Ximena Wortsman
Editor-in-Chief
Gregor B.E. Jemec
Co-Editor

Dermatologic Ultrasound with Clinical and Histologic Correlations

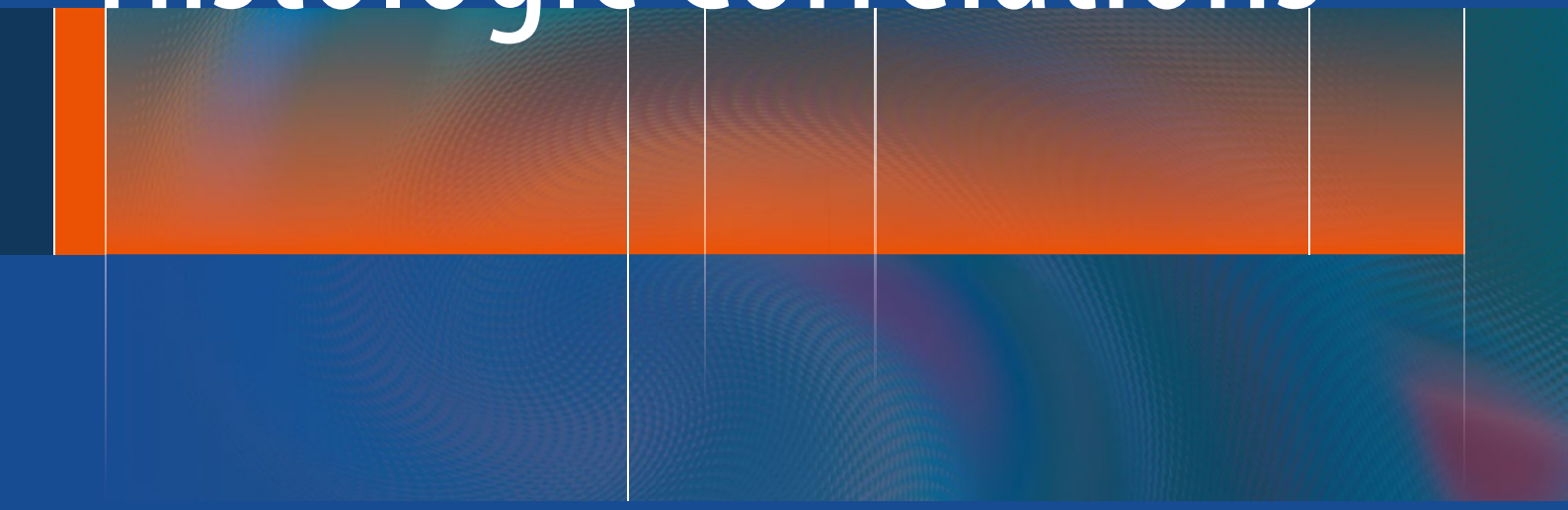

Springer

Dermatologic Ultrasound with Clinical and Histologic Correlations

Ximena Wortsman
Editor-in-Chief

Gregor B.E. Jemec
Co-Editor

Dermatologic Ultrasound with Clinical and Histologic Correlations

Springer

Editor-in-Chief
Ximena Wortsman, MD
Department of Radiology and Dermatology
Institute for Diagnostic Imaging
and Research of the Skin and Soft Tissues
Clinica Servet, Faculty of Medicine
University of Chile
Santiago
Chile

Co-Editor
Gregor B.E. Jemec, MD, DMSci
Department of Dermatology
Roskilde Hospital
Health Sciences Faculty
University of Copenhagen
Roskilde
Denmark

ISBN 978-1-4614-7183-7 ISBN 978-1-4614-7184-4 (eBook)
DOI 10.1007/978-1-4614-7184-4
Springer New York Heidelberg Dordrecht London

Library of Congress Control Number: 2013941862

Printed on acid-free paper

Springer is part of Springer Science+Business Media (www.springer.com)

To Gloria, Isaias, Benjamin, Camila, Claudio, and Marcelo for their continued support, encouragement, and love.

Ximena

Foreword

It is my great honor to write the foreword for *Dermatologic Ultrasound with Clinical and Histologic Correlations*. The editors and contributors of this book are some of the world's experts in the field of superficial ultrasound imaging, and they have created an exceptional book. High frequency ultrasound can depict pathologies of the skin and subcutaneous tissues with exquisite detail. Ultrasound has become an important tool in the evaluation of dermatologic conditions, but in order for the field to continue growing, there is a need for education among sonographers and ultrasound physicians. This book fills this important educational niche, and I predict that it will be an indispensable resource to ultrasound practitioners throughout the world.

Levon Nazarian, MD
Department of Radiology
Thomas Jefferson University Hospital
Philadelphia, PA
USA

Preface

Dermatologic Ultrasound with Clinical and Histologic Correlations is a compendium of experience over the past 10 years in the field of dermatologic ultrasound. During this time, significant technological advances have produced equipment that allows imaging of the skin with variable frequency ultrasound in hitherto unseen detail and provides a range of dynamic data that are currently unmatched by any other technology. The main purpose of this book is to serve as the starting point for anyone interested in this challenging area and to provide a practical approach to dealing with common dermatologic entities.

The material presented here is the result of the classic correlation of the clinical dermatologic lesions with the sonography and histologic findings. We believe that this type of correlation between different presentations of biological data can improve the understanding of not only of the ultrasound information but also of the physiopathology of dermatologic disorders. The cases featured in this book were carefully selected to represent a wide spectrum of diseases. In addition, clinical overviews, tips, and pitfalls are provided for a better understanding of both the pathologies and the methodological approach.

The book is organized in three main sections. The first section presents an introductory review of the technical considerations relating to color Doppler ultrasound of the skin and the normal anatomy of the skin, appendages, and adjacent structures. The second section highlights the wide range of dermatologic and pseudo-dermatologic diseases that may be approached with ultrasound imaging. The final section includes a glossary of dermatologic terms, dermatologic classifications, suggested protocols for dealing with common dermatologic conditions, and pre-surgical sonography assessment of skin lesion margins.

Dermatologic ultrasound requires simultaneous knowledge of both dermatology and sonography, both of which are challenging worlds. Nevertheless, when the concepts are mastered and the mutual exchange of information occurs, the utility is such that an increasing demand occurs for ultrasound imaging. Thus, we are convinced that this imaging tool can make a significant change in the quality of dermatologic management in daily practice and provide a wide open door to sonography. We hope that this book will encourage you and your team to develop this exciting imaging tool further.

Santiago, Chile — Ximena Wortsman, MD
Roskilde, Denmark — Gregor B.E. Jemec, MD, DMSci

Acknowledgments

Special thanks to:

To the team of contributors of this book who have enriched the material with their experience and work.

To the Department of Dermatology, Hospital Clinico U. Chile, Faculty of Medicine, University of Chile, for their continued support and provision of encouragement and challenge for developing this imaging field.

To Mrs. Adelina Varela, who has greatly supported the gathering of the data.

Contents

Contributors

Fernando Alfageme, MD, PhD Department of Dermatology, Hospital Puerta de Hierro Majadahonda, Universidad Autonoma de Madrid, Madrid, Spain

Ligia Aranibar, MD Department of Dermatology, Hospital Clínico Universidad de Chile, Faculty of Medicine, University of Chile, Santiago, Chile

Patricio Azocar, MD Department of Radiology, Hospital del Trabajador, Santiago, Chile

Robert Baran, MD Nail Diseases Center, Cannes, France

Department of Dermatology, Gustave Roussy Cancer Institute, Villejuif, France

Robert L. Bard, MD Department of Radiology, New York Medical College, New York, NY, USA

Marcio Bouer, MD Research Unit, Department of Radiology, University of São Paulo Medical School, São Paulo, São Paulo, Brazil

Department of Radiology, Fleury Laboratory, São Paulo, São Paulo, Brazil

Instituto de Radiologia, Hospital das Clínicas Da Universidade de São Paulo, São Paulo, São Paulo, Brazil

Jose Antonio Bouffard, MD Department of Orthopaedic Surgery and Sports Medicine, Sports Medicine Ultrasound, Detroit Medical Center, Sports Medicine Institute, Detroit, MI, USA

Perla E. Calderon, MD Department of Dermatology, Hospital Clínico Universidad de Chile, Faculty of Medicine, University of Chile, Santiago, Chile

Laura Carreño, MD Department of Pathology, Dermopathology Section, Hospital Clinico Universidad de Chile, Faculty of Medicine, University of Chile, Santiago, Chile

Orlando Catalano, MD First Department of Radiology, National Cancer Institute "Fondazione G. Pascale", Naples, Italy

Chih-Yen Chen, PhD Division of Applied Optics, Instrument Technology Research Center, National Applied Research Laboratories, Hsinchu, Taiwan

Huihua Kenny Chiang, PhD Institute of Biomedical Engineering, and Institute of Biophotonics Engineering, National Yang-Ming University, Beitou District, Taipei, Taiwan

Hong-Jen Chiou, MD Division of Musculoskeletal Radiology, Taipei Veterans General Hospital and School of Medicine, National Yang-Ming University, Taipei, Taiwan

Yi-Hong Chou, MD Division of Ultrasound and Breast Imaging, Taipei Veterans General Hospital and School of Medicine, National Yang-Ming University, Taipei, Taiwan

Maria Francisca Daza, MD Department of Dermatology, Clinica Alemana de Santiago, Santiago, Chile

Diana Gaitini, MD Unit of Ultrasound, Department of Medical Imaging, Rambam Health Care Campus, Haifa, Israel

Ruth and Bruce Rappaport, Faculty of Medicine, Technion – Israel Institute of Technology, Haifa, Israel

Gregor B.E. Jemec, MD, DMSci Department of Dermatology, Health Sciences Faculty, Roskilde Hospital, University of Copenhagen, Roskilde, Denmark

Claudia Morales, MD Department of Pathology, Dermopathology Section, Hospital Clinico Universidad de Chile, Faculty of Medicine, University of Chile, Santiago, Chile

Siegfried Peer, MD, PhD Department of Radiology, CTI GesmbH Innsbruck, Innsbruck, Tirol, Austria

Ivo Sazunic, MD Dermopathology Section, Faculty of Medicine, Histodiagnostico Malaga, University of Chile, Santiago, Chile

Fernando A. Valenzuela, MD Department of Dermatology, Hospital Clínico Universidad de Chile, Faculty of Medicine, University of Chile, Santiago, Chile

Christiane Voit, MD, PhD Department of Dermatology, Skin Cancer Center, Charité – University Medicine Berlin, Berlin, Germany

Jacobo Wortsman, MD Department of Medicine, Southern Illinois University School of Medicine, Springfield, IL, USA

Ximena Wortsman, MD Department of Radiology and Dermatology, Institute for Diagnostic Imaging and Research of the Skin and Soft Tissues, Clinica Servet, Faculty of Medicine, University of Chile, Santiago, Chile

Part I

The Requisites

Introduction to Color Doppler Ultrasound of the Skin

1

Diana Gaitini

A comprehensive review of the basics of ultrasound focused on the requisites for skin, nail and scalp examinations

Contents

1.1 Introduction

Ultrasound has become a unique medical imaging tool in the investigation of dermatological diseases. By providing high-resolution gray scale images and blood flow information in real time, ultrasound can provide detailed anatomic and physiologic data of skin lesions and deeper soft-tissue changes. Lesion size in three dimensions-lengths, width and depth, morphology, inner structure -solid, cystic or mixed, homogeneous or inhomogeneous, foci of calcifications or necrosis, location, and extension can be diagnosed. By defining vascularity in real time, color and spectral Doppler ultrasound have been proven useful in the study of localized lesions of the skin. Interventional procedures such as tumor biopsy, collection drainage, foreign body removement, and needle localization of lesions can safely be performed under ultrasound guidance. The detailed anatomic information provided by sonography is useful in planning surgery. Magnetic resonance imaging (MRI) is frequently recommended for preoperative assessment although it requires the use of intravenous contrast media and can be less efficient in detecting tumors <3 mm in diameter. Ultrasound is a non-invasive and non-radiating test and as so, follow-up examinations can be performed without potential radiation damage. Finally, operator skills and knowledge of the clinical setting and the question being asked are important in ultrasound success.

1.2 Technical Considerations

Modern digital ultrasound systems utilize *transducers* with a broad range of frequencies (broad bandwidth) [1]. High variable-frequency ultrasound (HVFUS) ranging from 6 to 18 MHz with a Doppler frequency ranging from 7 to 4 MHz is a recently available technique capable of clearly defining skin layers and deeper structures as well as vascularization patterns in real time (Fig. 1.1). With a wide array of frequency availability and adjustable focus, echo sources at different depths can be accurately pinpointed. Small footprint light-weight

D. Gaitini, MD
Unit of Ultrasound, Department of Medical Imaging,
Rambam Health Care Campus,
Ha'alya Ha'shnia 8, Haifa 31096, Israel

Ruth and Bruce Rappaport Faculty of Medicine,
Technion – Israel Institute of Technology, Haifa, Israel
e-mail: d_gaitini@rambam.health.gov.il

X. Wortsman, G.B.E. Jemec (eds.), *Dermatologic Ultrasound with Clinical and Histologic Correlations*,
DOI 10.1007/978-1-4614-7184-4_1,

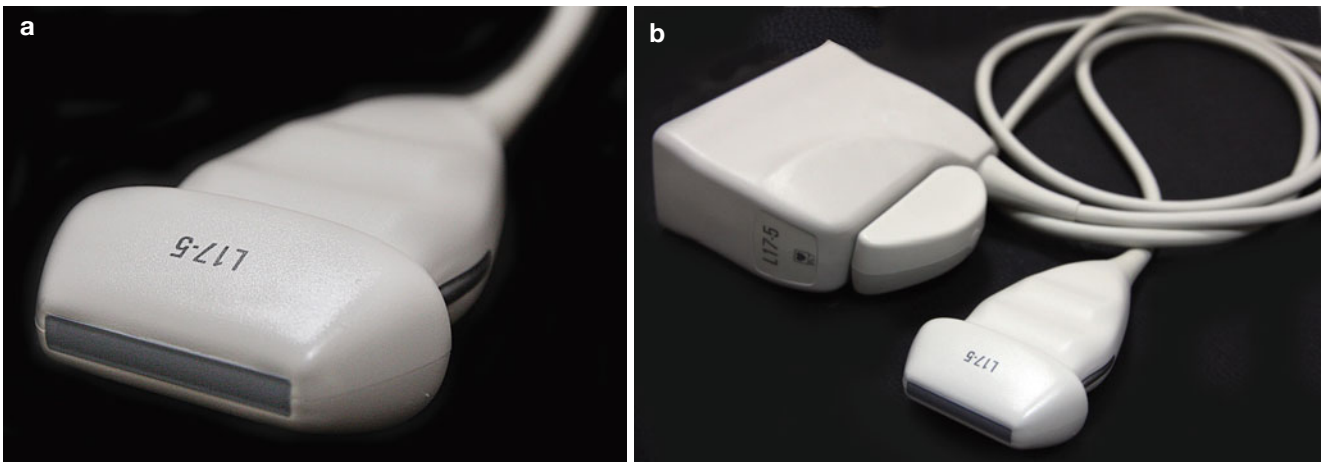

Fig. 1.1 HVFUS linear array transducer. (**a**, **b**) High-resolution (5.0–17.0 MHz) transducers are used for superficial applications: small parts, breast, superficial vascular, and musculoskeletal including skin

Fig. 1.2 HVFUS linear array "hockey stick" transducer. Versatile multi-frequency (up to 15 Mhz) compact 'hockey stick'-shape transducer, with a high Doppler and color flow sensitivity. The hockey stick-shape allows complete contact with the skin surface, reducing scattering artifacts, making it a good choice for superficial and vascular imaging

7–15 MHz linear array probes of compact "hockey stick" shape (Fig. 1.2) allow complete contact with the skin surface, reducing scattering *artifacts*. Hockey stick probes allow better access to mobile structures such as the tongue, or small appendixes such as children's fingers. Fixed (nonvariable) high-frequency ultrasound transducers are activated at a single high operating frequency (20–100 MHz) that determines both *resolution* and the depth of penetration (6–7 mm at 20 MHz; 3 mm at 75 MHz). Most lesions examined in skin ultrasound involve subepidermal structures that would be out of reach for devices of low penetrating power. Furthermore, images produced by fixed high-frequency ultrasound transducers are more pixeled. Deep subcutaneous tissues are not shown and real-time data on blood flow and vascular pattern are lacking [2–5]. In vivo confocal laser microscopy, another imaging technique, has a low penetration of only 0.5 mm, which limits its applicability to lesions of epidermis and papillary dermis [6]. Other imaging techniques such as MRI or positron emission tomography/computed tomography (PET-CT) have limited spatial resolution allowing definition of skin lesions only when greater than 5 mm. MRI and PET-CT require an intravenously administered contrast medium, are more expensive, and less available [7]. In comparison, HVFUS can define lesions in the submillimeter range (down to 0.1 mm). It can reach depths of 60 mm using a single probe with combinations of variable frequencies (7–15 MHz). Ultrasound using frequencies of 15 MHz or higher can clearly define skin layers morphology including changes in epidermal thickness. Although in its current version, ultrasound cannot detect lesions that are epidermal only or that measure less than 0.1 mm in depth. Adjustments of focus at a selected depth and selection of the transmission frequency provide a complete view of the skin and the deeper structures (muscles, tendons, and bone margins), with minimal dispersion of the sound energy waves. Frequencies in the upper range (14–15 MHz) are used for skin layer demonstrations and frequencies in the lower range (7–13 MHz) for the deeper tissues. The resulting composite imaging therefore integrates the effects of frequency-specific tissue reflectance

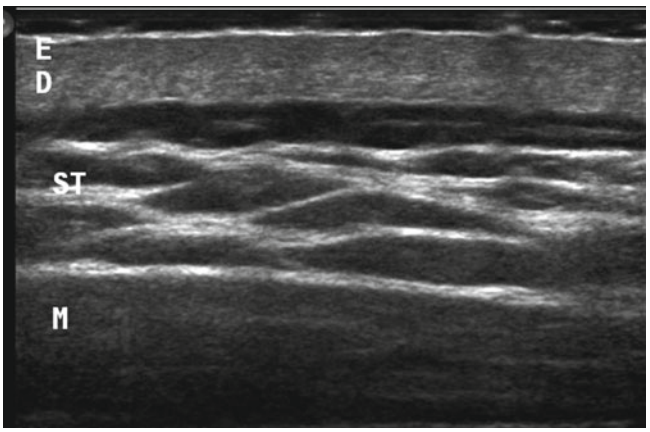

Fig. 1.3 HVFUS image of skin layers and deeper structures. Adjustments of focus at a selected depth and selection of the transmission frequency provide a complete view of the skin and the deeper structures Frequencies in the upper range (14–15 MHz) are used for skin layers and frequencies in the lower range (7–13 MHz) for the deeper tissues demonstration. *E* epidermis, *D* dermis, *ST* subcutaneous tissue, *M* muscle

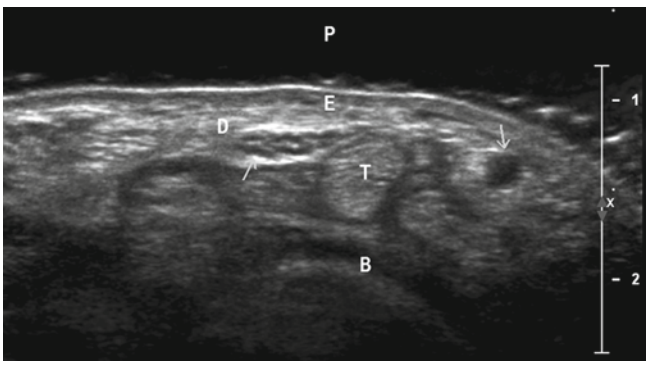

Fig. 1.4 HVFUS image of superficial structures. Axial scan at the level of the wrist. Variable frequency gives the best balance among spatial resolution and depth (2 cm penetration in this scan), generating good quality images of the skin (*E* epidermis, *D* dermis), tendons (*T*), and bone (*B*). Subcutaneous venous and arterial blood vessels appear as echofree ducts (*upper arrow*, ulnar artery). Nerves are seen as small hypoechoic dots surrounded by hyperechogenic tissue (*lower arrow*, median nerve). A gel pad (*P*) was interposed between the transducer and the skin, to reduce near field artifacts

and full-field automatic scanning. The images produced are sharp, obtained in real time, and provide quantitative estimation of blood flow. Thus, of all the imaging techniques available, HVFUS gives the best balance among spatial resolution, depth, and costs generating good quality images of all skin layers, muscles, tendons, and nerves (Fig. 1.3). Ultrasound examination is largely operator dependent – the quality of the obtained information depends mostly on the skill and experience of the examiner. Optimal adjustments of the technical settings are needed in every ultrasound scan. A good amount of gel over the skin is recommended to avoid artifacts from near field (Fig. 1.4). The operator should avoid pressing with the transducer because that may result in disappearing or false thinning of lesions.

Modern equipment software includes capabilities for *harmonic* imaging, *compound* image, extended field of view (EFOV), and *3-D ultrasound*. Tissue harmonic imaging reduces imaging artifacts caused by the interaction of the ultrasound beam with superficial structures or from aberrations at the edges of the beam profile. The artifact-producing signals are of low energy, insufficient to generate harmonic frequencies. Images generated exhibit reduced noise and improved spatial resolution (Fig. 1.5). Spatial compounding improves significant the contrast-to-noise ratio by reducing artifacts generated by the scattering of ultrasound from small tissue reflectors (speckle) [8] (Fig. 1.6). Extended EFOV allows acquisition and display of a panoramic image offering the possibility of viewing topographic anatomic structures with no loss in resolution [9] (Figs. 1.7 and 1.8). Three-dimensional (3D) imaging permits volume data to be displayed in multiple planes and allows accurate measurement of lesion volume.

High-resolution ultrasound imaging of normal skin shows a clear separation of skin layers [10]. The epidermis is seen as a thin *hyperechoic* line. In the palmar and plantar areas, the epidermis is thicker and bilaminar. The dermis is seen as a hyperechoic band of variable thickness, thin in the forearm and thicker in the lumbar region because of its high collagen content. The subcutaneous tissue is *hypoechoic*, generated by fat lobules, which are surrounded by hyperechoic fibrous septa. Subcutaneous venous and arterial blood vessels appear as thin *echo free* ducts. The bone margin appears as a distinct hyperechoic line (Fig. 1.9). The nail plates appear as two hyperechoic parallel lines. The nail bed and the matrix zone are hypoechoic – the matrix is slightly more hypoechoic than the proximal nail bed – contrasting with the hyperechogenicity of the overlying dermis (Fig. 1.10). On the ultrasound examination of healthy individuals, the epidermis shows a laminar hyperechoic appearance provided by the higher amount of keratin in this layer, and a mean epidermal thickness of 0.6 mm (SD 0.8–0.1 mm); normal plantar dermis appears as a hyperechoic band resulting from the higher presence of collagen, with a mean thickness of 1.1 mm. The subcutaneous tissue is a hypoechoic structure provided by fat lobules separated by hyperechoic fibrous septa. Blood flow is predominantly produced by thin (<1 mm) and easily compressible venous vessels in the subcutaneous tissue. No significant arterial vessels in the dermis are detected in healthy subjects.

The ability of sonography to show and characterize even minimal morphostructure was enhanced by the development of Doppler sonography [1]. Doppler ultrasound allows blood flow detection and definition of flow direction, characteristics, and velocity. The reflected ultrasound from a stationary target has the same frequency as the transmitted sound. Oppositely, the reflected sound from a moving target has a different frequency from the transmitted sound. The *Doppler effect* reflects the change in frequency and is directly propor-

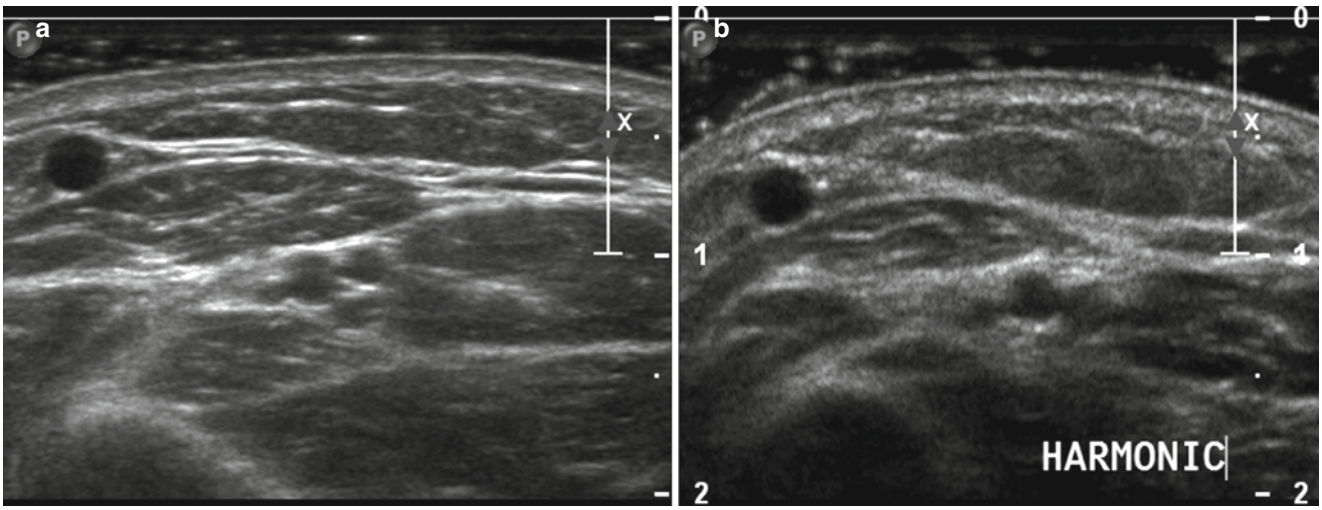

Fig. 1.5 (a,b) Harmonic tissue imaging. Split image at the same anatomic area (**a**) Compound scan. (**b**) Harmonic imaging. Harmonic imaging reduces near-field artifacts, caused by the interaction of the ultrasound beam with superficial structures. The generated images exhibit reduced noise and improved spatial resolution

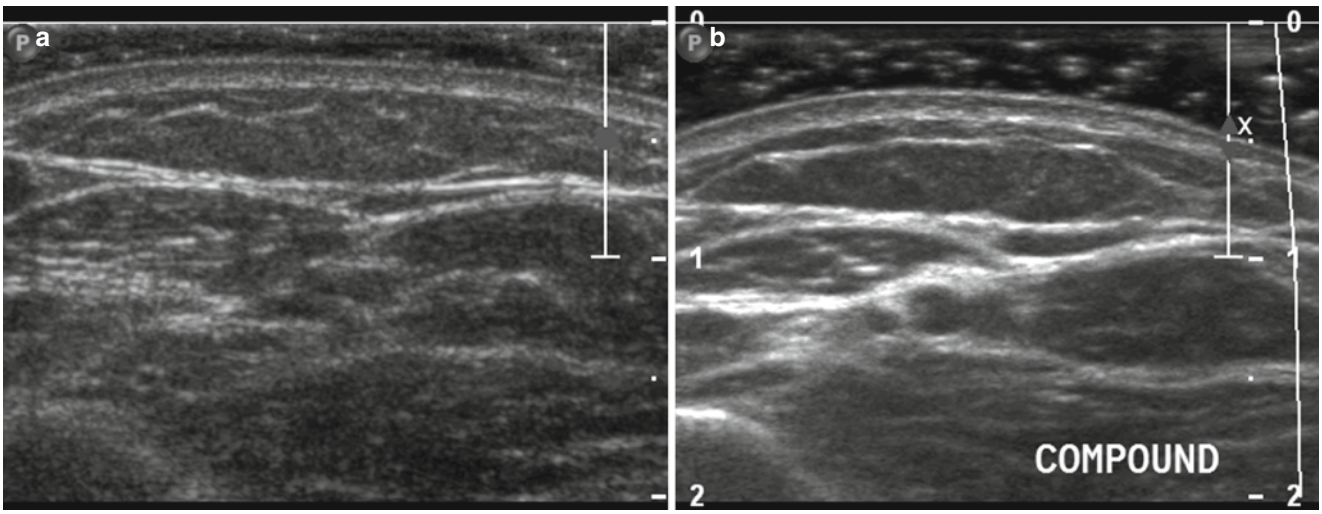

Fig. 1.6 (a, b) Spatial compounding imaging. Split image at the same anatomic area (**a**) Fundamental scan. (**b**) Compounding imaging. Compound significantly improves contrast-to-noise ratio by reducing artifacts generated by the scattering of ultrasound from small tissue reflectors (speckle)

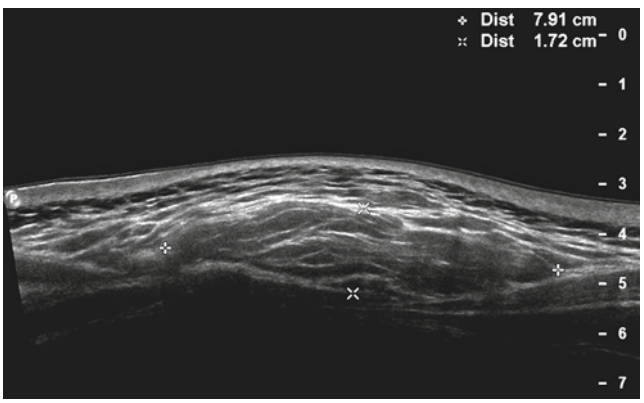

Fig. 1.7 Extended field of view (EFOV) imaging. EFOV−also termed panoramic view (*P* in left image corner)−allows acquisition and display of a panoramic image of large structures and the topographic anatomic relationships with the surrounding tissues, with no loss in resolution. In this case, an oval lesion in the subcutaneous tissue is seen, measuring 7.9 cm in length, compatible with a subcutaneous lipoma

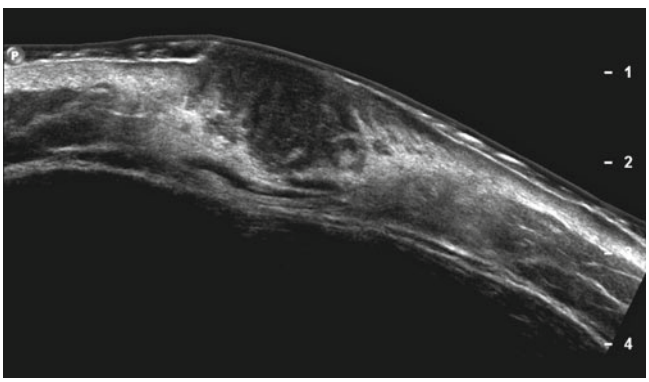

Fig. 1.8 Panoramic (EFOV) view. A malignant skin lesion (dermatofibrosarcoma) is presented. The tumor is hypoechogenic and poorly delimitated. Panoramic imaging shows lesion extension into the epidermis, dermis, and subcutaneous fat tissue

tional to the velocity of the moving target. Accurate estimation of target velocity requires precise measurement of the Doppler frequency shift and angle of insonation of the target in movement. Doppler measurements must be made at less than or equal to 60° the angle of insonation. Because the cosine of the angle changes rapidly for larger angles, and at an angle of 90° there is no relative movement of the target toward or away from the transducer, therefore no Doppler shift is detected. As Doppler frequency shifts fall in the audible range, the heard signal may provide information about flow characteristics. Doppler shifts can be displayed in graphic forms (Doppler frequency spectrum) and in color (color flow and power mode Doppler) (Fig. 1.11). The Doppler frequency spectrum shows changes in flow velocity and direction by vertical deflections of the waveform above and below the baseline. Doppler parameters such as maximum systolic, minimum diastolic, and mean blood flow velocity and the *pulsatility and the resistive indices* can be calculated (Fig. 1.12). Color flow imaging displays flowing blood in a color map, superimposed on the gray-scale image in real time. Color flow is able to provide flow direction (red towards the transducer, blue away from the transducer) and relative velocity information (lighter hues corresponding to higher velocities). Power mode uses a single color map to display the power or amplitude of the Doppler signals. Power mode has increased sensitivity for flow detection, but lacks information on flow direction and flow velocity. Low velocity flow and poorly vascularized lesions in the skin are better displayed by power Doppler. Color Doppler provides better information in higher flow velocity and hypervascular lesions, demonstrating flow direction and relative velocities. On color Doppler mode, color artifacts may be reduced to a minimum by optimizing the color Doppler amplification, degrading it until only pulsating color pixels are left. Absence of intralesion vessels may be proved by increasing Doppler amplification until many colored artifacts are seen around the lesion. Spectral Doppler display allows differentiation between venous and arterial flow. Flow velocity measurements and flow characteristics may be obtained (Fig. 1.13). Combining gray scale ultrasound with Doppler ultrasound, accurate definition of skin lesions features may be obtained, including internal echogenicity, size, shape, margins, skin layers involvement and blood flow (Fig. 1.14). Sonography may be useful to differentiate between inflammation, vascular lesions, and tumors. Increased dermal thickness (mean ± SD, 3.3 ± 1.0 mm vs. 1.4 ± 0.3 mm for normal individuals) allowed identifying subclinical lesions and the extension of lesions into clinically normal looking skin. Modern high-resolution equipments using high-frequency probes and a very sensitive power Doppler technique allows a clear definition of the cutaneous and muscular layers, as well as vascularity of skin and

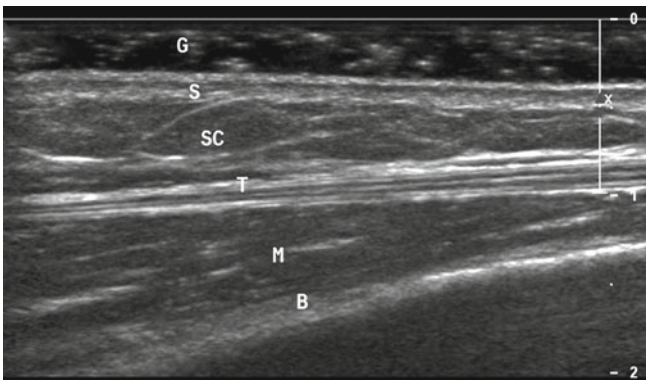

Fig. 1.9 High-resolution ultrasound image of normal skin and deeper structures. Longitudinal scan at the level of the forearm. A clear separation of skin layers (*S*) is shown. The epidermis is seen as a thin hyperechoic line. The dermis is seen as a hyperechoic band of variable thickness, thin in the forearm and thicker in the lumbar region because of a high collagen content. The subcutaneous tissue (*SC*) is hypoechoic, generated by fat lobules, which are surrounded by hyperechoic fibrous septa. Tendons (*T*) are hyperechogenic with parallel hypoechogenic lines. Muscles (*M*) are hypoechogenic, with parallel echogenic lines. The bone margin (*B*) appears as a distinct hyperechoic line. The focus is adjusted at the superficial level (*vertical line* on the right side of the image), to allow better definition of the skin. A good amount of gel (*G*) over the skin is recommended in order to avoid near-field artifacts

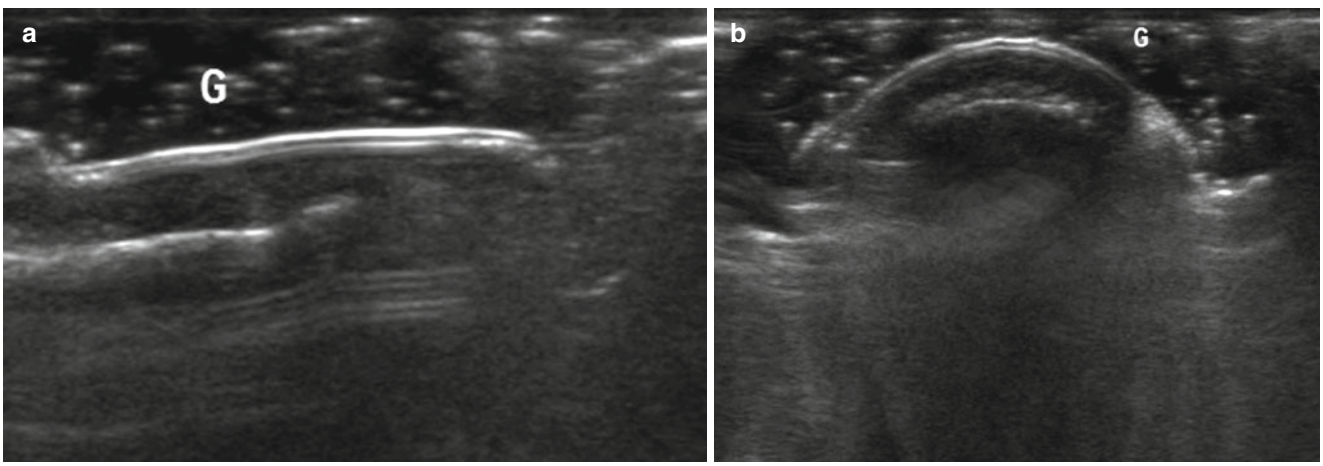

Fig. 1.10 High resolution US of the nail. (**a**) Longitudinal view. (**b**) Transverse view. The nail plates appear as two hyperechoic parallel lines. The nail bed and the matrix zone below the plates are hypoechoic. *G* gel spread over the nail

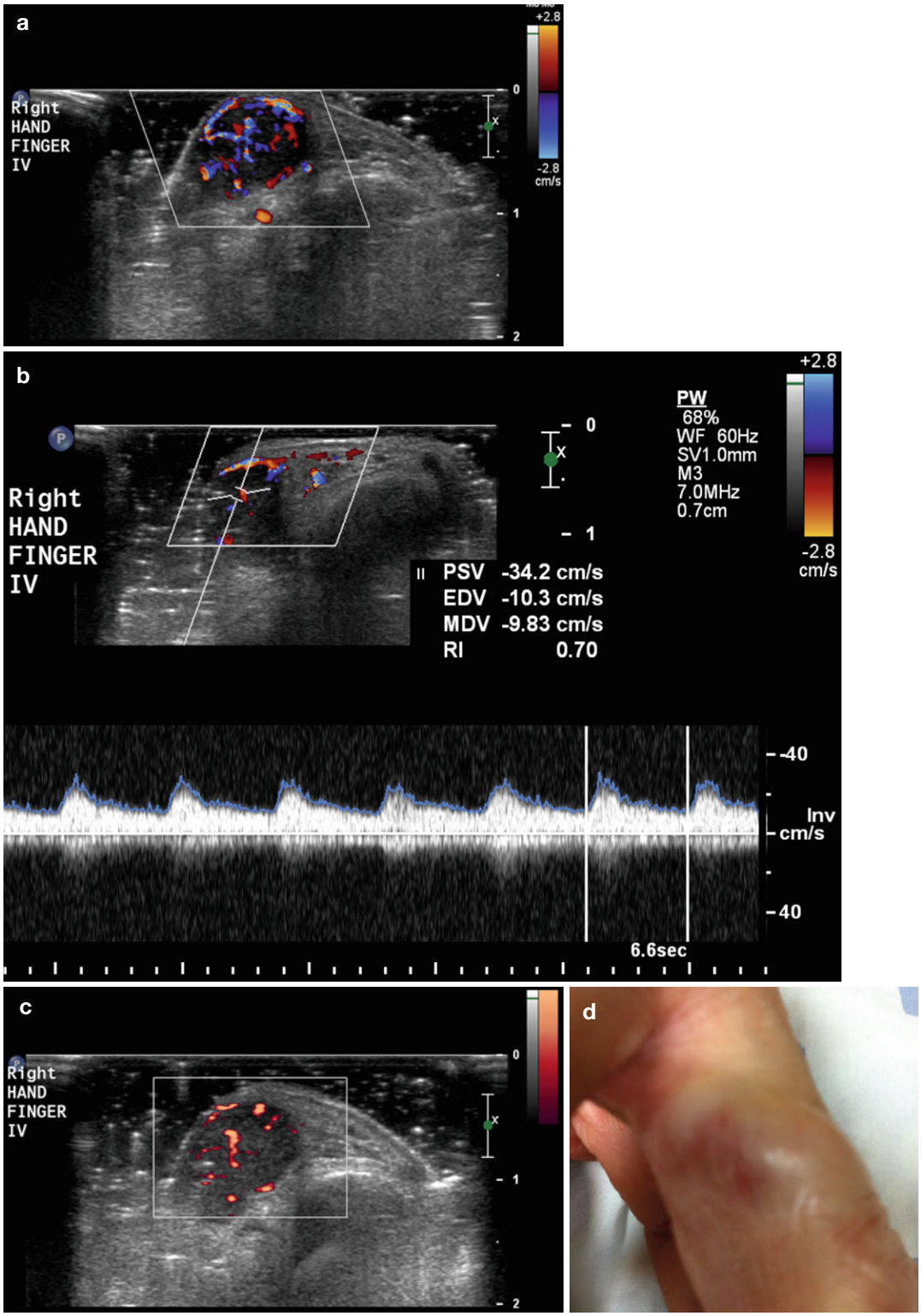

Fig. 1.11 Flow information provided by Doppler sonography. (**a**) Color Doppler flow. A rich vascularized lesion at the base of the right fourth hand finger, compatible with a vascular malformation is shown. Flowing blood is displayed in a color map, superimposed on the gray-scale image in real time. Flow direction: *red* toward the transducer and *blue* away from the transducer (see the *color bar* shown on the right side of the image), and relative velocity information (*lighter hues* corresponding to higher velocities) are provided. (**b**) Doppler frequency spectrum. Changes in flow velocity and flow direction are shown by vertical deflections of the waveform above the baseline. Doppler parameters are calculated: *PSV* (peak systolic velocity):34.2 cm/s; *EDV* (end diastolic velocity): 10.3 cm/s; *MDV* (mean blood flow velocity): 9.8 cm/s and *RI* (resistive index):0.70. (**c**) Power Doppler mode. Power flow uses a single color map to display the amplitude of the Doppler signals. Increased sensitivity for flow detection at lower velocities is achieved, although it lacks information on flow direction and flow velocity. (**d**) Anatomic picture of the lesion. A skin lump with skin redness is shown at the proximal fourth finger phalanx

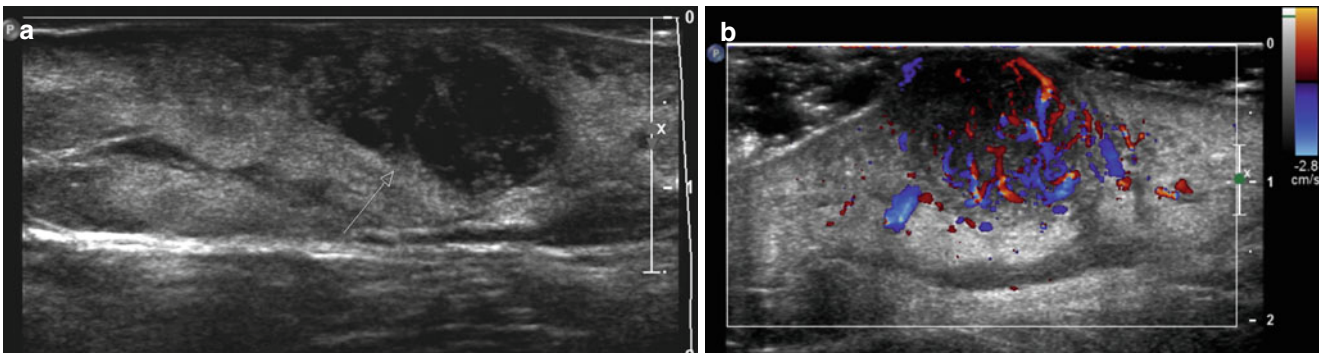

Fig. 1.12 Color Doppler sonography. Hypervascular lesion in the skin at the middle thigh, proved to be a dermatofibrosarcoma on histology. (**a**) On gray scale image, the tumor (*arrow*) is highly hypoechogenic and poorly delimitated. Hyperechogenic tissue surrounding the tumor represents edema in the subcutaneous fat. (**b**) Color Doppler shows a rich vascularity of the lesion

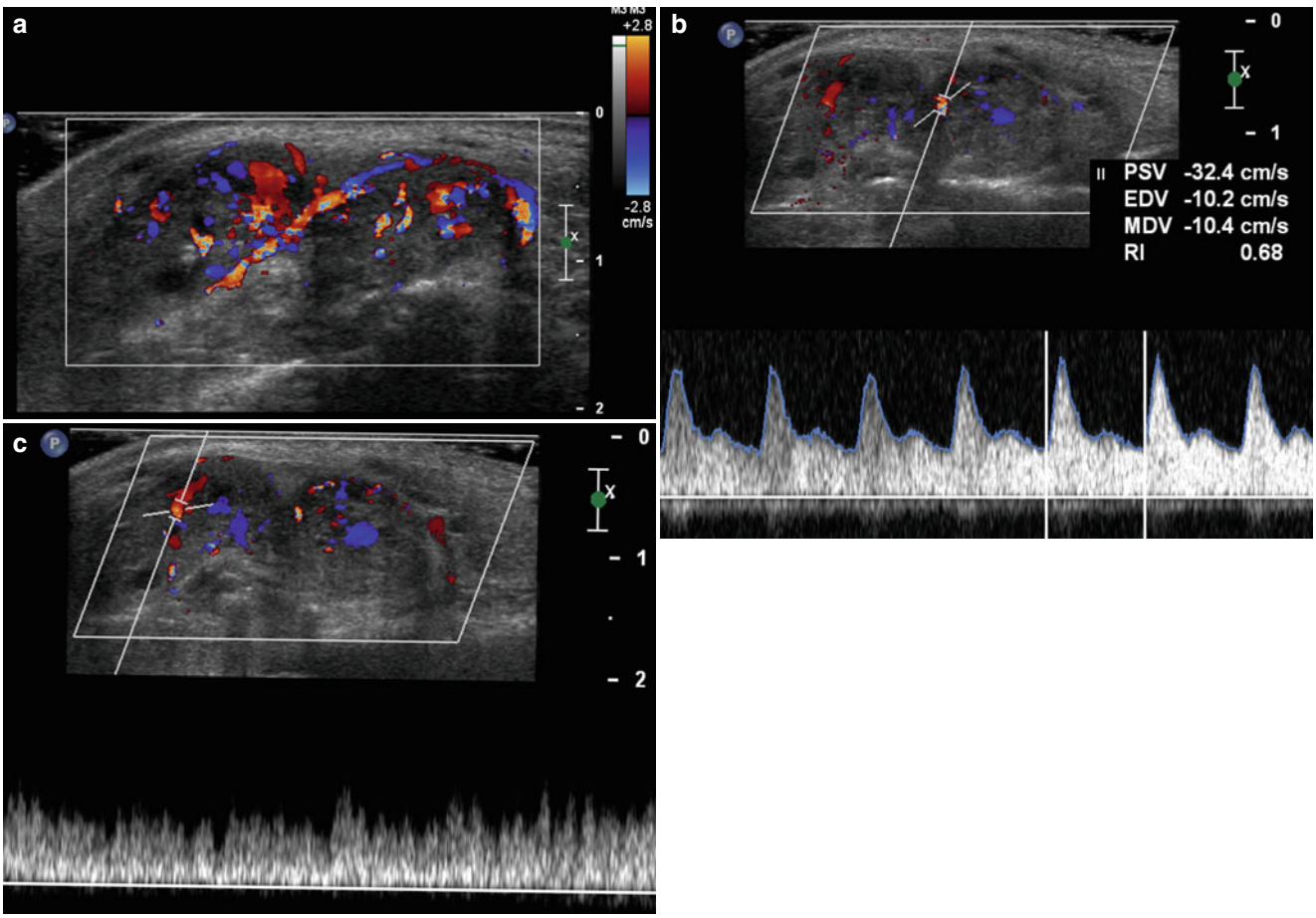

Fig. 1.13 Color and spectral Doppler sonography. A superficial hypervascular lesion at the dorsal left foot is shown. (**a**) Color Doppler display of vessels and flow direction. (**b**) Spectral Doppler display of arterial flow. Flow is displayed by placing the cursor (two parallel lines) into the vessel. Systolic, diastolic, and mean velocities are measured and resistive index calculated and displayed during one cardiac cycle (enclosed between the vertical lines on the spectral display, at the *bottom* of the image). (**c**) Spectral Doppler display of venous flow. Note that in this vein, flow direction is toward the transducer and as so, displayed in red and above the base line. Spectral Doppler allows differentiation between arterial and venous flow based on flow characteristics and flow velocities measurements

nail lesions. Wortsman et al. described glomus tumor of the nails evaluated with high-resolution color Doppler ultrasound using a compact linear probe 7–15 MHz in frequency [11]. The tumors appeared as hypoechoic nodules with high vascularity in the nail bed and remodeling of the underlying bone. Small tumors of 0.9 mm diameter could be identified and arterial flow was demonstrated in all tumors, with a varied peak systolic velocity, mean 11.3 ± 9.1 cm/s

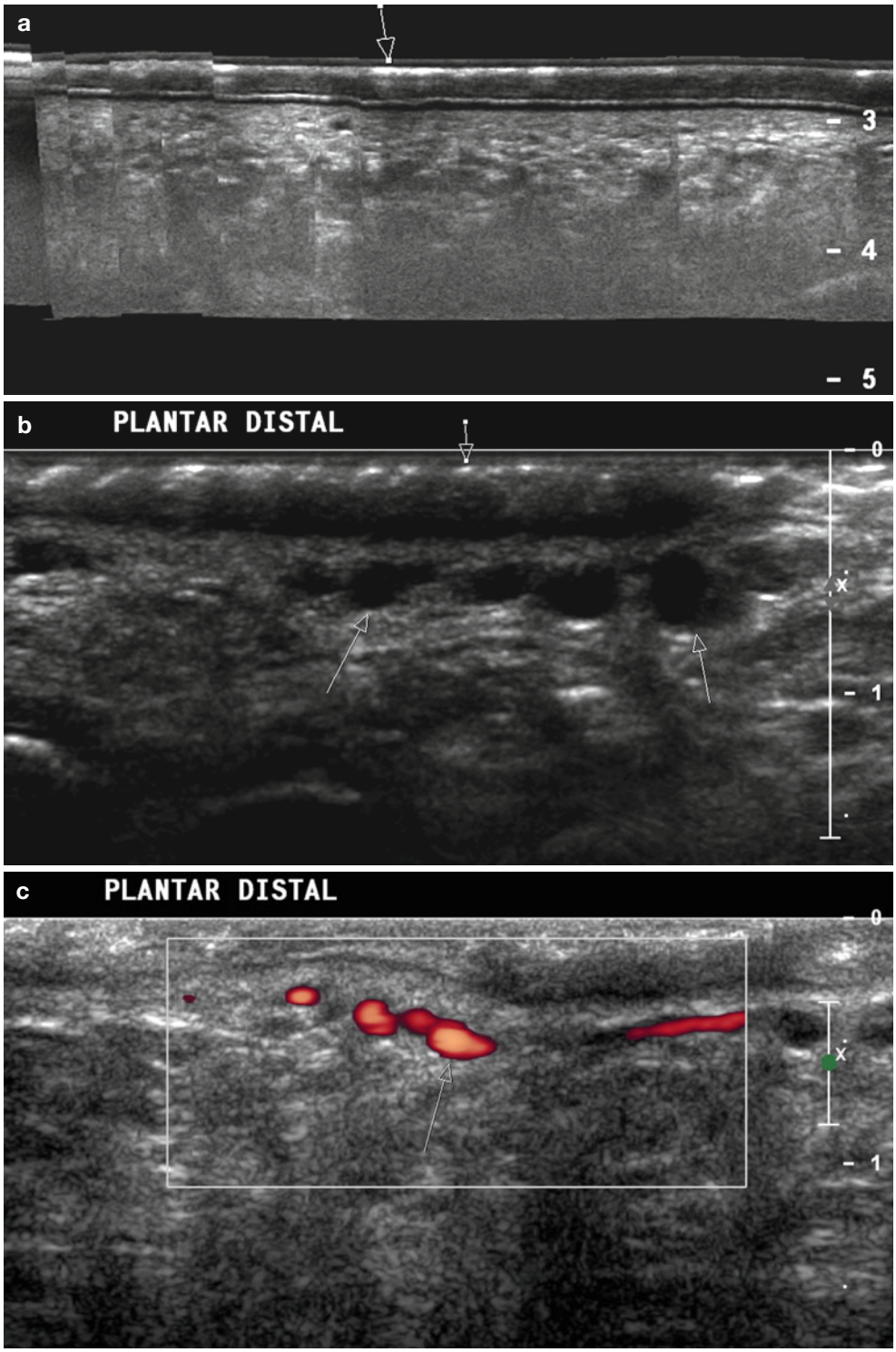

Fig. 1.14 Gray scale and color Doppler. Patient suffering from pachyonychia congenita, a rare autosomal dominant skin disorder characterized by hyperkeratosis on hands and feet. (**a**) Panoramic (EFOV) image performed over the blisters on the plantar foot. Hyperechoic (*white*) *dots* and *lines* are seen in the epidermis, representing hyperkeratosis (*arrow*). The anechoic layer interposed between the epidermis and the dermis is a result of water contained in the blisters. (**b**) Hyperechoic epidermis (*vertical short arrow*) and engorged varicose veins seen in the dermis as anechoic (*black*) dots (*oblique long arrows*). (**c**) Power Doppler sonography shows flow into the veins (*arrow*)

(range: 3.7–26.1 cm/s) Characteristic ultrasound pictures can be seen in psoriasis, cysts, vascular abnormalities, and other nail diseases [12]. Giovagnorio et al. described the ultrasound characteristics of 68 lesions suspicious of skin metastases [13]. Each nodule was classified by measurement of fundamental sonographic parameters- major diameter, shape, borders, echo texture, and homogeneity and by assessment of vascularity with color Doppler sonography - presence or absence of flow and vascular pattern. Of 68 nodules, 23 were malignant (21 metastases and 2 B-cell lymphomas), and 45 were benign (22 sebaceous cysts, 18 granulomas of different origins, 3 fibromas, and 2 neurofibromas). The nodules were localized in the subcutaneous space, had clearly demarcated borders, and were

hypoechoic. A circular or oval shape was predominant, but seven metastases had an irregular, polycyclic shape. On color Doppler sonography, none of the benign nodules or B-cell lymphomas showed signs of vascularity, whereas the metastatic nodules were all vascularized, with one or more peripheral poles (21 of 21 nodules) and internal vessels (11 of 21 nodules). A polycyclic shape and hypervascularity, with multiple peripheral poles and, eventually, internal vessels, should be considered the most indicative signs of metastasis. In a previous publication, 71 visible and palpable nodules of the skin and subcutaneous tissue were evaluated with color Doppler sonography [14]. The nodules were classified as avascular (type I), hypovascular with a single vascular pole (type II), hypervascular with multiple peripheral poles (type III), and hypervascular with internal vessels (type IV). Of the 32 malignant nodules, 9 % showed a type I pattern, 50 % had a type III pattern, and 41 % had a type IV pattern; of the 39 benign nodules, 86 % showed a type I pattern and 14 % had a type II pattern. The sensitivity and specificity of hypervascularity in malignant lesions were 90 and 100 % respectively; the sensitivity and specificity of hypovascularity in benign lesions were 100 and 90 % respectively. The authors conclude that color Doppler sonography is able to increase the specificity of ultrasonography in the evaluation of skin nodular lesions.

Benign tumors are associated with hyperemia and ectasia of the vessels but not with any appreciable formation of new vessels. It is well documented that many different kinds of malignant tumors are accompanied by angiogenesis. This vascularization is an important indicator of development and prognosis. The detection of Doppler signals is a simple, noninvasive method of analyzing this vascularization. Knowledge of the intratumoral vascularity can have an influence on the therapy, with regard to the extent of excision. Extensive vascularity in a primary tumor is probably an adverse prognostic factor for the possibility of early spread although, may be a good prognostic factor for chemotherapy treatment.

Hypervascularization is found both in inflammatory and malignant lesions at Doppler ultrasound examination of skin lesions, making difficult to differentiate between them. The introduction of *microbubble contrast injection for ultrasound* (*CEUS*) (Fig. 1.15) redefined the role of ultrasound in resolving vascular questions [15, 16]. CEUS can help delineate small vascular structures (0.1–0.3 mm in diameter) and enhance Doppler signals from low velocity small volumes of blood. Schroder et al. described the use of ultrasound contrast media for characterizing vascularization of benign and malignant skin tumors on enhanced color Doppler [15]. B-mode gray scale parameters such as tumor diameter, margins and echogenicity were evaluated. On color Doppler mode, rhythmically pulsating colored pixels corresponded to arterial vessels, which were confirmed by registering their Doppler spectrum. Afterwards, the mode was changed to the power Doppler mode without changing the technical settings. In most cases, the amplification had to be degraded to avoid confluence of the colored areas. Following conventional imaging, a signal-enhancing agent was intravenously injected. The main criterion of malignancy was the degree of the intratumoral vascularity as measured by the percentage vessel area (p.v.a.) of the lesions. The p.v.a. was defined as the ratio of colored intratumoral vessel areas to the other "gray" parts of the tumor. A significant difference was found between malignant and benign tumors ($p = 0.01$) with regard to the degree of vascularity. The mean p.v.a. of malignant tumors was 9.6 % before and 18.8 % on CEUS. The mean p.v.a. of benign tumors was 1.1 and 3.3 %, respectively. B-mode criteria - echogenicity, homogeneity, sharpness of the borders-and the calculated spectral Doppler values did not contribute to the differential diagnosis of the tumors. Analysis of tumor vascularity using the p.v.a. after injection of the signal enhancer was superior to B-mode, spectral Doppler ultrasound, and flow indices.

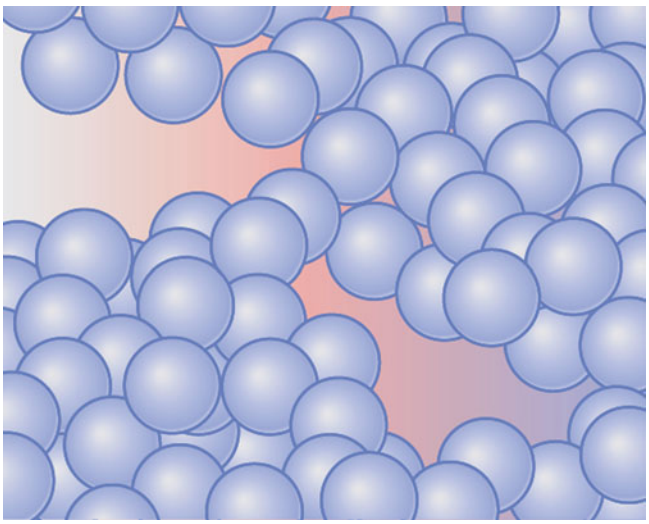

Fig. 1.15 Microbubbles for contrast enhancement in ultrasound imaging (*CEUS*). Encapsulated bubbles of gas, smaller than red blood cells. Intravascular agents capable of circulating freely (blood-pool agents), help delinate small vascular structures (0.1–0.3 mm in diameter) and enhance Doppler signals from low velocity small volumes of blood

Non-invasive preclinical imaging has evolved during the last decade for longitudinal studies of normal development and models of human disease in small animals [17]. High frequency 'micro-ultrasound' has steadily evolved in the post-genomic era. The upper limits of linear and phased arrays transducers have been pushed from about 20 to over 50 MHz enabling a broad range of new applications. Available imaging options are non- linear contrast agent imaging for relative vascularity and perfusion quantification (Fig. 1.16) and 3D imaging for anatomical and vascular

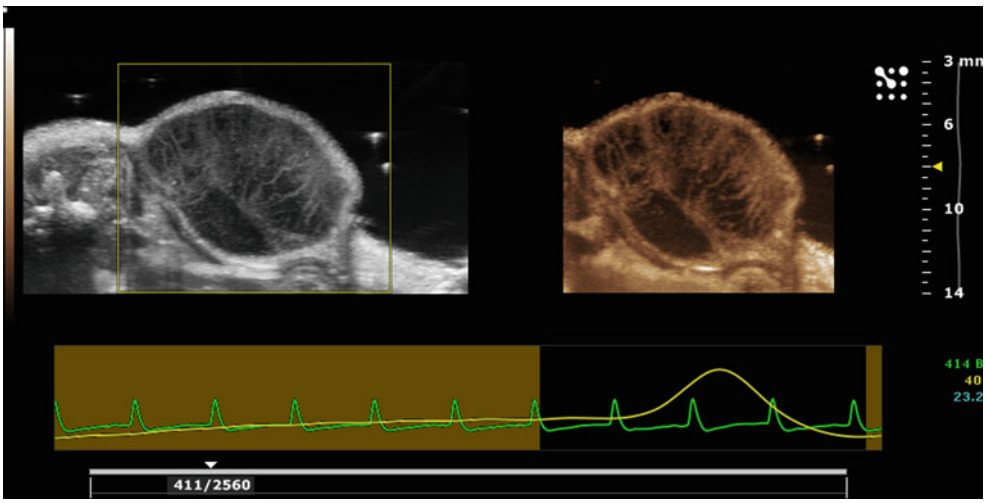

Fig. 1.16 Contrast enhancement in micro-ultrasound imaging. Tumor vascularization in a mouse tumor. Imaging is performed with a Vevo 2100 scanner using nonlinear contrast mode at 18 MHz. Wash-in of microbubble contrast agent (Vevo MicroMarker) following bolus injection in a tail vein. Ultrasound contrast agents are comprised of gas bubbles less than 5 μm in diameter encapsulated by a polymer or lipid shell. Signal acquisition is respiratory gated as shown in the image at the bottom of the picture. Tumor signals are suppressed by the nonlinear processing, leaving only the outline of the tumor. A branching pattern of vasculature is seen in the tumor, with a heterogeneous distribution

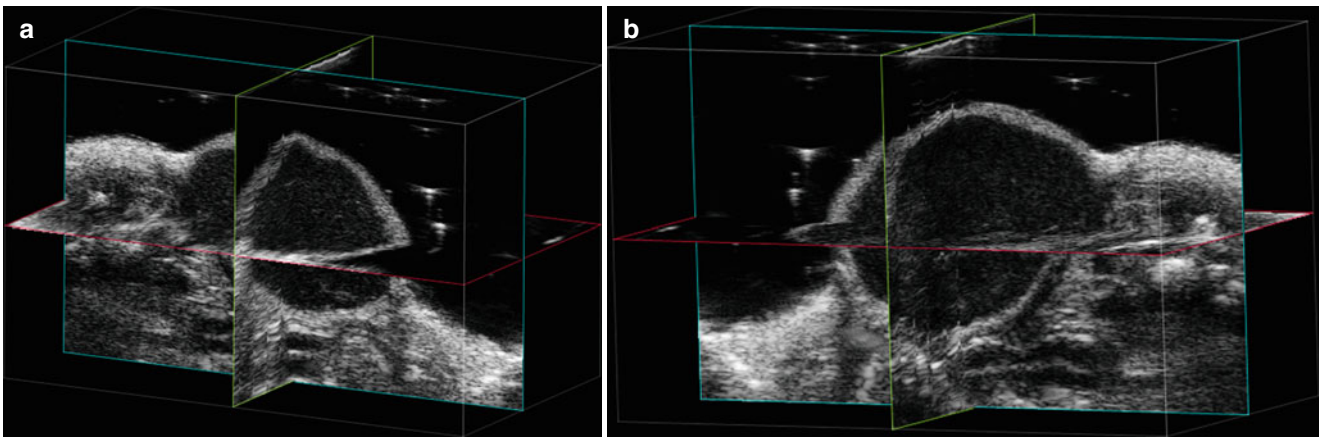

Fig. 1.17 3D-Mode imaging. (**a**, **b**) 3D images of a mouse tumor using a high frequency high resolution (30 μ resolution) linear array transducer (Vevo 2100 Imagin System. VisualSonics, Toronto). The intersecting planes can be displayed in arbitrary directions. Images can also be displayed as separate planes. 3D imaging combined with either B-Mode, Power Doppler Mode, or Nonlinear Contrast Imaging allows for quantification of volume and vascularity within a defined anatomical structure

visualization-when combined with power Doppler or contrast imaging- and volume and vascularity quantification (Fig. 1.17). Micro-ultrasound is playing an increasing role in preclinical studies and efforts are already underway to use the technology in clinical applications such as prostate, neonatal, ocular and skin imaging [18].

Tips and Teaching Points

1. High variable-frequency ultrasound transducers (HVFUS) 6–18 MHz with Doppler capability clearly define skin layers and deeper structures, and may show vascularization patterns and flow velocity.
2. Higher frequency transducers allow better resolution (as low as 0.1 mm), although the penetration depth decreases (6 mm depth at 20 MHz).
3. Power Doppler is more sensitive for low velocity flow, an thus better for poorly vascularized or low velocity flow lesions in the skin. No information on flow direction or flow velocity is provided.
4. Ultrasound examination is largely operator-dependent. It is advised to apply a large amount of gel over the skin and avoid compression with the transducer. Optimal adjustment of B-mode and Doppler technical settings must be made while performing US scans.

Conclusion

High-resolution gray scale sonography with color and spectral Doppler is a real-time noninvasive imaging technique that can be used as an adjunct to the clinical evaluation of skin and nail lesions. Superficial foreign bodies and hair fragments are easily identified. The procedure does not require administration of intravenous contrast media and provides good information about lesion characteristics and blood flow as well as surrounding structure invasion. Preoperative imaging aids in surgical planning by identifying the anatomical location and extent of a neoplasm and the presence of subclinical satellite lesions. Layers of involvement and vascularity patterns can be recognized in a non-invasive way. Measurements in ultrasound images have a good correlation with pathology. Sonographic monitoring of disease changes following medical treatment allows an objective verification of results and adjustment of treatment if necessary. Ultrasound may have a role in the evaluation of surgical treatment of skin lesions, allowing monitoring of therapeutic response, especially in suspicion of recurrence and in cases with persistent pain. Micro-ultrasound evolved in the last decade as a useful technique for preclinical studies and efforts are already under way for using it in clinical applications such as skin imaging.

Ultrasound is widely available and non-invasive and may therefore be used for longitudinal studies of skin lesions.

There are few limitations of the ultrasound technique, related mostly to its lack of sensitivity in detecting lesions localized to the epidermis or extremely thin (<0.1 mm) lesions, including port wine capillary vascular malformations and pigment deposits (melanin deposits), although epidermal thickening can be detected and can be particularly prominent in inflammatory or infectious conditions such as plantar warts.

Ultrasound examination is largely operator dependent. Optimal adjustment of B-mode and Doppler technical settings must be made while performing skin ultrasound.

Acknowledgment Edith Suss-Toby, Ph.D. and Michal Schlesinger-Lau, VMD, Imaging & Microscopy Unit, Multidisciplinary Laboratories, Faculty of Medicine, Technion, Israel Institute of Technology, Haifa, Israel, for the images on micro-ultrasound for preclinical imaging.

Glossary

Transducer Device that converts one form of energy into another. In ultrasound, the transducer converts electric energy provided by the transmitter to mechanical energy (acoustic pulses) and vice versa, reflected echoes to electric signals. Ultrasound transducers are made of thin piezoelectric materials that expand and contract to generate acoustic vibrations (frequencies).

Resolution Capacity to separate two objects in close proximity that are along the path of the ultrasound beam. Axial resolution is the smallest thickness while lateral resolution is the smallest width that can be resolved. Higher ultrasound frequencies raise the spatial resolution but lower the depth of penetration into the tissues.

Artifacts Source of imaging pitfalls, suggesting the presence of structures that are not actually present or obscuring real findings. Examples of artifacts suggesting structures that are not actually present are reverberation, refraction, and side lobes artifacts. Reverberation artifacts are a result of repeated reflection of the ultrasound signal between highly reflective interfaces usually near the transducer. Refraction artifacts are a result of bending of the sound beam causing targets that are not situated along the axis of the transducer to appear in a misleading location. Side lobes artifacts result from a strong out-of-plane reflector, generating confusing echoes. An example of artifact-obscuring findings is posterior acoustic shadowing. Acoustic shadow is a result of total reflection of the ultrasound waves by a strong reflector, causing loss of information on the tissues deep to the reflecting structure.

Harmonics Multiples or harmonic echoes of the transmitted fundamental frequency generated by the acoustic pulse as it travels within tissues.

Compounding Image resulting from summing ultrasound images obtained from different scanning angles.

Extended field of view (EFOV) Panoramic image generated by manual movement of a real-time probe in the direction of the transducer array. Imaging processing technology estimates translation and rotation of the probe by comparing successive images. The EFOV image buffer combines the images to produce a panoramic image.

3D Ultrasound Tissue volume acquired by dedicated 3D transducers employing hardware-based image registration, high density 2D arrays or software registration of scan planes.

Hypoechoic Reflected signals (echoes) of intermediate intensity or amplitude, generating images of low brightness in different shades of gray. Examples of hypoechoic tissues are the parenchymal organs such as the liver, spleen, renal parenchyma, and muscles.

Hyperechoic Reflected signals (echoes) of high intensity or amplitude, generating images of high brightness (white). Examples of hyperechoic tissues are fat, fibrous tissues, and bones. Foreign bodies and stones are examples of hyperechoic structures.

Echofree, sonolucent, or anechoic Absence of reflected signals (echoes), generating images in black. Examples of anechoic targets are normal vessels, gallbladder, urinary bladder, and cysts.

Doppler effect The result of the change in frequency of the sound when scattered by a moving target. The Doppler frequency shift is described by the Doppler equation:

$$\Delta F = (\mathrm{FR} - \mathrm{FT}) = (2\ \mathrm{FT}\ v / c)\cos\theta.$$

ΔF: Doppler frequency shift
FR: frequency of sound reflected from the moving target
FT: frequency of sound emitted from the transducer
v; target velocity
c: sound velocity in the medium
θ: angle between the flow axis and the incident ultrasound beam (angle of insonation). This angle must be kept at 60° or less.

Pulsatility index (PI) PI considers the tissue resistance to flow at each complete cardiac cycle. It is calculated as PI = PSV – EDV/mean velocity.

Resistive index (RI) RI considers the tissue resistance to blood flow at systole and diastole. It is calculated as RI = PSV – EDV/PSV

Contrast enhanced ultrasound agents (CEUS) Intravascular blood-pool agents comprised of encapsulated microbubbles of gas, smaller than red blood cells, capable of circulating freely. CEUS seek to enhance the echo amplitude by increasing the backscatter from moving red cells, while increasing attenuation from the static tissue.

References

1. Merrit CRB. Physics of ultrasound. In: Rumack CM, editor. Diagnostic ultrasound. 3rd ed. Philadelphia: Elsevier; 2005. p. 3–34.
2. Wortsman X, Wortsman J. Clinical usefulness of variable-frequency ultrasound in localized lesions of the skin. J Am Acad Dermatol. 2010;62:247–56.
3. Lassau N, Spatz A, Avril MF, et al. Value of high-frequency US for preoperative assessment of skin tumors. Radiographics. 1997;17:1559–651.
4. Cammarota T, Pinto F, Magliaro A, Sarno A. Current uses of diagnostic high-frequency US in dermatology. Eur J Radiol. 1998;27:215–23.
5. Szyman'ska E, Nowicki A, Mlosek K, et al. Skin imaging with high frequency ultrasound: preliminary results. Eur J Ultrasound. 2000;12:9–16.
6. Gerger A, Hofmann-Wellenhof R, Samonigg H, Smolle J. In vivo confocal laser scanning microscopy in the diagnosis of melanocytic skin tumors. Br J Dermatol. 2009;160:475–81.
7. Antoch G, Vogt FM, Freudenberg LS, Nazaradeh F, Goehde SC, Barkhausen J, et al. Whole-body dual-modality PET/CT and whole-body MRI for tumor staging in oncology. JAMA. 2003;290:3199–206.
8. Wortsman XC, Holm EA, Wulf HC, Jemec GBE. Real-time spatial compound ultrasound imaging of skin. Skin Res Technol. 2004;10:23–31.
9. Weng L, Tirumalai AP, Lowery CM, et al. US extended-field-of-view imaging technology. Radiology. 1997;203:877–80.
10. Hildegard Schmid-Wendtner M, Burgdorf W. Ultrasound scanning in dermatology. Arch Dermatol. 2005;14:217–24.
11. Wortsman X, Wortsman J, Soto R, et al. Benign tumors and pseudotumors of the nail: a novel application of sonography. J Ultrasound Med. 2010;29:803–16.
12. Gutierrez M, Wortsman X, Filippucci E, et al. High-frequency sonography in the evaluation of psoriasis: nail and skin involvement. J Ultrasound Med. 2009;28:1569–74.
13. Giovagnorio F, Valentini C, Paonessa A. High-resolution and color Doppler sonography in the evaluation of skin metastases. J Ultrasound Med. 2003;22:1017–22, quiz 1023–5.
14. Giovagnorio F, Andreoli C, De Cicco ML. Color Doppler sonography of focal lesions of the skin and subcutaneous tissue. J Ultrasound Med. 1999;18:89–93.
15. Schroder RJ, Maurer J, Zlowodski M, et al. Vascularization of malignant and benign skin tumors measured by D-galactose-based signal enhanced colour Doppler sonography. Acta Radiol. 2001;42:294–301.
16. Burns PN. Physics of ultrasound. In: Rumack CM, editor. Diagnostic ultrasound. 3rd ed. Philadelphia: Elsevier; 2005. p. 55–73.
17. Foster FS, Mehi J, Lukacs M, et al. A new 15–50 MHz array-based micro-ultrasound scanner for preclinical imaging. Ultrasound Med Biol. 2009;35:1700–8.
18. Foster FS, Hossack J, Lee Adamson S. Micro-ultrasound for preclinical imaging. Interface Focus. 2011;1:576–601.

Sonographic Anatomy of the Skin, Appendages, and Adjacent Structures

2

Ximena Wortsman, Jacobo Wortsman, Laura Carreño, Claudia Morales, Ivo Sazunic, and Gregor B.E. Jemec

The normal anatomy from a practical approach correlating clinical, ultrasound and histologic images

Contents

X. Wortsman, MD (✉)
Department of Radiology and Dermatology,
Institute for Diagnostic Imaging and Research of the Skin and Soft Tissues, Clinica Servet,
University of Chile, Faculty of Medicine,
Almirante Pastene 150, Providencia, Santiago, Chile
e-mail: xwo@tie.cl, xworts@yahoo.com, www.sonoskin.com

J. Wortsman, MD
Department of Medicine,
Southern Illinois University School of Medicine,
3128 Temple Drive, Springfield, IL 62704, USA

L. Carreño, MD • C. Morales, MD
Department of Pathology, Dermopathology Section,
Hospital Clinico Universidad de Chile, Faculty of Medicine,
University of Chile, Santiago, Chile
e-mail: lcarrenotoro@gmail.com; claudiamohuber@gmail.com

I. Sazunic, MD
Department of Dermatology, Dermatopathology Section,
Faculty of Medicine,
Histodiagnostico Malaga, University of Chile,
Santiago, Chile

G.B.E. Jemec, MD, DMSci
Department of Dermatology, Health Sciences Faculty,
Roskilde Hospital, University of Copenhagen,
Køgevej 7-13, Roskilde 4000, Denmark
e-mail: gbj@regionsjaelland.dk

X. Wortsman, G.B.E. Jemec (eds.), *Dermatologic Ultrasound with Clinical and Histologic Correlations*,
DOI 10.1007/978-1-4614-7184-4_2, © Springer Science+Business Media New York 2013

2.1 Introduction

The skin is the most superficial and largest body organ, and as such easily accessible to sonographic examination. It is however also a complex organ, and in spite of the approachable location, its great histologic and functional complexities present unique problems that must be addressed in ultrasound imaging.

The skin has a range of passive and active functions. While it mainly serves as the body's envelope protecting it against thermal and physical injuries, it is also the site for the photosynthesis of vitamin D_3, an indispensable factor in bone physiology. Furthermore, the skin regulates body temperature (through direct evaporation of water by the sweat glands or through the insulating properties of fatty tissue); and a communication organ as it connects the external and internal environments through a wide assortment of nerve receptors that serve not only to orientate the body in relation to the environment, but also in communication between individuals [1–3]. These many functions can only be fulfilled if the organ contains a broad range of different tissues and cell types.

Skin disorders are generally expressed with highly specific distribution patterns that reflect regional inhomogeneities in blood and nerve supply, immunologic variability in epitopes/antigens expression, and/or differences in immune cells distribution. Occasionally, primary alterations of superficial structures (tendons, ligaments, muscles, lymph nodes, or bony margins) may also simulate skin pathology or, be secondarily involved by primary skin disorders. Therefore the morphology of both the skin and of the adjacent organs must be properly identified when imaging the skin and establishing the differential diagnosis of a skin disease.

2.2 Technical Considerations

Appropriate sonographic examination of the skin requires both specialized equipment and thorough training of the operator. Initially, important data were generated with dedicated skin ultrasound performed at a fixed high frequency using heavy probes. Technological advances in ultrasound technology have however now opened the possibility for more thorough imaging of both the skin and the adjacent structures, providing a comprehensive and detailed image for analysis. It is now possible to use multichannel ultrasound machines fit with tunable (variable) frequency (≥15 MHz), and light-weight probes, making it possible to study the skin as well as the underlying tissues in a single process. Furthermore, the appearance of compact-linear type ("hockey-shaped" or "foot-print" transducers) has meant that more areas can now be studied because of the transducers' better adaptation to the irregular shape of the skin surface. Additional capabilities for sensitive color or power Doppler testing, extended field of view, and 3D reconstruction are also often useful.

The qualifications required of the operator in this field must include skills in both imaging as well as more than a basic knowledge of dermatology. The combined understanding is needed to properly correlate clinical findings with sonographic images. Real-time interpretation of the results allows for the prompt generation of clinical information, critical for consequent decisions on whether to extend the examination to a corporal segment not included in the initial request, thereby providing clinical utility.

Ultrasonography is not associated with adverse effects, and few preparations are needed in patients. Sedation is however routinely recommended for imaging studies in children younger than 4 years old to prevent movement artifacts as a result of crying or anxiety, as this may affect the spectral representation of the blood flow. Color Doppler ultrasound examination demands an environment that is quiet and comfortable for the child, the parents/guardians, and the operator. After the informed consent is signed by the parents or guardians, chloral hydrate (50 mg/kg) is administered orally; excellent sedation is regularly obtained and the examination is performed approximately 30 min later. The child is monitored with the Modified Aldrete Score (i.e., evaluation of activity, respiration, circulation [blood pressure], consciousness, and oxygen saturation), and discharge is recommended when the score reaches a value of 9 or higher.

To facilitate ultrasound wave focusing to the most superficial skin layers, copious amounts of gel must be applied; preferably, the gel is pre-warmed to decrease patient discomfort. The use of stand-off pads for further focus adjustment is not only unnecessary, but not recommended because the devices may compress small superficial vessels and interfere with the actual imaging process [4]; likewise, intravenous contrast medium is rarely if ever needed for basic studies.

2.3 Sonography of Cutaneous Layers

Like all epithelia, skin integrates passive and active barrier functions, mechanical functions, and other functions in a layered structure. The histologic skin layers such as the epidermis, dermis, and subcutaneous tissue can also be separated into sonographic equivalents of an outer layer (corresponding to the epidermis), a middle layer (dermis), and a deeper layer (subcutaneous tissue, subcutis, or hypodermis) [3, 5] (Fig. 2.1). Although the general organization of the skin is spatially maintained throughout the body, recognition of regional variations is of paramount importance for the correct analysis of sonographic findings.

Significant regional quantitative differences occur. The stratum corneum (i.e., the outermost layer of the epidermis) is thick in the palms and soles, and very thin on the eyelids. The epidermis is generally thinner in the forearm and thicker

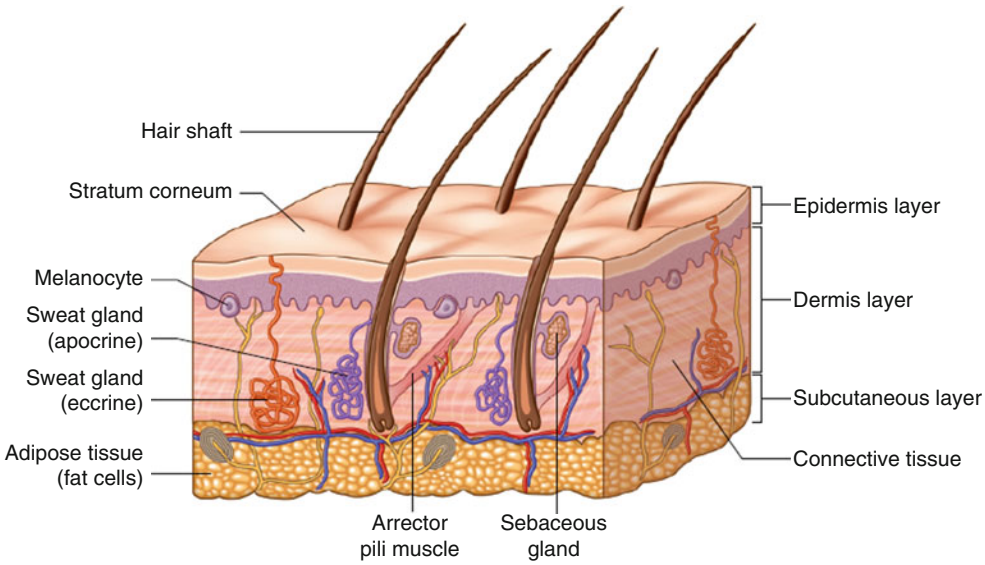

Fig. 2.1 Skin anatomy. Drawing shows the different components of the cutaneous layers

in the plantar or palmar regions; the dermis is thinner in the ventral forearm but thicker in the dorsal region; and the subcutaneous tissue is thinner in the dorsal aspect of the fingers but thicker in the trunk [6].

Qualitative differences also occur. The appendages are obviously also not evenly distributed over the body. Thus, hair follicles are prominent in the scalp, but absent in the soles of the feet (i.e., glabrous skin or devoid of hair). In addition, the skin exhibits important variations in the local density of melanocytes and blood supply [5].

All these characteristic properties must be considered when describing morphology, depth, and structural involvements by cutaneous lesions, as well as reference standards for the different skin imaging modalities.

2.3.1 Epidermis

2.3.1.1 Anatomy

The epidermis has a highly pleiotropic cellular content and is nonvascular. It is nourished through diffusional flow by the dermal circulation. The main cell populations of the epidermis are keratinocytes, melanocytes, and Langerhans cells. Small numbers of other cells, including Merkel cells (associated with sensory functions) are also present. The epidermis is in contiguity with the appendages, specialized dermal structures that transit through the epidermis lined with epithelial cells, with important potential for division and differentiation. Epidermal appendages include the hair follicles, nails, and sweat glands (with its apocrine, eccrine, and apoeccrine variants) and often stretch through the dermis as well, therefore, these will therefore be discussed elsewhere. The pilosebaceous unit is an epidermal invagination that contains the hair follicle (shaft and bulb portions), sebaceous glands, and the erector pili muscle (smooth muscle).

The interfollicular epidermis is divided into four epidermal layers or strata (from the most superficial to the deepest): corneum (acellular layer, keratin, and lipids), granulosum (granular cells), spinosum (prickly cells), and basale or germinativum (basal cells). There is an undulating basement membrane at the junction between epidermis and dermis providing adhesive support and is divided into lamina lucida and lamina densa. The thin lamina lucida lies directly beneath the basal keratinocytes epidermal layer, while the thicker lamina densa is in direct contact with the underlying dermis. These structures are the target of immunologic injury in autoimmune bullous disorders such as bullous pemphigoid and abnormalities in genetic structural disorders such as epidermolysis bullosa.

The epidermal diffusional flow through the dermoepidermal junction is critical for both nutrition supply and metabolite removal (including vitamin D_3). The epidermal appendages are separated from blood vessels, nerves, and cells in their dermal portion by a connective tissue sheath [3, 7].

2.3.1.2 Sonography

Echogenicity is determined by the capability to reflect the sound waves by the predominant or reflective component of the structure being studied; for example, epidermal keratin is highly echogenic, and heavily keratinized areas such as the thicker glabrous skin (palms of the hands and the soles of the feet) appear as bilaminar hyperechoic structures. In the lesser keratinized non-glabrous skin the epidermis appears as only a single, hyperechoic line that offers no major detail for interpretation (Figs. 2.2, 2.3, and 2.4) [4].

2.3.2 Dermis

2.3.2.1 Anatomy

The dermis is a supporting structure histologically dominated by organized bundles of collagen deposited by local fibroblasts providing not only the stroma for the epithelium but also the predominant mechanical functions of the skin.

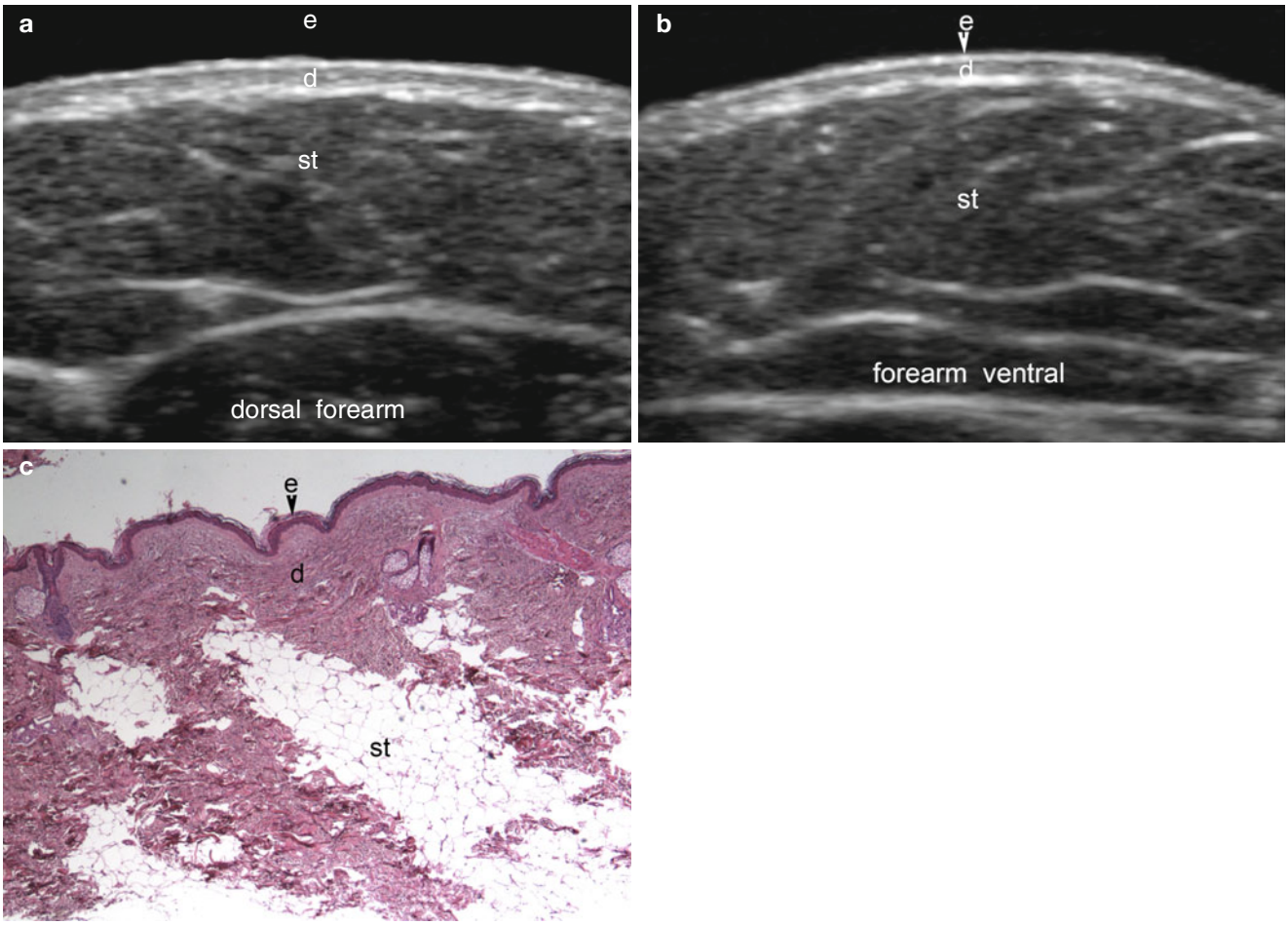

Fig. 2.2 (**a**–**c**) Normal skin, forearm. (**a**, **b**) Ultrasound (transverse view). (**a**) Dorsal forearm and (**b**) Ventral forearm. Note the thin ventral forearm dermis. (**c**) Histology (H&E ×40 zoom) demonstrates thin epidermis and dermis. *Abbreviations*: *e* epidermis, *d* dermis, *st* subcutaneous tissue

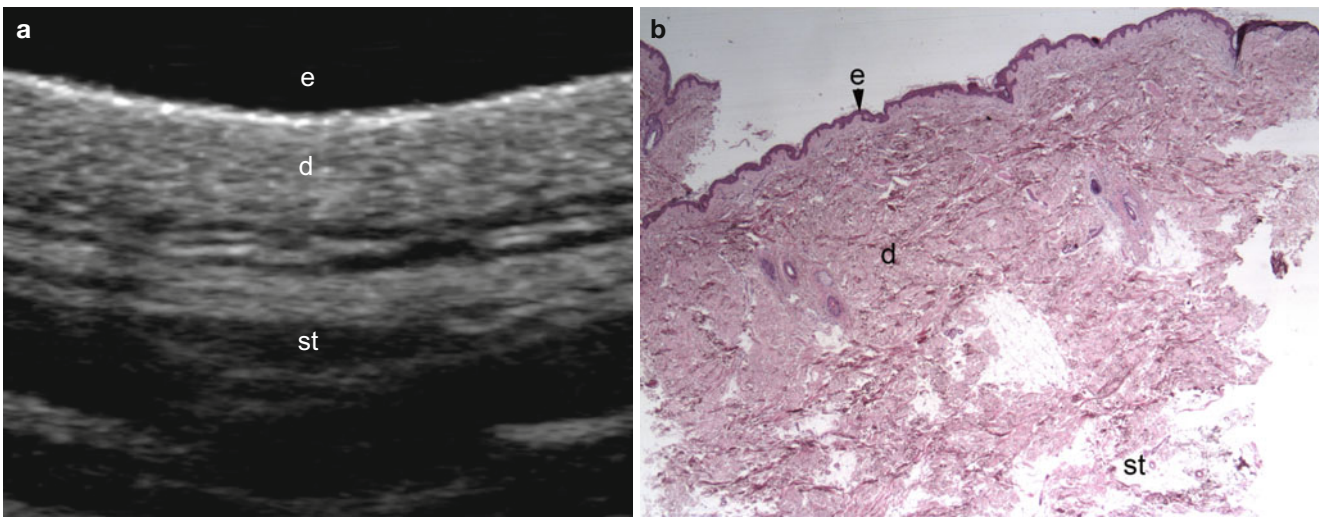

Fig. 2.3 (**a**, **b**) Normal dorsal skin. (**a**) Ultrasound (transverse view). Note the difference in dermis thickness compared to Fig. 2.2. (**b**) Histology (H&E ×40 zoom). Note high dermal collagen density and thickness. *Abbreviations*: *e* epidermis, *d* dermis, *st* subcutaneous tissue

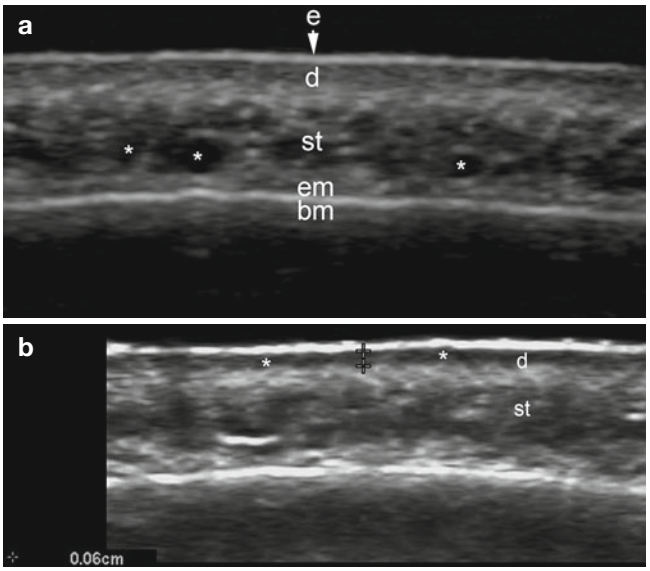

Fig. 2.4 (**a**, **b**) Normal frontal skin. (**a**) Ultrasound (transverse view). Note prominent subcutaneous veins (*). (**b**) Note subepidermal low echogenicity band (*, between markers), a sonographic sign of photoaging. *Abbreviations*: *e* epidermis, *d* dermis, *st* subcutaneous tissue, *em* epicranius muscle, *bm* bony margin of the skull

The dermis content also includes blood vessels, lymphatic vessels, nerve fibers, and the deep portions of hair follicles and sweat glands.

The dermis or corium consists of connective tissue (cells, collagen, and elastic fibers) arranged into two layers: a more superficial papillary dermis and the deeper reticular dermis. The thin papillary dermis is made of loose connective tissue containing mostly capillaries and fibers (elastic and reticular, with sparse collagen content). In the thick reticular dermis the connective tissue is denser, traversed by larger blood vessels, elastic fibers, coarse bundles of collagen fibers arranged in layers parallel to the skin surface, cells (fibroblasts, mast cells), nerve endings, lymphatic vessels, and epidermal appendages. The predominant form of collagen in the dermis is type I, followed by collagen III; the small amount of elastic fibers present in the dermis play an important functional role in the resistance to deformational forces, preventing the sagging of the skin. All dermal components are bound together by a gel-like ground substance made of various glycosaminoglycans (primarily hyaluronic acid, but also chondroitin sulfate), and glycoproteins.

The dermis exhibits a complex vascular system: the papillary dermis is supplied by a superficial vascular plexus at the border between papillary and reticular dermis through a candelabra-like capillary system; other specialized dermal vascular formations include arterio-venous anastomoses and the glomus bodies. Arterio-venous anastomoses function as valves allowing blood to bypass upper dermal capillaries, whereas glomus bodies, found in the fingertips, are rich vascular plexus of capillaries and lymphatics vessels that run along the dermal papillae, perpendicular to the skin surface. The dermal lymphatic circulation runs through an extensive network loosely arranged into superficial and deep plexuses [3, 8].

2.3.2.2 Sonography

Dermal echogenicity is determined by the collagen component that produces a hyperechoic band but trophic changes, as seen in older individuals after chronic exposure to sunlight, change dermal echogenicity from a single homogenous reflection to a more complex pattern with an additional subepidermal hypoechoic band (SLEB). The pathologic substrate for the latter is elastosis, a combination of elastin degeneration and local glycosaminoglycans deposition [4, 9] (Figs. 2.2, 2.3, and 2.4). With the current equipment, rarely blood flow is detected in the normal dermis on color Doppler.

2.3.3 Subcutaneous Tissue-Subcutis-Hypodermis

2.3.3.1 Anatomy

The subcutaneous fat is a tissue compartment further divided into lobules containing adipose cells and separated by thin fibro-vascular septa. The septa consist of collagen and reticulin fibers, and house blood, lymphatic vessels and cutaneous nerves. Each lobule is supplied by a small muscular artery (250–500 μm diameter) branching from the septa into centrilobular arterioles (100–300 μm in diameter) that generate capillary networks around each individual adipocyte; postcapillary venules drain into larger peripheral veins that also run along the septa. This arrangement has important clinical connotations because interferences with the arterial supply result in diffuse intra-lobular changes (panniculitis, mostly lobular), whereas venous occlusive disorders manifest with septal and paraseptal alterations (panniculitis, mostly septal). Of note, and in contrast to the rich connections of dermal vessels, the blood supply of the adipose microlobule is terminal, implying that there are no capillary connections between adjacent microlobules or between dermis and subcutaneous fat. As far as lymphatic circulation is concerned, subcutaneous fat septa contain dense lymphatic plexuses that transverse into the subcutaneous tissue, at first parallel to the surface of the skin and then perpendicular, to penetrate the deep fascia and drain into regional lymph nodes [10–12].

2.3.3.2 Sonography

The subcutaneous tissue with its fatty lobules appears hypoechoic with interspersed hyperechoic fibrous septa. Subcutaneous circulation can be visualized with color

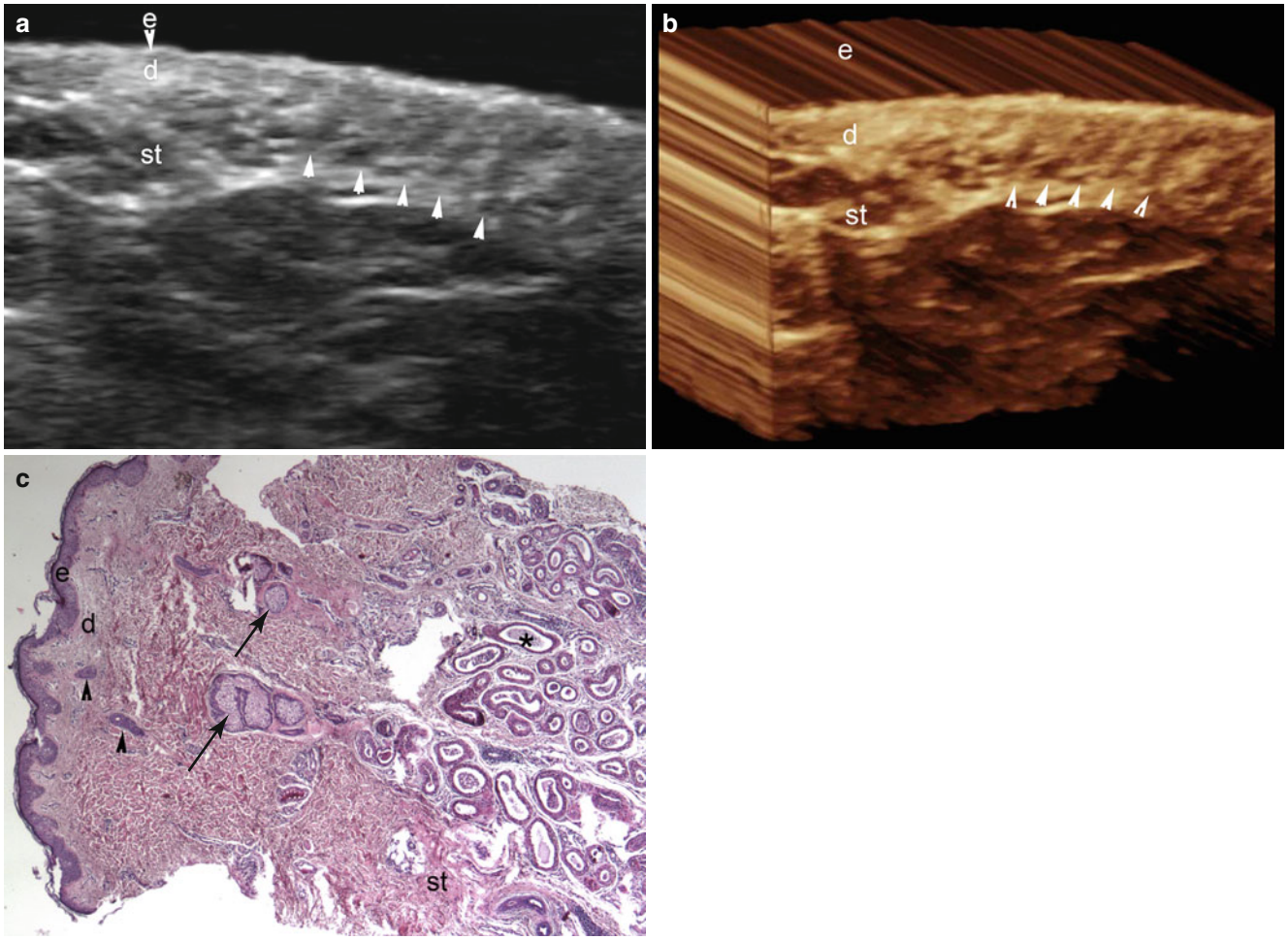

Fig. 2.5 (**a**–**c**) Normal skin at the axillary region. (**a**) Ultrasound (transverse view). The prominent dermal hypoechoic bands in the oblique axis correspond to hair follicles (*arrowheads*). (**b**) 3D ultrasound (transverse view). (**c**) Histology (H&E ×40 zoom) showing hair follicles (*arrowheads*) and sebaceous glands (*arrows*) in the dermis and apocrine glandular tissue (*) in the subcutaneous layer

Doppler examination that normally shows a low-flow pattern, detectable in arterial and venous vessels of the subcutaneous tissue [4] (Figs. 2.2, 2.3, 2.4, 2.5, and 2.6).

2.4 Appendages

2.4.1 Nail

2.4.1.1 Anatomy

The nail unit has a complex structure that involves three separate areas: the ungual plate that consists mostly of keratin, the nail bed that includes the matrix region, and the periungual region that includes the proximal and lateral nail folds. The nail plate presents keratinized epithelial cells and shows a curved shape (longitudinal and transverse axes) that facilitates attachment in the lateral and proximal nail folds. It is composed of dorsal and ventral layers that run transversely and a central layer that runs in longitudinal axis that may favor the resistance of the nail to trauma. The nail bed mostly presents a thin epidermis with prominent longitudinal ridges and a dermal layer without sebaceous or follicular appendages. The ungual matrix is the germinal layer that provides the keratinized cells that compose the nail plate. It is located in the proximal nail underlying the lunula (half moon) and also presents lateral proximal extensions (also called wings that are closely attached to the distal part of the lateral ligaments of the distal interphalangeal joint). The dermis underlying the ungual matrix shows prominent collagen. The periungual folds (lateral and proximal) are the cutaneous sites of insertion of the nail plate. Vascular supply to the nail is performed by four digital arteries, two on each side of the finger (ventral and dorsal aspect). The ventral (palmar) branches provide the main supply to the fingers and they show anastomoses in the distal arcades (dorsal and ventral). The ventral arch is located in the maximal padding of the finger pulp and the dorsal arch lies distal to the distal interphalangeal joint providing supply for the nail fold, extensor

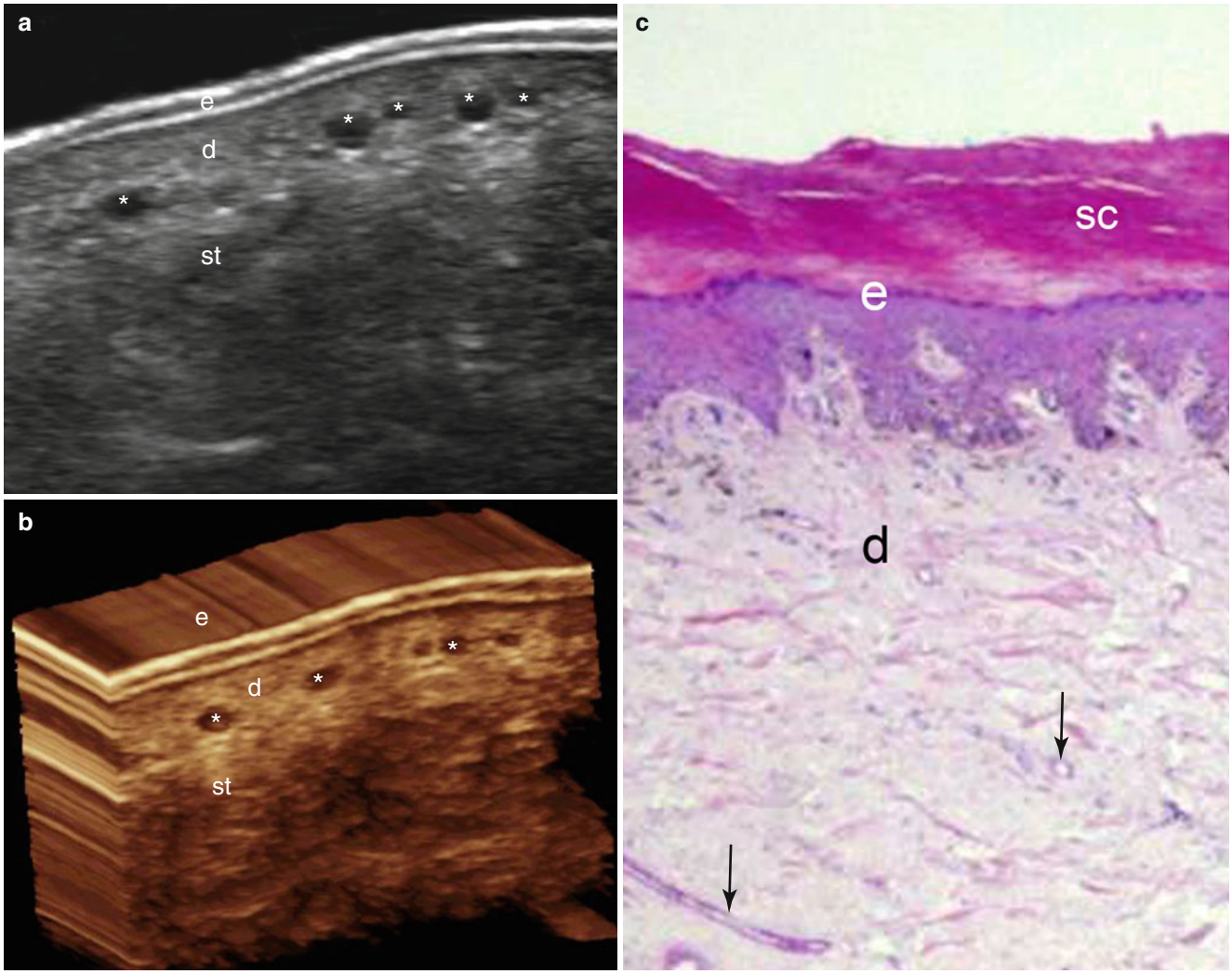

Fig. 2.6 (**a**–**c**) Normal plantar skin. (**a**) Ultrasound (transverse view) shows a bilaminar hyperechoic pattern of the epidermis. Dermal venous vessels (*) are prominent. (**b**) 3D ultrasound. (**c**) Histology (H&E ×40 zoom) showing marked stratum corneum (*sc*) thickness of the plantar epidermis, some thin vessels (*arrows*) and lack of hair follicles. *Abbreviations*: *e* epidermis, *d* dermis, *st* subcutaneous tissue, *sc* stratum corneum

tendon insertion, and the nail matrix. Deep and superficial veins conform a prominent network in the dorsal and ventral regions. Glomus bodies that are clusters of arteriovenous shunts surrounded by a prominent myoneural component are also present in the nail bed. It is supposed that these glomus bodies can serve in the regulation of the capillary network and may support the preservation of the peripheral blood flow under extreme cold conditions [13].

2.4.1.2 Sonography

The different parts of the nail apparatus have characteristic sonographic profiles. The ungual plate appears as a hyperechoic bilaminar structure: the two parallel lines, called dorsal and ventral plate, separated by an almost virtual hypoechoic space that tends to disappear at very high sound frequencies (≥22 MHz). The nail bed appears hypoechoic, but may turn slightly hyperechoic at proximal levels, beneath the ungual matrix. The periungual skin (lateral and proximal nail folds) has the sonographic morphology of normal skin with corresponding cutaneous layers, except for the almost total absence of adipose tissue. However, fatty lobules can be discerned in the hyponychium (distal periungual tissue) and the distal palmar aspect of the fingers. A pattern of low-flow vascularity (arterial and venous) is frequently detected in the nail bed close to the hyperechoic bony margin of the distal phalanx [14] (Figs. 2.7 and 2.8).

2.4.2 Hair

2.4.2.1 Anatomy

Hair, a unique mammalian trait, has important functional roles in thermoregulation, physical protection, sensory activity, and social interactions. Histologically, hair is divided

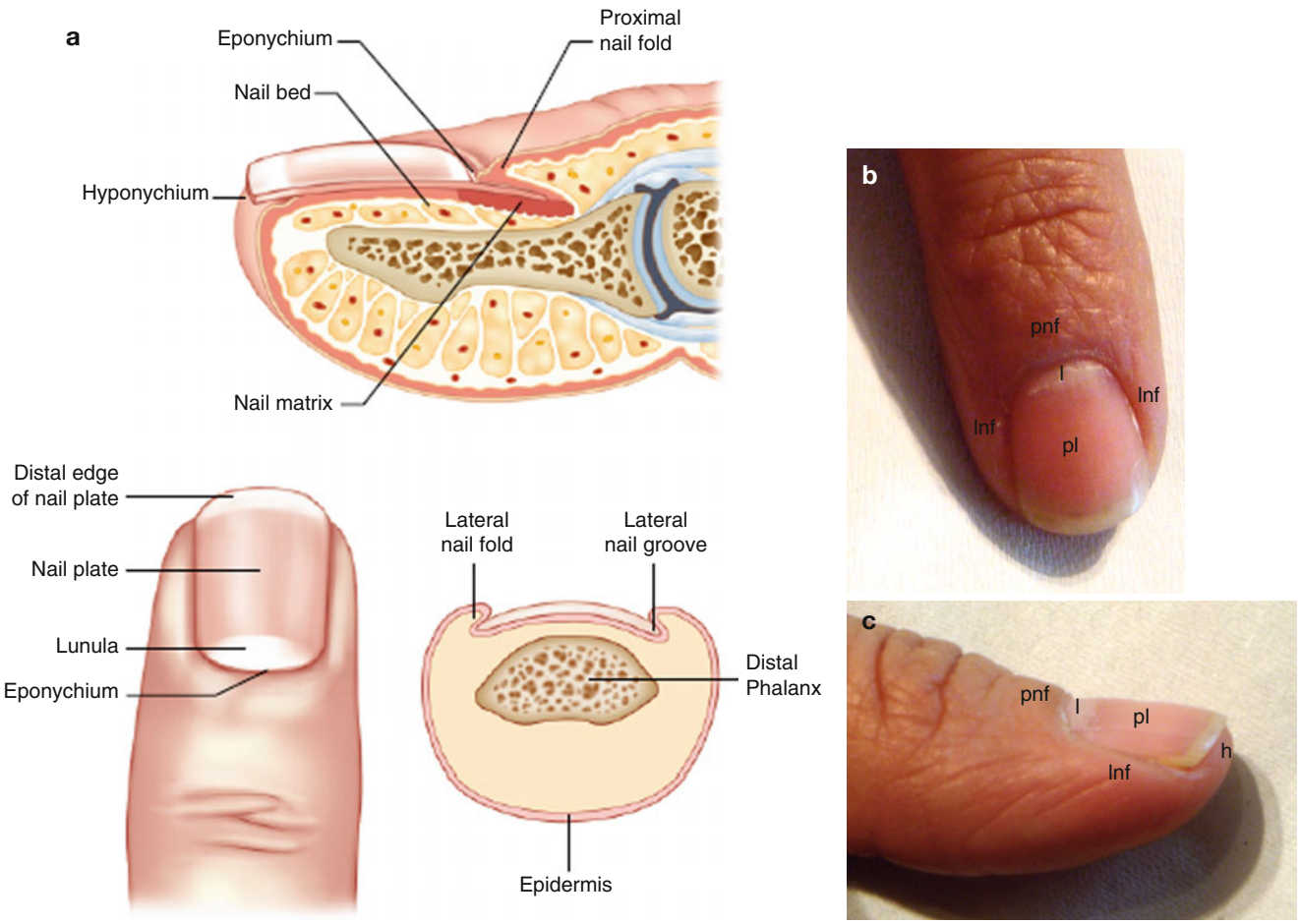

Fig. 2.7 (**a**–**c**) Nail anatomy. (**a**) Schematic representation of the nail. (**b**) Clinical frontal view of the nail. (**c**) Clinical lateral view of the nail. *Abbreviations*: *pl* ungual plate, *l* lunula, *pnf* proximal nail fold. *lnf* lateral nail fold, *h* hyponychium

into the hair follicle, located in the dermis, and the hair tract or shaft that emerges to the skin surface. Hair tracts are made of terminally differentiated keratinocytes produced by the hair follicles and consist of an outer layer or cuticle, analogous to the stratum corneum of the epidermis; a middle layer or cortex, made of hard keratin; and, an inner layer or medulla made of soft keratin. Hair follicles are distributed over the entire surface of the body with the notable exceptions of the soles of the feet, palms of the hands, glans penis, clitoris, labia minora, and muco-cutaneous junctions. The complex of sebaceous glands and hair follicle, in combination with the pili erector muscle form the pilosebaceous unit. At the proximal end or base of the hair follicle is the hair bulb, lying deep within the dermis and reaching down to the subcutaneous fat in the face. Because the hair bulb harbors a population of stem cells, the rich facial population of hair follicles results in rapid re-epithelization, even after deep cutaneous wounds. Contraction of the pili erector that connects the deep portion of the follicle to the superficial dermis (under control by the sympathetic nervous system) causes the follicle to assume a vertical direction ("goosebumps"). Hair density is highest in the scalp, where it is supplied by a centripetal vascular network derived from branches of the internal and external carotid arteries; the blood vessels traverse the subcutaneous tissue from the circumference of the scalp toward the midline, while progressively decreasing in size. After birth hair reaches maturity, undergoing active growth when hair follicles become anchored in the subcutaneous tissue, to be lost and regenerated periodically through cycles of growth (anagen), apoptosis-driven regression (catagen), and quiescence (telogen). Hair follicle orientation is oblique to the skin surface in Caucasians, and almost parallel in individuals of African ancestry; whereas in people of Asian ancestry, hair follicles are oriented vertically producing straight hairs [7, 8, 14–16].

2.4.2.2 Sonography

Hair follicles appear as slightly oblique hypoechoic bands usually wider at the bottom, occupying the dermis but reaching the subcutaneous border at maturity; scalp hair tracts are mostly

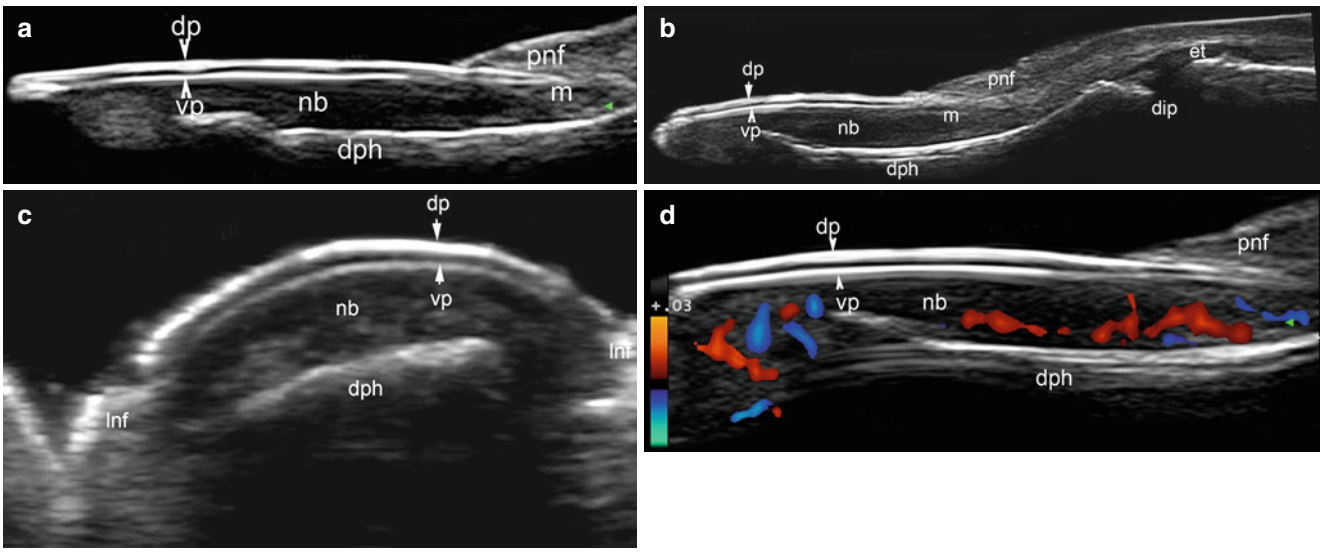

Fig. 2.8 (**a**–**d**) Nail anatomy. (**a**) Ultrasound of the nail unit (longitudinal view). (**b**) Ultrasound of the nail unit (longitudinal extended panoramic view) including the insertion of the extensor tendon (*et*) and the distal interphalangeal joint (*dip*). (**c**) Ultrasound of the nail unit (transverse view). Note lateral nail folds (*lnf*). (**d**) Color Doppler ultrasound (longitudinal view) showing visible blood flow within the nail unit. *Abbreviations*: *nb* nail bed, *dp* dorsal plate, *vp* ventral plate, *pnf* proximal nail fold, *lnf* lateral nail fold, *dph* distal phalanx, *dip* distal interphalangeal joint, et extensor tendon distal insertion

trillaminar hyperechoic structures, with the two outer lines corresponding to the cuticle-cortex complex and the inner line to the medulla. Vellous hairs such as the eyelashes may lack the center (medulla) and appear as a monolayer hyperechoic line.

Ultrasound makes it possible to identify the growth cycle phase, with shallow follicles marking the telogen phase (i.e., hair follicles located in the upper dermis) and deep follicles, the anagen phase(i.e., hair follicles with their bottom part reaching the border between the dermis and the subcutaneous tissue); intermediate stages indicate the catagen phase [17]. The variations in the orientation of the hair follicles (axis) can be recorded at the time of imaging examination to help prevent alopecia post-scalp surgery (Figs. 2.9 and 2.10).

2.4.3 Sebaceous Glands

2.4.3.1 Anatomy

Sebaceous glands are epidermal appendages and form an important part of the pilosebaceous unit. They are holocrine glands (the cellular cytoplasm is the secretion) that are widely distributed throughout the skin but most associated with hair and therefore concentrated in the face and scalp; they are absent from the palm of the hands and soles and dorsum of the feet. Sebaceous glands often open directly into the hair follicle and their secretion is sebum, an oily complex of triglycerides, fatty acids and their breakdown products, wax esters, squalene, and cholesterol and cholesterol esters. Because of its lipid-hydrophobic composition, sebum is a lubricant protecting the skin against friction while making it more impervious to moisture [14]. Meibomian and Montgomery's glands are sebaceous glands without associated hairs.

2.4.3.2 Sonography

Normal sebaceous glands are not visible by sonography on the machines currently in use, except as a part of the pilosebaceous unit.

2.4.4 Eccrine Glands

2.4.4.1 Anatomy

Sweat glands are eccrine glands (secrete a watery fluid) that are also widely distributed, being most concentrated in the palms of the hands, soles of the feet, and axillae; they are absent in the vermillion border of the lips, the external ear canal, the nail beds, the labia minora, the glans penis and the inner aspect of the prepuce. Sweat glands have a dermal coiled secretory portion and a straight distal duct connection to the epidermis. Sweat gland activity is controlled by the thermoregulatory center in the hypothalamus through sympathetic nerves [15]; sweat exerts a cooling effect on the body through heat loss by water evaporation.

2.4.4.2 Sonography

Normal eccrine glands are not visible using current ultrasound equipment.

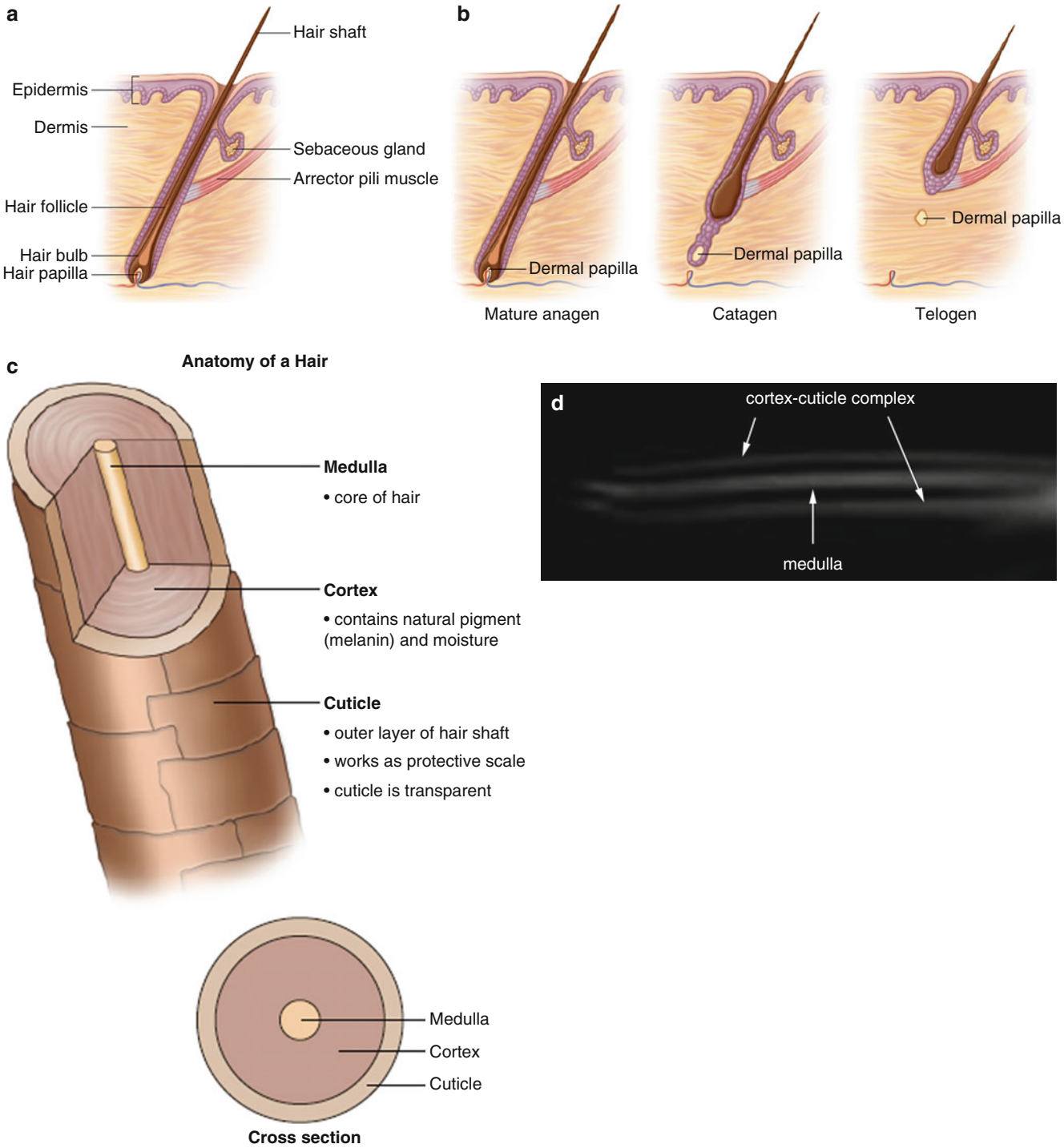

Fig. 2.9 (**a**–**d**) Hair. (**a**) Hair follicle structure. (**b**) Growth cycle of the hair follicle. (**c**) Normal structure of the hair tract. (**d**) Ultrasound of scalp hair shaft.

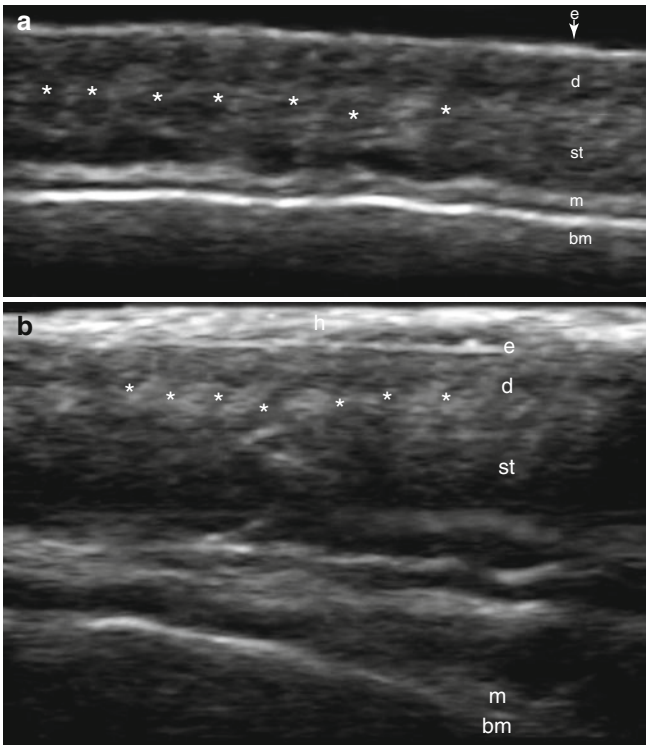

Fig. 2.10 (**a**, **b**) Sonographic anatomy of the scalp (longitudinal views). Note in dermis the hypoechoic, oblique direction of hair follicles (*). (**a**) Frontal region. (**b**) Occipital region. Note increased thickness of subcutaneous tissue. *Abbreviations*: *h* condensed hair tracts, *e* epidermis, *d* dermis, *st* subcutaneous tissue, *m* epicranius muscle, *bm* bony margin of the skull

2.4.5 Apocrine and Mammary Glands

2.4.5.1 Anatomy

Apocrine glands include cellular content in the secretory product and are found in the axillae, anogenital region; modified apocrine glands are found in the external ear canal (represented by the ceruminous glands), the eyelids (Moll's glands), and breasts (mammary glands). Most apocrine glands do not start functioning until after puberty and the secretion is often odorous [3, 8, 15]. Mammary glands are modified glands of the skin located on the milk lines. The glands are thought to be modified apocrine glands, and 15–20 glands are combined into the compound gland recognized clinically as the breast. The breast consists of secretory alveoli, lactiferous ducts, supportive connective tissue, and adipose tissue.

2.4.5.2 Sonography

The apocrine glands are not visible using sonography. Mammary glands are seen as hyperechoic fibroglandular tissue interspersed with hypoechoic fatty lobules. The subcutaneous tissue in the breast region may show a variable thickness of the fat component according to age, which is more prominent during late adulthood. Thin anechoic ducts can be detected in the areola region, and low flow vascularity is usually seen in the normal parenchyma.

2.5 Anatomy and Variants of Structures Adjacent to the Skin

2.5.1 Lymph Nodes

2.5.1.1 Anatomy

The oval-shaped organs belong to the immune system and show an outer capsule, mainly cellular, and an inner medulla with prominent ducts and sinuses. A fibrous macrocapsule surrounds the capsule with the exception of the vascular hilum region. B and T cells, plasma cells, and macrophages as well as a network of lymph sinuses ad ducts are present in the lymph nodes. Palpation of lymph nodes is a part of the routine clinical examination of patients, and the location of major conglomerates of lymph nodes is therefore well known. However, palpation is operator-dependent and additional information is therefore welcome, particularly where aberrant or abnormal nodes are found, or malignancy suspected.

2.5.1.2 Sonography

Lymph nodes appear as oval-shaped structures with hypoechoic rim (cortex) and hyperechoic center (medulla). The cortical rim is usually thin and of uniform thickness in all views. Color Doppler ultrasound shows the usually centrally located vascular hilum, generally detected in one of the aspects and typically consisting of low-flow arterial and venous vessels (Fig. 2.11).

2.5.2 Tendons

2.5.2.1 Anatomy

Tendons are composed of parallel bundles of collagen fibers that are held together by proteoglycans and connective tissue. A synovial sheath (lining) or a paratenon (loose connective tissue) can wrap around the tendon to protect it from friction or trauma. Superficial tendons are rarely directly involved in skin disease, but generalized diseases such as storage diseases and rheumatological diseases may require a more detailed description of tendons and the entheses.

2.5.2.2 Sonography

Tendons are hyperechoic cords, reflecting their high collagen content that exhibit a parallel fibrilar pattern. The normal synovial sheath is usually non-visible to ultrasound, with the exception of large groups of tendons such as the common extensor compartment in the wrist. The normal Achilles or patellar tendons present a "paratenon" usually not detected on ultrasound; synovial sheaths can contain a thin film of anechoic and compressible fluid surrounding the tendon that serves as a lubricant. Importantly, tendons may exhibit the sonographic artifact "anisotropy" (i.e., appearing bright on the screen when the ultrasound beam strikes the tendon at a 90° angle, but dark at other angles of approach). Anisotropy

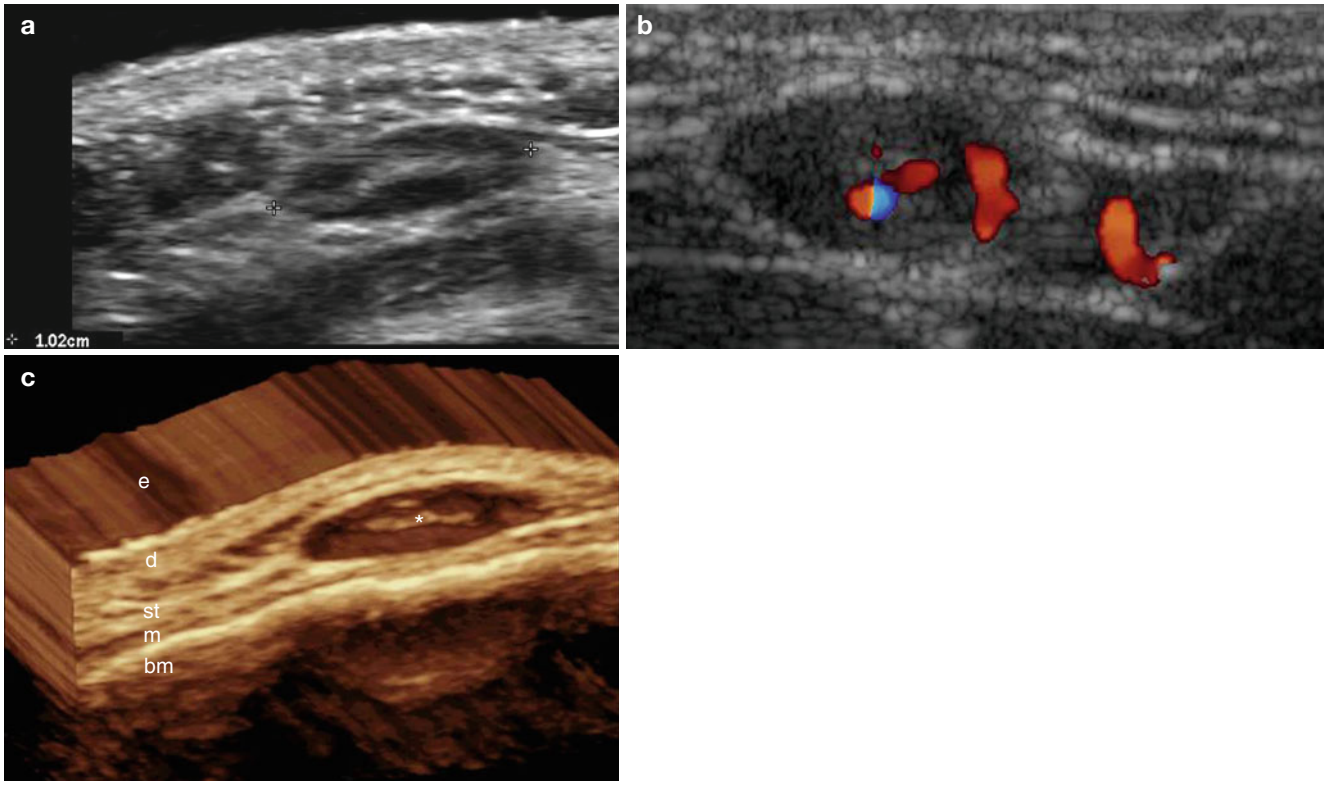

Fig. 2.11 (**a**–**c**) Lymph node anatomy. (**a**) Ultrasound (gray scale) shows 1.02 cm oval-shaped structure (between markers) with continuous hypoechoic cortex and well-defined hyperechoic center. (**b**) Color Doppler ultrasound. Note significant hilar blood flow. (**c**) 3D reconstruction. Note lymph node with the hyperechoic center (*). *Abbreviations*: *e* epidermis, *d* dermis, *st* subcutaneous tissue, *m* muscle, *bm* bony margin

may occasionally become a useful tracking signal in locating tendinous structures and should also be taken into account in the differential diagnosis of the tendon hypoechogenicity typical of tendinous tear or tendinosis. On sonography, accessory tendons exhibit morphology similar to normal tendons and maintain the hyperechoic fibrilar pattern. A common example is the accessory tendon of the abductor pollicis longus in the first extensor compartment of the wrist. Visualization of the accessory variant improves markedly if fluid is present within the synovial sheath of the tendon. Doubtful cases can be assisted using comparisons with the contralateral side. Ultrasound can also provide invaluable assistance by making it possible to visualize tendon movements in real time [18] (Fig. 2.12).

2.5.3 Muscle

2.5.3.1 Anatomy

Muscles are composed of myocytes, formed into muscle fibers are arranged in myofibrils that are packed in sarcomeres containing the proteins (actine and myosine, among others) that are necessary for the contraction process. Sequentially, the muscle fibers are surrounded by connective tissue layers that originate from the endomysium (i.e., covering of a muscle fiber) to the epimysium, covering the entire muscle. Skeletal muscles generally have one middle portion (belly) and two tendons (proximal and distal insertions), belly variations in number or shape result in the unipennate, bipennate, and/or circumpennate configurations. Bellies may also be separated by fibrous intersections, in the rectus abdominus or as a single belly and connect to multiple points of origins as in the quadriceps muscle. Several muscles are in close proximity to the skin in (e.g., the hands where assessment may be needed when inflammation is present). Accessory muscles are additional, anomalous, or supernumerary structures, usually discovered as asymptomatic findings but occasionally may cause soft-tissue swelling, becoming clinically relevant.

2.5.3.2 Sonography

Skeletal muscles are hypoechoic structures made of thick fascicles separated by hyperechoic adipose-fibrous septa (perimysium), and surrounded by an also hyperechoic fascia (Fig. 2.13). Fat deposits between the muscles can be identified, providing clinically useful inter-muscle separation planes. Sonographically, muscles are usually grouped functionally into compartments that change synchronously during a dynamic study (flexion-extension or rest-contraction) [19]. Accessory or supernumerary muscles

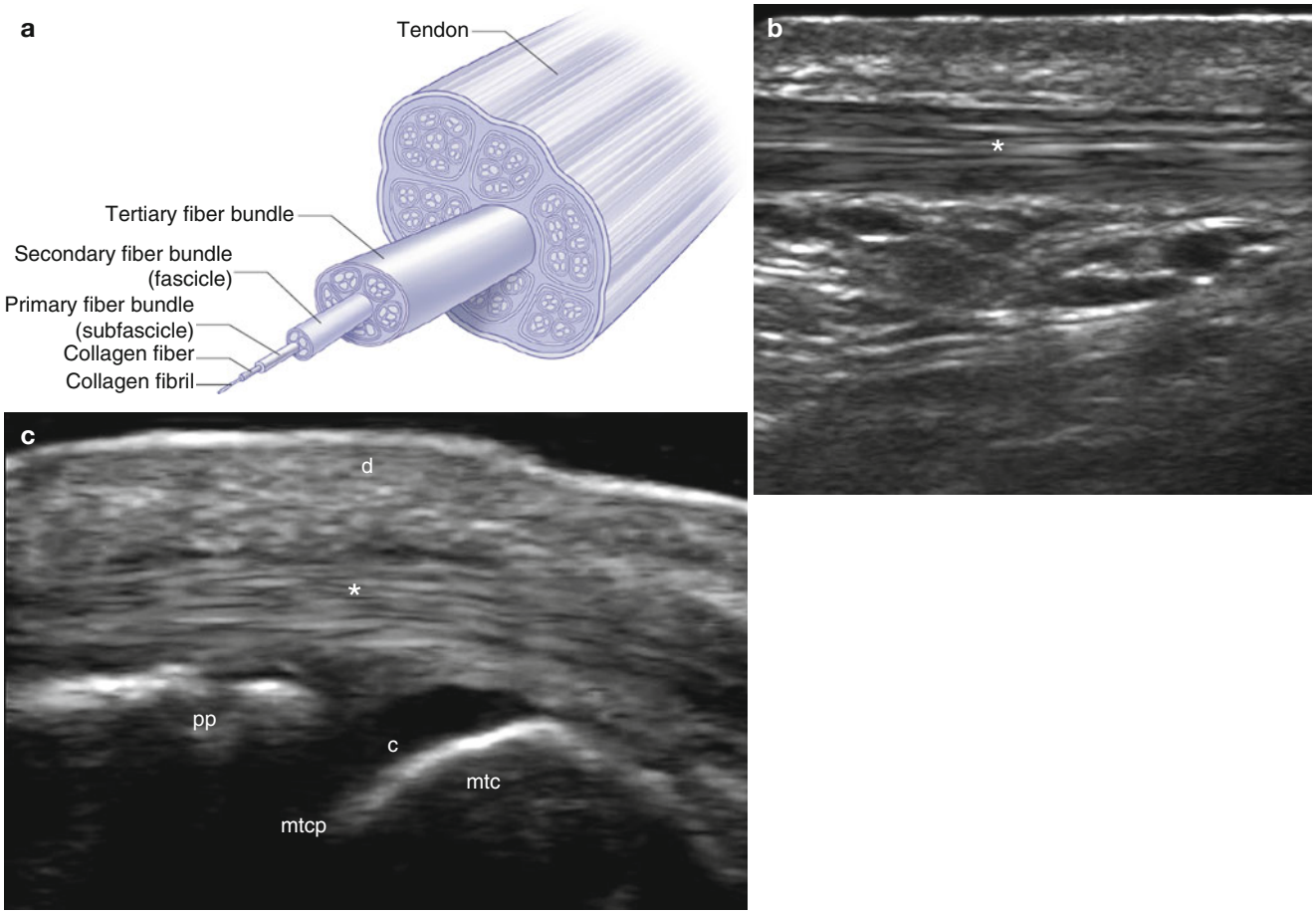

Fig. 2.12 (**a**–**c**) Anatomy of tendons. (**a**) Schematic representation of tendon structure. (**b**) Ultrasound of the anterior tibial tendon (longitudinal view). Note the hyperechoic fibrillar pattern (*). (**c**) Ultrasound of digital flexor tendon (*) at the metacarpophalangeal level in the hand (longitudinal view). *Abbreviations*: *d* dermis, *pp* proximal phalanx, *c* cartilage, *mtc* metacarpal bone, *mtcp* metacarpophalangeal joint

exhibit morphology similar to normal muscles (Fig. 2.14). Dynamic maneuvers may demonstrate the contraction process on short or transverse axis ultrasound, with the muscular belly showing increased anteroposterior size and decreased echogenicity. Common accessory muscles of the upper and lower limbs are listed on Table 2.1. Doubtful cases can be assisted using comparisons with the contralateral side [20].

2.5.4 Cartilage

2.5.4.1 Anatomy

Cartilage is composed of a hydrophilic matrix made of collagen fibers, glycosaminoglycans chondroitin, keratan sulfate, and cells (chondrocytes). According to the proportion of their collagen content, cartilages are classified into fibrocartilage (with high collagen content) and hyaline cartilage (with lower content). Cartilages are devoid of blood vessels and are supplied solely by diffusion from the synovial membrane or bone, and can be involved in locally destructive processes (e.g., Chondrodermatitis helicis of the ear) or systemic autoimmune disease.

2.5.4.2 Sonography

Articular hyaline cartilage appears as a well-defined intensely hypoechoic band adjacent to the hyperechoic bony margin (Fig. 2.15). In contrast, fibrocartilages such as the menisci in the knee or the triangular fibrocartilage in the wrist appear less hypoechoic than the hyaline cartilage with occasional hyperechoic areas reflecting calcium deposits [21].

2.5.5 Bursae

2.5.5.1 Anatomy

Bursae are sac-like structures with viscous fluid content that facilitates the movement of the musculoskeletal structures by reducing friction. Bursae are located superficially in the subcutaneous tissue, as the olecranon bursa in the elbow and the prepatellar bursa in the knee, or have deeper locations such as the subacromiosubdeltoid bursae in the

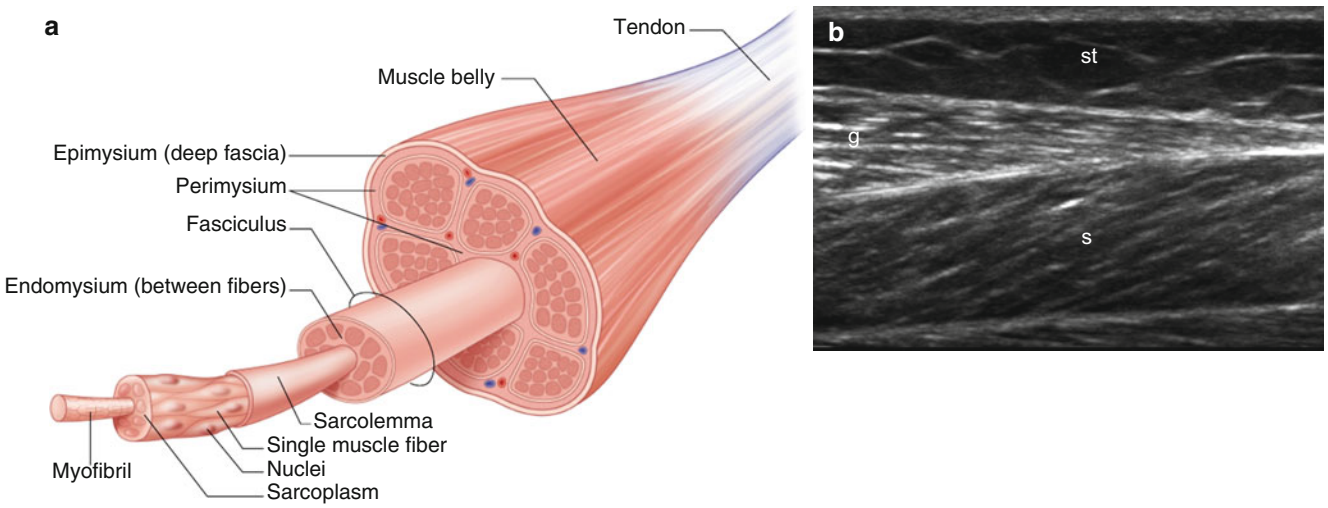

Fig. 2.13 (**a**, **b**) Anatomy of muscle. (**a**) Schematic representation of muscle. (**b**) Ultrasound of calf gastrocnemius muscle (longitudinal view). *Abbreviations*: *st* subcutaneous tissue, *g* gastrocnemius muscle belly, *s* soleous muscle

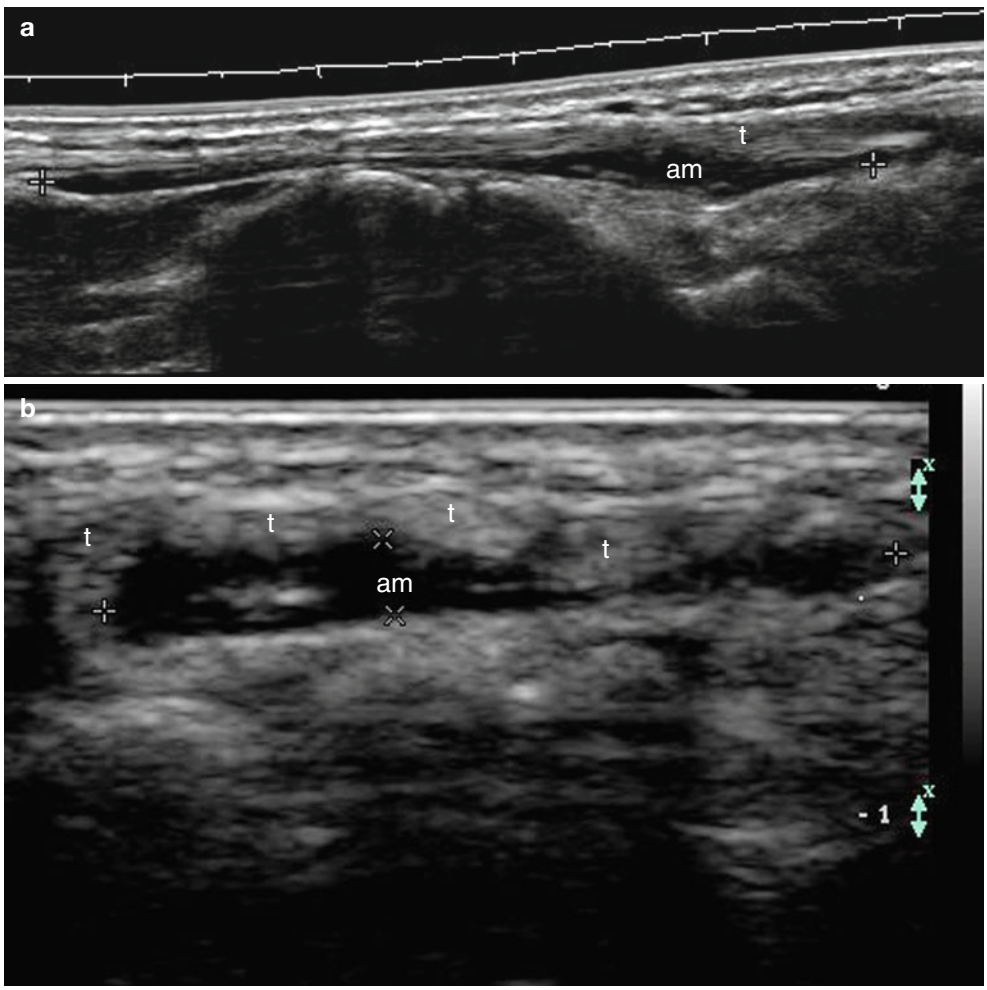

Fig. 2.14 (**a**, **b**) Accessory muscle. (**a**) Ultrasound of the dorsum of the wrist and hand (longitudinal panoramic view). The hypoechoic structure (*am*) attached to the common extensor tendons (*t*) corresponds to an accessory muscle (extensor digitorum brevis manus). (**b**) Ultrasound of the same dorsum of the wrist and hand in transverse view)

Table 2.1 Common limb accessory muscles

Muscle	Location
Chondroepitrocleariis	Arm
Anconeous	Elbow
Anoumalous palmaris longus	Forearm
Lumbrical muscles (proximal origin)	Wrist and hand
Flexor digitorum superficialis of the index finger	Wrist and hand
Abductor digiti minimi	Wrist and hand
Extensor digitorum brevis	Wrist and hand
Tensor fasciae surale	Knee
Accessory soleus	Ankle
Peroneous quartus	Ankle
Accessory flexor digitorum longus	Ankle

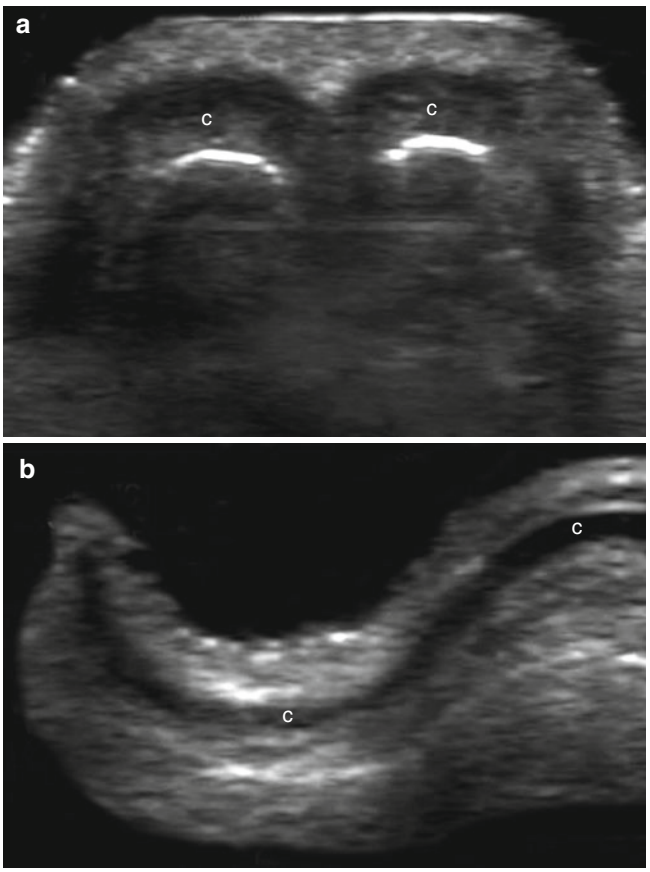

Fig. 2.15 (**a**, **b**) Anatomy of cartilage. (**a**) Ultrasound at the tip of the nose (transverse view). Note hypoechoic nasal cartilages (*c*). (**b**) Ultrasound at the middle third of the ear pinna (transverse view). Note hypoechoic sinuous band of the auricular cartilage (*c*)

shoulder and the gastrocnemius-semimembranous bursae in the knee. They may (for e.g., suprapatellar bursa) or may not (for e.g., infrapatellar bursa) communicate with the joint; bursae may even develop de novo, in response to friction or pressure over bony prominences as in hallux valgus, or exostoses. Under pathological conditions, bursae can undergo marked swelling and become large fluid-filled

Table 2.2 Subcutaneous bursae location

Bursa	Anatomic location
Olecranon	Posterior elbow
Baastrup	Spinous processes
Throcanteric	Hip
Prepatellar	Anterior knee
Infrapatellar	Anterior knee
Tibial tuberosity	Anterior knee
Calcaneal	Posterior ankle (Achilles tendon)

structures (bursitis); common locations of subcutaneous bursitis are shown in Table 2.2 [22].

2.5.5.2 Sonography

Inflamed bursae are commonly detectable using sonography and appearing as anechoic fluid-filled sac-like structures, sometimes surrounded by thick hypoechoic borders. In cases of mild inflammation, a hypoechoic band can be the only sonographic finding (Fig. 2.16).

2.5.6 Blood Vessels

2.5.6.1 Anatomy

Blood vessels are vascular channels that are part of the circulatory system and are separated in arteries, veins, and a capillary endothelial network. In contrast to veins, arteries present a smooth muscle layer, and the course of major blood vessels is well described in the literature. Clinical assessment involves palpation, however, a number of vascular diseases and abnormalities can be described more accurately using sonography.

2.5.6.2 Sonography

Blood vessels are characterized sonographically by their typical tubular shape and anechoic structure; veins usually collapse the lumen when compressed with the probe, while arteries do not collapse to compression. Atheromatosis may produce hypoechoic intimal thickening and, if calcified, may change to hyperechoic sometimes with posterior acoustic shadowing artifact. Phleboliths are calcifications that appear as hyperechoic deposits usually within the veins lumen. Color Doppler spectral curve analysis can readily distinguish arteries from veins; arterial vessels generally show systolic and diastolic peaks, while venous vessels exhibit monophasic tracings (Fig. 2.17).

2.5.6.3 Variant: Caliber Persistent Arteries (CPA)

CPAs are developmental alterations where arterial vessels fail to undergo the normal loss in caliber after penetrating the submucosal space. These anomalous arteries, often found in the lower lip as asymptomatic papules, can be misdiagnosed as malignant skin tumors, or can cause unexpected bleeding

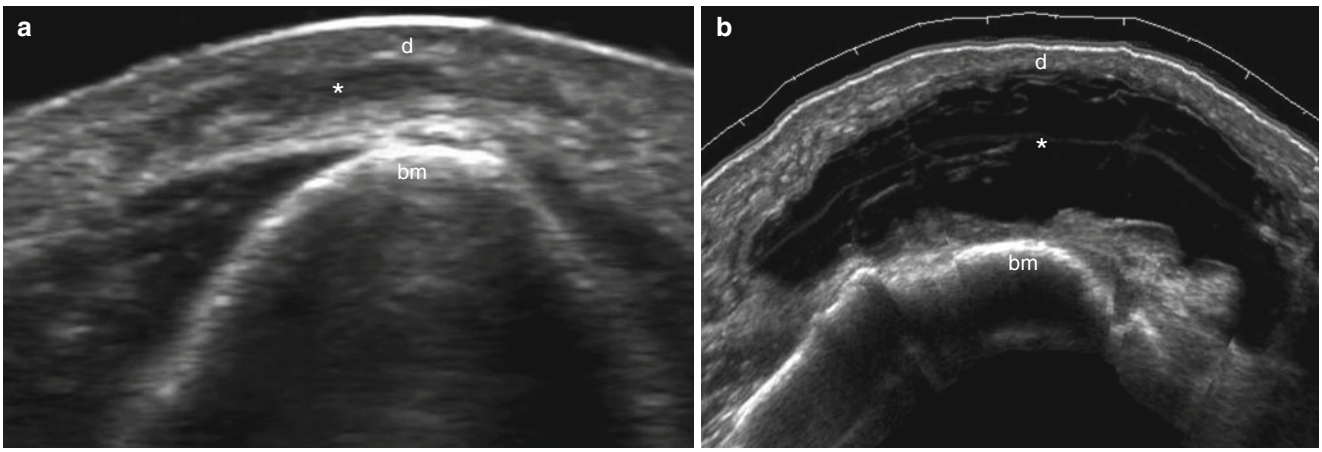

Fig. 2.16 (**a**, **b**) Anatomy of bursae. (**a**) Ultrasound at the tip of the olecranon (transverse view). Note slight hypoechoic thickening of olecranon bursa capsule (*). (**b**) Ultrasound at the posterior elbow (transverse panoramic view). The olecranon bursa is moderately enlarged with anechoic fluid (*). Abbreviations: *d* dermis, *bm* bony margin of the olecranon

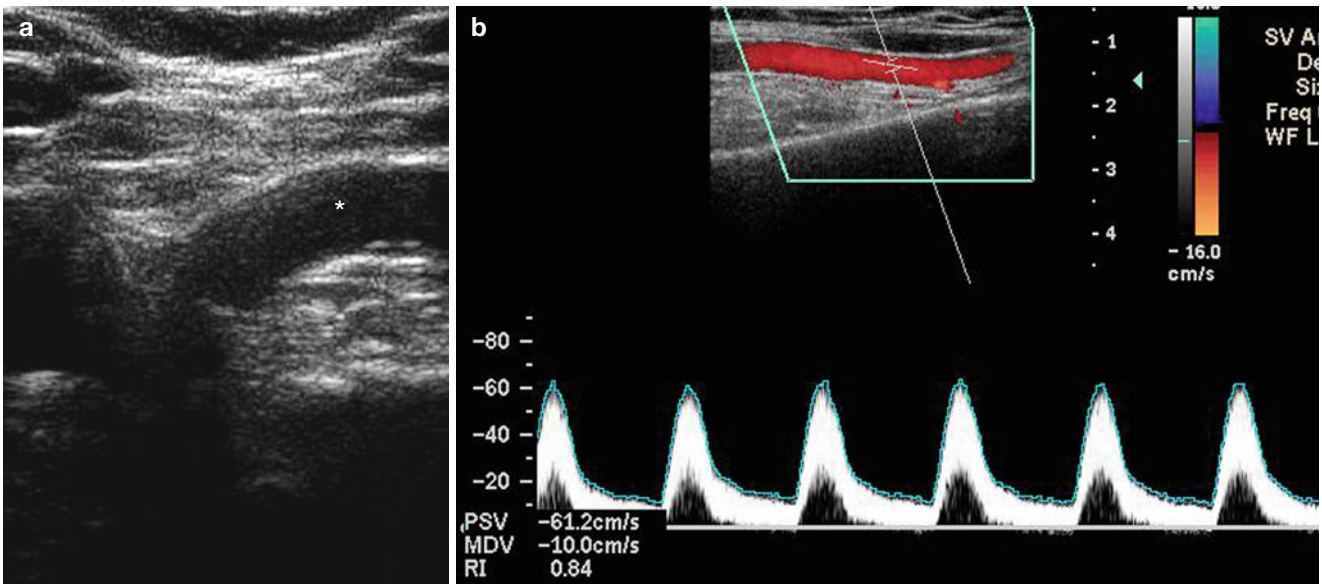

Fig. 2.17 (**a**, **b**) Anatomy of blood vessels. (**a**) Ultrasound at the supraclavicular region (transverse view). The tubular anechoic structure corresponds to the subclavian artery. (**b**) Color Doppler ultrasound with spectral curve analysis of blood flow at the axillary artery; plot of peak systolic velocity is depicted at the bottom

during biopsy or surgical procedures [23, 24]. On sonography, CPA appear as anechoic and often tortuous tubular structures of persistent caliber after entering the dermis of the lips. Color Doppler ultrasound demonstrates arterial pattern of flow within the anomalous vessel (Fig. 2.18).

2.5.7 Nerves

2.5.7.1 Anatomy

Peripheral nerves are made of axons held together by a thin endoneurium (inner layer), grouped into fascicles covered by the perineurium, and gathered into the nerve that is surrounded by the epineurium (outer layer). Nerves can be directly involved in disease, but imaging may also be used in connection with regional nerve blocks.

2.5.7.2 Sonography

Sonography shows nerves as hypoechoic structures with fine fascicular pattern; nerves on the traverse axis may resemble the sonographic appearance of the ovary in shape and echogenicity because they contain numerous hypoechoic dots corresponding to the fascicular disposition (Fig. 2.19). Nerves usually run close to vascular structures, and they are susceptible to suffering entrapment syndromes in selected anatomical locations that commonly involve fibro-osseous

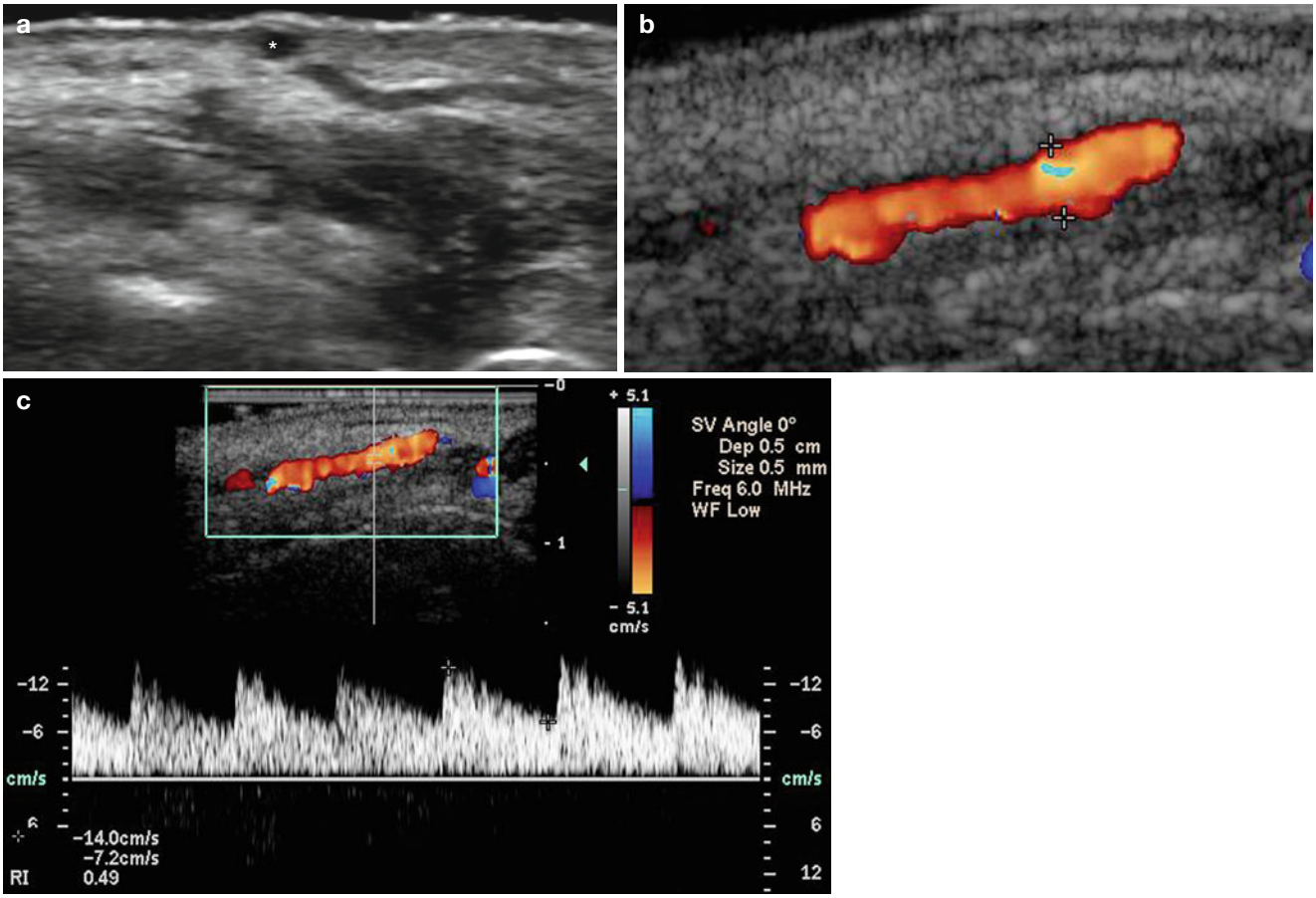

Fig. 2.18 (**a**–**c**) Caliber persistent artery of the lip. (**a**) Ultrasound (gray scale, transverse view) shows an anechoic round shaped nodule (*) in the dermis close to a tubular anechoic tract. (**b**) Color Doppler ultrasound (oblique view) demonstrates flow within the superficial tubular structure that was connected to the anechoic nodule and running superficially located to the orbicularis oris muscle. (**c**) Color Doppler ultrasound spectral curve analysis (oblique view) shows arterial blood flow within the vessel

tunnels such as the carpal or cubital tunnel in the wrist and elbow, respectively.

2.5.7.3 Variant: Bifid Median Nerve and Persistent Median Artery

Occasionally, nerves that normally present as single structures may instead present as two separate branches, a condition called bifid nerve that nevertheless shows similar fascicular echo-structures as single nerves. A common substrate for this anatomic variant is the median nerve that becomes bifid at the wrist, usually associated with a persistent median artery running between the branches; it is present in 15.4 % of healthy individuals and conversely, up to 63 % of the cases of persistent median artery are associated with a bifid median nerve. A unilateral persistent median artery is present in 20 % of normal subjects, and the bilateral form in 6 % of the general population. While the persistent median artery is most commonly seen as a hypoechoic thin fibrous remnant, it occasionally may show blood flow on color Doppler and rarely, vessel widening or even a hypoechoic thrombus within the lumen. Because of its superficial course close to the transverse carpal ligament, it has the potential for being injured during unrelated surgery and a preoperative diagnosis of persistent median artery can be clinically helpful [25–28] (Fig. 2.20).

2.5.8 Salivary Glands

2.5.8.1 Anatomy

Salivary glands are exocrine glands in charge of the secretion of saliva. They are located in proximity to the face and are easily detectable during sonographic examinations. They can be separated into major (parotid and submandibular) and minor salivary glands (oral cavity or lips region)

2.5.8.2 Sonography

The parotid glands are seen in their pre-auricular location in healthy individuals, with a characteristic sonographic hyperechoic parenchyma sometimes containing lymph nodes. Both submandibular glands appear as oval-shaped

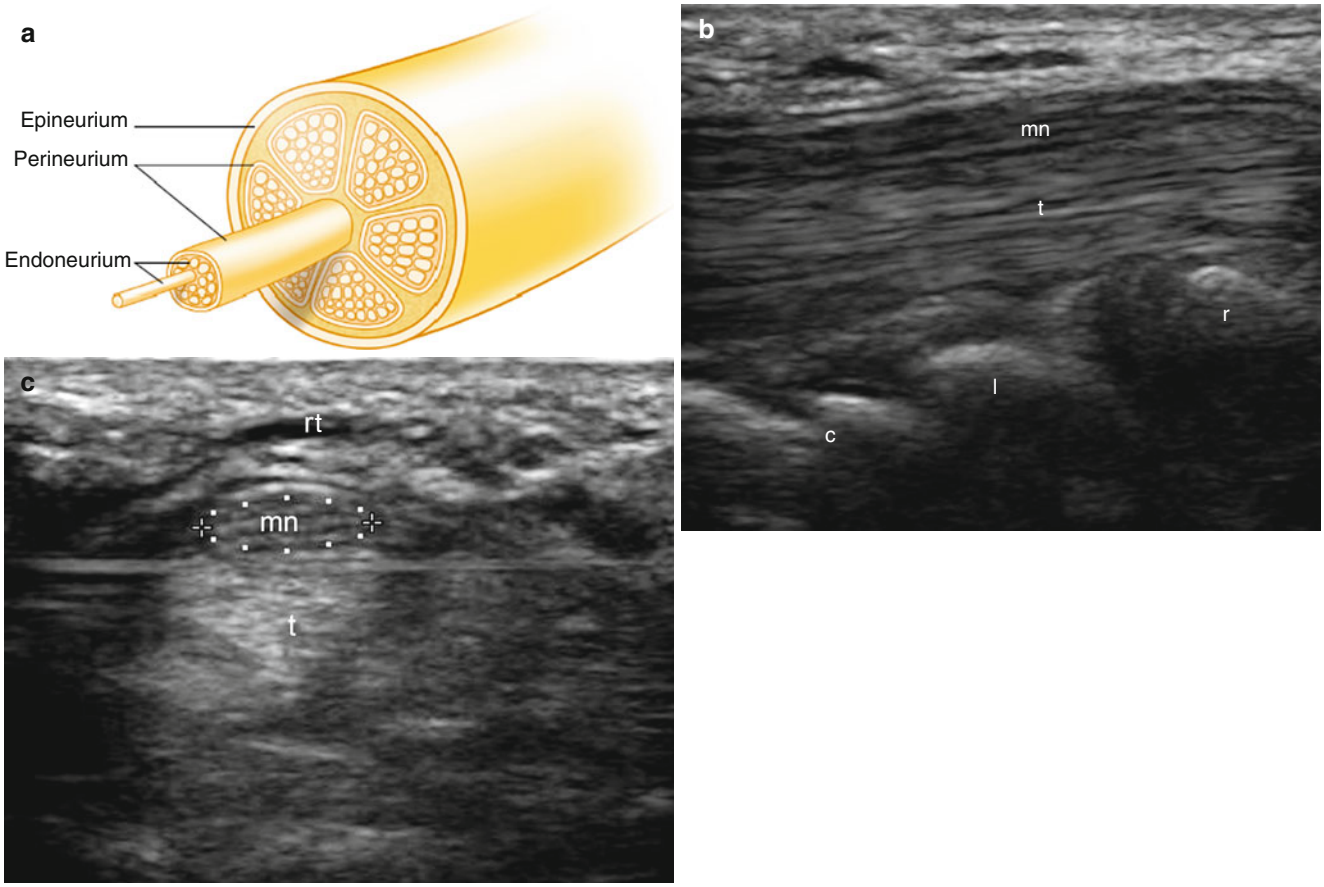

Fig. 2.19 (**a**–**c**) Normal anatomy of the nerve. (**a**) Schematic representation of a nerve. (**b**) Ultrasound of the median nerve at the wrist (longitudinal view). The hypoechoic pattern of the nerve allows easy separation from the hyperechoic tendons (*t*). (**c**) Ultrasound of the median nerve (transverse view) showing characteristic fascicular pattern with hypoechoic dots. *Abbreviations*: *mn* median nerve, *t* flexor tendons, *r* radius, *l* lunate, *c* capitate, *rt* flexor retinaculum

structures, either hyperechoic or slightly hypoechoic. Minor salivary glands appear as round-shaped hypoechoic structures (Fig. 2.21). On color Doppler low-velocity blood flow can be detected in the major glands.

2.5.8.3 Variant: Accessory or Anomalous Salivary Glands

Accessory or anomalous salivary glands are located in an ectopic location and with a well-formed ductal system; in contrast, heterotopic glands that are also in an abnormal location exhibit only rudimentary salivary tissue that consists solely of glandular acini. Accessory parotid glands are common, unilateral or bilateral, usually being found in the cheek, between the main parotid gland and the masseter fascia, immediately above the parotid duct, into where it drains through a tributary duct, and is found at autopsy in 21–56 % of normal adults. The differential diagnosis of the anomalous gland must include an anterior extension or "facial process" of the parotid gland fully connected to the main gland. Accessory parotid glands can occasionally produce facial swelling or asymmetry; they may become a source of complications during cosmetic facial procedures, or become affected by salivary glands tumors (up to 8 % of parotid tumors occur from accessory glands). If considering only malignant salivary gland tumors, the second most common location is the accessory salivary glands with a frequency of 22.6 %, immediately after the parotid glands with a relative frequency of 57.5 % [29–31]. On sonography, accessory glands show similar echostructure but smaller size than the main glands (Fig. 2.22).

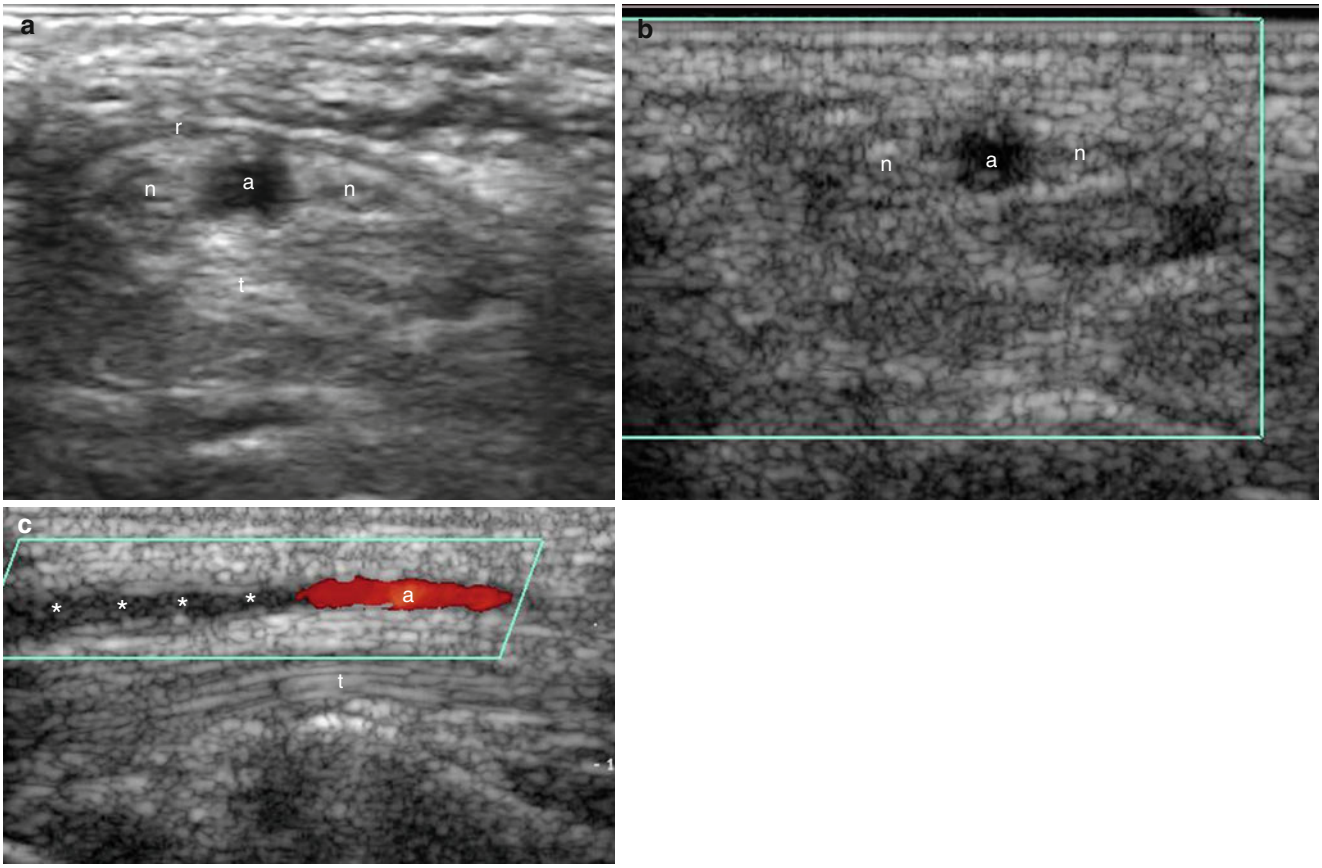

Fig. 2.20 (**a**, **b**) Bifid median nerve and persistent median artery. (**a**) Ultrasound of the wrist (transverse view). Two branches of the median nerve (*n*) are separated by a dilated persistent median artery (*a*). (**b**) Color Doppler ultrasound (longitudinal view) showing the vessel lumen to be partially hypoechoic indicaticating arterial thrombosis (*), with corresponding lack of blood flow signals. The proximal artery segment shows colorful blood flow. *Abbreviations*: *a* persistent median artery, *t* flexor tendons, *r* flexor retinaculum

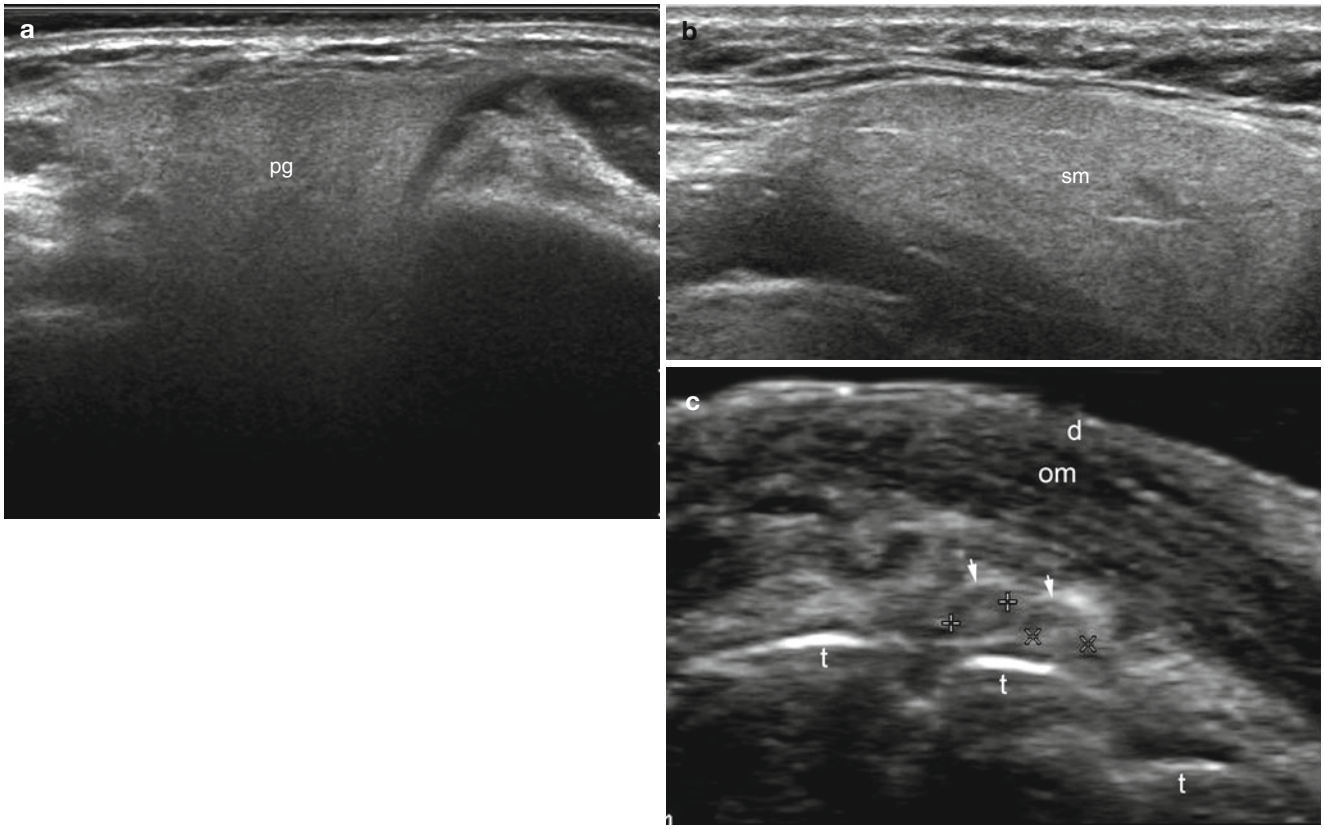

Fig. 2.21 (**a**–**c**) Anatomy of the salivary glands. (**a**) Ultrasound of the parotid gland (transverse view). Note hyperechoic homogenous pattern. (**b**) Ultrasound of the submandibular gland (transverse view) shows homogenous echogenicity and oval shape. (**c**) Ultrasound of the upper lip (transverse view). Minor salivary glands appear as hypoechoic round-shaped structures (*arrows* and between markers). *Abbreviations*: *d* dermis, *om* orbicularis oris muscle, *t* tooth, *pg* parotid gland, *sm* submandibular gland

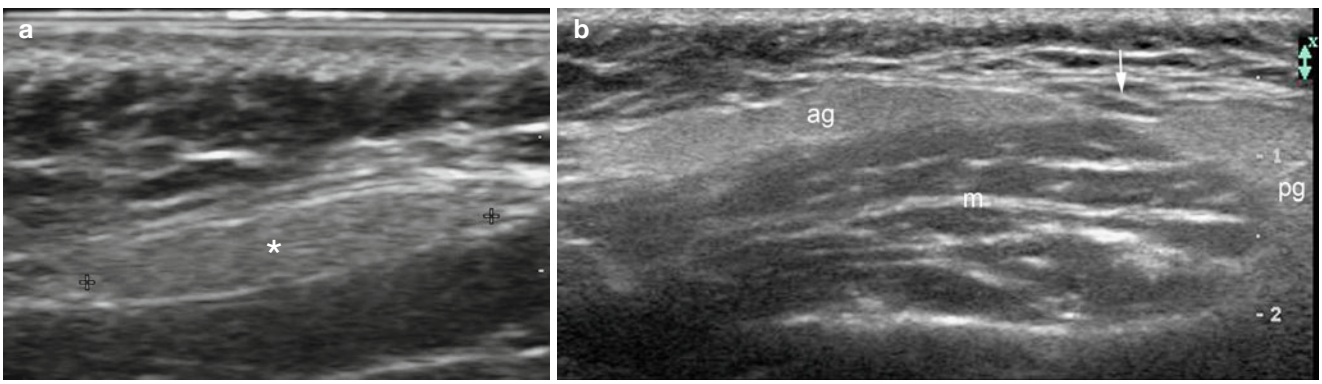

Fig. 2.22 (**a**, **b**) Accessory salivary glands. (**a**) Ultrasound (transverse view) at the right cheek shows hyperechoic oval-shaped and well-defined structure (*, between markers) adjacent to the surface of the masseter muscle. (**b**) Ultrasound in another case (transverse and wider view, left cheek). The accessory salivary gland is close to the masseter muscle, but separated from the parotid gland (*pg*). The separation is marked with an *arrow*

References

1. Proksch E, Brandner JM, Jensen JM. The skin: an indispensable barrier. Exp Dermatol. 2008;17:1063–72.
2. McKee P, Calonje E, Granter S. The structure and function of skin. In: McKee P, Calonje E, Granter S, editors. Pathology of the skin with clinical correlations. Philadelphia: Elsevier/Mosby; 2005. p. 1–36.
3. Ebling FJG, Eady RAJ, Leigh IM. Anatomy and organization of human skin. In: Rook AJ, Wilkinson DS, Ebling FJG, editors. Textbook of dermatology. Oxford: Blackwell Scientific Publications; 1992. p. 49.
4. Wortsman X, Wortsman J. Clinical usefulness of variable frequency ultrasound in localized lesions of the skin. J Am Acad Dermatol. 2010;62:247–56.
5. Farinelli N, Berardesca E. The skin integument: variation relative to sex, age, race, and body region. In: Serup J, Jemec GBE, Grove GL, editors. Handbook of non-invasive methods and the skin. 2nd ed. Boca Raton: Taylor and Francis; 2006. p. 27–31.
6. Wortsman XC, Holm EA, Wulf HC, Jemec GB. Real-time spatial compound ultrasound imaging of skin. Skin Res Technol. 2004; 10:23–31.
7. Kanitakis J. Anatomy, histology and immunohistochemistry of normal human skin. Eur J Dermatol. 2002;12:390–9.
8. Burns DA, Breathnach SM, Cox N, Griffiths CE, editors. Rook's textbook of dermatology. 7th ed. Malden: Blackwell Science; 2004. p. 3.1–3.84.
9. Gniadecka M, Gniadecki R, Serup J, Søndergaard J. Ultrasound structure and digital image analysis of the subepidermal low echogenic band in aged human skin: diurnal changes and interindividual variability. J Invest Dermatol. 1994;102:362–5.
10. Ackerman AB. Panniculitis. In: Ackerman AB, editor. Histopathologic diagnosis of inflammatory skin diseases. Philadelphia: Lea & Febiger; 1978. p. 779–825.
11. Segura S, Requena L. Anatomy and histology of normal subcutaneous fat, necrosis of adipocytes, and classification of the panniculitides. Dermatol Clin. 2008;26:419–24.
12. Requena L. Normal subcutaneous fat, necrosis of adipocytes and classification of the panniculitides. Semin Cutan Med Surg. 2007;26:66–70.
13. de Berker D, Baran R. Science of the nail apparatus. In: Baran R, de Berker D, Holzberg M, Thomas L, editors. Baran & Dawber diseases of the nails and their management. 4th ed. Oxford: Wiley-Blackwell; 2012. p. 1–50.
14. Wortsman X, Wortsman J, Soto R, Saavedra T, Honeyman J, Sazunic I, et al. Benign tumors and pseudotumors of the nail: a novel application of sonography. J Ultrasound Med. 2010;29: 803–16.
15. Amirlak B, Shahabi L, Campbell AC, Totonchi A, Soltanian H. Skin anatomy. Medscape. http://emedicine.medscape.com/article/1294744-overview#showall
16. Schneider MR, Schmidt-Ullrich R, Paus R. The hair follicle as a dynamic miniorgan. Curr Biol. 2009;19:R132–42.
17. Wortsman X, Wortsman J, Matsuoka L, Saavedra T, Mardones F, Saavedra D, et al. Sonography in pathologies of scalp and hair. Br J Radiol. 2012;85:647–55.
18. Van Holsbeeck M, Introcaso J. Sonography of tendons. In: Van Holsbeeck M, Introcaso J, editors. Musculoskeletal ultrasound. 2nd ed. St. Louis: Mosby; 2001. p. 77–129.
19. Van Holsbeeck M, Introcaso J. Sonography of muscle. In: Van Holsbeeck M, Introcaso J, editors. Musculoskeletal ultrasound. 2nd ed. St. Louis: Mosby; 2001. p. 23–75.
20. Wortsman X, Azocar P. Wrist ultrasound. In: Dogra V, Gaitini D, editors. Musculoskeletal ultrasound with CT and MRI correlation. 1st ed. New York/Stuttgart: Thieme; 2010. p. 46–70.
21. Wortsman X, Jemec GB. Sonography of the ear pinna. J Ultrasound Med. 2008;27:761–70.
22. Van Holsbeeck M, Introcaso J. Sonography of bursae. In: Van Holsbeeck M, Introcaso J, editors. Musculoskeletal ultrasound. 2nd ed. St. Louis: Mosby; 2001. p. 131–69.
23. Wortsman X, Calderón P, Arellano J, Orellana Y. High-resolution color Doppler ultrasound of a caliber-persistent artery of the lip, a simulator variant of dermatologic disease: case report and sonographic findings. Int J Dermatol. 2009;48:830–3.
24. Arellano J, Antoniazzi C, Wortsman X. Early diagnosis of a calibre persistent labial artery in a child: usefulness of ultrasonography. Australas J Dermatol. 2012;53:e18–9.
25. Granata G, Caliandro P, Pazzaglia C, Minciotti I, Russo G, Martinoli C, et al. Prevalence of bifid median nerve at wrist assessed through ultrasound. Neurol Sci. 2011;32:615–8.
26. Gassner EM, Schocke M, Peer S, Schwabegger A, Jaschke W, Bodner G. Persistent median artery in the carpal tunnel: color Doppler ultrasonographic findings. J Ultrasound Med. 2002;21:455–61.
27. Propeck T, Quinn TJ, Jacobson JA, Paulino AF, Habra G, Darian VB. Sonography and MR imaging of bifid median nerve with anatomic and histologic correlation. AJR Am J Roentgenol. 2000; 175:1721–5.
28. Iannicelli E, Chianta GA, Salvini V, Almberger M, Monacelli G, Passariello R. Evaluation of bifid median nerve with sonography and MR imaging. J Ultrasound Med. 2000;19:481–5.
29. Ostman J, Anneroth G, Gustafsson H, Tavelin B. Malignant salivary gland tumours in Sweden 1960–1989 – an epidemiological study. Oral Oncol. 1997;33:169–76.
30. Ito FA, Ito K, Vargas PA, de Almeida OP, Lopes MA. Salivary gland tumors in a Brazilian population: a retrospective study of 496 cases. Int J Oral Maxillofac Surg. 2005;34:533–6.
31. Cunnane M, Artz G. Histology epithelial metaplasias and non inflammatory and non neoplastic lesions of the salivary glands. In: Lee Witt R, editor. Salivary glands diseases: surgical and medical management. New York: Thieme; 2006. p. 50.

Part II

Clinical Applications

Congenital Diseases of the Skin

3

Ximena Wortsman, Jacobo Wortsman,
and Ligia Aranibar

Common congenital conditions that may challenge the diagnoses or follow ups

Contents

3.1 Introduction

Congenital disorders of the cutaneous layers and appendages are most often hereditary and are associated with extracutaneous alterations, as components of complex syndromes, and are expressed clinically at birth or early infancy; once the linkage to specific gene mutations has been established, the disorders are classified as "genodermatoses" [1]. Developmental alterations of the skin generally exhibit marked pleomorphism, affecting single or multiple body segments, with dermatome(s) restrictions characteristic for some disorders [2]. Because multi-structural involvement is common and can be non-discernable clinically on imaging studies, ultrasound may become particularly essential for both diagnosis and follow-up of these patients.

X. Wortsman, MD (✉)
Department of Radiology and Dermatology,
Institute for Diagnostic Imaging and Research of
the Skin and Soft Tissues, Clinica Servet,
University of Chile, Faculty of Medicine,
Almirante Pastene 150, Providencia, Santiago, Chile
e-mail: xwo@tie.cl, xworts@yahoo.com, www.sonoskin.com

J. Wortsman, MD
Department of Medicine,
Southern Illinois University School of Medicine,
3128 Temple Drive, Springfield, IL 62704, USA

L. Aranibar, MD
Department of Dermatology,
Hospital Clínico Universidad de Chile,
Faculty of Medicine, University of Chile,
Santos Dumont 999, Santiago 8380456, Chile
e-mail: liaranibar@gmail.com

X. Wortsman, G.B.E. Jemec (eds.), *Dermatologic Ultrasound with Clinical and Histologic Correlations*,
DOI 10.1007/978-1-4614-7184-4_3,

3.2 Pathology

3.2.1 Pits, Fistulae, and Sinus

These congenital malformations of the head and neck result from the failure to close of the first and second branchial arches that form the external ear canal; inheritance is autosomal dominant incomplete, with low penetrance and variable expression [1]. Defective arch closure results in the formation of unilateral or bilateral pits, sinuses, or fistulae in front of the pinna, varying in size from small dimples (preauricular pits) to large and deep lesions (sinuses or fistulae). Sonography of the skin, in addition to determining the lesion relationships to regional anatomic landmarks (superficial temporal artery, anterior crus of the helix or tragus), can accurately assess lesion extension delineating sinusal tracts that show as hypoechoic structures with occasionally inner echoes from debris and peri-lesional increases in vascularity.

Clinically, preauricular pits present as shallow invaginations on the skin anterior to the border of the crus of the helix (auricular cartilage) that may chronically discharge foul-smelling cheesy desquamated keratin debris. Preauricular fistulae or sinuses are deeper than the pit and lined by stratified squamous keratinizing epithelium; they may present with recurrent swelling from episodes of infection and purulent discharge. When the preauricular sinus opening is occluded, the sinusal cavity becomes dilated and turns into a cyst. Approximately 3–10 % of preauricular sinuses are manifestations of complex disorders, in particular, deafness and branchio-oto-renal (BOR) syndrome; thus, auditory testing and renal ultrasound should be considered at the time of diagnosis. While surgery is the preferred treatment, patients without pre-surgical ultrasound have recurrence rates of 9–42 %; in contrast, pre-operative planning that includes ultrasound has not been associated with reports of recurrences [2–4] (Figs. 3.1 and 3.2).

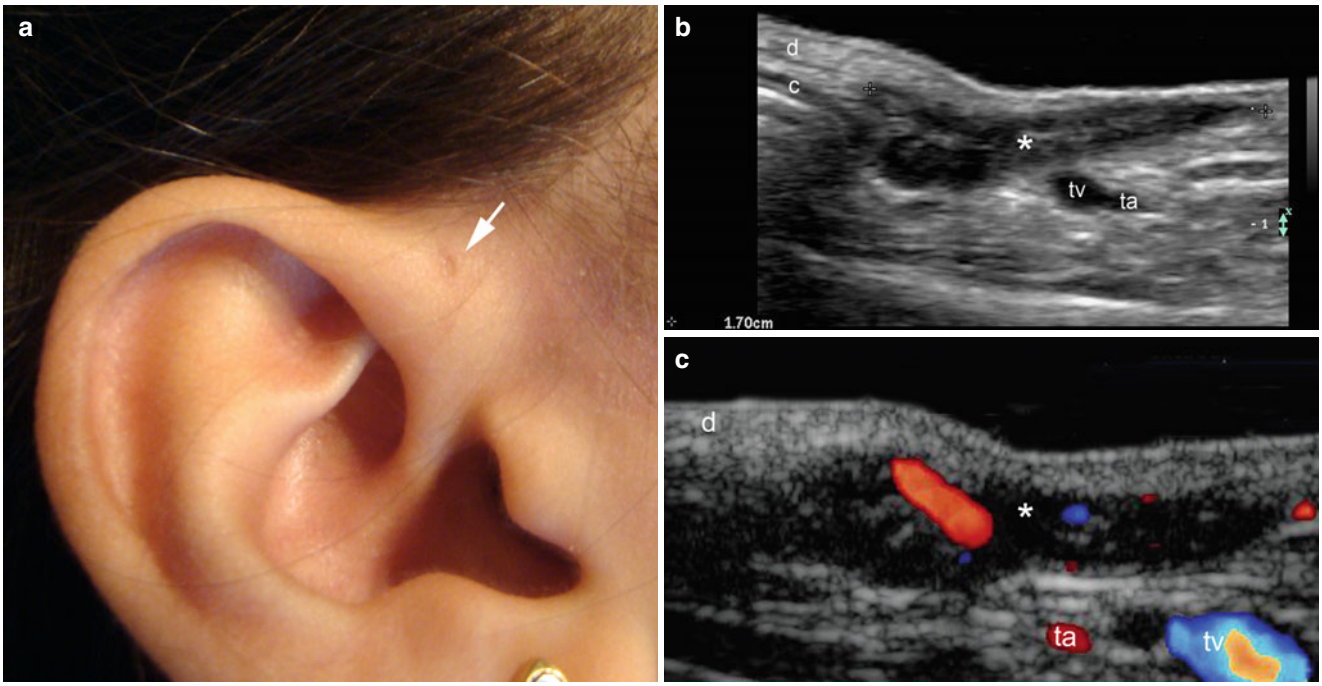

Fig. 3.1 (**a**–**c**) Preauricular sinus. (**a**) Clinical image shows a small dimple in the right pre-auricular region (*arrow*). (**b**) Ultrasound image (gray scale, transverse view) demonstrates 1.7 cm long hypoechoic sinus tract (*) located superficial to the temporal vessels and closely attached to the anterior aspect of the cartilage of the pinna (c). (**c**). Color Doppler ultrasound image (transverse view, higher level) shows vascularity in the periphery of the sinus tract (*) and also the temporal artery and vein in the vicinity. *Abbreviation*: *d* dermis, *ta* temporal artery, *tv* temporal vein

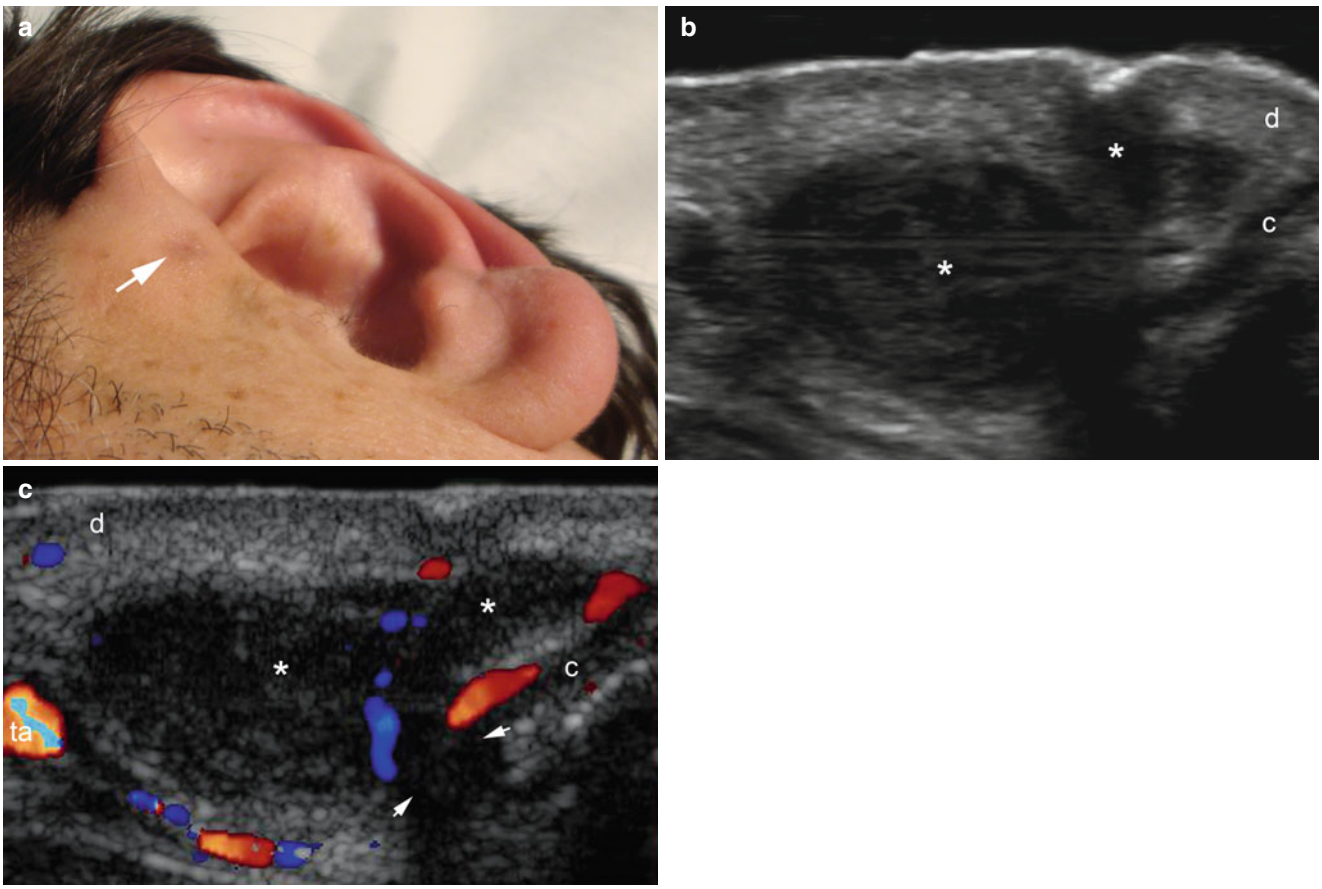

Fig. 3.2 (**a**–**c**) Dilated preauricular sinus. (**a**) Clinical image shows a small pit in the left pre-auricular region. (**b**) Ultrasound image (gray scale, transverse view) demonstrates dilated hypoechoic sinus tract (*) attached to the anterior aspect of the cartilage. (**c**) Color Doppler ultrasound image (transverse view) shows increased blood flow in the periphery of the sinus (*) and partial involvement (interruption, *arrows*) of the cartilage. *Abbreviations*: *d* dermis, *c* cartilage, *ta* temporal artery

3.2.2 Cysts

3.2.2.1 Branchial Clefts or Cysts

Brachial clefts or cysts are also the result of improper closure of branchial archs (most commonly the second arch), appearing as lesions in the upper neck, usually along the sternocleidomastoideus muscle. When presenting as cystic formations, they can drain externally or internally to the pharynx [4]. In most cases the sonographic appearance is that of well-defined cysts with wall thicknesses that range from almost imperceptible to very thick. Most commonly, cysts are anechoic and unilocular; hypoechoic forms with internal echoes or even hyperechoic with a pseudosolid appearance have also been described, and a multiloculated appearance with septations may occasionally be seen. The posterior acoustic enhancement typical of cystic entities is detected in up to 70 % of the lesions. Branchial clefts or tracts, usually seen as hypoechoic tortuous bands, can be connected to a cyst with or without debris, or septations [5, 6] (Fig. 3.3).

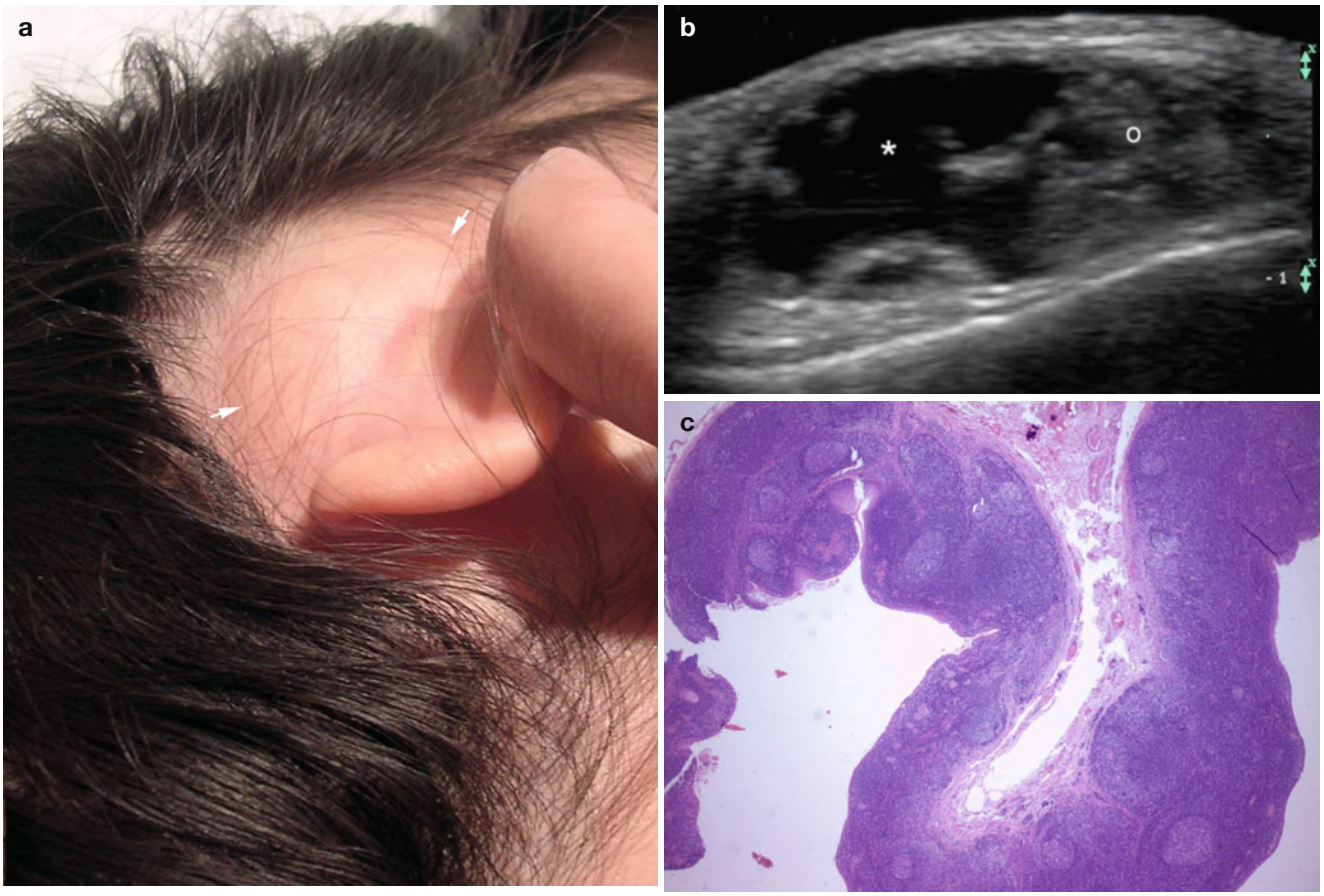

Fig. 3.3 (**a**–**c**) Branchial cyst. (**a**) Clinical image shows a lump (*arrows*) in the right retroauricular region. (**b**) Ultrasound image (gray scale, longitudinal view) demonstrates large anechoic cystic structure (*, *arrows*) with thick hypoechoic walls (o) located in the subcutaneous tissue. (**c**) Histology (HE zoom × 40 courtesy of Dr. Laura Carreño) shows a cystic cavity surrounded by stroma and epithelium with a rich lymphocytic component that conforms follicular nodules with germinal centers

3.2.2.2 Thyroglossal Cysts or Ducts

Thyroglossal cyst or duct anomalies result from defective migration of thyroid tissue from the base of the tongue to the anterior-lower neck, and may present as localized swelling in children or young adults. Cyst locations range from the tongue and submandibular regions to the suprahyoid area, hyoid bone, or infrahyoid region. On sonograms, thyroglossal cysts are well-circumscribed round or oval-shaped structures in the anterior neck close to the midline, most commonly anechoic, but hypoechoic; mixed patterns can also be seen. Most cysts have thin walls and show posterior acoustic enhancement; debris content noted occasionally represents proteinaceous secretion by the epithelial lining [7–9] (Fig. 3.4).

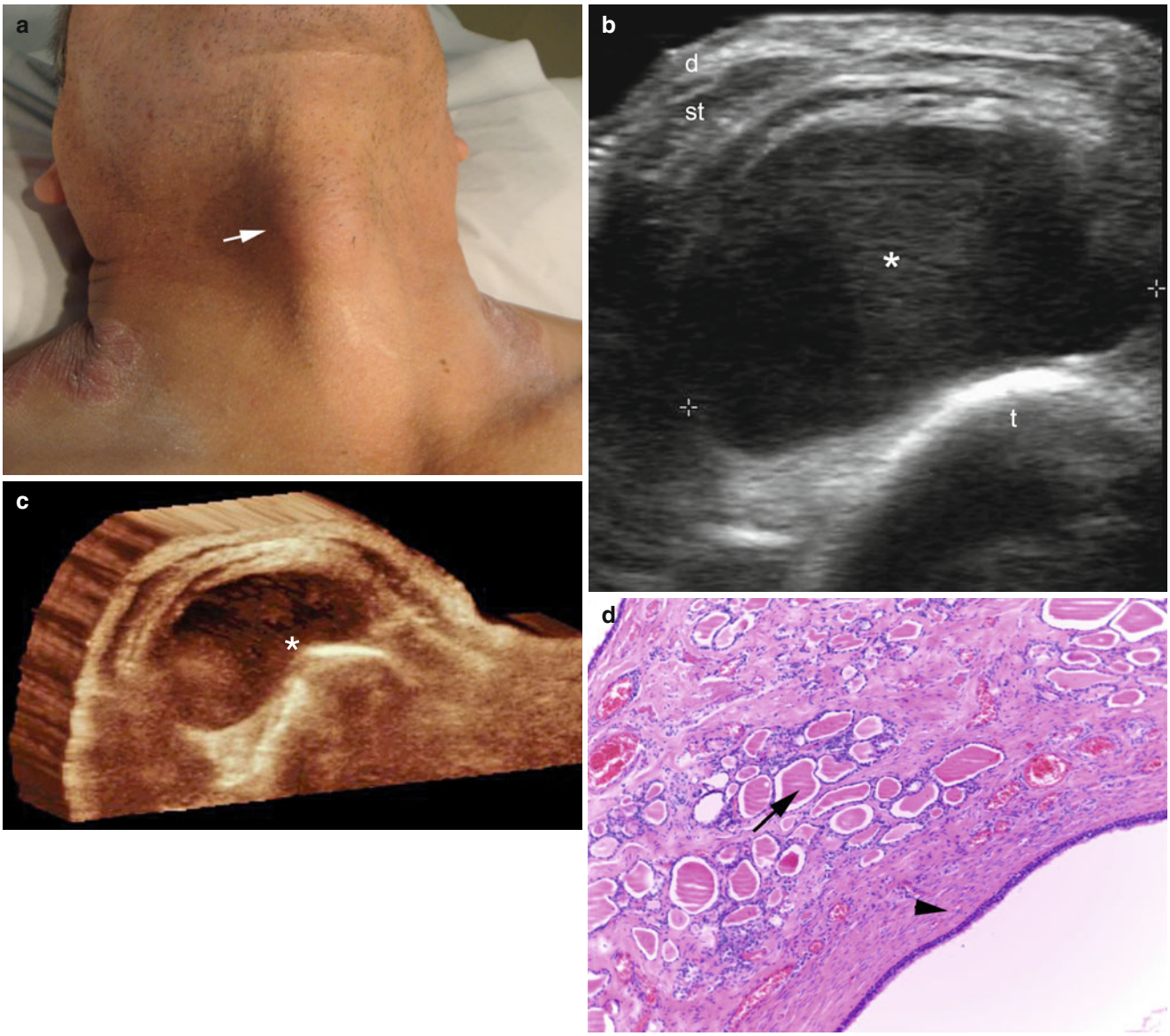

Fig. 3.4 (**a**–**d**) Thyroglossal cyst. (**a**) Clinical image shows a bump in the anterior aspect of the neck in a psoriatic patient. (**b**) Ultrasound image (gray scale, transverse view) demonstrates a well-defined *oval-shaped* anechoic structure (*, between markers) attached to the anterior aspect of the trachea close to the midline of the neck. (**c**) 3D ultrasound image (transverse view) of the same lesion (*). (**d**) Histology (HE zoom × 100 courtesy of Dr. Claudia Morales) shows the wall of the cyst composed by a layer of cylindrical ciliary epithelium (*arrowhead*), thyroid follicles (*arrow*) and fibrous stroma. *Abbreviations*: *d* dermis, *st* subcutaneous, *t* trachea

3.2.2.3 Broncogenic Cysts

Broncogenic cysts are cutaneous sequestrations of the respiratory epithelium and present as mostly asymptomatic solitary nodules; malignant transformation is exceptional, and sometimes they have connecting tracts to the epidermis that drain mucoid secretion. Broncogenic cysts are usually located in the supraesternal region, and rarely in the lateral neck or even the scapular region. On sonograms, the lesions are thick-walled, round- or oval- shaped, anechoic, or hypoechoic lesions. When the lesions become inflamed, vascularity can be increased at the periphery of the cysts [10–12] (Fig. 3.5).

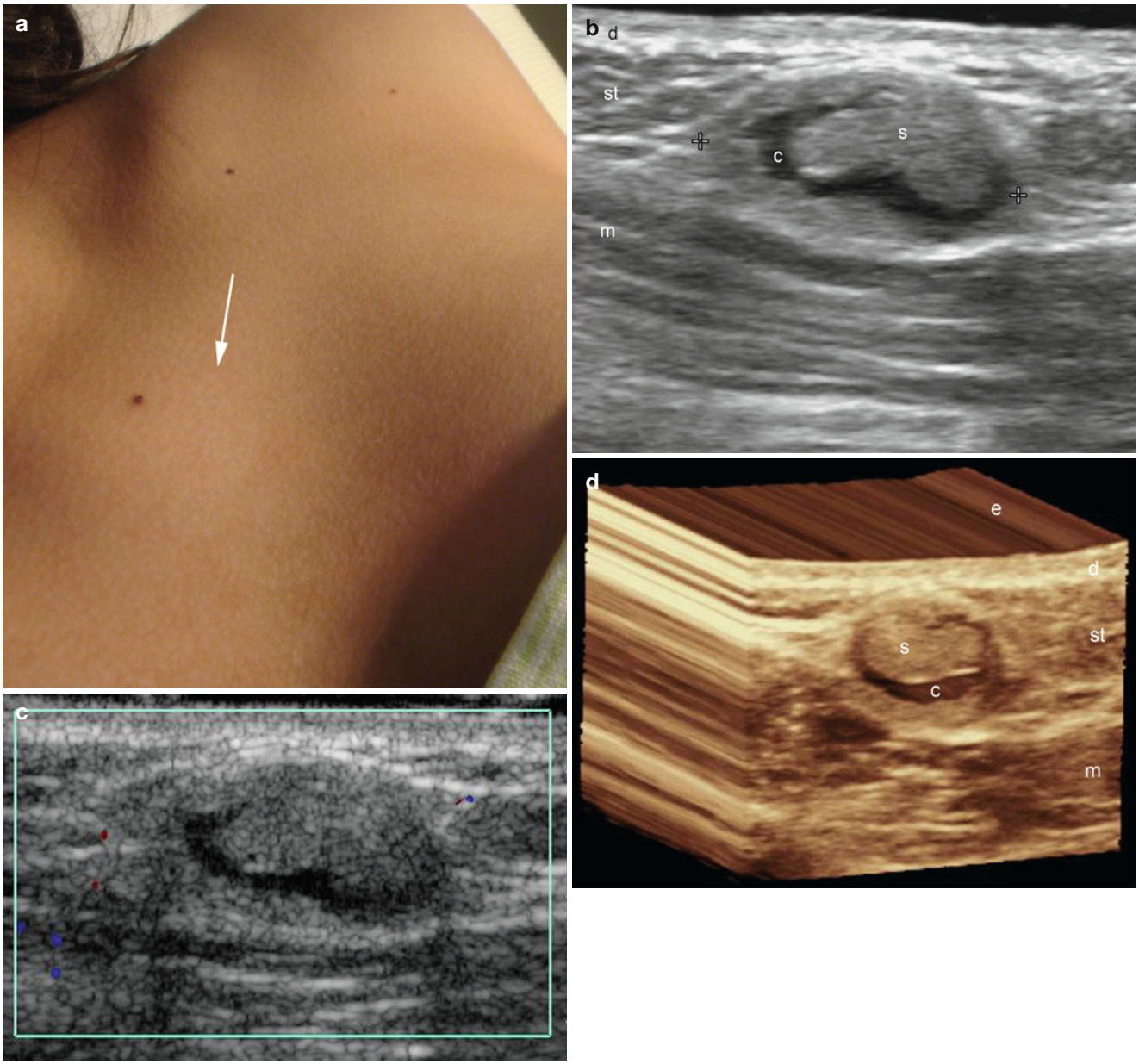

Fig. 3.5 (**a**–**d**) Broncogenic cyst. (**a**) Clinical image of the patient that presents a palpable lump in the sternal region (*arrow*). (**b**) Ultrasound image (gray scale, transverse view) shows oval shaped solid-cystic structure (between markers) in the subcutaneous tissue. The anechoic band corresponds to the cystic area and the hypoechoic region with the solid component. (**c**) Color Doppler ultrasound image (transverse view) demonstrates tiny vessels in the periphery and no detectable vascularity within the mass. (**d**) 3D reconstruction ultrasound image (transverse view) of the broncogenic cyst. *Abbreviations*: *e* epidermis, *d* dermis, *st* subcutaneous tissue, *m* muscle, *c* cystic, *s* solid

3.2.2.4 Dermoid Cysts

Dermoid cysts are typically found along the skull bone fusion lines (e.g., anterior fontanel, lateral frontal region, tail of the eyebrow, or submandibular region) presenting as non-tender and firm nodules, with sometimes bluish discoloration of the covering skin. Imaging studies are mandatory in dermoid cysts of the midline (nose, occipital region, or vertebral spine) to exclude the presence of tracts connecting to the central nervous system. At ultrasound examination the cysts are round or oval-shaped, anechoic, or of mixed echogenicity (anechoic- hypoechoic) sometimes with thick walls and with increased vascularity at the periphery when inflamed (Figs. 3.6 and 3.7). At times, floating bodies can appear in the cystic fluid that represent hypoechoic fat lobules, also called the "sac-of- marble" sign. Calcium deposits can also be found within dermoid cysts and show as hyperechoic deposits with fluidic movements upon compression [13–15].

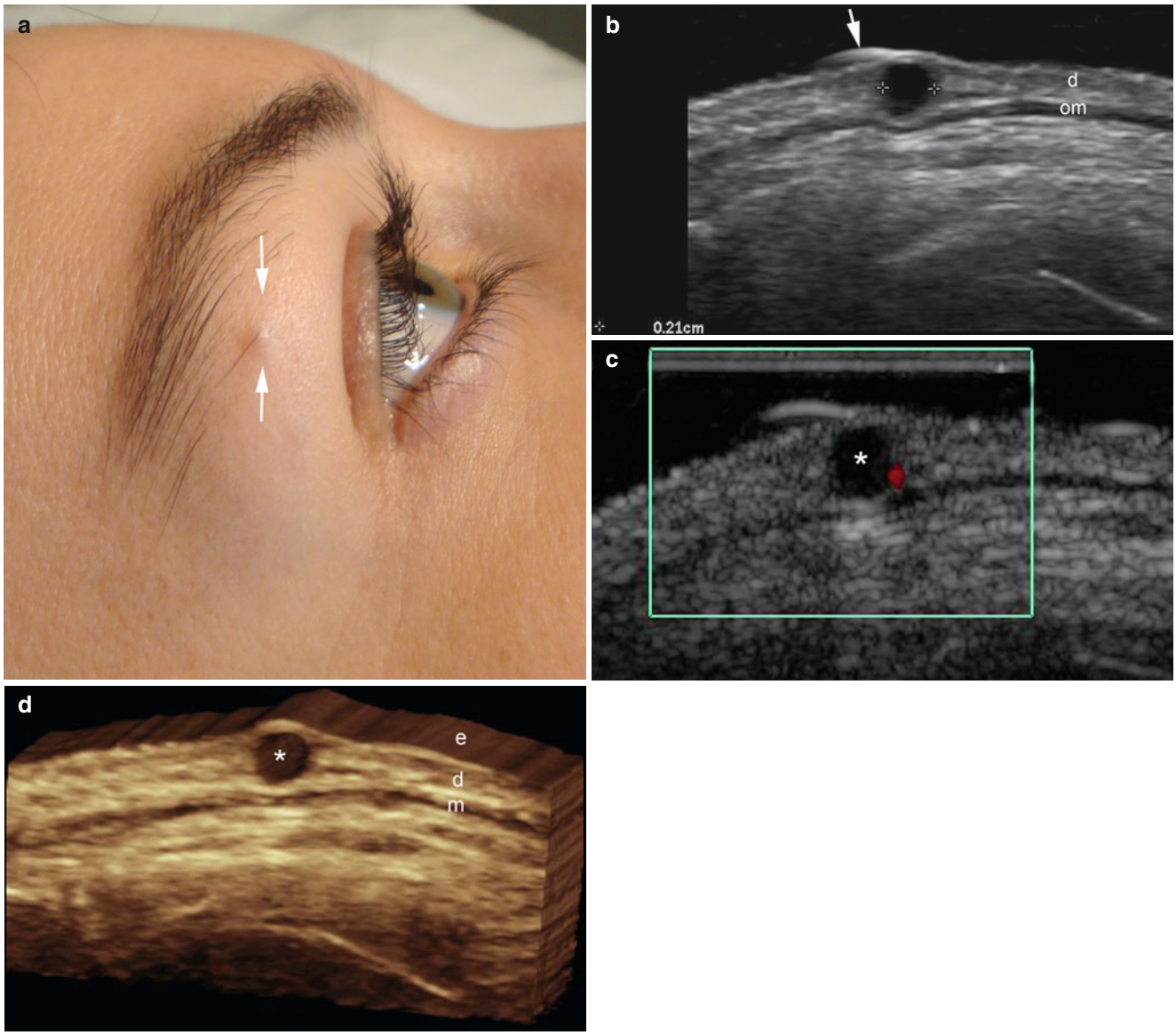

Fig. 3.6 (**a**–**d**) Small dermoid cyst. (**a**) Clinical image shows a tiny nodule in the right ciliar region. (**b**) Ultrasound image (transverse view) demonstrates a 2.1 mm well defined *round-shaped* anechoic cyst (between markers). Notice the hyperechoic line (*arrow*) on top of the cyst that corresponds to the hair tract also visible in the clinical image. (**c**) Color Doppler ultrasound image shows a small vessel in the periphery and no vascularity within the cyst. (**d**) 3D reconstruction of the cyst (*). *Abbreviations*: *e* epidermis, *d* dermis, *om* and *m* orbicular muscle of the eyelid

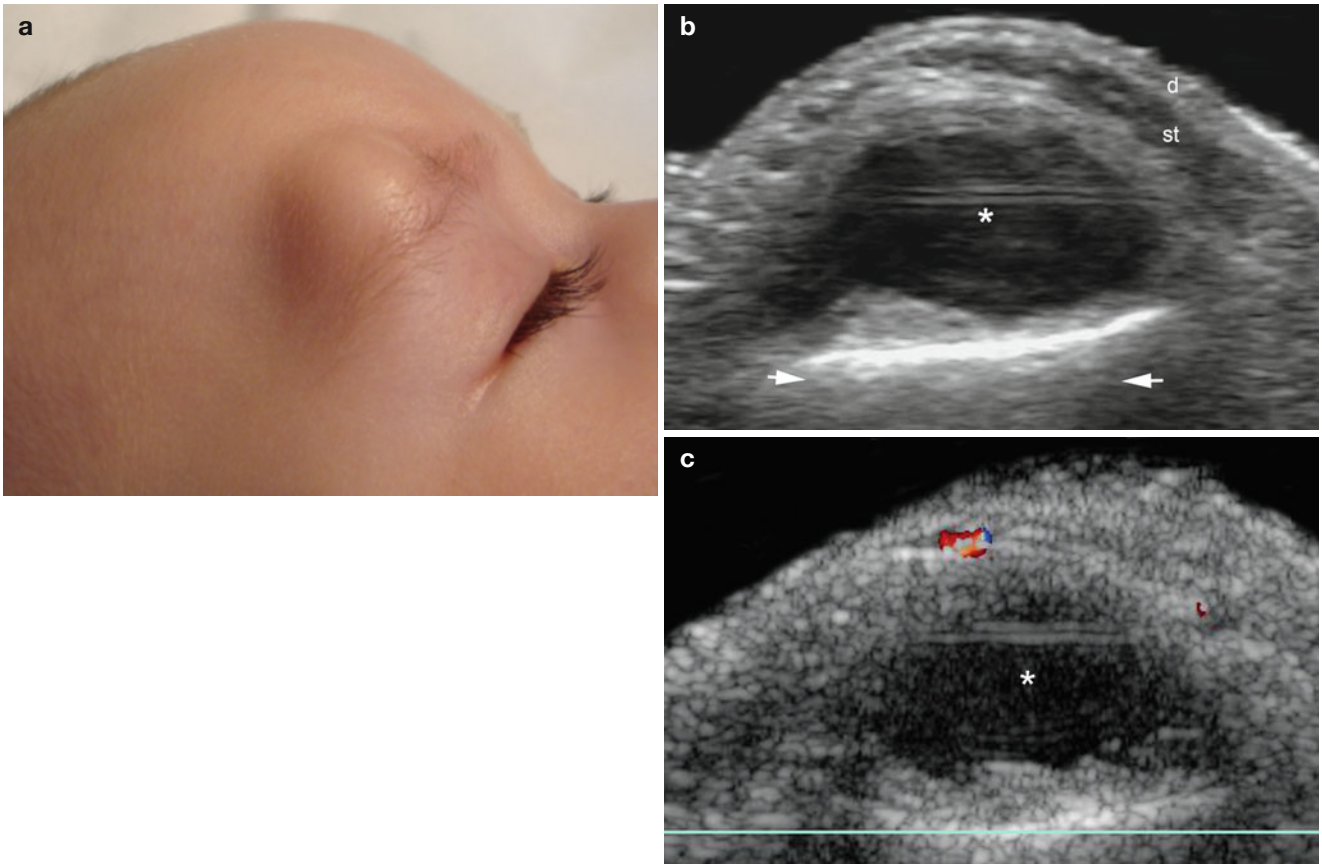

Fig. 3.7 (**a**–**c**) Large dermoid cyst. (**a**) Clinical image shows a swelling in the right ciliar region. (**b**) Ultrasound image (gray scale, transverse view) demonstrates well-defined *oval-shaped* anechoic cystic structure (*) that produces posterior acoustic enhancement artifact (*arrow*). (**c**) Color Doppler ultrasound image shows no vascularity within the cyst and scarce vascularity in the periphery

3.2.3 Hemangiomas of Infancy and Congenital Hemangiomas

Hemangiomas of infancy or common hemangiomas, the most frequent tumors found in infants, appear shortly after birth and go through an active growth phase over the first 2 years, ending in a slowly evolving involutional phase. Hemangiomas consist of localized endothelial proliferations in superficial or deep skin layers that can be highly localized segment-restricted tumors, or distributed through multiple locations. Hemangiomas are sometimes manifestations of dysmorphic conditions, such as in PHACES syndrome (posterior fossa malformations, hemangiomas of the cervicofacial region, arterial anomalies, cardiac anomalies, eye anomalies, and occasionally, sternal defects). The most common brain abnormality associated with PHACES is the Dandy–Walker malformation (of the cerebellar vermis), although hemangioma-associated anomalies may affect all the major cerebral arteries; coarctation of the transverse aorta in the great vessels is the most common arterial anomaly, and congenital heart defects, optic nerve hypoplasia, and abnormal retinal vessels have been also described. Complications of hemangiomas of infancy include ulceration, bleeding, infection, and scarring [16, 17].

The term "congenital hemangioma" was introduced to denote other less common types of hemangiomas that attain maximal size at birth without further postnatal growth. These tumors are classified according to their postnatal evolution into RICH (rapidly involuting congenital hemangiomas) and NICH (non-involuting congenital hemangiomas). RICH are more common, with the majority disappearing completely by the age of 12 months; NICH display a pattern of growth proportional to the physical growth and require eventual excision. RICH and NICH test negative for the endothelial tissue marker glucose transporter-1 protein, also called GLUT-1. This differs from the common hemangioma of infancy that tests positive for the same marker. RICH and NICH generally present clinically as large masses in the head or near a joint in the limbs with violaceous discoloration, prominent venous vessels, and telangiectasias [17, 18]. On histology, RICH are composed of variably sized vascular conglomerates around a central draining vein and adjacent fibrosis usually without microfistula or hobnailed endothelium. NICH commonly present as large conglomerates of small vessels with arteriovenous or arteriolymphatic microfistulae or hobnailed endothelial cells, often with regressive endothelial changes such as dystrophic calcifications and fibrosis [19]. On ultrasound, both hemangiomas of infancy and congenital hemangiomas appear as ill-defined masses, but congenital hemangiomas usually consist of a single large tumor. The sonographic appearance of hemangiomas of infancy depends on the activity phase: in the active growth phase the highly vascular proliferating tumoral areas appear hypoechoic, while the pattern becomes heterogeneous during the involution phase to end as a mostly hyperechoic and hypovascular or avascular structure (Figs. 3.8, 3.9, 3.10, and 3.11). Arterial and venous blood flow are usually detected within common hemangiomas of infancy, but arteriovenous shunts (arterialized venous flow) are typical of the proliferative phases. Calcifications (phleboliths), which are rarely founded in common hemangiomas of infancy, are more common in congenital hemangiomas. [19].Of interest, both RICH and NICH may show on color Doppler prominent venous vascularity that may extend to the local muscles that become swollen and congested, hardening the tumor to palpation, sometimes simulating a malignant tumor (Figs. 3.12 and 3.13). Therefore, variations in echogenicity, type of vessels, and presence or absence of calcifications, albeit subtle, can tilt the diagnosis in borderline cases toward common hemangioma of infancy or RICH/NICH congenital hemangiomas [20, 21]. Ultrasound is also important in evaluating the involvement of deeper structures such as tendons, muscles, cartilage, or bone.

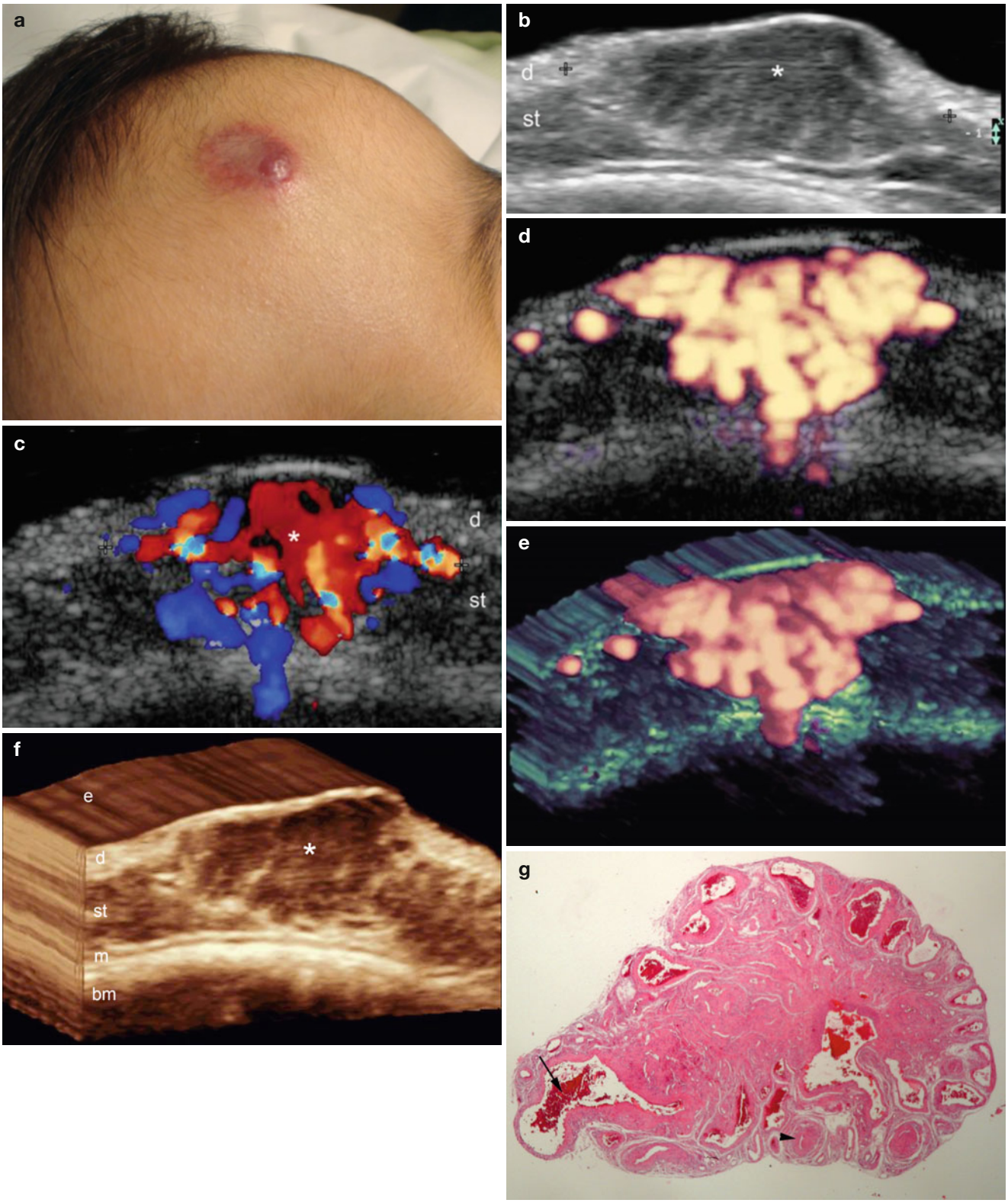

Fig. 3.8 (**a**–**g**) Hemangioma. (**a**) Clinical image of the lesion in the frontal region. (**b**) Ultrasound image (gray scale, transverse view) shows hypoechoic and heterogenous mass (*) that presents ill- defined borders and involves dermis and subcutaneous tissue. The most hypoechoic area corresponds to the most proliferative part of the hemangioma. (**c**) Color Doppler ultrasound image (transverse view) shows prominent blood flow within the mass. (**d**) Power Doppler image (transverse view) demonstrates increased and slow flow vascularity. (**e**) 3D power Doppler reconstruction shows the vessels within the lesion. (**f**) 3D ultrasound reconstruction of the lesion (*). (**g**) Histology (HE zoom × 20 courtesy of Dr. Laura Carreño) shows marked proliferation of vessels presenting variable thickness. Arteriolar vessels (*arrowhead*) and venous vessels (*arrow*) are detected. *Abbreviations*: *e* epidermis, *d* dermis, *st* subcutaneous tissue, *m* epicranius muscle, *bm* bony margin of the skull

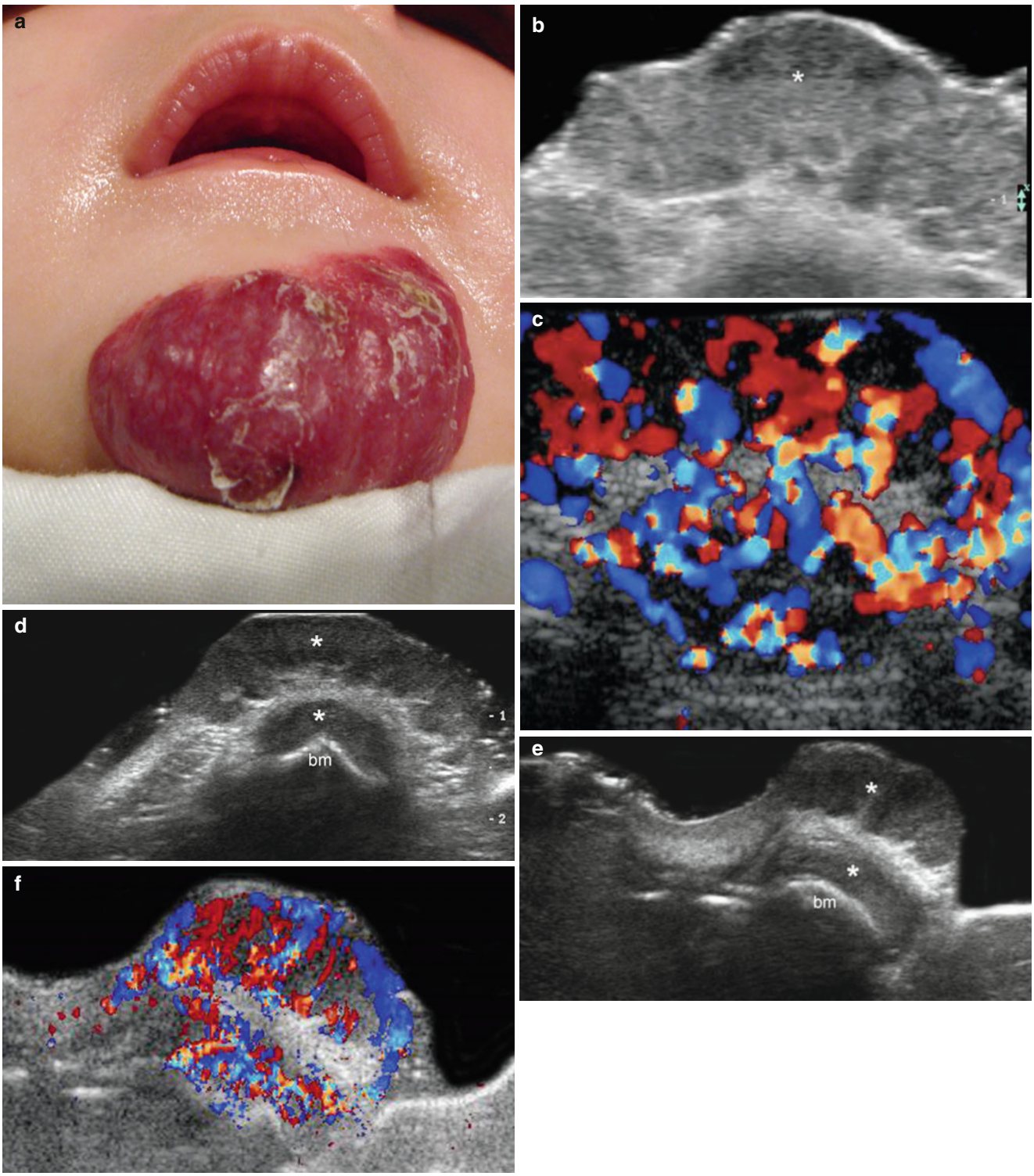

Fig. 3.9 (**a**–**f**) Hemangioma in proliferative phase. (**a**) Clinical image of a lesion in the chin. (**b**) Ultrasound image (gray scale, transverse view) shows hypoechoic mass (*) that involves dermis and subcutaneous tissue. (**c**) Color Doppler ultrasound image (transverse view) demonstrates high presence of vascularity within the mass. (**d**) Ultrasound image (gray scale, transverse panoramic wide view) shows the hypoechoic mass within the dermis and subcutaneous tissue, and also a deeper involvement composed by the hypoechoic tissue superficial to the bony margin of the mandible (*bm*). (**e**) Ultrasound image (gray scale, longitudinal panoramic wider view) demonstrates the mass (*) in the other axis. (**f**) Color Doppler ultrasound image (longitudinal panoramic view) shows the increased vascularity within the superficial and deep components of the hemangioma

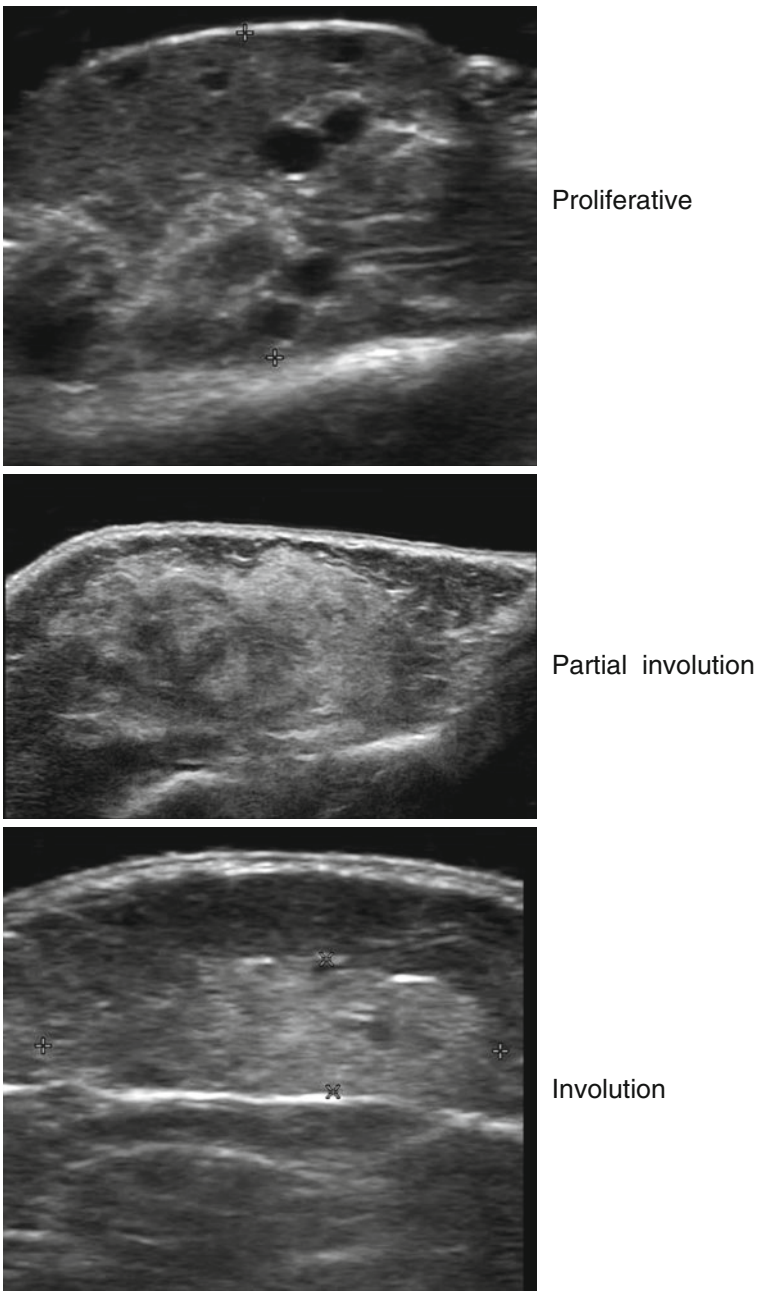

Fig. 3.10 Gray scale sonographic grading of echogenicity during the different phases of hemangiomas

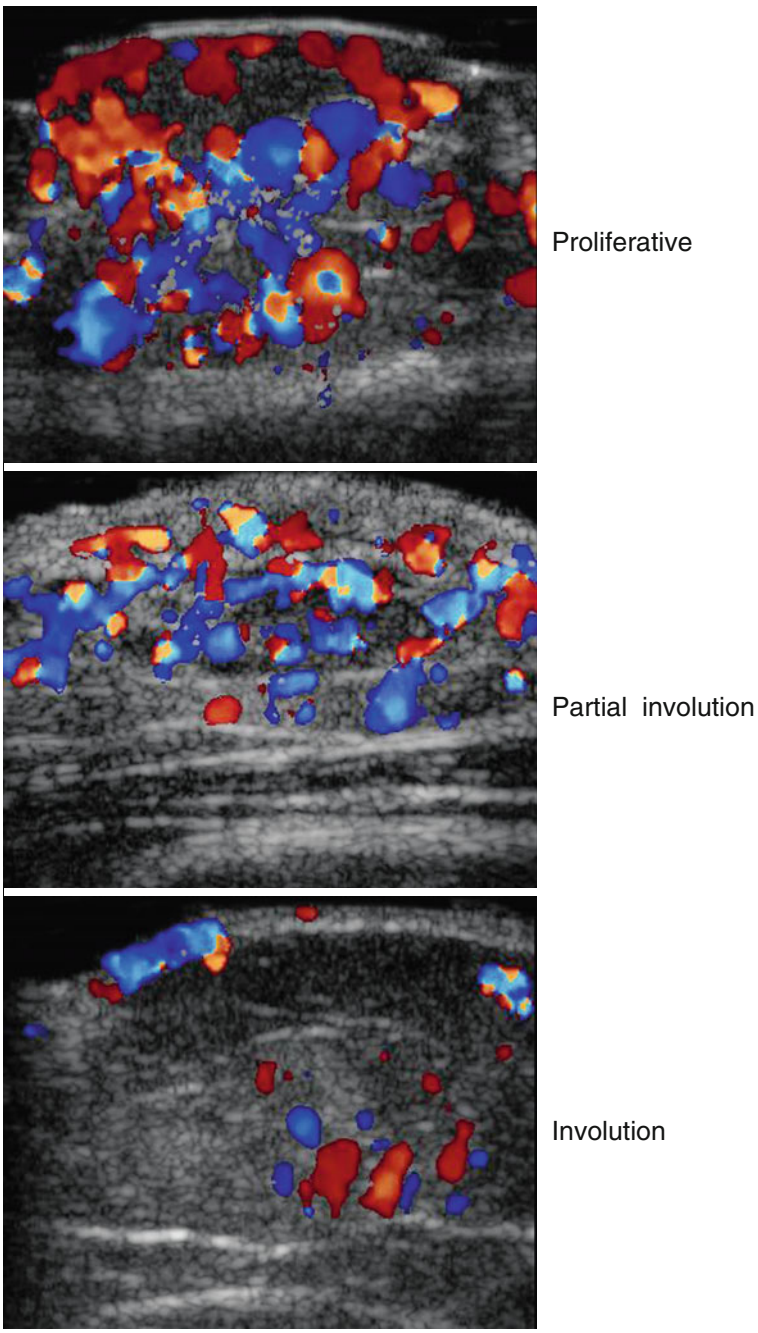

Fig. 3.11 Color Doppler sonographic grading of vascularity during the different phases of hemangiomas

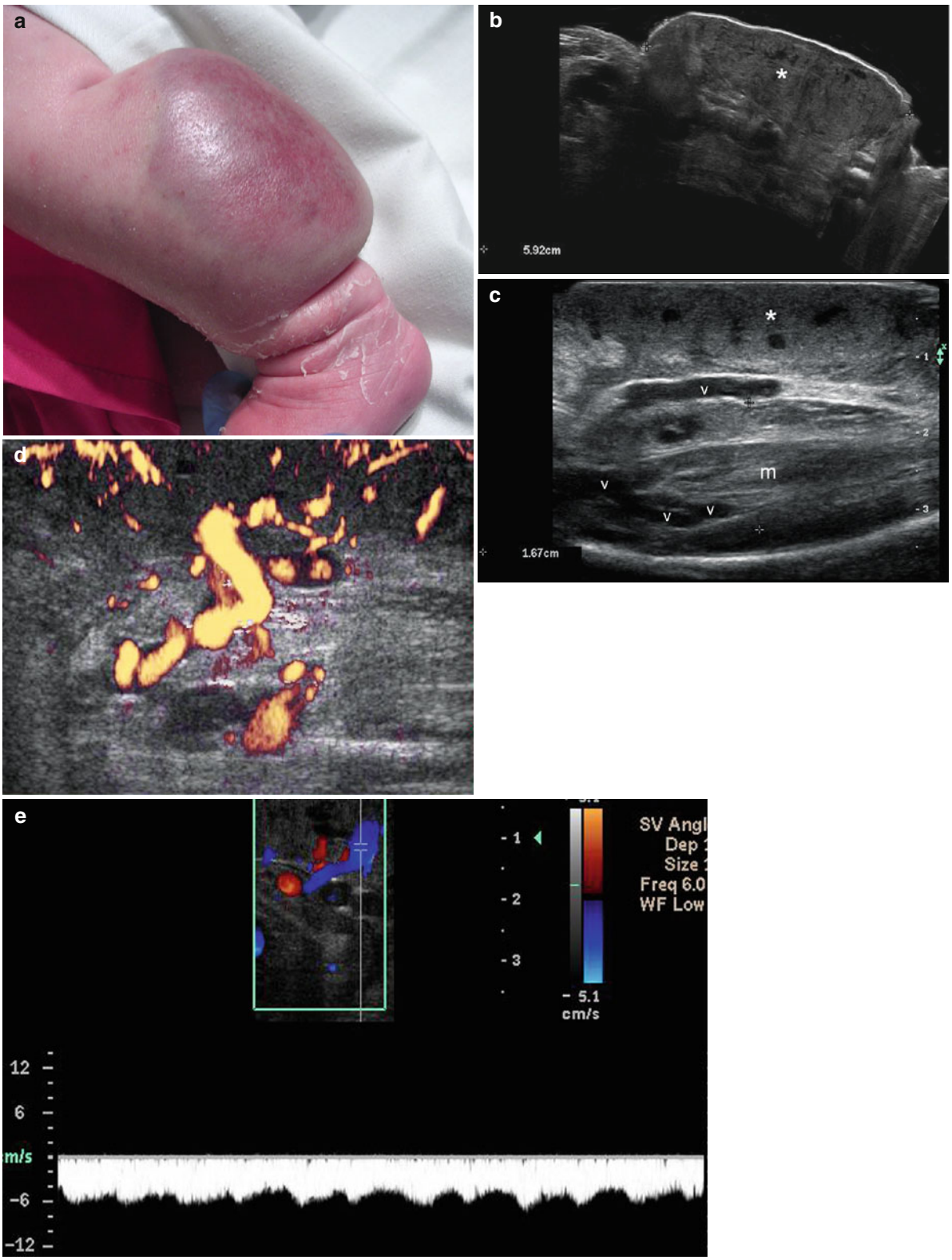

Fig. 3.12 (**a**–**e**) RICH (Rapidly involuting congenital hemangioma). (**a**) Clinical image of a lesion in the leg in a baby, 1 week after birth. (**b**) Ultrasound image (gray scale, longitudinal view) shows a 5.9 cm long hypoechoic mass (*) affecting the cutaneous layers of the leg. Notice the thick anechoic and tortuous venous vessels at the bottom of the lesion. (**c**) Ultrasound image (gray scale, longitudinal view at a deeper focal zone) shows ingurgitation of the lateral gastrocnemius muscle with prominent venous vessels. (**d**) Power Doppler ultrasound image (longitudinal view) demonstrates increased vascularity within the lesion. (**e**) Color Doppler ultrasound image (longitudinal view) shows venous flow within a thick lesional vessel. *Abbreviations*: *v* venous vessels, *m* lateral gastrocnemius muscle

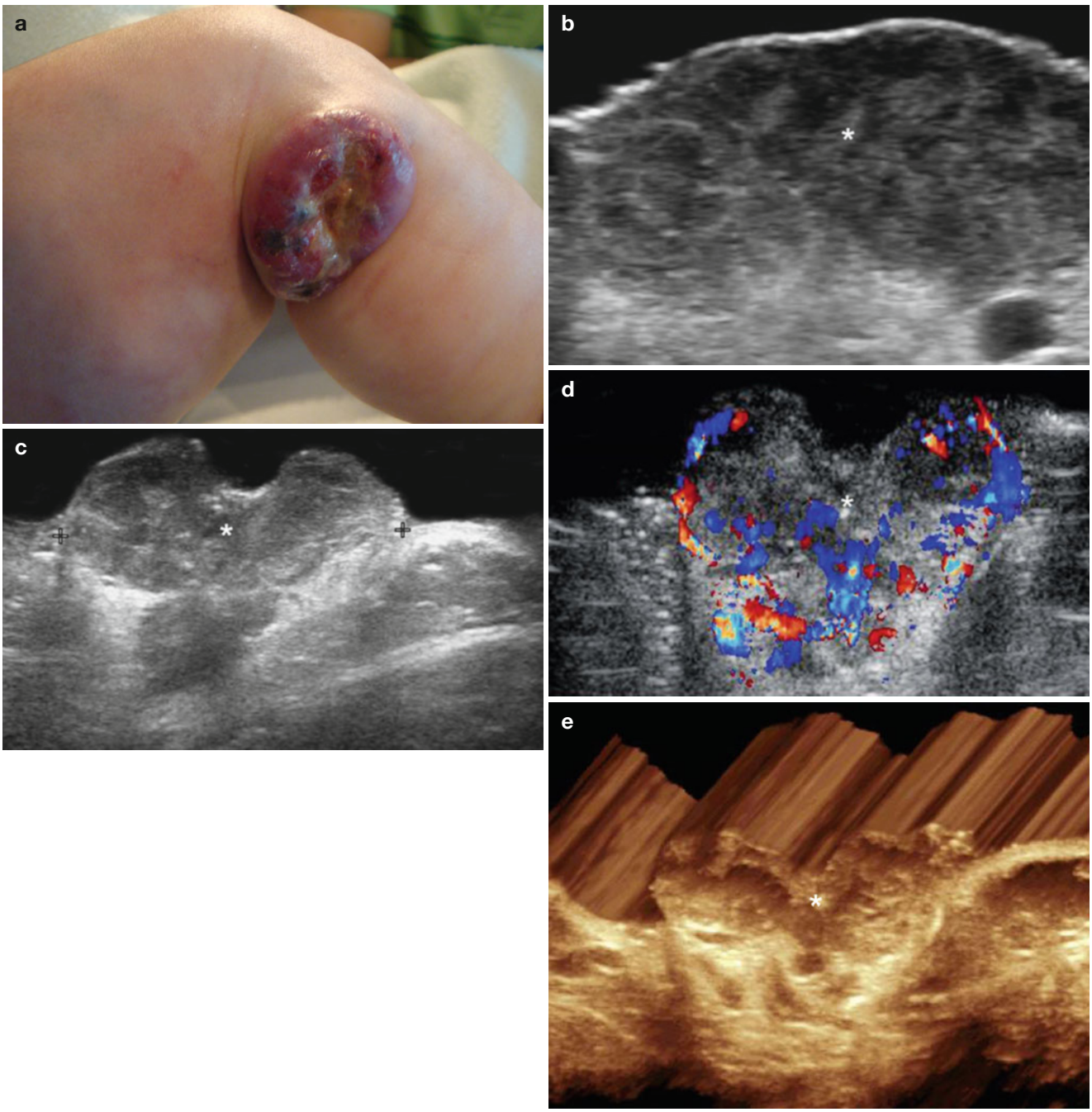

Fig. 3.13 (**a**–**e**) RICH (Rapidly involuting congenital hemangioma). (**a**) Clinical image of an ulcerated RICH lesion in the leg (male baby, 2 months old). (**b**) Ultrasound image (gray scale, transverse view) shows hypoechoic and slightly heterogenous lesion (*) that involves all the cutaneous layers. Notice the increased hyperechogenicity in parts of the epidermis and the hypoechogenictity of the dermis and subcutaneous tissue. (**c**) Ultrasound image (gray scale, transverse panoramic view) demonstrates the lobulated shape and the central depression of the lesion (*). (**d**) Color Doppler ultrasound image (transverse view) shows the increased vascularity within the lesional area (*). (**e**) 3D ultrasound reconstruction of the congenital hemangioma (*)

3.2.4 Vascular Malformations

Vascular malformations (VM) present as localized or diffuse defects that reflect defective morphogenesis and do not correspond to actual vascular tumors. The overall incidence of VM is 1.5 %, evenly distributed by sex and race; approximately two thirds are venous, and one third are arterial, capillary, lymphatic, or mixed. According to blood flow velocity, VM can be classified into high-flow (i.e., arterial and arterio-venous lesions), and low-flow (i.e., venous, lymphatic, and capillary entities) [22–25].

Unlike hemangiomas, VM remain basically unchanged after birth and are characterized by progressive ectasia of vascular structures resulting from increases in vessel diameter. Venous structures can be more selectively affected in complex congenital syndromes that include Sturge-Weber (angiomatosis encephalotrigeminal) and Cobb (cutaneomeningospinal angiomatosis) syndromes, as well as the Cutis Marmorata Telangiectatica Congenita, Phacomatosis Pigmentovascularis, Blue Rubber Bleb, Parkes-Weber, Maffuci, Klippel-Trenaunay, and Proteus syndromes (Table 3.1) [22].

VM are generally attributed to sporadic mutations; for example, in Klippel-Trenaunay syndrome, the associated genetic defect is the translocation t (8; 14) (q 22.3; q 13), whereas in the Proteus syndrome there appears to exist a mosaic expression of an activating mutation in AKT1 kinase [22]. The histology of VM shows normal-appearing endothelium, with the vascular expansion related to hypertrophy and not hyperplasia of the vascular tissue.

On color Doppler ultrasound, VM are seen as tubular anechoic structures (arterial, venous, arterio-venous), pseudocystic anechoic structures (arterial, venous or lymphatic), or focal hyperechoic areas without discernible vessels (capillary) (Figs. 3.14, 3.15, 3.16, 3.17, and 3.18). Flat capillary lesions such as Port Wine stains can sometimes appear as dermal areas of low echogenicity or as focal hyperechoic spots or refringence areas in the epidermis; nevertheless, when the lesions are extremely flat and superficial they ultimately may become undetectable on ultrasound. Phleboliths are seen as hyperechoic calcified spots and often present point to venous origin which can be further supported by the addition of spectral curve analysis to determine type and velocity of the blood flow, whereas pressure with the probe may also help by identifying the easily compressible venous malformations. VM are occasionally complicated by thrombosis (especially venous), that can be detectable on ultrasound as hypoechoic material within the lumen with absent flow on spectral curve analysis and lack of compressibility under probe pressure. VM may also produce local areas of subcutaneous fat hypertrophy or musculoskeletal overgrowth related to the chronic increase in blood flow and more rarely, result in segmental cutaneous atrophy. These reactive phenomena are readily detectable with ultrasound.

Table 3.1 Congenital syndromes associated with vascular malformations [22]

Syndromes	Vascular structure affected
Sturge Weber	Venules
Cobb	
Sacral venular	
Cutis marmorata congenita	
Phacomatosis pigmentovascularis	
Von Hippel-Lindau	
Blue rubber bleb nevus	Veins
Maffuci	
Glomuvenous malformations	
Klippel-Trenaunay	Mixed venules-veins-lymphatic
Proteus	
Parkes-Weber	Mixed venules-veins-arterio-venous fistula
Rendu-Osler-Weber	Arteriovenous
Mafucci	Veins or mixed venous-lymphatic
Gorham	

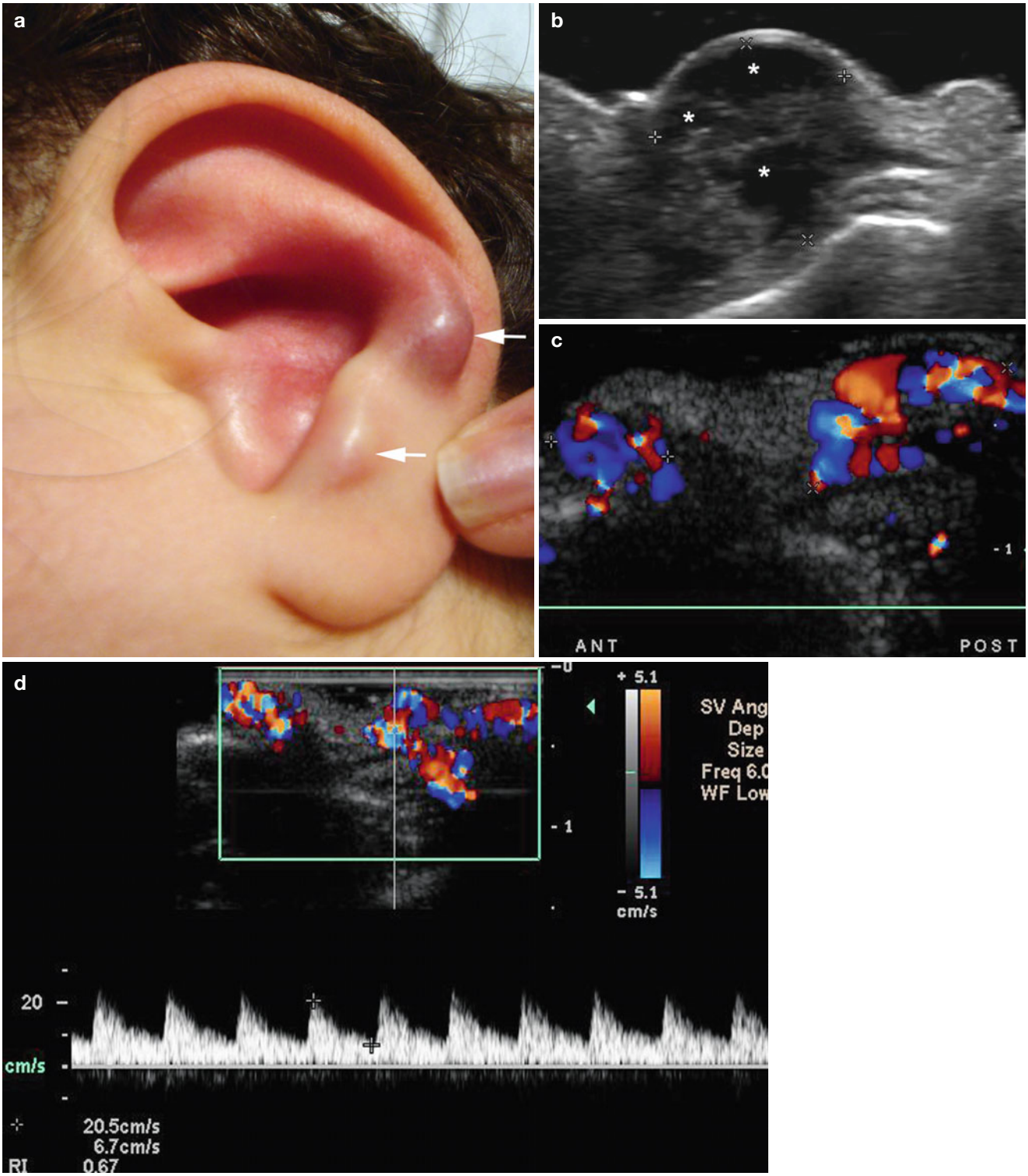

Fig. 3.14 (**a**–**d**) Arterial vascular malformation. (**a**) Clinical image of a patient presenting with two erythematous bumps in the left ear pinna. (**b**) Ultrasound image (gray scale, transverse view) at the most lateral and large bump demonstrates hypoechoic lesion (between markers) with anechoic tubular and pseudocystic areas (*) that partially involves the cartilage. (**c**) Color Doppler ultrasound image (panoramic transverse view) demonstrates increased vascularity within the two focal lesions (between markers). (**d**) Color Doppler spectral curve analysis shows 20.5 cm/s arterial peak systolic velocity within the lesions

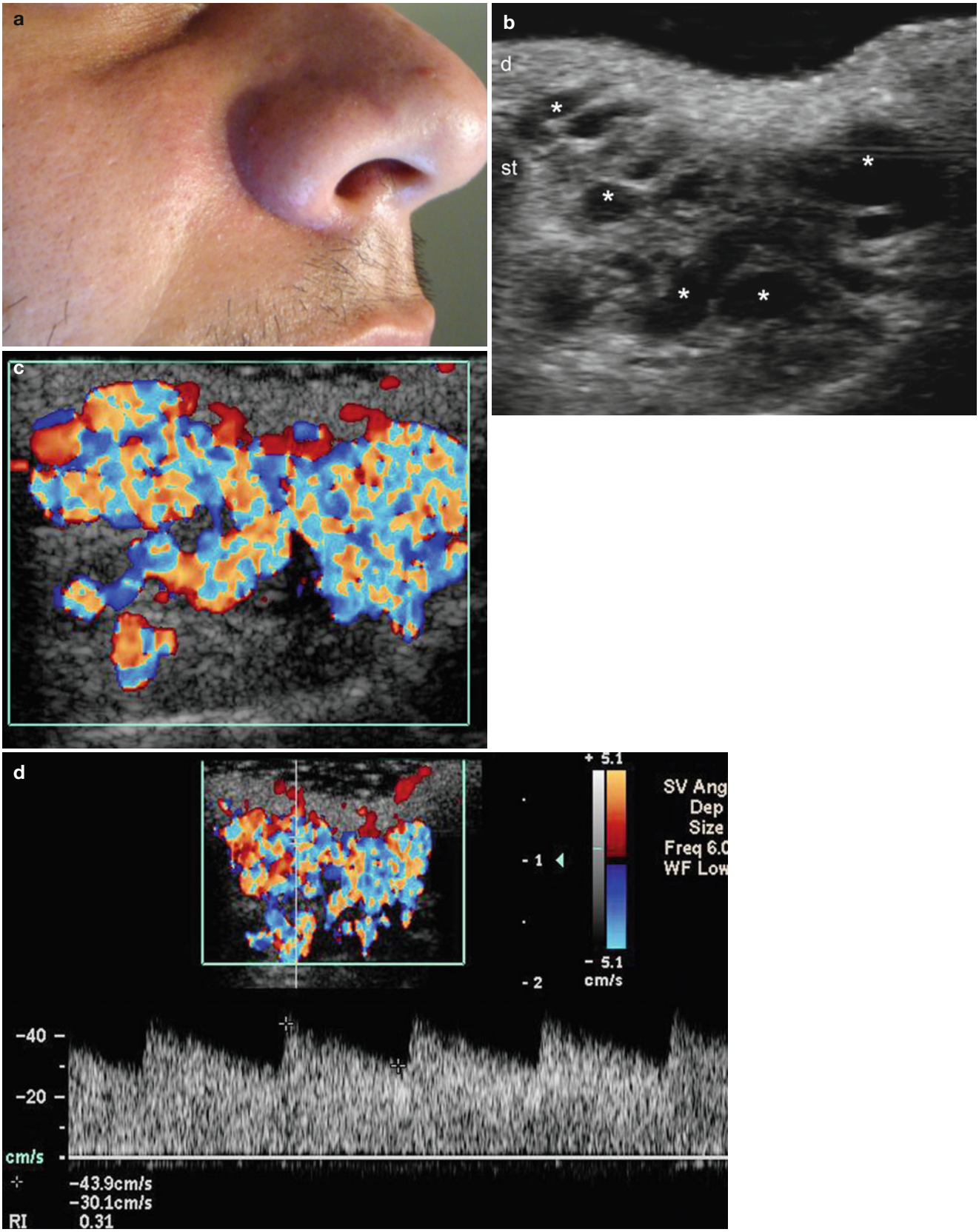

Fig. 3.15 (**a**–**d**) Arterial vascular malformation. (**a**) Clinical image shows a erythematous lump in the right nasofold line. (**b**) Ultrasound image (gray scale, transverse view) demonstrates multiple anechoic tubules and pseudocystic areas (*) in the subcutaneous tissue. (**c**) Color Doppler ultrasound image (transverse view) shows turbulent flow within the anechoic tubules and pseudocystic areas. (**d**) Color Doppler spectral curve analysis shows high arterial flow (43.9 cm/s peak systolic velocity) within the nest of vessels

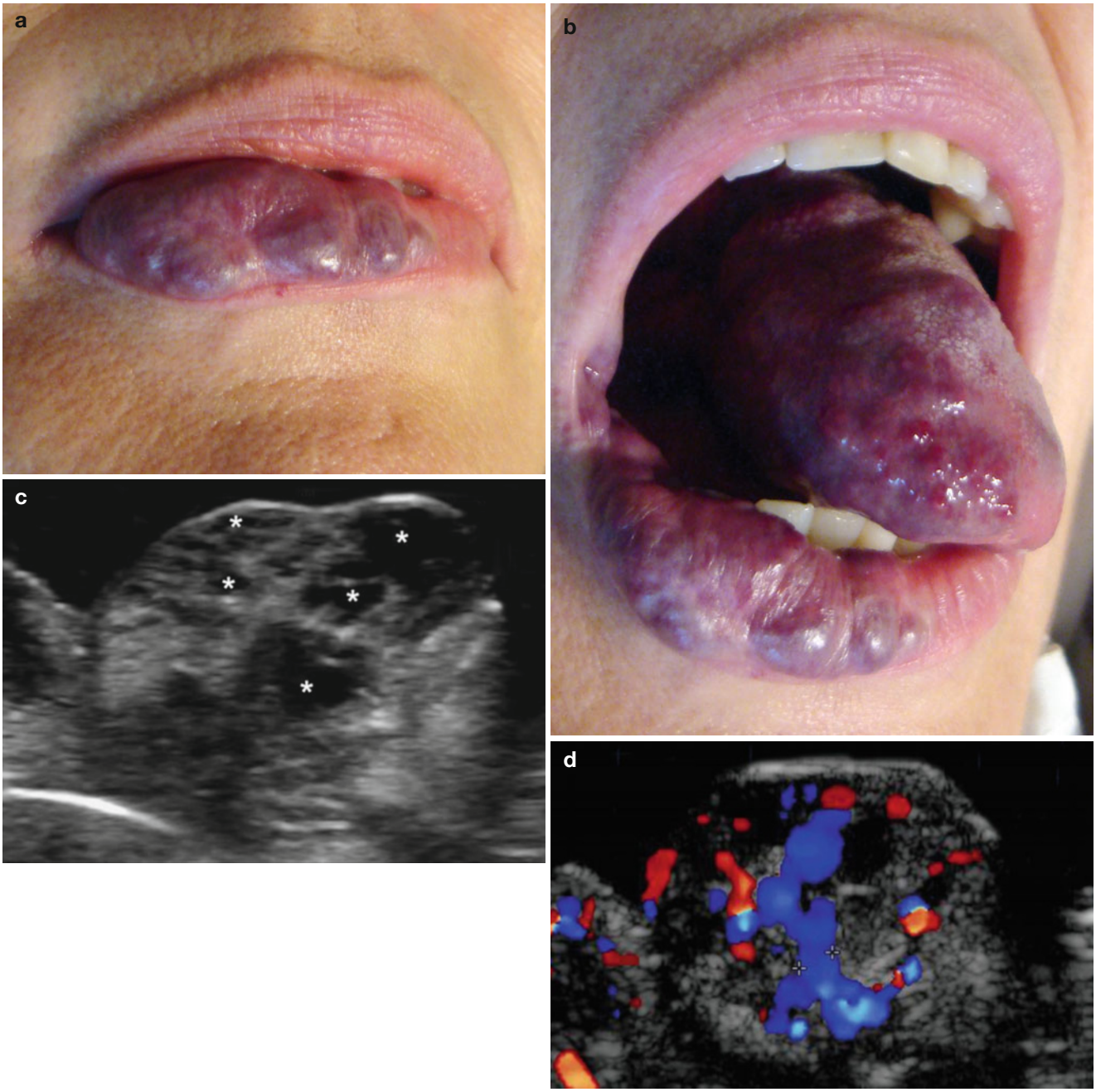

Fig. 3.16 (**a**–**g**) Venous vascular malformation. (**a**, **b**) Clinical images of the lesions at the lower lip and tongue. (**c**) Ultrasound image (gray scale, longitudinal view) at the lower lip shows multiple anechoic tubular and pseudocystic structures affecting the dermis and the orbicular muscle of the lip. (**d**) Color Doppler ultrasound image demonstrates increased flow within the tubular and pseudocystic areas. (**e**) Color Doppler spectral curve analysis shows venous flow within the structures. (**f**) Ultrasound transverse view in the right aspect of the floor of the oral cavity shows similar anechoic structures. (**g**) Ultrasound image (gray scale, transverse view) of the right peribuccal region shows anechoic tubular tracts (*) and a hyperechoic calcified phlebolith (*arrows*)

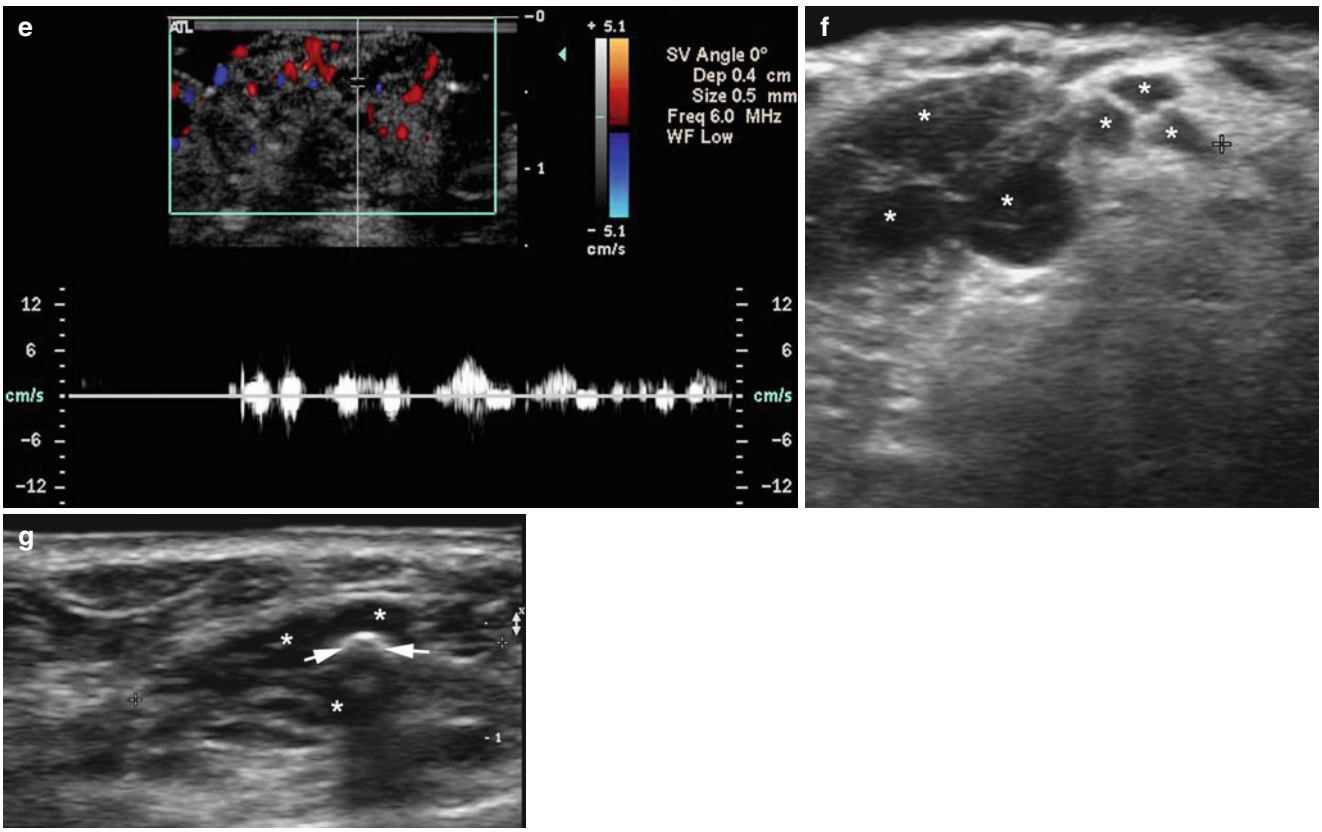

Fig. 3.16 (continued)

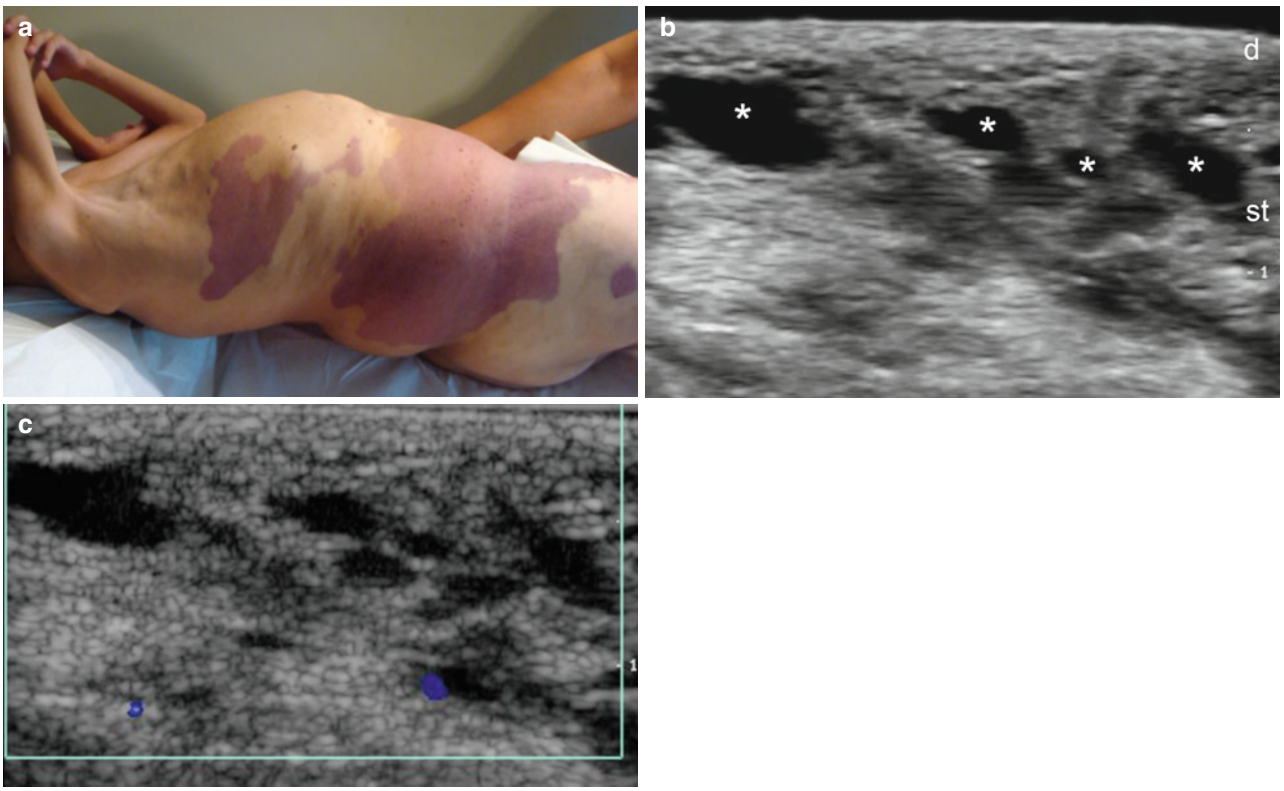

Fig. 3.17 (**a**–**f**) Venous vascular malformation in Proteous syndrome. (**a**) Clinical image of a patient with Proteus syndrome. (**b**) Ultrasound image (gray scale, transverse view at the right thoracic region) shows multiple anechoic pseudocystic structures (*) in the subcutaneous tissue. (**c**) Color Doppler ultrasound image (transverse view, right thoracic region) demonstrates scarce flow within the pseudocystic areas. (**d**) Color Doppler spectral curve analysis shows low monophasic venous flow in some of the structures. (**e**) Ultrasound image (longitudinal view, left thigh) demonstrates lack of subcutaneous tissue and direct contact between the dermis and the muscular compartment in a perilesional region. (**f**) Histology (HE ×20 zoom, courtesy of Dr. Laura Carreño) shows multiple dilated and tortuous vessels with thin walls and blood filled lumen (*). *Abbreviations*: *e* epidermis, *d* dermis, *st* subcutaneous tissue, *m* muscle

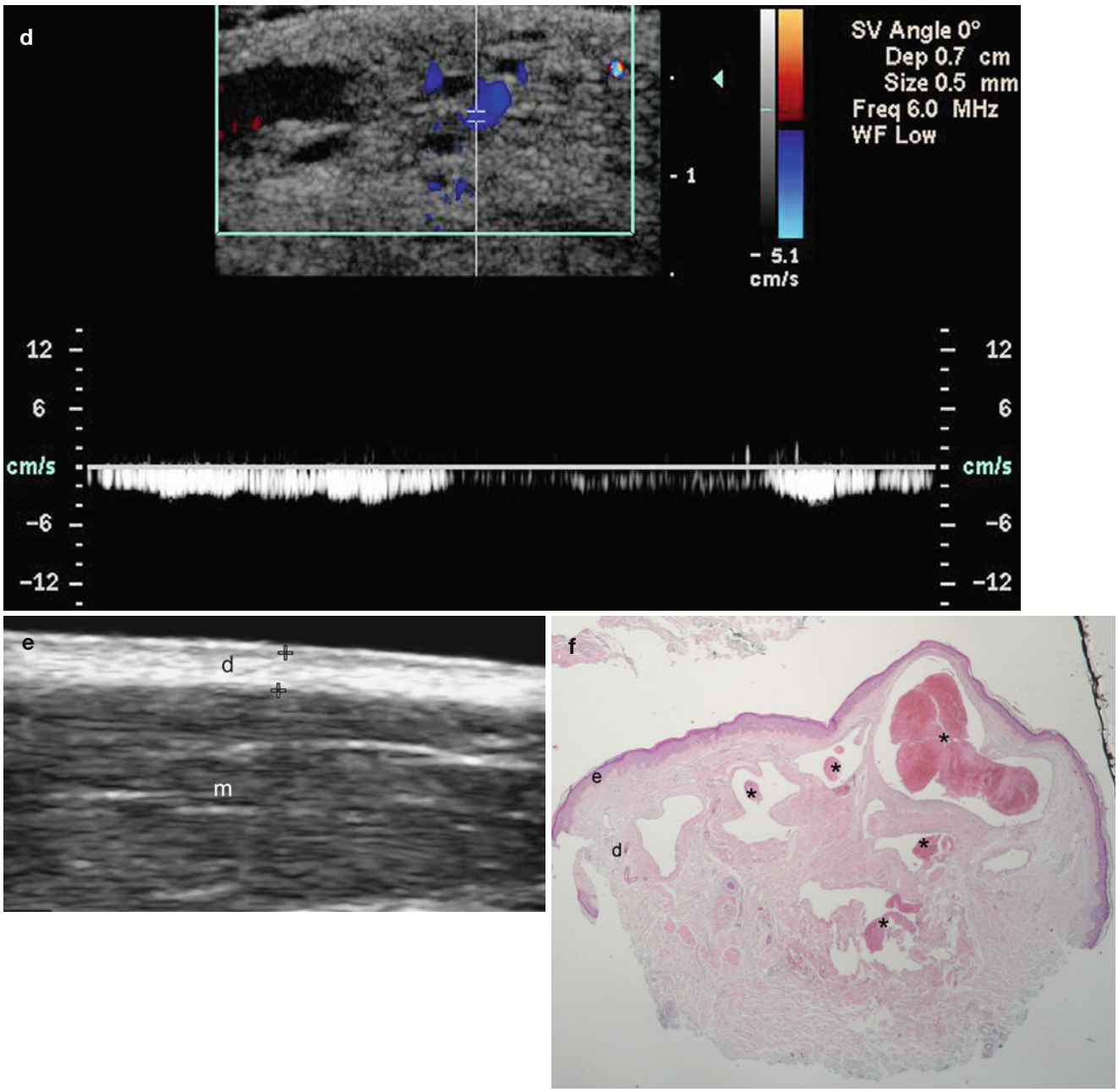

Fig. 3.17 (continued)

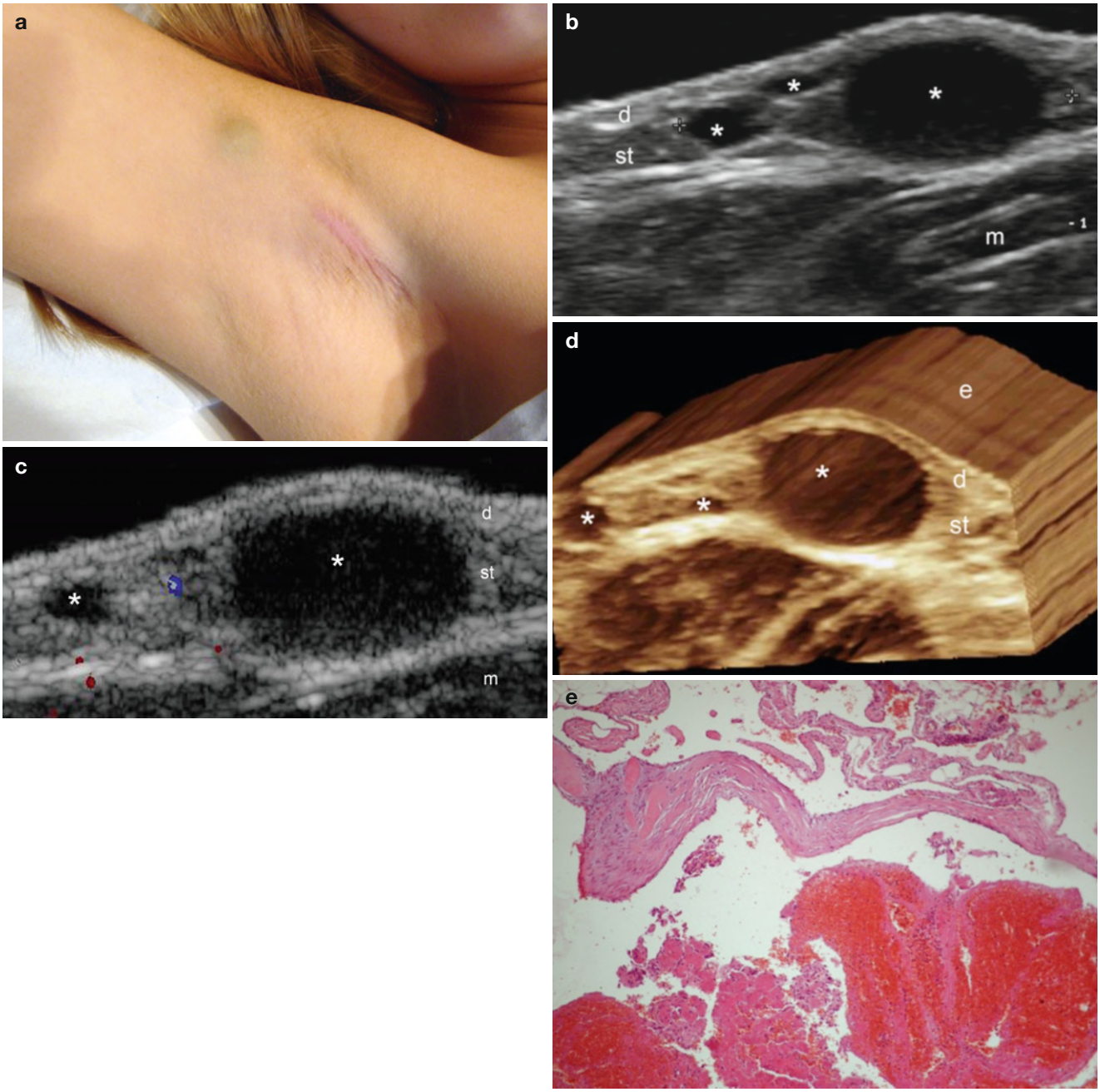

Fig. 3.18 (**a**–**e**) Lymphatic vascular malformation. (**a**) Clinical image of a lesion in the right arm. The scar in the axilla corresponds to a previous surgical removal of the malformation (without pre-surgical ultrasound). (**b**) Ultrasound image (gray scale, transverse view at the right arm) shows multiple round and oval-shaped anechoic structures (*) of variable sizes in the subcutaneous tissue. (**c**) Color Doppler ultrasound image (transverse view) demonstrates lack of detectable blood flow within the structures. (**d**) 3D ultrasound image (longitudinal view) of the lesional area (*). (**e**) Histology (HE 10× zoom courtesy of Dr. Claudia Morales) shows dilated endothelial spaces without content and smooth muscle cell. *Abbreviations*: *e* epidermis, *d* dermis, *st* subcutaneous tissue, *m* muscle

3.2.5 Aplasia Cutis

As implied by the name, aplasia cutis (AC) is characterized by the local absence (partial or total) of skin at birth; it affects more often the scalp especially the parietal regions. AC is a single lesion in 70 % of the patients, affecting multiple areas in the remaining 30 %. AC lesions involving the midline are considered markers for an incomplete fusion of the neural tube [26, 27]. AC generally present clinically as small round or starry erosion or ulceration with superficial scarring, as blisters draining serous fluid, or as a cutaneous defect or depression covered by a thin and bright membrane (membranous aplasia cutis) [28]. AC is rarely associated with an underlying bony defect that could potentially increase the rate of complications [29]. Sonography in AC usually shows subcutaneous tissue atrophy, dermal hypoechogenicity, and sometimes thinning of the dermis (Fig. 3.19). Although unusual, it is important to exclude the occurrence of subjacent bony defects under the cutaneous lesion, particularly in the scalp; because the meningeal layers can be in direct contact with the dermis, which can be a potential threat for the development of meningitis.

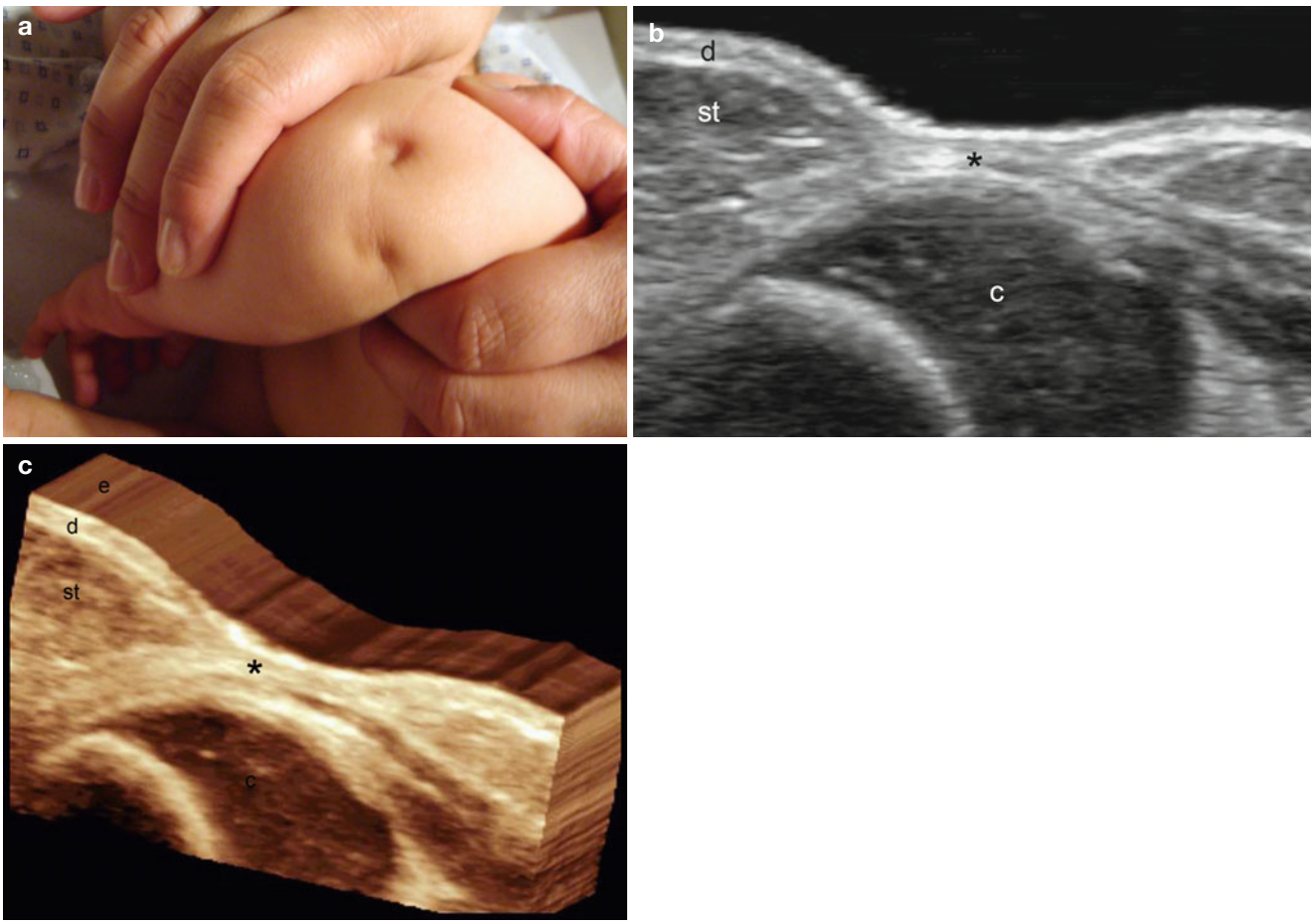

Fig. 3.19 (**a**–**c**) Aplasia cutis. (**a**) Clinical image of the lesional area showing two depression sites at the posterior aspect of the left elbow. (**b**) Ultrasound image (longitudinal view) demonstrates a focal lack of subcutaneous fatty tissue in the lesional area (*). Notice the close contact between the dermis and the cartilage of the olecranon process. (**c**) 3D ultrasound image (longitudinal view) of the same lesion (*). *Abbreviations*: *e* epidermis, *d* dermis, *st* subcutaneous tissue, *c* cartilage

3.2.6 Buske-Ollendorf Disease

Buske-Ollendorf disease, also called lenticular dermatofibrosis, is a genetic condition with an autosomal dominant pattern of inheritance, and results from mutations in the gene LEMD (12q14). Clinically, it is characterized by the presence of yellow colored skin papules in the dorsum of the hands, trunk, gluteal and lumbosacral regions [30–34]; furthermore, x-ray projections show isolated bony condensations or sclerosis (osteopoikilosis or osteopathia condensans disseminate) most commonly in the epiphyseal and metaphyseal regions of long bones, or in local clusters in the carpal or tarsal bones [35]. Sonography of the papules shows focal hypoechogenicity with dermal thickening, and usually, a hypovascular pattern on color Doppler ultrasound studies (Fig. 3.20).

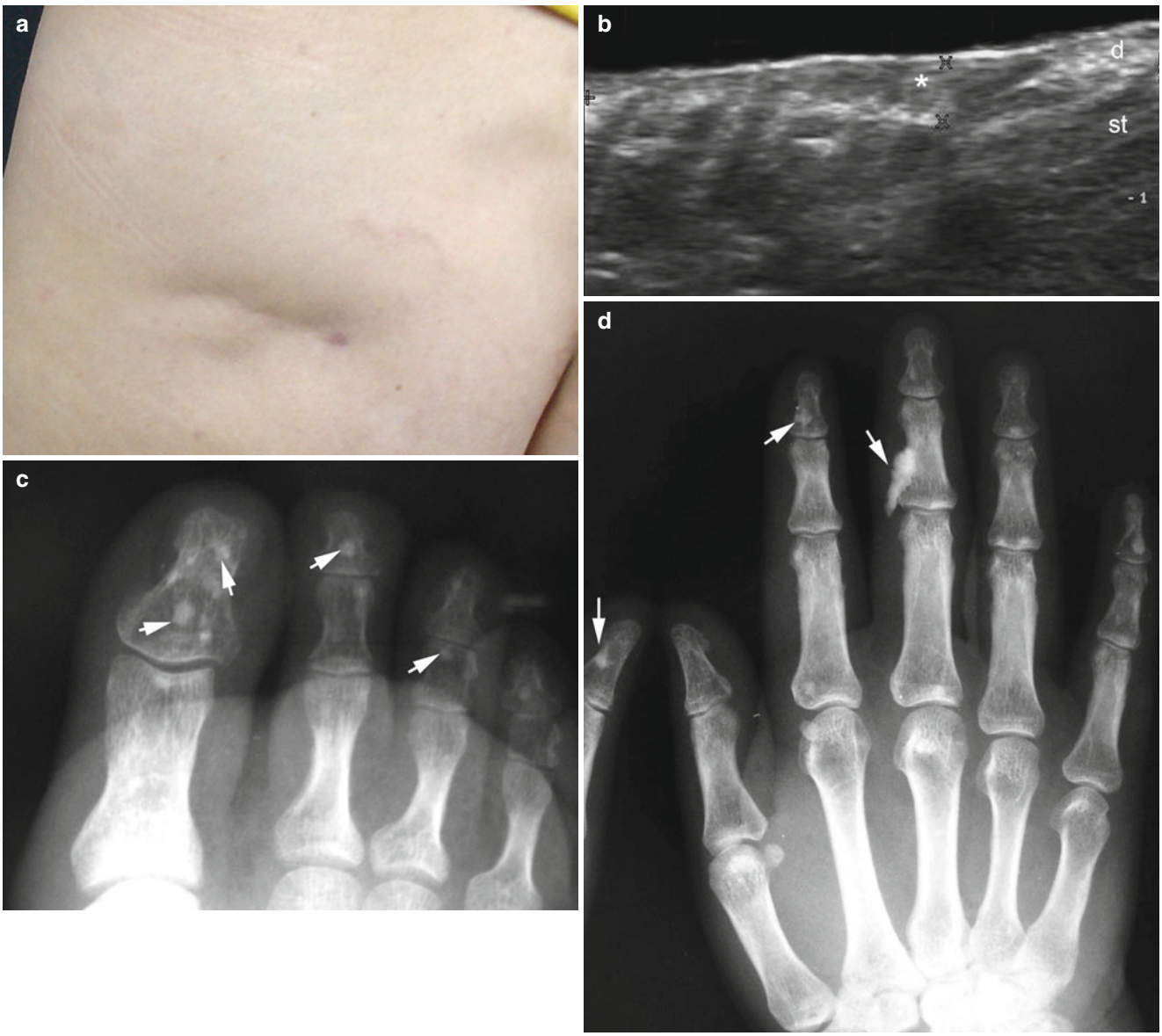

Fig. 3.20 (**a**–**d**) Bushke-Ollendorf disease. (**a**) Clinical lesion in the left gluteal region. (**b**) Ultrasound image (gray scale, transverse view, left gluteal region) shows hypoechoic dermal thickening (*). (**c**, **d**) Radiographs (anteroposterior view) of the left foot (**c**) and left hand (**d**) demonstrate multiple hyperdense calcified deposits (*arrows*) that correspond to the associated osteopoikilosis. *Abbreviations*: *d* dermis, *st* subcutaneous tissue

3.2.7 Lipoid Proteinosis

Lipoid proteinosis, also called lipoidoproteinosis or Urbach-Wiethe disease (U-W), represents an autosomal recessive genetic disorder apparently caused by a mutation in a gene localized in chromosome 1q21 that codes for ECM1, a protein in the extracellular matrix [36]. Clinically, it appears as white or yellow papules in the tongue, lips, and vocal cords that results in hoarseness and weak crying. It is manifested during infancy by vesicles and hemorrhagic crusts on the face, trunk, axilla, groin, elbows, dorsum of the hands, palm of the hands, and/or soles of the feet and extremities; upon healing, the lesions may leave varioliform scars or yellow-colored hyperkeratotic plaques. Involvement of the scalp can result in scarring alopecia. Lipoid proteinosis can result in blending of the papules (moniliform blepharosis) in the free border of the eyelid. This condition can also manifest by the production of hyaline deposits in the cornea, conjuntival region, and retina (Bruch's membrane) resulting in corneal opacities and secondary glaucoma from disruption of the trabecular meshwork. Diffuse lesional infiltration of the pharynx and larynx may result in dysphagia and respiratory insufficiency [37–40].

Sonography of the papules shows localized thickening and hypoechogenicity of the dermis or equivalent submucosal regions. On color Doppler ultrasound, blood flow can be increased overall within the lesional tissue, although typically with slow-flow vessels. Hyperechogenicity from lesional involvement of the vocal cords (deposits of lipoproteins) may explain the occasional development of dysphonia (Fig. 3.21). Skull radiographs and CT may show comma-shaped intracranial calcifications in the temporal regions [41].

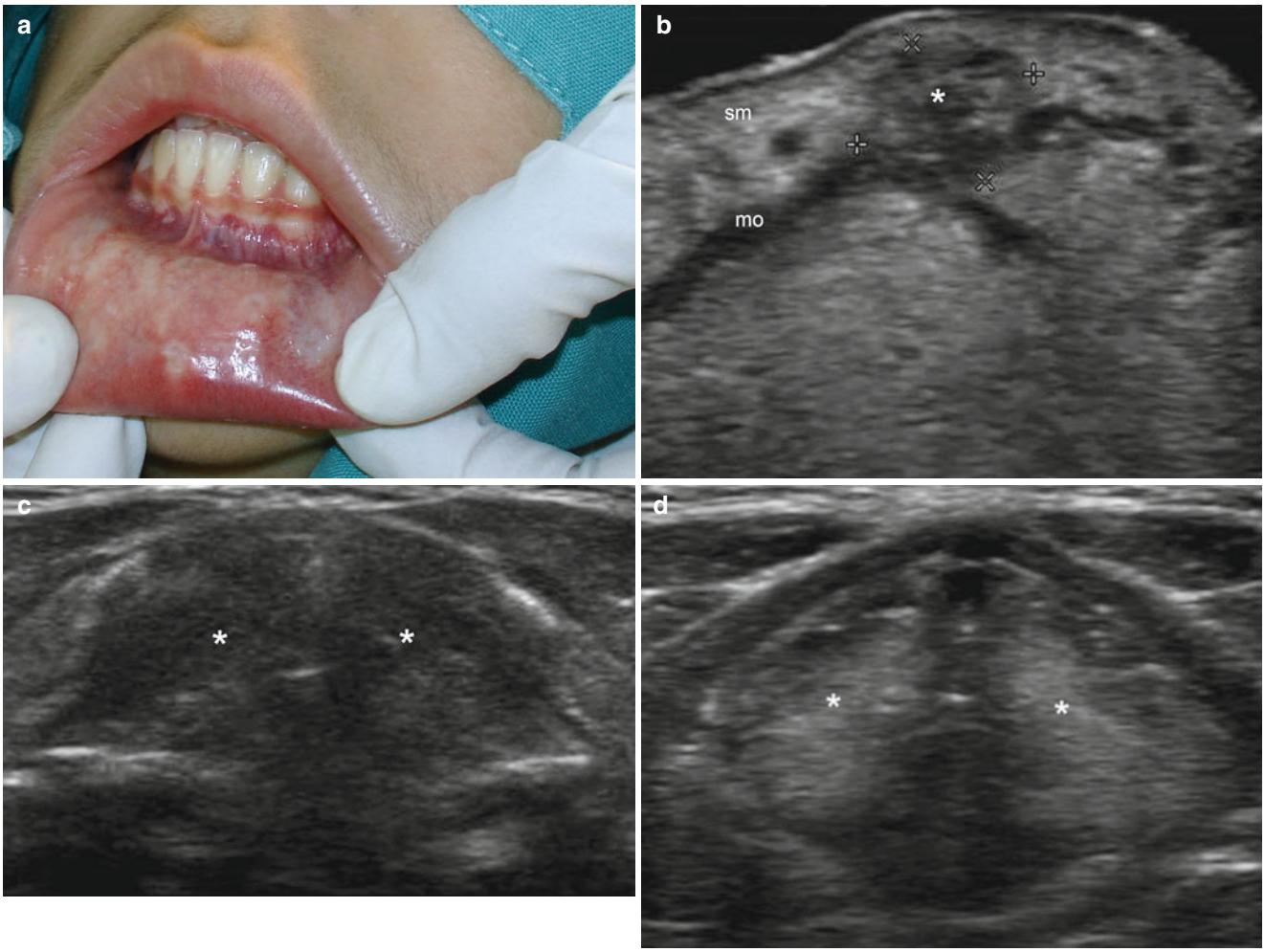

Fig. 3.21 (**a**–**d**) Lipoid proteinosis. (**a**) Clinical white papules in the mucosa of the lip. (**b**) Ultrasound image (gray scale, transverse view) shows a submucosal hypoechoic deposit (*, between markers) in the lower lip superficially located to the orbicularis oris muscle. (**c**) Ultrasound image (gray scale, transverse view) shows the normal sonographic echogenicity of the vocal cords. (**d**) Ultrasound image (gray scale, transverse view) demonstrates increased echogenicity of the vocal cords (*) in lipoid proteinosis. *Abbreviations*: *sm* submucosa, *mo* orbicularis oris muscle of the lip

3.2.8 Neurofibromatosis

Neurofibromatosis (NF) belongs to the group of phakomatoses (i.e., hereditary developmental anomalies of ectodermal tissues), and are nerve tumors that appear as hamartomas disseminated throughout the skin [42–46]. The genetic mutations causing NF occasionally occur de novo; the inheritance is autosomal dominant with variable penetration [42, 43].

Although eight different subtypes of NF have been recognized, NF-1 and NF-2 account for 99 % of cases. NF-1 (von Recklinhausen's disease), the most common presentation, is characterized by the presence of multiple café-au-lait spots in the skin, peripheral neurofibromas, and pigmented hamartomas of the iris (Lisch nodules). NF-2 accounts for 10 % of cases and affects the central nervous system in addition to the skin, inducing bilateral acoustic neurinomas, meningiomas, and spinal tumors [44].

Morphologically, there are three forms of presentation of cutaneous neurofibromas: localized, plexiform, and diffuse. Localized neurofibromas appear sonographically as ovoid or fusiform hypoechoic nodules, and although originating from a neural tract in only 50 % of cases, it is possible to define the central afferent and efferent neural branches of the nodule. Thus, the difficult differential diagnosis with another neurogenic tumor, schwannoma may be possible when eccentrically located afferent and efferent tracts characteristic of the latter tumor, are clearly identified sonographically. Vascularity of localized neurofibromas ranges from hypo- to hypervascular on color Doppler ultrasound; the presence of increased vascularity may be associated with hemorrhagic episodes appearing as highly localized fluid-containing anechoic areas within the lesions (Fig. 3.22).

Because plexiform neurofibromas involve long nerve segments and branches, the tumors adopting a serpentine structure are better described as "bag of worms". Ultrasound shows the affected nerves and branches as multiple and tortuous hypoechoic tracts, commonly hypovascular on color Doppler ultrasound (Fig. 3.23).

Diffuse neurofibromas are characterized by infiltrative tumoral growth into the subcutaneous and dermal tissues, with entrapment of structures normally traversing those layers. Sonograms usually show multiple tubular tracts or nodules that are hypoechoic and sometimes interconnected, surrounded by hyperechoic tissue in a plaque-like appearance; anechoic ductal structures may be evident within the lesional tissue. Blood flow patterns ranging from hypo- to hypervascular can be seen on color Doppler ultrasound (Fig. 3.24).

Histology shows a myxoid stroma infiltrated by tumoral cells and fibroblasts with occasional prominent vessels. In the diffuse form of NF, atypical Schwann cells with short fusiform contours are interspersed within a uniform matrix of fibrillar collagen [45–47].

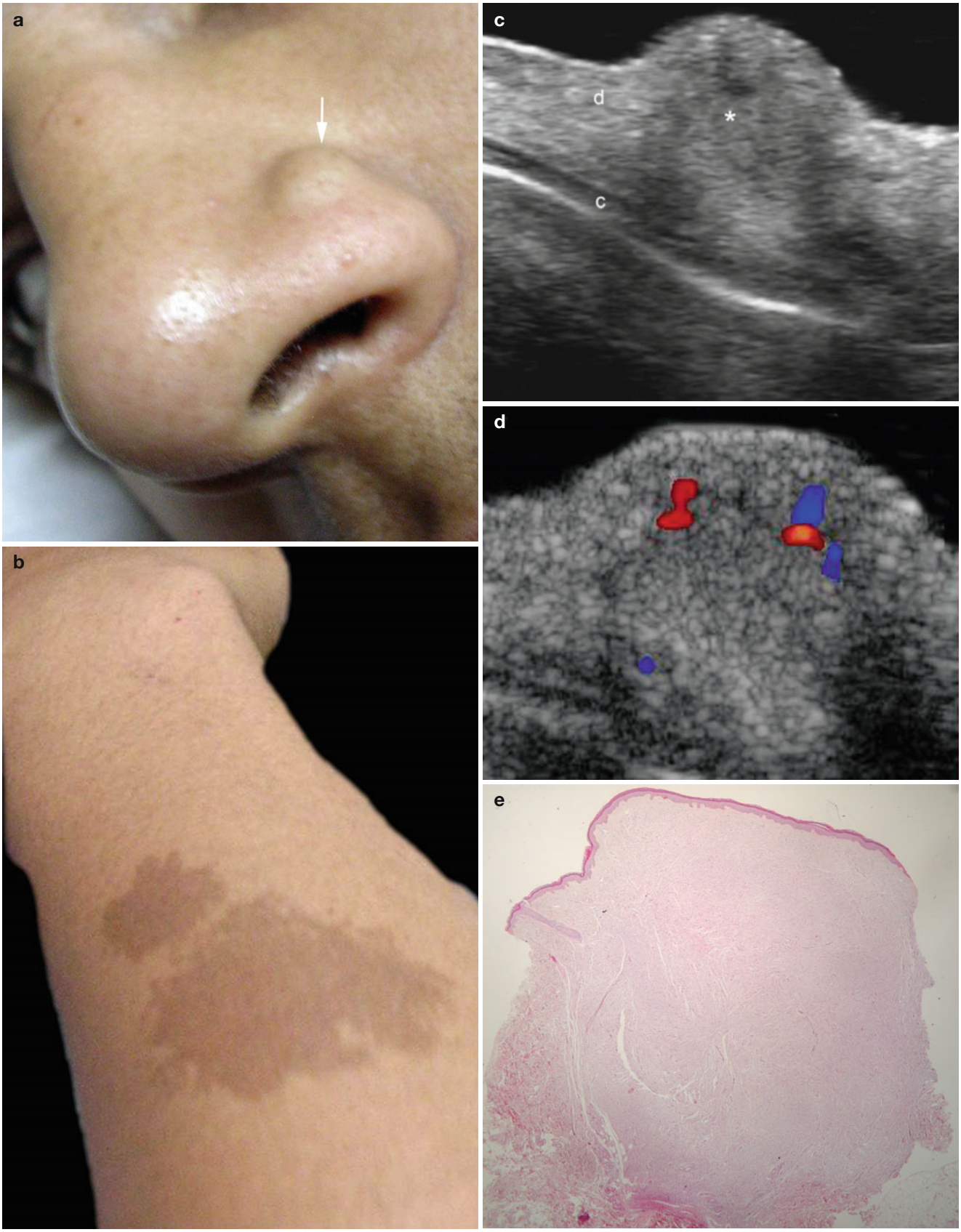

Fig. 3.22 (**a**–**d**) Localized neurofibroma. (**a**) Swelling at the left wing of the nose. (**b**) Café-au-lait spots in the left forearm of the same patient. (**c**) Ultrasound image (gray scale, transverse view) shows hypoechoic dermal nodule (*) in the left wing of the nose. (**d**) Color Doppler ultrasound image (transverse view) demonstrates a few vessels within the nodule. (**e**) Histology (HE zoom × 20, courtesy of Dr. Laura Carreño) shows a circumscribed nodule without encapsulation and with interlacing bundles of cells with ovoid-to-spindle nuclei with shorter fusiform contours and collagen fibrils. *Abbreviations*: *d* dermis, *c* nasal cartilage

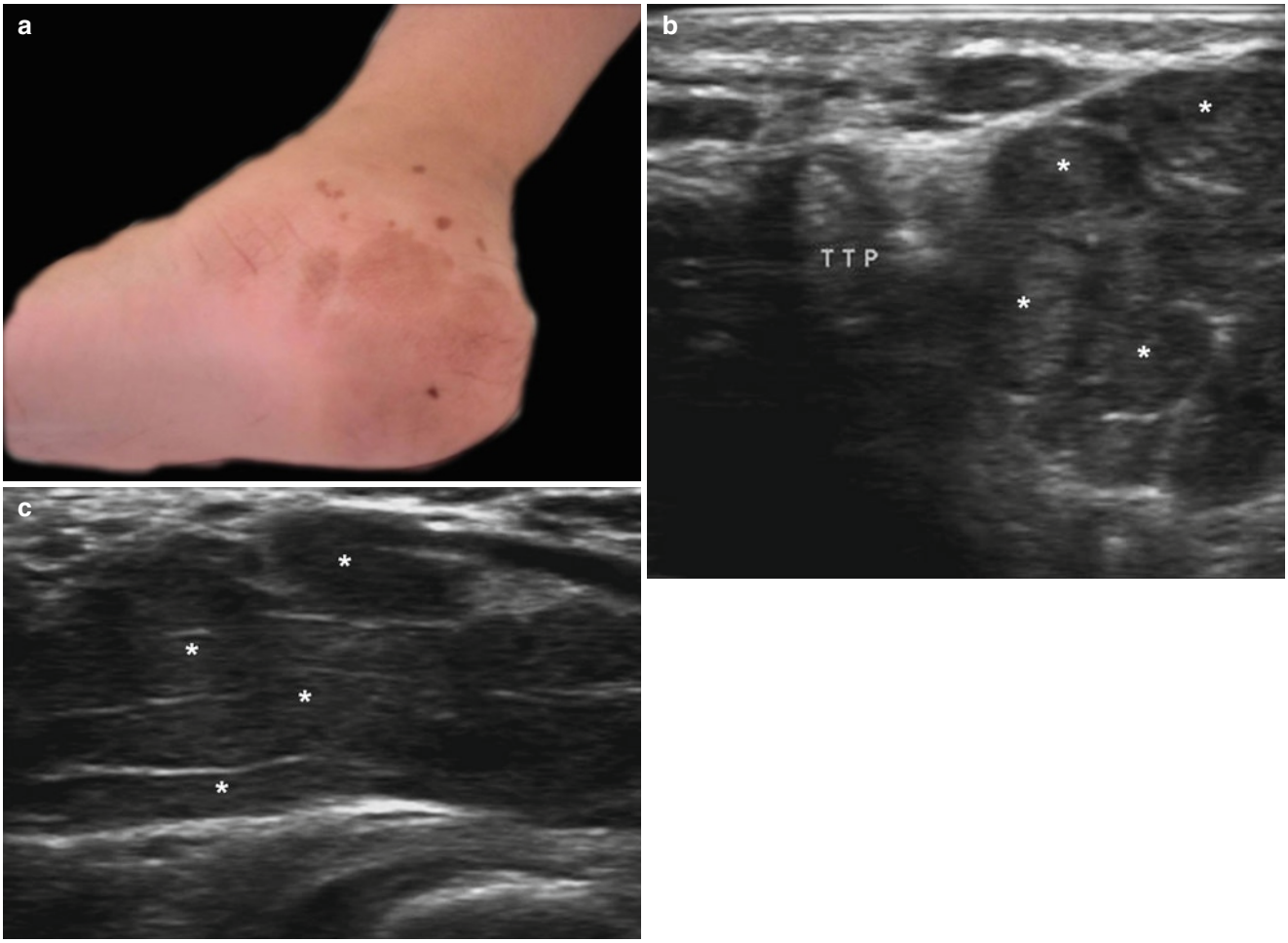

Fig. 3.23 (**a**–**c**) Plexiform neurofibroma. (**a**) Clinical image of child with café-au-lait spots in the medial aspect of the ankle. The child presented difficulties for walking. (**b**) Ultrasound image (gray scale, transverse view, medial aspect of the ankle) shows multiple hypoechoic round-shaped structures (*) following the course of the posterior tibial nerve and its branches. (**c**) Ultrasound image (gray scale, longitudinal view) demonstrates the thick fascicles (*) that compose an appearance of a "bag of worms"

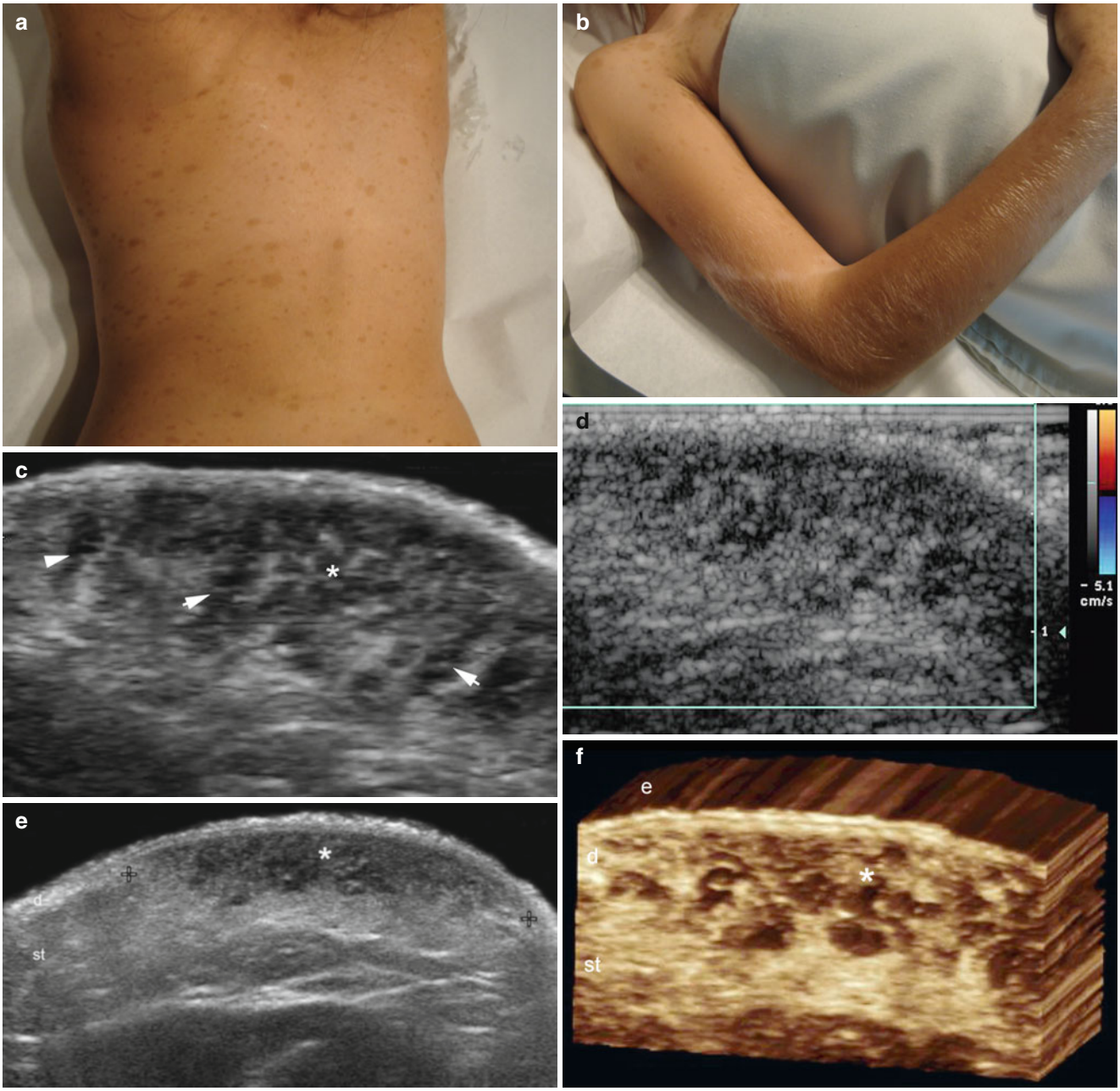

Fig. 3.24 (**a**–**f**) Diffuse neurofibromatosis. (**a**, **b**) Clinical image shows multiple café-au-lait spots in the dorsal (**a**) and right upper extremity (**b**) regions. (**c**) Ultrasound image (gray scale, transverse view, right arm) demonstrates a hypoechoic and heterogeneous dermal and subcutaneous plaque-like structure (*) with several hypoechoic tortuous tracts (*arrows*). (**d**) Color Doppler ultrasound image (transverse view) shows lack of detectable blood flow within the lesion. (**e**) Ultrasound image (gray scale, panoramic view) shows the extension of the lesion (between markers) both in dermis and subcutaneous tissue. (**f**) 3D ultrasound image (transverse view) of the lesion (*). *Abbreviations*: *e* epidermis, *d* dermis, *st* subcutaneous tissue

3.2.9 Neural Fibrolipomatosis

Neural fibrolipomatosis is considered a congenital tumor of the peripheral nerves (hamartoma) which undergo secondary adipose tissue infiltration. Most frequently it affects the median nerve (85 %), but may occasionally involve the acoustic, brachial, ulnar, and radial nerves or small nerve branches in the extremities [48, 49]. Clinically, neural fibrolipomatosis presents with diffuse or localized swelling adjacent to the affected nerves. It is associated with Lipomatous Macrodystrophia, a syndrome with circumscribed overgrowth of mesenchymal tissue that can, for example, affect the fingers (macrodactyly) [50–52].

Sonography shows the enlargement of small cutaneous nerve branches as hypoechoic tracts within the dermis and subcutaneous tissue, usually without accompanying hypervascularity on color Doppler. Involvement of larger nerves may also be detected (Fig. 3.25).

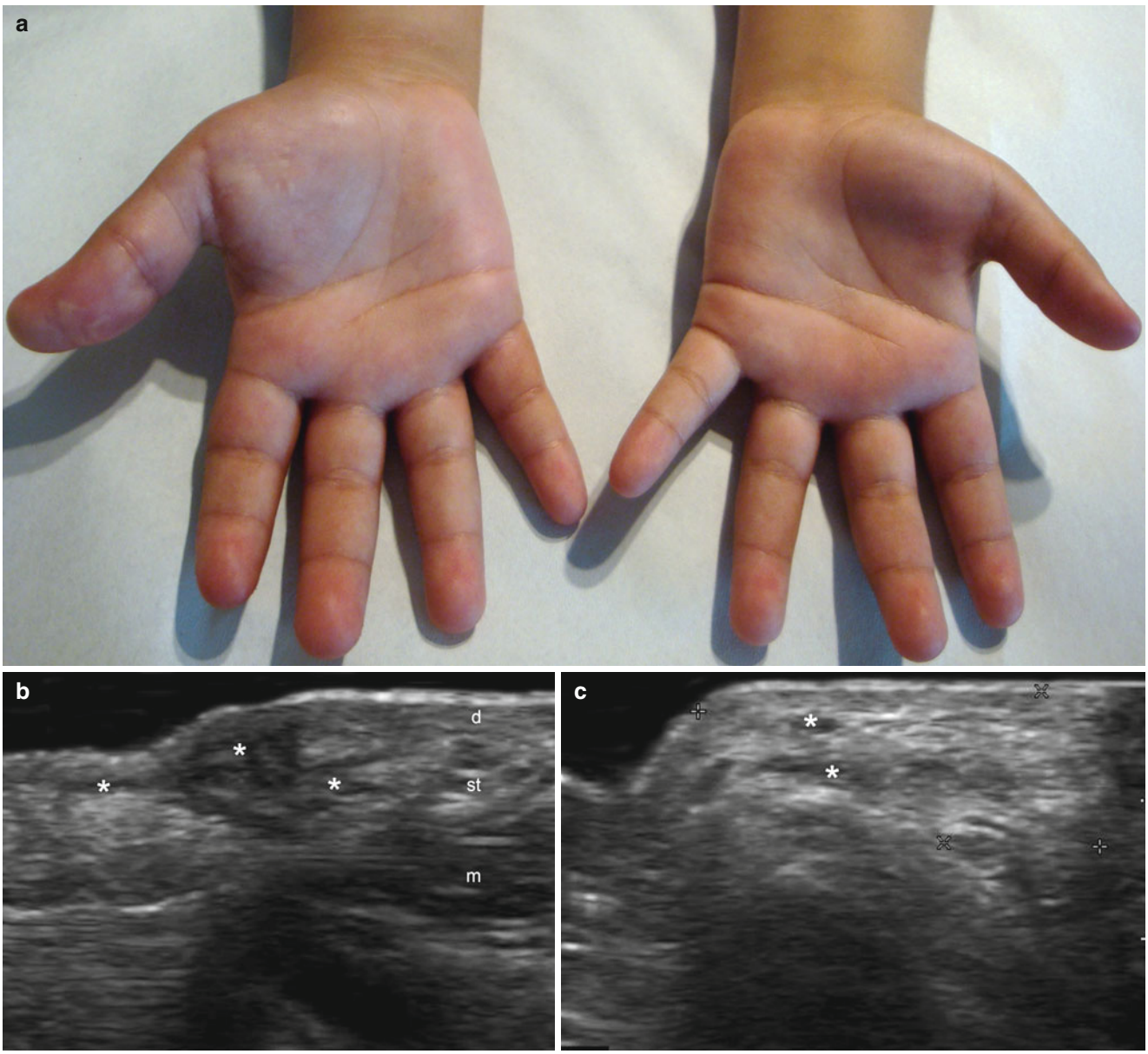

Fig. 3.25 (**a**–**c**) Neural fibrolipomatosis. (**a**) Clinical image of a child presenting macrodactyly in the right hand. (**b**) Ultrasound image (gray scale, longitudinal view at the thenar eminence) shows hypoechoic ill-defined pseudonodules and tracts (*) in the dermis and subcutaneous tissue. (**c**) Ultrasound image (gray scale, transverse view) demonstrates the hypoechoic tortuous tracts and hyperechogenicity of the surrounding tissue. *Abbreviations*: *d* dermis, *st* subcutaneous tissue, *m* muscle

3.2.10 Ichthyosis

Ichthyosis is a heterogeneous group of disorders of epidermal cornification, both inherited and acquired, that share the manifestations of generalized hyperkeratosis and/or scaling of the skin. Vulgar ichthyosis is the most common form, and also the mildest form, characterized by only slight scaling that spares the intertriginous areas and face. More severe forms of ichthyosis include X-chromosome linked recessive icthyosis, lamellar icthyosis, bullous erythrodermic icthyosis, and Harlechin-type icthyosis, that present with ectropion (eversion of the eyelids) of varying degrees, eclabion (eversion of the lips), and hypoplasia of nasal and auricular cartilages. The scalp can be covered with thick scales and also palmoplantar keratoderma (thickening of the skin of the palms and soles) and ungual dystrophies such as onychogriphosis (thickening and increased curvature of the nail), ungual keratosis (thickening of the ungual plates), and ungual fissures or sulcus that may also involve the skin. As a functional consequence of the cutaneous alterations, there can be severe interference with the perspiration process resulting in hyperthermia, hypothermia, or dehydration; there is even an increased potential for the development of toxic effects while using topical dermatologic products [53]. The skin manifestations of ichthyosis are amenable to examination and quantification with ultrasound and thus, it is possible to objectively assess the results of commonly used systemic and topical therapies.

Congenital autosomal recessive ichthyosis (CARI) or lamellar variant results from mutations in at least three chromosomal loci. This is generally compatible with normal life expectancy. It has an unusual phenotype typically diagnosed at birth by a characteristic appearance: babies with CARI are born with marked erythrodermia encased in a collodion-like membrane that appears as an extra layer of skin (babies with collodion); the membrane is shed in 2–3 weeks and replaced with darker brownish-gray color scales [54, 55]. Histology shows epidermal hyperkeratosis and hyperplasia. The unremarkable granular layer of the epidermis does not show signs of inflammation.

The Harlequin-type ichthyosis is of particular interest because it can be diagnosed sonographically while still in utero with the finding of “uneven skin” on prenatal ultrasound [56–61]. Postnatal ultrasound of the skin displays diffuse epidermal thickening with hyperechogenicity; there is also diffuse thickening of the nail plates in all fingernails and toenails with absent interplate space (the hypoechoic space that normally separates the ventral and dorsal ungual plates). The epidermis of the plantar regions appears as a single thick hyperechoic layer instead of the normal bilaminar pattern. Blood flow is generally normal (Fig. 3.26) [62].

Fig. 3.26 (**a**–**g**) Ichthyosis. (**a**) Clinical image shows the ectropion (eversion of the eyelids) in the right eye and the scalp covered with thick scales. (**b**) Clinical image of the plantar keratoderma (thickening and scaling of the skin of the soles). (**c**) Clinical image showing ungual dystrophies and ungual keratosis (thickening of the ungual plates). (**d**) Ultrasound image (gray scale, right plantar region) demonstrates thickening of the epidermis that lose the normal bilaminar pattern. (**e**) 3D ultrasound image (transverse view, plantar region) shows the epidermal thickening. (**f**) 3D ultrasound image (longitudinal view) demonstrates the thickening of the nail plate that lose the normal bilaminar pattern. (**g**) Histology (HE 40 × zoom courtesy of Dr. Claudia Morales) shows epidermal hyperkeratosis and hyperplasia. Notice the thickening of the epidermal stratum corneum (sc) without inflammation. *Abbreviations*: *e* epidermis, *d* dermis, *st* subcutaneous tissue, *pl* nail plate, *n* nail bed, *pnf* proximal nail fold, *dph* distal phalanx

References

1. Kugelman A, Hadad B, Ben-David J, et al. Preauricular tags and pits in newborn: the role of hearing tests. Acta Pediatr. 1997; 86:170–2.
2. Scheinfeld NS, Silverberg NB, Weinberg JM, Nozad V. The preauricular sinus: a review of its clinical presentation, treatment, and associations. Pediatr Dermatol. 2004;21:191–6.
3. Wortsman X, Jemec GBE. Ultrasound of the ear pinna. J Ultrasound Med. 2008;27:761–70.
4. Ahuja AT, Marshall JN, Roebuck DJ, King AD, Metreweli C. Sonographic appearances of preauricular sinus. Clin Radiol. 2000;55:528–32.
5. Maran AGD, Buchanan DR. Branchial cysts, sinuses and fistulae. Clin Otolaryngol. 1978;3:77–92.
6. Ahuja AT, King AD, Metreweli C. Second branchial cleft cysts: variability of sonographic appearances in adult cases. AJNR Am J Neuroradiol. 2000;21:315–9.
7. Wadsworth DT, Siegel MJ. Thyroglossal duct cysts: variability of sonographic findings. AJR Am J Roentgenol. 1994;163:1475–7.
8. Ahuja AT, King AD, King W, Metreweli C. Thyroglossal duct cysts: sonographic appearances in adults. AJNR Am J Neuroradiol. 1999;20:579–82.
9. Ahuja AT, Wong KT, King AD, et al. Imaging for thyroglossal duct cysts:the bare essentials. Clin Radiol. 2005;60:141–8.
10. Ozel SK, Kazez A, Koseogullari AA, Akpolat N. Scapular bronchogenic cysts in children: case report and review of the literature. Pediatr Surg Int. 2005;21:843–5.
11. Jona JZ. Extramediastinal bronchogenic cysts in children. Pediatr Dermatol. 1995;12:304–6.
12. Muramatsu T, Shirai T, Sakamoto K. Cutaneous bronchogenic cyst. Int J Dermatol. 1990;29:143–4.
13. Nocini P, Barbaglio A, Dolci M, et al. Dermoid cyst of the nose: a case report and review of the literature. J Oral Maxillofac Surg. 1996;54:357–62.
14. Tuba Sanal H. Ultrasound finding of dermoid cyst located in neck region:sack –of-marbles sign. KBB Forum 2008;7(1).www.KBB-Forum.net.
15. Smirniotopoulos JG, Chiechi MV. Teratomas, dermoids, and epidermoids of the head and neck. Radiographics. 1995;15: 1437–55.
16. Chim H, Drolet B, Duffy K, Koshima I, Gosain AK. Vascular anomalies and lymphedema. Plast Reconstr Surg. 2010;126: 55e–69e.
17. Fadell 2nd MF, Jones BV. Adams DM. Prenatal diagnosis and postnatal follow-up of rapidly involuting congenital hemangioma (RICH). Pediatr Radiol. 2011;41(8):1057–60.
18. Mulliken JB, Enjolras O. Congenital hemangiomas and infantile hemangioma: missing links. J Am Acad Dermatol. 2004;50: 875–82.
19. North PE, Waner M, James CA, Mizeracki A, Frieden IJ, Mihm Jr MC. Congenital nonprogressive hemangioma: a distinct clinicopathologic entity unlike infantile hemangioma. Arch Dermatol. 2001;137:1607–20.
20. Dubois J, Garel L, David M, Powell J. Vascular soft-tissue tumors in infancy: distinguishing features on Doppler sonography. AJR Am J Roentgenol. 2002;178:1541–5.
21. Gorincour G, Kokta V, Rypens F, Garel L, Powell J, Dubois J. Imaging characteristics of two subtypes of congenital hemangiomas: rapidly involuting congenital hemangiomas and noninvoluting congenital hemangiomas. Pediatr Radiol. 2005;35: 1178–85.
22. Redondo P. Vascular malformations (I). Concept, classification, pathogenesis and clinical features. Actas Dermosifiliogr. 2007; 98(3):141–58. spanish.
23. Mulliken JB, Glowacki J. Hemangiomas and vascular malformations in infants and children: a classification based on endothelial characteristics. Plast Reconstr Surg. 1982;69:412.
24. Gupta A, Kozakewich H. Histopathology of vascular anomalies. Clin Plast Surg. 2011;38(1):31–44.
25. Jackson IT, Carreño R, Potparic Z, Hussain K. Hemangiomas, vascular malformations, and lymphovenous malformations: classification and methods of treatment. Plast Reconstr Surg. 1993;91:1216–30.
26. Burkhead A, Poindexter G, Morrell DS. A case of extensive Aplasia Cutis Congenita with underlying skull defect and central nervous system malformation: discussion of large skin defects, complications, treatment and outcome. J Perinatol. 2009;29(8):582–4.
27. Ribuffo D, Costantini M, Gullo P, Houseman ND, Taylor GI. Aplasia cutis congenita of the scalp, the skull, and the dura. Scand J Plast Reconstr Surg Hand Surg. 2003;37(3):176–80.
28. Bharti G, Groves L, David LR, Sanger C, Argenta LC. Aplasia cutis congenita: clinical management of a rare congenital anomaly. J Craniofac Surg. 2011;22(1):159–65.
29. Frieden IJ. Aplasia cutis congenita: a clinical review and proposal for classification. J Am Acad Dermatol. 1986;14(4):646–60.
30. Schena D, Germi L, Zamperetti MR, Colato C, Girolomoni G. Buschke-ollendorff syndrome. Int J Dermatol. 2008;47(11): 1159–61.
31. Hassikou H, Tabache F, Safi S, Baai M, Hadri L. Buschke-ollendorff syndrome. Joint Bone Spine. 2008;75(2):212–4.
32. Vergara A, Isarría MJ, Sánchez-Caminero P, Rodríguez-Peralto JL, Guerra A. Family buschke-ollendorff síndrome. Actas Dermosifiliogr. 2005;96(1):52–3.
33. Yadegari M, Whyte MP, Mumm S, Phelps RG, Shanske A, Totty WG. Buschke-ollendorff syndrome: absence of LEMD3 mutation in an affected family. Arch Dermatol. 2010;146(1):63–8.
34. Verbov J, Graham R. Buschke-ollendorff syndrome–disseminated dermatofibrosis with osteopoikilosis. Clin Exp Dermatol. 1986; 11(1):1.
35. Roberts NM, Langtry JA, Branfoot AC, Gleeson J, Staughton RC. Case report: osteopoikilosis and the buschke-ollendorff syndrome. Br J Radiol. 1993;66(785):468–70. Review.
36. Horey L, Wollina DU, Ptikha T, Hafner A, Ingber A, Liu L, et al. Lipoid proteinosis: identification of two novel mutations in the human ECM-1 gene and lack of genotype-phenotype correlation. Acta Derm Venereol. 2009;89(5):528–9.
37. Pérez-Finol M, González-Alcira O, Reyna-Villasmil E. Urbach-wiethe disease. Med clin (Barc). 2009;133(7):278–9.
38. Wollina U, Konrad H, Schönlebe J. Lipoid proteinosis. Acta Dermatovenerol Alp Panonica Adriat. 2004;13(4):131–4.
39. Hamada T. Lipoid proteinosis. Clin Exp Dermatol. 2002;27(8): 624–9.
40. Uchida T, Hayashi H, Inaoki M, Miyamoto T, Fujimoto W. A failure of mucocutaneous lymphangiogenesis may underlie the clinical features of lipoid proteinosis. Br J Dermatol. 2007;156(1): 152–7.
41. Holme SA, Lenane P, Krafchik BR. What syndrome es this? Urbach-weithe syndrome (Lipoid proteinosis). Pediatr Dermatol. 2005;22(3):266–7.
42. Shah KN. The diagnostic and clinical significance of café-au-lait macules. Pediatr Clin North Am. 2010;57(5):1131–53.
43. Arnsmeier SL, Riccardi VM, Paller AS. Familial multiple café au lait spots. Arch Dermatol. 1994;130(11):1425–6.
44. Braffman B, Naidich TP. The phakomatoses: part I. Neurofibromatosis and tuberous sclerosis. Neuroimaging Clin N Am. 1994;4(2):299–324.
45. Hassell DS, Bancroft LW, Kransdorf MJ, Peterson JJ, Berquist TH, Murphey MD, et al. Imaging appearance of diffuse neurofibroma. AJR Am J Roentgenol. 2008;190(3):582–8.

46. Chen W, Jia JW, Wang JR. Soft tissue diffuse neurofibromas: sonographic findings. Soft tissue diffuse neurofibromas: sonographic findings. J Ultrasound Med. 2007;26(4):513–8.
47. Lin J, Martel W. Cross-sectional imaging of peripheral nerve sheath tumors: characteristic signs on CT, MR imaging, and sonography. AJR Am J Roentgenol. 2001;176(1):75–82.
48. Fuchs A et al. Lipomatous tumors of soft tissues in the extremities and the waist in adults. J Radiol. 2002;83(9 Pt 1):1035–57.
49. Yildirim S. Neural fibrolipoma of the ulnar nerve in the hand: a case report. Hand Surg. 2005;10(2–3):323–6.
50. Akisue T et al. Neural fibrolipoma of the superficial peroneal nerve in the ankle: a case report with immunohistochemical analysis. Pathol Int. 2002;52(11):730–3.
51. Kim YJ et al. Neural fibrolipoma. J Am Acad Dermatol. 2005;53(3):528–9.
52. Sobel E, Giorgini RJ, Potter GK, Schwartz RD, Chieco TM. Progressive pedal macrodactyly surgical history with 15 year follow-up. Foot Ankle Int. 2000;21:45–50.
53. Oji V, Traupe H. Ichthyosis: clinical manifestations and practical treatment options. Am J Clin Dermatol. 2009;10:351–64. doi:10.2165/11311070-000000000-00000.
54. Lefévre C, Audebert S, Jobard F, et al. Mutations in the transporter ABCA12 are associated with lamellar ichthyosis type 2. Hum Molec Genet. 2003;12:2369.
55. Berg C, Geipel A, Kohl M, Krokowski M, Baschat AA, Germer U, et al. Prenatal sonographic features of harlequin ichthyosis. Arch Gynecol Obstet. 2003;268:48–51.
56. Watson WJ, Mabee Jr LM. Prenatal diagnosis of severe congenital ichthyosis (harlequin fetus) by ultrasonography. J Ultrasound Med. 1995;14:241–3.
57. Meizner I. Prenatal ultrasonic features in a rare case of congenital ichthyosis (harlequin fetus). J Clin Ultrasound. 1992;20:132–4.
58. Mihalko M, Lindfors KK, Grix AW, Brant WE, McGahan JP. Prenatal sonographic diagnosis of harlequin ichthyosis. AJR Am J Roentgenol. 1989;153:827–8.
59. Kudla MJ, Timmerman D. Prenatal diagnosis of harlequin ichthyosis using 3- and 4-dimensional sonography. J Ultrasound Med. 2010;29:317–9.
60. Vohra N, Rochelson B, Smith-Levitin M. Three-dimensional sonographic findings in congenital (harlequin) ichthyosis. J Ultrasound Med. 2003;22:737–9.
61. Bongain A, Benoit B, Ejnes L, Lambert JC, Gillet JY. Harlequin fetus: three-dimensional sonographic findings and new diagnostic approach. Ultrasound Obstet Gynecol. 2002;20:82–5.
62. Wortsman X, Aranibar L, Morales C. Post-natal 2 D and 3D sonography of the skin and nail in congenital autosomal recessive Icthyosis correlated with cutaneous histology. J Ultrasound Med 2011;30:1437–9.

Inflammatory Diseases of the Skin

4

Ximena Wortsman, Laura Carreño, and Claudia Morales

An insight into the world of sonography in psoriasis, morphea, lupus, dermatomyositis, and hidradenitis suppurativa, among others

Contents

4.1 Introduction

This chapter comprises several entities from different origins that can vary from trauma to viral infections or autoimmune diseases. Sonography has been proved useful for unmasking the anatomical changes that affect the skin layers and deeper structures during the inflammatory phases and also may show variable degrees of activity such as active, inactive, or atrophic stages in these conditions. In this chapter we will review the most common cutaneous inflammatory entities that may undergo ultrasonography.

The sonographer usually plays an active role in the assessment of the staging of inflammatory entities, sometimes having to extend the examination to other regions initially not previously requested by the referring physician. Thus, dealing with inflammatory conditions may also imply examining single or multiple lesions during the course of the same examination; therefore, baseline knowledge of the common sites of involvement in some of the entities may facilitate the process. Additionally, details such as sequential lighting of the examination room should be considered to properly place the probe when dealing with multiple locations.

4.2 Pathology

4.2.1 Hematomas-Seromas

Fluid collections secondary to trauma comprise one of the common causes of ultrasound requests in the soft tissues. The difference between hematomas and seromas is that hematomas contain a high presence of red blood cells, blot clots, and inflammatory cells in the acute phase that also show fibrin, granulation tissue, and debris in the late phases. In contrast, seromas (also called lymphoceles) are mainly composed of clear serous lymph fluid usually generated by leaks in the lymphatic network. Patients presenting with hemophilia, Ehler-Danlos syndrome, and sickle cell anemia may also easily have hematomas in the soft tissues. Thus, fluid hematic

X. Wortsman, MD (✉)
Department of Radiology and Dermatology,
Institute for Diagnostic Imaging
and Research of the Skin and Soft Tissues,
Clinica Servet, University of Chile, Faculty of Medicine,
Almirante Pastene 150, Providencia, Santiago, Chile
e-mail: xwo@tie.cl, xworts@yahoo.com, www.sonoskin.com

L. Carreño, MD • C. Morales, MD
Department of Pathology,
Dermopathology Section,
Hospital Clinico Universidad de Chile, Faculty of Medicine,
University of Chile, Santiago, Chile
e-mail: lcarrenotoro@gmail.com;
claudiamohuber@gmail.com

X. Wortsman, G.B.E. Jemec (eds.), *Dermatologic Ultrasound with Clinical and Histologic Correlations*,
DOI 10.1007/978-1-4614-7184-4_4,

collections are frequently found in the cutaneous layers and can vary in their sonographic representation according to the main composition, phase of involvement, and presence of liquefaction that could also show a mixed pattern (sero-hematic collections). Hematomas may commonly present on sonography as anechoic collections that can turn to hypoechoic or heterogeneous within days or weeks. Seromas usually present as anechoic clean collections as a result of their serous component. At the beginning the fluid collections are usually compressible with the probe and at late stages, compression is hard to perform because the fluid has been replaced by fibrous tissue and scarring components. The size of the collection also varies over a short period of time (days) and the sonographic follow up could be an objective way to confirm the regression of the hematoma. The latter fact could be important when dealing with hemorrhagic soft-tissue tumors that can occasionally mimic hematomas, but these entities usually do not significantly regress over days. Hemorrhagic tumors commonly show a mixed echogenicity with hypoechoic-anechoic or heterogeneous echogenicity, and they present low or absent capability of compression with the probe. Color Doppler can show peripherical hypervascularity in hematomas at the initial stages and hypovascularity at the late phases [1–5] (Fig. 4.1).

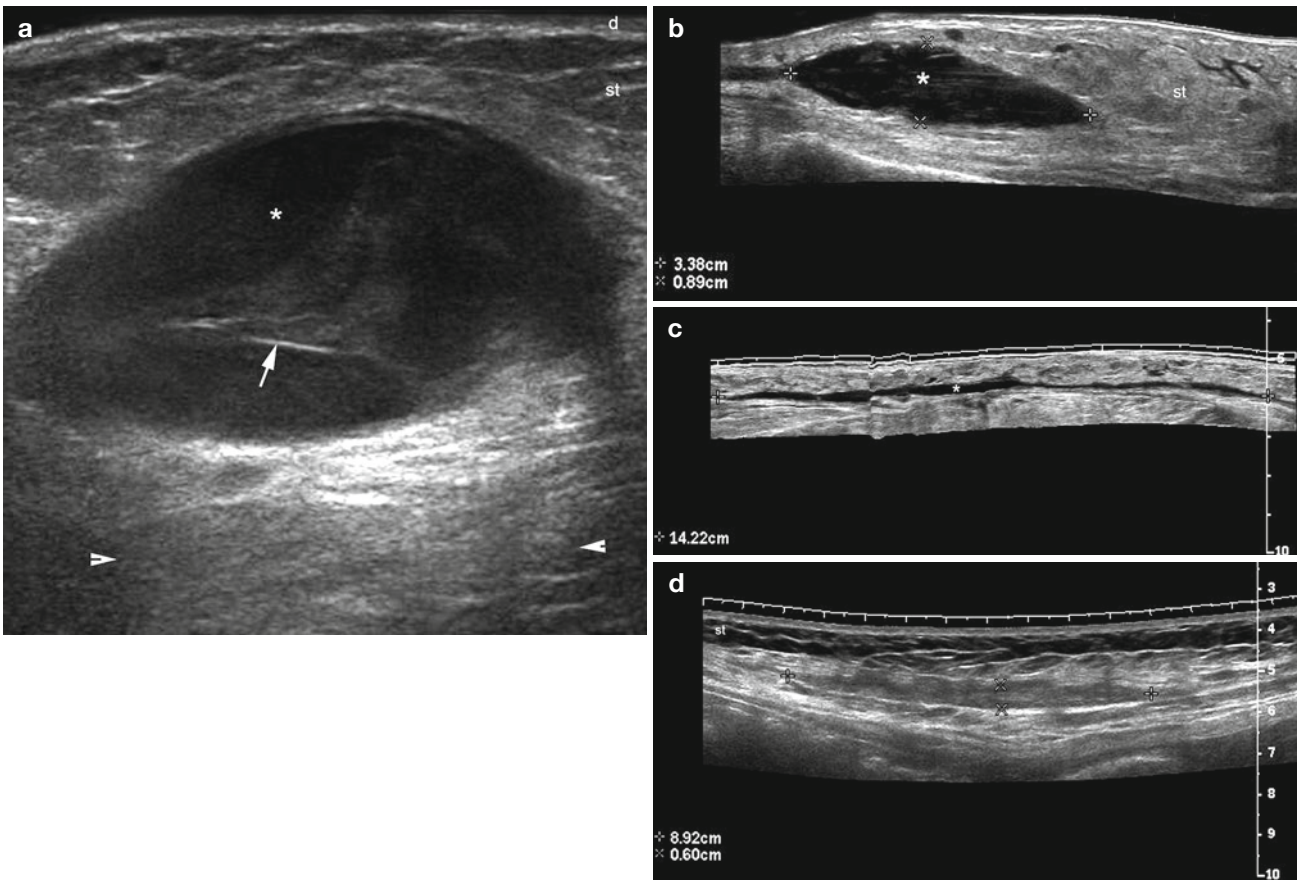

Fig. 4.1 (**a**–**d**) Hematomas. Sonographic appearances of hematic fluid collections (* and between markers) going from large (**a**, **b**) to laminar deposits (**c**, **d**). Notice the posterior acoustic reinforcement (*arrowheads*) and the internal septation (*arrow*) clearly depicted in (a). *Abbreviations*: *d* dermis, *st* subcutaneous tissue

4.2.2 Abscesses

Abscesses imply the presence of infection and/or pus within a fluid collection. Common causes of these organized collections are hematomas, ruptured epidermal cysts, inflamed pilonidal cysts, etc. Skin and soft-tissue infections are also the most common cause for hospital admission of injection drug users [6]. Abscesses present on ultrasound as distended anechoic or heterogeneous fluid collections, usually with multiple echoes or debris. They sometimes present anechoic communicating tracts to superficial (e.g., epidermal or subepidermal) or deep (e.g., muscular or articular) layers. Color Doppler usually demonstrates increase blood flow predominantly in the periphery of the collection [7]. Ultrasound-guided needle aspiration can be a useful technique for the identification of causative pathogens, and good results could be expected with ultrasound-guided gun biopsy culture from lesions without fluid collection [8] (Figs. 4.2 and 4.3).

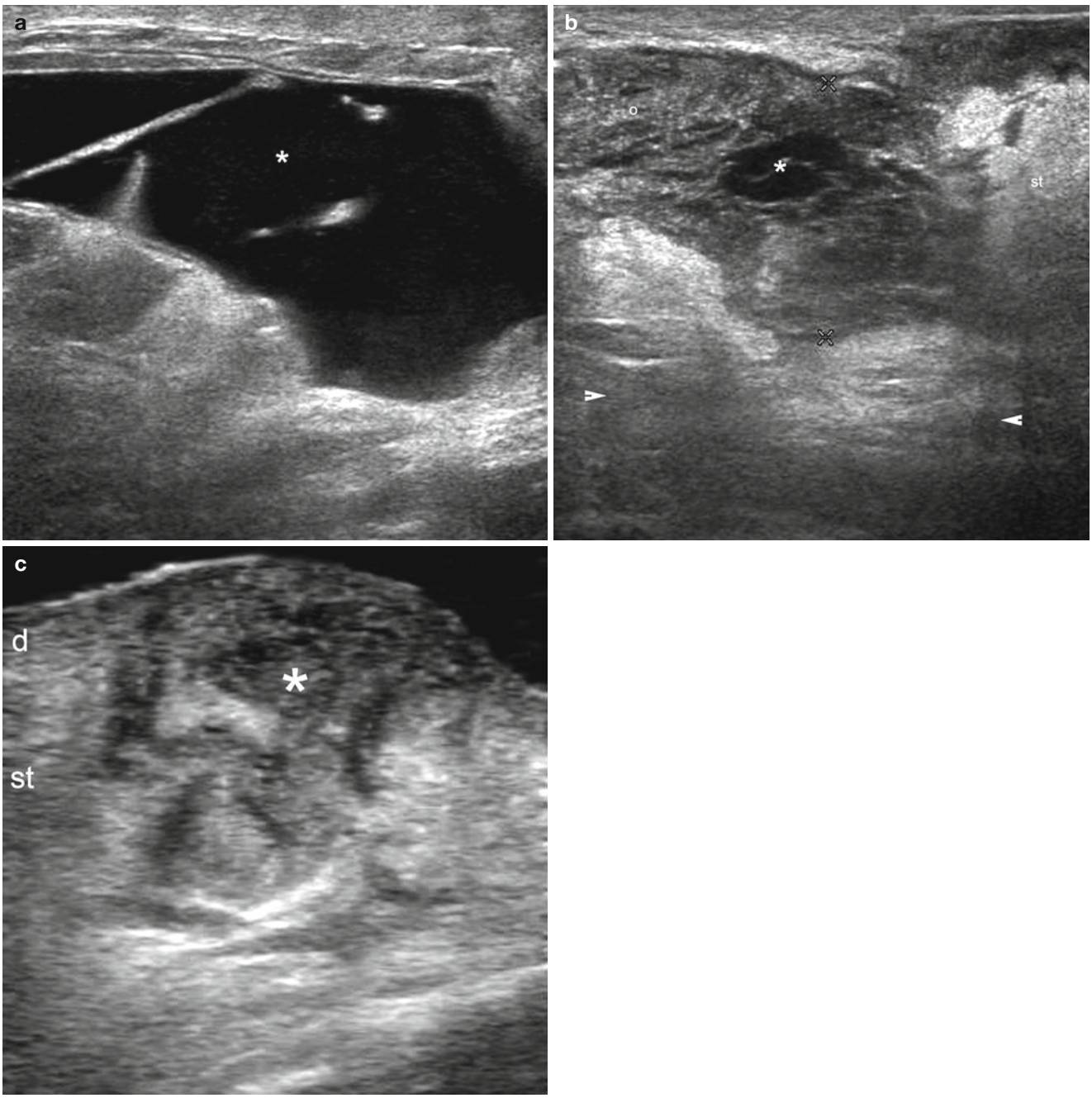

Fig. 4.2 (**a**–**c**) Abscesses. Variable sonographic appearances of cutaneous abscesses. (**a**) Large abscess that presents anechogenicity and prominent septa within the collection (*). (**b**) Abscess that shows heterogeneous echogenicity (o and *, hypoechoic and anechoic areas, respectively). A posterior acoustic reinforcement artifact (*arrowhead*) is also demonstrated. (**c**) There is an ill-defined fluid collection mostly hypoechoic and heterogeneous located in the dermis and subcutaneous tissue. *Abbreviations*: *d* dermis, *st* subcutaneous tissue

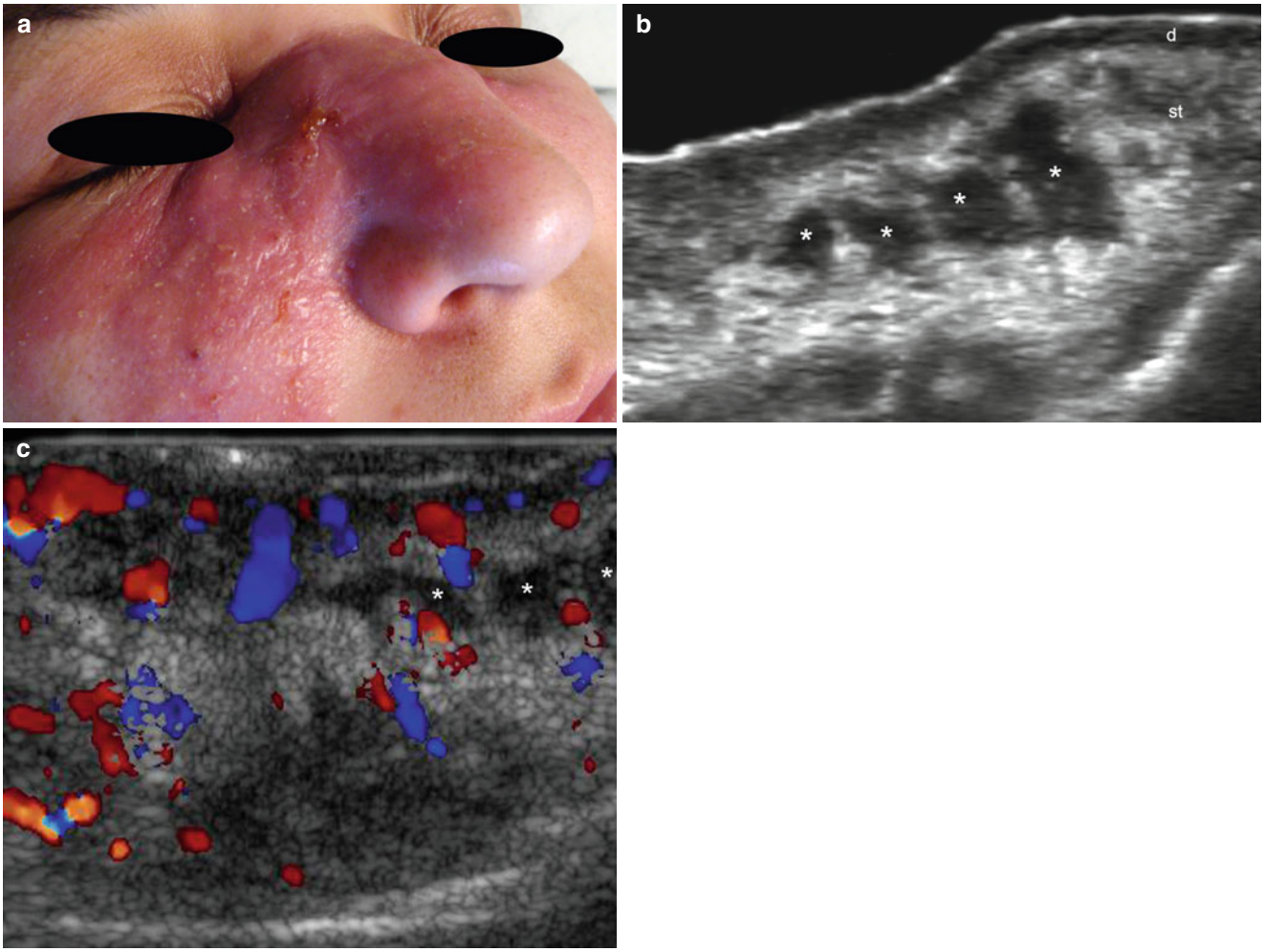

Fig. 4.3 (**a**–**c**) Multiple cutaneous abcesses. (**a**) Clinical lesion shows erythema and swelling at the right cheek. (**b**) Gray scale (transverse view) shows multiple round and oval shaped hypoechoic fluid collections (*) and increased echogenicity of the surrounding subcutaneous tissue. (**c**) Color Doppler (transverse view) demonstrates increased vascularity in the periphery of the collections (*). *Abbreviations*: *d* dermis, *st* subcutaneous tissue

4.2.3 Edema

The retention of fluid within the skin layers can be caused by various entities from trauma to inflammatory diseases. The venous and/or lymphatic systems usually fail to remove the excess of fluid that becomes stuck between the fatty lobules of the subcutaneous tissue. The incompetence of the lymphatic system is called lymphedema and differs from lipoedema, the latter being a different concept that implies an accumulation of fat abnormally distributed in the lower limbs [9]. Ultrasound has been reported to support the assessment of the changes in the thickness of the skin layers in post-thrombotic syndrome and the monitoring of the compression therapy in chronic venous disease [10]. Impairment of cutaneous microcirculation is a major predisposing factor in inflammation and ulceration in patients with chronic venous insufficiency (CVI). Increase of capillary filtration rate predisposes to the formation of edema. Local lymphedema is a complication of CVI and is often underdiagnosed [11]. On sonography, edema usually appears as anechoic fluid between the lobules of the subcutaneous tissue. In cases with lymphedema there is thickening of all the cutaneous layers, hypoechogenicity of the dermis, and increased echogenicity of the subcutaneous tissue in addition to the anechoic fluid between the fatty lobules of the hypodermis (Figs. 4.4 and 4.5).

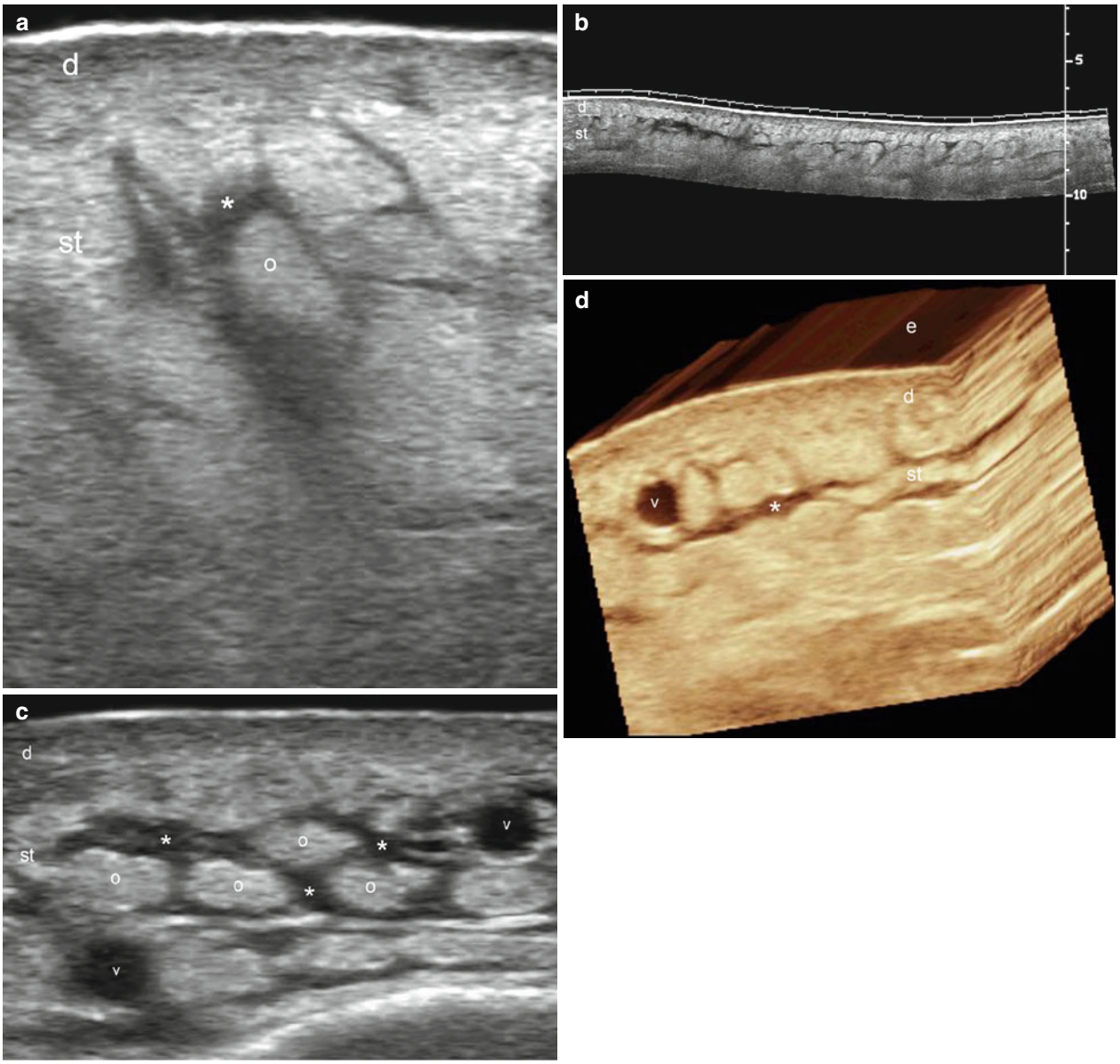

Fig. 4.4 (**a**–**d**) Cutaneous edema. Variable sonographic representations of cutaneous edema that show thickening and decreased echogenicity of the dermis and increased echogenicity of the fatty lobules (o) of the subcutaneous tissue. Notice the hypoechoic or anechoic fluid (*) in between the fatty lobules. Blurring of the borders of the lobules can be also detected (**a**, **b**). In (**c**), there is fluid surrounding the fatty lobules providing a "cobblestone" appearance. (**b**) Shows an extended field of view of the edema and (**d**) demonstrates the edema in 3D. *Abbreviations*: *d* dermis, *st* subcutaneous tissue, *v* vein

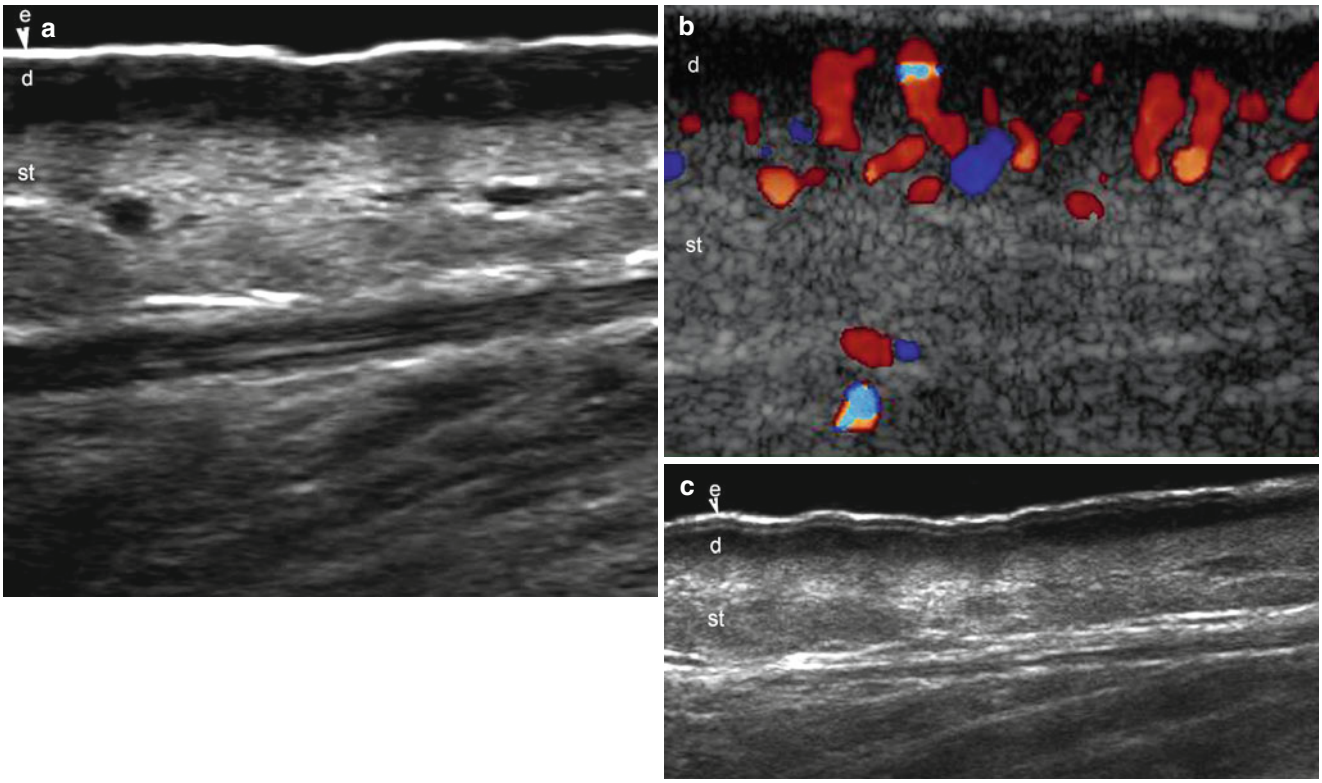

Fig. 4.5 (**a**–**c**) Lymphedema. (**a**) Gray scale ultrasound image shows marked and diffuse hypoechogenicity of the dermis and increased echogenicity of the subcutaneous tissue. Also, notice the prominent hyperechogenicity of the epidermis. (**b**) Color Doppler ultrasound image demonstrates increased vascularity in the dermis. (**c**) Extended field of view (gray scale) shows lymphedema that affect all the cutaneous layers of the leg. Notice the bilaminar appearance of the epidermis that resembles the pattern that is seen in glabrous skin and the prominent decrease of the echogenicity in the dermis and increased echogenicity in the subcutaneous tissue. *Abbreviations*: *e* epidermis, *d* dermis, *st* subcutaneous tissue

4.2.4 Chronic Venous Insufficiency-Lipodermatosclerosis-Liposclerosis

This is the result of an impairment of the main superficial veins and their tributaries that elicit microvascular changes derived from venous ecstasy. Thus, veins and capillaries become dilated, elongated, and tortuous and their endothelium is injured generating an increased extravasation, leading to an enlarged pericapillary space, edema in the interstitial tissue, and to the clinical finding of swelling. Hemoglobin from extravasated erythrocytes in the pericapillary space is degraded to hemosiderin and is responsible for hyperpigmentation. Microthrombosis in the capillaries causes microinfarction and micronecrosis. Hence, skin areas with severe microangiopathy have reduced numbers of perfused nutritional capillaries. Furthermore, the increased blood flow in the deeper skin layers does not contribute to nutrition of the superficial skin layers. The microvascular ischemia is patchy and appears to be the main factor determining trophic changes and venous ulceration. The process of microinfarction and micronecrosis is followed by the formation of a granulation tissue, proliferation of capillaries and fibroblasts, and finally wound healing by formation of scar tissue destroying the microlymphatic network. Clinically this process leads to lipodermatosclerosis, also called liposclerosis (i.e., induration and hyperpigmentation), atrophy, and in its most extreme form, to ulceration where the compensating mechanisms are no longer able to repair the damage. Thus, incompetence of the superficial venous system can generate dilation and secondaryt edema in the skin layers. The most common affected veins are the saphenous venous system (greater and lesser saphenous veins), the perforans veins (i.e., drain superficial structures directly into the deep venous system, therefore, crossing the fascial plane), and communicating veins (i.e., connecting veins in the same fascial plane and venous system). The incompetent vessels and their venous reflux are detectable using sonography, the latter being a feature usually well demonstrated on color Doppler and spectral curve analysis, and mainly when performing the Valsalva maneuver, which is even more evident when the patient is in upright position. Clinically, the skin shows varicose veins (i.e., dilated, tortuous, and palpable veins), reticular veins (i.e., dilated but non-palpable veins), and/or telangiectasias (small reddish to purple non-palpable dilated venous tracts) [12, 13]. Ultrasound has been reported as useful for guiding treatments such as sclerotherapy supporting the localization of the insufficient venous tracts [14]. Lipodermatosclerosis is a consequence of deep venous insufficiency and a risk factor for the occurrence of venous leg ulceration. It is characterized by induration and hyperpigmentation of the skin involving one or both of the lower legs in a characteristic "inverted champagne bottle" appearance. Associated with venous insufficiency, chronic lipodermatosclerosis is most common in middle-aged women. In addition to the chronic form of presentation there is an acute form that exhibits symptoms of severe pain. On sonography, lipodermatosclerosis presents as a diffuse thickening and decreased echogenicity of the dermal layer commonly associated with superficial venous insufficiency signs [15–17] (Figs. 4.6, 4.7 and 4.8).

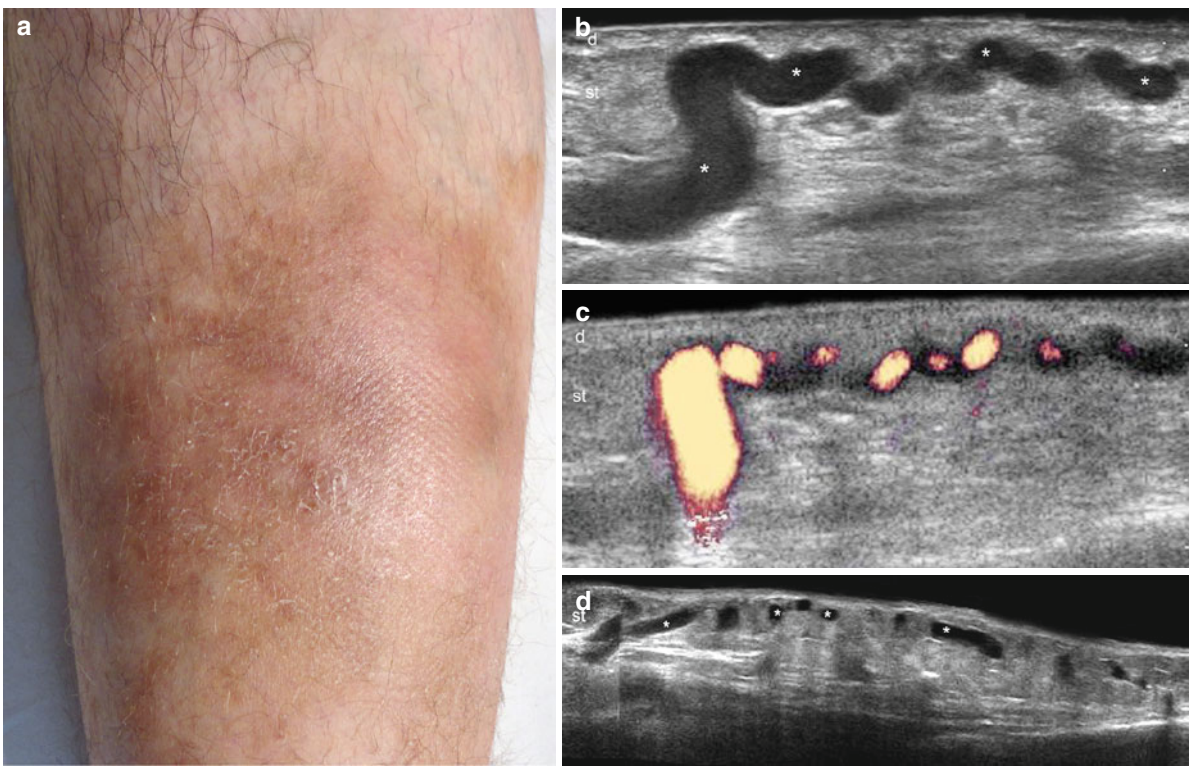

Fig. 4.6 (**a**–**d**) Venous insufficiency. (**a**) Clinical view shows hyperpigmentation and swelling in the anterior aspect of the leg. (**b**) Gray scale ultrasound image (longitudinal view) demonstrates dilated and tortuous perforans venous vessels (*) affecting mostly the upper subcutaneous tissue. (**c**) Power Doppler ultrasound image (longitudinal view) demonstrates flow within the vessels. (**d**) Gray scale ultrasound image (longitudinal extended field of view) shows a wider view of the venous vessels (*) and increased echogenicity of the underlying subcutaneous tissue. *Abbreviations*: *d* dermis, *st* subcutaneous tissue

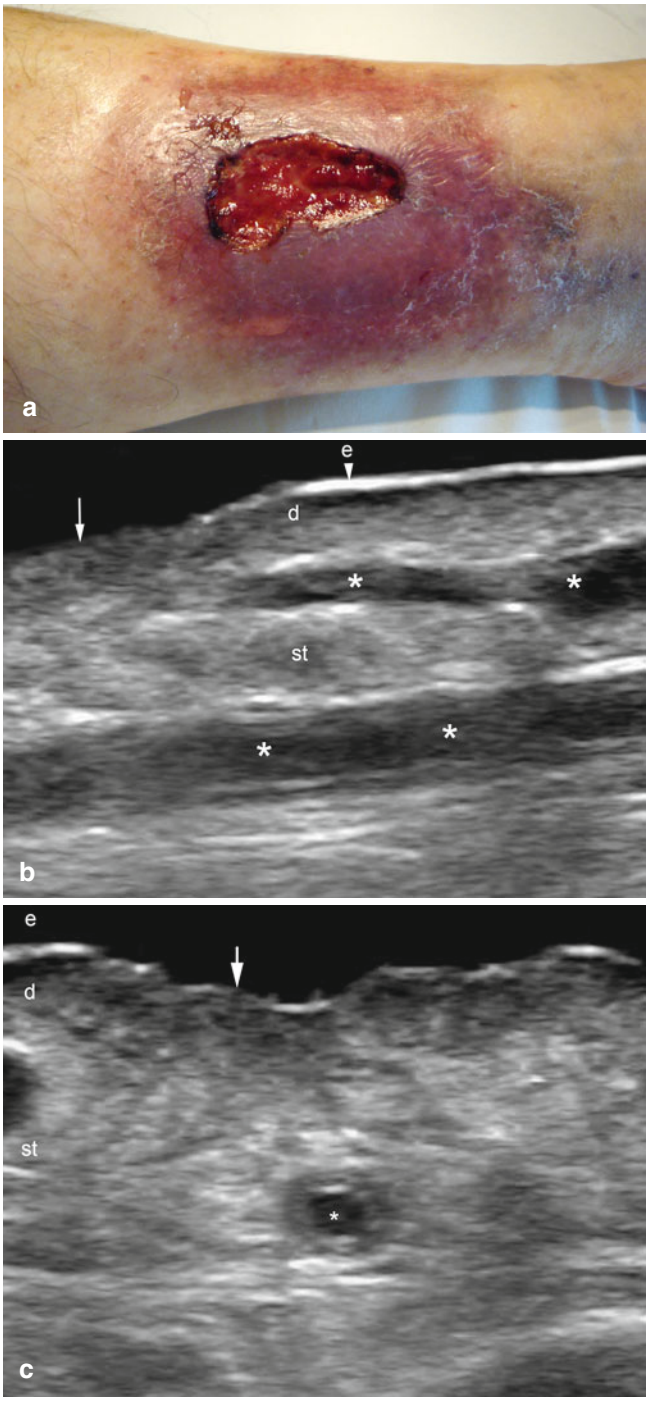

Fig. 4.7 (**a**–**c**) Venous ulcer. (**a**) Clinical lesion. (**b**) Gray scale ultrasound image (longitudinal axis) at the border of the ulcer shows interruption of the epidermis (*arrow*) and dilated anechoic venous vessels (*) in the underlying subcutaneous tissue. Increased echogenicity of the subcutaneous fatty tissue is also detected. (**c**) Gray scale ultrasound image (transverse view) demonstrates increased thickness of the wall of a subcutaneous venous vessel (*) secondary to inflammation. The *arrow* is pointing out the disruption of the epidermal layer. *Abbreviations*: *e* epidermis (*arrowhead*), *d* dermis, *st* subcutaneous tissue

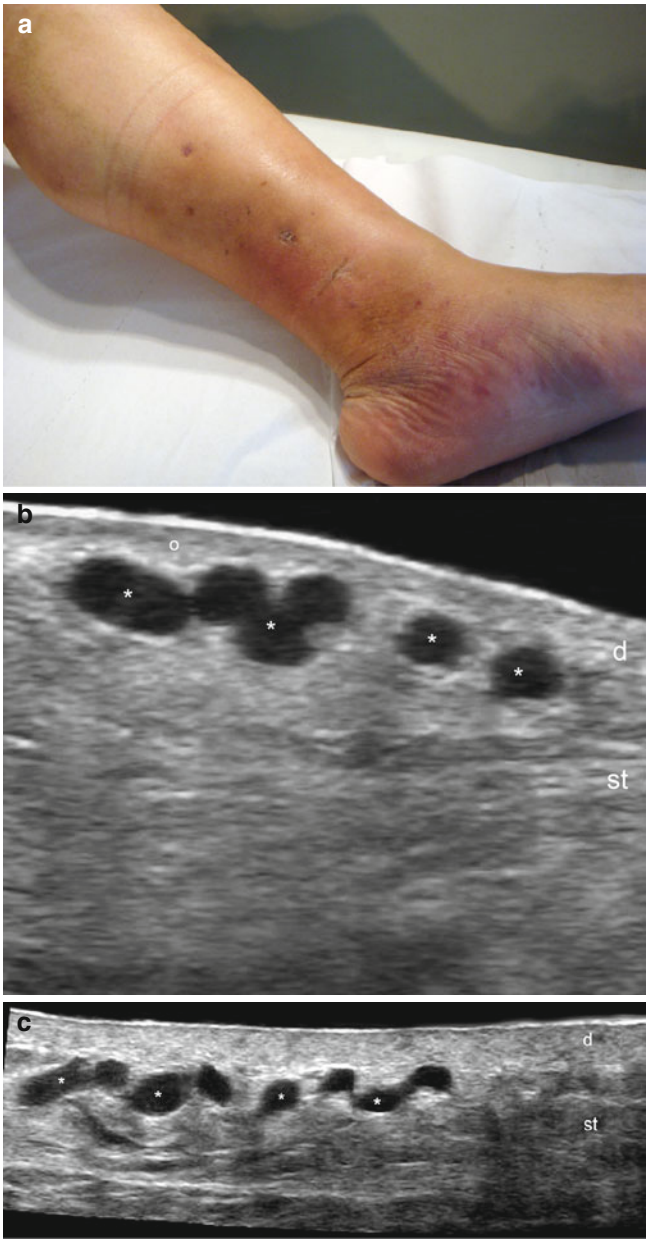

Fig. 4.8 (**a**–**c**) Chronic venous insufficiency. (**a**) Clinical image shows swelling and light pigmentation of the medial aspect of the leg. (**b**) Gray scale ultrasound image (longitudinal view) shows dilated and tortuous anechoic venous vessels (*) in the upper subcutaneous tissue. There is decreased echogenicity of the dermis (*, *d*) and increased echogenicity of the subcutaneous tissue. (**c**) Gray scale ultrasound image (longitudinal extended field of view) demonstrates the wide extension of the dilated and tortuous subcutaneous venous tracts (*). *Abbreviations*: *d* dermis, *st* subcutaneous tissue

4.2.5 Panniculitis

Panniculitis implies the presence of inflammation in the adipose tissue of the subcutaneous layer. It can be associated with a wide range of systemic diseases or local injuries such as trauma or cold, among others.

Clinically, panniculitis is characterized by red, purplish, or skin-colored lumps. Nevertheless, the clinical features frequently show low specificity and can cause trouble with obtaining a diagnosis on the physical examination.

Panniculitis is usually somewhat mixed because the inflammatory infiltrate involves both the septa and lobules; however, histologically, panniculitis can be classified according to the main affected component in the subcutaneous tissue, hence it can be separated into two types: septal and lobular panniculitis, and then each subtype can be subdivided according to presence of vasculitis as follows:

1. Septal panniculitis with vasculitis
2. Septal panniculitis without vasculitis
3. Lobular panniculitis with vasculitis
4. Lobular panniculitis without vasculitis

Septal panniculitis with vasculitis includes leukocytoclastic vasculitis involving the small blood vessels of the septa; superficial thrombophlebitis resulting from inflammation and subsequent thrombosis of large veins of the septa; and cutaneous polyarteritis nodosa, which is a vasculitis that involves the arteries and arterioles of the septa of subcutaneous fat with few or no systemic manifestations. Often septal panniculitis without vasculitis is the consequence of dermal inflammatory processes extending to the subcutaneous fat, such as necrobiosis lipoidica, subcutaneous granuloma annulare, scleroderma, rheumatoid nodule, and necrobiotic xanthogranuloma. However, in other cases, the inflammatory process is primarily located in the fibrous septa of the subcutis with or without involvement of the overlying dermis such as in erythema nodosum, the most frequently seen septal panniculitis (without vasculitis). Erythema nodosum in fully developed lesions is characterized histopathologically by Miescher's radial granulomas in the septa. On sonography, septal panniculitis (SP) shows prominent thickening and hypoechogenicity of the septa, in addition to the increased echogenicity of the fatty tissue. In contrast, lobular panniculitis primarily affects the lobules of the fatty subcutaneous tissue and can be observed in a wide spectrum of diseases such as erythema induratum of Bazin (nodular vasculitis), the most common variant of lobular panniculitis with vasculitis, or sclerosing panniculitis that results from chronic venous insufficiency of the lower extremities; calciphylaxis and oxalosis, which implies panniculitis with calcification of the vessel walls, sclerema neonatorum, an inflammatory disease with crystals within the adipocytes, subcutaneous fat necrosis of the newborn, and post-steroid panniculitis, among others. Lobular panniculitis may also be an expression of infections, trauma, or factitial causes involving subcutaneous fat. Lipodystrophies are common sequelae of panniculitis and can be separated in hypertrophic or atrophic, according to the increase or decrease in the fatty component [18–20]. On sonography, lobular panniculitis presents as marked blurriness and increased echogenicity of the fatty lobules of the subcutaneous tissue. Although the septa may present some degree of thickening and hypoechogenicity, these changes are less prominent compared with SP. In the presence of fat necrosis, anechoic or hypoechoic round-shaped pseudocystic structures have been reported as the result of fat liquefaction [21]. On color Doppler imaging, vascularity can be variable going from low to high although the hypovascularity in the subcutaneous tissue on the ultrasound examination does not detract the presence of vasculitis. Therefore, the primary role of ultrasound should be directed to assess the presence of panniculitis and ideally support the difference between mostly septal or lobular panniculitis (Figs. 4.9, 4.10, 4.11, 4.12 and 4.13).

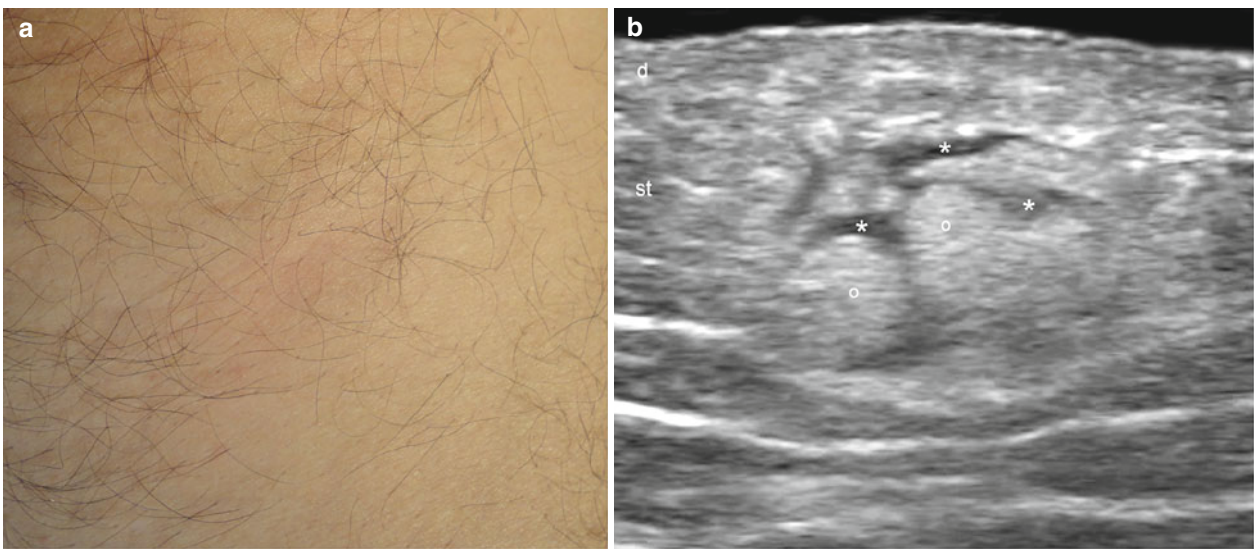

Fig. 4.9 (**a**–**e**) Mostly septal panniculitis. (**a**) Clinical image shows slight erythema and induration. (**b**) Gray scale (longitudinal view) demonstrates focal increased echogenicity of the fatty lobules (o) of the subcutaneous tissue with prominent hypoechoic septa (*). (**c**) Color Doppler ultrasound image (longitudinal view) shows a thick vessel running through the lesional area. (**d**) The lesional area in 3D (5–8 s transverse axis sweep). (**e**) Histology (HE 100× zoom) shows thickening and inflammation of the septa (*arrows*) that surround the fatty lobules (o) of the subcutaneous tissue. *Abbreviations*: *e* epidermis, *d* dermis, *st* subcutaneous tissue

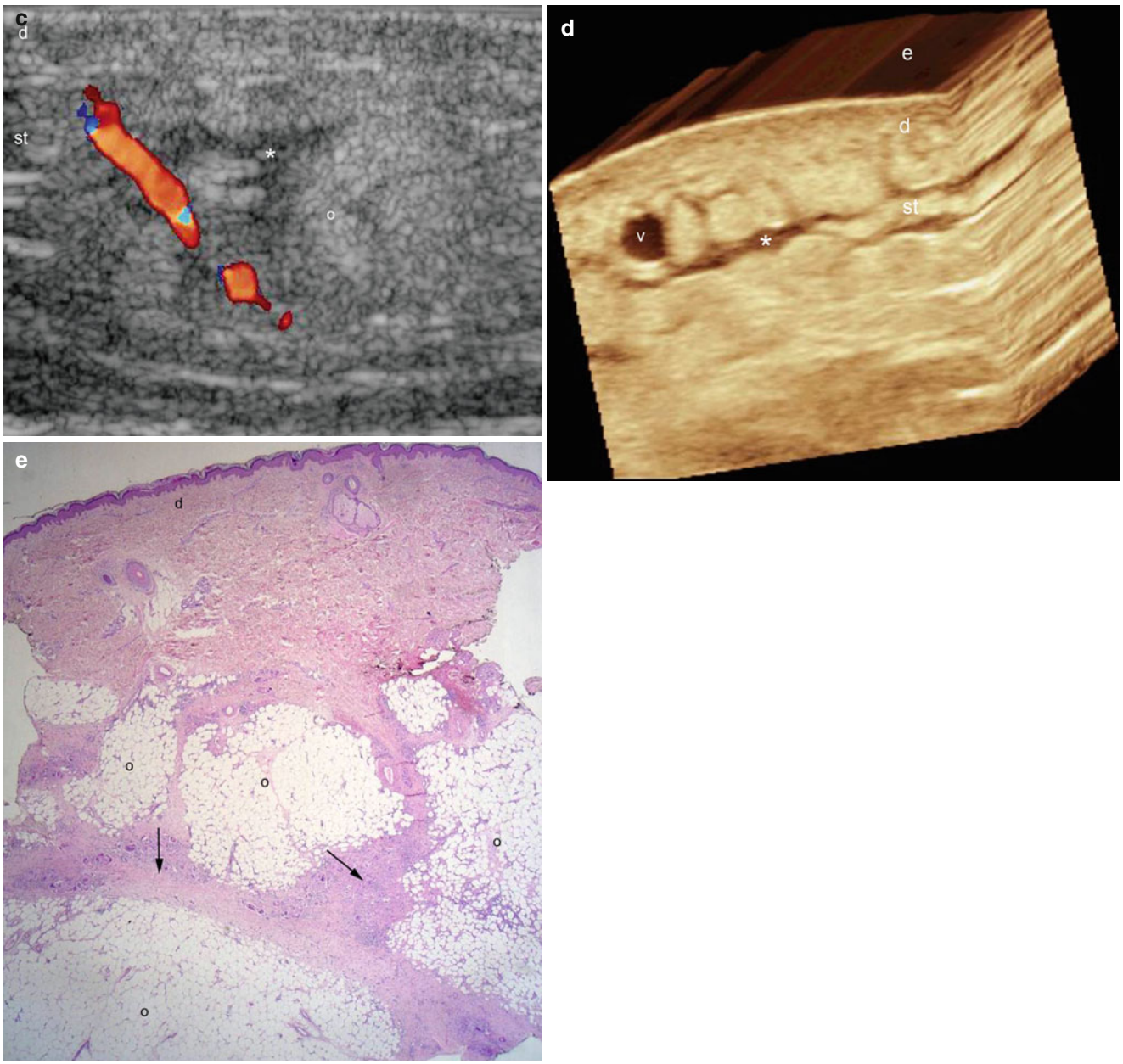

Fig. 4.9 (continued)

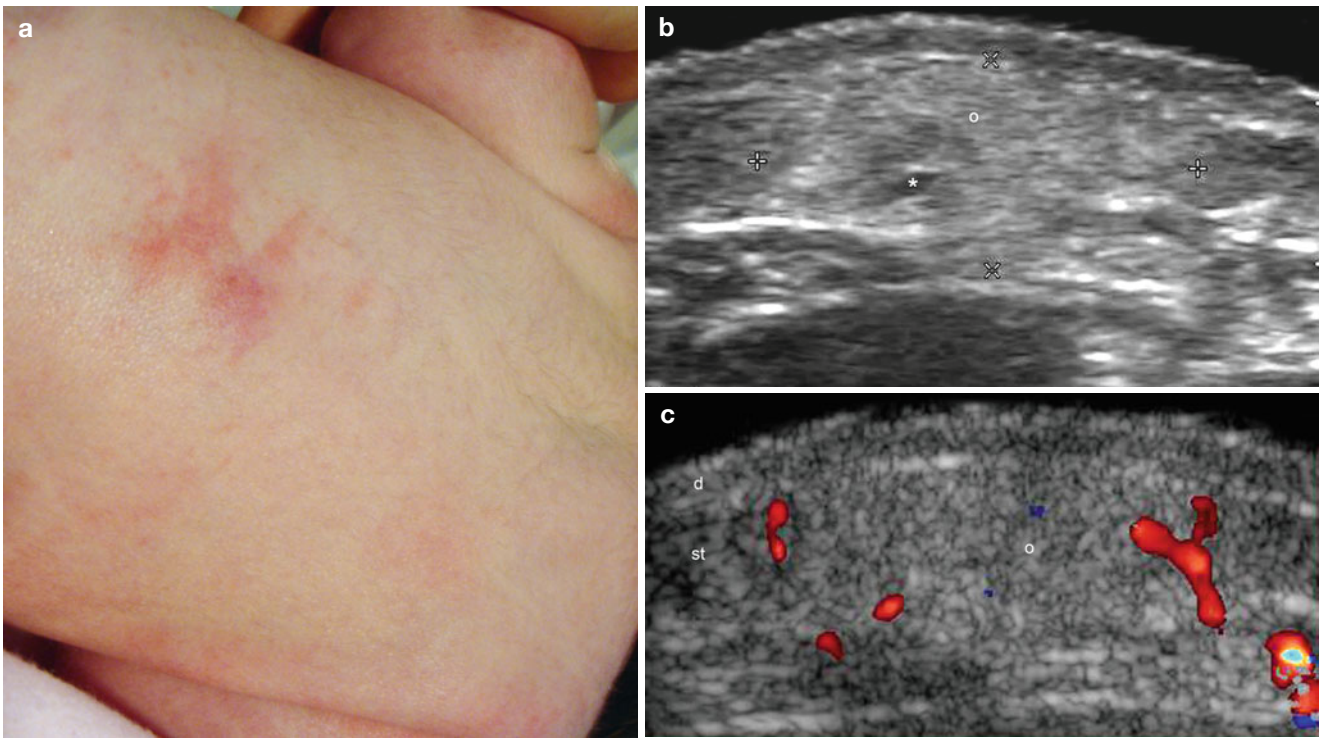

Fig. 4.10 (**a**–**c**) Mostly lobular panniculitis. Fat Necrosis of the newborn. (**a**) Clinical image shows erythema and swelling in the dorsolumbar region in a newborn. (**b**) Gray scale ultrasound image (transverse view) demonstrates increased echogenicity of the fatty lobules of the subcutaneous tissue with blurriness of the borders of the lobules (o). In-between the fatty tissue there is a small anechoic round-shape pseudocystic hypoechoic structure (*) that corresponds to a fat liquefaction area. (**c**) Color Doppler ultrasound image (transverse view) shows increased vascularity in the periphery of the lesional area and hypovascularity within the lesion (o). *Abbreviations*: *d* dermis, *st* subcutaneous tissue

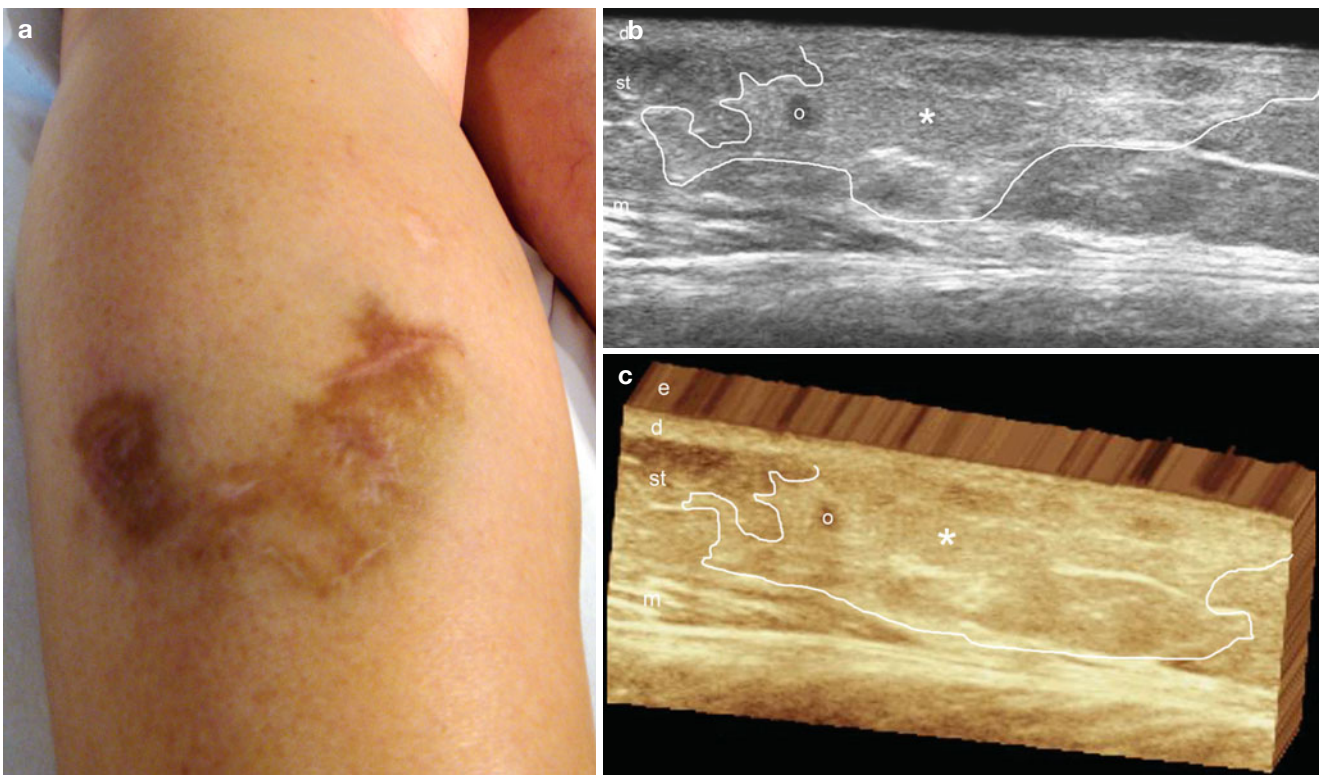

Fig. 4.11 (**a**–**c**) Mostly lobular panniculitis secondary to a dog bite. (**a**) Clinical lesion 8 months after dog bite in the calf shows a scarring, swelling and hyperpigmentation. (**b**) Gray scale ultrasound image (longitudinal view) demonstrates increased echogenicity and blurriness of the fatty lobules of the subcutaneous tissue (* and outlined) and a focal pseudocystic round-shaped hypoechoic structure (o) that corresponds to a liquefaction area of the fat (fat necrosis). (**c**) The lesion in 3D (5–8 s sweep). *Abbreviations*: *e* epidermis, *d* dermis, *st* subcutaneous tissue, *m* medial gastrocnemious muscle

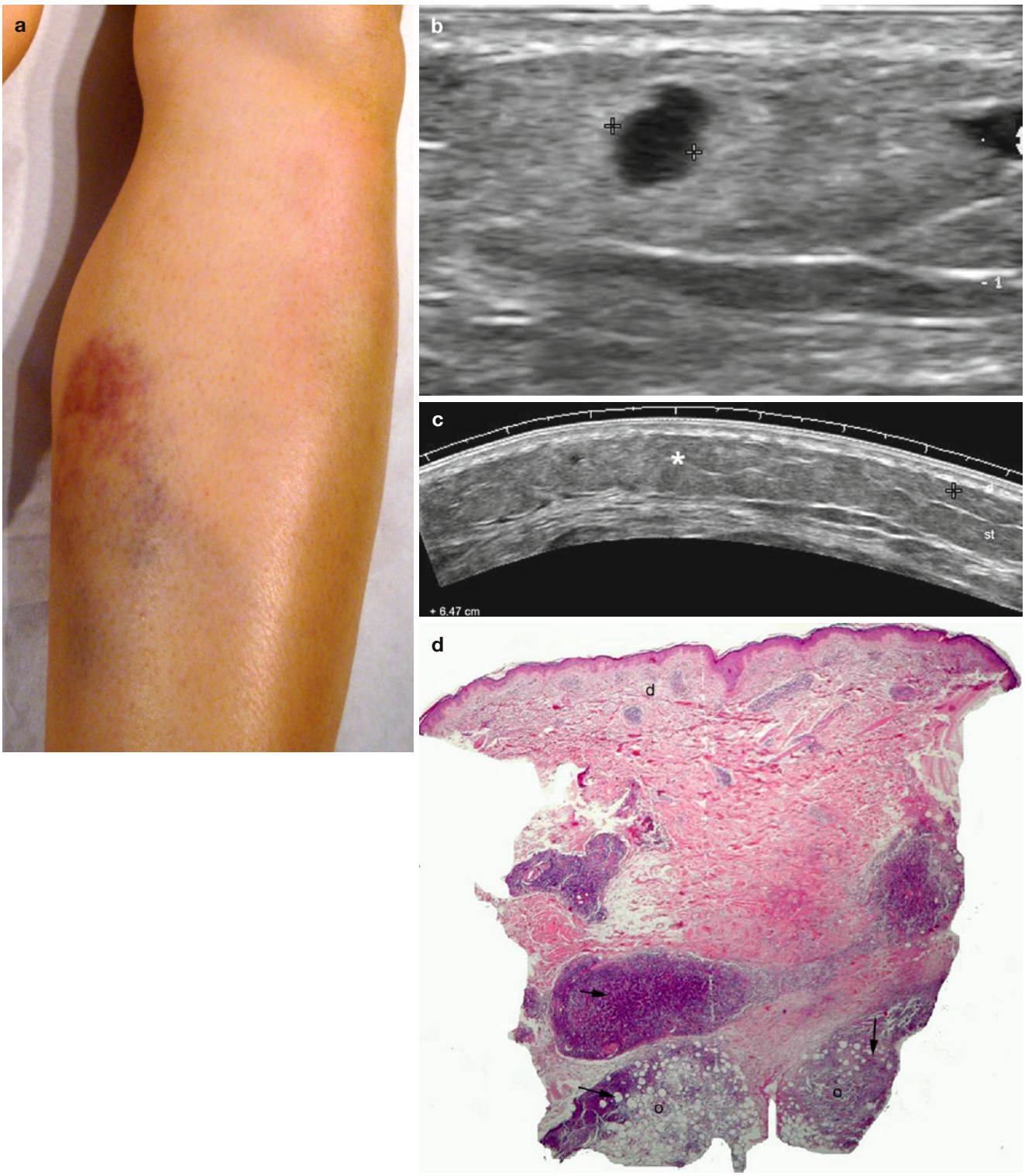

Fig. 4.12 (**a**–**d**) Mostly lobular panniculitis secondary to insect bite. (**a**) Clinical lesion shows erythema and ecchymosis in the site of the bite (spider). (**b**) Gray scale ultrasound image (longitudinal view) demonstrates increased echogenicity of the subcutaneous tissue and a round-shaped anechoic pseudocystic structure (between markers) that corresponds to fat liquefaction (fat necrosis). (**c**) Gray scale ultrasound image (transverse extended field of view) demonstrates a 6.47 cm area with increased echogenicity of the subcutaneous tissue. Notice the blurriness of the borders of the lobules and the septa in the lesional area. (**d**) Histology (HE 20× zoom) shows inflammatory infiltrates (*arrows*) affecting the fatty lobules (o) of the subcutaneous tissue. *Abbreviations*: *d* dermis

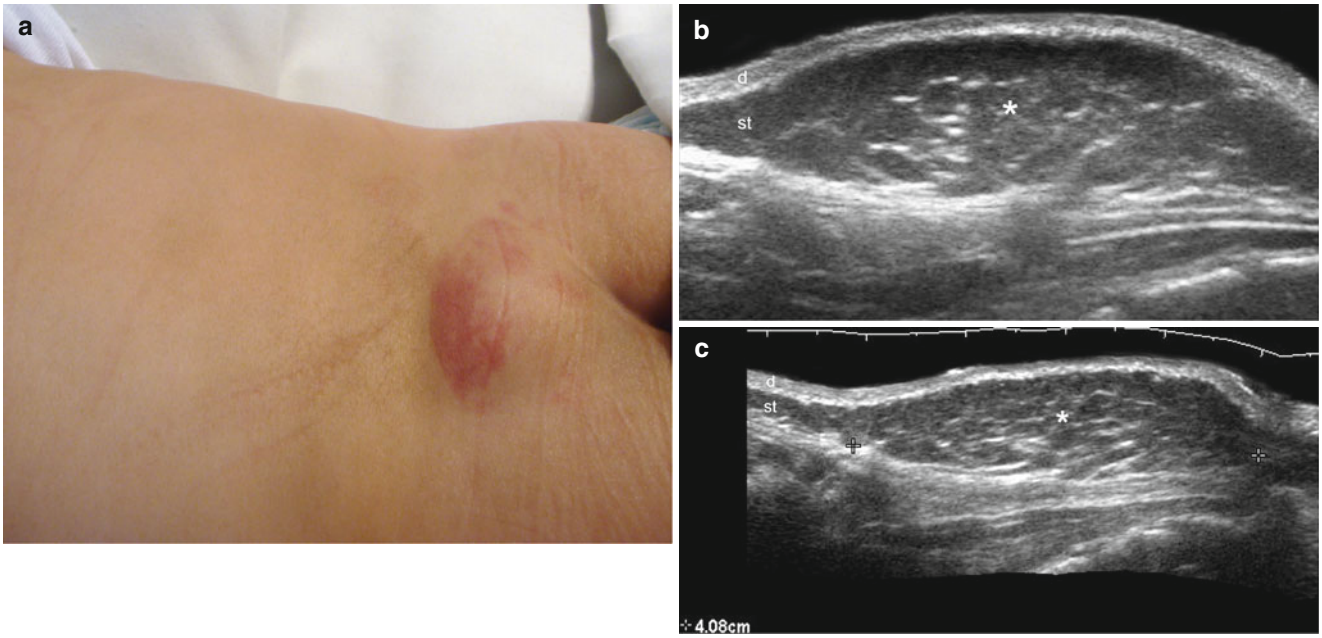

Fig. 4.13 (**a**–**c**) Hypertrophic lipodystrophy (congenital). (**a**) Clinical lesion in the lumbosacral region shows swelling and erythema. (**b**) Gray scale ultrasound image (transverse view) demonstrates a focal region with increased thickness of the subcutaneous tissue. No well-defined nodular structure or capsule can be detected. (**c**) Gray scale ultrasound image (longitudinal view) shows a 4.08 cm long lesional tissue (*, between markers) with increased thickness of the subcutaneous tissue. Notice that there is no abnormality in the echostructure of the subcutaneous tissue or the dermal layer. *Abbreviations*: *d* dermis, *st* subcutaneous tissue

4.2.6 Odontogenic Fistula

These fistulous tracts are commonly originated in dental inflammatory and infectious processes that drain into the soft tissues and open into the subepidermal or epidermal zones, commonly the maxillae or mandibular regions of the face. Clinically, these odontogenic fistulae may mimic a dermatologic origin, appearing as erythematous or bluish papulae that could drain viscous fluid. These lesions can also clinically mimic malignant skin tumors.

On sonography, the fistulous tracts usually appear as hypoechoic, sometimes slightly heterogeneous bands. The connection between the bony margin of the maxillae or mandible is usually assessed using sonography and commonly an erosion can be detected in the bony margin. With color Doppler imaging there is frequently hypervascularity in the periphery of the tracts [22, 23] (Figs. 4.14 and 4.15).

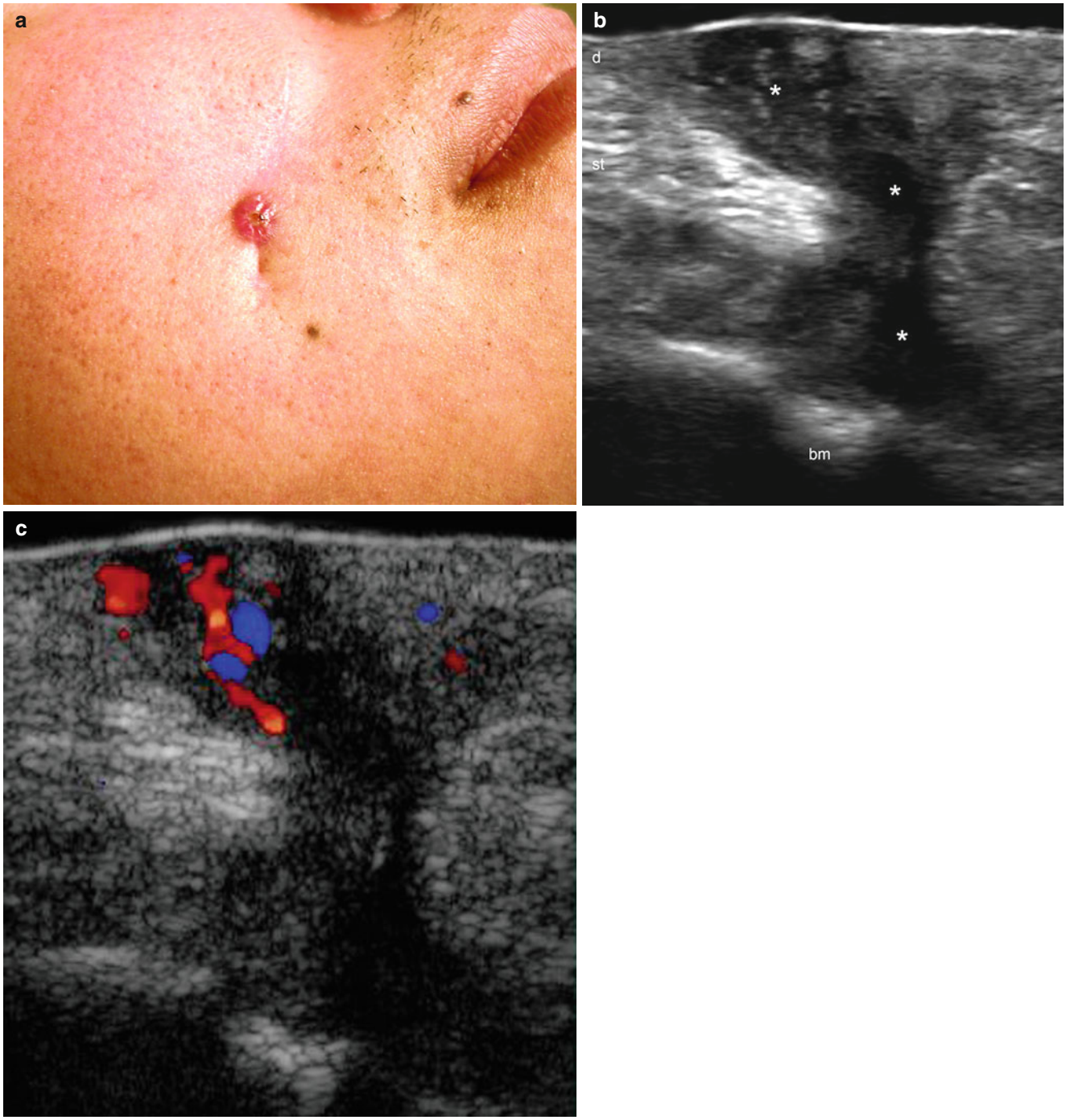

Fig. 4.14 (**a**–**c**) Odontogenic fistula. (**a**) Clinical lesion shows erythematous papule in the right cheek. (**b**) Gray scale ultrasound image (oblique longitudinal view) demonstrates tortuous hypoechoic fistulous tract (*) that connects the dermis and subcutaneous tissue with the bony margin of the upper maxilla. Notice the scalloping of the bony margin (*bm*) at the site of attachment of the fistula. (**c**) Color Doppler ultrasound image (oblique longitudinal view) shows increased vascularity in the periphery of the fistula. *Abbreviations*: *d* dermis, *st* subcutaneous tissue

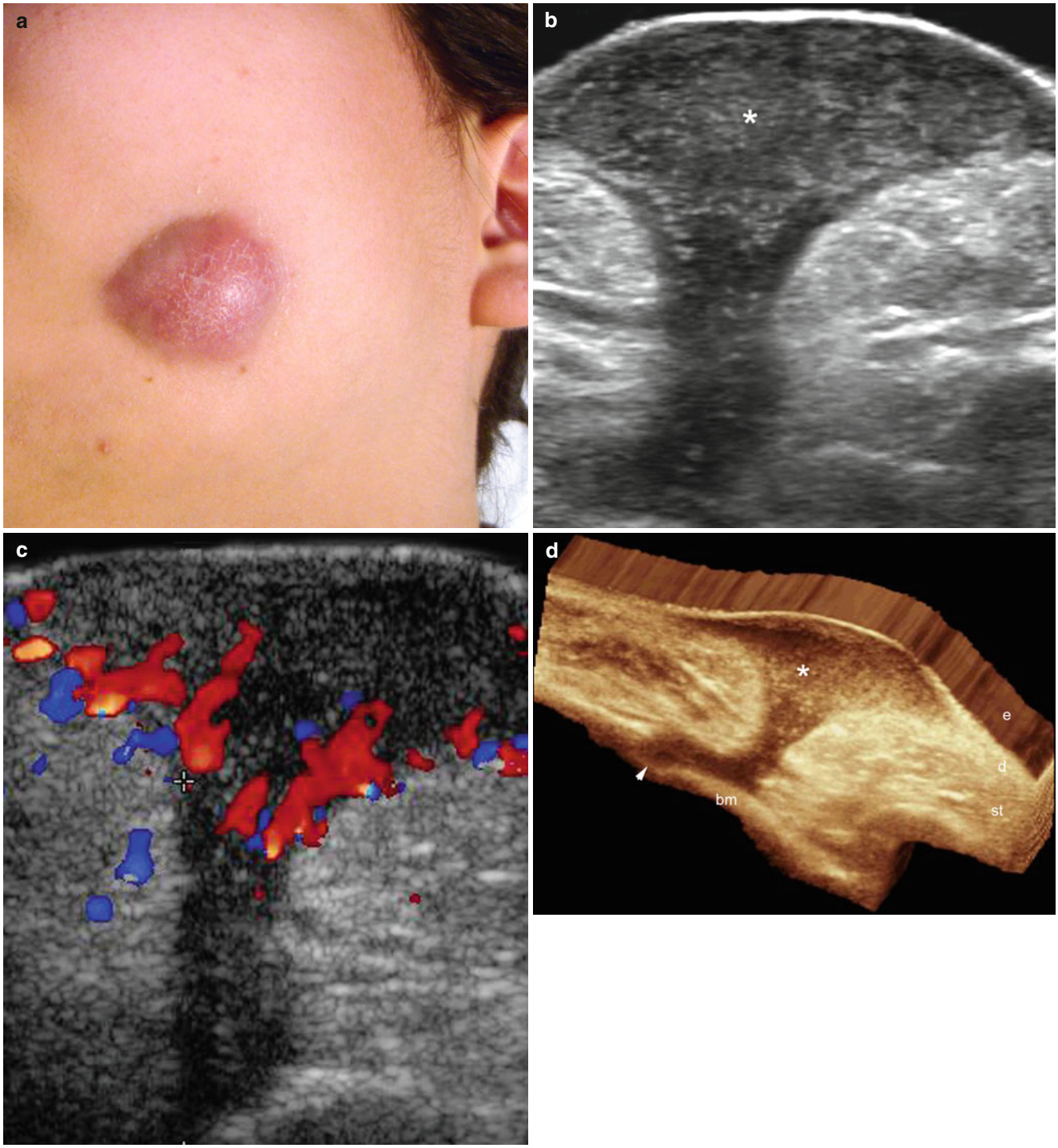

Fig. 4.15 (**a**–**d**) Odontogenic fistula. (**a**) Clinical lesion shows erythematous nodule in the left cheek. (**b**) Gray scale ultrasound image (transverse view) demonstrates hypoechoic "champignon-shaped" structure (*) in the dermis and subcutaneous tissue wider in the surface and narrow in the deepest portion (hypoechoic tract). (**c**) Color Doppler ultrasound image (longitudinal view) shows increased vascularity in the periphery of the lesional area. (**d**) 3D reconstruction of the fistula clearly shows the attachment of the fistula to the bony margin of the upper maxilla (scalloping area of the bone that is pointed out with an *arrow*). *Abbreviations*: *e* epidermis, *d* dermis, *st* subcutaneous tissue, *bm* bony margin of the upper maxilla

4.2.7 Mondor's Disease

Mondor's disease is a superficial vein thrombosis usually located in the subcutaneous tissue. The clinical sign is a cord-like palpable structure that tends to disappear over time. On sonography, the affected venous tract can be recognized as a tubular hypoechoic structure in correlation with the cord-like structure. Occasionally increased echogenicity of the subcutaneous tissue that surrounds the superficial vein can be found. On color Doppler imaging, no flow is detectable within the vessel in the acute phase. After a few weeks, the vascularity may return in concordance with the disappearance of the palpable cord-like structure and the ultrasound changes. Importantly, sonography may provide a tool to differentiate Mondor's disease from linear morphea [24] (Fig. 4.16).

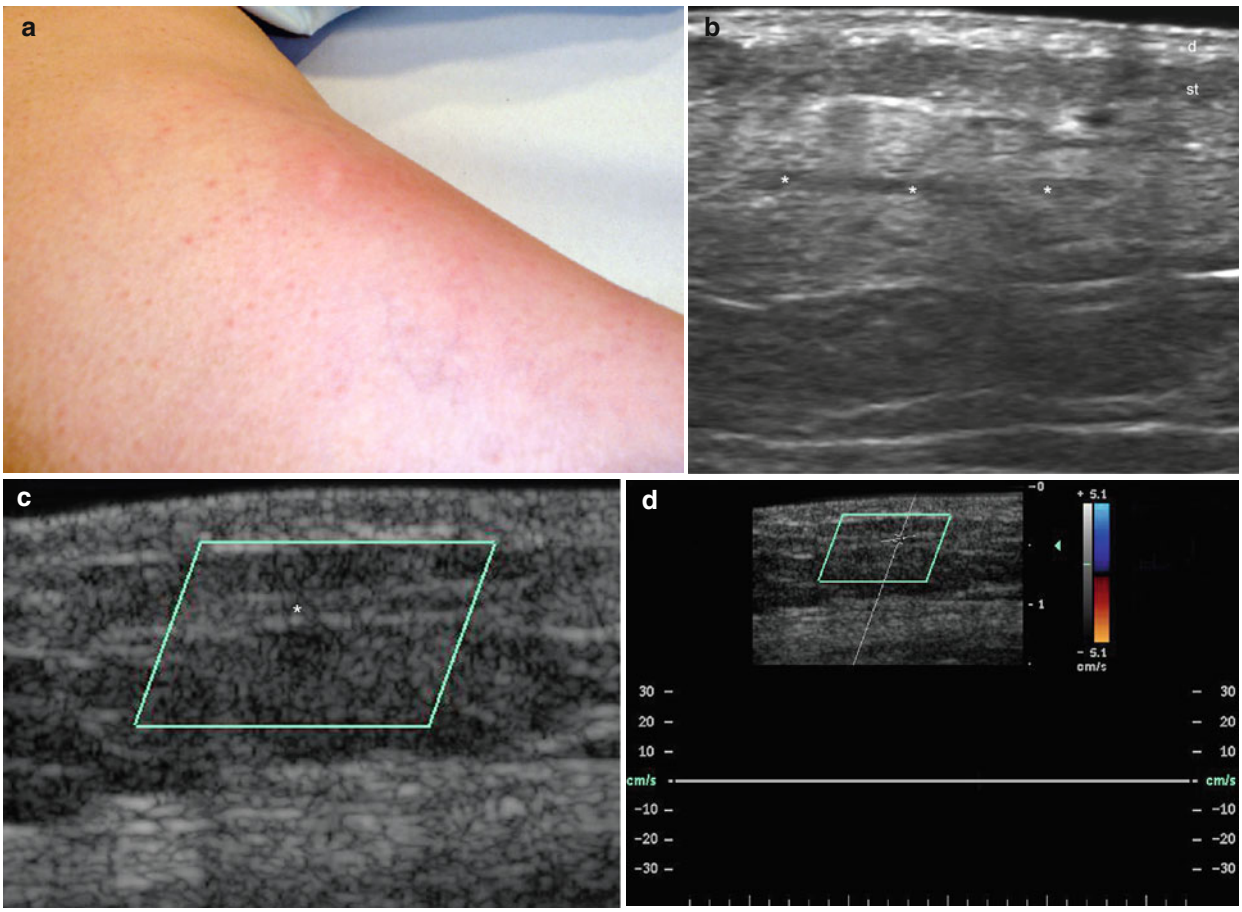

Fig. 4.16 (**a**–**d**) Mondor's disease. (**a**) Clinical image shows erythema in the medial aspect of the right thigh. There was also a palpable cord-like structure. (**b**) Gray scale ultrasound image (longitudinal view) demonstrates a dilated vessel in the subcutaneous tissue filled with hypoechoic thrombotic material (*). Increased echogenicity is detected in the surrounding subcutaneous tissue. (**c**) Color Doppler ultrasound image (longitudinal view) shows no vascularity within the vessel (*). (**d**) Color Doppler spectral curve analysis confirms the lack of vascularity. *Abbreviations*: *d* dermis, *st* subcutaneous tissue

4.2.8 Warts

Warts are common entities caused by the infection with the human papilloma (HP) virus and can generate painful lesions that can clinically mimic a foreign body or Mortons' neuroma when they are located in the plantar region. On physical examination, warts present as painful hyperkeratotic lesions frequently located in the soles of the feet. Warts can also affect other regions of the body, such as the hands. The HP virus causes an ingrown proliferation that usually shows an oval fusiform hypoechoic structure on sonography that affects the epidermis and dermis. Vascularity is variable and can go from hypo- to hypervascular in the sublesional dermis. Additionally, inflammatory changes in the vicinity of the wart that commonly affect the underlying plantar bursae can be detected. Painful warts (symptomatic) are usually associated with a higher presence of vascularity and bursitis [25, 26] (Figs. 4.17, 4.18, 4.19, 4.20 and 4.21).

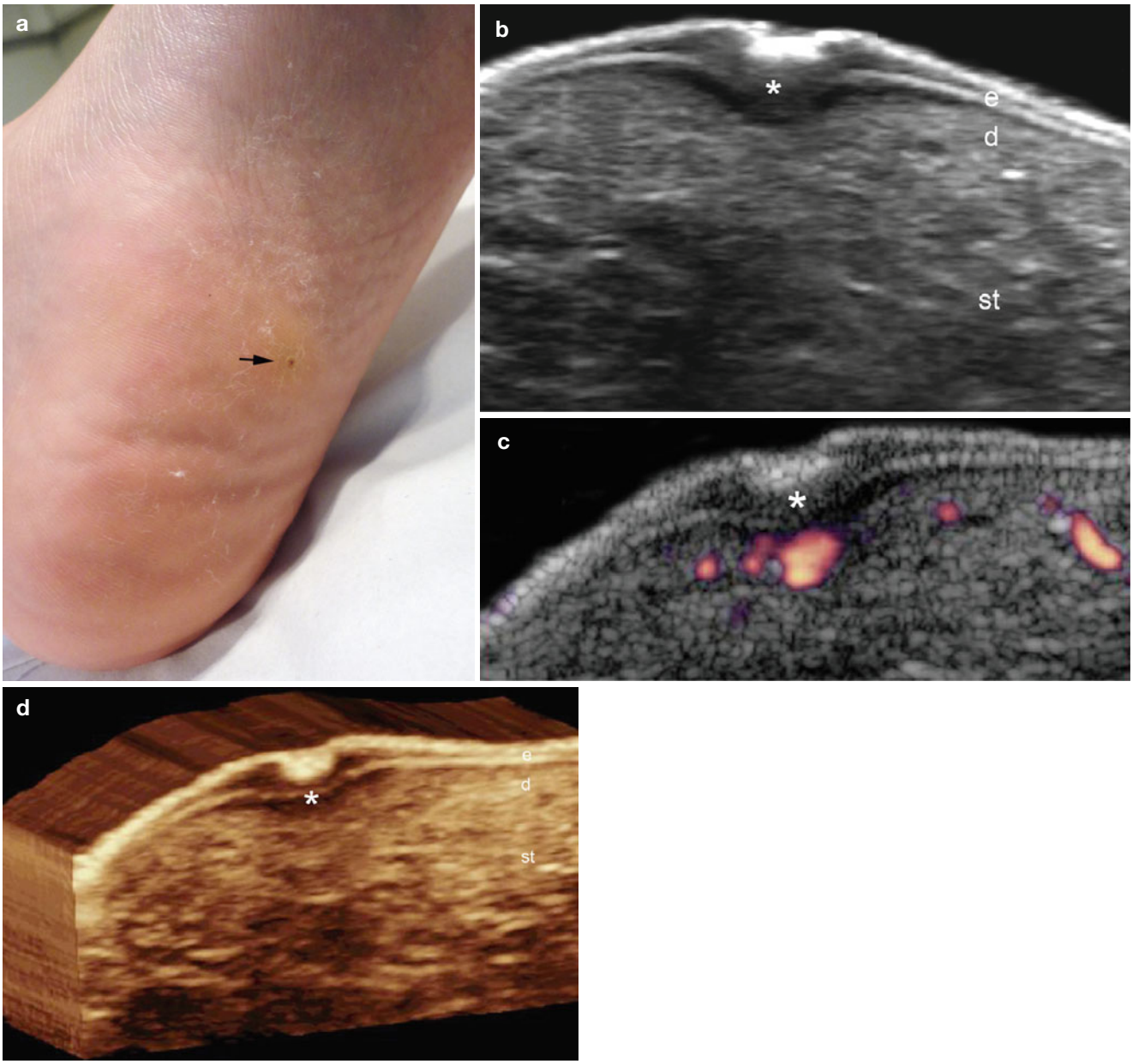

Fig. 4.17 (**a**–**d**) Plantar wart. (**a**) Clinical image shows hyperkeratotic lesion in the sole of the left foot. (**b**) Gray scale ultrasound image (transverse view) demonstrates fusiform shaped hypoechoic structure (*) that involves epidermis and dermis. The central hyperechoic epidermal depression corresponds to the clinical scab. (**c**) Color Doppler power angio (transverse view) demonstrates increased sublesional blood flow. (**d**) The lesion (*) in 3D (5–8 s reconstruction). *Abbreviations*: *e* epidermis, *d* dermis, *st* subcutaneous tissue

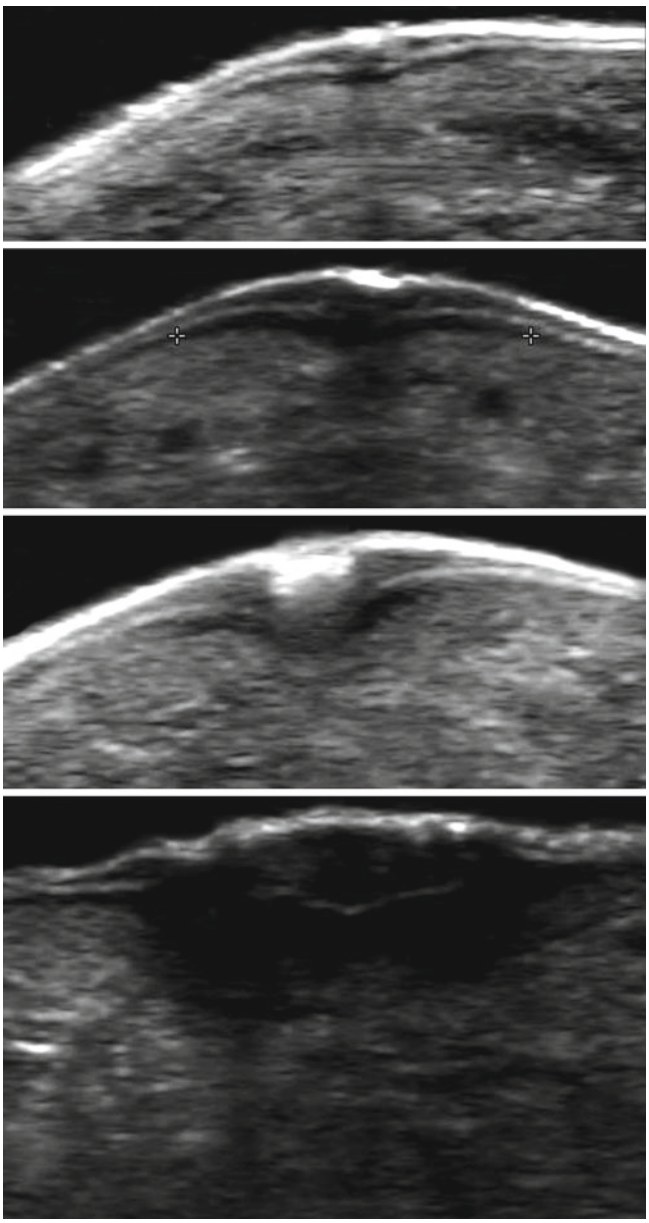

Fig. 4.18 Degree of depth involvement in plantar warts going from superficial (*top*) to deep (*bottom*). Notice the ingrown pattern of involvement of the warts within the cutaneous layers

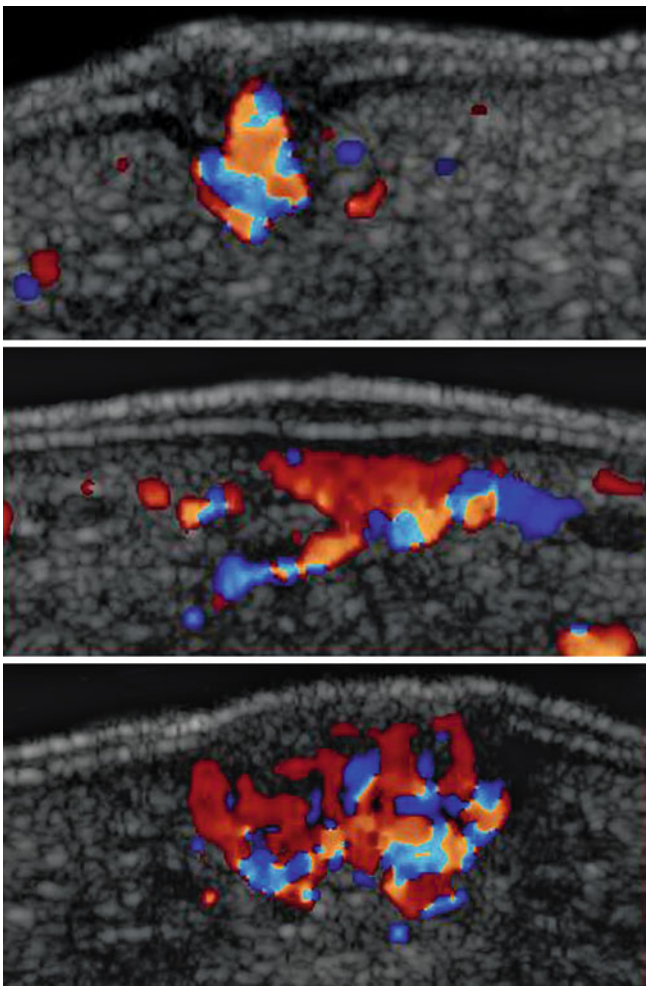

Fig. 4.19 Degree of vascularization of plantar warts going from hypovascular (*top*) to hypervascular (*bottom*)

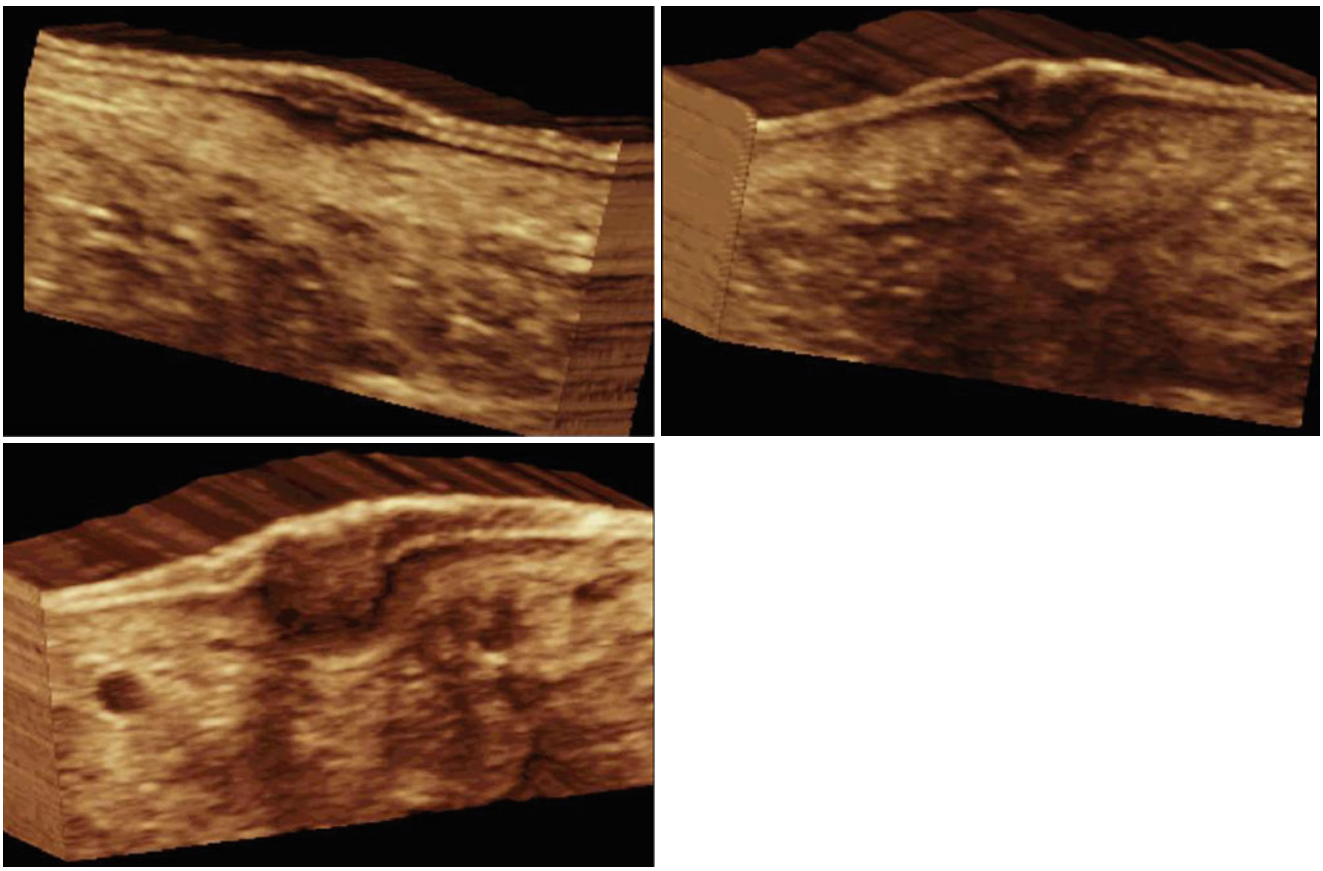

Fig. 4.20 3D reconstructions (5–8 s sweep) of the patterns of involvement in plantar warts

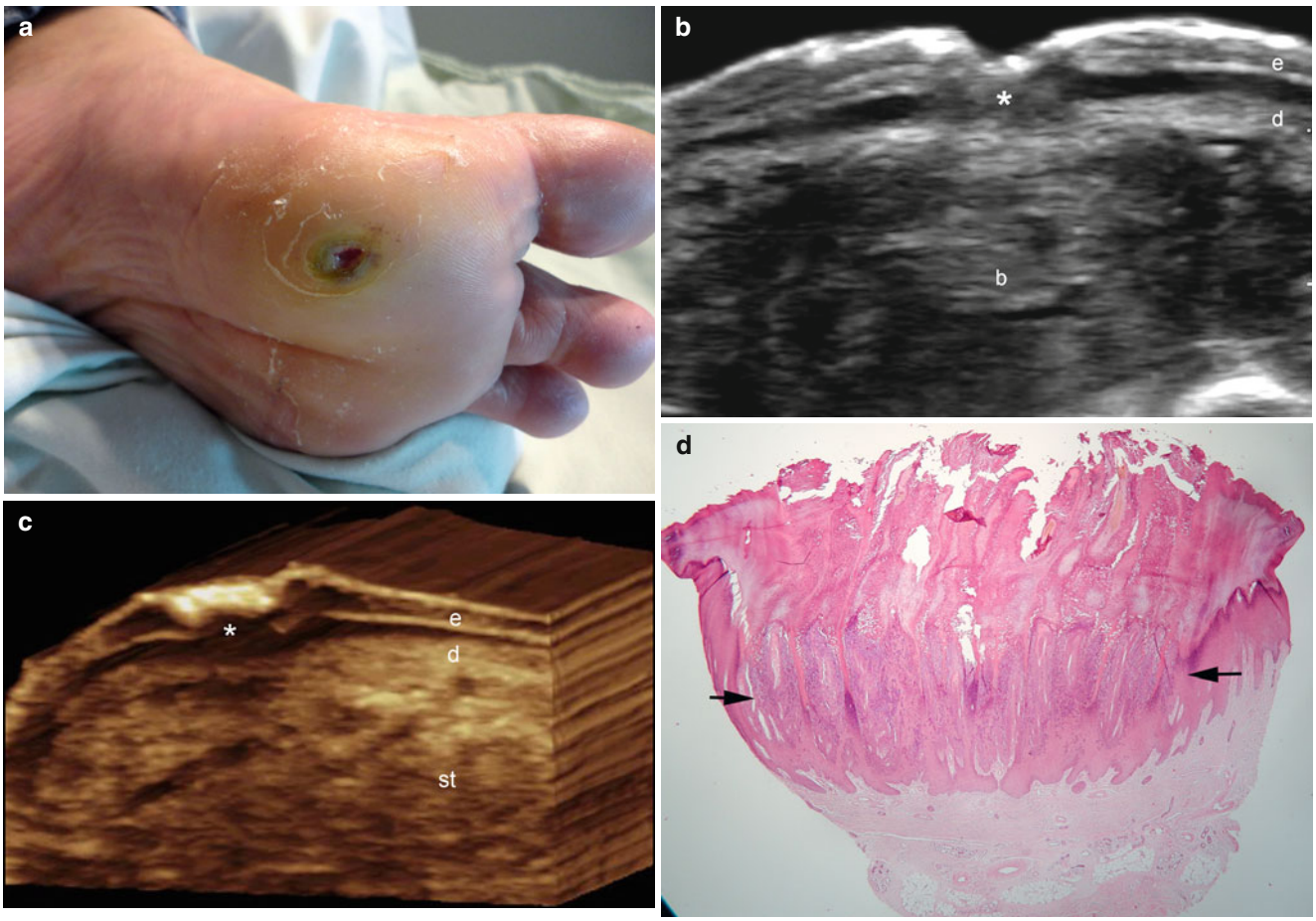

Fig. 4.21 (**a**–**d**) Plantar wart and bursitis. (**a**) Clinical lesion with ulceration and hyperkeratosis. (**b**) Gray scale ultrasound image (transverse view) shows fusiform shaped hypoechoic involvement (*) of the epidermis and dermis. There is distention and synovial proliferation of the plantar bursa (*b*) underlying the lesion. (**c**) 3D reconstruction of the lesional area (*, 5– 8 s sweep). (**d**) Histology (HE 20× zoom) demonstrates the viral infiltration (*between arrows*) with hyperkeratosis, acanthosis, hypergranulosis and papillomatosis. There is also dilation of venous vessels in the dermal papillae. *Abbreviations*: *e* epidermis, *d* dermis, *st* subcutaneous tissue

4.2.9 Psoriasis

Psoriasis is an autoimmune inflammatory disease that affects the skin, nails, enthesis and joints. Clinically, typical psoriatic plaques are characterized by erythematous, itchy, and elevated areas with increased scaling. Commonly, patients may recognize that new lesions appear at sites of injury to the skin (Koebner's phenomenon). These plaques commonly affect the extensor aspects and the scalp, but there are other forms of presentation that can also involve the flexor and intertriginous areas (i.e., axilla, groin, umbilical region, inframammary folds) with low or absent scaling. Less frequent types of psoriasis are guttate psoriasis, an acute form most commonly found in children after an upper respiratory infection and characterized by small droplike, salmon or pink papules, with fine scales; and pustular psoriasis (localized or generalized) that shows persistent pinhead-sized, sterile, sub-corneal pustules, persistent pustular eruptions of the hands and feet (localized) or affecting the skin in general. These pustules grow and merge into larger regions that can facilitate a secondary bacterial infection. The latter conditions can also affect the oral mucosa and the lips. Erythrodermic psoriasis, another rare and severe form of psoriasis, shows a widespread inflammation and erythroderma (i.e., exfoliative dermatitis) over most of the body surface. It can be accompanied by severe itching, swelling, and pain [27].

Nail involvement is extremely common in psoriasis and affects approximately 50 % of patients. In less than 5 % of the cases, the involvement of the nails can appear without cutaneous lesions. About 10–20 % of people with psoriasis also have psoriatic arthritis, and 80 % of patients with psoriatic arthritis (PsA) present nail psoriasis. Clinical manifestations of nail psoriasis are pitting, discoloration, onycholysis (i.e., separation of the nail plate from the nail bed), and subungual hyperkeratosis as well as nail plate crumbling and splinter hemorrhages [28].

Other types of inflammatory involvement in psoriasis include the joints, enthesis, and the bowel. PsA is a chronic inflammatory arthropathy associated with psoriasis, and is included among the seronegative spondyloarthropathies. The presence of cutaneous psoriasis is very important for correct and early diagnosis of PsA because the cutaneous lesions commonly precede the appearance of joint manifestations [29].

Histologically, psoriatic plaques show acanthosis (elongation of the rete ridges and corresponding dermal papillae), parakeratosis (presence of nucleated inmature keratinocytes in the stratum corneum), orthokeratosis (hypertrophy of the stratum corneum), loss of the granular cell layer, spongiform pustules, dermal mononuclear infiltrates, and parakeratotic microabscesses. At the nail, there is hyperkeratosis of the nail plates. Synovial proliferation is detected in the articular areas [30].

On sonography, psoriatic plaques show thickening of the epidermis and hypoechogenicity and thickening of the upper dermis. Occasionally, undulation of the epidermis can be detected. On color Doppler imaging, increased dermal blood flow is usually detected within the lesions. Ungual sonographic involvement varies according to the phase of activity of the disease, hence, going from early to late phases: thickening and decreased echogenicity of the ungual bed, focal hyperechoic spots in the ventral plates, and wavy plates and thickening of both plates (dorsal and ventral) can be found. Blood flow is usually increased in the proximal nail bed with low flow arterial vessels especially during the active phases of the disease. Joints can show prominent synovium, anechoic fluid, and periarticular erosions commonly in the interphalangeal joints. Tendinopathy that shows hypo- or heterogeneous echogenicity, usually at the insertion sites of the tendineous structures, has also been sonographically reported in patients with psoriasis even at subclinical stages. Increased blood flow may detected in the synovium on color Doppler imaging in active phases. Sonographic monitoring of treatment in psoriasis has been recently reported [31–33] (Fig. 4.22).

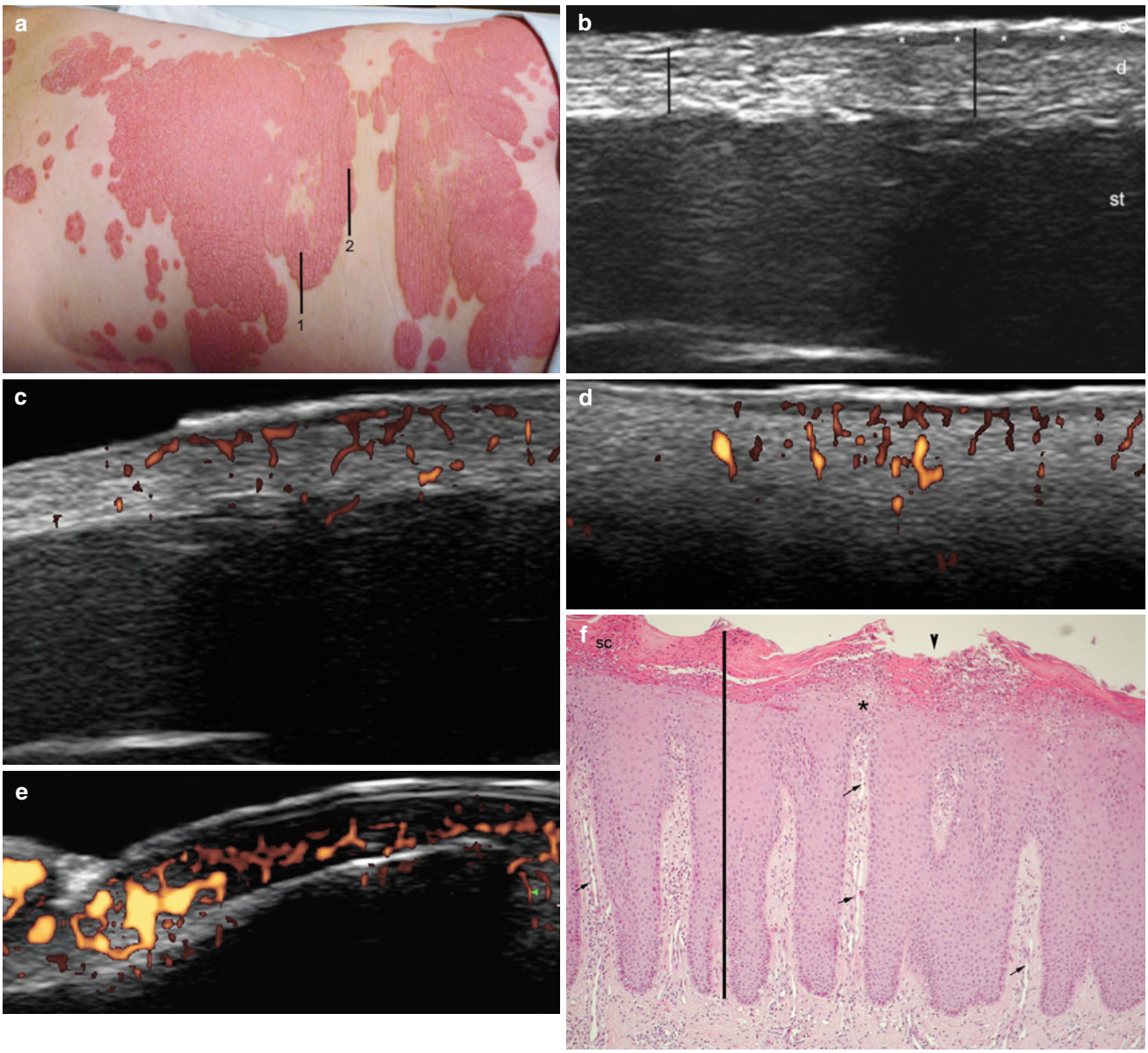

Fig. 4.22 (**a**–**f**). Psoriasis. (**a**) Clinical image shows multiple erythematous psoriatic plaques in the dorsolumbar region. The *black lines* [1, 2] show the orientation of the following ultrasound images. (**b**) Gray scale ultrasound image (transverse view, line 1 in (a)) demonstrates thickening of the epidermis and dermis with an hypoechoic band (*) in the upper dermis. The *vertical black lines* illustrate the different thicknesses in the abnormal (plaque, right side) and normal skin (*left side*). (**c**) Power Doppler ultrasound image (transverse view, line 1 in (a)) demonstrates increased blood flow in the upper dermis of the psoriatic plaque. (**d**) Power Doppler ultrasound image (transverse view, line 2 in (a)) shows similar morphology of the hypervascularity in the psoriatic plaque (*right side*) in comparison with the normal skin (*left side*) (**e**) Power Doppler ultrasound image of the nail (longitudinal view) of the left thumb in the same patient shows increased vascularity in the ungual bed. (**f**) Histology (HE 100 × zoom) demonstrates hyperkeratosis, acanthosis, agranulosis and suprapapillary thinning (*) of the epidermis (*black line*). There is also a small pustule in the stratum corneum (*arrowhead*) and prominent vascularity (*arrows*). *Abbreviations*: *e* epidermis, *d* dermis, *st* subcutaneous tissue, *sc* stratum corneum

4.2.10 Morphea

Also known as localized scleroderma, morphea is a fibrosing disorder of the skin and underlying tissues. Morphea is differentiated from systemic sclerosis because of the absence of sclerodactyly, Raynaud phenomenon, and nail fold capillary changes. Nevertheless, patients with morphea commonly have systemic symptoms such as malaise, fatigue, arthralgias, and myalgias, as well as positive autoantibody serologies. However, morphea is almost uniformly limited to those tissues derived from the mesoderm. The underlying pathogenesis of morphea is not completely understood at this time, but ultimately it results in an imbalance of collagen production and destruction. Early morphea lesions present as erythematous to purple indurated lesions that turn into sclerotic, atrophic, hairless plaques with varying amounts of post-inflammatory hyperpigmentation. There are several clinical subtypes of morphea, the most common is the plaque type, also called circumscribed morphea, that presents as fewer that three discrete indurated plaques. The superficial variant is more frequent and localized and limited to the epidermis and dermis. The deep variant of plaque morphea is also called subcutaneous or deep; morphea can affect the subcutaneous tissue, fascia, and muscular layers. Some classifications included in the plaque-morphea variants are the guttate (drop-like) presentation, the atrophoderma of Pasini and Pierini, keloidal type, and the lichen sclerosis et atrophicus. Generalized morphea is defined as more than four indurated plaques larger than 3 cm and/or involving two or more corporal regions but sparing the face and hands. Linear morphea is the most common subtype in children and can present as "en coup de sabre" (ECDS), progressive hemifacial atrophy (Parry-Romberg syndrome [PRS]), or linear limb involvement. In these three subtypes the lesions progress rapidly to atrophy of the skin. ECDS can be associated with ocular and central nervous system involvement and usually presents on the paramedian forehead. Deep morphea involves the skin and deeper layers, such as muscle or bone. This type includes the morphea profunda that affect the subcutaneous tissue; eosinophilic fasciitis, which is a variant of deep morphea that affects the fascial plane; and pansclerotic morphea, that produces a circumferential involvement of the epidermis, dermis, subcutaneous tissue, muscle, and bone. The latter subtype elicits muscle atrophy, joint contractures, and non-healing ulcers. Patients with pansclerotic morphea and chronic wounds have been reported to present a high risk of squamous cell carcinoma of the skin. There is also a mixed variant of morphea composed by a combination of two or more subtypes [34, 35]. Histologically, the appearance of morphea can vary according with the phase of the disease. In the early stages, thickening of the collagen bundles, perivascular inflammatory infiltrates composed mainly of lymphocytes, plasma cells, and eosinophils can be detected. In the late stages, the inflammatory infiltrate regress and the dermal collagen bundles become more prominent and eosinophilic, and the eccrine glands, vessels, and subcutaneous fat become atrophic [34].

The activity of the disease can be monitored using sonography, therefore, the lesions can vary from hypoechogenicity and thickening of the dermis with hyperechogenicity of the subcutaneous tissue in the active phase, to thinning of the dermis and subcutaneous tissue in the atrophy phase. At the end stage (atrophy), a direct contact between the dermis and the muscle layer can be detected. Increased blood flow is commonly detected in the cutaneous layers during active phases. Nevertheless, the lesions become hypovascular on color Doppler imaging at the end stages. It is possible to detect the partial or full thickness involvement of the lesions and their asynchronic presentation using sonography (i.e., multiple lesions in different phases of activity). The most sensitive sonographic signs for detecting activity are cutaneous hypervascularity and increased echogenicity of the underlying subcutaneous tissue (100 % sensitivity and specificity for both). In patients that present with PRS (progressive hemifacial atrophy), the ipisilateral parotid gland has been reported to be affected with signs of inflammation [35–38] (Figs. 4.23, 4.24, 4.25, 4.26, 4.27, 4.28 and 4.29).

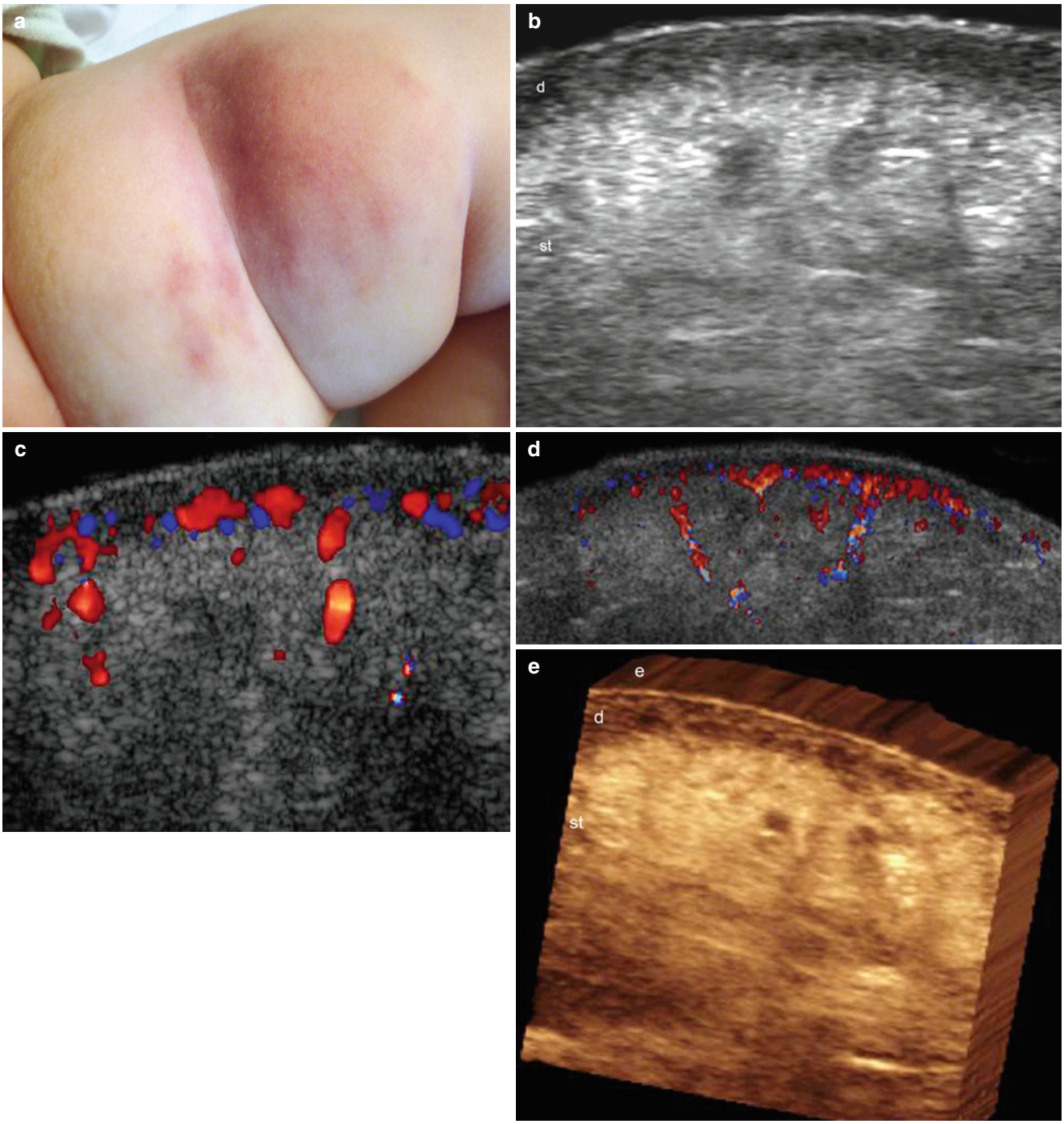

Fig. 4.23 (**a**–**e**) Active morphea (inflammatory phase). (**a**) Clinical erythematous swelling in the left thigh of an infant. (**b**) Gray scale ultrasound image (transverse view) shows thickening and decreased echogenicity of the dermis and increased echogenicity of the subcutaneous tissue. (**c**) Color Doppler ultrasound image (transverse view) demonstrates increased blood flow in the dermis and upper subcutaneous tissue. (**d**) Color Doppler ultrasound image (extended field transverse view) of the lesional area. (**e**) The lesion in 3D (5–8 s sweep). *Abbreviations*: *e* epidermis, *d* dermis, *st* subcutaneous tissue

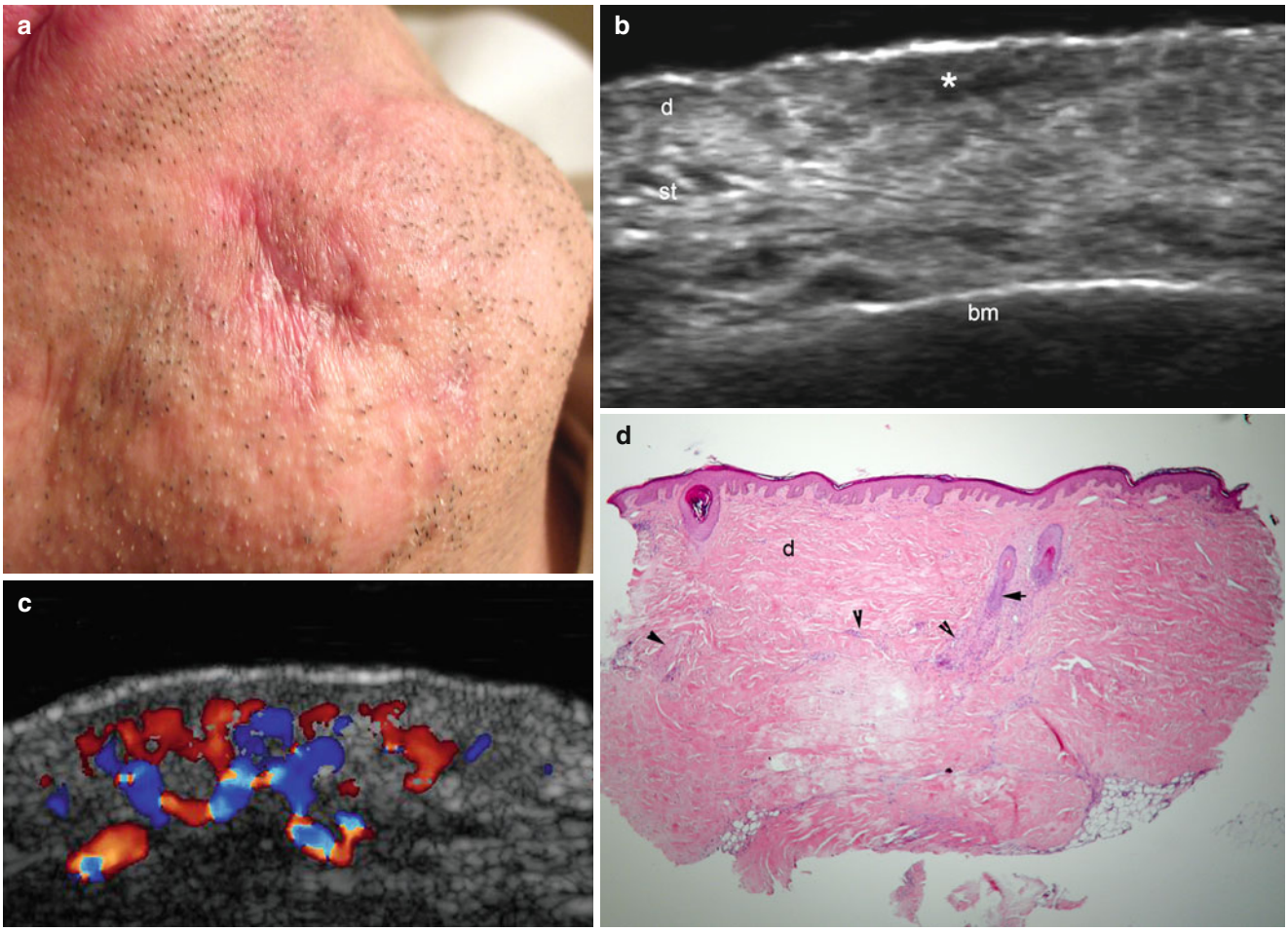

Fig. 4.24 (**a**–**d**) Active morphea (inflammatory phase). (**a**) Clinical lesion shows erythema, swelling and retraction in the chin. (**b**) Gray scale ultrasound image (transverse view) demonstrates thickening and decreased echogenicity of the dermis (*) and increased echogenicity of the subcutaneous tissue. (**c**) Color Doppler ultrasound image (transverse view) shows increased vascularity in the dermis and upper subcutaneous tissue. (**d**) Histology (HE 20 × zoom) illustrates the thick collagen bundles in the dermis (*d*) and the inflammatory infiltrates (*arrowheads*). There is also atrophy of the adnexal structures (*arrow*; i.e., hair follicles and perifollicular glands). *Abbreviations*: *d* dermis, *st* subcutaneous tissue, *bm* bony margin of the mandible

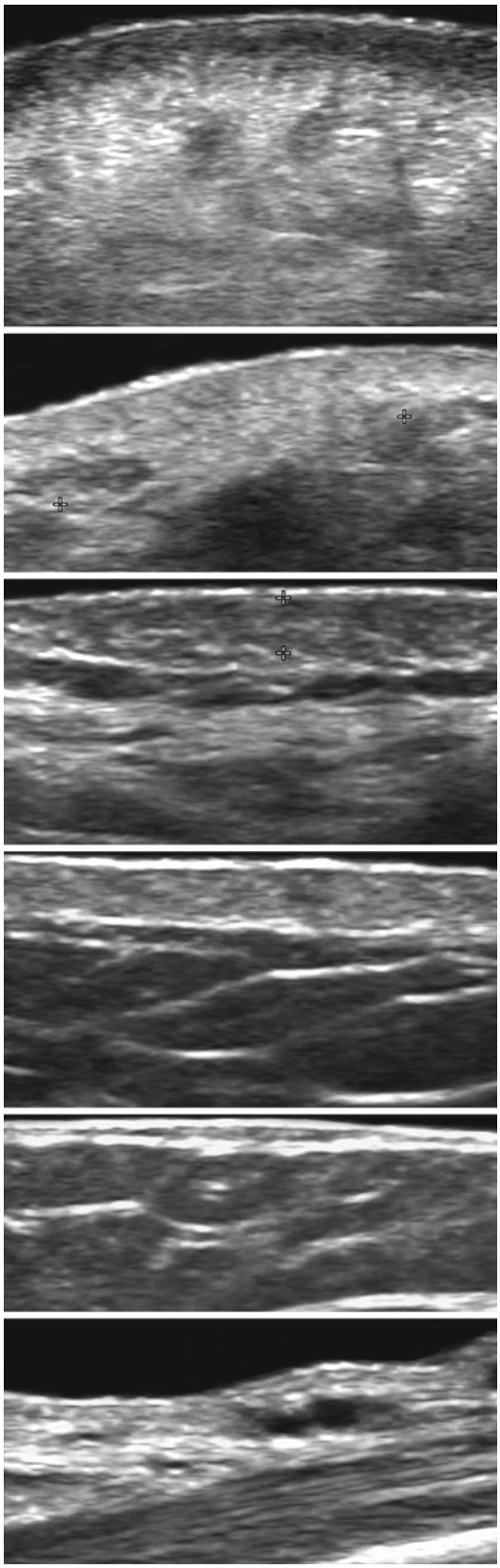

Fig. 4.25 Grading of activity in morphea (grey scale) going from active (*top*) to atrophy (*bottom*) phases

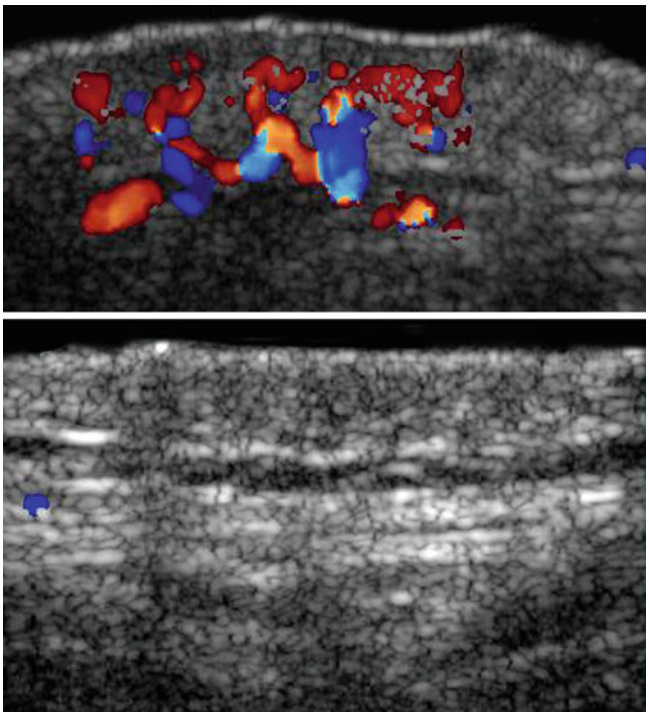

Fig. 4.26 Grading of activity in morphea (color Doppler ultrasound image) going from active (*top*, hypervascular) to atrophy (*bottom*, hypovascular) phases

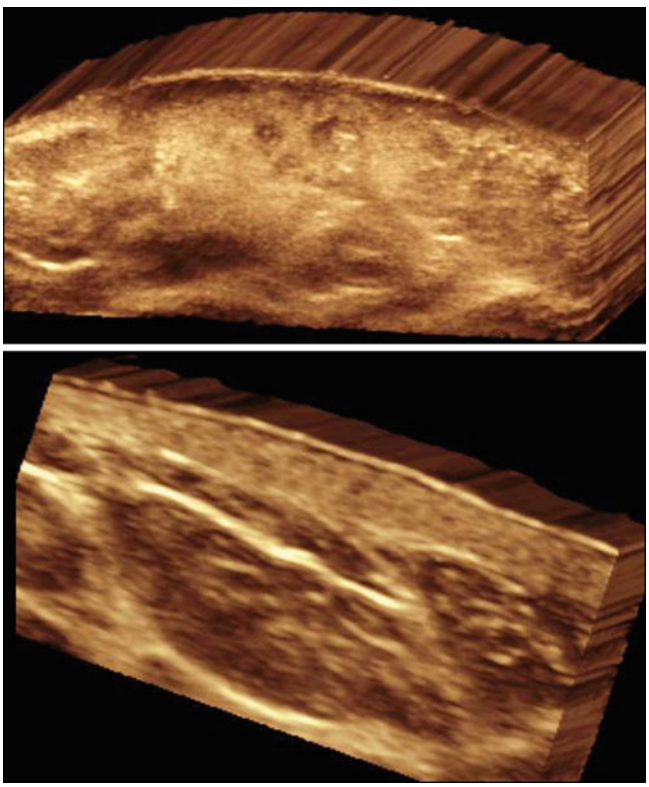

Fig. 4.27 Grading of activity in morphea (3D reconstructions) going from active (*top*) to inactive (*bottom*)

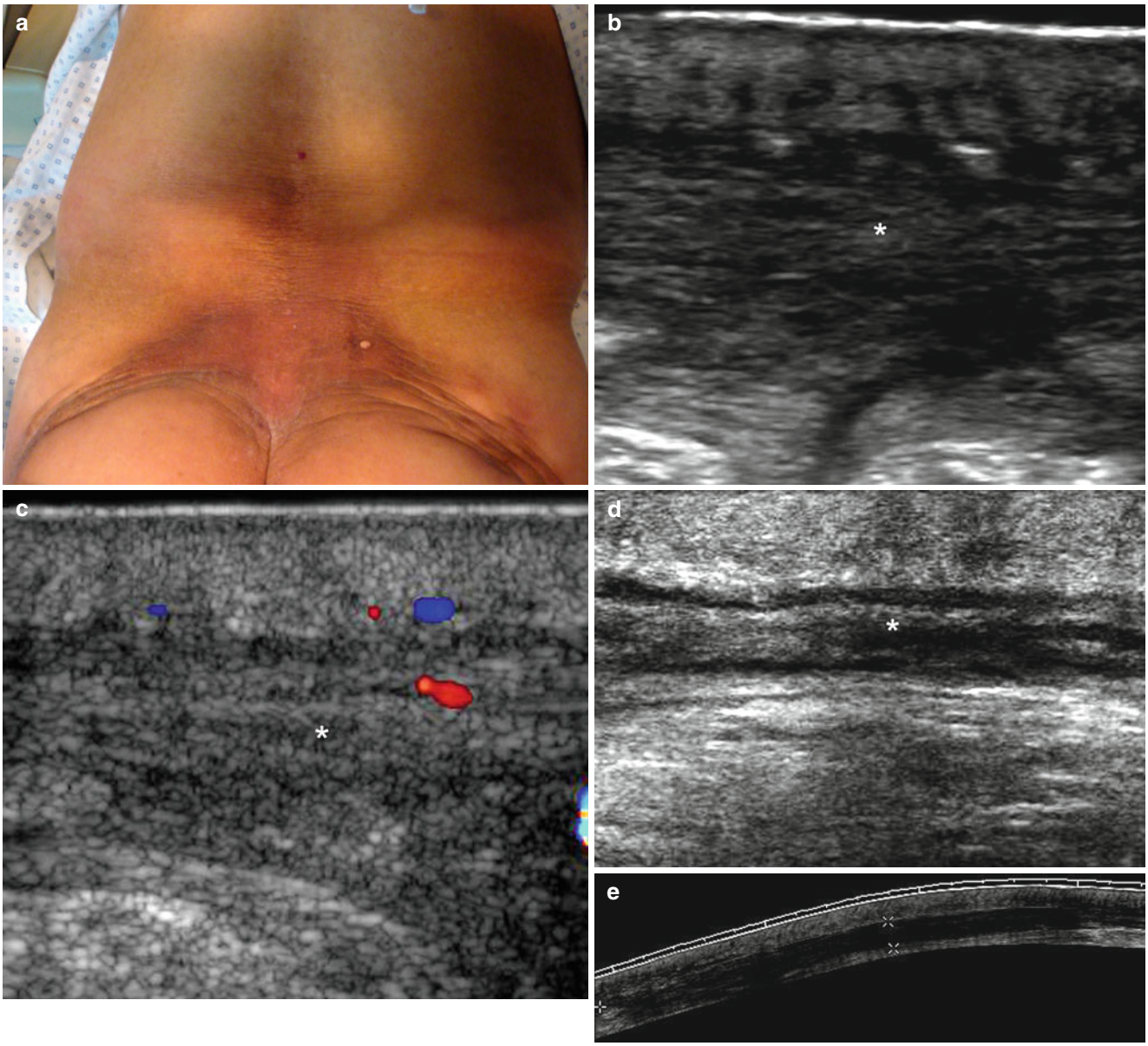

Fig. 4.28 (**a**–**e**) Deep morphea-eosinophilic fasciitis. (**a**) Clinical lesion shows hyperpigmented and indurated plaque in the lumbar and gluteal region. (**b**) Gray scale ultrasound image (transverse view) demonstrates increased thickening and decreased echogenicity of the fascial plane (*). There is also decreased echogenicity and thickening of the dermis. (**c**) Color Doppler ultrasound image (transverse view) shows increased blood flow in the lower dermis and fascial layer (*). (**d**) Gray scale ultrasound image (transverse view) depicts the decreased echogenicity and thickening of the fascia (*). (**e**) Gray scale (extended field of view, transverse axis) shows the wide extension of the lesion that involves the fascial layer (between markers)

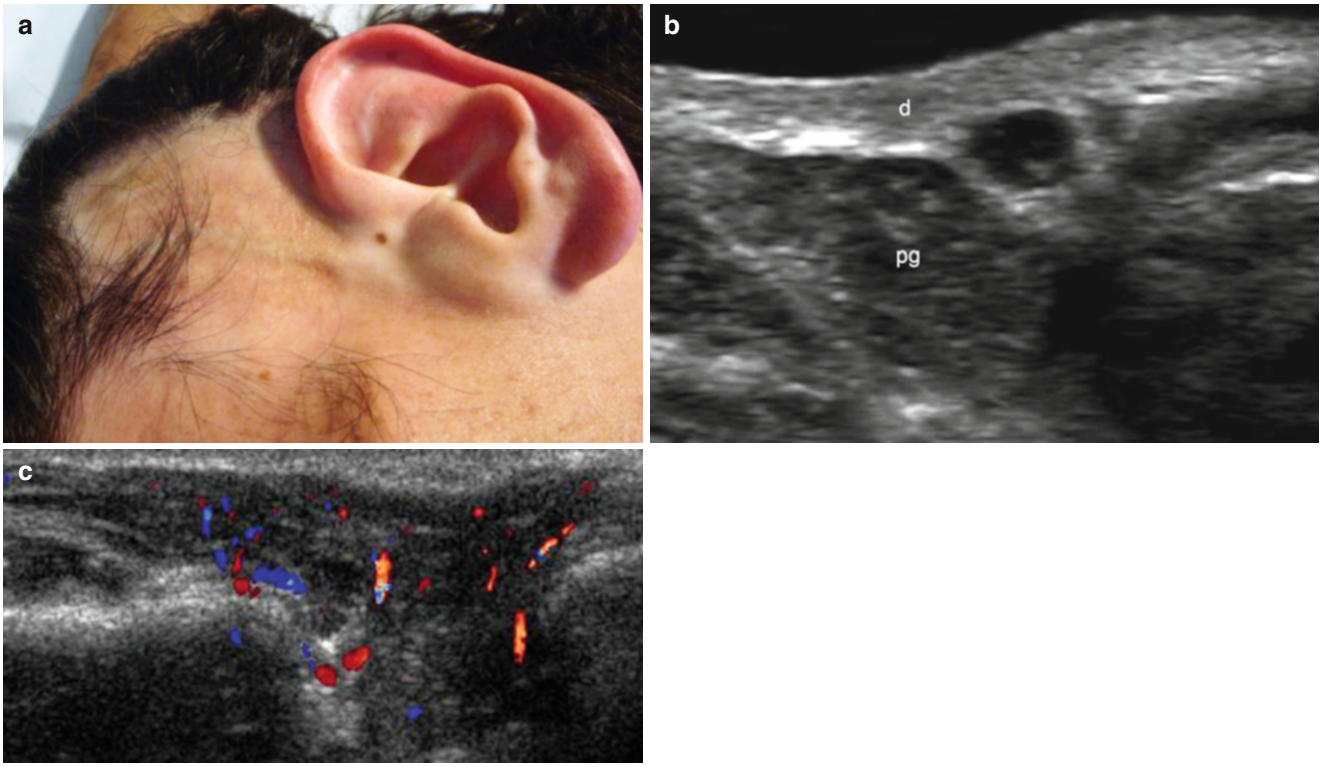

Fig. 4.29 (**a**–**c**) Morphea at the phase of atrophy (Parry-Romberg syndrome). (**a**) Clinical image shows atrophy of the left side of the face and baldness in the regional scalp. (**b**) Gray scale ultrasound image (transverse view at the left cheek) demonstrates lack of fat in the subcutaneous tissue and decreased echogenicity of the dermis (*d*). The underlying parotid gland (*pg*) presents hypoechogenicity. (**c**) Color Doppler ultrasound image (transverse view) shows hypoechogenicity and increased vascularity in the left parotid gland

4.2.11 Cutaneous Lupus

Cutaneous lupus is the cutaneous form of lupus erythematous (LE) and may precede systemic involvement. The term 'cutaneous lupus erythematosus' (CLE) comprises several related autoimmune skin disorders, defined as 'specific' skin manifestations of LE. The spectrum of clinical presentation of CLE is wide, reaching from mild erythema to disseminated scarring skin lesions, all of them photosensitive dermatosis [39]. According to the phase of activity and presentation of the disease, there are three forms of cutaneous lupus: acute cutaneous lupus (classical malar erythematous eruption with a butterfly pattern in the midface and/or a generalized erythematous maculopapular eruption), subacute cutaneous lupus (non-scarring, non–atrophy-producing), and chronic cutaneous (discoid) lupus (scarring, atrophy producing) [40]. Nonspecific skin lesions such as generalized or acrolocalized (i.e., peripheral location such as limbs, fingers, or ears) vasculitis, livedo reticularis, and alopecia are frequently seen in patients with cutaneous lupus. Other typical cutaneous lupus subsets, such as lupus profundus/panniculitis, lupus tumidus, urticaria vasculitis, hypertrophic lupus, and bullous lupus are rather rare variants. Butterfly rash and/or macular exanthema are characteristic skin lesions of systemic LE rarely found in patients with cutaneous lupus [41]. It is the localized cutaneous form of lupus characterized by erythematous plaques or swellings that can evolve to atrophic or depigmented plaques at the end stage. Histologically, lupus presents mucin deposits, thick collagen, and inflammatory cells according to the stage of the disease.

On sonography, active cutaneous lupus shows hypoechogenicity and thickening of the dermis and increased echogenicity of the subcutaneous tissue. The hypoechogenicity of the dermis tends to adopt a fusiform shape. Lesional hypervascularity is commonly detected in active stages. Atrophy of the cutaneous layers and hypovascularity are common at the end stages (discoid lupus). Information about the involvement of vessels, such as the digital arteries, can be obtained. These vessels can present thrombotic and vasculitis phenomena, which can complicate the treatment and/or prognosis of the disease. These thromboses present as hypoechoic filling of the vessels using sonography. Absence of flow is demonstrated on the spectral curve analysis on color Doppler ultrasound [22, 42, 43] (Figs. 4.30, 4.31, 4.32, 4.33 and 4.34).

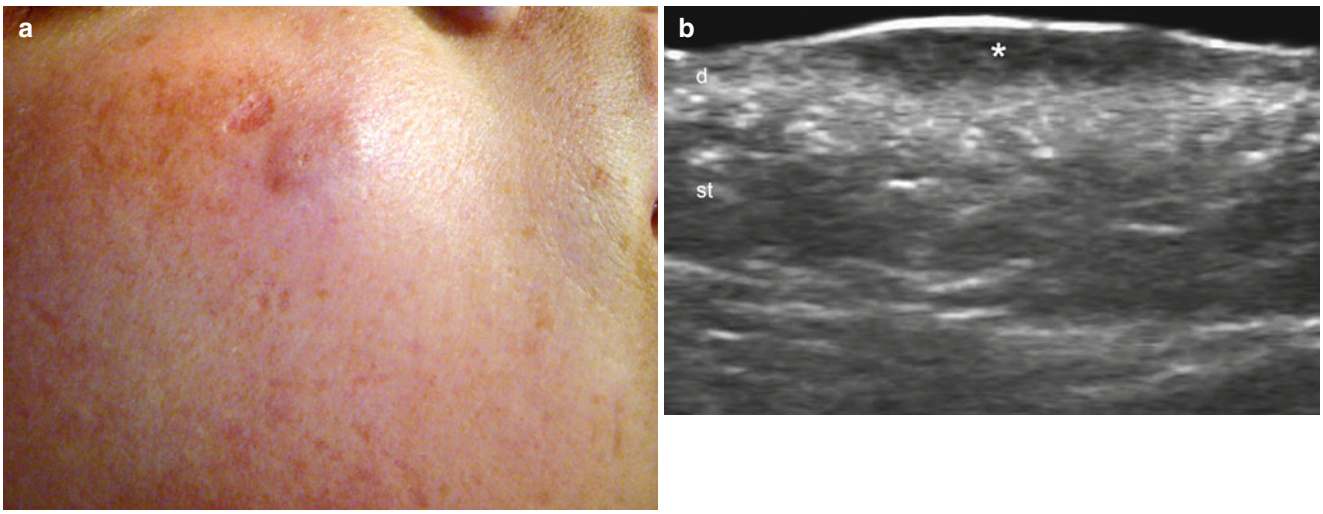

Fig. 4.30 (**a**–**e**) Cutaneous lupus (active phase) (**a**) Clinical image shows erythematous swelling in the right cheek. (**b**) Gray scale ultrasound image (transverse view) demonstrates fusiform-shaped thickening and decreased echogenicity of the upper dermis (*). There is also increased echogenicity of the lower dermis and upper subcutaneous tissue. (**c**) Color Doppler ultrasound image (transverse view) shows increased vascularity in dermis and subcutaneous tissue. (**d**) Histology (HE × 20 zoom) demonstrates interface vacuolar alterations, extensive perivascular and periadnexial inflammatory reaction, and mucin deposits. (**e**) (Alcian Blue ×100 zoom) shows prominent mucin deposition (*blue color*) in dermis between the collagen bundles. *Abbreviations*: *d* dermis, *st* subcutaneous tissue

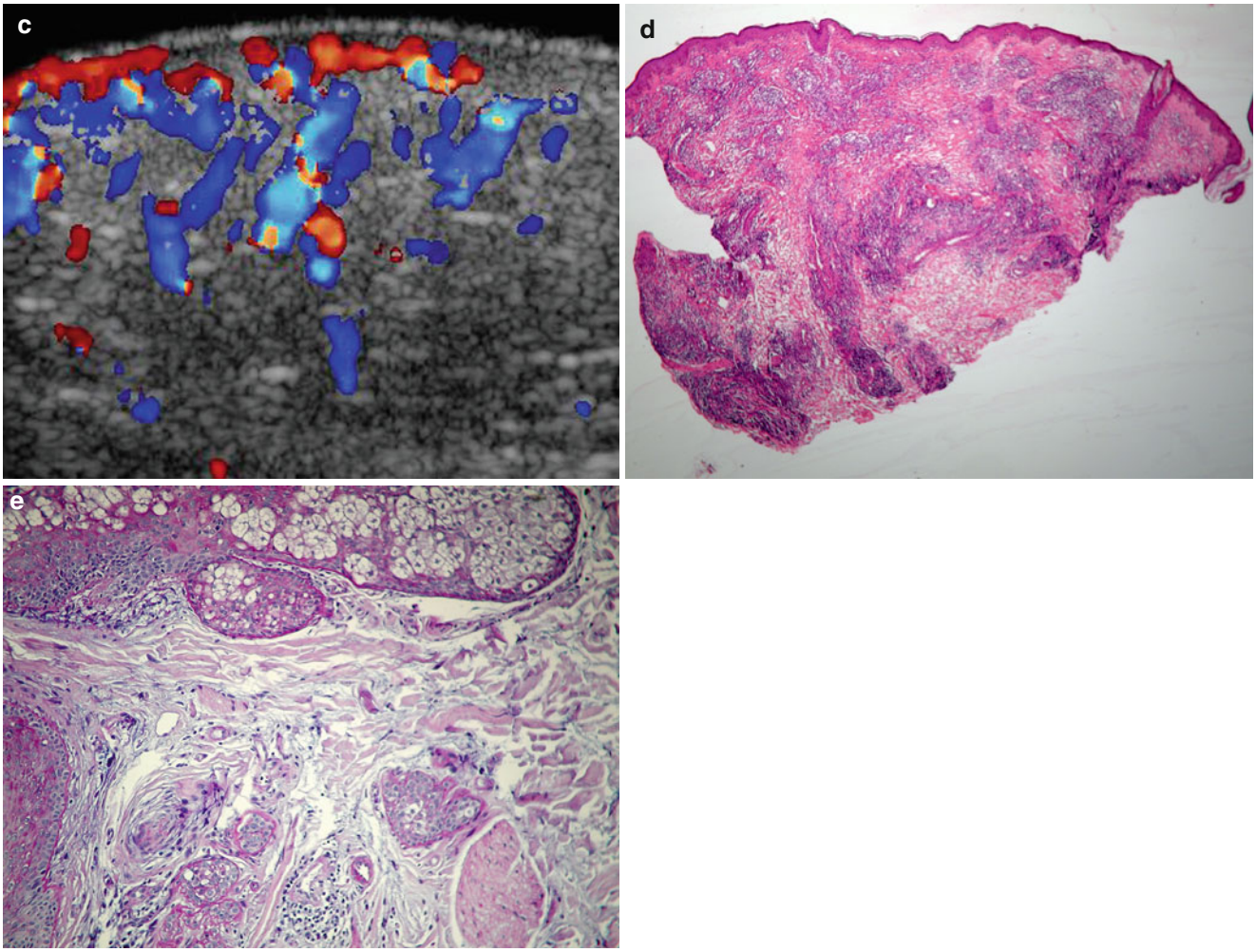

Fig. 4.30 (continued)

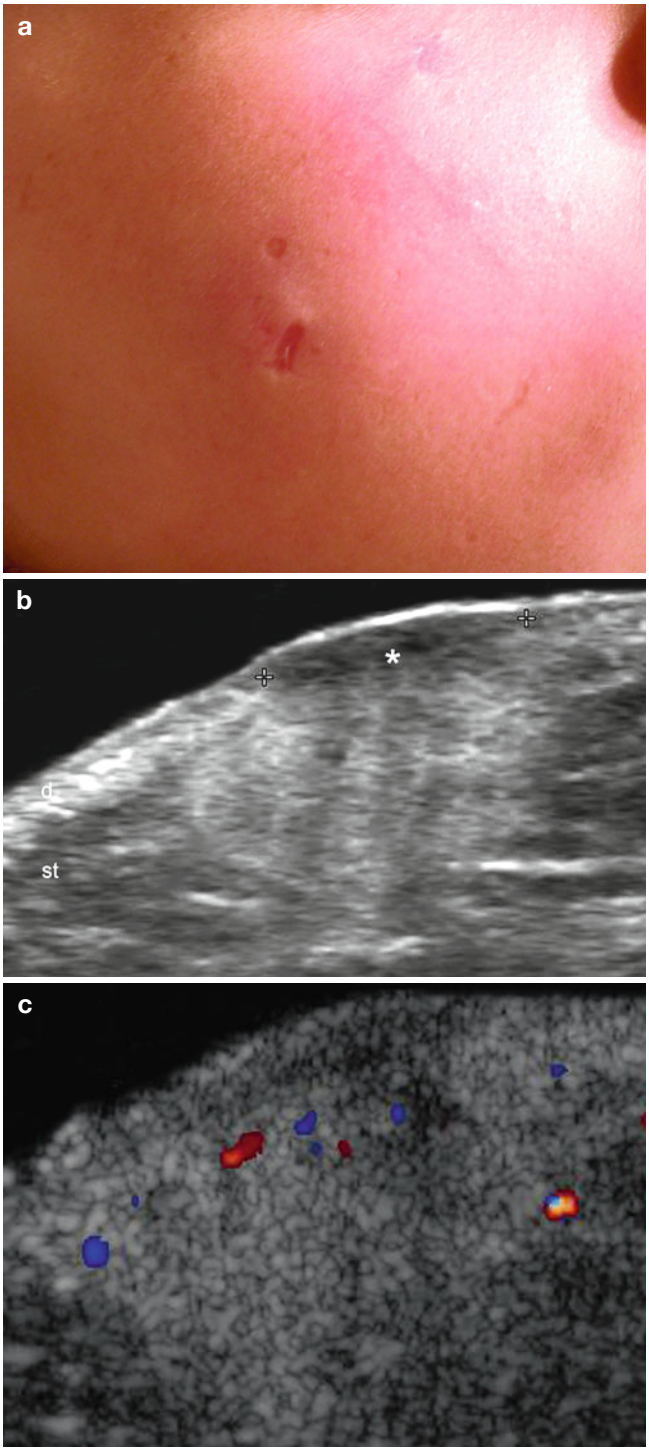

Fig. 4.31 (**a**–**c**) Cutaneous lupus (active phase). (**a**) Clinical image with erythema and swelling in the right cheek. (**b**) Gray scale ultrasound image (transverse view) shows fusiform shaped decreased echogenicity and thickening of the dermis (*) as well as increased echogenicity of the subcutaneous tissue. (**c**) Color Doppler ultrasound image (transverse view) demonstrates increased vascularity in the lesional site. *Abbreviations*: *d* dermis, *st* subcutaneous tissue

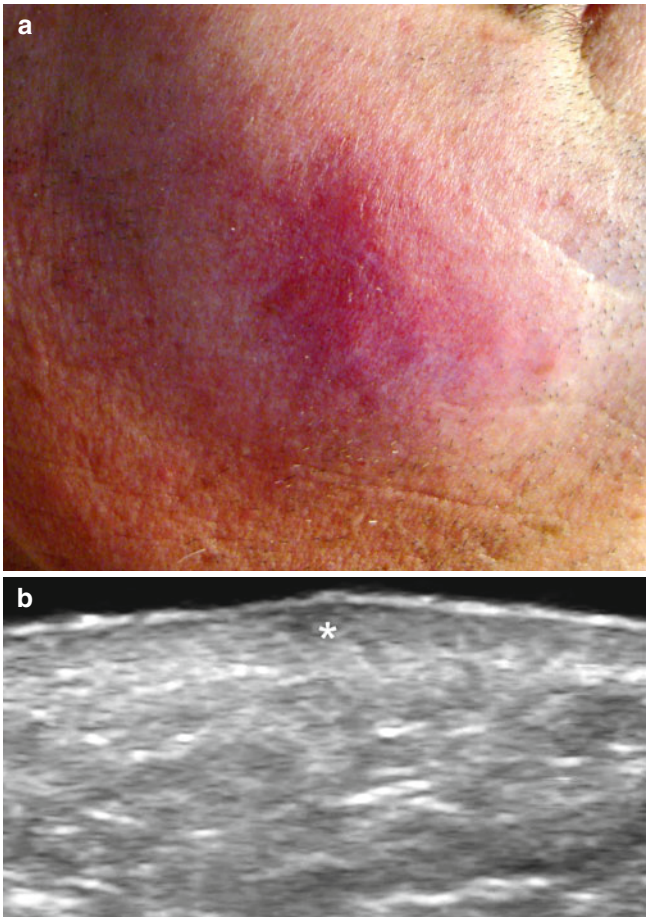

Fig. 4.32 (**a**, **b**) Cutaneous lupus (active phase). (**a**) Clinical image demonstrates erythema and swelling in the right cheek. (**b**) Gray scale ultrasound image (transverse view) shows thickening and decreased echogenicity of the dermis (*). Increased echogenicity of the upper subcutaneous tissue is also detected

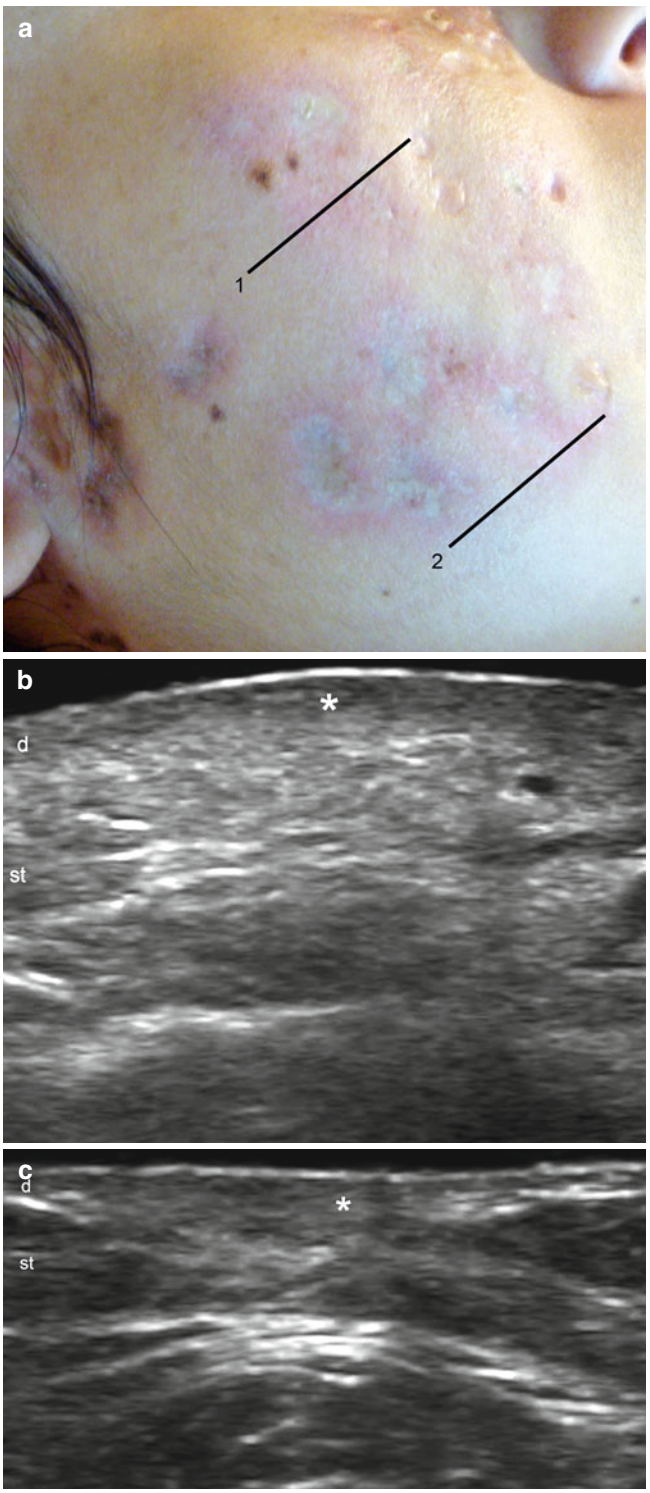

Fig. 4.33 (**a**–**c**) Discoid cutaneous lupus. (**a**) Clinical image shows disk shaped erythematous lesions and scarring in the right cheek. The *black lines* illustrate the level and orientation of the following ultrasound views. (**b**) Gray scale ultrasound image (transverse view, level 1) shows decreased echogenicity of the upper dermis (*) and increased echogenicity of the lower dermis and subcutaneous tissue. (**c**) Gray scale ultrasound image (transverse view) shows thickening and decreased echogenicity of the dermis (*). Increased echogenicity and lack of fatty lobules in the subcutaneous tissue is also detected. *Abbreviations*: *d* dermis, *st* subcutaneous tissue

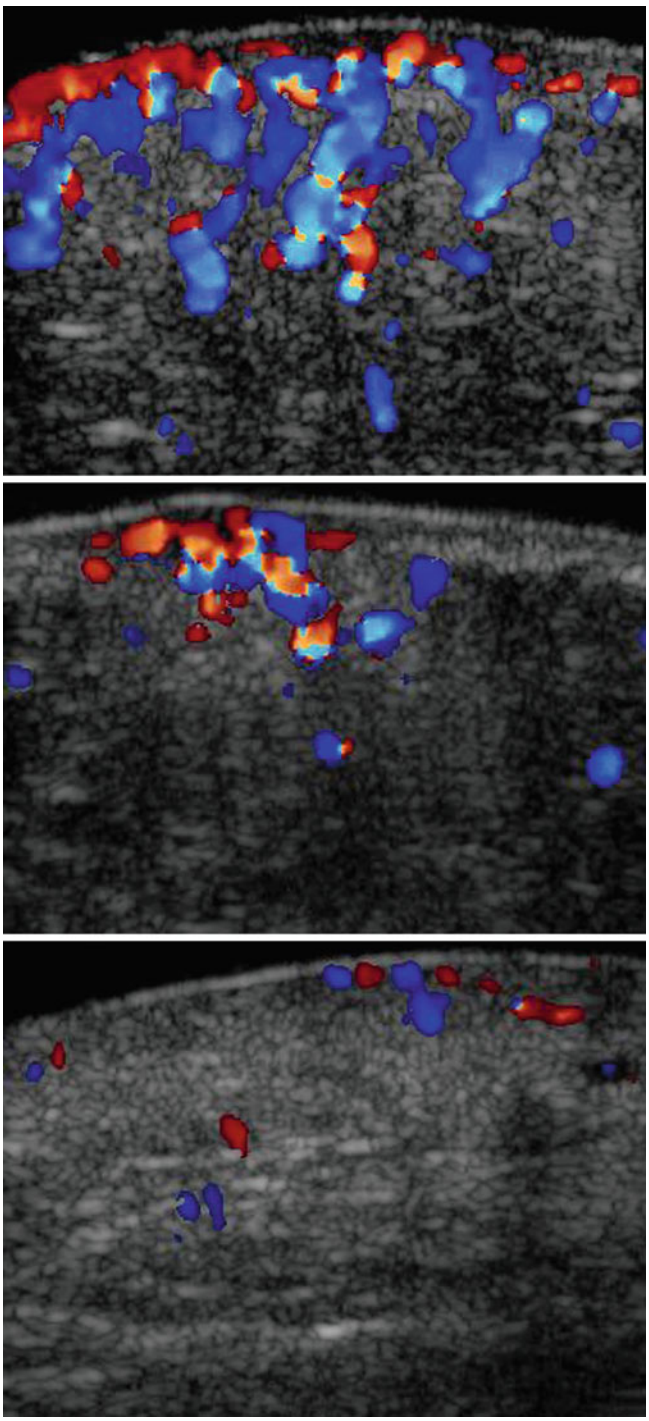

Fig. 4.34 Grading of vascularity in cutaneous lupus going from hypervascular (*top*) to hypovascular (*bottom*)

4.2.12 Dermatomyositis

Dermatomyositis is a systemic autoimmune disease that primarily affects skeletal muscle, skin, and the lungs. Although the disorder is rare, with a prevalence of one to ten cases per million in adults and one to 3.2 cases per million in children, early recognition and treatment are important ways to decrease the morbidity of systemic complications. Dermatomyositis is characterized by autoantibodies, tissue inflammation, parenchymal cell damage and death, and vasculopathy. Clinically, these patients present with "Gottron's papules" (erythematous, usually symmetric and keratotic macules located over the methacarpal and interphalangeal joints that can mimic psoriasis), "heliotrope rash" (violaceous eruption on the upper eyelids and rarely on the lower eyelids), the shawl sign (erythematous, poikilodermatous macules distributed in a "shawl" pattern over the shoulders, arms, and upper back), the V-sign (erythematous eruption in a V-shaped distribution over the anterior neck and chest), and periungual telangiectasias. Calcinosis is usually subclinical, although when the deposits are large, they can be palpable as an induration and associated to hyperpigmentation. Proximal muscle weakness or pain (upper or lower extremity and trunk) and elevated serum creatine kinase or aldolase levels are common. The diagnosis is confirmed by histology that shows a mixed B- and T-cell perivascular inflammatory infiltrate and perifascicular muscular fiber atrophy on the muscle biopsy.

Increased echogenicity of the muscle secondary to edema can be detected on sonography. Contrast-enhanced ultrasound with its capability of measuring perfusion has been reported as a useful tool for diagnosing acute inflammation in poly- and dermatomyositis. Calcinosis can be also detected on sonography and presents as hyperechoic spots, usually with posterior acoustic shadowing. Increased echogenicity of the subcutaneous tissue secondary to panniculitis has also been reported [22, 44–47] (Figs. 4.35 and 4.36).

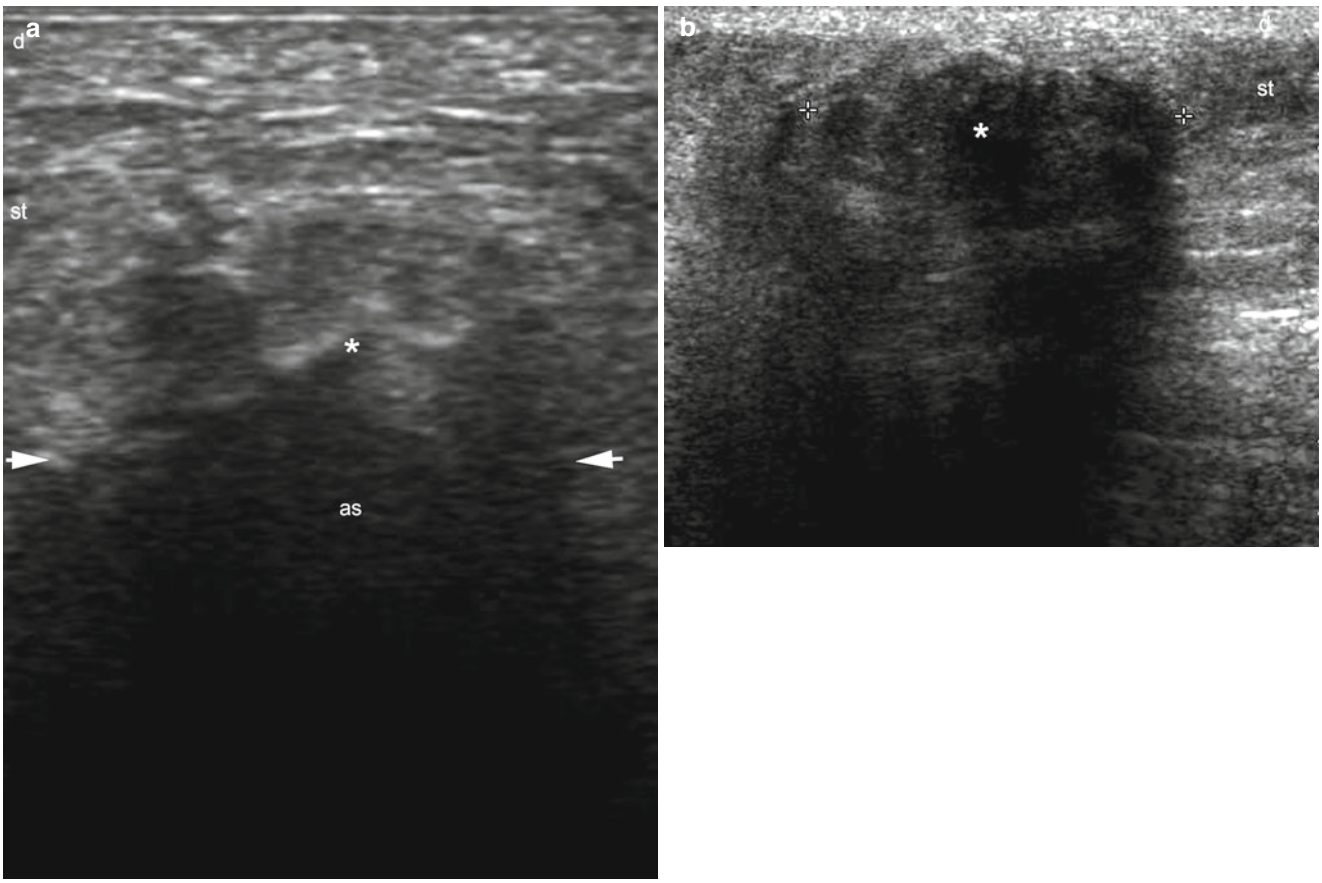

Fig. 4.35 (**a**, **b**) Calcinosis in dermatomyositis. (**a**, **b**) Gray scale ultrasound images (**a**: transverse view, left hip region and **b**: longitudinal view, left gluteal region) show hyperechoic deposits (*) in the subcutaneous tissue that generates strong posterior acoustic shadowing artifact (as, *arrows* (a) and markers (b)). *Abbreviations*: *d* dermis, *st* subcutaneous tissue

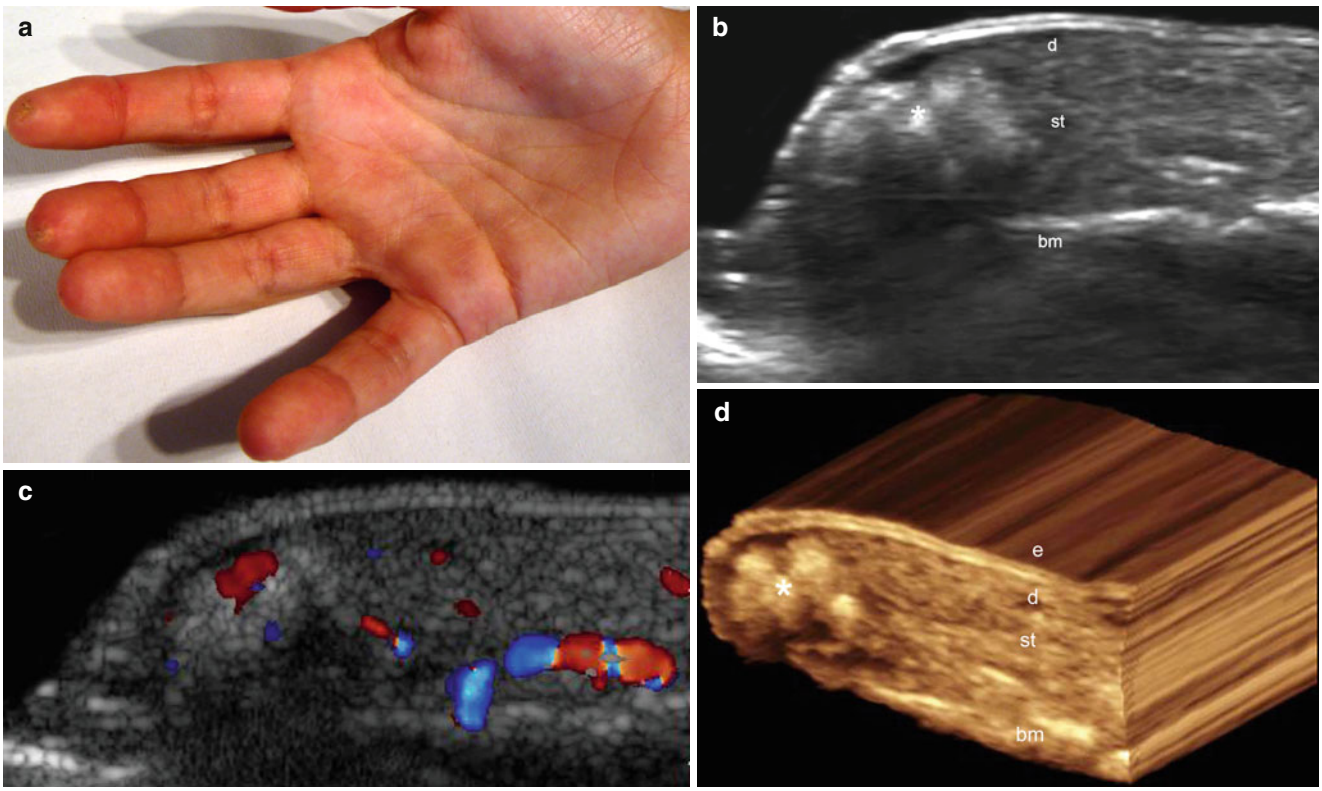

Fig. 4.36 (**a**–**d**) Calcinosis in dermatomyositis. (**a**) Clinical image shows bumps in the tip of the right index and middle fingers. (**b**) Gray scale ultrasound image (longitudinal view, index finger) demonstrates hyperechoic calcium deposits (*) in dermis and subcutaneous tissue. There is also hypoechogenicity of the upper dermis suggestive of inflammation and posterior acoustic shadowing artifact. (**c**) Color Doppler ultrasound image (longitudinal view, index finger) shows increased vascularity in the periphery of the calcium deposits. (**d**) The calcium deposits (*) in 3D (5–8 s, longitudinal reconstruction). *Abbreviations*: *e* epidermis, *d* dermis, *st* subcutaneous tissue, *bm* bony margin of the distal phalanx

4.2.13 Hidradenitis Suppurativa

Hidradenitis suppurativa (HS), also called acne inversa, is a chronic and recurrent inflammatory disease affecting the skin that bears prominent hair follicles and apocrine glands. The exact cause is still controversial but seems to present an autoimmune origin. Clinically, HS shows painful, deep seated inflamed lesions including nodules, sinus tracts, and abscesses with scarring and inflammation in the axillae and groin regions. This disease can less commonly affect the buttock, vulvar, or inframammary regions. The severity of the disease can be clinically assessed using Hurley's classification that separates the stages in: I mild, II moderate and III severe [48]. Histology shows follicular occlusion and inflammatory involvement of the apocrine glands with dense lymphocytic infiltrates around the hair follicle, and acute and chronic inflammatory cells around the apocrine glands. The inflamed sinus tracts frequently contain desquamated keratin, histiocytes, giant cells, and hair shafts within dense fibrosis. Squamous epithelium lined cyst or sinuses in the dermis all containing keratin and containing half hair shafts are usually observed [49]. On sonography, anechoic fluid collections with echoes (debris) and fragments of hair shafts, hypoechoic fistulous tracts in the dermis and subcutaneous tissue, thickening and hypoechogenicity of the dermis, and enlargement of the hair follicles can be detected. Frequently increased vascularity is observed in the periphery of the collections and regional lymph nodes seem to conserve the size, although they may present some cortical thickening during the inflammatory phases. Additionally, anechoic or hypoechoic dermal pseudocystic subclinical lesions in the dermis can be seen [50, 51]. Sonography may support the diagnosis and the assessment of severity in this recurrent disease [52] (Figs. 4.37, 4.38, 4.39, 4.40, 4.41, 4.42, 4.43 and 4.44).

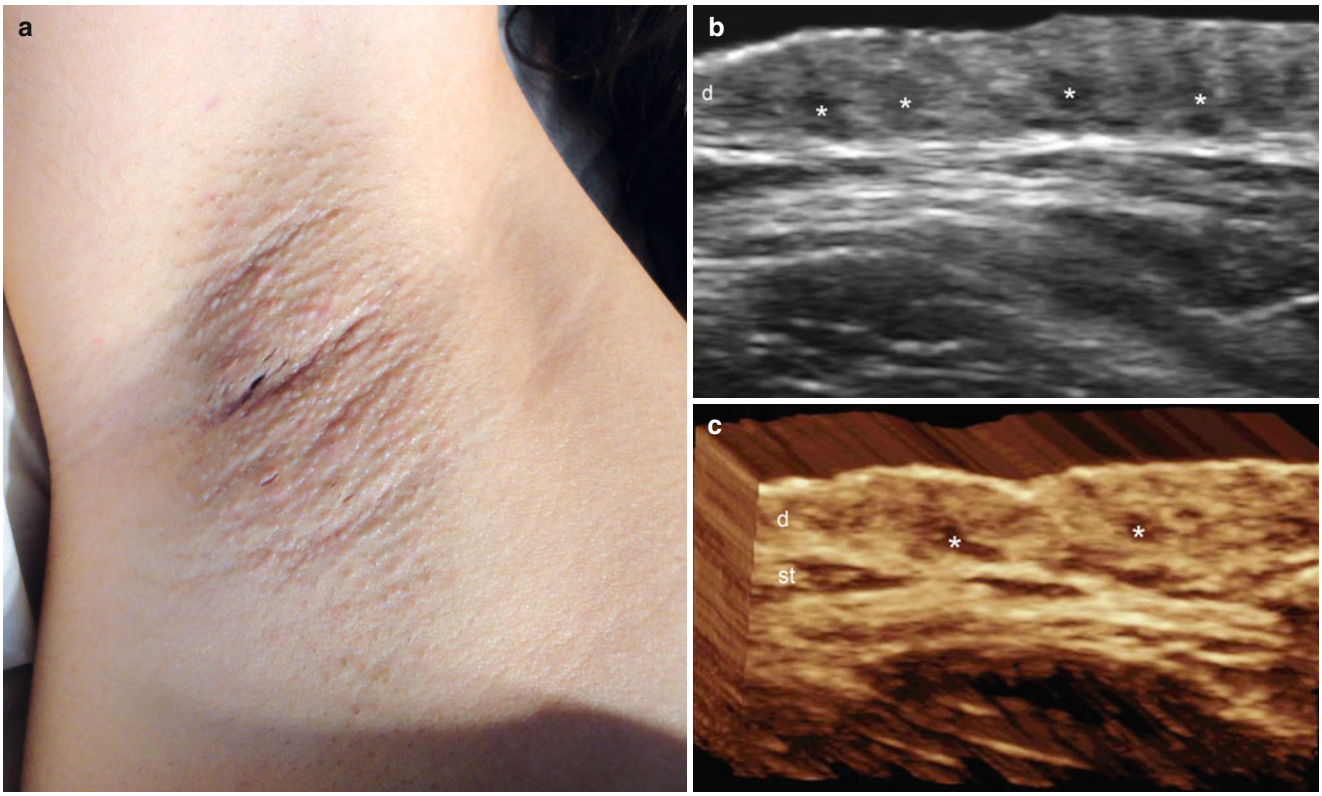

Fig. 4.37 (**a**–**c**) Hidradenitis suppurativa. (**a**) Clinical image shows erythema in the right axilla (Hurley I). (**b**) Gray scale ultrasound image (transverse view) demonstrates enlargement of the base of the hair follicles (*), decreased echogenicity and thickening of the dermis. (**c**) The lesional area in 3D (transverse view, 5–8 s reconstruction). *Abbreviations*: *d* dermis, *st* subcutaneous tissue

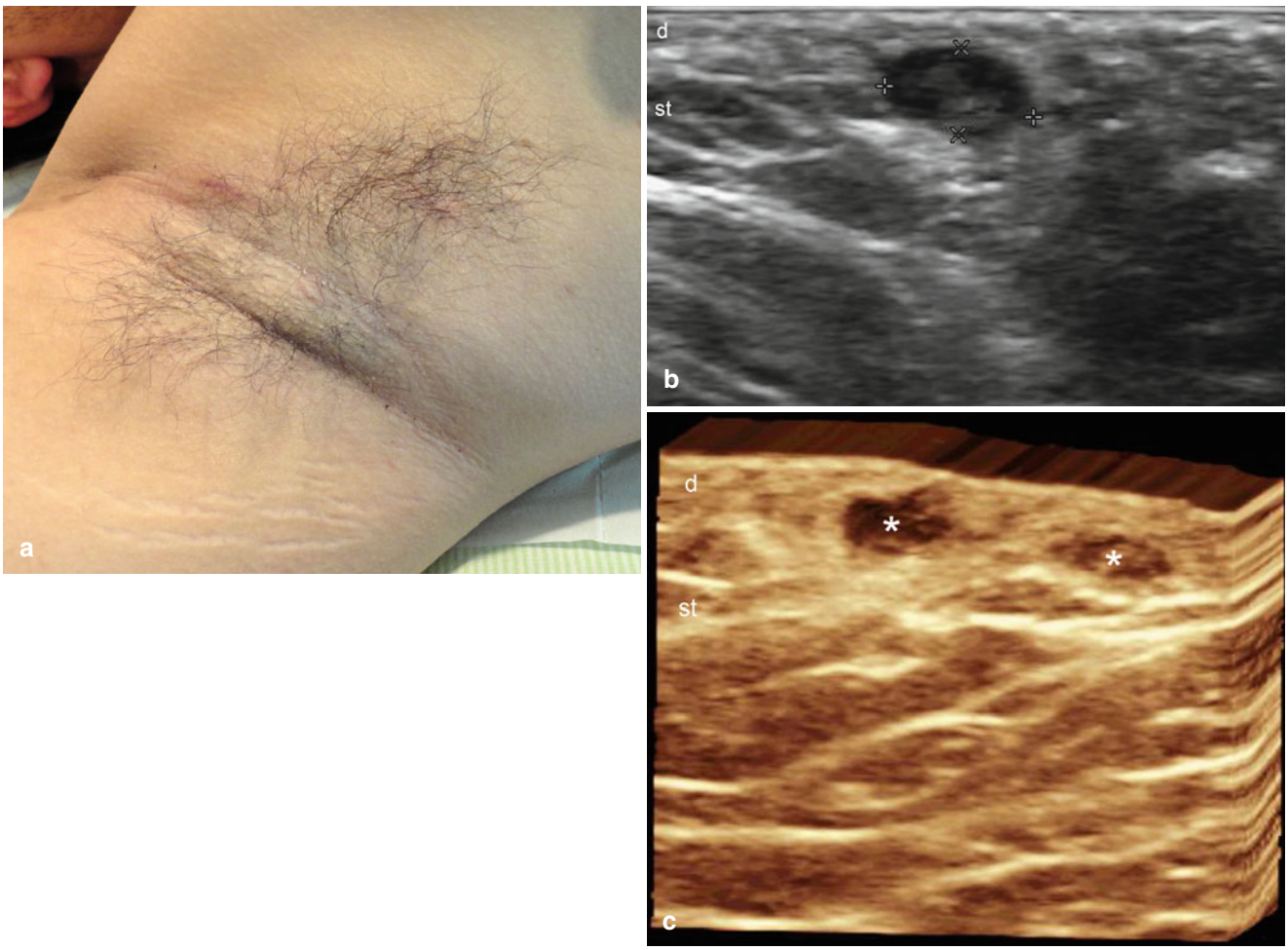

Fig. 4.38 (**a**–**c**) Hidradenitis suppurativa. (**a**) Clinical image shows patchy erythematous areas in the right axilla (Hurley I). (**b**) Gray scale ultrasound image (transverse view) demonstrates hypoechoic oval shaped pseudocystic structure (between markers) in the dermis and upper subcutaneous tissue. (**c**) 3D reconstruction (5–8 s reconstruction, transverse axis) depicts two hypoechoic round shaped pseudocystic lesions (*) in the dermis. *Abbreviations*: *d* dermis, *st* subcutaneous tissue

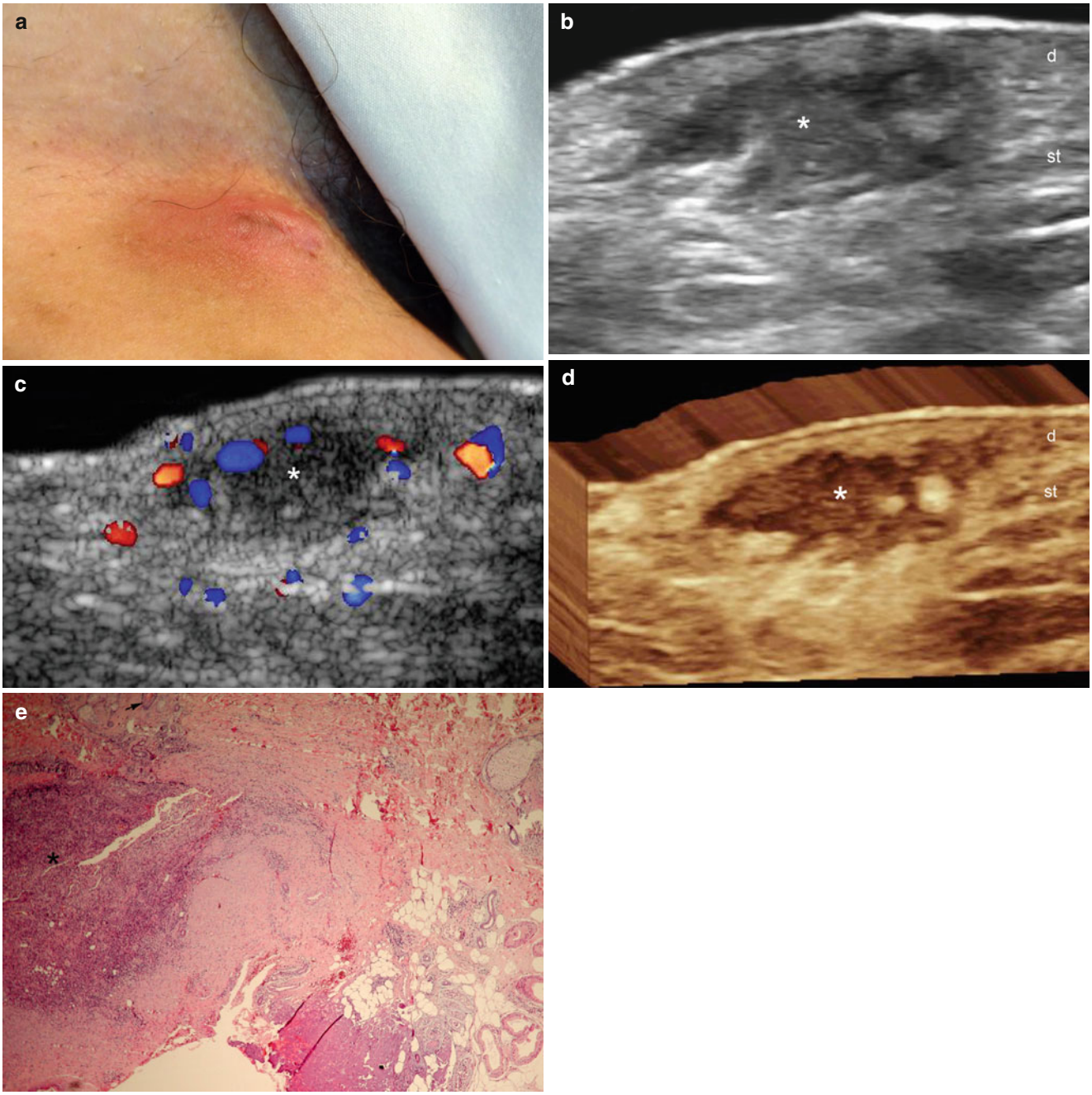

Fig. 4.39 (**a**–**e**) Hidradenitis suppurativa. (**a**) Clinical image shows erythematous swelling in the right groin (Hurley II). (**b**) Gray scale ultrasound image (transverse view) demonstrates hypoechoic collection (*) with echoes (debris) and irregular borders in the dermis and subcutaneous tissue that connects to the base of the hair follicles. Thickening and decreased echogenicity of the dermis is also detected. (**c**) Color Doppler ultrasound image (transverse view) shows increased vascularity in the periphery of the collection (*). (**d**) The collection (*) in 3D (5–8 s sweep reconstruction). (**e**) Histology (HE × 100 zoom) depicts a suppurative inflammatory reaction with polymorphonuclear cells and fibrosis (*). The base of a hair follicle is detected in the upper part of the figure (*arrow*). Adipose cells and apocrine glands are shown in the right side of the image (*bottom*). *Abbreviations*: *d* dermis, *st* subcutaneous tissue

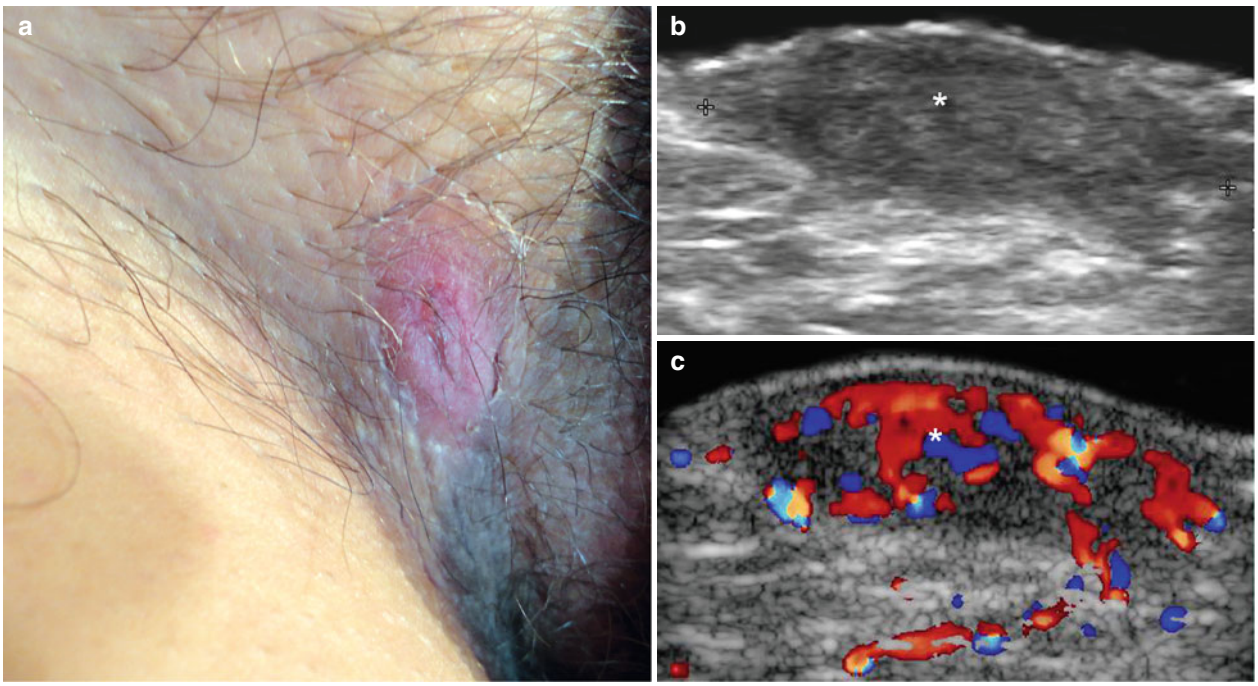

Fig. 4.40 (**a**–**c**) Hidradenitis suppurativa. (**a**) Clinical image shows erythematous bump in the right groin (Hurley I). (**b**) Gray scale ultrasound image (transverse view) demonstrates hypoechoic fluid collection with prominent echoes (debris and inflammatory/granulomatous tissue) (*, between markers) in the dermis and upper subcutaneous tissue. (**c**) Color Doppler ultrasound image (transverse view) shows increased blood flow in the collection

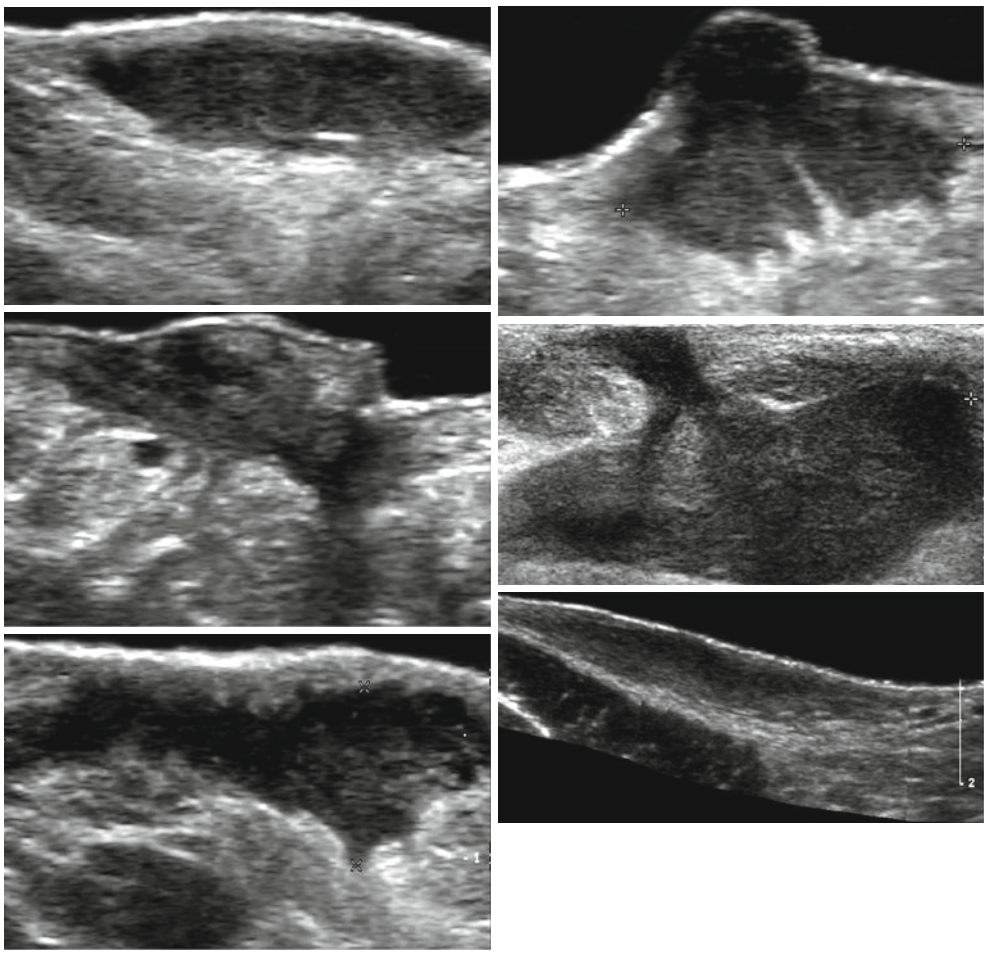

Fig. 4.41 Variable appearance of the fluid collections in hidradenitis suppurativa

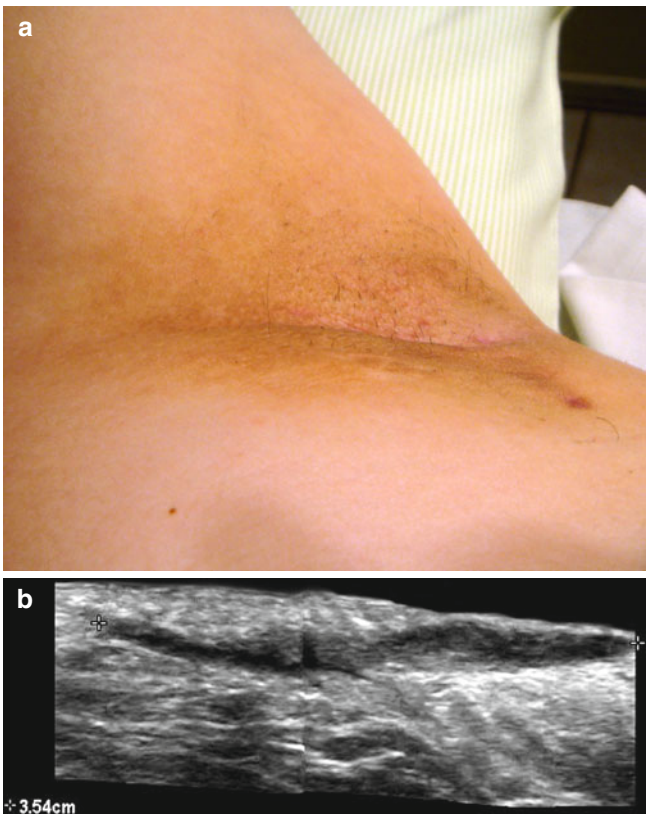

Fig. 4.42 (**a**, **b**) Hidradenitis suppurativa. (**a**) Clinical image shows slight erythema and retraction in the left axilla (Hurley I). (**b**) Gray scale ultrasound image (longitudinal view) depicts 3.54 cm hypoechoic fistulous tract (between markers) running in the dermis and upper subcutaneous tissue

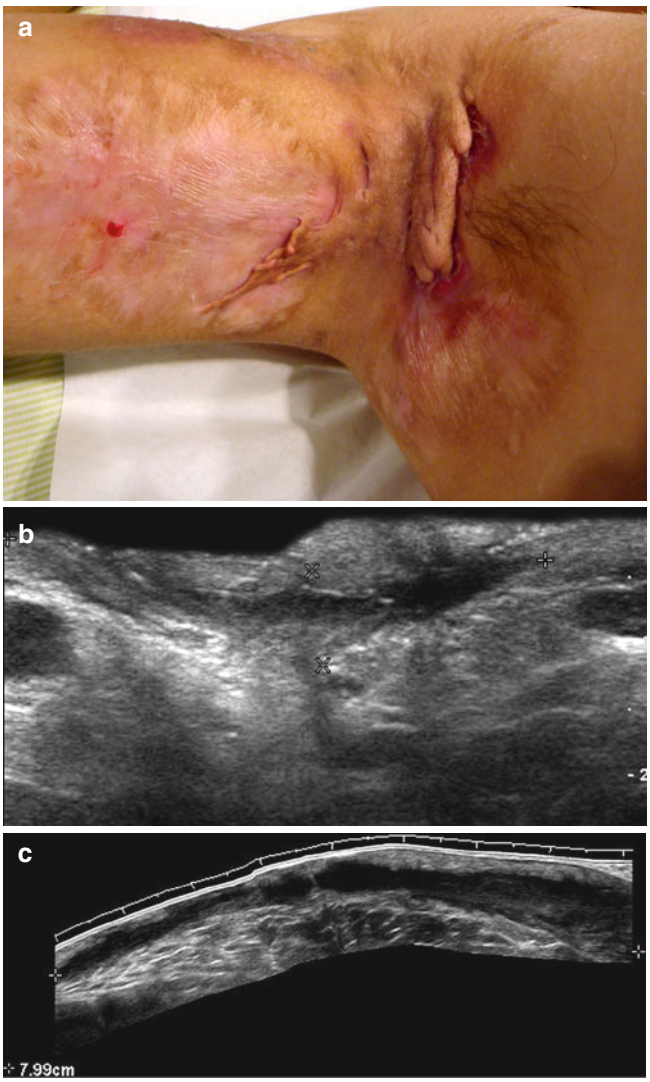

Fig. 4.43 (**a**–**c**) Hidradenitis suppurativa. (**a**) Clinical image shows extensive scarring, erythema and bumps in the right axilla (Hurley III). (**b**) Gray scale ultrasound image (transverse view) demonstrates one of the several hypoechoic fistulous tracts (between markers). (**c**) Gray scale extended field of view (longitudinal view) shows a 7.99 cm long hypoechoic fistulous tract (between markers) located in dermis and subcutaneous tissue in the same patient

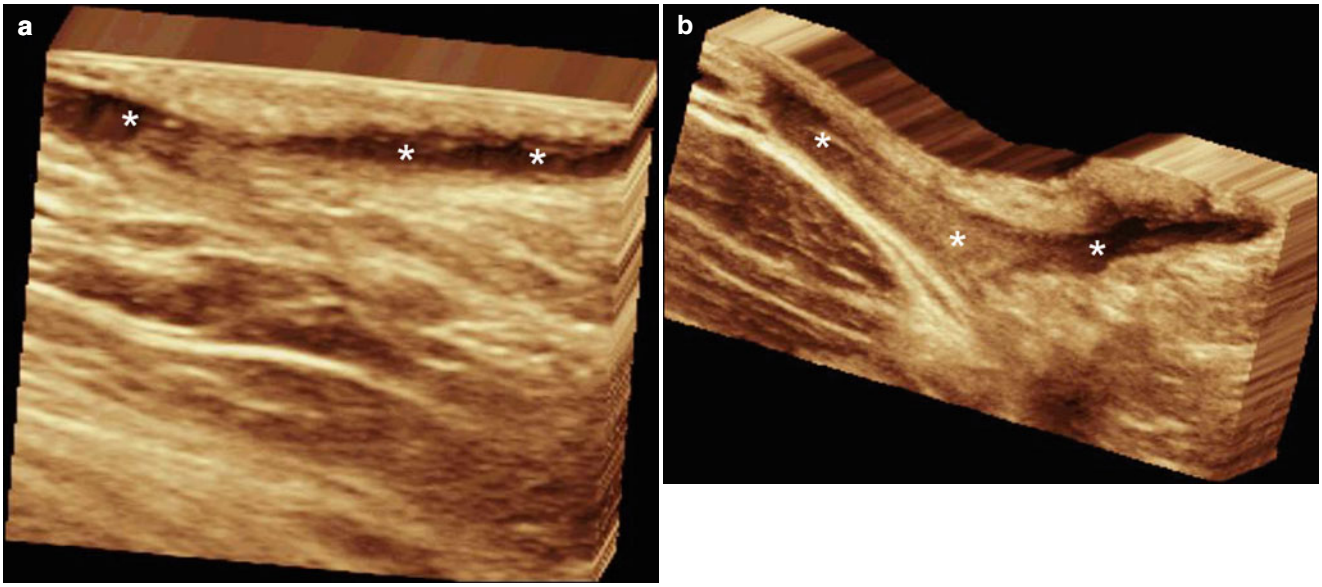

Fig. 4.44 (**a**, **b**). 3D of fistulous tracts (*) in hidradenitis suppurativa (5–8 s longitudinal view reconstructions)

4.2.14 Foreign Bodies

Foreign bodies are exogenous components that can be retained in the skin through many mechanisms commonly related to trauma. Occasionally, patients are not aware of the retained material but clinically they present with induration, erythema, and scarring. There are two main types of foreign bodies according to origin: organic (derived from living structures) such as splinters of wood or thorns of roses, or inert, also called synthetic, such as pieces of glass or metal.

Histology shows giant cells, macrophages, and inflammatory cells. Some foreign bodies such as wood, suture material, or glass are birefringent and can be identified using polarized light.

On sonography, foreign bodies appear as hyperechoic linear or band-like structures. Inert materials such as glass or metal usually show a posterior reverberance artifact. Commonly, there is hypoechoic granulomatous tissue surrounding the foreign body. Fluid collections in the vicinity such as hematomas or abscesses, or the involvement of deeper structures, can be ruled out. Occasionally, these foreign bodies may migrate and/or can be found far from the puncture wound level; therefore, it is suggested to examine a wide range of tissue. Sonography may prove their existence, assess the exact axis, location and measurements and also guide the removal. In an acute setting, the sonographer should avoid the contamination of the open wound with gel, therefore, the usage of sterile gel is recommended. In the presence of soft-tissue emphysema, a lateral approach to the wound or a water bath (when the lesional area is located in the distal arm or leg) can help [53–55] (Figs. 4.45, 4.46 and 4.47).

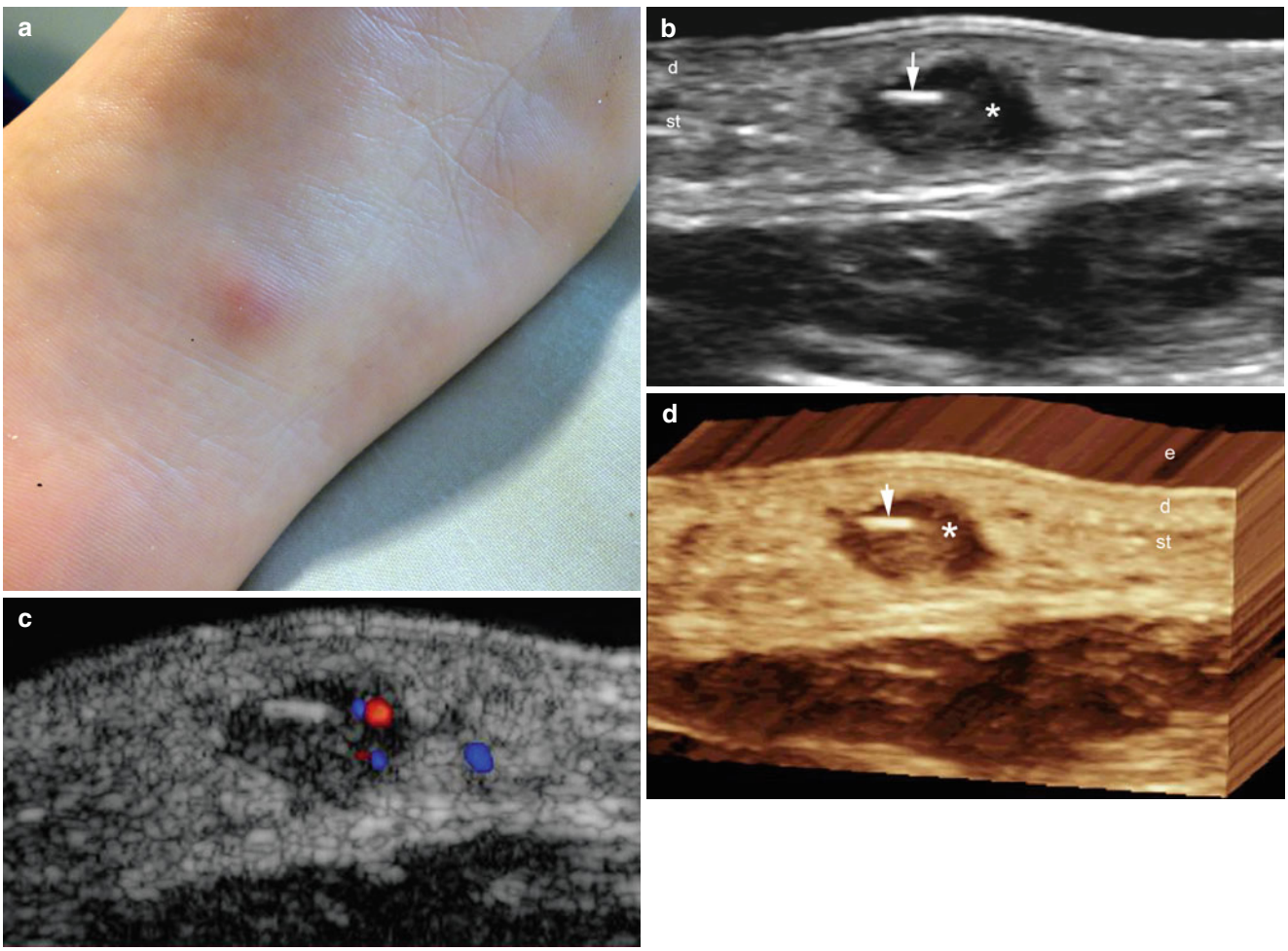

Fig. 4.45 (**a**–**d**) Organic foreign body. (**a**) Clinical image shows erythematous swelling in the medial aspect of the sole of the left foot. (**b**) Gray scale ultrasound image (longitudinal view) demonstrates hyperechoic line (*arrow*) in the subcutaneous tissue that corresponds to a fragment of a splinter of wood. Hypoechoic granulomatous tissue (*) surrounds the foreign body. Notice the bilaminar normal appearance of the plantar epidermis. (**c**) Color Doppler ultrasound image (transverse view) shows increased blood flow in the hypoechoic granulomatous tissue. (**d**) 3D reconstruction of the foreign body (5–8 s transverse view sweep). *Abbreviations*: *e* epidermis, *d* dermis, *st* subcutaneous tissue

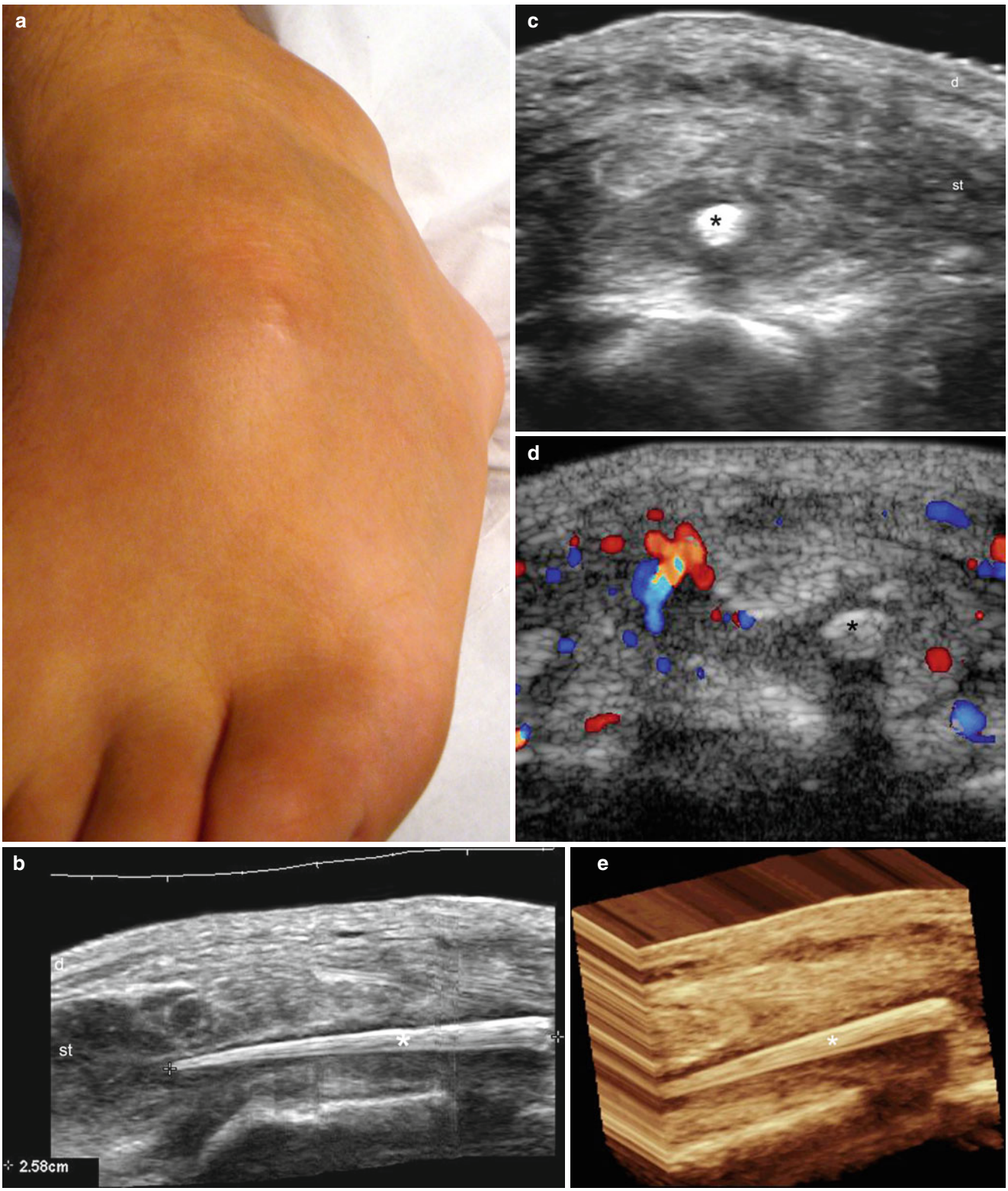

Fig. 4.46 (**a**–**e**) Organic foreign body. (**a**) Clinical image shows a swelling in the anterolateral aspect of the left foot. (**b**) Gray scale ultrasound image (longitudinal view) demonstrates a 2.58 cm, well defined, hyperechoic band (*) with tapering of its distal part, located in the subcutaneous tissue that corresponded to a fragment of a leaf of a palm tree. (**c**) Gray scale ultrasound image (transverse view) demonstrates the foreign body (*) and the surrounding hypoechoic granulomatous tissue in the periphery. (**d**) Color Doppler ultrasound image (transverse view) shows increased blood flow surrounding the foreign body. (**e**) 3D reconstruction of the foreign body (5–8 s longitudinal sweep). *Abbreviations*: *d* dermis, *st* subcutaneous tissue

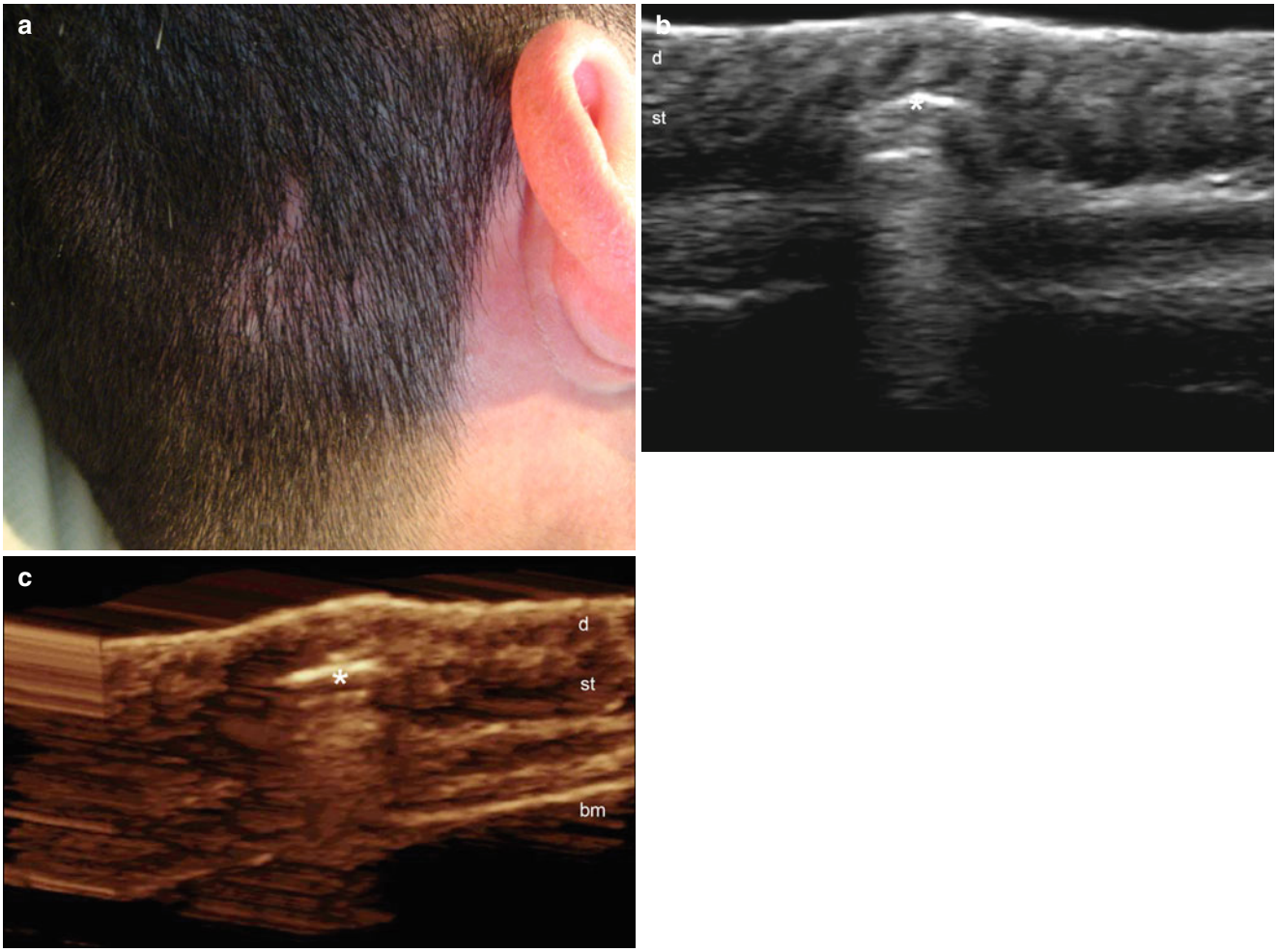

Fig. 4.47 (**a**–**c**) Inert foreign body. (**a**) Clinical image shows focal baldness and erythema in the right occipital region. (**b**) Gray scale ultrasound image (longitudinal view) demonstrates hyperechoic band (*) in the subcutaneous tissue that produces a posterior reverberance artifact that corresponded to a piece of glass. Notice the enlargement of the hair follicles superficially located and the compression of the superficial hair follicles performed by the foreign body. (**c**) 3D of the foreign body (5–8 s longitudinal view reconstruction). *Abbreviations*: *d* dermis, *st* subcutaneous tissue

References

1. Wortsman XC, Holm EA, Wulf HC, Jemec GB. Real-time spatial compound ultrasound imaging of skin. Skin Res Technol. 2004;10:23–31.
2. Hermann G, Gilbert MS, Abdelwahab IF. Hemophilia: evaluation of musculoskeletal involvement with CT, sonography, and MR imaging. AJR Am J Roentgenol. 1992;158:119–23.
3. Badauy CM, Gomes SS, Sant'Ana Filho M, Chies JA. Ehlers-Danlos syndrome (EDS) type IV: review of the literature. Clin Oral Investig. 2007;11:183–7.
4. Sidhu PS, Rich PM. Sonographic detection and characterization of musculoskeletal and subcutaneous tissue abnormalities in sickle cell disease. Br J Radiol. 1999;72:9–17.
5. Török L, Kirschner A, Ocsai H, Olasz K. Hematoma-like metastasis in melanoma. J Am Acad Dermatol. 2003;49:912–3.
6. Ebright JR, Pieper B. Skin and soft tissue infections in injection drug users. Infect Dis Clin North Am. 2002;16:697–712.
7. Latifi HR, Siegel MJ. Color Doppler flow imaging of pediatric soft tissue masses. J Ultrasound Med. 1994;13:165–9.
8. Noh JY, Cheong HJ, Song JY, Hong SJ, Myung JS, Choi WS, et al. Skin and soft tissue infections: experience over a five-year period and clinical usefulness of ultrasonography-guided gun biopsy-based culture. Scand J Infect Dis. 2011;43:870–6.
9. Naouri M, Samimi M, Atlan M, Perrodeau E, Vallin C, Zakine G, et al. High-resolution cutaneous ultrasonography to differentiate lipoedema from lymphoedema. Br J Dermatol. 2010;163:296–301.
10. Volikova AI, Edwards J, Stacey MC, Wallace HJ. High-frequency ultrasound measurement for assessing post-thrombotic syndrome and monitoring compression therapy in chronic venous disease. J Vasc Surg. 2009;50:820–5.
11. Wollina U, Abdel-Naser MB, Mani R. A review of the microcirculation in skin in patients with chronic venous insufficiency: the problem and the evidence available for therapeutic options. Int J Low Extrem Wounds. 2006;5:169–80.
12. Leu AJ, Leu HJ, Franzeck UK, Bollinger A. Microvascular changes in chronic venous insufficiency-a review. Cardiovasc Surg. 1995;3:237–45.
13. Meissner MH. Lower extremity venous anatomy. Semin Intervent Radiol. 2005;22:147–56.
14. Liu X, Jia X, Guo W, Xiong J, Zhang H, Liu M, et al. Ultrasound-guided foam sclerotherapy of the great saphenous vein with sapheno-femoral ligation compared to standard stripping: a prospective clinical study. Int Angiol. 2011;30:321–6.
15. Miteva M, Romanelli P, Kirsner RS. Lipodermatosclerosis. Dermatol Ther. 2010;23:375–88.
16. Kirsner RS, Pardes JB, Eaglstein WH, Falanga V. The clinical spectrum of lipodermatosclerosis. J Am Acad Dermatol. 1993;28:623–7.
17. Gniadecka M, Karlsmark T, Bertram A. Removal of dermal edema with class I and II compression stockings in patients with lipodermatosclerosis. J Am Acad Dermatol. 1998;39:966–70.
18. Chopra R, Chhabra S, Thami GP, Punia RP. Panniculitis: clinical overlap and the significance of biopsy findings. J Cutan Pathol. 2010;37:49–58.
19. Requena L, Yus ES. Panniculitis. Part I. Mostly septal panniculitis. J Am Acad Dermatol. 2001;45:163–83.
20. Requena L, Sánchez Yus E. Panniculitis. Part II. Mostly lobular panniculitis. J Am Acad Dermatol. 2001;45:325–61.
21. Avayú HE, Rodríguez AC, Wortsman CX, Corredoira SY, Serman VD, Strauch BG, et al. Newborn fat necrosis: case-report. Rev Chil Pediatr. 2009;80:60–4. Spanish.
22. Wortsman X, Gutierrez M, Saavedra T, Honeyman J. The role of ultrasound in rheumatic skin and nail lesions: a multi-specialist approach. Clin Rheumatol. 2011;30:739–48.
23. Cohen PR, Eliezri YD. Cutaneous odontogenic sinus simulating a basal cell carcinoma: case report and literature review. Plast Reconstr Surg. 1990;86:123–7.
24. Wortsman X, Wortsman J. Skin ultrasound, Chap. 9. In Dogra V, Gaitini D, editors. Musculoskeletal ultrasound with CT and MRI correlation,1st edn. Thieme, Stuttgart; 2010. p. 147–170.
25. Wortsman X, Sazunic I, Jemec GB. Sonography of plantar warts: role in diagnosis and treatment. J Ultrasound Med. 2009;28:787–93.
26. Wortsman X, Jemec GB, Sazunic I. Anatomical detection of inflammatory changes associated with plantar warts by ultrasound. Dermatology. 2010;220:213–7.
27. Johnson MA, Armstrong AW. Clinical and Histologic diagnostic guidelines for psoriasis: a critical review. Clin Rev Allergy Immunol. 2013;44:166–72.
28. Baran R. The burden of nail psoriasis: an introduction. Dermatology. 2010;221 Suppl 1:1–5.
29. Yamamoto T. Psoriatic arthritis: from a dermatological perspective. Eur J Dermatol. 2011;21:660–6.
30. Murphy M, Kerr P, Grant-Kels JM. The histopathologic spectrum of psoriasis. Clin Dermatol. 2007;25:524–8.
31. Gutierrez M, Wortsman X, Filippucci E, De Angelis R, Filosa G, Grassi W. High-frequency sonography in the evaluation of psoriasis: nail and skin involvement. J Ultrasound Med. 2009;28:1569–74.
32. Gutierrez M, De Angelis R, Bernardini ML, Filippucci E, Goteri G, Brandozzi G, et al. Clinical, power Doppler sonography and histological assessment of the psoriatic plaque: short-term monitoring in patients treated with etanercept. Br J Dermatol. 2011;164:33–7.
33. Kaeley GS. Review of the use of ultrasound for the diagnosis and monitoring of enthesitis in psoriatic arthritis. Curr Rheumatol Rep. 2011;13:338–45.
34. Fett N, Werth VP. Update on morphea: part I. Epidemiology, clinical presentation, and pathogenesis. J Am Acad Dermatol. 2011;64:217–28.
35. Wollina U, Buslau M, Heinig B, Petrov I, Unger E, Kyriopoulou E, et al. Disabling pansclerotic morphea of childhood poses a high risk of chronic ulceration of the skin and squamous cell carcinoma. Int J Low Extrem Wounds. 2007;6:291–8.
36. Li SC, Liebling MS, Haines KA. Ultrasonography is a sensitive tool for monitoring localized scleroderma. Rheumatology (Oxford). 2007;46:1316–9.
37. Li SC, Liebling MS. The use of Doppler ultrasound to evaluate lesions of localized scleroderma. Curr Rheumatol Rep. 2009;11:205–11.
38. Wortsman X, Wortsman J, Sazunic I, Carreño L. Activity assessment in morphea using color Doppler ultrasound. J Am Acad Dermatol. 2011;65:942–8.
39. Wenzel J, Zahn S, Tüting T. Pathogenesis of cutaneous lupus erythematosus: common and different features in distinct subsets. Lupus. 2010;19:1020–8.
40. Rothfield N, Sontheimer RD, Bernstein M. Lupus erythematosus: systemic and cutaneous manifestations. Clin Dermatol. 2006;24:348–62.
41. Tebbe B. Clinical course and prognosis of cutaneous lupus erythematosus. Clin Dermatol. 2004;22:121–4.
42. Delle Sedie A, Riente L, Filippucci E, et al. Ultrasound imaging for the rheumatologist. XV. Ultrasound imaging in vasculitis. Clin Exp Rheumatol. 2008;26:391–4.
43. Wortsman X. The traces of sound: taking the road to skin. Curr Rheumatol Rev. 2011;3:231–8.

44. Kao L, Chung L, Fiorentino DF. Pathogenesis of dermatomyositis: role of cytokines and interferon. Curr Rheumatol Rep. 2011;13:225–32.
45. Koler RA, Montemarano A. Dermatomyositis. Am Fam Physician. 2001;1(64):1565–72.
46. Weber MA. Ultrasound in the inflammatory myopathies. Ann N Y Acad Sci. 2009;1154:159–70.
47. Stonecipher MR, Jorizzo JL, Monu J, Walker F, Sutej PG. Dermatomyositis with normal muscle enzyme concentrations. A single-blind study of the diagnostic value of magnetic resonance imaging and ultrasound. Arch Dermatol. 1994;130(10):1294–9.
48. Jemec GB. Clinical practice. Hidradenitis suppurativa. N Engl J Med. 2012;366:158–64.
49. Layton A. Pathology of Hidradenitis Suppurativa. In: Jemec GBE, Revuz J, Leyden J, editors. Hidradenitis Suppurativa. Berlin: Springer- Verlag; 2006. p. 25–33.
50. Wortsman X, Jemec GB. Real-time compound imaging ultrasound of hidradenitis suppurativa. Dermatol Surg. 2007;33:1340–2.
51. Wortsman X, Revuz J, Jemec GB. Lymph nodes in hidradenitis suppurativa. Dermatology. 2009;219:22–4.
52. Kelekis NL, Efstathopoulos E, Balanika A, Spyridopoulos TN, Pelekanou A, Kanni T, et al. Ultrasound aids in diagnosis and severity assessment of hidradenitis suppurativa. Br J Dermatol. 2010;162:1400–2.
53. Halaas GW. Management of foreign bodies in the skin. Am Fam Physician. 2007;76:683–8.
54. Valle M, Zamorani MP. Skin and subcutaneous tissue. In: Bianchi S, Martinoli C, editors. Ultrasound of musculoskeletal system. Berlin: Springer- Verlag; 2007. p. 27–31.
55. Wortsman X. Common applications of dermatologic sonography. J Ultrasound Med. 2012;31:97–111.

Common Benign Non-vascular Skin Tumors

5

Ximena Wortsman and Marcio Bouer

The most common benign entities with tips to recognize them on sonography

Contents

5.1 Introduction

Presently, ultrasound has been proved useful for studying common benign cutaneous tumors [1]. Thus, the application of sonography allows the assessment of important characteristics of the tumors not frequently evident during the physical examination. The purpose of the ultrasound examination should be to provide additional information for the examination different from the one already deduced by the naked eye of a well-trained physician [2]. Among the characteristics that could be unveiled or confirmed by ultrasound examinations are: the nature of the lesion (solid or cystic), the extension, the anatomical location, and the degree of vascularity among others. This detailed information can be useful for planning surgery and improving the cosmetic prognosis of the patient at a later date.

Before the performance of an ultrasound examination in any type of skin tumor, a visual inspection of the lesion should take place. The latter procedure allows for properly locating the transducer and correlates the clinical and sonographic findings [3].

This chapter discusses the potential of this technique as pertains to common dermatological tumors and pseudotumors, and provides an orientation to the reader about how to handle these conditions on ultrasound imaging.

X. Wortsman, MD (✉)
Department of Radiology and Dermatology,
Institute for Diagnostic Imaging
and Research of the Skin and Soft Tissues,
Clinica Servet, Faculty of Medicine, University of Chile,
Almirante Pastene 150, Providencia, Santiago, Chile
e-mail: xwo@tie.cl,
xworts@yahoo.com,
www.sonoskin.com

M. Bouer, MD
Research Unit, Department of Radiology,
University of São Paulo Medical School,
São Paulo, São Paulo, Brazil

Department of Radiology, Fleury Laboratory,
São Paulo, São Paulo, Brazil

Instituto de Radiologia,
Hospital das Clínicas Da Universidade de São Paulo,
Rua Senador Cesar Lacerda de Vergueiro, 511 ap 162,
São Paulo, São Paulo, Brazil
e-mail: mbouer@gmail.com

X. Wortsman, G.B.E. Jemec (eds.), *Dermatologic Ultrasound with Clinical and Histologic Correlations*,
DOI 10.1007/978-1-4614-7184-4_5, © Springer Science+Business Media New York 2013

5.2 Benign Tumors

Benign cutaneous tumors are the reason for common requests of ultrasound examinations. According to the nature of the lesion they can be classified in cystic or solid.

5.2.1 Cystic

5.2.1.1 Epidermal Cyst

Epidermal cysts are caused by the implantation of epidermal components in the dermis and subcutaneous tissue. Common causes are congenital, traumatic, or related to previous surgery. Histologically, epidermal cysts are composed of a stratified squamous epithelium with a granular layer but without a sebaceous basis. Therefore, the term "sebaceous cyst" is a misnomer and can be anatomically confusing [3]. Clinically, they appear as a palpable and/or erythematous nodule that can discharge oily debris. On sonography, epidermal cysts show a variable appearance according to the integrity of their walls (Fig. 5.1). If the cyst is intact, a round-shaped anechoic structure located in the dermis and subcutaneous tissue can be detected. Frequently, an anechoic or hypoechoic tract connecting to the epidermis, also called "punctum", is seen on the ultrasound examination. There are cases in which giant epidermal cysts can present a "pseudotestes appearance" (i.e., brighter inner echoes and anechoic filiform areas), that contain highly compacted deposits of keratin, cholesterol crystals, and occasionally some dystrophic calcium deposits [4]. In the presence of inflammation or rupture, the cyst can show irregular or blurry borders and the keratin, mixed with inflammatory components, can spread to the surrounding tissues producing a hypoechoic foreign-body–like reaction. The posterior acoustic enhancement artifact that is typically seen in cystic structures is usually conserved and can give a clue to their identification. On color Doppler ultrasound, increased vascularity can be detected in the periphery of the cyst under inflammation or rupture phases. The detection of the phase of the cyst (intact or ruptured) using sonography can modify the surgical technique to approach the lesion from a small enucleation to a wide excision of the disintegrated cyst, or it can change the decision to start antibiotic treatment to decrease the inflammatory reaction [5] (Figs. 5.1, 5.2, 5.3, 5.4, 5.5, 5.6, 5.7, and 5.8).

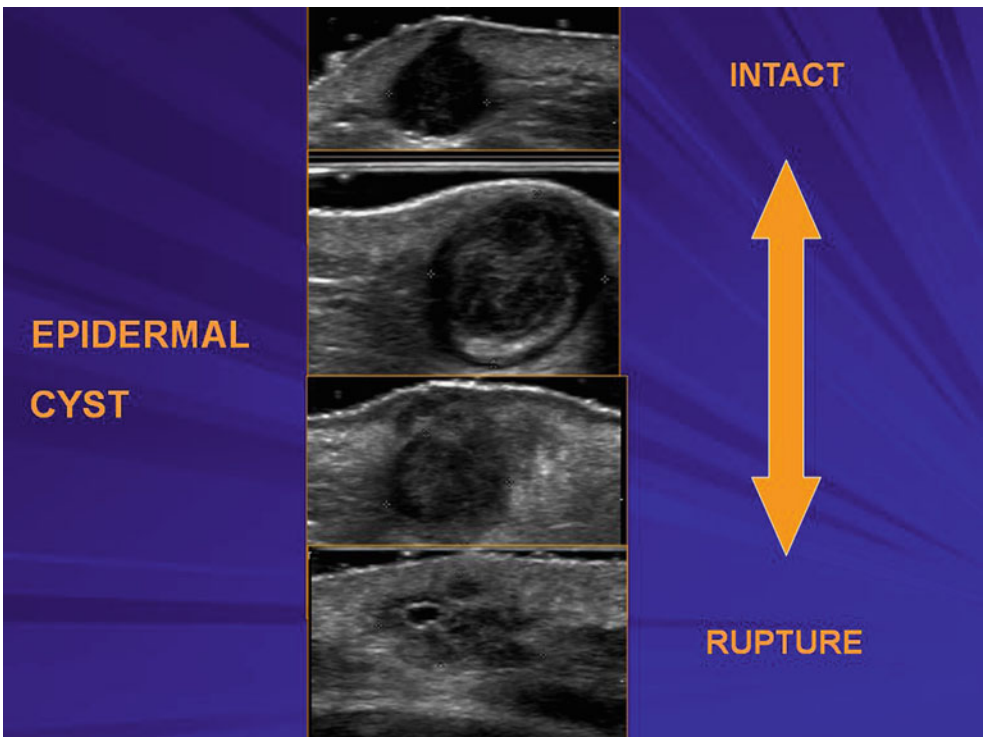

Fig. 5.1 Sonographic patterns of epidermal cysts going from intact (*top*) to total rupture phase (*bottom*). There is inflammation and partial rupture phases in the middle part of the figure. A well-defined round shaped anechoic structure is detected when the cyst is intact. Under inflammation the cyst becomes enlarged and is filled with dense keratin and inflammatory components. When a partial rupture occurs, the keratin is released to the surrounding tissues eliciting a foreign body-like reaction in the vicinity. During the end-stage phase (total rupture), an irregular hypoechoic shape can be seen. In spite of the phase, notice that the posterior acoustic reinforcement is conserved

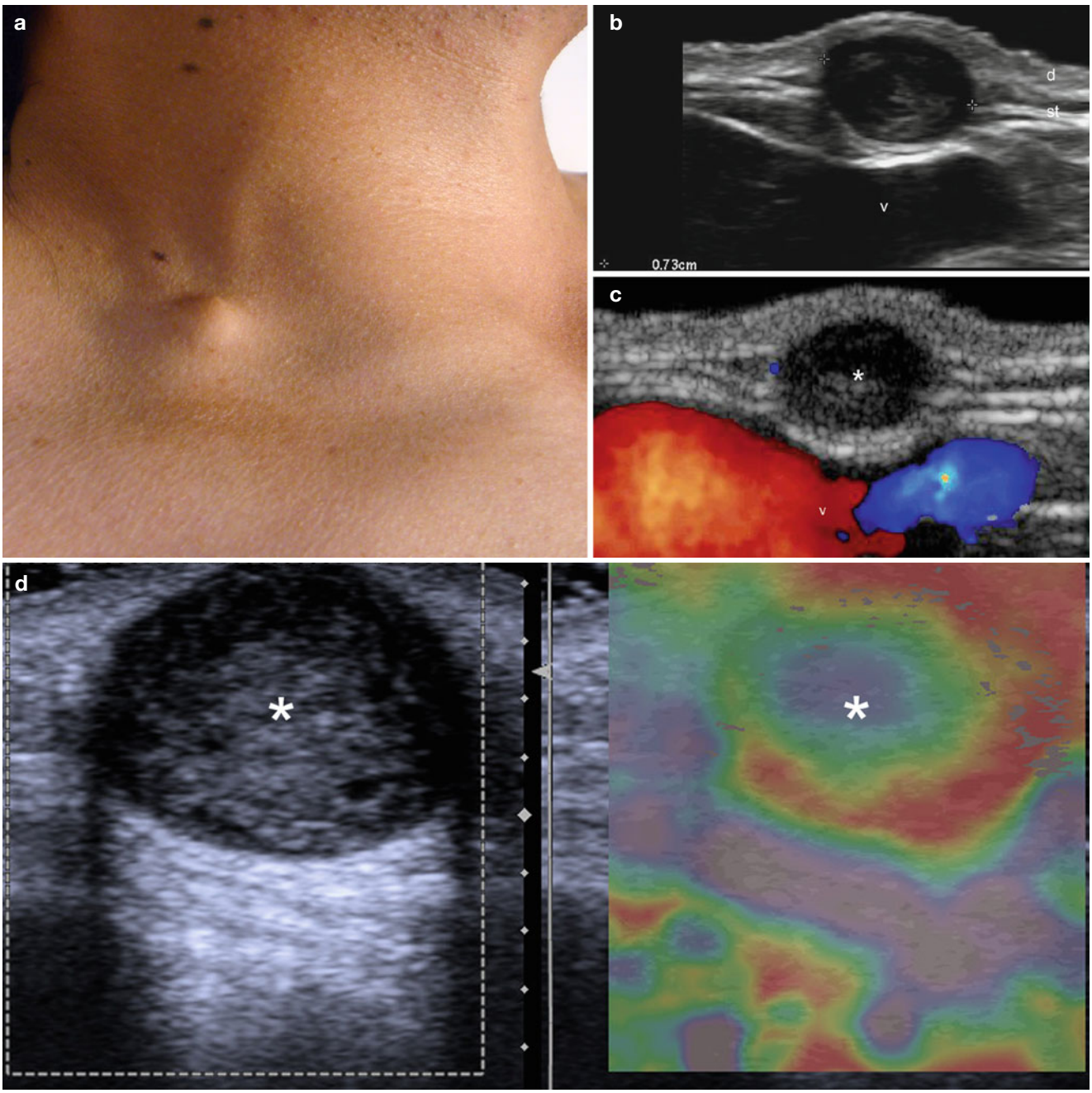

Fig. 5.2 (**a**–**e**) Intact epidermal cyst. (**a**) Clinical image shows a skin-colored bump in the right supraclavicular region. (**b**) Grey scale ultrasound image (transverse view) demonstrates 0.73 cm well-defined round-shaped anechoic structure in the dermis and subcutaneous tissue. The subclavian vein (*v*) runs deep into the cyst. (**c**) Color Doppler ultrasound image (transverse view) shows the avascular nature of the cyst (*) and the flow within the subclavian vein (*colors*). (**d**) Sonoelastography image (transverse, comparative view with grey scale) demonstrates the soft nature of the cyst (*). (**e**) Histology (HE× 20 zoom courtesy of Dr. Laura Carreño) shows a cystic lesion covered by squamous epithelium with a granular layer that contains desquamated keratin. *Abbreviations*: *d* dermis, *st* subcutaneous tissue, *v* subclavian vein

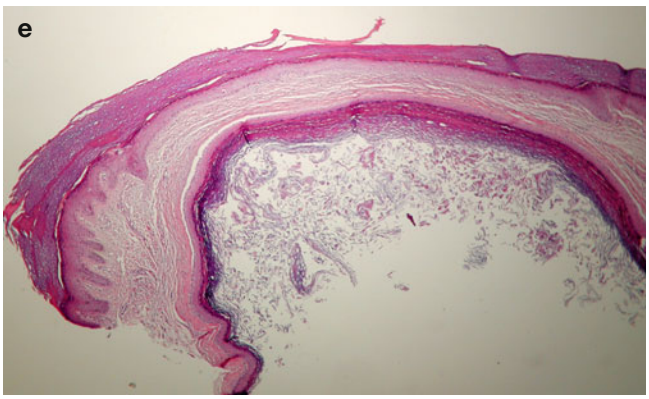

Fig. 5.2 (continued)

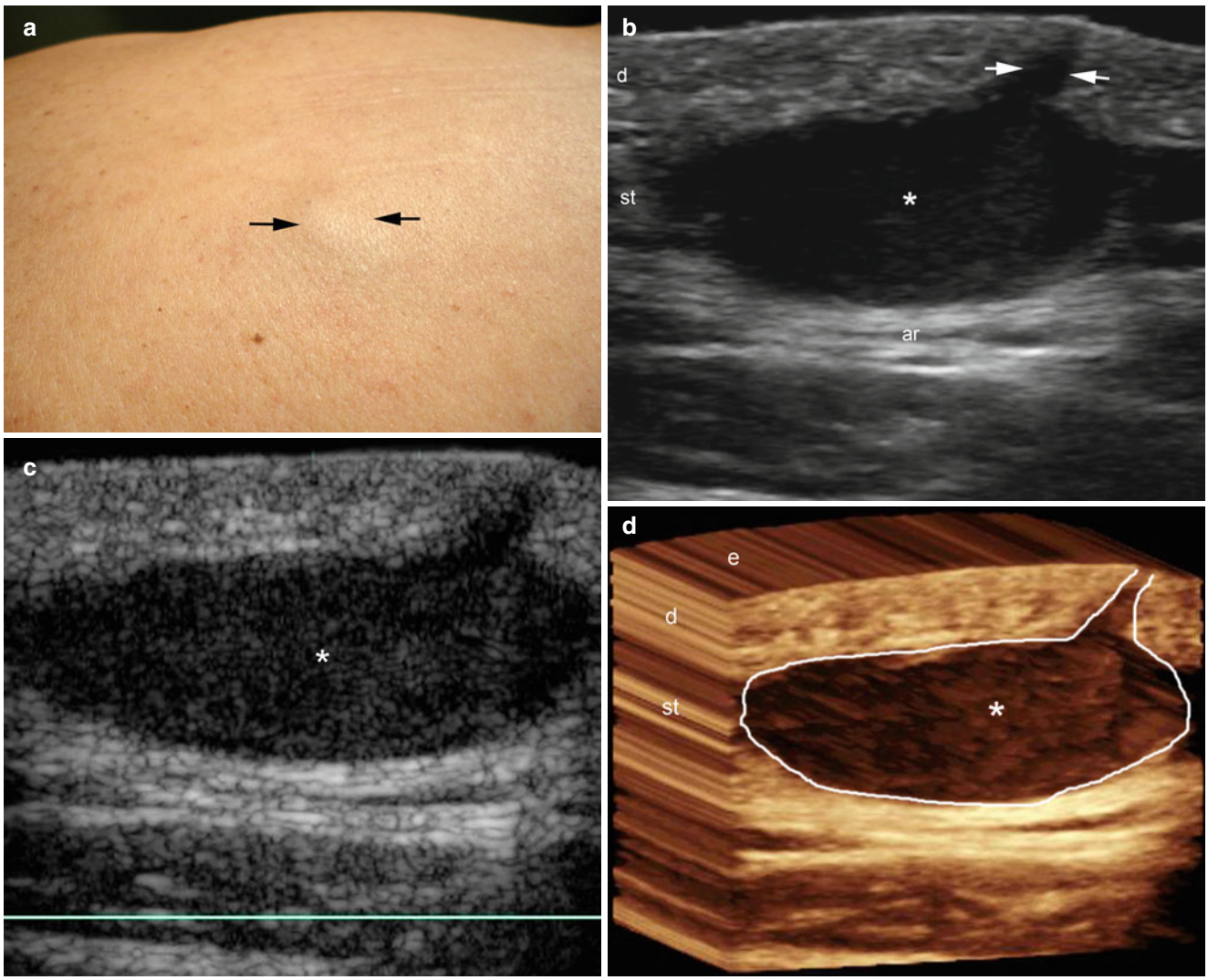

Fig. 5.3 (**a**–**d**) Intact epidermal cyst. (**a**) Clinical lesion shows a skin colored swelling (*arrows*) in the left dorsal region. (**b**) Grey scale ultrasound image (transverse view) demonstrates a well-defined, oval-shaped anechoic structure (*) located in the dermis and subcutaneous tissue. Notice the communicating tract, also called punctum (*arrows*) to the subepidermal zone. (**c**) Color Doppler ultrasound image (transverse view) shows no signs of vascularity in the lesional area. (**d**) 3D reconstruction (transverse view; 5–8 s sweep) of the lesion. *Abbreviations*: *e* epidermis, *d* dermis, *st* subcutaneous tissue

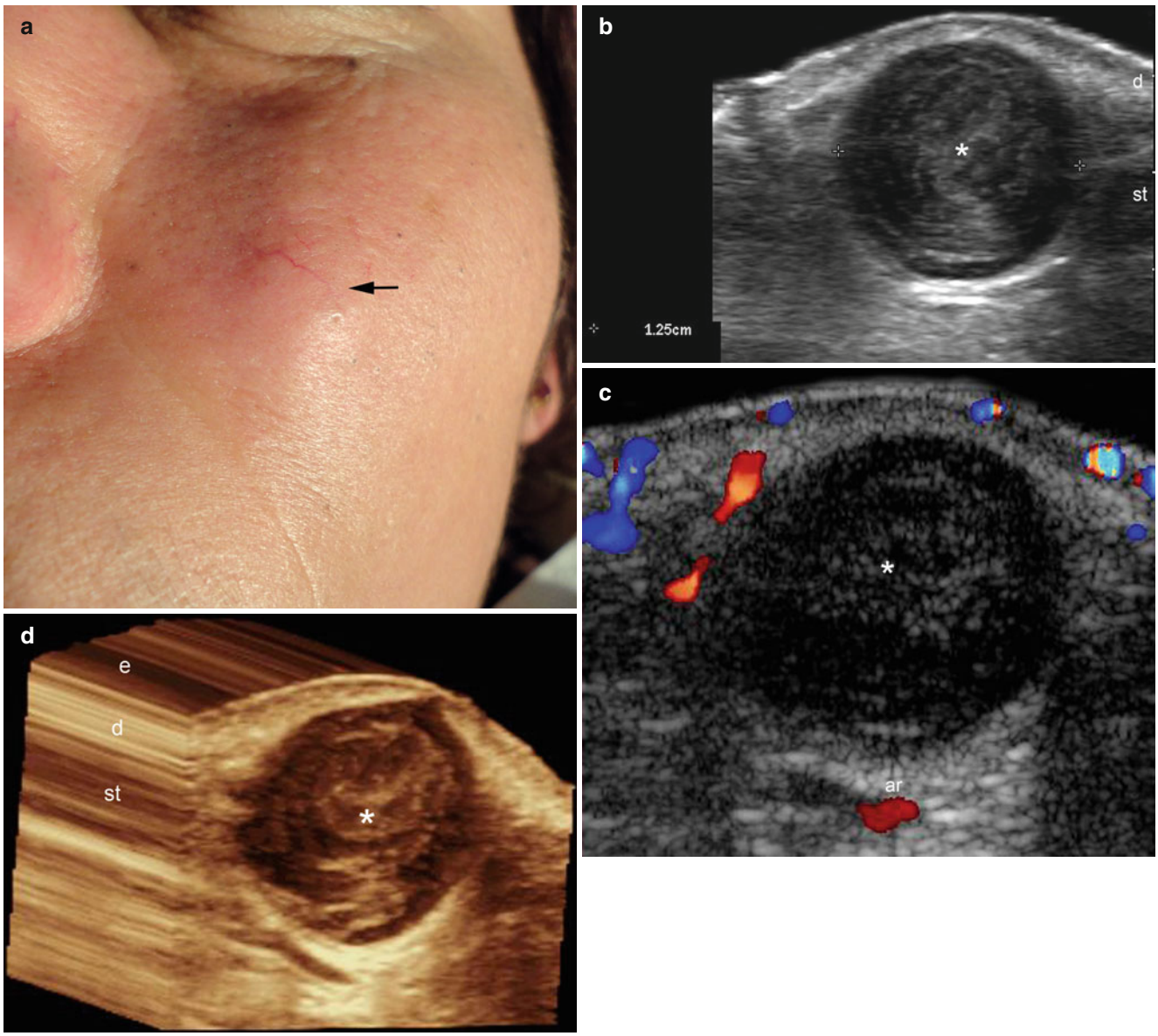

Fig. 5.4 (**a**–**d**) Inflammed epidermal cyst. (**a**) Clinical erythematous swelling in the left cheek. (**b**) Grey scale ultrasound image (transverse view) demonstrates a 1.25 cm well-defined round shaped hypoechoic structure (*) located in dermis and subcutaneous tissue. (**c**) Color Doppler ultrasound image (transverse view) shows increased blood flow in the periphery of the structure (*). Notice the posterior acoustic reinforcement artifact (*ar*), typical of the fluid filled lesions. (**d**) 3D of the lesion (*, transverse view, 5–8 s sweep). *Abbreviations*: *e* epidermis, *d* dermis, *st* subcutaneous tissue

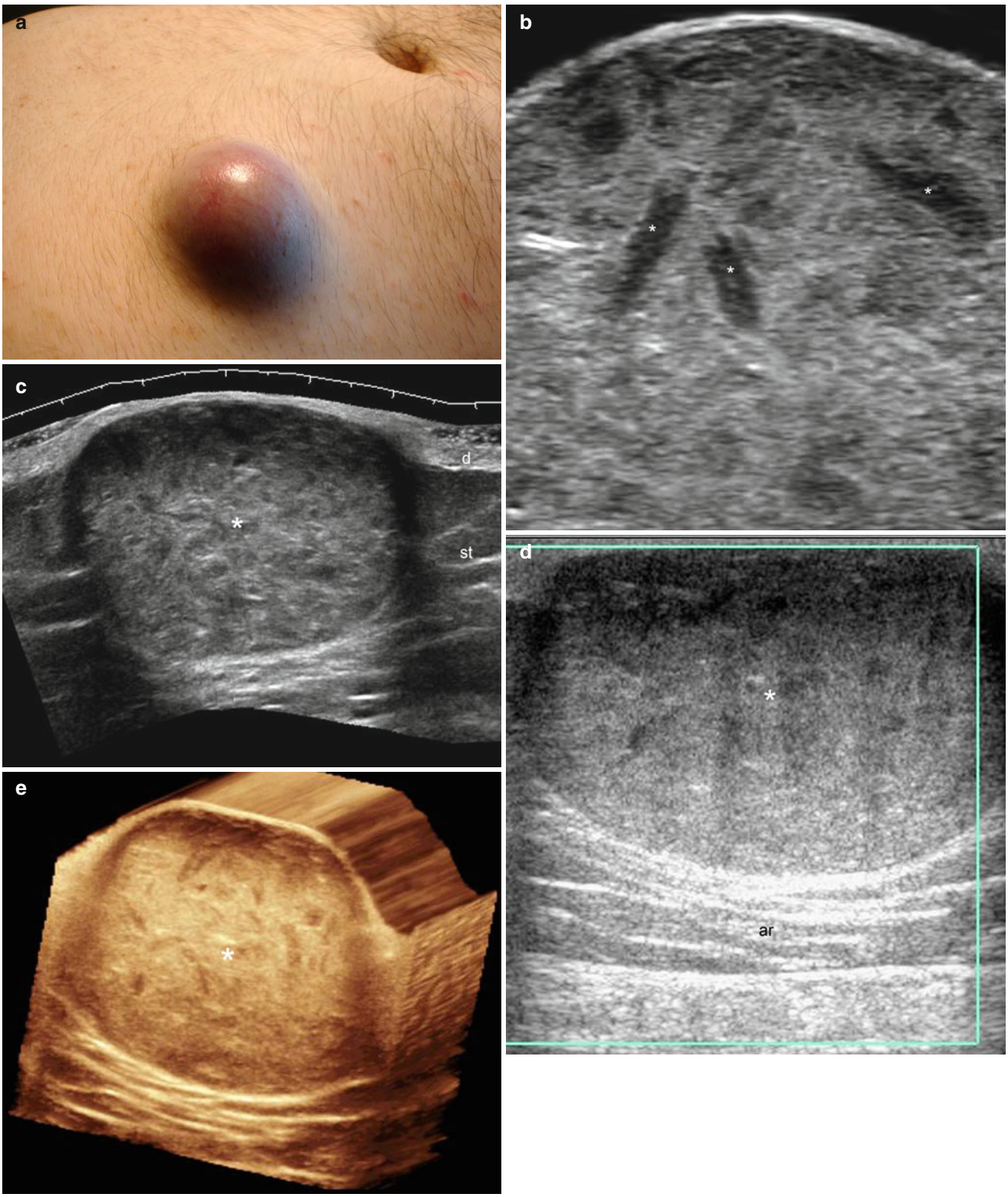

Fig. 5.5 (**a**–**e**) Epidermal cyst with "pseudotestes" appearance. (**a**) Clinical lesion shows an erythematous swelling in the right aspect of the abdominal wall. (**b**) Grey scale ultrasound image (transverse view) demonstrates the upper part of the cyst in the dermis and subcutaneous tissue. There is echoic material that corresponds to compact keratin and some hypoechoic bands (*) that represent cholesterol deposits. (**c**) Grey scale ultrasound image (extended transverse field of view) of the cyst shows a well-defined hypoechoic and heterogeneous dermal and subcutaneous structure (*) that presents some hypoechoic bands. (**d**) Color Doppler ultrasound image (transverse view) demonstrates the hypovascular nature of the lesion. Notice the posterior acoustic reinforcement artifact (*ar*). (**e**) 3D reconstruction of the lesion (*), (transverse view, 5–8 s sweep). *Abbreviations*: *d* dermis, *st* subcutaneous tissue

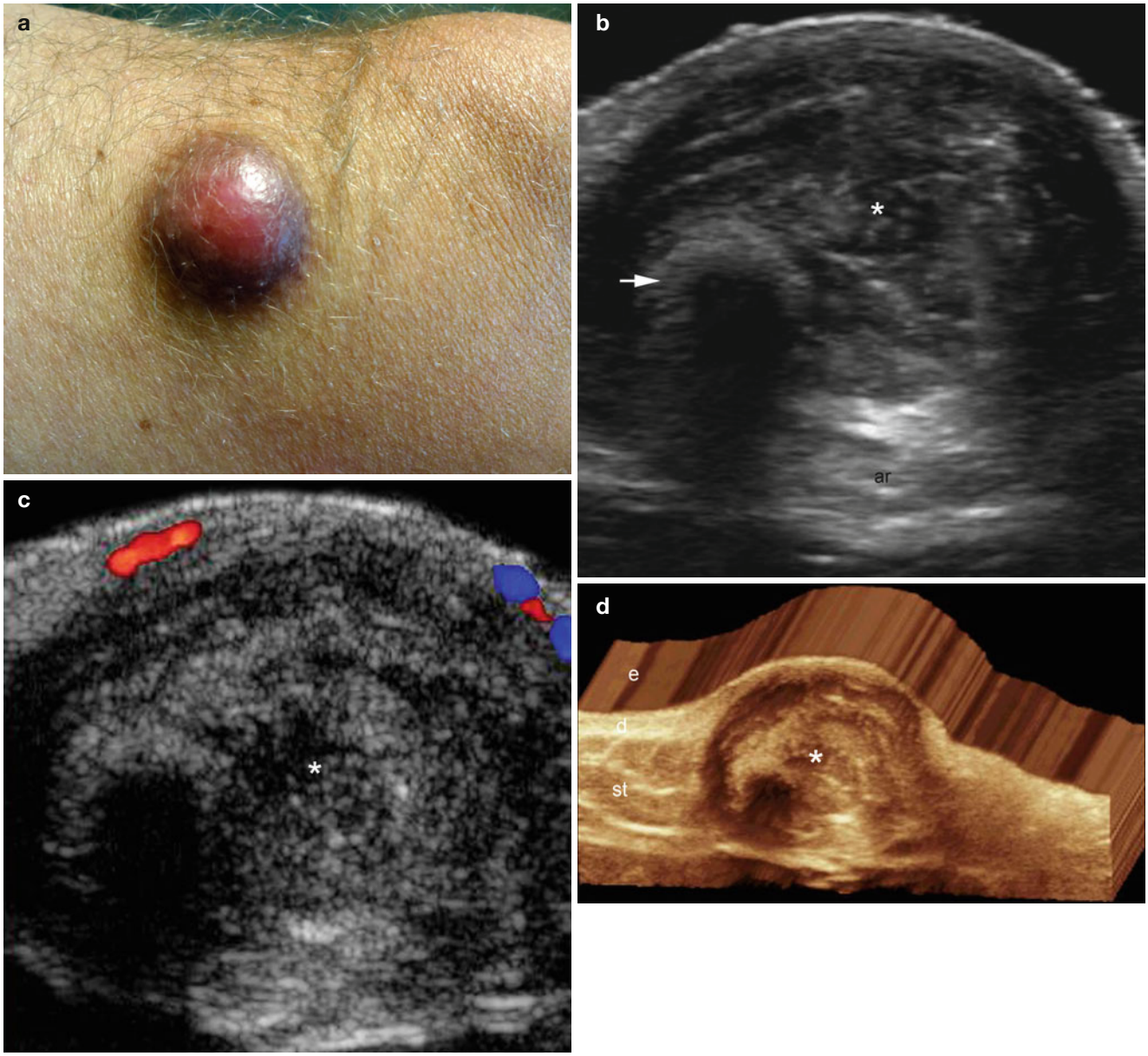

Fig. 5.6 (**a**–**d**) Giant inflammed epidermal cyst. (**a**) Clinical lesion shows an erythematous swelling in the right thigh. (**b**) Grey scale ultrasound image (longitudinal view) demonstrates a well-defined oval shaped hypoechoic structure (*) located in the dermis and subcutaneous tissue. The hyperechoic spot (*arrow*) in the left aspect of the figure corresponds to a calcium deposit within the cyst. Notice the posterior acoustic reinforcement artifact (*ar*). (**c**) Color Doppler ultrasound image (longitudinal view) shows slight hypervascularity in the periphery of the cyst. (**d**) The lesion (*) in 3D (5–8 s longitudinal reconstruction). *Abbreviations*: *e* epidermis, *d* dermis, *st* subcutaneous tissue

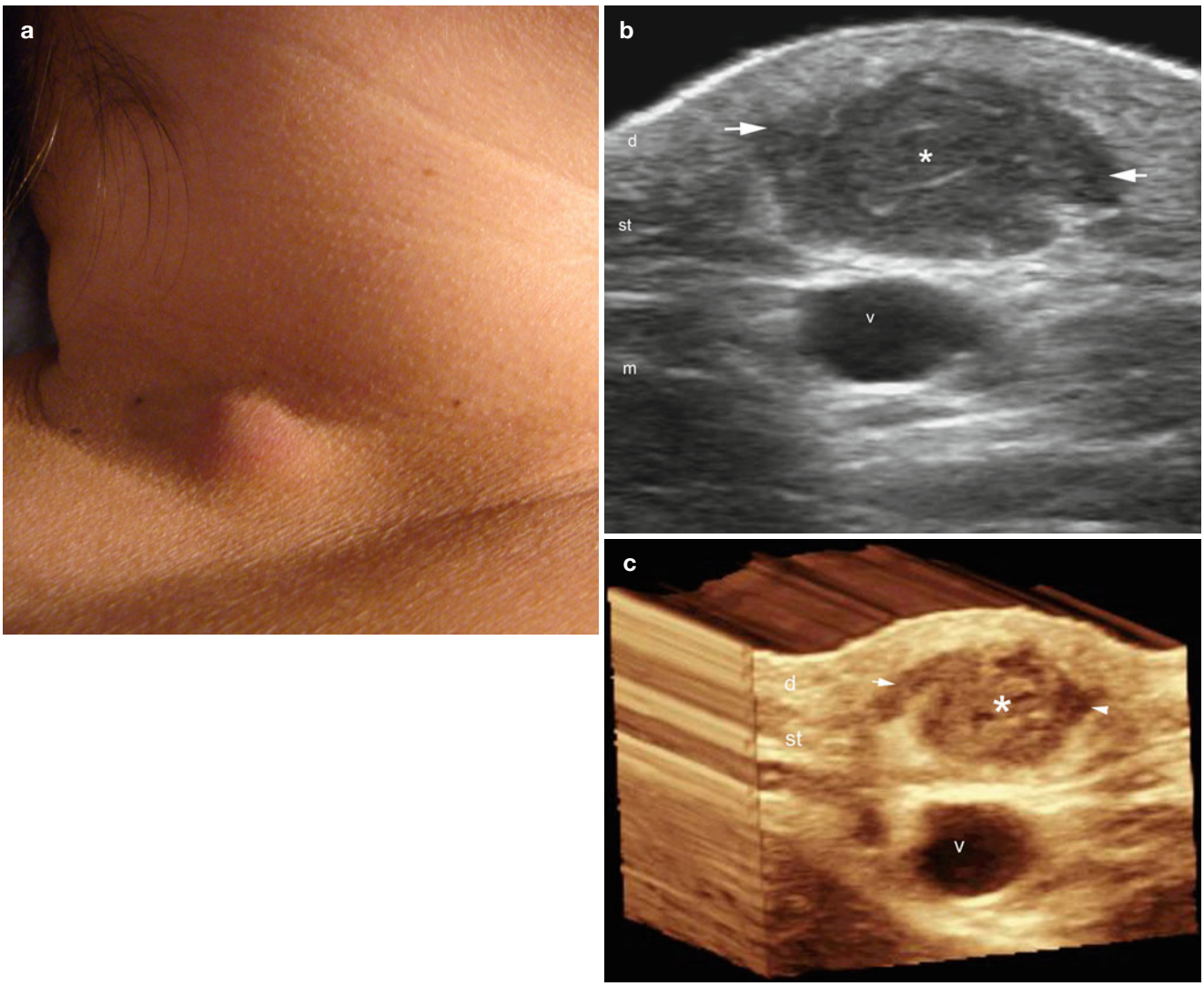

Fig. 5.7 (**a**–**c**) Epidermal cyst with partial rupture. (**a**) Clinical image shows erythematous swelling in the right aspect of the neck. (**b**) Grey scale ultrasound image (transverse view) demonstrates hypoechoic lesion (*) in the dermis and subcutaneous tissue with lobulated and irregular borders (*arrows*) that corresponds to the sites of rupture. The external jugular vein (*v*) is located immediately deep to the cyst. (**c**) The cyst in 3D (5–8 s sweep reconstruction). *Abbreviations*: *d* dermis, *st* subcutaneous tissue, *m* muscle

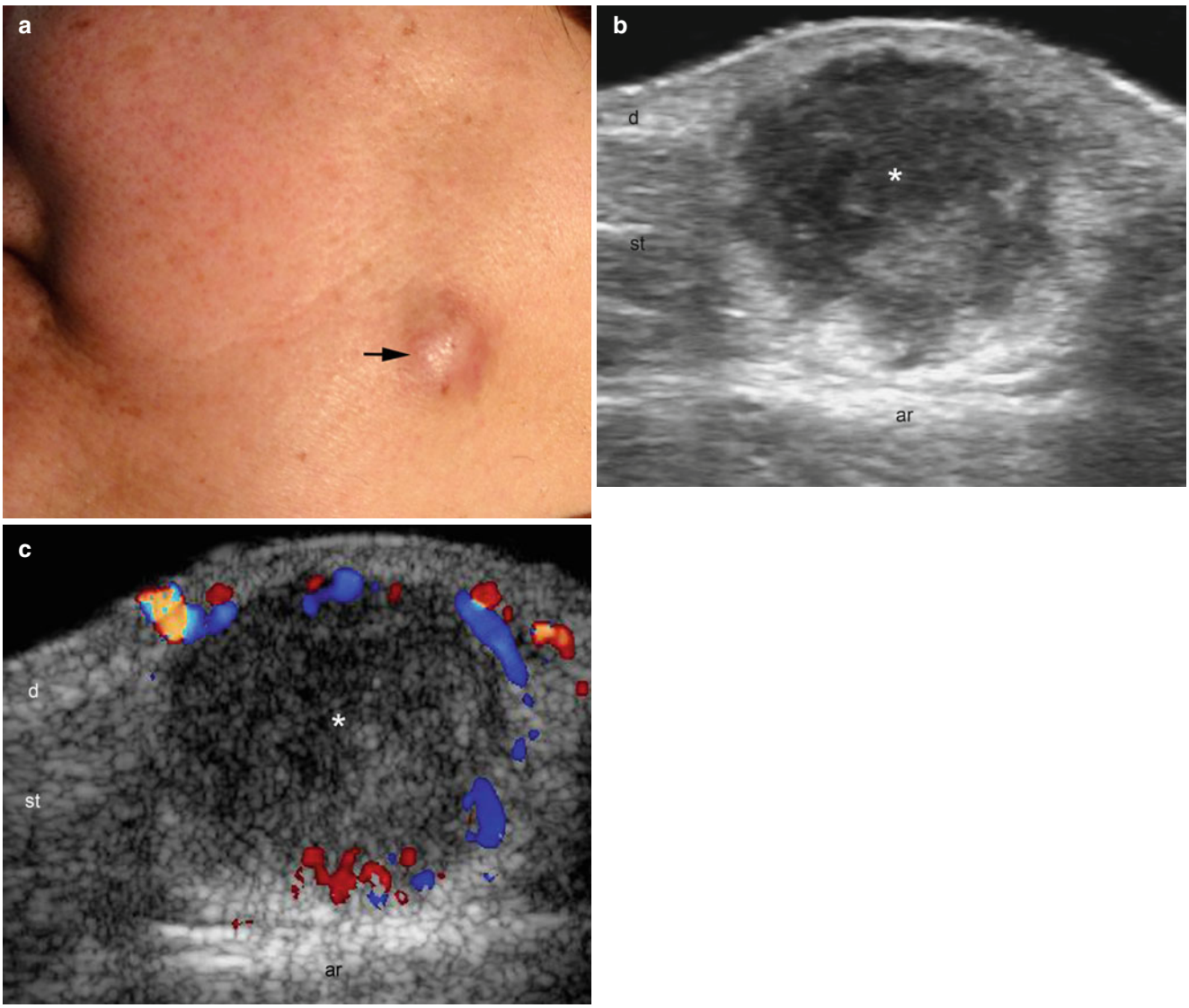

Fig. 5.8 (**a**–**c**) Epidermal cyst with total rupture. (**a**) Clinical lesion shows erythematous swelling (*arrow*) in the left aspect of the cheek. (**b**) Grey scale ultrasound image (transverse view) shows hypoechoic structure (*) with irregular borders located in the dermis and subcutaneous tissue. Notice the posterior acoustic reinforcement artifact (*ar*). (**c**) Color Doppler ultrasound image (transverse view) demonstrates increased vascularity in the periphery of the lesion. *Abbreviations*: *d* dermis, *st* subcutaneous tissue, *ar* posterior acoustic reinforcement

Tip

- Look for the posterior acoustic enhancement when dealing with epidermal cysts.

Pitfall

- Ruptured epidermal cysts can mimic other soft-tissue tumors because they can present irregular borders. Use the tip previously commented on and search for the connecting tract (punctum) to the subepidermal region.

5.2.1.2 Steatocystoma Multiplex

Steatocystoma multiplex (SM) is an uncommon disorder of the pilosebaceous unit characterized by the development of sebaceous dermal cysts, commonly multiple. SMs are lined by stratified squamous epithelium, and flattened sebaceous gland cells are identified in the cystic walls. SMs may present variable sizes and are usually located in the axilla, upper limbs, neck, and torso. Rarely can they be found in the scalp. They may drain thick material to the epidermal surface through a thin connection. When multiple lesions are detected, it indicates that autosomic dominant inheritance could be present. On sonography, most SMs present as round or oval-shaped, hypoechoic or anechoic cystic structures located in the dermis and subcutaneous tissue with well-defined or lobulated borders and posterior acoustic enhancement [6–8]. Calcium deposits, septa, and loculations can also be detected (Fig. 5.9).

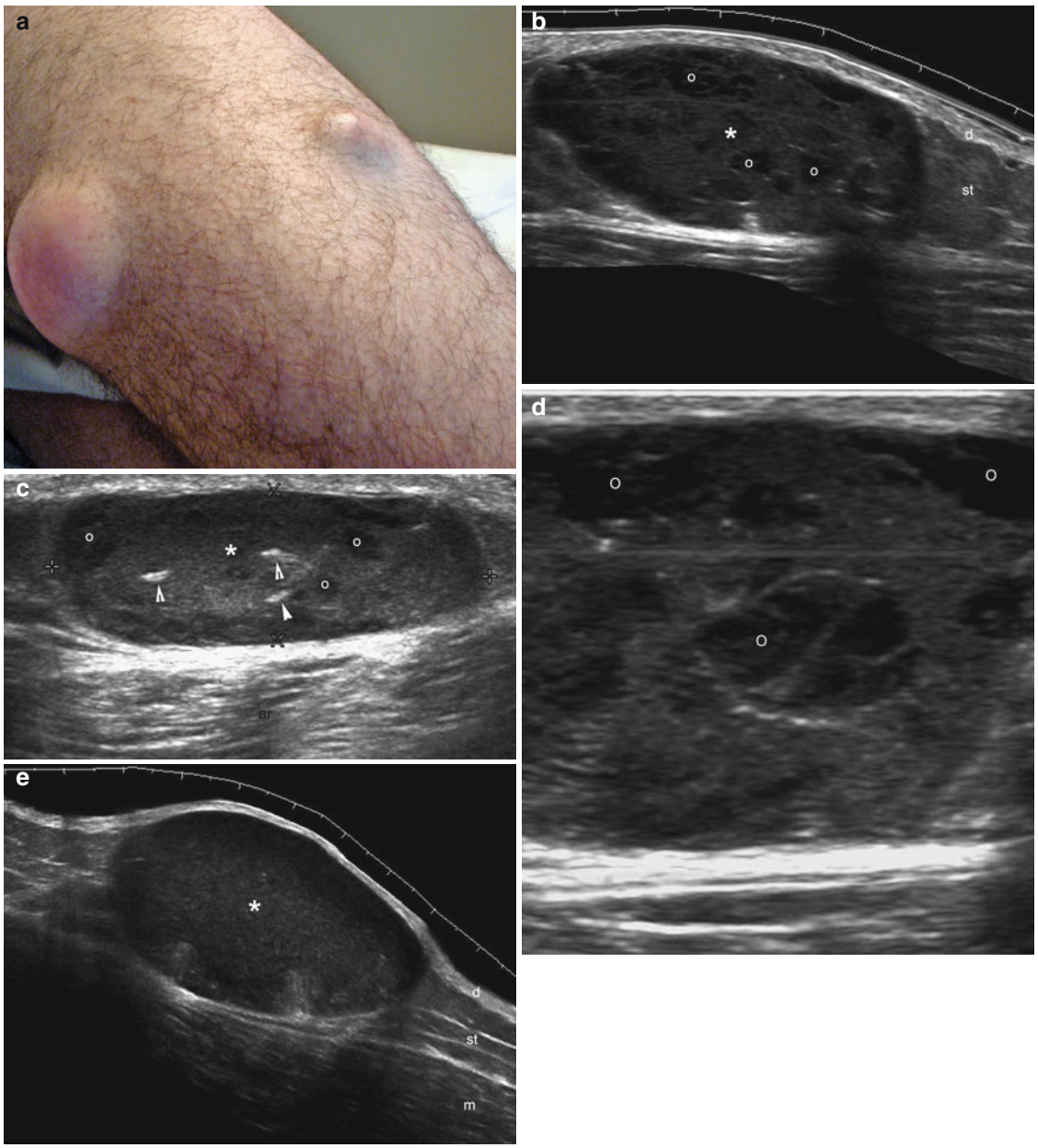

Fig. 5.9 (**a**–**g**) Steatocystoma multiplex Appearances. (**a**) Clinical image shows two erythematous lumps in the left leg. (**b**–**d**) Grey scale ultrasound images (**b** and **c** longitudinal views and **d** superficial zoom view) demonstrates well-defined oval-shaped hypoechoic structures (*) in the subcutaneous tissue. There are oval and round shaped anechoic areas (*) within the cysts, some of them presenting septa or loculations. Notice the tiny hyperechoic bands (arrowheads) and the posterior acoustic reinforcement artifact (*ar*) in figure (c). (**e**) Other steatocystoma multiplex in the same patient shows a well-defined, oval-shaped hypoechoic appearance. (**f**) In the same patient a different steatocystoma multiplex lesion demonstrates a hypoechoic and lobulated structure. The hyperechoic band in the right side of the image corresponds to a calcium deposit. (**g**) Histology (HE× 20 zoom, courtesy of Dr. Claudia Morales). Unilocular cystic lesion lined by squamous epithelium with a corrugated eosinophilic cuticle and without a granular layer. *Abbreviations*: *d* dermis, *st* subcutaneous tissue, *ar* acoustic reinforcement

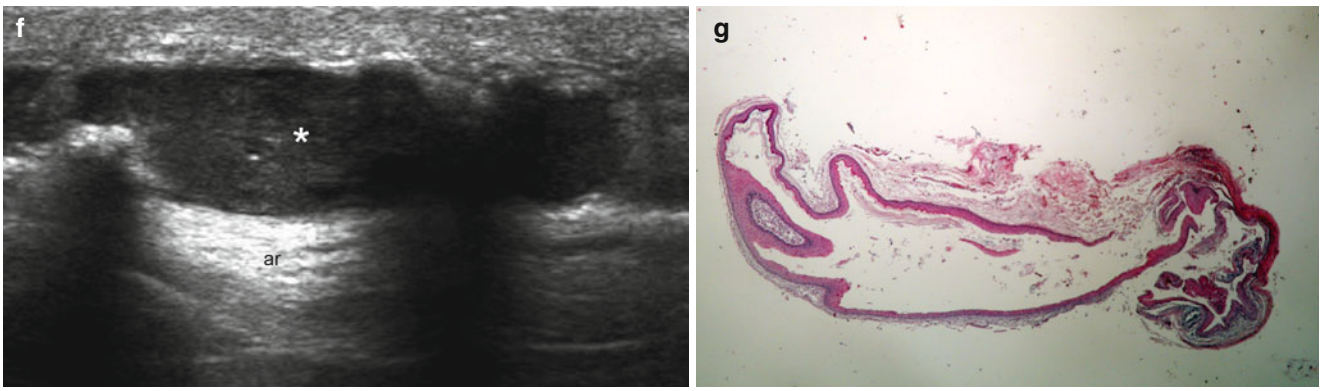

Fig. 5.9 (continued)

5.2.1.3 Trichilemmal Cyst

Also called pilar cysts, trichilemmal cysts are derived from the external sheath of the hair follicle and their most common location is the scalp. They are lined with cuboidal epidermal cells and in contrast to epidermal cysts, they do not contain a granular layer. Content is amorphous or compacted keratinous with oily material sometimes prone to calcification. Presentation could be single or multiple palpable nodules, that in the scalp region can be associated to localized baldness. They do not usually show communicating tracts (punctum) to the epidermal surface. When these cysts show a non-scalp location, recent rapid growth, or size greater than 5 cm, a malignant or proliferative transformation should be ruled out [9]. On sonography, they usually present as anechoic or hypoechoic cystic structures in the dermis and subcutaneous tissue that contain inner echoes or debris. Hyperechoic spots or linear deposits within the cyst that correspond to calcium and/or compacted hair tracts deposits can be detected and these calcifications have also been reported by other imaging modalities such as computed tomography [10] (Figs. 5.10, 5.11, and 5.12).

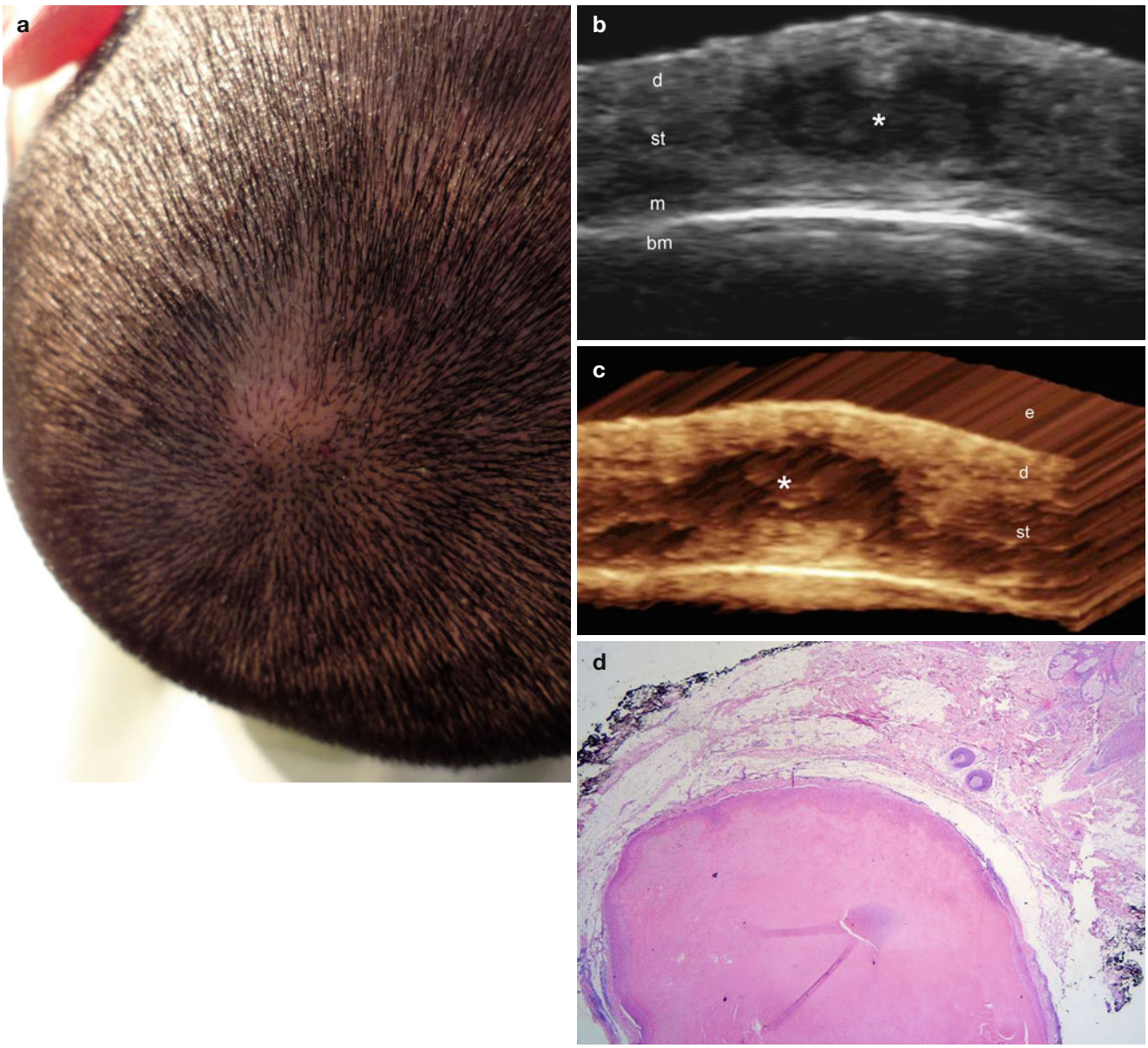

Fig. 5.10 (**a**–**d**) Trichilemmal cyst. (**a**) Clinical image shows a focal hair loss in the scalp. (**b**) Grey scale ultrasound image (transverse view) demonstrates a well-defined, oval-shaped, anechoic structure in the subcutaneous tissue that bulges into the dermis. (**c**) The lesion (*) in 3D (5–8 s sweep reconstruction, transverse view). (**d**) Histology (HE× 20 zoom, courtesy of Dr. Laura Carreño): unilocular cyst covered by squamous epithelium that shows abrupt keratinization without a granular layer. *Abbreviations*: *e* epidermis, *d* dermis, *st* subcutaneous tissue, *m* epicranius muscle, *bm* bony margin of the skull

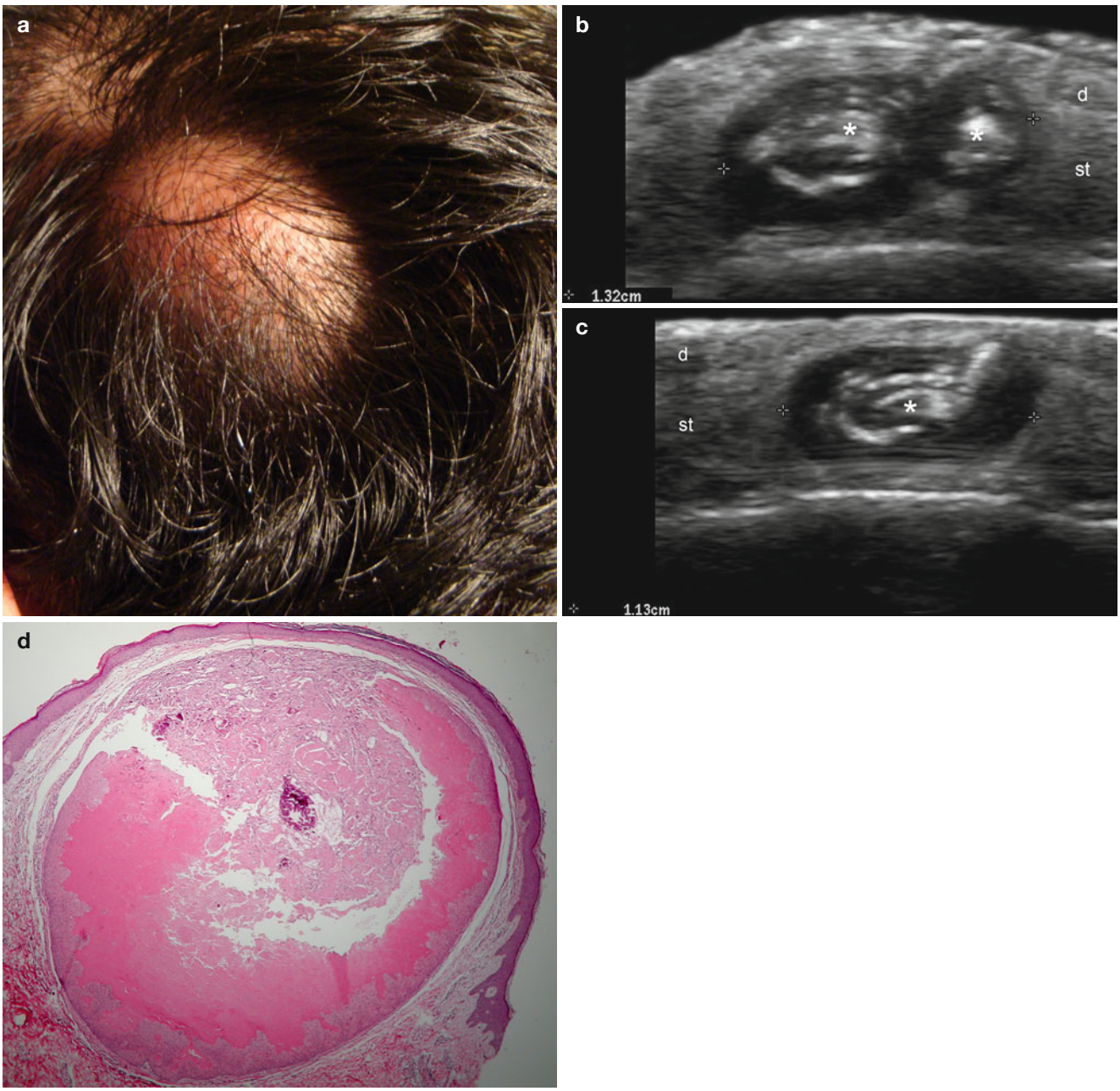

Fig. 5.11 (**a**–**d**) Trichilemmal cyst. (**a**) Clinical image shows focal alopecia and swelling in the scalp. (**b**) Grey scale ultrasound image (transverse view) demonstrates two adjacent well-defined oval and round-shaped structures (*). These lesions present an hypoechoic rim and hyperechoic center with linear disposition. (**c**) Grey scale ultrasound image (longitudinal view) of the smallest size cyst demonstrates a 1.13 cm oval-shaped lesion in the subcutaneous tissue with similar echogenicity patterns. (**d**) Histology (HE 20× zoom, courtesy of Dr. Laura Carreño): unilocular cyst lined by squamous epithelium with abrupt keratinization and a central calcium deposit. No granular layer is detected. *Abbreviations*: *d* dermis, *st* subcutaneous tissue

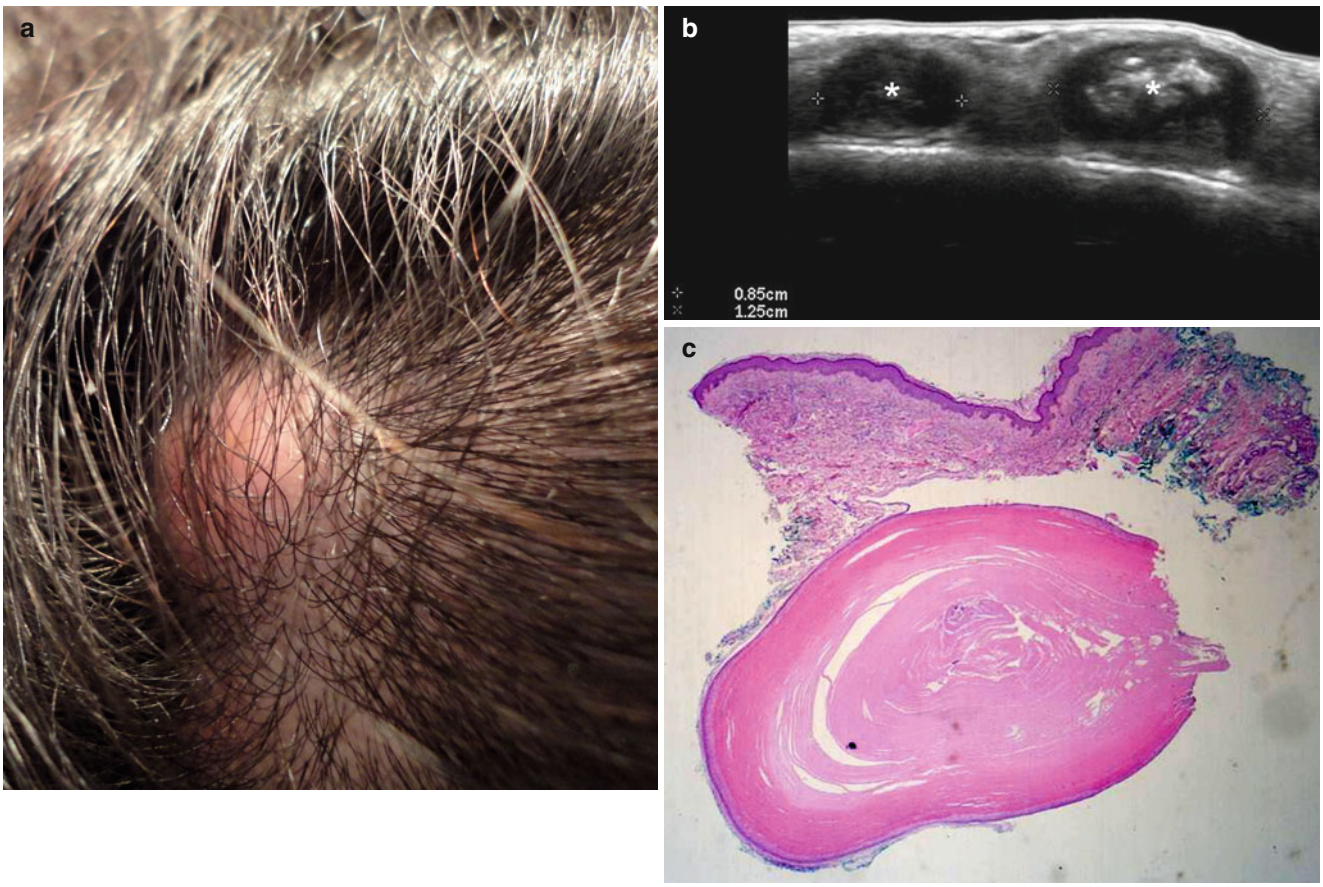

Fig. 5.12 (**a**–**c**) Sonographic appearance of trichilemmal cysts. (**a**) Clinical image shows focal alopecia and erythematous swelling in the scalp. (**b**) Grey scale ultrasound image (transverse view) demonstrates two adjacent oval-shaped structures (*) in the subcutaneous tissue. There is a 0.85 cm homogeneous hypoechoic cyst in the left side of the figure. A 1.25 cm mixed echogenicity cyst with hypoechoic rim and hyperechoic center that corresponds to calcium deposits and some hair tract fragments is detected in the right side of the figure. (**c**) Histology (HE× 20 zoom courtesy of Dr. Claudia Morales): unilocular cyst covered by squamous epithelium without a granular layer. There is also abrupt keratinization

Tip

- Trichilemmal cysts are commonly located on the scalp. Think about them when you deal with a cystic lesion in that location.

Pitfalls

- Trichilemmal cysts can present dystrophic calcifications and compacted hair tracts that can show a central hyperechoic linear pattern which may simulate other tumors such as pilomatrixomas, especially when thick hypoechoic fluid, usually as a result of packed keratin, is present within the cyst.
- It is important to remember to look for the posterior acoustic enhancement artifact typical of cystic structures and to check the appearance of the center of the lesion in cases with hyperechogenicity that is usually more linear on trichilemmal cysts and spot-like in pilomatrixomas.

5.2.1.4 Dermoid Cyst

Dermoid cysts (DCs) are composed of remnants of cutaneous tissues along the embryonal lines of closure. Clinically, they present as single non-tender swelling on the lateral aspect of the upper eyelid or eyebrow region. Other less common locations include the midline of the neck, nasal root, forehead, mastoid area, scalp, and torso. DCs are commonly seen in children or young adults. Histologically, DCs present with stratified squamous epithelium with hair follicles and sebaceous glands. Eccrine sweat glands and apocrine glands may also be present. Smooth muscle is a common finding but in contrast to benign cystic teratoma, cartilage and bone are not usually present. On sonography, DCs show as anechoic round or oval-shaped cystic structures located in the dermis and subcutaneous tissue that occasionally may present as echoes or debris. DCs can have thin or thick walls, and occasionally hyperechoic lines in the periphery of the cysts can also be seen because of hair tracts fragments. Septa or calcifications are uncommon in these types of cysts, and DCs show no signs of vascularity within the lesions on color Doppler ultrasound [11–14]. Scalloping of the underlying bony margin may also be found (Figs. 5.13, 5.14, and 5.15).

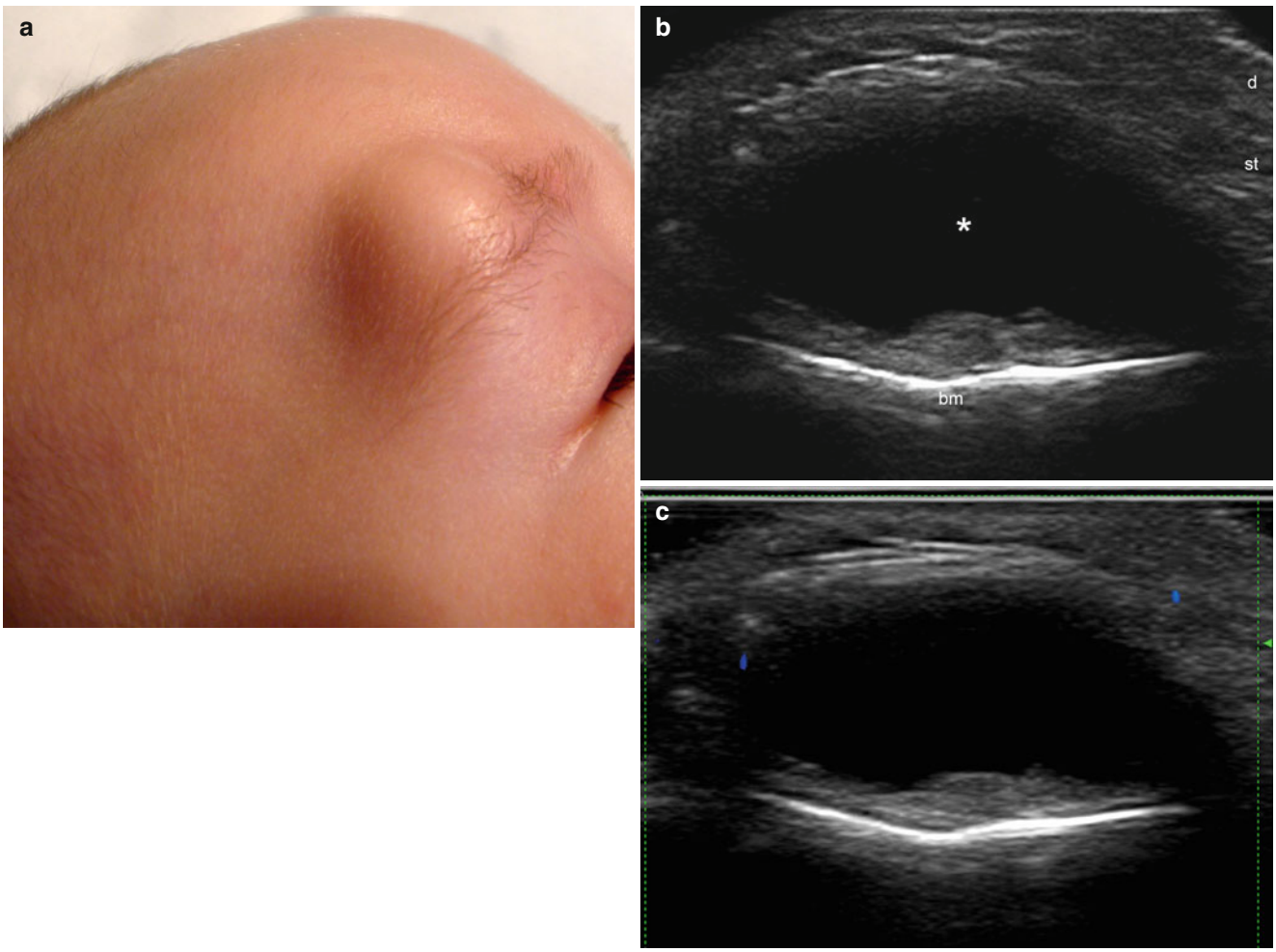

Fig. 5.13 (**a**–**c**) Dermoid cyst. (**a**) Clinical image shows a skin-colored swelling in the right eyebrow. (**b**) Grey scale ultrasound image (transverse view) demonstrates a well-defined, oval-shaped anechoic structure with a thick hypoechoic posterior wall located in the deep subcutaneous tissue. Additionally, posterior acoustic reinforcement artifact and scalloping of the margin of the frontal bone are detected. (**c**) Color Doppler ultrasound image (transverse view) shows lack of vascularity within the cyst

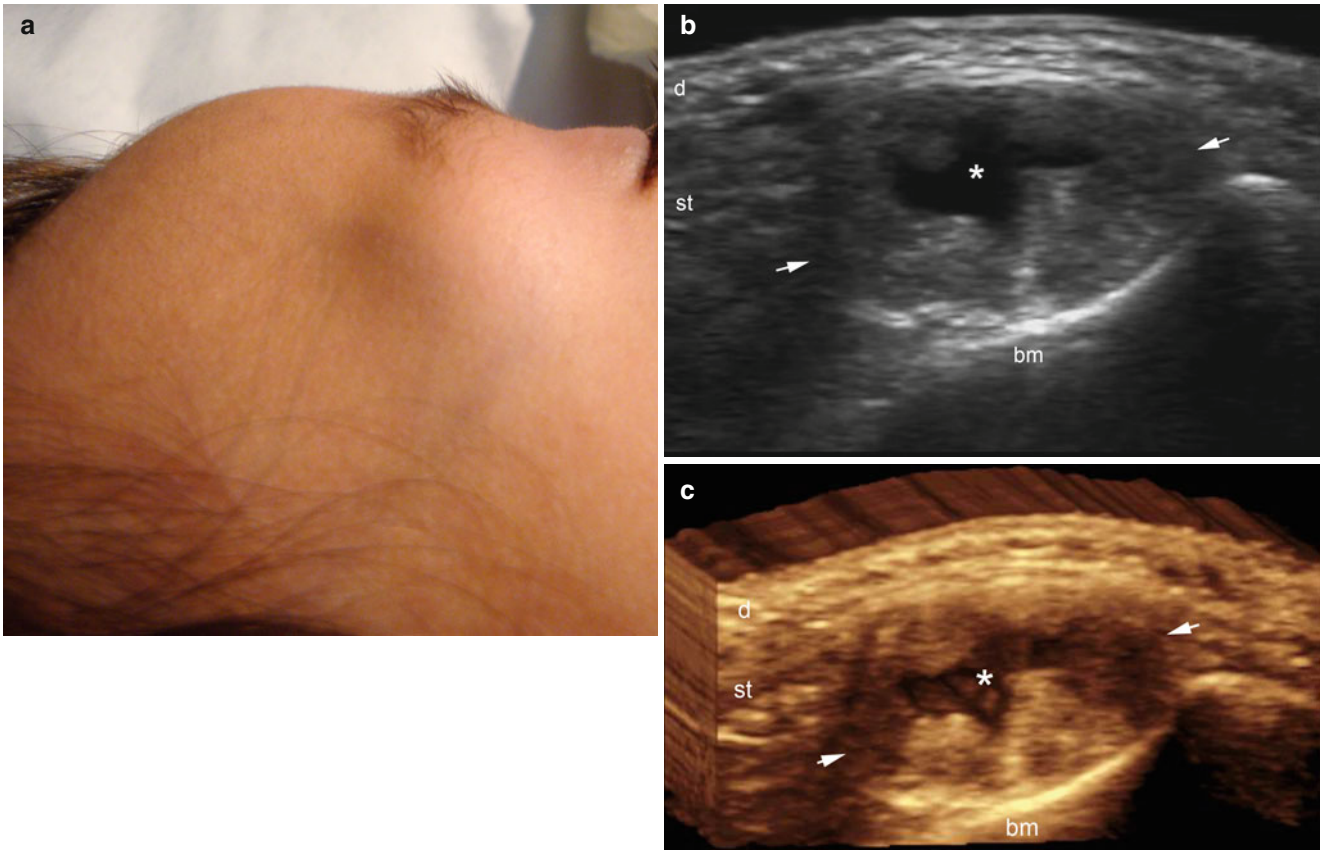

Fig. 5.14 (**a**–**c**) Dermoid cyst. (**a**) Clinical image shows a skin-colored lump in the external region of the right eyebrow. (**b**) Grey scale ultrasound image (transverse view) demonstrates a well-defined, anechoic structure (*) with thick hypoechoic walls (*arrows*) located in the subcutaneous tissue. There are posterior acoustic reinforcement and scalloping of the bony margin. (**c**) The lesion in 3D (5–8 s sweep reconstruction in transverse view). *Abbreviations*: *d* dermis, *st* subcutaneous tissue, *bm* bony margin

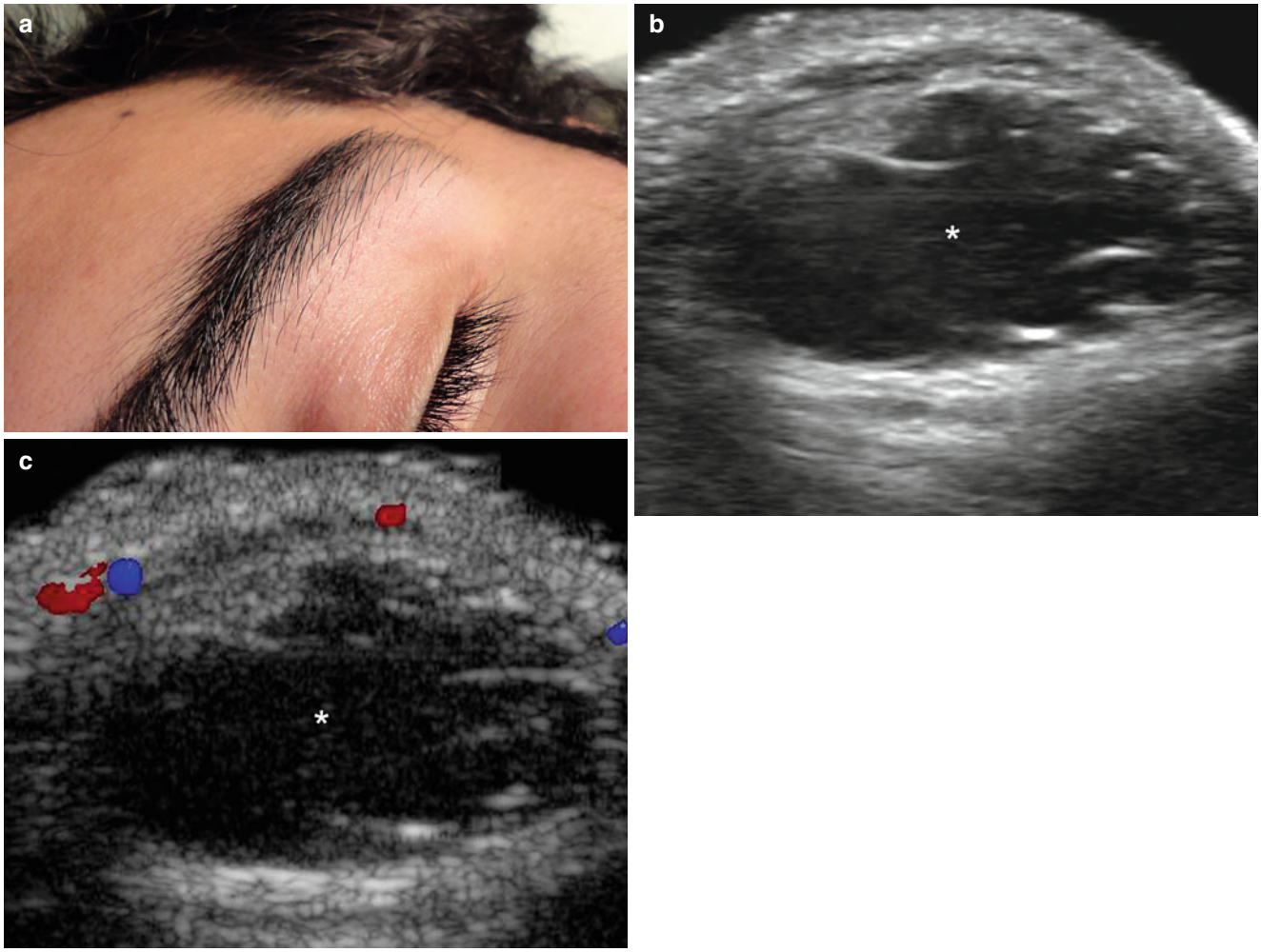

Fig. 5.15 (**a**–**c**) Dermoid cyst. (**a**) Clinical photograph shows a skin colored swelling in the external border of the left eyebrow. (**b**) Grey scale ultrasound image (transverse view) demonstrates a well-defined oval-shaped anechoic structure (*) located in the subcutaneous tissue. Hyperechoic lines are detected in the periphery of the cyst that corresponds to hair tract fragments. A posterior acoustic reinforcement artifact is also detected (**c**) Color Doppler ultrasound image (transverse view) shows some vessels in the periphery of the cyst and lack of blood flow within the cystic structure (*)

Tip

- The upper eyelid or eyebrow regions are frequent anatomical locations for dermoid cysts. It is important to remember that!

5.2.1.5 Pilonidal Cyst

Pilonidal cysts, also called pilonidal sinus or "jeep disease", are composed of pseudocystic structures that contain a nest of hair tracts and keratin. These cysts are commonly founded in the intergluteal region and originate by the patient`s own hair penetrating the skin directly or via dilated follicular ostia. Among the most common risk factors are chronic regional trauma with continuous friction movements and/or patients that present excessive body hair, obesity, and sweating or occupations requiring sitting. The most frequent location is the sacrococcygeal region and usually affects young male adults. Commonly, pilonidal cysts become inflamed and turn into recurrent pilonidal abscesses. On sonography, pilonidal cysts present as oval-shaped anechoic or hypoechoic sinus structures in the dermis and subcutaneous tissue that contain hyperechoic lines that correspond to the hair tracts. Hypoechoic bands connecting to the base of the regional hair follicles and the presence of hypoechoic branches of cyst may also be detected. On color Doppler ultrasound, hypervascularity can be found in the periphery of the cysts. Sonography can detect the axes of the cysts and their branches allowing the improvement of the surgical planning, the cosmetic prognosis, and a potential decrease of the recurrences [15, 16] (Figs. 5.16, 5.17, and 5.18).

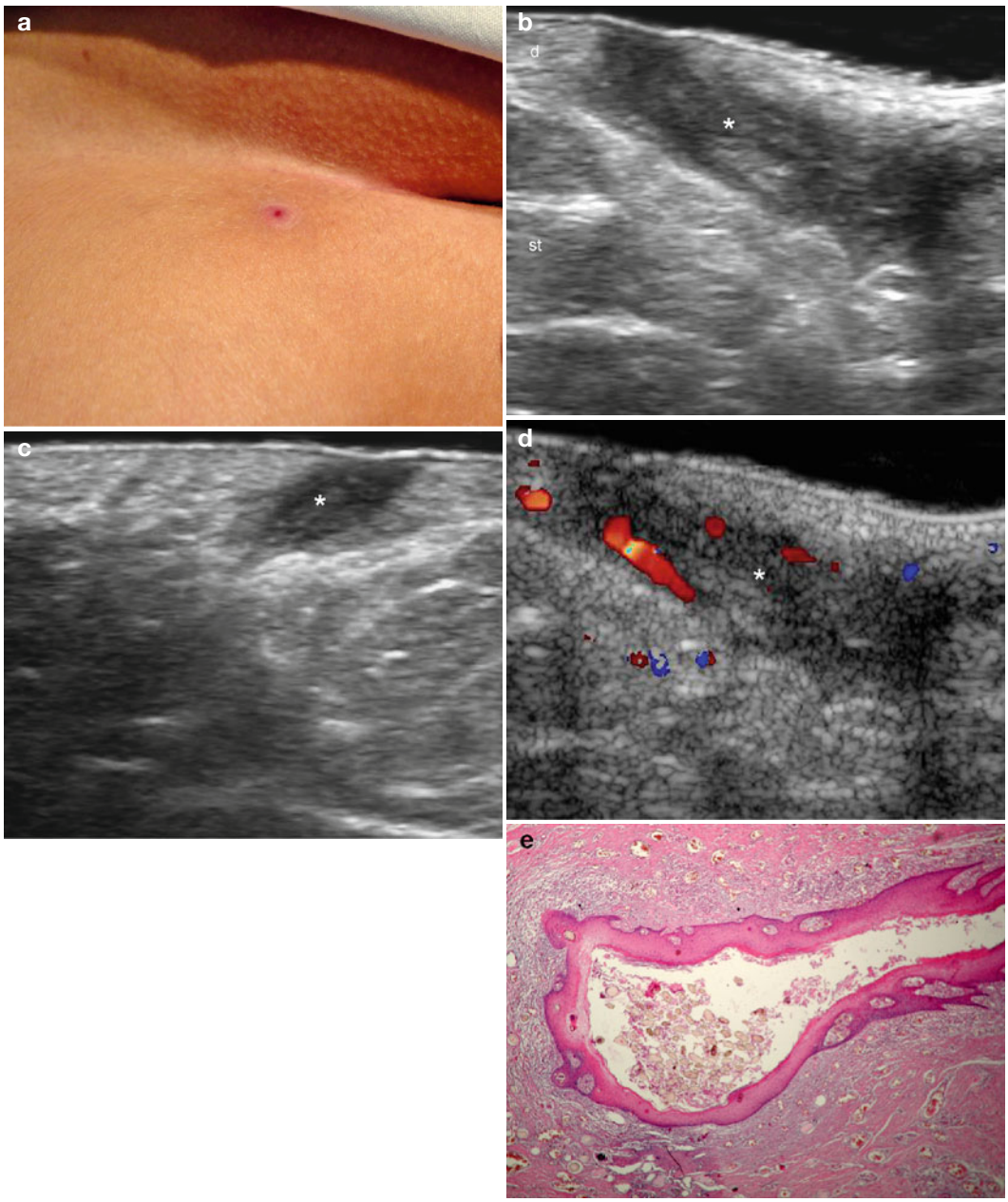

Fig. 5.16 (**a**–**e**) Pilonidal cyst. (**a**) Clinical erythematous lesion in the intergluteal region. (**b**) Grey scale ultrasound image (longitudinal view) demonstrates hypoechoic sinus (*) that runs through the dermis and upper subcutaneous tissue. (**c**) Grey scale image (transverse view) of the cyst (*). (**d**) Color Doppler ultrasound image (longitudinal view) shows increased blood flow in the periphery of the lesion. (**e**) Histology (HE 20× zoom, courtesy of Dr. Laura Carreño): Cyst lined by mature squamous epithelium and containing fragments of hair tracts

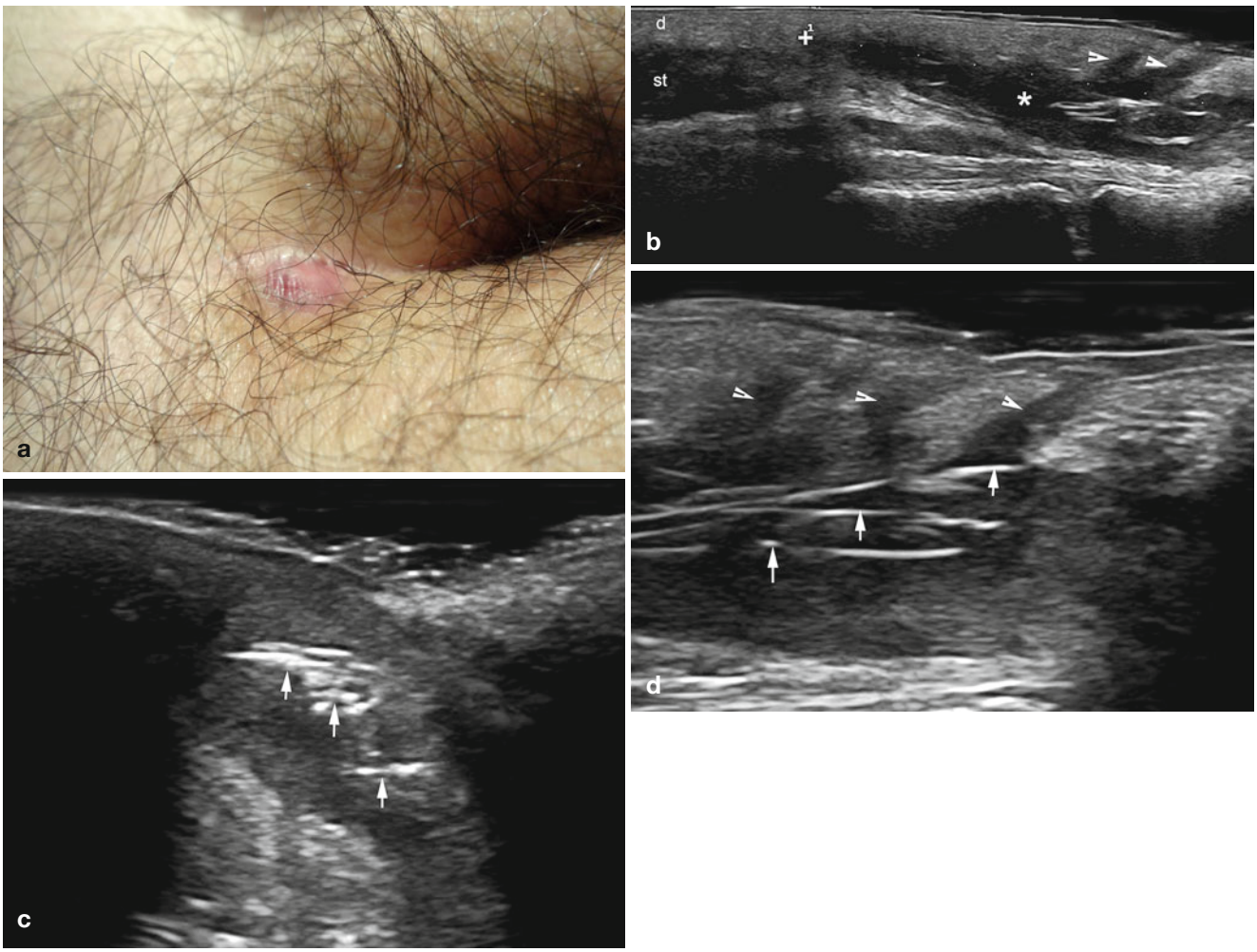

Fig. 5.17 (**a**–**e**) Pilonidal cyst. (**a**) Clinical image shows erythematous swelling in the intergluteal region. (**b**) Grey scale ultrasound image (longitudinal view) demonstrates a well-defined oval-shaped anechoic-hypoechoic structure in the dermis and upper subcutaneous tissue. There are hyperechoic lines that correspond to fragments of hair tracts. Notice the hypoechoic branches of the cyst that communicate with the base of the hair follicles (*arrowheads*). (**c**) Grey scale ultrasound image (zoom, transverse view) shows a hypoechoic sinus with hyperechoic lines (*arrows*) that represent the hair tract fragments. (**d**) Grey scale ultrasound image (zoom, longitudinal view) demonstrating the connecting hypoechoic branches (*, *arrowheads*) to the base of the hair follicles and the hyperechoic hair tracts (*arrows*) within the cyst. (**e**) Grey scale longitudinal serial reconstruction of the cyst in the different parts

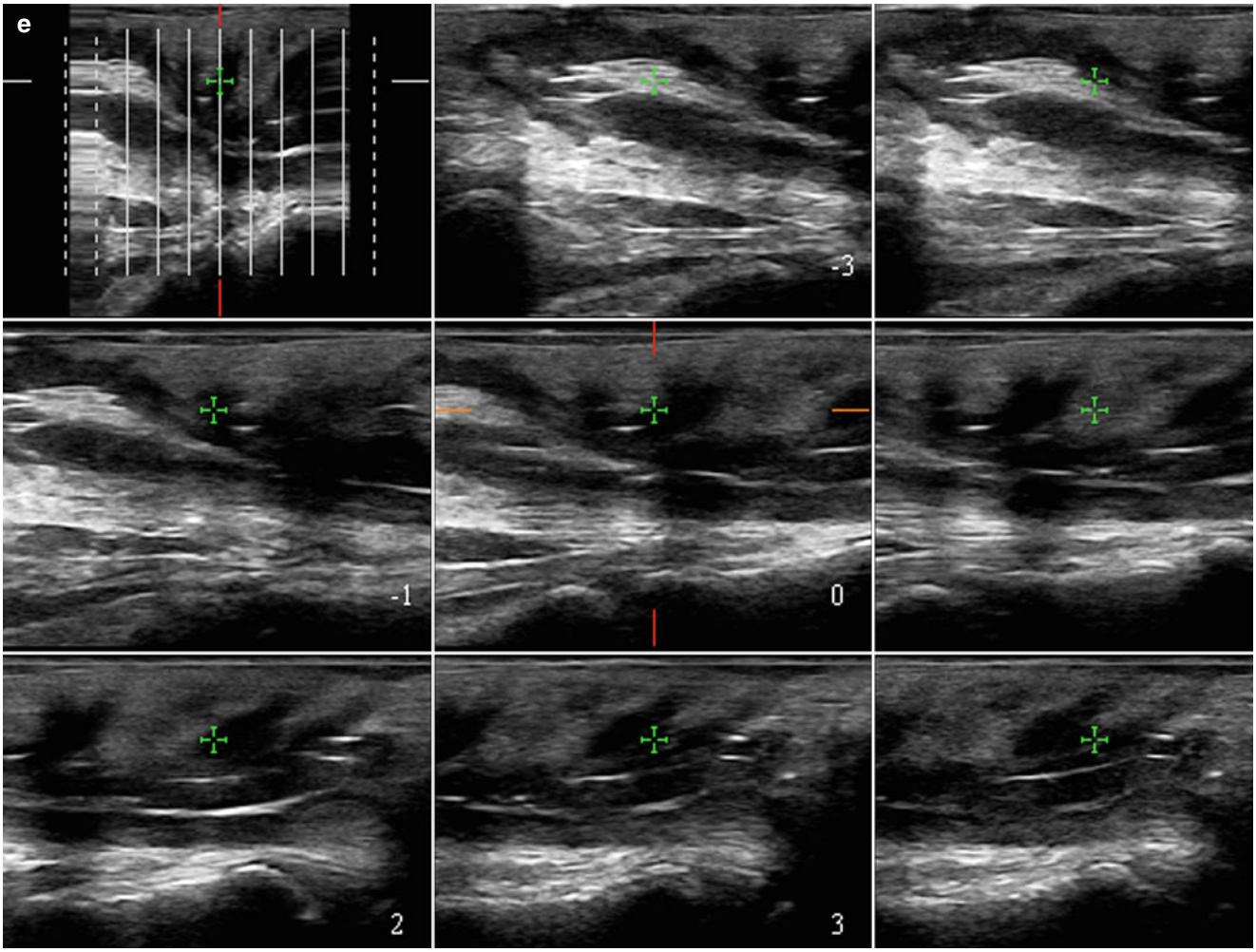

Fig. 5.17 (continued)

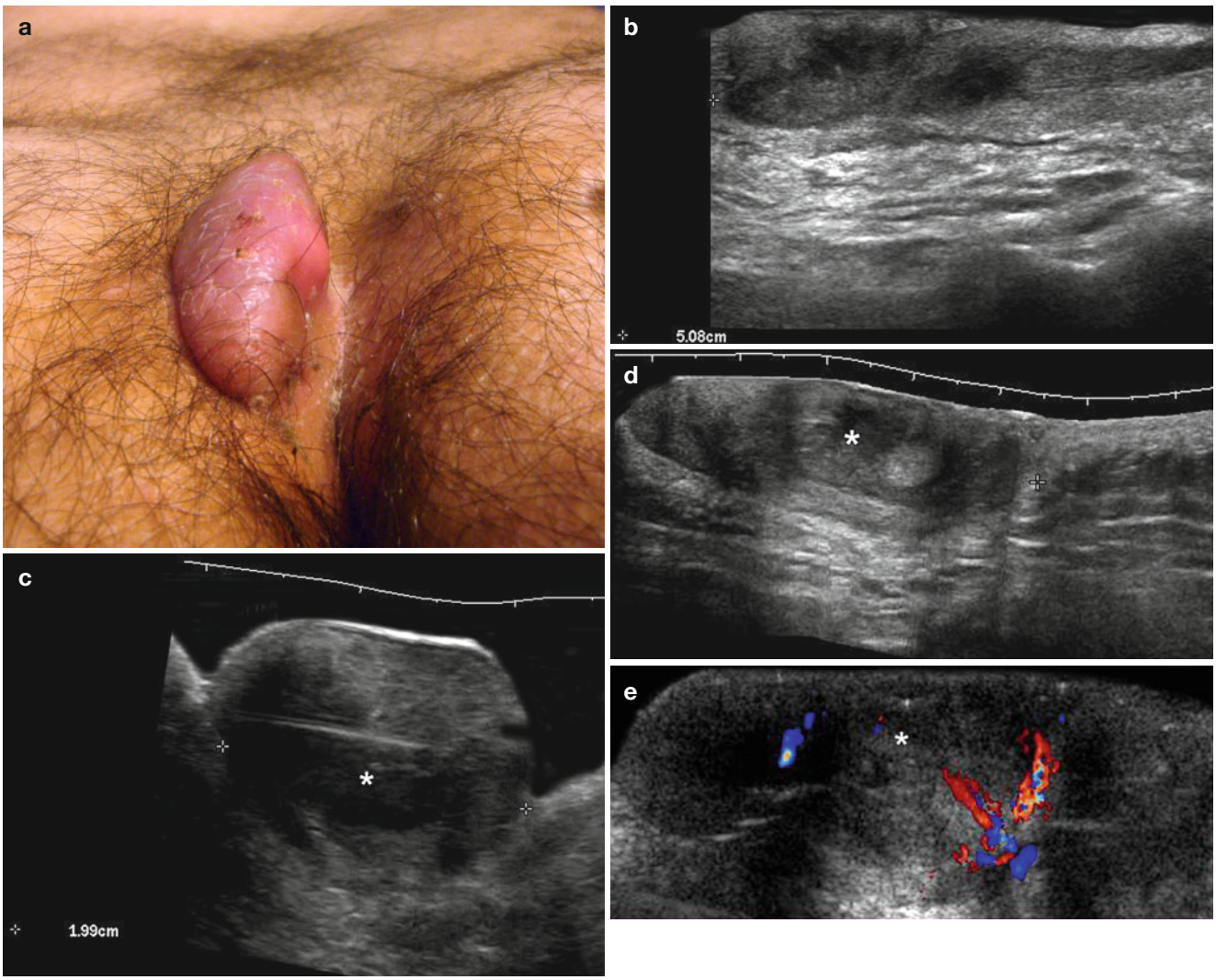

Fig. 5.18 (**a**–**e**) Pilonidal cyst with scarring. (**a**) Clinical erythematous swelling in the intergluteal region. (**b**) Grey scale ultrasound image (longitudinal view) shows a 5.08 cm well-defined hypoechoic sinus in the dermis and subcutaneous tissue. (**c**) Grey scale image (transverse view) demonstrates a 1.99 cm hypoechoic sinus that bulges into the epidermis and dermis. (**d**) Grey scale ultrasound image (longitudinal view) focused in the upper part of the lesion demonstrates the hypoechogenicity within the lesion (*). (**e**) Color Doppler ultrasound image (longitudinal view) shows increased blood flow that predominantly affects the periphery of the cyst but also involves the lesion

Tip

- Perform a broad sonographic sweep when examining pilonidal cysts, including all axes. Keep in mind that the axis and branches of the lesion may present a variable anatomical distribution and could be located upward, downward, oblique, transverse, or longitudinal with respect to the cutaneous lesion.

5.2.1.6 Synovial Cyst

Synovial cysts have a synovial lining and are usually attached to joints or tendon sheaths most commonly in the hands and feet. Synovial cysts contain a myxoid material and are therefore also called myxoid cysts. Another common location for synovial cysts is the periungual region where they can compress the ungual matrix and produce secondary dystrophic changes in the ungual plates. These cysts originate in deeper layers and can bulge into the skin. On sonography, synovial cysts show as round or oval-shaped well-defined anechoic structures in the dermis and subcutaneous tissue that can have a connecting anechoic or hypoechoic tract to the nearest joint. These connecting tracts commonly run through the lateral aspects of the interphalangeal joints of the fingers (Figs. 5.19, 5.20, and 5.21).

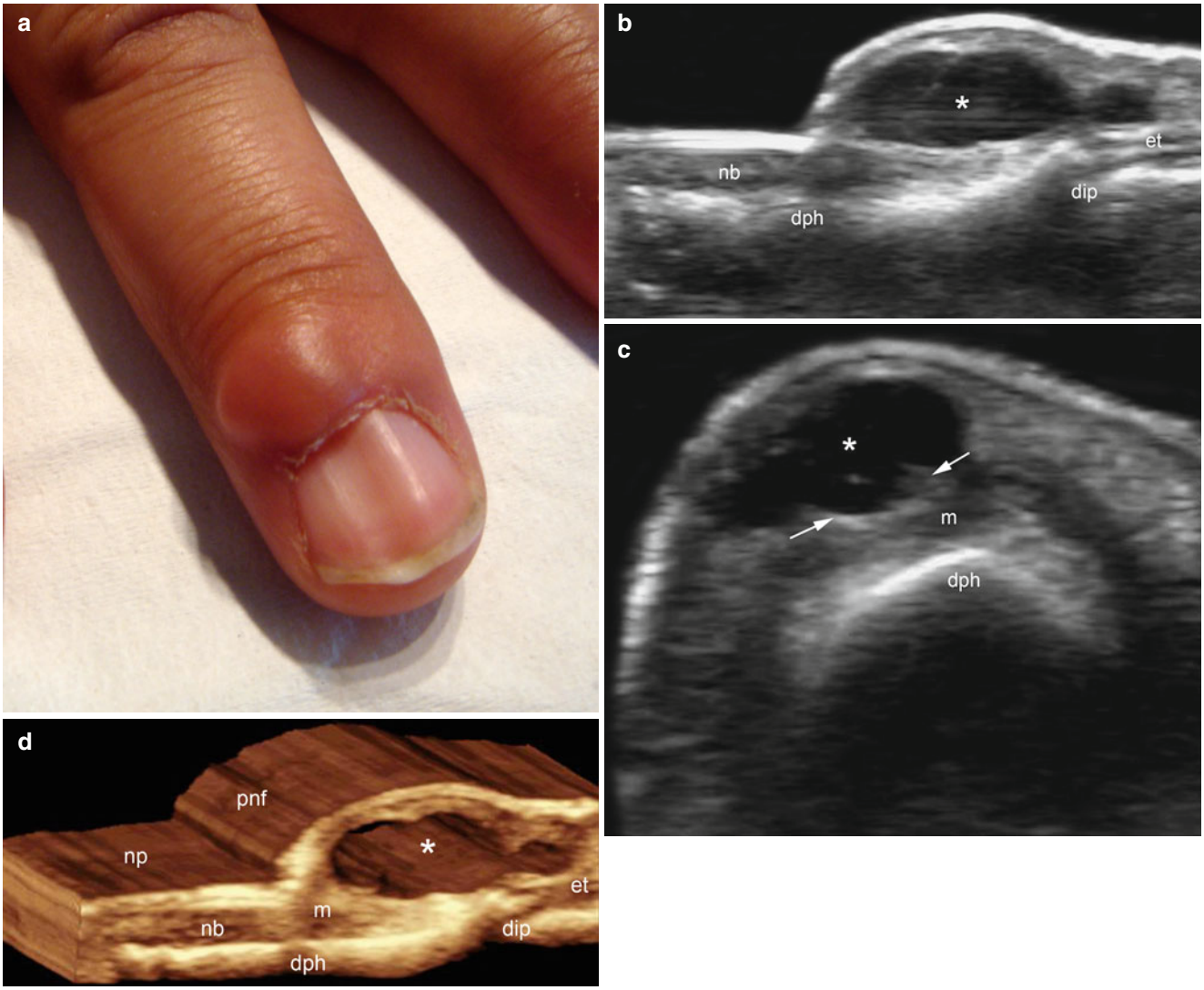

Fig. 5.19 (**a**–**d**) Periungual synovial cyst. (**a**) Clinical image shows periungual swelling in the proximal nail fold and dystrophic changes with concavity of the nail plate. (**b**) Grey scale ultrasound image (longitudinal view) demonstrates a well-defined, oval-shaped anechoic cystic structure in the subcutaneous tissue of the proximal nail fold. (**c**) Grey scale ultrasound image (transverse view) demonstrates extrinsic compression (*arrows*) of the ungual matrix by the cyst (*). (**d**) The cyst (*) in 3D (5–8 s sweep reconstruction). *Abbreviations*: *nb* nail bed, *m* ungual matrix, *np* nail plate, *pnf* proximal nail fold, *dip* distal interphalangeal joint, *et* extensor tendon, *dph* distal phalanx

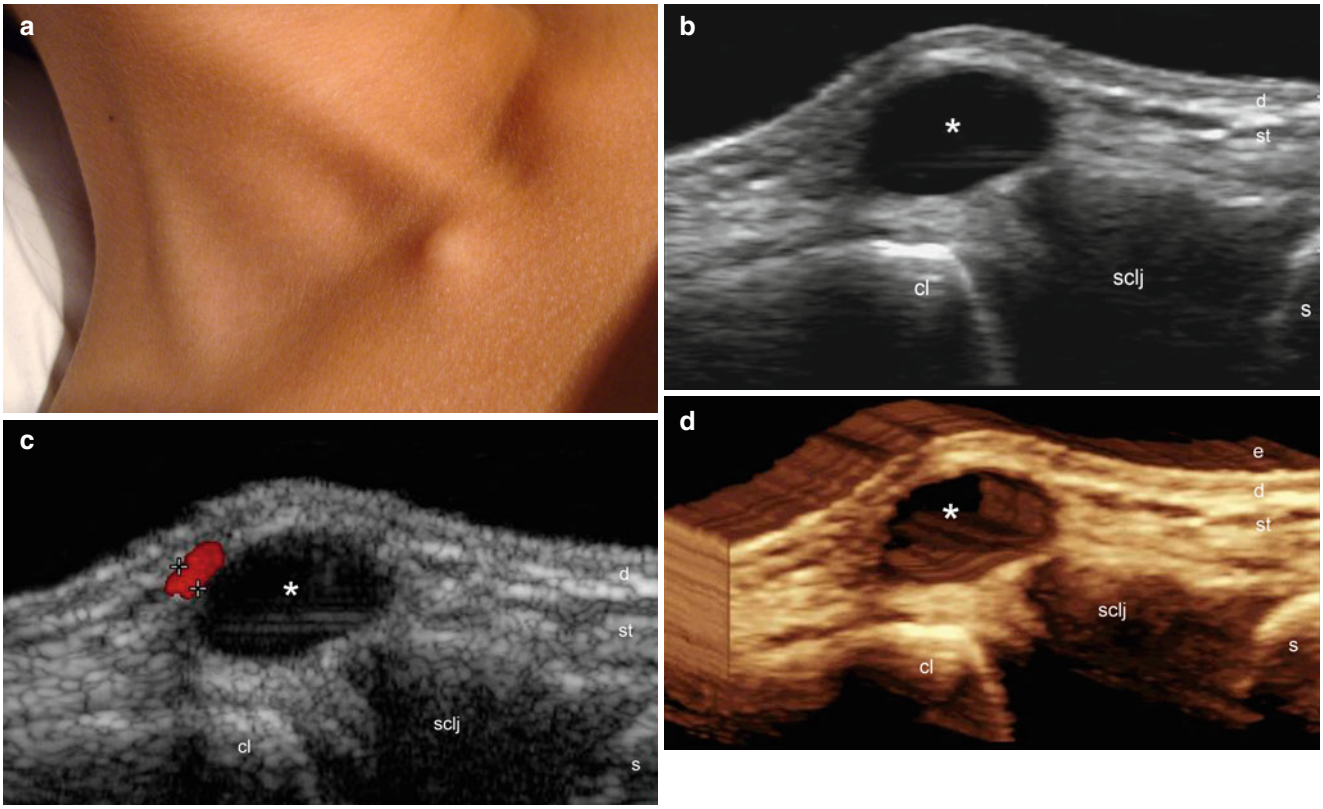

Fig. 5.20 (**a**–**d**) Synovial cyst. (**a**) Clinical figure shows a skin-colored lump in the right upper sternal region. (**b**) Grey scale ultrasound image (transverse view) demonstrates a well-defined, oval-shaped, anechoic structure (*) in the subcutaneous tissue that is attached to the sternoclavicular joint (sclj). (**c**) Color Doppler ultrasound image (transverse view) shows no signs of vascularity within the cyst and a small vessel in the periphery. (**d**) The cyst in 3D (5–8 s reconstruction sweep). *Abbreviations*: *e* epidermis, *d* dermis, *st* subcutaneous tissue, *cl* clavicle, *sclj* sternoclavicular joint, *s* sternum

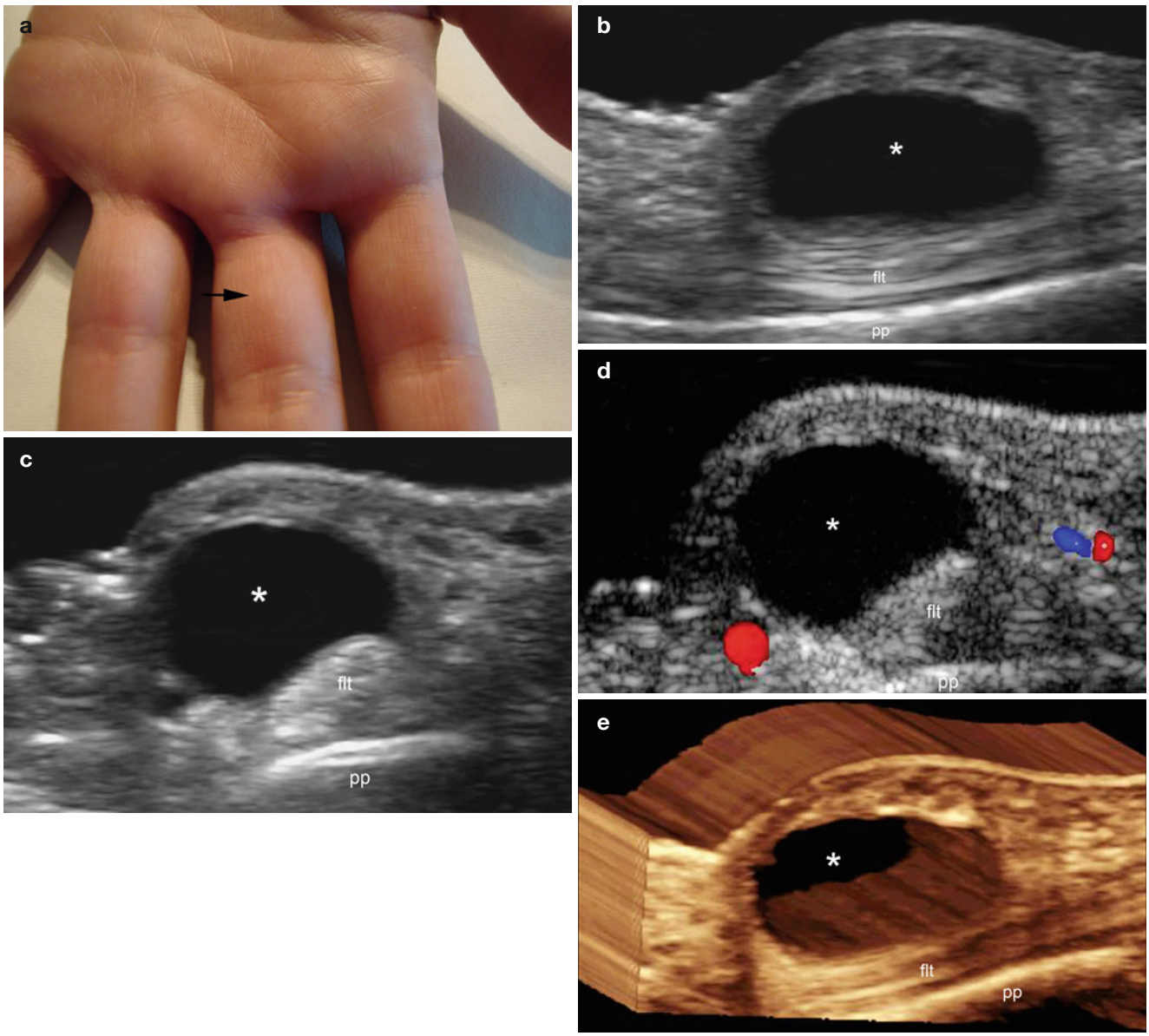

Fig. 5.21 (**a**–**e**) Synovial cyst. (**a**) Clinical photograph shows a skin colored swelling (*arrow*) in the base of the middle finger. (**b**, **c**) Grey scale ultrasound image (**b** longitudinal view and **c** transverse view) demonstrates a well-defined, oval-shaped anechoic cystic structure (*) attached to the flexor tendon sheath. (**d**) Color Doppler ultrasound image (transverse view) shows lack of vascularity within the cyst (*). (**e**) The cyst (*) in 3D (5–8 s sweep reconstruction, longitudinal view). *Abbreviations*: *flt* flexor tendon, *pp* proximal phalanx

Tip

- Look for the connecting tract to the joint or synovial sheath when dealing with synovial cysts

Pitfall

- Mucous cysts are usually found in the nail bed and may simulate synovial cysts. Mucous cysts are generated by the degeneration of collagen, therefore, they commonly do not connect with the joint (See Chap. 18).

5.2.2 Solid

5.2.2.1 Lipomatous Tumors

Lipomatous tumors are composed of mature adipose cells and variable degrees of fibrous (fibrolipoma) or capillary (angiolipoma) components. Lipomas are the most common soft-tissue tumors and they are usually single but can also be multiple in number. Clinically, lipomatous tumors show as nonpainful swelling or palpable nodules; nevertheless, they can be painful if they compress neural structures in close vicinity. The anatomical location of lipomas can be of critical importance when they are in risky locations such as in the neck or temple, among others regions, where main vascular structures can be found in the surrounding tissues. On sonography, they present as well-defined oval or round-shaped structures that follow the axis of the skin layers. Fibrolipomas tend to appear as hypoechoic whereas angiolipomas appear hyperechoic and heterogeneous. Hyperechoic fibrous septa can frequently be detected within the tumors. They commonly show hypovascularity on color Doppler ultrasound, and when hypervascularity is detected in a lipoma, an atypical or neoplastic transformation should be rule out [5, 17–20] (Figs. 5.22, 5.23, and 5.24).

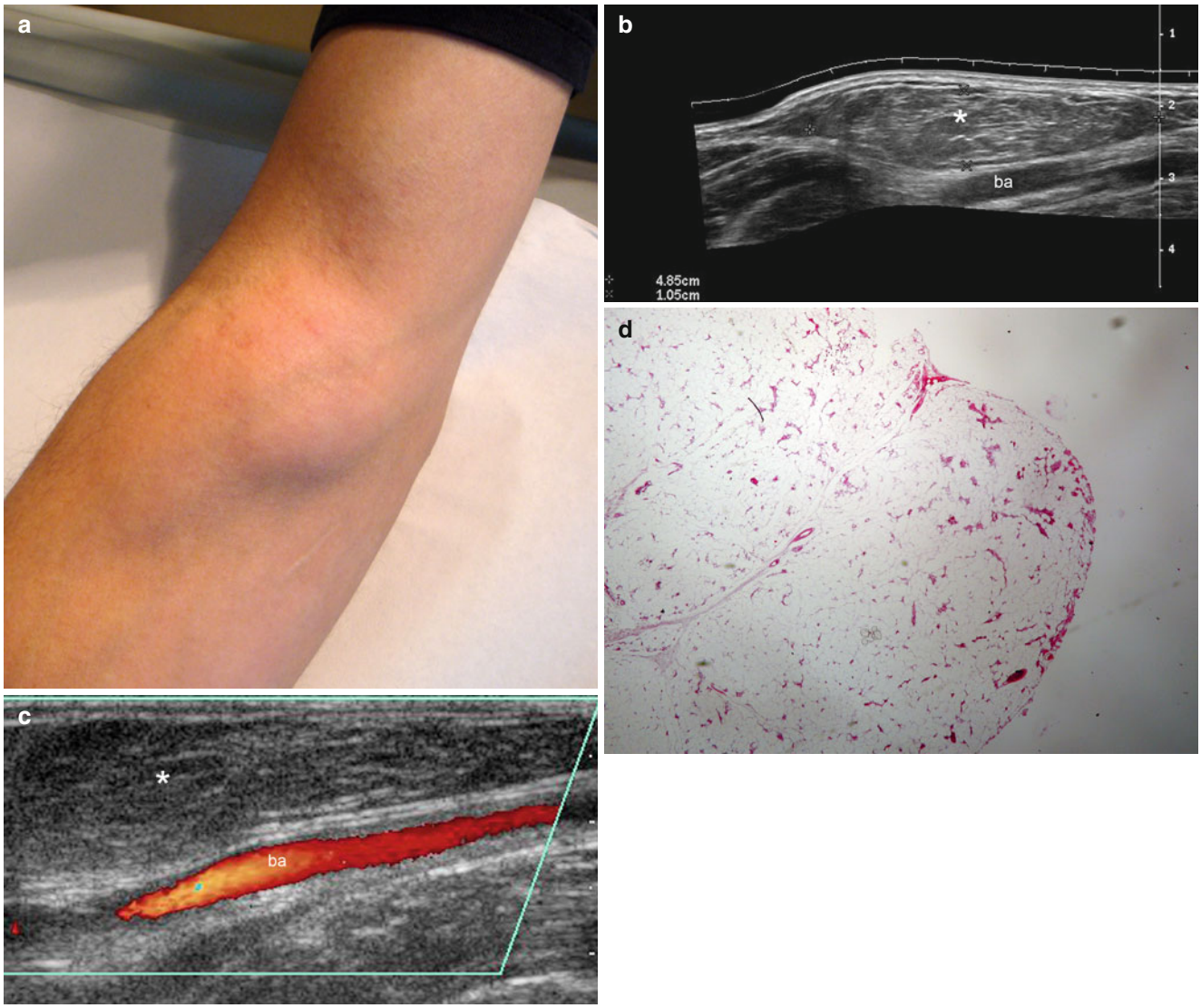

Fig. 5.22 (**a**–**d**) Lipoma. (**a**) Clinical image shows skin-colored swelling in the left forearm. (**b**) Grey scale ultrasound image (longitudinal view) demonstrates a 4.85 × 1.05 cm well-defined, oval-shaped, hypoechoic structure in the subcutaneous tissue. The brachial artery (*ba*) runs deep to the solid mass. (**c**) Color Doppler ultrasound image (longitudinal view) shows the flow within the brachial artery deep to the mass. (**d**) Histology (HE 20× zoom, courtesy of Dr. Laura Carreño): mature adipocytes with small eccentric nuclei

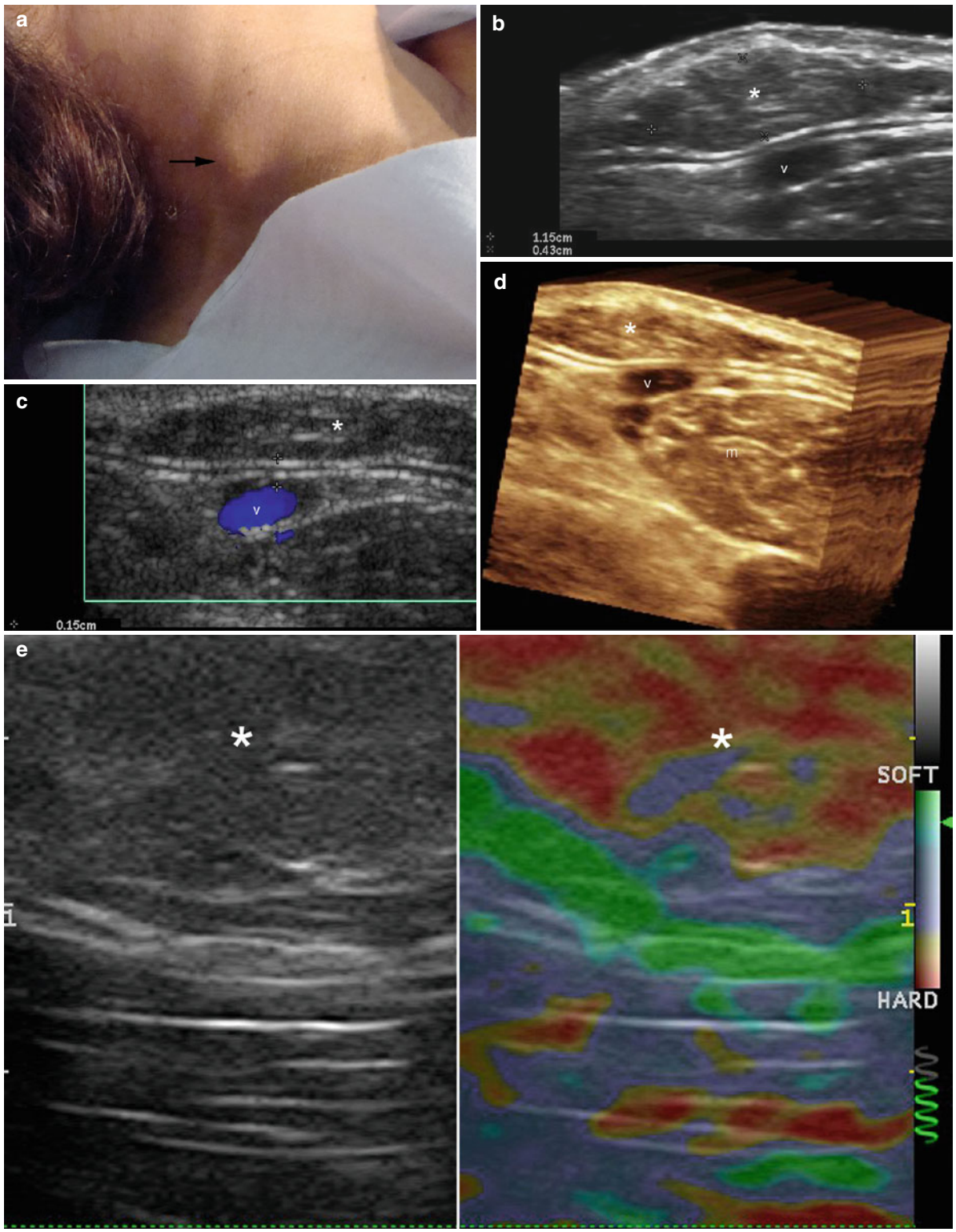

Fig. 5.23 (**a**–**e**) Lipoma. (**a**) Clinical photograph shows a skin-colored swelling in the right side of the neck (*arrow*). (**b**) Grey scale ultrasound image (transverse view) demonstrates1.15 × 0.43 cm well-defined oval-shaped hypoechoic mass (*, between markers) in the subcutaneous tissue that follows the axis of the skin layers. The external jugular vein (*v*) is located deep to the mass. (**c**) Color Doppler ultrasound image (transverse view) shows the flow within the external jugular vein and the distance between the mass and the vein (1.5 mm). (**d**) The mass in 3D (5–8 s reconstruction, transverse view). (**e**) Sonoelastography image (comparative, longitudinal view) in other case demonstrates the soft nature of the lipomatous structure

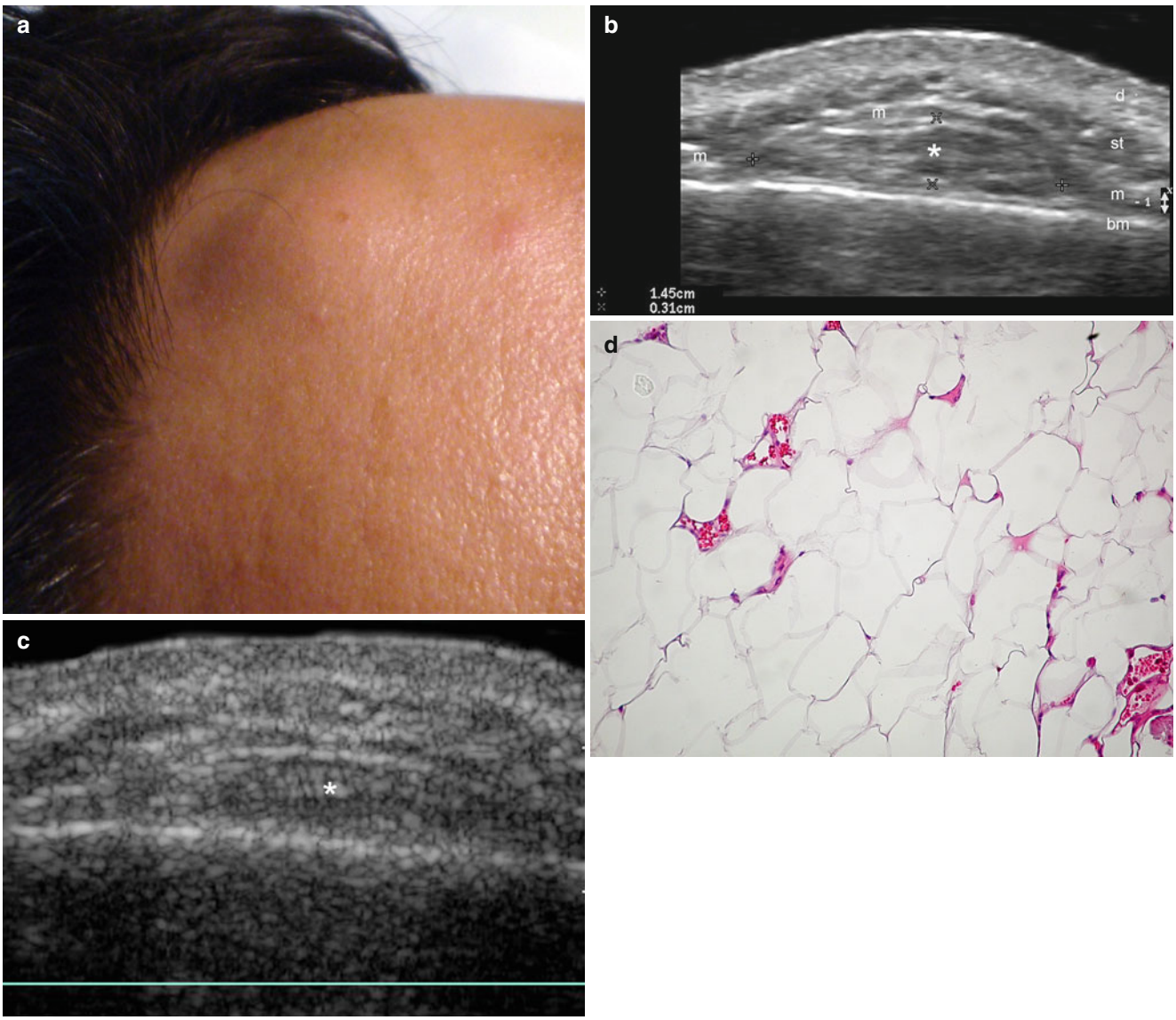

Fig. 5.24 (**a**–**d**) Subgaleal lipoma. (**a**) Clinical image shows skin-colored swelling in the frontal region. (**b**) Grey scale ultrasound image (transverse view) demonstrates a 1.45×0.31 cm, well-defined, oval-shaped hypoechoic nodule (*) located between the epicranius muscle and the bony margin of the skull. Notice that the muscle is displaced upward. (**c**) Color Doppler ultrasound image (transverse view) shows lack of detectable vascularity within the nodule. (**d**) Histology (HE 100× zoom, courtesy of Dr. Claudia Morales): proliferation of mature adipocytes with large clear cytoplasms an small eccentric nuclei. *Abbreviations*: *d* dermis, *st* subcutaneous tissue, *m* epicranius muscle, *bm* bony margin of the skull

Tips

- It is important to remember that there are risky locations for the lipomas where the skin is thin and there are relevant anatomical structures located more superficially, such as in the temple region (temporal artery), neck (carotid arteries and jugular veins), and ventral forearm (brachial artery) among others.
- Describe in your report the relevant anatomic structures in the vicinity of the lipomatous tumor, such as thick vessels (arteries or veins), nerves, tendons, or muscles.

Pitfall

- An oval hypoechoic or heterogeneous structure that does not follow the axis of the skin layers usually does not correspond to a lipoma.

5.2.2.2 Fibromatous Tumors

There are different types of fibromatous lesions that may affect the skin layers.

5.2.2.2.1 Dermatofibromas

Dermatofibromas, also called fibrous histiocytomas and histiocytomas cutis, occur most commonly in the lower extremities or torso of middle-age women. Clinically, they present as erythematous or brown firm and painless nodules. The origin of these lesions is controversial, whether reactive to trauma such as insect bites or a neoplastic process; dermatofibromas grow slowly and do not tend to regress over time. Histologically, they are composed of spindle cells embedded in a hyaline collagenous stroma. Scattered lipid-laden histiocytes, multinucleated giant cells, and hemosiderin deposition are frequently seen [21]. On sonography, they appear as ill-defined hypoechoic lesions, commonly heterogeneous, that affect the dermis and less frequently the upper subcutaneous tissue. Dermatofibromas may produce a distortion or enlargement in the regional hair follicles. On color Doppler ultrasound, dermatofibromas are frequently hypovascular but they can occasionally present increased vascularity with slow flow arterial or venous vessels (Figs. 5.25 and 5.26).

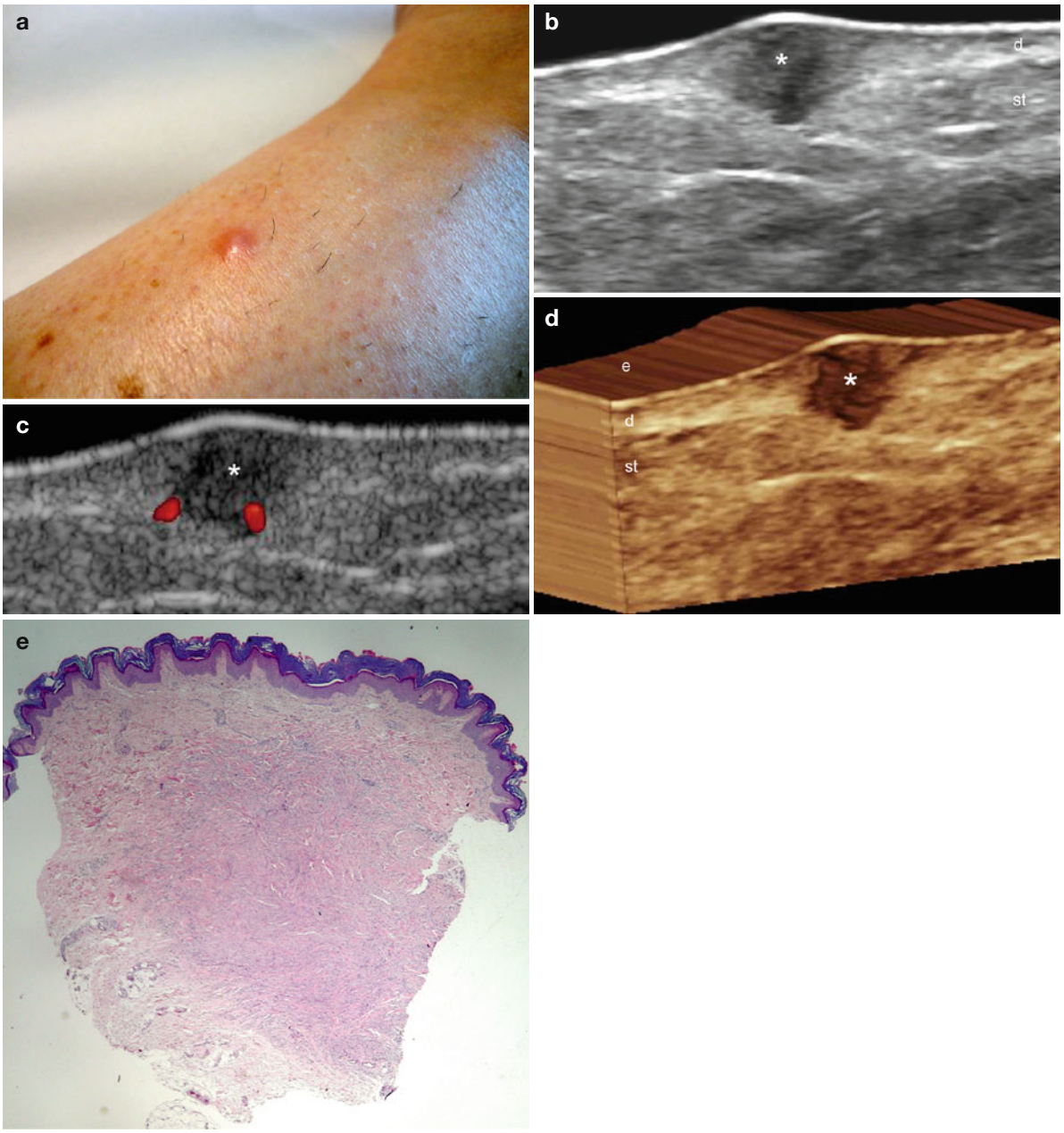

Fig. 5.25 (**a**–**e**) Dermatofibroma. (**a**) Erythematous swelling in the lateral aspect of the left leg. (**b**) Grey scale ultrasound image (longitudinal view) demonstrates an ill-defined hypoechoic and heterogeneous structure (*) in the dermis and upper subcutaneous tissue. (**c**) Color Doppler ultrasound image (longitudinal view) shows two small vessels in the sublesional region. (**d**) The lesion in 3D (5–8 s sweep reconstruction, longitudinal view). (**e**) Histology (HE 20× zoom, courtesy of Dr. Laura Carreño): dense spindle cell infiltrate with capillary vessels and thick bundles of collagen in the periphery. The epidermis shows acanthosis. *Abbreviations*: *e* epidermis, *d* dermis, *st* subcutaneous tissue

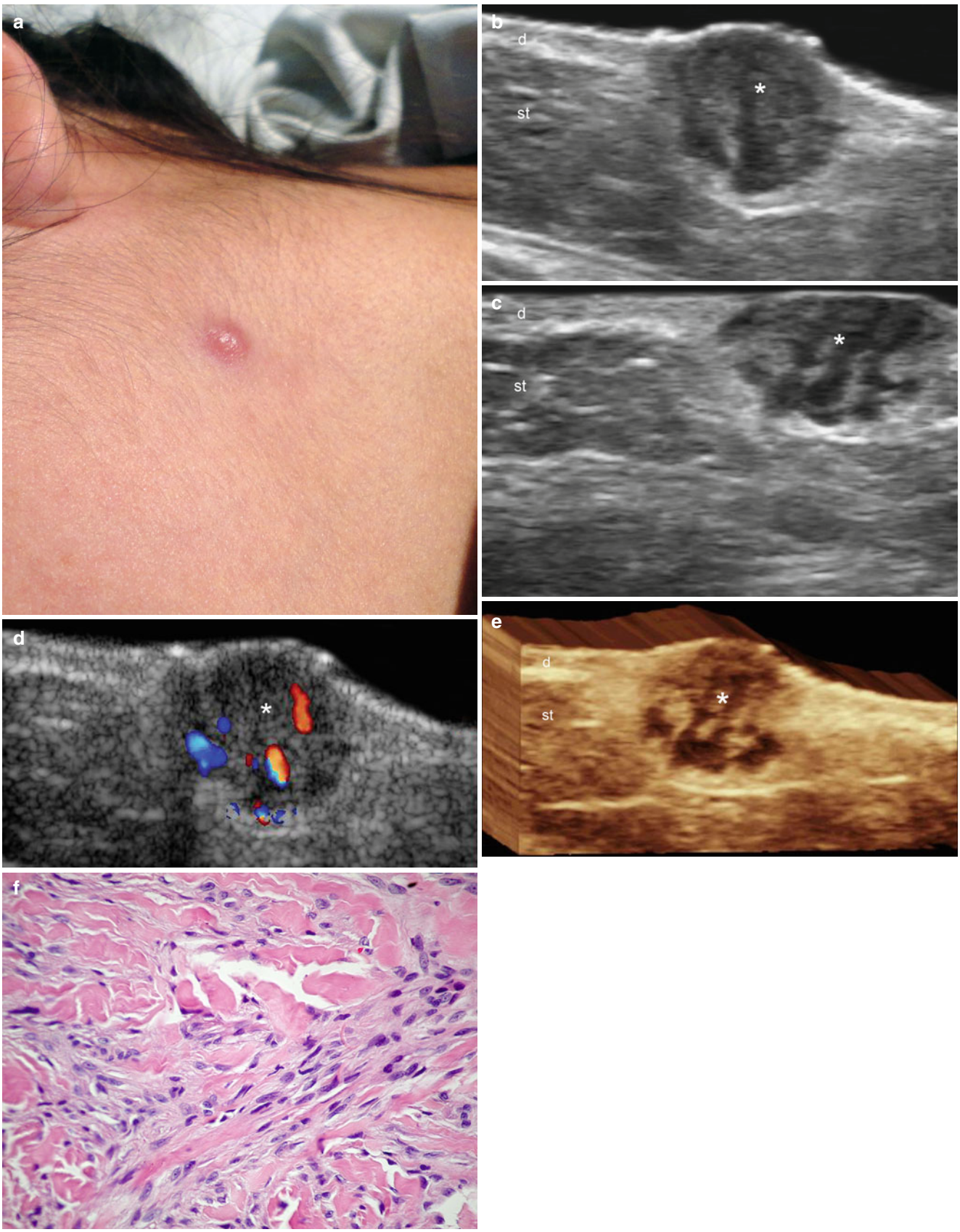

Fig. 5.26 (**a**–**e**) Dermatofibroma. (**a**) Clinical photograph shows erythematous swelling in the left aspect of the neck. (**b**, **c**) Grey scale ultrasound images (**b** transverse and **c** longitudinal views) demonstrate an ill-defined hypoechoic and heterogeneous structure (*) with hypoechoic bands located in the dermis and subcutaneous tissue. (**d**) Color Doppler ultrasound image (longitudinal view) shows increased vascularity within the structure (*). (**e**) 3D reconstruction of the lesion (*, 5–8 s sweep, longitudinal view). (**f**) Histology (HE 400× zoom, courtesy of Dr. Laura Carreño): spindle cell infiltrate with thick bundles of collagen in the periphery. *Abbreviations*: *e* epidermis, *d* dermis, *st* subcutaneous tissue

Nodular Fasciitis

Nodular fasciitis (NF), also called pseudosarcomatous fibromatosis, is thought to represent a reactive process of unknown etiology that is most commonly seen in young or middle-aged adults particularly in the extremities, and mainly at the forearms, but can also be present on the torso. NF tends to grow rapidly, therefore these entities may clinically mimic a sarcomatous lesion. NF presents as palpable firm nodules, sometimes painful and in 10–15 % of cases, a history of trauma can be found. Histologically, NF is composed of plump spindle cells within a loose myxoid and collagenous stroma with a typically feathery, microcystic appearance. Numerous thin-walled blood vessels, usually lined with prominent endothelial cells in radial arrangement, are also seen. Foci of hemorrhage, sparse chronic inflammatory infiltrates with lymphocytes, histiocytes and multinucleate osteclast-type giant cells within a myxoid stroma with a rich cellular array of spindle-shaped fibroblasts, and numerous mitotic figures are frequent findings. On sonography, they present as oval or round-shaped well-defined and sometimes lobulated nodules, located in the subcutaneous tissue. Echogenicity can vary from hypoechoic to heterogeneous, and multiple punctate echogenic foci have been described within the tumor. Occasionally, NF is associated with hyperechogenicity of the surrounding tissue because of edema. Lesional blood flow may also be variable and could range from hypo- to hypervascularity frequently with slow flow arterial vessels [21, 22] (Fig. 5.27).

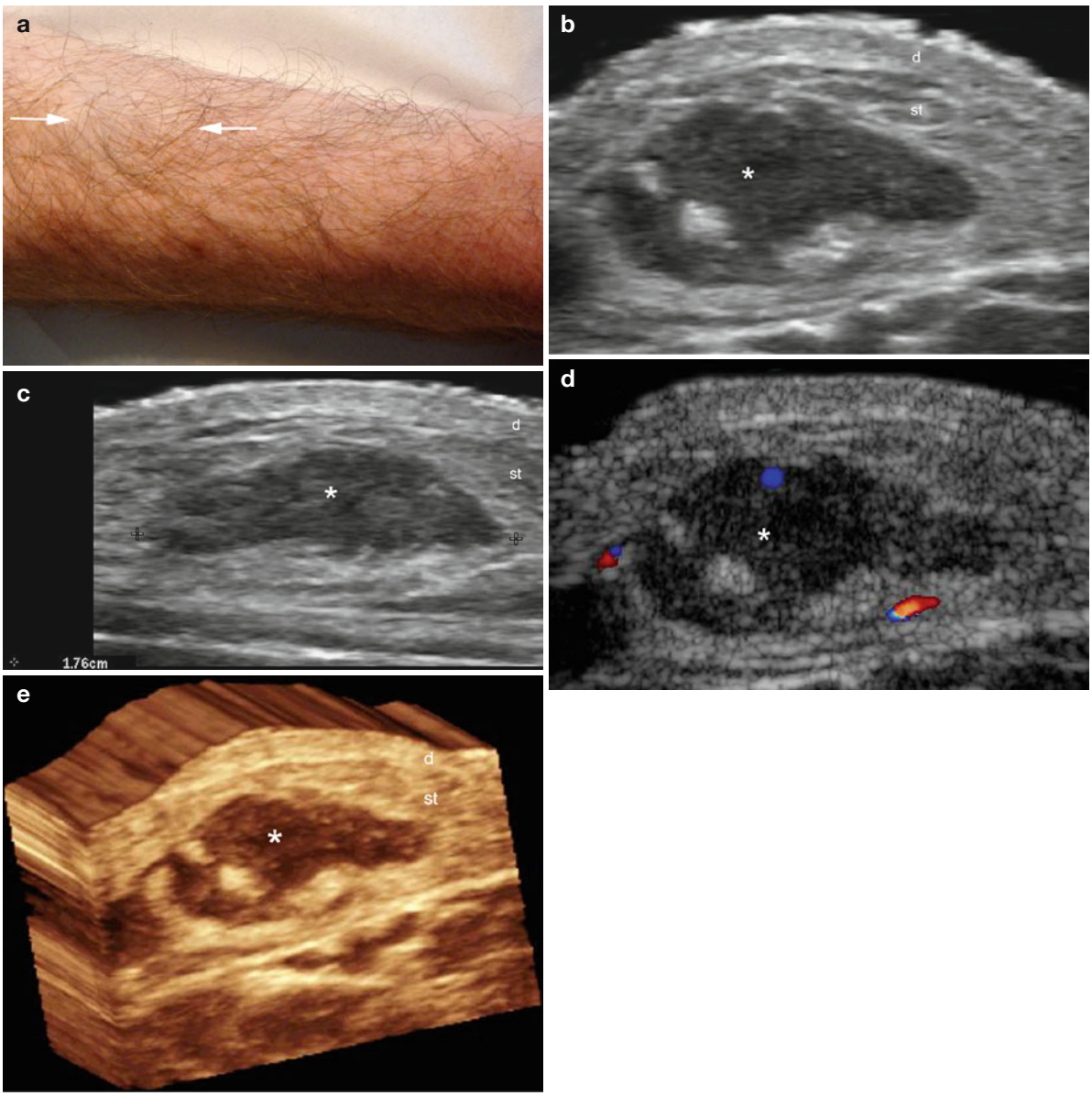

Fig. 5.27 (**a**–**e**) Nodular fasciitis. (**a**) Clinical image shows a skin-colored palpable lump (*arrows*) in the palmar aspect of the right forearm. (**b**) Grey scale ultrasound image (transverse view) demonstrates an oval-shaped hypoechoic and heterogeneous solid nodule (*) in the subcutaneous tissue. (**c**) Grey scale ultrasound image (longitudinal view) shows a 1.76 hypoechoic/heterogeneous oval-shaped subcutaneous nodule (*). (**d**) Color Doppler ultrasound image (transverse view) presents a few small vessels in the periphery of the nodule. (**e**) The nodule (*) in 3D (5–8 s sweep, transverse view). *Abbreviations*: *d* dermis, *st* subcutaneous tissue

Elastofibroma Dorsi

Elastofibroma dorsi (ED) is a rare, slow-growing reactive pseudotumor of connective tissue typically located in the subscapular region (93 %) and bilateral in 54 % of cases. A common location for ED is beneath the rhomboid major and latissimus dorsi muscles and adjacent to the inferior angle of the scapula. ED is more common over the age of 40 years and is frequently reported in elderly people. ED has a female predominance, and depending on its size, may cause pain (the most common symptom). Although some have suggested that ED can be a response to repeated trauma or friction between the lower scapula and the underlying chest wall, this has never been confirmed, particularly for examples located in extrascapular sites. It is composed histologically of an ill-defined unencapsulated mass that merges with the adjacent connective tissue and conformed by paucicellular collagen, entrapped mature fat cells, and large elastic fibers. On ultrasound, the lesions appear as ill-defined, mostly oval multilayered masses fixed to the deep costal plane, but mobile with respect to the scapula. For a better visualization of ED, a dynamic maneuver with abduction of the arm should be performed in order to mobilize the mass away from the scapula. Thus, the most common presentation of ED is a heterogenous fasciculated mass with hyperechoic fibrous and hypoechoic fat strands. The remaining less frequent sonographic patterns of ED can vary from hypoechoic to hyperechoic according to the grade of fibroelastic (hyperechoic) or fatty (hypoechoic) components [23–25] (Fig. 5.28).

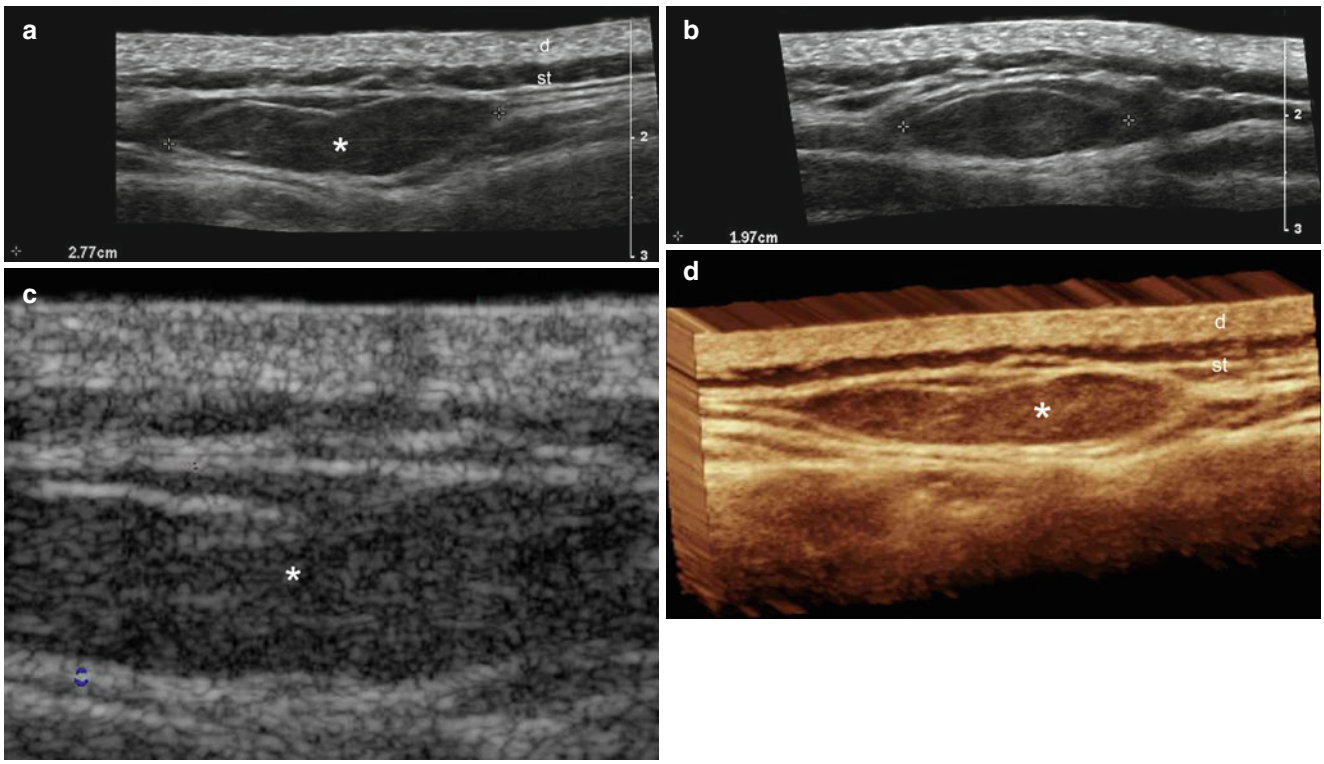

Fig. 5.28 (**a**–**d**) Elastofibroma dorsi. (**a**, **b**) Grey scale ultrasound images (**a** longitudinal and **b** transverse view) show a 2.77 cm long × 1.97 cm transverse axis well-defined oval-shaped hypoechoic and slightly lobulated solid mass in the subcutaneous tissue of the left scapular region. (**c**) Color Doppler ultrasound image (transverse view) shows no signs of vascularity within the mass. (**d**) The mass in 3D (5–8 s sweep reconstruction, longitudinal view). *Abbreviations*: *d* dermis, *st* subcutaneous tissue

Tip

- The scapular or subscapular locations are the key for diagnosing this tumor.
- It is important to remember to perform the dynamic maneuver with abduction of the arm to visualize the elastofibroma.

5.2.2.3 Neurogenic Tumors

Neurogenic tumors usually present clinically as non painful palpable lumps. There are many types of neurogenic structures, the most common are described below.

5.2.2.3.1 Schwannoma

Schwannomas, also called, neurilemmomas, are neurogenic entities clinically presenting as slow-growing painless lumps of variable size most frequently located in the limbs and followed by the head and neck; they are usually single but can also be multiple. Histologically, they are composed of Schwann cells and present as packed spindle cells with tapering and elongated wavy nuclei; palisading is prominent and scattered spindle or stellate cells set in an abundant loose myxoid stroma. Chronic inflammatory cells and small blood vessels with hyalinized walls are common and microcystic or macrocystic changes, hemorrhage, calcifications, and hemosiderin deposition can be also detected. Inmuno-histochemistry usually shows S-100 positive [26].

Their appearance tends to be well-defined on ultrasound, with round or oval-shaped solitary hypoechoic or heterogeneous nodules located in the subcutaneous tissue. They may occasionally present some anechoic areas as a result of cystic degeneration. Moreover, there is a cystic variant of schwannoma that shows prominent anechoic areas. Hyperechoic spots resulting from calcifications can sometimes be found within the mass. Rarely, afferent and efferent hypoechoic neural tracts can be detected and may support the diagnosis. Schwannomas may also show increased vascularity on color Doppler ultrasound, however they are commonly hypovascular [27, 28] (Figs. 5.29 and 5.30).

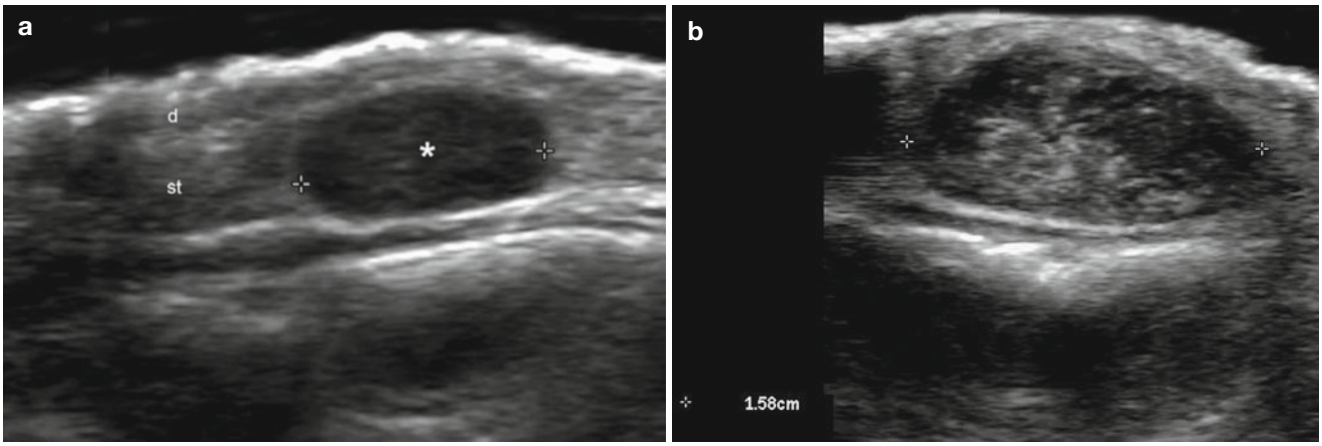

Fig. 5.29 (**a**–**e**) Schwanoma. (**a**, **b**) Grey scale ultrasound images (longitudinal view) of the left retroauricular region (**a** basal and **b** 1-year follow-up) shows a well-defined, oval-shaped hypoechoic nodule that becomes more heterogeneous and increases in size in the follow-up examination (from 0.74 to 1.58 cm). Notice that the nodule is located in the subcutaneous tissue in the basal ultrasound image but bulges into the dermis in the follow-up ultrasound image. (**c**, **d**) Color Doppler ultrasound images (longitudinal view, **c**: basal and **d**: follow-up) demonstrate that peripheral vessels increase in number in the follow-up examination. (**e**) The nodule in 3D (5–8 s sweep, longitudinal reconstruction of the follow-up examination). *Abbreviations*: *d* dermis, *st* subcutaneous tissue

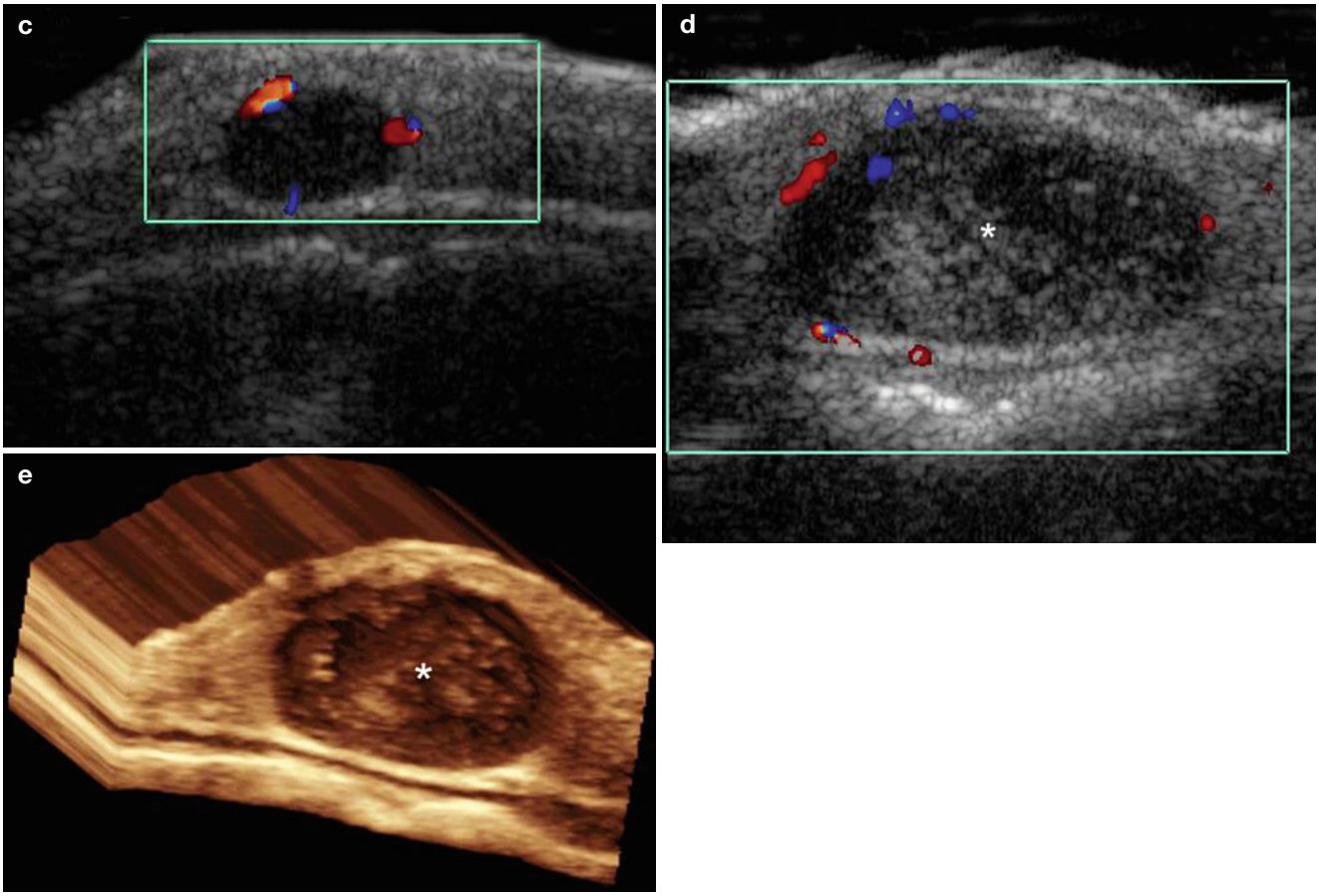

Fig. 5.29 (continued)

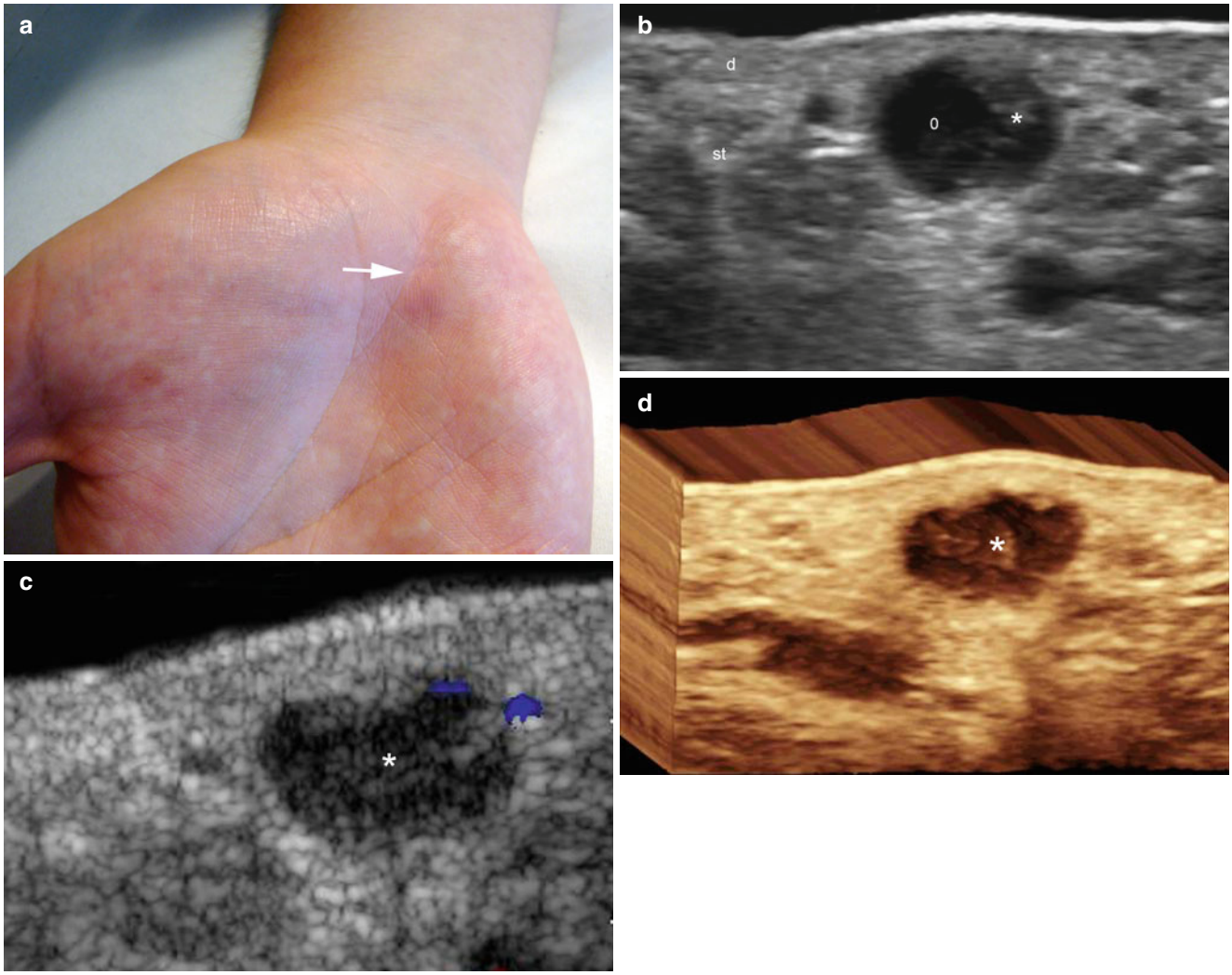

Fig. 5.30 (**a**–**d**) Schwanoma. (**a**) Clinical image shows a skin-colored swelling in the palmar aspect of the right hand (*arrow*). (**b**) Grey scale ultrasound image (transverse view) demonstrates a well-defined nodule in the subcutaneous tissue that presents mixed echogenicity (*, hypoechoic and o, anechoic) areas. (**c**) Color Doppler ultrasound image (transverse view) shows tiny vessels in the periphery of the nodule (*). (**d**) 3D reconstruction of the nodule (5–8 s sweep, transverse view). *Abbreviations*: *d* dermis, *st* subcutaneous tissue

Tip

- Be aware of anechoic areas within schwannomas that represent cystic degeneration zones and may mimic a cystic lesion on sonography.
- It is important to remember that schwannomas do not usually present as connecting tracts to the subepidermal region.

5.2.2.3.2 Neurofibroma

Neurofibromas are tumors that originate in the nerve sheath and commonly show as single nodules but when multiple in number, they can be associated to von Recklinghausen 's disease (neurofibromatosis type I). In the latter situation, patients may clinically show café-au-lait spot besides the usual lumps, swelling, or cutaneous soft papulae.

Histologically, neurofibromas are composed by multiple small nerve fibers arranged with spindle cells of scanty pale cytoplasm and elongated wavy nuclei set in a fibrillar, collagenous, and sometimes fibrous stroma. Few inflammatory components can be seen, mainly conformed by mast cells and also stromal collagen, mucin, and hyalinized collagen. Inmunohistochemistry shows S-100 positive in 30–50 % of cells and variable CD34.

Neurofibromatosis can present in three forms: localized, diffuse, and plexiform (see Chap. 3, congenital diseases).

Localized neurofibromas appear on ultrasound as round, ovoid, or fusiform-shaped hypoechoic nodules. Centrally located afferent and efferent hypoechoic neural branches can be found, mainly when neurofibromas are located in the subcutaneous tissue. In contrast, schwannomas have been reported to present eccentrically located hypoechoic afferent and efferent tracts. Nevertheless, the latter findings may not be easy to detect and there are controversial reports about the sensitivity of these afferent and efferent tracts signs. There are variable degrees of vascularity reported in localized neurofibromas on color Doppler ultrasound that can vary from hypo- to hypervascular and neurofibromas can also be associated with hemorrhagic episodes.

Plexiform neurofibromas involve branches of nerves that can adopt a serpentine shape that has been also called "bag of worms". Histologically they are composed of thick nerves or nerve fibers with prominent myxoid changes, in addition to the background of typical neurofibromas. Multiple and tortuous hypoechoic tracts following the course of a neural branch can be detected using sonography. These tracts are frequently hypovascular on color Doppler ultrasound.

Diffuse neurofibromas are characterized by extensive tumoral growth located in the dermis and subcutaneous tissue within a collagenous stroma. On ultrasound, they present as ill-defined plaque-like lesions with mixed echogenicity (hyperechoic and hypoechoic areas) sometimes with multiple hypoechoic tubule-like and tortuous tracts or nodules. On color Doppler ultrasound, vascularity may vary from hypo- to hypervascular [28–32] (Figs. 5.31, 5.32, 5.33, 5.34, 5.35, and 5.36).

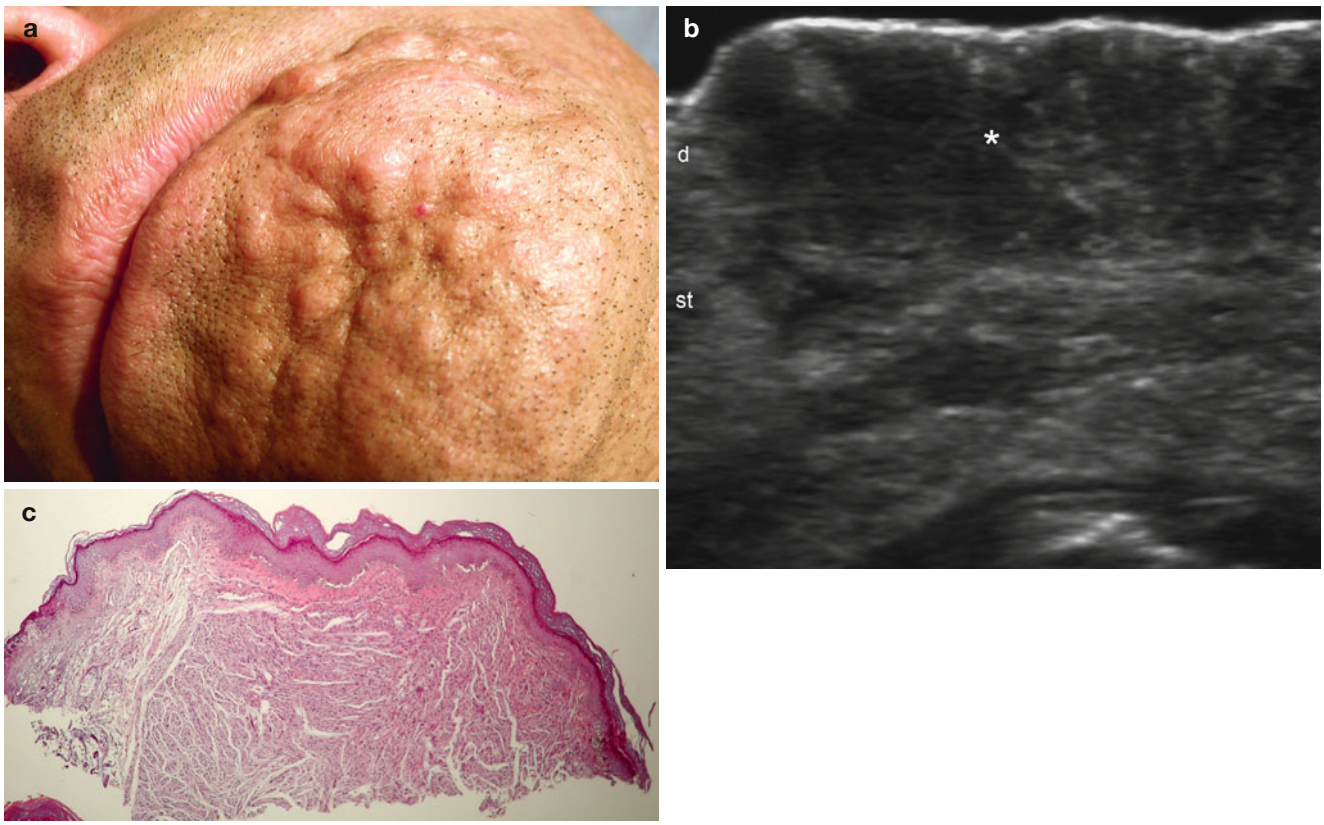

Fig. 5.31 (**a**–**c**) Diffuse neurofibromas. (**a**) Clinical image shows multiple skin-colored bumps in the chin and lower lip regions. (**b**) Grey scale ultrasound image (transverse view, chin region) demonstrates hypoechogenicity and heterogeneous thickening (*) of the dermis and upper subcutaneous tissue with some hyperechoic spots. (**c**) Histology: (HE 40× zoom courtesy of Dr. Claudia Morales): homogeneous proliferation of spindle cells. *Abbreviations*: *d* dermis, *st* subcutaneous tissue

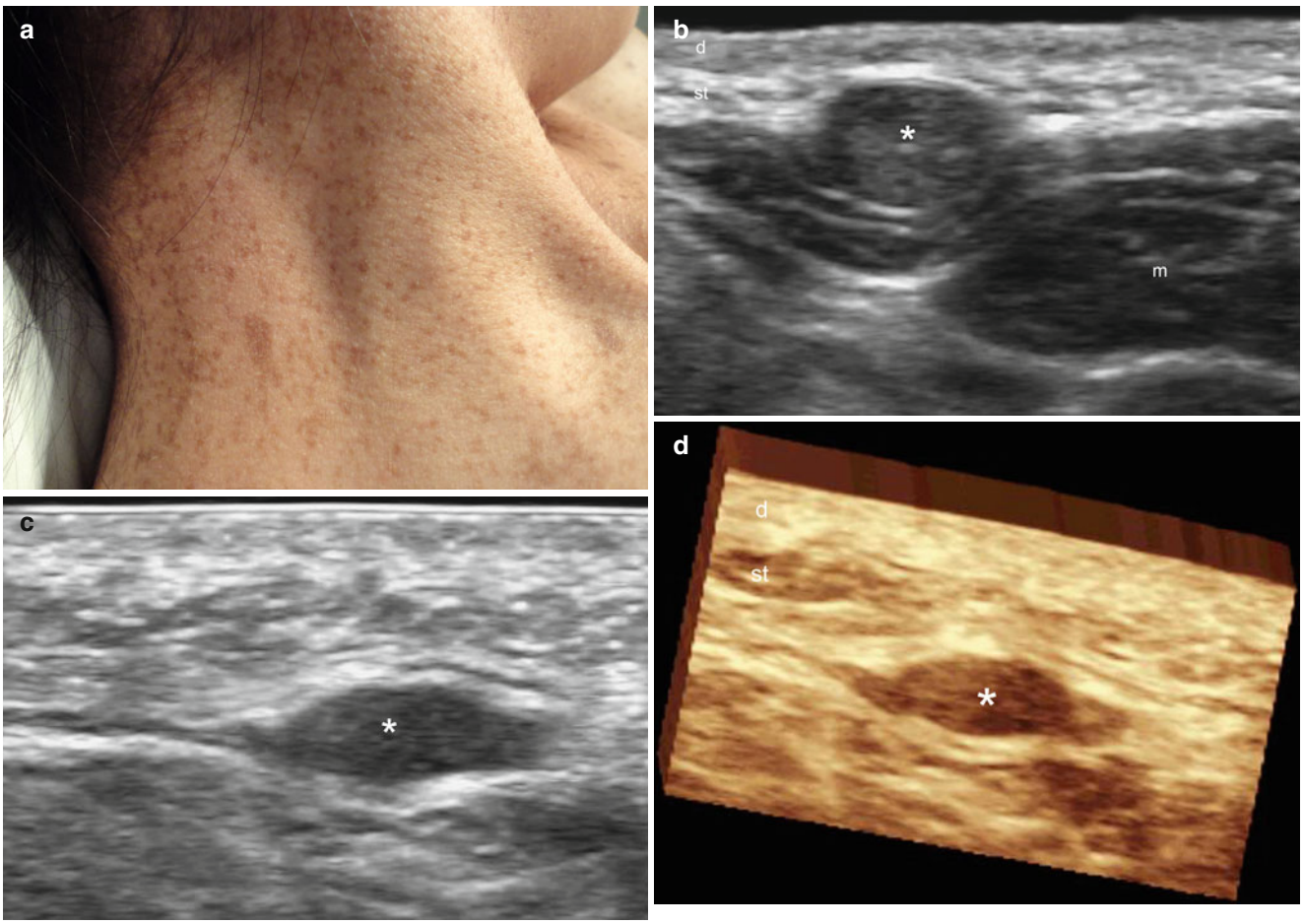

Fig. 5.32 (**a**–**d**) Localized neurofibroma. (**a**) Clinical image shows multiple cafe-au-lait spots in the neck region. (**b**) Grey scale ultrasound image (transverse view, right aspect of the neck) demonstrates a well-defined, round-shaped nodule (*) in the subcutaneous tissue. (**c**) Grey scale ultrasound image (longitudinal view, medial aspect of the right gluteal region in the same patient) shows a well-defined, oval-shaped hypoechoic nodule. A hypoechoic afferent tract can be detected in the left side of the nodule. (**d**) 3D of the lesion (*) located in the right gluteal region (longitudinal view). *Abbreviations*: *d* dermis, *st* subcutaneous tissue

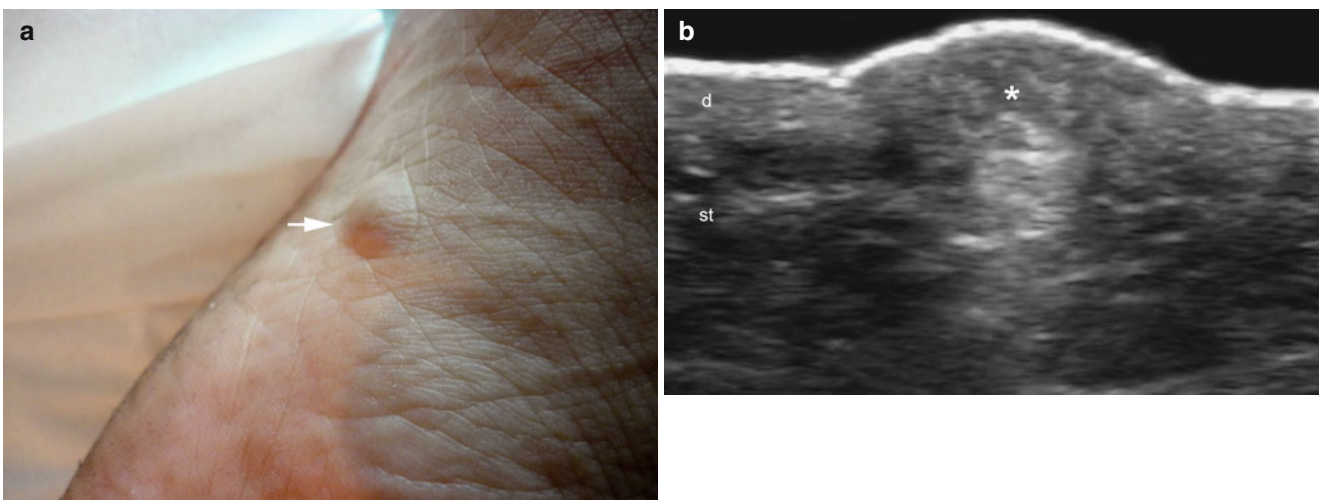

Fig. 5.33 (**a**–**c**) Diffuse neurofibroma. (**a**) Clinical image shows a skin-colored bump in the medial aspect of the plantar region of the left foot (*arrow*). (**b**) Grey scale ultrasound image (longitudinal view) demonstrates an ill-defined lesion (*) that presents heterogeneous echogenicity and is located in the dermis and subcutaneous tissue. (**c**) Histology (HE 20× zoom courtesy of Dr. Claudia Morales): nodular proliferation of spindle cells. *Abbreviations*: *d* dermis, *st* subcutaneous tissue

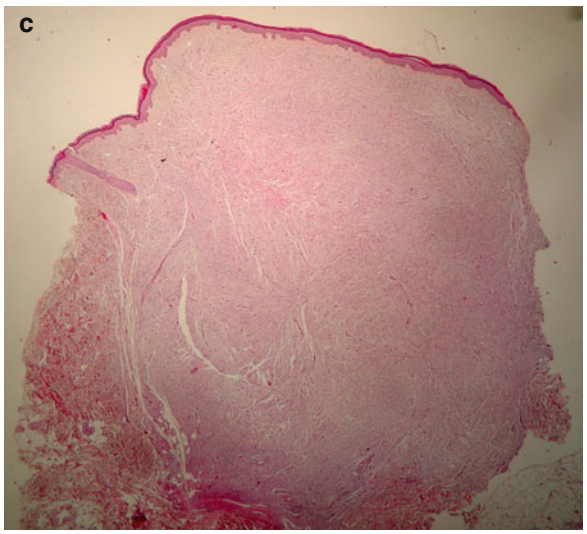

Fig. 5.33 (continued)

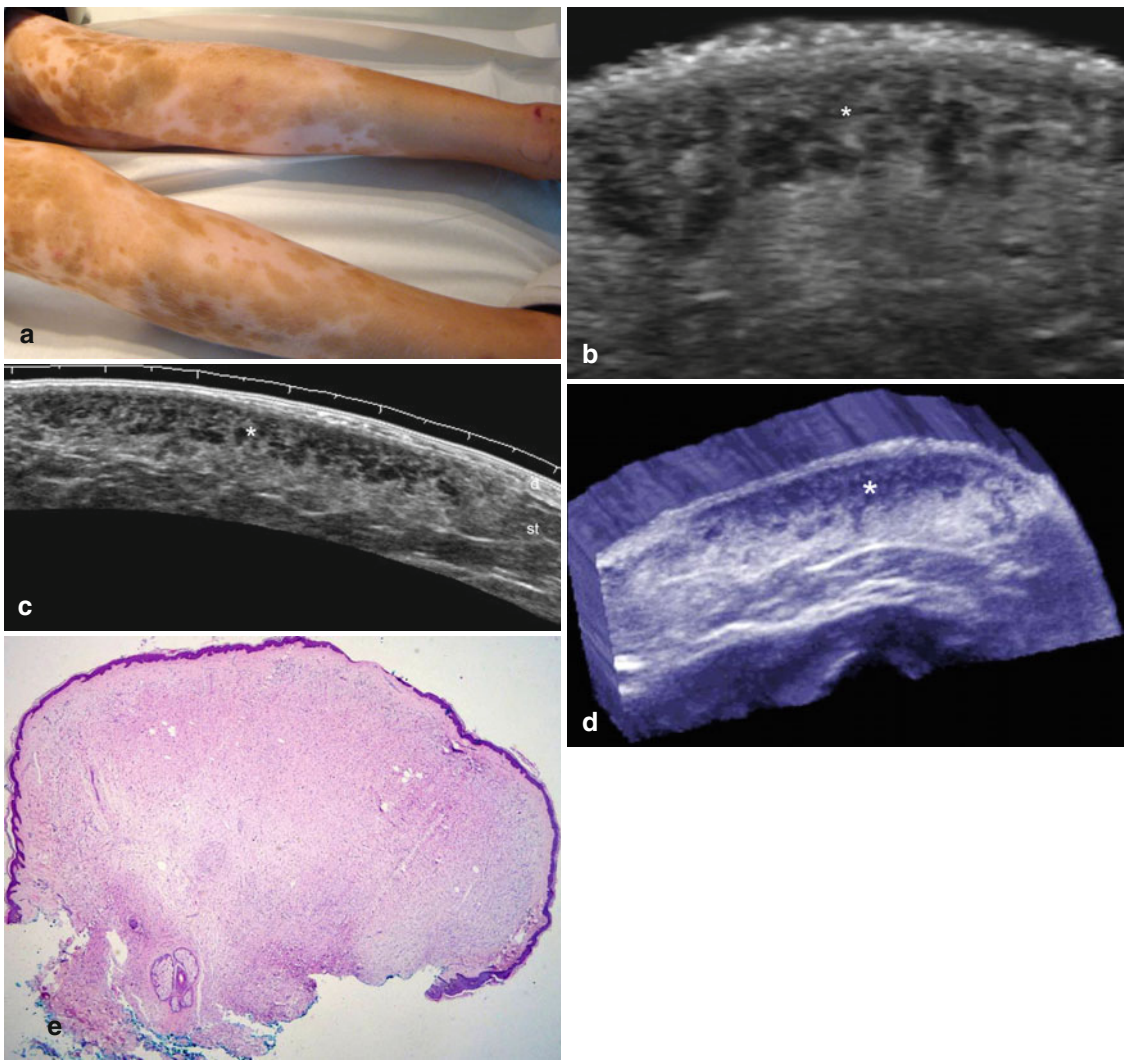

Fig. 5.34 (**a**–**e**) Diffuse neurofibromatosis. (**a**) Clinical image shows multiple café-au-lait spots in the legs. (**b**, **c**) Grey scale ultrasound images (longitudinal views of the left leg; **b** extended field of view and **c**: zoomed image) demonstrates an ill-defined thickening of the dermis and upper subcutaneous tissue that presents heterogeneous echogenicity and some hypoechoic areas. (**d**) The lesion in 3D (5–8 s reconstruction, transverse view). (**e**) Histology (HE 20× zoom, courtesy of Dr. Claudia Morales) shows proliferation of spindle cells with ill-defined borders that displaces upward the epidermal surface. *Abbreviations*: *d* dermis, *st* subcutaneous tissue

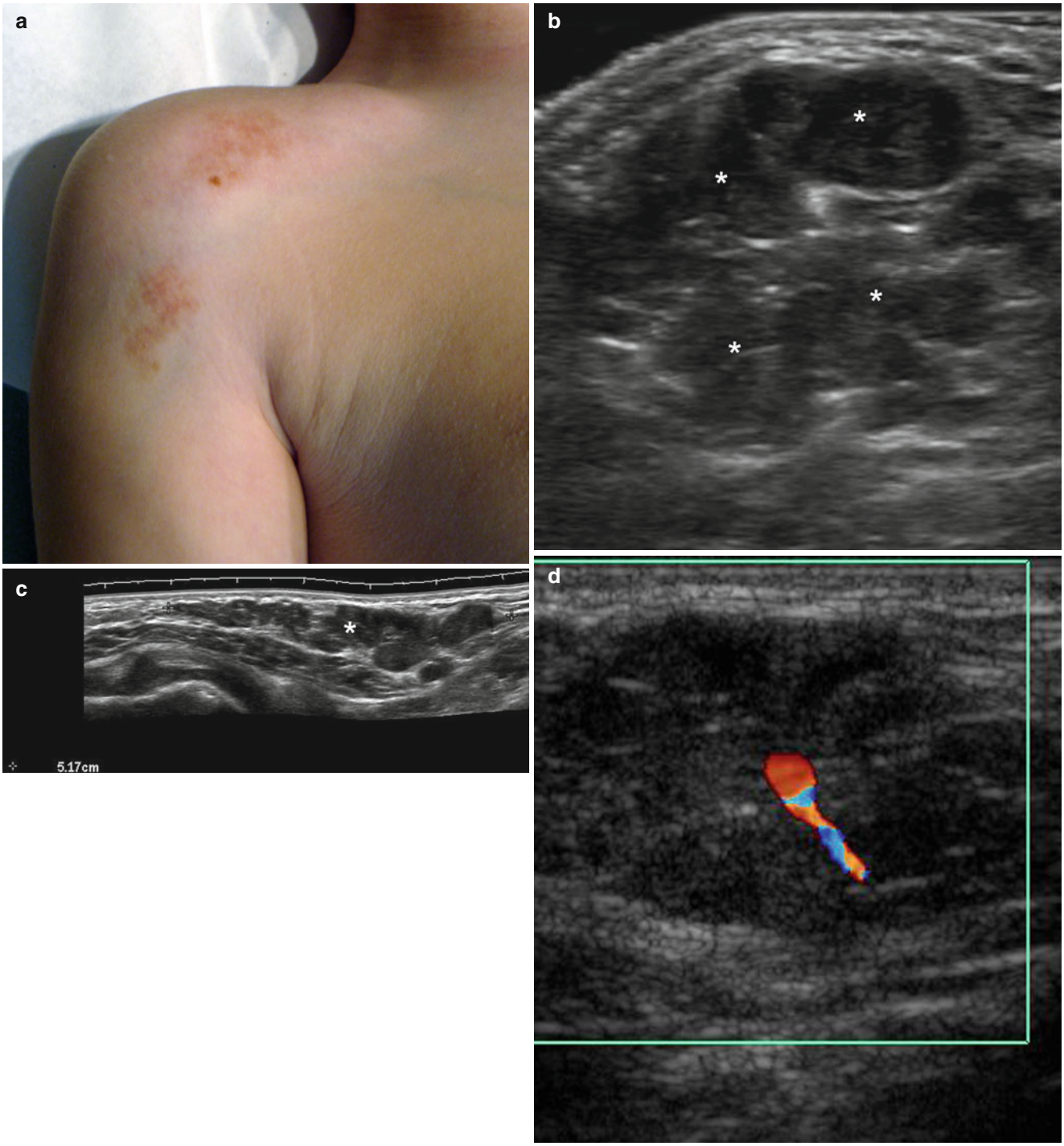

Fig. 5.35 (**a**–**d**) Plexiform neurofibromatosis. (**a**) Clinical image shows cafe-au-lait spots in the right shoulder and arm. (**b**) Grey scale ultrasound image (transverse view, right shoulder region) demonstrates several and confluent hypoechoic nodules (*) in the subcutaneous tissue. (**c**) Grey scale ultrasound image (extended field of longitudinal view) shows a 5.17 cm long hypoechoic solid nodules and tracts ("bag of worms" appearance) located in the subcutaneous tissue. (**d**) Color Doppler ultrasound image demonstrates scarce vascularity in between the nodules

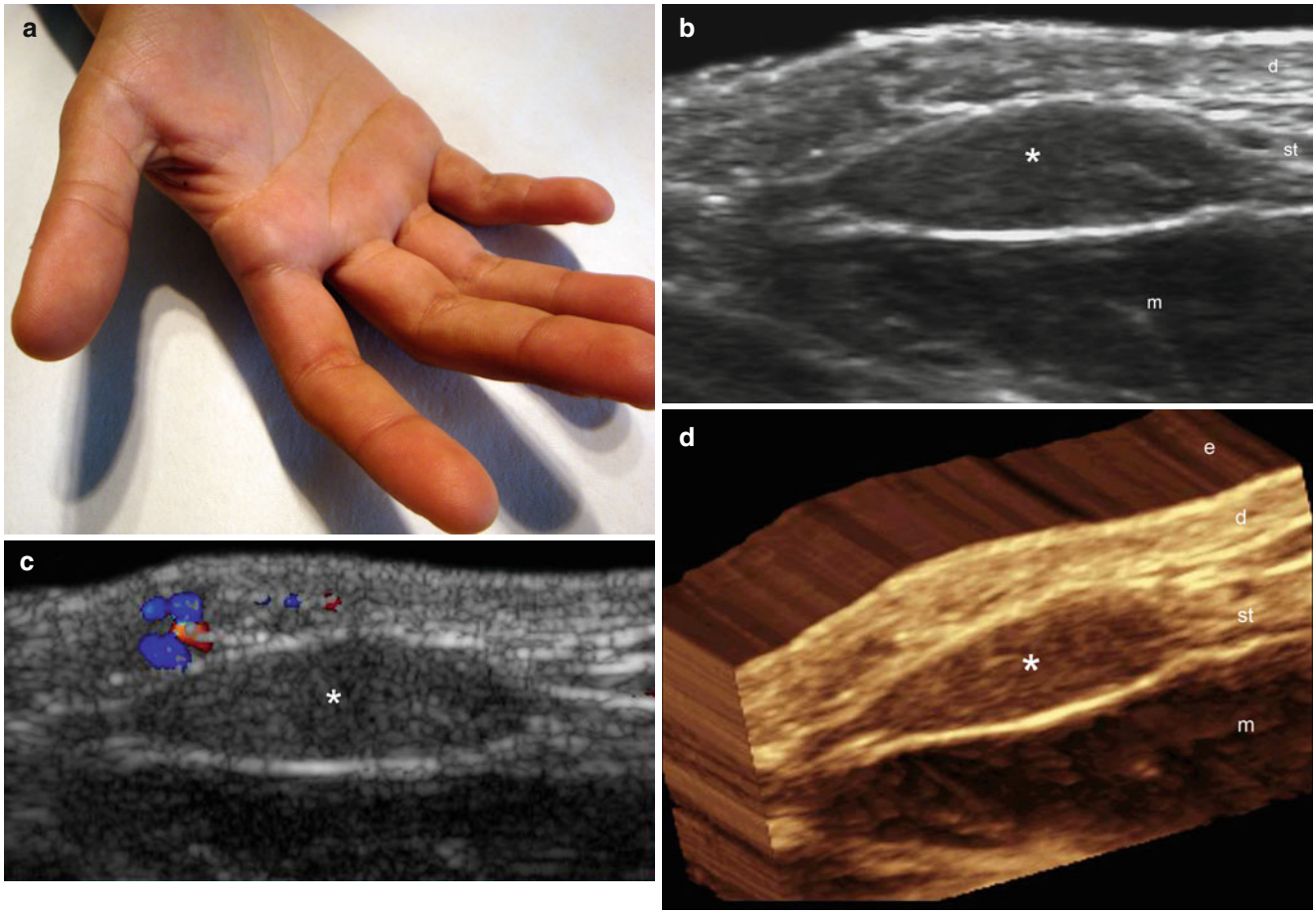

Fig. 5.36 (**a**–**d**) Localized neurofibroma. (**a**) The patient presented with a palpable lump in the right thenar eminence. (**b**) Grey scale ultrasound image (transverse view) shows well-defined, oval-shaped, hypoechoic nodule (*) in the subcutaneous tissue. An afferent hypoechoic tract is detected in the left side of the nodule. (**c**) Color Doppler ultrasound image (transverse view) demonstrates no signs of vascularity within the nodule. A few small vessels are detected in the dermis and upper subcutaneous tissue. (**d**) The nodule in 3D (5–8 s sweep reconstruction, transverse view). *Abbreviations*: *e* epidermis, *d* dermis, *st* subcutaneous tissue, *m* muscle

Tip

- Look for the afferent and efferent tract in localized neurofibromas. It is not always present, but may help.
- The "bag of worms" appearance in plexiform neurofibromas is a classic sonographic pattern that follows the course of the nerve tracts.
- Examine the patient and look for the cafe-au-lait spots. These clinical signs may direct you.

5.2.2.3.3 Neuroma

Neuromas are not true neurogenic tumors, and are composed of reactive proliferative hyperplastic reactions commonly secondary to peripheral nerve damage after trauma (acute or chronic) or surgery, such as amputation or partial transection. Neuromas are most commonly located in the lower extremities, followed by the head and neck. The oral cavity is also a frequent location after tooth extraction. Other sites include the radial nerve and the brachial plexus. Clinically, they may produce exquisite pain, numbness, discomfort, tingling, or electric shock-like symptoms.

Histologically, neuromas are composed of multiple and non-encapsulated axons, Schwann cells, endoneurial cells, and perineurial cells, surrounded by prominent scar tissue with dense collagen. Dystrophic calcifications are rarely seen in the lesional area.

On sonography, neuromas are usually located in the subcutaneous tissue. Traumatic neuromas caused by amputation tend to present a bulbous hypoechoic end continuous with the remnant neural tract. If the damage is produced by a chronic injury such as friction or irritation, neuromas tend to present as focal ill-defined and sometimes fusiform structures. On color Doppler ultrasound, neuromas are frequently hypovascular structures.

Morton's neuroma represents perineural fibrosis of the plantar digital nerve. Morton's neuroma occurs most frequently in the space between the third and fourth head of the metatarsal bones but can also affect other metatarsal spaces. A dynamic sonographic maneuver, by applying pressure with the fingers of the sonographer to the intermetatarsal space (dorsal or plantar aspects) may be needed for detecting Morton's neuromas. The probe should be positioned in the contrary aspect to the finger of the examiner. On sonography, Morton's neuroma presents a variable appearance that goes from well-defined hypoechoic rounded or oval-shaped lesions, to ill-defined hypoechoic structures. This variation can be produced by the degree of perineural fibrosis that involves the digital nerve [21, 32] (Fig. 5.37).

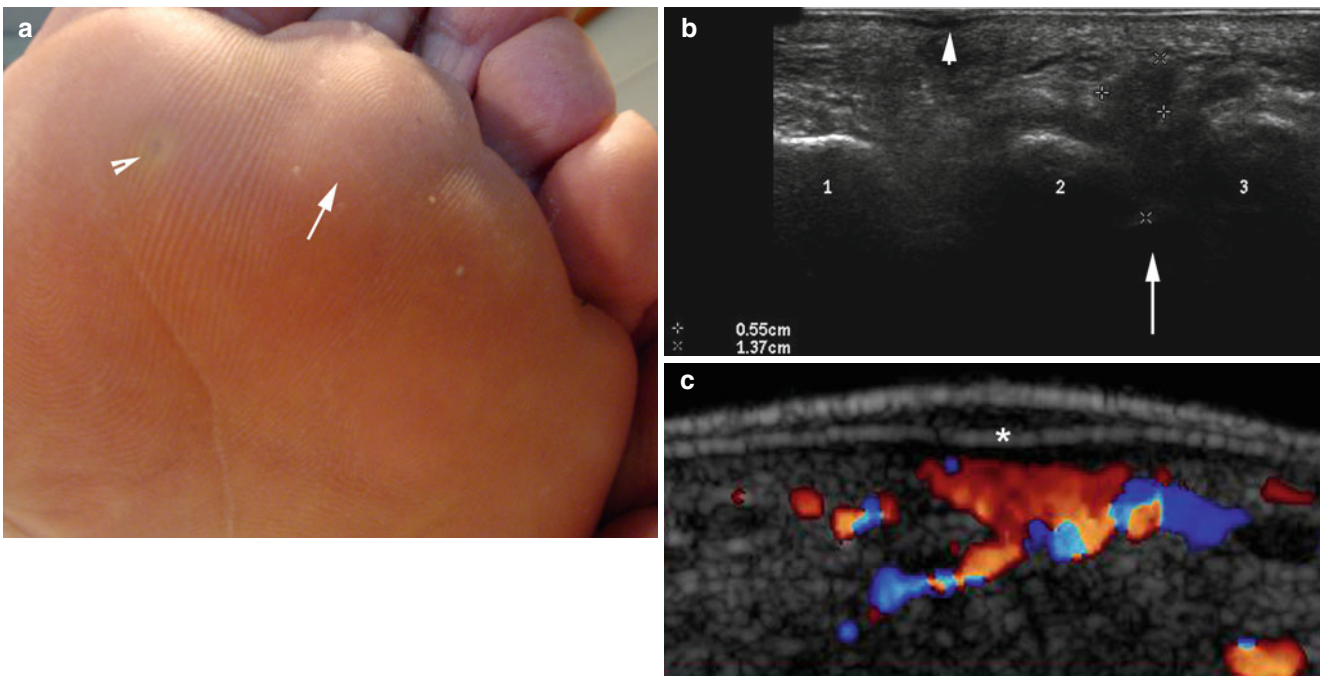

Fig. 5.37 (**a**–**c**) Morton's neuroma and plantar wart. (**a**) Clinical image shows a hyperkeratotic lesion (*arrowhead*) in the sole of the left foot. Nevertheless, the patient presented with exquisite pain in the second intermetarsal space (*arrow*, between the 2nd and 3rd metatarsal bones). (**b**) Grey scale ultrasound image (transverse view, metatarsal level) shows a 0.55×1.37 cm hypoechoic mass (*large arrow*) in the second intermetatarsal space. Notice the hypoechoic and fusiform-shaped structure in the epidermis and dermis of the first metatarsal space that corresponds to a concomitant plantar wart (*small arrow*). (**c**) Color Doppler ultrasound image (transverse view) shows signs of dermal hypervascularity in the plantar wart

Tips

- Traumatic neuromas can be painful, therefore, try to not press too hard with the probe for a long time and use more gel than usual. The patient will appreciate the gentleness.
- Morton's neuromas may not be able to be detected during a rest examination. A dynamic study specifically dedicated to looking for these pseudotumors should be performed.
- When examining patients who are suspected of having Morton's neuroma, keep in mind the possibility of differential diagnoses such as plantar warts and foreign bodies.

5.2.2.4 Tumors of the Pilosebaceous Unit

5.2.2.4.1 Pilomatrixoma

Pilomatrixomas, also known as pilomatricomas and calcifying epitheliomas of Malherbe, are tumors that arise from the hair matrix and appear clinically as slow growing firm to hard nodules, most commonly located in the head, neck, and extremities. Pilomatrixomas usually affect children and young adults and are typically flesh colored, but may also appear erythematous or bluish. They frequently appear as single nodules, but occasionally can present as multiple nodules. Clinical misdiagnosis has been reported in up to 56 % of cases and these benign tumors can easily mimic other common benign lesions, such as epidermal cysts, on physical examination.

Histologically, pilomatrixomas are composed of lobules conformed by basaloid and ghost cells, eosinophilic keratinous debris, and calcifications. A fibrous pseudocapsule of compressed connective tissue usually surrounds the lobules.

The classic appearance on ultrasound is a target lesion characterized by a round-shaped and/or lobulated nodule with a hypoechoic rim and hyperechoic center located in the dermis and subcutaneous tissue. Commonly, the center shows hyperechoic deposits that correspond to calcium deposits. The degree of calcification in pilomatrixomas is variable and can range from a low presence of calcium to completely calcified structures. Nevertheless, on sonography the presence of calcium is a key element for diagnosing pilomatrixomas, and has been reported in 68–80 % of the cases. Additionally, there is a cystic variant of pilomatrixomas characterized by anechoic fluid and septa that separate the rim from the center, usually as a result of hemorrhage.

On color Doppler ultrasound, pilomatrixomas can present a variable degree of vascularity, going from hypovascular to hypervascular. In cases with prominent vascularity, clinical signs can be confusing and can be mistaken for hemangioma; therefore, sonography may help to perform the differential diagnosis between these entities [33–38] (Figs. 5.38, 5.39, 5.40, 5.41, and 5.42).

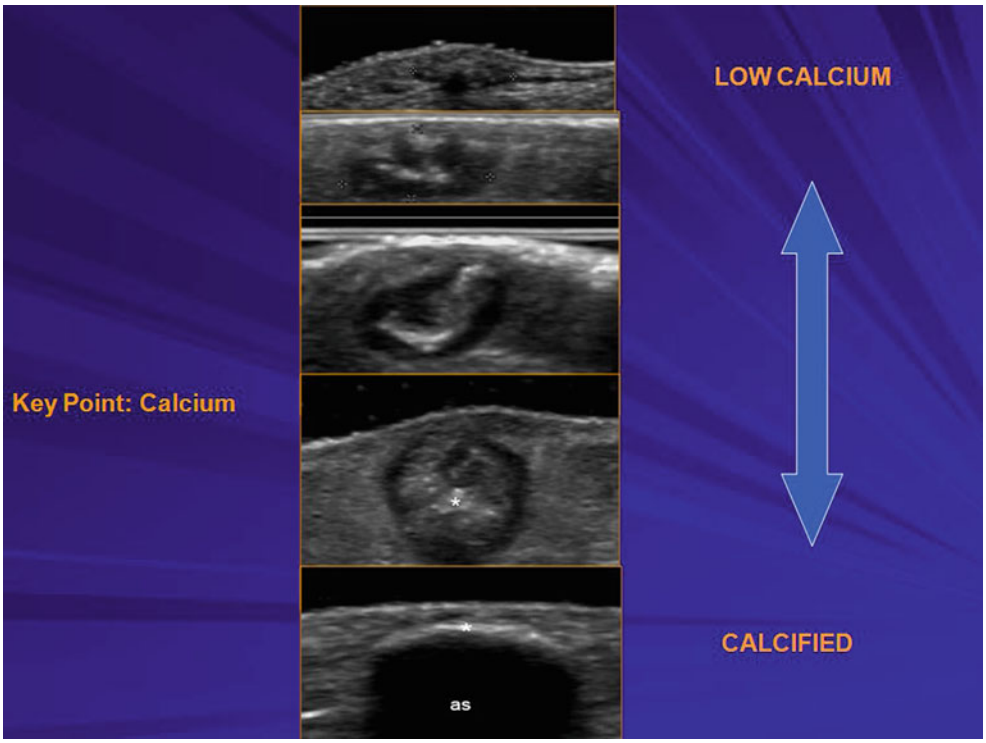

Fig. 5.38 Variable sonographic appearances of pilomatrixomas going from low calcium deposits (*top*) to completely calcified (*bottom*)

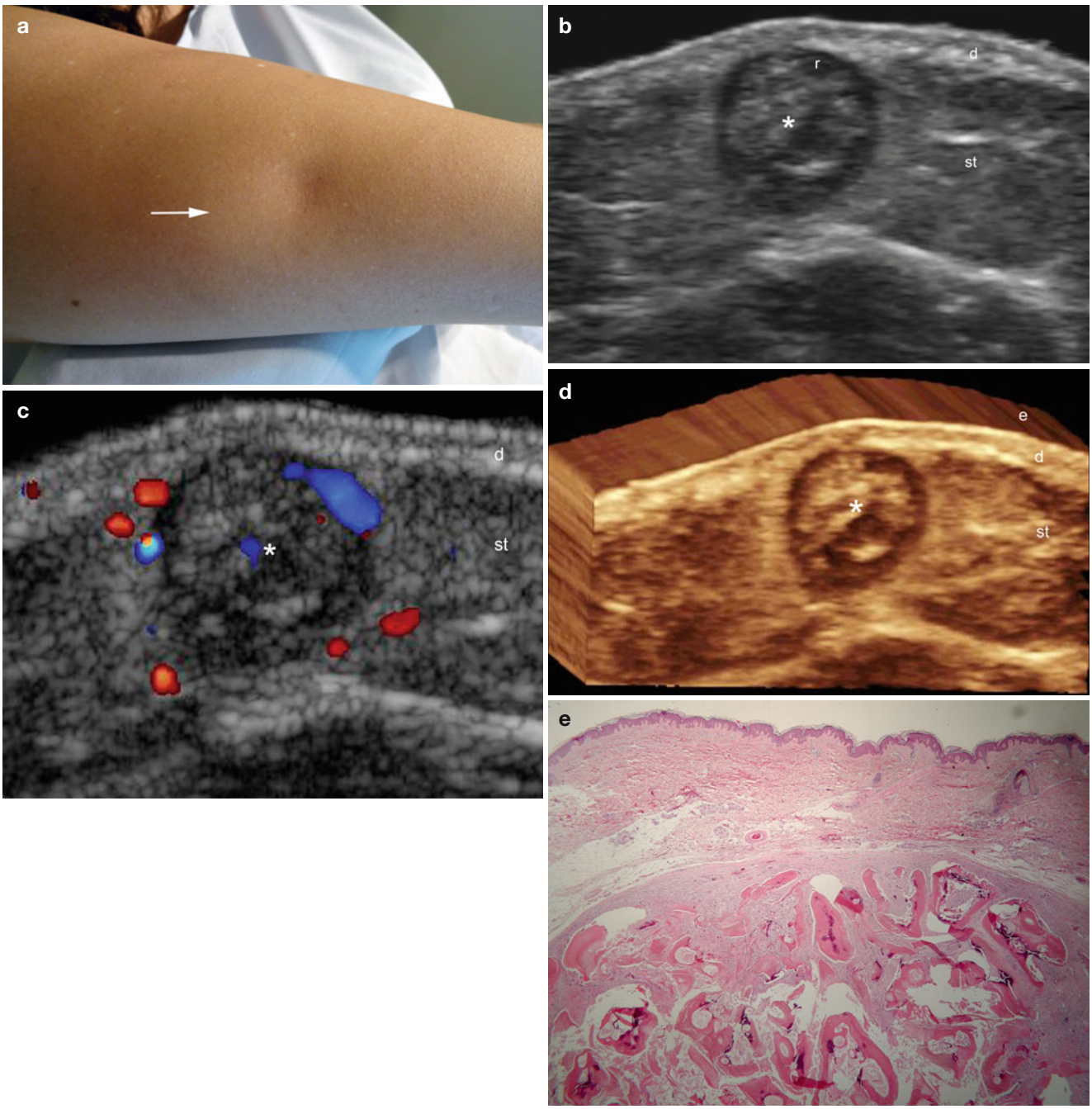

Fig. 5.39 (**a**–**e**) Pilomatrixoma. (**a**) Palpable lump in the dorsal right arm (*arrow*). (**b**) Grey scale ultrasound image (transverse view) shows a well-defined round-shaped subcutaneous solid nodule that presents a hypoechoic rim (*r*) and hyperechoic center (*, calcium deposits). This is the classic "target appearance" of pilomatrixomas. (**c**) Color Doppler ultrasound image (transverse view) demonstrates increased vascularity in the periphery and within the nodule (*). (**d**) The lesion (*) in 3D (5–8 s sweep, transverse view reconstruction). (**e**) Histology (HE 40× zoom courtesy of Dr. Laura Carreño): proliferation of eosinophilic ghost cells with calcium deposits and surrounded by a fibrous stroma. *Abbreviations*: *e* epidermis, *d* dermis, *st* subcutaneous tissue

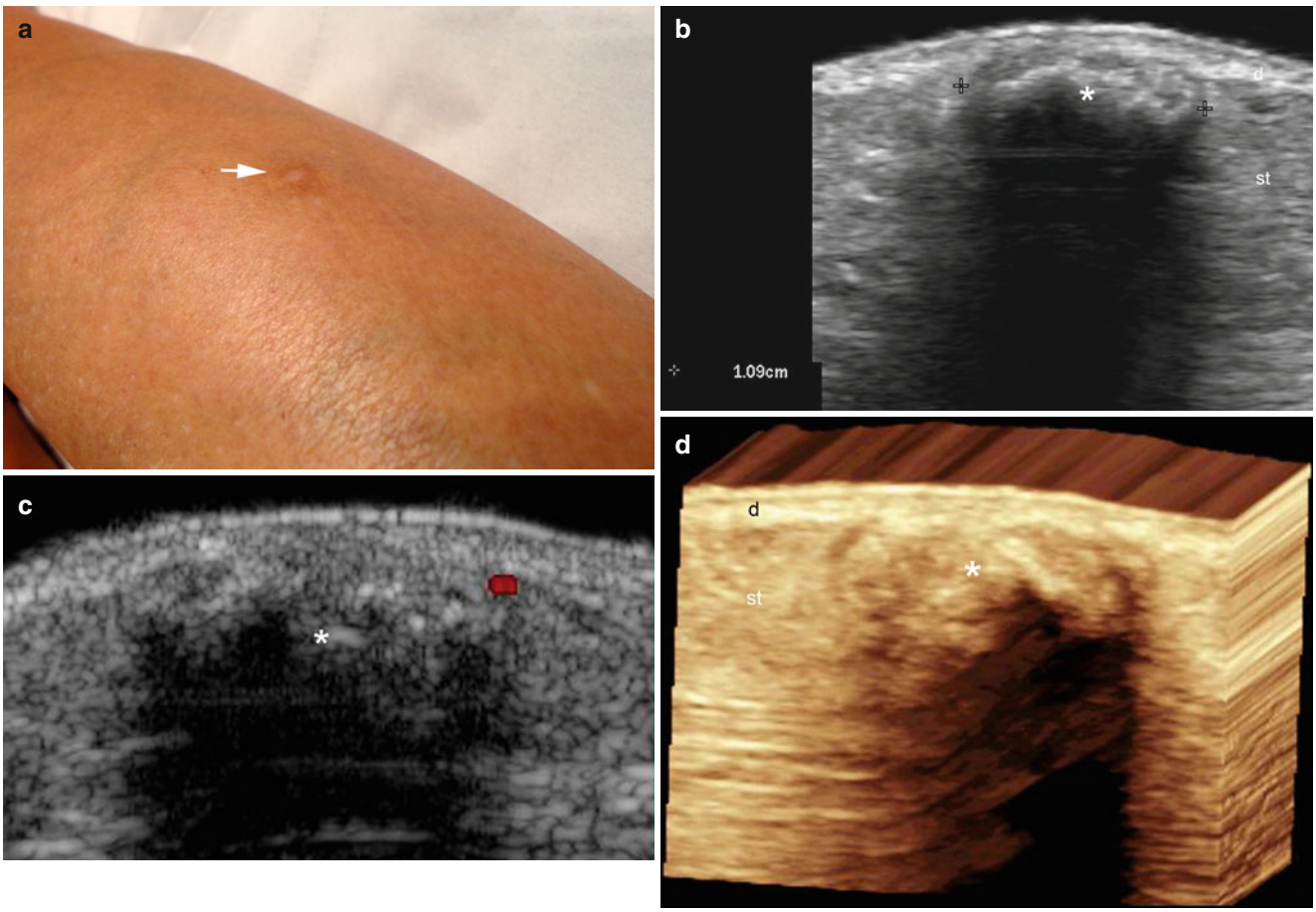

Fig. 5.40 (**a**–**d**) Pilomatrixoma. (**a**) Clinical photograph shows a skin-colored lump (*arrow*) in the lateral aspect of the left leg. (**b**) Grey scale ultrasound image (transverse view) demonstrates a 1.0 cm "target-like" nodule (*) with a hypoechoic rim and hyperechoic calcified center located in the subcutaneous tissue that slightly bulges into the dermis. Notice the posterior acoustic shadowing artifact generated by the calcium deposits. (**c**) Color Doppler ultrasound image (transverse view) shows a small vessel in the periphery of the lesion (*). (**d**) 3D reconstruction of the nodule (*, transverse view, 5–8 s sweep). *Abbreviations*: *d* dermis, *st* subcutaneous tissue

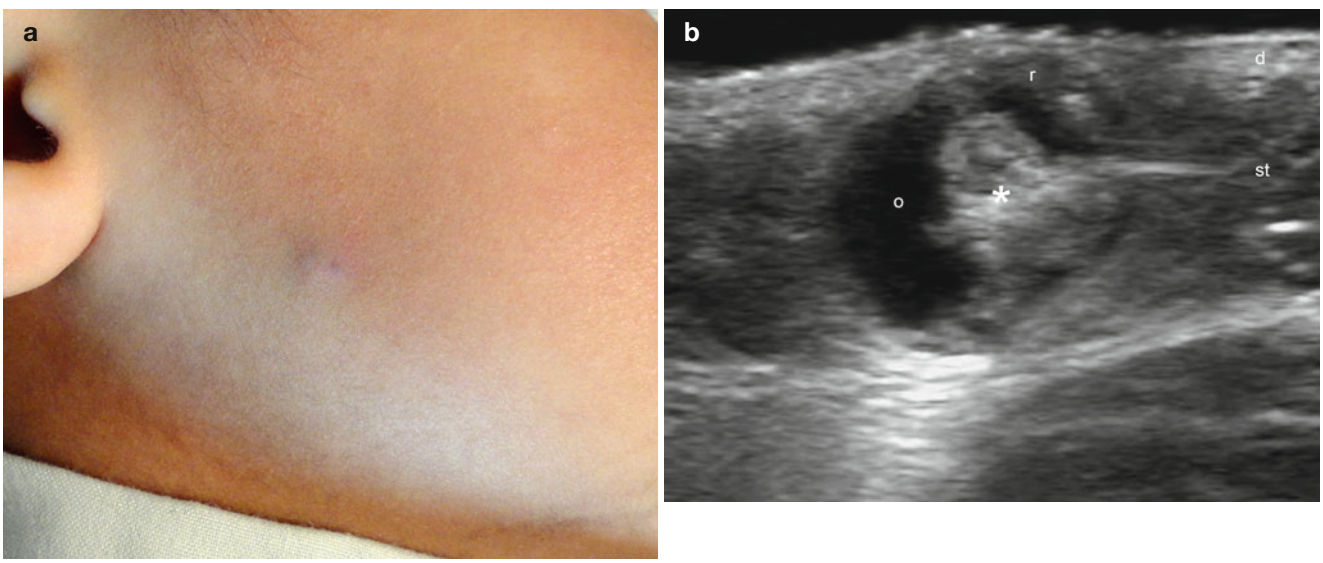

Fig. 5.41 (**a**–**e**) Cystic pilomatrixoma. (**a**) Clinical image shows an erythematous and bluish bump in the right cheek. (**b**) Grey scale ultrasound image (transverse view) demonstrates a nodule with a hypoechoic rim (*r*) and a mixed echogenicity center composed by hypoechoic (*, solid) and anechoic (*o*, cystic) areas. The nodule is located in the dermis and subcutaneous tissue. Tiny hyperechoic spots are detected within the hypoechoic central part. (**c**) Color Doppler ultrasound image (transverse view) shows increased vascularity in the periphery of the lesion. (**d**) The nodule in 3D (5–8 s sweep reconstruction). (**e**) Histology (HE 400× zoom, courtesy of Dr. Laura Carreño): eosinophilic ghost cells with calcium deposits and surrounded by a fibrous stroma. *Abbreviations*: *e* epidermis, *d* dermis, *st* subcutaneous tissue

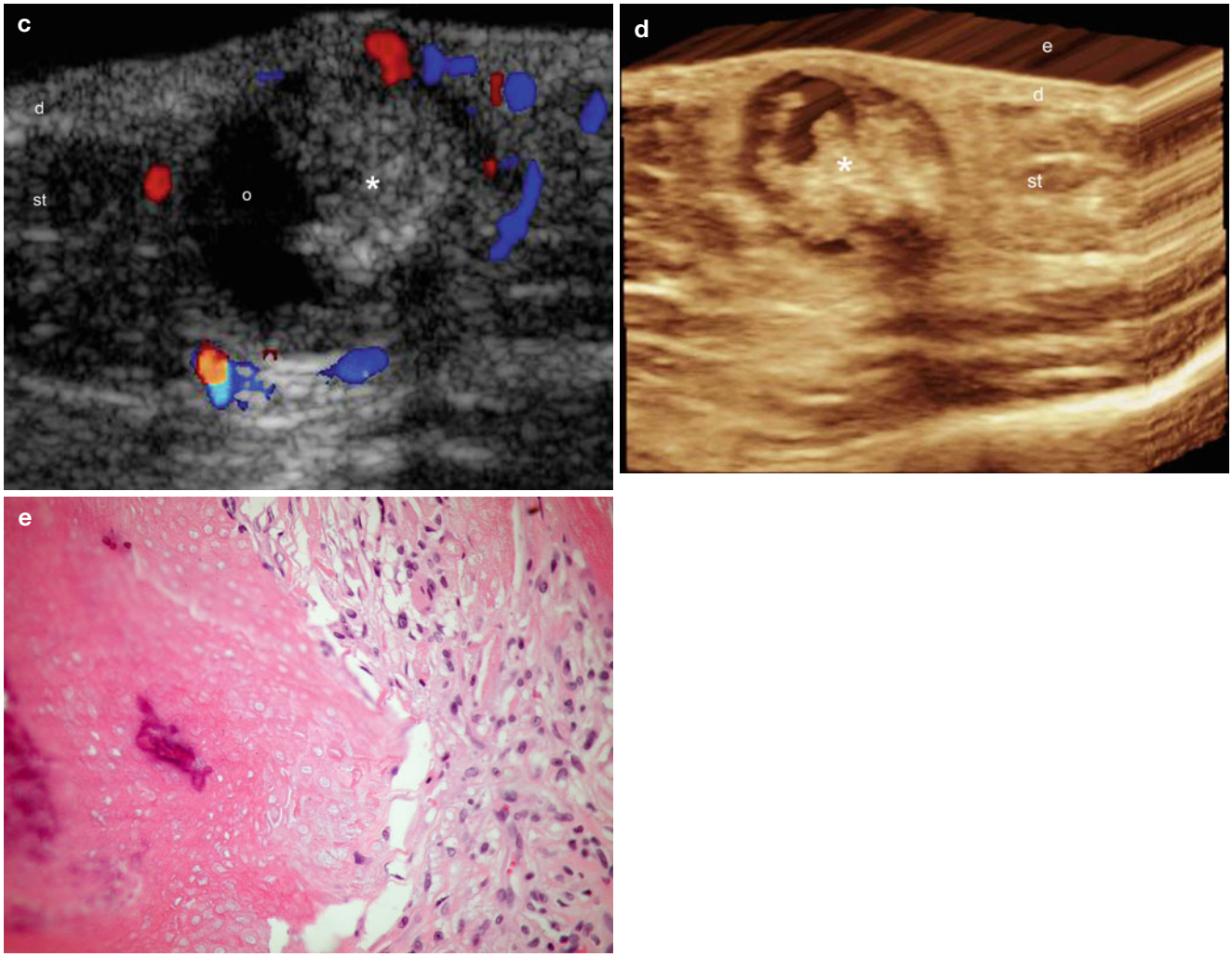

Fig. 5.41 (continued)

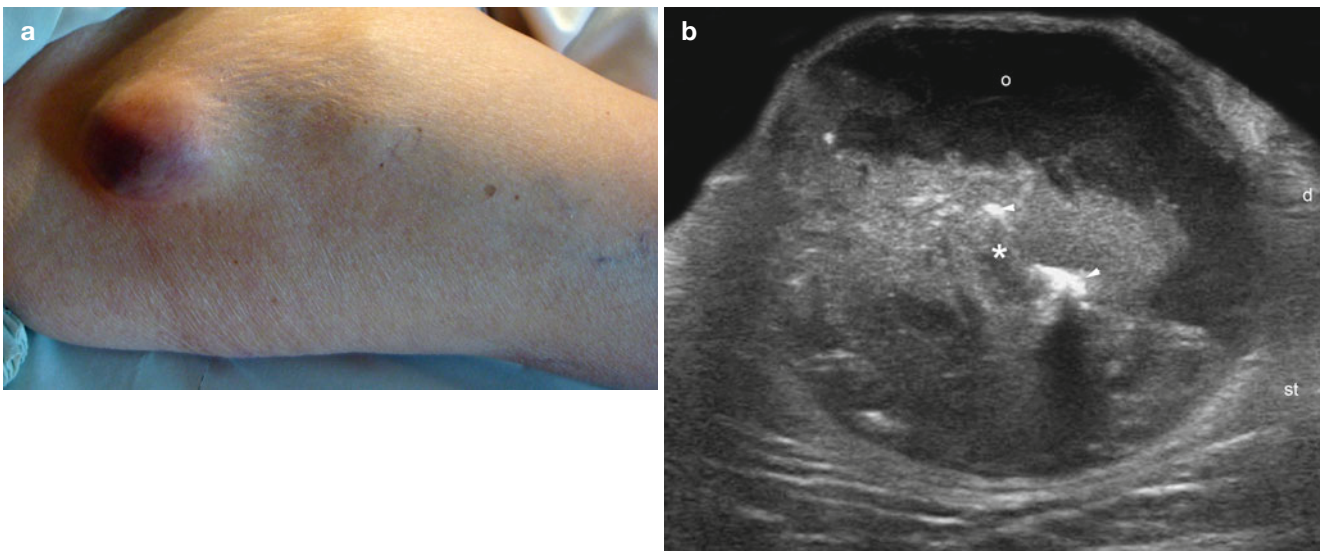

Fig. 5.42 (**a**–**f**). Cystic pilomatrixoma. (**a**) Erythematous lump in the lateral aspect of the right thigh. (**b**–**d**) Grey scale ultrasound images (**b** transverse view; **c** longitudinal view; **d** zoomed longitudinal view) demonstrate a mixed echogenicity mass in the dermis and subcutaneous tissue. There is a hypoechoic solid area (*) with a hyperechoic spot that corresponds to a calcium deposit (*arrowhead*), and an anechoic cystic zone (*o*) within the same lesion. A hyperechoic linear inner septa is also detected (*arrow*) in the mass. (**e**) Color Doppler ultrasound image (transverse view) shows no signs of vascularity in the lesional area. (**f**) The mass in 3D (5–8 s sweep reconstruction). *Abbreviations*: *d* dermis, *st* subcutaneous tissue

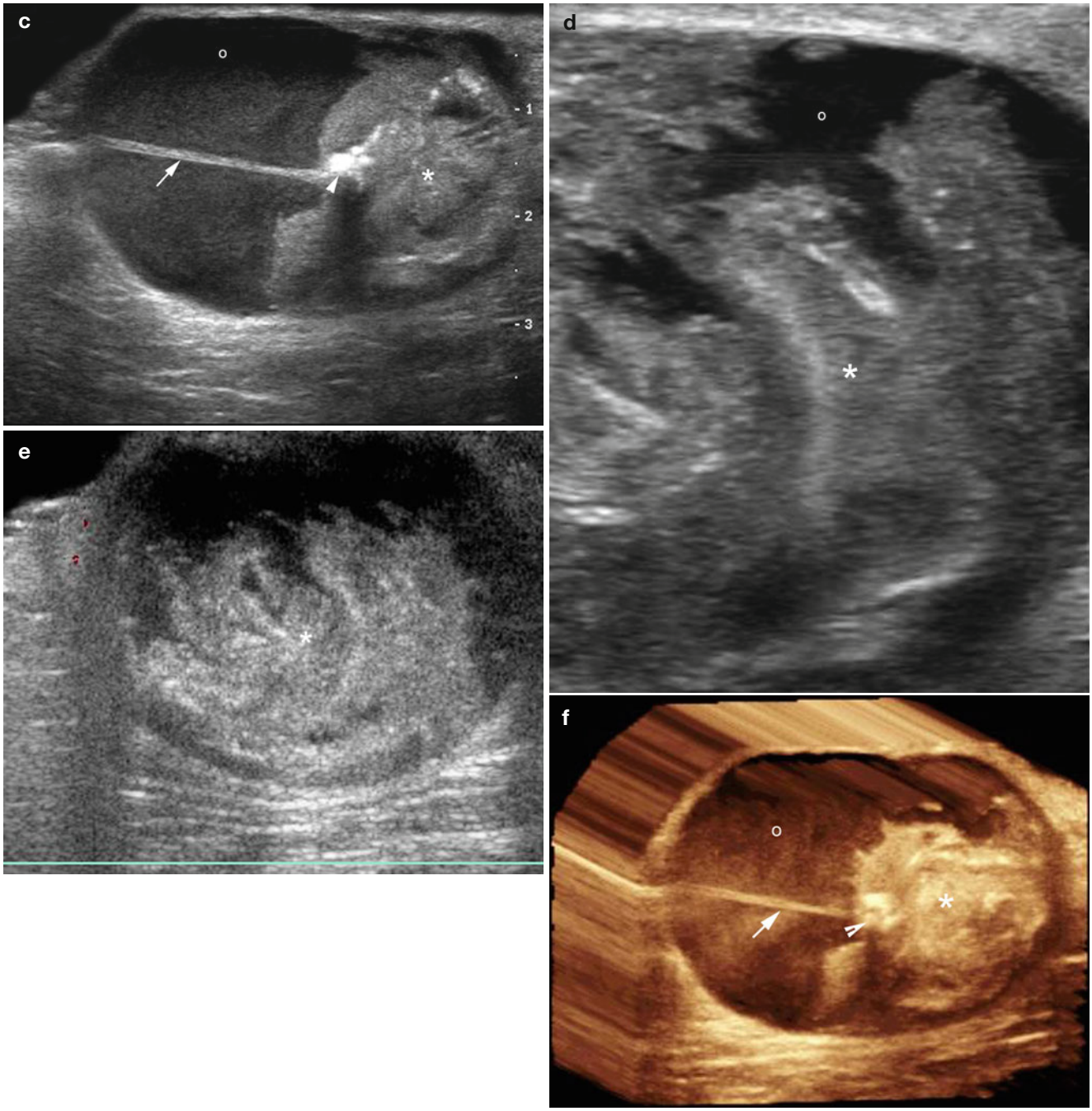

Fig. 5.42 (continued)

Tip

- The presence of hyperechoic spots in the center of the nodules traduces the amount of the calcium component, and the calcification by itself conforms a key element for diagnosing pilomatrixomas.

5.2.2.4.2 Tricoepithelioma

Tricoepithelioma is a hamartomatous entity that derives from hair matrix components and is clinically characterized by multiple painless flesh-colored or erythematous papules with a symmetrical distribution on the face. Germline mutations in the cylindromatosis gene have been described in families with trichoepitheliomas. Thus, Brooke-Spiegler syndrome, an autosomal dominant predisposition to skin appendageal neoplasms, includes trichoepitheliomas and other tumors such as cylindromas and/or spiradenomas. Histologically, tricoepitheliomas show lobules of basaloid cells and keratocysts embedded in dense connective tissue and may present primitives hair bulbs.

On sonography, this benign condition presents as a diffuse hypoechoic plaque-like thickening of the dermis with multiple and tiny hyperechoic spots. These tumors usually show hypovascularity on color Doppler ultrasound [39, 40] (Fig. 5.43).

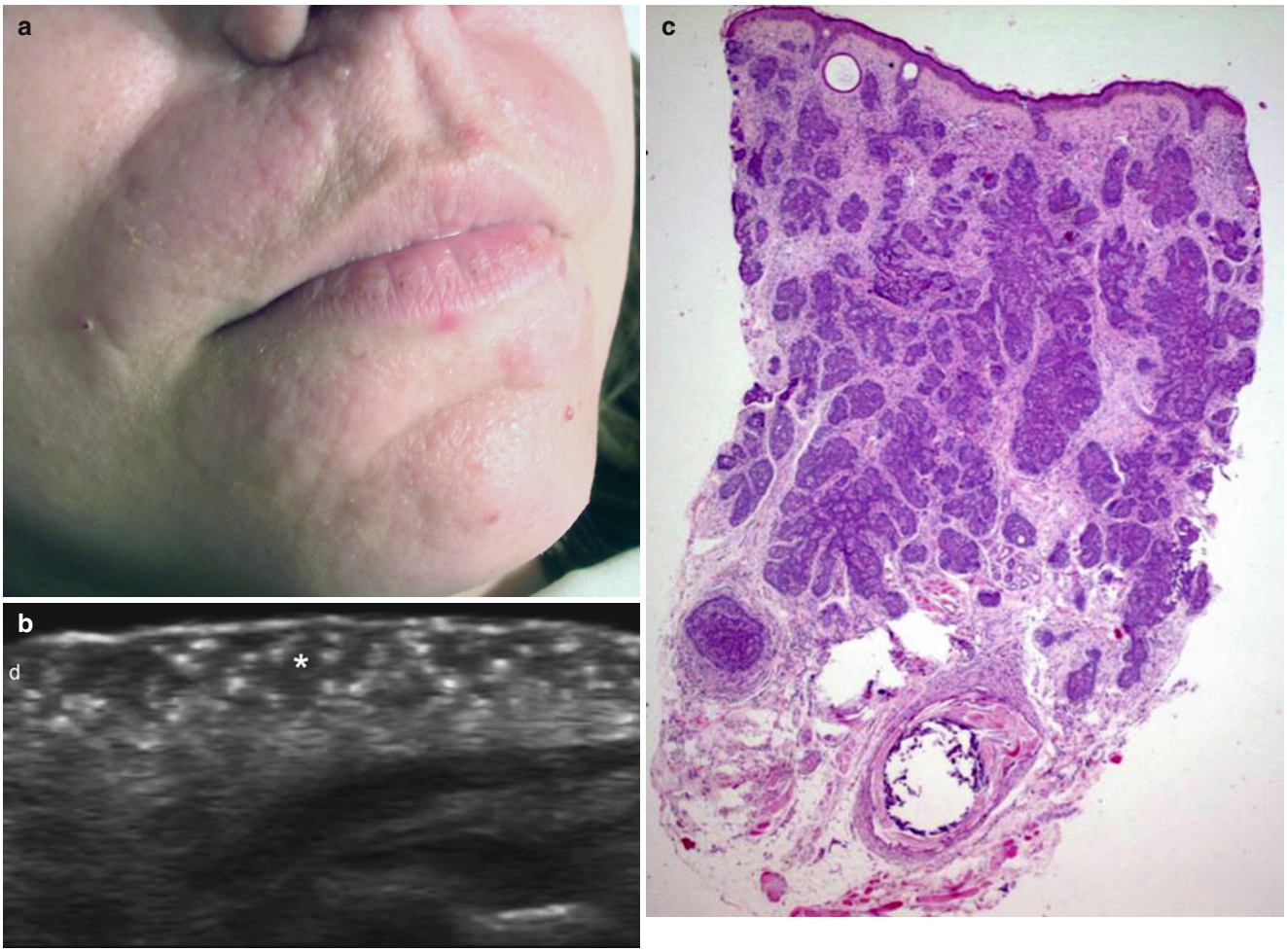

Fig. 5.43 (**a**–**c**) Tricoepithelioma. (**a**) Clinical photograph shows hyperechoic swelling and papules in the lower face. (**b**) Grey scale ultrasound image (right nasofold line and upper lip, transverse view) shows a thick hypoechoic dermal plaque-like lesion (*) with hyperechoic spots. (**c**) Histology (HE 20× zoom, courtesy of Dr. Laura Carreño): dermis with nests of basaloid cells, calcifications, germs and papillae structures

5.2.2.5 Other origins

5.2.2.5.1 Mastocytoma

Mastocytomas are tumors that are conformed by mast cells, and are most commonly found in young children. They represent 10 % of mastocytosis diseases that also include other forms of mastocytosis, such as urticaria pigmentosa, diffuse cutaneous mastocytosis, and systemic mastocytosis. They appear clinically as a solitary reddish brown, pink, or yellow nodule or plaque most frequently on the extremities or torso but these entities can also affect the head. Spontaneous involution is common and they are usually not associated with systemic involvement [41, 42].

On histology, mast cells with abundant eosinophilic cytoplasm and eosinophils are detected in the dermis. Subepidermal vesiculation and edema of the papillary dermis may also be seen [43].

On sonography, solitary mastocytomas present as hypoechoic band-like, oval or fusiform-shaped dermal lesions that usually follow the axis of the skin layers. On color Doppler ultrasound, there is a variable pattern of blood flow going from hypovascular to hypervascular lesions (Fig. 5.44).

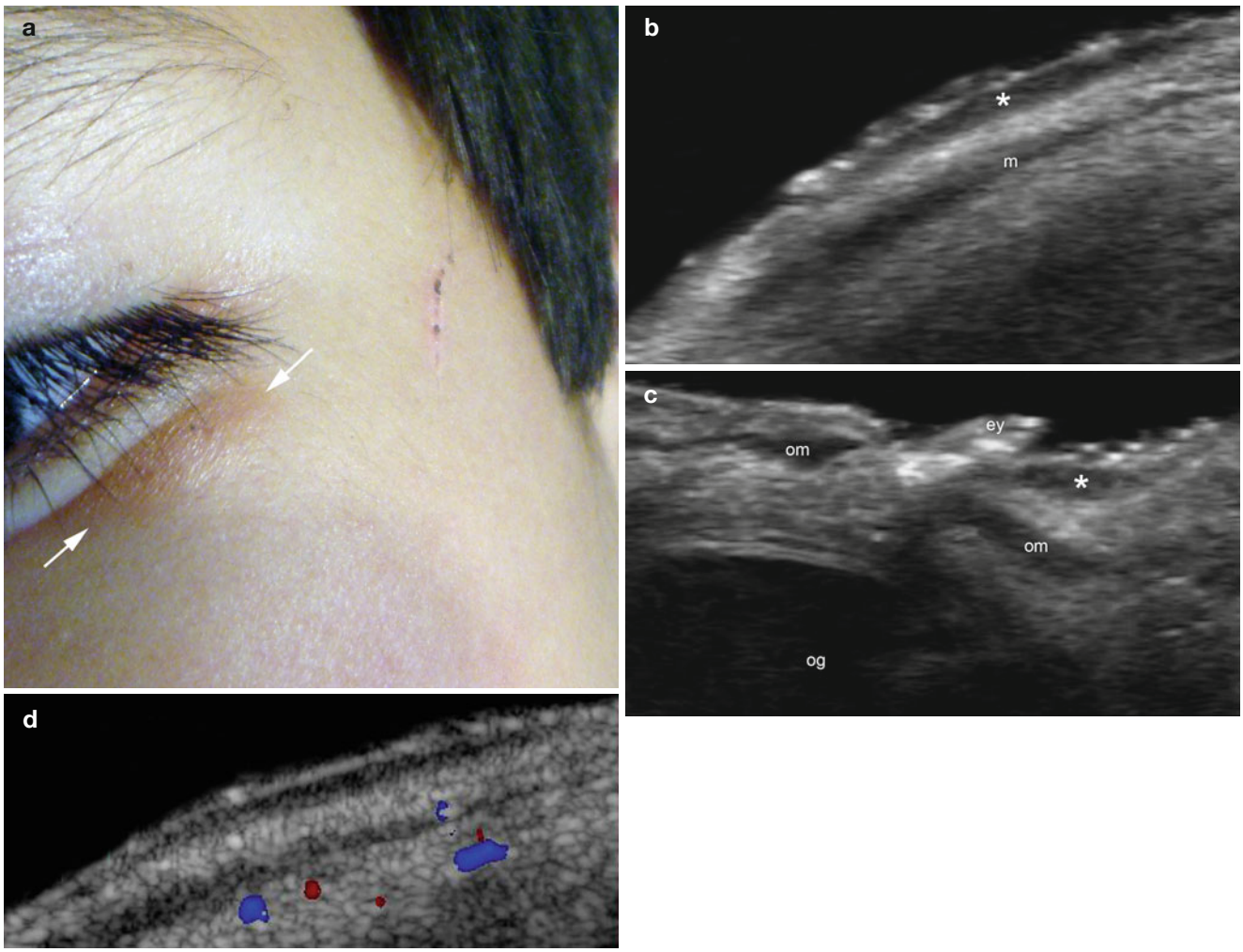

Fig. 5.44 (**a**–**d**) Solitary mastocytoma. (**a**) Clinical photograph shows light brown plaque (*arrows*) in the left lower eyelid. (**b**, **c**) Grey scale ultrasound images (**b** transverse view; **c** longitudinal view) demonstrate a hypoechoic dermal plaque (*) that follows the axis of the skin layers. (**d**) Color Doppler ultrasound image (transverse view) shows lack of vascularity in the lesional area. *Abbreviations*: *m* orbicularis muscle, *ey* eyelashes, *og* ocular globe

5.2.2.5.2 Cutaneous Lymphoid Hyperplasia

Cutaneous lymphoid hyperplasia (CLH), also known as pseudolymphoma, pseudolymphoma of Spiegler and Fendt, sarcoidosis of Spiegler and Fendt, Spiegler–Fendt, borrelial lymphocytoma, lymphadenosis benigna cutis, and lymphocytoma cutis. CLH is composed of benign hyperplastic polyclonal lymphoid infiltrates. Therefore, CLH correlates with a reactive inflammatory response and commonly presents after insect bites or trauma. On physical examination, CLH is characterized by erythematous, plum or bluish-colored nodules and patches, predominantly on the face, earlobe, chest, and extremities. Lesions are usually single in number and children are affected the most. Histologically, CLH shows dense lymphoid infiltrates with conspicuous germinal centers. On sonography, lesions show as oval or fusiform hypoechoic lesions located in the dermis. On color Doppler ultrasound, CLH can present variable vascularity going from hypo- to hypervascular [44] (Figs. 5.45 and 5.46).

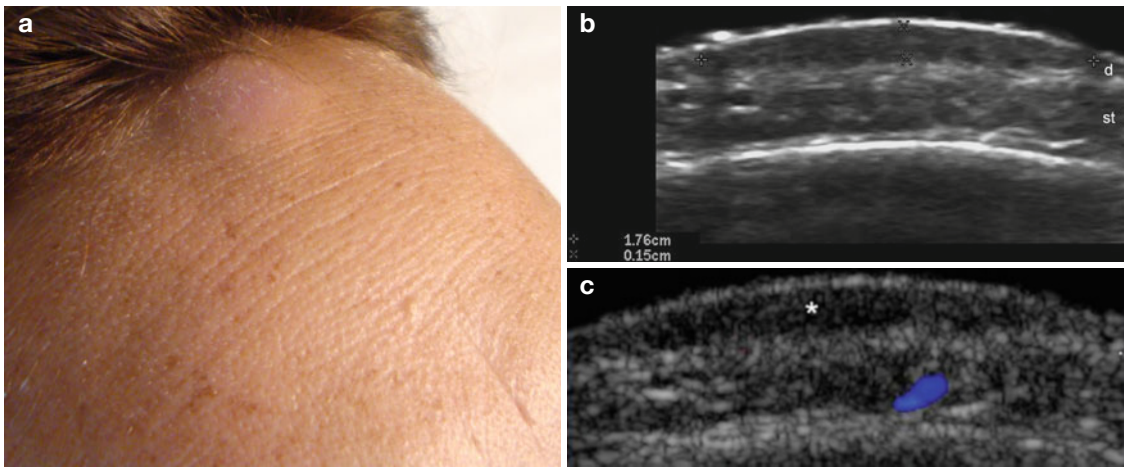

Fig. 5.45 (**a**–**c**) Cutaneous lymphoid hyperplasia (lymphocytoma cutis, pseudolymphoma). (**a**) Clinical photograph shows erythematous swelling in the frontal region. (**b**) Grey scale ultrasound image (transverse view) demonstrates an oval-shaped hypoechoic lesion (*) located in the dermis. (**c**) Color Doppler ultrasound image (transverse view) shows no detection of vascularity within the lesion

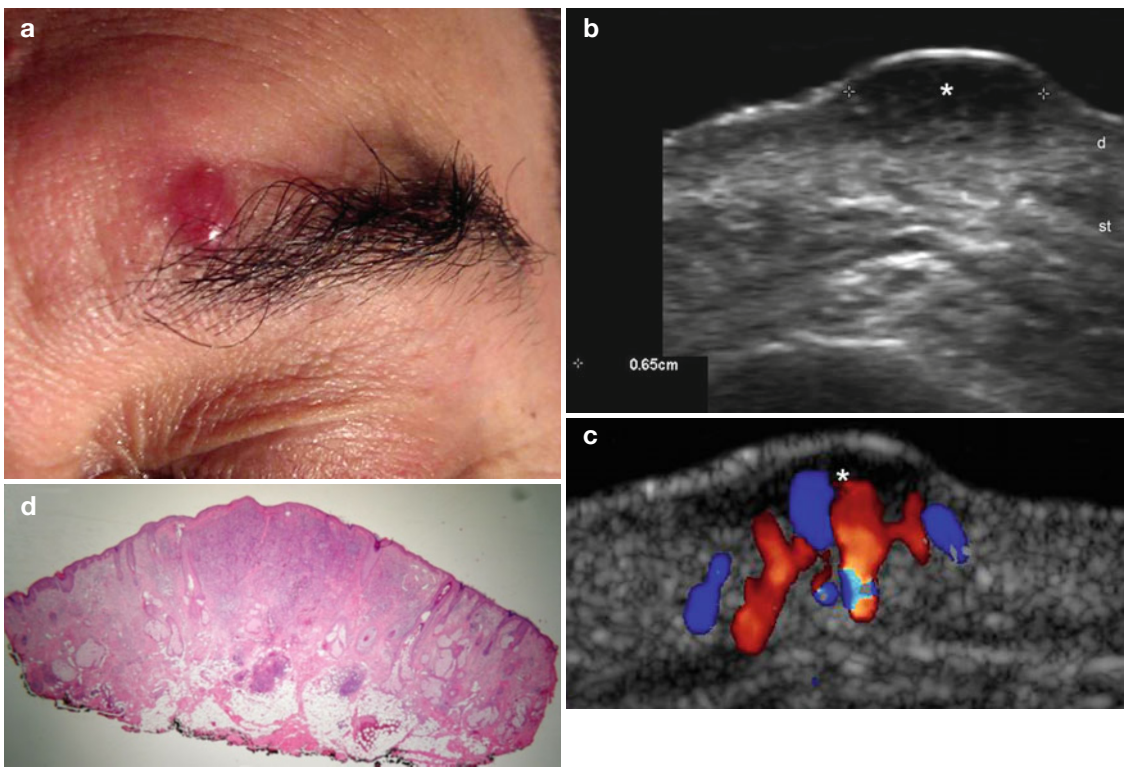

Fig. 5.46 (**a**–**d**) Cutaneous lymphoid hyperplasia (lymphocytoma cutis, pseudolymphoma). (**a**) Clinical image of erythematous papule in the medial aspect of the left eyebrow region. (**b**) Grey scale ultrasound image (transverse view) demonstrates a 6.5 mm oval-shaped, hypoechoic lesion (*, between markers) located in the dermis and upper subcutaneous tissue. (**c**) Color Doppler ultrasound image (transverse view) shows increased blood flow at the bottom of the lesion. (**d**) Histology (HE 20× zoom, courtesy of Dr. Ivo Sazunic): diffuse and nodular inflammatory infiltrate in dermis and subcutaneous tissue. *Abbreviations*: *d* dermis, *st* subcutaneous tissue

5.2.2.5.3 Keloid

Keloids are pseudotumors that are reactive proliferations produced by an abnormal healing process with exhuberant scarring that tend to grow and extend beyond the borders of the original injury. In contrast, hypertrophic scars usually conserve the borders of the previous wound and tend to decrease over time. Histologically, keloids present spindle cells and thick bundles of eosinophilic hyalinized collagen. On ultrasound, they present as hypoechoic or heterogeneous echogenicity plaque-like structures or pseudonodule(s) located in the dermis that also present a hyperechoic linear fibrillar pattern. These hyperechoic lines within the lesions usually correlate well with the presence of thick bundles of collagen fibers. Occasionally, hypoechoic dermal and/or subcutaneous fistulous tracts or branches that emerge from, or connect to, the lesions can be found. On color Doppler ultrasound, a variable degree of vascularity can be detected in the lesional region. The presence of blood flow usually tend to correlate well with the activity of the keloids [45, 46] (Figs. 5.47, 5.48, 5.49, 5.50, and 5.51).

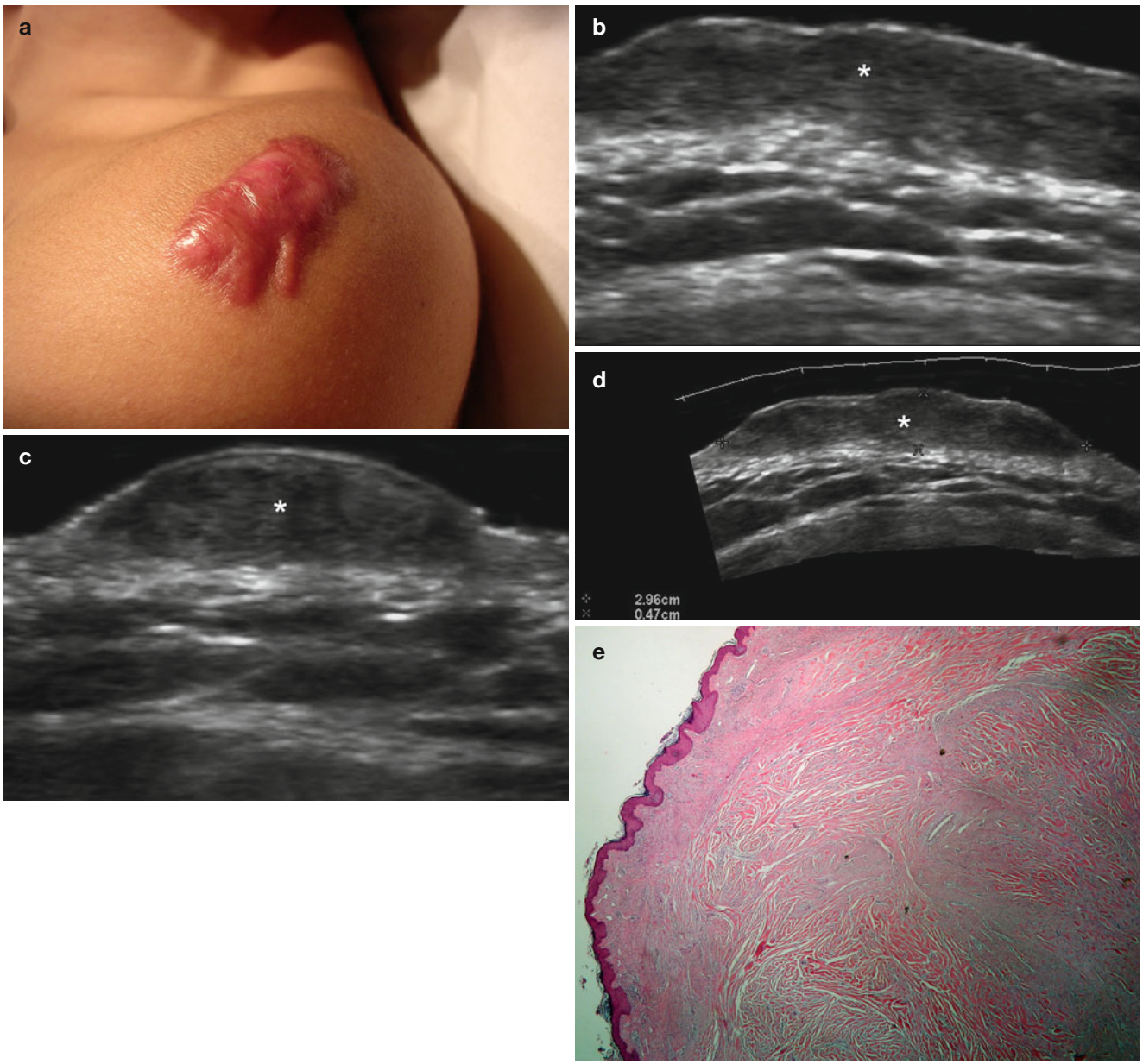

Fig. 5.47 (**a**–**e**) Keloid. (**a**) Clinical photograph shows erythematous lump in the lateral aspect of the left arm. (**b**–**d**) Grey scale ultrasound images (**b** longitudinal view; **c** transverse view; **d** extended field of longitudinal view) demonstrate a 2.96×0.47 cm hypoechoic thick plaque-like structure (*) located in the dermis that presents a linear fibrillar pattern. (**e**) Histology (HE 100× zoom, courtesy of Dr. Claudia Morales): dermis with keloidal bundles of collagen

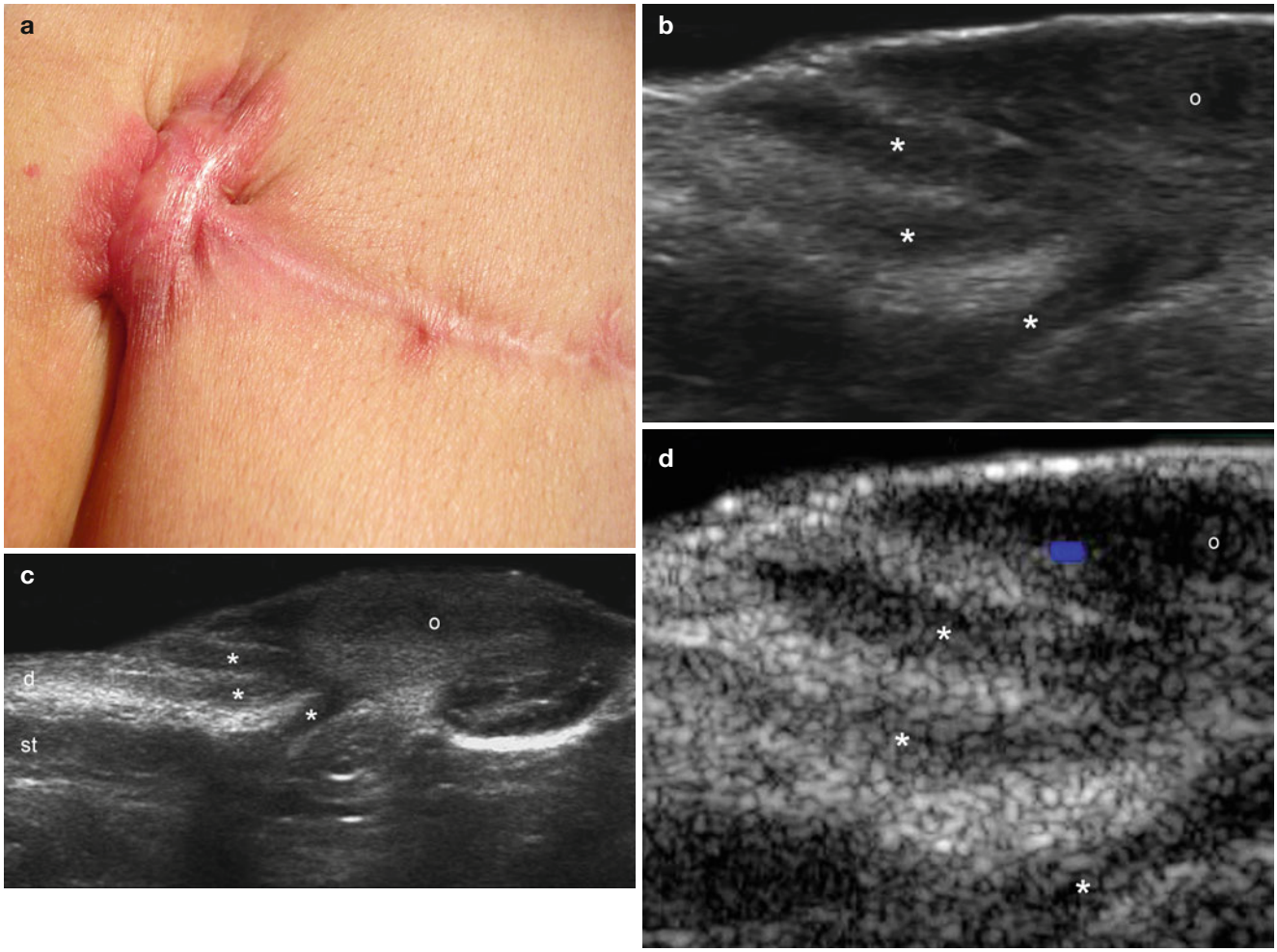

Fig. 5.48 (**a**–**d**) Keloid. (**a**) Clinical image shows an erythematous lump in the upper part of a scar in the abdominal wall. (**b**, **c**) Grey scale ultrasound images (**b** zoomed and **c** extended field of transverse views) demonstrate an oval-shaped hypoechoic lesion (*o*) located in the dermis that presents a fibrillar pattern. Notice the three hypoechoic fistulous branches with scarring (*) that emerge from the lesional area (*left side* of the figure). (**d**) Color Doppler ultrasound image (transverse view) shows scarce blood flow within the lesion

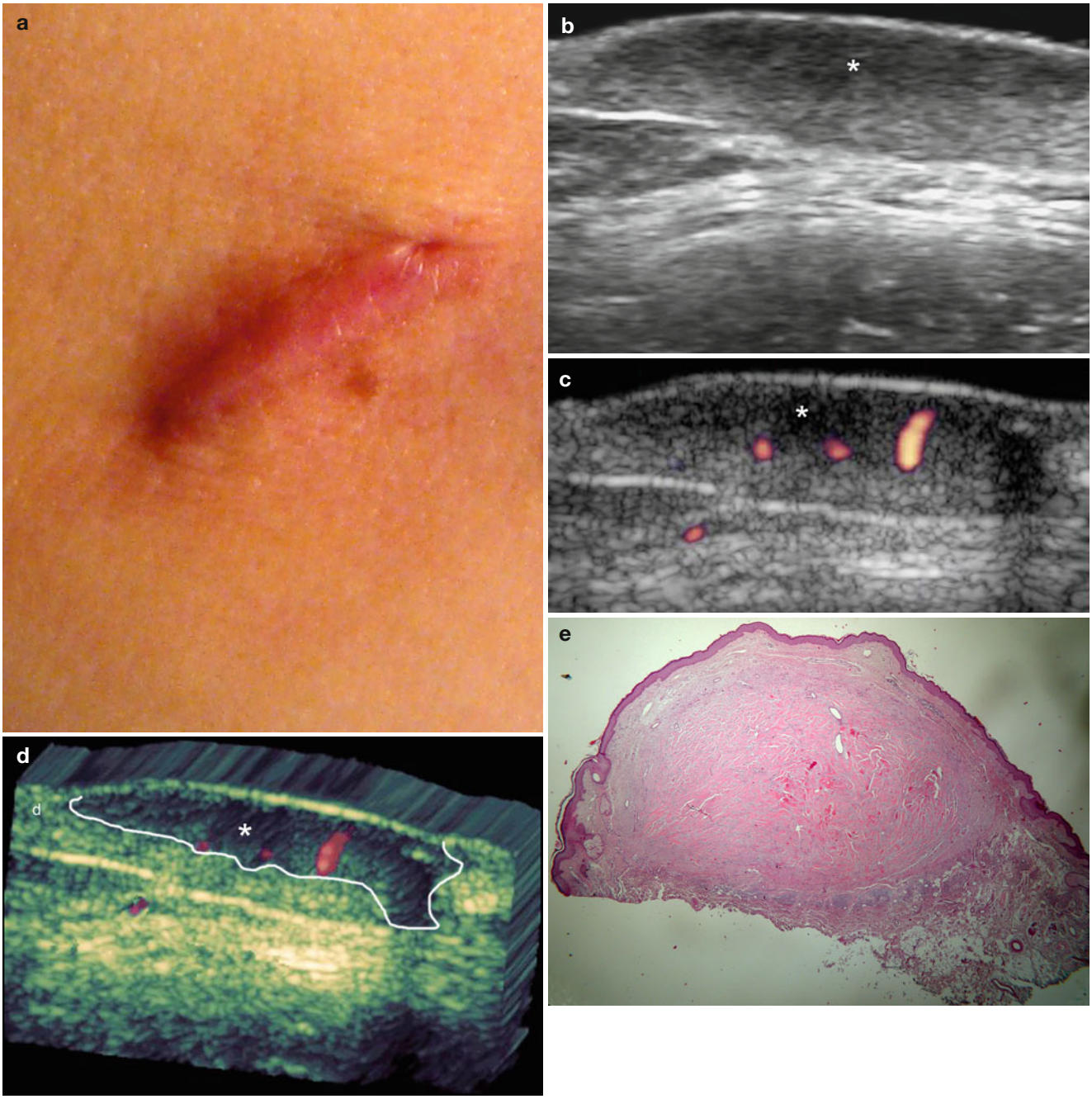

Fig. 5.49 (**a**–**e**) Active keloid. (**a**) Clinical erythematous swelling in the left dorsal region. (**b**) Grey scale ultrasound image (transverse view) demonstrates a hypoechoic thickening (*) of the dermis with a fibrillar pattern. (**c**) Power angio Doppler ultrasound image (transverse view) shows increased blood flow within the lesion (*). (**d**) 3D power angio Doppler reconstruction ultrasound image (transverse view) demonstrating the lesion (*, outlined, 5–8 s sweep). (**e**) Histology (HE 20× zoom, courtesy of Dr. Claudia Morales): dermal proliferation of keloidal bundles of collagen. *Abbreviation*: *d* dermis

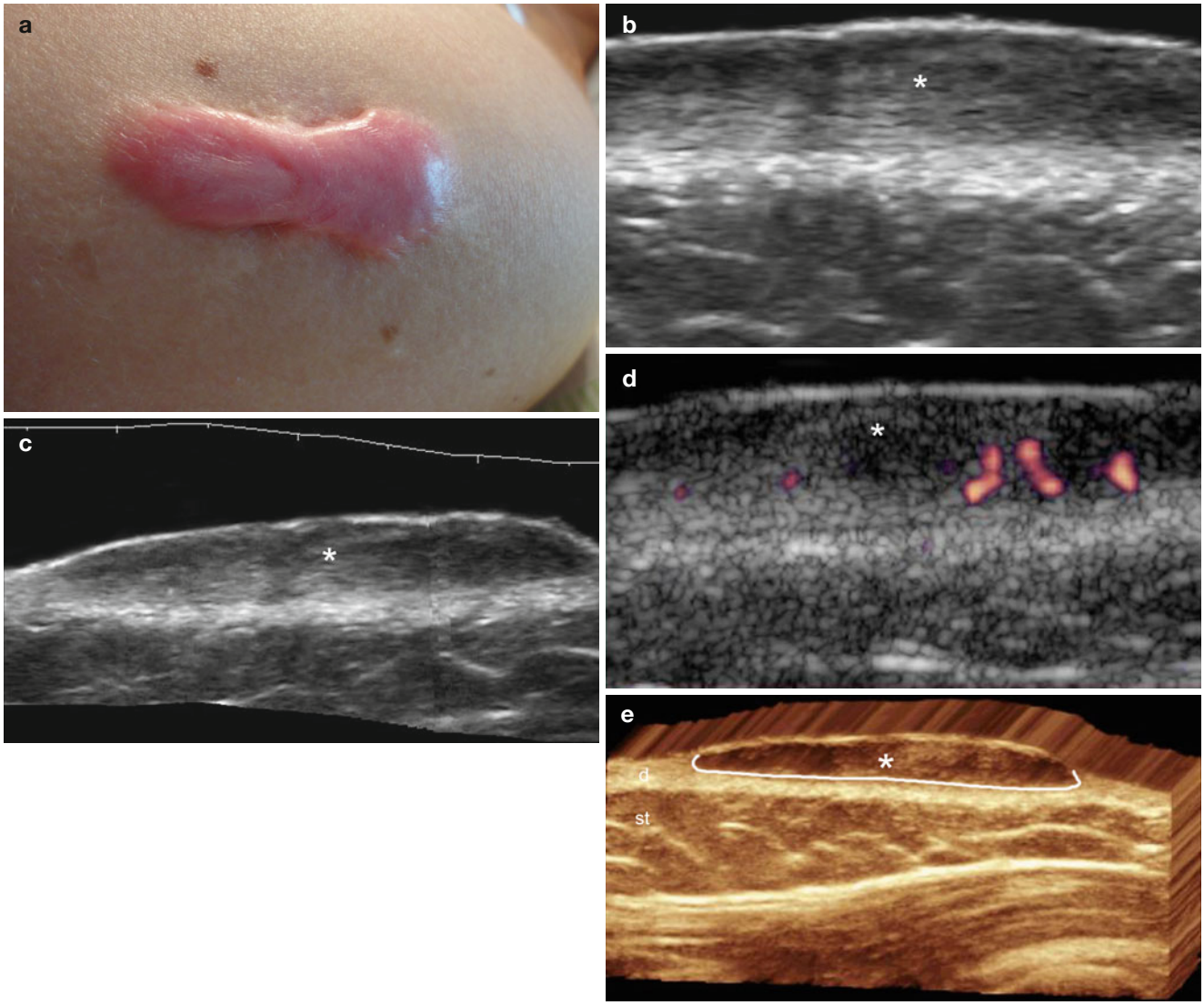

Fig. 5.50 (**a**–**e**) Active keloid. (**a**) Clinical photograph shows erythematous swelling in the left arm. (**b**, **c**) Grey scale ultrasound images (**b** zoomed and **c** extended field longitudinal view images) demonstrate hypoechoic thickening of the dermis with a fibrillar pattern. (**d**) Power angio Doppler ultrasound image shows increased blood flow within the lesion. (**e**) The lesion in 3D (*, outlined). *Abbreviations*: *d* dermis, *st* subcutaneous tissue

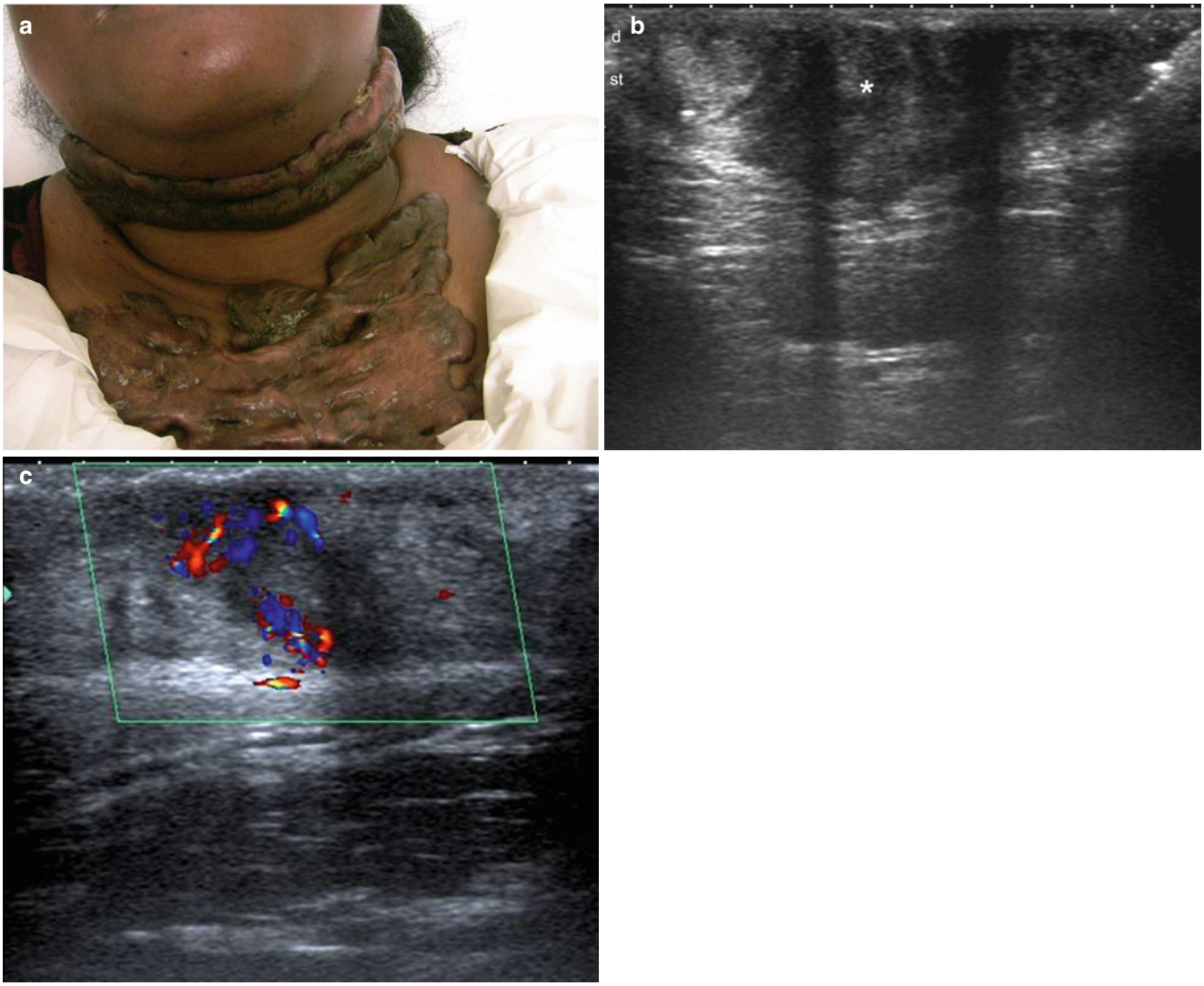

Fig. 5.51 (**a**–**c**) Active keloid. (**a**) Clinical photograph shows multiple pigmented lumps in the neck and upper thoracic regions. (**b**) Grey scale ultrasound image (longitudinal view) demonstrates hypoechoic and heterogeneous pseudonodular structure (*) with a fibrillar pattern. (**c**) Color Doppler ultrasound image (longitudinal view) demonstrates increased blood flow within the lesion

Tip

- Look for the hyperechoic lines in the dermis when dealing with keloids.
- Color Doppler ultrasound may unveil the increased vascularity within the lesions that tend to correlate well with the activity of the keloid.

Pitfall

- Hypertrophic scars (HS) can be clinically confused with keloids, but HS are commonly hypoechoic and they usually do not present hyperechoic lines and do not extend beyond the borders of the original injury.

5.2.2.5.4 Hydrocystoma

Hydrocystomas, also named cystadenomas, Moll's gland cysts, or sudoriferous cysts, correspond to cystic forms of sweat gland adenomas that result from proliferation of the apocrine or eccrine secretory glands and/or obstruction of the sweat gland ducts immediately above the glandular coil within the deep dermal layer following an inflammatory process or trauma. They can present as single or multiple lesions of varying sizes, generally situated on the head (mainly on the face): the forehead, cheeks, and eyelids (glands of Moll), with the outer canthus of the lower eyelid being the most common site of presentation.

Hydrocystomas can be separated in two histological types: apocrine and eccrine. The apocrine hydrocystoma or cyst of Moll involves the eyelid border and generally appears following an obstruction of the apocrine secretory duct of the gland of Moll (apocrine and eccrine sweat glands). Clinically, they consist of small, painless, round, translucent, fluid-filled vesicles. The eccrine hydrocystoma or cyst of the eccrine sweat glands originates from the eccrine sweat gland, also known as the gland of Moll, and is a rare disorder. It generally presents as multiple cutaneous vesicles on the lower eyelid. The most common site for cysts of Moll is close to the eyelashes, the route of lacrimal drainage, while the most common site for eccrine hydrocystomas is on the skin of the eyelid.

Histologically, apocrine hydrocystomas (Moll's cysts) present with multiple large cystic spaces and papillary projections in the dermis, covered by two layers of secretory cells. The innermost cells are columnar-shaped with eosinophilic cytoplasm with typical apical projections and decapitation secretion, periodic acid-Schiff-positive, and diastase-resistant granules. Eccrine hydrocystomas are retention cysts characterized by a single, partially collapsed cystic cavity in the dermis, with no papillary projections, surrounded by one or two layers of small cuboid epithelial cells. The content of the cysts sometimes has a brownish coloring because of the lipofuscin secreted by the neighboring cell, giving it a clinical appearance of blue nevus or melanoma [47].

The capability of differentiating these entities (apocrine vs eccrine origin) using sonography has not been reported. Moreover, both conditions present as well-defined anechoic subepidermal cystic structures without internal vascularity [48]. On ultrasound, hydrocystomas usually appear as well-defined, round or oval-shaped anechoic cystic structures. They can displace the epidermal layer upward and generate a slight secondary compression in the underlying muscles, especially when hydrocystomas affect the orbital region. On color Doppler ultrasound, they most commonly show no signs of vascularity (Fig. 5.52).

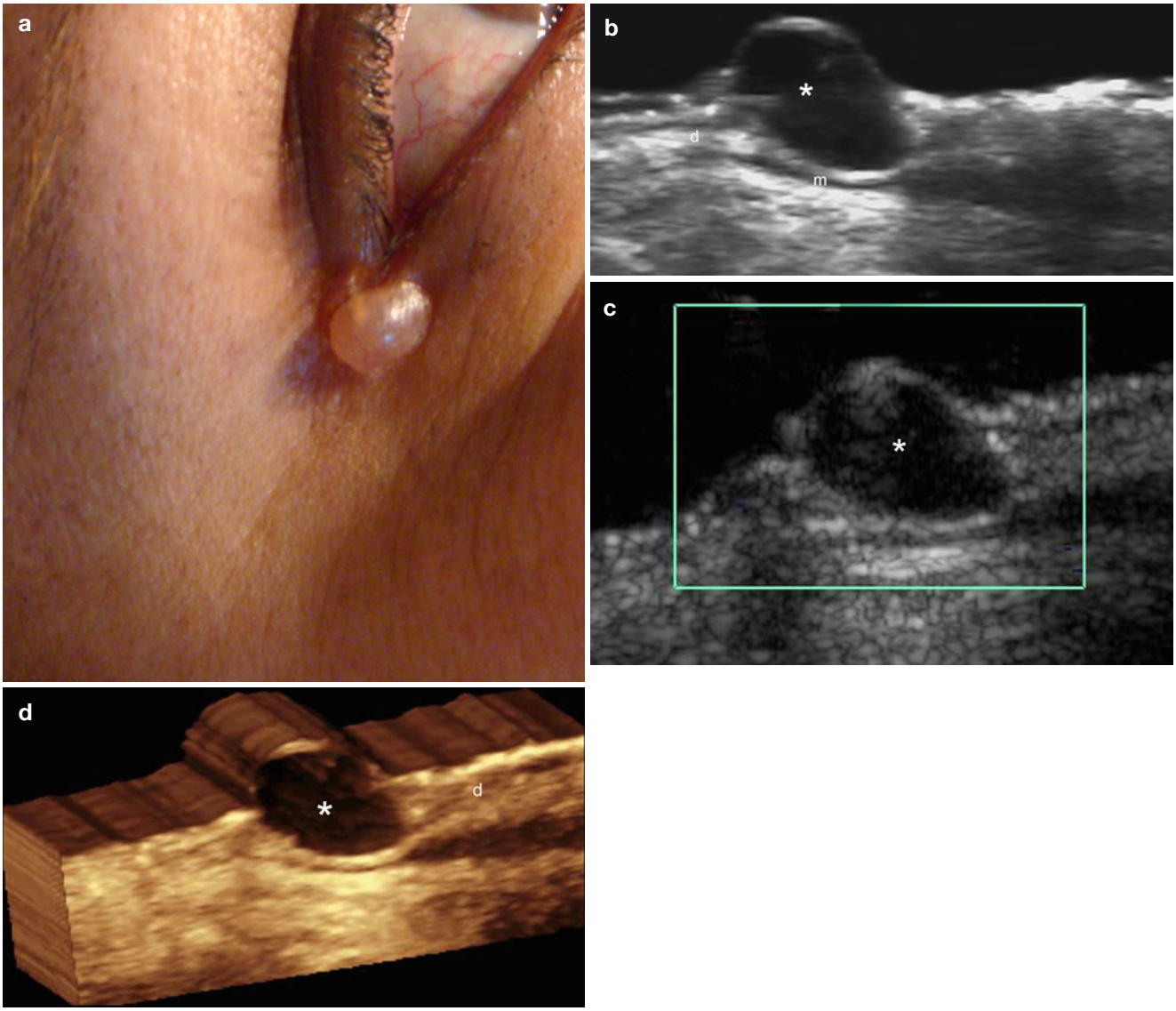

Fig. 5.52 (**a**–**d**) Hydrocystoma. (**a**) Clinical image shows a translucent, fluid-filled vesicle in the lateral canthus of the right eye. (**b**) Grey scale ultrasound image (transverse view) demonstrates a well-defined oval-shaped anechoic cystic lesion (*) located in the dermis (*d*). The cyst displaces the epidermal layer upward and generates a slight extrinsic compression in the underlying orbicularis oris muscle (*m*) of the lower eyelid. (**c**) Color Doppler ultrasound image (transverse view) shows no signs of vascularity in the lesional area. (**d**) 3D reconstruction of the hydrocystoma (5–8 s sweep, transverse view)

Conclusion

Sonography is a reliable imaging tool for studying common dermatologic benign entities. Using sonography can unveil information that is otherwise unavailable to the naked eye of a clinician.

References

1. Wortsman X, Wortsman J. Clinical usefulness of variable frequency ultrasound in localized lesions of the skin. J Am Acad Dermatol. 2010;62:247–56.
2. Wortsman X, Jemec G. Common inflammatory diseases of the skin: from the skin to the screen. Adv Psoriasis Inflamm Skin Dis. 2010;2:9–15.
3. Wortsman X. Common applications of dermatologic sonography. J Ultrasound Med. 2012;31:97–111.
4. Jin W, Ryu KN, Kim GY, Kim HC, Lee JH, Park JS. Sonographic findings of ruptured epidermal inclusion cysts in superficial soft tissue: emphasis on shapes, pericystic changes, and pericystic vascularity. J Ultrasound Med. 2008;27:171–6.
5. Kuwano Y, Ishizaki K, Watanabe R, Nanko H. Efficacy of diagnostic ultrasonography of lipomas, epidermal cysts, and ganglions. Arch Dermatol. 2009;145(7):761–4.
6. Mester J, Darwish M, Deshmukh SM. Steatocystoma multiplex of the breast: mammographic and sonographic findings. AJR. 1998;170:115–6.
7. Park KY, Oh KK, Noh TW. Steatocystoma multiplex: mammographic and sonographic manifestations. AJR. 2003;180:271–4.
8. Lee D, Chun JS, Hong SK, Seo JK, Choi JH, Koh JK, et al. Steatocystoma multiplex confined to the scalp with concurrent alopecia. Ann Dermatol. 2011;23 Suppl 2:S258–60.
9. Folpe AL, Reisenauer AK, Mentzel T, Rütten A, Solomon AR. Proliferating trichilemmal tumors: clinicopathologic evaluation is a guide to biologic behavior. J Cutan Pathol. 2003;30:492–8.
10. Chang SJ, Sims J, Murtagh FR, McCaffrey JC, Messina JL. Proliferating trichilemmal cysts of the scalp on CT. AJNR Am J Neuroradiol. 2006;27:712–4.
11. Al-Khateeb TH, Al-Masri NM, Al-Zoubi F. Cutaneous cysts of the head and neck. J Oral Maxillofac Surg. 2009;67:52–7.
12. Kirwan LA. Dermoid cyst of the lateral third of the eyebrow. Practitioner. 1985;229:771–3.
13. MacKee P, Calonje E, Granter S. Cutaneous cysts. In: MacKee P, Calonje E, Granter S, editors. Pathology of the skin with clinical correlation. 3rd ed. Philadelphia: Elsevier/Mosby; 2005. p. 1673–4.
14. Choudur HN, Hunjan JS, Howey JM, DeNardi F. Unusual presentation of a dermoid cyst in the ischiorectal fossa. Magnetic resonance imaging and ultrasound appearances. Skeletal Radiol. 2009;38:921–4.
15. Harlak A, Mentes O, Kilic S, Coskun K, Duman K, Yilmaz F. Sacrococcygeal pilonidal disease: analysis of previously proposed risk factors. Clinics (Sao Paulo). 2010;65:125–31.
16. Mentes O, Oysul A, Harlak A, Zeybek N, Kozak O, Tufan T. Ultrasonography accurately evaluates the dimension and shape of the pilonidal sinus. Clinics (Sao Paulo). 2009;64:189–92.
17. Inampudi P, Jacobson JA, Fessell DP, et al. Soft-tissue lipomas: accuracy of sonography in diagnosis with pathologic correlation. Radiology. 2004;233:763–7.
18. Hsu YC, Shih YY, Gao HW, Huang GS. Subcutaneous lipoma compression the common peroneal nerve and causing palsy: sonographic diagnosis. J Clin Ultrasound. 2010;38:97–9.
19. Yang DM, Kim HC, Lim JW, Jin W, Ryu CW, Kim GY, et al. Sonographic findings of groin masses. J Ultrasound Med. 2007;26:605–14.
20. Fornage BD, Tassin GB. Sonographic appearances of superficial soft tissue lipomas. J Clin Ultrasound. 1991;19:215–20.
21. MacKee P, Calonje E, Granter S. Tumors of fibrous and myofibroblastic tissue. In: MacKee P, Calonje E, Granter S, editors. Pathology of the skin with clinical correlation. 3rd ed. Philadelphia: Elsevier/Mosby; 2005. p. 1669–723.
22. Nikolaidis P, Gabriel HA, Lamba AR, Chan NG. Sonographic appearance of nodular fasciitis. J Ultrasound Med. 2006; 25(2):281–5.
23. Ramos R, Ureña A, Macía I, Rivas F, Ríus X, Armengol J. Elastofibroma dorsi: an uncommon and under-diagnosed tumour. Arch Bronconeumol. 2011;47:262–3.
24. Battaglia M, Vanel D, Pollastri P, Balladelli A, Alberghini M, Staals EL, et al. Imaging patterns in elastofibroma dorsi. Eur J Radiol. 2009;72:16–21.
25. Bianchi S, Martinoli C, Abdelwahab IF, Gandolfo N, Derchi LE, Damiani S. Elastofibroma dorsi: sonographic findings. AJR Am J Roentgenol. 1997;169:1113–5.
26. MacKee P, Calonje E, Granter S. Neurilemmoma. In: MacKee P, Calonje E, Granter S, editors. Pathology of the skin with clinical correlation. 3rd ed. Philadelphia: Elsevier/Mosby; 2005. p. 1669–723.
27. Lee JY, Kim SM, Fessell DP, Jacobson JA. Sonography of benign palpable masses of the elbow. J Ultrasound Med. 2011;30:1113–9.
28. Tsai WC, Chiou HJ, Chou YH, Wang HK, Chiou SY, Chang CY. Differentiation between schwannomas and neurofibromas in the extremities and superficial body: the role of high-resolution and color Doppler ultrasonography. J Ultrasound Med. 2008;27:161–6.
29. Hassell DS, Bancroft LW, Kransdorf MJ, Peterson JJ, Berquist TH, Murphey MD, et al. Imaging appearance of diffuse neurofibroma. AJR Am J Roentgenol. 2008;190:582–8.
30. Gruber H, Glodny B, Bendix N, Tzankov A, Peer S. High-resolution ultrasound of peripheral neurogenic tumors. Eur Radiol. 2007;17:2880–8.
31. Chen W, Jia JW, Wang JR. Soft tissue diffuse neurofibromas: sonographic findings. J Ultrasound Med. 2007;26:513–8.
32. Murphey MD, Smith WS, Smith SE, Kransdorf MJ, Temple HT. From the archives of the AFIP imaging of musculoskeletal neurogenic tumors: radiologic-pathologic correlation. Radiographics. 1999;19:1253–80.
33. Roche NA, Monstrey SJ, Matton GE. Pilomatricoma in children: common but often misdiagnosed. Acta Chir Belg. 2010; 110:250–4.
34. Hwang JY, Lee SW, Lee SM. The common ultrasonographic features of pilomatricoma. J Ultrasound Med. 2005;24:1397–402.
35. Choo HJ, Lee SJ, Lee YH, Lee JH, Oh M, Kim MH, et al. Pilomatricomas: the diagnostic value of ultrasound. Skeletal Radiol. 2010;39:243–50.
36. Solivetti FM, Elia F, Drusco A, Panetta C, Amantea A, Di Carlo A. Epithelioma of Malherbe: new ultrasound patterns. J Exp Clin Cancer Res. 2010;29:42.
37. Wortsman X, Wortsman J, Arellano J, Oroz J, Giugliano C, Benavides MI, et al. Pilomatrixomas presenting as vascular tumors on color Doppler ultrasound. J Pediatr Surg. 2010;45:2094–8.
38. Hassanein AH, Alomari AI, Schmidt BA, Greene AK. Pilomatrixoma imitating infantile hemangioma. J Craniofac Surg. 2011;22:734–6.
39. Blake PW, Toro JR. Update of cylindromatosis gene (CYLD) mutations in Brooke-Spiegler syndrome: novel insights into the role of deubiquitination in cell signaling. Hum Mutat. 2009;30:1025–36.
40. Brenn T, MacKee P. Tumors of the hair follicle. In: MacKee P, Calonje E, Granter S, editors. Pathology of the skin with clinical correlation. 3rd ed. Philadelphia: Elsevier/Mosby; 2005. p. 1519–63.

41. Bulat V, Mihi LL, Situm M, Buljan M, Blaji I, Pusi J. Most common clinical presentations of cutaneous mastocytosis. Acta Clin Croat. 2009;48:59–64.
42. Horny HP, Sotlar K, Valent P. Mastocytosis: state of the art. Pathobiology. 2007;74:121–32.
43. Jr Marney SR. Mast cell disease. Allergy Proc. 1992;13:303–10.
44. Gilliam AC, Wood GS. Cutaneous lymphoid hyperplasias. Semin Cutan Med Surg. 2000;19:133–41.
45. Gupta S, Sharma VK. Standard guidelines of care: keloids and hypertrophic scars. Indian J Dermatol Venereol Leprol. 2011;77:94–100.
46. Viera MH, Caperton CV, Berman B. Advances in the treatment of keloids. J Drugs Dermatol. 2011;10:468–80.
47. Couto Júnior Ade S, Batista GM, Calafiori IG, Radael VC, Mendes WB. Hidrocystoma: surgical management of cystic lesions of the eyelid. An Bras Dermatol. 2010;85:368–71.
48. Chin K, Finger PT, Iacob C. High-frequency ultrasound imaging of periocular hidrocystomas. Optometry. 2003;74:760–4.

6 The Computer-Aided Diagnosis of Soft-Tissue Tumors Using Sonographic Morphology and Texture Features

Hong-Jen Chiou, Chih-Yen Chen, Yi-Hong Chou, and Huihua Kenny Chiang

Contents

H.-J. Chiou, MD (✉)
Division of Musculoskeletal Radiology,
Taipei Veterans General Hospital, School of Medicine,
National Yang-Ming University, No. 201, Section 2, Shih-Pa Road,
Taipei 112, Taiwan
e-mail: hjchiou@gmail.com

C.-Y. Chen, PhD
Division of Applied Optics, Instrument Technology Research Center,
National Applied Research Laboratories, No. 20 R&D Road,
Hsinch Science Park, Hsinchu, Taiwan
e-mail: cychen@itrc.narl.org.tw

Y.-H. Chou, MD
Division of Ultrasound and Breast Imaging, Taipei Veterans General Hospital, and School of Medicine, National Yang-Ming University,
No. 201, Section 2, Shih-Pai Rd, Taipei, Taiwan
e-mail: yhchou@vghtpe.gov.tw

H.K. Chiang, PhD
Institute of Biomedical Engineering, and
Institute of Biophotonics Engineering, National Yang-Ming University,
No. 155, Sec. 2, Linong Street, Beitou District, Taipei, Taiwan
e-mail: hkchiang@ym.edu.tw

6.1 Introduction

Over the past years, great improvement of sonographic technique has been made and this has made it possible to prospectively evaluate prognostic factors in patients. Furthermore, sonography is a useful and helpful imaging modality that is primarily used as an in vivo screening tool for examining anatomical structures. This progress facilitates sonography in becoming a first-line screening modality in diagnosing tumors, and capable of characterizing the sizes, shapes, locations, and echogenicity of soft-tissue tumors [1, 2]. However, a suitable and reliable diagnosis of soft-tissue tumors needs long-term training for the inexperienced physicians [3–5].

Generally, the characteristics of morphologic features for malignant tumors are directly into local invasion of the pseudocapsule and peripheral structural tissues [6]. In comparison with the benign tumors sonographically, shapes of malignant tumors are revealing to the behaviors of irregularity and protrusion. Furthermore, texture features retrieved from the visual perception can be regarded as another useful tool for tumor diagnosis to represent the characteristics of smooth and homogeneous echogenicity for benign tumors; on the contrary, the characteristics of high echogenicity and contrast are likely to be malignant tumors. The other useful features include margin and posterior echogenicity behavior, although they have shown various influences on each individual [7]. It is noteworthy that applying these criteria is highly dependent on the experiences, making it is difficult for young and inexperienced physicians to apply these principles in a consistent manner in an unknown case.

Fortunately, this problem can be solved by using a computer-aided diagnosis (CAD) system to provide useful information and reduce misdiagnosis. In the past two decades, the main research for the CAD system has focused on the most commonly occurring tumors (e.g., breast cancer, lung cancer, liver cancer, etc.), and most of them have been verified in practical use clinically. However, some uncommon tumors (soft-tissue tumors) are difficult for radiologists to learn

X. Wortsman, G.B.E. Jemec (eds.), *Dermatologic Ultrasound with Clinical and Histologic Correlations*,
DOI 10.1007/978-1-4614-7184-4_6,

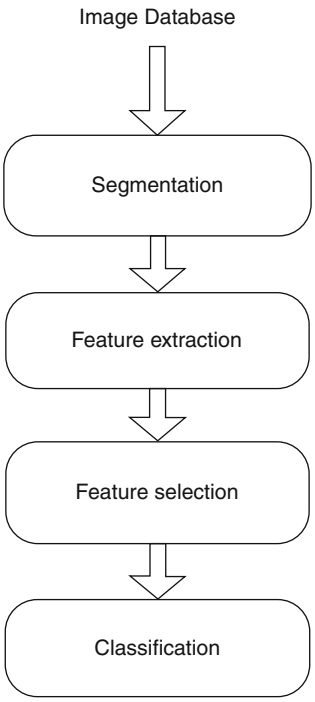

Fig. 6.1 Flowchart of the CAD diagnosis algorithm for the differentiation of benign tumors from malignant soft-tissue tumors

about and to accumulate diagnostic experiences regarding them. If a CAD system of on soft-tissue tumors on sonography could be developed for assisting radiologists with an objective and stable diagnostic tool, the radiologist can increase his or her diagnostic confidence and performance. Another advantage is that unnecessary biopsy may also be decreased [8].

Figure 6.1 shows a flowchart of the various steps of the general CAD algorithm for tumor diagnosis. Because of the various surrounding tissue and many different histological subtypes of soft-tissue tumors, it makes the automatic segmentation hard to implement. Therefore, the segmentation step will be omitted and the other steps, such as feature extraction, feature selection, and classification will be discussed and how to build a CAD system. Each of the algorithm's modules will be discussed in detail in the following sections, concerning studies will be present with the goal of developing a CAD algorithm based sonographically onsoft-tissue tumors. Moreover, the morphologic and texture features of soft-tissue tumors would be integrated for a tumor classification model.

6.2 Feature Extraction

In general, malignant tumors can present certain properties such as rapid growth, infiltrative contour, high vascular velocity, low Doppler resistive index, and enhanced calcium concentration [9–11]. Accordingly, the sonography-based diagnosis of tumors can fall into the following criteria: location, size, shape, contour, echogenicity, and the structure of blood vessels [1, 11–13] and radiologists usually take into consideration such properties for distinguishing the benign tumors from malignant tumors. We will also discuss the differentiation between benign and malignant soft-tissue tumors in more detail.

6.2.1 Morphologic Feature Set

Tumor shape can contain important diagnostic information about the severity of malignant changes. According to previous reports, many researchers have found that most malignant soft-tissue tumors spreading in a spherical fashion will infiltrate the tumor pseudo-capsule and adjacent structures [8, 12, 14]. Because of the infiltration property of malignancy, morphologic features of benign and malignant tumors are appear with differences. The shapes of malignant soft-tissue tumors probably exhibit microlobulation and macrolobulation, but benign tumors are likely to present slight macrolobulation and ovoid shapes [8, 12, 15, 16].

Tumors with irregular curvature and shape are frequently pronounced with a high-grade malignancy [12, 17]. Skaane et al. have further categorized tumors into different classes such as round, ovoid, macrolobulated, microlobulated, and irregular [15]. The main reason might be that malignant tumors typically present with irregular and infiltrated margins, but benign tumors tend to have smooth and regular borders. A set of morphologic features containing important diagnostic information is presented below based on radiologists' experience regarding the morphological characteristics of tumor shapes.

First, for direct impression in clinical evaluation, benign tumors tends to be smaller than malignant tumors, therefore, tumor area is quite useful and helpful for the clinical diagnosis. In spite of that, a reliable and accurate CAD system is still needed with improved features. Second, a shape-based approach, the matching relationship between the tumor contour and the closest matching polygon is another morphologic feature set that includes circularity, compactness, eccentricity, ellipticity, rectangularity, as well as others [12, 18, 19]. In Fig. 6.2, both a benign and a malignant tumor are showing matching ellipses as an example.

In Fig. 6.2, the characteristic of the closest matching ellipse is shown in (a) a benign and (b) a malignant tumor. The white solid line reveals the tumor contour and the dashed line indicates the best morphology of matching ellipse.

The third major feature set is a lobular shape that can be used to characterize many soft-tissue tumors. A tumor with multiple lobulations, the number of substantial protuberances, and depressions can be well formulated to describe a

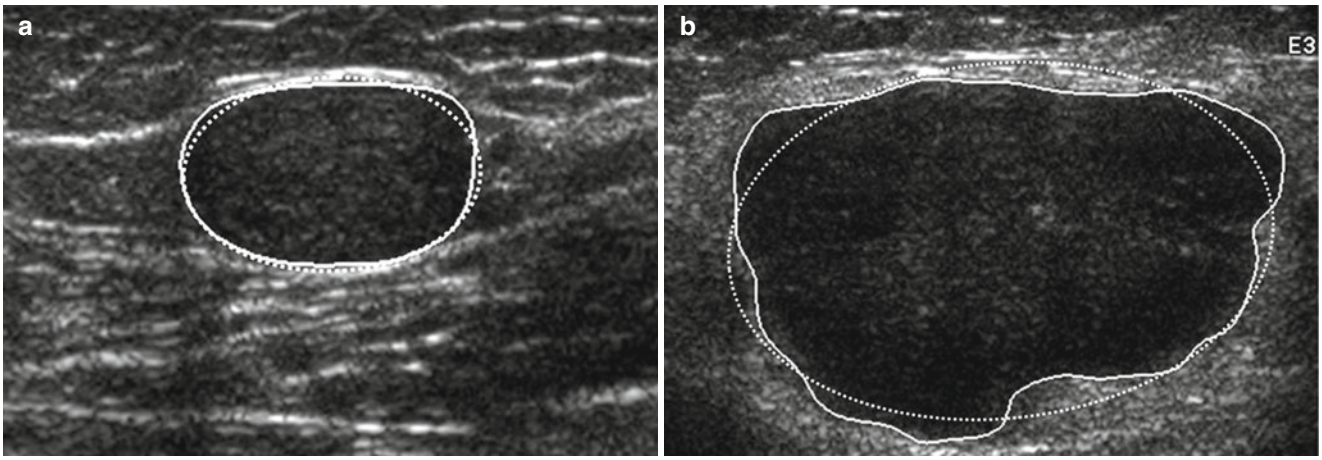

Fig. 6.2 Characteristics of the closest matching ellipse are shown in (**a**) a benign and (**b**) a malignant tumor. The *white solid line* reveals the tumor contour and the *dashed line* indicates the best morphology of matching ellipse

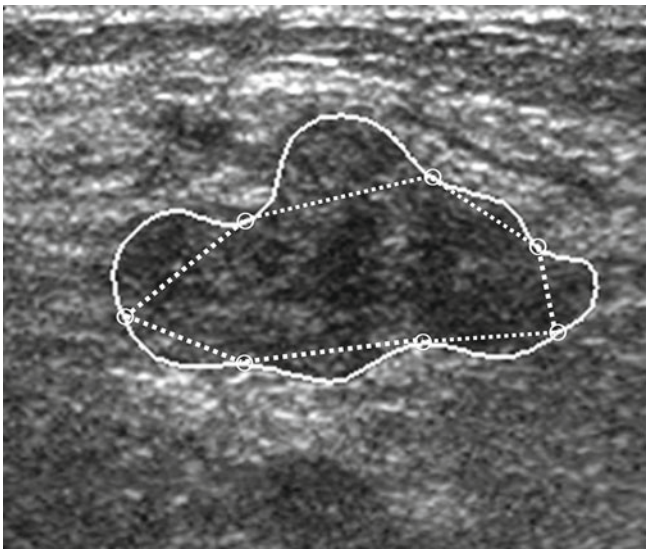

Fig. 6.3 Subimage of a malignant tumor with concave points (*open points*). *Solid line* indicates the tumor contour and *dashed line* indicates the connection of the concave points

malignant tumor. In Fig. 6.3, the concave points of the tumor contour are computed with labels of open points. The greater the convex and concave points exhibited in a tumor contour, the more likely it is to be a malignant tumor [18].

6.2.2 Texture Feature Set

The sonographic pattern produced by a tissue itself is usually described as a texture feature, which began approximately in the early 1980s for sonographic tumor analysis. The evaluation of image texture is largely dependant on radiologist experience but is not easily characterized. Thus, the computer-extracted texture feature for image interpretation that acts as a visual perception of the naked eye, can be designed to capture important differences between malignant and benign masses [12, 18, 20]. Some of the texture feature sets are from the contextual properties associating with the spatial distributions of gray levels [21] and others are related to directional characteristics (i.e., rotational variance). To quantitatively extract textural information, the used texture feature sets include the grey-level co-occurrence matrix [22], gray-level difference matrix [23], run-length matrix [24], fractal dimension[25], Markov random field [26], Gabor filters [27], wavelet transformation [28], Laws' texture [29], among others, are defined. Therefore, many of the textural approaches based on spatial distribution of grey values are preferred for their reported superiority at analysis of medical imaging.

6.3 Classification Method

The final part of a CAD system is choosing an appropriate classifier, and can be grouped as supervised and unsupervised. The most commonly used classifiers contain linear discriminant analysis (LDA) [7, 30], multi-layer perceptron network (MLP) [31–34], support vector machine [35–38], as well as others. The main process is transforming the quantitative input (i.e., features) to qualitative output (i.e., diagnosis, prognosis, etc.). Output from the classifier can be either a distinct value, indicating one of the predefined classes, or a real value vector, reflecting a likelihood that a sample has originated from a specific class [39]. To optimize the performance of the classifier, the most important thing is to search the optimal classification function. In simple terms, the diagnosis task is regarded as a two-class classification (e.g., either benignancy or malignancy).

Setting up a classifier usually requires three stages: the training stage, the testing stage, and the performance evaluation stage. The k-fold cross-validation is a recommended

criterion to verify the classification result of the CAD system [40], and means that all the adopted cases are randomly partitioned into k subsets with similar size according to the machine type and the pathological result. Each subset is then regarded as test set exactly once and classified by a CAD system trained by the other subsets. An advantage of cross-validation is that all data are used for training and testing, a disadvantage is the requirement of computational complexity. Furthermore, an extreme variation of cross-validation is overestimation. Nevertheless, the leave-one-out cross-validation is definitely the superior procedure for evaluating the system with reliability and stability.

6.4 Classification Results for Soft-Tissue Tumors

To date, little research has been reported and discussed regarding the development of a CAD system sonographically based on soft-tissue tumors [41] and [42] have reported success for soft-tissue tumor diagnosis. The reason for so few publications may be because of the rare occurrence, but various types of soft-tissue tumors has limited the accumulation of results in a clinical database. In the study by Chen et al., they focused on the selection of shape-based features (five geometric features and 11 morphologic features) and a statistic-based classifier (LDA) for classification. Their conclusion demonstrated that tumor shape features play a specific role in the diagnosis of benign or malignant status. Furthermore, a complete study of tumor characterization should also include the feature of image texture to overcome the lack of complete comprehension clinical analysis. Therefore, the texture feature set was included and the combination of both morphologic and texture features of soft-tissue tumors sonographically was performed in the latter study. According to the classification results of the combining feature sets, the area under the receiver operator characteristic curve, A_z values, with the two classifiers (LDA and MLP classifiers) have shown identical sequences as follows: the combination of two feature sets greater than morphologic features greater than texture features. This finding suggested that the assessment of combined morphologic and texture features has a similar concept of complementary information to radiologists. Furthermore, the analysis using the morphologic features is simply better than using the texture features. This result can be explained by the fact that some benign and most malignant soft-tissue tumors own similar appearances of heterogeneous echotexture on sonography [12, 43, 44]. Another interesting experiment was comparing the performance between the radiologists' rankings and the CAD, with the result showing the performance of the optimal CAD result was slightly better than the radiologists' evaluations.

Conclusion

The clinical interpretation of soft-tissue tumors depends greatly on the clinical examination, imaging, and histological analysis. With the rapid improvement in ultrasound technology, high-resolution sonography has complemented more sophisticated anatomy structures than previously and has enabled the diagnosis of soft-tissue tumors with high sensitivity [1, 3, 45]. In this chapter we have shown that a CAD system integrating the different features is capable of assisting radiologists in the diagnosis of soft-tissue tumors on sonography. In the characterization of benign and malignant soft-tissue tumors, the CAD system successfully implements the classification using two feature sets that include morphologic features and texture features. Notably, the performance of the morphologic features is shown to be greater in the determination of the tumor status. Importance should be emphasized that both of the morphologic and texture features are important properties at the time of visual interpretation of soft-tissue tumors.

In a comparison between the CAD system and clinical evaluations, the optimal results of the CAD system are superior to radiologist performance. Because of the subjectivity of visual interpretation, qualitative evaluations can vary over a wide range among different radiologists or at different time periods. Therefore, it is indicated that the computerized method in terms of decision-making rules is applicable in practical use for assisting radiologists with information that is more objective for making diagnostic decisions.

References

1. Chiou HJ, Chou YH, Chiou SY, Wang HK. High-resolution ultrasonography in superficial soft tissue tumors. J Med Ultrasound. 2007;15:152–74.
2. Gandhi MR, Benson MD. Ultrasound of soft tissue masses. World J Surg. 2000;24:227–31.
3. Garcia-Gomez JM, Vidal C, Marti-Bonmati DL, Galant J, Sans N, Robles M, et al. Benign/malignant classifier of soft tissue tumors using MR imaging. MAGMA. 2004;16:194–201.
4. Verstraete KL, Vanzieleghem B, De Deene Y, Palmans H, De Greef D, Kristoffersen DT, et al. Static, dynamic and first-pass MR imaging of musculoskeletal lesions using gadodiamide injection. Acta Radiol. 1995;36:27–36.
5. Clark MA, Fisher C, Judson I, Thomas JM. Soft-tissue sarcomas in adults. N Engl J Med. 2005;353:701–11.
6. Morton L, Antman KH, Tepper J. Soft tissue sarcomas cancer medicine. 4th ed. Philadelphia: Williams & Wilkins; 1997. p. 2559–92.
7. Horsch K, Giger ML, Venta LA, Vyborny CJ. Computerized diagnosis of breast lesions on ultrasound. Med Phys. 2002;29:157–64.
8. Hadjiiski L, Chan HP, Sahiner B, Helvie MA, Roubidoux MA, Blane C, et al. Improvement in radiologists characterization of malignant and benign breast masses on serial mammograms with computer-aided diagnosis: an ROC study1. Radiology. 2004;233:255–65.

9. McNally EG. Practical musculoskeletal ultrasound. Philadelphia, PA: Elsevier Churchill Livingstone; 2005.
10. Fisher C. Soft tissue sarcomas: diagnosis, classification and prognostic factors arthroscopy. J Arthrosc Relat Surg. 1996;49:27–33.
11. Adler RS. Musculoskeletal system ultrasound in medicine. Ultrasound Med Biol. 2000;26–27:S125.
12. Chou YH, Tiu CM, Hung GS, Wu SC, Chang TY, Chiang HK. Stepwise logistic regression analysis of tumor contour features for breast ultrasound diagnosis. Ultrasound Med Biol. 2001;27: 1493–8.
13. Bodner G, Schocke MF, Rachbauer F, Seppi K, Peer S, Fierlinger A, et al. Differentiation of malignant and benign musculoskeletal tumors: combined color and power doppler US and spectral wave analysis. Radiology. 2002;223:410–6.
14. Olsson H. An updated review of the epidemiology of soft tissue sarcoma. Acta Orthop Scand Suppl. 2004;75:16–20.
15. Skaane P, Engedal K. Analysis of sonographic features in the differentiation of fibroadenoma and invasive ductal carcinoma. AJR Am J Roentgenol. 1998;170:109–14.
16. Stavros AT, Thickman D, Rapp CL, Dennis MA, Parker SH, Sisney GA. Solid breast nodules: use of sonography to distinguish between benign and malignant lesions. Radiology. 1995;196:123–34.
17. Sintzoff SA, Gillard I, Van Gansbeke D, Gevenois PA, Salmon I, Struyven J. Ultrasound evaluation of soft tissue tumors. J Belge Radiol. 1992;75:276–80.
18. Chen CM, Chou YH, Han KC, Hung GS, Tiu CM, Chiou HJ, et al. Breast lesions on sonograms: computer-aided diagnosis with nearly setting-independent features and artificial neural networks. Radiology. 2003;226:504.
19. Chang RF, Wu WJ, Moon WK, Chen DR. Automatic ultrasound segmentation and morphology based diagnosis of solid breast tumors. Breast Cancer Res Treat. 2005;89:179–85.
20. Wu WJ, Moon WK. Ultrasound breast tumor image computer-aided diagnosis with texture and morphological features. Acad Radiol. 2008;15:873–80.
21. Pau LF, Wang PSP. Handbook of pattern recognition and computer vision. Singapore: World Scientific Publishing Company; 1999.
22. Haralick RM, Shanmugam K, Dinstein I. Textural features for image classification. Syst Man Cy IEEE Trans. 1973;3:610–21.
23. Van Gool L, Dewaele P, Oosterlinck A. Texture analysis anno 1983. Comp Vision Graph Image Process. 1985;29:336–57.
24. Milan S, Vaclav H, Roger B. Image processing analysis and machine vision. Peking: Photocopy Edition Posts & Telecom Press; 2002.
25. Tuceryan M, Jain AK. Texture analysis, handbook of pattern recognition & computer vision. River Edge: World Scientific Publishing Co., Inc.; 1993.
26. Chellappa R, Chatterjee S. Classification of textures using gaussian markov random fields. IEEE Trans Acoust Speech Signal Proc. 1985;33:959–63.
27. Teuner A, Pichler O, Hosticka BJ. Unsupervised texture segmentation of images using tuned matched gabor filters. IEEE Trans Image Process. 1995;4:863–70.
28. Mallat SG. A theory for multiresolution signal decomposition: the wavelet representation. Pattern Anal Mach Intell IEEE Trans. 1989;11:674–93.
29. Laws KI. Texture energy measures. 1979.
30. Lefebvre F, Meunier M, Thibault F, Laugier P, Berger G. Computerized ultrasound B-scan characterization of breast nodules. Ultrasound Med Biol. 2000;26:1421–8.
31. Chen DR, Chang RF, Kuo WJ, Chen MC, Huang Y. Diagnosis of breast tumors with sonographic texture analysis using wavelet transform and neural networks. Ultrasound Med Biol. 2002;28:1301–10.
32. Zheng K, Wang T, Lin J, Li D. Recognition of breast ultrasound images using a hybrid method. In: Complex Medical Engineering, 2007. CME 2007. IEEE/ICME international conference on, Beijing; 2007, pp 640–643.
33. Alvarenga AV, Pereira WC, Infantosi AF, Azevedo de CM. Classification of breast tumours on ultrasound images using morphometric parameters. Intelligent Signal Processing, 2005 IEEE international workshop on, Portugal: Coimbra University; 2005, pp 206–210.
34. Joo S, Yang YS, Moon WK, Kim HC. Computer-aided diagnosis of solid breast nodules: use of an artificial neural network based on multiple sonographic features. IEEE Trans Med Imaging. 2004;23:1292–300.
35. Chang RF, Wu WJ, Moon WK, Chen DR. Improvement in breast tumor discrimination by support vector machines and speckle-emphasis texture analysis. Ultrasound Med Biol. 2003;29:679–86.
36. Huang YL, Chen DR. Support vector machines in sonography: application to decision making in the diagnosis of breast cancer. Clin Imaging. 2005;29:179–84.
37. Piliouras N, Kalatzis I, Dimitropoulos N, Cavouras D. Development of the cubic least squares mapping linear-kernel support vector machine classifier for improving the characterization of breast lesions on ultrasound. Comput Med Imaging Graph. 2004;28: 247–55.
38. Rodrigues PS, Giraldi GA, Provenzano M, Faria MD, Chang RF, Suri JS. A new methodology based on q-entropy for breast lesion classification in 3-D ultrasound images. In: Engineering in Medicine and Biology Society, 2006. EMBS'06. 28th Annual International Conference on, New York; 2006, pp 1048–1051.
39. Jain AK, Duin RP, Mao J. Statistical pattern recognition: a review. Pattern Anal and Mach Intell IEEE Trans. 2000;22:4–37.
40. Stone M. Cross-validatory choice and assessment of statistical predictions. J R Stat Soc Ser B (Methodol). 1974;36:111–47.
41. Chen CY, Chiou HJ, Chou YH, Chiou SY, Wang HK, Chou SY, et al. Computer-aided diagnosis of soft tissue tumors on high-resolution ultrasonography with geometrical and morphological features. Acad Radiol. 2009;16:618–26.
42. Chen CY, Chiou HJ, Chou SY, Chiou SY, Wang HK, Chou YH, et al. Computer-aided diagnosis of soft-tissue tumors using sonographic morphologic and texture features. Acad Radiol. 2009;16:1531–8.
43. Kransdorf MJ, Jelinek JS, Moser Jr RP. Imaging of soft tissue tumors. Radiol Clin North Am. 1993;31:359–72.
44. Widmann G, Riedl A, Schoepf D, Glodny B, Peer S, Gruber H. State-of-the-art HR-US imaging findings of the most frequent musculoskeletal soft-tissue tumors. Skeletal Radiol. 2009;38:637–49.
45. Tierney JF, Stewart LA, Parmar MKB. Adjuvant chemotherapy for localised resectable soft-tissue sarcoma of adults: meta-analysis of individual data. Lancet. 1997;350:1647–54.

Hemangiomas and Vascular Malformations

7

Siegfried Peer and Ximena Wortsman

How to deal with the most common forms of vascular tumors and their ultrasound findings

Contents

7.1 Introduction

While a so-called "angel's kiss" is a harmless finding–typically with spontaneous resolution within the first 2 years of life–one in one hundred newborns is affected by a vascular soft-tissue lesion, which warrants further investigation. Our main goal is to separate the "don't touch" lesions, such as most hemangiomas–that can simply be observed for a period of time, awaiting spontaneous involution– from lesions that need to be observed more closely or those that should undergo early therapeutic intervention. Such a decision must be made by an interdisciplinary team of pediatricians, dermatologists, surgeons, and radiologists, however, "too many cooks may spoil the broth," especially if they don't speak the same language. A confusing historical nomenclature has been used for many years for the classification of a vascular anomaly: even specialists have applied the term "cavernous hemangioma" to a port wine stain, which gives the false impression of a possibility for spontaneous involution of the lesion. Various hybrid names such as "capillary hemangioma" further added to the confusion. The correct classification of a lesion by clinicians, and especially radiologists and sonographers, however, is of utmost importance to avoid misinterpretations in terms of prognosis and choice of optimal treatment.

7.2 Classification of Vascular Anomalies

The work of Mulliken and Glowacki has greatly improved our understanding of vascular anomalies [1]. In their work dating back to 1982, they classified vascular anomalies according to their endothelial characteristics into two main categories: hemangioma and vascular malformations. While a hemangioma is a benign vascular tumor, characterized by an initial rapid growth of endothelial cells, followed by later slow involution, vascular malformations by definition are not tumors; they are composed of dysplastic vascular channels without accompanying endothelial proliferation. The basic

S. Peer, MD, PhD (✉)
Department of Radiology, CTI GesmbH Innsbruck,
Klostergasse 4, Innsbruck, Tirol 6020, Austria
e-mail: info@siegfried-peer.at

X. Wortsman, MD
Department of Radiology and Dermatology,
Faculty of Medicine, Institute for Diagnostic Imaging
and Research of the Skin and Soft Tissues,
Clinica Servet, University of Chile,
Almirante Pastene 150, Providencia, Santiago, Chile
e-mail: xwo@tie.cl, xworts@yahoo.com, www.sonoskin.com

X. Wortsman, G.B.E. Jemec (eds.), *Dermatologic Ultrasound with Clinical and Histologic Correlations*,
DOI 10.1007/978-1-4614-7184-4_7, © Springer Science+Business Media New York 2013

Table 7.1 ISSVA-Classification of vascular anomalies

	Vascular Malformations	
Vascular Tumors	Simple	Combined
Hemangioma	Arterial/ Capillary	Arteriovenous fistula
		Arteriovenous malformation
		Capillary-venous malformation
		Capillary-lymphatic-venous malformation
Other	Lymphatic	Lymphatic-venous malformation
Kaposiform hemangioendothelioma		Capillary-lymphatic-arteriovenous malformation
Hemangiopericytoma		
Pyogenic granuloma		
Spindle-cell hemangioendothelioma		
	Venous	

ISSVA International Society for the Study of Vascular Anomalies

classification by Mullicken/Glowacki was later modified by Burrows et al. [2], who introduced the subclassification of vascular malformations into high-flow and low-flow varieties. Currently, a generally accepted classification is recommended by the Society for the Study of Vascular Anomalies [3], which is based on the cellular origin of the lesion, its clinical behavior, and its flow characteristics. In that classification, proliferating neoplasms are distinguished from congenital vascular malformations (Table 7.1). In terms of treatment planning, additional differentiation of lesions into "high-flow," "intermediate-flow," and "low-flow," as proposed by Kawanabe et al. and Inoue et al., is of practical value [4, 5]. While in high-flow lesions a combination of transarterial catheter embolization with or without venous embolization or sclerotherapy is feasible, percutaneous sclerotherapy alone may be the best choice for slow-flow lesions.

Teaching Point
Hemangiomas are true endothelial tumors and malformations are developmental anomalies. Correct classification is mandatory to institute optimal treatment!

7.3 General Considerations for Imaging of Vascular Anomalies

Ultrasound imaging–which will be covered in more detail later in the chapter–is definitely the first line evaluation of hemangiomas and vascular malformations, although at times additional imaging studies are needed. While conventional radiography and computed tomography (CT) have only little impact, magnetic resonance imaging (MRI), digital subtraction angiography (DSA), and venous angiography are important adjuncts for the study of vascular anomalies.

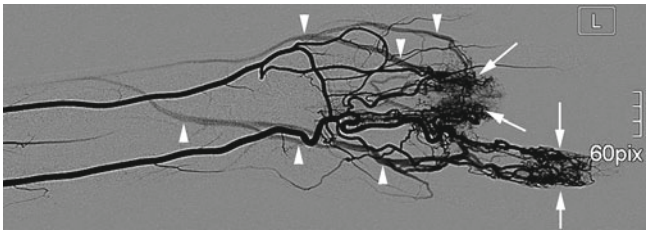

Fig. 7.1 Arterial DSA in a patient with recurrent arteriovenous malformation in the hand after previous surgery. Dense arterial nidus (*arrows*) and early venous drainage (*arrowheads*) is demonstrated

DSA is typically performed to define the arterial component of combined high-flow arteriovenous malformations and arteriovenous fistulae (Fig. 7.1). However, in hemangiomas and other types of malformations (low or intermediate flow), it is hardly indicated. The lesions that should undergo DSA can be judged through careful evaluation of the individual flow characteristics during examination with color Doppler and duplex ultrasound or MRI. Depending on the location of the lesion, DSA is performed with either retrograde or antegrade cannulation of the femoral artery and endovascular treatment is typically performed during the same session. In low-flow venous malformations, angiographic lesion visualization is performed through direct percutaneous phlebography for differential diagnosis or during sclerotherapy (Fig. 7.2). This topic is covered in more detail in the section on venous malformations.

A complete work up of a hemangioma is normally feasible with ultrasound alone, whereas an indication for MRI is in critical regions in deep lying hemangiomas, such as the pelvic area or in distinct locations of the craniofacial region (orbit, nasopharyngeal space, etc.). Typically, hemangiomas are hyperintense on T2-weighted images and isointense to muscle on T1-weighted sequences with marked enhancement after administration of a contrast agent (Fig. 7.3).

In cases with large or multiple vascular malformations we opt for a combination of ultrasound with MRI and magnetic resonance angiography (MRA) which can provide the complete extent of the lesion and its relationship to surrounding soft tissues (muscles, nerves, bone, tendons, subcutaneous tissue, and skin).

Teaching Point
Combined ultrasound and MRI is ideal for imaging of large and multiple vascular malformations. It combines functional and morphological information.

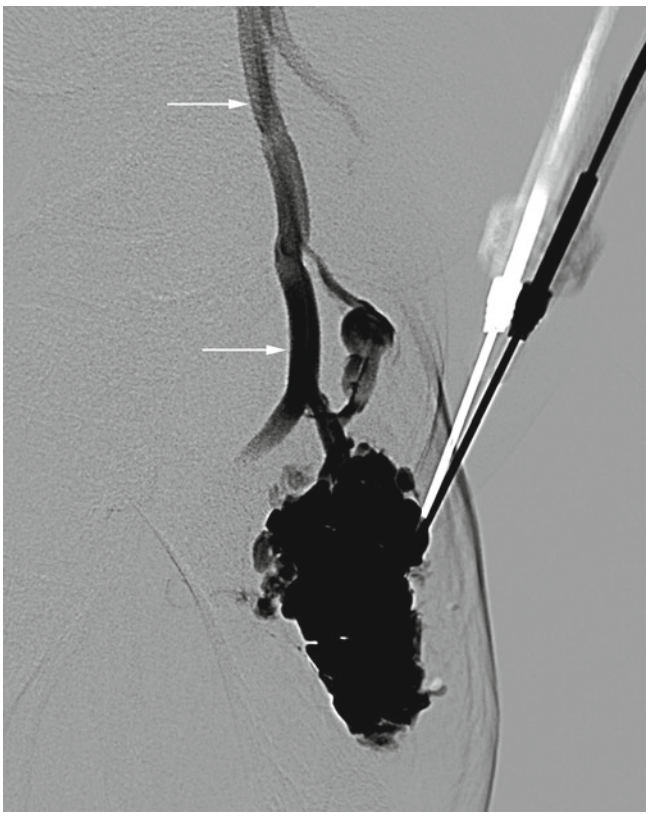

Fig. 7.2 Direct puncture phlebography in a patient with a venous malformation around the knee. Rapid venous drainage into the superficial femoral vein (*arrows*) is demonstrated

Vascular malformations are best distinguished from adjacent fatty structures on fat-suppressed sequences (STIR [short tau inversion recovery] or frequency selective fat saturation) (Fig. 7.4). Low-flow venous malformations consist of blood-filled pouches of variable size that appear as homogeneous hyperintense areas without flow void signals on T2-weighted or STIR images (Fig. 7.4). In contrast, high-flow malformations are characterized by signal voids in serpiginous structures corresponding to high-flow feeders (Fig. 7.5). A pathognomonic feature of venous malformations is intralesional phleboliths caused by stagnation of blood flow with partial thrombosis and calcification of clot, and can be detected as low signal foci on T2-weighted or STIR images (Fig. 7.6). MRA has gained widespread acceptance in the pre-treatment evaluation of vascular malformations (Fig. 7.7), and in terms of technique, it can be performed as conventional MRA, typically with fast 3D gradient-echo sequences in coronal orientation after intravenous injection of 0.1 mmol/kg of a gadolinium contrast agent. A more timely approach is contrast-enhanced time-resolved MRA, which combines high temporal resolution and the ability to visualize flow dynamics in a manner similar to that of DSA [6].

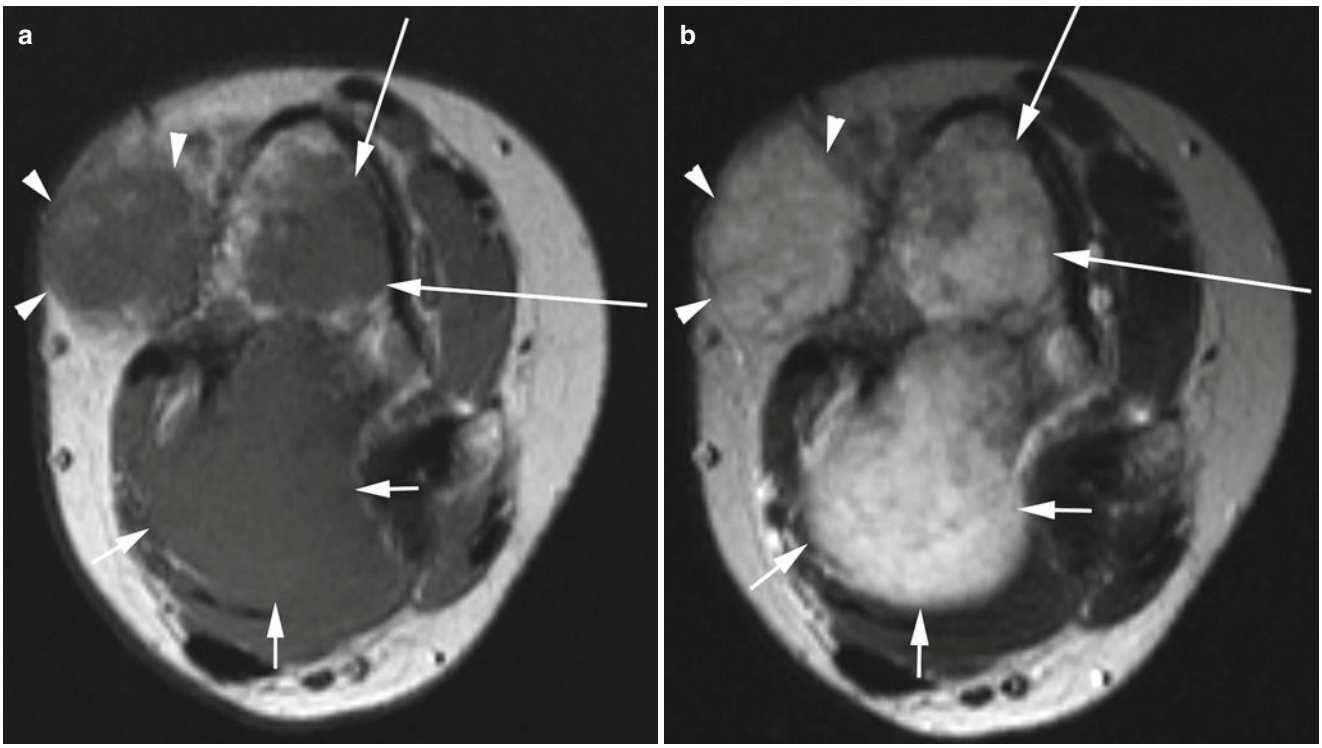

Fig. 7.3 (**a**–**c**) Multiple hemangiomas in a patient with Mafucci syndrome, located in the subcutaneous tissue (*arrowheads*), muscle (*short arrows*), and bone (*long arrows*). In the T1-weighted image (**a**) intramuscular hemangioma (*short arrows*) is isointense to muscle tissue and hardly discernible from normal muscle. In the T2-weighted image (**b**) the hemangiomas are hyperintense and thus more easily discerned from muscle but not so from subcutaneous tissue. In the T1-weighted image after administration of gadolinium contrast (**c**) all hemangiomas show marked inhomogeneous uptake

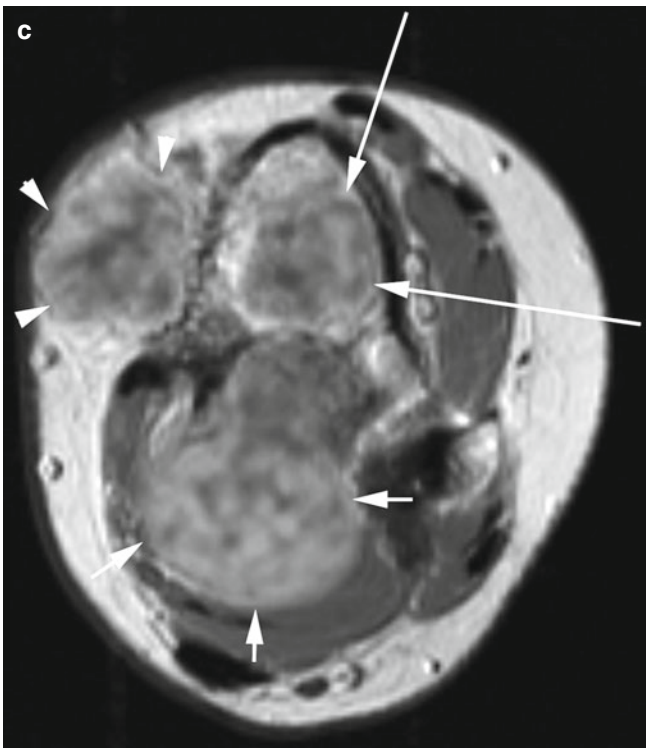

Fig. 7.3 (continued)

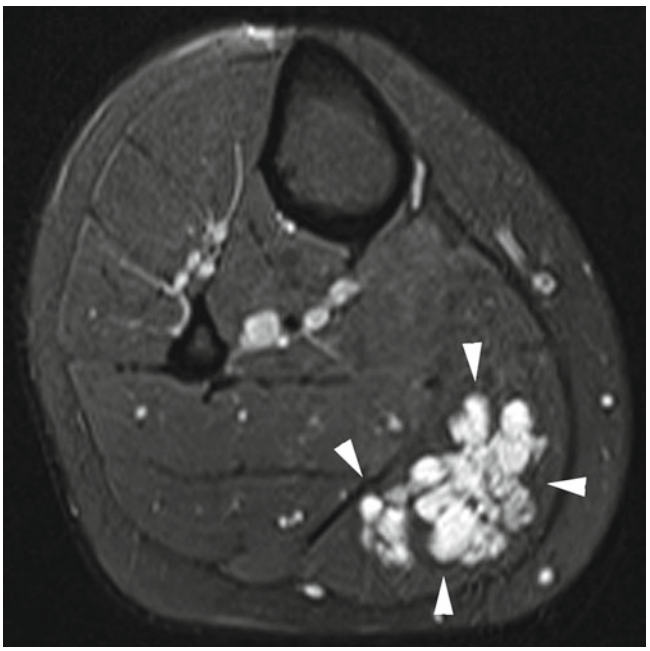

Fig. 7.4 Fat saturated transverse MR image in a patient with a slow-flow venous malformation (*arrowheads*) inside the medial gastrocnemius muscle. High signal intensity fluid-filled venous caverns are demonstrated

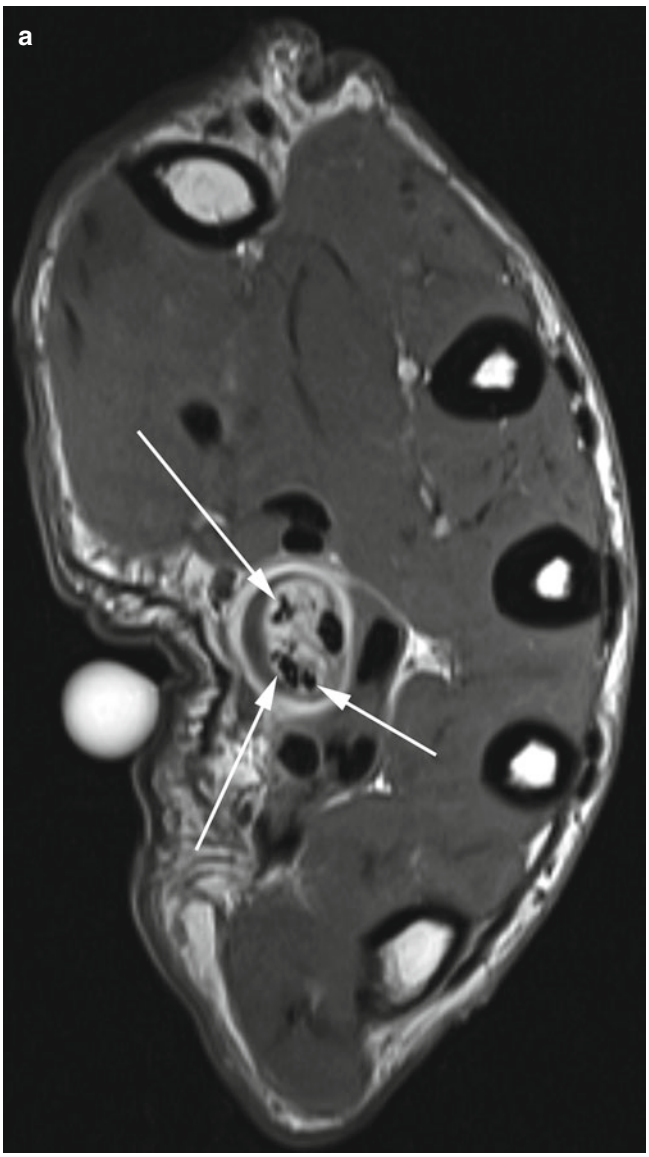

Fig. 7.5 (**a**) T1-weighted MR image in a patient with high-flow AVM. Multiple small signal voids (*arrows*) are seen inside carpal tunnel and adjacent to the flexor tendons. (**b**) Grey scale ultrasound image shows hypoechoic longitudinal vascular channels (*arrows*) interspersed with flexor tendons (*arrowheads*). (**c**) Duplex ultrasound demonstrates high arterial systolic flow velocity arterial feeder

Fig. 7.5 (continued)

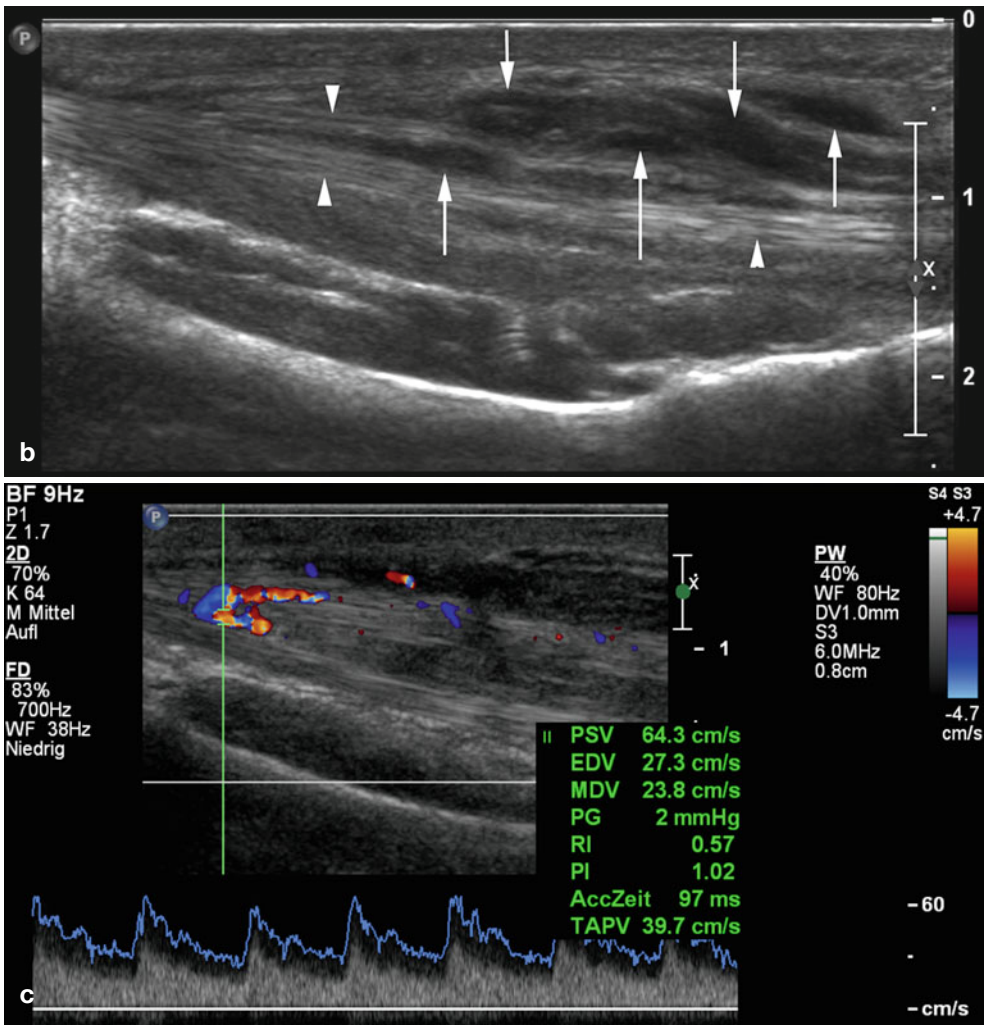

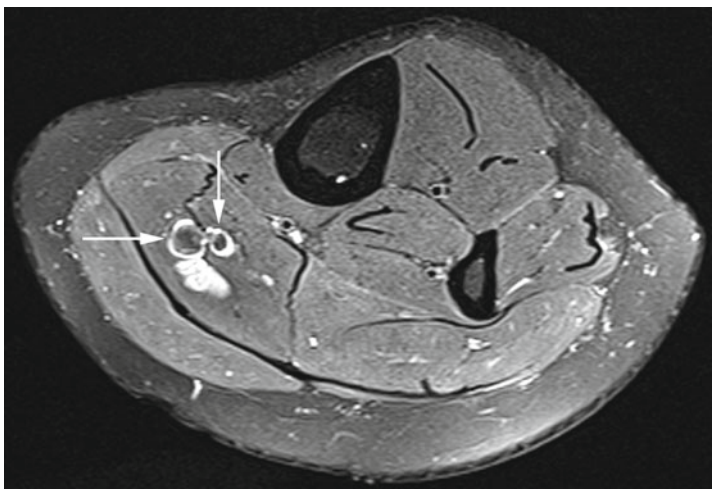

Fig. 7.6 Axial T2-weighted fat saturated MR image in a patient with a venous malformation. The venous malformation is of hyperintense fluid equivalent signal with two small roundish low signal structures = phleboliths (*arrows*)

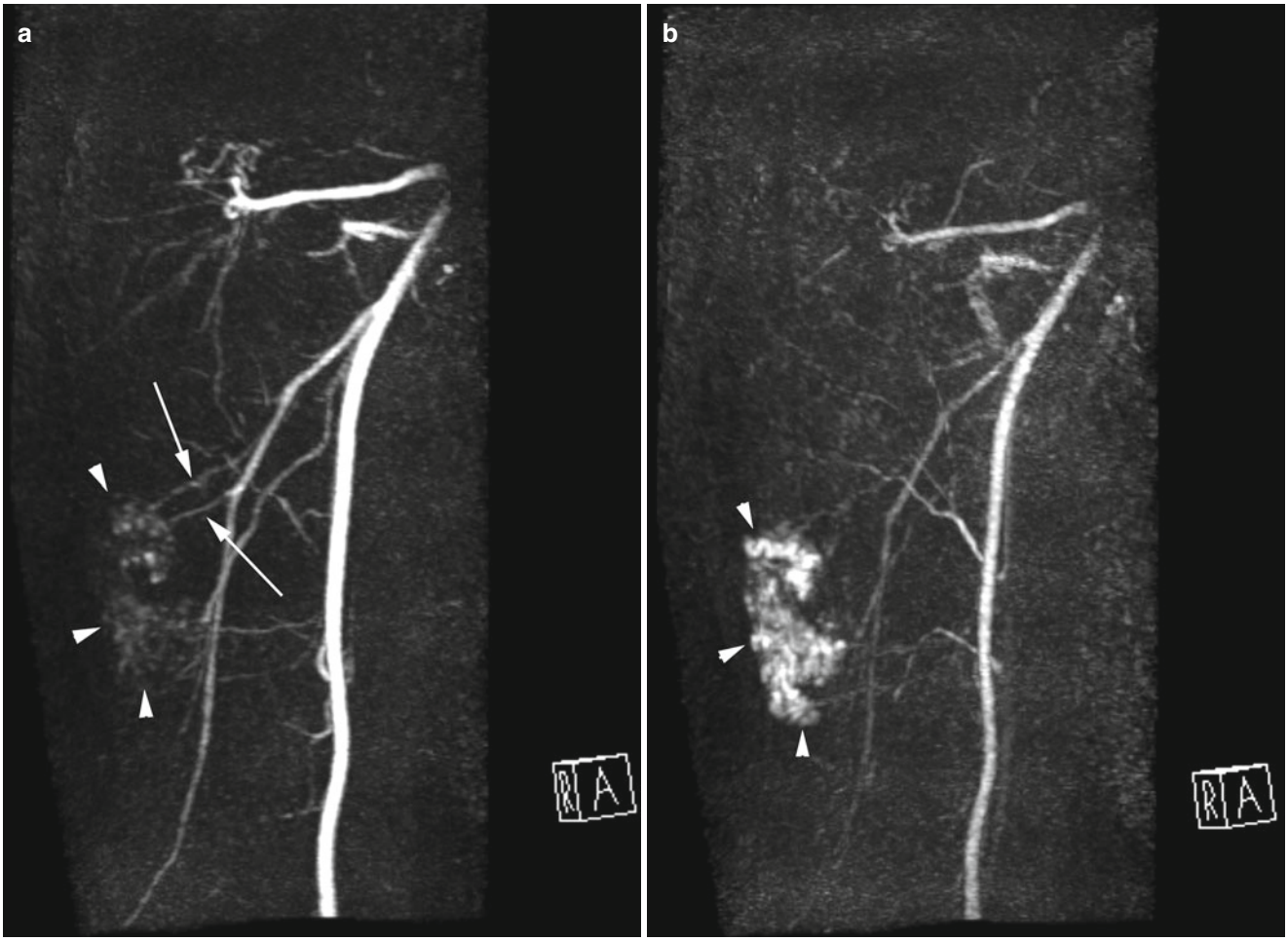

Fig. 7.7 (**a**–**b**) MR angiography of low-flow arteriovenous malformation (*arrowheads*): (**a**) early angiographic phase, (**b**) late angiographic phase. Slow progressive filling of malformation through small arterial feeders (*arrows* in **a**)

7.4 Ultrasound: General Considerations and Technical Requirements

A modern ultrasound equipment with high-resolution scanning software is well suited for the imaging of vascular anomalies. Companies combine special beam-forming software with broad-band transducers, which enhances the system's ability for high-resolution imaging and powerful color Doppler and duplex ultrasound. New matrix transducers deliver an ultra-thin, targeted ultrasound beam, which results in extraordinary tissue uniformity, while decreasing noise surrounding the region of interest. This results in fewer artifacts and better image quality in terms of resolution and image sharpness.

All lesions are initially evaluated in B mode and documented and measured in two orthogonal planes. We carefully evaluate the echotexture of the lesion (hypo- or hyperechoic, homogeneous or heterogeneous) and its borders toward surrounding tissue (well delineated, infiltrative, etc.). We especially look for any solid component, which is an important finding for the differentiation of a "true" tumor (i.e., hemangioma) and a malformation (Fig. 7.8). Any presence of cystic or tubular vascular channels inside a lesion is also recorded.

Color Doppler ultrasound is used to define the vascular pattern of a lesion (optimized low-flow color Doppler settings must be used to permit detection of small vessels, low-velocity arteries, and veins); hypovascular lesions are differentiated from lesions with little or dense vascularization. Vessel location is categorized as predominantly central, peripheral, or combined (central and peripheral). Vessel density inside a tumor is documented in a modified semi-quantitative fashion according to Dubois et al. [7, 8] (Fig. 7.9): the area of greatest vascular density is identified and color flow signals can be counted within an area of 1 cm^2. A vessel is defined as a linear or punctuate colored signal not associated with adjacent color noise (optimized setting of color gain is of utmost importance to reduce artifacts). Vessel density is defined as low (fewer than two vessels per square centimeter), moderate (2–4 vessels per square centimeter), or high (five or more vessels per square centimeter).

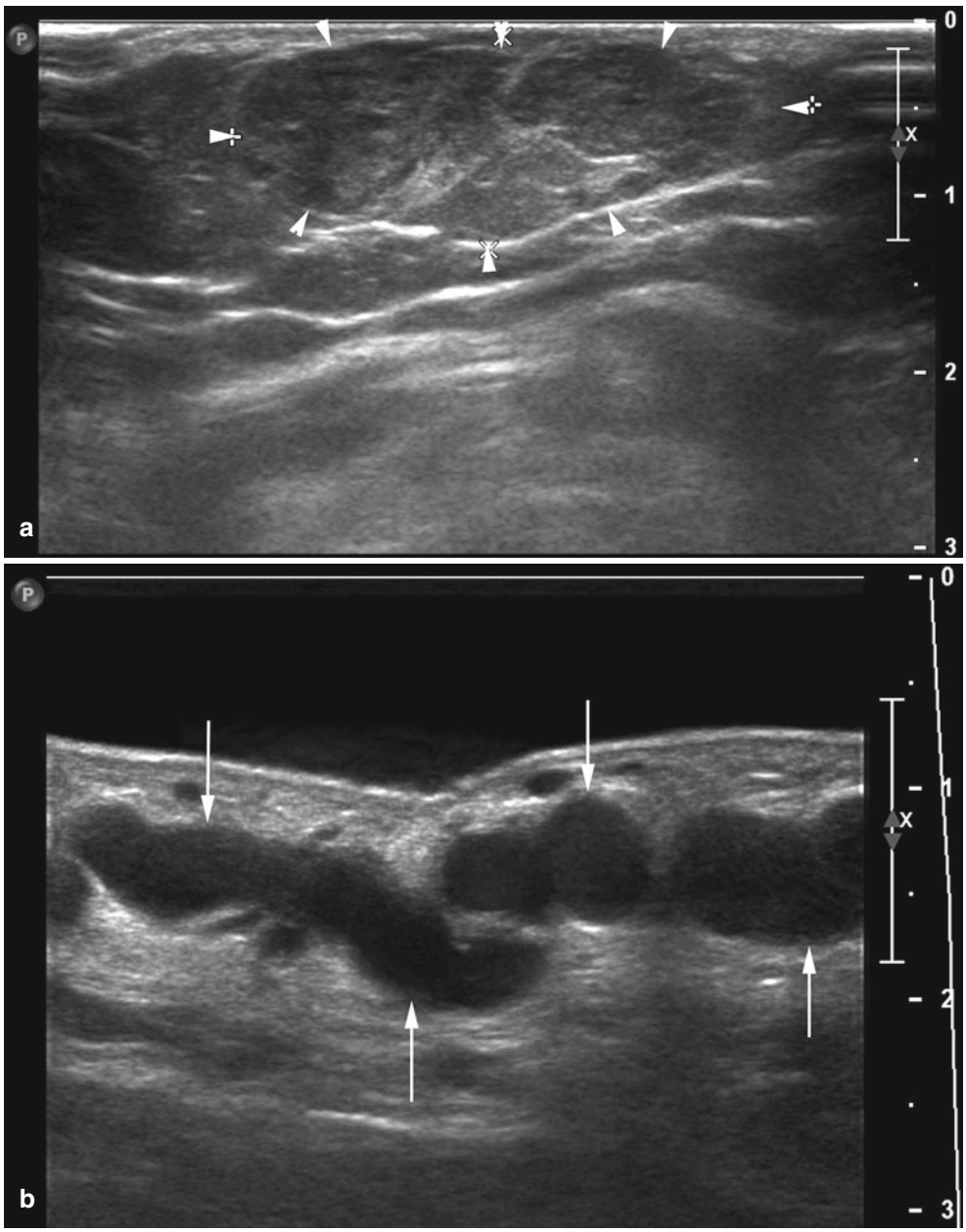

Fig. 7.8 (**a**) Typical hemangioma presenting a slightly hyperechoic and heterogeneous lobulated solid mass with distinct outer contour i.e., "true" soft-tissue tumor (*arrowheads*). (**b**) In contrast an arteriovenous malformation consisting of dilated anechoic vascular channels only (*arrows*) without a solid component

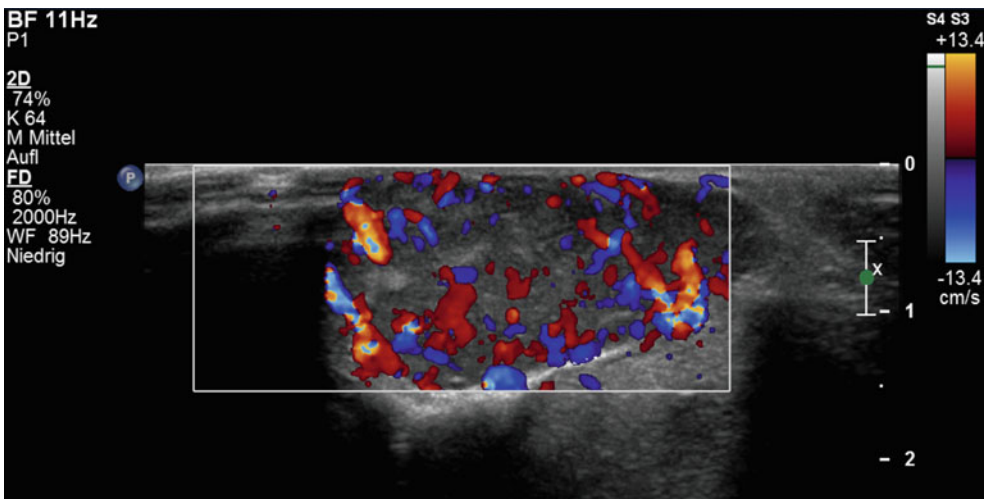

Fig. 7.9 Periorbital hemangioma in a child: a high vessel count of >5 is demonstrated inside a region of one square centimeter

An important additional tool for the differentiation of lesions with color Doppler ultrasound is the "compression test": with light compression of a lesion and subsequent release of transducer pressure a bidirectional venous flow can be induced inside the blood filled pouches of a venous malformation. A corresponding change of color encoding from red to blue is seen in the image, depending on transducer pressure (Fig. 7.10).

Teaching Point
A color Doppler ultrasound compression test shows bidirectional flow inside a lesion typical for venous malformations.

Duplex ultrasound and spectral wave analysis are used to characterize the types of vessels that exist inside the lesion: presence of venous/arterial vessels, arteriovenous shunts (high diastolic flow and resistive index (RI) below 0.5) (Fig. 7.11), and measurement of flow velocities to define a lesion as low, intermediate, or high flow. In the latter, flow volume or shunt volume across the lesion should also be evaluated (Fig. 7.12).

Contrast-enhanced ultrasound (CEUS) with application of microbubble contrast agents is not essentially new, but the value of CEUS for the examination of vascular anomalies has not been studied in detail [9]. Microbubbles circulate freely inside the body and constitute a true intravascular contrast agent; therefore, they permit analysis of tumor perfusion and regional blood flow. It is known from CEUS of soft-tissue tumors that microbubble-enhanced ultrasound can improve

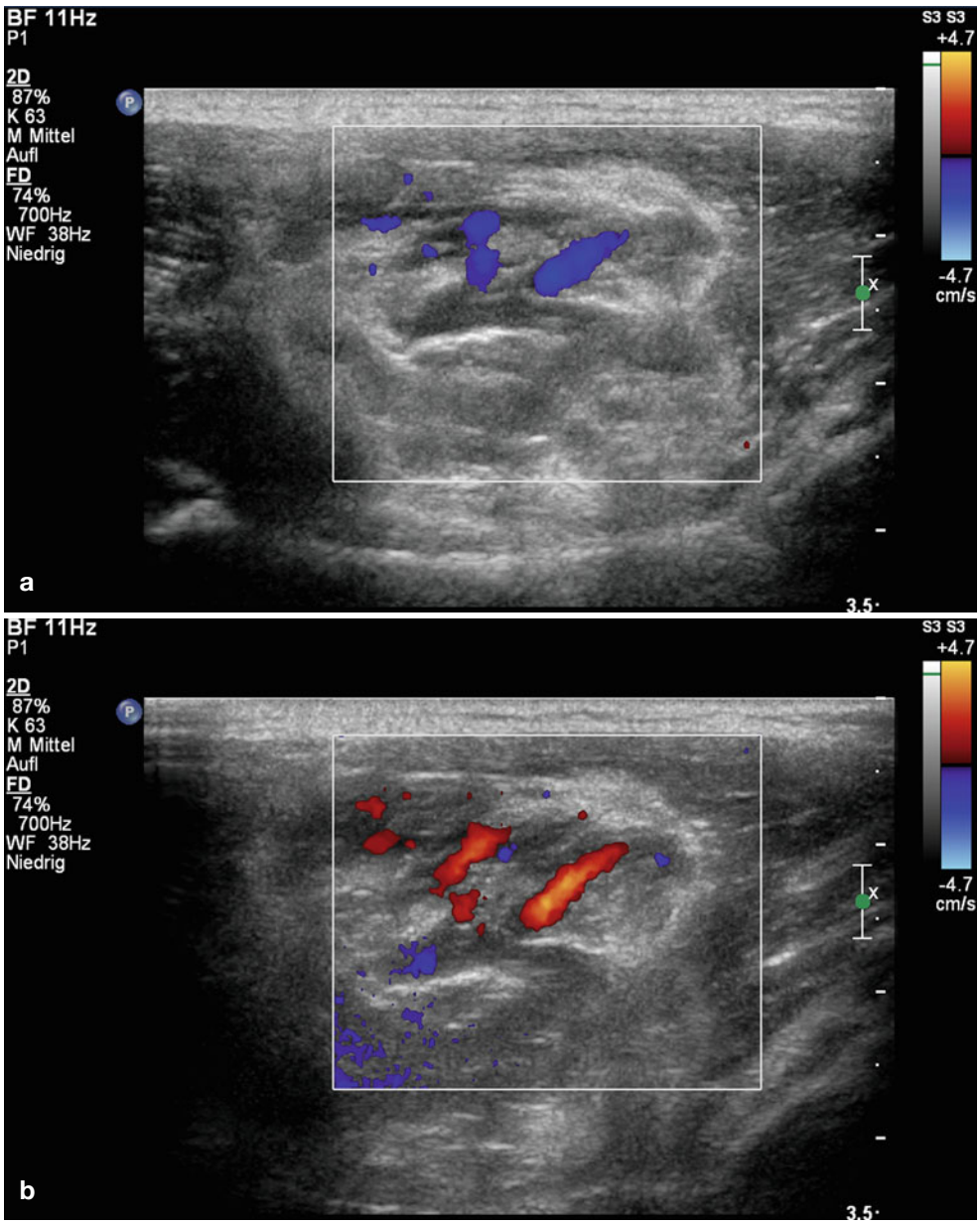

Fig. 7.10 (**a**, **b**) Compression ultrasound in a patient with low flow venous malformation: note color change from red to blue during the compression test confirming bidirectional venous flow

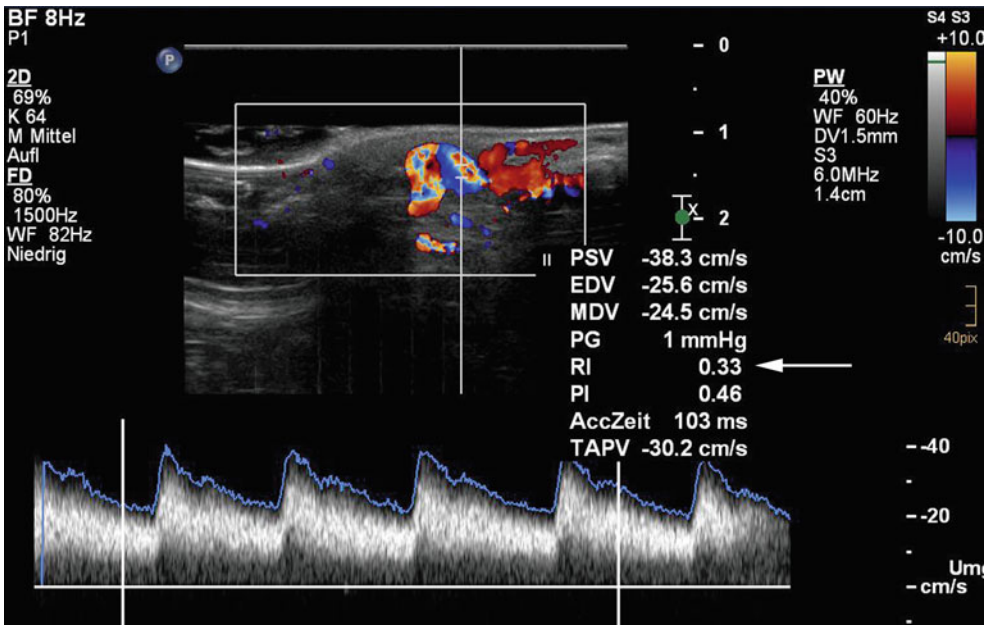

Fig. 7.11 High flow arteriovenous malformation, spectral wave analysis: demonstration of arteriovenous shunt flow with RI (resistive index) < 0.5 (*arrow*)

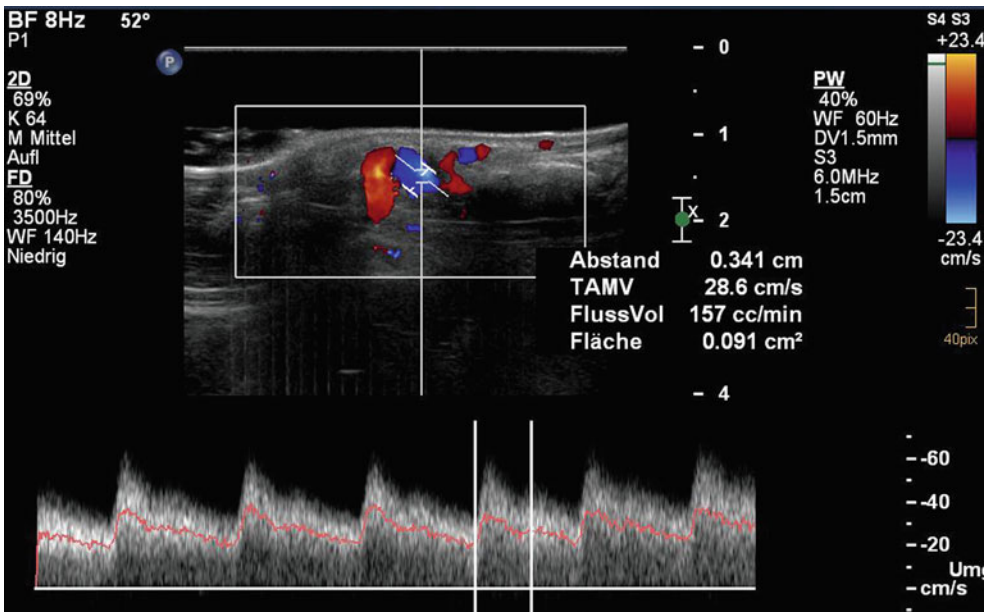

Fig. 7.12 Measurement of flow volume across the shunt: a shunt volume of 157 ml/min is demonstrated

the detection of perfusion compared with color Doppler ultrasound: in a substantial number of tumors that appear only sparsely vascularized with color Doppler ultrasound, CEUS gives a completely different impression by depicting more vessels and more intense perfusion. In particular, CEUS may offer improved detection of small arteriovenous shunts, which might have an impact on the grading of vascular anomalies into low-flow or intermediate/high-flow subtypes, and especially on evaluation of therapeutic success (extent of devascularization) after sclerotherapy (Fig. 7.13).

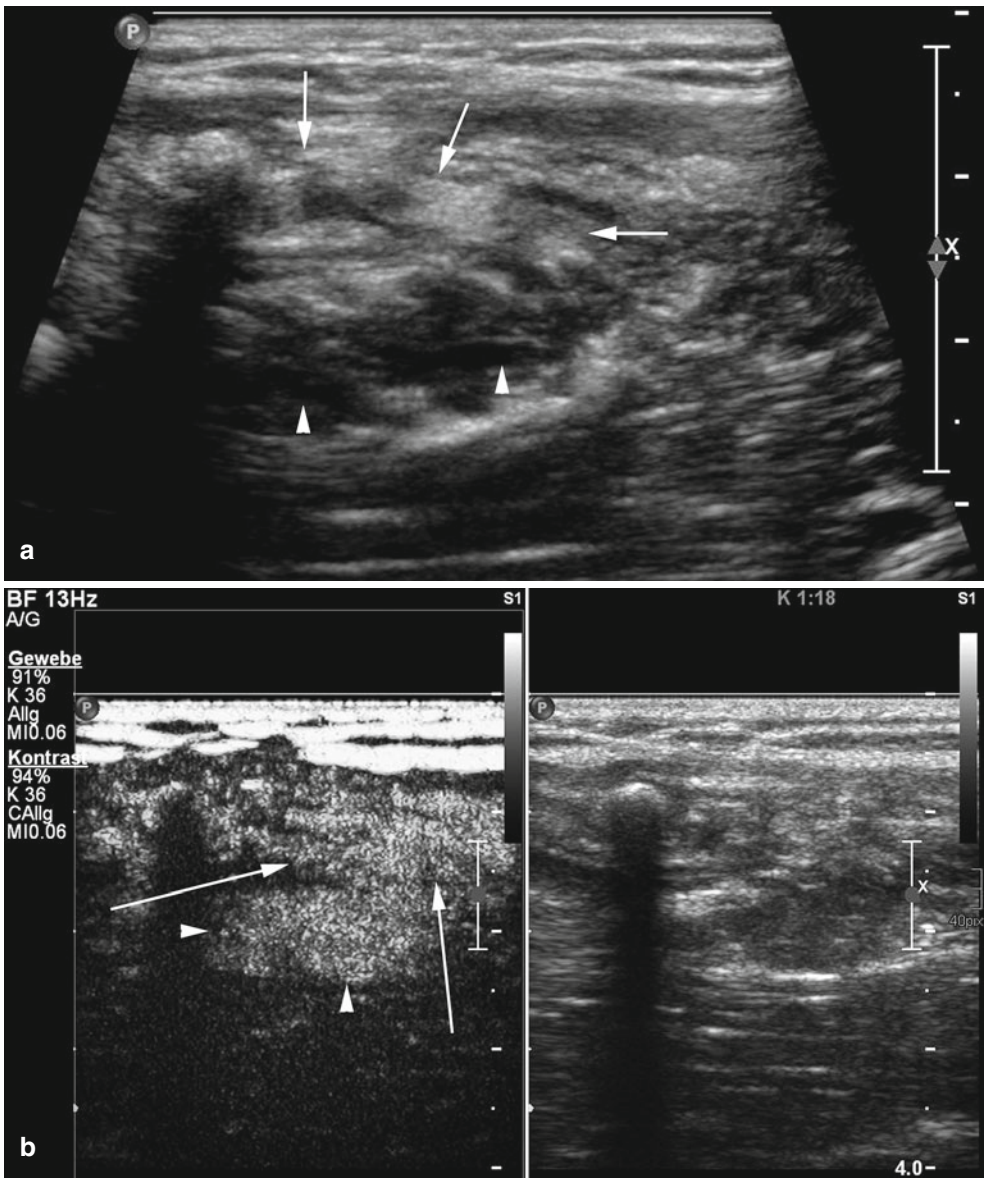

Fig. 7.13 (**a**) Grey scale ultrasound image in a patient with venous malformation after sclerotherapy. While some deep-lying blood-filled venous caverns are seen (*arrowheads*), the superficial part of the malformation seems largely fibrotic (*arrows*) corresponding with at least partial success. (**b**) Contrast-enhanced ultrasound image in the same patient (split screen image, left: tissue harmonic imaging mode, right: corresponding grey scale image): note dense contrast enhancement in venous caverns (*arrowheads*) and the superficial part of the malformation also (*arrows*) which was considered fibrotic on grey scale images

7.5 Hemangioma

7.5.1 Clinical Background

Hemangiomas of infancy are benign vascular tumors typically present at birth. In contrast to vascular malformations, hemangiomas show an initial proliferative phase, followed by slow involution during early childhood. A second proliferative phase may precede regression in some hemangiomas. The time at which regression occurs differs substantially: around 50 % of hemangiomas regress completely by the age of 5 years and almost 90 % by the age of 9–10 years. Despite involution, the prognosis of a hemangioma can be disappointing resulting from cosmetic impairment, and furthermore, hemangiomas may pose a clinical problem, depending on their location: perioral, perianal, or orbital hemangiomas may bleed, impair vision, or cause other problems [10]. In contrast to simple hemangiomas, an extensive imaging work-up is advocated in the latter type. Ultrasound may often suffice, but for particularly deep-lying hemangiomas (such as lesions inside the orbit), MRI may be a better choice. In contrast to vascular malformations, most hemangiomas do not need invasive treatment.

7.5.2 Ultrasound Characteristics

Hemangiomas differ in their appearance according to the phase; thus, lesions in the proliferative stage appear as hypoechoic hypervascular ill-defined structures on ultrasound

that become heterogeneous (i.e., hypoechoic and hyperechoic areas) during partial involution. The intensity of the vascularity that can be detected within the lesions also varies during the different degrees of involution going from hypervascular to hypovascular. In the end stage of involution, hemangiomas tend to show hyperechogenicity and hypo- or lack of vascularity (Figs. 7.14, 7.15, 7.16, 7.17, 7.18, 7.19, 7.20, 7.21, 7.22, 7.23, 7.24, and 7.25).

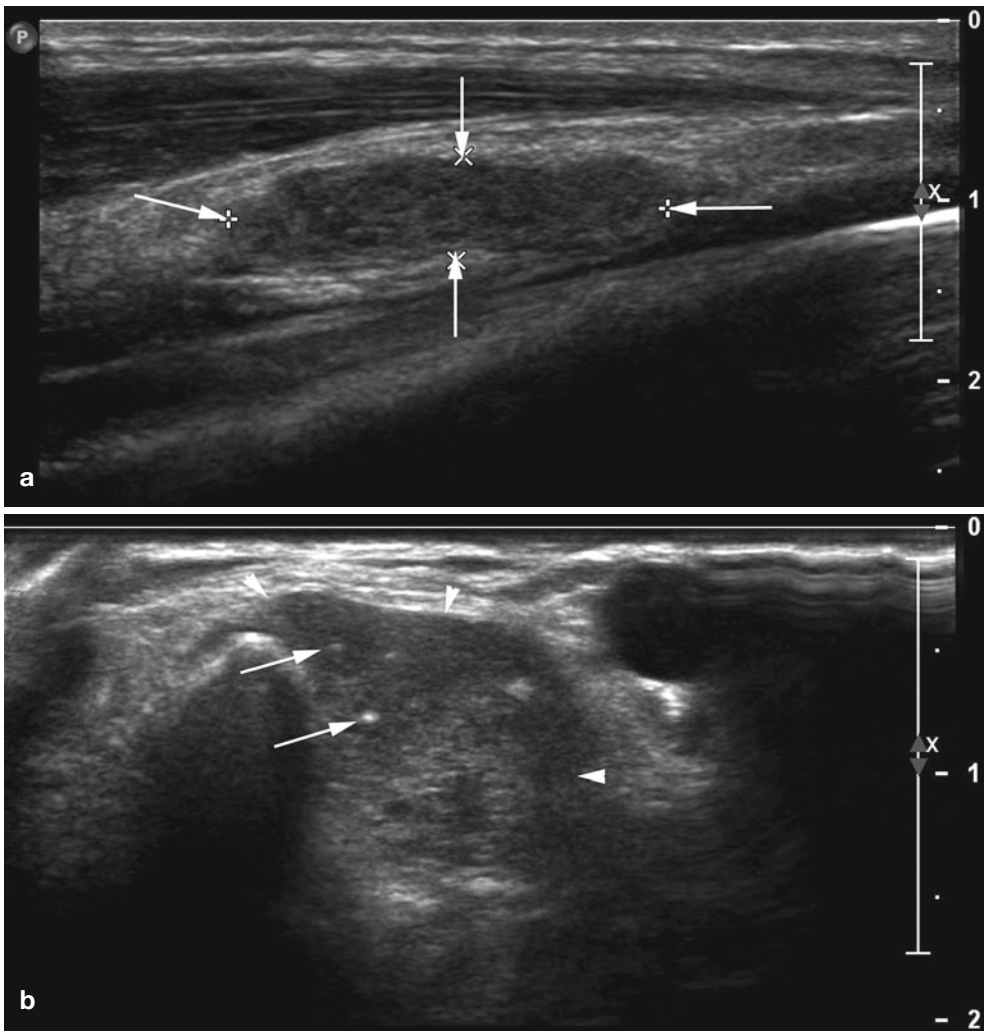

Fig. 7.14 (**a**) Hemangioma with distinct outer border and relatively homogeneous texture, slightly hyperechoic to muscle. (**b**) Hemangioma in another patient with distinct capsule (*arrowheads*) but more inhomogeneous texture and tiny calcific foci (*arrows*)

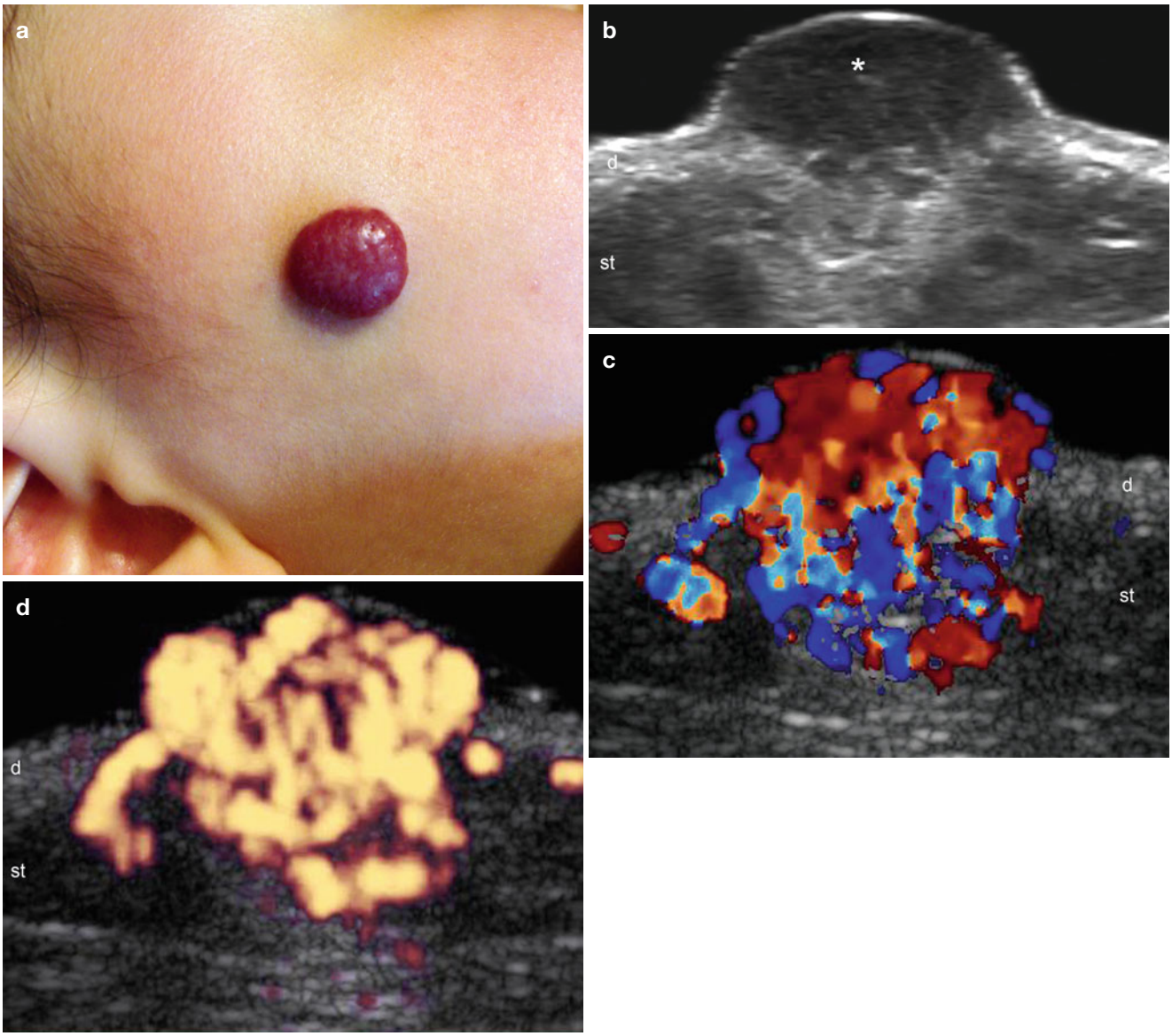

Fig. 7.15 (**a**–**f**) Hemangioma (proliferative phase). (**a**) Clinical erythematous bump in the right cheek. (**b**) Grey scale ultrasound image (transverse view) shows hypoechoic tissue (*) in the dermis that displaces the epidermis upward. Hyperechogenicity of the subcutaneous tissue is also detected. (**c**) Color Doppler ultrasound image and (**d**) power Doppler ultrasound image (transverse view) demonstrates prominent vascularity in the lesional area. (**e**, **f**) Color Doppler ultrasound spectral curve analysis (transverse view) shows arterial (**e**) and venous (**f**) flow within the mass. *Abbreviations*: *d* dermis, *st* subcutaneous tissue

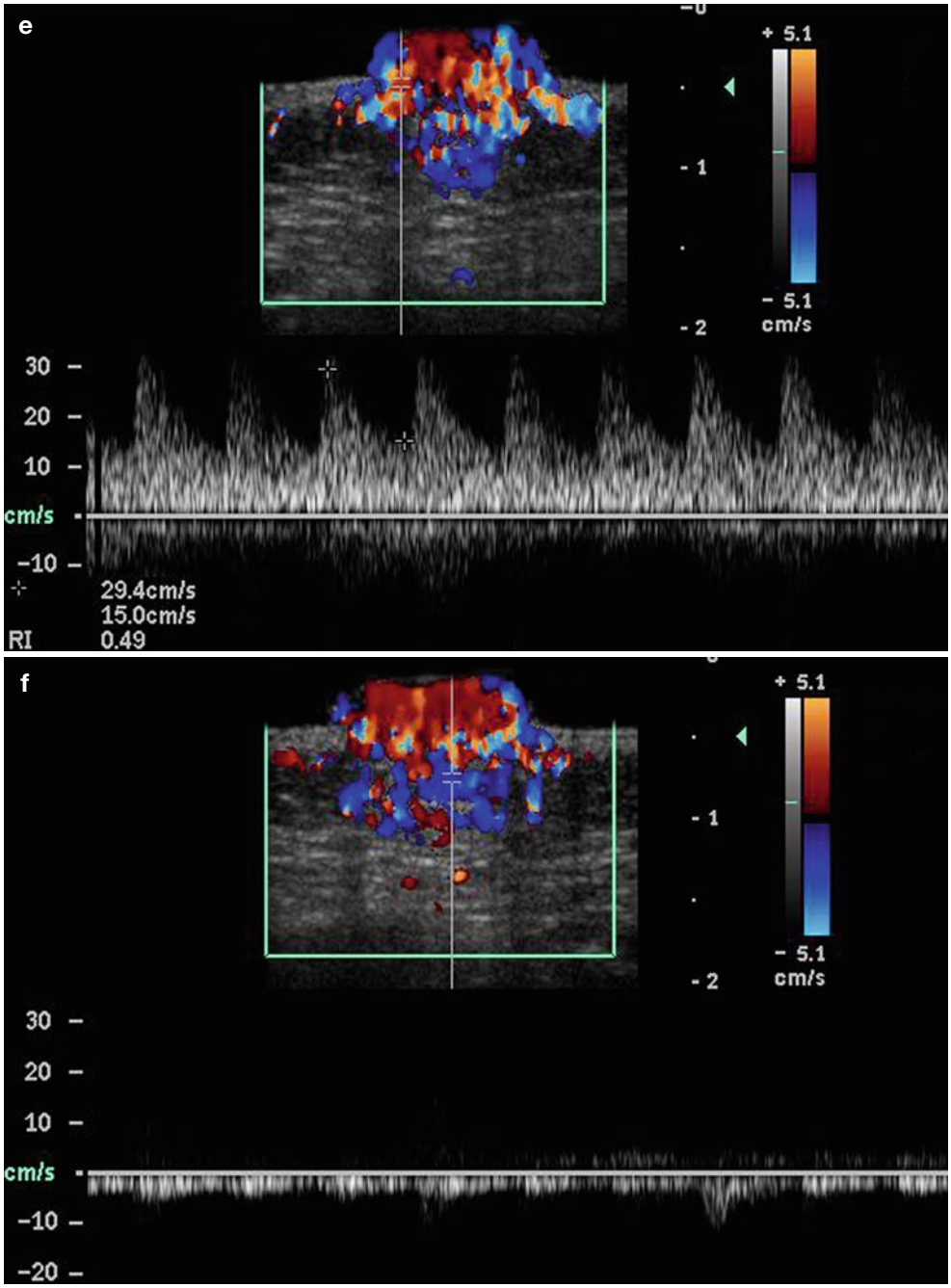

Fig. 7.15 (continued)

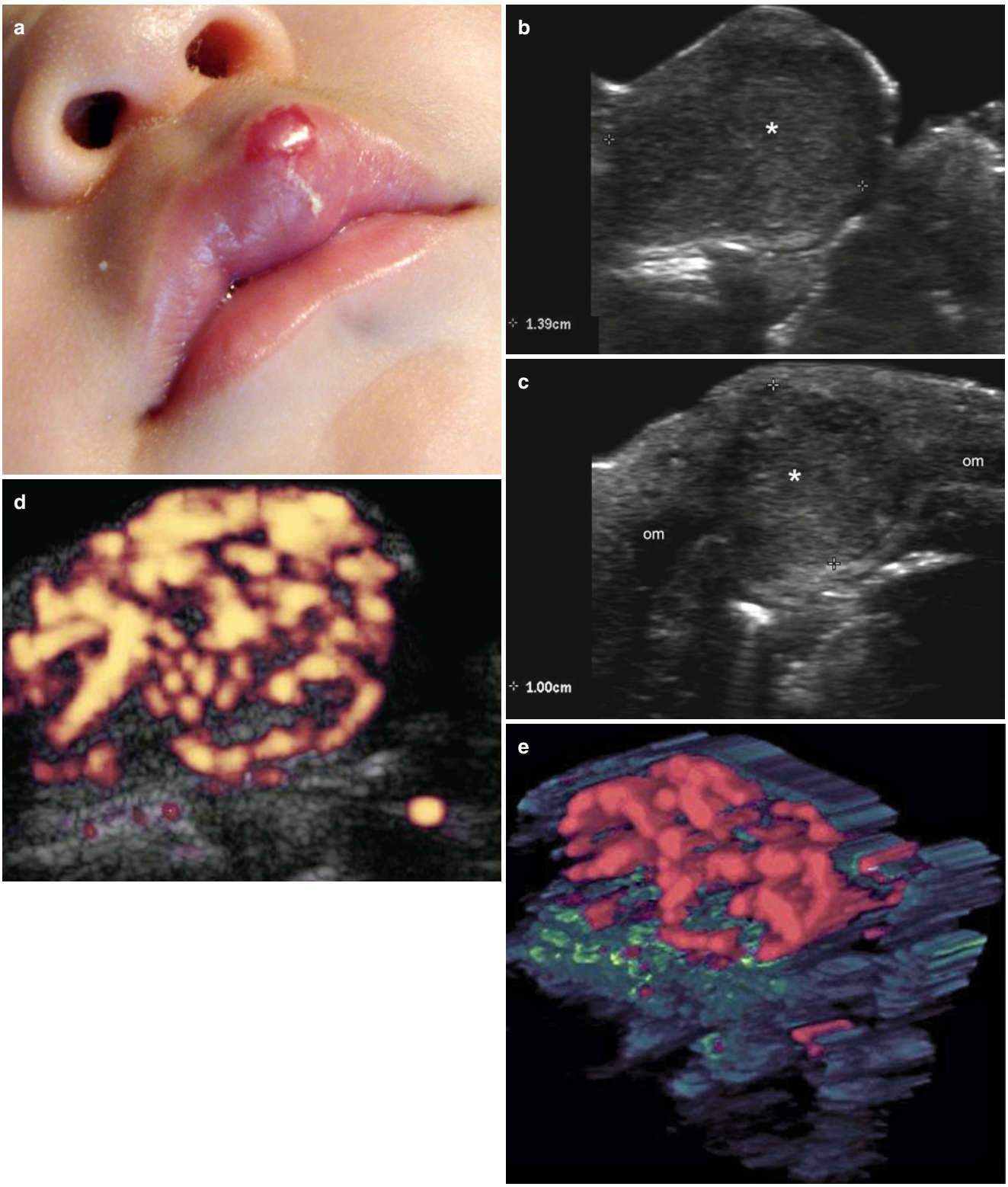

Fig. 7.16 (**a**–**g**) Hemangioma (proliferative phase) (**a**) Clinical lesion shows erythematous swelling in the upper lip. (**b**) Grey scale ultrasound image (longitudinal view) demonstrates 1.39 cm long hypoechoic mass (*) in the upper lip that involves the cutaneous layers and the orbicularis muscle. (**c**) Grey scale ultrasound image (transverse view) shows 1.0 cm depth hypoechoic mass. Notice the discontinuity of the orbicularis muscle (*om*). (**d**) Power Doppler ultrasound image and (**e**) 3D reconstruction power angio (longitudinal view) demonstrates the prominent vascularity within the mass. (**f**, **g**) Spectral curve analysis shows the arterial (**f**) and arterialized venous flow shunts (**g**) in the same mass

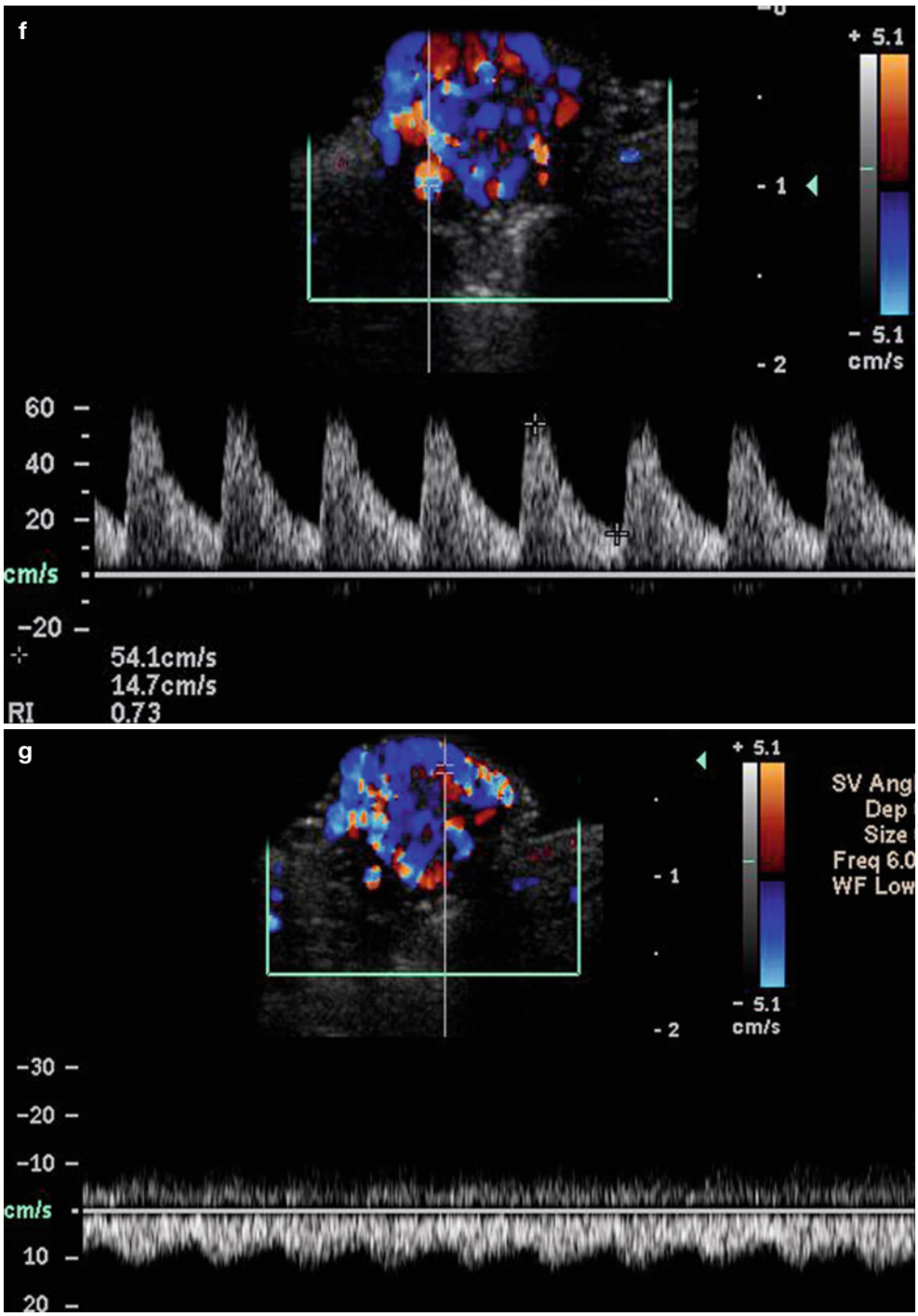

Fig. 7.16 (continued)

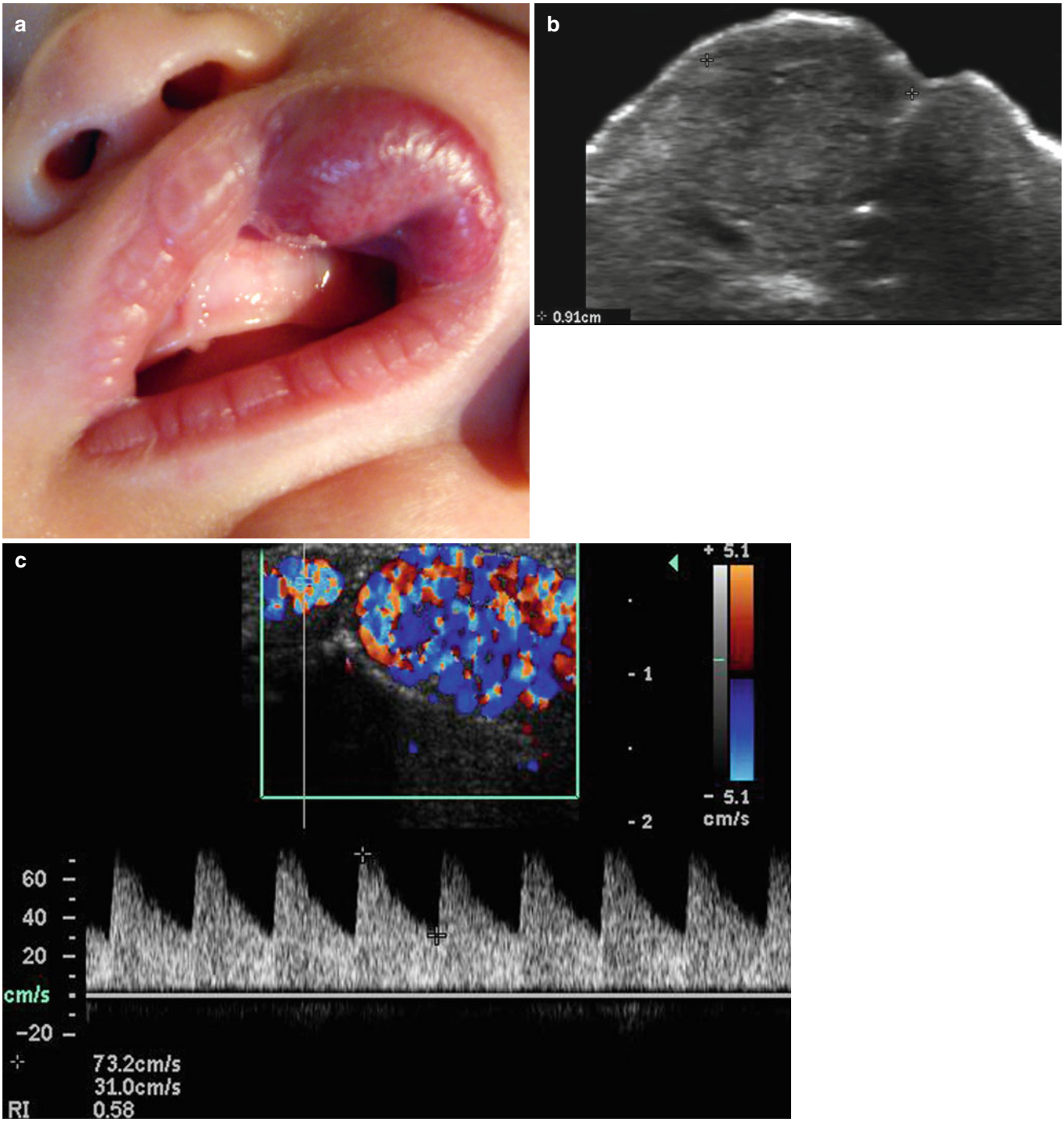

Fig. 7.17 (**a**–**d**) Hemangioma (proliferative phase). (**a**) Clinical image shows erythematous swelling, retraction, and deformation of the upper lip. (**b**) Grey scale ultrasound image (longitudinal view) demonstrates 0.9 cm long ill-defined hypoechoic mass that affects the cutaneous layers and the orbicularis oris muscle. (**c**) Color Doppler ultrasound spectral curve analysis (transverse view) shows a high peak of systolic velocity within the arterial vessels (73.2 cm/s). (**d**) Power angio 3D reconstruction demonstrates the hypervascularity of the mass

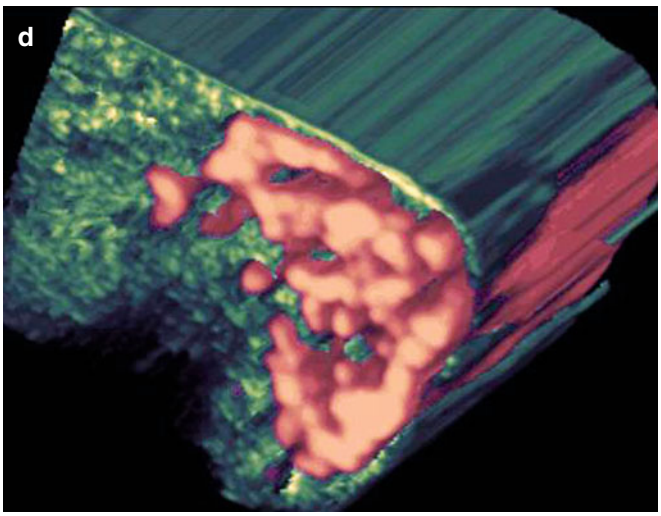

Fig. 7.17 (continued)

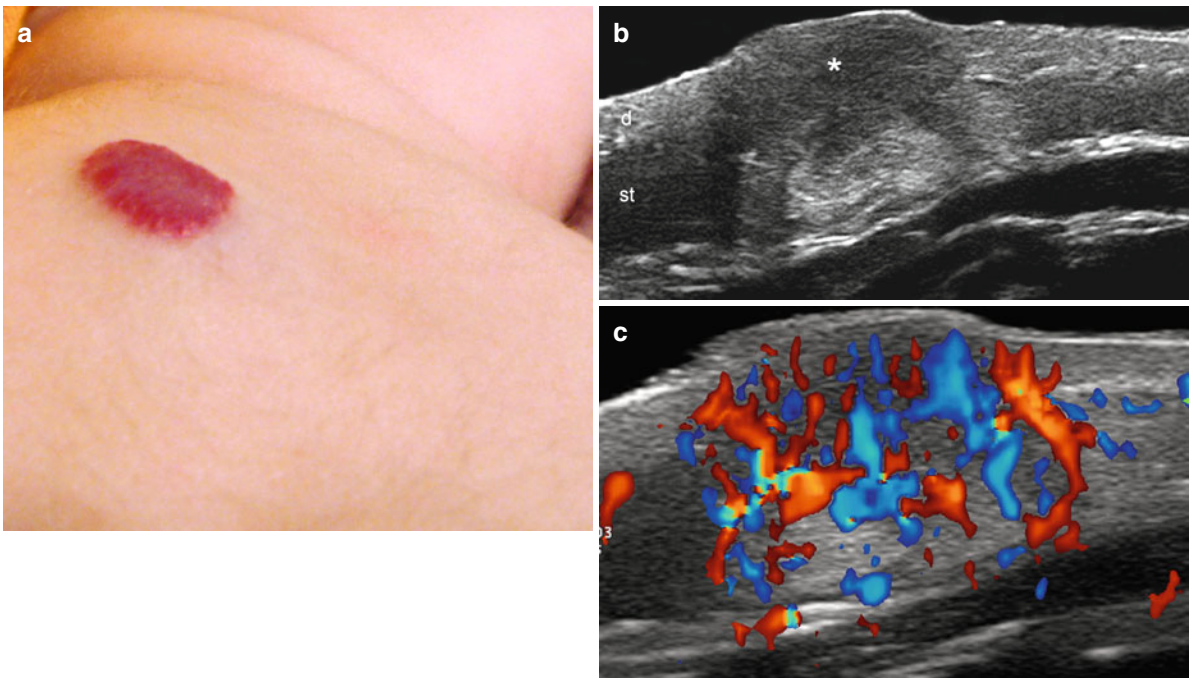

Fig. 7.18 (**a**–**c**) Hemangioma (mostly proliferative phase). (**a**) Clinical lesion shows erythematous bump in the dorsal region. (**b**) Grey scale ultrasound image (transverse view) demonstrates a mass with prominent hypoechogenicity (*) in the dermis and upper subcutaneous tissue. Hyperechogenicity is detected in the lower subcutaneous tissue. (**c**) Color Doppler ultrasound image (transverse view) shows hypervascularity within the mass. *Abbreviations*: *d* dermis, *st* subcutaneous tissue

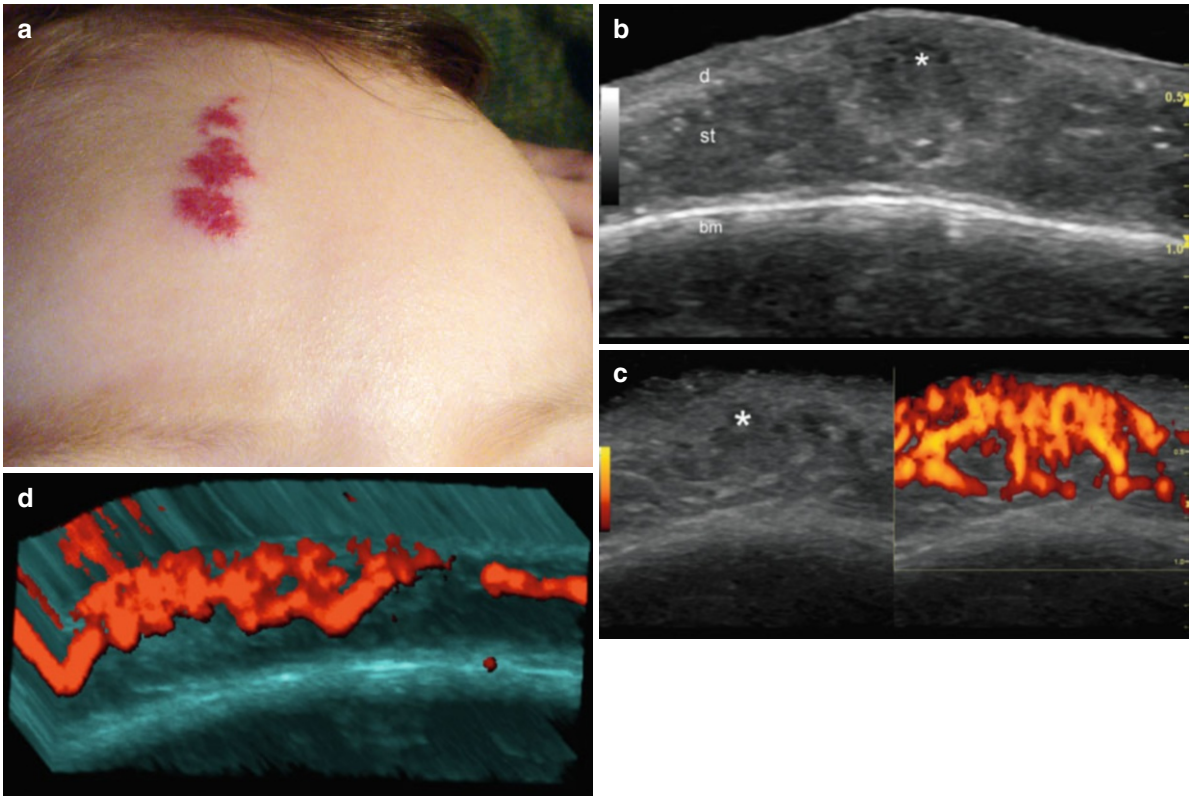

Fig. 7.19 (**a**–**d**) Hemangioma (mostly proliferative phase). (**a**) Clinical image demonstrates an erythematous swelling in the right frontal region. (**b**) Grey scale ultrasound image (transverse view) shows ill-defined hypoechoic lesion (*) that affects the dermis and upper subcutaneous tissue. (**c**) Grey scale ultrasound image and power. Doppler ultrasound image (comparative images) demonstrates prominent vascularity within the mass (*). (**d**) Power angio 3D reconstruction (5–8 s) of the lesion. *Abbreviations*: *d* dermis, *st* subcutaneous tissue, *bm* bony margin of the skull

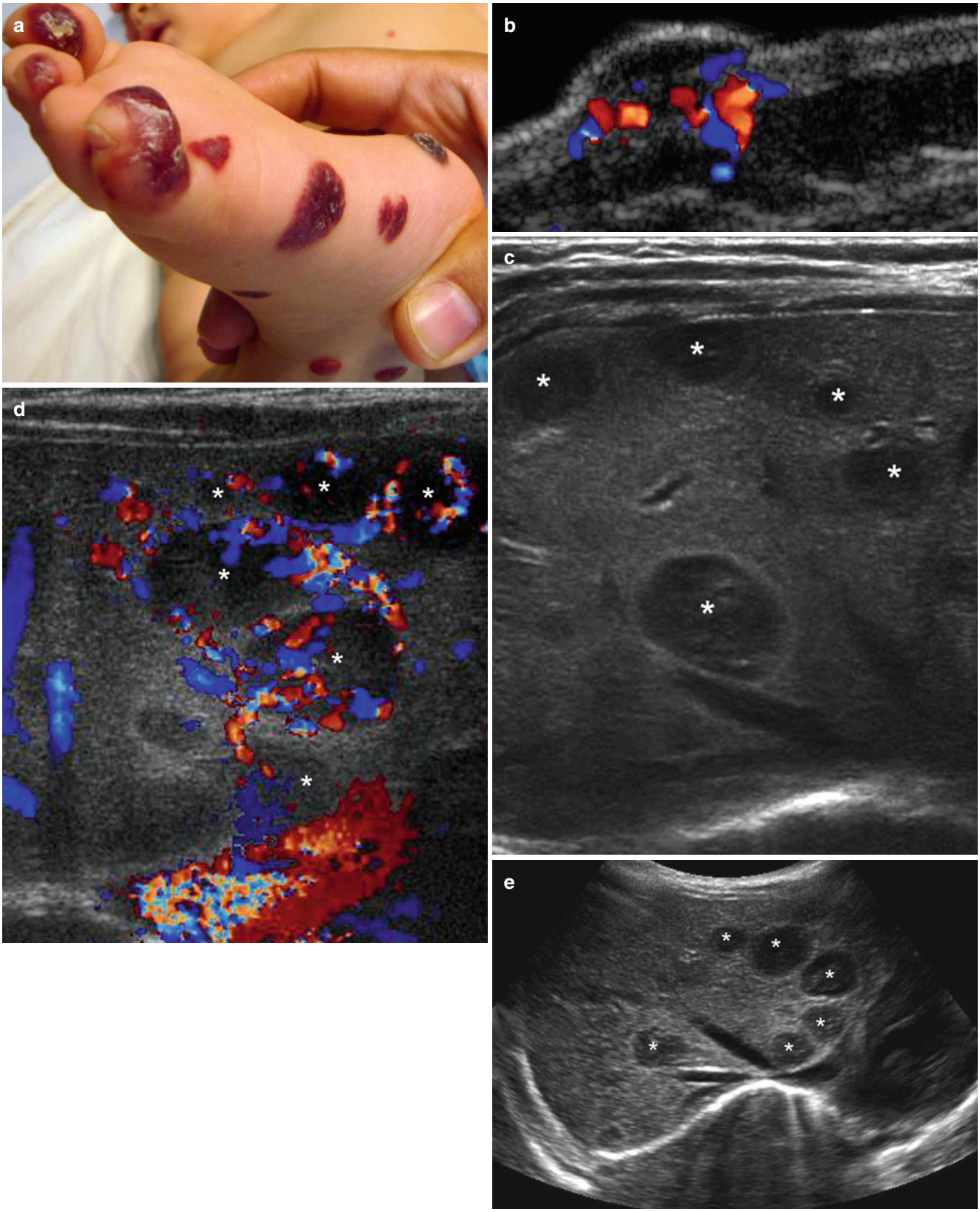

Fig. 7.20 (**a**–**e**) Multiple cutaneous and hepatic hemangiomatosis (proliferative phase). (**a**) Clinical image shows multiple cutaneous hemangiomas in the right foot. (**b**) Grey scale ultrasound image (transverse view) of one of the lesions demonstrates hypoechoic mass affecting dermis and subcutaneous tissue with increased blood flow. (**c**) Grey scale ultrasound image of the liver (transverse view) in the same patient shows multiple hypoechoic nodules suggestive of hemangiomas. (**d**) Color Doppler ultrasound image (transverse view) demonstrates increased vascularity in the periphery and within the hepatic nodules (*). (**e**) Grey scale ultrasound image (extended transverse axis) shows a wider view of the multiple hepatic nodules (*)

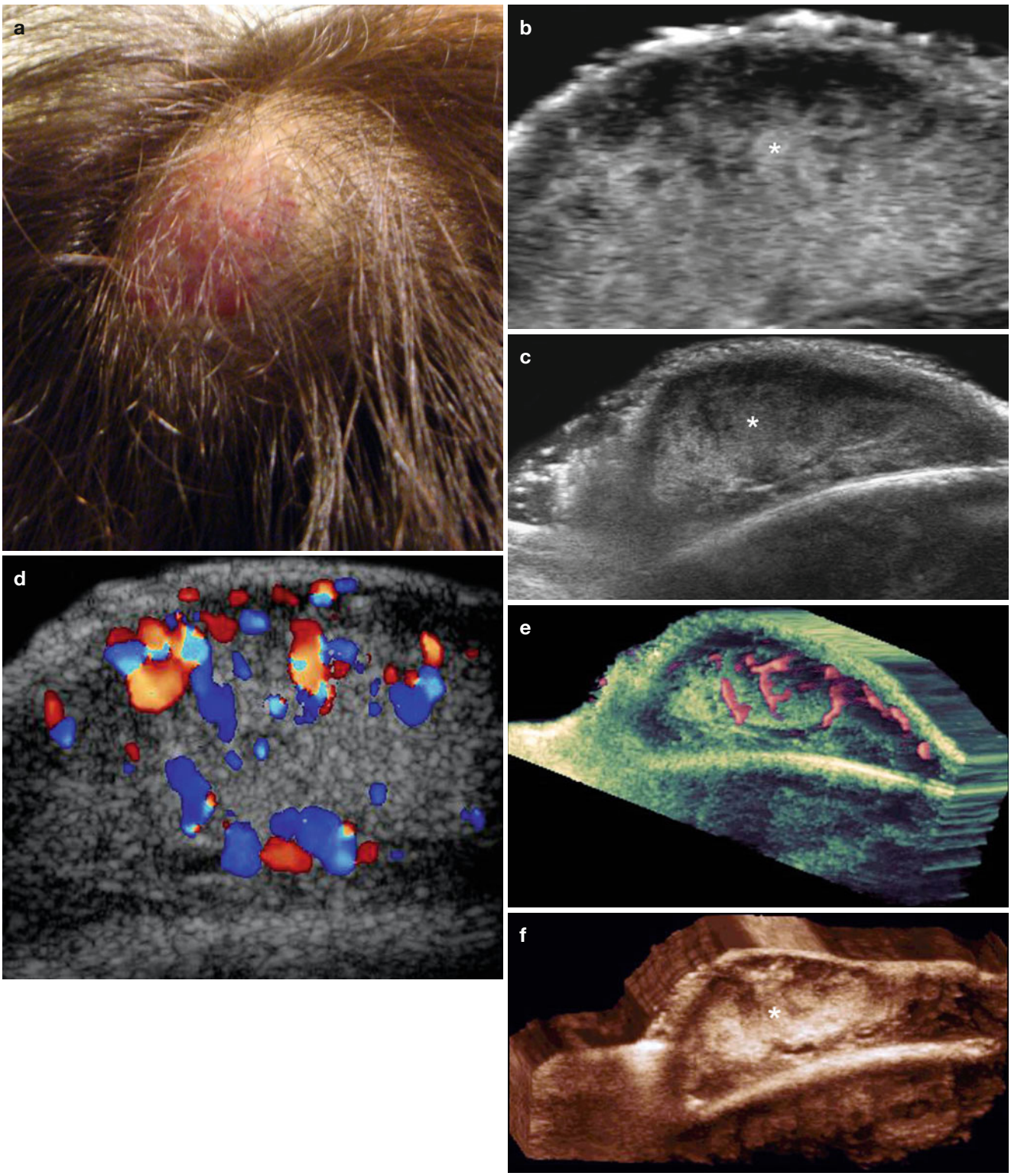

Fig. 7.21 (**a**–**f**) Hemangioma (partial regression phase). (**a**) Clinical erythematous lesion in the scalp. (**b**) Grey scale ultrasound image (transverse view) and (**c**) Grey scale ultrasound image (extended transverse view) shows a mixed echogenicity ill-defined mass (*) that involve dermis and subcutaneous tissue (*). (**d**) Color Doppler ultrasound image (transverse view) demonstrates increased vascularity within the mass. Nevertheless, the blood flow is less prominent compared with the previous cases in proliferative phase. (**e**) 3D power and (**f**) grey scale reconstructions of the hemangioma

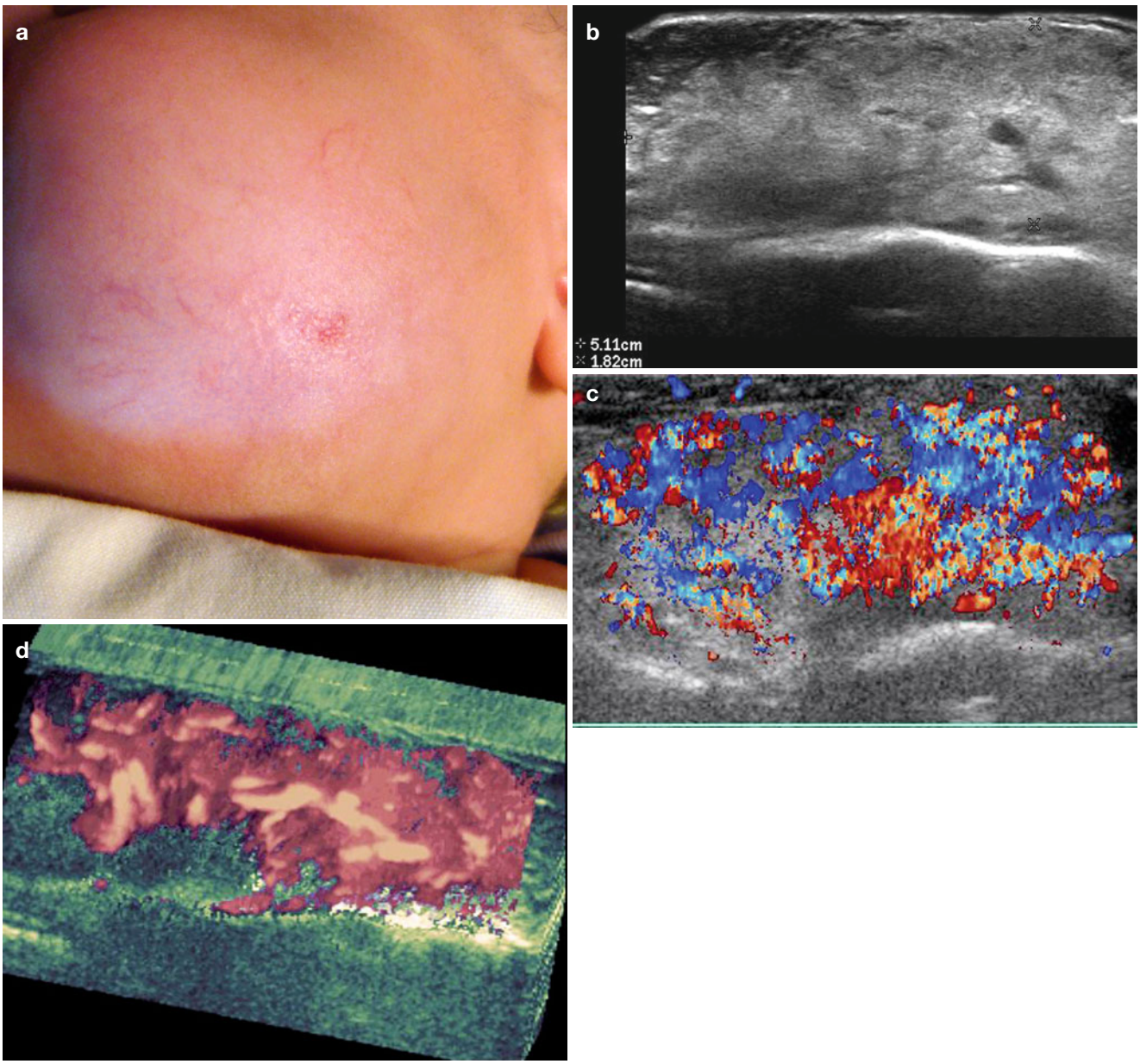

Fig. 7.22 (**a**–**d**) Hemangioma (partial regression phase). (**a**) Clinical erythematous lesion in the left cheek. (**b**) Grey scale ultrasound image (transverse view) that shows 5.11 × 1.82 cm Ill-defined heterogeneous mass that involves dermis, subcutaneous tissue and the masseter muscle. (**c**) Color Doppler ultrasound image (transverse view) and (**d**) 3D Power angio reconstruction (transverse view, 5–8 s) demonstrate increased vascularity within the mass

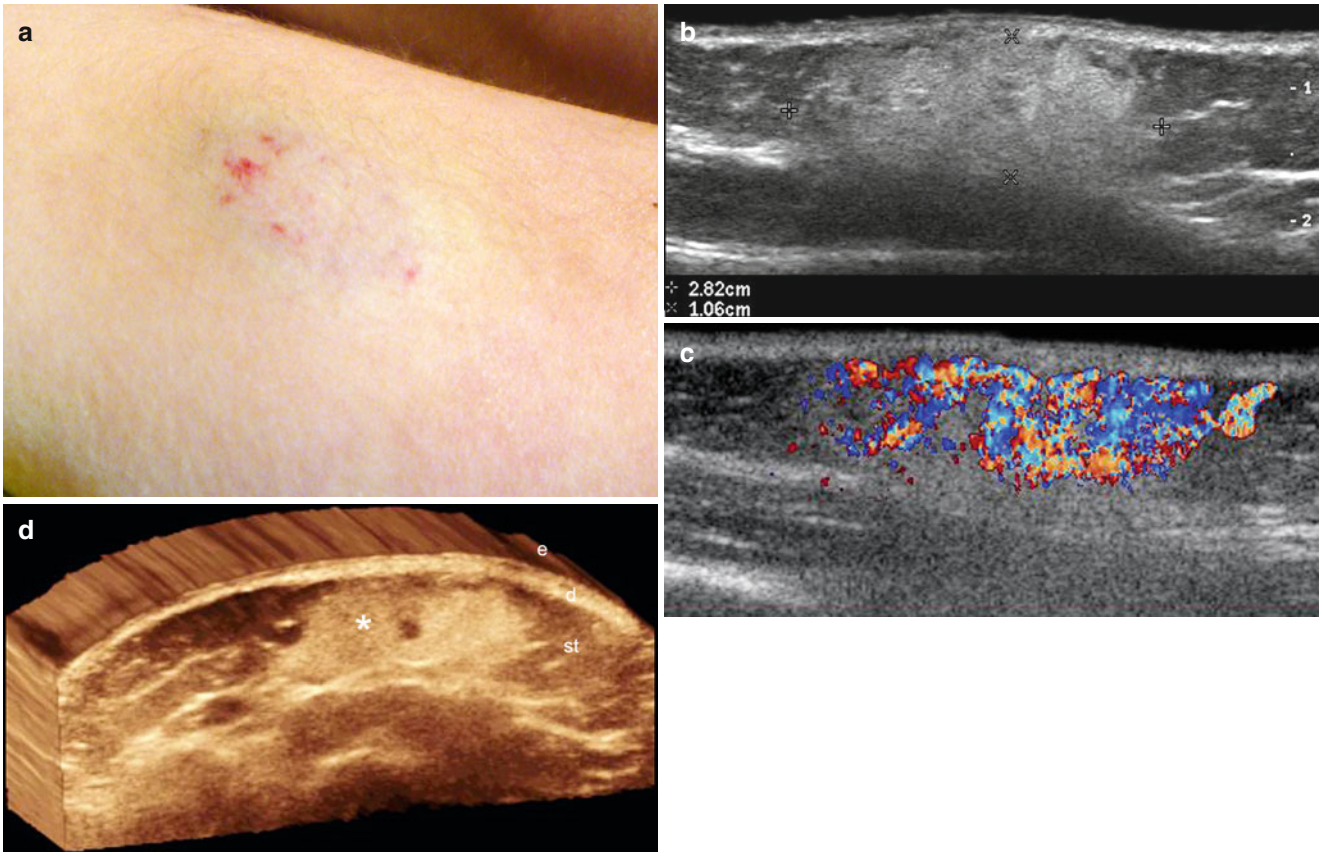

Fig. 7.23 (**a**–**d**) Hemangioma (partial regression phase). (**a**) Clinical image shows erythematous lesion in the left arm. (**b**) Grey scale ultrasound image (longitudinal view) demonstrates 2.82 × 1.06 cm Ill-defined hyperechoic and heterogeneous mass that mostly affects the subcutaneous tissue. (**c**) Color Doppler ultrasound image (longitudinal view) shows increased turbulent blood flow within the lesion. (**d**) 3D reconstruction (transverse view, 5–8 s) of the lesion (*). *Abbreviations*: *e* epidermis, *d* dermis, *st* subcutaneous tissue

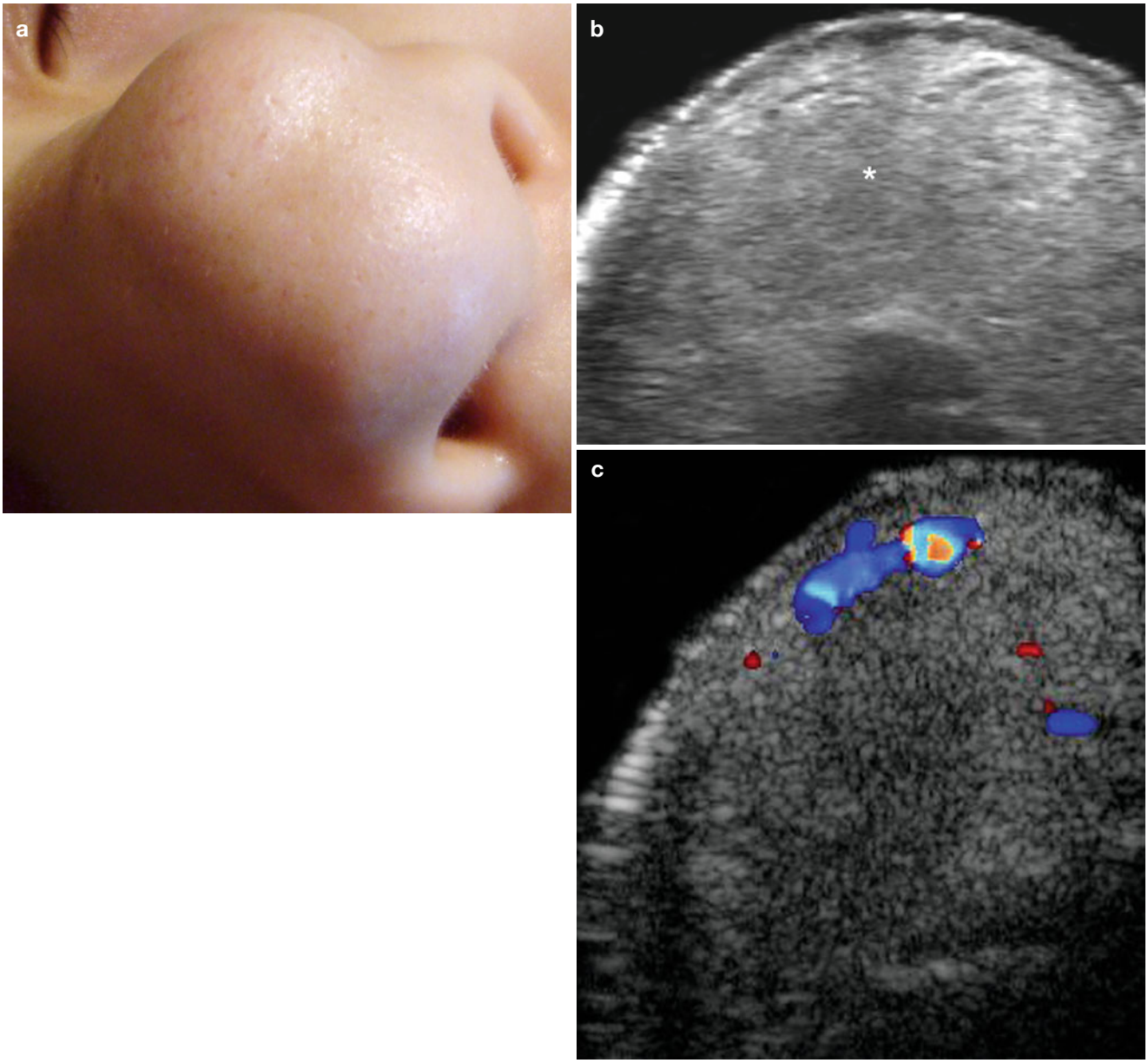

Fig. 7.24 (**a**–**c**) Hemangioma (complete regression phase). (**a**) Clinical image shows a lump in the tip of the nose. (**b**) Grey scale ultrasound image (transverse axis) demonstrates ill-defined hyperechoic mass (*) that affects the cutaneous layers and the nasal cartilages. (**c**) Color Doppler ultrasound image (transverse view) shows scarce presence of vascularity within the mass in comparison with the previous cases

Vascular channels, pouches, or pseudocystic structures large enough to be seen on B-mode are not a typical feature of hemangiomas [7]. Nevertheless, most hemangiomas show blood flow through many small vessels that may not be detectable with B-mode ultrasound. Therefore, on color Doppler ultrasound, hemangiomas are typically hypervascular with intense perfusion and high vessel density according to the criteria mentioned above (five or more vessel counts per square centimeter) (Fig. 7.24). With duplex ultrasound the arterial vessels inside a hemangioma have a Doppler shift of >2 KHz, or in other words show high systolic flow velocities (Fig. 7.26). Together with a high vessel count this is a highly specific feature for the diagnosis of hemangiomas and the combination of high vessel count and high-flow velocity results in a positive predictive value of 97 % [7]. Proliferative hemangiomas show prominent arterial blood flow, low-velocity venous vessels, and occasionally arteriovenous shunts. During the involution phase, the arteriovenous shunts start to disappear and the peak systolic velocity of the arterial vessels tends to decrease.

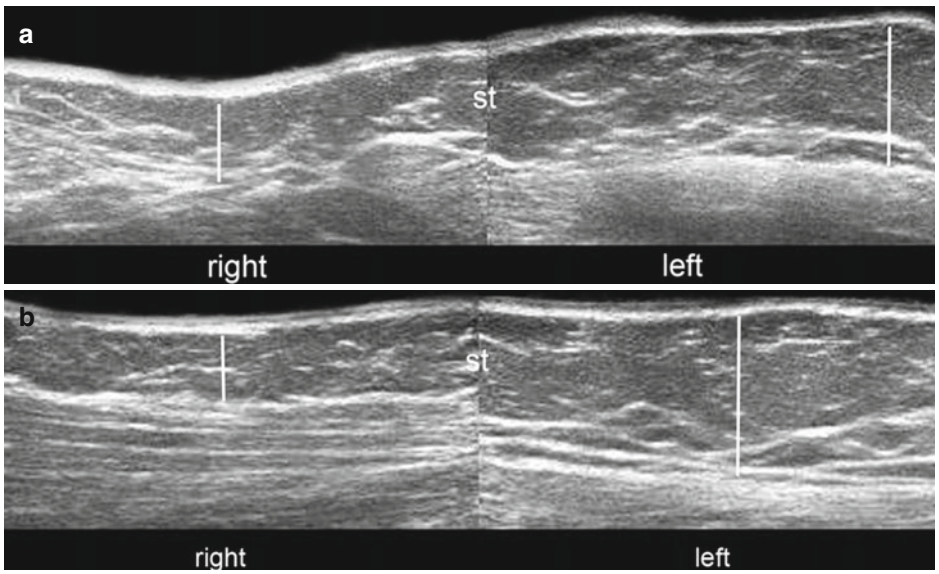

Fig. 7.25 (**a**, **b**) Hypertrophic lipodystrophy secondary to a hemangioma (total regression phase). Grey scale ultrasound images in (**a**) (transverse view) and (**b**) (longitudinal view) show side by side comparisons of the chest region. Notice the hypertrophy of the subcutaneous tissue in the left side (hemangioma site) in comparison with the normal right side (*white vertical lines*). The echogenicity of the subcutaneous tissue is unremarkable (total regression phase). *Abbreviation*: *st* subcutaneous tissue

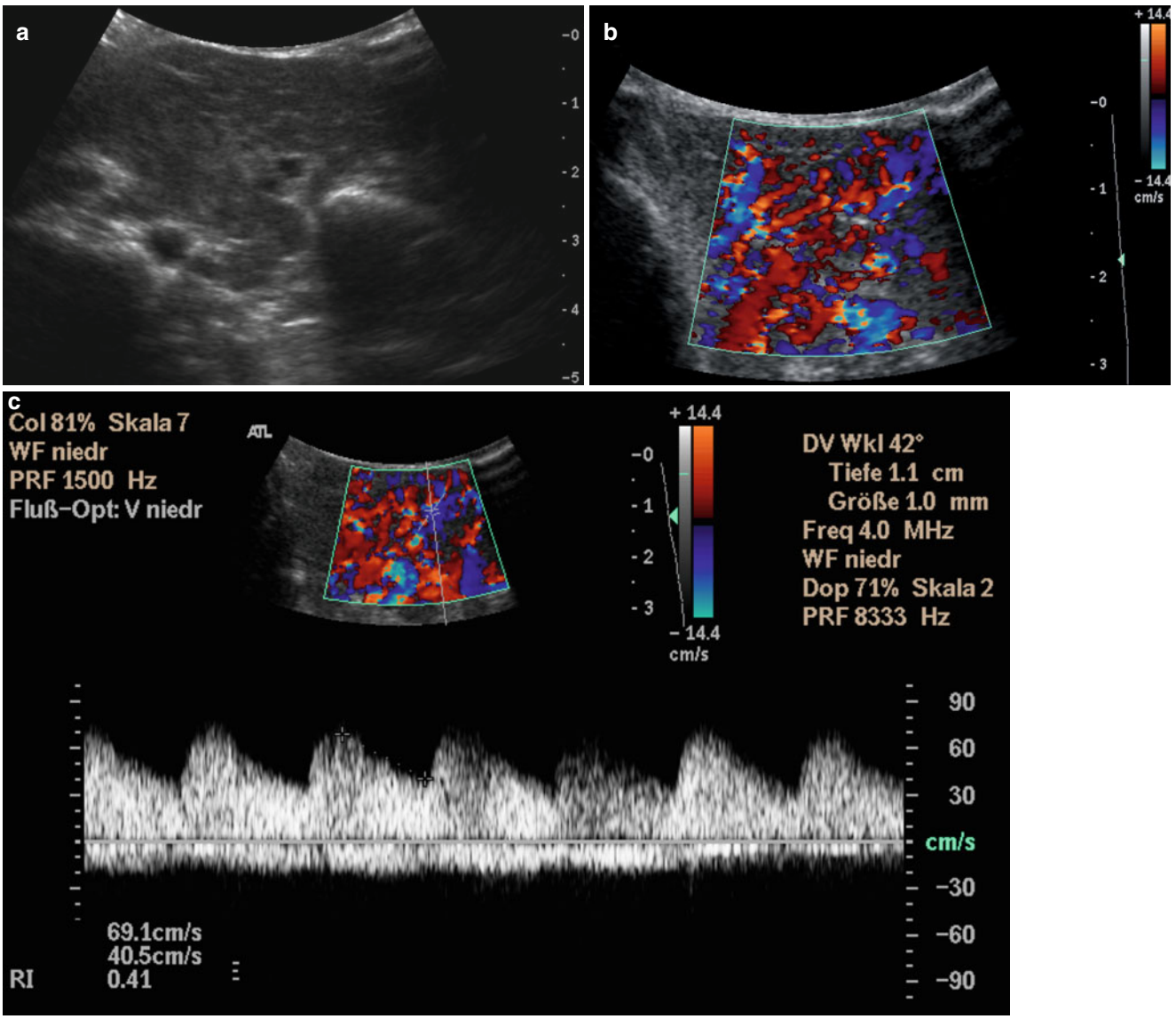

Fig. 7.26 (**a**) Transverse grey scale image of hemangioma inside the parotid gland. (**b**) Color Doppler ultrasound image shows a high vascular density with more than five vessel counts per square centimeter. (**c**) Spectral curve analysis: maximum systolic flow velocity of 70 cm/s and high diastolic flow resulting in an resistive index (RI) of < 0.5 is demonstrated

Teaching Point
A high vessel density throughout the entire lesion along with high velocity arterial and venous signals inside a solid lesion is highly specific for hemangioma.

As mentioned previously, hemangiomas (benign lesions) and soft-tissue sarcomas are not easily differentiated using B-mode ultrasound alone. What about color Doppler ultrasound and duplex ultrasound? The problem is that both types of lesions (hemangiomas and malignant tumors) are capable of stimulating the host into creating new vessels, usually from existing endothelial cells, by secreting angiogenesis factors. This is the reason why hemangiomas, in contrast to other benign soft-tissue tumors, show high vascularization. These newly produced vessels lack normal wall architecture (the muscularis layer is absent) and therefore have a high velocity with low resistance. In this regard, hemangiomas may resemble malignant soft-tissue tumors, however, in the latter, vessels are mostly found at the periphery of the tumor (active infiltrative tumor tissue) while in hemangioma the vessels are distributed more evenly throughout the lesion [11] (Fig. 7.27), which is why a high vessel density throughout the lesion is unlikely to be found in a malignant soft-tissue sarcoma.

7.6 Vascular Malformations

7.6.1 Arterial and ArterioVenous Malformations

7.6.1.1 Clinical Background

Arterial and arteriovenous malformations (AVMs) have no relationship to endothelial proliferation, but represent abnormal differentiation of vessels during embryogenesis. They are congenital lesions that are typically present at birth but often initially not detected. Additional growth, vascular factors, trauma, or endocrine changes result in clinical manifestation of the evolutive lesions, resulting in detection that is sometimes delayed into adolescence. Unlike hemangiomas, vascular malformations typically increase in size during growth. The main locations are the head and neck (40 % of cases), extremities (40 %), and torso (20 %) [12]. They represent a superficial soft-tissue mass that is typically soft and patchy with bluish or red discoloration of the skin. They derive from aberrant vessels and consist of a nest of arterial vessels or direct connections between arterial, venous, capillary, and also lymphatic vessels. This collection of tortuous vessels is called a nidus where shunting between vessels occurs, without existence of a capillary bed. These high-flow vascular malformations can contain several such nidi.

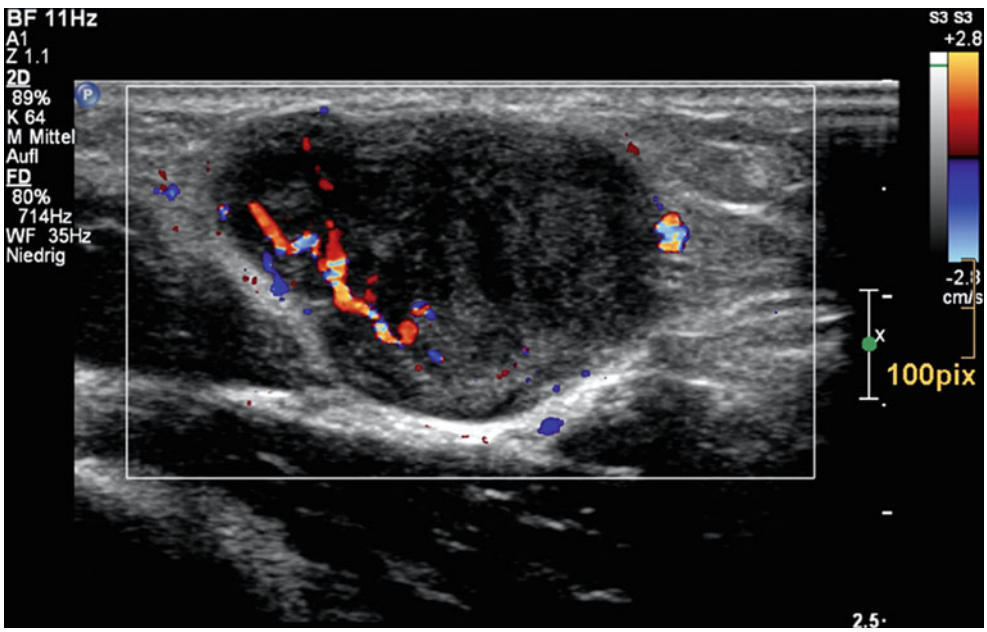

Fig. 7.27 Hypervascularized soft-tissue tumor (leiomyosarcoma) with slightly inhomogeneous texture and in contrast to hemangioma peripherally located vessels (compare with distribution of vessels in Figs. 7.9 and 7.26)

Teaching Point
A nidus with arteriovenous shunting is the hallmark of an AVM and several such nidi may exist inside a single malformation.

The high recurrence rate of vascular malformations results from their cellular origin from early mesenchymal cells, and have the potential to enlarge and recur. Because of this feature, AVMs can progress into highly destructive lesions with gross deformity of a finger or limb and substantial cosmetic impairment.

7.6.1.2 Ultrasound Characteristics

The presentation of arterial and AVMs on B-Mode ultrasound is quite variable. Typically located superficially in the subcutaneous tissue and they may result in thickening of the skin and subcutis. A nest of anechoic ducts can usually be detected, even though in some cases a anechoic pseudocystic appearance can be encountered (Figs. 7.28, 7.29, 7.30, 7.31, and 7.32). Additionally, a mixed pattern composed by hyperechoic vascular stroma and anechoic vascular channels of different size and diameter may be found [8]. The overall appearance of AVMs can be quite inhomogeneous, especially because of the different amount of arterial and venous elements inside the lesion (Figs. 7.33 and 7.34). Typically arterial malformations and AVMs do not have a soft-tissue component [8]. If the latter is encountered, the physician should always be concerned about a different differential diagnosis, such as a highly vascularized soft-tissue tumor. A criterion which may help is the distribution of vessels inside the lesions: while vessels and shunts are mainly centered inside the lesion in AVMs, in soft-tissue sarcomas, these vessels are more often found in the periphery because of their infiltrative growth. A coexisting surrounding edema or infiltrative borders are also a hallmark of sarcomas. AVMs often have indistinct outer borders and sometimes the vessels inside an AVM are so small that they are hardly seen with B-Mode ultrasound, and only detected when color Doppler ultrasound is applied.

Teaching Point
AVMs do not have soft-tissue components. If high-flow vessels and shunting are present together with a soft-tissue mass–think sarcoma.

As mentioned previously, AVMs consist of arterial and venous connections forming a so-called vascular nidus. The arterial feeders and draining veins of the AVM may sometimes be detected in the periphery of the lesion, but this is not always possible. A characteristic of all AVMs however, which must be sought as it comprises a diagnostic feature, is the presence of arteriovenous shunt flow. With color Doppler ultrasound, this is represented by aliasing inside the lesion; in this regard the correct setting of the scanner is of utmost importance to not take artifacts for true aliasing! With duplex ultrasound arteriovenous shunts show high diastolic flow above the baseline and resistance indices below 0.5 (Figs. 7.33 and 7.34). The differentiation of high-flow and low-flow AVMs is important in terms of treatment planning and therefore direct measurement of shunt flow across the lesion with duplex ultrasound is mandatory.

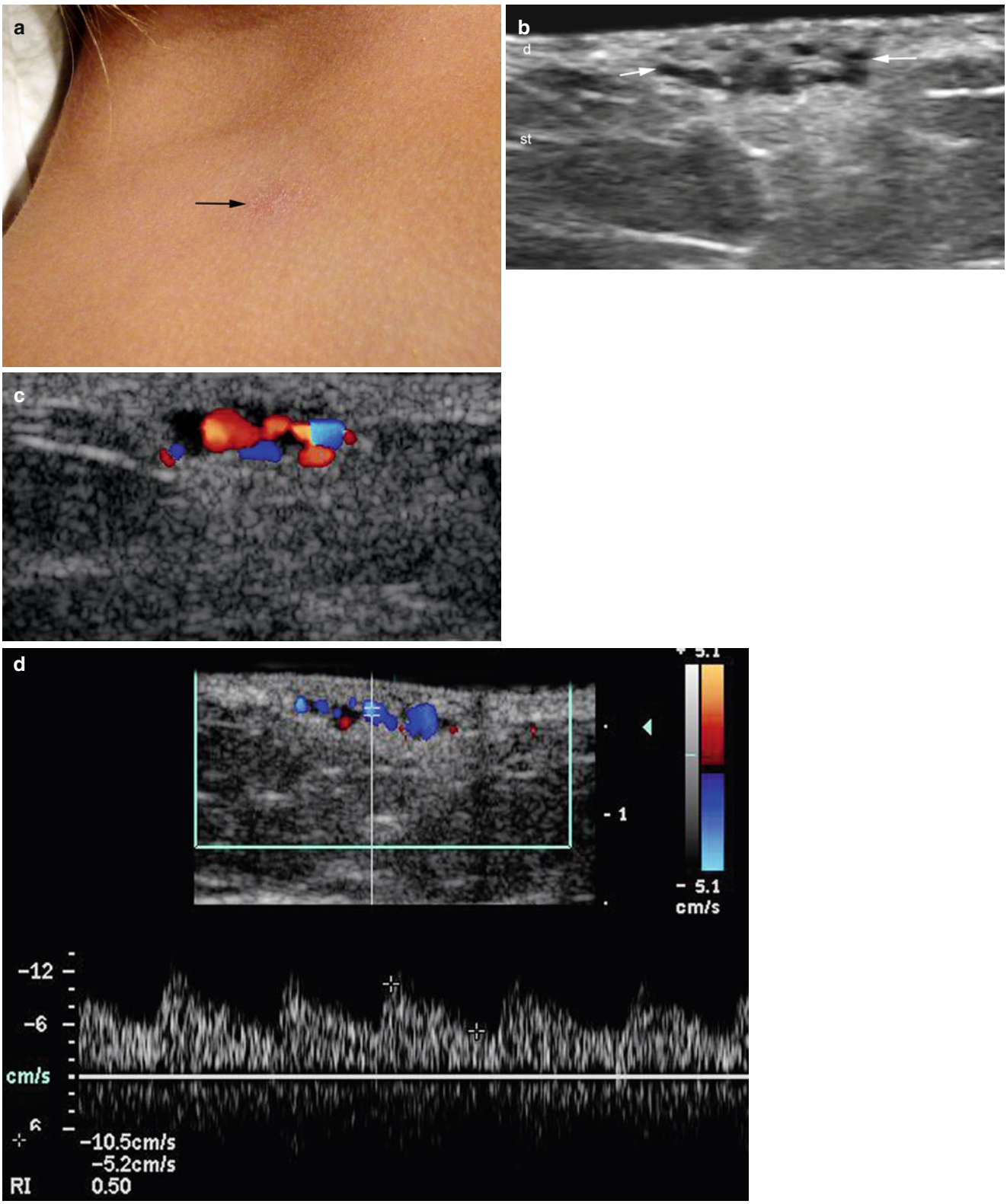

Fig. 7.28 (**a**–**d**) High-flow arterial vascular malformation. (**a**) Clinical erythematous and scaly lesion in the right clavicular region. (**b**) Grey scale ultrasound image (transverse view) shows multiple anechoic tubules (*arrows*) in the dermis and subcutaneous tissue. (**c**) Color Doppler ultrasound image (transverse view) demonstrates increased blood flow within the channels. (**d**) Color Doppler ultrasound spectral curve analysis shows arterial flow in the tubules. *Abbreviations*: *d* dermis, *st* subcutaneous tissue

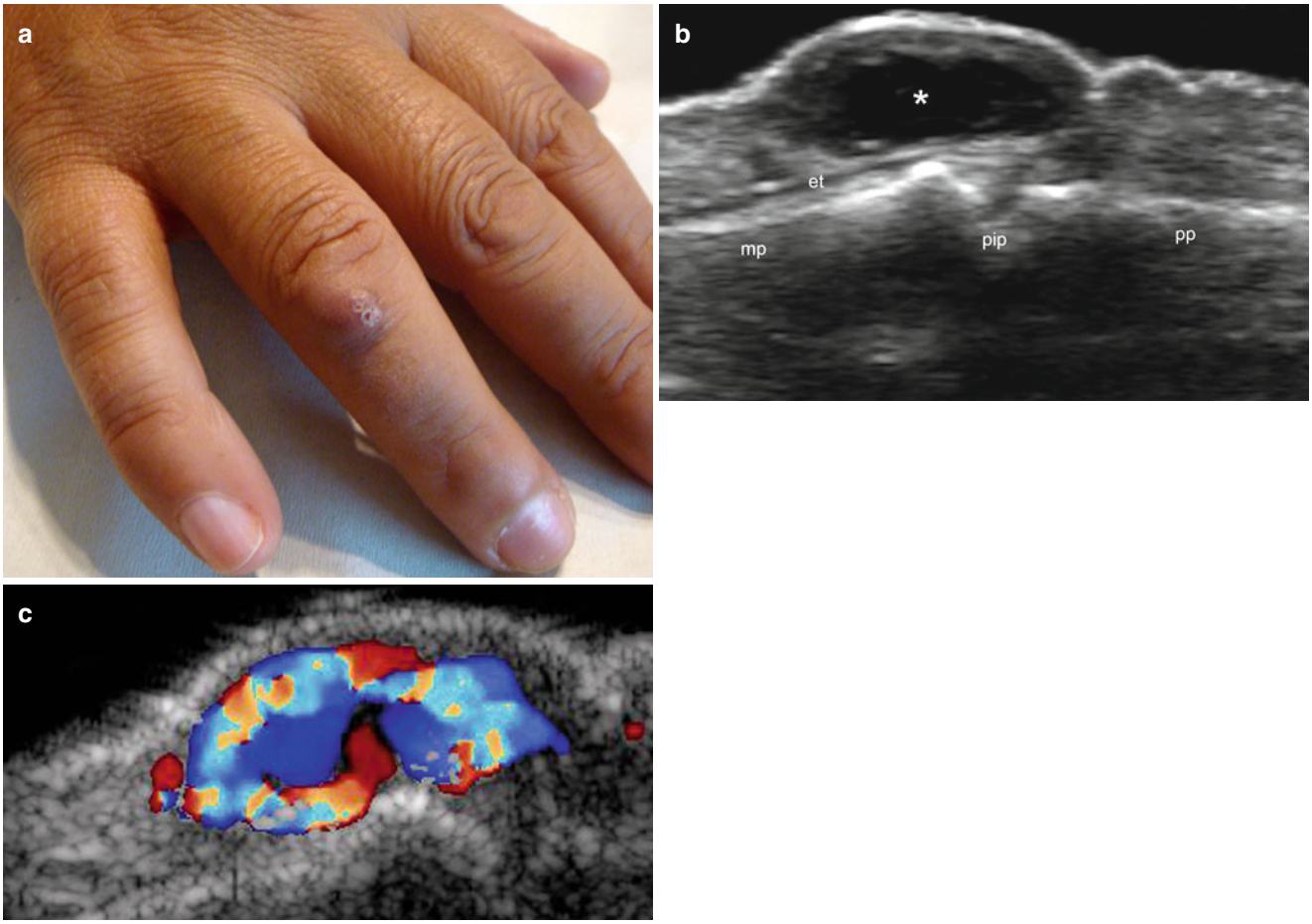

Fig. 7.29 (**a**–**e**) High-flow arterial vascular malformation. (**a**) Clinical image shows erythematous and scaly bump in the right ring finger. (**b**) Grey scale ultrasound image (longitudinal view) demonstrates oval-shaped anechoic pseudocystic structure in the subcutaneous tissue on top of the extensor tendon and proximal interphalangeal joint. (**c**) Color Doppler ultrasound image (longitudinal view) shows a nest of vessels filling the pseudocystic structure. (**d**) Color Doppler ultrasound spectral curve analysis demonstrates arterial flow within the vessels. (**e**) 3D power angio reconstruction of the lesion. *Abbreviations*: *et* extensor tendon, *mp* middle phalanx, *pp* proximal phalanx, *pip* proximal interphalangeal joint

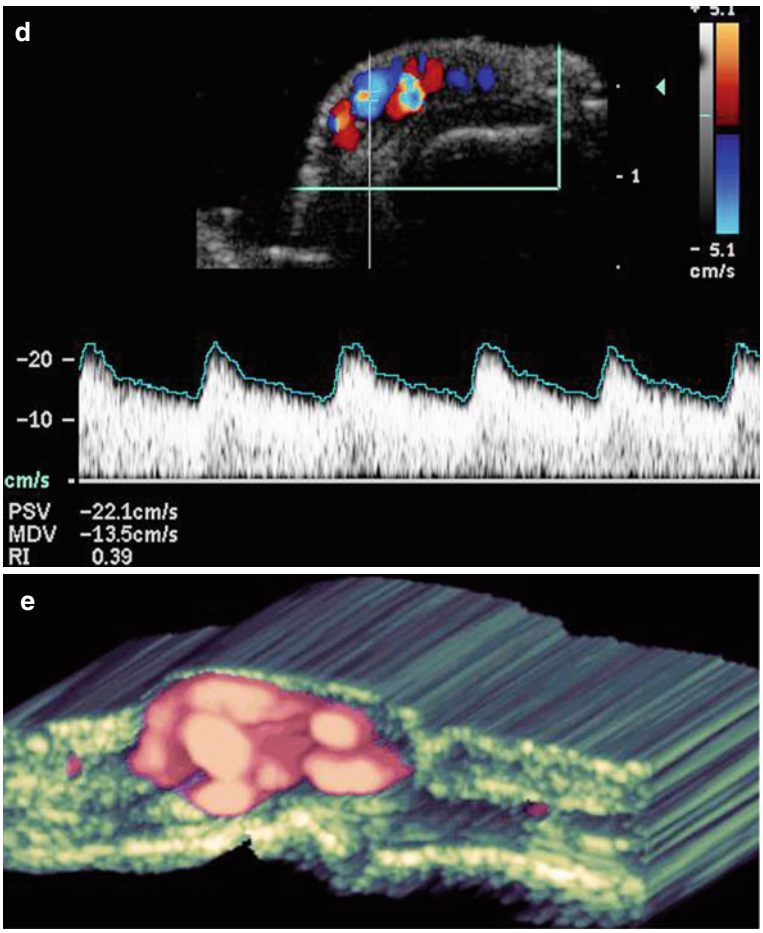

Fig. 7.29 (continued)

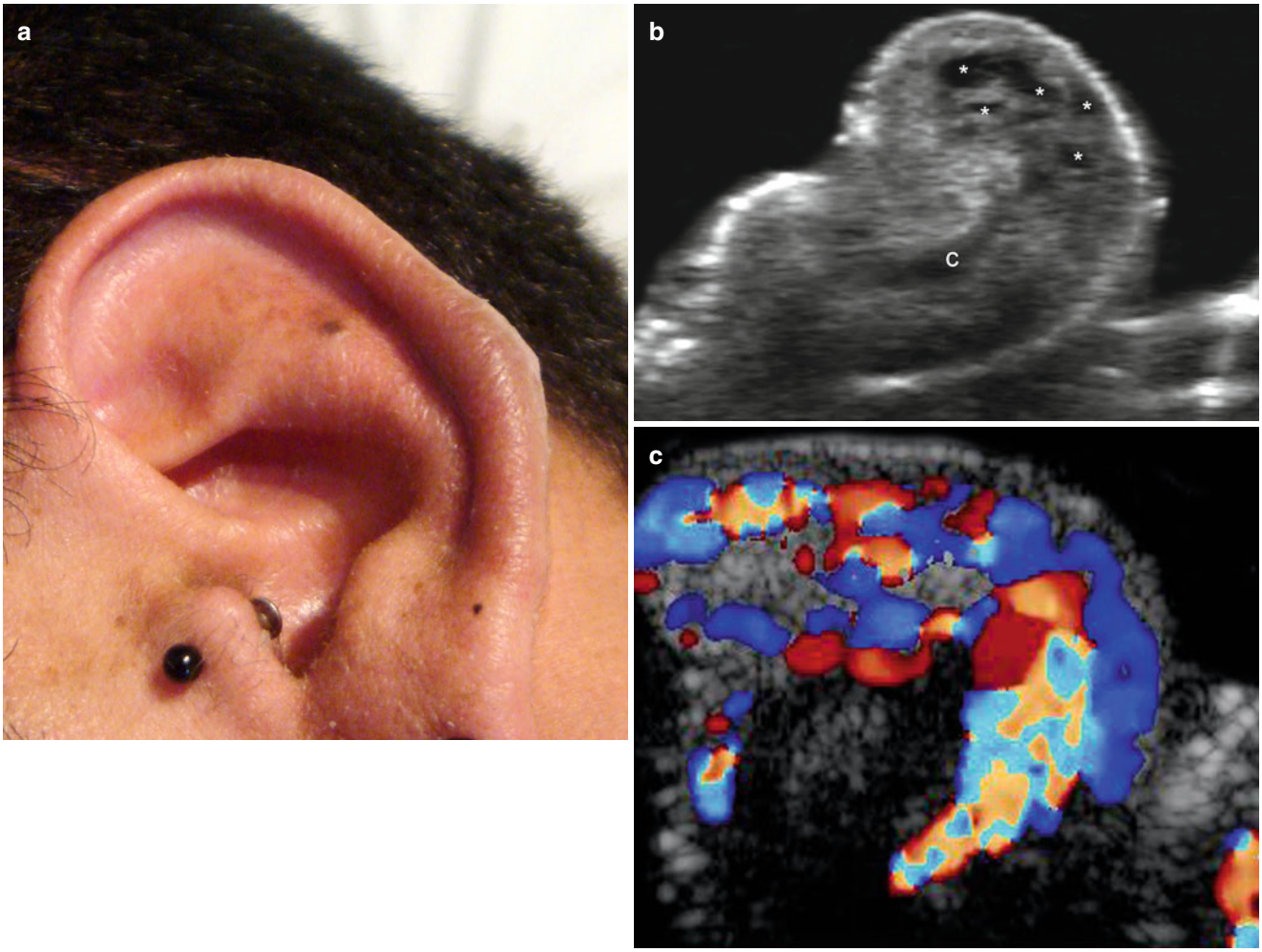

Fig. 7.30 (**a**–**e**) High-flow arterial vascular malformation. (**a**) Clinical lesion shows erythematous swelling in the helix of the left ear pinna. (**b**) Grey scale ultrasound image (transverse view) demonstrates multiple anechoic tubules (*) affecting the dermis and part of the auricular cartilage. (**c**) Color Doppler ultrasound image (transverse view) shows prominent vascularity within the tubules. (**d**) Color Doppler ultrasound spectral curve analysis shows high arterial flow within the tubules (peak systolic velocity: 87 cm/sec). (**e**) 3D power angio reconstruction of the vascular lesion

Fig. 7.30 (continued)

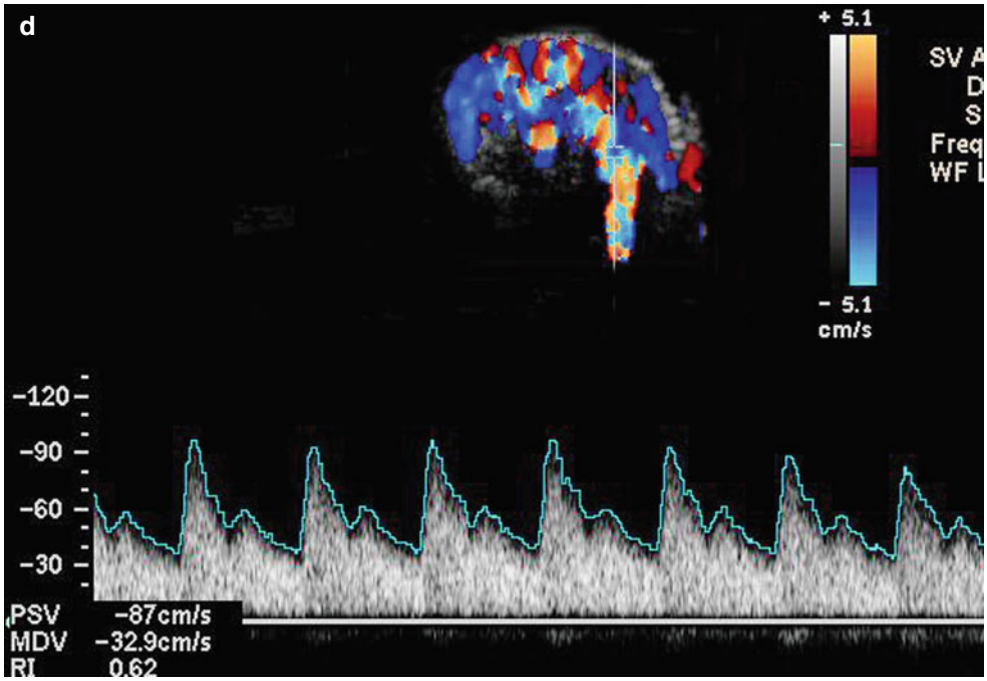

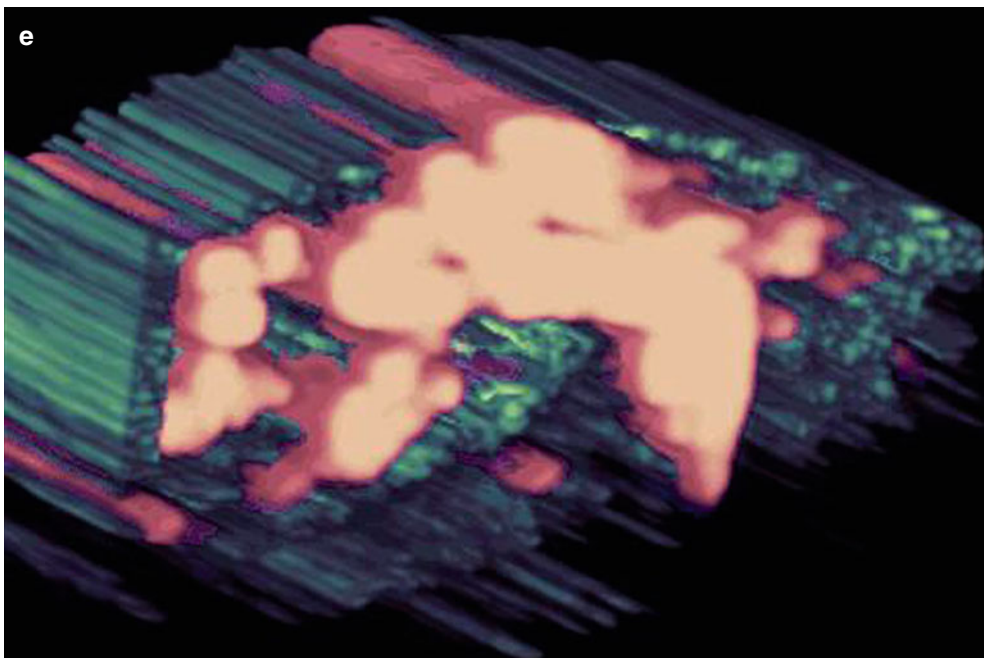

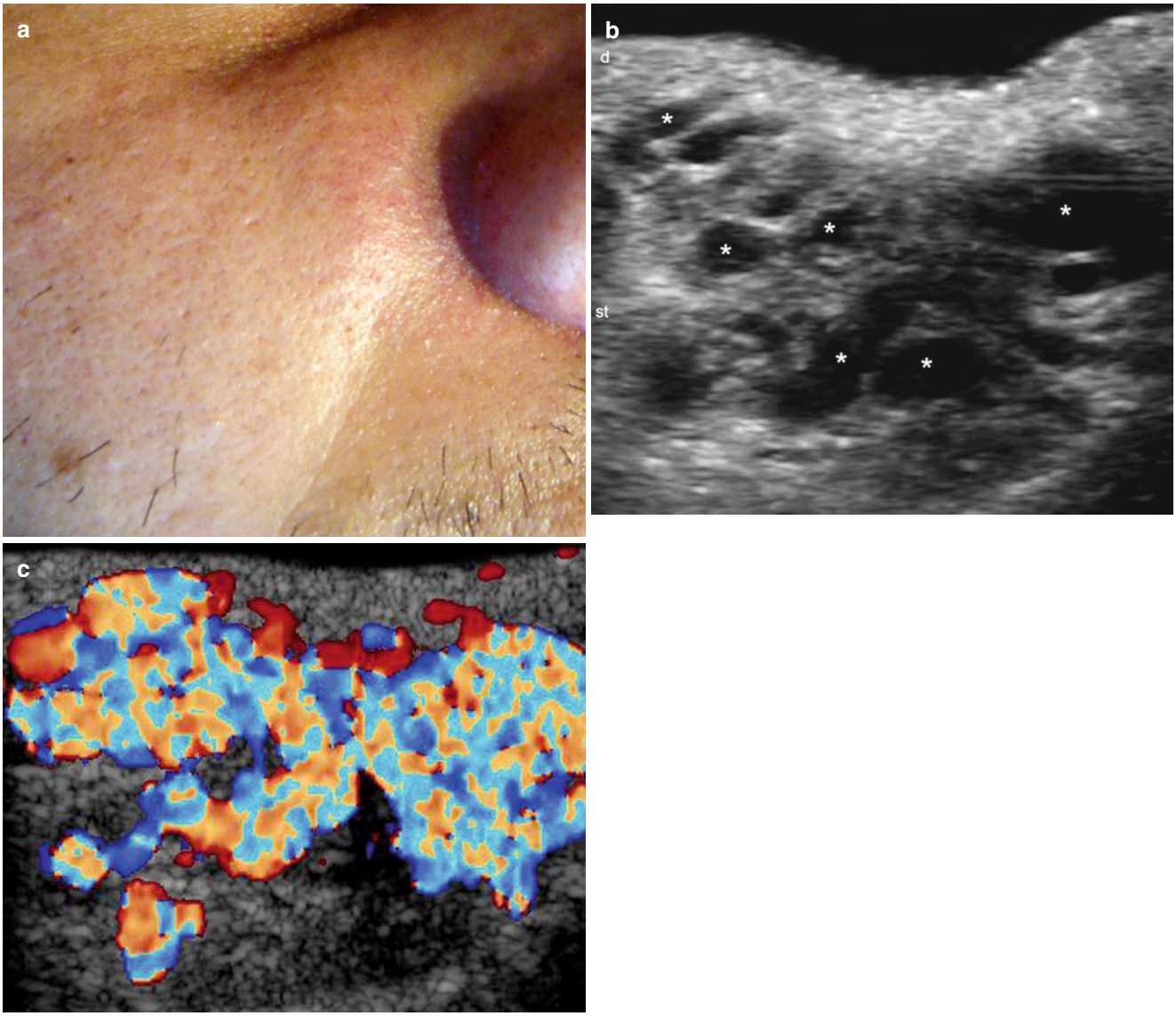

Fig. 7.31 (**a**–**e**) High-Flow arteriovenous vascular malformation. (**a**) Clinical lesion shows slightly erythematous swelling in the right cheek. (**b**) Grey scale ultrasound image (transverse view) demonstrates multiple anechoic ducts (*) in the subcutaneous tissue without a solid component. (**c**) Color Doppler ultrasound image (transverse view) shows high and turbulent flow within the ducts. (**d**, **e**) Color Doppler ultrasound spectral curve analysis demonstrates high velocity arterial (**d**) and venous (**e**) in the channels

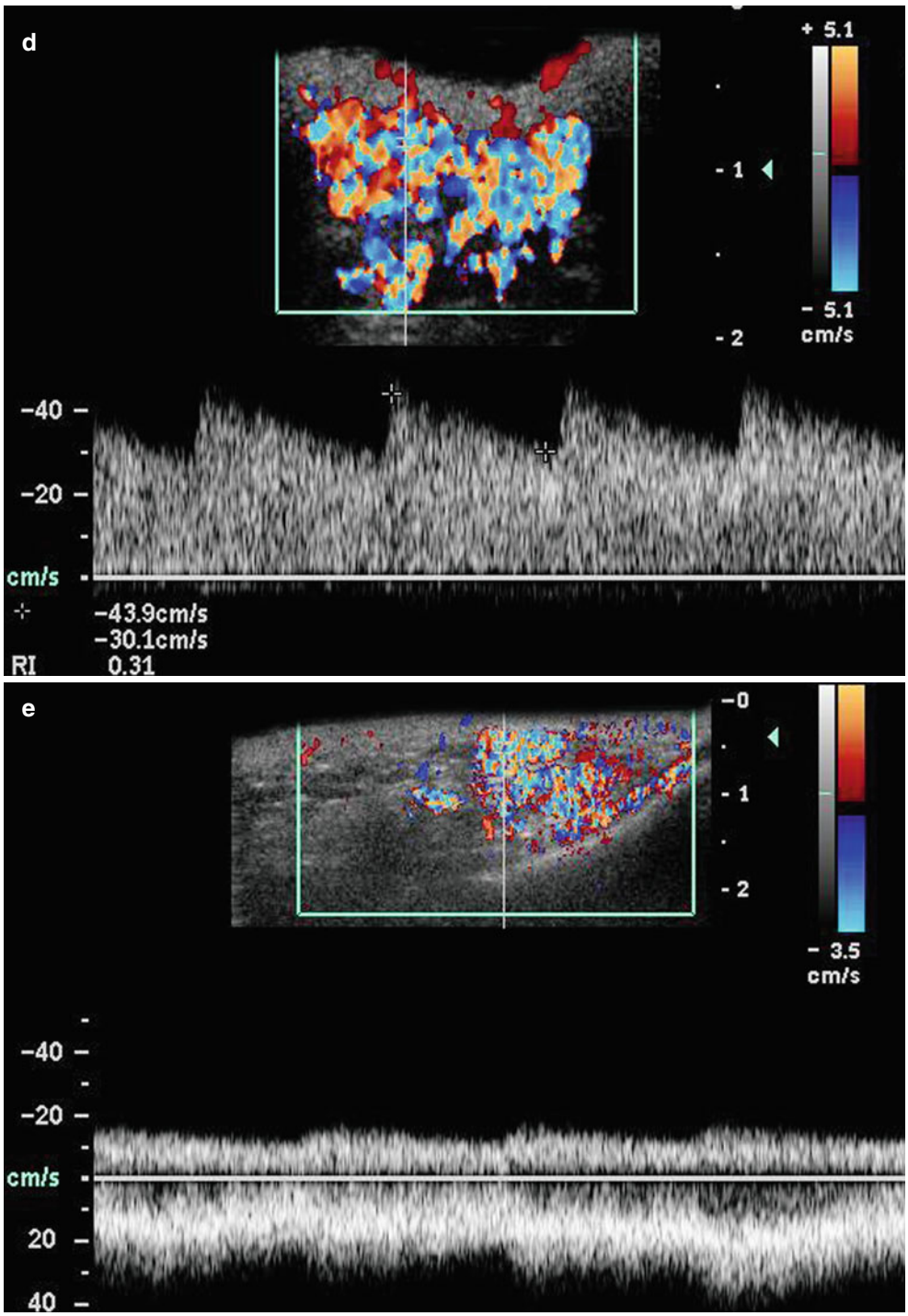

Fig. 7.31 (continued)

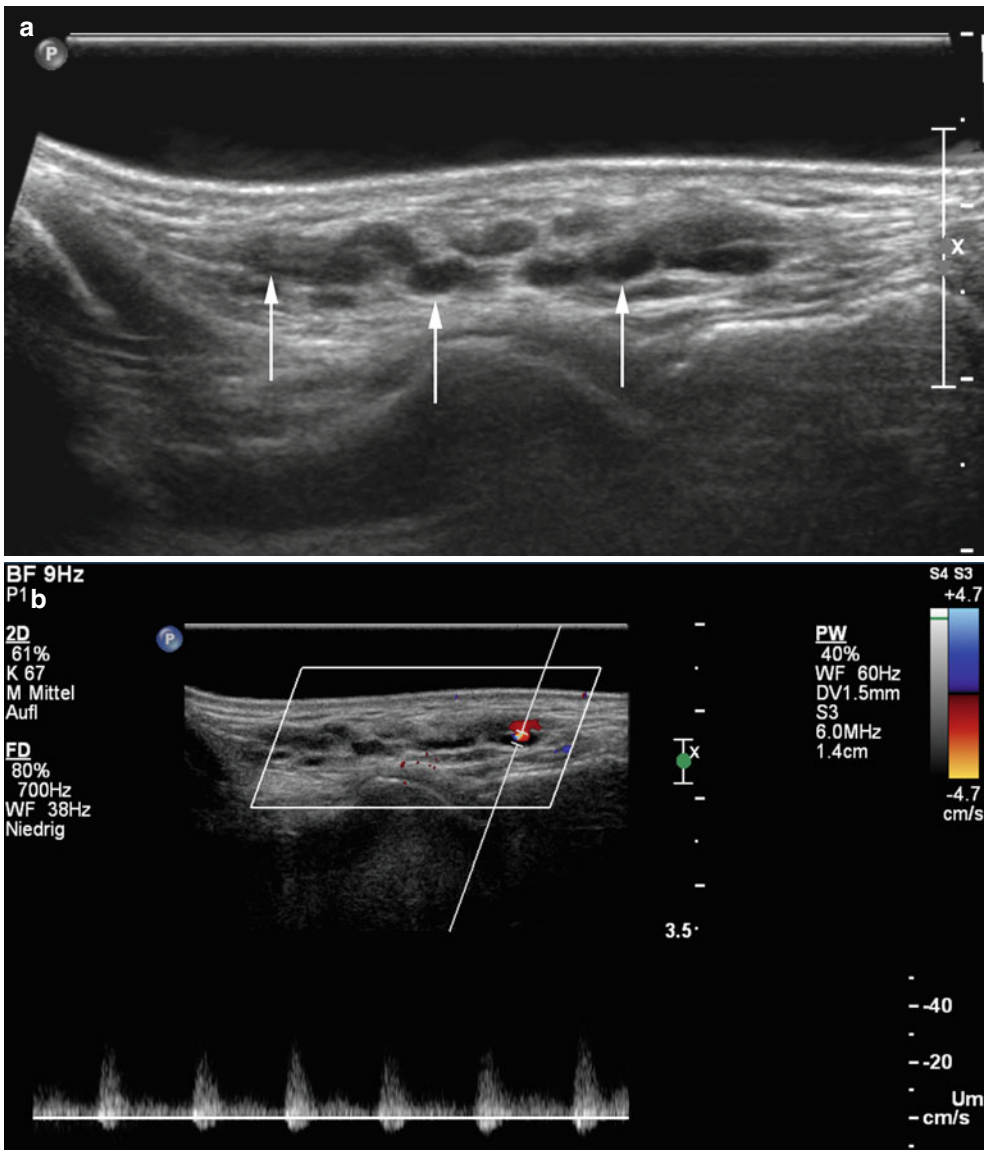

Fig. 7.32 (**a**, **b**) High-flow arteriovenous vascular malformation. (**a**) Grey scale ultrasound image of a small subcutaneous lesion consisting mainly of tortuous venous components (*arrows*). (**b**) At the lower pole of the lesion however a small arterial feeder is demonstrated, corresponding with a high-flow arteriovenous malformation

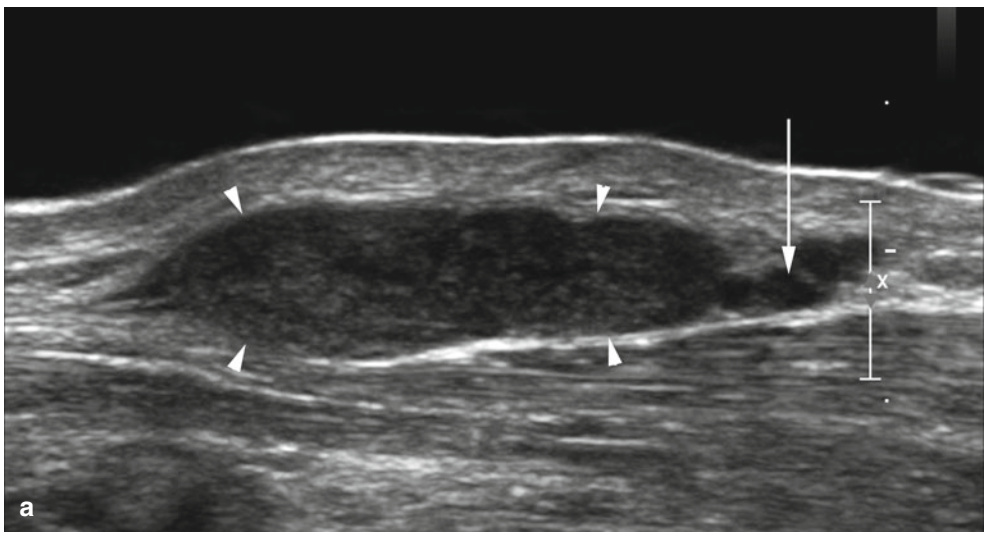

Fig. 7.33 (**a**–**c**) High-flow arteriovenous vascular malformation. (**a**) Grey scale ultrasound image of subcutaneous soft tissue mass (*arrowheads*) with a thick vascular structure on its right border (*arrow*). (**b**) Duplex ultrasound confirms highly vascularized lesion with a large peripheral high flow feeding artery and (**c**) draining vein

Fig. 7.33 (continued)

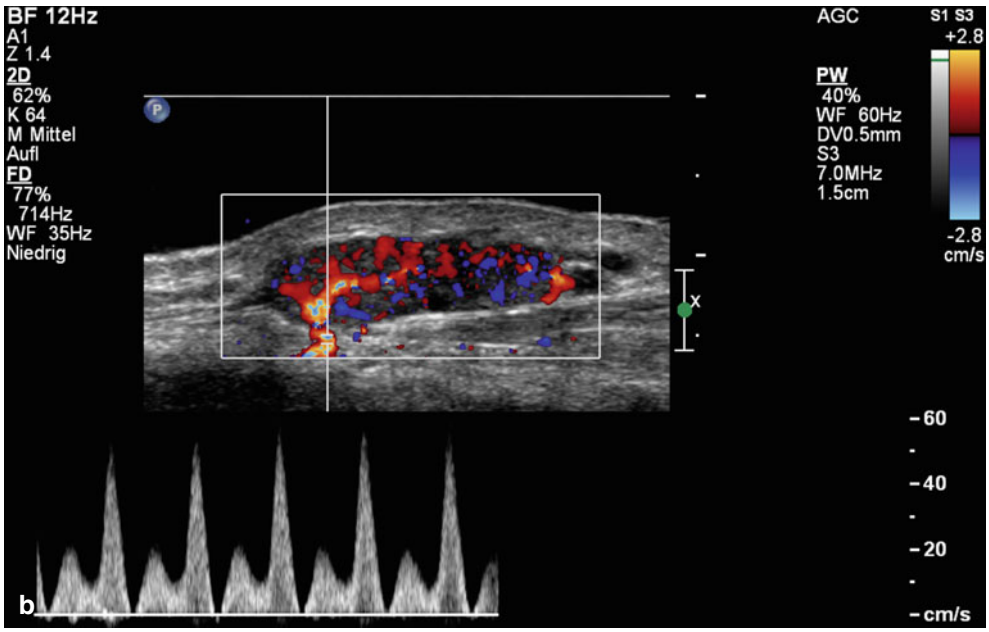

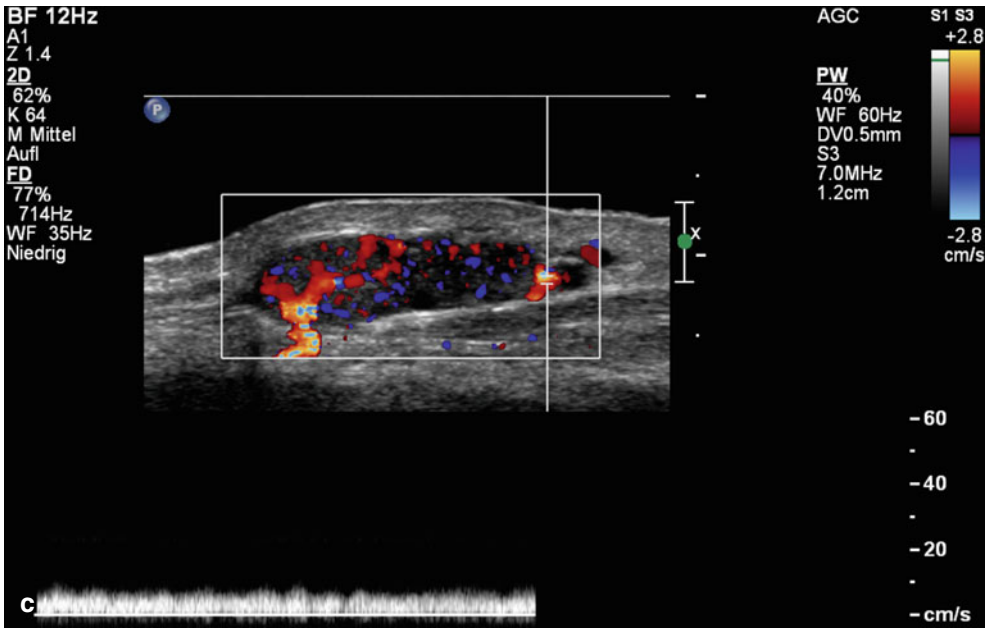

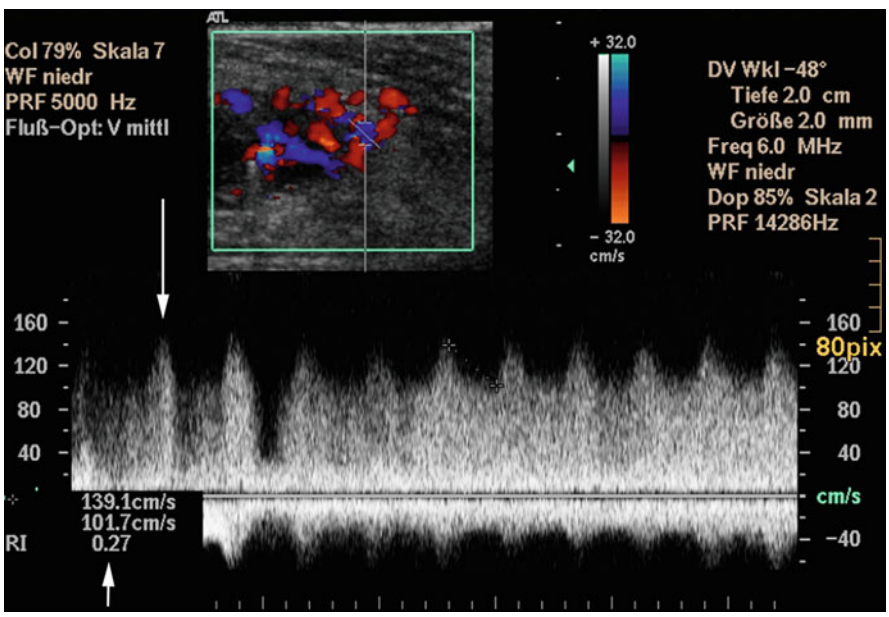

Fig. 7.34 High-flow arteriovenous malformation. Duplex ultrasound: note high-flow velocity of around 139.1 cm/s (*long arrow*) and high diastolic flow resulting in resistive index (RI) < 0.5 (*short arrow*) corresponding with marked arterio-venous shunting

7.6.2 Venous Malformations

7.6.2.1 Clinical Background

Venous malformations have certain similarities to arterial malformations and AVMs: both are congenital, both do not regress, but may most commonly enlarge during growth and both may go undetected for a period of time until they become clinically symptomatic. Venous malformations are bluish in color, they are compressible, and typically increase in size during a Valsalva maneuver [13]. While venous malformations are often asymptomatic, they may become painful when thrombophlebitis or thrombosis occurs, or in the case of involvement of muscles and joints. Histologically, they consist of venous channels with dilated, sponge-like caverns of different sizes. In terms of treatment planning, venous malformations may be further divided into four subtypes according to a classification system proposed by Puig et al. [14] (Table 7.2). The classification is based on lesion drainage and has important implications on sclerotherapy because types 3 and 4 lesions carry a higher risk of complications.

Teaching Point
The type of drainage has implications on the treatment of venous malformations as type 3 and type 4 lesions have a higher rate of complications during sclerotherapy.

A variety of syndromes can be associated with venous malformations: Klippel-Trenaunay syndrome (venous and lymphatic malformations in combination with capillary malformations and skeletal or soft-tissue hypertrophy), Parkes-Weber syndrome (similar to Klippel-Trenaunay but with presence of additional high-flow malformations), Sturge-Weber syndrome (cutaneous, facial venular malformations; i.e., port wine stain in the facial area supplied by the V1 branch of the trigeminal nerve and subcutaneous lymphatic malformations with secondary maxillofacial bone hypertrophy), Maffuci syndrome (a variant of Ollier's disease, with venous malformations associated with multiple enchondromas), among others.

Table 7.2 Classification of venous malformations based on venous drainage according to Puig et al. [14]

Type	Description
Type I	Isolated malformation without peripheral drainage
Type II	Malformation drains into normal veins
Type III	Malformation drains into dysplastic veins
Type IV	Venous ectasia

7.6.2.2 Ultrasound Characteristics

Venous malformations are anechoic or slightly hypoechoic, sponge-like structures on B-mode sonograms and they consist of multiple blood-filled caverns of different sizes. Varicose veins, complex and communicating venous channels are seen in only about 50 % of lesions [15]. Typically venous malformations have only little fibrous stroma, but the walls of the individual caverns range from very thin septae to thick fibrous bridges (Figs. 7.35, 7.36, and 7.37), which is why approximately 80 % of venous malformations are somewhat inhomogeneous on B-mode with a mixture of hypoechoic caverns and sometimes hyperechoic septations [16]. If large parts of the malformation are filled with thrombotic material, it can resemble a soft-tissue tumor with mixed echogenity making it difficult to differentiate from hemangiomas or other soft-tissue lesions [16, 17]. The inhomogeneous texture of the lesion can sometimes prevent distinction from surrounding normal tissue and exact measurement of size, this is especially the case when tiny finger-like protrusions of the lesion invade into the surrounding soft tissues. Tiny roundish calcifications resembling phleboliths inside thrombosed caverns are a diagnostic hallmark of venous malformations but are seen in only 20 % of lesions [15, 16] (Figs. 7.36, 7.37, 7.38, 7.39, 7.40, and 7.41). Echotexture alone does not allow differentiation of venous malformations from hemangioma or lymphangioma, in contrast to the latter however, venous malformations are easily compressed with the transducer. A color Doppler ultrasound compression test is a comparable and important equivalent test for the diagnosis of a venous malformation. With correct color Doppler ultrasound settings, the signal inside the blood-filled caverns shows a change from red to blue and vice versa during transducer pressure/release of pressure on the malformation (Fig. 7.10). No flow is detected in approximately 15–20 % of lesions; this may be due to either thrombosis, substantially low flow inside the malformation, or to inappropriate Doppler settings [15]. In lesions with low flow, no color signal may be seen at all unless light pressure is applied. Nevertheless, flow inside venous malformations could be quite variable, and according to Trop et al. [16], 16 % of lesions do not show any flow at all, 78 % have slow monophasic venous flow, and 6 % have biphasic low flow. Venous malformations do not harbor arteriovenous shunts, therefore, it is important to search for regions with aliasing (turbulence) using color Doppler ultrasound and for shunt flow with spectral wave analysis. If a shunt is detected, the lesion is by definition not a venous malformation but either an arteriovenous malformation and this is an important distinction in terms of treatment planning.

Teaching Point
If arteriovenous shunts are detected inside a malformation it is by definition not a simple venous malformation.

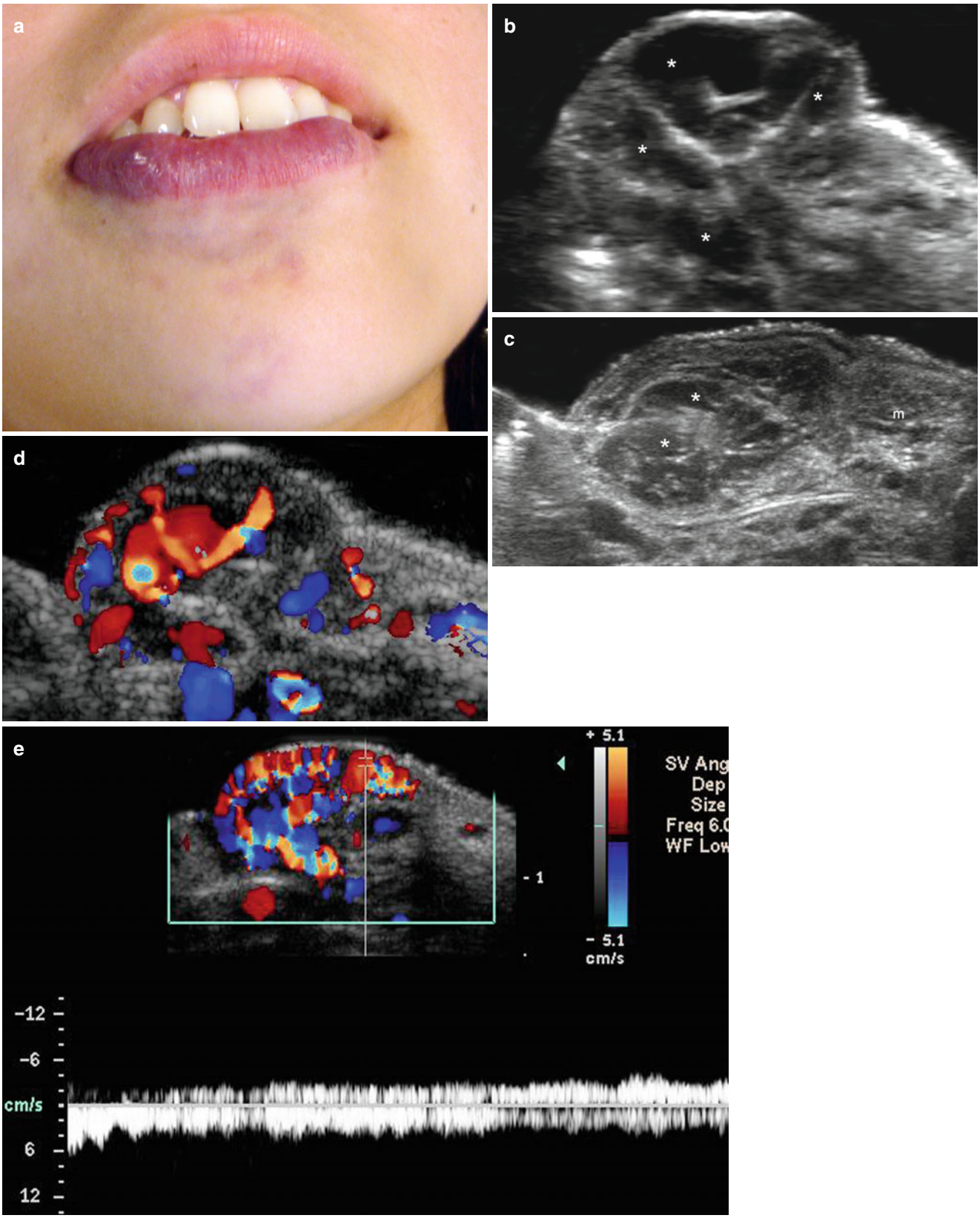

Fig. 7.35 (**a**–**e**) Low-flow venous vascular malformation. (**a**) Clinical erythematous lesion in the right border of the lower lip. (**b**) Grey scale ultrasound image (longitudinal view) and (**c**) (transverse extended view) show multiple anechoic tubules and pseudocytic structures (*) that involve the dermis and the orbicularis muscle. (**d**) Color Doppler ultrasound image demonstrates increased blood flow within the tubules. (**e**) Spectral curve analysis shows venous flow in the ducts

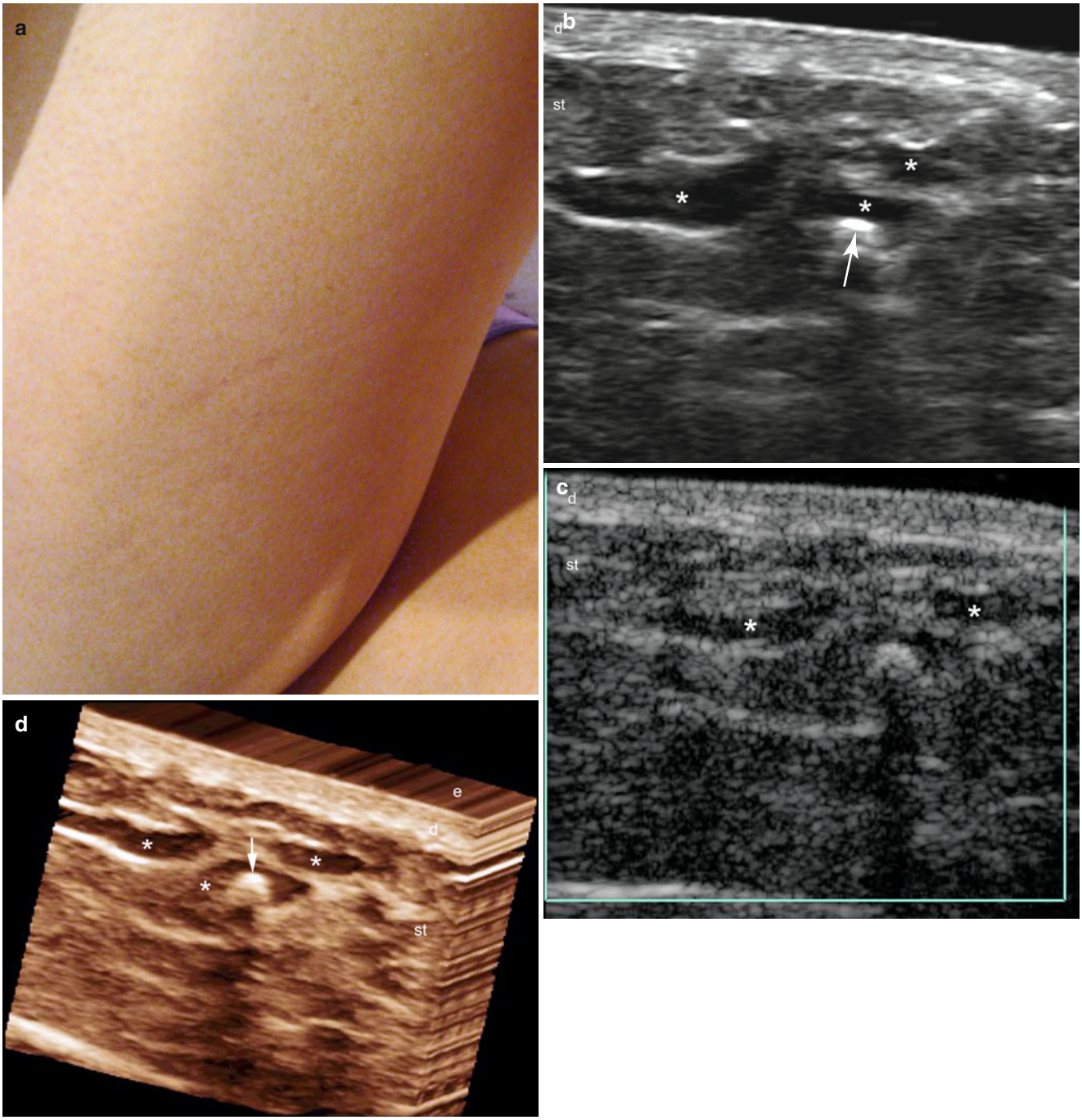

Fig. 7.36 (**a**–**d**) Low-flow venous vascular malformation. (**a**) Clinical lesion demonstrates slight erythema in the posterior aspect of the right thigh. (**b**) Grey scale ultrasound image (transverse view) shows anechoic ducts (*) in the subcutaneous tissue. Notice the hyperechoic nodule that corresponds to a phleboliths (*arrow*). (**c**) Color Doppler ultrasound image demonstrates no detectable vascularity within the lesion. (**d**) 3D ultrasound reconstruction (5–8 s sweep) of the lesion highlighting the anechoic tubules (*) and the phlebolith (*arrow*)

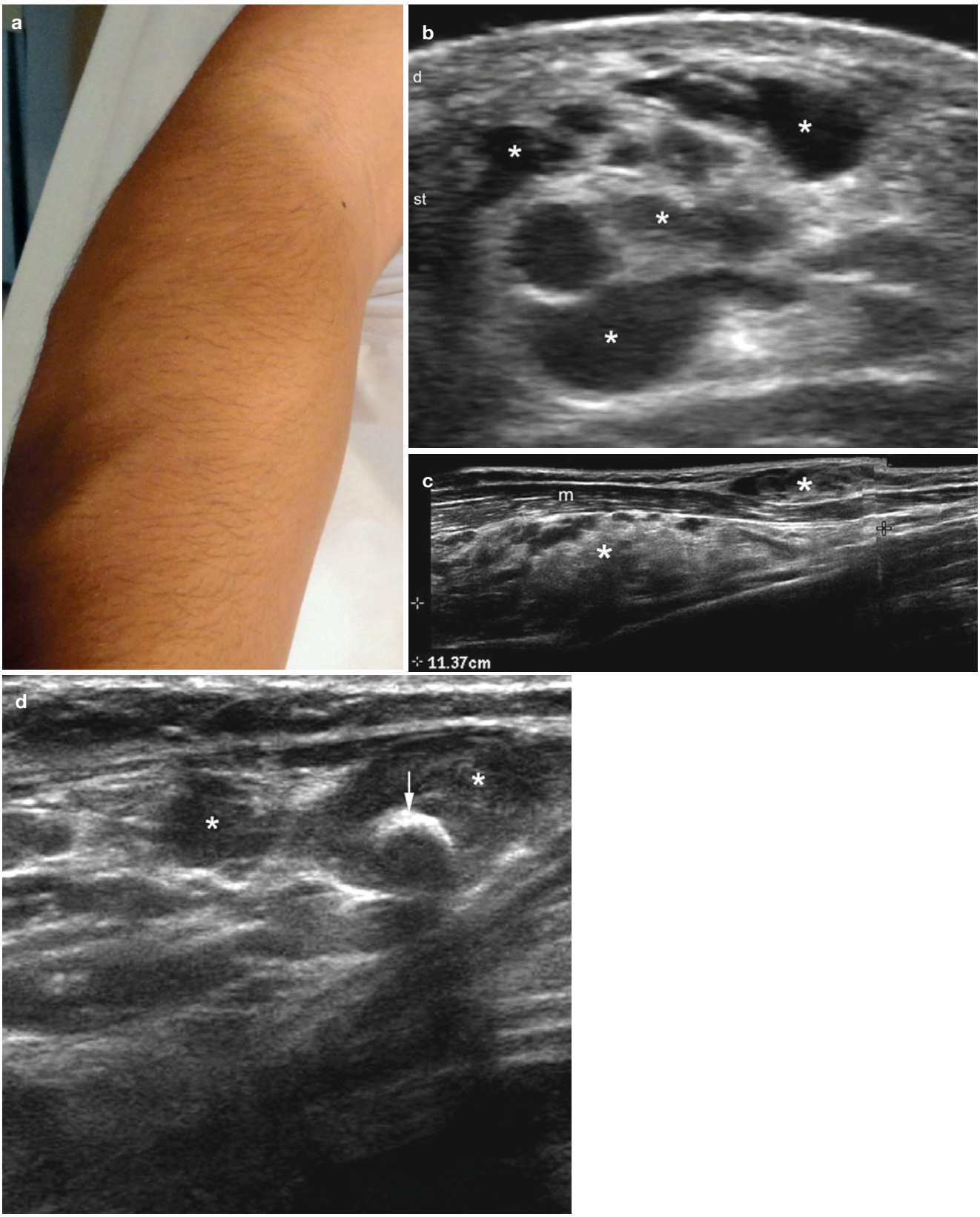

Fig. 7.37 (**a**–**e**) Low-flow venous vascular malformation. (**a**) Clinical lesion shows a swelling in the right arm and forearm. (**b**) Grey scale ultrasound image (transverse view) shows multiple anechoic pseudocystic structures (*) in the subcutaneous tissue. (**c**) Grey scale ultrasound image (extended field longitudinal view) in the forearm demonstrates subcutaneous and miofascial involvement (*). (**d**) Grey scale ultrasound image (longitudinal view) shows an hyperechoic phlebolith (*arrow*) within the pseudocystic cavities (*). (**e**) Color Doppler ultrasound spectral curve analysis with monophasic venous flow. *Abbreviation: m* muscle

Fig. 7.37 (continued)

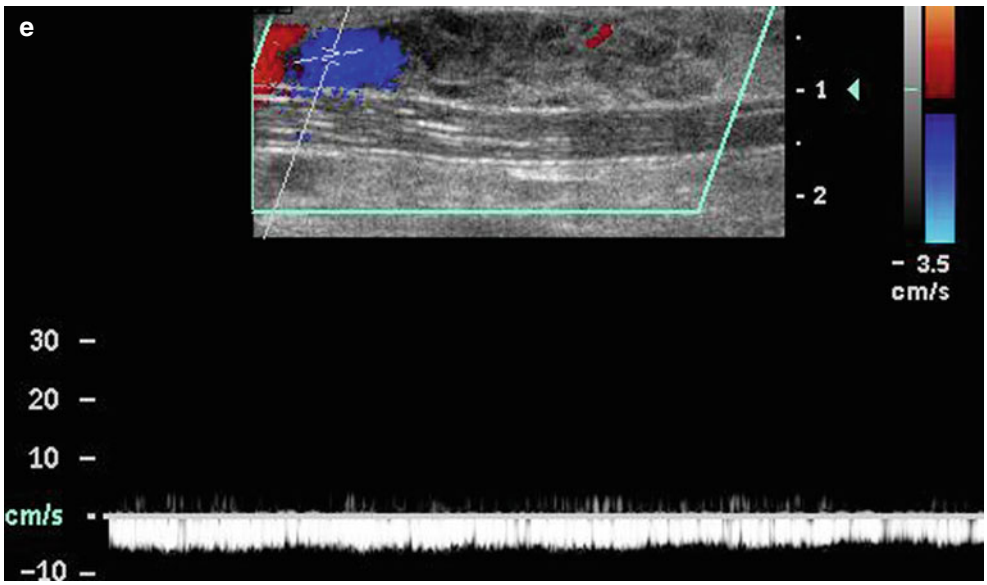

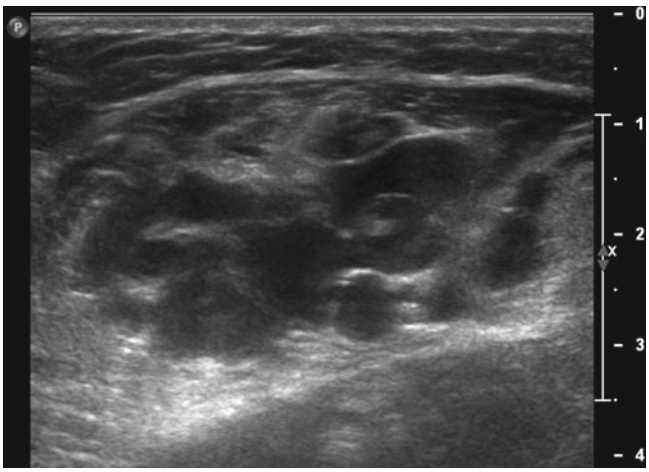

Fig. 7.38 Grey scale ultrasound image of a patient with a venous malformation at the distal thigh consisting of thin walled anechoic sponge-like caverns

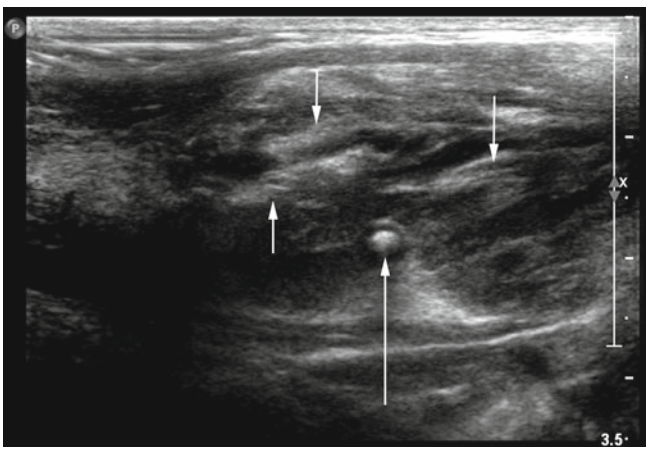

Fig. 7.39 In contrast to the lesion in Fig. 7.38, this venous malformation shows thick fibrous septae (*small arrows*). A small phlebolith is also demonstrated (*long arrow*)

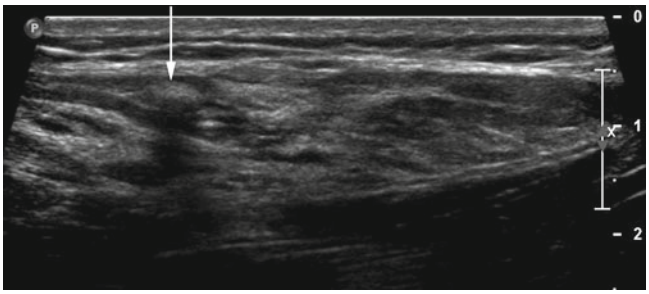

Fig. 7.40 Transverse grey scale image showing large roundish calcification (*arrow*) inside venous channel, a hallmark of a low flow venous malformation

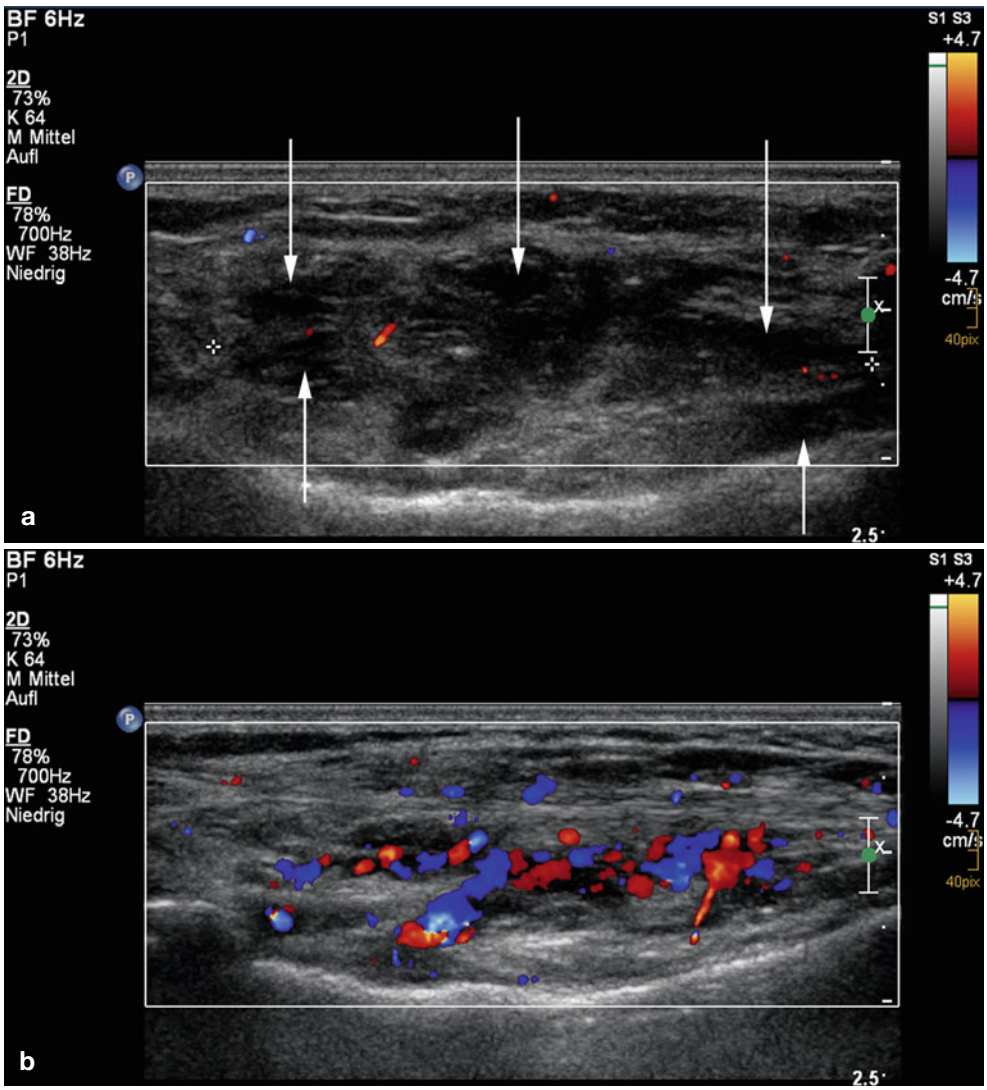

Fig. 7.41 (**a**) Soft-tissue lesion consisting of anechoic and hypoechoic caverns (*arrows* in **a**) with no detectable flow during normal ultrasound. Only with compression (**b**) venous flow inside the lesion is demonstrated

7.6.2.3 Direct Percutaneous Phlebography

The value of direct percutaneous phlebography in venous anomalies is twofold: it can be performed as a diagnostic procedure and if contrast-filled abnormal venous cavities are demonstrated, this confirms the presence of a venous malformation and virtually excludes the presence of a soft-tissue tumor. The second, and in our opinion, more important aspect, is to perform direct percutaneous phlebography as the first step during sclerotherapy of a venous malformation (Fig. 7.42): A 21-gauge needle is inserted into the malformation under ultrasound guidance and connected to a syringe via a length of tubing. Under suction, the needle is positioned until blood is withdrawn and 5 ml of iodinated contrast is injected by hand to observe the characteristics of venous opacification and filling of the drainage vein. According to Puig et al. [14] and Dubois et al. [15], different drainage patterns may be observed: some malformations are mere fluid-filled caverns without any detectable drainage. The most common is a cavitary pattern with late and slow venous drainage without detection of abnormal veins. The third is a malformation consisting of spongy vascular channels draining into dysplastic veins, with the fourth a venous ectasia with rapid drainage. In cases with immediate drainage, compression of the drainage vein using a tourniquet to avoid spilling of the sclerosant into the systemic circulation and to increase local exposure inside the malformation, is strongly advised (Fig. 7.42b).

Teaching Point

Direct puncture phlebography is necessary before sclerotherapy to define the type of drainage in malformations.

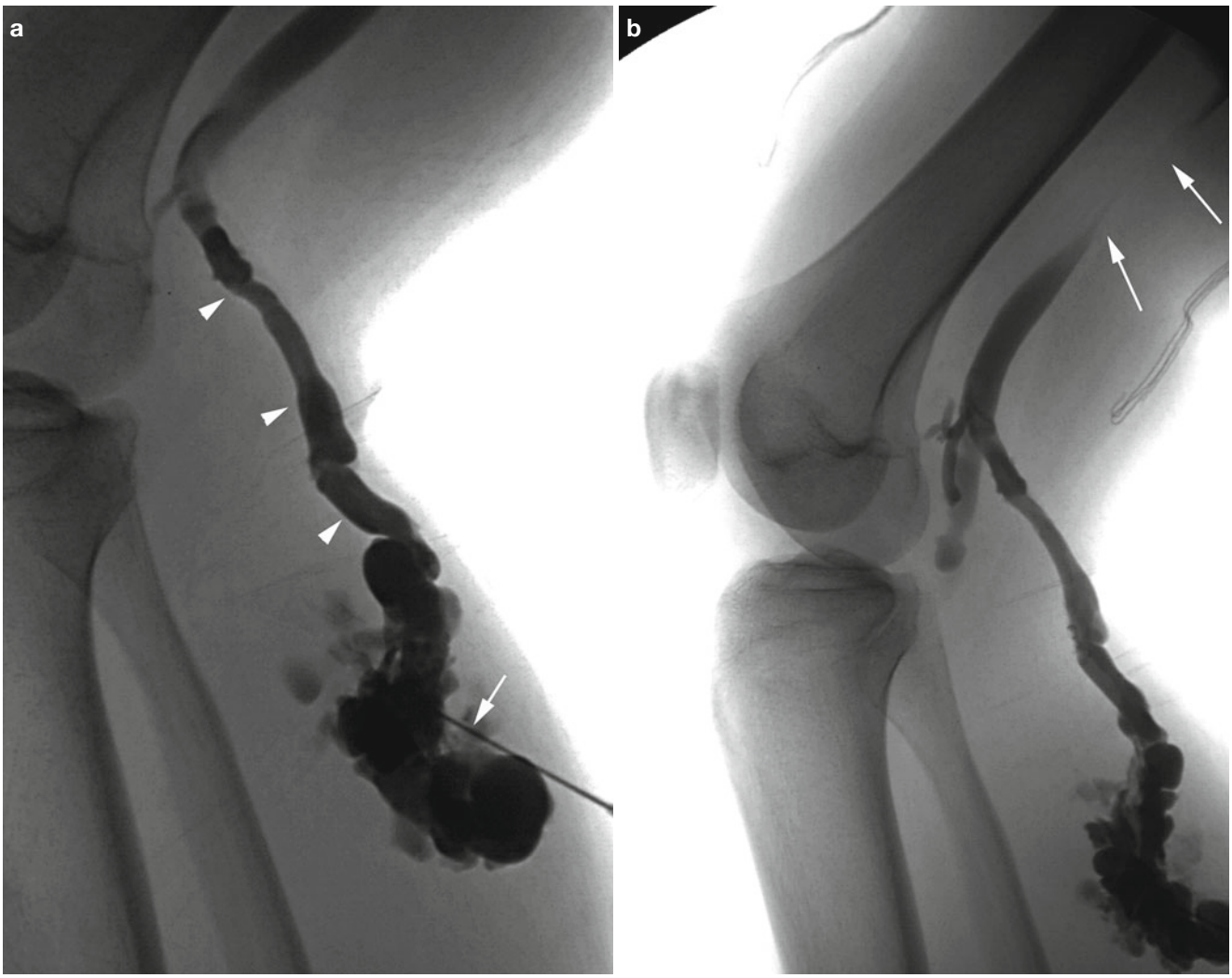

Fig. 7.42 (**a**) Direct puncture phlebography via a 21-gauge needle (*arrow*) in a patient with a large venous malformation inside the medial gastrocnemius muscle. Rapid drainage via a large communicating vein (*arrowheads* in **a**) into the distal femoral vein is seen. (**b**) Venous drainage is largely reduced after fastening of a tourniquet (*arrows* in **b**) and sclerotherapy with slow injection of the sclerosant is begun

7.6.3 Lymphatic Malformations

7.6.3.1 Clinical Background

Lymphatic malformations also called lymphangiomas, arise from a developmental defect in the communication between lymph vessels and their draining channels during embryogenesis [17, 18]. Histologically, they are thin-walled fluid-filled cysts of different sizes surrounded by a variable amount of connective tissue stroma; while the microcystic variant consists of multiple tiny cysts within a thick solid matrix, macrocystic variants consist mainly of large thin-walled spaces filled with proteinaceous fluid. The head and neck are most frequently affected and cervicofacial lymphatic malformations represent a rough 70 % of cases. About 60 % of lymphatic malformations are present at birth and the other 40 % become symptomatic during the first 2 years of life. The macrocystic variants may enlarge with growth of the child and compress surrounding soft tissues. Involvement of the tongue and orbit is well known and may result in impaired vision or speech. Tissue overgrowth may result in macroglossia, deformities of the bony palate and jaw, and thus problems with dentition or malocclusion. The infiltrative growth is more common with microcystic variants and can result in considerable cosmetic impairment. Lymphatic malformations in the limbs can also result in progressive lymphedema and skin changes.

The distinction of lymphatic malformations from other congenital vascular anomalies is important because they represent proliferative lesions, which warrants closer observation and more aggressive treatment. Lymphatic malformations may exist alone or be part of several syndromes with a complex mixture of arteriovenous and lymphatic anomalies such as Klippel-Trenaunay or Proteus syndrome. In terms of

therapy, lymphatic malformations pose a severe problem: while surgical resection is considered the gold standard, complete resection is often impossible, the recurrence rate is high, and the risk of severe cosmetic impairment is considerable. Therefore, various approaches for percutaneous treatment under ultrasound or CT/MRI guidance are reported in the literature [19, 20]: simple direct drainage, aspiration, and sclerotherapy with ethanol or picibanil (OK-432) are most frequently used with varying success.

7.6.3.2 Ultrasound Characteristics

Simple macrocystic lymphatic malformations are septate caverns of large size filled with anechoic fluid (Figs. 7.43, 7.44, 7.45, 7.46, 7.47, 7.48). Bleeding or infection may sometimes result in mixed echogenity of fluid in different caverns and/or the presence of debris layered at the bottom of the caverns. The lesion itself may be mobile against the surrounding soft tissues, but typically the caverns themselves are not compressible with the transducer; as previously mentioned, this is an important sign for the differential diagnosis of venous malformations. Microcystic malformations may exhibit extremely small cysts barely visible with sonography, tightly packed within a solid echoic matrix. This is why they may sometimes resemble proliferating hemangioma on B-mode.

Using color Doppler ultrasound, small arteries or veins may be found inside cyst walls or the surrounding stroma of mere lymphatic malformations, and according to Paltiel et al. [8], that is the case in approximately 60 % of cases. However, cysts themselves are not vascularized at all, unless a combined venolymphatic malformation is present. Only in the latter can a color change be seen in a color Doppler ultrasound compression test. Only slow flow is detected inside veins and arteries of lymphatic malformations using spectral wave analysis.

Teaching Point

A negative result using the color Doppler ultrasound compression test in a cavernous malformation is diagnostic for cystic lymphangioma.

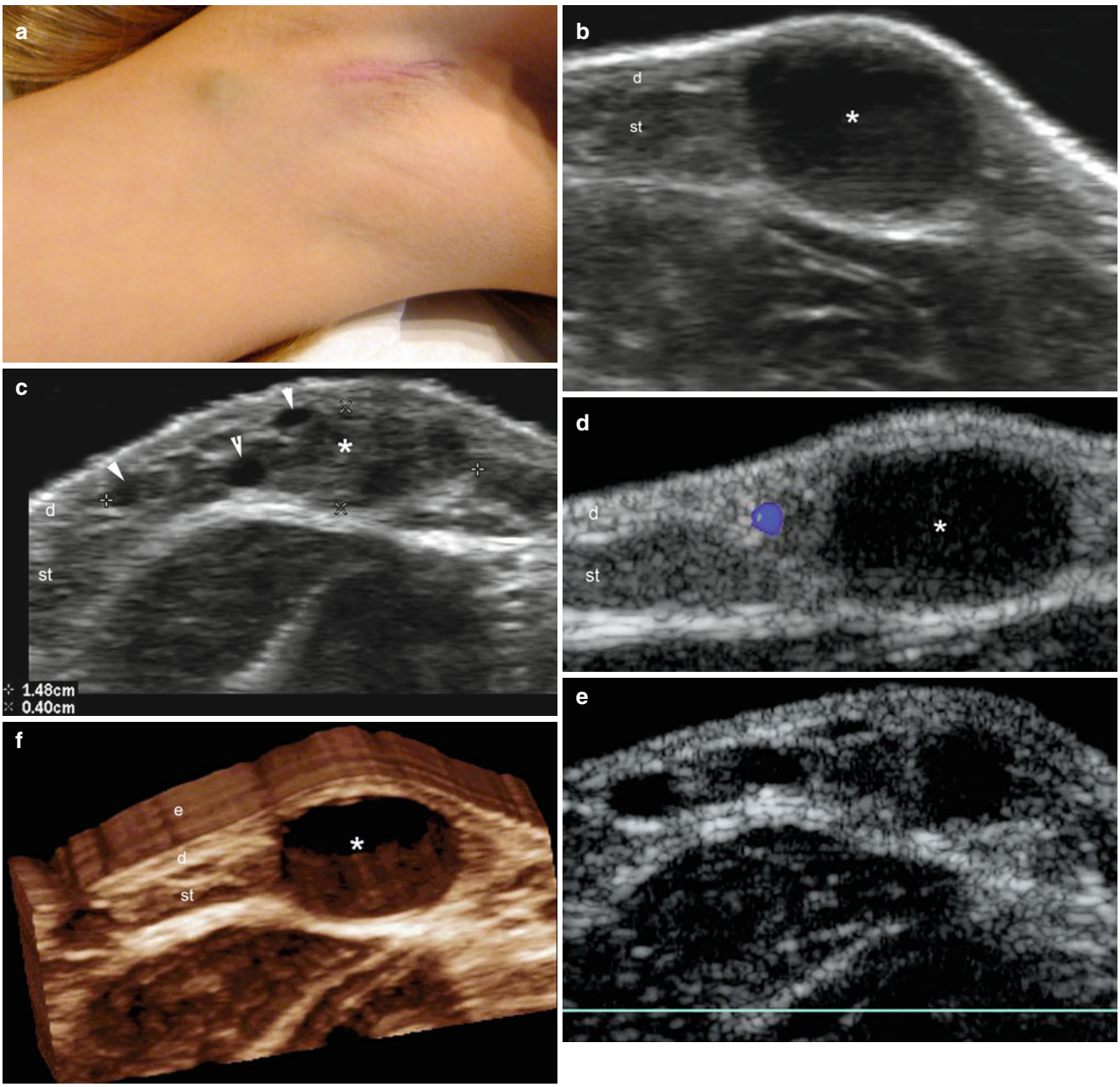

Fig. 7.43 (**a**–**f**) Low-flow lymphatic vascular malformation. (**a**) Clinical image shows a lesion with swelling in the inner aspect of the right arm. Notice the erythematous scar in the axilla secondary to a previous partial removal of the lymphatic malformation. (**b**, **c**) Grey scale ultrasound images (transverse view) demonstrate multiple well-defined round-shaped anechoic pseudocystic structures in the dermis and subcutaneous tissue. B (large pseudocyst, *) and C (multiple small pseudocysts–*arrows*) in between the normal subcutaneous tissue (*). (**d**, **e**) Color Doppler ultrasound images (transverse views) show lack of vascularity within the pseudocystic structures. (**f**) 3D reconstruction (5–8 s sweep) of the lesional area. *Abbreviations*: *e* epidermis, *d* dermis, *st* subcutaneous tissue

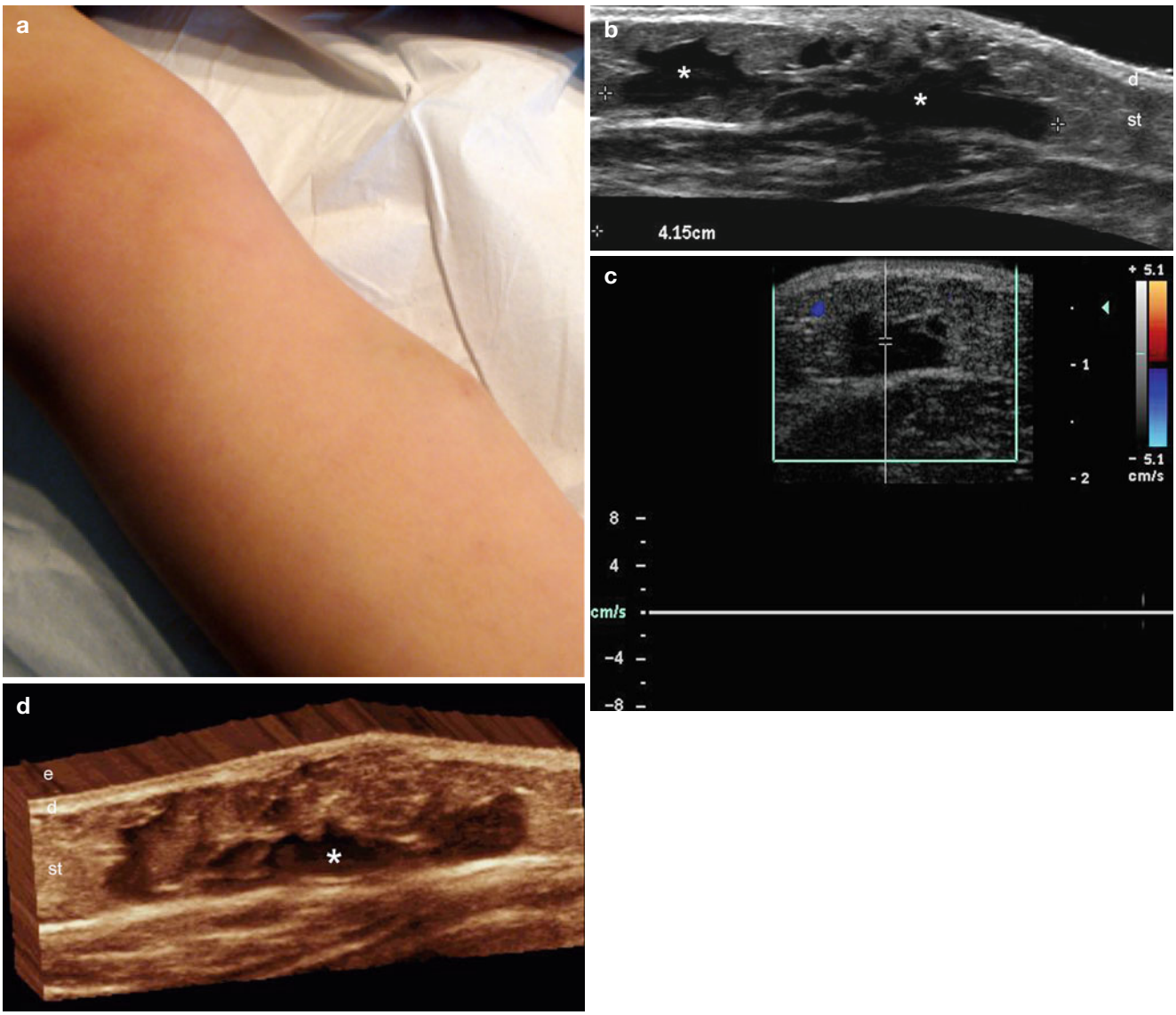

Fig. 7.44 (**a**–**d**) Low-flow lymphatic vascular malformation. (**a**) Clinical image shows swelling in the inner aspect of the right leg. (**b**) Grey scale ultrasound image (extended field of longitudinal view) demonstrates 4.15 cm long anechoic pseudocystic structures (*) mostly in the subcutaneous tissue. (**c**) Color Doppler ultrasound spectral curve analysis shows lack of vascularity within the pseudocystic spaces. (**d**) 3D ultrasound reconstruction of the lesion (*). *Abbreviations*: *e* epidermis, *d* dermis, *st* subcutaneous tissue

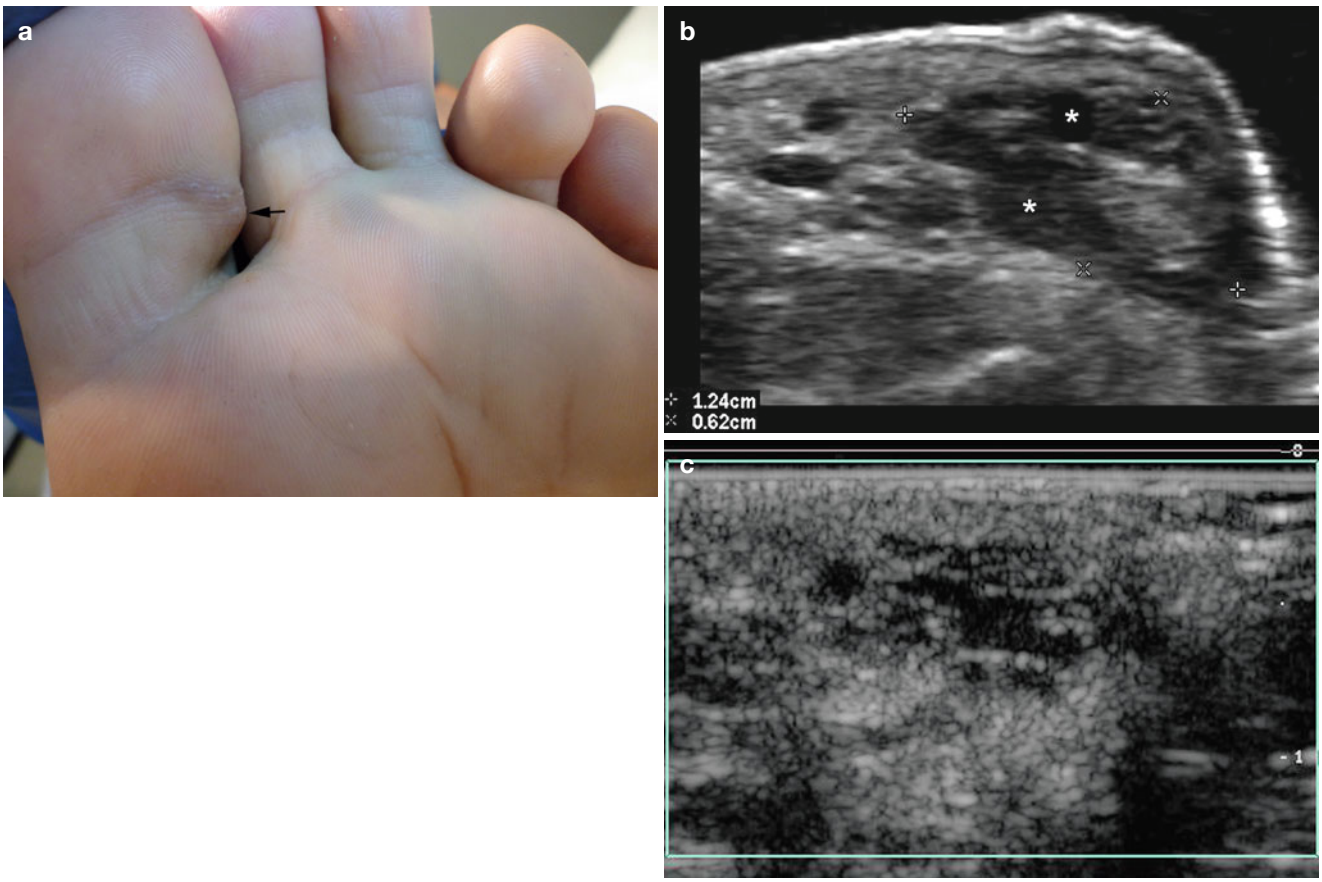

Fig. 7.45 (**a**–**c**) Low-flow lymphatic vascular malformation. (**a**) Clinical image demonstrates slightly erythematous swelling (*arrow*) in the lateral aspect of the left toe. (**b**) Grey scale ultrasound image (transverse view) shows 1.24 × 0.62 cm area with multiple anechoic tubules and pseudocystic structures (*) in the subcutaneous tissue. (**c**) Color Doppler ultrasound image (transverse view) demonstrates lack of vascularity within the tubules and pseudocystic spaces

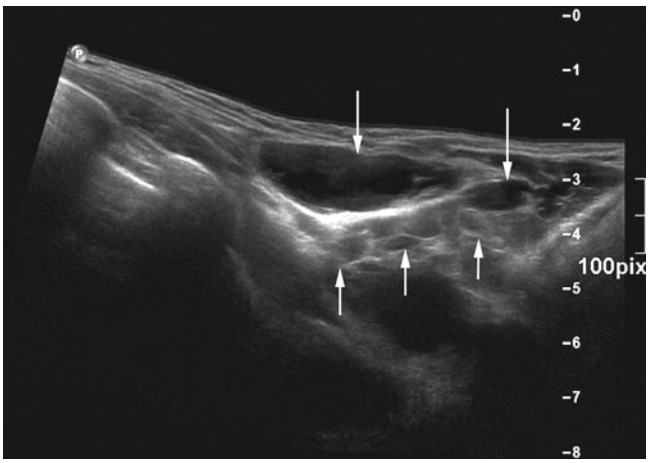

Fig. 7.46 Macrocystic lymphangioma consisting of variously sized fluid-filled cysts (*arrows*)

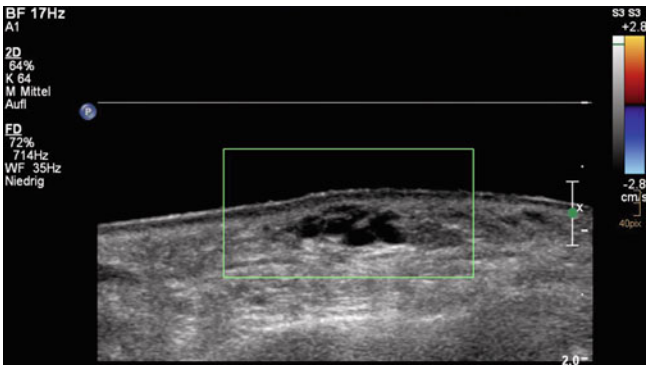

Fig. 7.47 Microcystic lymphangioma: subcutaneous lesion consisting of multiple equally sized tiny cysts without detectable flow (compression scan)

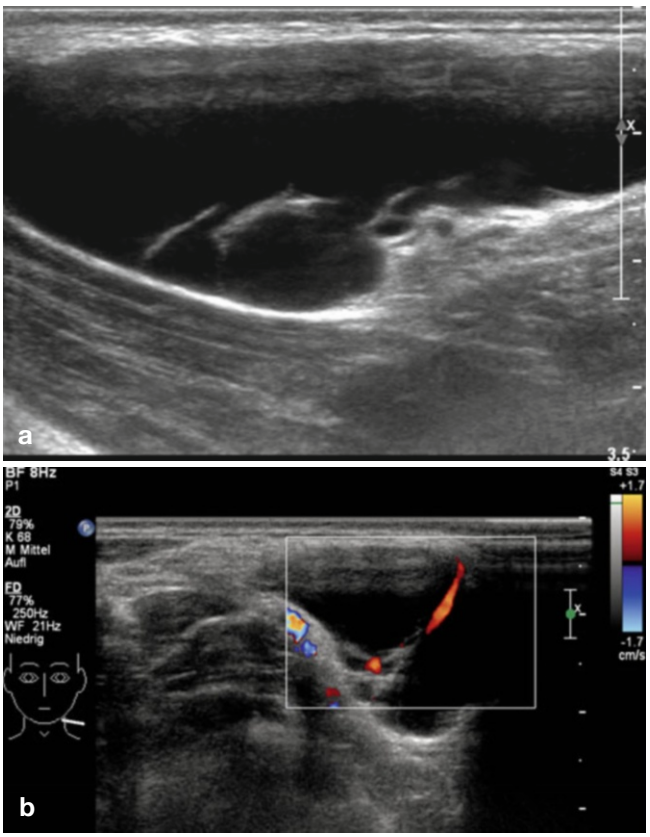

Fig. 7.48 Transverse grey scale (**a**) and Color Doppler ultrasound images (**b**) of a patient with lymphangioma. A small vessel is demonstrated inside a thick septum (**b**) in this otherwise avascular lesion

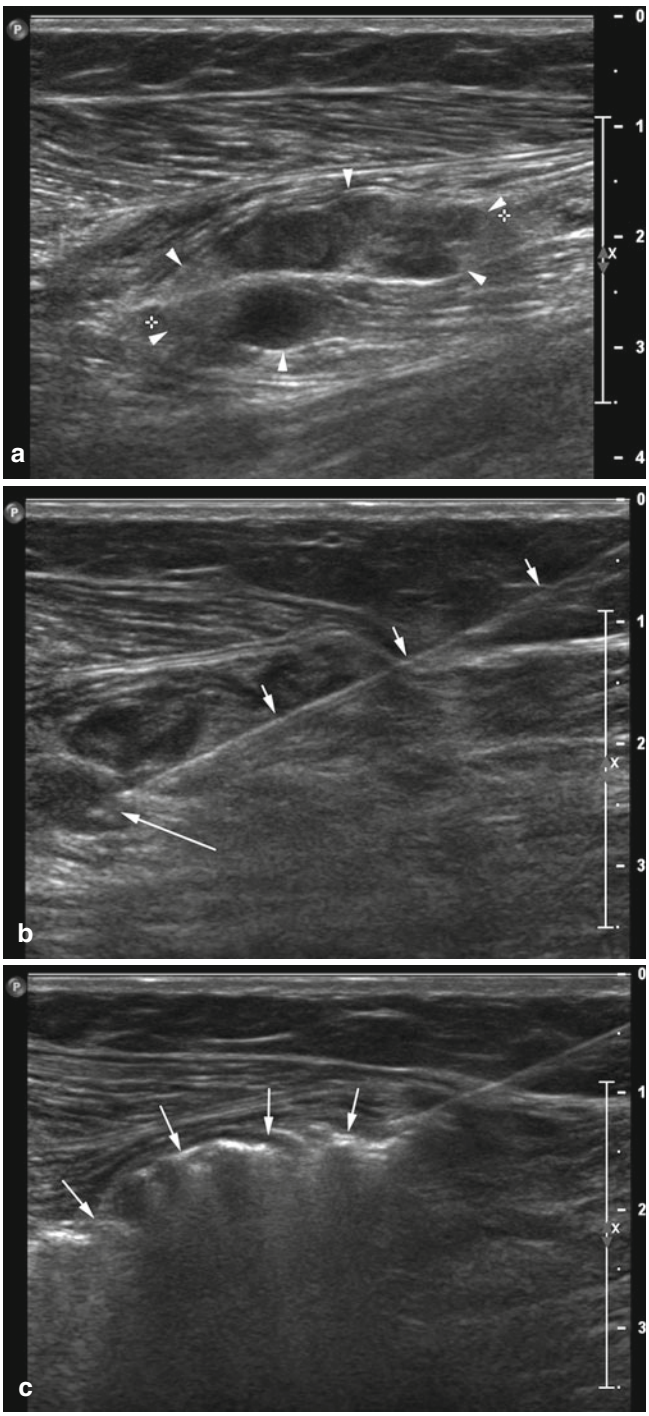

Fig. 7.49 (**a**) Transverse grey scale image of a small intramuscular venous malformation (*arrowheads*) (same patient as in Fig. 7.6). (**b**) Direct puncture under sonographic control with a 21-gauge needle (*arrowheads*). The needle tip (*arrow*) is positioned inside the deepest lying cavern. (**c**) Homogeneous distribution of polidocanol foam inside the lesions (*arrows*)

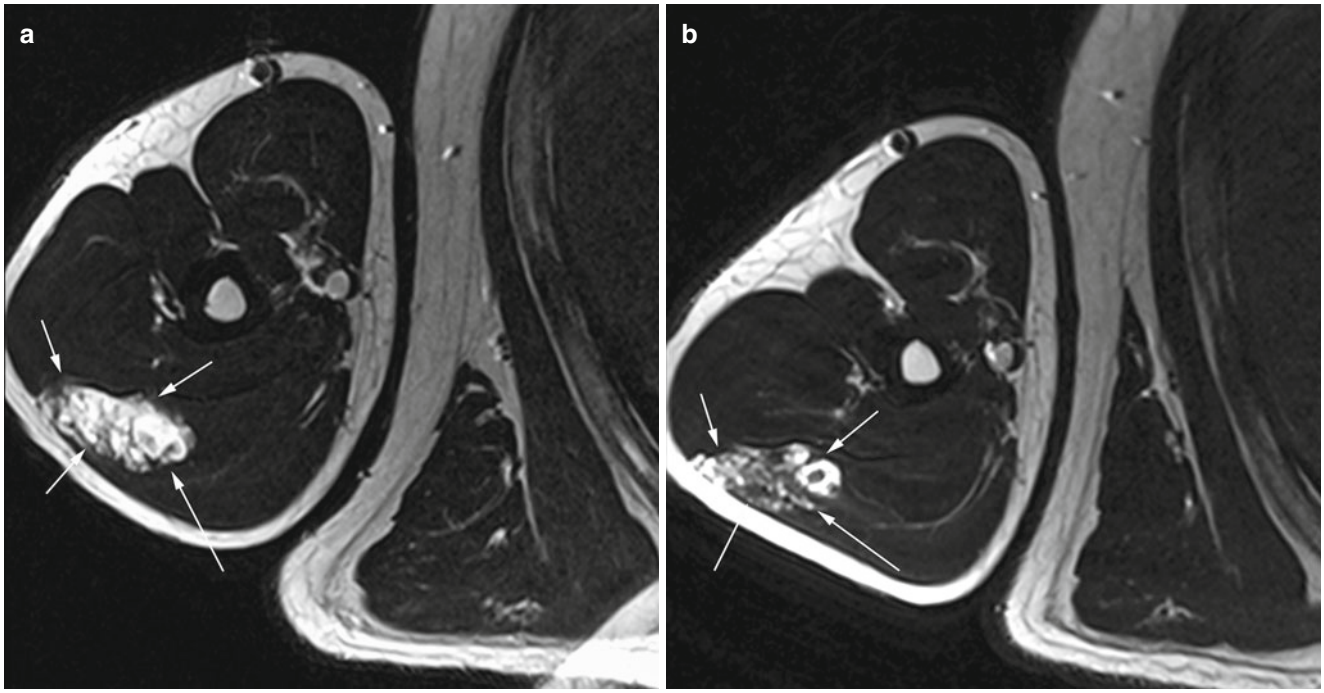

Fig. 7.50 (**a**, **b**) Transverse T2-weighted MR images of venous malformation (*arrows*) in the right triceps muscle, (**a**) before, (**b**) after sclerotherapy with polidocanol. Note marked reduction of hyperintense areas inside the malformation in (b), consistent with good response to sclerotherapy

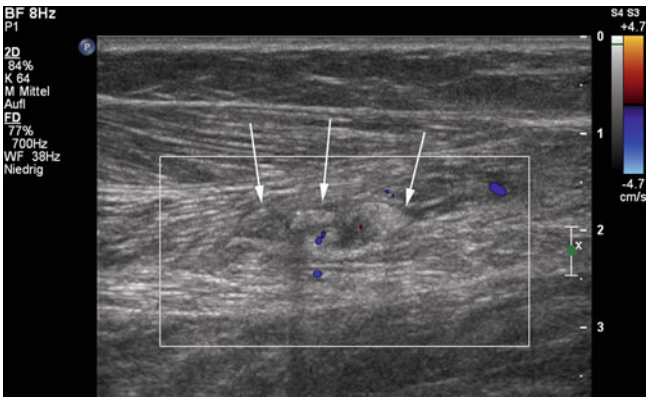

Fig. 7.51 Color Doppler ultrasound image after sclerotherapy of venous malformation: a marked reduction of lesion volume, fibrous remodeling (*arrows*) and no detectable flow is demonstrated confirming good response

7.7 Percutaneous Ultrasound-Guided Therapy

Traditionally the accepted treatment for a vascular malformation was surgery. Because of the complex architecture of vascular malformations, however, surgical resection often does not allow for complete excision of the lesion, or only at the risk of severe cosmetic impairment. This is especially true for complex AVMs with high flow. Generally speaking, malformations are lesions that respond to a variety of external stimuli: minor trauma (and thus also surgical incision) may result in accelerated growth of residual parts of a malformation with disastrous consequences. Therefore, current treatment concepts favor a multidisciplinary approach that on the one hand avoids overaggressive surgery, and overtly conservative approaches on the other. Treatment of vascular malformations has two major aims: complete destruction or resection of the lesion, if feasible, or at least amelioration of clinical symptoms by reduction of local blood flow and/or extent of the lesion. Ideally, the nidus of an AVM must be completely destroyed, complete thrombosis and later fibrous remodeling of a slow-flow malformation must be achieved, and cosmetic or functional impairment must be kept at a minimum. In this regard, sclerotherapy may be the sole treatment for a venous malformation, may be used in conjunction with arterial embolotherapy, or implemented as a preoperative or postoperative adjunct therapy.

While the nidus of an AVM is typically treated by transarterial catheter embolization, venous channels inside an AVM or slow-flow venous malformation (Fig. 7.49) may be attacked by a variety of sclerosing agents that include absolute ethanol, polidocanol (aethoxysklerol), and ethanolamine oleate. In experienced hands, percutaneous sclerotherapy is usually a safe procedure, however, certain complications exist and therefore the decision to treat must be based on a thorough clinical and imaging work-up. We generally recommend a complete color Doppler ultrasound examination with spectral wave analysis, including measurement of

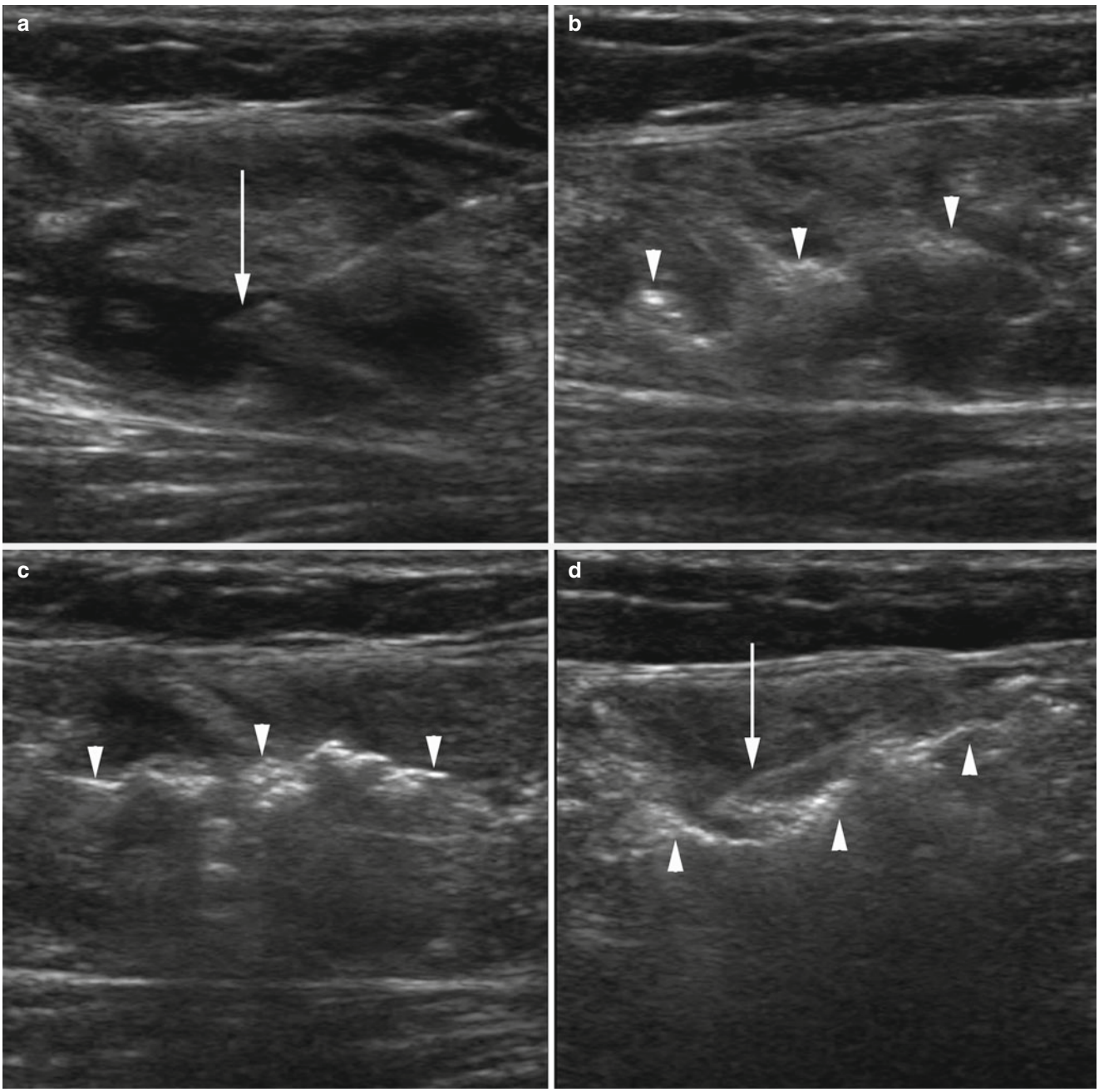

Fig. 7.52 (**a**–**d**) Sclerotherapy with polidocanol in a patient with a slow-flow venous malformation: initially the needle tip is positioned deep inside the lesion (*arrow* in **a**), with injection of polidocanol foam progressive filling of venous caverns is seen (*arrowheads* in **b** and **c**). The needle is repositioned to a more superficial location (*arrow* in **d**). Note the posterior acoustic shadowing in caverns already filled with echogenic foam (*arrowheads* in **d**) that prevents visualization of the deep lying area in the later phase of sclerotherapy

shunt flow in combined AVMs and MRI with inclusion of MRA. In the case of a combined AVM, conventional angiography is performed to define the configuration of the nidus and the existing feeders, and a first session of transcatheter arterial embolization is usually performed after diagnostic angiography. In selected cases, percutaneous sclerotherapy of the venous component is performed in the same session. For venous malformations, direct puncture percutaneous phlebography is performed and a first sclerotherapy session follows after definition of the venous drainage (see above). Patients with lymphangioma go directly toward sclerotherapy after diagnostic imaging with ultrasound and MRI.

The same imaging work-up detailed above is used to assess treatment success after sclerotherapy. Judging the effect of sclerotherapy is difficult because there is a high discrepancy

between the clinical and morphological response [21]; while some patients show good response in terms of regression of lesion volume as defined on imaging, clinical improvement can be unsatisfactory, and vice versa.

Teaching Point
Clinical improvement and results of imaging studies after sclerotherapy are highly discrepant.

To our knowledge, there are no reliable data on how to define a "good response" based on imaging criteria, but generally a reduction of lesion volume ≥50 % is considered acceptable (Fig. 7.50). This is true for low-flow venous malformations, but for high-flow lesions, an attempt to complete devascularization should be made. If only partial reduction is achieved, the risk of recurrence with increased perfusion of the persisting feeders and subsequent enlargement of the malformation is high. In general, better success rates are achieved in malformations with low flow and only small draining vessels. Another important aspect for better success rates is even distribution of the sclerosant throughout the malformation and a longer local dwell time in the target, which are achieved by multiple punctures and repositioning of the needle and effective reduction of venous drainage by compression of drainage veins, or the use of a sclerosant with better endothelial contact (i.e., foam). Given this reasoning, lesions with distinct margins on pre-interventional imaging, few drainage veins and no or slow drainage are good candidates for sclerotherapy.

Percutaneous sclerotherapy may be used to treat lymphangiomas [19]. Withdrawal of the cyst fluid before instillation of the sclerosant is mandatory, particularly in large lymphangiomas, to achieve better contact of the drug with the cyst wall and to reduce the volume of the sclerosant.

In general, multiple sclerotherapy sessions are needed for the treatment of larger malformations and especially large lymphangiomas.

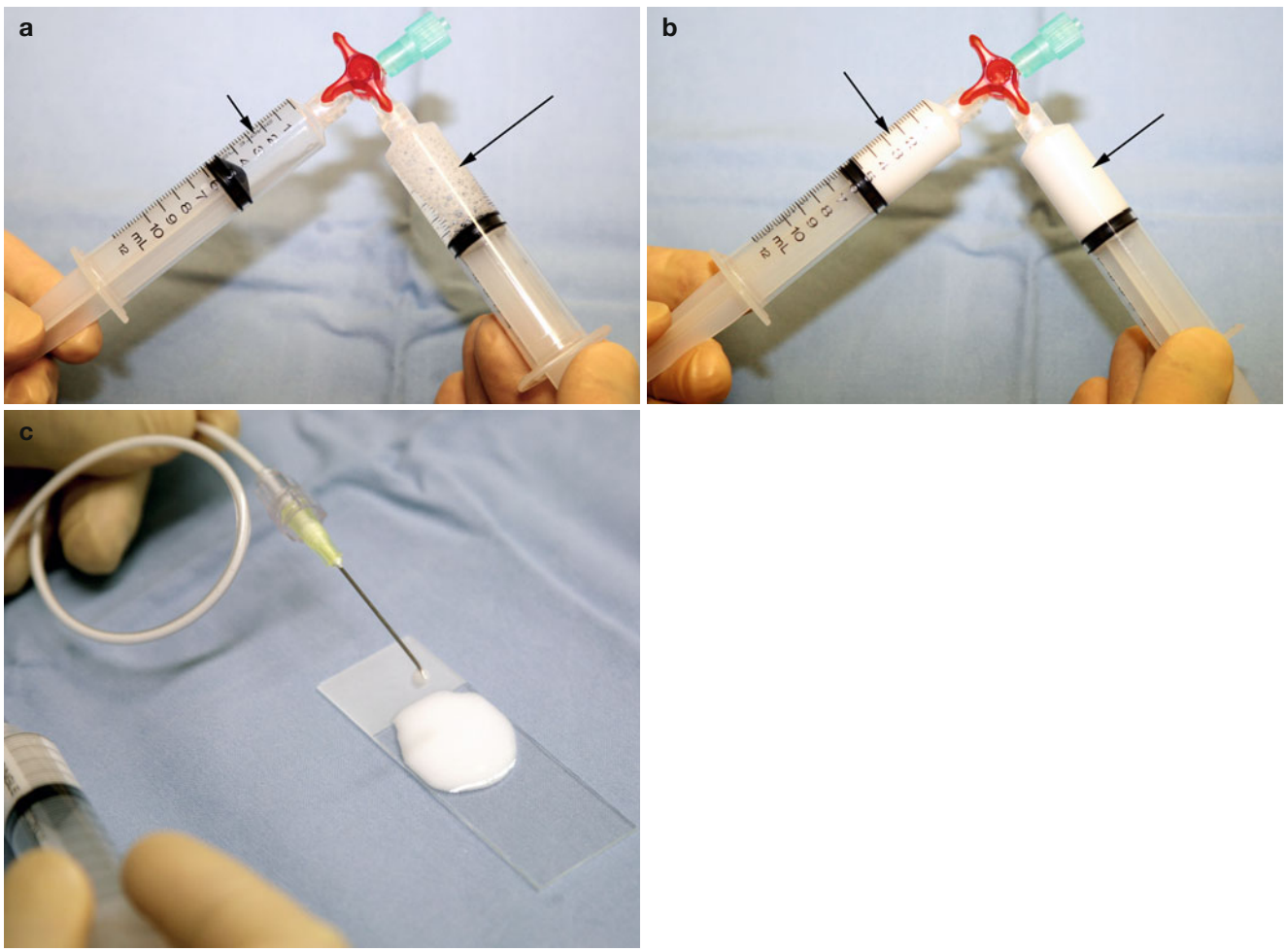

Fig. 7.53 (**a**) An equal amount of polidocanol (*long arrow*) and air (*short arrow*) is mixed by using a disposable three-way stopcock and two syringes. (**b**) Air and liquid polidocanol are pumped through the stopcock from one syringe into the other until dense foam is formed (*arrows*). (**c**) The stable foam is administered via a 21-gauge needle and tubing

7.7.1 Absolute Ethanol

Absolute ethanol has long been the main agent for treatment of lesions that are surgically inaccessible. Ethanol causes endothelial damage, thrombosis with later fibrosis, and occlusion of vascular channels. A response rate between 64 and 96 % is reported for venous malformations in terms of reduction of lesion size and volume and/or improvement of symptoms [12] (Fig. 7.51). The rate of complication is not to be underestimated with skin changes (blisters, necrosis), superficial cellulitis, deep vein thrombosis, pulmonary embolus, and cardiopulmonary collapse. It is possible for systemic alcohol contamination to also occur. Because of severe pain associated with the procedure, we generally only perform ethanol sclerotherapy under general anesthesia (a nerve block may be an alternative in selected cases). Blood-flow monitoring is mandatory because of the risk of cardiovascular reactions. Except for venous malformations with no detectable drainage or hemangioma, a tourniquet is used to reduce venous drainage and the sclerosant is injected slowly through an 18–22 gauge needle. In contrast to other researchers, we do not perform injection under fluoroscopic guidance, but with sonographic control only. For large cavernomatous malformations it is advised to gradually inject only small amounts of the sclerosant with frequent repositioning of the needle to achieve even distribution of the scelrosant inside the malformation. In our experience, this results in a better sclerosing effect throughout the lesion.

7.7.2 Polidocanol

Polidocanol (aethoxysclerol) is a substance that has been used with good success for the treatment of lower extremity and esophageal varices and thus an agent with good sclerosing potential for venous malformations [22]. It is a detergent consisting of 95 % hydroxypolyethoxydodecane, which induces overhydration of endothelial cells, resulting in a cascade of vascular injury, thrombosis, and fibrotic remodeling similar to ethanol. Because polidocanol has an anesthetic effect, it can be applied without any need for additional anesthesia, which makes it the agent of choice for sclerotherapy in an outpatient setting. Because severe cardiovascular complications are known, it should not be seen as a "Mickey-Mouse treatment," which is why the same precautions are to be taken as in ethanol sclerotherapy (blood-flow monitoring, use of tourniquets, etc.). We observe patients for at least half an hour after treatment, or longer depending on the extent of the lesion and the type of venous drainage. Generally, 1 ml of a 1 % solution of polidocanol is used for each centimeter of the lesion, with a maximum of 6–10 ml. The injection is done with real-time ultrasound guidance and repositioning of the needle or repeat punctures as specified above for ethanol treatment (Fig. 7.52). A special type of application using a polidocanol foam preparation has been presented in the literature for the treatment of varicose veins [23], which may also be used successfully for the treatment of venous malformations [24]. An equal amount of polidocanol and air is mixed by using a disposable three-way stopcock and two syringes. The air and liquid polidocanol are pumped through the stopcock from one syringe into the other until dense foam is formed [23] (Fig. 7.53). The stopcock may be gradually locked to reduce the opening of the hole and produce foam with tinier microbubbles and thicker texture. Afterward, the foam is injected as specified above under ultrasound guidance. In our experience, foam sclerotherapy has several advantages: foam provides better surface contact with the endothelium and therefore results in a better effect on the endothelial lining; it is highly echogenic and therefore the distribution of the sclerosant inside the malformations is better visualized with ultrasound compared with a liquid preparation.

Teaching Point

Polidocanol foam allows for better sonographic control of sclerotherapy and yields better results at a lower risk for complications.

Care must be taken to first fill the deep-lying caverns of a malformation (Fig. 7.52): if superficial parts fill with bubbles at the beginning of the injection, the deep-lying parts are no longer accessible because of overshadowing and a lack of needle visualization. Based on personal experience of foam sclerotherapy of varicose veins, because to our knowledge no data from larger controlled trials exist, we know that the risk of spilling the sclerosant into draining vessels and extravasation into the surrounding soft tissues is reduced with foam for the treatment of malformations.

Conclusion

Hemangiomas and vascular malformations are a complex subset of soft-tissue lesions. Their differentiation from other soft-tissue tumors and the correct classification of malformations and hemangiomas is important because it is the basis for adequate treatment. Ultrasound is the ideal first line modality for imaging and may be supplemented by MRI and MRA for further work-up. Invasive imaging such as arterial angiography or direct puncture phlebography is only needed for the planning and control of interventional treatment, but otherwise unnecessary. As hemangiomas and malformations are overtly complex in terms of clinical presentation, diagnosis, therapy, and prognosis, they must be covered by an interdisciplinary team of specialists dedicated to the management of these patients.

References

1. Mulliken JB, Glowacki J. Hemangiomas and vascular malformations in infants and children: a classification based on endothelial characteristics. Plast Reconstr Surg. 1982;69:412–22.
2. Burrows PE, Mulliken JB, Fellows KE, Strand RD. Childhood hemangiomas and vascular malformations: angiographic differentiation. Am J Roentgenol. 1983;141:483–8.
3. Enjolras O. Classification and management of the various superficial vascular anomalies: hemangiomas and vascular malformations. J Dermatol. 1997;24:701–10.
4. Kawanabe T, Wakita S, Harii K, Hayashi N, Inoue Y. Sclerotherapy of hemangiomas and vascular malformations in lips. Jpn J Plast Reconstr Surg. 1996;16:852–62.
5. Inoue Y, Wakita S, Yoshikawa K, et al. Evaluation of flow characteristics of soft-tissue vascular malformations using technetium-99 m labeled red blood cells. Eur J Nucl Med. 1999; 26:367–72.
6. Kramer U, Ernemann U, Fenchel M, et al. Pretreatment evaluation of peripheral vascular malformations using low-dose contrast-enhanced time-resolved 3D MR angiography: initial results in 22 patients. Am J Roentgenol. 2011;196:702–11.
7. Dubois J, Patriquin HB, Garel L, et al. Soft tissue hemangiomas in infants and children: diagnosis using Doppler sonography. Am J Roentgenol. 1998;171:247–52.
8. Paltiel HJ, Burrows PE, Kozakewich HPW, Zurakowski D, Mulliken JB. Soft tissue vascular anomalies: utility of US for diagnosis. Radiology. 2000;214:747–54.
9. Oe Y, Orr L, Laifer-Narin S, et al. Contrast-enhanced sonography as a novel tool for assessment of vascular malformations. J Angiogenesis Res. 2010;2:25.
10. Enjolras O, Riche MC, Merland JJ, Escnde JP. Management of alarming hemangiomas in infancy: a review of 25 cases. Pediatrics. 1990;85:491–8.
11. Taylor KJW, Ramos I, Carter D, Morse SS, Snower D, Fortune K. Correlation of Doppler US tumor signals with neovascular morphologic features. Radiology. 1988;166:57–62.
12. Hyodoh H, Masakazu H, Akiba H, et al. Peripheral vascular malformations: imaging, treatment approaches, and therapeutic issues. Radiographics. 2005;25:159–71.
13. Puig S, Casati B, Staudenherz A, Paya K. Vascular low-flow malformations in children: current concepts for classification, diagnosis and therapy. Eur J Radiol. 2005;53:35–45.
14. Puig S, Aref H, Chigot V, Bonin B, Brunelle F. Classification of venous malformations in children and implications for sclerotherapy. Pediatr Radiol. 2003;33:99–103.
15. Dubois J, Soulez G, Oliva VL, et al. Soft-tissue venous malformations in adult patients: imaging and therapeutic issues. Radiographics. 2001;21:1519–31.
16. Trop I, Dubois J, Guibaud L, et al. Soft tissue venous malformations in pediatric and young adult patients: diagnosis with Doppler US. Radiology. 1999;212:841–5.
17. Abernethy LJ. Classification and imaging of vascular malformations in children. Eur Radiol. 2003;13:2483–97.
18. Blei F. Congenital lymphatic malformations. Ann NY Acad Sci. 2008;1131:185–94.
19. Impellizzeri P, Romeo C, Borruto FA, et al. Sclerotherapy for cervical cystic lymphatic malformations in children. Our experience with computed tomography-guided 98 % sterile ethanol insertion and a review of the literature. J Pediatr Surg. 2010;45:2473–8.
20. Bloom DC, Perkins AJ, Manning SC. Management of lymphatic malformations. Curr Opin Otolaryngol Head Neck Surg. 2004;12:500–4.
21. Yun WS, Kim YW, Lee KB, et al. Predictors of response to percutaneous ethanol sclerotherapy (PES) in patients with venous malformations: analysis of patient self-assessment and imaging. J Vasc Surg. 2009;50:581–9.
22. Jain R, Bandhu S, Sawhney S, Mittal R. Sonographically guided percutaneous sclerosis using 1 % polidocanol in the treatment of vascular malformations. J Clin Ultrasound. 2002;30:416–23.
23. Tessari L, Cavezzi A, Frullini A. Preliminary experience with a new sclerosing foam in the treatment of varicose veins. Dematol Surg. 2001;27:58–60.
24. Bergan J, Cheng V. Foam sclerotherapy of venous malformations. Phlebology. 2007;22(6):299–302.

Cutaneous Vascular Tumors

8

Ximena Wortsman, Laura Carreño, and Claudia Morales

Contents

X. Wortsman, MD (✉)
Department of Radiology and Dermatology,
Faculty of Medicine, Institute for Diagnostic Imaging
and Research of the Skin and Soft Tissues,
Clinica Servet, University of Chile, Almirante Pastene, 150,
Providencia, Santiago, Chile
e-mail: xwo@tie.cl, xworts@yahoo.com, www.sonoskin.com

L. Carreño, MD • C. Morales, MD
Department of Pathology, Dermopathology Section,
Hospital Clinico U. Chile,
Faculty of Medicine, University of Chile,
Santiago, Chile

8.1 Introduction

There are many types of vascular tumors that can affect the skin. The most common vascular tumors are hemangiomas of infancy that were reviewed in the previous chapter. Additionally, congenital hemangiomas [rapidly involuting congenital hemangioma (RICH) and non-involuting congenital hemangioma (NICH)] are discussed in Chap. 3 (Congenital Conditions). In this chapter we will discuss other types of cutaneous vascular entities that can be referred for a sonographic examination.

8.2 Vascular Tumors

8.2.1 Benign

8.2.1.1 Angiokeratoma

Angiokeratoma is conformed by dilated vessels and hyperkeratosis. Current classification distinguishes between widespread forms (angiokeratoma corporis diffusum), which are usually associated with an inborn error of metabolism, and localized forms, that include solitary angiokeratoma, Fordyce's angiokeratoma, angiokeratoma circumscriptum naeviforme, and angiokeratoma of Mibelli [1]. Thus, there are several variants that predominantly affect the trunk and limbs with reddish papulae that present a wart-like appearance clinically. Histologically, these lesions present a similar appearance in all variants showing multiple dilated capillaries in the papillary dermis that can extend to the epidermis, with acanthosis and hyperkeratosis also being detected. On sonography, angiokeratomas presents as a hypoechoic band or region that affects the dermis with thickening of the epidermis. The keratotic component can generate a tiny posterior acoustic shadowing artifact, and frequently, they present hypovascularity on color Doppler imaging because of their slow flow capillary component (Fig. 8.1).

X. Wortsman, G.B.E. Jemec (eds.), *Dermatologic Ultrasound with Clinical and Histologic Correlations*,
DOI 10.1007/978-1-4614-7184-4_8, © Springer Science+Business Media New York 2013

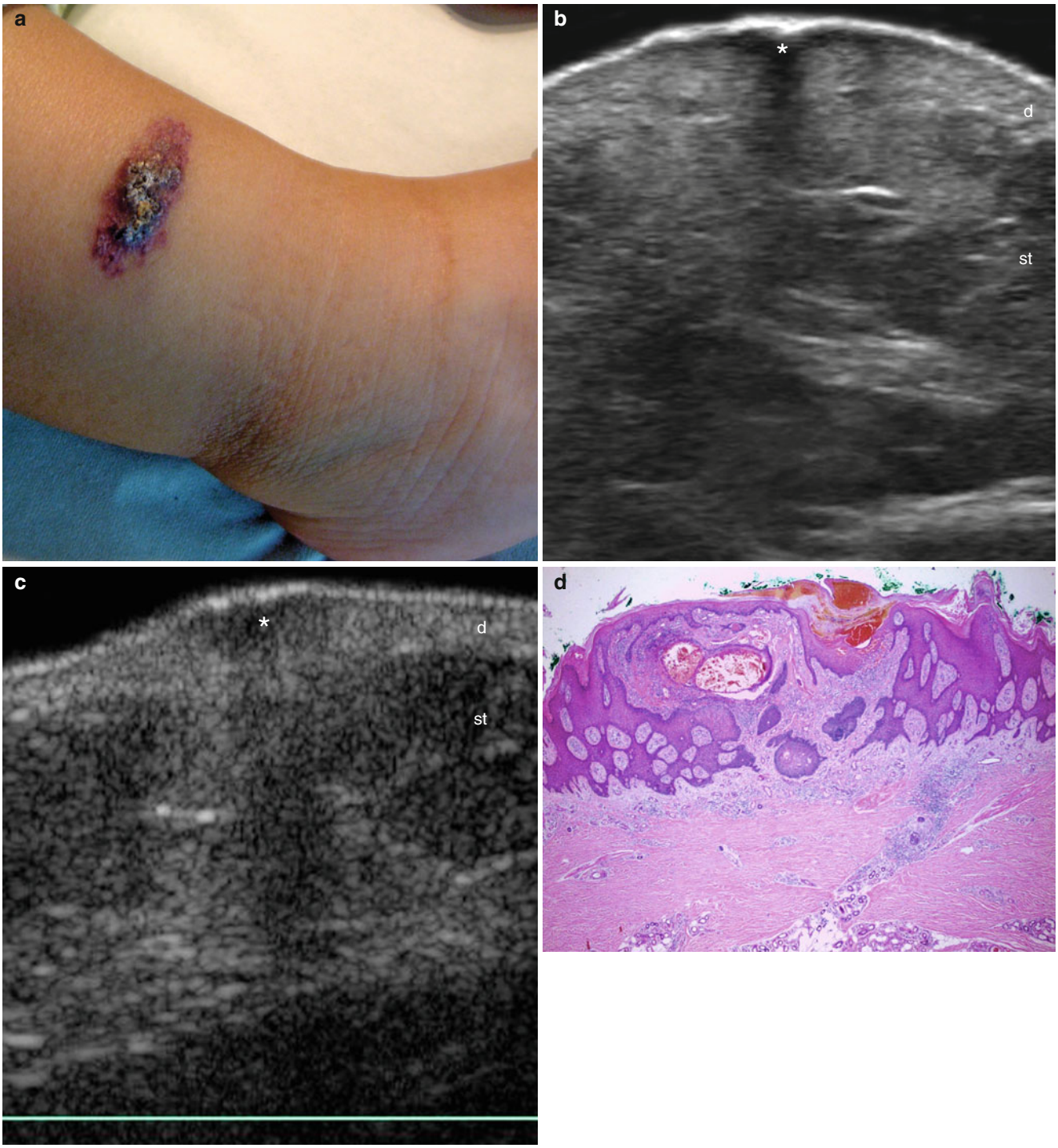

Fig. 8.1 (**a**–**d**) Angiokeratoma. (**a**) Clinical reddish lesion in the anterior aspect of the right leg. (**b**) Grey scale ultrasound (transverse view) shows hypoechoic region (*) in the dermis that generates a tiny posterior acoustic shadowing artifact. Notice the thickening of the epidermal layer. (**c**) Color Doppler ultrasound image (transverse view) demonstrates lack of detectable vascularity within the lesion. (**d**) Histology (HE × 40 zoom): proliferation of dermal vessels with epidermal acanthosis and hyperkeratosis

8.2.1.2 Verrucous Hemangioma

Verrucous hemangioma (VH) is a confusing name because it shows similar clinical and histological characteristics to angiokeratoma, with the exception that VH also involves the subcutaneous tissue. Clinically, it affects children with warty dark blue or reddish nodules predominantly on the limbs [2]. On sonography, VHs present as hypoechoic dermal bands with thickening of the epidermis and hyperechogenicity of

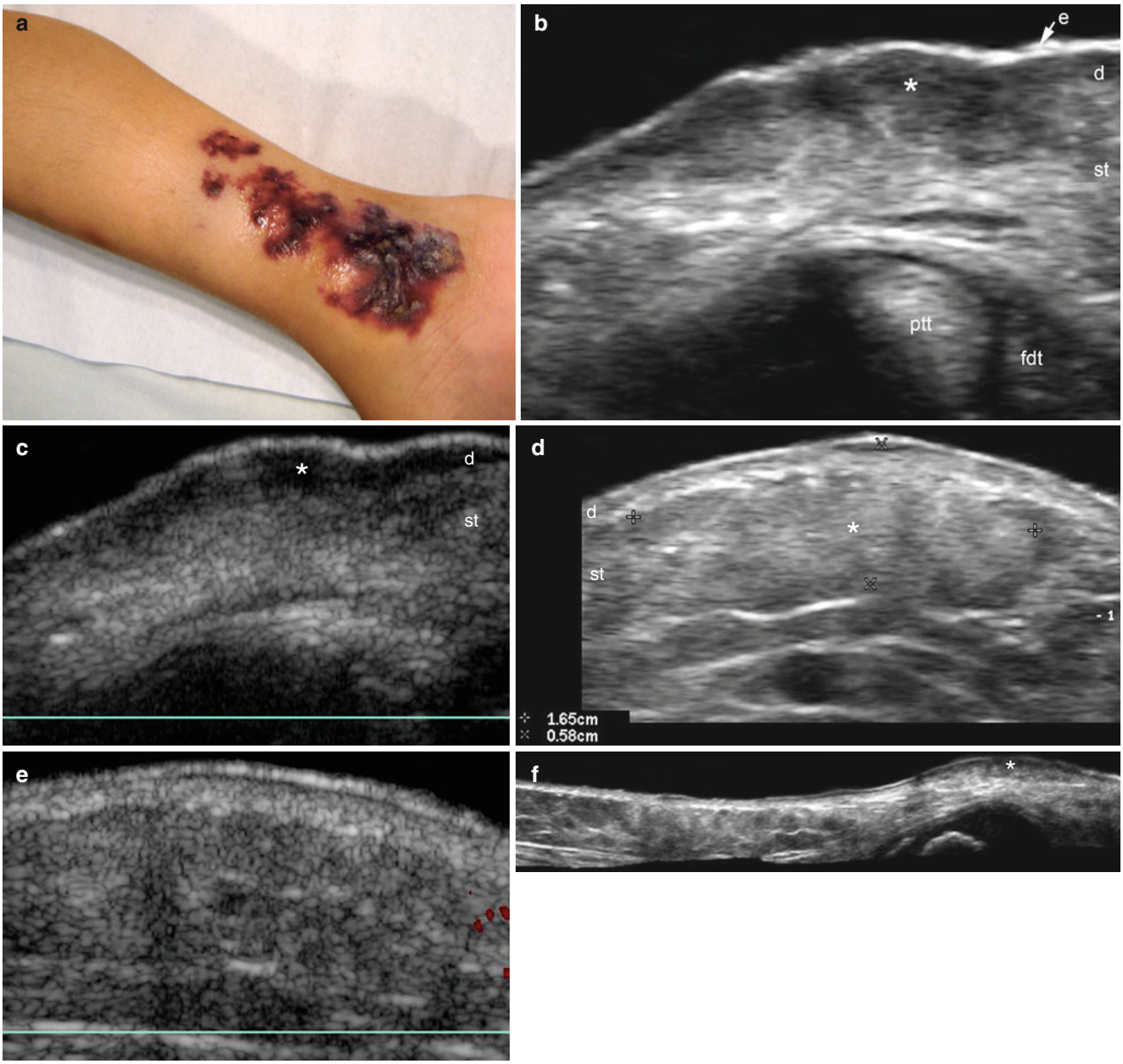

Fig. 8.2 (**a**–**f**) Verrucous Hemangioma. (**a**) Clinical reddish lesion in the medial aspect of the right leg and ankle. (**b**) Grey scale ultrasound image (transverse view, ankle region) shows the lesional area (*) with hypoechogenicity and thickening of the dermis and upper subcutaneous tissue. Also notice the thickening of the epidermis (arrow). (**c**) Color Doppler ultrasound (transverse view, ankle region) demonstrates lack of detectable vascularity within the tumor (*). (**d**) Grey scale ultrasound (transverse view, leg region) shows hyperechogenicity of the subcutaneous tissue. (**e**) Color Doppler ultrasound (transverse view, leg region) demonstrates hypovacularity of the subcutaneous tissue in the lesional area. (**f**) Grey scale (extended field of view in longitudinal axis) shows the heterogeneous echostructure in the dermis (mostly hypoechoic) and subcutaneous tissue (mostly hyperechoic) in the medial aspect of the leg and ankle. *Abbreviations*: *e* epidermis, *d* dermis, *st* subcutaneous tissue, *ptt* posterior tibial tendon, *fdt* flexor digitorum tendon

the subcutaneous tissue. The lesions are usually hypovascular on color Doppler ultrasound that can be related to the slow capillary flow component (Fig. 8.2).

8.2.1.3 Kaposiform Hemangioendothelioma

Kaposiform hemangioendothelioma (KH) are tumors that are common in children and young adults often manifesting later than infantile hemangioma. KH can be associated with lymphangiomatosis and has no known association with Kaposi sarcoma related to human immunodeficiency virus infection, and demonstrates aggressive local behavior with invasion but not distant metastasis. KH shows predilection for the limbs, head, and neck and is characterized by its common association with Kasabach–Merrit syndrome (i.e., consumptive coagulopathy)

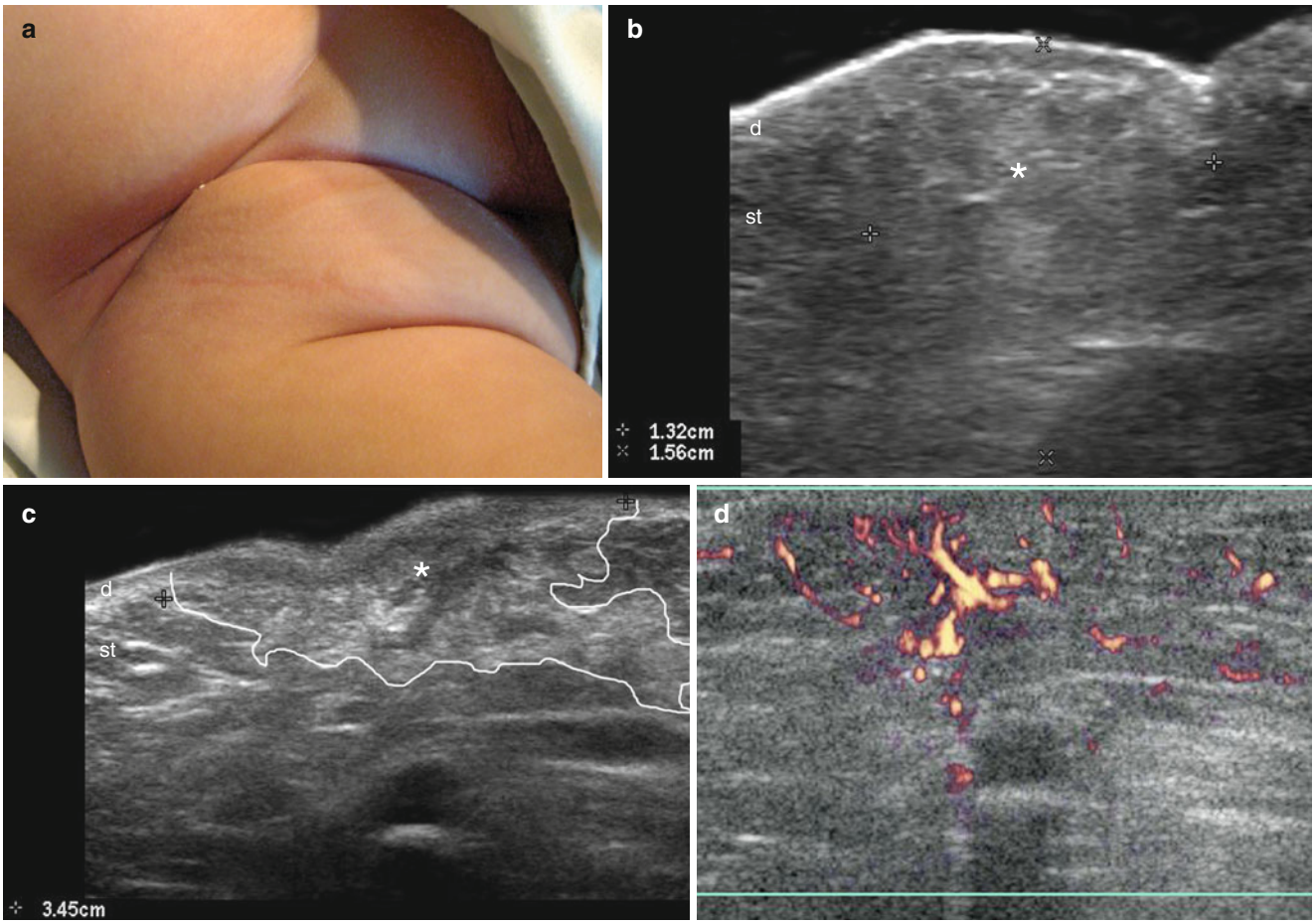

Fig. 8.3 (**a**–**d**) Kaposiform hemangioendothelioma. (**a**) Clinical swelling in the right groin. (**b**) Grey scale ultrasound (transverse view) shows ill-defined hyperechoic and heterogeneous region (*, measuring 1.32 × 1.56 cm, between markers; transverse and depth axis respectively) that affects mostly the subcutaneous tissue and to a lesser extent the dermal layer. (**c**) Grey scale ultrasound (longitudinal view) demonstrates 3.45 cm long ill-defined hyperechoic and heterogeneous lesion (*, outlined, between markers). (**d**) Color Doppler ultrasound (transverse view) shows irregular hypervascularity within the lesional area. *Abbreviations*: *d* dermis, *st* subcutaneous tissue

that can cause a high mortality rate among patients. Clinically, KH shows as reddish nodules or swelling that rapidly grows and infiltrates the soft tissues. Histologically, the tumors are lobular, infiltrative, and composed of spindle cells, congested capillaries, slit-like vascular spaces, and occasional pale epithelial cells. Thrombotic phenomena can be detected in parts of the lesion. Endothelial cells test positive for CD31, CD34, and FLI1 but negative for GLUT1 and LeY in inmunohistochemistry [3–5]. On sonography, KH tend to show an ill-defined heterogeneous echogenicity that commonly affects the dermis and subcutaneous tissue and easily involves deeper structures such as muscle. On color Doppler ultrasound, tumor vascularity may present a variable grading from hyper- to hypovascular (Fig. 8.3).

8.2.1.4 Glomus Tumor-Glomangioma

Glomus tumor or glomangioma are conformed by rare neoplasms arising from the subcutaneous glomus apparatus (i.e., neuromyoarterial component). They account for 1–5 % of soft-tissue tumors of the upper extremity, occurring in most cases in the nail bed. When located on the nail, the typical clinical presentation includes reddish spots, paroxysmal pain, and hypersensitivity. Nevertheless, occasionally painless subungual glomus tumors can be detected. Recently, the tumors comprised of glomus cells have been categorized into two major subtypes: the glomus tumor and the glomangioma. Glomangiomas differ clinically from glomus tumors in that they present in children and young adults, are usually asymptomatic, do not have a predilection for the subungual region, and often are multifocal. They can vary in color from pink to blue and often become darker with age; they can be plaque-like or nodular. Multiple glomangiomas are rare and comprise about 10 % of all glomus tumors. Because glomangiomas are not neoplastic and resemble venous malformations, it has been suggested that they should more precisely be called lineal glomuvenous malformations.

Histopathologic features of glomangiomas contain more-dilated venous channels than do glomus tumors and that is why they resemble venous malformations. Unlike venous malformations, they demonstrate single-to-multiple rows of surrounding cuboidal glomus cells. These cells stain positively for vimentin and α-smooth-muscle actin but are negative for desmin, von Willibrand factor, and S-100. Another

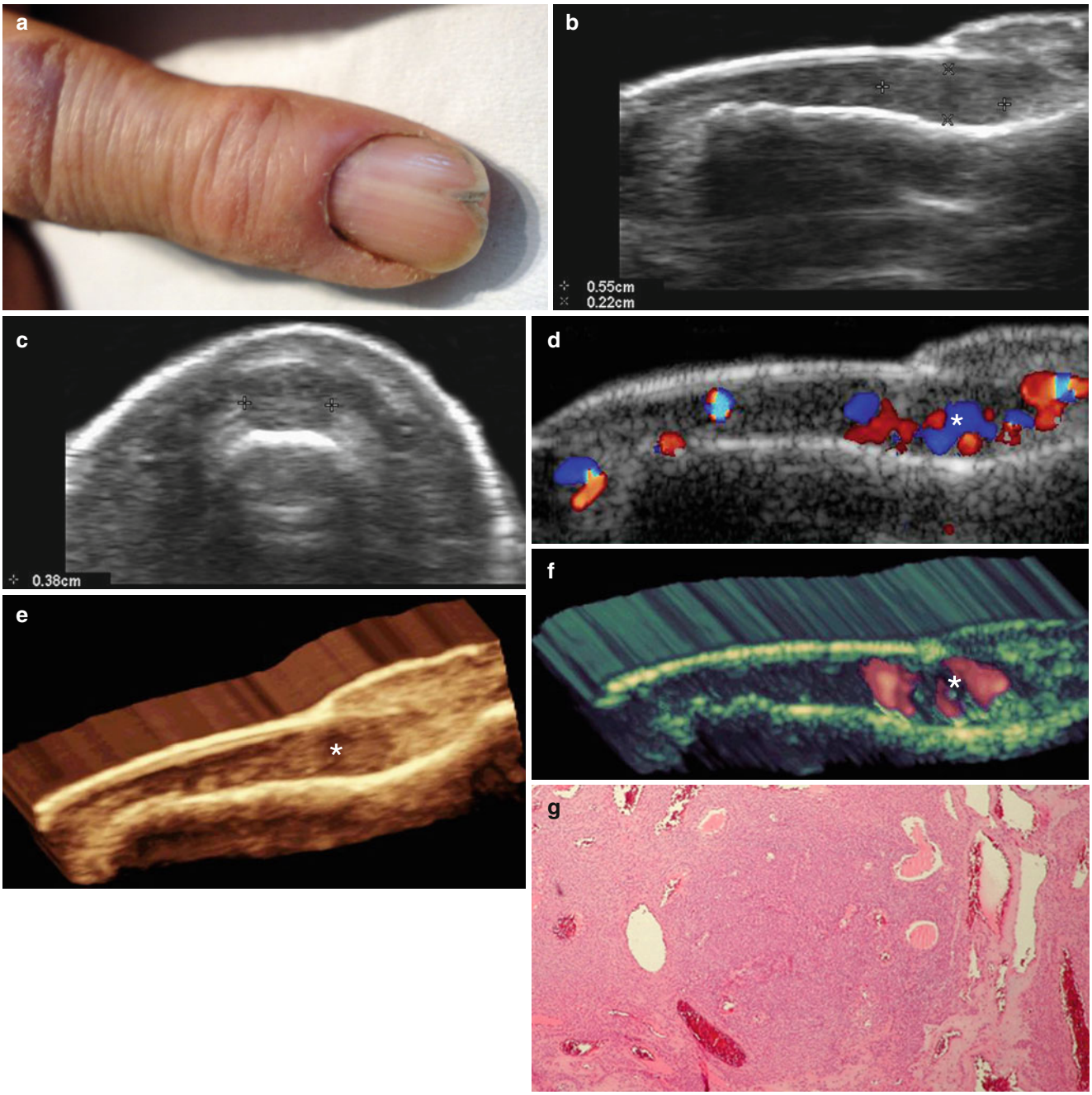

Fig. 8.4 (**a**–**g**) Glomus tumor of the nail. (**a**) Clinical dystrophy of the nail of the left index finger. (**b**) Grey scale ultrasound (longitudinal view) shows 0.55 × 0.22 cm (long and depth axis, respectively), well-defined, oval -shaped, hypoechoic nodule in the proximal nail bed. Notice the slight upward displacement of the nail plates and the remodeling of the bony margin of the distal phalanx. (**c**) Grey scale ultrasound (transverse view) also demonstrates the 0.38 cm hypoechoic nodule in the proximal nail bed. (**d**) Color Doppler ultrasound (longitudinal view) shows increased blood flow within the tumor (*). (**e**) (grey scale) and (**f**) (power angio) are different 3 D reconstructions of the tumor (*) (5–8 s sweep). (**g**). Histology (HE × 40 zoom): intradermal vascular proliferation surrounded by cuboidal cells that conform a solid pattern

difference is that histologically glomangiomas are less likely to have a capsule than glomus tumors. Glomus tumors lye in the deep reticular dermis where there are dilated vascular spaces that are lined by cuboidal cells with round nuclei and eosinophilc cytoplasm.

On ultrasound, these entities tend to present as well-defined hypoechoic nodules slightly heterogeneous and occasionally with anechoic areas. In the nail bed they tend to be centrally located (without involvement of the periungual region) and usually remodel the bony margin of the distal phalanx underneath the tumor. On color Doppler ultrasound, glomus tumors often show hypervascularity with low flow arterial and venous vessels, although there are some hypovascular subtypes (Fig. 8.4). In contrast, glomangiomas may show a variable morphology that goes from being well-defined, hypervascular, and nodular to ill-defined and

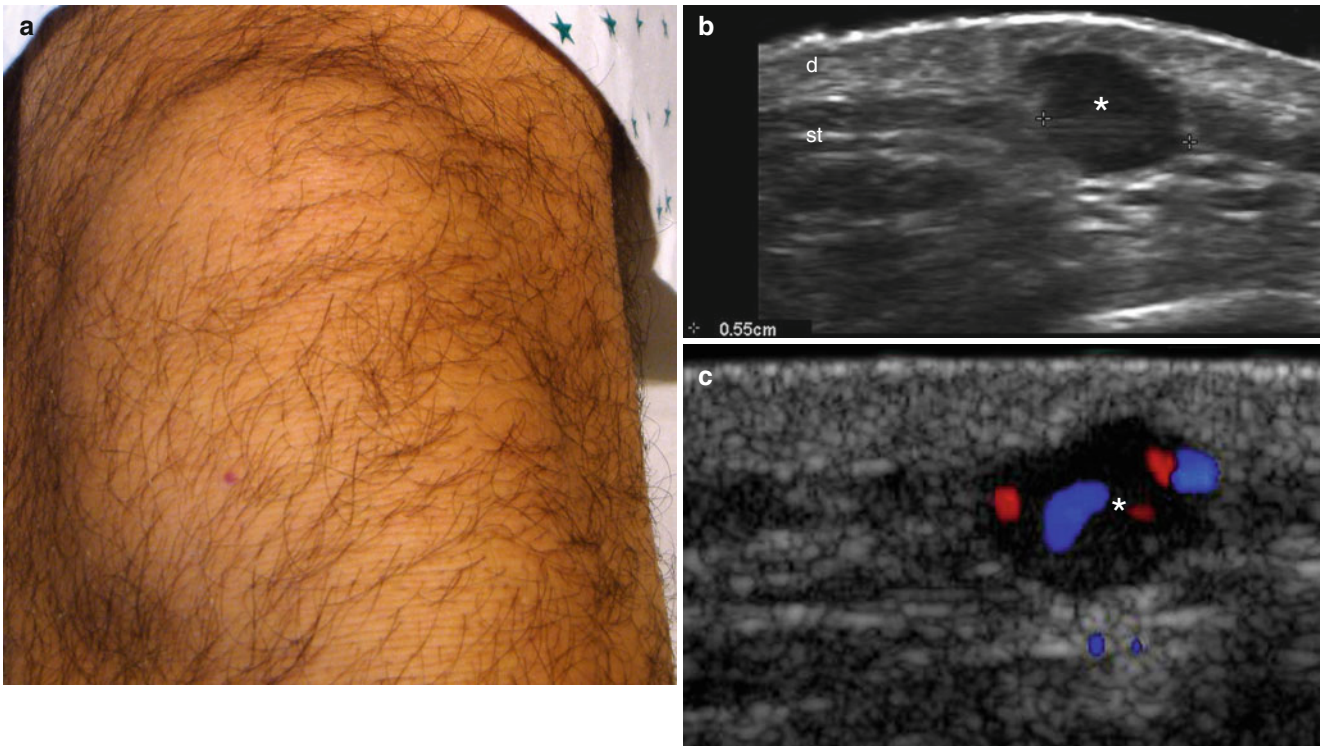

Fig. 8.5 (**a**–**c**) Glomangioma. (**a**) Unremarkable clinical view of the anterior aspect of the knee. Nevertheless, the patient presented with tenderness in correlation with the sonographic findings. (**b**) Grey scale ultrasound (transverse view) demonstrates 0.55 cm well-defined hypoechoic nodule in the dermis and upper subcutaneous tissue. (**c**) Color Doppler ultrasound (longitudinal view) demonstrates increased vascularity within the nodule (*)

hypovascular depending on the amount and size of the vessels. These benign entities are usually composed of slow flow and capillary structures (Fig. 8.5). Thus, glomangiomas are commonly located in the dermis and subcutaneous tissue and may present clinically as multiple linear bluish and serpiginous lesions that demonstrate a nodular appearance on ultrasound as previously described [6–12].

8.2.1.5 Pyogenic Granuloma

Pyogenic granuloma (PG), also called telangiectatic granuloma and lobular capillary hemangioma, is a lesion that is a reactive and lobular proliferation of capillary vessels that commonly affects the skin of the head, neck and limbs, the nail, and the oral mucosa. PG appears more frequently in children, young adults, and pregnant women and shows a fast initial growth. Clinically, it appears as erythematous or bluish swelling or polypoid lesions that easily ulcerates and bleeds. Histologically, these entities are composed of lobules with multiple capillary vessels within a loose collagenous. Mitosis is frequent and the lesion may also show inflammatory cells and fibrosis during late stages. On sonography, PG presents as hypoechoic pseudonodules or structures usually located in the dermis and subcutaneous tissue. On color Doppler imaging, prominent vascularity is commonly detected with slow flow arterial and venous vessels [13, 14] (Fig. 8.6).

8.2.1.6 Epithelioid Hemangioma

Epithelioid hemangioma, also called angiolymphoid hyperplasia with eosinophilia, atypical pyogenic granuloma, pseudopyogenic granuloma, inflammatory angiomatous nodule, papular angioplasia, and intravenous atypical vascular proliferation, is a benign, reactive vaso-proliferative disease, presenting with painless, reddish or purple, single or multiple nodules in the dermal and subcutaneous tissues of the head and neck, particularly around the ear. Blood eosinophilia is present in up to 15 % of the cases and a male predominance has been noted in selected Asian studies and presents most commonly in patients 20–50 years old, with a mean onset of 30–33 years [15].

Histology shows nodules or masses conformed by multiple vascular spaces lined with rounded endothelial cells with prominent eosinophilic cytoplasm. Blood vessels lined with cuboidal endothelial cells and numerous eosinophils are also detected.

On sonography, hypoechoic and slightly heterogeneous nodules or pseudonodules are located in the dermis and occasionally in the subcutaneous tissue. Color Doppler imaging demonstrates increased vascularity within the nodules usually with slow flow arterial vessels. When this entity affects the ear, it may cause a thinning of the auricular cartilage (Fig. 8.7).

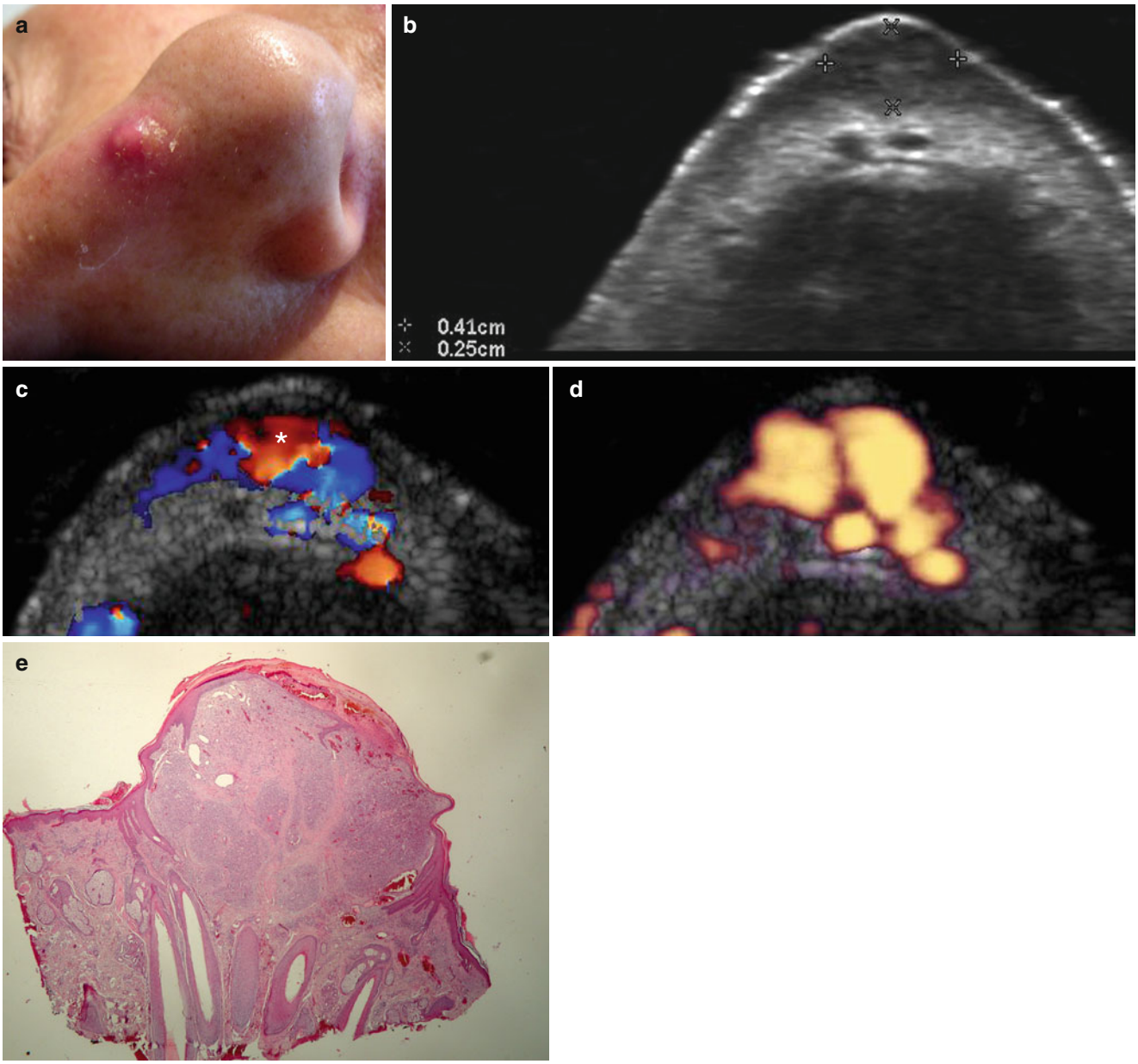

Fig. 8.6 (**a**–**e**) Pyogenic Granuloma. (**a**) Clinical image shows erythematous swelling in the dorsum of the nose. (**b**) Grey scale ultrasound (transverse view): 0.41 × 0.25 cm hypoechoic nodule that affects dermis and upper subcutaneous tissue. (**c**) Color Doppler ultrasound and (**d**) Power Angio (transverse view) demonstrate increased vascularity within the nodule (*). (**e**) Histology (HE 20 × zoom): proliferation of capillary intradermal vessels with a lobulated pattern and covered by excoriated epidermis

8.2.1.7 Lymphangioma

Lymphangiomas are congenital malformations of the lymphatic system that can involve the skin. They account for 4 % of all vascular tumors, but comprise 25 % of benign vascular growths in children. They are hamartomatous in nature and can be grouped into cutaneous lymphangioma circumscriptum (CLC), cavernous lymphangiomas, and cystic hygromas. CLC appears localized to the dermis, although frequently extends deeper and laterally. Clinically, lymphangioma circumscriptum shows clusters of flesh-colored to translucent clear, pink, red, or black papules that measure 1 to 4 mm, overlying hyperpigmented and erythematous indurated plaques [16, 17]. On sonography, they may present as mixed echogenicity nodules with a variable degree of anechoic and hypoechoic areas in the cutaneous layers. On color Doppler imaging, lymphangiomas are predominantly hypovascular. However, hypervascularity can be found in part of the tumor because of stromal components (Fig. 8.8).

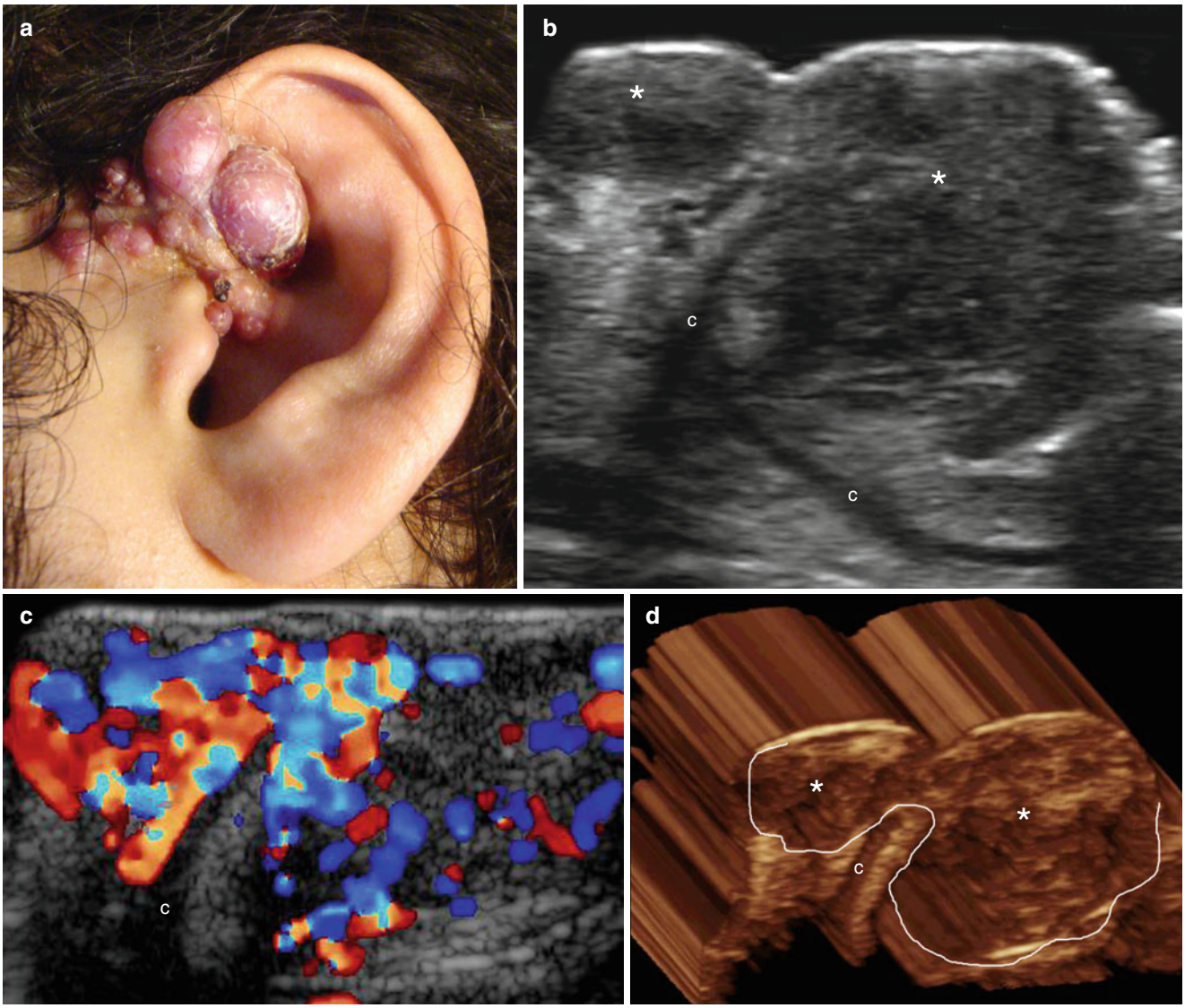

Fig. 8.7 (**a**–**d**) Epithelioid hemangioma (angiolymphoid hyperplasia with eosinophilia). (**a**) Clinical lesion shows multiple erythematous bumps that affect the left ear pinna and pre-auricular region. (**b**). Grey scale ultrasound (transverse view) demonstrates hypoechoic and confluent nodules and pseudonodules (*) that involve the cutaneous layers of the helix. Notice that there is thinning of the ear cartilage (*c*) that conserves its hypoechogenicity. (**c**) Color Doppler ultrasound (transverse view) shows prominent vascularity within the nodules. (**d**) 3D reconstruction of the lesion (*, and outlined; transverse axis, 5–8 s sweep). *Abbreviations*: *c* cartilage

8.2.1.8 Cutaneous Angiomyxoma

Cutaneous angiomyxoma (CA), also called superficial angiomyxoma, is a condition that affects all ages, with a peak incidence in the third and fourth decades and arises in the trunk, lower limb, head, and neck regions. Approximately one third of CAs recur locally, but there have been no metastases reported. Patients with multiple lesions may have the Carney complex (i.e., autosomal dominant condition conformed by myxomas of the heart and skin, hyperpigmentation of the skin [lentiginosis], and endocrine overactivity). CA affects females approximately seven times more often as it does males.

Clinically, CA presents as cutaneous papules, nodules, swellings or polypoid lesions. Tumors can show variable size and may measure 10 cm or more in diameter, demonstrate local infiltration of the surrounding tissues, and recur in approximately 50 % of cases [18].

Histology shows extensive myxoid stroma, numerous small blood vessels, varying cellularity, acellular mucin pools, stellate or bipolar fibroblastic cells, muciphages, a sparse and mixed inflammatory cell infiltrate with notable neutrophils, and occasional plumper cells with eosinophilic cytoplasm. Cytologic atypia is reported as mild. In approximately 20 % of cases, the primary lesion or its recurrence contained epithelial structures, including epidermoid cysts, thin strands of squamous epithelium, and small buds of basaloid cells. Immunohistochemically, tumor cells are negative for S-100 protein, smooth muscle actin, and pankeratin [19, 20].

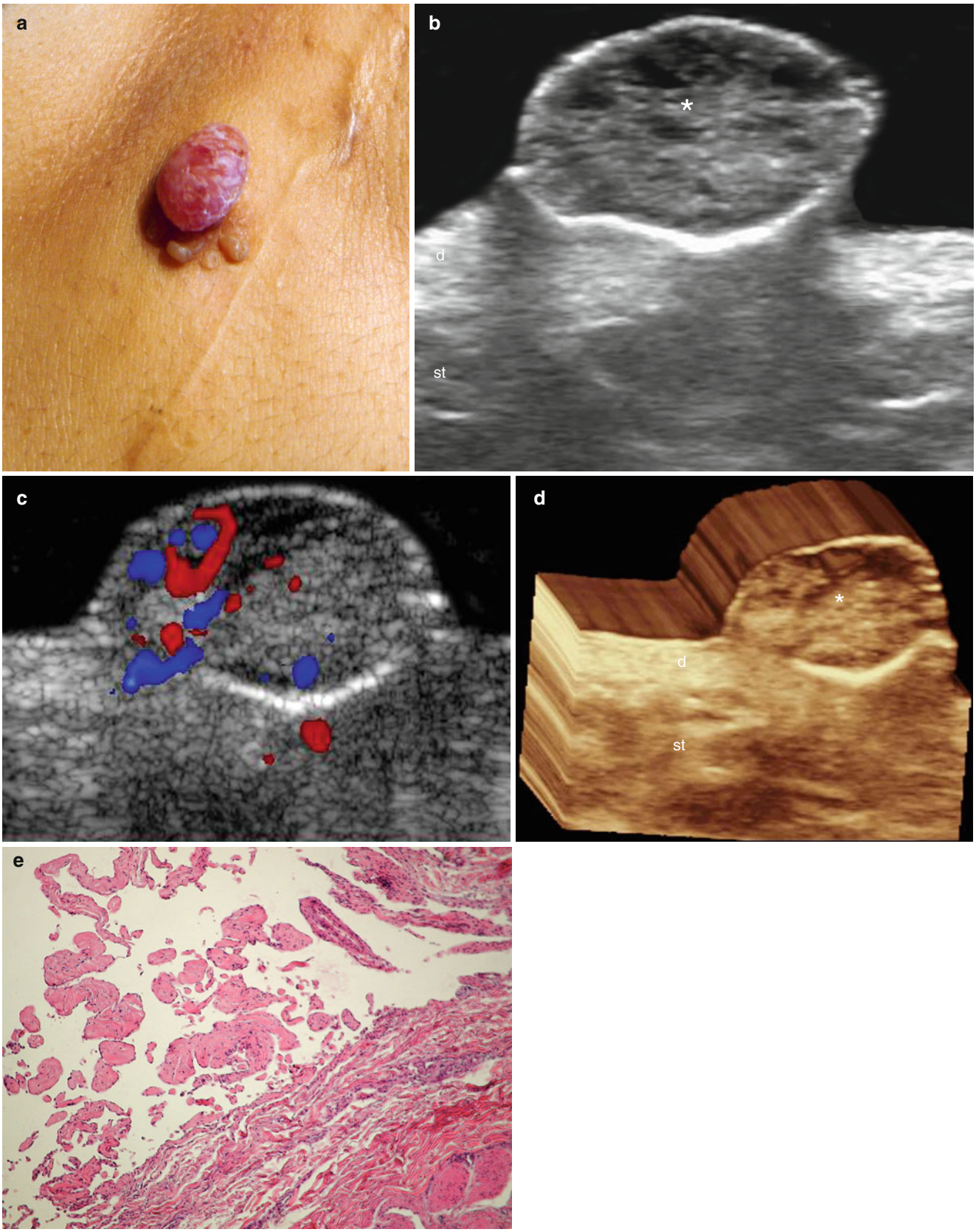

Fig. 8.8 (**a**–**e**) Recurrent lymphangioma circumscriptum. (**a**) Clinical image shows erythematous and translucent cutaneous lumps and papules that recurred 2 years after surgery. (**b**) Grey scale ultrasound (transverse view in the large nodule) shows a well-defined mixed echogenicity oval-shaped nodule with anechoic and hypoechoic areas that emerges from the dermis and protrudes into the epidermal region. (**c**) Color Doppler (transverse view) demonstrates increased vascularity in part of the lesion (mostly *left* border of the image) and hypovascularity in the remaining areas. (**d**) The lesion in 3D (5–8 s sweep). (**e**) Histology (HE 100 × zoom): vascular spaces without content and covered by a monolayer of flat endothelial cells. *Abbreviations: d* dermis, *st* subcutaneous tissue

On sonography, there are ill-defined areas with round or oval-shaped hypoechoic nodules and some anechoic pseudocystic structures that usually involve the subcutaneous tissue with additional increased echogenicity of the vicinity. On color Doppler imaging, these areas are mostly hypovascular or show slow flow vessels (Fig. 8.9).

8.2.2 Malignant

8.2.2.1 Cutaneous Angiosarcoma

Cutaneous angiosarcoma are rare soft-tissue sarcomas of the endothelial cells most commonly affecting the head and neck and particularly the scalp, but can also involve other corporal regions such as the limbs. A subset of patients presents with multifocal disease and/or positive regional nodes,

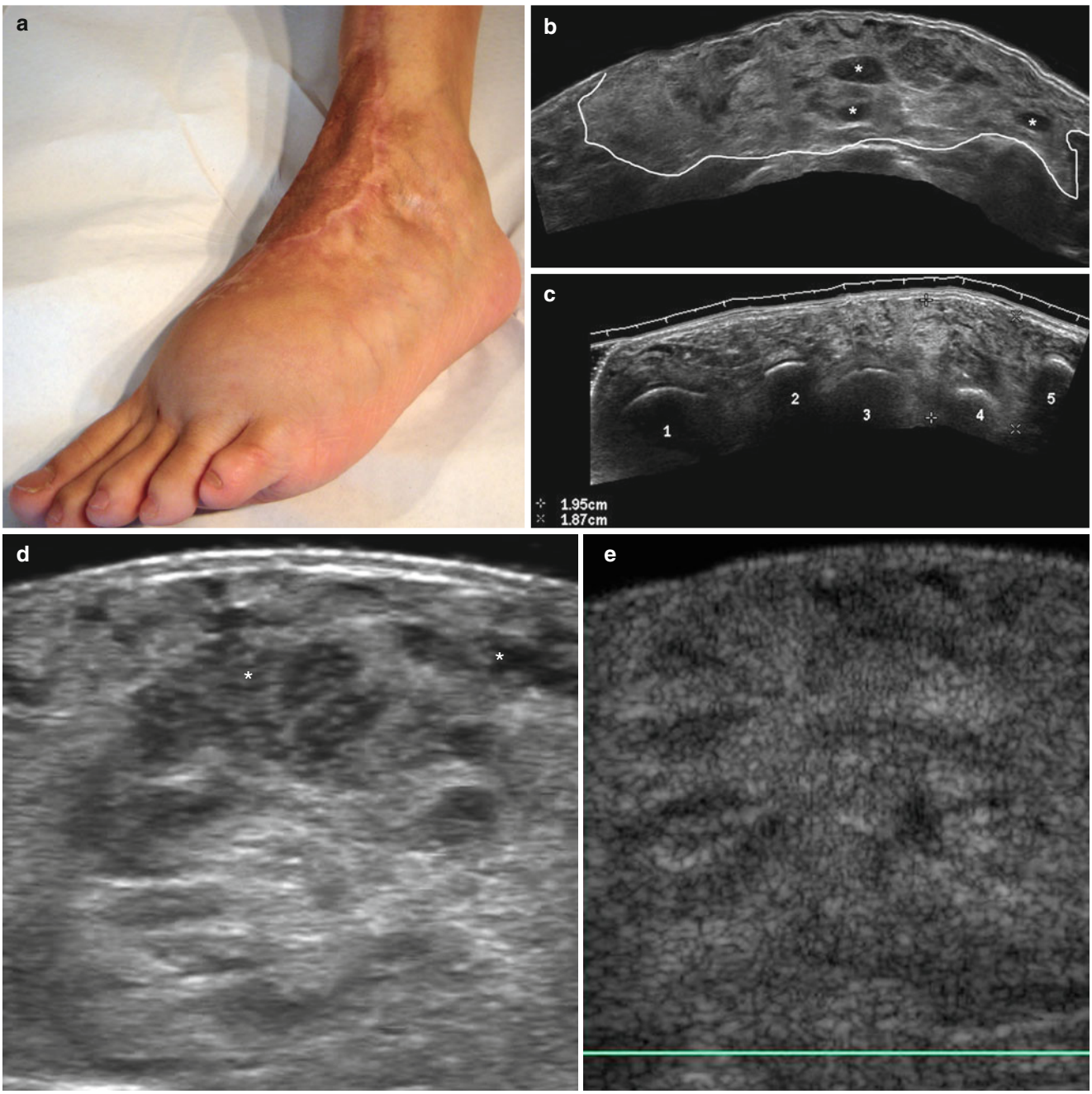

Fig. 8.9 (**a**–**g**) Recurrent angiomyxoma. (**a**) Clinical image shows swelling in the dorsum of the left foot. The patient was operated on 1 year previously (scar) and the biopsy was positive for angiomyxoma. (**b**–**d**) Grey scale ultrasound (transverse axis; b, ankle level; c, foot-metatarsal level (numbers); d, zoom dorsum of the foot level) demonstrates ill-defined heterogeneous structure with some oval-shaped hypoechoic areas (*) that mostly involve the subcutaneous tissue. (**e**) Color Doppler ultrasound (transverse view, dorsum of the foot) shows lack of detectable vascularity within the lesional area. (**f**) The lesion in 3D (5–8 s sweep). (**g**) Histology (HE × 100 zoom): proliferation of capillary vessels within a myxoid stroma

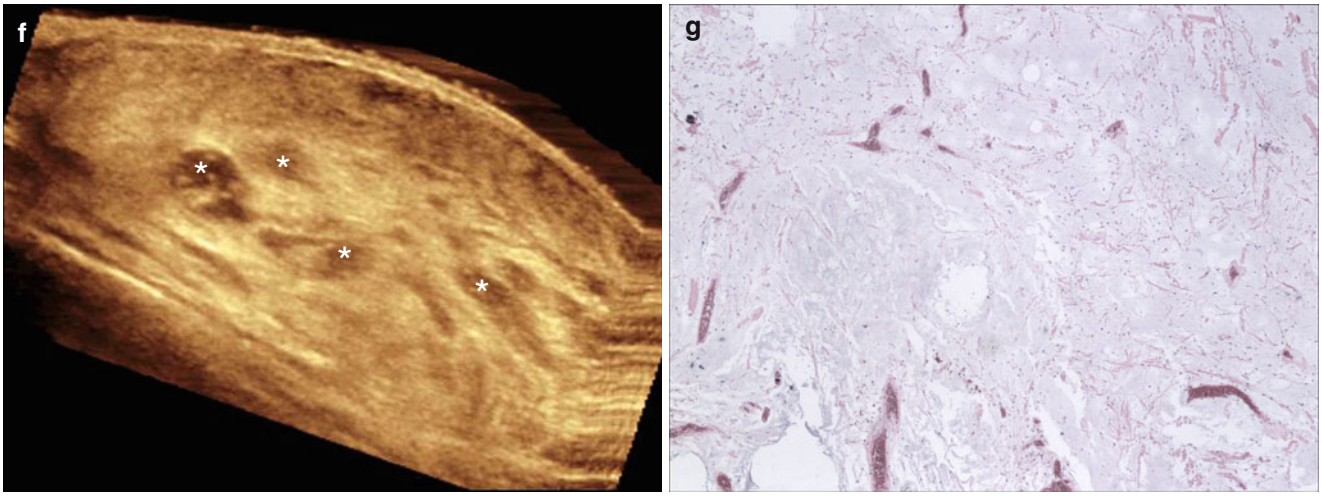

Fig. 8.9 (continued)

and the probability of metastasis is relatively high [21]. This condition is thought to be a collection of hemangiosarcoma, lymphangiosarcoma, tumors that cannot be classified as being of vascular and lymphatic origin, or mixed tumor of both. Thus, based on immunohistochemistry, cutaneous angiosarcoma can be divided into vascular, mixed, and lymphatic types [22].

Clinically, lesions show as rapidly growing, erythematous or purple, bruise-like swellings, sometimes with ulceration. Histology shows extensive infiltration with pleomorphic, multilayered endothelial cells that show a high rate of mitosis, embedded in a collagen matrix [21].

On sonography, cutaneous angiosarcomas present as hypoechoic and sometimes lobulated solid masses that affect the cutaneous layers and commonly deeper structures. Hyperechoic fibrous septa can be detected within the mass and on color Doppler imaging, increased vascularity, with asymmetric and irregular disposition of the vessels is usually found within the lesion (Fig. 8.10)

8.2.2.2 Kaposi's Sarcoma

Kaposi's sarcoma (KS) is a malignancy of endothelial skin cells with multifocal localization on the skin, lymph nodes, and visceral organs. KS comprises four clinical variants:

(a) Classic KS, also called Mediterranean KS that affects middle-aged men of Mediterranean and Jewish descent,
(b) Iatrogenic KS, in iatrogenically immunosuppressed patients (e.g., post transplant),
(c) African endemic KS,
(d) AIDS-related, also called epidemic AIDS-KS.

All variants are associated with human herpesvirus-8 (HHV-8), and they display very similar histopathological features, with the proliferation of spindle cells (considered as the KS tumor cells) associated with inflammation and neoangiogenesis.

Clinically, KS is characterized by violaceous and/or reddish macules and papules, which over the course of months or years tend to merge into plaques and nodules (in some cases ulcerated), commonly associated with edema, particularly evident in the lower limbs. However, definitive diagnosis is based on histopathological evidence of spindle cell and the presence of HHV-8 latency associated nuclear antigen, in spindle cells, and vascular or lymphatic endothelial cells.

The clinical progression of classic KS is generally slow and not very aggressive, although cases with rapidly growing lesions and with signs of local invasiveness, can be observed as well as forms that fail to respond to physical or systemic treatment. By contrast, the natural history of AIDS-KS, which can affect mucous membranes, lymph nodes, the gastrointestinal tract, and the lungs, is more aggressive, particularly in untreated HIV-infected individuals.

Preliminary results have suggested that small cutaneous KS lesions–in both classic KS and AIDS-KS patients–display similar B-mode ultrasound patterns conformed by hypoechoic and/or heterogeneous lesions, localized in the epidermis and dermis and sometimes affecting the subcutaneous tissue. On color Doppler imaging, vascularity is variable although lesional blood flow has been reported to be more prominent in cases with AIDS-KS [23–26] (Fig. 8.11).

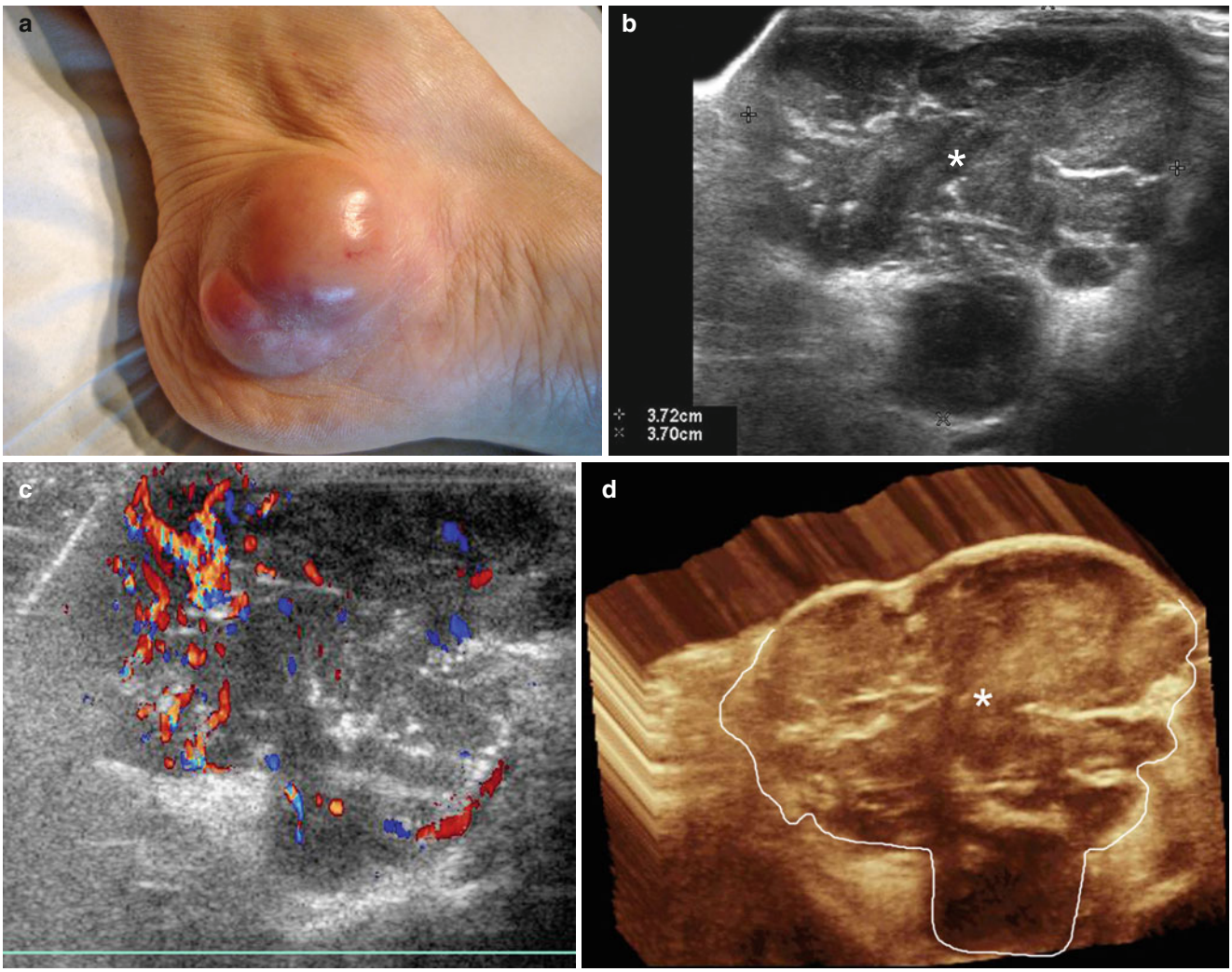

Fig. 8.10 (**a**–**d**) Cutaneous angiosarcoma. (**a**) Clinical image shows erythematous lump in the inner aspect of the left foot. (**b**) Grey scale ultrasound (transverse view) demonstrates 3.72×3.70 cm lobulated, hypoechoic and solid mass (*) that involves the subcutaneous tissue and also affects the dermis. (**c**) Color Doppler ultrasound (transverse view) shows irregular and asymmetric hypervascularity within the mass. (**d**) The tumor in 3D (*, and outlined, 5–8 s sweep)

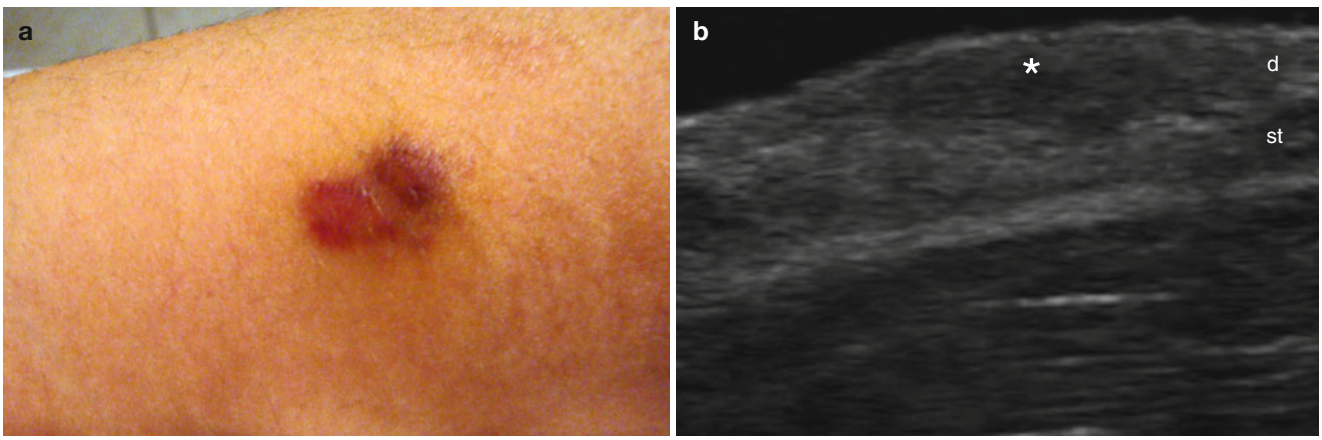

Fig. 8.11 (**a**–**f**) Kaposi's sarcoma. (**a**) Clinical reddish lesion in the inner aspect of the left arm (HIV positive patient). (**b**) Grey scale ultrasound (longitudinal view) shows ill-defined, focal hypoechogenic thickening (*) that involves the dermis and upper subcutaneous tissue. There is increased echogenicity of the lower subcutaneous tissue. (**c**) Power angio (longitudinal view) demonstrates increased blood flow within the lesion (*). (**d**) 3D reconstruction of the lesion (*, transverse axis). (**e**) 3D power angio reconstruction of the lesional area (5–8 s sweep). (**f**) Histology (HE 40 × zoom) shows a dermal vascular proliferation. *Abbreviations*: *e* epidermis, *d* dermis, *st* subcutaneous tissue, *m* muscle

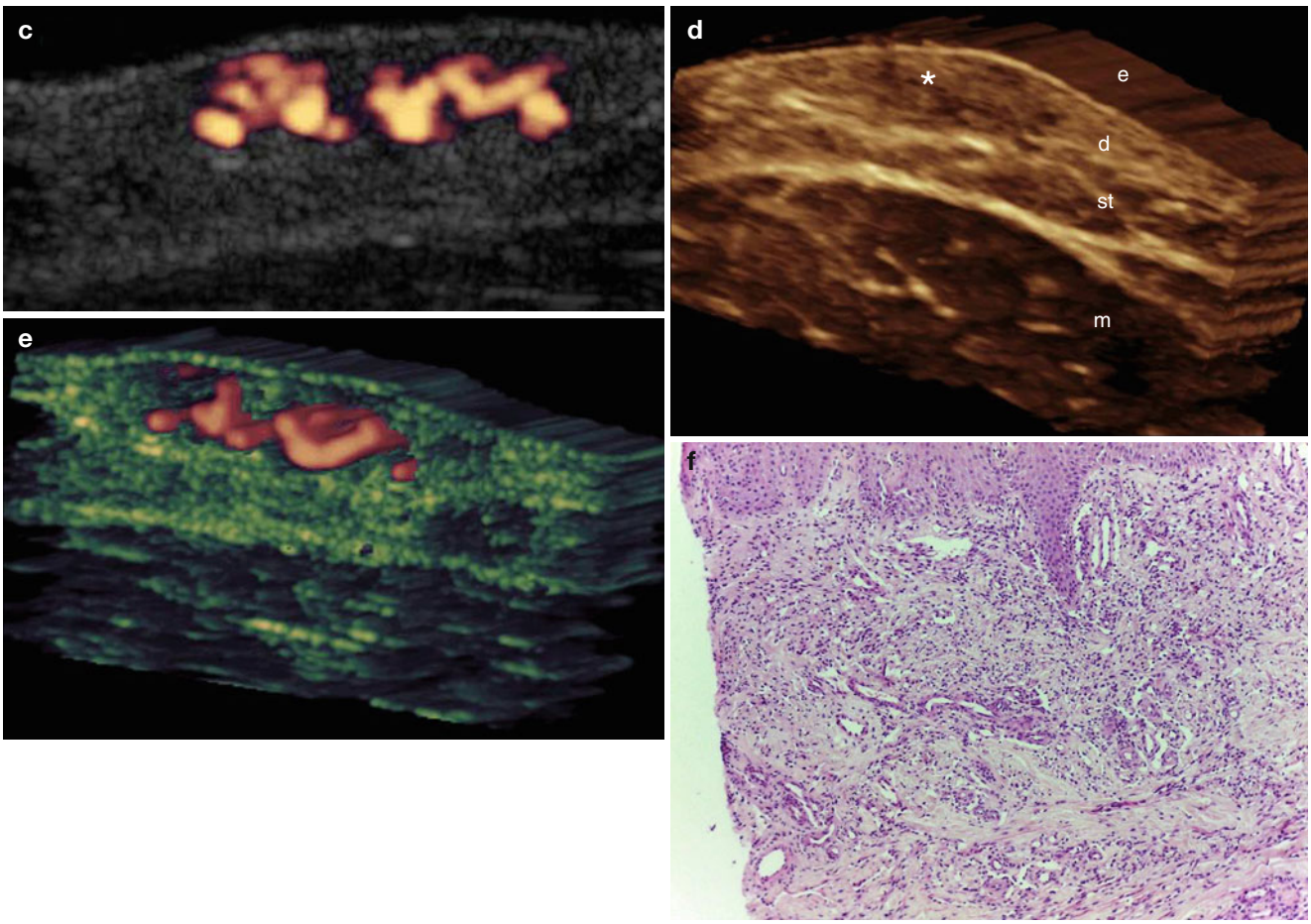

Fig. 8.11 (continued)

References

1. Schiller PI, Itin PH. Angiokeratomas: an update. Dermatology. 1996;193:275–82.
2. Clairwood MQ, Bruckner AL, Dadras SS. Verrucous hemangioma: a report of two cases and review of the literature. J Cutan Pathol. 2011;38:740–6. doi:10.1111/j.1600-0560.2011.01733.x.
3. Fernández Y, Bernabeu-Wittel M, García-Morillo JS. Kaposiform hemangioendothelioma. European Journal of Internal Medicine. 2009;20:106–13.
4. Vin-Christian K, McCalmont TH, Frieden IJ. Kaposiform hemangioendothelioma. An aggressive, locally invasive vascular tumor that can mimic hemangioma of infancy. Arch Dermatol. 1997;133:1573–8.
5. Lyons LL, North PE, Mac-Moune Lai F, Stoler MH, Folpe AL, Weiss SW. Kaposiform hemangioendothelioma: a study of 33 cases emphasizing its pathologic, immunophenotypic, and biologic uniqueness from juvenile hemangioma. Am J Surg Pathol. 2004;28:559–68.
6. Paliogiannis P, Trignano E, Trignano M. Surgical management of the glomus tumors of the fingers: a single center experience. Ann Ital Chir. 2011;82:465–8.
7. Wortsman X, Wortsman J, Soto R, Saavedra T, Honeyman J, Sazunic I, et al. Benign tumors and pseudotumors of the nail: a novel application of sonography. Journal of Ultrasound in Medicine. 2010;29:803–16.
8. Wortsman X, Jemec GBE. Role of high variable frequency ultrasound in preoperative diagnosis of glomus tumors: a pilot study. Am J Clin Dermatol. 2009;10:23–7.
9. Park HJ, Jeon YH, Kim SS, Lee SM, Kim WT, Park NH, et al. Gray-scale and color Doppler sonographic appearances of nonsubungual soft-tissue glomus tumors. Journal of Clinical Ultrasound. 2011;39:305–9.
10. Leger M, Patel U, Mandal R. Glomangioma. Dermatol On Line J. 2010;16(11):11. http://dermatology-s10.cdlib.org/1611/articles/11_2010-04-20/leger.html
11. McEvoy BF et al. Multiple hamartomatous glomus tumors of the skin. Arch Dermatol. 1971;104:188.
12. Aranibar L, Rivera L, Kutz AM, Wortsman X, Henriquez A. Lineal glomuvenous malformation. Rev Chil Dermatol. 2011;27:82–6.
13. Lin RL, Janniger CK. Pyogenic granuloma. Cutis. 2004;74:229–33.
14. Gonçales ES, Damante JH, Fischer Rubira CM, Taveira LA. Pyogenic granuloma on the upper lip: an unusual location. Journal of Applied Oral Science. 2010;18:538–41.
15. Al-Muharraqi MA, Faqi MK, Uddin F, Ladak K, Darwish A. Angiolymphoid hyperplasia with eosinophilia (epithelioid hemangioma) of the face: an unusual presentation. Int J Surg Case Rep. 2011;2:258–60.
16. Patel GA, Schwartz RA. Cutaneous lymphangioma circumscriptum: frog spawn on the skin. Int J Dermatol. 2009;48:1290–5.
17. Heller M, Mengden S. Lymphangioma circumscriptum. Dermatology Online Journal. 2008;15:14–27.

18. Young RJ, Brown NJ, Reed MW, Hughes D, Woll PJ. Angiosarcoma. The Lancet Oncology. 2010;11:983–91.
19. Wilk M, Schmoeckel C, Kaiser HW, Hepple R, Kreysel HW. Cutaneous angiomyxoma: a benign neoplasm distinct from cutaneous focal mucinosis. J Am Acad Dermatol. 1995;33: 352–5.
20. Calonje E, Guerin D, McCormick D, Fletcher CD. Superficial angiomyxoma: clinicopathologic analysis of a series of distinctive but poorly recognized cutaneous tumors with tendency for recurrence. Am J Surg Pathol. 1999;23:910–7.
21. Mendenhall WM, Mendenhall CM, Werning JW, Reith JD, Mendenhall NP. Cutaneous angiosarcoma. Am J Clin Oncol. 2006;29:524–8.
22. Kamo R, Ishii M. Histological differentiation, histogenesis and prognosis of cutaneous angiosarcoma. Osaka City Medical Journal. 2011;57:31–44.
23. Solivetti FM, Elia F, Latini A, Cota C, Cordiali-Fei P, Di Carlo A. AIDS-kaposi sarcoma and classic kaposi sarcoma: are different ultrasound patterns related to different variants? J Exp Clin Cancer Res. 2011;13:30–40.
24. Tornesello ML, Biryahwaho B, Downing R, Hatzakis A, Alessi E, Cusini M, et al. Human herpesvirus type 8 variants circulating in Europe, Africa and North America in classic, endemic and epidemic Kaposi's sarcoma lesions during pre-AIDS and AIDS era. Virology. 2010;398:280–9.
25. Gessain A, Duprez R. Spindle cells and their role in Kaposi's sarcoma. Int J Biochem Cell Biol. 2005;37:2457–65.
26. Sullivan RJ, Pantanowitz L, Casper C, Stebbing J, Dezube BJ. Epidemiology, pathophysiology and treatment of Kaposi sarcoma-associated herpesvirus disease: Kaposi sarcoma, primary effusion lymphoma, and multicentric Castleman disease. Clin Infect Dis. 2008;47:1209–15.

Skin Cancer: The Primary Tumors

9

Ximena Wortsman, Laura Carreño, and Claudia Morales

How to deal and what to look for in the primary lesion

Contents

9.1 Introduction

Skin cancer is the most common form of cancer in human beings, therefore a frequent cause of dermatological consultation. Cutaneous cancer can be categorized into two main types: non-melanoma skin cancer (NMSC) and melanoma. NMSC constitutes up to 95 % of skin malignancies, and melanoma up to 5 %. The most frequent forms of presentations of NMSC are basal cell carcinoma (BCC) and squamous cell carcinoma (SCC) [1].

Less common skin malignancies are dermatofibrosarcoma protuberans, angiosarcoma, Merkel's cell carcinoma, Kaposi's sarcoma, and cutaneous lymphomas.

The goal of this chapter is to review the sonographic patterns of the most common forms of skin cancer and the role of sonography in the evaluation of these entities.

9.2 Non-Melanoma Skin Cancer

NMSC (BCC and SCC) is most frequent on areas exposed to the sun, and can be associated with functional and cosmetic problems that can complicate the evolution and prognosis in highly exposed areas of the body. Thus, NMSC presents frequently in facial locations that include the skin of the eyelids, nose, lips, and ears where the cutaneous layers are thin and involvement of cartilage and orbicular muscles may easily occur. Recurrences and multiple locations are not uncommon and can make the management of patients even more difficult. Incomplete excision of primary NMSC lesions has been reported in up to 45.5 % of cases [2].

X. Wortsman, MD (✉)
Department of Radiology and Dermatology,
Institute for Diagnostic Imaging and
Research of the Skin and Soft Tissues,
Clinica Servet, University of Chile, Faculty of Medicine,
Almirante Pastene 150, Providencia, Santiago, Chile
e-mail: xwo@tie.cl, xworts@yahoo.com, www.sonoskin.com

L. Carreño, MD • C. Morales, MD
Department of Pathology, Dermopathology Section,
Hospital Clinico Universidad de Chile, Faculty of Medicine,
University of Chile, Santiago, Chile
e-mail: lcarrenotoro@gmail.com; claudiamohuber@gmail.com

X. Wortsman, G.B.E. Jemec (eds.), *Dermatologic Ultrasound with Clinical and Histologic Correlations*,
DOI 10.1007/978-1-4614-7184-4_9,

9.2.1 Basal Cell Carcinoma

BCC, also called epithelioma, is the most frequent form of cancer among human beings and composes 75–95 % of all skin cancers. It is rarely fatal but could be highly disfiguring [1–3]. Clinically, BCC appears as a slow-growing, painless, erythematous, pearly papule or nodule that usually easily bleeds after minor trauma or may ulcerate (rodent ulcer). These tumors can also mimic a scar on physical examination.

Greater than 70 % of BCC tumors are located on the face, and the most frequent locations are the nose and eyelids [2, 3]. This type of skin cancer rarely metastasizes, although in areas where the skin is thin, there is a significant risk of involvement of deeper layers such as muscle, cartilage, or bone.

BCCs can be separated into several subtypes: superficial or in situ multifocal (15–35 %); diffuse or infiltrative that include morpheaform and micronodular subtypes (4–17 %); nodular, that also include nodulocystic, adenoid, and ulcerative subtypes (45–60 %); and pigmented (1–7 %). There are also other less common histological variants of BCC such as pleomorphic, clear cell, signet ring, granular, infundibulocystic, metaplastic, and keloidal subtypes, among others. Additionally, the different categories can be mixed within the same lesion or the patient may present multiple lesions with more than one subtype. Histologically, BCC is composed of a fibrous stroma and islands of basaloid cells that are dependent cells similar to the basal cells of the epidermis and hair follicles. The cells show indistinct cytoplasmic borders and oval basophilic vesicular nuclei. The nodulocystic subtype shows cysts with abundant mucin and the adenoid variant presents a pseudoglandular appearance. The morpheaform subtype shows narrow epithelial strands compressed by dense fibrous stroma and hyalinization [4] (Figs. 9.1, 9.2, 9.3, 9.4, 9.5, 9.6, and 9.7).

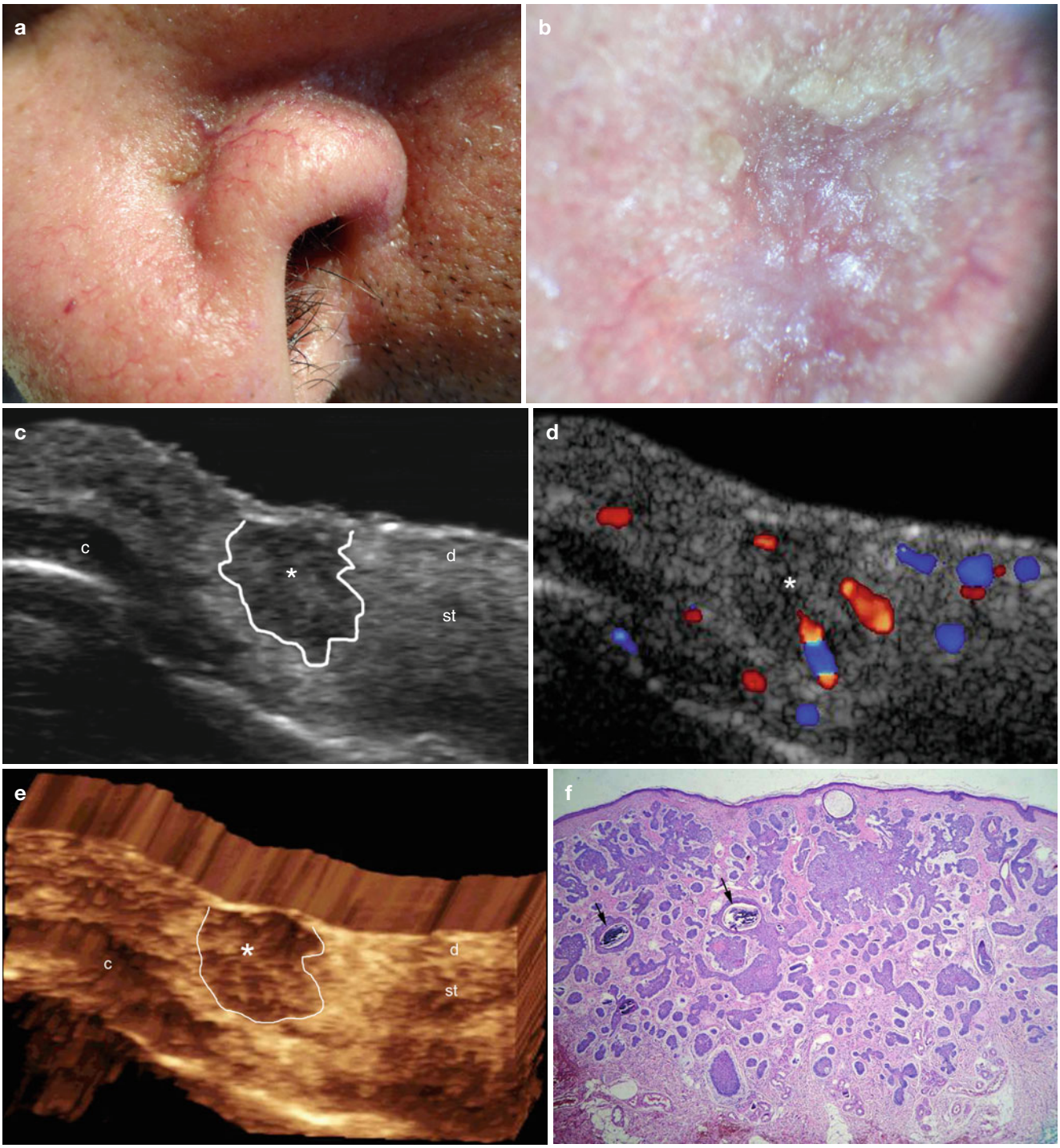

Fig. 9.1 (**a**–**f**) Basal cell carcinoma. (**a**, **b**) Clinical images (**a** photograph and **b** dermoscopy) of a pearly and erythematous lesion in the left nasal wing. (**c**) Grey scale ultrasound image (transverse view) shows well-defined hypoechoic structure (*, outlined) with irregular borders located in the dermis and subcutaneous tissue. The left nasal cartilage is unremarkable. (**d**) Color Doppler ultrasound image (transverse view) demonstrates increased blood flow in the lesional area. (**e**) The lesion shown in 3D (5–8 s sweep, transverse view). (**f**) Histology (HE × 40 zoom) shows small and large nests of basaloid cells suggestive of macro- and micronodular basal cell carcinoma. Calcium deposits (*arrows*) are also detected. *Abbreviations*: *d* dermis, *st* subcutaneous tissue, *c* nasal cartilage

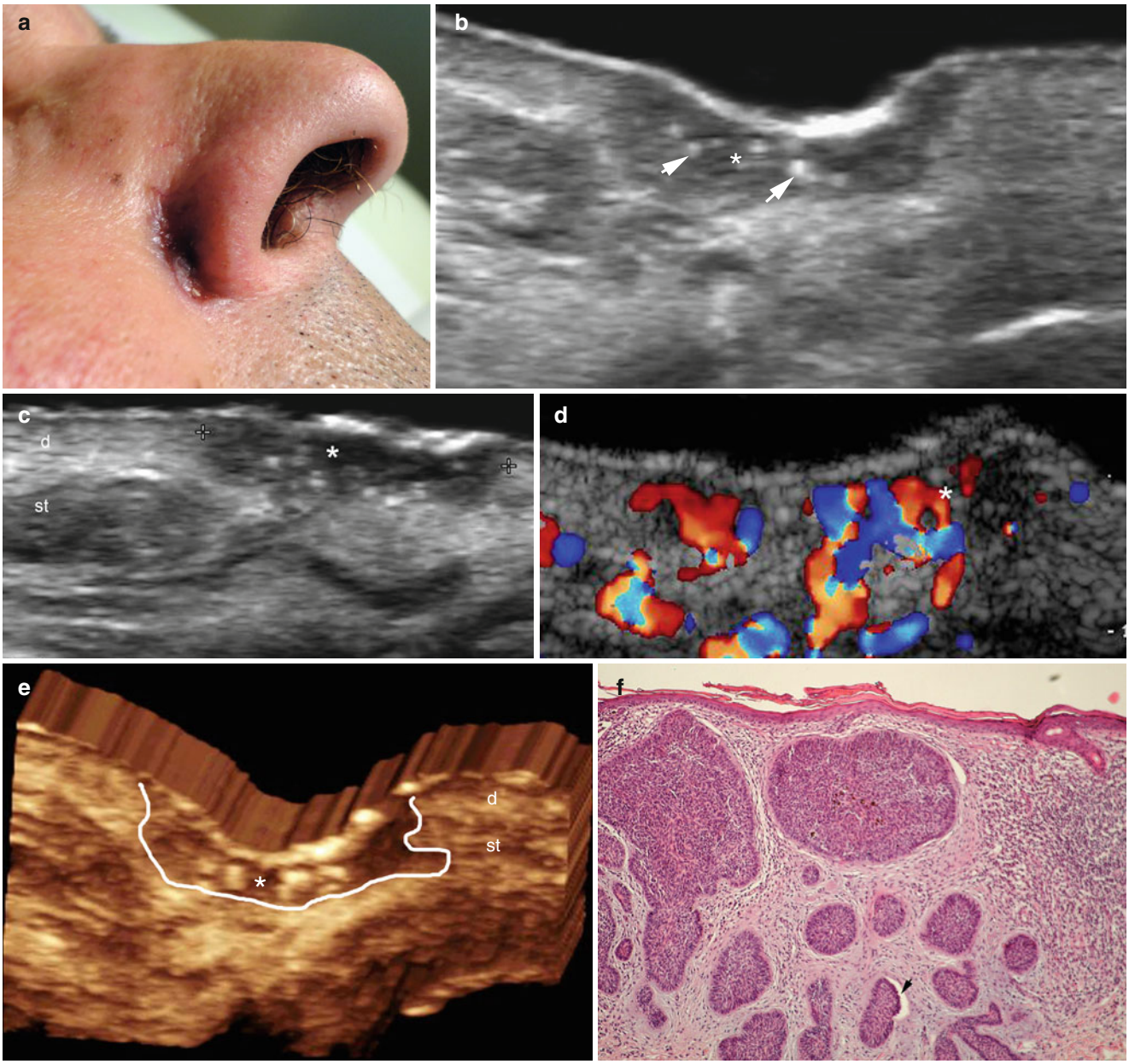

Fig. 9.2 (**a**–**f**) Basal cell carcinoma. (**a**) Clinical photograph shows a reddish swelling in the right nasofold line. (**b**, **c**) Grey scale ultrasound images (**b** transverse and **c** longitudinal views) demonstrate a well-defined oval-shaped hypoechoic lesion (*) located in the dermis and upper subcutaneous tissue. Notice the hyperechoic spots (*arrows*) within the structure. The right nasal cartilage is unremarkable. (**d**) Color Doppler ultrasound image (longitudinal view) shows increased blood flow within the lesion. (**e**) 3D reconstruction of the tumor (*, outlined; 5–8 s sweep, transverse view). (**f**) Histology (HE 100 × zoom): Macro- and micronodular infiltrate of basaloid cells with a palisade arrangement. A cleft is noted surrounding a cell nest. Fibrous stroma and inflammatory cells are also detected. *Abbreviations*: *d*, dermis; *st*, subcutaneous tissue

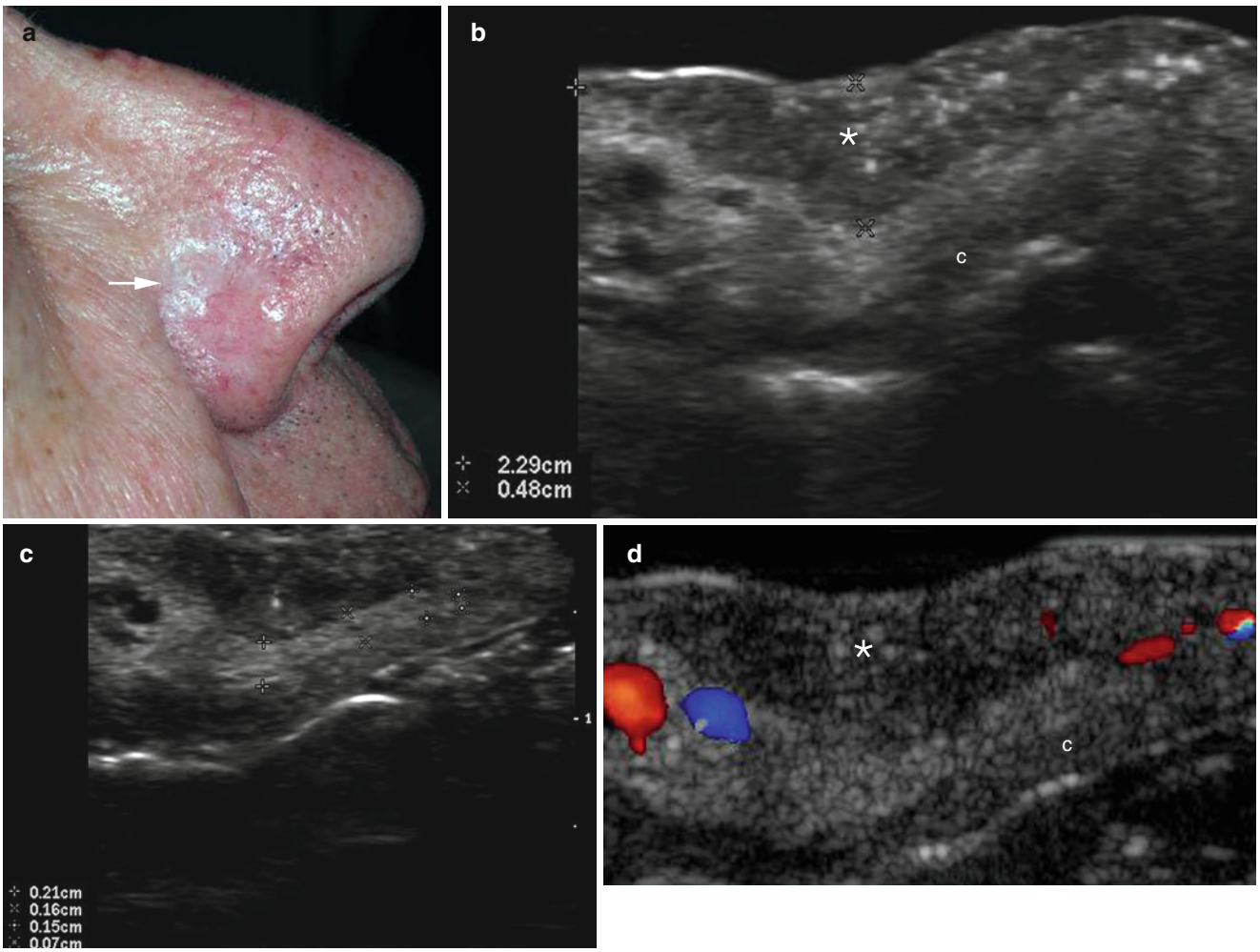

Fig. 9.3 (**a**–**g**) Morpheaform basal cell carcinoma. (**a**) Clinical image shows a pearly and erythematous nodule (*arrow*) in the right nasal wing. (**b**, **c**) Grey scale ultrasound images (transverse views; **b** superficial and **c** deep focus) demonstrate a 2.29 × 0.48 cm well-defined fusiform hypoechoic lesion located in the dermis and upper subcutaneous tissue. Notice the multiple hyperechoic spots within the lesion and the tapering of the distance (0.21–0.07 cm going from the posterior to anterior aspect) between the tumor and the right nasal cartilage (**c**). The right nasal cartilage is unremarkable. (**d**) Grey scale ultrasound image demonstrates a small vessel within the lesion (*). (**e**) The surgical defect (Mohs's surgery). (**f**) The lesion after surgical reconstruction. (**g**) Histology (HE × 100 zoom): cords and angular nests of atypical basaloid cells (*arrows*). (Figs. **a**, **e**, and **f** are courtesy of Dr. Daniela Saavedra) *Abbreviations*: *d* dermis, *st* subcutaneous tissue, *c* nasal cartilage.

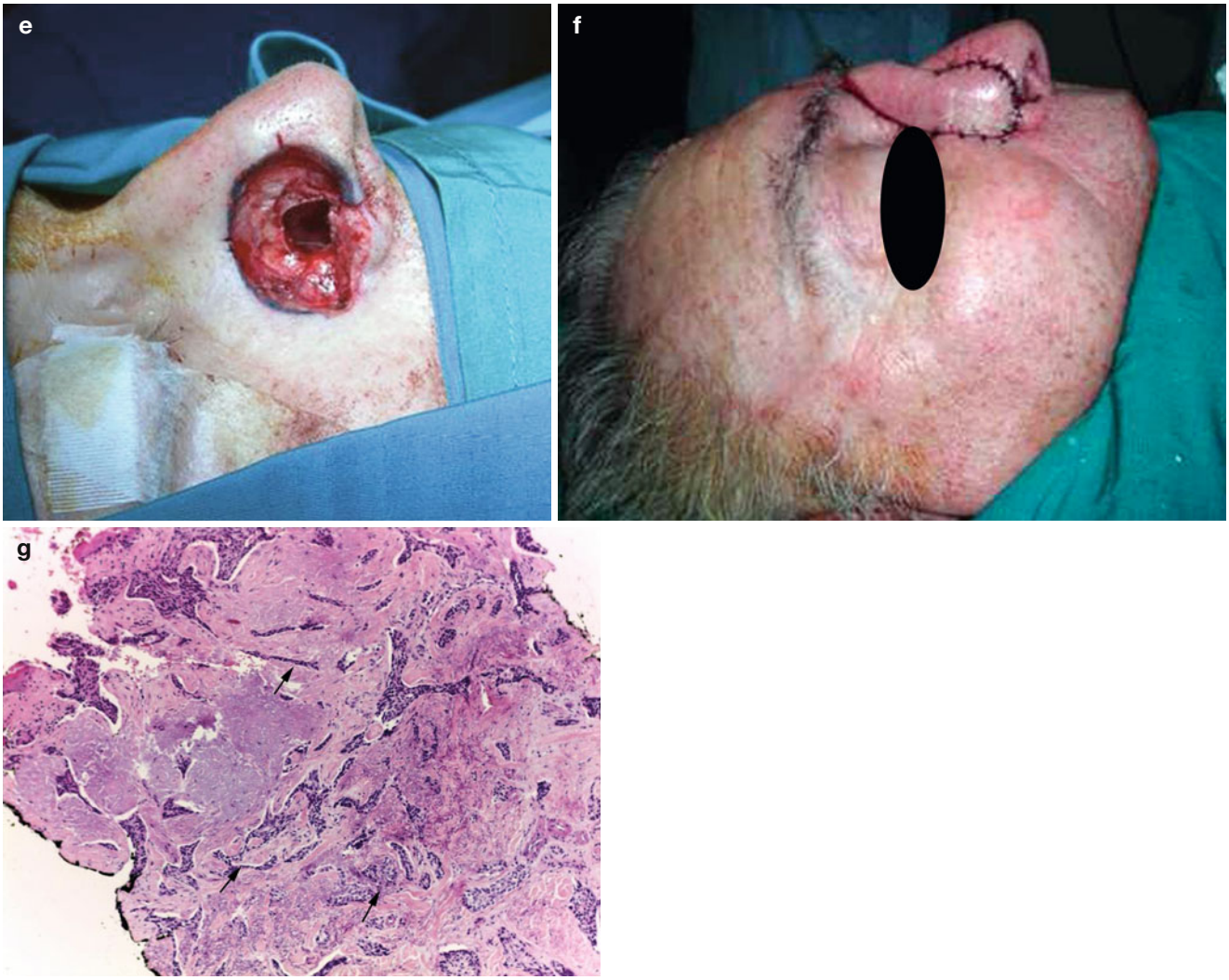

Fig. 9.3 (continued)

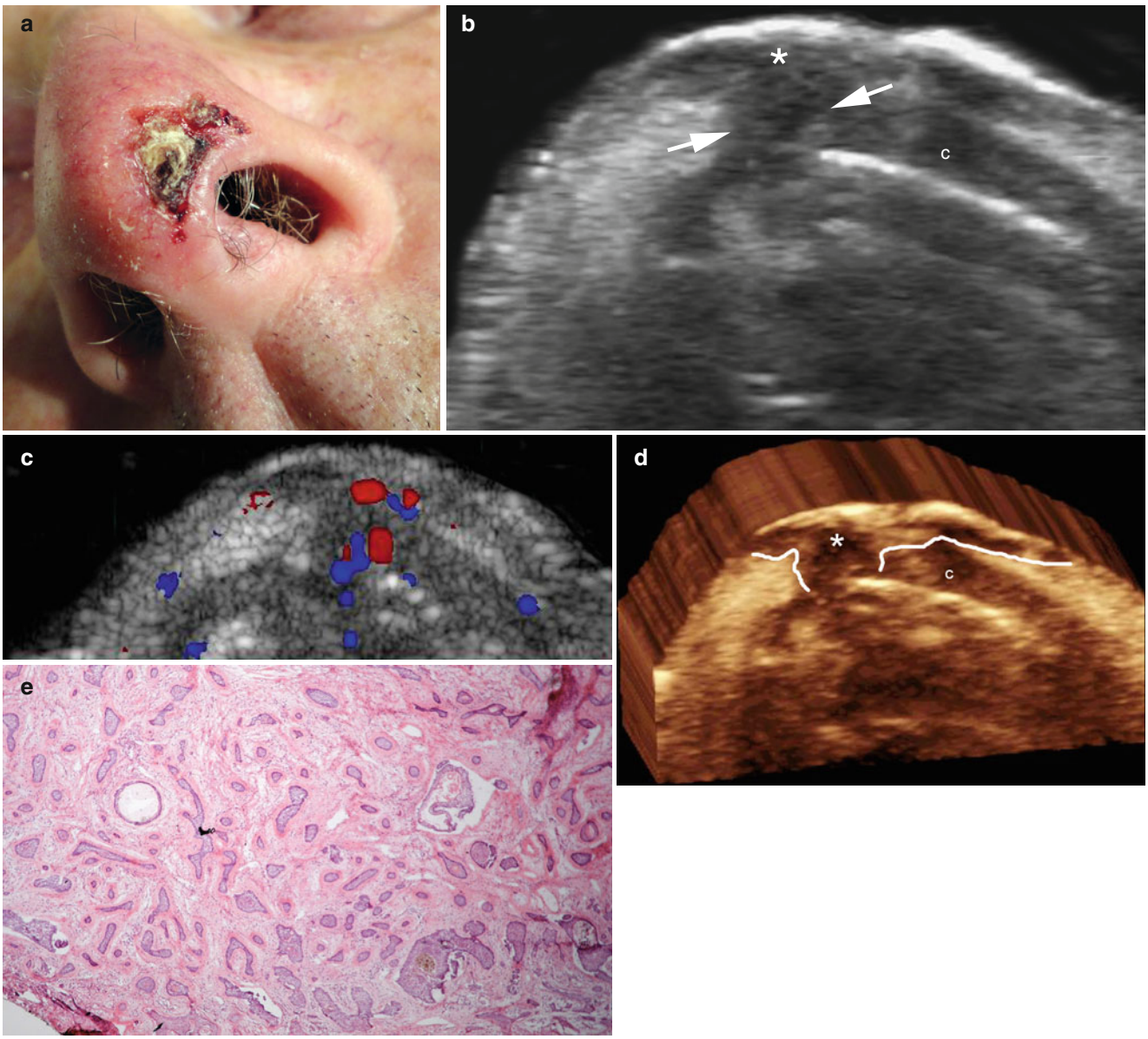

Fig. 9.4 (**a**–**e**) Basal cell carcinoma with involvement of the nasal cartilage. (**a**) Clinical photograph shows ulcerated erythematous lesion in the left nasal wing. (**b**) Grey scale ultrasound image (transverse view) demonstrates hypoechoic solid lesion (*) that involves the anterior aspect (*arrows*) of the left nasal cartilage. (**c**) Color Doppler ultrasound image (transverse view) shows increased vascularity in the lesional area including the nasal cartilage. (**d**) 3D view of the tumor (*, transverse view, outlined, 5–8 s sweep). (**e**) Histology (HE ×40 zoom): dermis with nests of atypical basaloid cells of variable sizes and shape. The small size nests predominate within the tumor that is surrounded by a fibrous stroma. *Abbreviations*: *d* dermis, *st* subcutaneous tissue, *c* cartilage

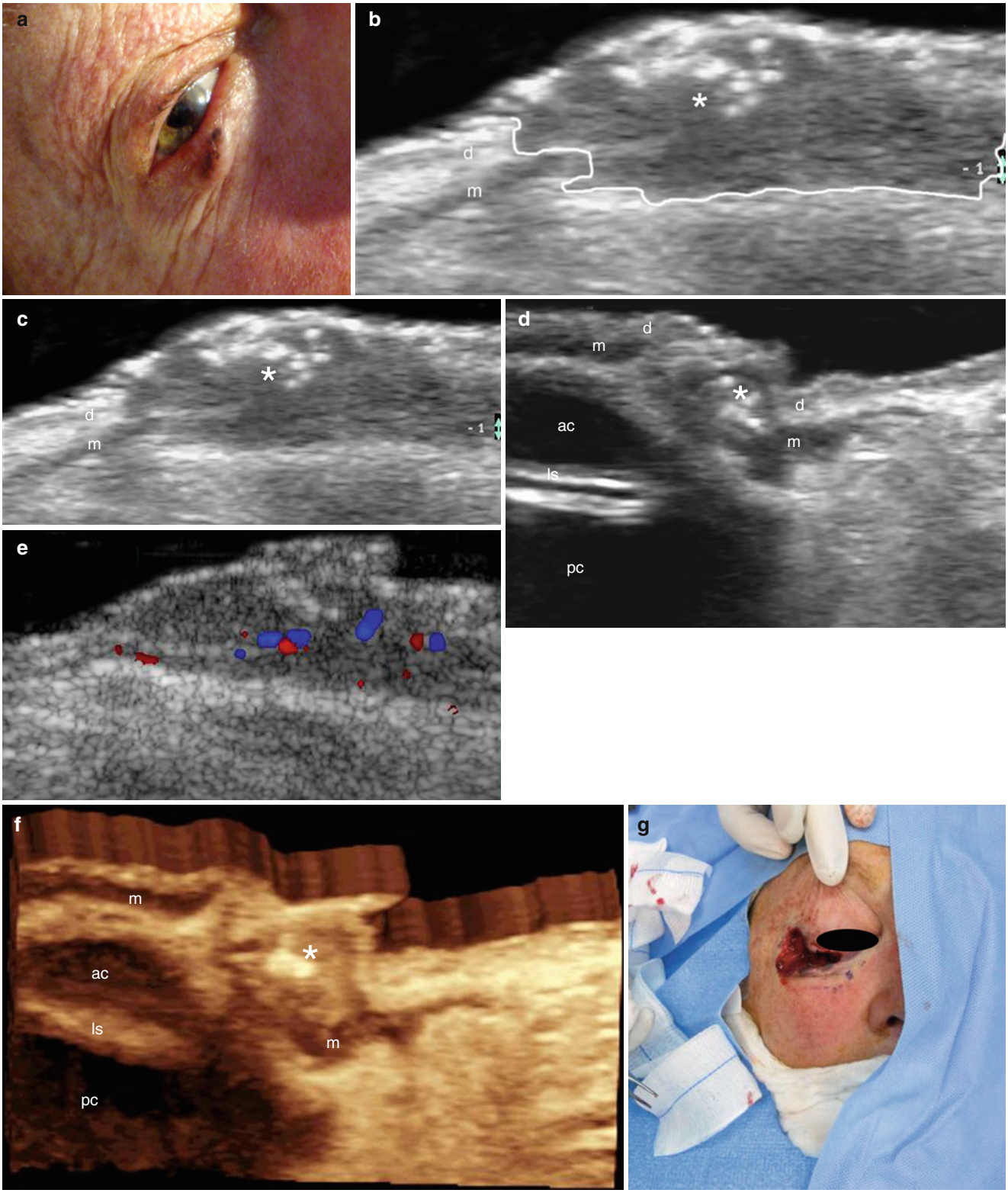

Fig. 9.5 (**a**–**g**) Basal cell carcinoma with involvement of the orbicular muscle of the lower eyelid. (**a**) Clinical photograph shows a pigmented and erythematous lump in the right lower eyelid. (**b**–**d**).Grey scale ultrasound images (**b** and **c** transverse views; **d** longitudinal view) demonstrated ill-defined hypoechoic lesion (*) that involves the dermis and the underlying orbicularis muscle. The tumor presents irregular borders that are outlined in figure (**b**). Notice the hyperechoic spots within the tumor. (**e**) Color Doppler ultrasound image (transverse view) shows increased vascularity within the lesional area. (**f**) 3D reconstruction of the tumor (longitudinal view; 5–8 s sweep). (**g**) The surgical excision of the tumor (Mohs's surgery). Images **a** and **g** are courtesy of Dr. Daniela Saavedra. *Abbreviations*: *d* dermis, *m* orbicularis muscle of the eyelid, *ac* anterior chamber of the ocular globe, *pc* posterior chamber of the ocular globe, *l* lens

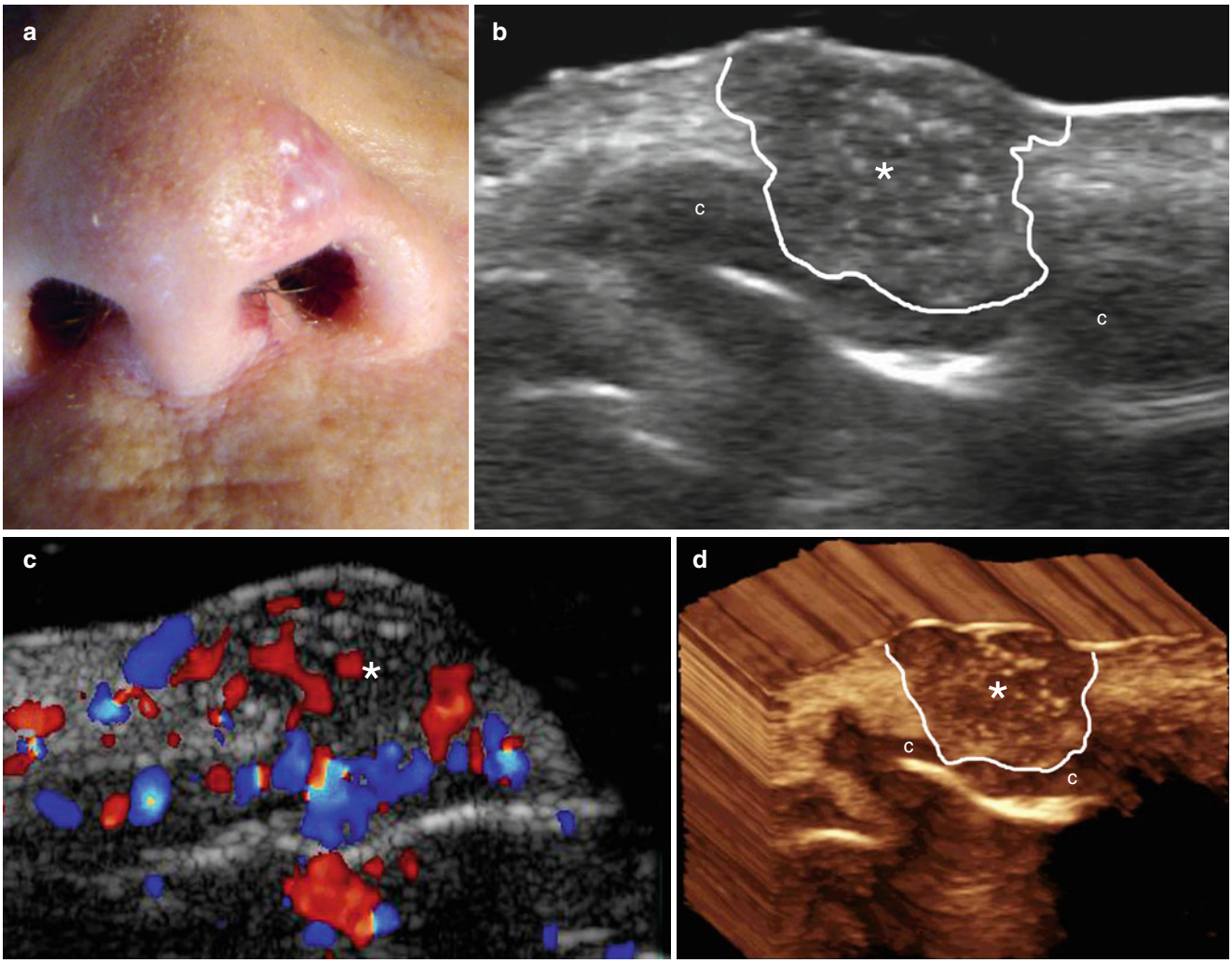

Fig. 9.6 (**a**–**d**) Basal cell carcinoma with involvement of the left nasal cartilage. (**a**) Clinical photograph shows pearly erythematous swelling in the left nasal wing. (**b**) Grey scale ultrasound image (transverse view) demonstrates well-defined hypoechoic solid lesion (*) with irregular borders (outlined) that involves the skin layers and the underlying nasal cartilage. Notice the hyperechoic spots within the tumor. (**c**) Color Doppler ultrasound image (longitudinal view) shows increased vascularity in the lesional area (*). (**d**) 3D reconstruction of the tumor (*, outlined). *Abbreviation*: *c* nasal cartilage

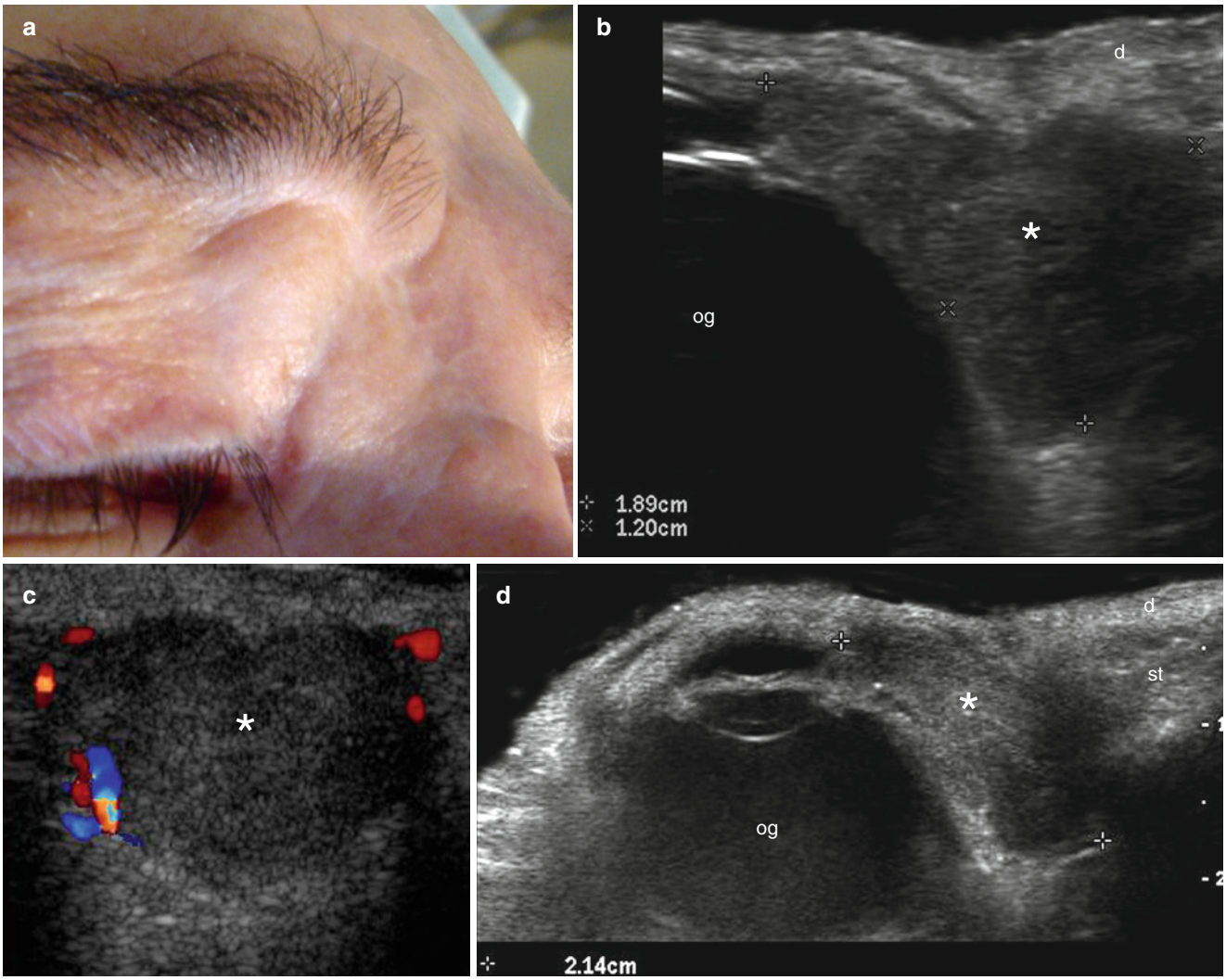

Fig. 9.7 (**a**–**d**) Recurrent basal cell carcinoma. (**a**) Clinical photograph shows skin-colored swelling in the medial aspect of the right upper eyelid. (**b**) Grey scale ultrasound image (transverse view) demonstrates 1.89 × 1.20 cm well-defined hypoechoic mass (*) that affects the subcutaneous tissue and extends into the medial aspect of the orbit. (**c**) Color Doppler ultrasound image (longitudinal view) shows increased vascularity in the periphery of the tumor. (**d**) Grey scale ultrasound image (extended field of transverse view) demonstrates a wide transverse extension of the tumor (*, 2.14 cm wide). *Abbreviations*: *d* dermis, *st* subcutaneous tissue, *og* ocular globe

9.2.2 Squamous Cell Carcinoma

Cutaneous SCC is the second most common skin cancer, accounting for 20% of all cutaneous malignancies. Most of the tumors are found on the head and neck skin, and cumulative ultraviolet exposure is believed to be the most likely etiological factor. Most deaths from SCC occur in a high-risk group of patients that is composed of tumors greater than 2 cm in diameter; tumor thickness over 4 mm; moderately/poorly differentiated or desmoplastic histological SCC subtype; ear, lip, hand, feet, or genital tumor site; perineural or lymphovascular invasion; nodal metastasis at presentation; recurrent SCC; SCC arising from scars or chronic skin disease, for example, chronic ulcers; and SCC arising in immunosuppressed patients [5]. Furthermore, thickness (or depth of invasion) is an important predictor of metastases in SCC [6]. Thus, ultrasound may support identification of the high-risk SCC group that is associated with a greater mortality and morbidity.

Additionally, there are SCC-related lesions: Bowen's disease, the in situ form of SCC, and actinic keratosis, a precancerous skin lesion that usually appears in photodamaged skin that potentially can become a squamous cell cancer.

SCC presents clinically as a slow-growing usually painless, indurated lesion with a rough, scaly, erythematous surface that easily bleeds and can be nodular, ulcerated, plaque-like, or verrucous. The ulceration can present with a necrotic center and a prominent rim. Common locations are the lips, ear pinna, scalp, and dorsal aspect of the hands. Hence, infiltration of the deeper layers and metastasis is more frequent with SCC. Metastasis can occur to the regional lymph nodes and also to the liver, bones, lungs, and brain.

Histologically, SCC presents as infiltrating sheets and islands of variably differentiated squamous epithelium and a variable degree of mitotic activity (pleomorphism). Keratocysts and keratin pearls may also be found, with neurotropism and lymphovascular invasion providing poor prognosis. There are variants of SCC such as clear cell SCC, spindle cell, desmoplastic acantholytic, pseudovascular or pseudoangiosarcomatous, adenosquamous, mucoepidermoid, and verrucous [7] (Figs. 9.8, 9.9, 9.10, 9.11, and 9.12)

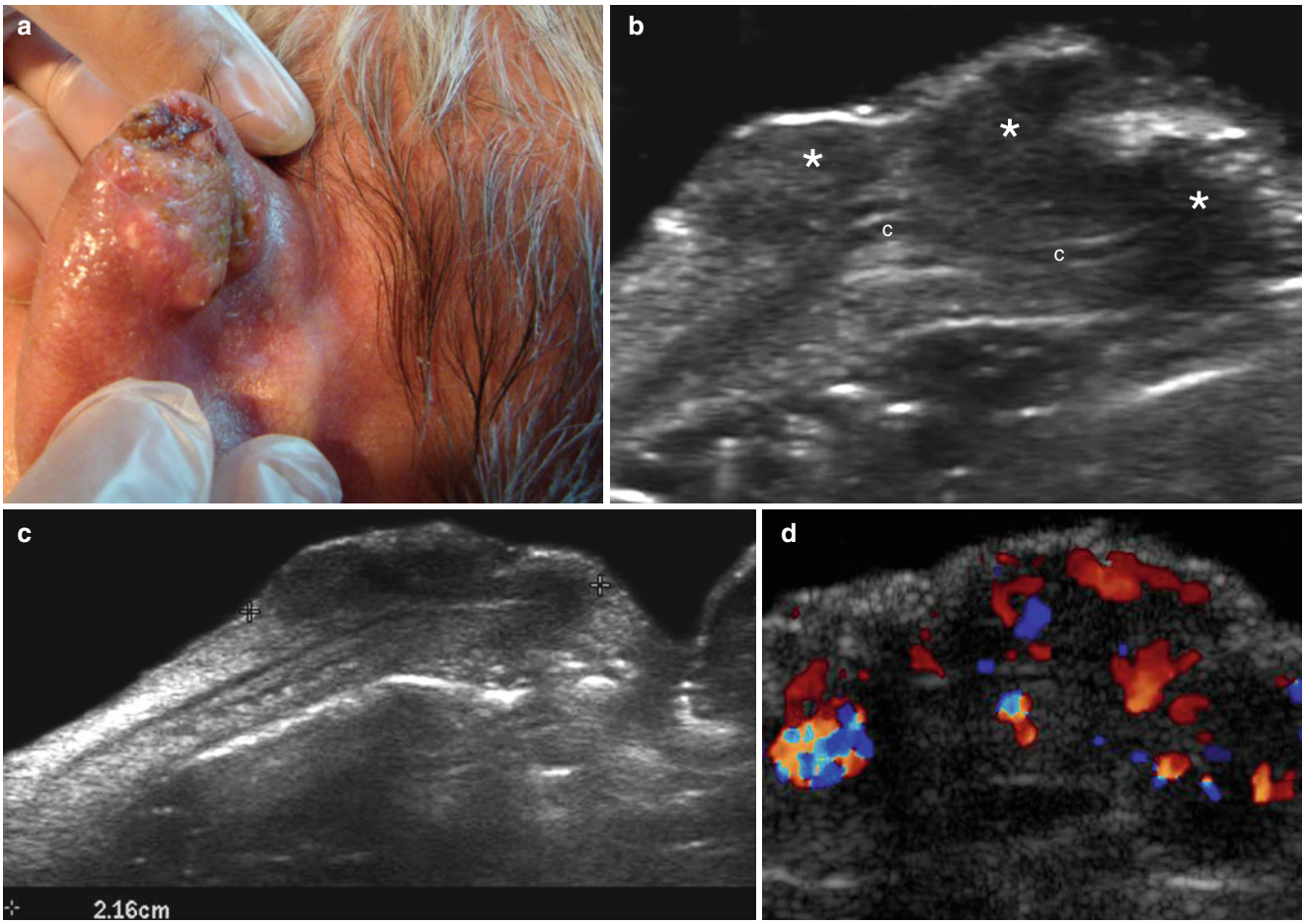

Fig. 9.8 (**a**–**d**) Squamous cell carcinoma. (**a**). Clinical photograph shows ulcerated erythematous swelling in the left ear pinna. (**b**, **c**) Grey scale ultrasound images (transverse views from the posterior aspect of the ear pinna; **b** zoomed image; **c** extended field of view) shows hypoechoic mass (*) that presents irregular borders and involves the posterior and anterior skin layers. The lesion embraces the ear cartilage and measures 2.16 cm in transverse axis. (**d**) Color Doppler ultrasound image (transverse view) demonstrates increased vascularity within the lesion. *Abbreviation*: *c* cartilage

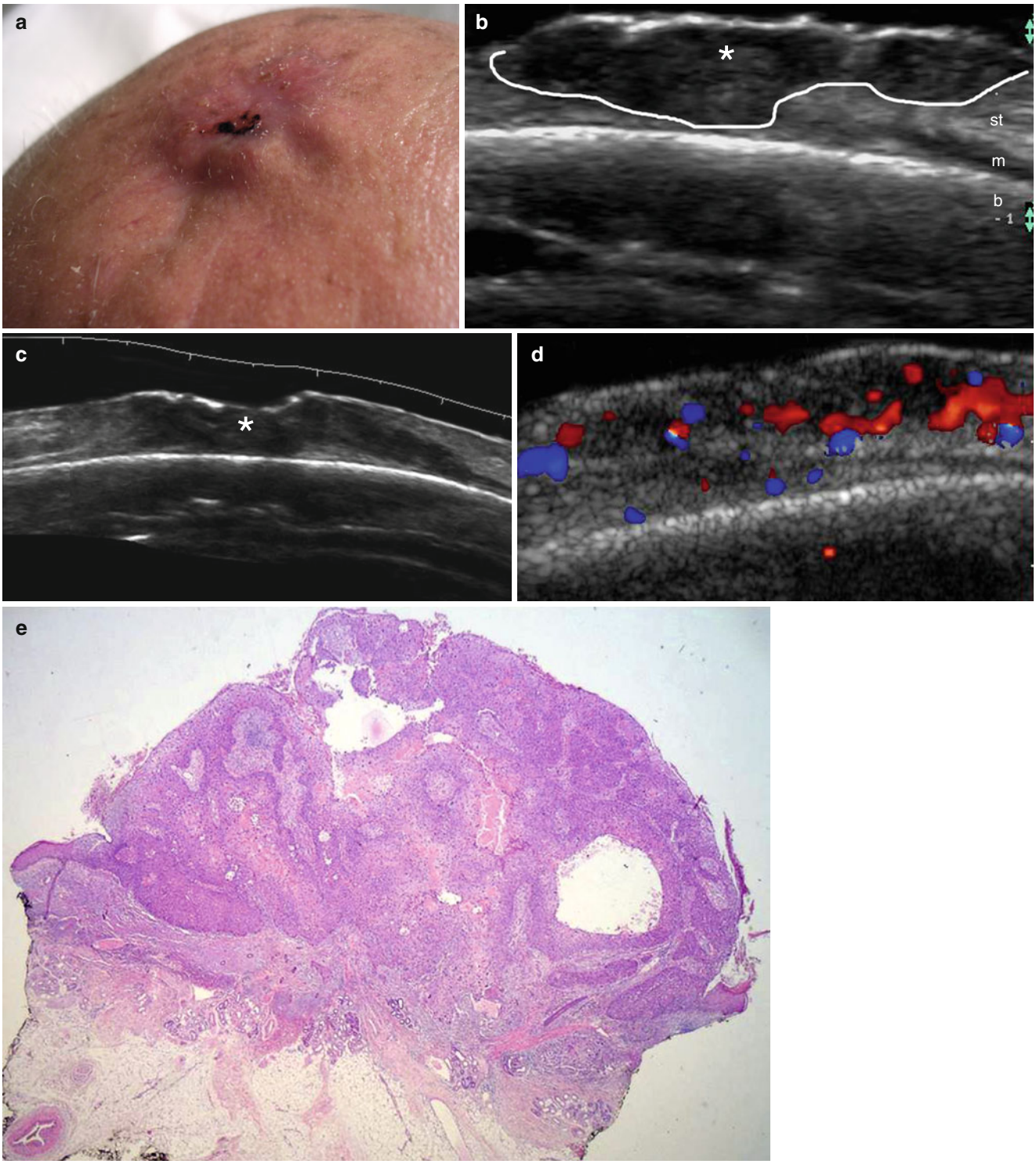

Fig. 9.9 (**a**–**e**) Squamous cell carcinoma. (**a**) Clinical photograph shows ulcerated erythematous swelling in the scalp. (**b**, **c**) Grey scale ultrasound images (**b** zoomed image and **c** extended field of view) demonstrate hypoechoic solid lesion (*, outlined) that involves the epidermis, dermis, subcutaneous tissue, and part of the epicranius muscle. The bony margin of the skull is unremarkable. (**d**) Color Doppler ultrasound image (transverse view) shows increased blood flow in the lesional area. (**e**) Histology (HE 40× zoom): neoplastic proliferation of atypical squamous cells with irregular disposition. *Abbreviations*: *st* subcutaneous tissue, *m* epicranius muscle, *b* bony margin of the skull

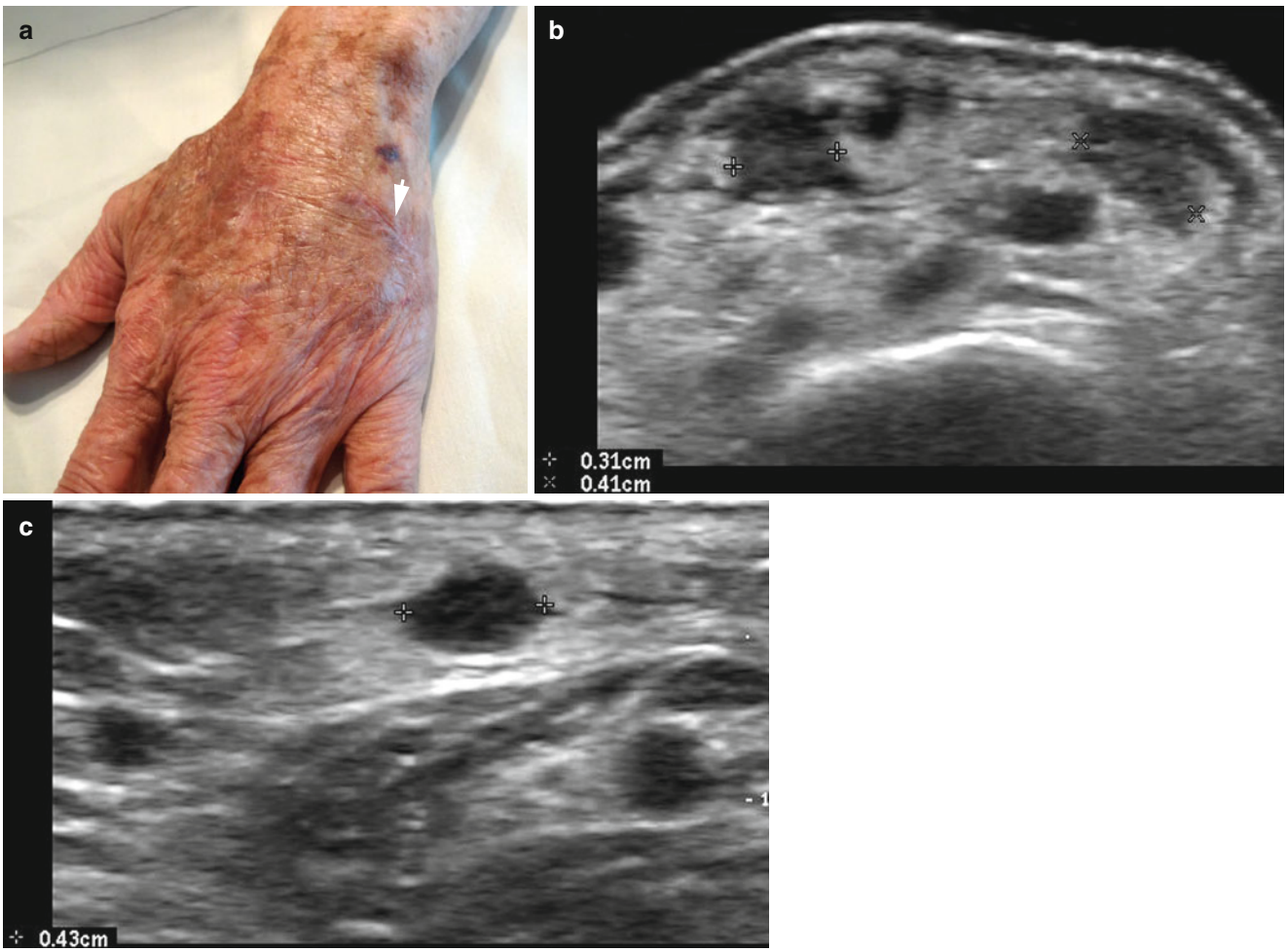

Fig. 9.10 (**a**–**c**) Satellite lesions in recurrent squamous cell carcinoma (SCC). (**a**) Clinical photograph shows an erythematous scar (*arrow*) in the dorsum of the left hand. The patient presented with a history of removal of an SCC lesion 6 months prior. (**b**, **c**) Grey scale ultrasound images (**b** transverse view located 0.5 cm proximal to the scar and **c** longitudinal view 0.5 distal to the scar level) show three well-defined hypoechoic nodules (between markers) located in the subcutaneous tissue that range in size between 0.3 and 0.43 cm. Increased echogenicity of the surrounding subcutaneous tissue is also detected

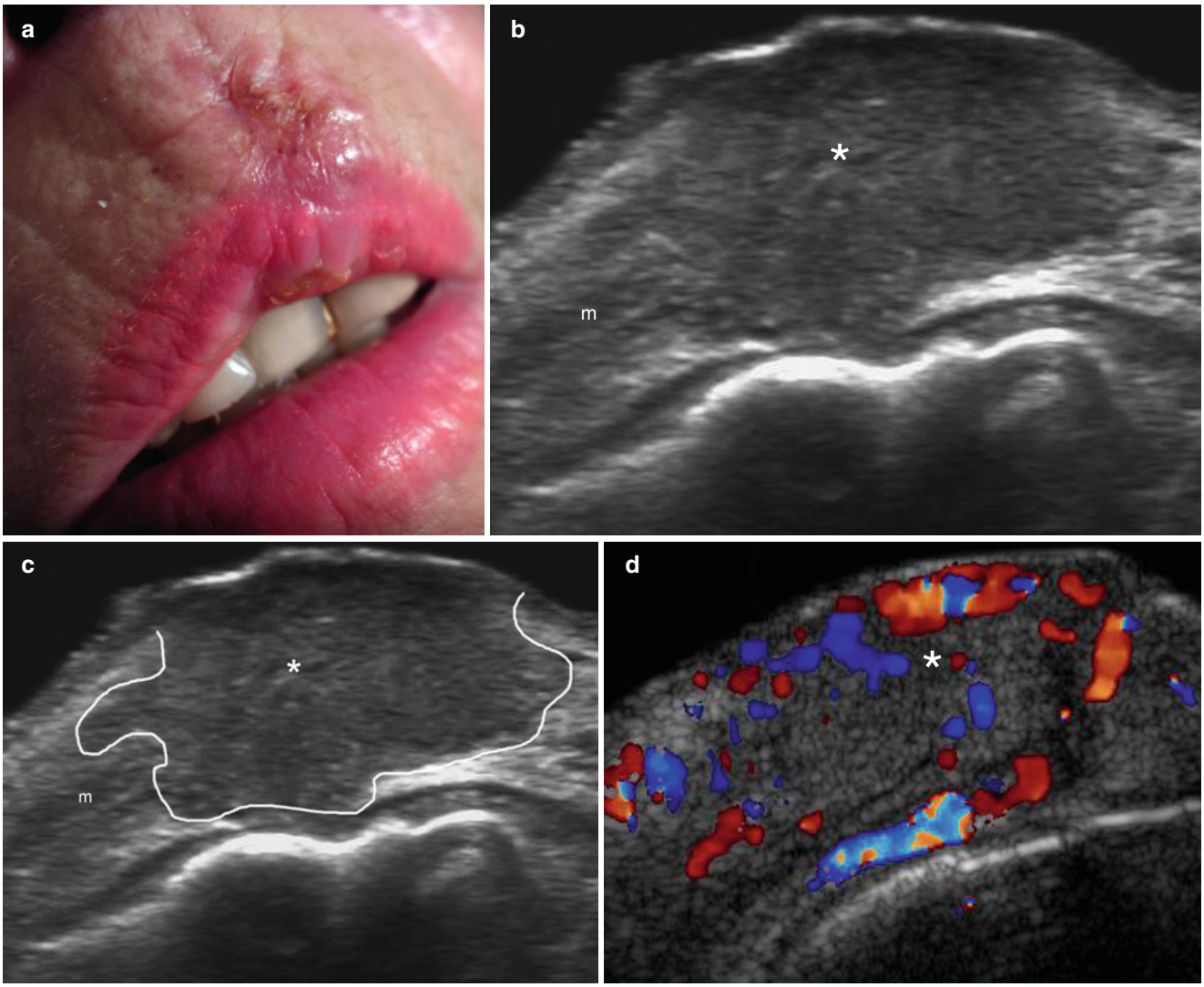

Fig. 9.11 (**a**–**d**) Recurrent squamous cell carcinoma (SCC) that involves the orbicularis muscle of the upper lip. (**a**) Clinical photograph shows erythematous swelling in the scar area. The patient has a history of removal of an SCC lesion 1 year prior in the same region. (**b**, **c**) Grey scale ultrasound images (transverse views; **c** the tumor is outlined) show a hypoechoic solid mass (*) that involves the skin layers and the orbicularis muscle of the upper lip. The tumor also bulges into the vestibular aspect of the lip. (**d**) Color Doppler ultrasound image (longitudinal view) demonstrates increased blood flow within the lesional region (*). *Abbreviation*: *m* orbicularis muscle of the lip

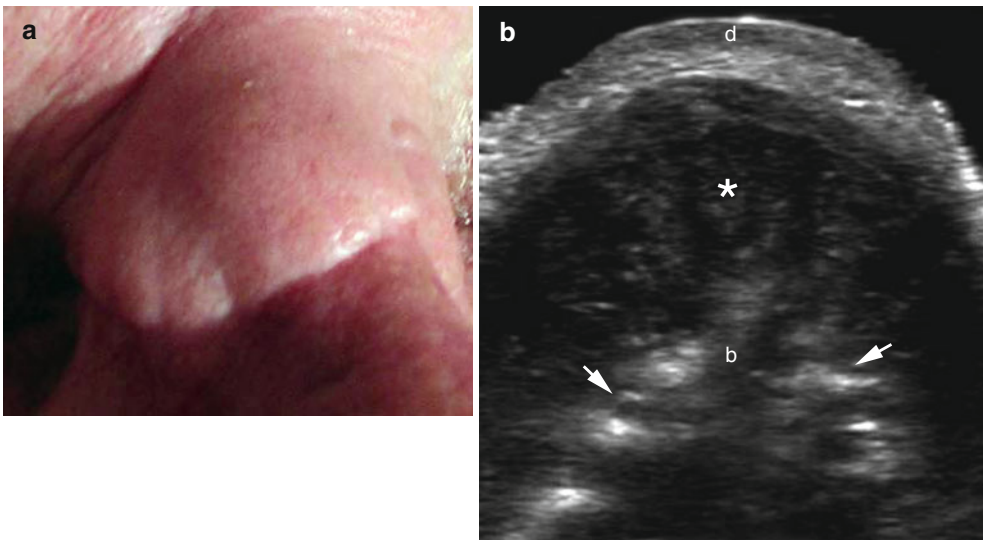

Fig. 9.12 (**a**–**b**) Recurrent squamous cell carcinoma (SCC) with involvement of the bony margin of the nasal bones. (**a**) Clinical image shows skin-colored swelling in the dorsum of the nose. The patient presented with a history of removal of an SCC lesion 3 years prior. (**b**) Grey scale image (transverse view) demonstrates a hypoechoic solid mass (*) that involves the subcutaneous tissue and the bony margin of the nasal bones (*arrows*). Notice the erosion of the bony margin of the nasal bones (*arrows*). *Abbreviations*: *d* dermis, *b* bony margin of the nasal bones

9.2.3 Staging of NMSC

Current staging of NMSC is based on the clinical measure of the tumor size, depth, loco-regional lymph node involvement, and distant metastasis. Tumors measuring ≥2 cm on the lips, ear, eye, or nose present a poor prognosis.

Not formally included among high-risk NMSC lesions are the ones present in immunosuppressed patients who show a higher incidence of NMSC under long-term immunosuppressive therapy or conditions. Thus, renal transplantation is associated with an increased incidence of NMSC caused by immunosuppressive treatments, and under this context, NMSC exhibits more aggressive biological and clinical courses, with higher rates of recurrence and mortality than in the general population. In renal transplants, SCC represents the most frequent skin malignancy (64.1 %), followed by BCC (17.9 %), Bowen's disease (10.2 %), basosquamous carcinoma (5.1 %), and a rare case of invasive sebaceous carcinoma (2.6 %) according to some reports [8, 9]

SCC is the most severe complication and most common cause of death in patients with junctional and recessive dystrophic epidermolysis bullosa [10, 11].

The inclusion of the sonographic parameters (diameter in all axes, blood flow, presence of deeper layers involvement and satellite lesions) may support the clinical staging of NMSC providing valuable data that can match the anatomical involvement for each patient. The latter features may help to perform a one-time treatment, decreasing the possibility of recurrences and improving the cosmetic prognosis of the patient.

9.2.4 NMSC Sonographic Characteristics

NMSC usually presents as hypoechoic and heterogeneous cutaneous tumors with irregular borders. Hyperechoic spots are frequently detected within BCC tumors. Low flow arterial vessels are commonly detected in the lesion and its periphery. The vascularity in BCC is commonly prominent at the bottom of the tumor [12, 13]. Nevertheless, squamous carcinoma is more aggressive upon presentation, therefore, infiltration of the deeper structures and/or loco-regional lymph nodes should be ruled out on the ultrasound examinations. Vascularity in SCC is frequently more prominent compared with BCC and shows greater presence of vessels within the lesion.

Two sonographic artifacts have been reported in BCC lesions. The first is termed the "angles at the bottom" of the lesion, which is produced by inflammatory components that include dilated vessels and giant cells. The second is termed the "blurry tumor" which is generated by a large presence of hyperplastic sebaceous glands that are isoechogenic with the primary lesion and can decrease the definition of the borders of the tumor [12].

Tips for BCC
- Well defined
- Hypoechoic
- Hyperechoic spots within the tumor
- Increased vascularity at the bottom of the lesion

Tips for SCC
- Hypoechoic lesion with irregular borders
- Involvement of deeper layers
- Increased vascularity within the tumor

9.3 Primary Cutaneous Melanoma

Primary cutaneous melanoma is the most aggressive type of cutaneous malignancy and constitutes 4–11 % of all skin cancers comprising greater than 75 % of cutaneous cancer-related deaths and provoking greater than 8,000 deaths per year in the United States [14]. Recurrence has been reported in up to 35.9 % of the treated cases, and can be even higher (46.1 %) when the head and neck region is considered [15, 16]. Melanomas usually present clinically in 95 % of the cases as hyperpigmented macules or nodules that can show irregular borders and ulcerations. Approximately 5 % of melanomas lack pigment and are called amelanotic melanomas. Amelanotic melanomas contain few and/or deeper granules of melanin that are commonly not detected by the naked eye which can delay diagnosis.

The staging of melanoma is based on the Breslow classification that relies on the sequential tumor infiltration (depth) of the cutaneous layers detected by histology which considers the measurement of the microscopic invasion from the stratum granulosum of the epidermis to the deepest portion of the tumor (Table 9.1) [17]. Thus, knowledge of the thickness of the tumor will modify important decisions pertaining to the management of the tumor, such as the size of the excision, the performance of a sentinel node procedure, or the final prognosis of the patient.

On histology, melanomas appear as nests of atypical melanocytes with irregular nuclei, nuclear pleomorphism, prominent nucleoli, spindle or epitheliod cells, and marked mitotic activity. The level of invasion is graded according to the Clark classification (Table 9.1) and the depth of the invasion is assessed using the Breslow index (Table 9.2), which are important prognostic factors for melanoma [18].

On sonography, melanomas usually appear as well-defined, oval- or fusiform-shaped, homogeneous, hypoechoic lesions with smooth borders, increased acoustic transmission, and variable degrees of vascularity, even though they commonly show hypervascularity on color Doppler imaging [19–25]. Sonography has been proved useful for discriminating melanomas thicker and thinner than 1 mm which is relevant for deciding the performance of a sentinel node procedure that is indicated in melanomas that measure greater than 1 mm in thickness [26], the vessels are commonly located within the lesion and may also be tracked using contrast-enhanced ultrasound. Assessment of the vascularity, including the peak systolic velocity of the arterial vessels, may provide an idea of the angiogenic power of the tumor that can correlate with the metastatic potential [27–29]. In cases with ulcerations, the epidermis can show irregularities or discontinuities, and increased echogenicity in the subcutaneous tissue may also be found. Because melanomas can show asymmetry in their thickness, the sonographic measurements should be performed at the deepest point. In the vicinity of the primary lesion, satellite lesions (arising within 2 cm from the primary tumor) or in transit metastasis (arising greater than 2 cm from the primary tumor) can be detected [24, 29, 30]. These secondary lesions appear as hypoechoic oval- or round-shaped with smooth or lobulated contours, mild to moderate heterogenicity, and enhanced acoustic through transmission structures frequently located in the subcutaneous tissue and with variable degrees of vascularity [18, 24, 31]. Ultrasound has been reported to alter the management of patients by detecting impalpable metastasis and helping to differentiate between benign and malignant masses [16, 31]. Usually, there is increased vascularity within the metastases on color Doppler imaging, although the presence of internal vessels can show a variable appearance that can go from hypo- to hypervascular. Occasionally, these metastases can present an irregular appearance and anechogenicity and can be sonographically misdiagnosed as abscesses. This challenging anechoic appearance has been reported as related more to hypercellularity and not as a result of necrosis [32]. The balloon shape, nodular thickening of the cortex, and loss of hyperechogenicity of the medullae are signs of malignant infiltration in regard to nodal infiltration [24]. The use of lower frequency probes in bulky primary melanomas may help to reach to the bottom of the lesion and provide a better definition of the extension (Figs. 9.13, 9.14, 9.15, 9.16, and 9.17).

Table 9.1 Clark classification of the levels of invasion in melanoma

Level I: in situ melanoma
Level II: invasion of the papillary dermis by single cells or small nets
Level III: invasive tumor usually as an expansile nodule abutting on the reticular dermis
Level V: invasion of the subcutaneous fat

Table 9.2 Breslow classification of the depth of melanoma

Tumor depth (mm)	Approximate 5-year survival (%)
<1	95–100
1–2	80–96
2.1–4	60–75
>4	50

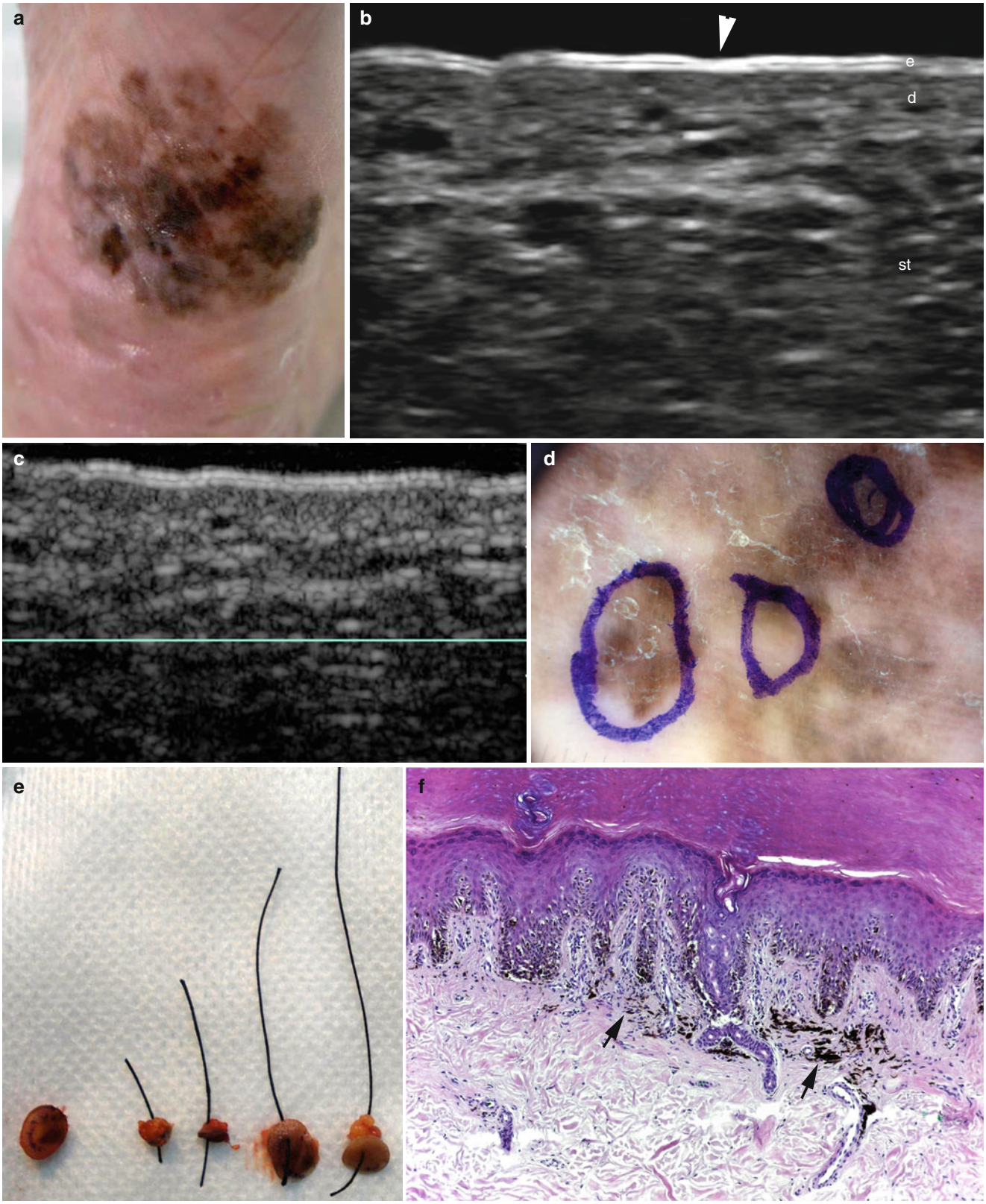

Fig. 9.13 (**a**–**f**) Melanoma in situ. (**a**) Clinical photograph shows hyperpigmented and irregular lesion in the sole of the left foot. (**b**) Grey scale ultrasound image (longitudinal view) demonstrates loss of the bilaminar pattern of the epidermis (*arrowhead*) in part of the lesion. Nevertheless, no sign of solid mass is detected. Notice the bilaminar appearance of the normal epidermis that is typically seen in the plantar region (glabrous skin). (**c**) Color Doppler ultrasound image (longitudinal view) shows no sign of regional hypervascularity. (**d**) Cutaneous marking of the biopsy sites. (**e**) Biopsy samples. (**f**) Histology (HE 40× zoom). Acral skin with atypical melanocytic proliferation in the dermo-epidermal junction. Deposition of melanin in the dermal melanophages. *Abbreviations*: *e* epidermis, *d* dermis, *st* subcutaneous tissue. (a, d, and e are courtesy of Drs. Veronica Catalan and Carlo Pezo)

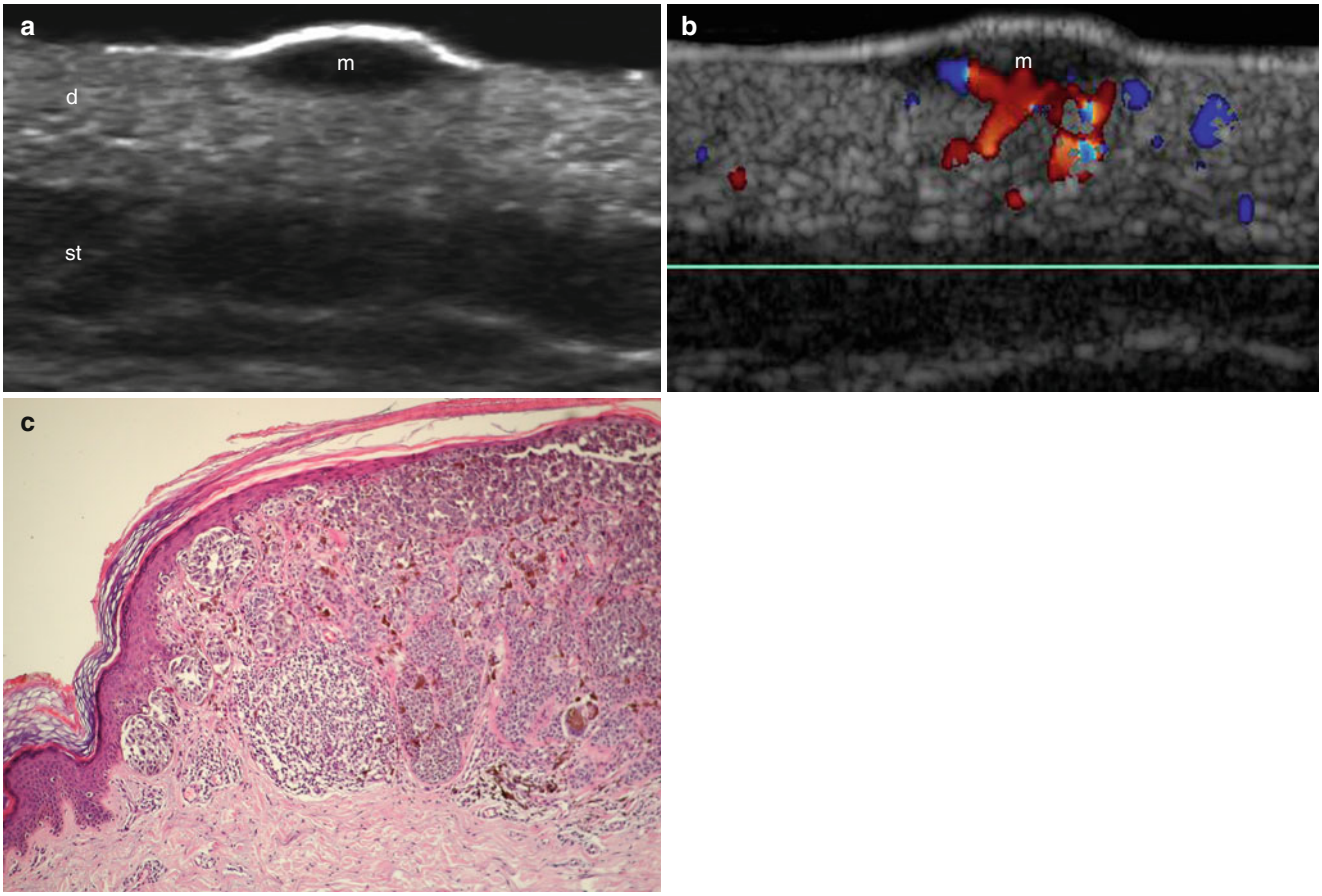

Fig. 9.14 (**a**–**c**) Melanoma. (**a**) Grey scale ultrasound image (transverse view) in the dorsal region shows a well-defined fusiform-shaped hypoechoic lesion (*m*) in the dermis. (**b**) Color Doppler ultrasound image (transverse view) demonstrates increased vascularity within the tumor (m). (**c**) Histology (HE 40 × zoom): melanocytic proliferation composed by nests of different sizes in the dermo-epidermal junction and the dermis. Fibrous stroma and melanophages surround the atypical cells. *Abbreviations*: *d* dermis, *st* subcutaneous tissue, *m* melanoma

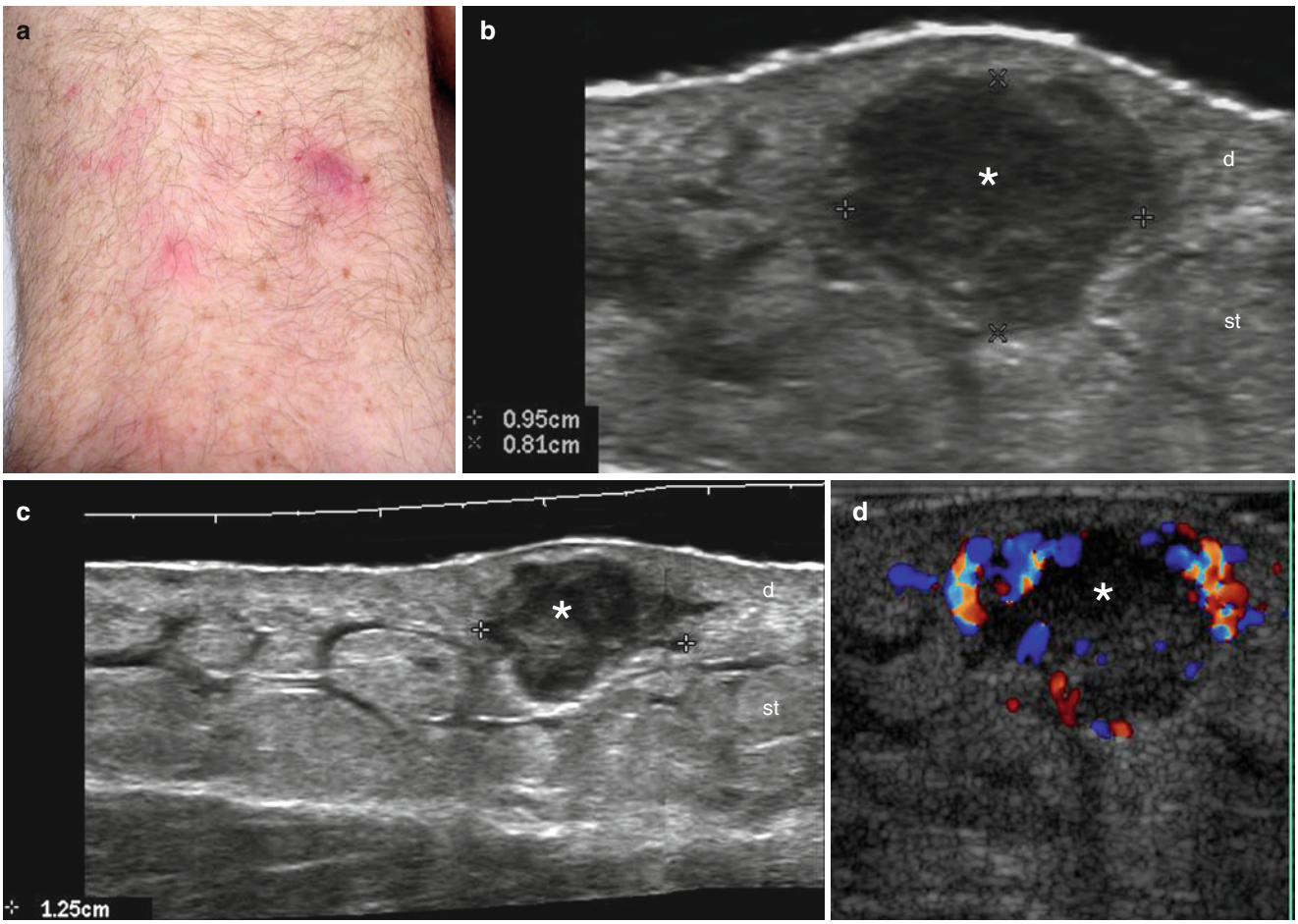

Fig. 9.15 (**a**–**d**) Melanoma in-transit metastasis. (**a**) Clinical image shows erythematous papules in the dorsum of the left thigh. The patient has history of a melanoma surgery in the left ankle. (**b**, **c**) Grey scale images (**b** zoomed, transverse view and **c** extended field of longitudinal view of the large size cutaneous lesion) demonstrate 1.25 × 0.81 cm oval-shaped hypoechoic structure located in the dermis and subcutaneous tissue. Increased echogenicity and septal anechoic bands in the surrounding subcutaneous tissue suggestive of edema are also detected. (**d**) Color Doppler ultrasound image (transverse view) shows increased blood flow in the periphery of the lesion

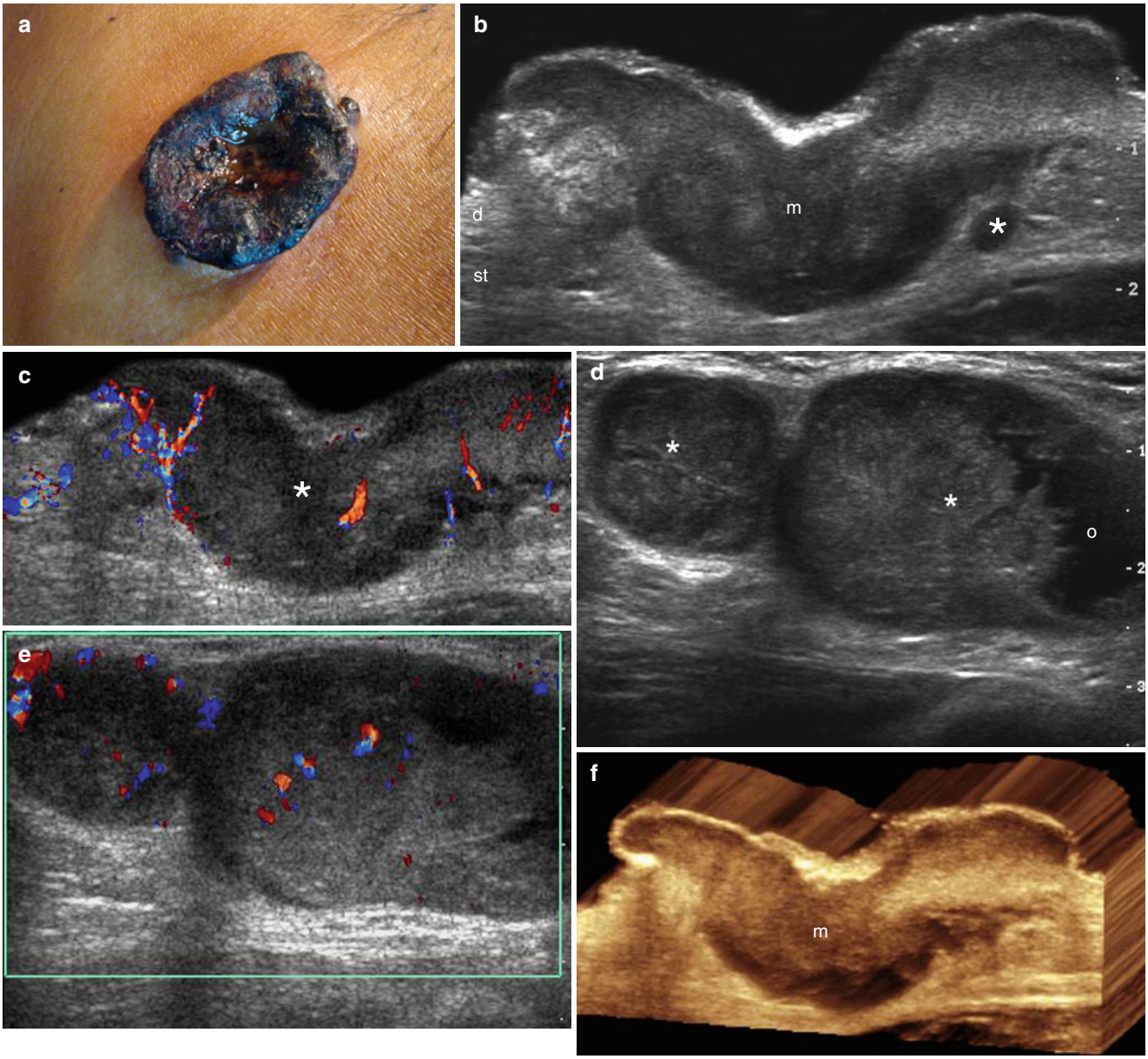

Fig. 9.16 (**a**–**f**) Primary melanoma, satellite and nodal metastasis. (**a**) Clinical photograph shows exophytic and ulcerated hyperpigmented lesion in the right aspect of the abdominal wall. (**b**) Grey scale ultrasound image (transverse view) demonstrates a well-defined fusiform-shaped hypoechoic solid structure (*m*) that involves the epidermis, dermis, and subcutaneous tissue. Notice the satellite nodule (*) located in the subcutaneous tissue adjacent to the main lesion. (**c**) Color Doppler ultrasound image (transverse view) shows increased vascularity in the lesional area. (**d**) Grey scale ultrasound image (transverse view, right axilla) demonstrates two well-defined, oval-shaped structures located in the subcutaneous tissue suggestive of nodal metastases. Notice the anechoic area (*o*) in one of the lesions. (**e**) Color Doppler ultrasound image (transverse view) shows increased blood flow with an asymmetric and irregular pattern within the nodules. (**f**) 3D reconstruction of the lesion (transverse view, 5–8 s sweep)

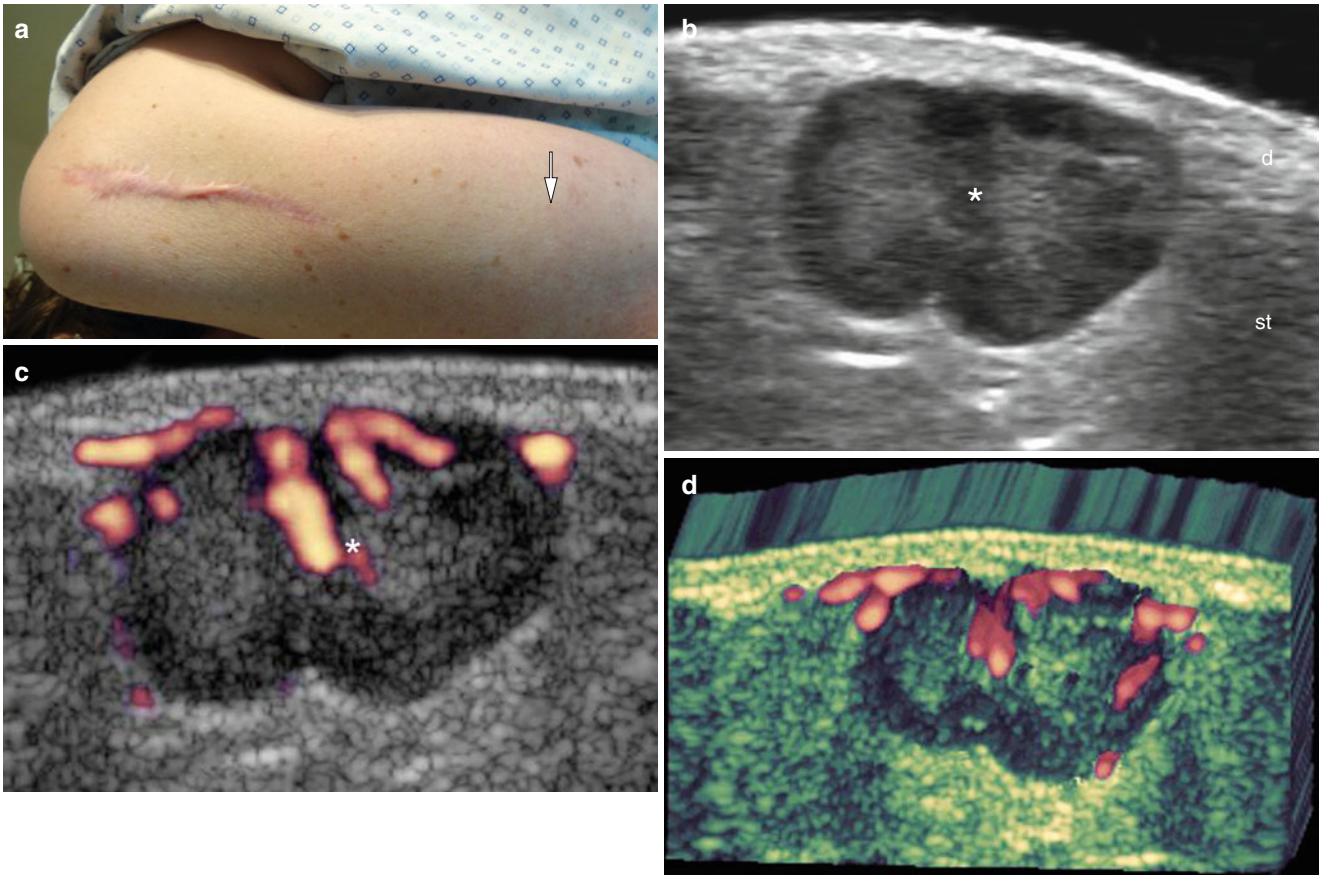

Fig. 9.17 (**a**–**d**) Melanoma in-transit metastasis. (**a**) Clinical photograph shows a patient with a history of a recent melanoma surgery in the left arm and a palpable lump (*arrow*) distal to the scar. (**b**) Grey scale (transverse view) demonstrates a well-defined, oval-shaped lobulated solid structure (*) in the subcutaneous tissue that bulges into the dermis. The nodule presents a hypoechoic rim and a slightly hyperechoic center. (**c**) Power Doppler image (transverse view) shows increased vascularity within the nodule (*) with thick and irregular vessels. (**d**) 3D power angio Doppler reconstruction of the lesion (5–8 s sweep)

9.3.1 Contrast-Enhanced Ultrasound in Melanoma

Intravenous contrast medium, conformed by gas-filled microbubbles that enhance the echogenicity of the vessels, has been progressively used in melanoma and loco-regional staging for obtaining early information about the effectiveness of the treatment of the primary lesion and clarifying a doubtful cortical thickening at the lymph nodes [27–29]. It is also a promising tool to reduce the number of patients who should undergo fine-needle aspiration cytology of lymph nodes with focal cortical thickening in melanoma [33, 34]. The vascular density in melanoma has already been correlated with metastatic potential using color Doppler ultrasound. Thus, neovascularization has been reported as a prognostic factor for metastasis equivalent to the Breslow index [35]. Furthermore, contrast-enhanced ultrasound imaging of tumor neovascularity has been mentioned in the literature as providing a noninvasive marker of angiogenesis corresponding to the expression of vascular endothelial growth factor in mice that were implanted with the human melanoma cell line DB-1 that can become a useful tool for monitoring clinical anti-angiogenic therapies [36]. Lymphosonography (i.e., contrast-enhanced ultrasound after interstitial injection of a contrast agent) has been reported as statistically better than lymphoscintigraphy for the detection of sentinel lymph nodes in an animal model [37].

The limitations of the usage of contrast medium are the current short-life time of the bubbles within the systemic circulation that commonly provides minutes for performing the analysis, the cost, and the invasive nature of the intravenous injection. Nevertheless, lymphosonography can require seconds to identify the movement of the contrast within lymphatic channels and present a higher spatial resolution than lymphoscintigraphy. The sonographic signs for malignancy in lymphosonography are heterogenous or sparse enhancement in sentinel lymph nodes. In contrast, uniform enhancement in small (<5 cm) sentinel lymph nodes suggest benignancy [37]. Thus, contrast-enhanced ultrasound can improve the management of melanoma by allowing detection and characterization of the primary and secondary lesions, guidance of biopsy, and prompt assessment of the effectiveness of the pharmacodynamic response [31].

9.3.2 Elastography in Cutaneous Melanoma

As of yet, few reports that show the experience or usefulness of sonoelastography in cutaneous melanoma are available [38, 39]. There are reports on acousto-optical elastography, an experimental imaging modality for quantifying the mechanical behavior of skin lesions. The method relies on stimulating the tissue with a low frequency acoustic force and imaging the resulting strains in the tissue by means of quantifying the magnitude of the dynamic shift in a back-reflected laser speckle pattern from the skin. The magnitude of the shift reflects the local stiffness of the tissue, which has shown promising results when comparing benign melanocytic nevi with melanoma [40]. However, to date there are no reports that have altered management in terms of detecting undisclosed malignancies, although it may increase the diagnostic confidence of less-experienced operators performing ultrasound. Therefore, the assessment of the role of elastography in melanoma and other cutaneous tumors probably will require further investigation [37].

9.3.3 High-Intensity Focused Ultrasound in Cutaneous Melanoma

High-intensity focused ultrasound (HIFU) is a focused sonic energy that heats and destroys the tissue through thermal ablation. Currently, scarce reports on the effects of HIFU in melanoma are available. However, significant tumor necrosis and absent local serum-vascular endothelial growth factor have been described in animal models [41, 42].

Tips for Melanoma

- Hypoechoic
- Fusiform lesion
- Increased vascularity
- Check for satellite (≤2 cm from the primary tumor), in-transit (≥2 cm from the primary tumor), or nodal metastasis
- Provide extension in all axes

9.4 Other Malignant Skin Tumors

9.4.1 Dermatofibrosarcoma Protuberans

Dermatofibrosarcoma protuberans (DFSP) is an unusual, locally aggressive cutaneous fibroblastic neoplasm that mainly affects the torso and proximal extremities of young and middle-aged adults. DFSP presents as a slow-growing, multinodular, and plaque-like erythematous or purple mass that tends to infiltrate and show local recurrence but rarely metastasizes to distant organs [43].

On histology, there is a proliferation of spindle cells with elongated nuclei with little or no pleomorphism. DFSP usually affects the dermis and subcutaneous tissue although it can also involve deeper layers. Inmunohistochemical markers such as CD34 are commonly positive [43, 44]. On sonography, two sonographic patterns have been described The first is a well-defined oval hypoechoic structure and the second is composed of an ill-defined heterogeneous structure, with hyper- and hypoechoic areas and lobulated or pseudopodia-like protrusions commonly affecting the dermis and subcutaneous tissue. DFSP can also send projections to the fascial or muscular layers. Nevertheless, this condition usually tends to spread horizontally, and the degree of vascularization is variable but commonly presents slow flow vessels [45, 46] (Figs. 9.18 and 9.19).

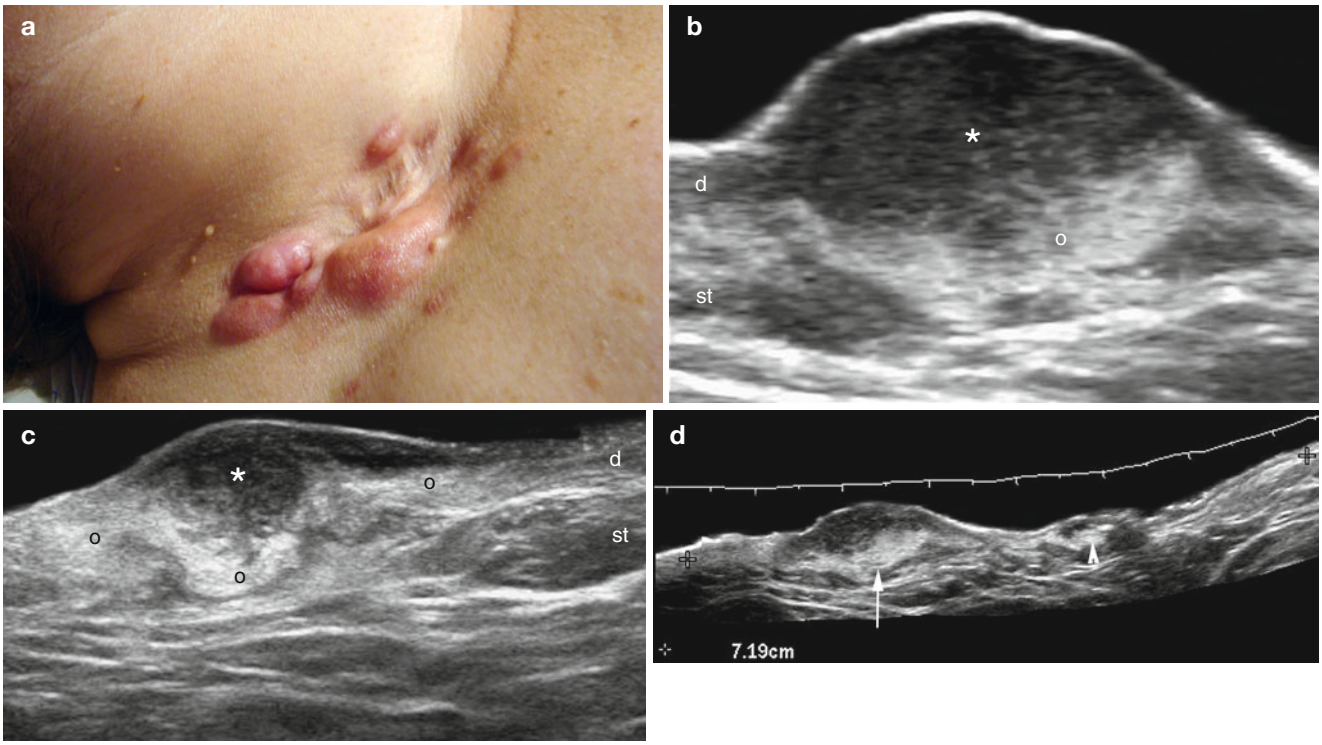

Fig. 9.18 (**a**–**h**) Dermatofibrosarcoma protuberans. (**a**) Clinical image shows erythematous lumps in the right aspect of the neck. (**b**–**d**) Grey scale ultrasound images (**d**: zoomed longitudinal view; **c** transverse view; **d** extended field of longitudinal view) demonstrate a 7.19 cm long, ill-defined mixed echogenicity lesion that involves the dermis and subcutaneous tissue. The lesion is composed of a superficial lobulated hypoechoic pseudonodular region (*) and a deep hyperechoic region (o). Notice the two pseudonodular regions in figure (**d**) that present a large size (*arrow*) and small size (*arrowhead*) lesion. (**e**) Color Doppler ultrasound image (transverse view) demonstrates increased vascularity within the lesion. (**f**) 3D power angio reconstruction of the tumor (5–8 s sweep). (**g**) The tumor at surgery. (**h**) Histology (HE 100× zoom): atypical spindle cell proliferation that surrounds adipocytes

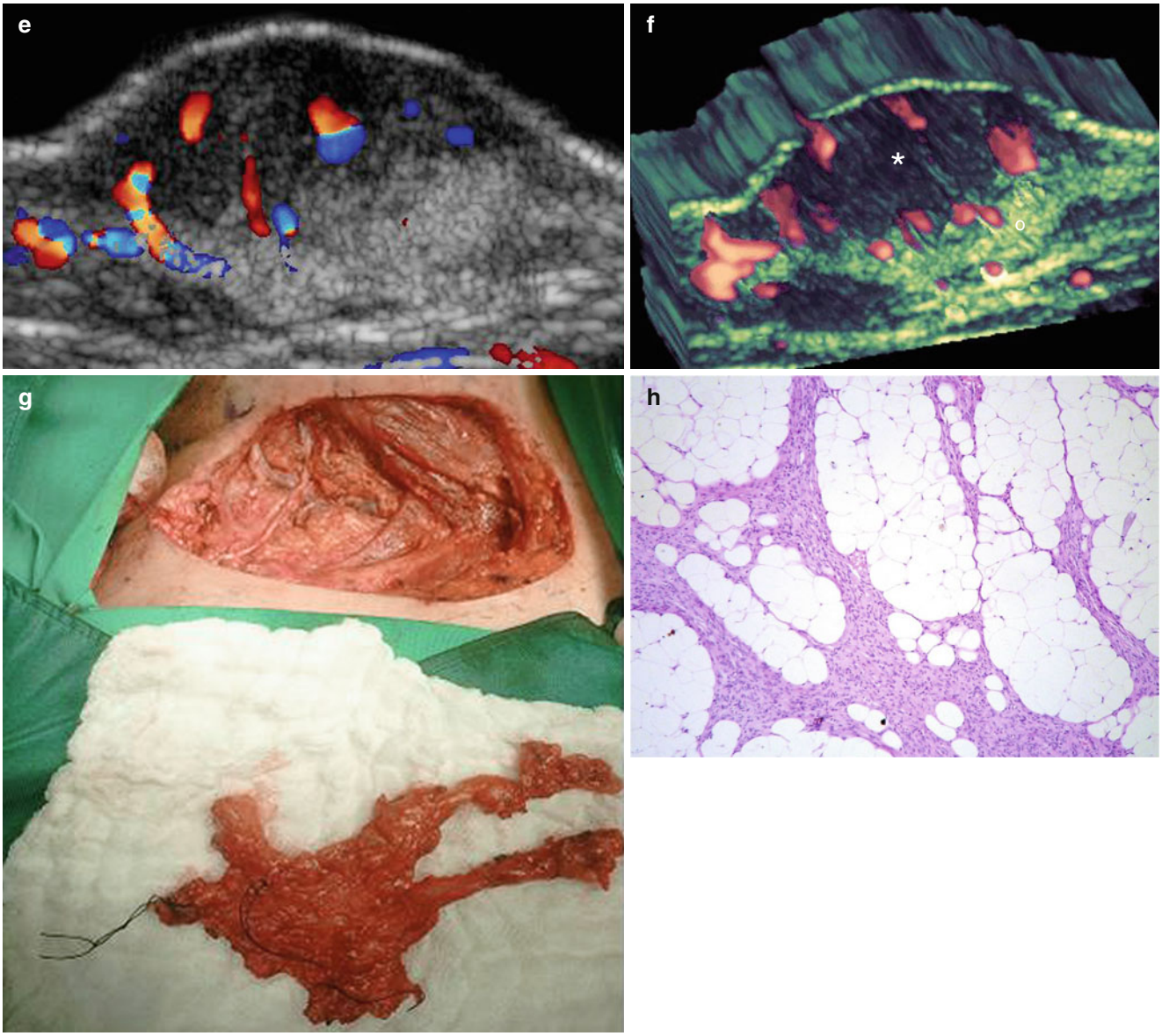

Fig. 9.18 (continued)

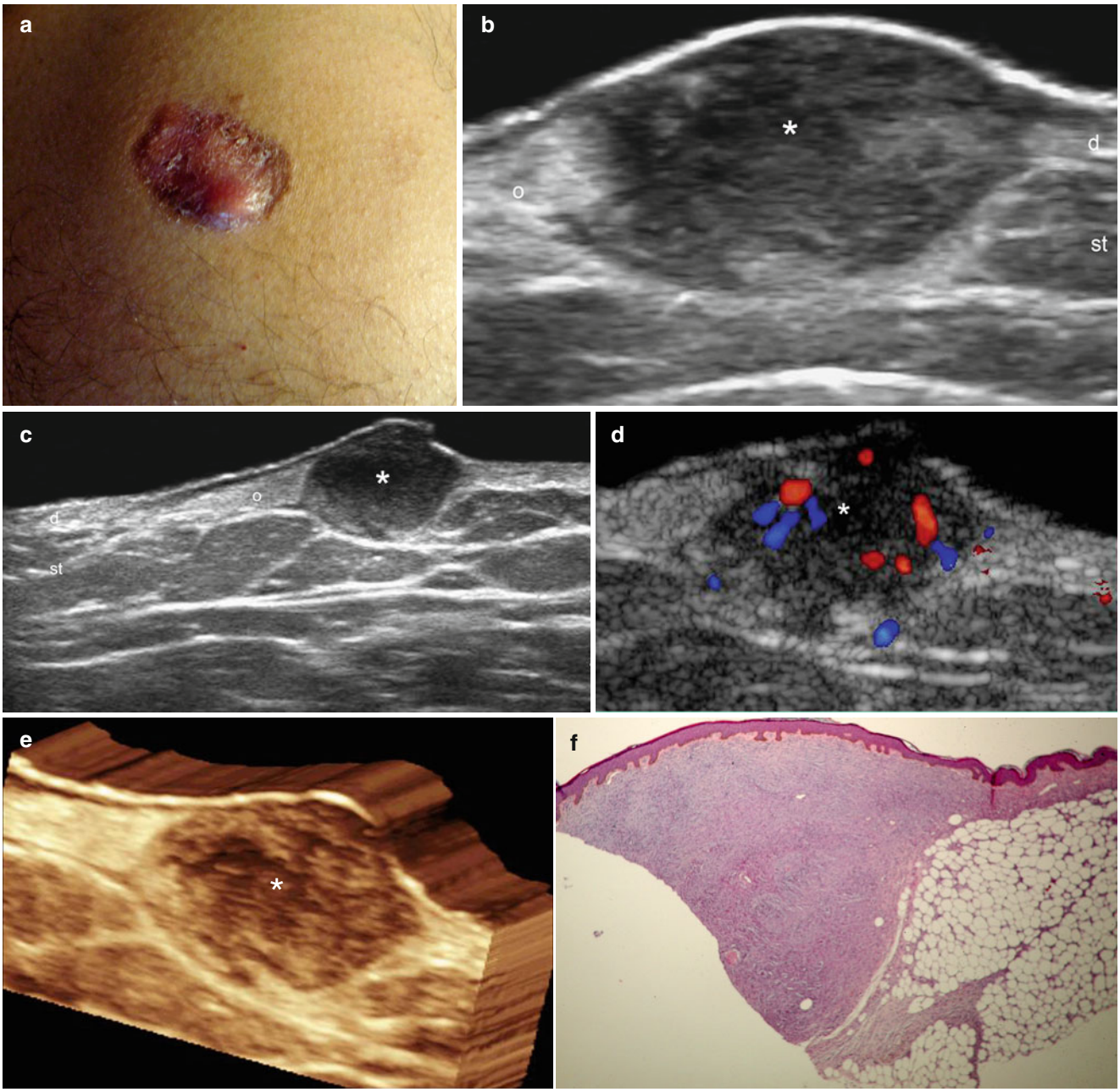

Fig. 9.19 (**a**–**f**) Dermatofibrosarcoma protuberans. (**a**) Clinical photograph shows an erythematous lump in the right thigh. (**b**, **c**) Grey scale ultrasound images (**b** transverse view; **c** longitudinal view) demonstrate ill-defined mixed echogenicity lesion located in the dermis and subcutaneous tissue. It presents a superficial hypoechoic and lobulated pseudonodular part (*) and an increased echogenicity (o) of the vicinity. (**d**) Color Doppler ultrasound image (longitudinal view) shows increased blood flow within the hypoechoic part. (**e**) 3D reconstruction of the lesion (*, 5–8 s sweep, transverse view). (**f**) Histology (HE 20 × zoom): dermal and hypodermal proliferation of atypical spindle cells. *Abbreviations*: *d* dermis, *st* subcutaneous tissue

9.4.2 Cutaneous Angiosarcoma

Cutaneous angiosarcoma is a rare malignant tumor of endothelial origin that often presents an aggressive course, with 60 % of angiosarcomas primarily located in the skin and mainly affect older patients (>50 years of age) with a peak incidence in the eighth decade. The 5-year survival rate ranges from 12 % to 20 % and angiosarcoma often undergoes distant metastasis most commonly in the liver, lymph nodes, and spleen. The most important prognostic feature is tumor size, and other significant factors are depth of invasion >3 mm, mitotic rate, positive surgical margins, local recurrence, and metastases.

The head and neck form of angiosarcoma is the most frequent subtype, also called idiopathic angiosarcoma, and accounts for 50–60 % of all cases. The latter form is frequently seen on the scalp of elderly men.

Clinically, angiosarcomas show as a bruise-like erythematous or violaceous plaques or mass that becomes larger and ill-defined over time. Pain, bleeding, and swelling have been also described. A higher incidence of angiosarcomas occurs in female patients that have received radiation therapy for breast cancer, patients that present with chronic extremity lymphedema (Stewart-Treves syndrome), and pre-existing vascular malformations have been reported [47, 48].

Histologically, the masses consist of ill-defined hemorrhagic and occasionally blood-filled cystic spaces. The cutaneous layers and sometimes deeper structures are commonly replaced by a diffuse, irregular, and anastomosing network of endothelial-lined erythrocyte containing variably slit-like to medium-sized sinusoidal to larger blood-filled cystic spaces. The endothelial cells are enlarged and contain hobnailed hyperchromatic round to oval nuclei with condensed chromatin. Other forms show a solid pattern with epithelioid and spindle cells with little intervening stroma [49–51].

On sonography, angiosarcoma appears as an ill-defined or lobulated hypoechoic mass with prominent vascularity commonly with low flow arterial and venous vessels. This tumor usually infiltrates the dermis and subcutaneous tissue but can also affect deeper structures. (See Fig. 8.10.)

9.4.3 Kaposi's Sarcoma

Kaposi's sarcoma (KS) is a low-grade mesenchymal tumor involving blood and lymphatic vessels. There are four variants of the disease, each presenting a different clinical manifestation: classic or sporadic, African or endemic, organ transplant-related or iatrogenic, and AIDS-related or epidemic. This condition is the most common tumor among patients with HIV infection [52]. KS is a low-grade malignancy that is associated with human herpesvirus-8, and composes a multifocal tumor that most commonly affects mucocutaneous sites. It might also involve lymph nodes and visceral organs, in particular of the respiratory and gastrointestinal tract, but it can affect every organ system [53].

Histologically, in its early stages, KS contains blood vessels with a fine endothelium passing through the dermal collagen bundles. In the plaque and nodular stages, the vessel lumens are visible more clearly and there is a progressive increase in the number of neoplastic spindle cells with a low degree of pleomorphism and atypia, and occasional mitoses. The infiltrate is made up of lymphocytes and plasma cells [54].

On sonography, KS lesions appear as hypoechoic or heterogeneous lesions, as a plaque-like thickening of the dermis, sometimes with a nodular appearance. Vascularity is variable within the lesion and infiltration of deeper structures, such as muscles, has been reported [55]. Ultrasound has been used as an objective tool for measuring the degree of remission of the disease [56, 57] (See Fig. 8.11).

9.4.4 Merkel Cell Carcinoma

Merkel cell carcinoma (MCC) originates from a cutaneous mechanoreceptor cell (Merkel cell) located in the basal layer of the epidermis [58]. MCC is a rare neuroendocrine carcinoma of the skin that is found primarily in older individuals and exhibits a bad prognosis mainly because of a high rate of local recurrence. Risk factors associated with the development of MCC include exposure to ultraviolet radiation and immunosuppression, with a viral etiology (polyomavirus) also being proposed. Thirty-six percent of cases of MCC are located on sun-exposed areas such as the face and 50 % are located on the head and neck.

MCC presents clinically as a single firm flesh-colored to erythematous dome-shaped nodule with a smooth shiny surface, sometimes with telangiectasia.

Regional lymph nodes are involved in 15–66 % of patients and distant metastases are found in 1–6 % of patients.

Histologically, MCC appears as a dermal nodule or plaque that frequently extends into the subcutaneous tissue. It may show a nodular or infitrative pattern with lymphovascular invasion. Small blue cells with basophilic nuclei and minimal cytoplasm are detected. Mitoses are frequent and apoptosis index is high. Inmunohistochemistry using CK (cytokeratin)-20 positive and thyroid transcription factor-1 negative may help to assess the diagnosis, among other markers.

Tumor size ≥2 cm, lymph node involvement, deeper structure involvement (muscle, fascia or cartilage), infiltrative pattern on histology, and distant metastasis (liver, lung, bone, brain) present a worse prognosis [59].

On sonography, MCC tumors will present as a hypoechoic ill-defined nodule or mass that usually affects the dermis and subcutaneous tissue and presents prominent vascularity (Fig. 9.20).

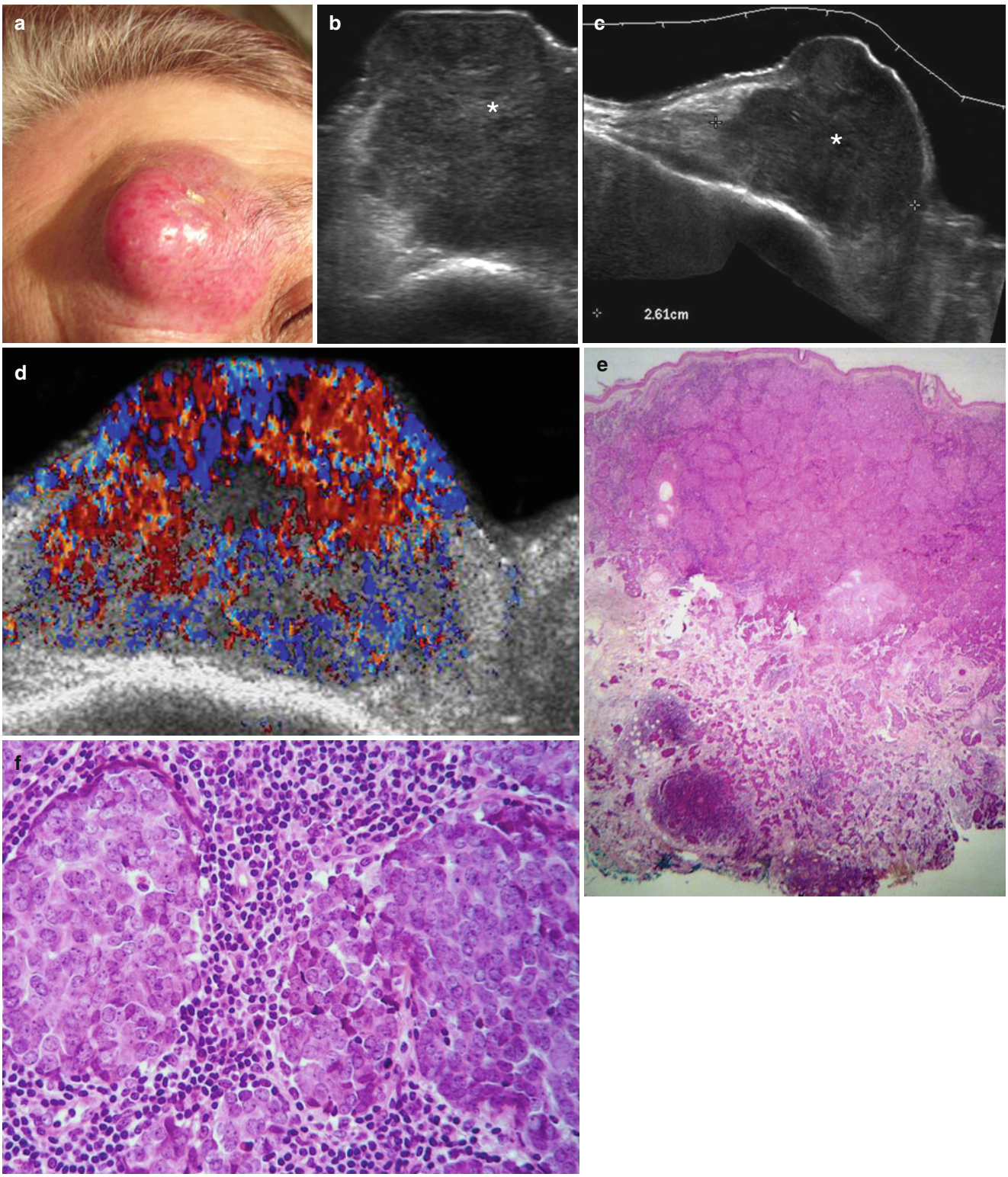

Fig. 9.20 (**a**–**f**) Merkel cell carcinoma. (**a**) Clinical photograph shows erythematous and exophytic lump in the medial aspect of the left frontal region. (**b**, **c**) Grey scale ultrasound images (**b** zoomed transverse view; **c** longitudinal view) demonstrate a 2.61 cm long oval-shaped hypoechoic solid mass with irregular borders that involves the dermis and subcutaneous tissue. (**d**) Color Doppler ultrasound image (transverse view) shows prominent vascularity within the mass. (**e**, **f**) Histology (e: HE × 20 zoom; f: HE× 400 zoom) demonstrates dense and irregular aggregates of pyknotic cells with little cytoplasm, fine chromatin, and lymphoid stroma. Immunohistochemically, the neoplastic cells stained positive for chromogranin, synaptophysin, and perinuclear cytokeratin 20

9.4.5 Cutaneous Lymphoma

Cutaneous lymphoma comprises a heterogeneous group of lymphoproliferative cutaneous disorders separated mainly by the predominant type of lymphoid cell present in the tumor. Hence, they can be classified into two groups: T-cell and B-cell lymphomas [60]. The most common type of T-cell lymphomas are mycosis fungoides, named for its mushroom-like tumors that are commonly seen at the end stage of the disease and Sezary's syndrome, a leukemic erythrodermic lymphoma variant. The three major histological subgroups of primary cutaneous B-cell lymphoma are: follicle center, marginal zone B-cell, large B-cell and leg type.

9.4.5.1 Mycosis Fungoides

Mycosis fungoides is the most frequent form of primary cutaneous T-cell lymphoma that is a low-grade cutaneous lymphoma characterized by skin-homing CD4+ T cells. Clinically, it shows highly symptomatic progressive skin lesions including patches, plaques, tumors, scaling, poikiloderma, and erythroderma, and has a poorer prognosis during later stages [61].

Histologically, mycosis fungoides presents as hyperkeratosis, psoriasiform hyperplasia, and superficial perivascular lymphocytic infiltrates. Scarring and atypical lymphocytes with hyperchromatic nuclei can also present. Folliculotropic mycosis fungoides (FMF) is a variant of cutaneous T-cell lymphoma that affects the hair follicles.

9.4.5.2 Sezary's Syndrome

The leukemic form of Sezary's syndrome is most common in the fifth to seventh decades of life and is characterized by intense pruritus, edema, scaling (especially in the palms and soles [palmoplantar keratoderma]), and a generalized infiltrative erythroderma. Lymphadenopathy and atypical circulating lymphocytes (Sezary's cells) in the peripheral blood are also commonly found.

Histologically, Sezary's syndrome shows infiltrates composed of highly convoluted cerbriform lymphocytes with hyperkeratosis, acanthosis, and sometimes microabscesses.

9.4.5.3 Subcutaneous Panniculitic T-Cell Lymphoma

Subcutaneous panniculitic T-cell lymphoma is a less common form of presentation of T-cell lymphoma that can clinically mimic chronic panniculitis and present as multiple ulcerated and erythematous or violaceous nodules or plaques that most commonly affect the torso and extremities. Histologically, panniculitic T-cell lymphoma presents with vesicular and hyperchromatic nuclei and conspicuous erythrophagocytosis. The atypical lymphocytes involve the subcutaneous tissue and rim fat cells with a lace-like appearance. Fat necrosis with xanthoma cells and hemorrhage are also commonly found.

9.4.5.4 B-Cell Cutaneous Lymphomas

B-cell cutaneous lymphomas cab be either primary or metastatic. The marginal zone B-cell lymphoma is the most common primary cutaneous type. Clinically, this type shows as single or multiple asymptomatic, erythematous, brown or violaceous papules, nodules, or plaques sometimes surrounded by an erythematous border. The torso, especially the back, is the most affected area. In contrast to mucosae, the skin does not have an associated B-cell lymphocyte population, therefore it has been suggested that skin-associated lymphoid tissue may develop following chronic antigen stimulation, such as chronic inflammation or autoimmune diseases. Histologically, there is a dense atypical B-cell lymphoid infiltrate in B-cell cutaneous lymphoma that dissects the collagen with inmunoblasts that present central eosinophilic nuclei and scattered eosinophils [62].

On sonography, lymphomas can present as focal hypoechoic or heterogeneous thickening of the dermis or as diffuse lesions that involve the dermis and subcutaneous tissue. The diffuse form of presentation usually appears as heterogeneous involvement with mixed echogenicity (anechoic, hypoechoic, and hyperechoic areas). When the lesions are anechoic, they can mimic fluid collections. Diffuse forms of presentation may show single or multiple locations and anechoic or hypoechoic plaque-like structures. Subcutaneous panniculitic T-cell lymphoma (STCL) can present with prominent and hyperechoic fatty lobules as well as anechoic or hypoechoic septa in the subcutaneous tissue. The latter form of presentation (STCL) may mimic cellulitis. The vascularity is variable and can go from hypovascular to hypervascular (63, 64) (Figs. 9.21, 9.22, 9.23, and 9.24).

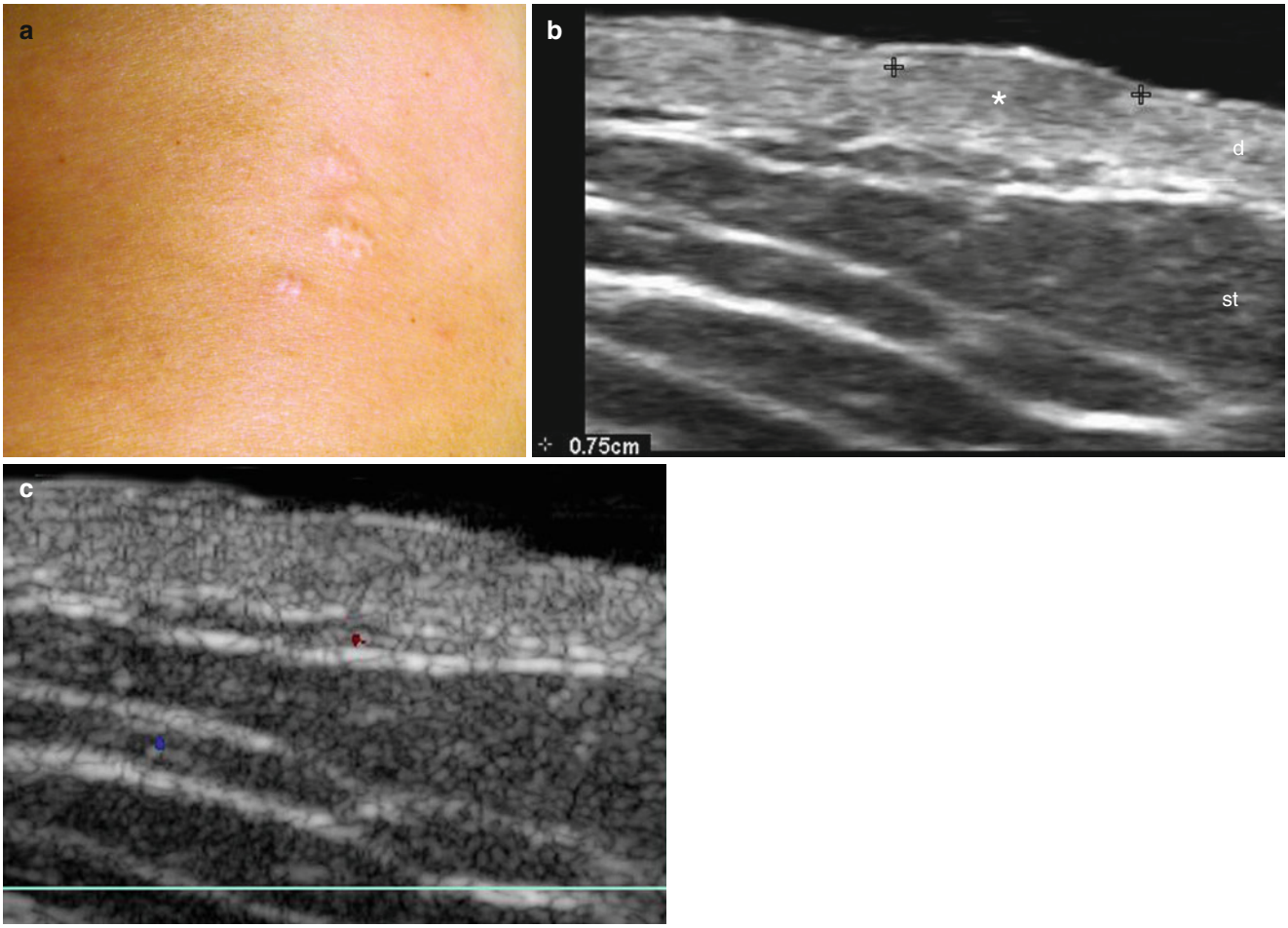

Fig. 9.21 (**a**–**c**) Cutaneous lymphoma (mycosis fungoides). (**a**) Clinical image shows hypopigmented lumps in the left side of the anterior aspect of the thoracic region. (**b**) Grey scale ultrasound image (longitudinal view) demonstrates 0.75 cm ill-defined hypoechoic and heterogeneous structure (*) in the dermis. (**c**) Color Doppler ultrasound image (longitudinal view) demonstrates no signs of hypervascularity in the lesional region

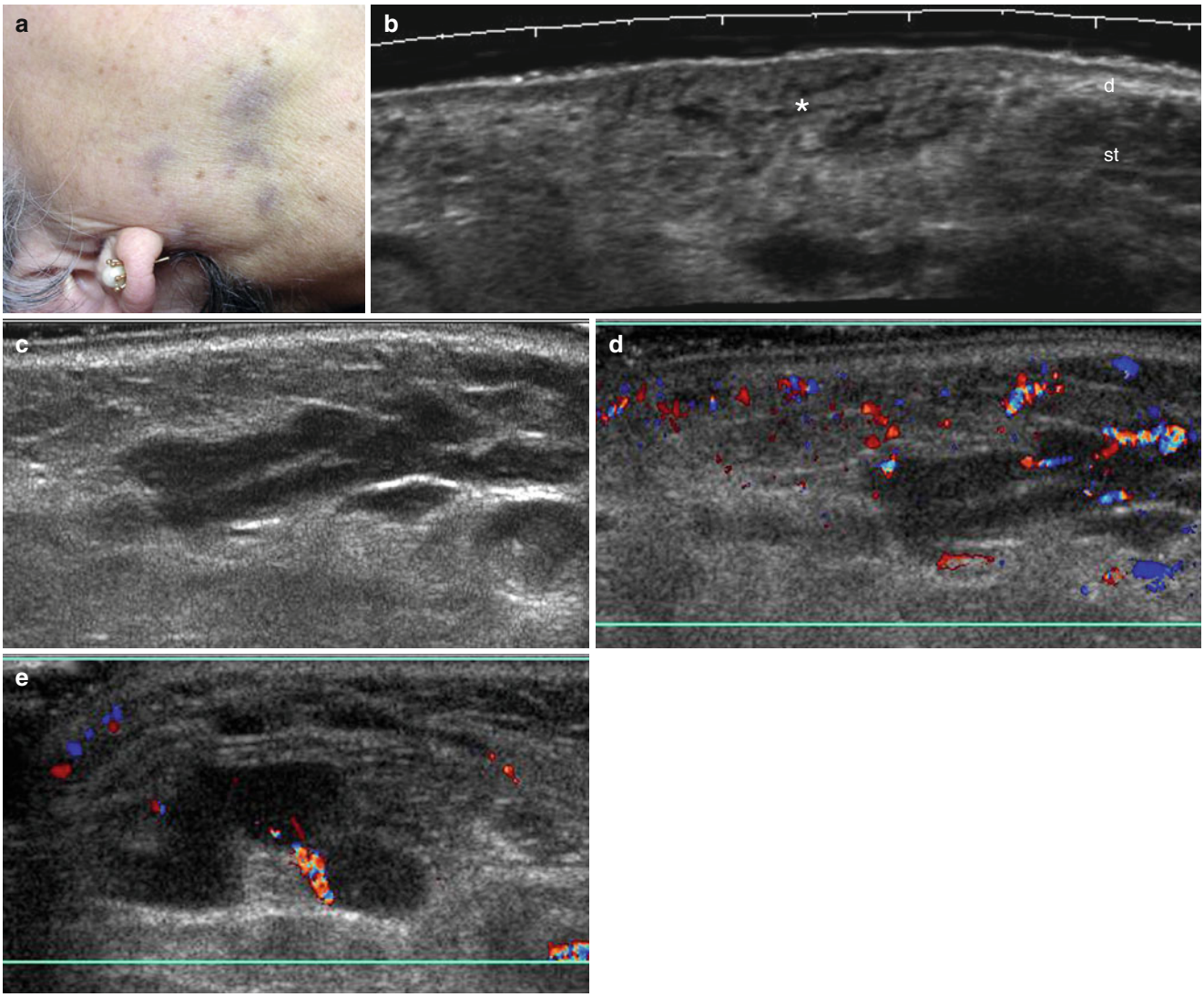

Fig. 9.22 (**a**–**e**) Cutaneous lymphoma. (**a**) Clinical photograph shows purple bruise-like lesions in the right mandible and neck regions. (**b**) Grey scale ultrasound image (transverse view) demonstrates ill-defined heterogeneous echogenicity area (*) in the dermis and subcutaneous tissue. (**c**) Grey scale ultrasound image (longitudinal view) presents hypoechoic plaque-like structures in the subcutaneous tissue. (**d**) Color Doppler ultrasound image (longitudinal view) shows increased vascularity in the lesional region. (**e**) Color Doppler ultrasound image (transverse view, neck region) demonstrates oval-shaped hypoechoic nodules with loss of the hyperechoic center and compatible with infiltrated lymphadenopathies

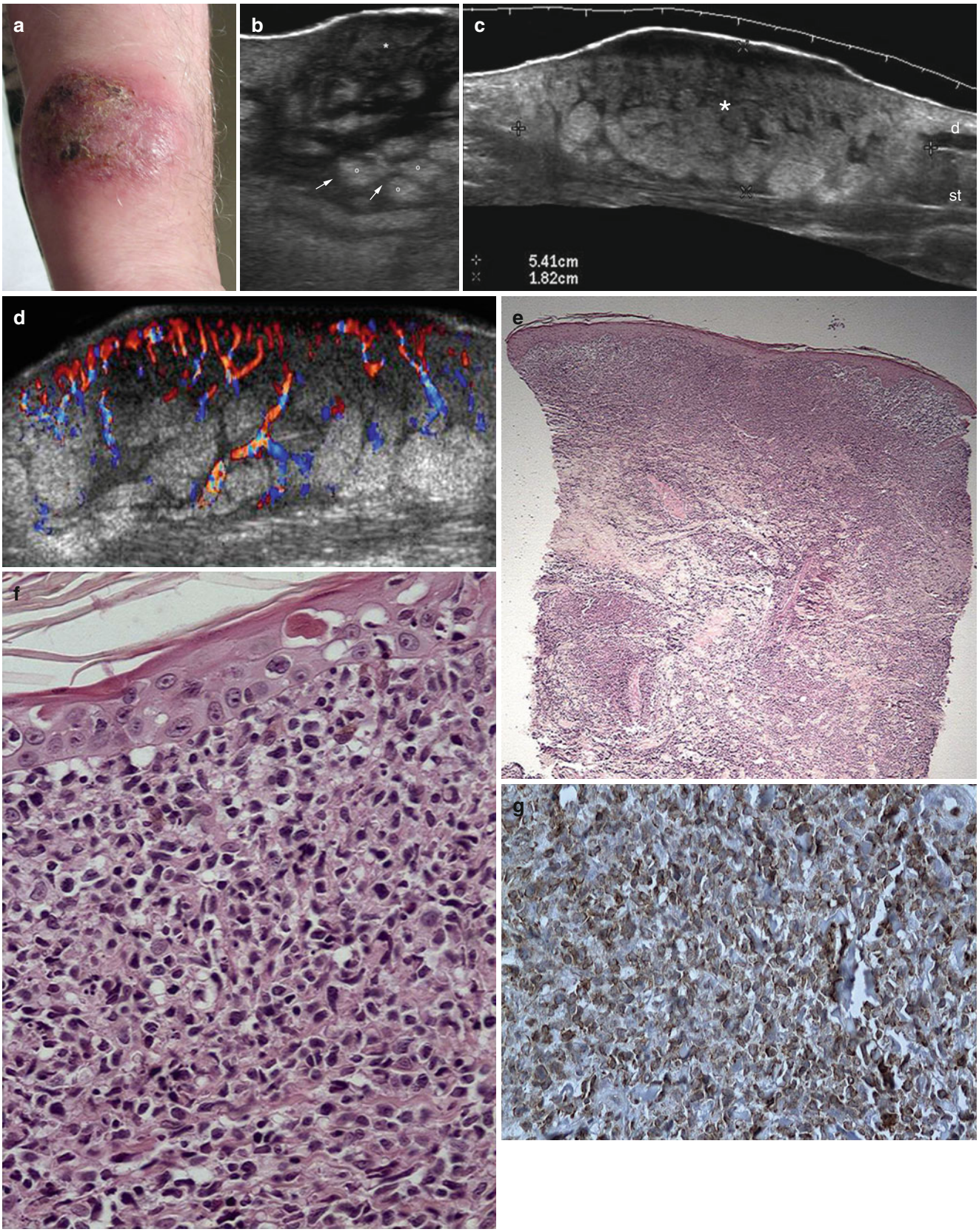

Fig. 9.23 (**a**–**g**) Subcutaneous panniculitic T-cell lymphoma. (**a**) Clinical photograph shows a crusty and erythematous lesion in the left arm. (**b**, **c**) Grey scale ultrasound images (**b** zoomed and **c** extended field of longitudinal views) demonstrats a 5.41 × 1.82 cm focal area (*, between markers) that presents increased thickness of the dermis and subcutaneous tissue with hypoechogenicity of the dermis and hyperechogenicity of the subcutaneous tissue. Notice the prominent and hyperechoic fatty lobules (o) and the thick and hypoechoic septa (*arrows*) in the subcutaneous tissue with a "cobblestone" appearance. (**d**) Color Doppler ultrasound image (longitudinal view) shows increased vascularity in the lesional region. (**e**, **f**) Histology (e: HE ×20 zoom; f: HE ×40 zoom) demonstrates a dense infiltrate with atypical lymphoid cells. (**g**) Immunohistochemistry (400× zoom) shows CD 3 positive T-lymphoid cells

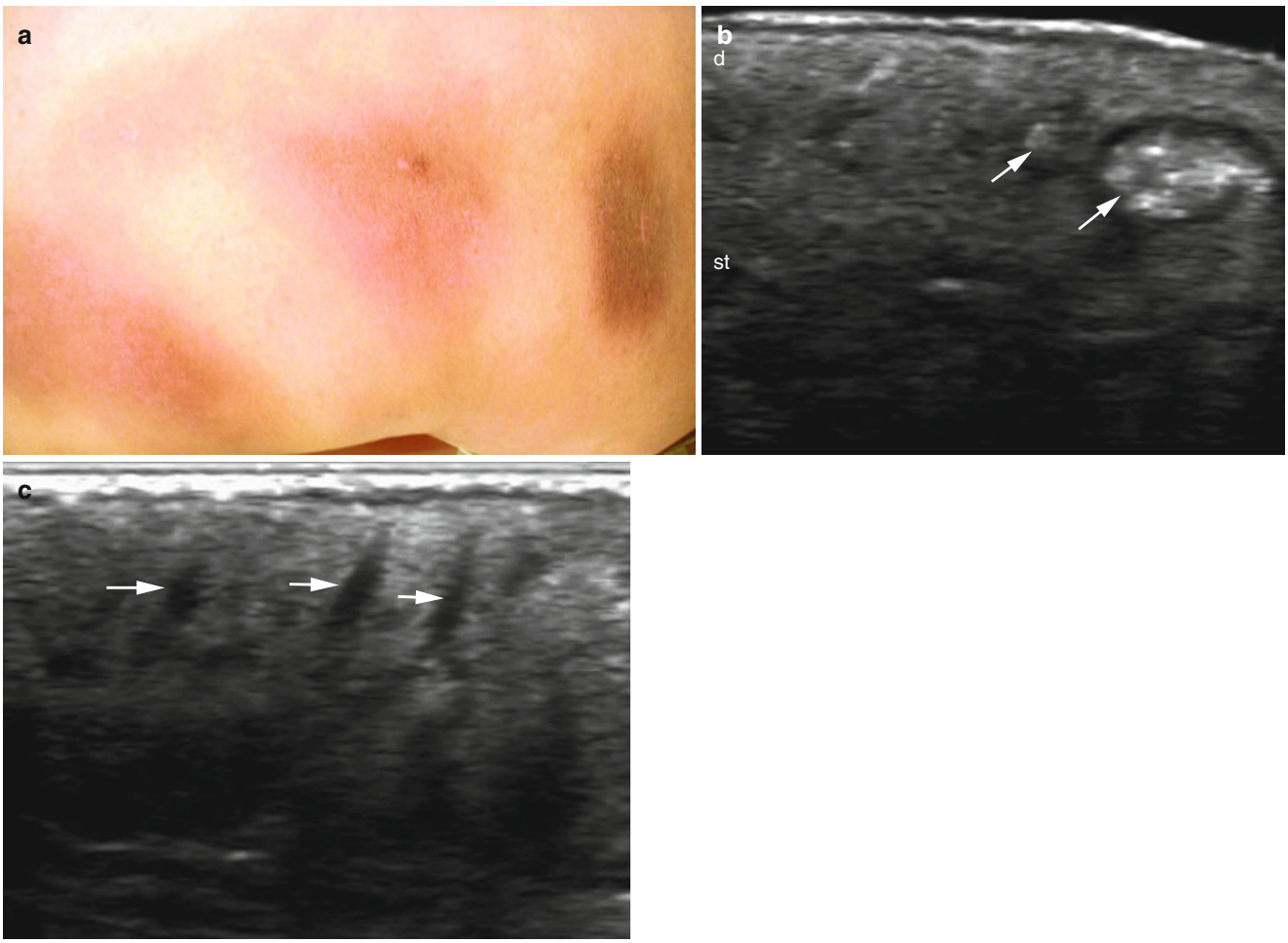

Fig. 9.24 (**a**–**c**) Folliculotropic mycosis fungoides (FMF). (**a**) Clinical photograph shows erythematous and slightly pigmented indurations in the dorsal region. (**b**, **c**) Grey scale ultrasound images (transverse views) demonstrate round and oval-shaped, hyperechoic deposits (*arrows*) attached to the dermal hair follicles (Figure b). Notice that the hair follicles are also enlarged (*arrows* in figure c)

References

1. Hong H, Sun J, Cai W. Anatomical and molecular imaging of skin cancer. Clin Cosmet Investig Dermatol. 2008;1:1–17.
2. Bartoš V, Pokorný D, Zacharová O, Haluska P, Doboszová J, Kullová M, et al. Recurrent basal cell carcinoma: a clinicopathological study and evaluation of histomorphological findings in primary and recurrent lesions. Acta Dermatovenerol Alp Panonica Adriat. 2011;20:67–75.
3. Goto M, Kai Y, Arakawa S, Oishi M, Ishikawa K, Anzai S, et al. Analysis of 256 cases of basal cell carcinoma after either one-step or two-step surgery in a Japanese institution. J Dermatol. 2012;39:68–71.
4. Brenn T, Mc Kee P. Tumors of the surface epithelium. In: Mc Kee P, Calonje E, Granter S, editors. Pathology of the skin with clinical correlations. 3rd ed. Philadelphia: Elsevier/Mosby; 2005. p. 1167–82.
5. Samarasinghe V, Madan V, Lear JT. Management of high-risk squamous cell carcinoma of the skin. Expert Rev Anticancer Ther. 2011;11:763–9.
6. Veness MJ. High-risk cutaneous squamous cell carcinoma of the head and neck. J Biomed Biotechnol. 2007;2007(3):80572.
7. Brenn T, Mc Kee P. Tumors of the surface epithelium. In: Mc Kee P, Calonje E, Granter S, editors. Pathology of the skin with clinical correlations. 3rd ed. Philadelphia: Elsevier/Mosby; 2005. p. 1199–228.
8. Gniadecki R, Normal DT. Basal cell carcinoma—clinical guidelines, Danish dermatological society. Forum for Nord Derm Ven. 2009;14(1):4–6.
9. Zavos G, Karidis NP, Tsourouflis G, Bokos J, Diles K, Sotirchos G, et al. Nonmelanoma skin cancer after renal transplantation: a single-center experience in 1736 transplantations. Int J Dermatol. 2011;50:1496–500.
10. Yuen WY, Jonkman MF. Risk of squamous cell carcinoma in junctional epidermolysis bullosa, non-Herlitz type: report of 7 cases and a review of the literature. J Am Acad Dermatol. 2011;65:780–9.
11. Huang L, Wong YP, Burd A. A novel homozygous splice site mutation in COL7A1 in a Chinese patient with severe recessive dystrophic epidermolysis bullosa and squamous cell carcinoma. Int J Dermatol. 2011;50:52–6.
12. Bobadilla F, Wortsman X, Muñoz C, Segovia L, Espinoza M, Jemec GB. Pre-surgical high resolution ultrasound of facial basal cell carcinoma: correlation with histology. Cancer Imaging. 2008;8:163–72.

13. Uhara H, Hayashi K, Koga H, Saida T. Multiple hypersonographic spots in basal cell carcinoma. Dermatol Surg. 2007;33:1215–9.
14. Ekwueme DU, Guy G, Li C, Rim SH, Parelkar P, Chen SC. The health burden and economic costs of cutaneous melanoma mortality by race/ethnicity-United States, 2000 to 2006. J Am Acad Dermatol. 2011;6(S1):S133–43.
15. Reintgen DS, Vollmer R, Tso CY, Seigler HF. Prognosis for recurrent stage I malignant melanoma. Arch Surg. 1987;122:1338–42.
16. Nazarian LN, Alexander AA, Kurtz AB, Capuzzi Jr DM, Rawool NM, Gilbert KR, et al. Superficial melanoma metastases: appearances on gray-scale and color Doppler sonography. AJR Am J Roentgenol. 1998;170:459–63.
17. Netscher DT, Leong M, Orengo I, Yang D, Berg C, Krishnan B. Cutaneous malignancies: melanoma and nonmelanoma types. Plast Reconstr Surg. 2011;127:37e–56.
18. McKee P, Calonje E, Granter S. Melanoma. In: MacKee P Calonje E, Granter S. editors. Pathology of the skin with clinical correlations. 3rd ed. Philadelphia: Elsevier/Mosby; 2005. p. 1309–56.
19. Wortsman X. Sonography of the primary cutaneous melanoma: a review. Radiol Res Pract. 2012;2012:814396.
20. Tacke J, Haagen G, Horstein O, Huettinger G, Kiesewetter F, Schell H, et al. Clinical relevance of sonometry-derived tumour thickness in malignant melanoma—a statistical analysis. Br J Dermatol. 1995;132:209–14.
21. Guitera P, Li LX, Crotty K, Fitzgerald P, Mellenbergh R, Pellacani G, et al. Melanoma histological Breslow thickness predicted by 75-MHz ultrasonography. Br J Dermatol. 2008;159:364–9.
22. Hoffmann K, Jung J, el Gammal S, Altmeyer P. Malignant melanoma in 20-MHz B scan sonography. Dermatology. 1992;185:49–55.
23. Kaikaris V, Samsanavičius D, Maslauskas K, Rimdeika R, Valiukevičienė S, Makštienė J, et al. Measurement of melanoma thickness–comparison of two methods: ultrasound versus morphology. J Plast Reconstr Aesthet Surg. 2011;64:796–802.
24. Catalano O, Siani A. Cutaneous melanoma: role of ultrasound in the assessment of locoregional spread. Curr Probl Diagn Radiol. 2010;39:30–6.
25. Vilana R, Puig S, Sanchez M, Squarcia M, Lopez A, Castel T, et al. Preoperative assessment of cutaneous melanoma thickness using 10-MHz sonography. AJR Am J Roentgenol. 2009;193:639–43.
26. Music MM, Hertl K, Kadivec M, Pavlović MD, Hocevar M. Preoperative ultrasound with a 12–15 MHz linear probe reliably differentiates between melanoma thicker and thinner than 1 mm. J Eur Acad Dermatol Venereol. 2010;24:1105–8.
27. Lassau N, Mercier S, Koscielny S, Avril MF, Margulis A, Mamelle G, et al. Prognostic value of high-frequency sonography and color doppler sonography for the preoperative assessment of melanomas. AJR Am J Roentgenol. 1999;172:457–61.
28. Lassau N, Koscielny S, Avril MF, Margulis A, Duvillard P, De Baere T, et al. Prognostic value of angiogenesis evaluated with high-frequency and color Doppler sonography for preoperative assessment of melanomas. AJR Am J Roentgenol. 2002;178:1547–51.
29. Lassau N, Spatz A, Avril MF, Tardivon A, Margulis A, Mamelle G, et al. Value of high-frequency US for preoperative assessment of skin tumors. Radiographics. 1997;17:1559–65.
30. Voit C, Van Akkooi AC, Schäfer-Hesterberg G, Schoengen A, Kowalczyk K, Roewert JC, et al. Ultrasound morphology criteria predict metastatic disease of the sentinel nodes in patients with melanoma. J Clin Oncol. 2010;28:847–52.
31. Nazarian LN, Alexander AA, Rawool NM, Kurtz AB, Maguire HC, Mastrangelo MJ. Malignant melanoma: impact of superficial US on management. Radiology. 1996;199:273–7.
32. Catalano O, Voit C, Sandomenico F, Mandato Y, Petrillo M, Franco R, et al. Previously reported sonographic appearances of regional melanoma metastases are not likely due to necrosis. J Ultrasound Med. 2011;30:1041–9.
33. Tombesi P, Tassinari D, Sartori S. Contrast-enhanced ultrasound for characterizing lymph nodes with focal cortical thickening in patients with cutaneous melanoma. AJR Am J Roentgenol. 2011;197:W371.
34. Rubaltelli L, Beltrame V, Tregnaghi A, Scagliori E, Frigo AC, Stramare R. Contrast-enhanced ultrasound for characterizing lymph nodes with focal cortical thickening in patients with cutaneous melanoma. AJR Am J Roentgenol. 2011;196:W8–12.
35. Lassau N, Chami L, Chebil M, Benatsou B, Bidault S, Girard E, et al. Dynamic contrast-enhanced ultrasonography (DCE-US) and anti-angiogenic treatments. Discov Med. 2011;11:18–24.
36. Forsberg F, Ro RJ, Liu JB, Lipcan KJ, Potoczek M, Nazarian LN. Monitoring angiogenesis in human melanoma xenograft model using contrast-enhanced ultrasound imaging. Ultrason Imaging. 2008;30:237–46.
37. Goldberg BB, Merton DA, Liu JB, Forsberg F, Zhang K, Thakur M, et al. Contrast-enhanced ultrasound imaging of sentinel lymph nodes after peritumoral administration of Sonazoid in a melanoma tumor animal model. J Ultrasound Med. 2011;30:441–53.
38. Bhatia KS, Yuen EH, Cho CC, Tong CS, Lee YY, Ahuja ATA. Pilot study evaluating real-time shear wave ultrasound elastography of miscellaneous non-nodal neck masses in a routine head and neck ultrasound clinic. Ultrasound Med Biol. 2012;38:933–42.
39. Hinz T, Wenzel J, Schmid-Wendtner MH. Real-time tissue elastography: a helpful tool in the diagnosis of cutaneous melanoma? J Am Acad Dermatol. 2011;65:424–6.
40. Kirkpatrick SJ, Wang RK, Duncan DD, Kulesz-Martin M, Lee K. Imaging the mechanical stiffness of skin lesions by in vivo acousto-optical elastography. Opt Express. 2006;14:9770–9.
41. Rouffiac V, Duret JS, Péronneau P, Dehez N, Opolon P, Roche A, et al. Combination of HIFU therapy with contrast-enhanced sonography for quantitative assessment of therapeutic efficiency on tumor grafted mice. Ultrasound Med Biol. 2006;32:729–40.
42. Xing Y, Lu X, Pua EC, Zhong P. The effect of high intensity focused ultrasound treatment on metastases in a murine melanoma model. Biochem Biophys Res Commun. 2008;375:645–50.
43. Oliveira-Soares R, Viana I, Vale E, Soares-Almeida LM, Picoto A. Dermatofibrosarcoma protuberans: a clinicopathological study of 20 cases. J Eur Acad Dermatol Venereol. 2002;16:441–6.
44. Nouri K, Lodha R, Jimenez G, Robins P. Mohs micrographic surgery for dermatofibrosarcoma protuberans: University of Miami and NYU experience. Dermatol Surg. 2002;28:1060–4.
45. Thornton SL, Reid J, Papay FA, Vidimos AT. Childhood dermatofibrosarcoma protuberans: role of preoperative imaging. J Am Acad Dermatol. 2005;53:76–83.
46. Shin YR, Kim JY, Sung MS, Jung JH. Sonographic findings of dermatofibrosarcoma protuberans with pathologic correlation. J Ultrasound Med. 2008;27:269–74.
47. Donghi D, Kerl K, Dummer R, Schoenewolf N, Cozzio A. Cutaneous angiosarcoma: own experience over 13 years. Clinical features, disease course and immunohistochemical profile. J Eur Acad Dermatol Venereol. 2010;24:1230–4.
48. Wollina U, Hansel G, Schönlebe J, Averbeck M, Paasch U, Uhl J, et al. Cutaneous angiosarcoma is a rare aggressive malignant vascular tumour of the skin. J Eur Acad Dermatol Venereol. 2011;25:964–8.
49. Morgan MB, Swann M, Somach S, Eng W, Smoller B. Cutaneous angiosarcoma: a case series with prognostic correlation. J Am Acad Dermatol. 2004;50:867–74.
50. Kamo R, Ishii M. Histological differentiation, histogenesis and prognosis of cutaneous angiosarcoma. Osaka City Med J. 2011;57:31–44.
51. Costache M, Ene AM, Simionescu O, Sajin M. Histopathological diagnosis of cutaneous vascular sarcomas. Rom J Morphol Embryol. 2010;51:105–9.
52. Gasparetto TD, Marchiori E, Lourenço S, Zanetti G, Vianna AD, Santos AA, et al. Pulmonary involvement in Kaposi sarcoma: correlation between imaging and pathology. Orphanet J Rare Dis. 2009;4:18.

53. Restrepo CS, Ocazionez D. Kaposi's sarcoma: imaging overview. Semin Ultrasound CT MR. 2011;32:456–69.
54. Requena L, Requena C. Histopathology of the more common viral skin infections. Actas Dermosifiliogr. 2010;101:201–16.
55. Solivetti FM, Elia F, Latini A, Cota C, Cordiali-Fei P, Di Carlo A. AIDS-kaposi sarcoma and classic kaposi sarcoma: are different ultrasound patterns related to different variants? J Exp Clin Cancer Res. 2011;30:40.
56. Haddow LJ, Davies S, Buckingham S, Miller RF. Kaposi's sarcoma infiltrating skeletal muscle. Sex Transm Infect. 2002;78:464–5.
57. Bogner JR, Zietz C, Held M, Späthling S, Sandor P, Kronawitter U, et al. Ultrasound as a tool to evaluate remission of cutaneous Kaposi's sarcoma. AIDS. 1993;7:1081–5.
58. Duprat JP, Landman G, Salvajoli JV, Brechtbühl ER. A review of the epidemiology and treatment of Merkel cell carcinoma. Clinics (Sao Paulo). 2011;66:1817–23.
59. Nicolaidou E, Mikrova A, Antoniou C, Katsambas AD. Advances in Merkel cell carcinoma pathogenesis and management: a recently discovered virus, a new international consensus staging system and new diagnostic codes. Br J Dermatol. 2012;166:16–21.
60. Pileri Jr A, Patrizi A, Agostinelli C, Neri I, Sabattini E, Bacci F, et al. Primary cutaneous lymphomas: a reprisal. Semin Diagn Pathol. 2011;28:214–33.
61. Galper SL, Smith BD, Wilson LD. Diagnosis and management of mycosis fungoides. Oncology (Williston Park). 2010;24: 491–501.
62. McKee P, Calonje E, Granter S. Cutaneous lymphoproliferative diseases and related disorders. In: MacKee P Calonje E, Granter S, editors. Pathology of the skin with clinical correlations. 3rd ed. Philadelphia: Elsevier/Mosby; 2005. p. 1357–457.
63. Oztürk E, Sipahioglu S, Han U, Yücesoy C, Dilli A, Hekimoğlu B. Ultrasonography and MRI findings of cutaneous B-cell lymphoma, leg type. JBR-BTR. 2011;94:81–2.
64. Ushiki T, Nikkuni K, Higuchi T, Takai K. Multimodality imaging of subcutaneous panniculitis-like T-cell lymphoma. Intern Med. 2011;50:1265.

Contrast Enhanced Ultrasound in Squamous Cell Carcinoma

10

Marcio Bouer

Contents

10.1 Introduction

Squamous cell carcinoma (SCC) is a cutaneous malignant neoplasm derived from epidermal suprabasal keratinocytes. The incidence of this tumor is estimated to be 200,000 new cases per year in the U.S. The most affected group of individuals are at the approximate age group of 40 years, with the largest predisposing factor being sun exposure throughout life. In addition to ultraviolet radiation, other related factors are ionizing radiation, environmental carcinogens, immunosuppression, scars, burns, chronic exposure to heat, inflammatory skin diseases, human papillomavirus, and genodermatosis.

Most SCCs occur from precursor lesions such as actinic keratosis and Bowen's disease (in situ SCC). The clinical presentation of these tumors varies, and their biological behavior, which can be only superficial invasion, demands easy care or deep invasion and metastasis, and therefore more complex treatment. The most common clinical forms are: erythematous keratotic papule or plaque, ulcer, nodule, cutaneous horn, warty, or abscess. Verrucous carcinoma and keratoacanthoma clinical forms are considered separately because of the peculiarity of biological behavior.

Lower lip squamous cell carcinoma (LLSCC) usually begins as actinic cheilitis or scaly leucoplakia with slow progression to a tumor nodule. It is related to sun exposure and cigarette smoking. LLSCC can have local invasion and present occasional metastases.

The characteristic histopathology of SCC is the presence of atypical keratinocytes beyond the basal membrane zone and within the dermis. The histological grade of SCC is based on the degree of cell differentiation. In 1932, Broders introduced a classification system based on the percentage of undifferentiated cells present in the tumor, which is still used currently (Table 10.1).

The risk of recurrence and metastasis is defined by the following factors listed: diameter greater than 2 cm, deeper than 4 mm; Clark level IV or V; tumor involvement of muscle, nerve, or bone; location on the lip or ear; tumor on the

M. Bouer, MD
Research Unit, Department of Radiology,
University of São Paulo Medical School,
São Paulo, São Paulo, Brazil

Department of Radiology, Fleury Laboratory,
São Paulo, São Paulo, Brazil

Instituto de Radiologia, Hospital das Clínicas Da
Universidade de São Paulo, Rua Senador Cesar Lacerda de Vergueiro,
511 ap 162, São Paulo, São Paulo, Brazil
e-mail: mbouer@gmail.com

X. Wortsman, G.B.E. Jemec (eds.), *Dermatologic Ultrasound with Clinical and Histologic Correlations*,
DOI 10.1007/978-1-4614-7184-4_10,

Table 10.1 Classification of borders

Grade	Undifferentiated cells (%)	Other features
1	<25	Keratinization
2	<50	
3	<75	
4	>75	Atypia, loss of intercellular bridges

scar; Broders grade 3 or 4; immunocompromised patient; or absence of inflammatory infiltrate.

The treatment of SCC is selected according to the risk of recurrence and metastasis. Ablative techniques such as electrocoagulation and curettage, cryosurgery with liquid nitrogen, CO2 laser, photodynamic therapy, and intralesional chemotherapy do not allow histological control of margins, and therefore are only suitable for SCC with low risk of recurrence and metastasis. Techniques of surgical excision are recommended for SCC with high risk of recurrence and metastasis and may be conventional excision or Moh's micrographic surgery, the latter being indicated in deeply infiltrating tumors; previously irradiated sites; involvement of muscle, nerve or bone; immunosuppression; recurrent tumor or very large, ill-defined margins; and preservation of important local tissue (nasal tip, lip, eyelid, ear, genitals).

The follow-up of patients with SCC should be every 3–12 months depending on the type of tumor, and the risk of the patient developing a new SCC is higher than that for the general population [1, 2].

10.2 Ultrasonography and Contrast-Enhanced Ultrasound

In the late 1970s, Alexander and Miller first used a high-frequency transducer (15 MHz) to generate images of the skin. Since then, progress in the development of transducers and equipment has allowed an increased application of ultrasound Doppler in the study of various skin diseases with satisfactory results in many cases.

Among the tumors studied, melanomas have received the most attention, mainly by their degree of malignancy and the importance of early diagnosis. In these tumors, determining the depth of the lesions has shown positive results and vascular mapping studied by the Doppler method, has shown an association with the degree of malignancy in preliminary studies [3, 4].

SCC has been studied by B-mode ultrasound and Doppler ultrasound in order to describe the morphological and topographic aspects and establish the degree of malignancy. The main results of such studies can be chronologically listed as follows:

- In 1993, with the use of a 20-MHz transducer, 45 malignant skin lesions were analyzed; three were SSCs that were hypoechogenic and with irregular contours and ten were considered SCC in situ (Bowen disease) with smaller thickness than the others, but also with irregular contours, two with mixed echogenicity and the others hypoechogenic; no features were found that might differentiate those tumors from other primary malignancies of the skin [5].
- In 1999, using transducers of different frequencies ranging from 5 MHz to 13 MHz, six SCCs were studied, with emphasis on the color Doppler analysis of the vascular mapping, with the following results: all the cases presented hypervascularization, three with multiple peripheral poles and three with internal vessels [6].
- In 2001, with the use of a 12-MHz transducer and carrying out vascular mapping with color Doppler before and after intravenous contrast injection (LevovistR), 81 skin tumors were evaluated, among which ten were SCCs. The study showed better visualization of the internal vasculature of the tumors with the use of the Doppler and contrast media; more evident neovascularization in malignant tumors than in the benign ones; and difficulty differentiating the hypervascularization of the tumors from the inflammatory lesions [7].
- In 2001, with the use of a 10-MHz transducer and vascular mapping with "Power" Doppler, 71 cases of skin tumors other than melanoma were evaluated, among which 15 were SCCs, with the following results: presence of mixed vascularization in all the cases. The pattern of tumoral vascularization was significantly correlated only with the thickness of the tumor, showing that mixed and peripheral patterns of vascularization occur more frequently in malignant tumors [8].
- A problem related to SCC studies is that the hyperkeratotic epidermis in these tumors could turn totally reflexive, preventing the passage of sound beam [9].
- Experimental SCC was induced subcutaneously in 16 nude mice. Centrally located vessels were found in 12 tumors using color-coded sonography. Histology, however, showed their presence in all 16 tumors. Interestingly, the failure of sonography in detecting vessels did not

correlate with tumor size. It seemed that the detection of such vessels was particularly difficult in those tumors that grew very fast [10].

10.3 Microbubble Contrast

Discovered by Raymond Gramiak at the end of the decade in 1960 during studies on the heart, the contrast with microbubbles in ultrasound has been improved by at least three decades [11]. They consist of stabilized microbubbles for different substances and have the advantage of being eliminated by breath staying longer in circulation. The development of new methods for evaluating contrast on ultrasound such as harmonics (harmonic pulse inverted and second harmonic), has allowed a more powerful effect of sonography for enhancing resolution in vascular studies [12, 13]. Normally, the microbubbles oscillate in response to external stimuli (sound) during scanning, in a nonlinear way enabling the use of nonlinear techniques such as harmonics, to better detect the microbubbles specifically. The effect on the behavior of microbubbles is dependent on the sound pressure created by the ultrasonic beam. Generally, the increase in pressure causes increased reflection, then increased vibration, and finally the rupture of microbubbles, however, this behavior change may induce undesirable effects. The level of mechanical index is responsible for the pressure in the microbubbles and therefore its behavior, as well as the properties of the contrast agent and image mode selected [14]. Several studies were published with different types of contrast microbubbles in ultrasound, however the ESDP (Perfluorpropane-Exposed Sonicated Dextrose Albumin) is currently the most widely accepted [13]. The ESDP is composed of a mixture of 5 % dextrose and 5 % saline human albumin solution added to perfluorpropane gas. The average size of the microbubbles is 4.65 μm and the concentration is 1.46 × 10(9) bubbles/ml.

To date there are no reports in the literature on the isolated assessment of SCC of the skin to ultrasound with Doppler and with contrast and their association with histological findings.

We conducted a study to determine the value of ultrasound using a commercial transducer in the preoperative evaluation of SCC of the skin and to evaluate the usefulness of microbubble contrast and Doppler ultrasound to determine a classification of different types of vascularization of SCC, correlating them with histological findings.

Between 2006 and 2007 were performed ultrasound examinations for evaluation of nodules with clinical suspicion of squamous cell and later proven by pathologic SCC of the skin. The device used was a multifrequency linear transducer of 5–12 MHz and adjusted only for skin assessment. For evaluation of the lesions, a gel layer interposed between the skin and the transducer was used, necessary and sufficient to obtain the best focus of the injury with minimal pressure applied with the transducer over the region under study to avoid changes in measurements.

The survey had the following sequence: first B-mode evaluation of contours, echogenicity, morphology and dimensions; then with the pulsed Doppler resistivity index, with color Doppler, the presence or absence of vascularization, the type of vascularity (peripheral, central or mixed), presence of tortuous vessels and vascular density. After the administration of a microbubble contrast agent that was injected in bolus into a peripheral vein (4 ml), followed by a "flush" of 10 ml of saline, a color Doppler analysis was made for the presence or absence of vascularization, the type of vascularity (peripheral, central or mixed), presence of tortuous vessels, and vascular density.

We saw that the tumor was always evident on ultrasound, as well as the affected regions, borders, echotexture, and size; factors that assist in surgical planning. We noticed an improvement in the view of the vascularization of tumors with the use of contrast. Perhaps the best sensitivity of the new devices with the use of Doppler ultrasound can make it possible to verify a small vessel without the use of contrast. A fact that may represent little improvement in the assessment of vascularity after contrast in some cases is the fugacity of the contrast in these superficial tumors.

Comparing the measurements of the dimensions of the tumors with the clinical pathology, there was poor consistency and agreement in all lines studied which can be related to the inability to fully separate the tumor from the non-tumoral tissue, which is associated with the axial resolution of the transducers.

Testing for the analysis of resistivity index according to the anatomic classification showed a p value of 0.024, with the following average values for grade 1, 0.64; for grade 2, 0.69; and for grade 3, 0.60; concluding that there is significant differentiation between the resistivity indices. Obviously, as the number of cases is reduced, this variation should be further investigated (Figs. 10.1a–f, 10.2a–f, 10.3a–f, 10.4a–f, and 10.5a–e).

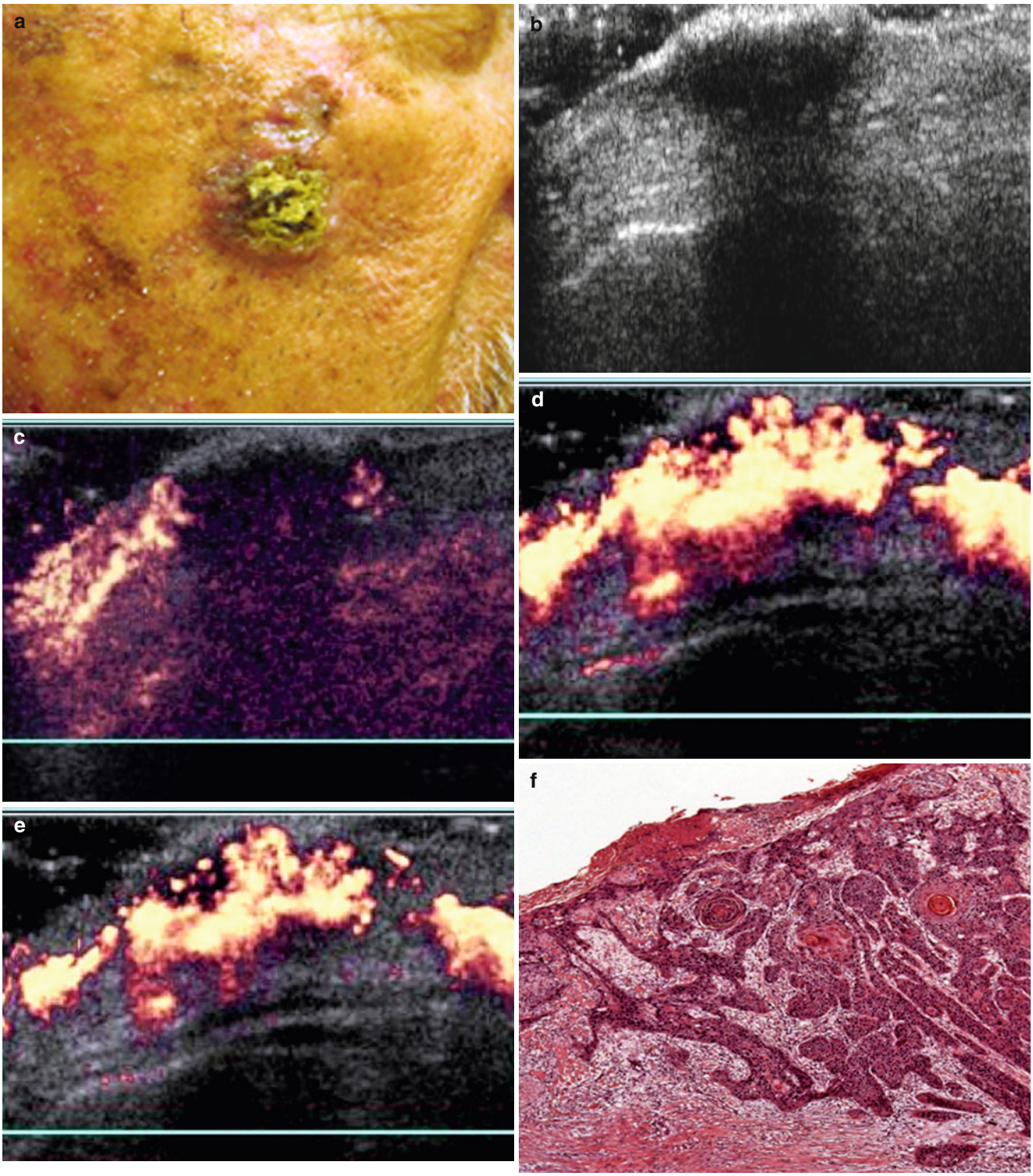

Fig. 10.1 (**a**) Squamous cell carcinoma in malar region. (**b**) Grey scale ultrasonography—Lesion partially characterizated with attenuation of sound beam caused by hyperkeratosis. (**c**) Power Doppler ultrasound image before contrast. (**d**, **e**) Power Doppler ultrasound image after contrast—lesion better seen after contrast, hypervascularizated. (**f**) Histological aspect

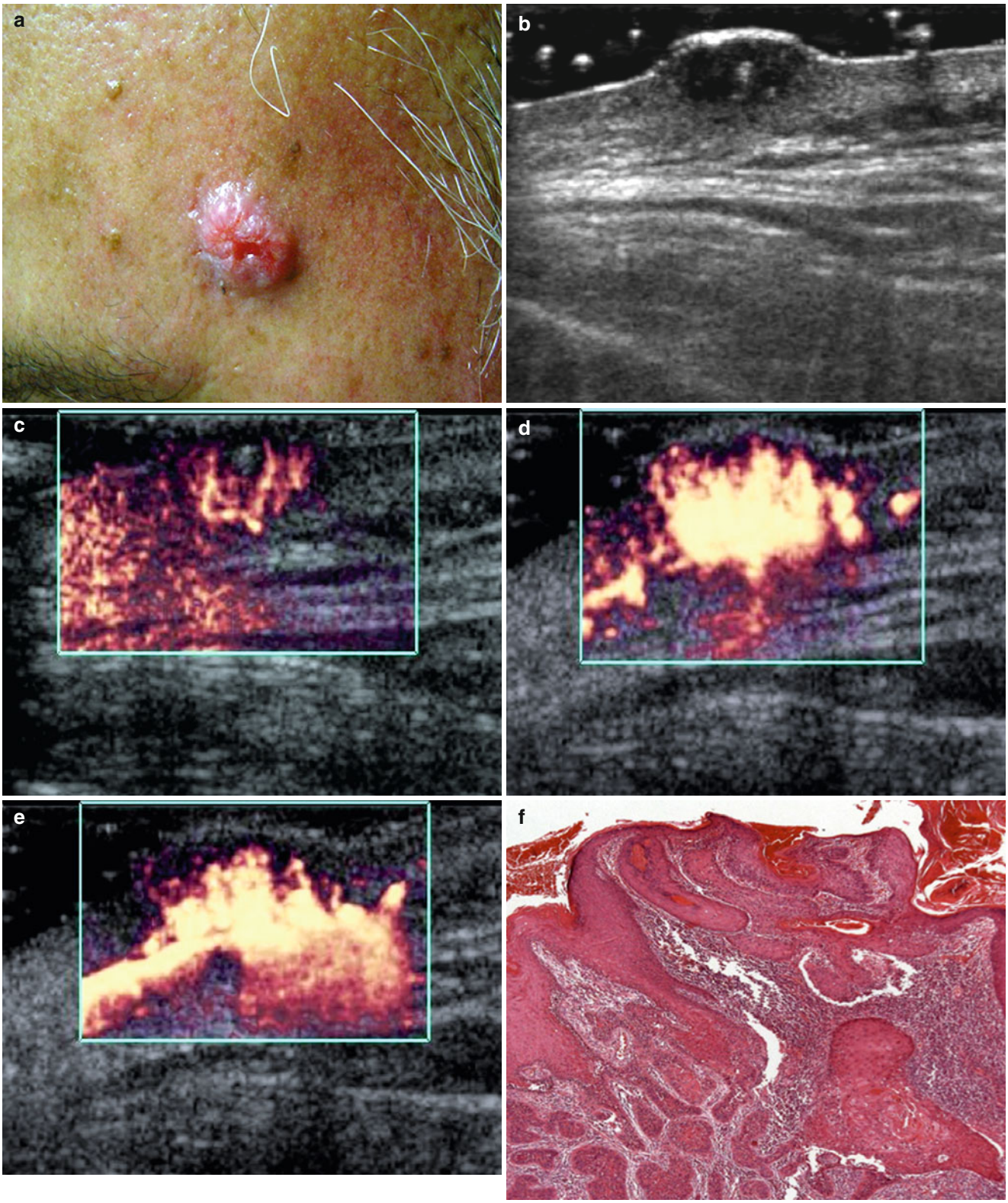

Fig. 10.2 (**a**) Squamous cell carcinoma in temporal region. (**b**) Grey scale ultrasound image—Lesion occupying dermis. (**c**) Power Doppler ultrasound image before contrast—some vessels seen in central region. (**d**, **e**) Power Doppler ultrasound image after contrast—lesion better seen after contrast, hypervascularizated. (**f**) Histological aspect

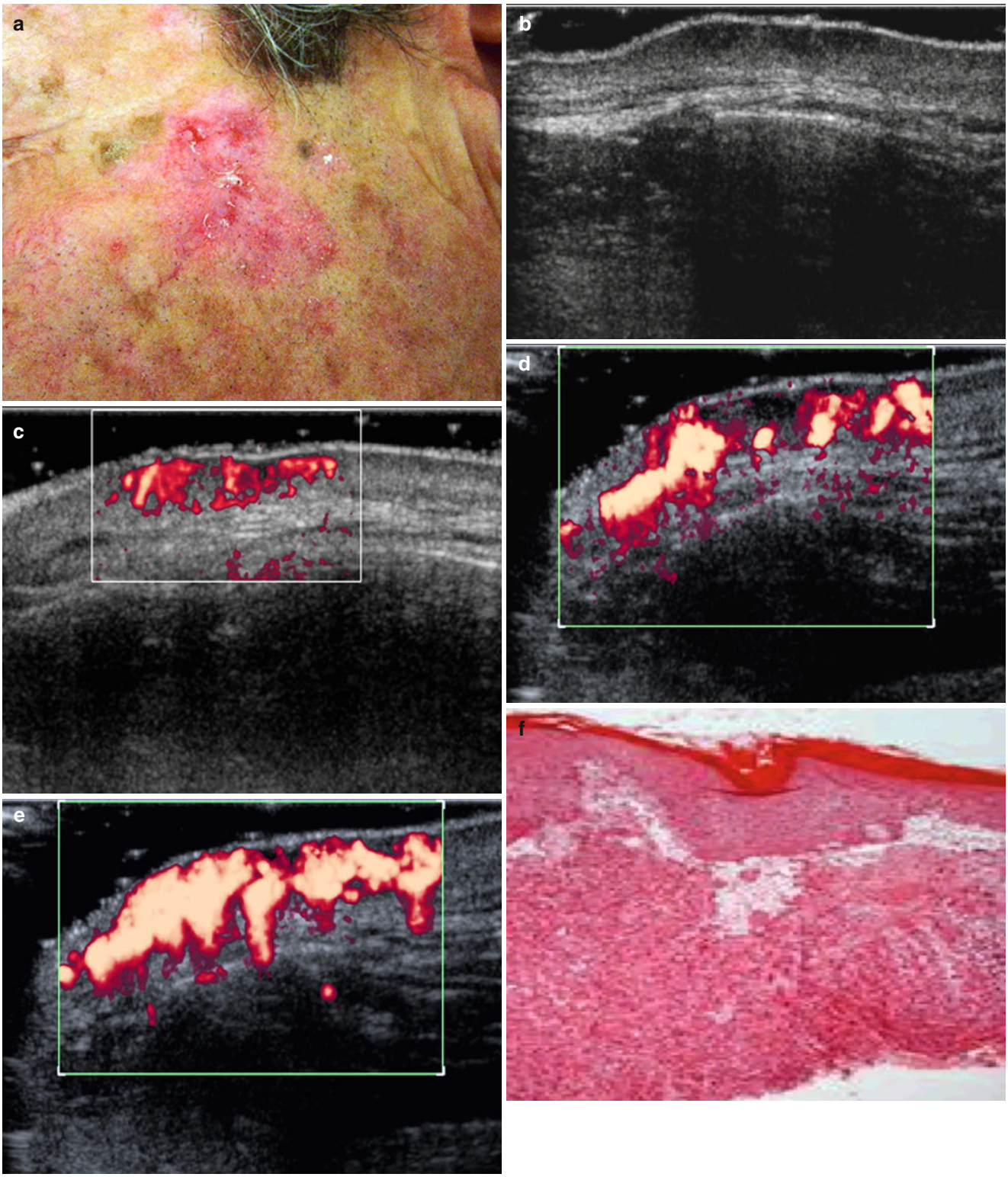

Fig. 10.3 (**a**) Squamous cell carcinoma in malar region. (**b**) Grey scale ultrasound image—Lesion occupying dermis. (**c**) Power Doppler ultrasound image before contrast—some vessels seen in central and peripheric region. (**d**, **e**) Power Doppler ultrasound image after contrast—lesion better seen after contrast, hypervascularizated. (**f**) Histological aspect

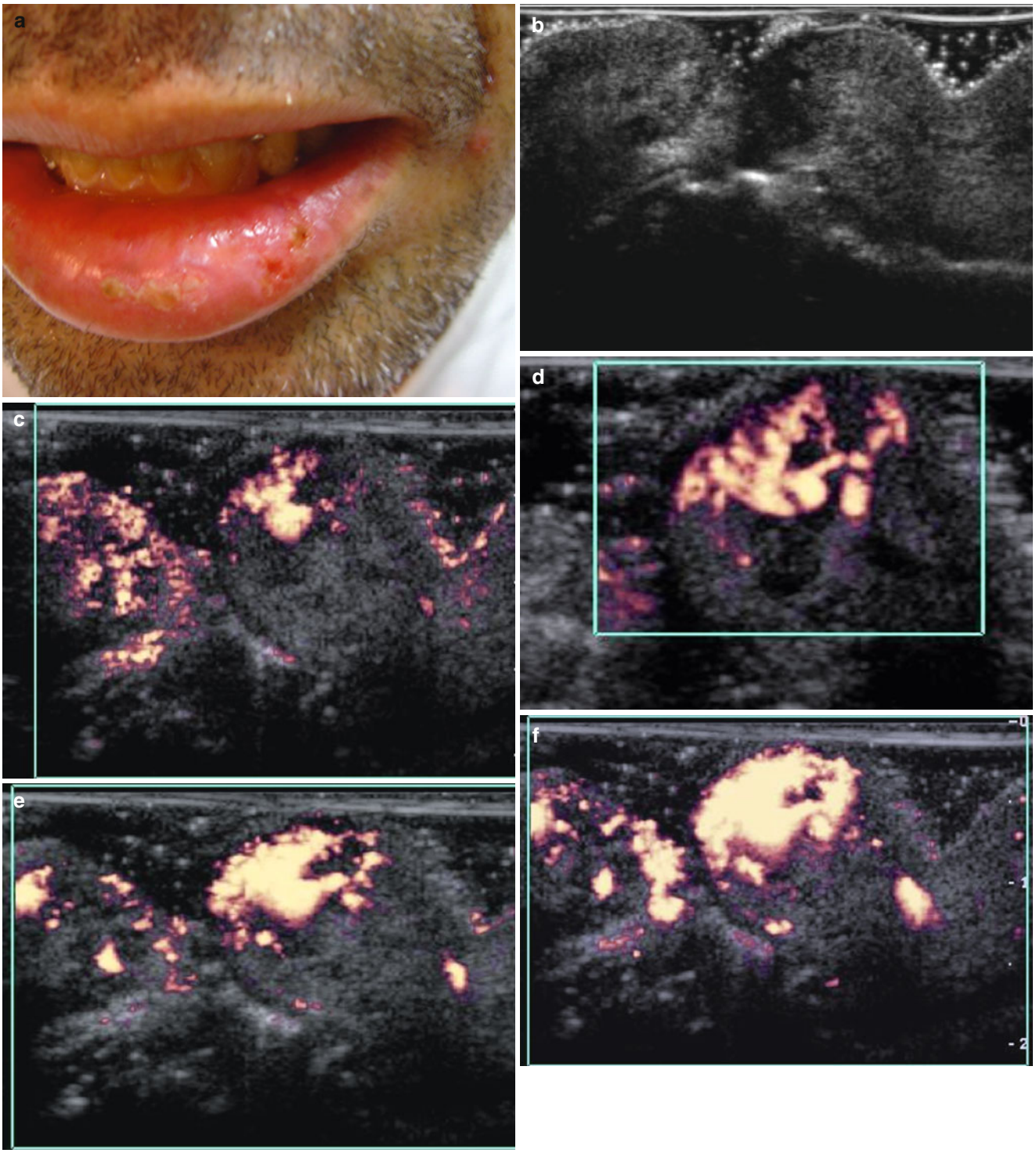

Fig. 10.4 (**a**) Lower lip squamous cell carcinoma. (**b**) Grey scale ultrasound image. (**c**, **d**) Power Doppler ultrasound image before contrast—some vessels seen in central region. (**e**, **f**) Power Doppler ultrasound image after contrast—lesion better seen after contrast, hypervascularized

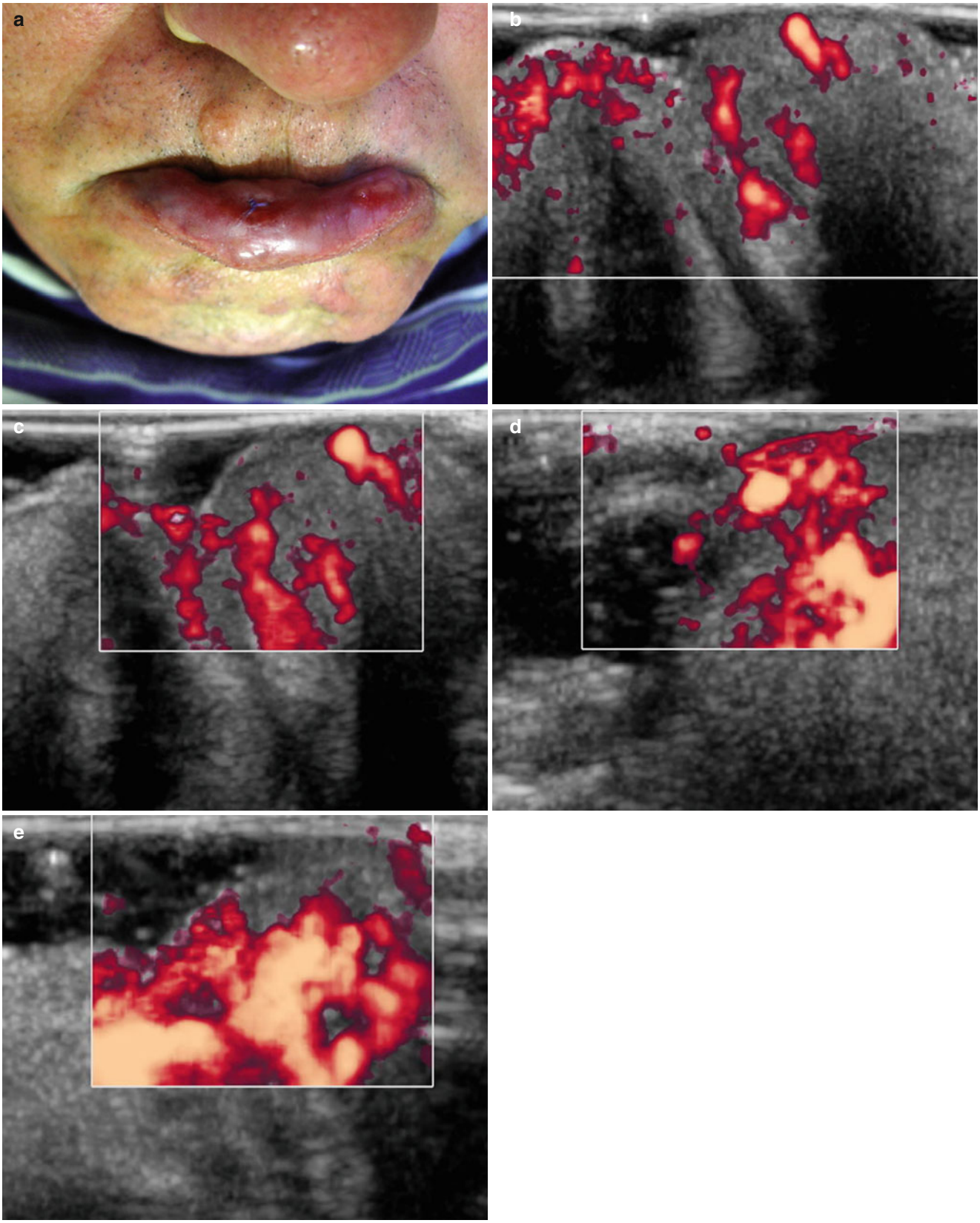

Fig. 10.5 (**a**) Lower lip squamous cell carcinoma. (**b**, **c**) Power Doppler ultrasound image before contrast—some vessels seen in central and peripheric region. (**d**, **e**) Power Doppler ultrasound image after contrast—lesion better seen after contrast, hypervascularizated

References

1. Grossman D, Leffell DJ. Squamous cell carcinoma, Chap. 80. In: Fitzpatrick's dermatology in general medicine, 6th ed. New York: McGraw-Hill; 2003. p. 737–47.
2. Sampaio SAP, Rivitti EA. Tumores epiteliais malignos. In: Sampaio SAP, Rivitti EA, editors. Dermatologia. 2nd ed. São Paulo: Artes Médicas; 2001. p. 842–5.
3. Srivastava A, Hughes LE, Woodcock JP, Laidler P. Vascularity in cutaneous melanoma detected by Doppler sonography and histology: correlation with tumour behaviour. Br J Cancer. 1989;59:89–91.
4. Lassau N, Mercier S, Koscielny S, Avril M-F, et al. Prognostic value of high-frequency sonography and color Doppler sonography for the preoperative assessment of melanomas. Am J Roentgenol. 1999;172:457–61.
5. Cammarota T, Pinto F, Magliaro A, Sarno A. Current uses of diagnostic high-frequency US in dermatology. Eur J Radiol. 1998;27:S215–23.
6. Giovagnorio F, Andreoli C, De Cicco ML. Color Doppler sonography of focal lesions of the skin and subcutaneous tissue. J Ultrasound Med. 1999;18:89–93.
7. Schröder R-J, Mäurer J, Zlowodski M, Hidajat N, et al. Vascularization of malignant and benign skin tumours measured by d-galactose-based signal-enhanced colour Doppler sonography. Acta Radiol. 2001;42:294–301.
8. Karaman GC, Karaman CZ, Sendur N, Akdilli A, et al. Power Doppler ultrasonography for the evaluation of skin tumors other than malignant melanoma. Eur Radiol. 2001;11:1111–6.
9. Schmid-Wendtner MH, Burgdorf W. Ultrasound scanning in dermatology. Arch Dermatol. 2005;141(2):217–24.
10. Jecker P, Brieger J, Doring S. The sonographic detection of experimentally induced squamous cell carcinoma compared with the histological image. Ultraschall Med. 2005;26(5):399–405.
11. Gramiak R. The beginnings of ultrasound contrast. In: Goldberg BB, editor. Ultrasound contrast agents. London: Martin Dunitz; 1997.
12. Muhagh et al. Contrast echocardigraphy: current and future applications. J Am Soc Echocardiogr. 2000;13(4):331–41.
13. Mattrey R, Pelura TJ. Perflurocarbon-based ultrasound contrast agents. In: Goldberg BB, editor. Ultrasound contrast agents. London: Martin Dunitz; 1997.
14. Jakobsen J, Oyen R, Thomsen H, Morcos S. Safety of ultrasound contrast agents. Eur Radiol. 2005;15:941–5.

Locoregional Staging of Melanoma

11

Orlando Catalano and Christiane Voit

How to perform an adequate locoregional staging

Contents

11.1 Introduction

Melanoma is the most aggressive and most deadly type of skin cancer. It is a relatively frequent disease, especially in some geographical areas, and its incidence has significantly increased worldwide during recent decades. Despite a higher detection rate and an increasing trend to thinner lesions [1], its mortality has increased [2]. The Breslow index (i.e., the primary tumor thickness in millimeters as measured histologically after excision biopsy) is the single most important predictor of survival in patients with melanoma, correlating with the probability of lymph-node metastasis and distant metastasis. Additional key points for staging of disease and prognosis include primary tumor ulceration, primary tumor mitotic rate, number of affected lymph nodes, and nodal metastatic burden [3].

Melanoma has complex metastatic pathways, including local extension, regional spread to lymph nodes, and spread to distant organs (including the skin) [4]. Most metastases will develop within the first 3 years and about two thirds of all recurrences are lymph-node metastases [5]. Thus, in most cases, melanoma spreads along the lymphatic ducts toward the regional lymph node station (approximately 70 % of all metastases involve the regional lymphatic basin). In 1996, a meta-analysis covering several publications revealed that once the lymph nodes are involved, the 5-year survival rate decreases to about 37 % [6]. Lymphatic diffusion includes satellite metastasis (<2 cm from the primary lesion), in-transit metastasis (>2 cm from the primary lesion), and lymph-node metastasis. Satellite and in-transit metastases are included in the N staging parameter featuring an N2 parameter when not combined with nodal metastases and an N3 parameter when found jointly [3]. Other superficial metastases (skin, subcutaneous layer, non-regional lymph nodes) are included in the M parameter as M1a and have a more favorable prognosis than the other M classifications [3, 7].

Sentinel lymph node (SN) staging is based on the well-supported hypothesis that melanoma lymphatic metastases follow an orderly progression through afferent lymphatic channels to

O. Catalano, MD (✉)
First Department of Radiology, National Cancer Institute "Fondazione G. Pascale", via M.Semmola, Naples 80131, Italy
e-mail: orlandcat@tin.it

C. Voit, MD, PhD
Department of Dermatology, Skin Cancer Center, Charité – University Medicine Berlin, Charitéplatz 1, Berlin, 10117, Germany
e-mail: christiane.voit@t-online.de

X. Wortsman, G.B.E. Jemec (eds.), *Dermatologic Ultrasound with Clinical and Histologic Correlations*,
DOI 10.1007/978-1-4614-7184-4_11, © Springer Science+Business Media New York 2013

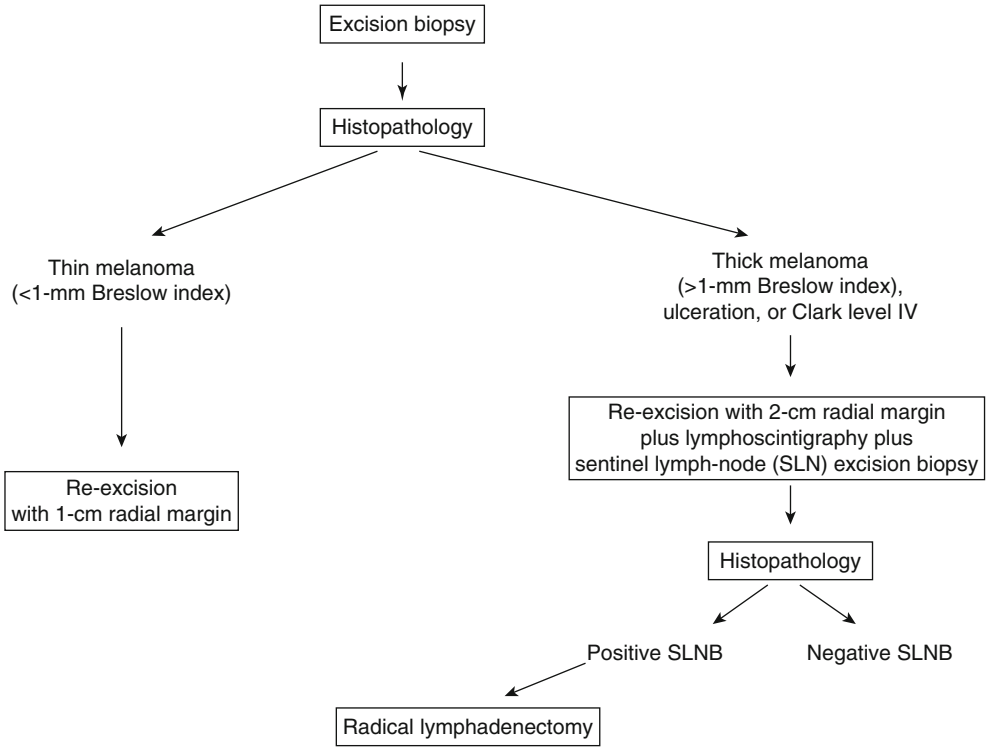

Fig. 11.1 Current, worldwide-accepted flow chart for management of patients with melanoma, not including sonography

SNs before spreading to other regional, non-sentinel nodes [8]. The SN is defined as the first draining lymph node from a tumor and its status is regarded as the best predictor of patient survival from melanoma to date. The SN has the greatest risk to harbor (occult) metastases, as it is the first station in the metastatic cascade. The SN is selectively harvested through a minimally invasive, targeted procedure, the sentinel lymph-node biopsy (SLNB). Thereafter, the SN is examined through the use of an extensive pathology protocol. The result of this assessment should be able to accurately predict both survival and further non-sentinel lymph-node metastases in the same lymph node station [9]. Thus, the SLNB is the basis for treatment planning (Fig. 11.1): if the SN is positive the patient undergoes completion lymphadenectomy (CLND), where in the case of a negative SLNB, a radical lymphadenectomy will be avoided. Radical lymphadenectomy was the standard of care prior to the introduction of the SLNB and it is now called elective lymphadenectomy (ELND). However, a benefit in terms of overall survival following an ELND has not been proved [10–13]. Because the rate of occult micrometastases in patients having undergone ELND is about 20 %, it means that 80 % of patients with melanoma have been operated on in vain and have been confronted with the risk of postsurgical complications such as persisting lymphedema. By introducing SLNB to patients with melanoma, the surgical management has been simplified [8–14]. SLNB is the less, but still invasive standard procedure for defining the N status accompanied by some morbidity. This procedure was originally developed as a means of identifying patients with nodal metastasis without the morbidity associated with a complete lymph node dissection [8–15]. Additionally, particularly for torso melanomas, it allows for recognizing the site of the regional lymphatic station, something that is sometimes hard to predict on the sole basis of anatomy. As a general rule, SLNB is reserved for intermediate thickness lesions because those <1 mm only rarely have nodal involvement, whereas very thick melanomas have a high probability of direct hematogenous spread.

Real-time, high-resolution ultrasound is a feasible and inexpensive modality [16]. It has become the main noninvasive imaging tool used for staging and follow-up of locoregional tumor spread in patients with cutaneous melanoma [17–20]. Sonography is now used in a variety of clinical scenarios including the initial assessment of lymph node status (avoidance of the SLNB procedure in case of overt metastatization) [21] (Fig. 11.2), detection of satellite and in-transit metastases; differential diagnosis with nonmelanomatous lesions; lymphatic basin surveillance (both in the subject managed conservatively after SLNB and in the patient submitted to radical lymphadenectomy); guidance for fine-needle aspiration cytology (FNAC); and for presurgical marker placement [22–24]. Several articles [17, 19, 25] have reported a higher accuracy for ultrasound over physical examination in the detection of in-transit and nodal lesions. The combination of ultrasound-guided FNAC allows maximizing the overall accuracy [26–28]. Nevertheless, ultrasound imaging of patients with melanoma requires specific expertise [29–31]. False negative results can result from inadequate operator training, use of not updated or not adequately set equipment, failure to enclose the lymph node in the scanned areas, and presence of subtle malignant changes or micrometastasis. False positive results can

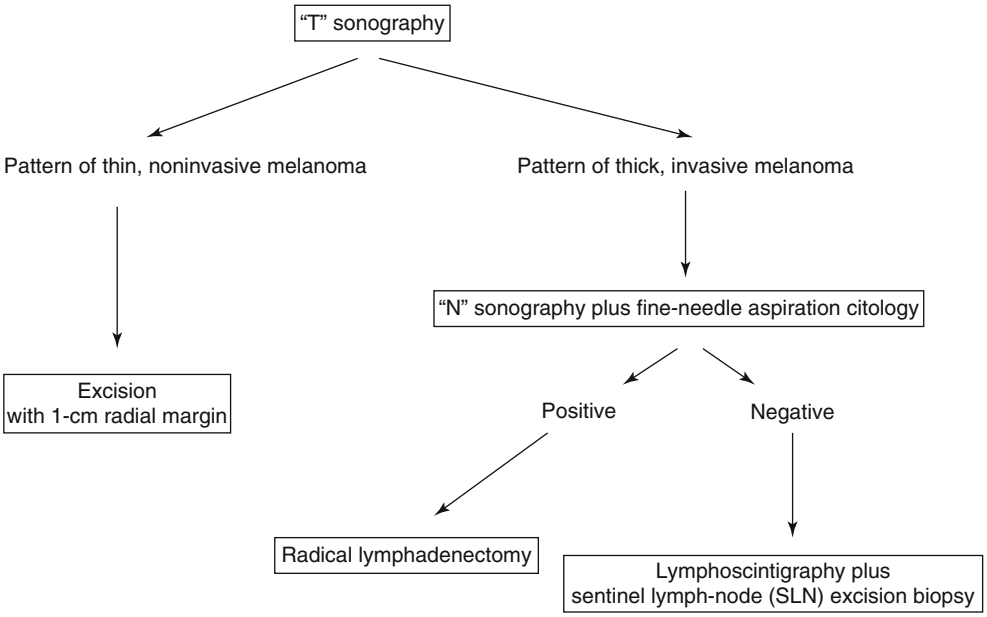

Fig. 11.2 Theoretical flow chart for management of patients with melanoma including sonography in all steps

also be a result of inadequate equipment or insufficient skill, as well erroneous image interpretation (benign lymphadenopathy, benign soft-tissue abnormality, etc.).

11.2 Technical Considerations

11.2.1 Sonography

State-of-the-art scanners, a complete set of high-frequency probes, and specifically trained operators are all mandatory. Although sonography for melanoma has been performed for more than 20 years [17, 32], only modern, top-level equipment allows detection of very small soft-tissue metastases and subtle lymph node changes.

Primary cutaneous melanoma has been investigated both with 7.5–13 MHz and recently up to 18 MHz transducers (high-resolution ultrasound), which are those most commonly used in clinical practice (Fig. 11.3). Additionally, 20–75 MHz transducers have been used, although mainly for scientific purposes (Fig. 11.4). The higher the transmission frequency is, the better the spatial resolution, but the lower the tissue penetration results. Furthermore, melanomas that are very thick and exceed the explored depth (when using very high-frequency probes) cannot be imaged adequately, it is then best to change to a lower frequency probe because thick melanomas can easily be depicted using frequencies as low as 10–12 MHz. It is important to avoid any compression of the skin surface or lesion flattening, and to use an adequate amount of gel to separate the transducer from the skin. Lesion flattening caused by exerting too much pressure on the lesion can lead to a false low measurement of tumor thickness. The use of gel stand-off pads is recommended for lesions that are located superficially, such as primary tumors, to shift the focus to where the lesion is located

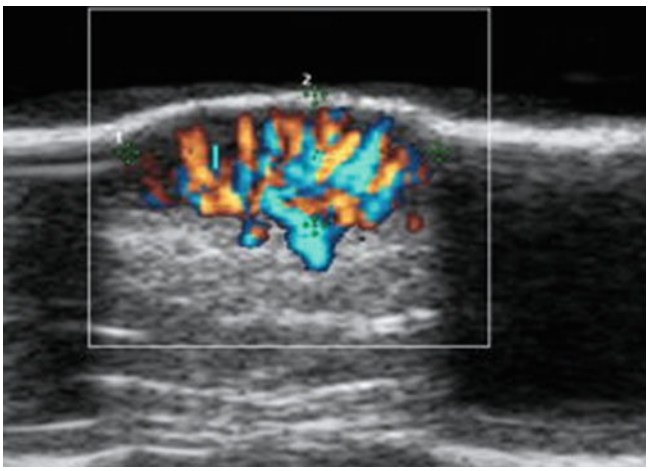

Fig. 11.3 Primary melanoma. Directional power Doppler image. Vascularization shown at the basis of the lesion. Tumor thickness is 4 mm

(Fig. 11.5). Care must be taken to minimize the pressure applied to the skin [33], and when using frequencies that are very high, water is also used as a medium between the probe and the skin [34]. Application of saline approximately 15 min prior to ultrasound can be helpful to overcome the post-lesional deletion of echoes behind hyper-echoic/echo-rich structures in lesions showing hyperkeratosis [35]. It can be difficult to adequately place the probe in certain body areas (i.e., scalp, ear, fingers), and this is where the gel stand-off pad is extremely helpful in making incongruent structures "smooth". The images are recorded with the gain curve allowing tumor-to-tissue contrast. The focal zone is set superficially, and as mentioned previously, can be adapted according to the tumor position in the superficial tissue. Magnification is increased as needed [35].

In order to image the locoregional spread of melanoma lesions, the scanner must be equipped with a high-resolution

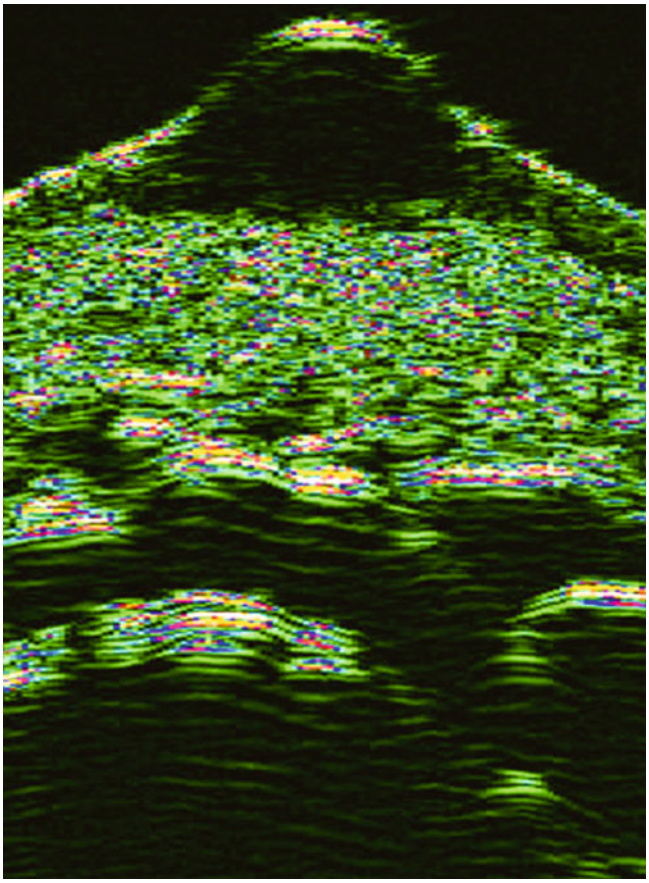

Fig. 11.4 20 MHz ultrasound image of a melanoma on the lower extremity using water as a conductor medium

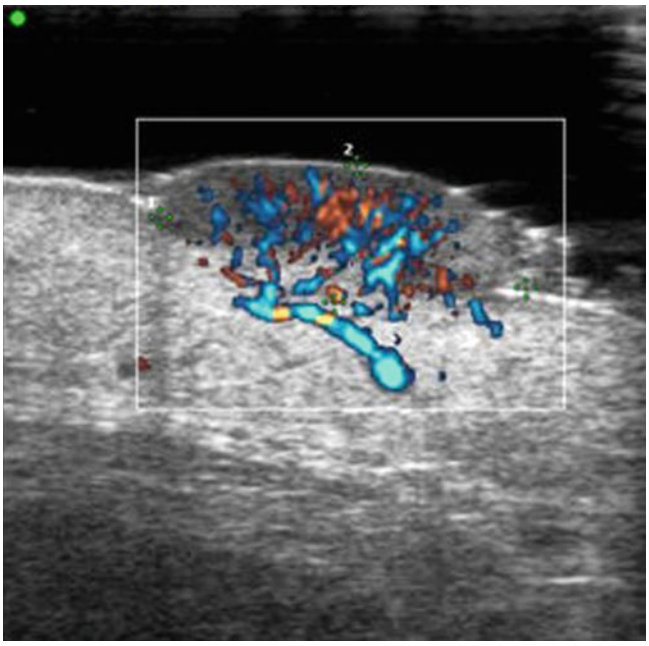

Fig. 11.5 Melanoma, primary tumor on the calf. Directional power Doppler image. Because of the prominent shape a gel stand-off pad was used. Note the already marked perfusion

(>7.5 MHz), multi-frequency linear transducer. Ideally, two linear transducers differing in probe length and frequency range should be available. The choice of the right transducer depends mostly on the depth of the area being explored. Summarizing its application, gel stand-off pad can be used for lesions that are superficial and for those causing an irregular skin surface [29, 30, 32, 36]. The pad not only allows better aim of the beam at the level of the lesion on B-mode scans, but also detects otherwise missed intra-lesional flow signals on Doppler imaging (Figs. 11.6, 11.7, and 11.8). It is important to use a dynamic regulation of the scan; in general, higher frequencies are necessary for superficial lesions and lower frequencies for deeper lesions (Fig. 11.9). The beam is aimed directly below the area of interest and care should be taken to use an adequate regulation of signal amplification and time-gain compensation curve which helps to avoids the development of artifact echoes within anechoic structures as well as the suppression of subtle echoes within hypoechoic structures.

Real-time, extended field-of-view (EFOV) reconstructions can be obtained electronically, beginning with a lateral translation movement of the probe over the skin of the patient. EFOV images allow panoramic display of the area of interest and can be helpful in improving image correlation during serial scanning and to give to the surgeon images that are more anatomically oriented and comprehensive; thus creating a map-like picture of a whole area by adding up scans and those pieces of a puzzle that contribute to a complete image. EFOV images are particularly helpful in measuring bulky masses or measuring the distance between multiple melanoma lesions typically located along the muscular fascia of the in-transit distance or between a given lesion and an anatomic landmark (i.e., vessels, bony promontories, etc.) [37] (Figs. 11.10, 11.11, and 11.12).

A systematic exploration modality is mandatory. The skin around the primary tumor (or, more frequently, its scar) is scanned carefully to first rule out satellite (first 2–3 cm) and then in-transit metastases. An area around the lesion (or its scar) of at least 10 cm in diameter, particularly in the direction of the related regional lymphatic station, is initially explored. The transducer is then moved along the presumable course of the lymphatic vessels toward the regional lymph node station. If done carefully, sonography may allow a panoramic exploration of a large body part such as an entire limb, although it is seen mostly as a non-comprehensive imaging modality. Although it is a time-consuming practice, the technician should always try to assess the body segment lying between the primary melanoma site and the lymph node station(s) [31]. Lymphatic spread is not always predictable on the sole basis of anatomy; metastases can involve multiple regional stations simultaneously or can develop in non-regional lymphatic stations. The lymphatic drainage can show significant changes, particularly after radical lymphadenectomy, which should always be kept in mind during follow-up ultrasound. The supraclavicular and axillary

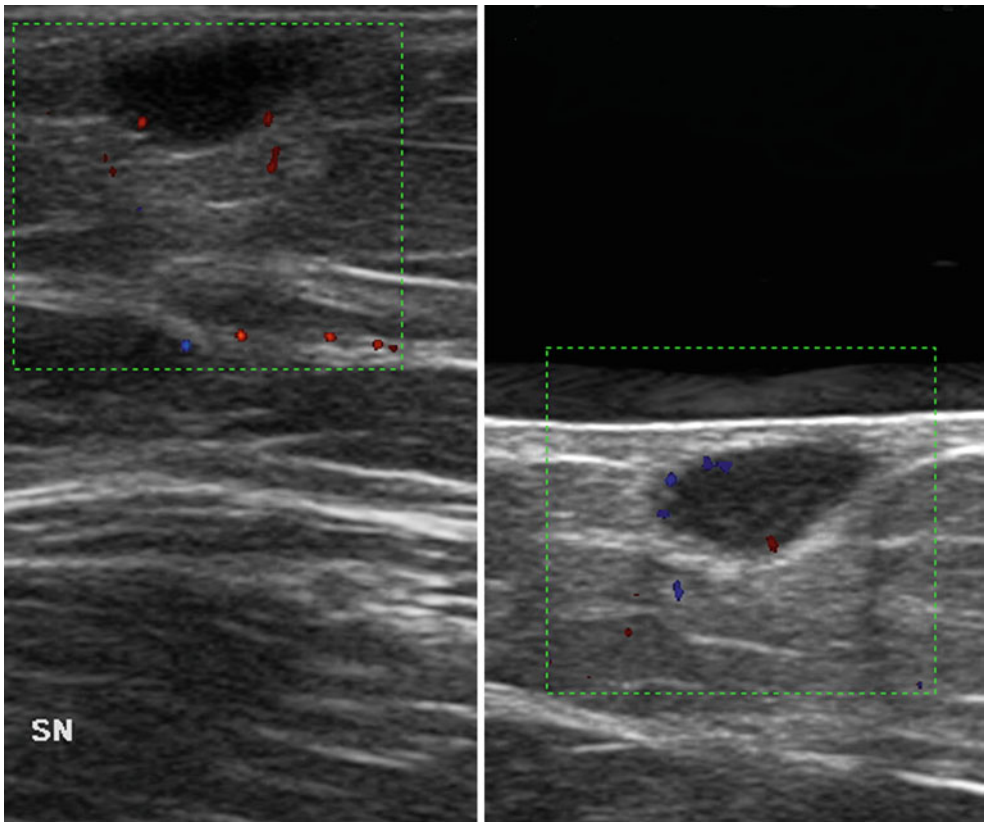

Fig. 11.6 Post-surgical inguinal recurrence. Directional power Doppler image without and with use of a gel pad spacer. More flow signals can be detected within the small cutaneous nodule by using a spacer, which allows to better focus the beam superficially

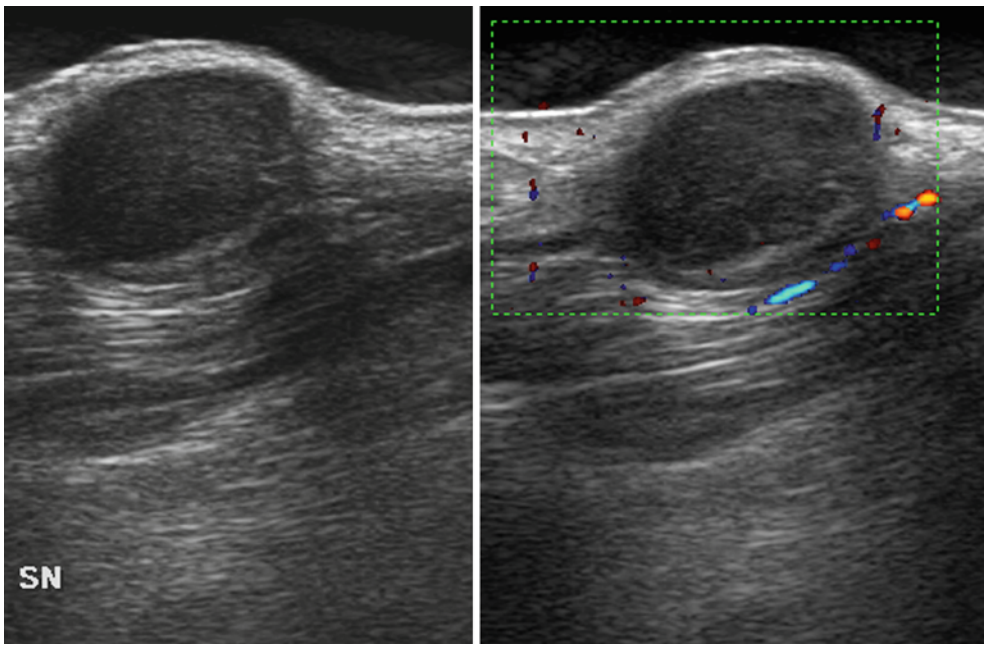

Fig. 11.7 Recurring melanoma lesion of the neck. Use of a gel pad to adequately depict the hypoechoic, bulging nodule at sonography and power Doppler imaging

nodes as well as the deep pectoral and infraclavicular nodes should be scanned in melanomas in the torso. When the primary melanoma is in the head or neck, the supraclavicular stations must be examined bilaterally, not only the cervical stations. In melanomas of the upper limbs and upper trunk melanomas, the supraclavicular and infraclavicular stations should also be included. When the primary melanoma site is at the level of the limbs, the status of the axillary, inguinal, and even iliac lymphatic basins is assessed. Although contralateral lymphadenopathies are encountered rarely, and mostly in patients having undergone radical lymphadenectomy, the contralateral (axillary or inguinal) lymphatic basin must always be

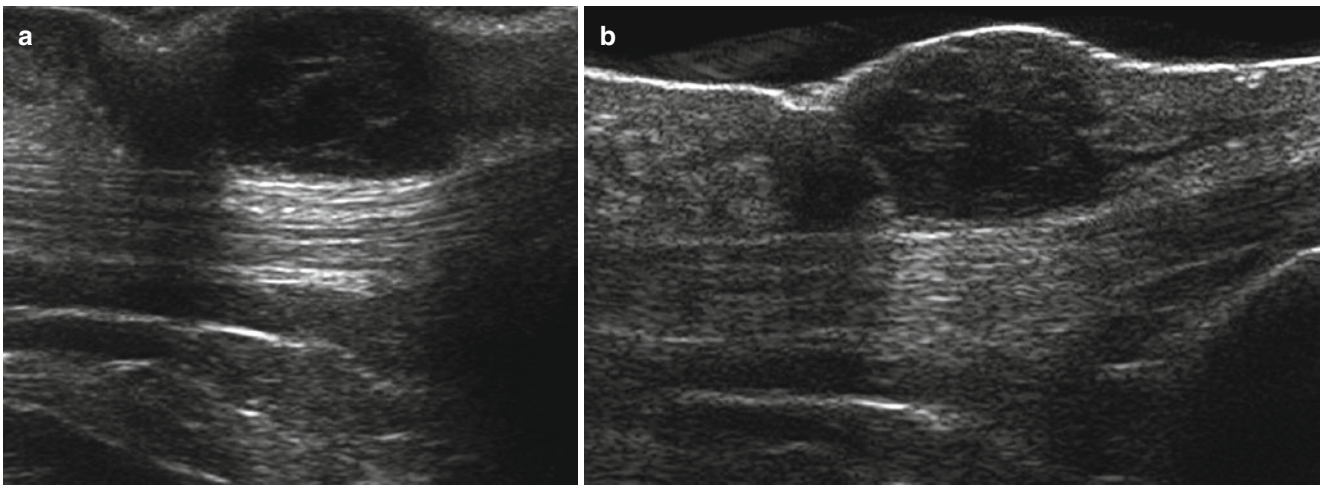

Fig. 11.8 Post-surgical recurrence of a heel melanoma. Because of the protruding position of the nodule, the ultrasound image is fair (**a**). However, by using a gel pad spacer, it is possible to achieve an adequate depiction of the hypoechoic nodule (**b**)

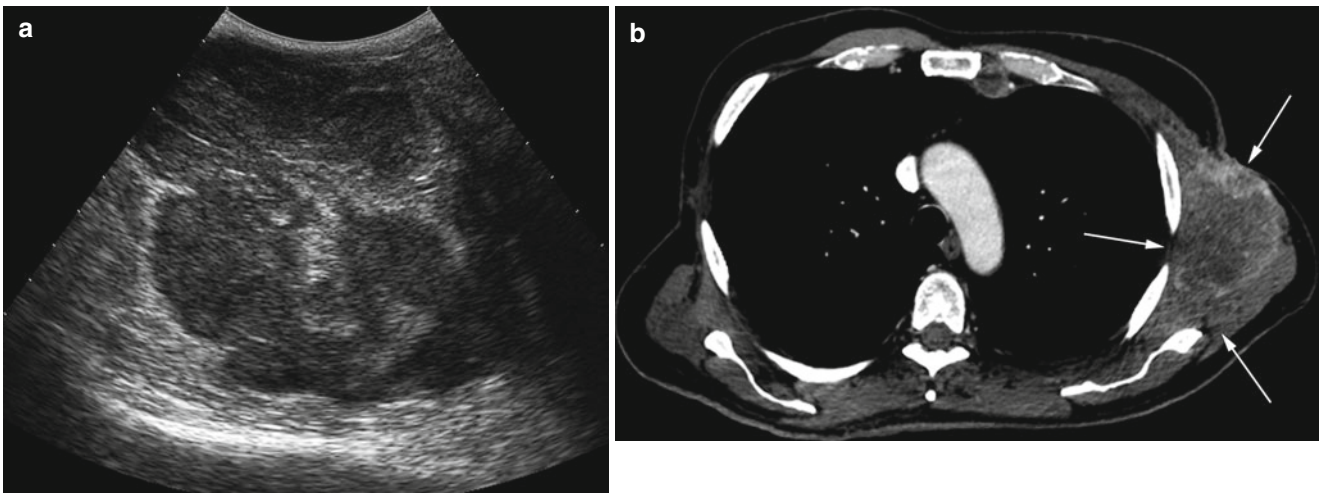

Fig. 11.9 Use of an "abdominal" transducer to evaluate superficial but bulky melanoma metastases. (**a**) Axillary metastasis, sonography. (**b**) Computed tomography, axial scan (*arrows*)

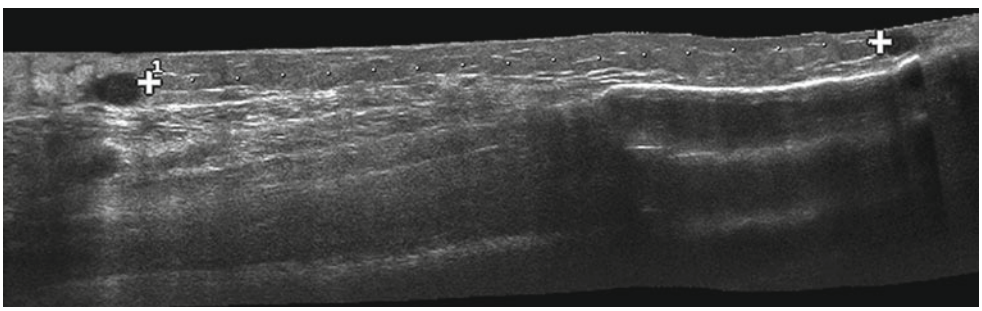

Fig. 11.10 Extended field-of-view ultrasound image allowing for direct measurement of the distance between two in-transit melanoma metastases of the thigh (162 mm)

explored. However, the contralateral lymphatic station represents a useful reference because some sort of symmetry can normally be found in the number, size, and overall appearance of the lymph nodes and an overt difference between the two sides is already suspicious by itself [31, 38]. It is best to start the examination with the "healthy" side to get insight into the individual shape, number, and grade of activation of the individual patient and then compare with the other "sick" side (the lymph node basin that must be checked).

The exploration of each lymphatic station should be extensive. In the neck, not only the anterior and laterocervical stations, but all possible sites of spread should be explored including the nuchal, retroauricular, and intraparotid nodes. In the case of facial melanoma, the cheeks and the submen-

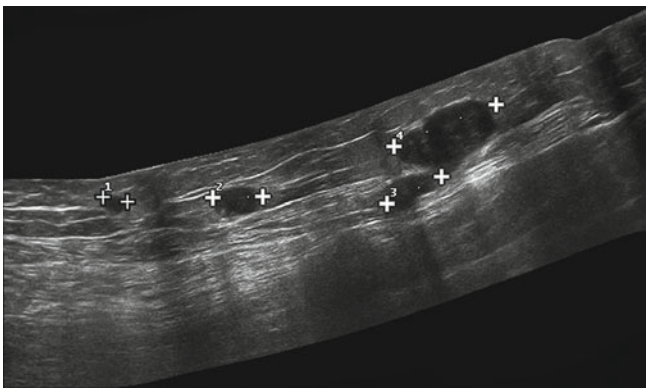

Fig. 11.11 Extended field of view (ultrasound allowing depiction and measurement of multiple melanoma metastases of the thigh

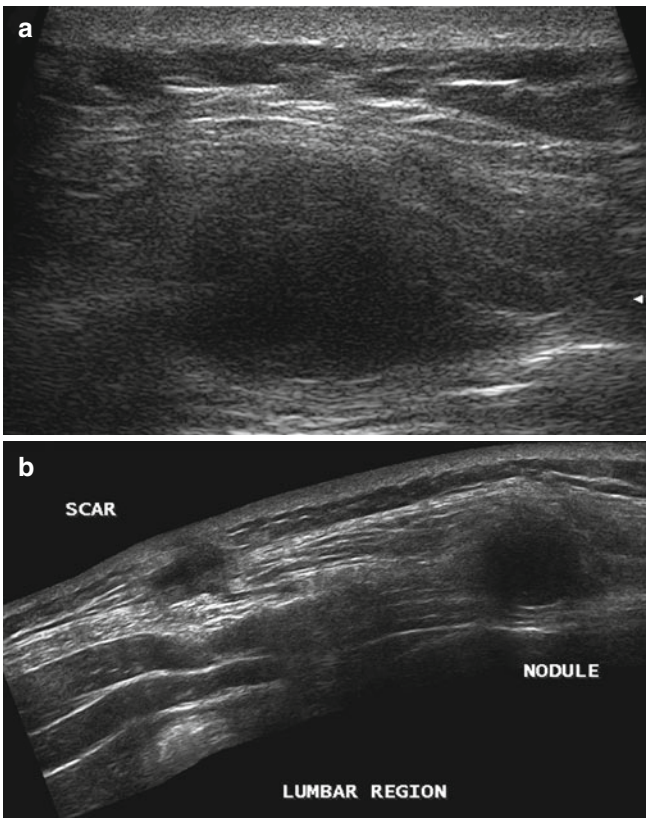

Fig. 11.12 Lumbar recurrence. Ultrasound image revealing a deep nodule raising 5 cm far from the primary melanoma scar (**a**). Extended field of view reconstruction allowing for comprehensive depiction of the anatomic relationship between the scar and the new nodule (**b**)

tal region should be included. At level of the axillae, not only is the axillary cavity (both medially and laterally to the main vessels) explored, but also the posterior column toward the latissimus dorsi muscle, the beginning of the upper arm, the subaxillary region, and the mammary prolongation. The inguinal region should be scanned for both superficial and deep nodes, both medially and laterally to the main vessels, extending the scan to the crural region

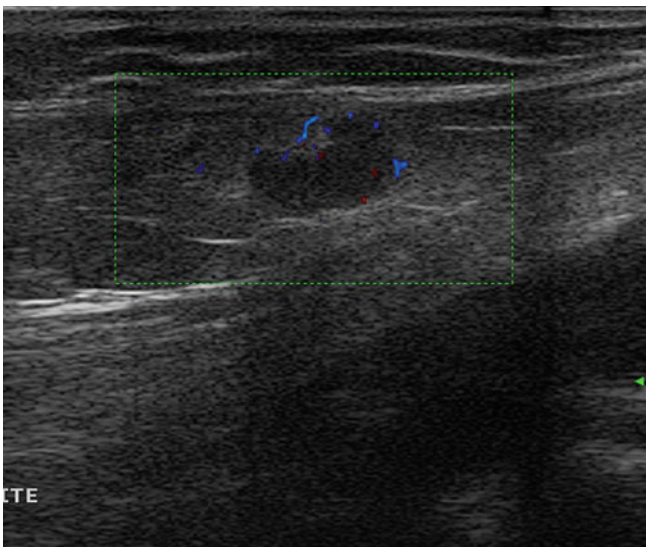

Fig. 11.13 Interval lymph-node metastasis within the popliteal fossa. Directional power Doppler image. The lymph node is oval with a small and eccentric hilum and with multiple peripheral flow signals

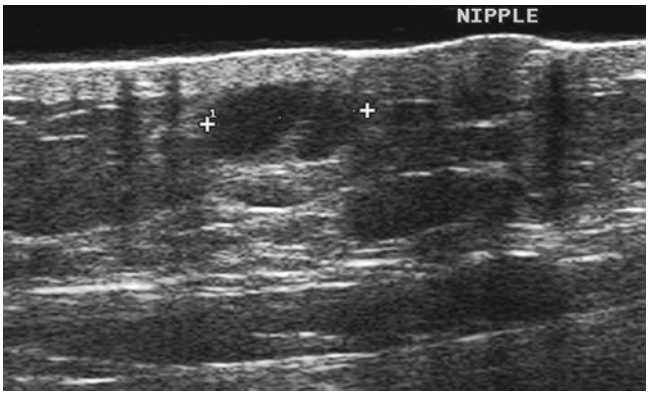

Fig. 11.14 Interval lymph-node metastasis (*calipers*) close to the nipple in a patient with chest wall primary melanoma and axillary nodal melanoma metastases

toward the thigh and above the ligamentum inguinale to the suprainguinal portion of the anterior abdominal wall. An attempt should also be made to evaluate the external iliac nodes, particularly those that are most superficial (using both a linear and a convex probe) [38, 39]. Because pelvic lymph nodes are frequently positive, ilioinguinal dissection should be considered for all patients, particularly those with macroscopic metastases to groin lymph nodes [40].

It is important to explore the retroareolar and the upper-external lump portions in patients with torso primary melanoma, the epitrochlear area in patients with forearm or hand primary melanoma (particularly for ulnar side melanomas), and the popliteal fossa in patients with leg or foot primary melanoma (particularly for lateral heel melanomas) to rule out any interval lymphadenopathy (i.e., any non-regional lymphatic station placed along the pathway of melanoma spread) [31, 41–43] (Figs. 11.13 and 11.14).

Additionally, it is important to write a clear description of the ultrasound findings, even accompanied by a small sketch to forward useful information to the next technician or surgeon. It would be even better if there were consistency in the technicians, meaning that those difficult cases showing multiple metastases would always be examined by the same technician to prevent inter-observer variability.

11.2.2 Color Doppler Imaging

Color Doppler imaging requires a scanner setting adequate to detect superficial, slow flows: highest Doppler frequencies, relatively low-pulse repetition frequency (the lowest not causing aliasing or excessive reduction in the frame rate), the lowest wall filter, color gain immediately below the noise threshold. The power Doppler mode in most scanners is more sensitive in depicting very slow flows than is the color Doppler mode, and should therefore be the preferred mode. Care should be taken to avoid excessive compression with the transducer, capable of suppressing the flow signal from very small and superficial lesions [31] (Fig. 11.15). In addition to the morphological description of the sentinel node in B-mode, this combination enables the registration of all functional information regarding blood flow in the sentinel node. Thus, any neo-angiogenesis as event early in the course of each metastasization can be made visible [44, 45].

11.2.3 Contrast-Enhanced Ultrasound

The detection of flow signals within the primary melanoma can be improved through the use of ultrasound contrast media because they increase the Doppler sensitivity for slow

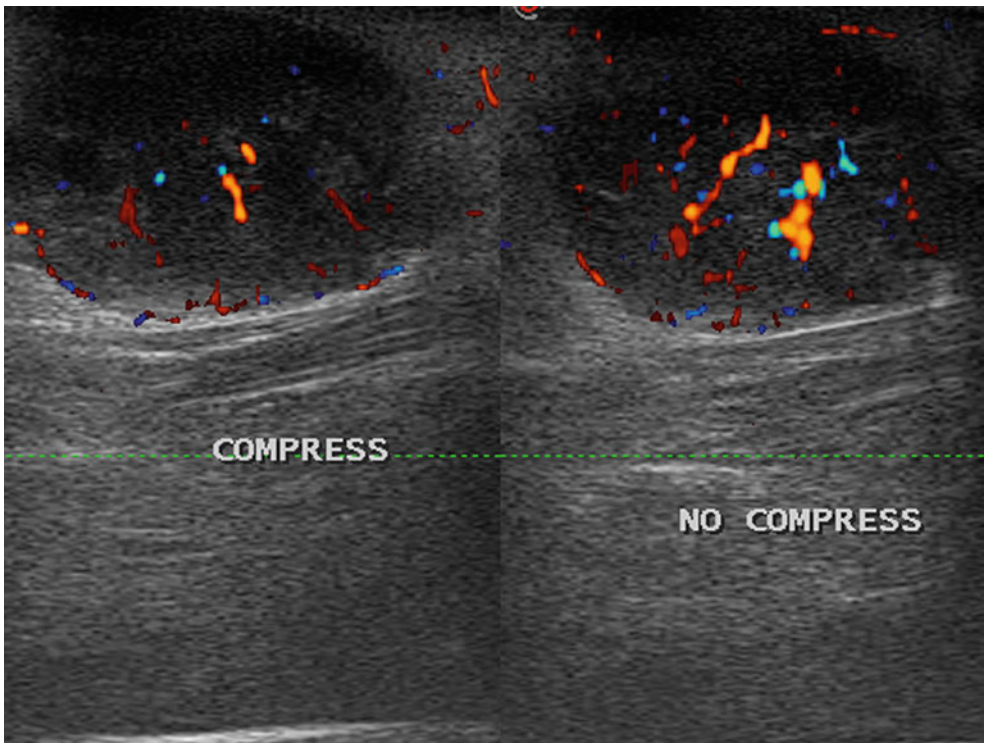

Fig. 11.15 Ankle melanoma metastasis. Directional power Doppler image with and without (intentional) compression. Attention should be paid to avoiding excessive compression with the transducer that can consistently attenuate the flow signals

flows [46]. However, these contrast agents are not available in all countries and are not in clinical practice for this reason. Some authors [47, 48] have used intravenously injected contrast media on ultrasound to increase the intra-nodal vascular signals in patients with melanoma. However, it is our opinion that the Doppler mode sensitivity of current scanners is sufficient, and consequently, its further intensification usually does not add relevant information (but will increase the costs).

Currently, ultrasound contrast media are rarely used as Doppler signal enhancers, but instead are used to obtain grey scale, real-time images based on tissue perfusion similarly to contrast-enhanced computed tomography or magnetic resonance. Thus contrast-enhanced ultrasound (CEUS) is used mostly for special cases, such as for the detection and differential diagnosis of liver metastasis in abdominal sonography. The use of CEUS for melanoma imaging is still preliminary. CEUS has been used for the assessment and quantification of perfusion in cases of superficial melanoma metastases, particularly in the early assessment of response to treatment (isolated limb perfusion) [46]. There is also some preliminary experience on the use of contrast media to enhance grey scale images, showing the different perfusion behaviors of reactive and of metastatic lymph nodes [49]. A recent article reported that CEUS was useful to further evaluate focal thickenings of the lymph node cortex in patients with melanoma [50]. Focal tumor deposits are seen as perfusion defects within the enhanced lymph node (Figs. 11.16 and 11.17); however, we think that the focal thickening of the cortex that can actually be observed in early lymph-node metastasis is nearly always accompanied by slight peripheral flows and the latter can be depicted with the use of power Doppler ultrasound with a low pulse repetition frequency.

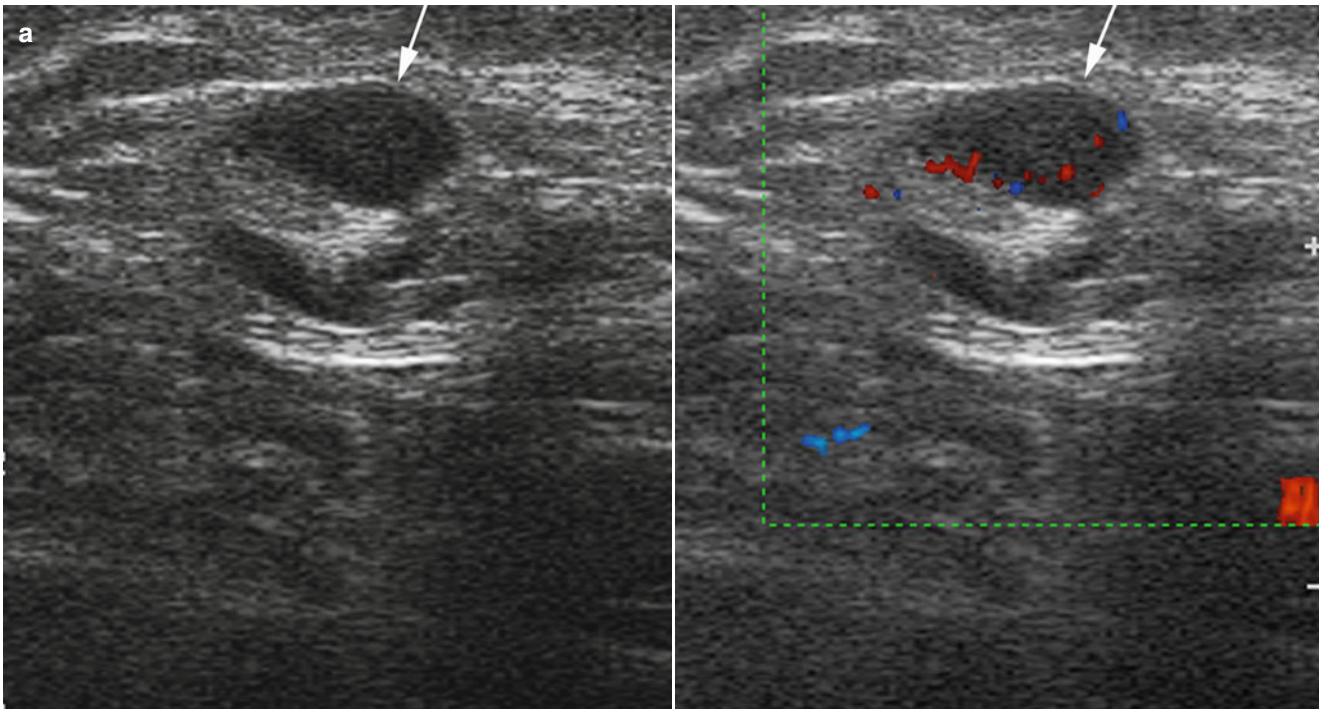

Fig. 11.16 Focal tumor deposit detected using contrast-enhanced ultrasound. The color Doppler image (**a**) shows an asymmetrical, vascularized cortical thickening (*arrow*) of an inguinal lymph node in a patient with leg melanoma. The contrast-enhanced ultrasound image in dual real-time mode (**b** 27 s from injection; **c** 37 s from injection) clearly depicts a focal enhancing defect and consequently allows a definitive diagnosis

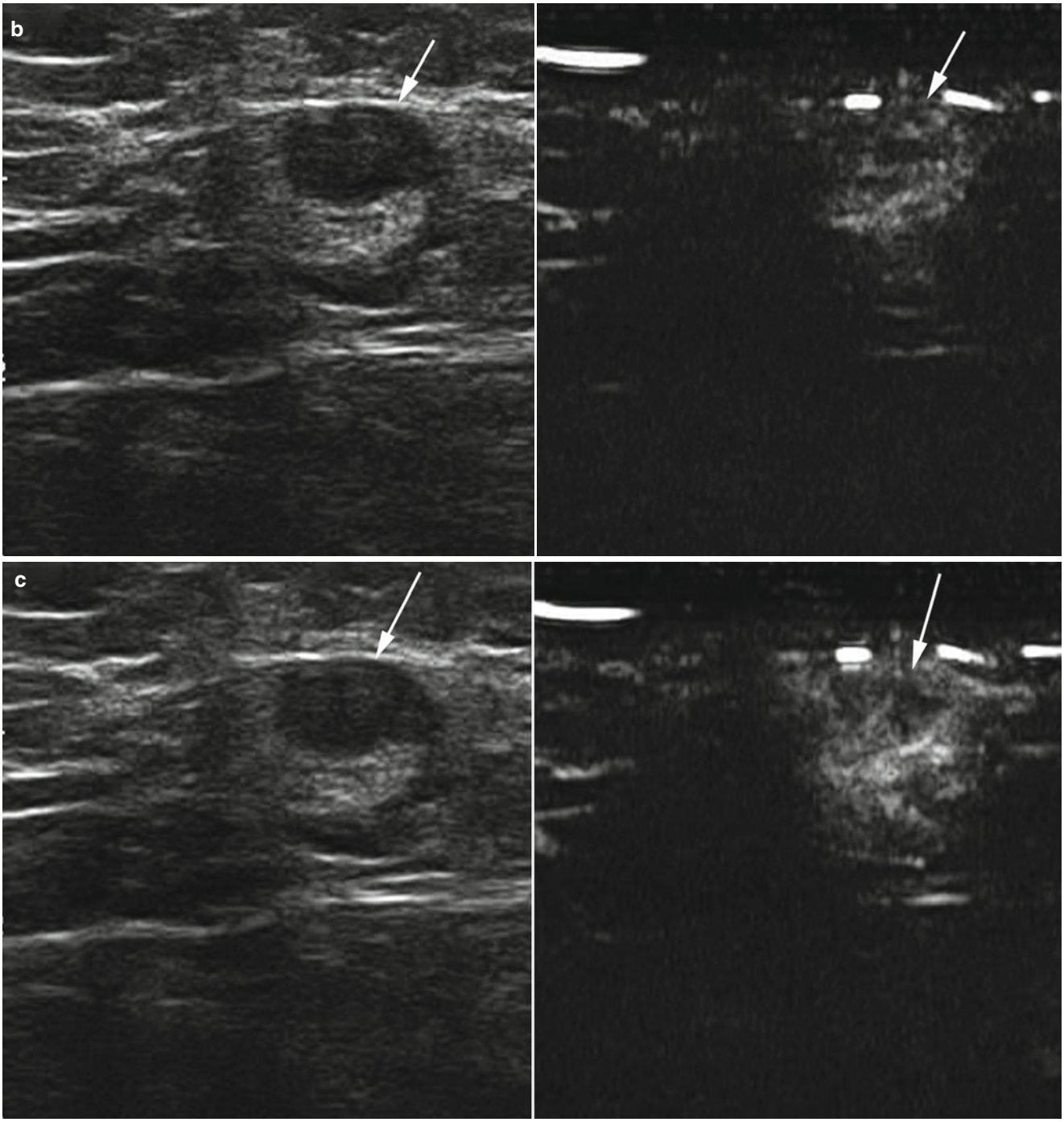

Fig. 11.16 (continued)

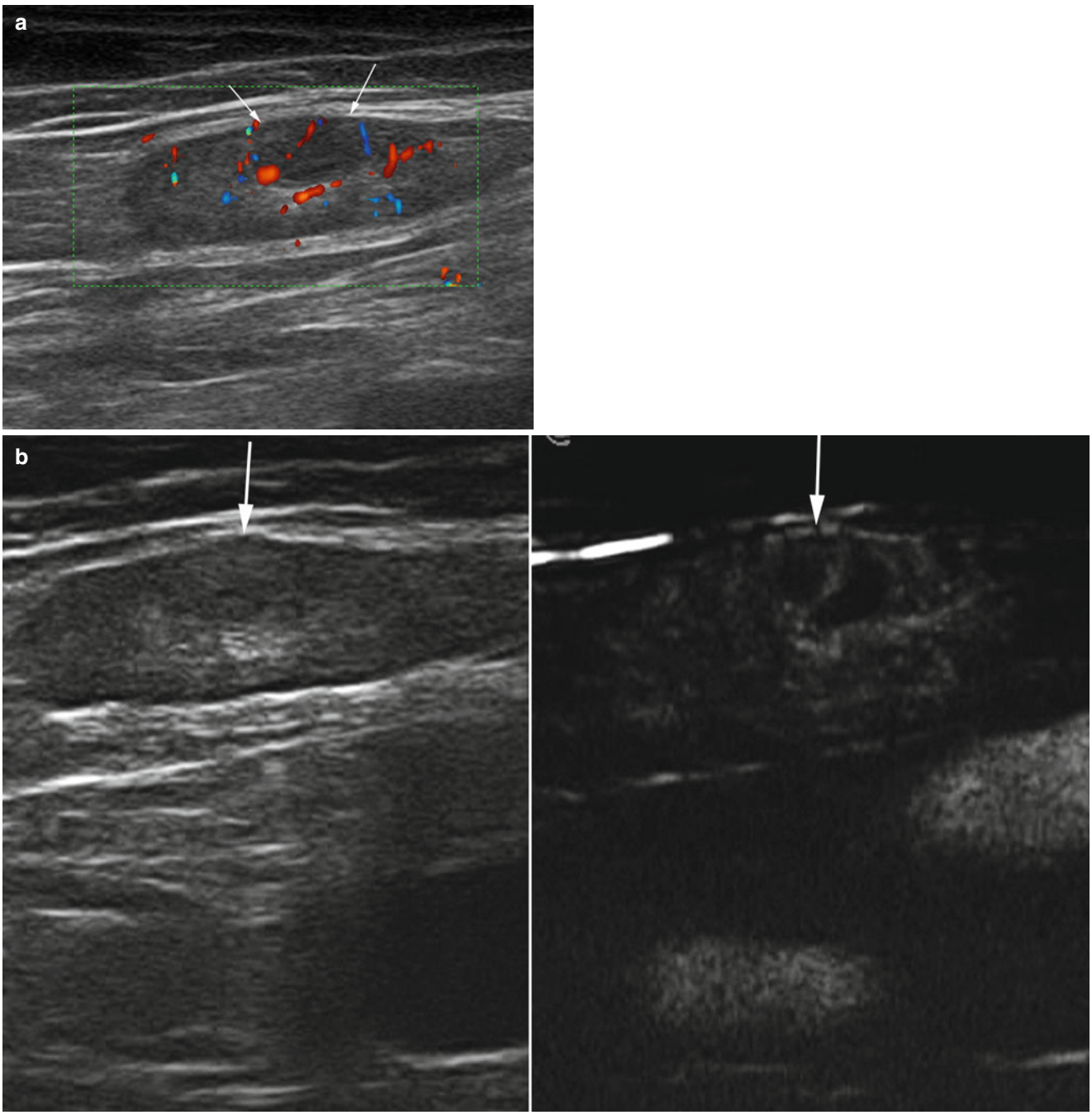

Fig. 11.17 Focal tumor deposit detected using contrast-enhanced ultrasound. The color Doppler image (**a**) shows a subtle, hypoechoic, vascularized, area (*arrows*) within an inguinal lymph node in a patient with recurring heel melanoma. The contrast-enhanced ultrasound image in dual real-time mode (**b** 29 s from injection; **c** 56 s from injection) depicts a focal heterogeneity and consequently allows a definitive diagnosis

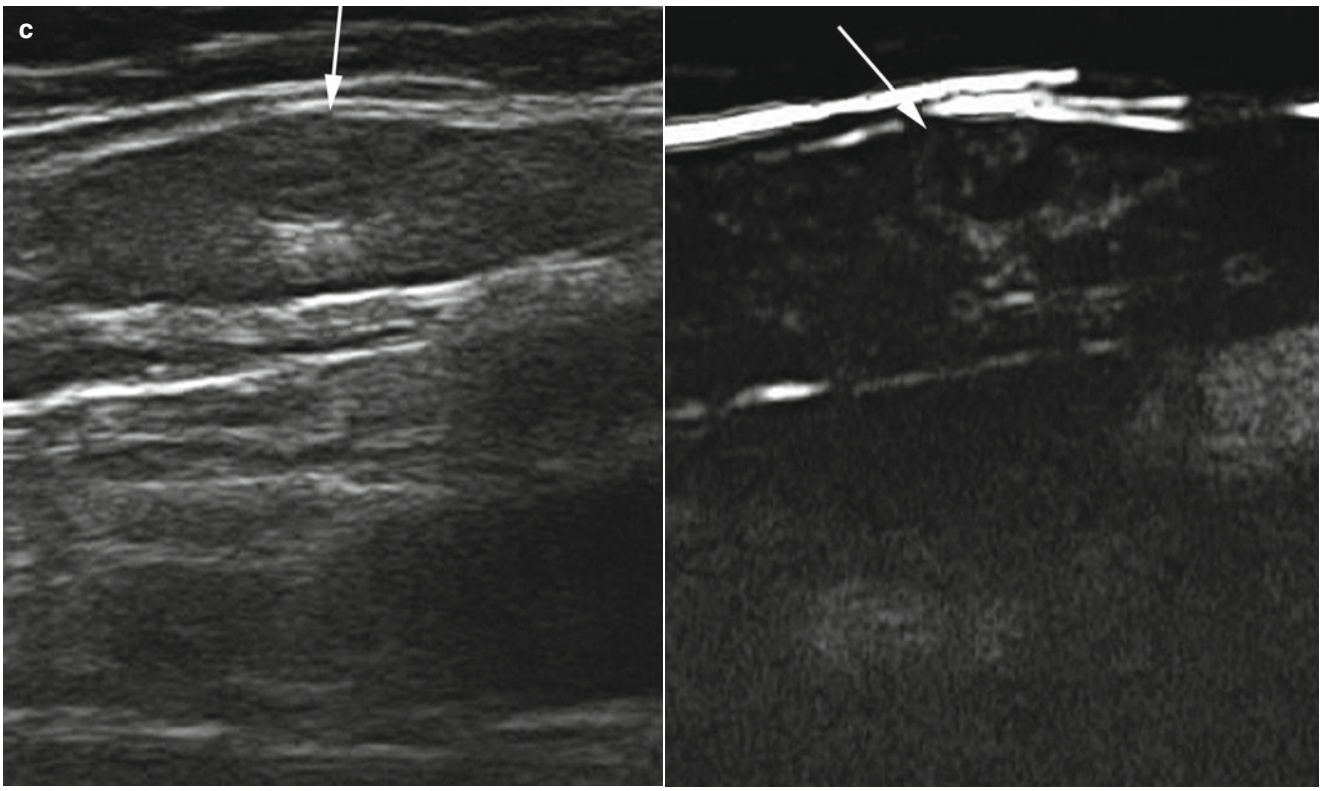

Fig. 11.17 (continued)

11.3 Sonography Findings

11.3.1 Sonography of Primary Melanoma Lesions

Management of primary cutaneous melanoma is usually a two-step procedure. First, an excision biopsy is performed to determine the melanoma subtype and to measure the tumor thickness (Breslow index) and other pathological features such as Clark level, mitotic index [51], immunohistopathology consisting of staining against Melan A and HMB 45, and in rare cases, against S100. Subsequently, the lesion is re-excised with a free margin of variable width (depending on tumor thickness) with a wide excision currently ranging between 1 and 2 cm. From a theoretical point of view, a swift pre-surgical, noninvasive assessment of tumor thickness (using ultrasound) and tumor vascularization (using Doppler techniques) may allow for defining the appropriate surgical margin extent, avoiding the preliminary biopsy and directly performing a single-step tumor resection (combined with the SLNB, if appropriate). Excision biopsy has its own drawbacks: the lymphatic drainage can be altered (with worsening consequences on the subsequent SLNB) while very wide lesions or lesions in anatomically critical sites (such as the sole of the foot) can be difficult to biopsy [35]. However, in current clinical practice, excision biopsy is difficult to replace with sonography. Aside from the technical limitations mentioned previously, avoiding excision biopsy would be feasible only when the diagnosis of melanoma is clinically and dermatoscopically certain, something only possible in some cases.

Cutaneous melanoma grows radially at the beginning radially (i.e., horizontally within the epidermal and superficial dermal layers). This growth pattern is also reflected by the superficially spreading melanoma subtype, which is the most frequent melanoma subtype about 65 % of the time. As long as cells have not passed the basal layers and have not made contact with the lymphatic or blood vessels, the tumor does not have the capacity to metastasize. With time, the pattern of growth assumes a vertical component, and the melanoma grows downward into the deeper dermal layers. Consequently, the metastasization probability can be predicted by simply measuring the depth of invasion of the vertical growth phase nodule below the epidermis.

Primary lesions are examined using ultrasound for their margin delineation, lesion shape, lesion thickness (maximal vertical measure from lower edge of the skin surface to the deepest point of the lesion posterior margin), internal texture, and echogenicity (compared with the adjacent dermal tissue) [52] (Figs. 11.18, 11.19, and 11.20).

Melanomas usually appear as hypoechoic, homogeneous lesions, while nevi usually have a more inhomogeneous echotexture. However, sonography does not normally allow for differentiation of benign from malignant lesions (although it generally allows for the distinction of melanoma/nevi from other skin lesions) [38]. The tumor is sometimes near anechoic, resembling a cystic lesion, although with a different shape.

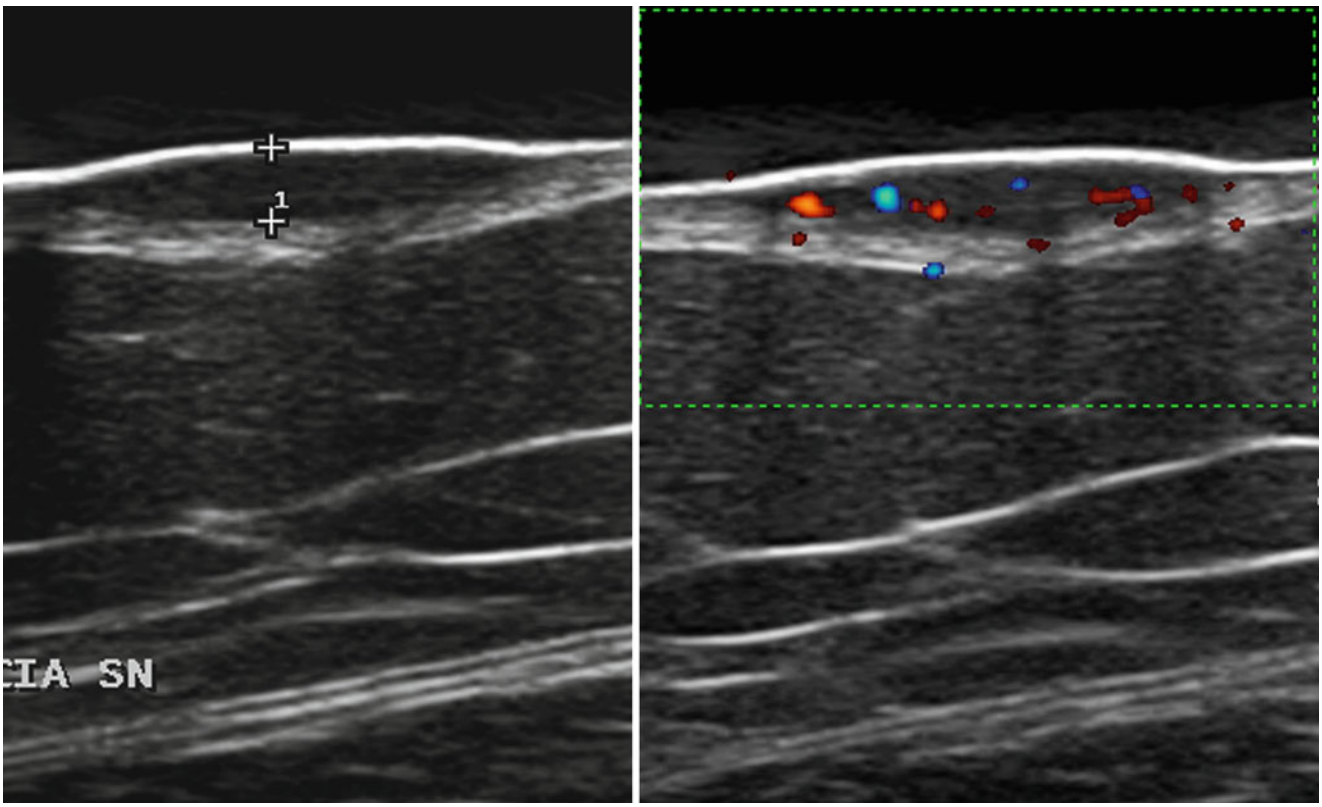

Fig. 11.18 Primary melanoma of the thigh. Image taken with a gel pad spacer. The 1.9-mm thick melanoma shows multiple internal flow signals in the power Doppler side of the split mode image

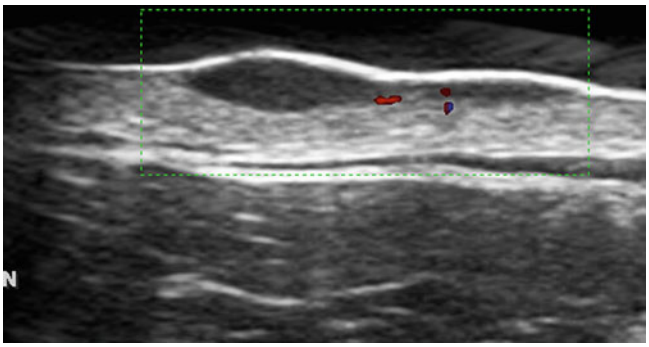

Fig. 11.19 Primary melanoma of the shoulder. Image taken with a gel pad spacer. Directional power Doppler scan. The bilobated melanoma shows multiple little internal flow signals

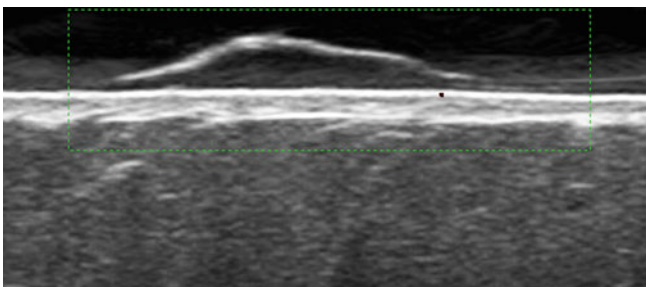

Fig. 11.20 Primary melanoma of the forearm. Image taken with a gel pad spacer. Directional power Doppler scan. The raised melanoma lesion shows no substantial flow signals internally

The lesion appears linear, an oval-shaped or elongated lesion, bordered superficially by the intact echogenic epidermal surface. The entry echo may become irregular in cases of verrucous forms and interrupted in cases of ulcerated forms. The deep margin is generally sharp, occasionally with enhanced through transmission. Irregularity typically indicates infiltration of deeper tissue with possible recognition of spreading tumor buttons. There can be an inflammatory-reactive infiltrate (present in up to one-third of cases) in this deeper aspect of the lesion, which appears as hypoechoic as the lesion, and therefore indistinguishable from the tumor itself (although sometimes this infiltrate determines a subtle inhomogeneity of the deeper aspect of the lesion). This fact can lead to false high measurements of the primary tumor thickness using sonography. Finally, the lateral borders of the tumor should be analyzed, being irregular in the case of invasion.

Melanomas that are very thin (<0.4 mm) may not be able to be visualized in the elderly, at least when using common transducer frequencies (10–20 MHz) [33, 53, 54]. Additionally, sonography at frequencies lower than 20 MHz can overestimate the tumor thickness, mostly because of lymphocytic infiltration, regression changes, and nevus remnant [34]. A recent systematic review [53], yielding 14 studies published from 1987 to 2007, showed good to high correlation coefficients, generally greater than 0.9. Thinner melanomas are particularly those that may be incorrectly measured [55]. Data available from 7 of 14 studies showed predictive values of adequate

margins in at least 72 % of lesions [53]. The discrimination between tumors <1-mm thick and those >1 mm-thick is feasible [33]. High frequencies, up to 75 MHz, clearly allow a higher correlation with the Breslow index for thinner melanomas (owing to the increased spatial resolution) [34, 35]. However, these probes are not as widely available as others and are used mostly for study or research purposes and not in routine application. Aside from the probe utilized, it is believed that given the formalin fixation for Breslow assessment, some degree of tension loss and shrinkage tends to occur [56], and consequently the sonography measure may not directly correlate with the pathological measure as a result of overestimation. Underestimation of the lesion thickness is less common; in the case of ulceration, the thickness can be measured lower than it really is, particularly if the signal gain is not set appropriately.

Melanoma growth is dependent on the development of new capillaries that vascularize the tumor, a phenomenon that is called neoangiogenesis [57]. Microvessel density is an independent prognostic variable in vertical melanoma growth because the development of abundant vessels corresponds to the phase of rapid tumor growth [54, 58, 59]. The degree of color Doppler signals is an indicator of tumor vascularization, correlating with the pathological parameters, specifically with microvessel density [58]. Intra-tumoral Doppler vascularization can be categorized into absent, limited (only one intratumor vessel visualized), and abundant (more than one vessel visualized) [54, 58]. Flow signals are usually seen at the lesion base and are typically absent at the lateral borders [59]. Doppler vascularization is seen mostly in thicker melanomas and correlates with patient prognosis, being statistically linked to tumor relapse, lymph node status, and ulceration [59, 60]. Consequently, an abundant vascularization can be an indicator of the need for closer patient follow-up.

According to one study, color Doppler detection of intralesional vessels had 100 % specificity and 34 % sensitivity in the distinction of melanomas from other pigmented skin lesions. Consequently, sonography coupled with color Doppler imaging was considered a reliable tool for the management of pigmented skin lesions [61]. High peak velocities have been detected in patients with melanoma who developed metastasis [59]. However, sampling the small intratumor vessels for spectral analysis is not always feasible.

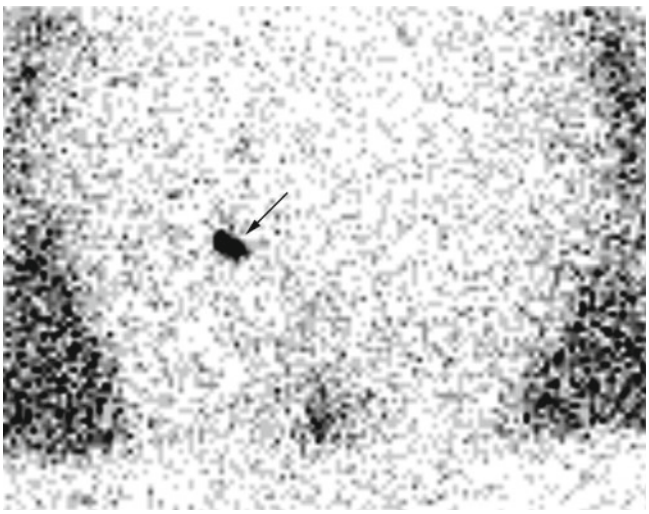

Fig. 11.21 Sentinel lymph-node procedure. Lymphoscintigraphy. Sentinel lymph-node uptake at the right inguinal station (*arrow*)

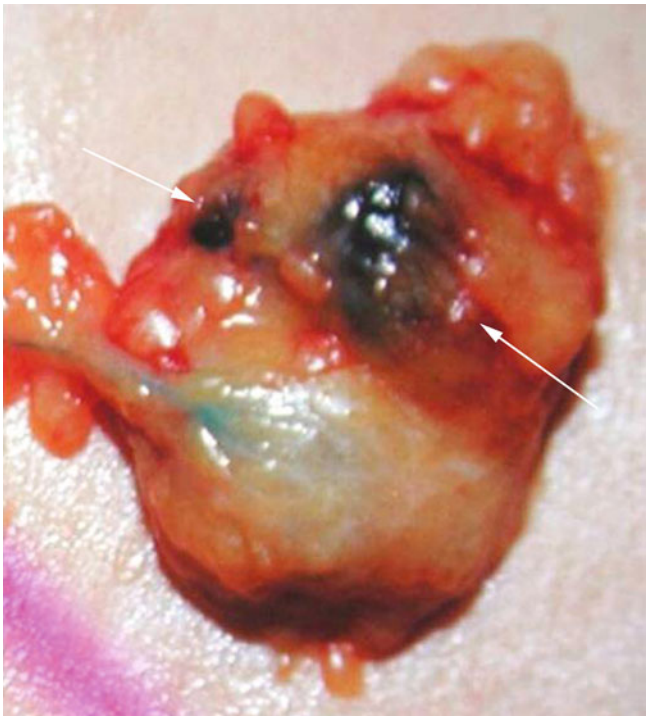

Fig. 11.22 Excised lymph node after the sentinel lymph node biopsy. Two small melanoma deposits can be seen (*arrows*)

11.3.2 Sonography of Locoregional Melanoma Spread

At initial melanoma staging in patients scheduled for the SLNB, the operator must try to detect any abnormality suspicious for metastasis to a regional lymph node. In this case the SLNB, which is an expensive, invasive (general anesthesia, surgical morbidity), and logistically demanding modality can theoretically be avoided.

SN positivity rates in the literature show some spread, yet on average, an SN positivity rate of 15–20 % is reported, with variations of 10–30 % depending on the percentage of ulcerated primary tumors, mean/median Breslow thickness of the population, and the extent of the pathological work-up used to examine the SN [9] (Figs. 11.21 and 11.22). Considering that only about 20 % of all patients with melanoma show an involved SN, this means that 80 % do not, and are then relatively "over-treated" undergoing an SLNB.

The search for an alternate staging modality showed that pre-SLNB sonography is less invasive and quite promising [62] (Figs. 11.23 and 11.24). Having detected some abnormality in sonography, this suspicious finding should be

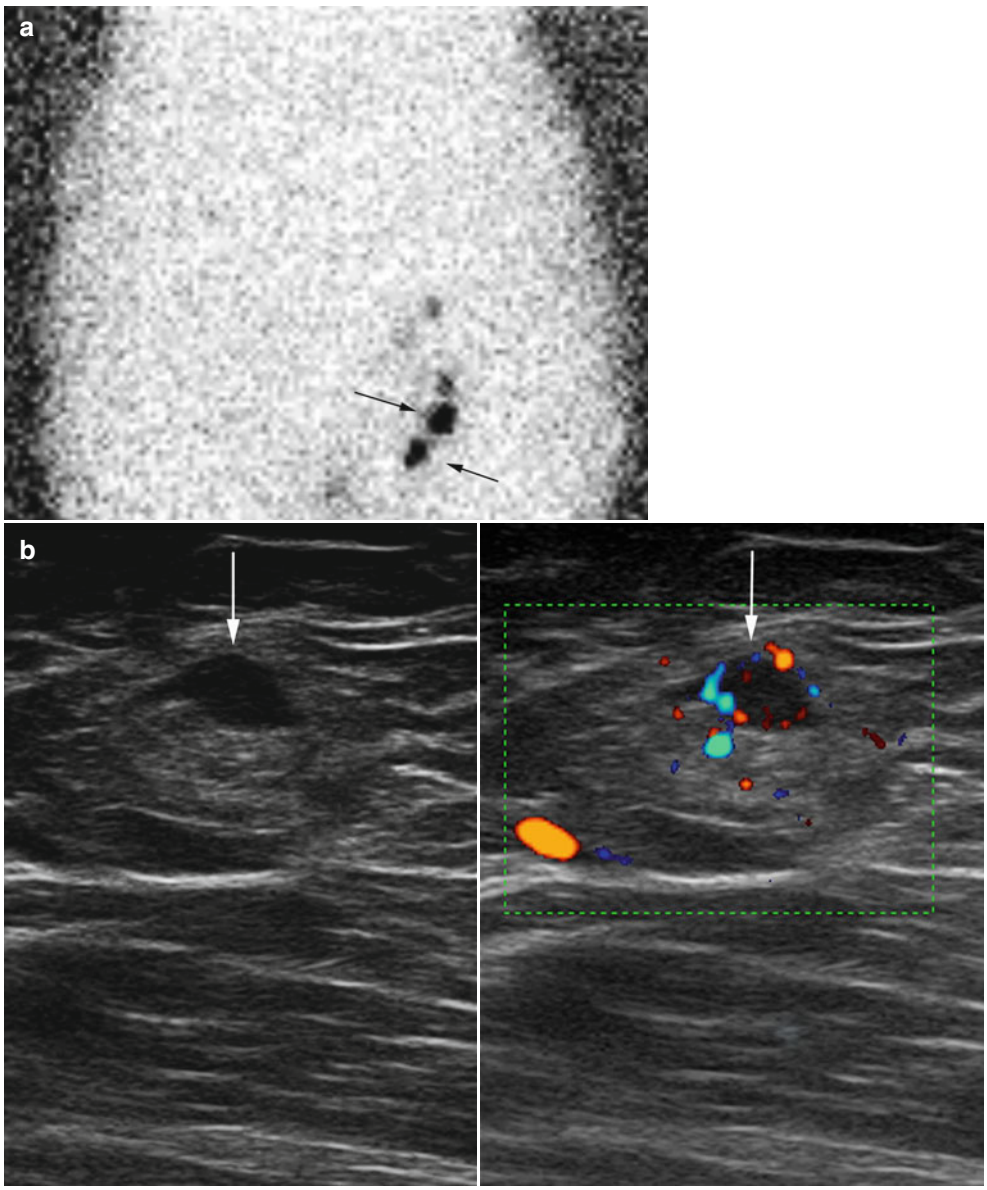

Fig. 11.23 Sentinel lymph-node procedure. Lymphoscintigraphy (**a**) and sonography (**b**). Sentinel lymph-node uptake at the left inguinal station (**a** *arrows*). The ultrasound image shows a hump-like, vascularized thickening of a small, superficial lymph node. Subsequent excision biopsy confirmed melanoma metastasis

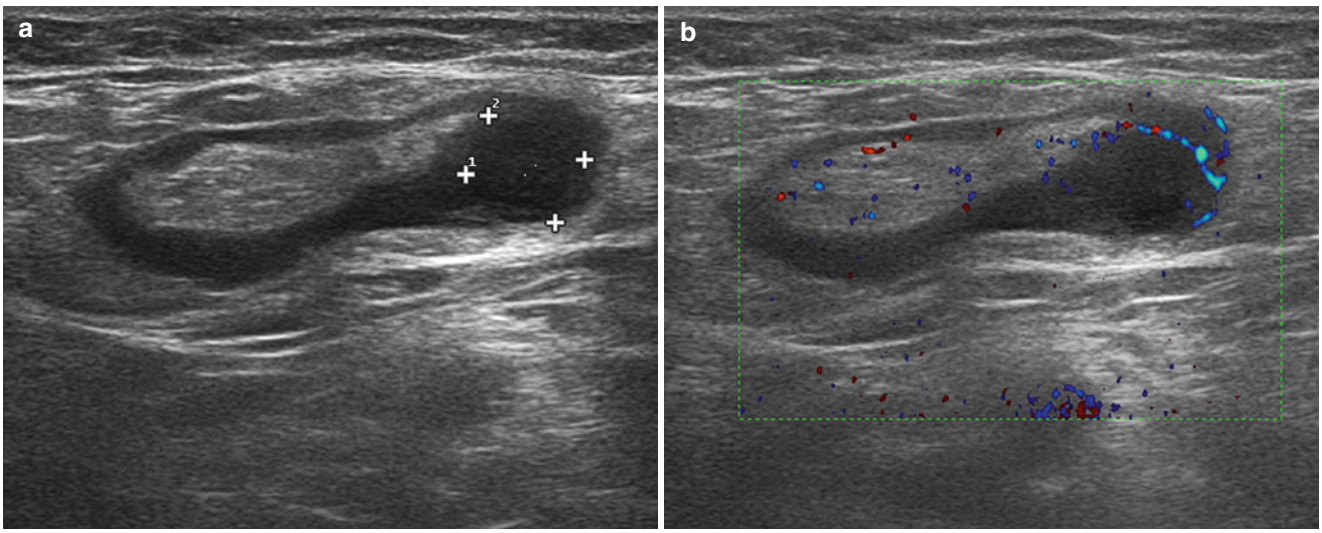

Fig. 11.24 Ultrasound image from pre-sentinel lymph node biopsy. A focal hypoechoic, 9×8 mm deposit is detected within an elongated inguinal lymph node (**a** *calipers*). The directional power Doppler scan demonstrates multiple flow signals within the nodule (**b**). Metastasis was confirmed at subsequent sentinel lymph node biopsy

Table 11.1 Studies on non-targeted sonography performed before sentinel lymph node biopsy in patients with melanoma

First author/journal and publication year/reference	Center	Study design	Patients number	Enrollment period	Transducers	Sensitivity	Specificity
Starritt/*Ann Surg Oncol* 2005 [65]	Sidney, Australia	Prospective monocentric	31	2001–2002	5–10 MHz, linear	N/A	N/A
Voit/*Ann Surg Oncol* 2006 [27]	Berlin, Germany	Prospective monocentric	127	2001–2003	Three, between 3.5 MHz and 14 MHz	79 % (82 % when combined with FNAC)	72 % (72 % when combined with FNAC)
Kunte/*Dermatol Surg* 2009 [69]	Munich, Germany	Prospective monocentric	25	2002–2003	7.5–10 MHz, linear	33.3 %	100 %
Voit/*J Clin Oncol* 2009 [28]	Berlin, Germany	Prospective monocentric	400	2001-unknown	Three transducers, between 3.5 MHz and 14 MHz	65 %	99 %
Sanki/*J Clin Oncol* 2009 [64]	Sidney, Australia	Prospective monocentric	716	2001–2005	First 5–10 MHz and then 10–14 MHz, both linear	24.3 %	96.8 %
Voit/*J Clin Oncol* 2010 [45]	Berlin, Germany	Prospective monocentric	650	2001–2007	Three transducers, between 3.5 MHz and 14 MHz	82 %	80 %

verified using FNAC. The idea is that after a positive ultrasound-guided FNAC confirmation, the patient can directly undergo radical lymphadenectomy.

Some initial studies on the value of ultrasound-guided FNAC reported sensitivity rates at around 30 % [62–64]. Those and other studies concluded that sonography is not a tool reliable enough to be used pre-operatively prior to SLNB [63, 64]. A study from the Melanoma Institute Australia, Sydney covered large numbers of patients with melanoma examined before SLNB [64]. In their study the median histologic minimum cross-sectional area of the SN metastatic deposits was 0.39 mm^2 (12.75 mm^2 for sonography true-positive results and 0.22 mm^2 for sonography false-negative results). Ultrasound-detected true-positive SNs had significantly greater cross-sectional areas than undetected SN metastases showing that most of the metastases were too small and thus escaped ultrasound detection [64]. The same group had calculated a nest size of at least 4.5 mm as crucial for the detection of involvement using sonography [65]. However, other experienced and dedicated centers have not achieved similarly promising results.

Therefore, many centers still prefer to perform SLNB, being the universally accepted standard. In a recent, large series, ultrasound-guided FNAC before the SLNB procedure identified up to 65 % of all nodal metastases [28]. New sonography morphologic criteria have significantly increased the sensitivity of this technique. Peripheral perfusion has been shown to be an early sign of metastases (77 % sensitivity, 52 % positive predictive value), whereas a balloon-shaped lymph node was a late sign of metastases (30 % sensitivity, 96 % positive predictive value) [45]. Those morphological patterns had been detected, described, and then prospectively scored and tested in a large patient population. The predetermined set of morphological criteria was compared with the golden standard of histopathology of the excised SN. Moreover, all morphology patterns were correlated to the SN tumor burden measured according to the Rotterdam criteria [66]. Additionally, they were correlated to the location of tumor nests within the SN (subcapsular vs. intraparenchymal), also known as Dewar criteria [67] or combined Rotterdam criteria [68], thus providing a correlation of the pattern and the grade of involvement. Thus, even a chronological development of certain patterns over time, from early involvement to late metastasis, could be observed [44]. In combination, these new morphology criteria were able to accurately demonstrate metastases in the mentioned 65 % of SN positive patients.

Pre-SLNB sonography can be performed in a non-targeted modality, looking for any abnormal lymph node within the regional lymphatic stations and guiding its cytological sampling. In this case the operator does not know where and which is the SN. The published articles on non-targeted sonography of patients with melanoma patient summarized in Table 11.1. As an alternative, sonography can be carried out in a targeted way, guided by lymphoscintigraphy to examine the hot lymph node (i.e., SN) that has been marked on the skin by the nuclear medicine physician. This approach is more complex because it requires that lymphoscintigraphy, sonography plus FNAC, and cytological analysis are all performed on the same day as the SLNB. The published articles on targeted sonography of the patients with melanoma are listed in Table 11.2. Another major difference between the studies by Voit et al. and the former studies might be that FNAC was performed frequently, as indicated by the early signs mentioned above. If we look at the sensitivity of the balloon-shaped lymph node, when the lymph node is echo-free and the architecture has been nearly completely destroyed by tumor cells, we see that the yield of this one morphological criterion, the balloon-shaped lymph node, resulted in 30 % sensitivity, comparable with the results of previous studies [62, 63, 65]. Yet, the introduction of a new morphology criterion, namely the presence of peripheral perfusion as a very early sign, often only visible with a very sensitive power mode, lead to a massive increase in sensitivity of 77 % [45]. At the same time, far smaller lesions were found using sonography, and even lesions >0.5 mm (measure on the histopathological glass slide) were successfully confirmed by cytology [45]. Such lesions are not visible as distinct lesions

Table 11.2 Studies on targeted sonography performed after lymphoscintigraphy and before sentinel lymph node biopsy in patients with melanoma

First author/journal and publication year	Center	Study design	Patients number	Enrollment period	Transducers	Sensitivity	Specificity
Rossi/*Eur J Cancer* 2000 [86]	Padova, Italy	Unknown	69	1993–1999	10 MHz, linear	33 %	100 %
Rossi/*J Surg Oncol* 2003 [62]	Padova, Italy	Prospective monocentric	125	1997–2000	10–13 MHz, linear	39 %	100 %
Hocevar/*Melanoma Res* 2004 [87]	Ljubljana, Slovenia	Prospective monocentric	57	2002–2003	12–15 MHz, linear	71 %	84 %
Testori/*Melanoma Res* 2005 [80]	Milan, Italy	Retrospective monocentric	88	1998–2000	10–12 MHz, linear	94.1 %	89.8 %
Van Rijk/*Ann Surg Oncol* 2006 [63]	Amsterdam, The Netherlands	Prospective monocentric	107	2000–2004	First, 7.5 MHz, linear, and then, 6–12 MHz, linear	34 % (4.7 % when combined with FNAC)	87 % (100 % when combined with FNAC)
Sibon/*Melanoma Res* 2007 [88]	Boulogne, France	Prospective monocentric	131	1999–2005	7.5–12 MHz, linear	8.8 %	95.9 %

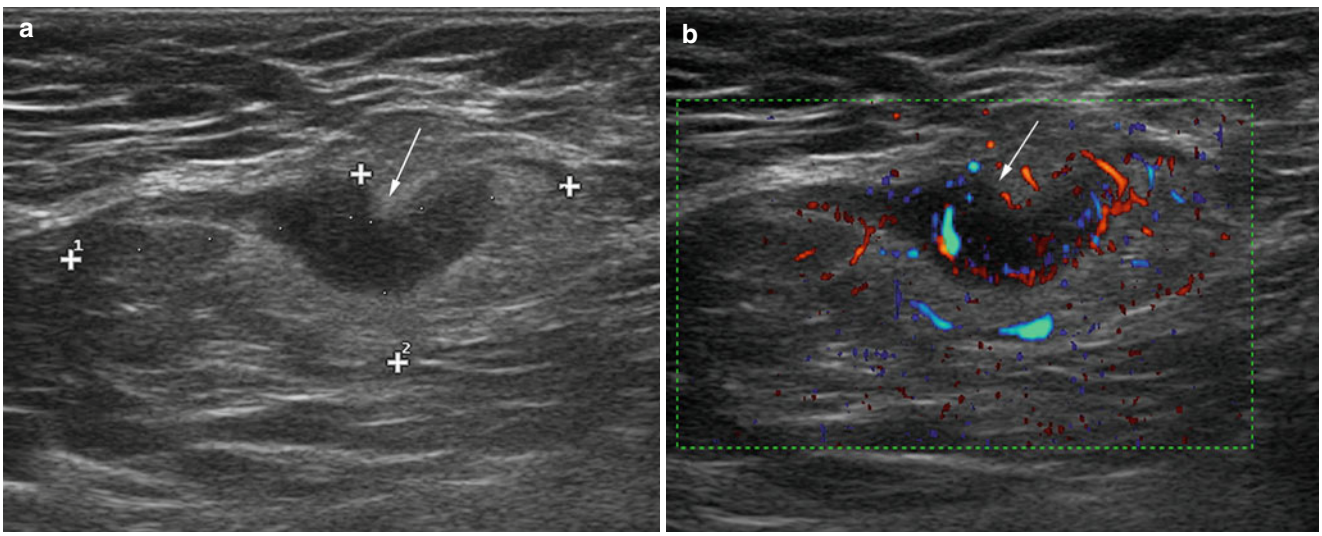

Fig. 11.25 Lymph-node metastasis 2 months after excision of a dorsal cutaneous melanoma (negative sentinel lymph node biopsy). Focal cortical thickening (**a** *arrow*) in a 37×14 mm axillary lymph node. The directional power Doppler image (**b**) demonstrates intense vascularization of the thickened cortical portion

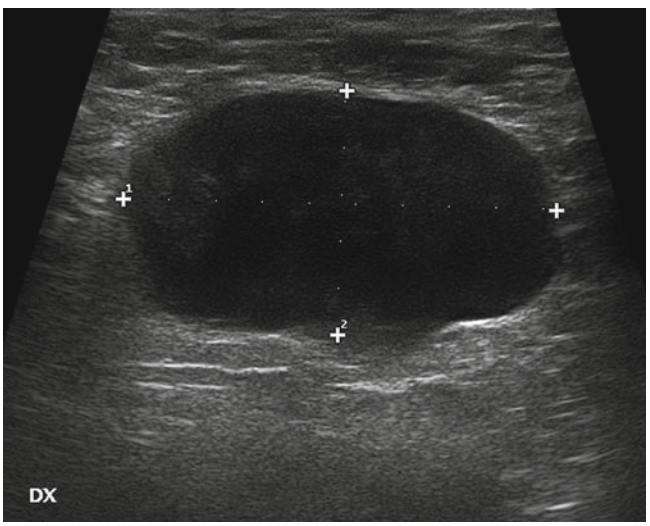

Fig. 11.26 Lymph-node metastasis 6 months after excision of a back cutaneous melanoma and negative sentinel lymph node biopsy. A large (46×26 mm) homogeneously and markedly hypoechoic lymphadenopathy is visible

but are suspected because of the early signs through the changed structural appearance of the lymph node and the emergence of peripheral perfusion, and later the starting loss of central echoes [9]. Moreover, the possibility of obtaining cytology results overnight made it possible to immediately influence treatment and perform CLND, where SN was originally planned.

Sonography can be used as a guidance tool during lymphoscintigraphy to assist with lymph node localization and to decrease the number of false negative results. It is ideal to transfer all necessary information directly to the operation table, because often the location of lymph nodes discovered by lymphoscintigraphy and marked on the skin, and that disclosed by sonography differ. Additionally, nearby structures (i.e., vessels) should be communicated to the surgeon. Sonography is also helpful in detection of other lymph-node metastasis in patients having undergone a negative or failed SLNB. It is uncommon, but the SLNB can fail to detect or excise the SN [21] (Figs. 11.25, 11.26, 11.27, 11.28, and

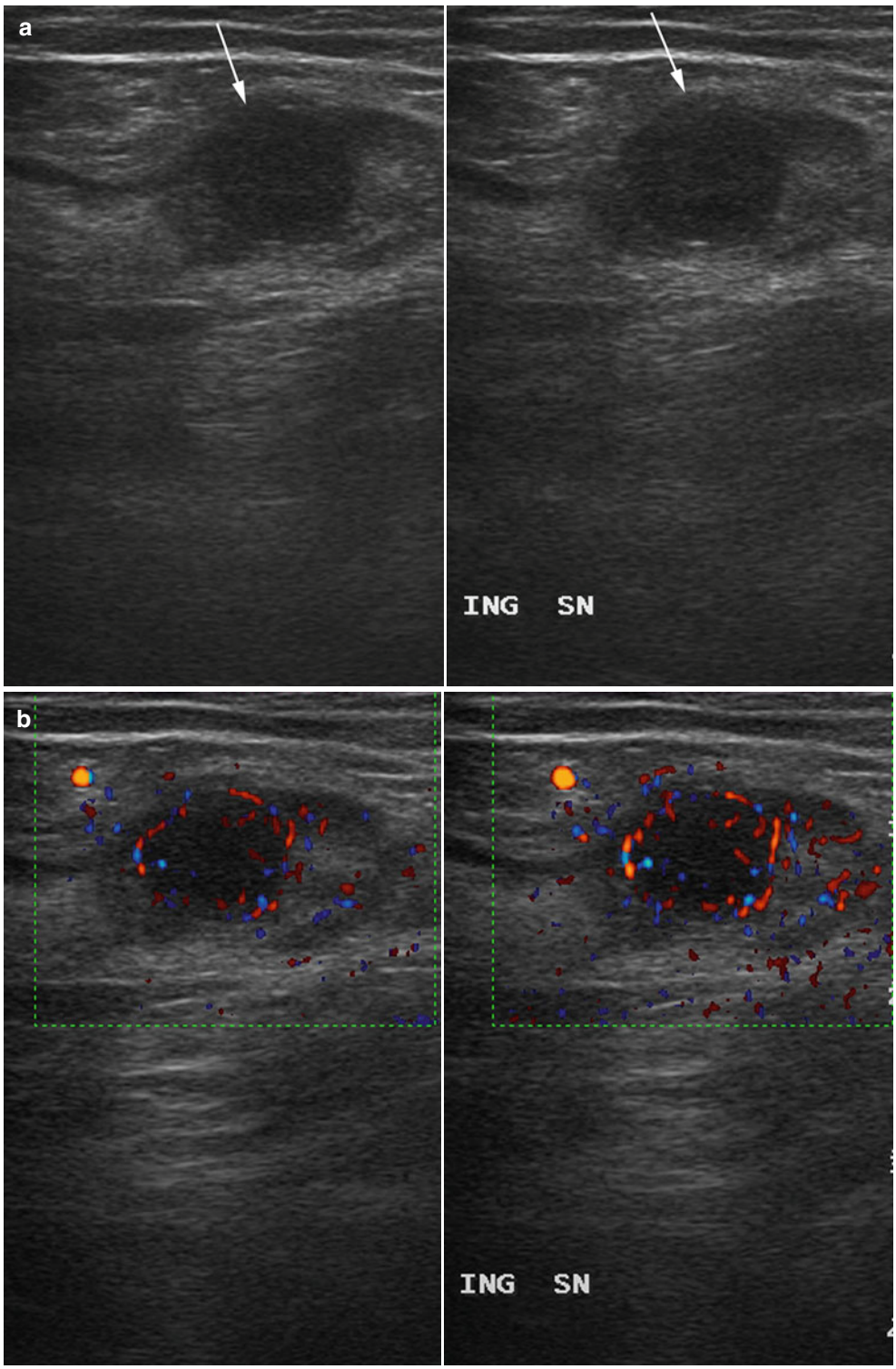

Fig. 11.27 Contralateral lymph-node metastasis after lymphadenectomy. The patient presented with abdominal wall cutaneous melanoma and had undergone right inguinal radical lymp hadenectomy after positive sentinel lymph node biopsy (SLNB) 3 months prior. The SLNB was negative on the left side but the ultrasound survey detected a focal tumor deposit (**a** *arrows*) within a left inguinal lymph node. The tumor nodule shows intense vascularization on the directional power Doppler image (**b**)

11.29). In other occurrences that are similarly uncommon, the tumor can recur at level of a lymphatic station where SN has been found to be negative during an SLNB procedure performed weeks or months prior [70]. The failure/false negativity of SLNB can result from various causes relating to the lymphoscintigraphy technique, the operative procedure, the experience of the surgeon and his/her personal learning curve, or with the histopathologic examination of the SN. The potential occurrence false-negative results of SLNB prompts the need for short-term clinical, and possibly sonographic, monitoring of the regional lymphatic stations after a negative SLNB result. While scanning the lymphatic station after the SLNB, the radiologist should consider the potential pitfalls, such as the presence of a lymphocele that can be

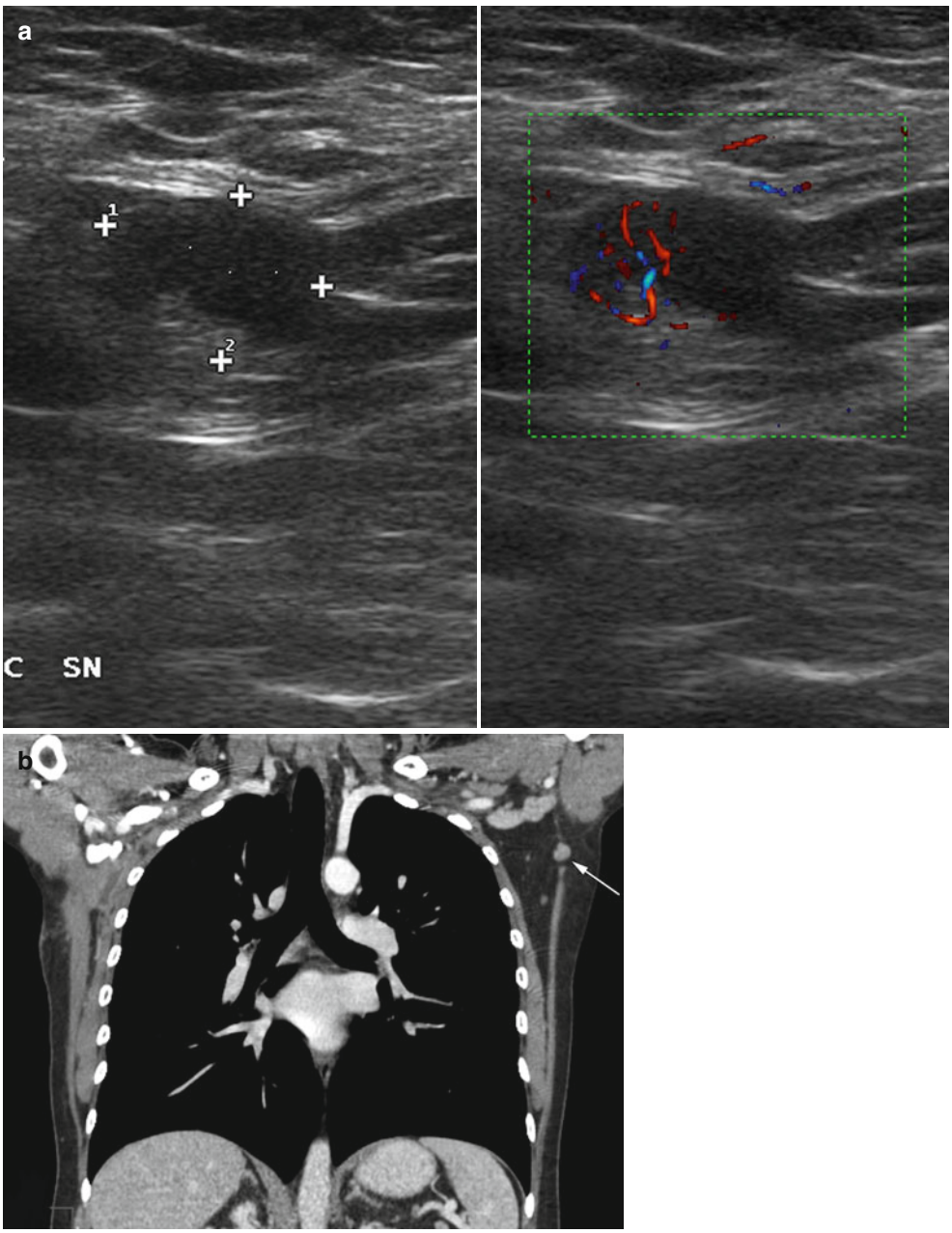

Fig. 11.28 Contralateral lymph-node metastasis after lymphadenectomy. The patient presented with dorsal cutaneous melanoma and had undergone right axillary completion lymphadenectomy after positive sentinel lymph node biopsy (SLNB) 5 months prior. The SLNB was negative on the left side. However, subsequent ultrasound follow-up detected a focal, vascularized tumor deposit within a 13×9 left axillary lymph node (**a** *calipers*). The coronal reconstruction from the contrast-enhanced computed tomography scan confirms the left axillary metastasis (**b** *arrow*)

misinterpreted as an enlarged lymph node. The occurrence of a lymphocele/seroma is not a rare event following SLNB. The use of color Doppler ultrasound will again help to differentiate the lymphocele (no signals) from the suspicious lymph node. The lymphocele can then be easily removed by a making a puncture to remove the surplus fluid (Figs. 11.30, 11.31, and 11.32).

This is based on physical examination as the first line assessment in what relates to follow-up of patients with melanoma. Patients who had been operated on for melanoma are initially followed-up with for 3- or 6-month visits, depending on patient risk of recurrence (i.e., depending on the primary tumor features, the sentinel node status, the recommendations of the skin cancer guidelines of each country, and consensus meetings) [71] (Figs. 11.33, 11.34, 11.35, 11.36, 11.37, 11.38, 11.39, and 11.40). Thereafter, patients are evaluated annually. Sonography is currently also being used for follow-up of patients with melanoma for the surveillance of the primary tumor area (10-cm radial area around the scar) and of the regional lymph-node stations [31, 72]. When an indeterminate lymph node is found during patient follow-up, there are two main decision approaches: immediate FNAC or 2–8 week follow-ups [19, 25, 29, 30]. The choice between the two options depends on several factors including the level of clinical and sonography confidence, facility access to cytology, patient anxiety status, and operator skill.

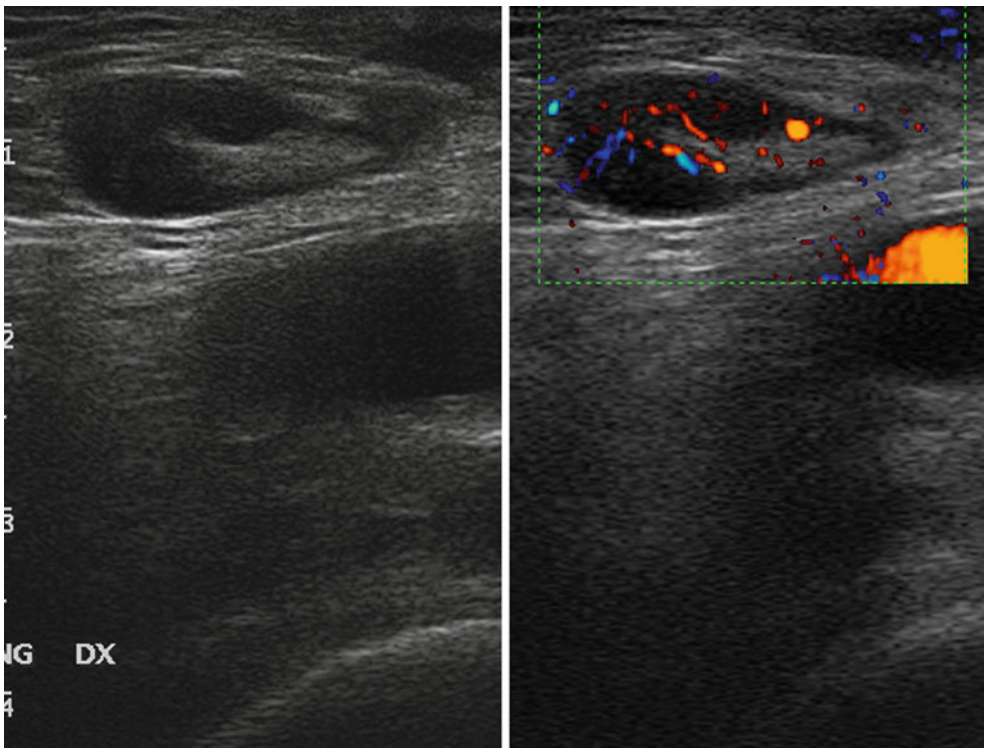

Fig. 11.29 Lymph node metastasis 2 months after negative inguinal sentinel lymph node biopsy. Image showing detection of a superficial lymph node with asymmetrical cortical thickening and multiple flow signals (directional power Doppler side of the split-mode image)

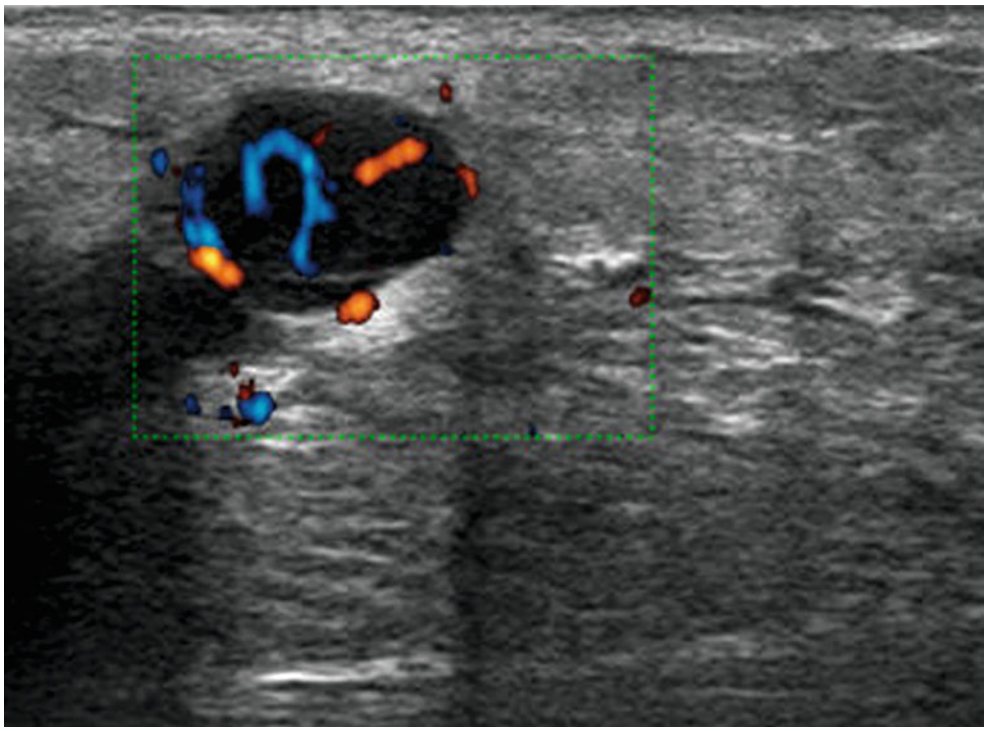

Fig. 11.30 Seroma vs. metastasis. Directional power Doppler image. In pure B-mode the posterior enhancement of the echoes would be misleading for a diagnosis of seroma. However, the artificially written question mark, depicted here by power mode, easily leads to raise the diagnosis of a metastasis

Satellite and in-transit metastases, as well as hematogenous subcutaneous metastases, appear as subcutaneous and hypoechoic nodules (Figs. 11.41, 11.42, 11.43, 11.44, 11.45, 11.46, 11.47, 11.48, 11.49, and 11.50). Because melanin scarcely reflects the sound beam, melanoma metastasis typically presents as a marked hypoechogenicity, sometimes approaching cyst-like anechogenicity with possible acoustic enhancement [22, 36, 73]. The shape is round, oval, or lobulated and the contour is usually sharp. The best way to differentiate them from small lymphoceles in the in-transit distance through the use of color Doppler ultrasound or a higher power mode because these metastases regularly

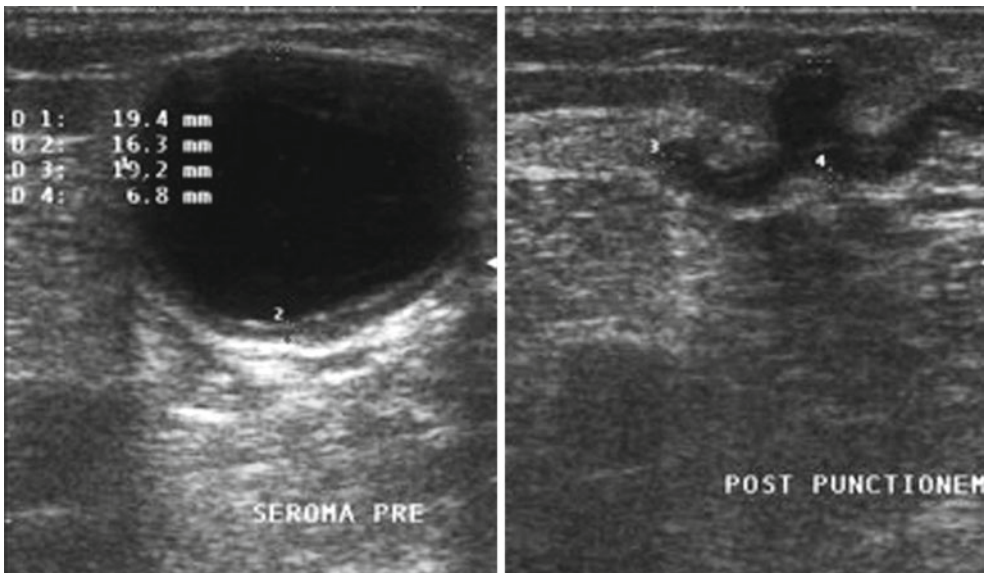

Fig. 11.31 Seroma. Left side pre- and right side post-puncture, leaving just a small "octopus-like" structure

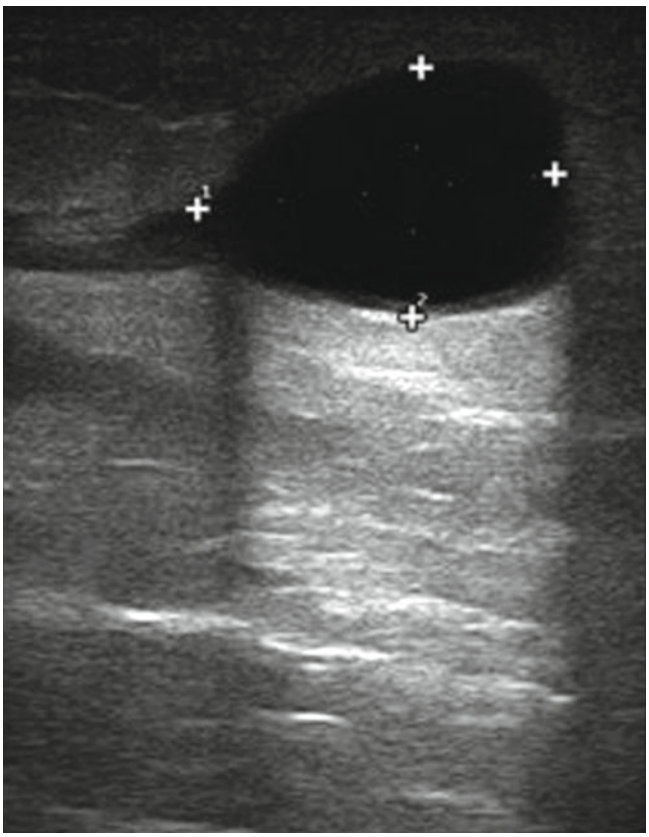

Fig. 11.32 Seroma-like widening of the lymphatics and dilated canal toward the seroma

present faint peripheral signals of vascularization (Figs. 11.51 and 11.52). Because in-transit nodules grow along the lymphatic ducts, in some cases it is possible to note a hypoechoic band entering the metastasis on one side and exiting on the other, which is the direct image of the dilated duct filled with melanoma cells (Fig. 11.53). In other cases, the lesions merge with each other while progressively growing to develop an elongated lesion (Fig. 11.54). Melanoma metastases show a variable degree of vascularization, ranging from scarce and peripheral, to diffuse and intense, and depends on the grade of involvement and the chronological age of the metastasis. While the presence of flow signals is helpful in proving that a lesion is solid, the absence of vascularization is not helpful in excluding a melanoma metastasis [74]. The vascularization have a false-negative result when the preset of the sonography device has not been chosen correctly, the device is not sensitive enough, or if the examiner exerts too much pressure on the transducer.

Lymph node assessment is based on analyzing the size, shape, border, and internal echotexture of the node (Figs. 11.55, 11.56, 11.57, 11.58, and 11.59). A recent critical review [75] has shown how the diagnostic criteria for melanoma nodal metastasis diagnosis used in published articles are extremely heterogeneous and sometimes unclear, emphasizing the need to establish definitive, clearly defined, and univocal diagnostic criteria to be applied in daily clinical practice as well as to be used for publications. Some dated published studies considered a longitudinal diameter >2 cm [76, 77] or >3 cm [78] as a suspicion criterion. However, we have seen enough examples where patients present with a longitudinal diameter of a lymph node of ≥ 4 cm, and have been neither FNAC (e.g., sentinel nodes that had been fine needled within the scope of a study even if they did not seem suspicious on sonography) [27] nor in sonography follow-up of the lymph nodes. The nodal size by itself is currently no longer regarded as a diagnostic criterion. However, a lymph node with a non-specific appearance (i.e., slightly thickened cortex) becomes more suspicious when it is also large in size. Small-sized lymph nodes may sometimes appear round, or

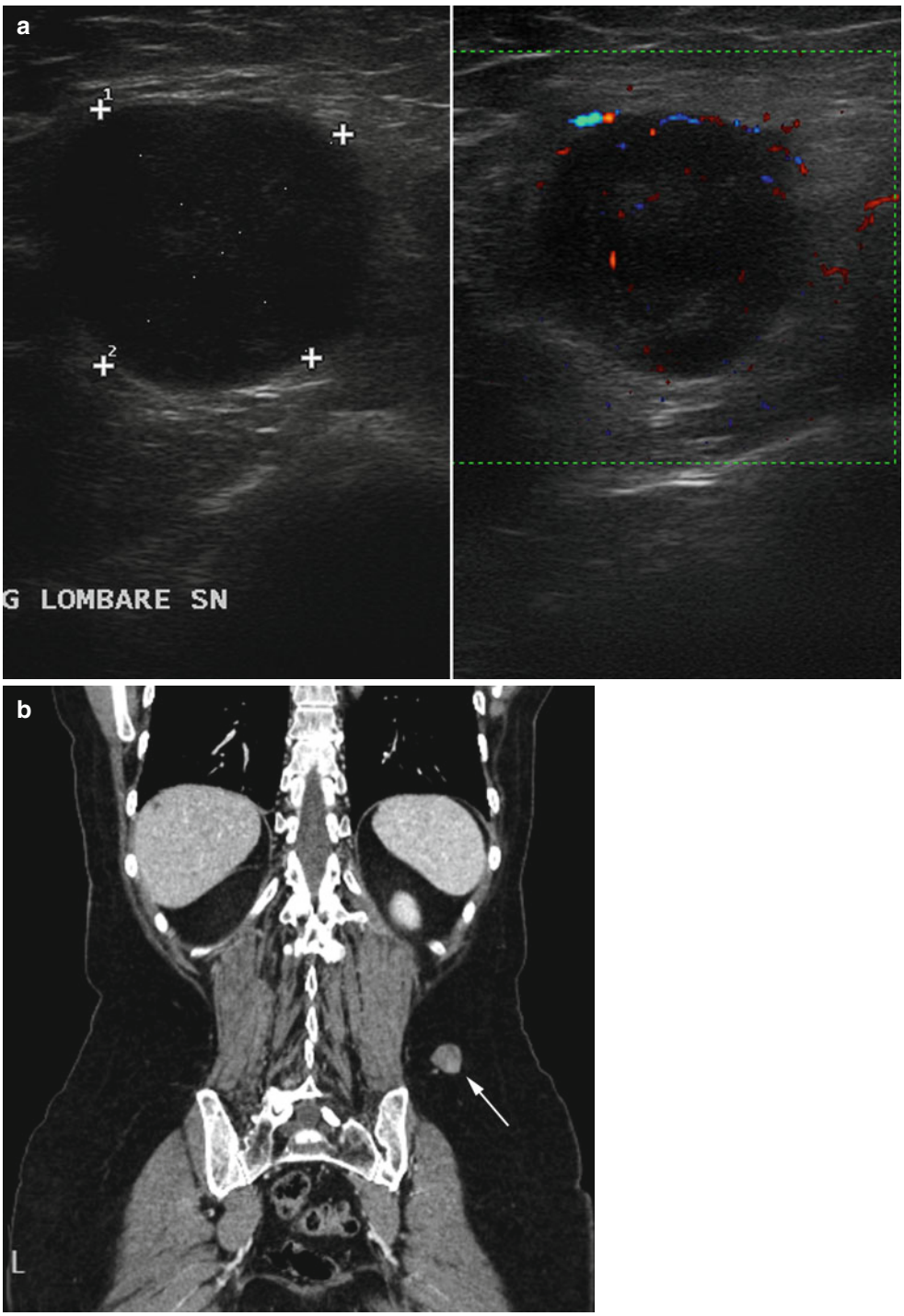

Fig. 11.33 Lumbar recurrence. Detection of an in-transit 26×25 mm nodule of the loin (**a**) 1 year after excision of a flank cutaneous melanoma. The directional power Doppler portion of the split-mode image (**a**) shows multiple, peripheral flow signals. The coronal reconstruction of the contrast-enhanced computed tomography scan confirms the subcutaneous nodule (**b** *arrow*)

may show a loss of the hilum hyperechogenicity or a cortical thickening, but most patients will still be considered as benign if these changes are not marked. Even in cases of small nodes where the changes are not marked, the use of fine-needle aspiration is recommended. A total of 2,446 FNACs were performed in 1,279 patients, of which 421 FNACs (20.9 %) were performed in lesions <10 mm, and 216 lesions <6 mm and 149 lesions <5 mm were successfully punctured, with sensitivities of 96.3 % and 96.9 %, respectively. In the 5-mm lesions a specificity of 98.1 %, a positive predictive value of 98.9 %, and a negative predictive value of 94.4 % were achieved [79]. The same changes would be more easily considered suspicious in large-sized lymph nodes.

The lymph node is considered suspicious when oval-shaped or even more when round while it is not suspicious when markedly elongated. Some authors consider a longitudinal/

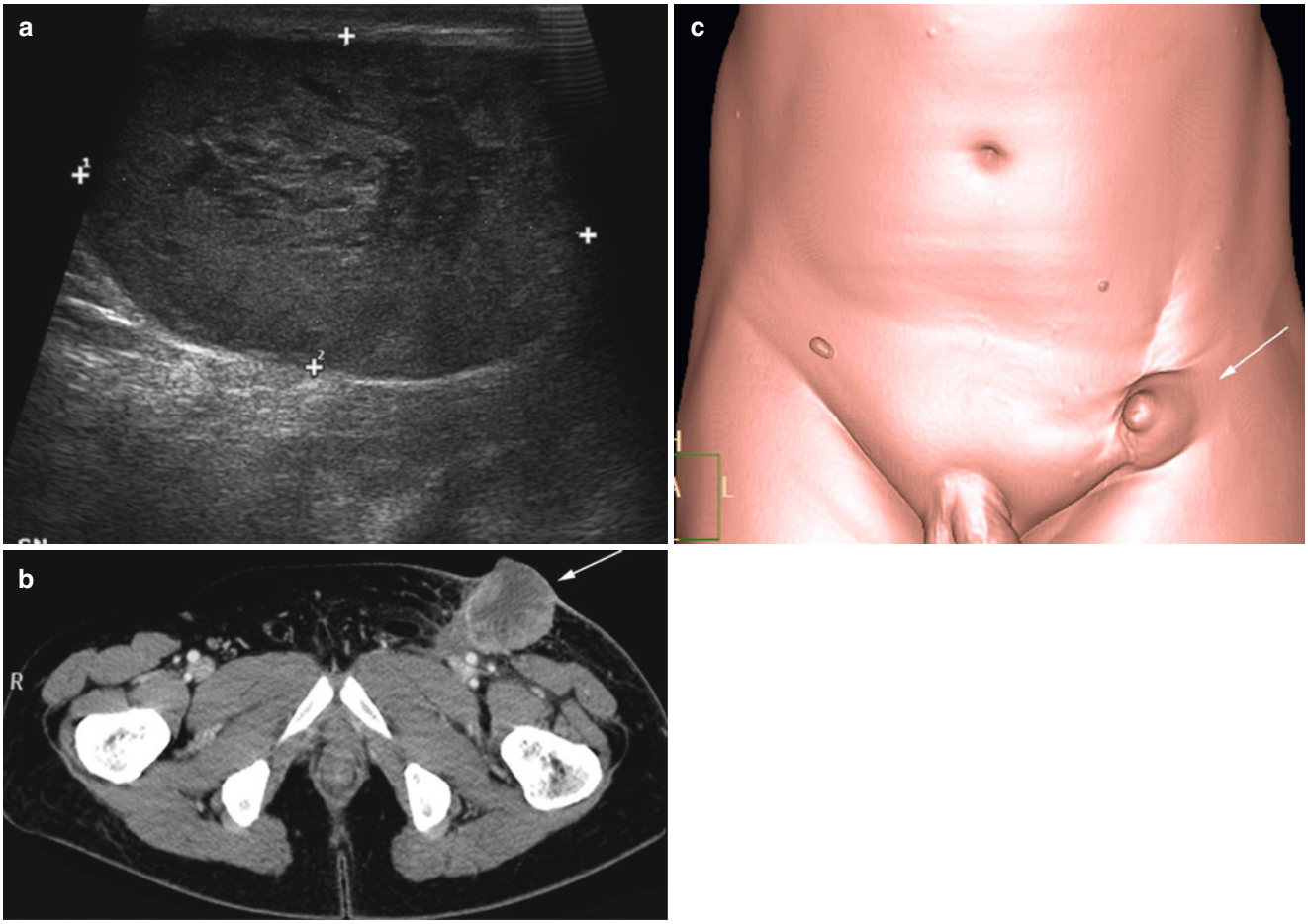

Fig. 11.34 Post-surgical recurrence. A large (56×36 mm) lymph-node mass is seen 8 months after inguinal radical lymphadenectomy (**a** *calipers*). The contrast-enhanced axial computed tomography image (**b** *arrows*) confirms the internally necrotic, left inguinal lesion. The surface reconstruction from the volumetric CT data set depicts cutaneous bulging (**c** *arrows*)

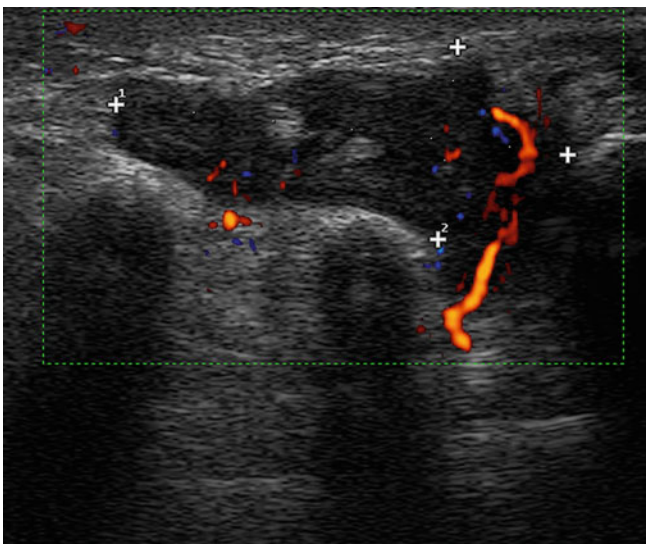

Fig. 11.35 Local melanoma recurrence. Tumor tissue (*calipers*, 29×12 mm) with flow signals at directional power Doppler is seen deep into the foot near the metatarsal bones

transverse (L/T) diameter <2 [69, 76, 80] as suspect, while other authors including us, consider an L/T ratio of <1.5 [36, 81, 82] as threshold (Fig. 11.60). A 1.5 threshold probably increases the rather low specificity of the size criterion. Additionally, the use of the L/T ratio, also called the Vassallo or Solbiati Index, has been prospectively tested [45]. A Vasallo/Solbiati Index showing a threshold of >2 in most cases of benign lymph nodes was checked [83, 84] and was not a statistically significant predictor of involvement, nor was it a predictor of non-involvement. Similarly, the size of the lymph nodes was not a useful characteristic for involvement (i.e., increasing size was not translated into an increasing number of detected malignant SNs) [45]. In any case, the nodal shape should not be used as a stand-alone criterion for diagnosing malignancy. More relevance has currently been placed on cortical changes, which can indicate an early stage of lymph node metastasization, eventually preceding the typical finding of a round and diffusely hypoechoic lymph node [31]. The lymph nodes exhibiting a diffuse but symmetric (circumferential) thickening of the cortex as the only abnormality should be

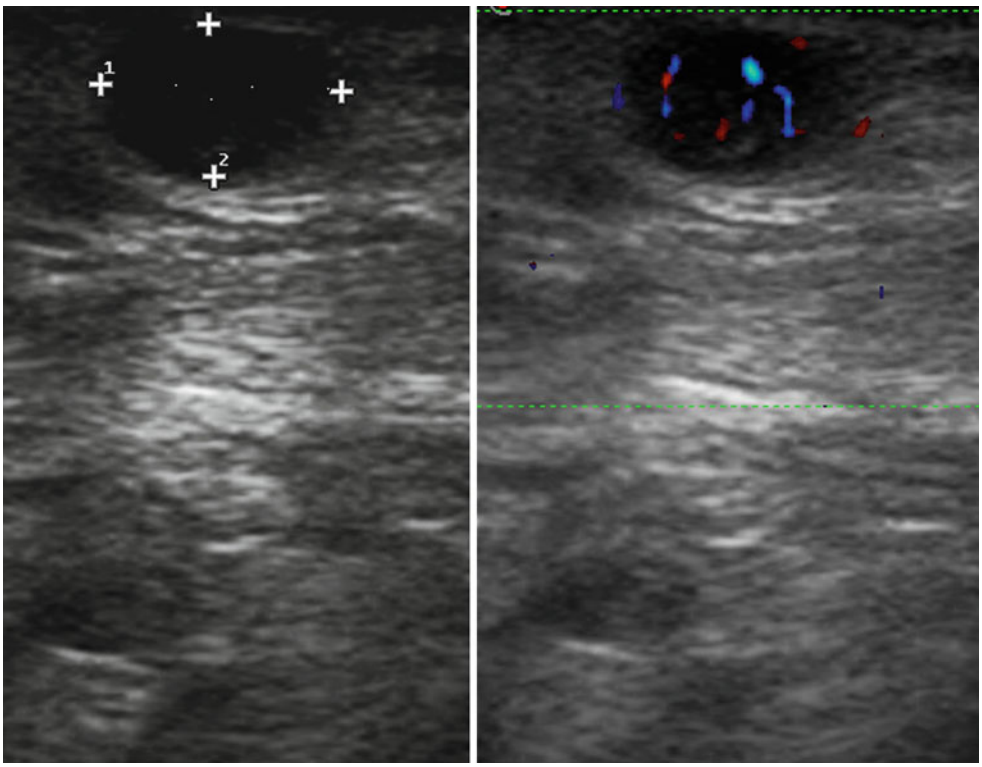

Fig. 11.36 Local recurrence after radical lymphadenectomy. Detection of a subcutaneous 6×4 mm hypoechoic nodule with multiple flow signals in the directional power Doppler side of the split mode image

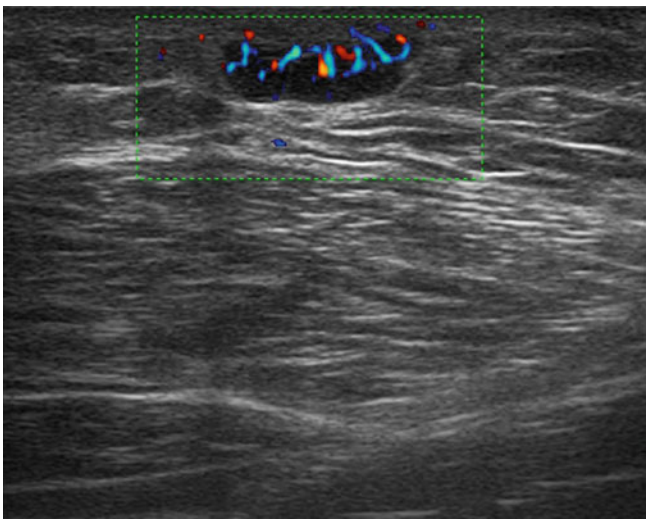

Fig. 11.37 Cutaneous metastasis of the chest. Directional power Doppler image shows flat hypoechoic nodule with intense vascularization

considered indeterminate. However, the lymph nodes showing an asymmetric (unilateral) cortical thickening should be considered suspicious (Figs. 11.61, 11.62, 11.63, 11.64, 11.65, and 11.66).

Finally, lymph nodes with a focal, eventually nodular, thickening of the cortex are generally diagnosed as metastatic (Figs. 11.67, 11.68, 11.69, 11.70, 11.71, 11.72, 11.73, 11.74, 11.75, 11.76, 11.77, and 11.78). The "node within the node" may vary in size from millimetric to a large deposit involving most of the lymph node. It has been described as the "hump sign" because at onset it looks extremely similar to a hump on the back of a camel [45]. This has been depicted using a sketch in a recent publication [70]. Sketches are useful for describing certain patterns of a lymph node and are helpful to examiners in re-detecting a lymph node when it is under observation. The hump can be isoechoic or hypoechoic in comparison with the rest of the cortex but in both cases virtually indicates a partial metastasis when compared with a slight perfusion in this area. Focal metastasis may develop in lymph nodes, being oblong and not just oval, with an evident echoic hilum with a very thing cortex in all other areas, but that lymph node will still be diagnosed with confidence as metastatic because of the asymmetric broadening of the parenchyma.

Other tumors produce focal protuberances of the lymph-node contour but the nodules are usually isoechoic to the remaining cortex (hypoechoic by itself). In conjunction with evaluating the appearance of the cortex, attention should be given to the changes within the central hyperechoic "hilum". The hilum region can be displaced, reduced in size, become overtly inhomogeneous, or totally disappear. A small hilum can be a non-specific finding, however, a hilar displacement by an asymmetric or focal cortical thickening or a partial or total substitution of the hilum with hypoechoic tissue indicates metastasis. In a recent publication, this pattern was described as "wandering of the central echo to the rim" and in the chronological course of time it can end up in a so-called complete loss of central echoes until tumor cells have finally

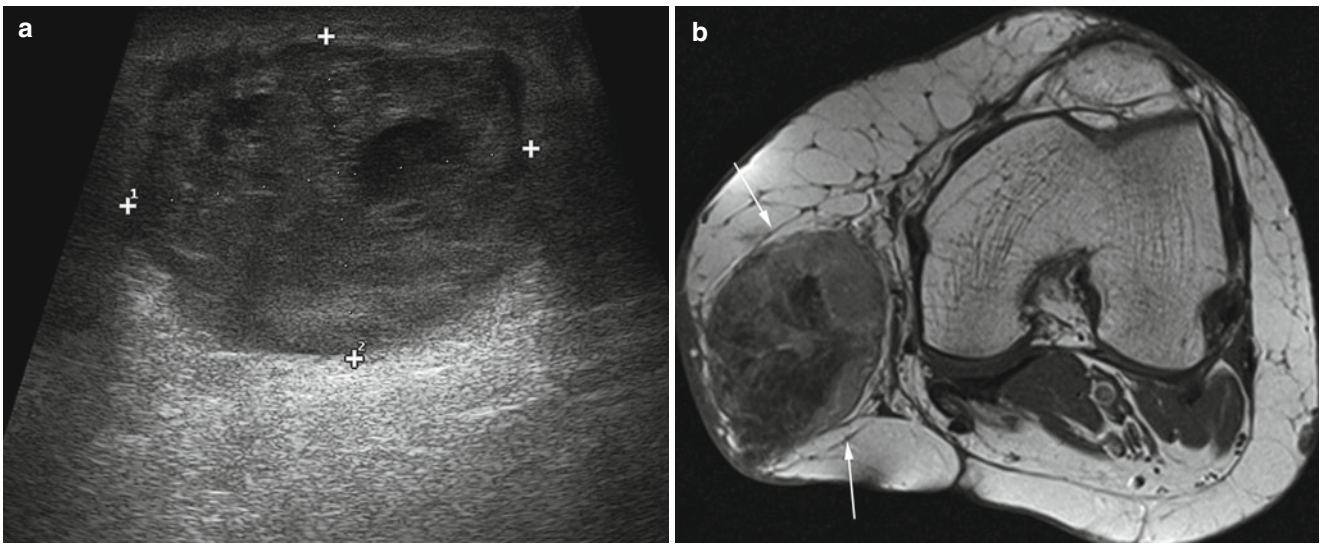

Fig. 11.38 Knee metastasis in a patient with history of cutaneous melanoma in the leg. Ultrasound image shows a partially necrotic, 44×35 mm mass (**a** *calipers*). The subcutaneous lesion is also evident on the axial magnetic resonance image (**b** *arrows*)

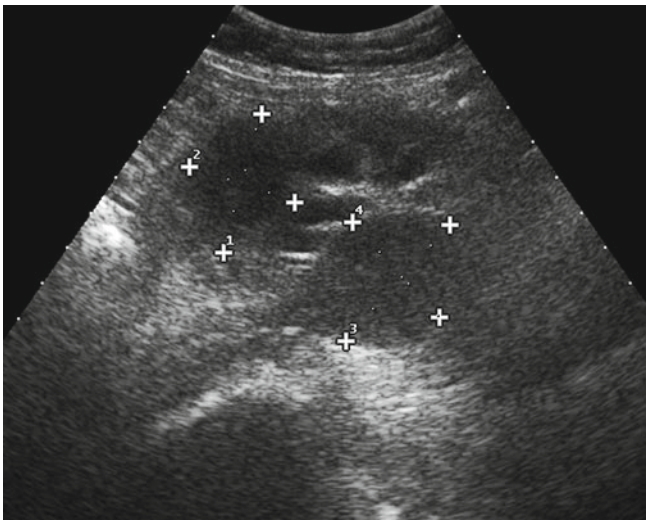

Fig. 11.39 Iliac recurrence after inguinal radical lymphadenectomy. The ultrasound image obtained using an abdominal, low-frequency probe shows two hypoechoic, iliac lymphadenopathies (34×26 and 36×30 mm)

destroyed the complete lymph node architecture [45]. The borders of a metastatic lymph node are commonly described as being sharp, eventually irregular in most cases, while reactive lymphadenopathy are said to show both sharp or blurred margins [82]. However, the nodal border too subjective of a criterion and is usually not taken in consideration [31]. Anechoic necrotic areas of variable extent can sometimes be seen internally within larger metastatic lymph nodes (Figs. 11.79 and 11.80).

Color Doppler and power Doppler imaging should be routinely used to investigate any abnormal lymph nodes or subcutaneous lesions encountered. There are two different main vascular patterns should be distinguished: benign lymph nodes show a monopolar vascularization, with vessels entering the lymph node hilum and distributing regularly toward the periphery (without reaching the nodal cortex); in malignant lymph nodes the "color hilum" is lost or displaced while multiple vessels penetrate the nodal capsule and enter the lymph node distributing anarchically [30] (Figs. 11.81, 11.82, 11.83, 11.84, 11.85, 11.86, 11.87, 11.88, 11.89, and 11.90). Doppler ultrasound is particularly helpful in indeterminate circumstances, improving operator confidence in suspecting malignancy. When a lymph node shows diffuse thickening of the cortex (i.e., a lower than usual size of the echoic hilum, meaning that the broadening of the parenchyma is often gained by a loss of the hilum), detecting a hilar vascularization decreases the4 suspicion. On the other hand, an abnormal vessel distribution prompts further investigation. Furthermore, when the B-mode demonstrates an isoechoic asymmetric thickening of the lymph node cortex or a focal bulging of the cortex, Doppler ultrasound techniques may allow for detecting a somehow different vascularization of the suspected area. The vascularization can range from being more or less vascularized than the remaining portions of the lymph node or clearly showing capsular vessels directly related to that area. Finally, as mentioned previously, when a small subcutaneous lesion is found, possibly indicating a an in-transit nodule or a metastatic lymphadenopathy, the detection of even minimal flow signals can allow the proper differentiation from other abnormalities such as small seromas or cysts.

Spectral Doppler imaging is time-consuming and requires being of sufficient caliber for the detection of vessels (Fig. 11.91). Additionally, there is a significant overlap between the spectrum of benign and malignant lymph nodes in patients with melanoma when using Doppler imaging.

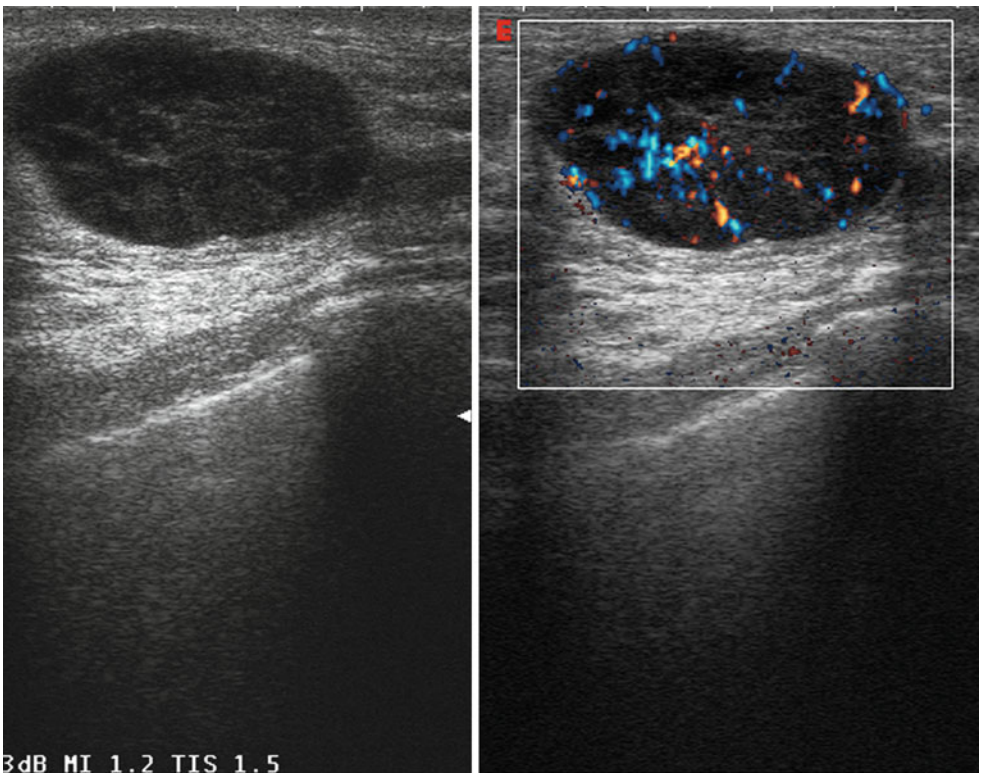

Fig. 11.40 Breast melanoma metastasis. Intramammary inhomogeneously hypoechoic nodule showing intense vascularization on the directional power Doppler portion of the split-mode image

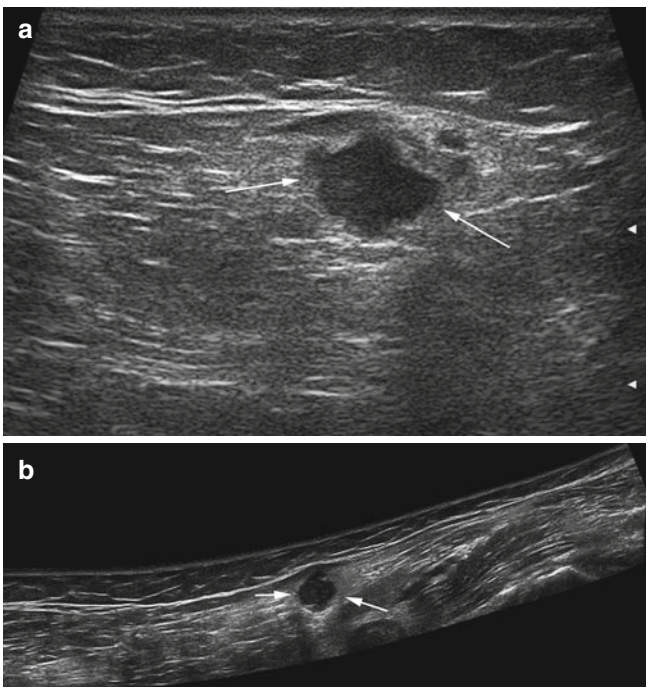

Fig. 11.41 In-transit metastasis. The ultrasound image (**a** *arrows*) shows an abnormal lymph node within the popliteal fossa. The extended field-of-view image demonstrates the topographic relationships of the lymph node (**b** *arrows*)

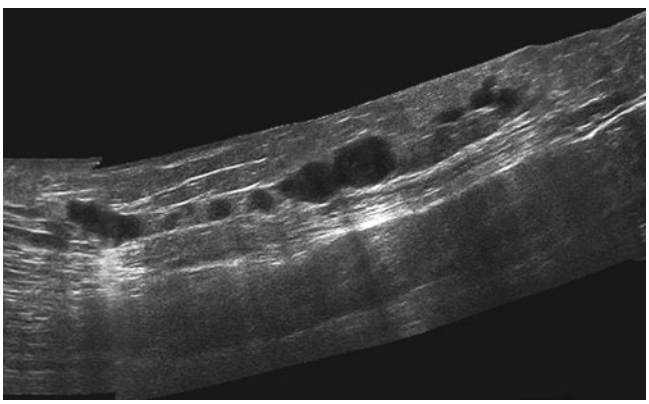

Fig. 11.42 In-transit metastases. Extended field-of-view image allows a comprehensive depiction of multiple melanoma nodules disposed longitudinally along the thigh

A round or oval lymph node with (markedly) hypoechoic texture is virtually diagnostic for metastasis, aside from its size. Various conditions can be associated with a nodular hypoechoic image within the soft tissues including normal or abnormal vessels, dense scars, fluid collections (seromas, hematomas, lymphoceles, etc.), cysts, abscesses, and benign tumors [23]. Nevertheless, patient history combined with B-mode and color Doppler imaging findings usually allows for an adequate differentiation. The operator should be adequately

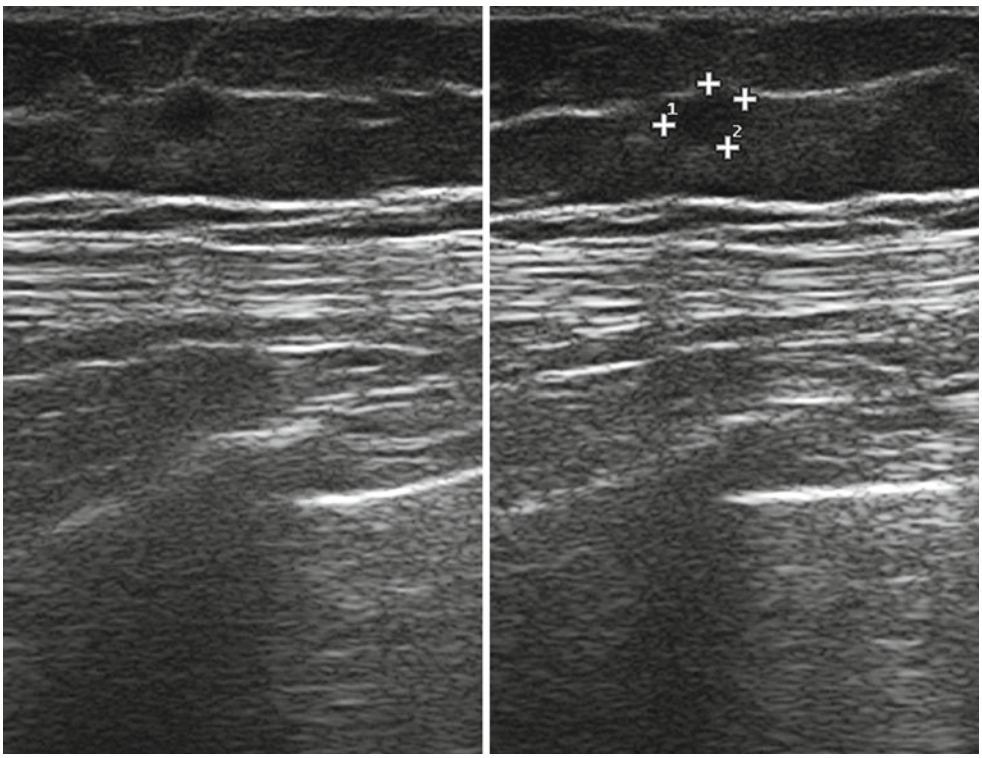

Fig. 11.43 In-transit metastasis. Detection of a 4 × 3 mm metastatic nodule (*calipers*) within the subcutaneous layer of the thigh

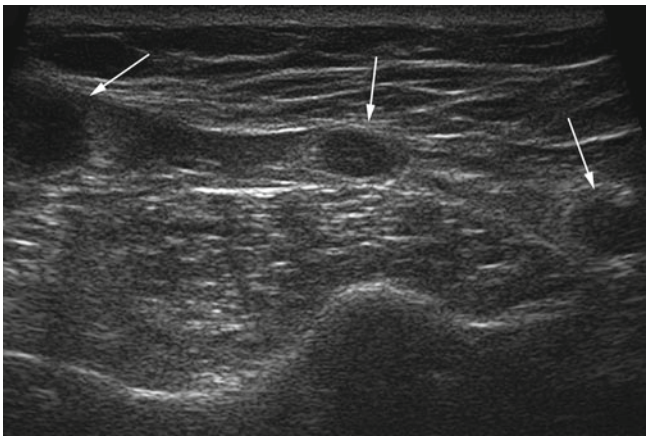

Fig. 11.44 In-transit metastases. Three metastatic nodules (*arrows*) are seen within the soft tissues of the shoulder

aware of the appearance on sonography of normal, reactively enlarged, involutively enlarged (fatty metamorphosis), inflammatory (acute and chronic lymphadenitis), and neoplastic lymph nodes. The fatty metamorphosis can very often imitate hypoechoic areas within the lymph node which can easily be mistaken for intranodal metastases described as echo-free islands [45]. The echoes are difficult to see in B-mode if you increase the gain in the fatty metamorphosis, while the intranodal metastasis seems to be more echo-free, therefore, making it difficult to distinguish one from the other. Additionally, the use of the color Doppler and power Doppler mode is again helpful. Fatty metamorphosis regularly does not present with any vascularization. The sonography operator should consider the fact that the appearance of normal lymph nodes can differ between the various lymphatic stations (neck, axilla, and inguinal region) and in young and old patients [85].

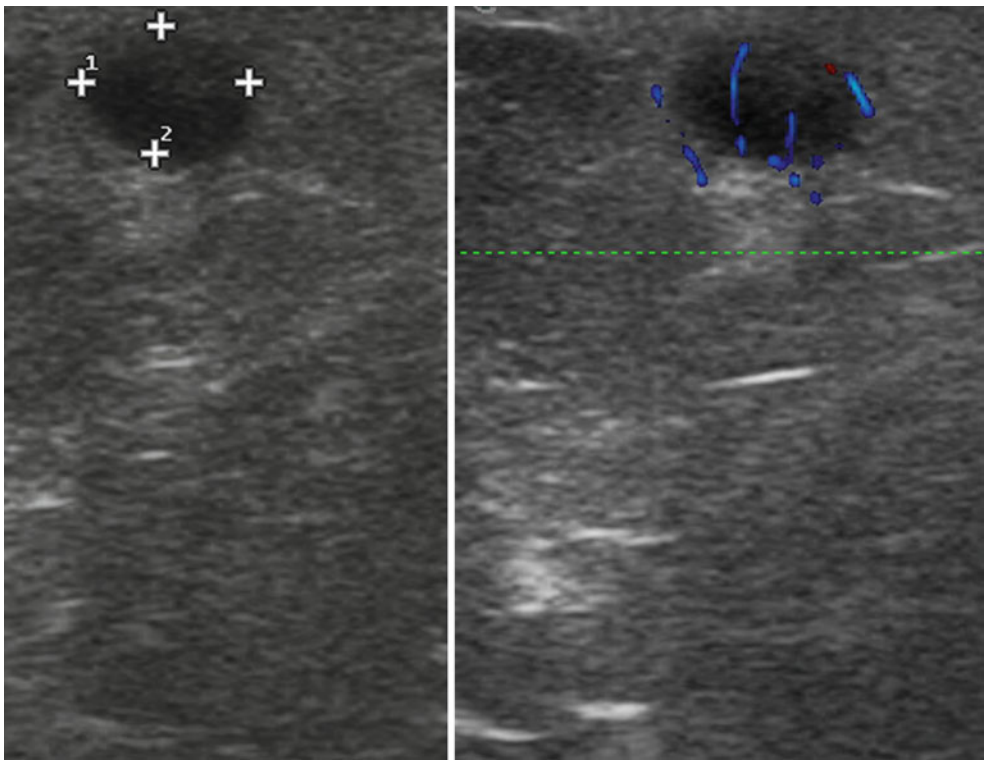

Fig. 11.45 In-transit metastasis. Small (4×3 mm) melanoma nodule is detected within the thigh subcutaneous layer. Despite the very small size, multiple vessels are visible on the color Doppler side of the split-mode image

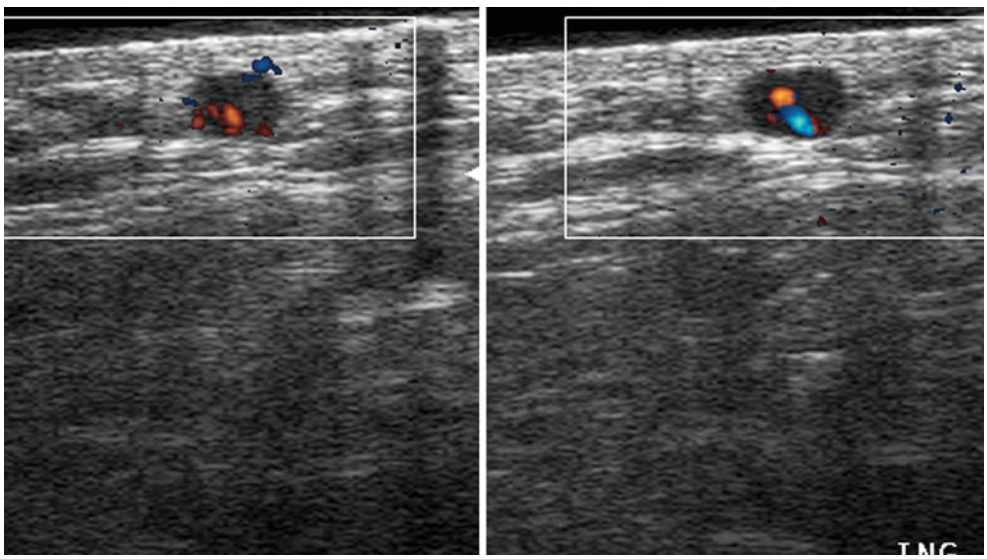

Fig. 11.46 In-transit metastasis. Small (4 mm) melanoma nodule is visible within the inguinal region. Despite the very small size, flow signals are visible on the directional power Doppler image

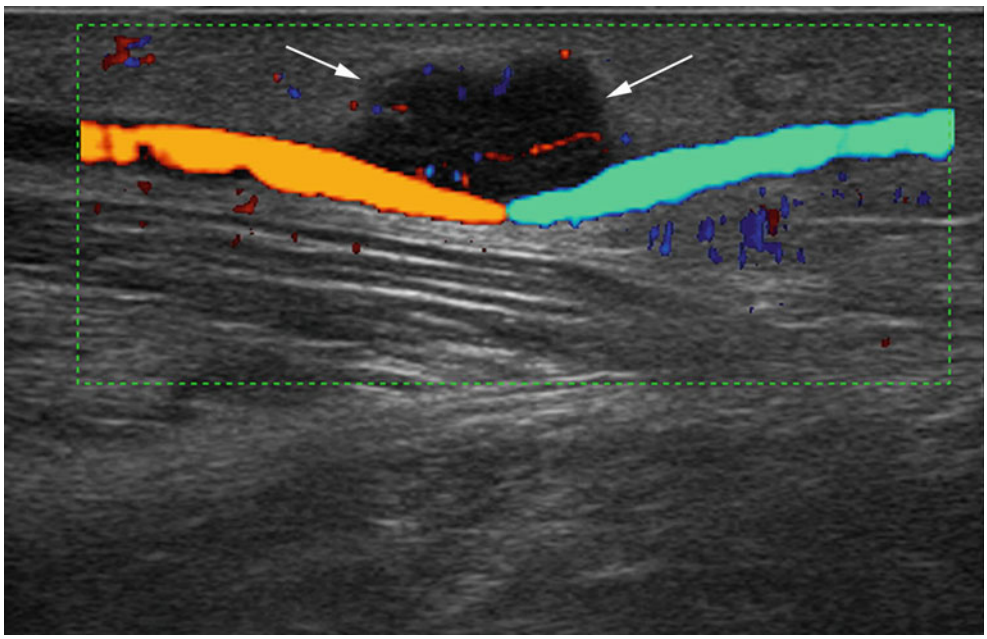

Fig. 11.47 In-transit metastasis. Directional power Doppler image. Melanoma nodule of the leg (*arrows*) is seen compressing the internal saphenous vein

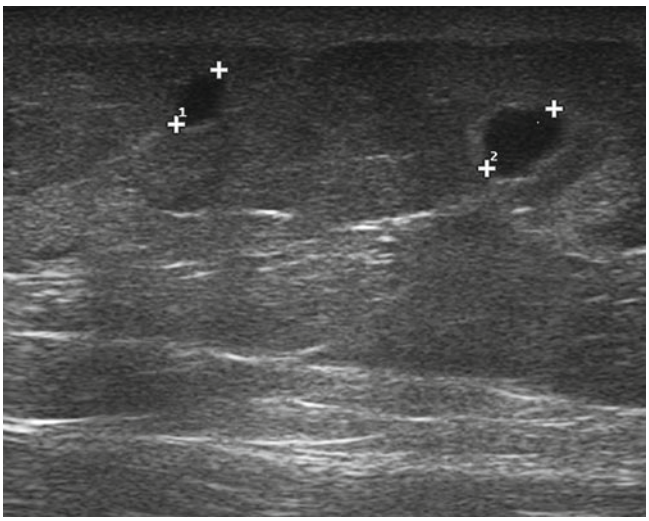

Fig. 11.48 In-transit metastases. Two small subcutaneous nodules (*calipers*, 6 and 5 mm) are visible within the subcutaneous layer of the thigh

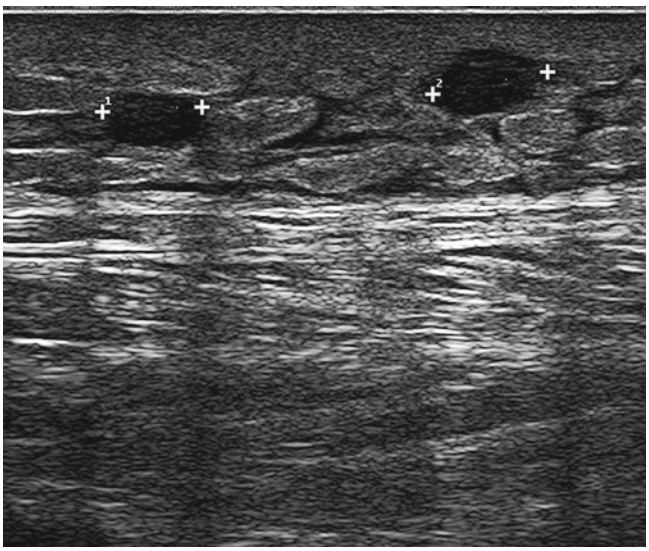

Fig. 11.49 In-transit metastases. Two subcutaneous nodules (*calipers*, 7 mm and 6 mm) are visible within the subcutaneous layer of the leg. Note diffuse subcutaneous edema

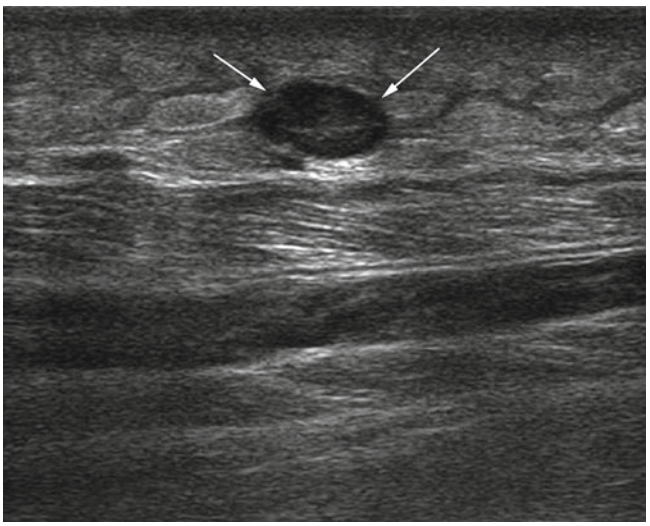

Fig. 11.50 In-transit metastasis. Subcutaneous nodule (*arrows*) is seen within the subcutaneous layer of the leg. Note diffuse subcutaneous edema

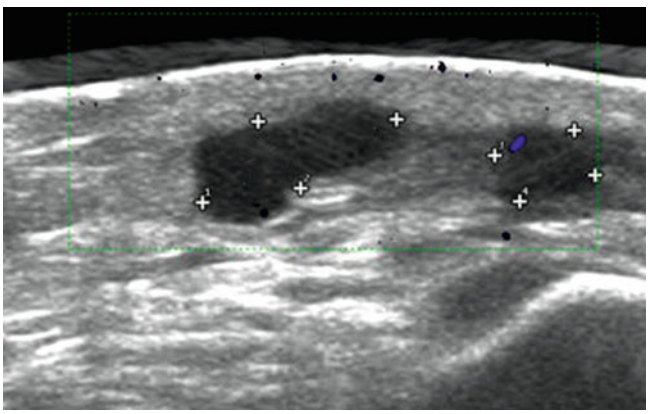

Fig. 11.51 Echo-poor aspect of in-transit metastases. Directional power Doppler image. Slightest traces of vascularization give the right hint towards in-transit metastases, which have been proved by fine-needle aspiration cytology

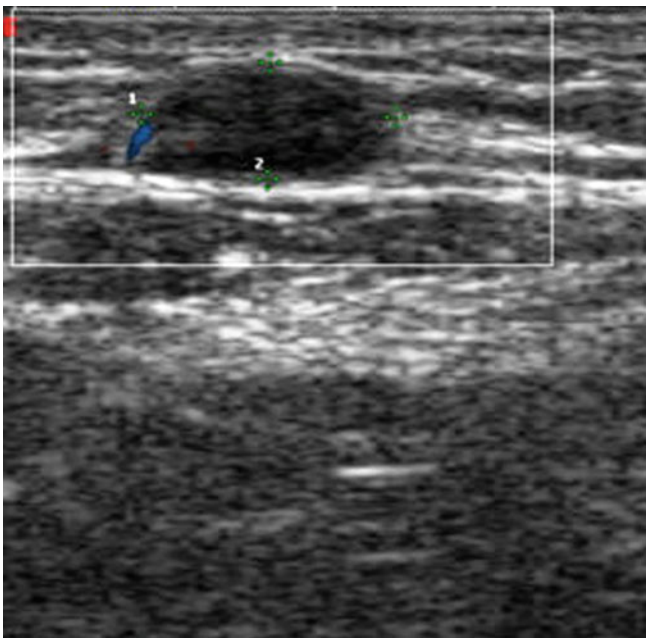

Fig. 11.52 In-transit metastasis. Directional power Doppler image. Small in-transit nodule with slight perfusion at periphery

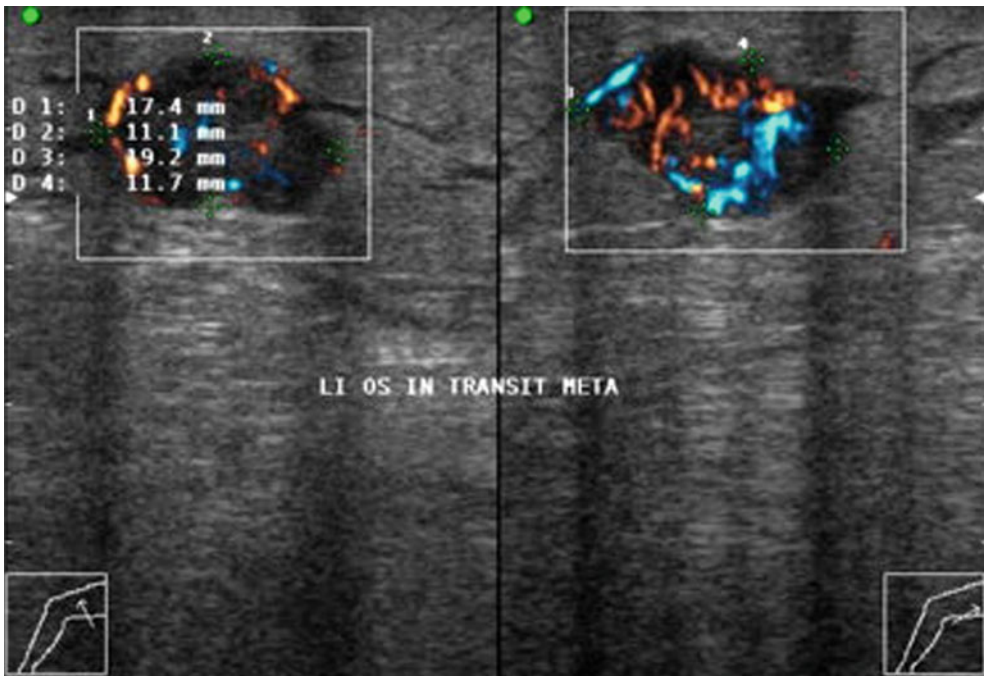

Fig. 11.53 Directional power Doppler image. In-transit metastases with dilated lymphways in the surrounding and enhanced vascularization

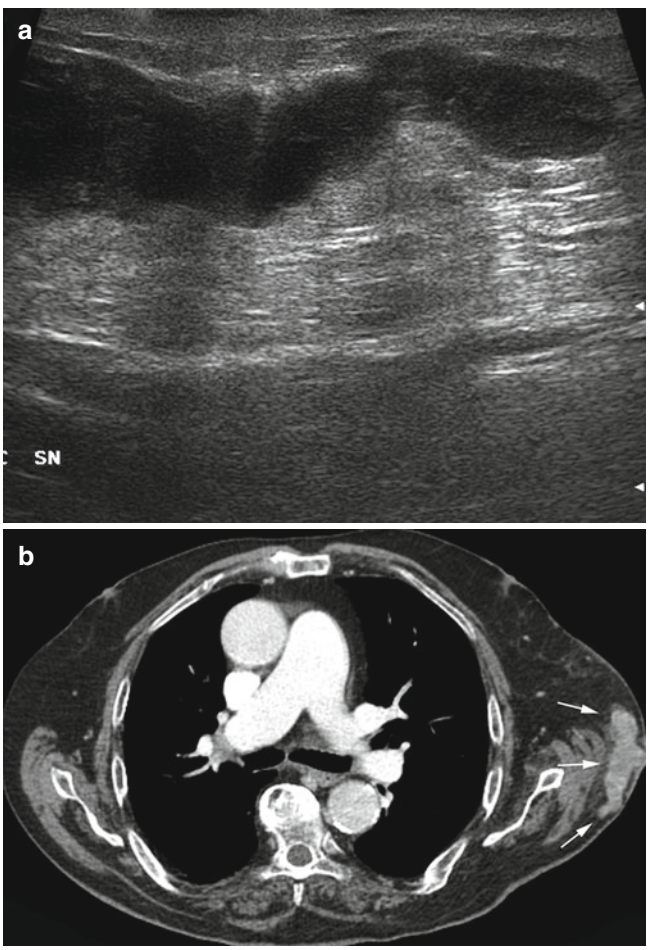

Fig. 11.54 In-transit metastases. Multiple melanoma nodules have merged into a single, very elongated one (**a**). Computed tomography confirmation (**b**, *arrows*)

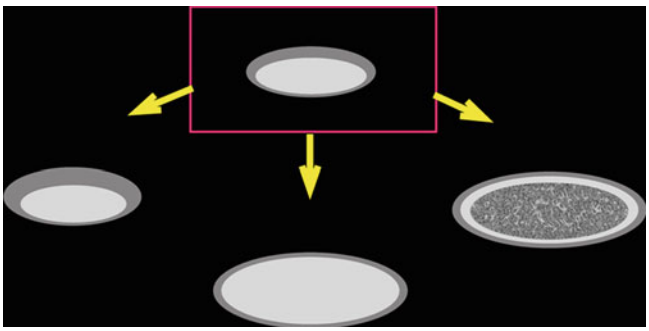

Fig. 11.55 Benign lymph-node changes. The normal lymph node may turn into reactive, fatty (hyperechoic), or fatty (hypoechoic)

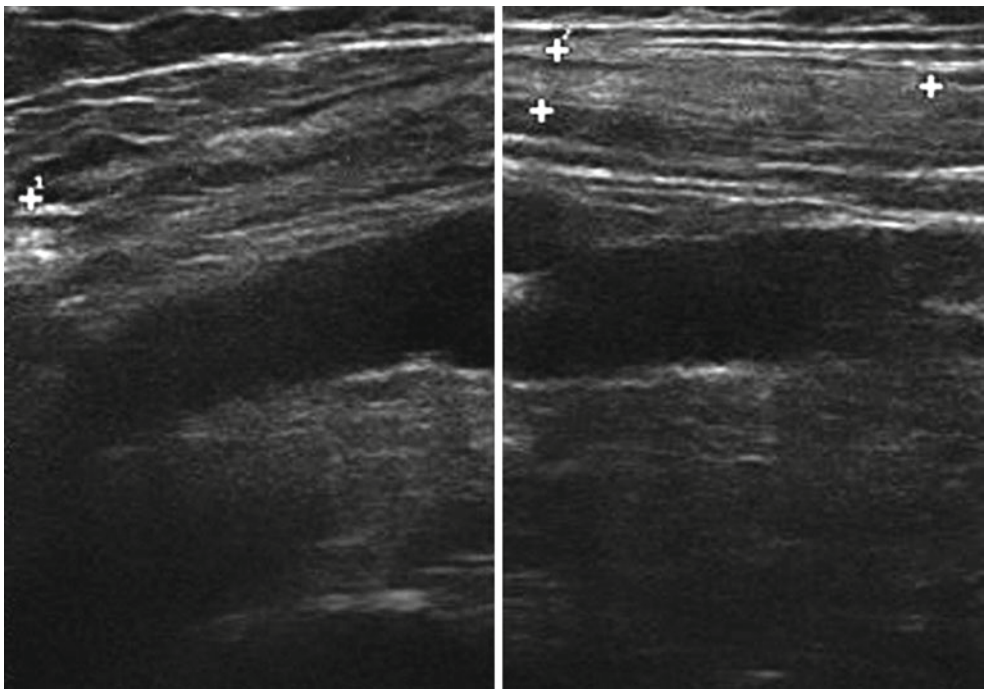

Fig. 11.56 Benign lymph node. Panoramic image of a long, longitudinally shaped lymph node in the groin region spanning the common femoral artery close to its bifurcation

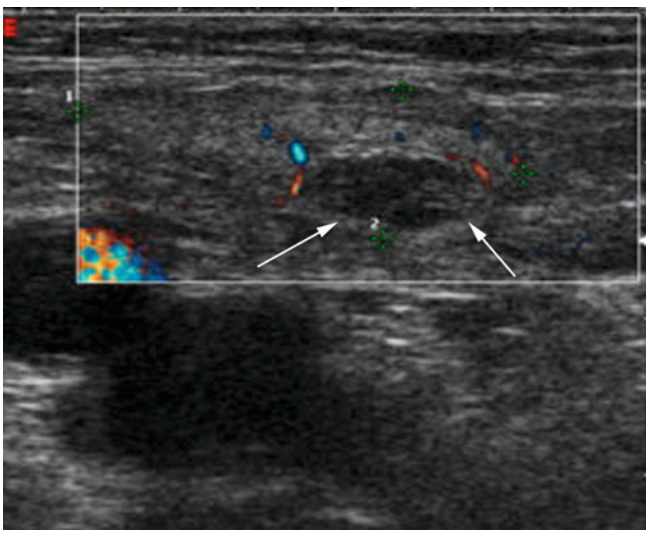

Fig. 11.57 Fatty metamorphosis. Directional power Doppler image. Predominantly echo-rich, 29×10 mm lymph node with an echo-free, non-vascularized area (*arrows*). Using fine-needle aspiration cytology in this echo-poor area, tissue was verified as fatty metamorphosis

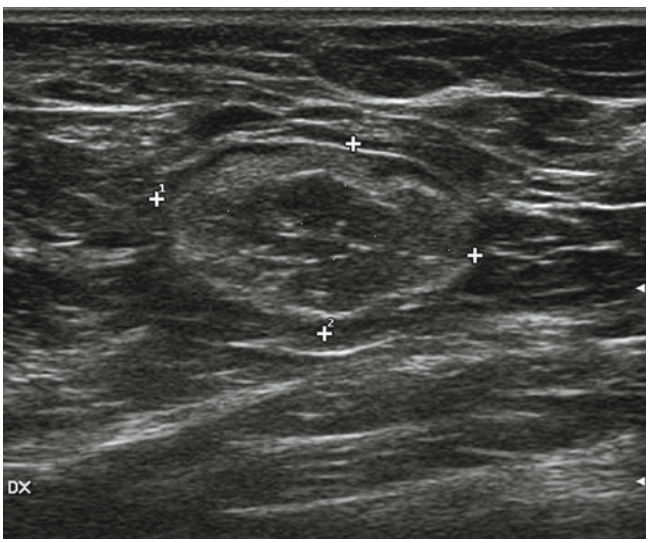

Fig. 11.58 Benign lymph node of the axilla (fatty metamorphosis). Despite the size and shape (22×13 mm – L/T 1.7) this lymph node is overtly benign, with a very thin hypoechoic cortex and a very large, hyperechoic "hilum"

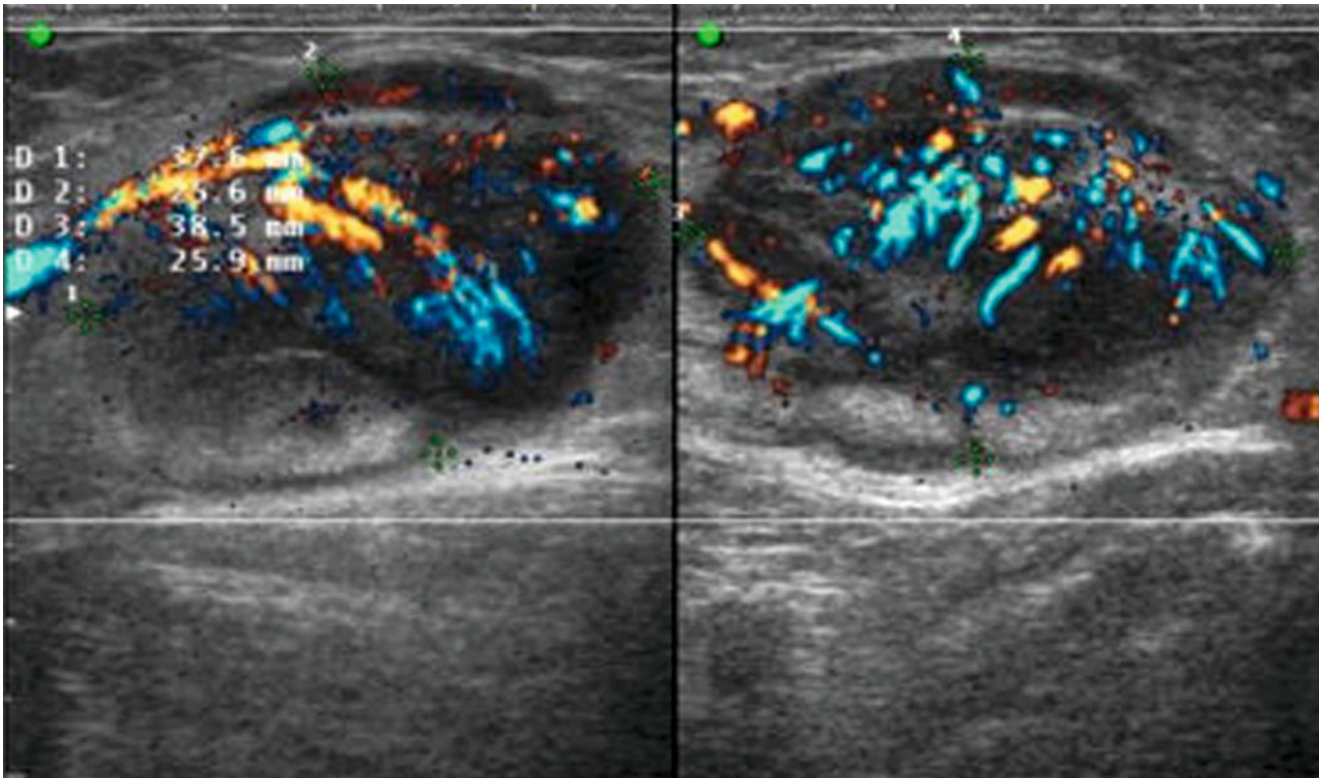

Fig. 11.59 Benign lymphadenopathy. Directional power Doppler image. Granulomatous lymphadenopathy, proved using fine-needle aspiration cytology, and the typical appearance of a large lymph node with intensified vascularization

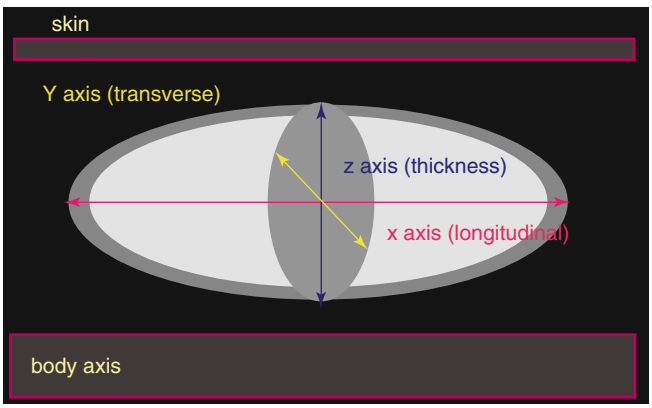

Fig. 11.60 Measurement of lymph-node diameters. Thickness, transverse diameter, and longitudinal diameter

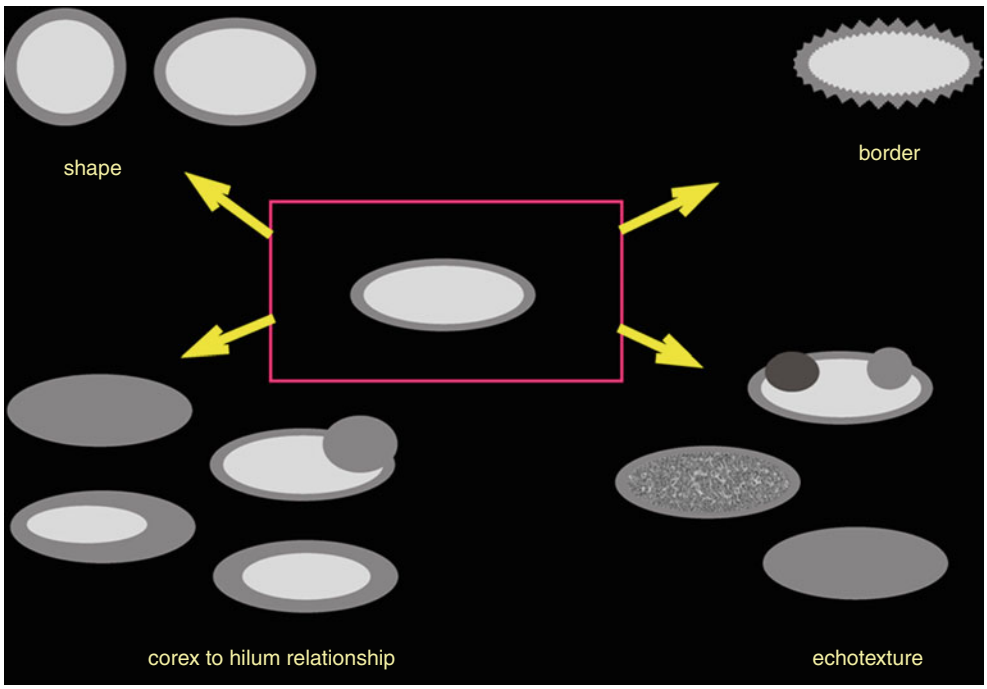

Fig. 11.61 Malignant lymph-node changes. The normal lymph node may change its shape (to round or oval), its margins, its "hilum" (absent, displaced, eccentrically diminished, or concentrically diminished), or its texture (focal isoechoic nodule, focal hypoechoic nodule, diffuse homogenous hypoecogenicity, or diffuse heterogeneous hypoecogenicity)

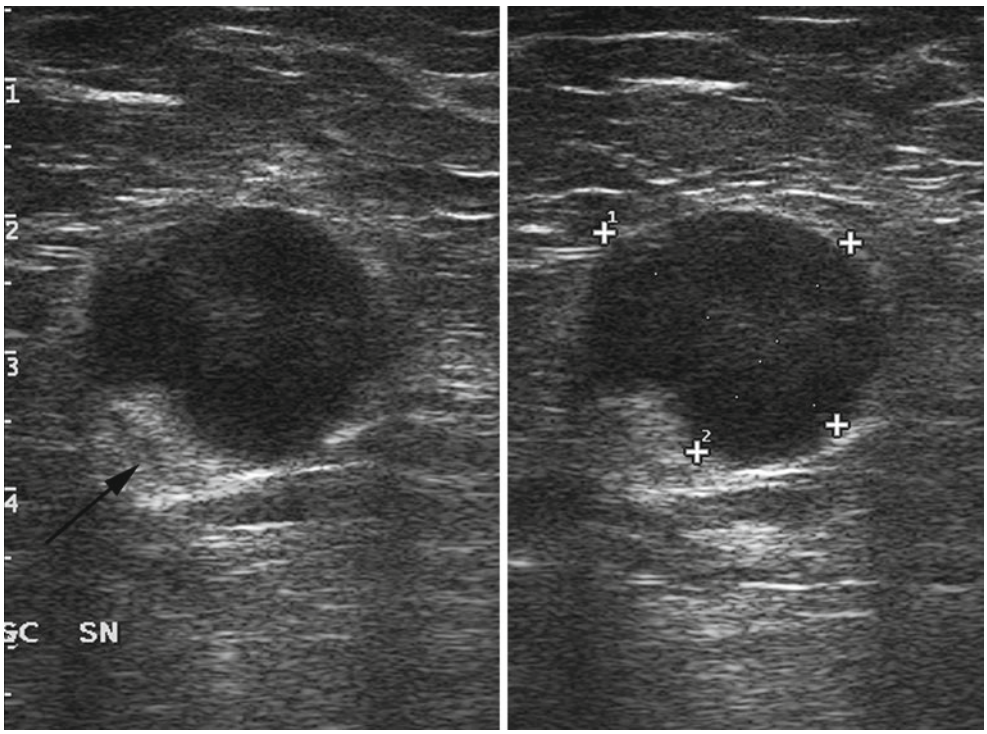

Fig. 11.62 Metastatic lymph node. Round, hypoechoic, 22×19 mm, axillary lymph node (*calipers*). A small, echoic hilum is displaced marginally (*arrow*)

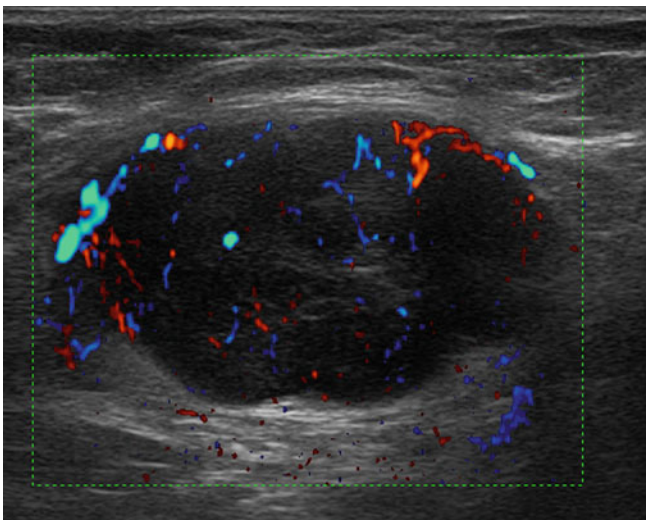

Fig. 11.63 Metastatic lymph node. Large, metastatic lymph node of the axilla showing diffuse and anarchic vascularization at directional power Doppler imaging

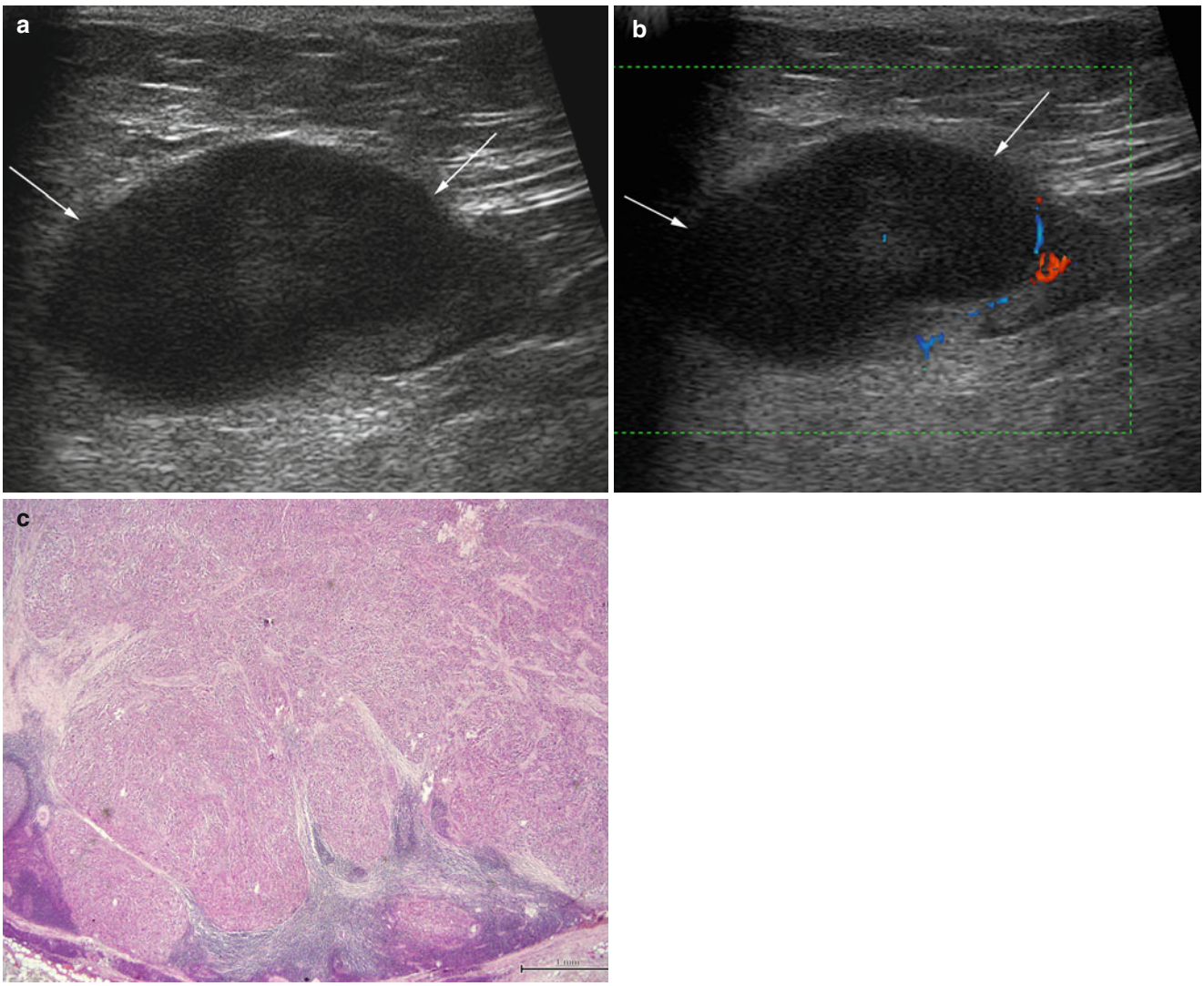

Fig. 11.64 Metastatic lymph node. Large metastatic nodule within an inguinal lymph node (**a**, *arrows*). The color Doppler image (**b**) shows displaced hilar vessels and little vascularization of the nodule (*arrows*). The post-lymphadenectomy histological image (**c**, H&E 2×) demonstrates the metastatization

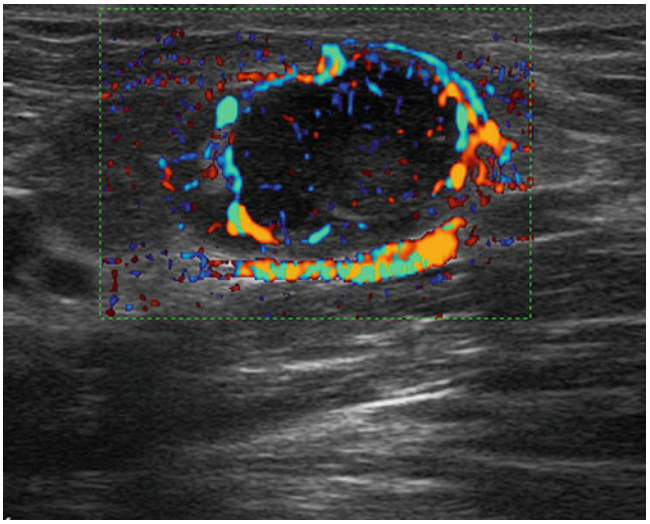

Fig. 11.65 Metastatic lymph node of the groin. Intense, peripheral vascularization using directional power Doppler imaging

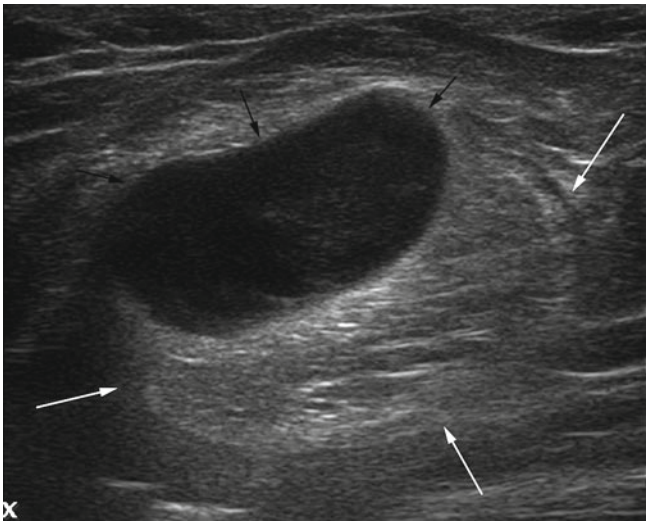

Fig. 11.67 Focal nodal metastasis. Hypoechoic nodule (*black arrows*) within an otherwise normal (fatty) axillary lymph node (*white arrows*)

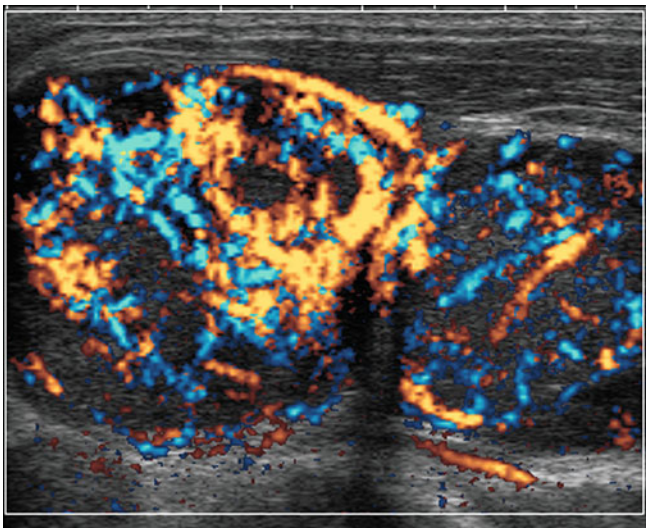

Fig. 11.66 Metastatic lymph nodes of the supraclavicular region. Intense, peripheral vascularization using directional power Doppler imaging for two adjacent lymph nodes

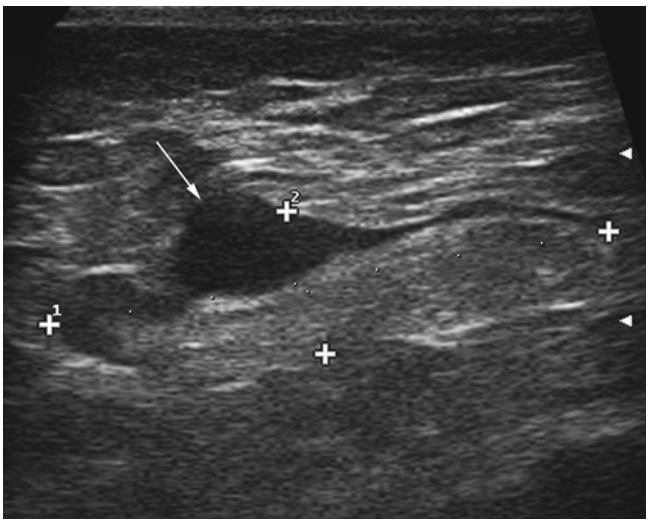

Fig. 11.68 Focal nodal metastasis. Despite the elongated shape of the inguinal lymph node (34×9 mm – L/T 3.8), metastasis is present (*arrow*). It would take a lot of time for this metastatic lymph node to become round (if ever!)

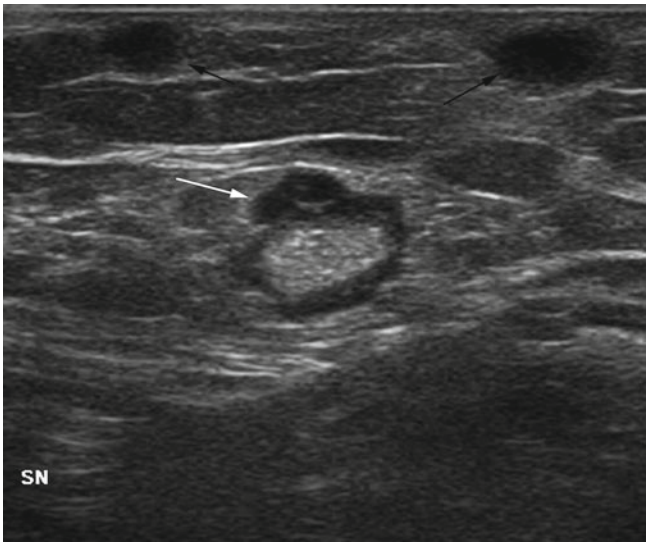

Fig. 11.69 Focal nodal metastasis. Hypoechoic, focal cortical thickening (*arrow*) of an inguinal lymph node

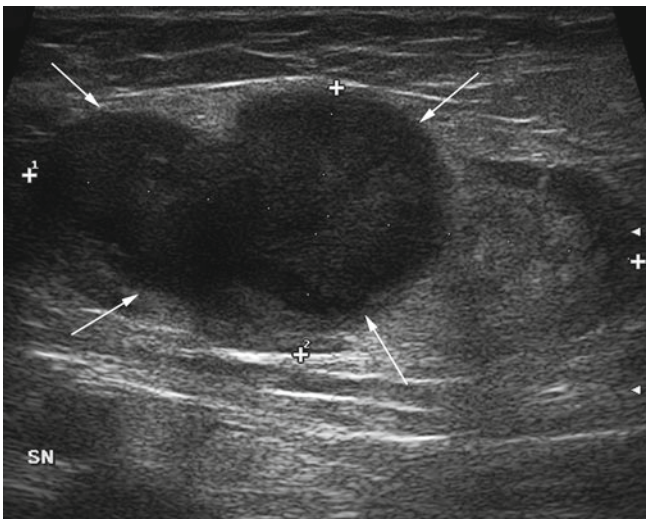

Fig. 11.70 Focal nodal metastasis. Hypoechoic nodule (*arrows*) within an otherwise normal inguinal lymph node (51 × 22 mm)

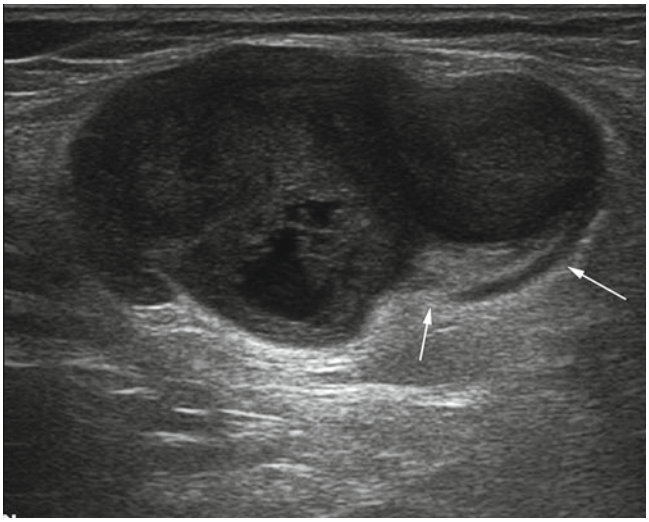

Fig. 11.71 Focal nodal metastasis. Large hypoechoic nodule within an inguinal lymph node. Residual normal nodal tissue (cortex and "hilum") (*arrows*)

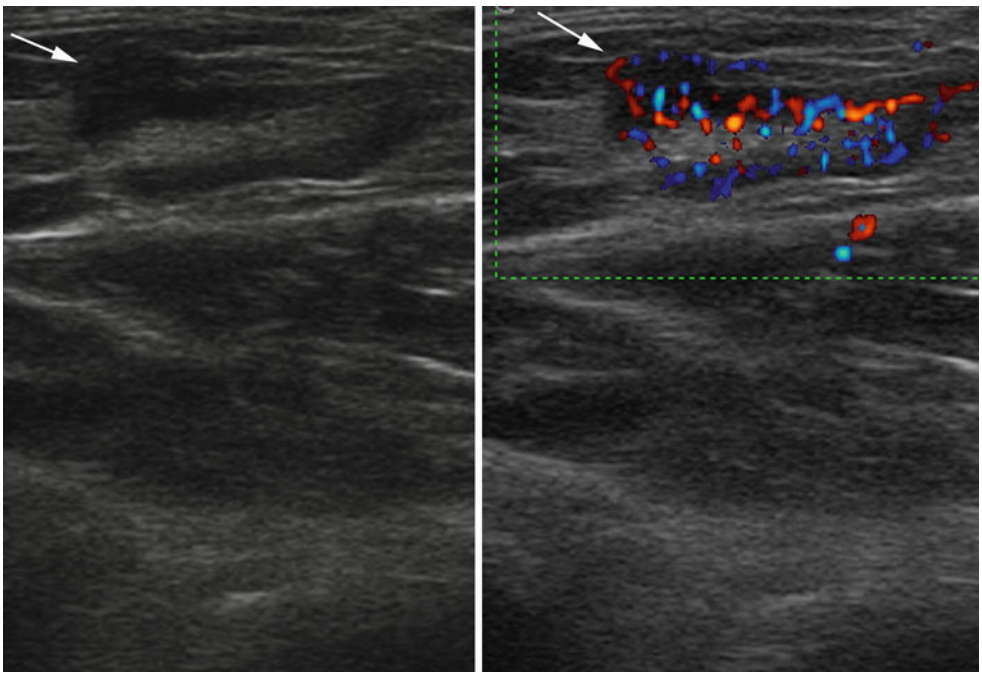

Fig. 11.72 Focal nodal metastasis. Focal nodule (*arrows*) within an inguinal lymph node. The directional power Doppler side of the split-mode image shows multiple hilar vessels within the lymph node but also multiple nonhilar vessels within the nodule

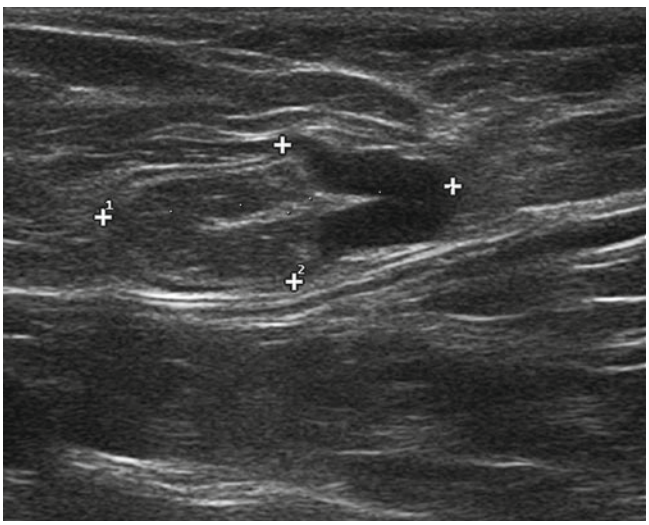

Fig. 11.73 Partial lymph-node metastasis. The crural lymph node (25×10 mm) shows a thin cortex on the right side (*left part* of the image) shows a thick cortex on the left side (*right part* of the image)

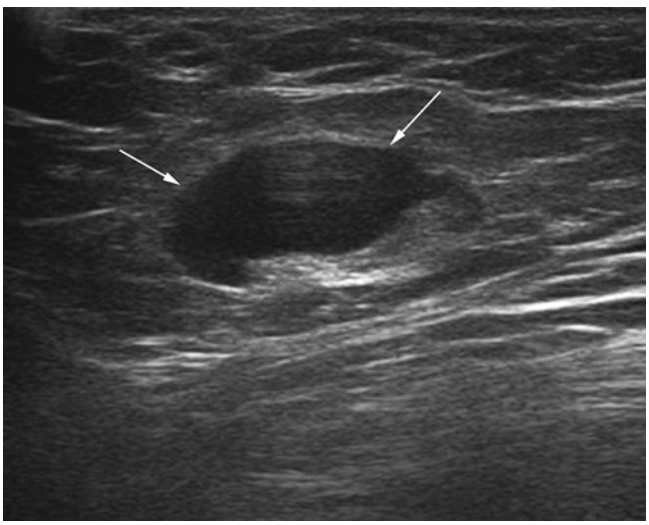

Fig. 11.74 Focal nodal metastasis. Large hypoechoic nodule (*arrows*) within an inguinal lymph node in a patient with anterior abdominal wall primary melanoma

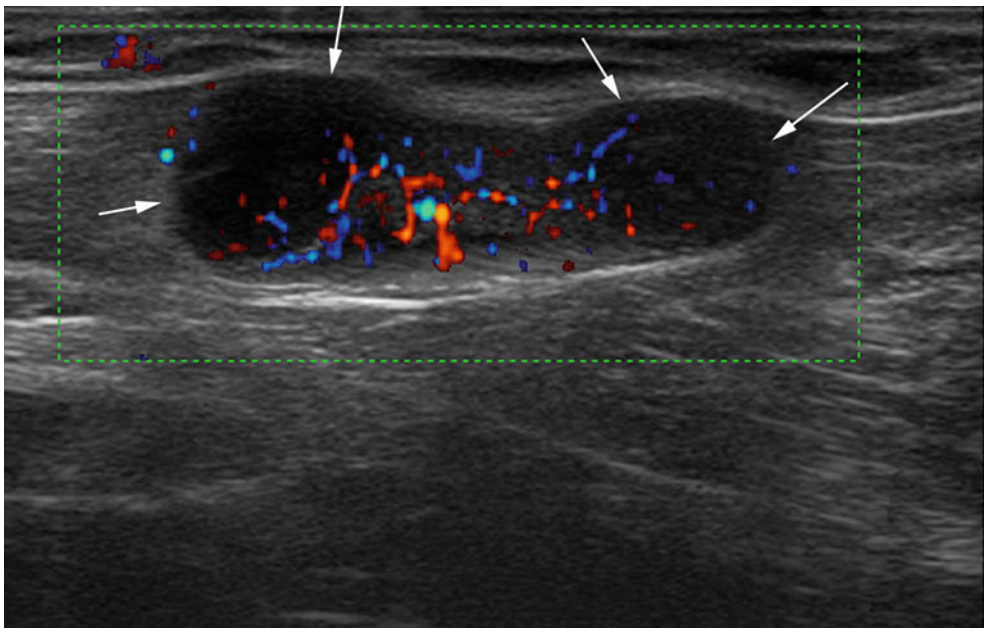

Fig. 11.75 Focal nodal metastasis. Directional power Doppler image. Two hypoechoic nodules (*arrows*) within an inguinal lymph node. Multiple flow signals are evident both at the nodal hilum and from the capsule

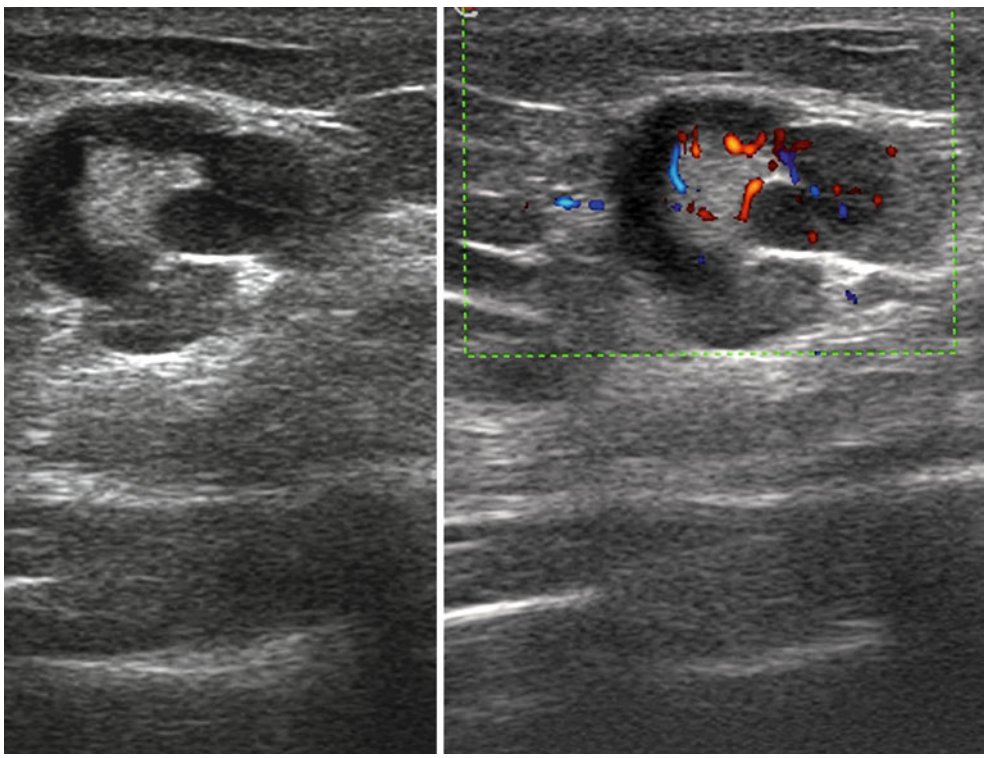

Fig. 11.76 Focal lymph-node metastasis. Hypoechoic nodule within a lymph node placed between the breast and the axilla in a patient with previous abdominal wall cutaneous melanoma. Note multiple intranodular flow signals in the directional power Doppler part of the split-mode image

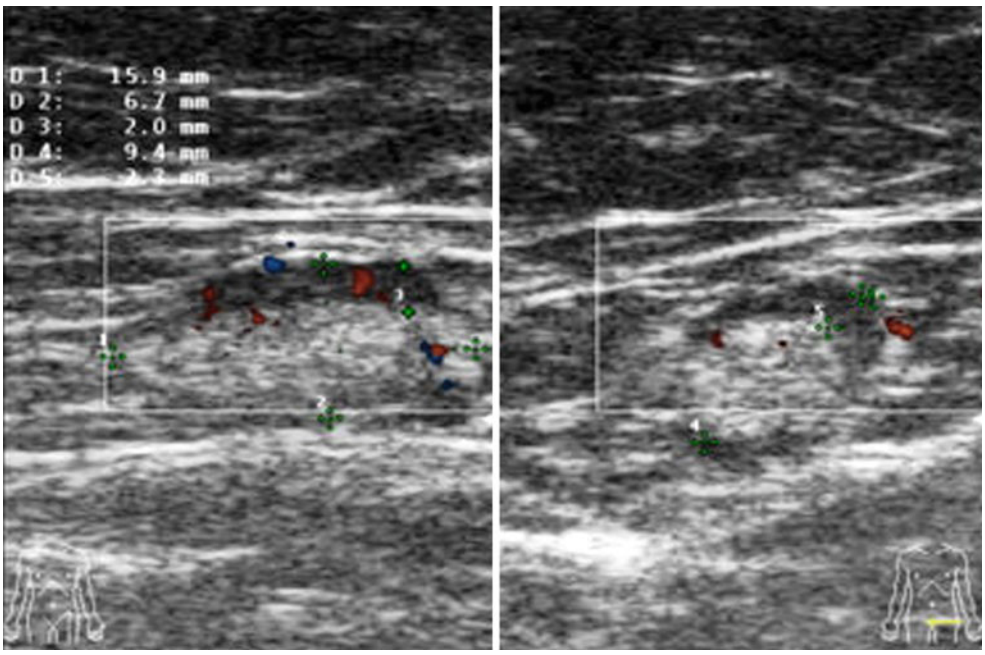

Fig. 11.77 Metastatic lymph node, hump sign. Directional power Doppler image. Very slight changes; the echo-free parenchyma becomes more obvious here because the B-gain has mistakenly been turned to to a too high position to make the contrast visible. Note the simultaneous hyperperfusion

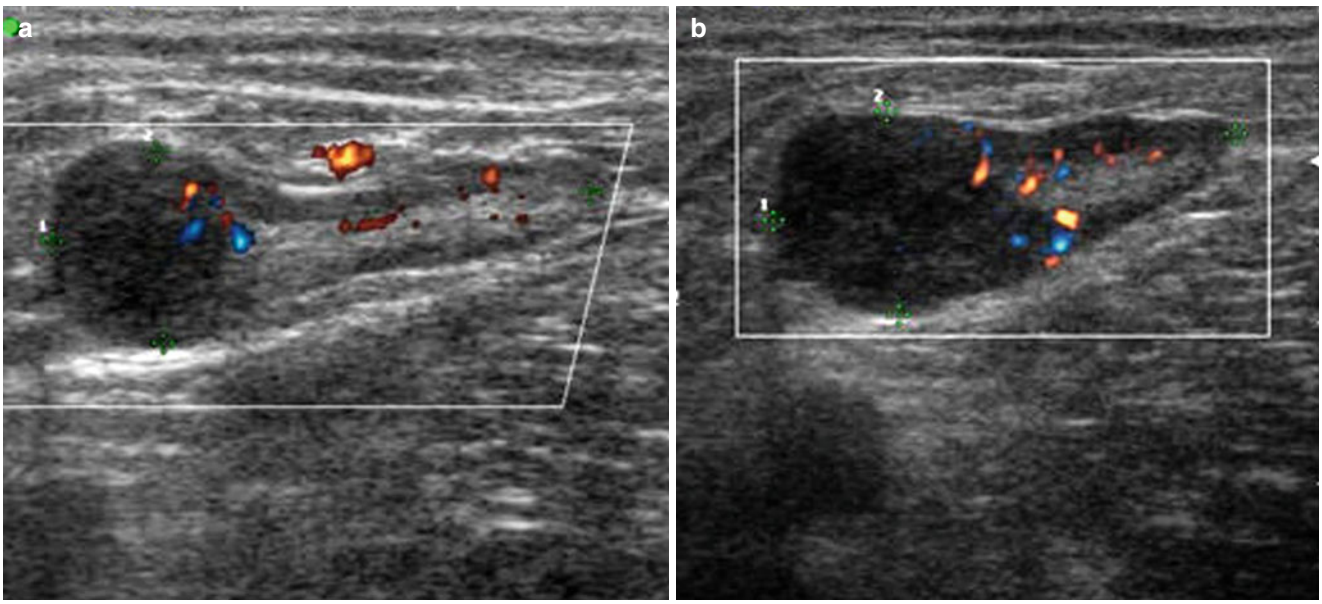

Fig. 11.78 Chronological development of a focal nodal metastasis. Directional power Doppler image (**a**, **b**). Changes observed over a time period of 3 weeks (patient had first refused to undergo fine-needle aspiration cytology or operation)

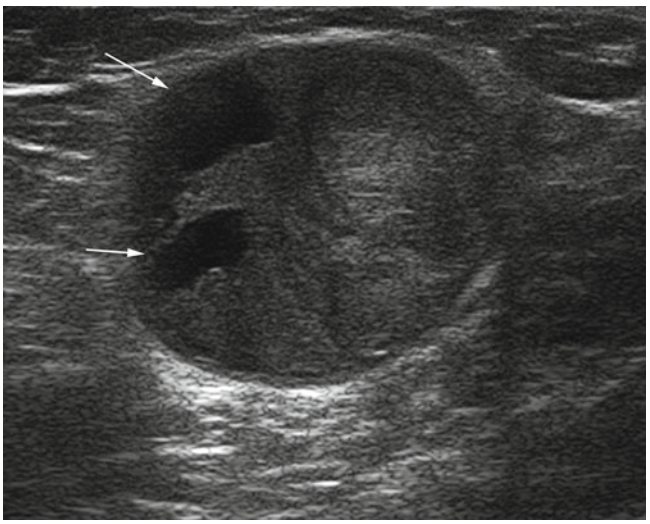

Fig. 11.79 Metastatic lymph node with necrotic areas. Large and round inguinal lymph node with anechoic necrotic areas (*arrows*) internally

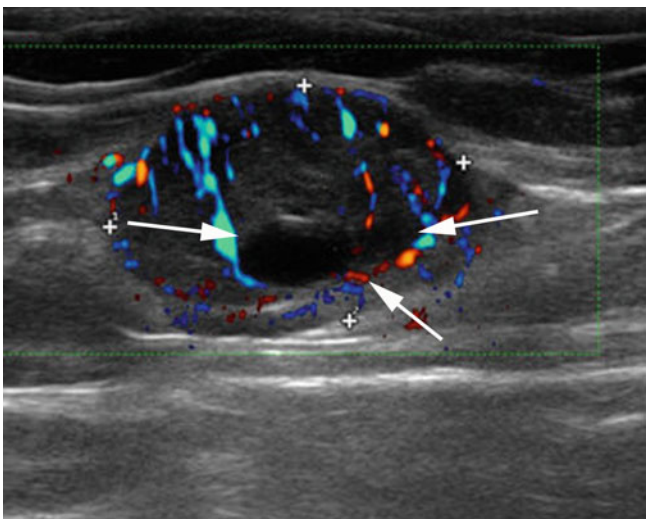

Fig. 11.80 Metastatic lymph node. Directional power Doppler image. Balloon-shaped, 24×16 mm lymph node with totally vanished central hilum and irregular perfusion. Note the area without any vascularization (*arrows* – necrotic area?) and the overall three-dimensional impression

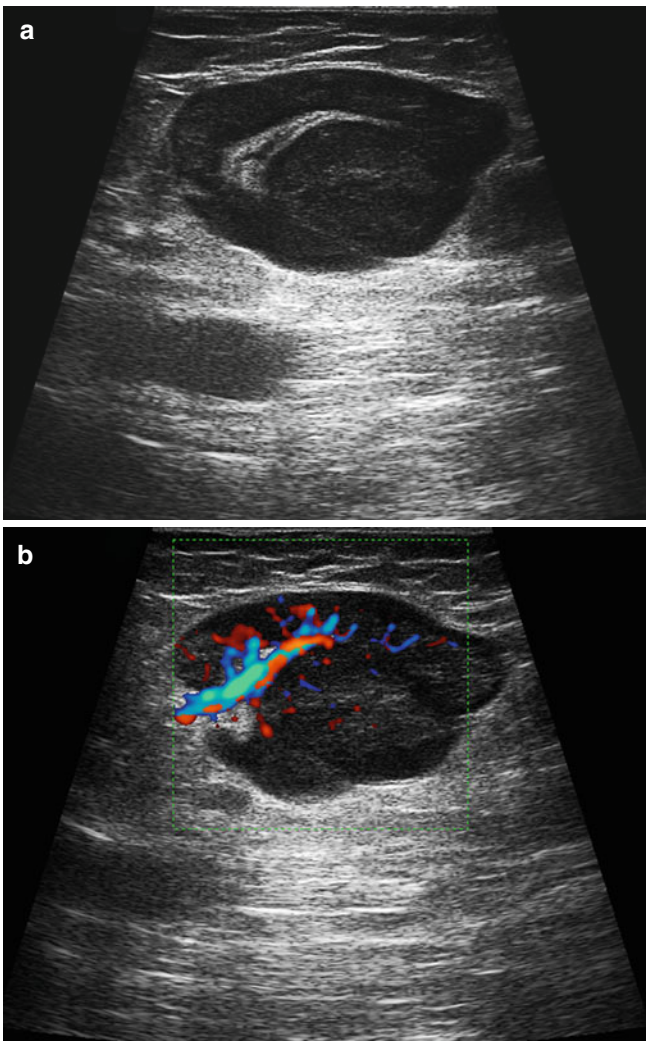

Fig. 11.81 Lymph-node metastasis. Diffuse thickening of the nodal cortex (**a**). Despite this, the hilar vascularization is preserved on the directional power Doppler image (**b**), with no capsular vessel evident

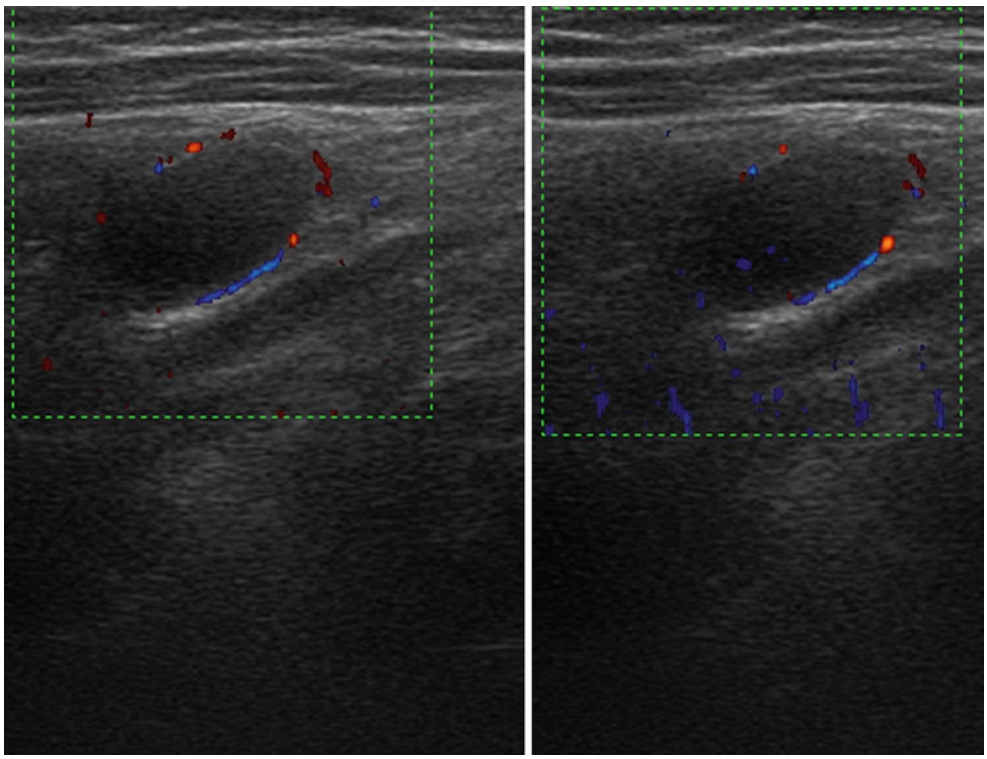

Fig. 11.82 Lymph-node metastasis. Homogeneously hypoechoic lymph node with multiple peripheral flow signals using directional power Doppler ultrasound

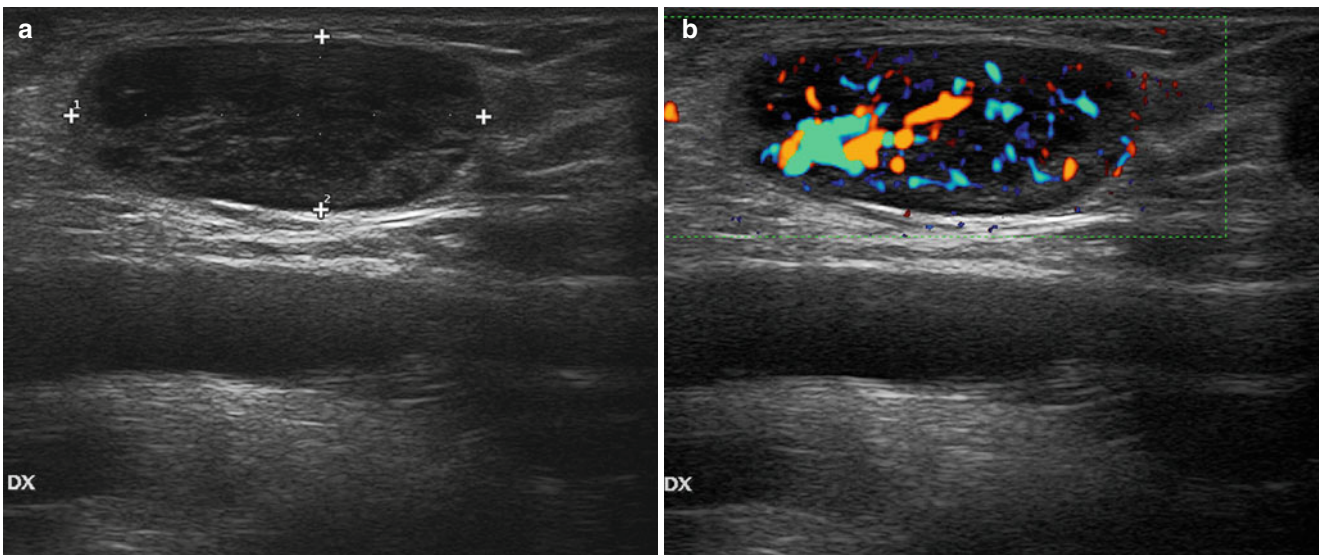

Fig. 11.83 Lymph-node metastasis. Heterogeneously hypoechoic inguinal lymph node (27×11 mm, **a**) with multiple peripheral flow signals on directional power Doppler imaging (**b**)

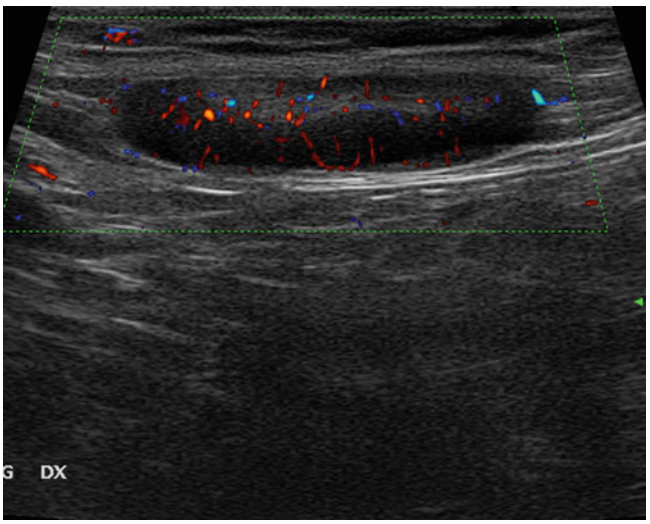

Fig. 11.84 Lymph-node metastasis. Inguinal lymph node with diffuse but asymmetric cortical thickening and multiple peripheral flow signals using directional power Doppler imaging. Despite its elongated shape, the lymph node proved to be metastatic at surgery

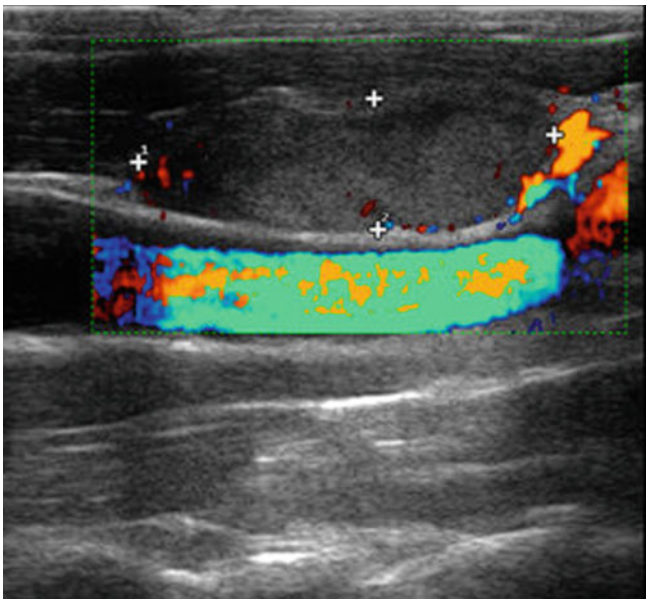

Fig. 11.85 Lymph-node metastasis. Directional power Doppler image. Melanoma metastasis neighbors the sternocleidomastoid muscle and the carotid artery

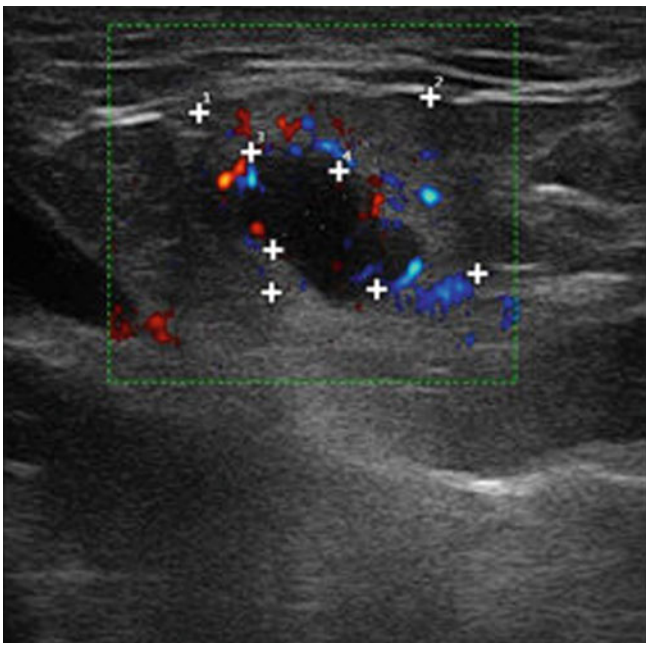

Fig. 11.86 Metastatic lymph node. Directional power Doppler image. So-called echo-free Island

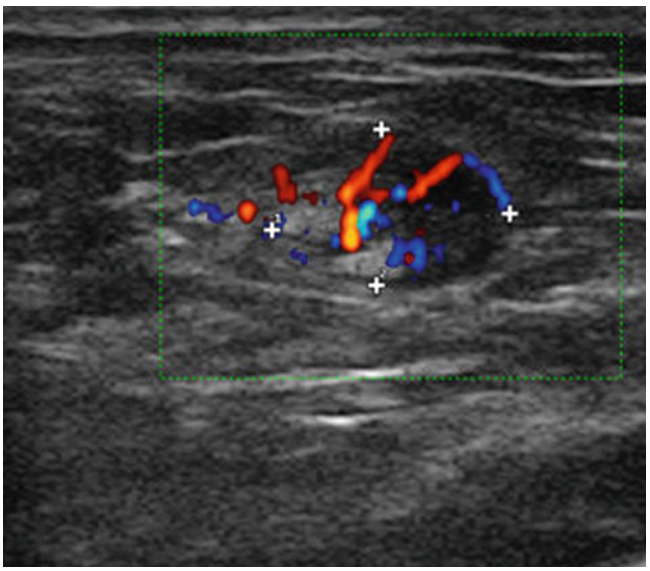

Fig. 11.87 Metastatic lymph node. Directional power Doppler image. Asymmetrical broadening of the nodal cortex, accompanied in this case by a hypervascularization

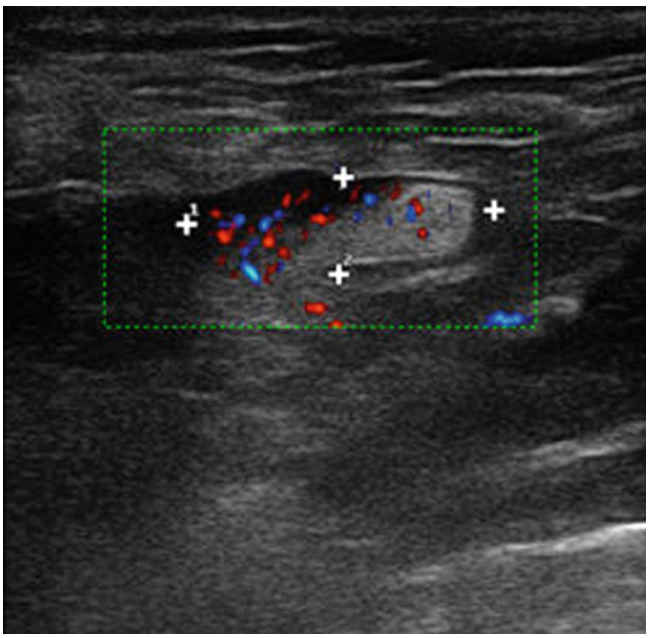

Fig. 11.88 Metastatic lymph node. Directional power Doppler image. Asymmetrical broadening of the parenchyma, accompanied by a hyperperfusion selectively in this area

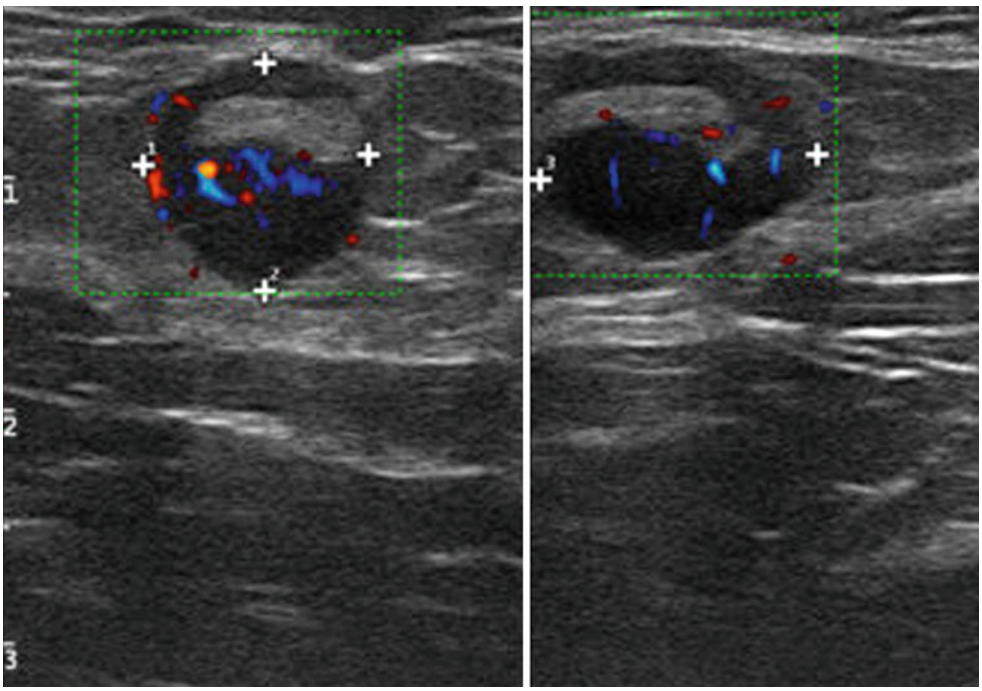

Fig. 11.89 Metastatic lymph node. Directional power Doppler image. So-called "wandering" of the central echo to the border of the lymph node

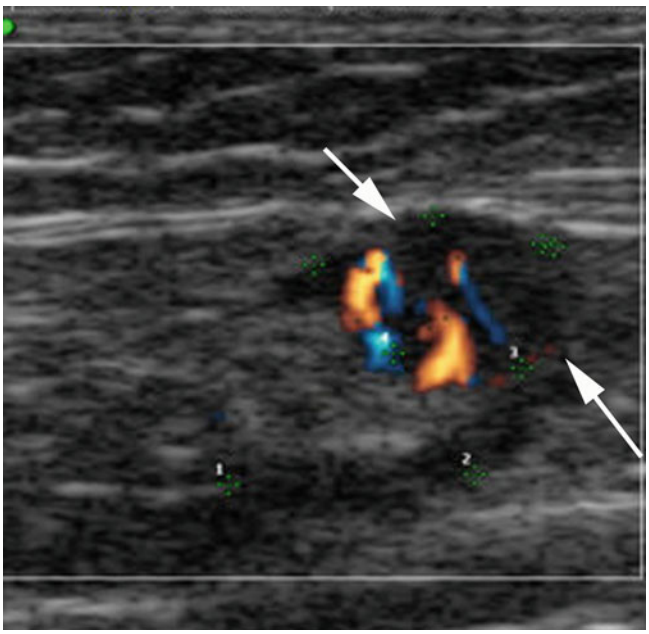

Fig. 11.90 Metastatic lymph node, echo-free island. Directional power Doppler image. Lymph node of 12×8 mm (see set cursors) with an echo-free, hypervascularized island (6×5 mm, *arrows*)

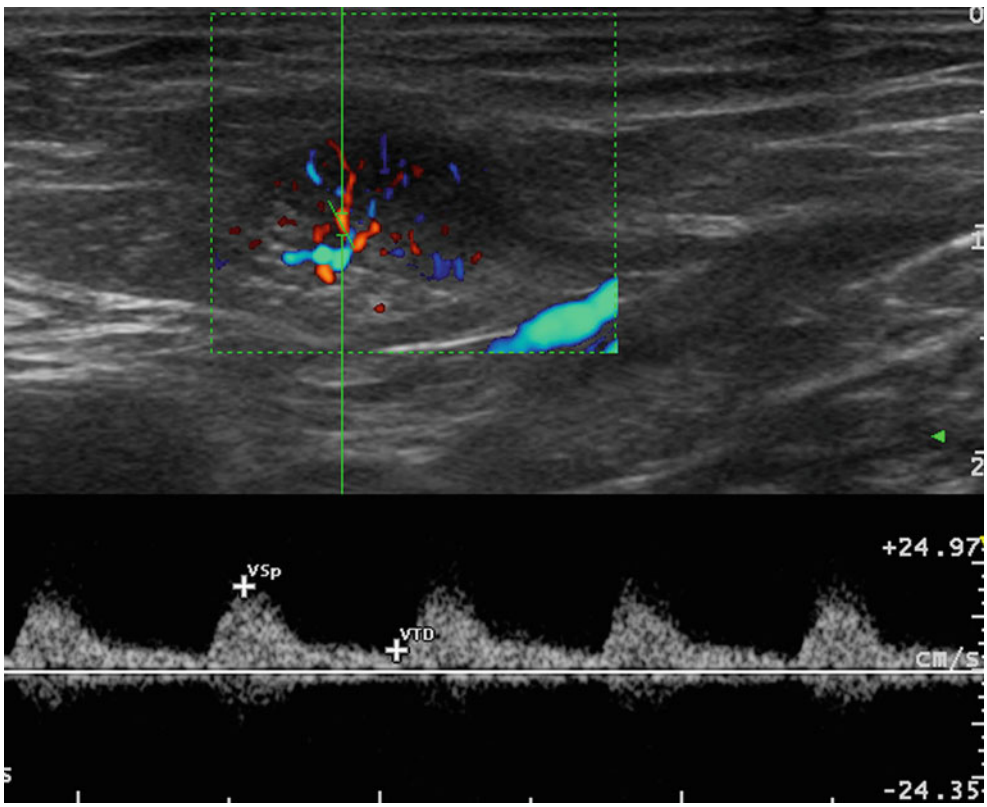

Fig. 11.91 Spectral analysis of a metastatic inguinal lymph node. The flowmetry below the directional power Doppler image depicts a moderate raise in flow speed (16 cm/s peak systolic flow) and flow resistance (0.75 resistive index)

11.3.3 Ultrasound-Guided Intervention

Several series of studies [26–28] have shown the superiority of ultrasound-guided FNAC over palpation-guided FNAC (Figs. 11.92, 11.93, 11.94, and 11.95). In particularly, it is known that ultrasound guidance helps to reduce the number of false-negative samplings by indicating the most suspicious lymph node within a given station, by driving the needle toward targets that are very small (not palpable), and by demonstrating that the needle tip is actually within the lymph node. Ultrasound guidance is used in a targeted way, directing the needle toward the most suspicious area of the lymph node such

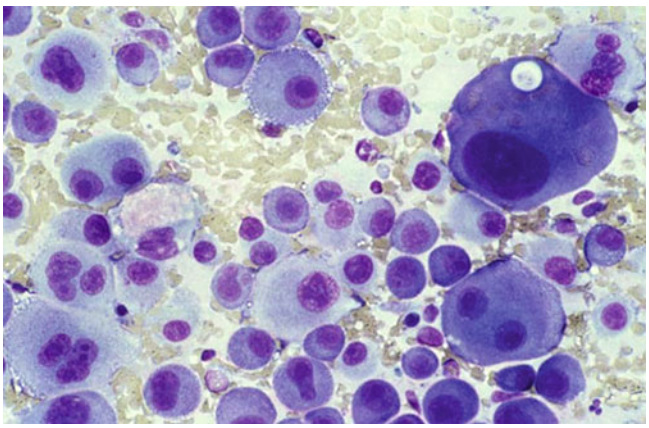

Fig. 11.92 Cytology of malignant melanoma

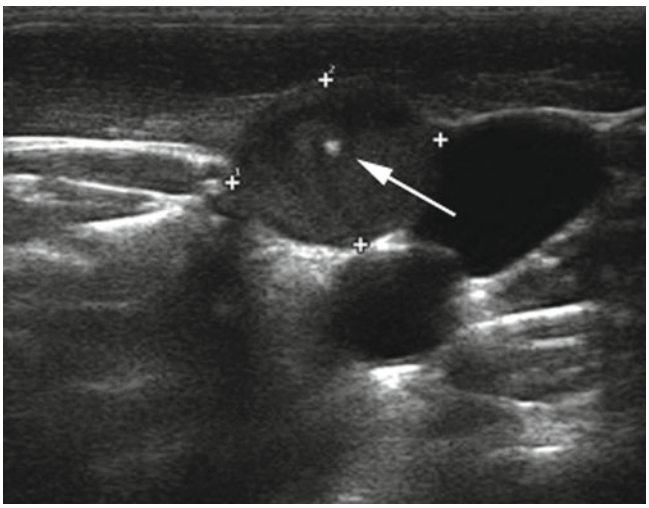

Fig. 11.93 Fine-needle aspiration cytology. White reflex of a fine needle tip (*arrow*) within a relatively echo-rich, 15 × 12 mm melanoma metastasis close to jugular vein and carotid artery

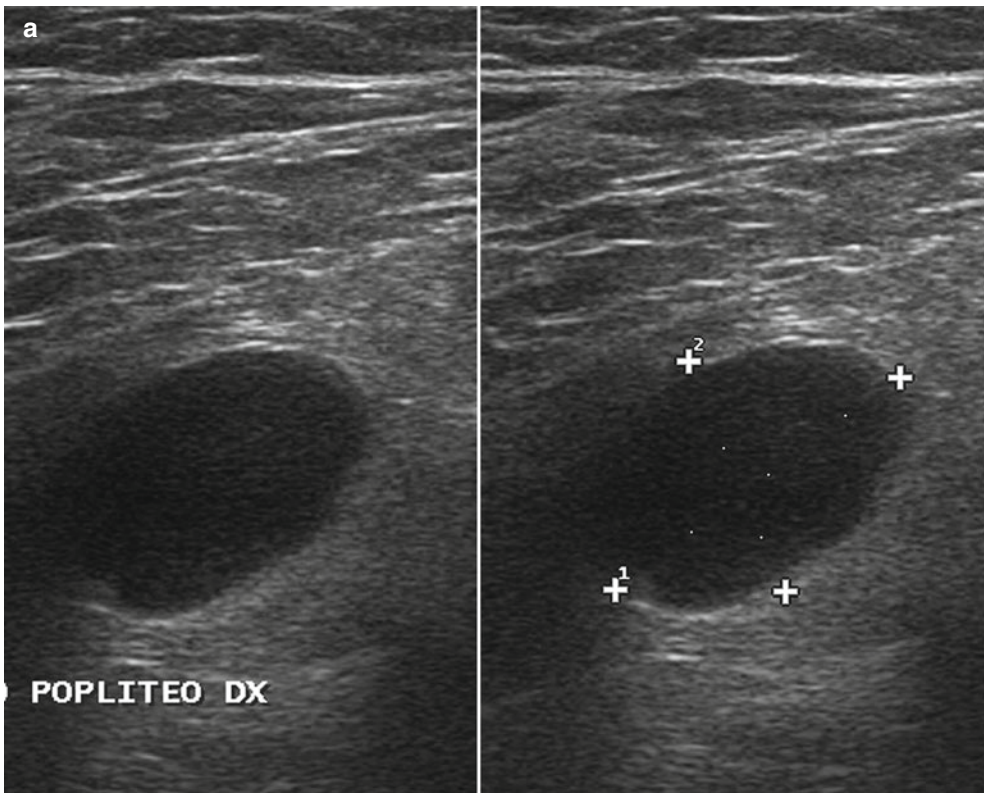

Fig. 11.94 Fine-needle aspiration cytology (FNAC) of an interval popliteal lymph node. A 18–13 hypoechoic popliteal nodule is detected at follow-up in a patient with history of foot melanoma (**a** *caliper*). Confirmatory ultrasound-guided FNAC is subsequently performed. Note the needle (**b** *arrows*) penetrating obliquely into the nodule

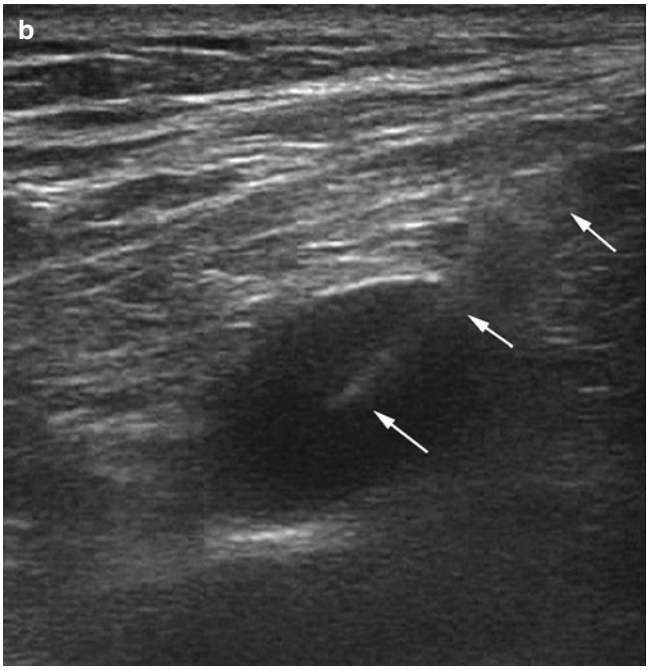

Fig. 11.94 (continued)

as a hypoechoic area, focal thickening of the cortex, or the thickest and most vascularized area of the cortex. Instead, sampling should avoid the areas at greater risk of necrotic content such as those with an echo-poor texture and without Doppler flow signals. Thus, the samples containing non-diagnostic material can be reduced to a minimum.

Wherever possible, all FNAC samplings should be extemporarily evaluated by the on-site cytopathologist. The evaluation can be performed either from air-dried slides with rapid Romanowsky coloration, or from air-dried slides with May-Gruenwald Giemsa staining which tops the morphological information of the single cell as compared with Romanowsky staining. The puncture is repeated immediately in the event of an indeterminate/unrepresentative smear or when there are discrepancies in the clinical, sonography, and cytology findings. Papanicolaou staining is then used for definitive assessment. The cytopathologic assessment should include an immunocytochemical analysis with special reference to the HMB-45 marker. Using strict morphological criteria however, renders the use of immunocytochemical analysis unnecessary because melanoma cells are extremely easy to aspirate and easily follow the under-pressure into the needle. The cells present as well-conserved cells in a dissociated pattern with a large basophile cytoplasm often showing nucleus inclusions and binuclear cells.

In select cases, ultrasound guidance is used for presurgical targeting of nonpalpable melanoma metastases (Figs. 11.96, 11.97, 11.98, 11.99, and 11.100), and in the case of deep and/

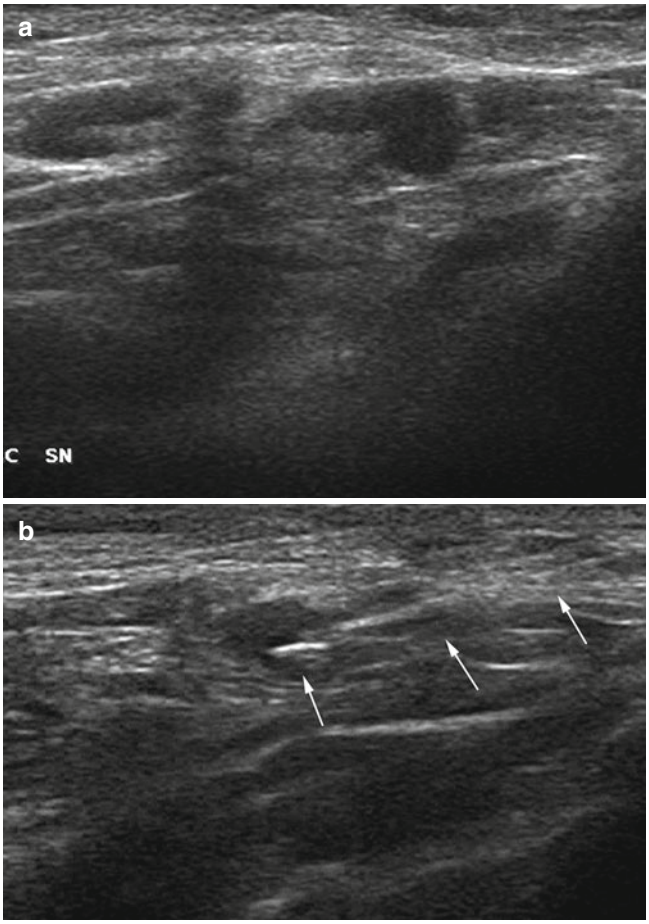

Fig. 11.95 Fine-needle aspiration cytology (FNAC) of a metastatic axillary lymph node. A lymph mode with a hypoechoic nodule is detected in a patient scheduled for sentinel lymph-node biopsy (**a**). Targeted, ultrasound-guided FNAC is subsequently performed. Note the needle (**b**, *arrows*) penetrating obliquely into the tumor deposit

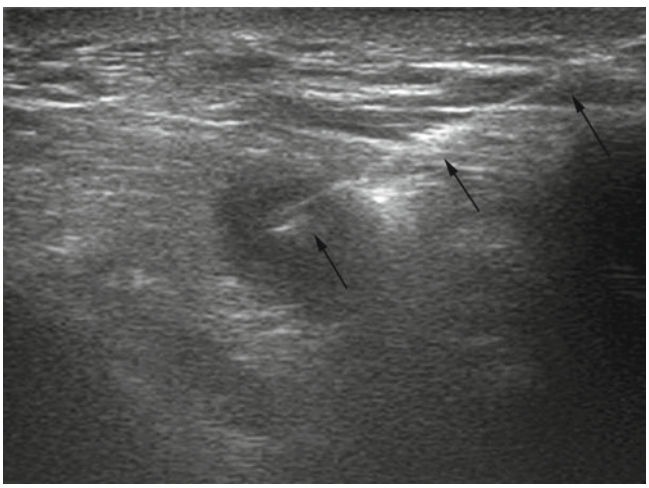

Fig. 11.96 Presurgical guidewire. The wire (*arrows*) is inserted into a metastatic supraclavicular (not palpable) lymph node before surgery

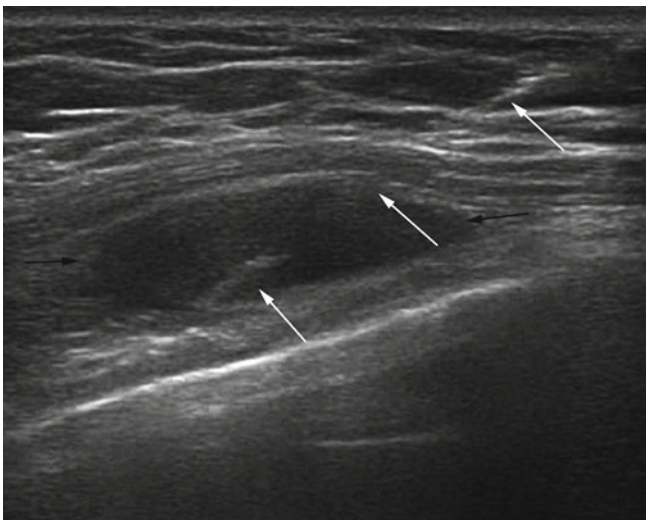

Fig. 11.97 Presurgical guidewire. The wire (*arrows*) is inserted into a metastatic, not palpable, melanoma metastasis placed between the pectoralis muscle and the ribs

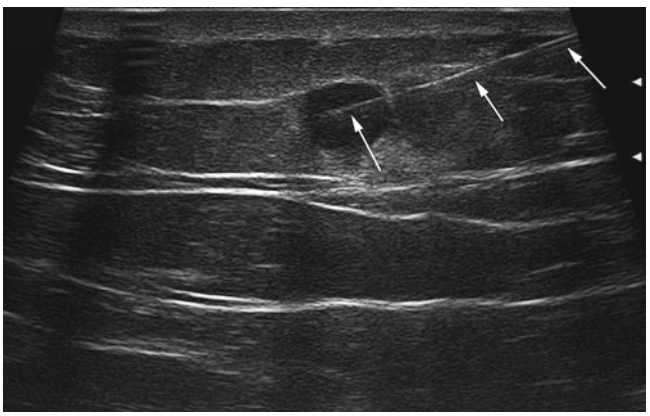

Fig. 11.98 Presurgical guidewire. The wire (*arrows*) is inserted into a small, hardly palpable subcutaneous nodule of the lumbar region before surgery

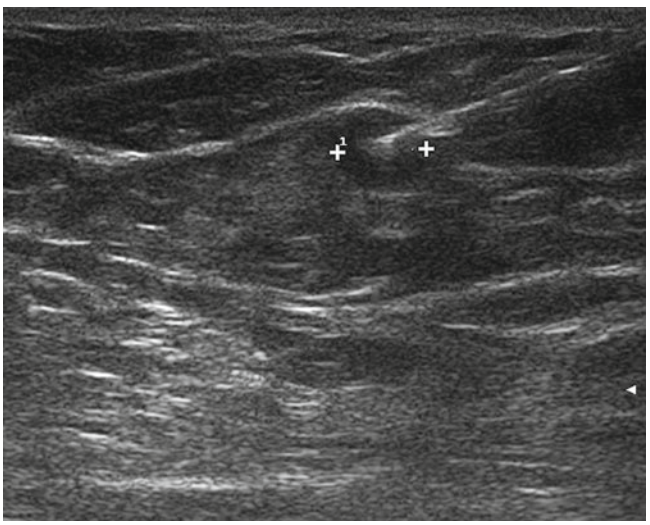

Fig. 11.99 Presurgical guidewire. The wire is inserted into an in-transit nodule (4 mm, *calipers*) detected at the lateral aspect of the chest wall in a patient with abdominal wall primary melanoma on ultrasound before sentinel lymph-node biopsy

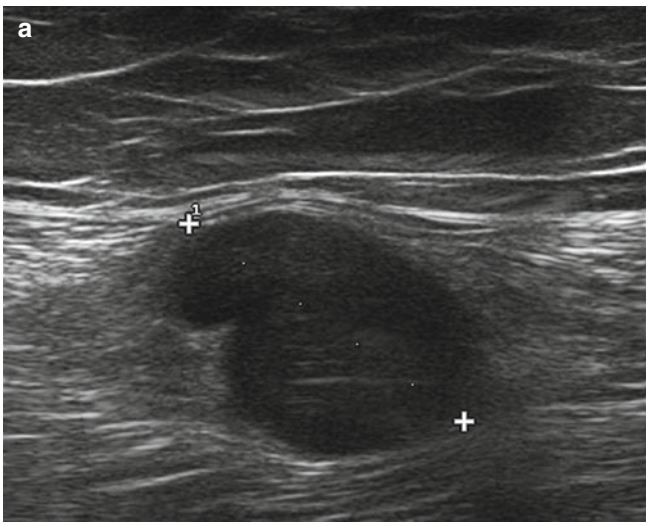

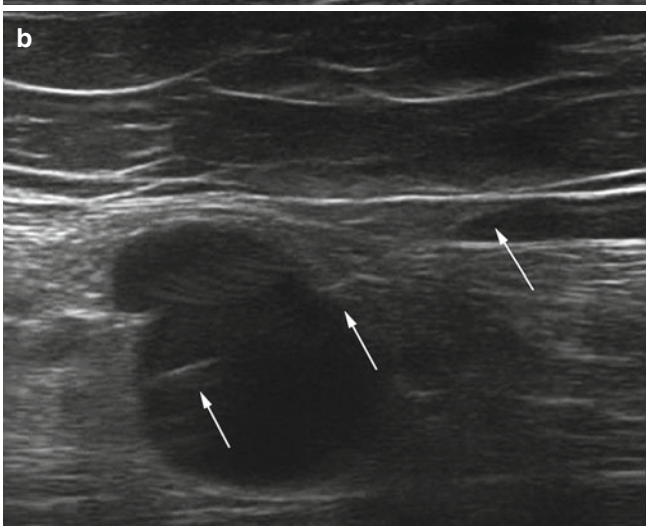

Fig. 11.100 Presurgical guidewire. Ultrasound image (**a** *calipers*) shows a 24-mm intramuscular melanoma metastasis of the thigh. A wire (**b** *arrows*) is inserted into the large but deep lesion before surgery

or small locoregional metastasis, help the surgeon by marking the overlying skin with a black marker or, if necessary, by placing a percutaneous guidewire preoperatively [24]. Skin marking in two cross areas, accompanied by additional information about the depth of the lesion, is useful not only immediately before surgery but also when a non-palpable abnormality is found during patient follow-up and the patient is sent back to the referring clinician.

Conclusion

Sonography has the potential to be used in the preliminary assessment of suspicious cutaneous lesions scheduled for excision biopsy. However, the assessment of primary cutaneous melanoma using ultrasound and Doppler has not yet been put into clinical practice in all facilities.

Sonography plays an increasing role in the assessment of the superficial spread of melanoma, but is being used

increasingly in the staging and follow-up of patients with cutaneous melanoma. However, state-of-the-art equipment and careful exploration by trained operators is necessary to maximize the results and knowledge of the usual spreading routes for melanoma and of typical and atypical sonography features is also mandatory.

References

1. Coory M, Baade P, Aitken J, Smithers M, McLeod GR, Ring I. Trends for in situ and invasive melanoma in Queensland, Australia, 1982–2002. Cancer Causes Control. 2006;17(1):21–7.
2. de Vries E, Coebergh JW. Cutaneous malignant melanoma in Europe. Eur J Cancer. 2004;40:2355–66.
3. Balch CM, Gershenwald JE, Soong SJ, Thompson JF, Atkins MB, Byrd DR, et al. Final version of 2009 AJCC melanoma staging and classification. J Clin Oncol. 2009;27:6199–206.
4. Meier F, Will S, Ellwanger U, Schlagenhauff B, Schittek B, Rassner G, et al. Metastatic pathways and time courses in the orderly progression of cutaneous melanoma. Br J Dermatol. 2002;147:62–70.
5. Balch CM, Buzaid AC, Soong SJ, Atkins MB, Cascinelli N, Coit DG, et al. Final version of the American Joint Committee on Cancer staging system for cutaneous melanoma. J Clin Oncol. 2001; 19:3635–48.
6. Buzzell RA, Zitelli JA. Favorable prognostic factors in recurrent and metastatic melanoma. J Am Acad Dermatol. 1996;34(5 Pt 1): 798–803.
7. Balch CM, Soong SJ, Gershenwald JE, Thompson JF, Reintgen DS, Cascinelli N, et al. Prognostic factors analysis of 17,600 patients with melanoma: validation of the American Joint Committee on Cancer melanoma staging system. J Clin Oncol. 2001;19: 3622–34.
8. Morton DL, Wen DR, Wong JH, Economou JS, Cagle LA, Storm FK, et al. Technical details of intraoperative lymphatic mapping for early stage melanoma. Arch Surg. 1992;127:392–9.
9. van Akkooi AC, Voit CA, Verhoef C, Eggermont AM. New developments in sentinel node staging in melanoma: controversies and alternatives. Curr Opin Oncol. 2010;22:169–77.
10. Veronesi U, Adamus J, Bandiera DC, Brennhovd IO, Caceres E, Cascinelli N, et al. Inefficacy of immediate node dissection in stage 1 melanoma of the limbs. N Engl J Med. 1977;297:627–30.
11. Sim FH, Taylor WF, Ivins JC, Pritchard DJ, Soule EH. A prospective randomized study of the efficacy of routine elective lymphadenectomy in management of malignant melanoma. Preliminary results. Cancer. 1978;41:948–56.
12. Balch CM, Soong SJ, Bartolucci AA, Urist MM, Karakousis CP, Smith TJ, et al. Efficacy of an elective regional lymph node dissection of 1 to 4 mm thick melanomas for patients 60 years of age and younger. Ann Surg. 1996;224:255–63.
13. Cascinelli N, Morabito A, Santinami M, MacKie RM, Belli F. Immediate or delayed dissection of regional nodes in patients with melanoma of the trunk: a randomised trial. WHO melanoma programme. Lancet. 1998;351:793–6.
14. Wong JH, Cagle LA, Morton DL. Lymphatic drainage of skin to a sentinel lymph node in a feline model. Ann Surg. 1991;214: 637–41.
15. Amersi F, Morton DL. The role of sentinel lymph node biopsy in the management of melanoma. Adv Surg. 2007;41:241–56.
16. van Akkooi AC, Voit CA, Verhoef C, Eggermont AM. Potential cost-effectiveness of US-guided FNAC in patients with melanoma as a primary procedure and in follow-up. Ann Surg Oncol. 2010; 17:660–2.
17. Prayer L, Winkelbauer H, Gritzmann N, Winkelbauer F, Helmer M, Pehamberger H. Sonography versus palpation in the detection of regional lymph-node metastases in patients with malignant melanoma. Eur J Cancer. 1990;26:827–30.
18. Blum A, Schlagenhauff B, Stroebel W, Breuninger H, Rassner G, Garbe C. Ultrasound examination of regional lymph nodes significantly improves early detection of locoregional metastases during the follow-up of patients with cutaneous melanoma: results of a prospective study of 1288 patients. Cancer. 2000;88:2534–9.
19. Voit C, Mayer T, Kron M, Schoengen A, Sterry W, Weber L, et al. Efficacy of ultrasound B-scan compared with physical examination in follow-up of patients with melanoma. Cancer. 2001;91: 2409–16.
20. Schmid-Wendtner MH, Paerschke G, Baumert J, Plewig G, Volkenandt M. Value of ultrasonography compared with physical examination for the detection of locoregional metastases in patients with cutaneous melanoma. Melanoma Res. 2003;13:183–8.
21. Lam TK, Uren RF, Scolyer RA, Quinn MJ, Shannon KF, Thompson JF. False-negative sentinel node biopsy because of obstruction of lymphatics by metastatic melanoma: the value of ultrasound in conjunction with preoperative lymphoscintigraphy. Melanoma Res. 2009;19:94–9.
22. Catalano O, Siani A. Cutaneous melanoma: role of ultrasound in the assessment of locoregional spread. Curr Probl Diagn Radiol. 2010;39:30–6.
23. Nazarian LN, Alexander AA, Rawool NM, Kurtz AB, Maguire HC, Mastrangelo MJ. Malignant melanoma: impact of superficial US on management. Radiology. 1996;199:273–7.
24. Voit C, Proebstle TM, Winter H, Kimmritz J, Kron M, Sterry W, et al. Presurgical ultrasound-guided anchor-wire marking of soft tissue metastases in stage III patients with melanoma. Dermatol Surg. 2001;27:129–32.
25. Machet L, Nemeth-Normand F, Giraudeau B, Perrinaud A, Tiguemounine J, Ayoub J, et al. Is ultrasound lymph node examination superior to clinical examination in melanoma follow-up? A monocentre cohort study of 373 patients. Br J Dermatol. 2005;152:66–70.
26. Voit C, Mayer T, Proebstle TM, Weber L, Kron M, Krupienski M, et al. Ultrasound-guided fine-needle aspiration cytology in the early detection of melanoma metastases. Cancer. 2000;90:186–93.
27. Voit C, Kron M, Schafer G, Schoengen A, Audring H, Lukowsky A, et al. Ultrasound-guided fine needle aspiration cytology prior to sentinel lymph node biopsy in patients with melanoma. Ann Surg Oncol. 2006;13:1682–9.
28. Voit CA, van Akkooi AC, Schafer-Hesterberg G, Schoengen A, Schmitz PI, Sterry W, et al. Rotterdam criteria for sentinel node (SN) tumor burden and the accuracy of ultrasound (US)-guided fine-needle aspiration cytology (FNAC): can US-guided FNAC replace SN staging in patients with melanoma? J Clin Oncol. 2009;27:4994–5000.
29. Voit C, Schoengen A, Schwurzer-Voit M, Weber L, Ulrich J, Sterry W, et al. The role of ultrasound in detection and management of regional disease in patients with melanoma. Semin Oncol. 2002;29: 353–60.
30. Schafer-Hesterberg G, Schoengen A, Sterry W, Voit C. Use of ultrasound to early identify, diagnose and localize metastases in patients with melanoma. Expert Rev Anticancer Ther. 2007;7:1707–16.
31. Catalano O, Setola SV, Vallone P, Mattace Raso M, Gallipoli D'Errico A. Sonography for locoregional staging and follow-up of cutaneous melanoma: how we do it. J Ultrasound Med. 2010;29: 791–802.
32. Fornage BD, Lorigan JG. Sonographic detection and fine-needle aspiration biopsy of nonpalpable recurrent or metastatic melanoma in subcutaneous tissues. J Ultrasound Med. 1989;8:421–4.
33. Vilana R, Puig S, Sanchez M, Squarcia M, Lopez A, Castel T, et al. Preoperative assessment of cutaneous melanoma thickness using 10-MHz sonography. AJR Am J Roentgenol. 2009;193:639–43.
34. Guitera P, Li LX, Crotty K, Fitzgerald P, Mellenbergh R, Pellacani G, et al. Melanoma histological breslow thickness predicted by 75-MHz ultrasonography. Br J Dermatol. 2008;159: 364–9.

35. Hayashi K, Koga H, Uhara H, Saida T. High-frequency 30-MHz sonography in preoperative assessment of tumor thickness of primary melanoma: usefulness in determination of surgical margin and indication for sentinel lymph node biopsy. Int J Clin Oncol. 2009;14:426–30.
36. Nazarian LN, Alexander AA, Kurtz AB, Capuzzi Jr DM, Rawool NM, Gilbert KR, et al. Superficial melanoma metastases: appearances on gray-scale and color Doppler sonography. AJR Am J Roentgenol. 1998;170:459–63.
37. Catalano O, Sandomenico F, Siani A. Value of the extended field of view modality in the sonographic imaging of cutaneous melanoma: a pictorial essay. Dermatol Surg. 2010;36:1300–4.
38. Ulrich J, Voit C. Ultrasound in dermatology. Part II. Ultrasound of regional lymph node basins and subcutaneous tumours. Eur J Dermatol. 2001;11:73–9.
39. Mall JW, Reetz C, Koplin G, Schafer-Hesterberg G, Voit C. Neuss H [surgical technique and postoperative morbidity following radical inguinal/iliacal lymph node dissection – a prospective study in 67 patients with malignant melanoma metastatic to the groin]. Zentralbl Chir. 2009;134:437–42.
40. Spillane AJ, Haydu L, McMillan W, Stretch JR, Thompson JF. Quality assurance parameters and predictors of outcome for ilioinguinal and inguinal dissection in a contemporary melanoma patient population. Ann Surg Oncol. 2011;18(9):2521–8.
41. Uren RF, Howman-Giles R, Thompson JF, McCarthy WH, Quinn MJ, Roberts JM, et al. Interval nodes: the forgotten sentinel nodes in patients with melanoma. Arch Surg. 2000;135:1168–72.
42. McMasters KM, Chao C, Wong SL, Wrightson WR, Ross MI, Reintgen DS, et al. Interval sentinel lymph nodes in melanoma. Arch Surg. 2002;137:543–7.
43. Marone U, Caraco C, Chiofalo MG, Botti G, Mozzillo N. Resection in the popliteal fossa for metastatic melanoma. World J Surg Oncol. 2007;5:8.
44. Ulrich J, van Akkooi AJ, Eggermont AM, Voit C. New developments in melanoma: utility of ultrasound imaging (initial staging, follow-up and pre-SLNB). Expert Rev Anticancer Ther. 2011;11:1693–701.
45. Voit C, van Akkooi AC, Schafer-Hesterberg G, Schoengen A, Kowalczyk K, Roewert JC, et al. Ultrasound morphology criteria predict metastatic disease of the sentinel nodes in patients with melanoma. J Clin Oncol. 2010;28:847–52.
46. Lassau N, Chami L, Peronneau P. Imaging of melanoma: accuracy of ultrasonography before and after contrast injection for diagnostic and early evaluation of treatments. Bull Cancer. 2007;94:93–8.
47. Schmid-Wendtner MH, Dill-Muller D, Baumert J, Wagner A, Eberle J, Tilgen W, et al. Lymph node metastases in patients with cutaneous melanoma: improvements in diagnosis by signal-enhanced color doppler sonography. Melanoma Res. 2004;14:269–76.
48. Schmid-Wendtner MH, Burgdorf W. Ultrasound scanning in dermatology. Arch Dermatol. 2005;141:217–24.
49. De GV, Gori A, Grazzini M, Rossari S, Marino G, D'Elia G, et al. Contrast-enhanced ultrasound: a filter role in AJCC stage I/II patients with melanoma. Oncology. 2010;79:370–5.
50. Rubaltelli L, Beltrame V, Tregnaghi A, Scagliori E, Frigo AC, Stramare R. Contrast-enhanced ultrasound for characterizing lymph nodes with focal cortical thickening in patients with cutaneous melanoma. AJR Am J Roentgenol. 2011;196:W8–12.
51. Thompson JF, Soong SJ, Balch CM, Gershenwald JE, Ding S, Coit DG, et al. Prognostic significance of mitotic rate in localized primary cutaneous melanoma: an analysis of patients in the multi-institutional American Joint Committee on Cancer melanoma staging database. J Clin Oncol. 2011;29:2199–205.
52. Jemec GB, Gniadecka M, Ulrich J. Ultrasound in dermatology. Part I. High frequency ultrasound. Eur J Dermatol. 2000;10:492–7.
53. Machet L, Belot V, Naouri M, Boka M, Mourtada Y, Giraudeau B, et al. Preoperative measurement of thickness of cutaneous melanoma using high-resolution 20 MHz ultrasound imaging: a monocenter prospective study and systematic review of the literature. Ultrasound Med Biol. 2009;35:1411–20.
54. Lassau N, Koscielny S, Avril MF, Margulis A, Duvillard P, De BT, et al. Prognostic value of angiogenesis evaluated with high-frequency and color doppler sonography for preoperative assessment of melanomas. AJR Am J Roentgenol. 2002;178:1547–51.
55. Serrone L, Solivetti FM, Thorel MF, Eibenschutz L, Donati P, Catricala C. High frequency ultrasound in the preoperative staging of primary melanoma: a statistical analysis. Melanoma Res. 2002;12:287–90.
56. Salmhofer W, Rieger E, Soyer HP, Smolle J, Kerl H. Influence of skin tension and formalin fixation on sonographic measurement of tumor thickness. J Am Acad Dermatol. 1996;34:34–9.
57. Fallowfield ME, Cook MG. The vascularity of primary cutaneous melanoma. J Pathol. 1991;164:241–4.
58. Cosgrove D, Lassau N. Assessment of tumour angiogenesis using contrast-enhanced ultrasound. J Radiol. 2009;90(1 Pt 2):156–64.
59. Srivastava A, Hughes LE, Woodcock JP, Laidler P. Vascularity in cutaneous melanoma detected by Doppler sonography and histology: correlation with tumour behaviour. Br J Cancer. 1989;59:89–91.
60. Lassau N, Lamuraglia M, Koscielny S, Spatz A, Roche A, Leclere J, et al. Prognostic value of angiogenesis evaluated with high-frequency and colour Doppler sonography for preoperative assessment of primary cutaneous melanomas: correlation with recurrence after a 5 year follow-up period. Cancer Imaging. 2006;6:24–9.
61. Bessoud B, Lassau N, Koscielny S, Longvert C, Avril MF, Duvillard P, et al. High-frequency sonography and color Doppler in the management of pigmented skin lesions. Ultrasound Med Biol. 2003;29:875–9.
62. Rossi CR, Mocellin S, Scagnet B, Foletto M, Vecchiato A, Pilati P, et al. The role of preoperative ultrasound scan in detecting lymph-node metastasis before sentinel node biopsy in patients with melanoma. J Surg Oncol. 2003;83:80–4.
63. van Rijk MC, Teertstra HJ, Peterse JL, Nieweg OE, Olmos RA, Hoefnagel CA, et al. Ultrasonography and fine-needle aspiration cytology in the preoperative evaluation of patients with melanoma eligible for sentinel node biopsy. Ann Surg Oncol. 2006;13:1511–6.
64. Sanki A, Uren RF, Moncrieff M, Tran KL, Scolyer RA, Lin HY, et al. Targeted high-resolution ultrasound is not an effective substitute for sentinel lymph node biopsy in patients with primary cutaneous melanoma. J Clin Oncol. 2009;27:5614–9.
65. Starritt EC, Uren RF, Scolyer RA, Quinn MJ, Thompson JF. Ultrasound examination of sentinel nodes in the initial assessment of patients with primary cutaneous melanoma. Ann Surg Oncol. 2005;12:18–23.
66. van Akkooi A, de Wilt J, Verhoef C, Schmitz P, van Geel A, Eggermont A, et al. Clinical relevance of melanoma micrometastases (<0.1 mm) in sentinel nodes: are these nodes to be considered negative? Ann Oncol. 2006;17:1578–85.
67. Dewar DJ, Newell B, Green MA, Topping AP, Powell BW, Cook MG. The microanatomic location of metastatic melanoma in sentinel lymph nodes predicts nonsentinel lymph node involvement. J Clin Oncol. 2004;22:3345–9.
68. van der Ploeg AP, van Akkooi AC, Rutkowski P, Nowecki ZI, Michej W, Mitra A, et al. Prognosis in patients with sentinel node-positive melanoma is accurately defined by the combined Rotterdam tumor load and Dewar topography criteria. J Clin Oncol. 2011;29:2206–14.
69. Kunte C, Schuh T, Eberle JY, Baumert J, Konz B, Volkenandt M, et al. The use of high-resolution ultrasonography for preoperative detection of metastases in sentinel lymph nodes of patients with cutaneous melanoma. Dermatol Surg. 2009;35:1757–65.

70. Voit CA, van Akkooi AJ, Schafer-Hesterberg G, Sterry W, Eggermont AM. Multimodality approach to the sentinel node: an algorithm for the use of presentinel lymph node biopsy ultrasound (after lymphoscintigraphy) in conjunction with presentinel lymph node biopsy fine needle aspiration cytology. Melanoma Res. 2011;21(5):450–6.
71. Garbe C, Hauschild A, Volkenandt M, Schadendorf D, Stolz W, Reinhold U, et al. Evidence and interdisciplinary consense-based German guidelines: diagnosis and surveillance of melanoma. Melanoma Res. 2007;17:393–9.
72. Catalano O, Caracò C, Mozzillo N, Siani A. Locoregional spread of cutaneous melanoma: sonography findings. AJR Am J Roentgenol. 2010;194:735–45.
73. Solivetti FM, Di Luca SA, Pirozzi G, Coscarella G, Brigida R, Eibenshutz L. Sonographic evaluation of clinically occult in-transit and satellite metastases from cutaneous malignant melanoma. Radiol Med (Torino). 2006;111:702–8.
74. Alexander AA, Nazarian LN, Capuzzi Jr DM, Rawool NM, Kurtz AB, Mastrangelo MJ. Color doppler sonographic detection of tumor flow in superficial melanoma metastases: histologic correlation. J Ultrasound Med. 1998;17:123–6.
75. Catalano O. Critical analysis of the ultrasonographic criteria for diagnosing lymph-node metastasis in patients with cutaneous melanoma: a systematic review. J Ultrasound Med. 2011;30: 547–60.
76. Rossi CR, Seno A, Vecchiato A, Foletto M, Tregnaghi A, De Candia A, et al. The impact of ultrasound scanning in the staging and follow-up of patients with clinical stage I cutaneous melanoma. Eur J Cancer. 1997;33:200–3.
77. Brountzos EN, Panagiotou IE, Bafaloukos DI, Kelekis DA. Ultrasonographic detection of regional lymph node metastases in patients with intermediate or thick malignant melanoma. Oncol Rep. 2003;10:505–10.
78. Machet L, Perrinaud A, Giraudeau B. Routine ultrasonography in melanoma follow-up? Lancet Oncol. 2005;6:2.
79. Voit CA, van Akkooi AC, Eggermont AM, Schäfer-Hesterberg G, Kron M, Ulrich J, Sterry W, Schoengen A, Rademaker J. Fine needle aspiration cytology of palpable and nonpalpable lymph nodes to detect metastatic melanoma. J Natl Cancer Inst. 2011;103:1771–7.
80. Testori A, Lazzaro G, Baldini F, Tosti G, Mosconi M, Lovati E, et al. The role of ultrasound of sentinel nodes in the pre- and postoperative evaluation of stage I patients with melanoma. Melanoma Res. 2005;15:191–8.
81. Saiag P, Bernard M, Beauchet A, Bafounta ML, Bourgault-Villada I, Chagnon S. Ultrasonography using simple diagnostic criteria vs palpation for the detection of regional lymph node metastases of melanoma. Arch Dermatol. 2005;141:183–9.
82. Tregnaghi A, De Candia A, Calderone M, Cellini L, Rossi CR, Talenti E, et al. Ultrasonographic evaluation of superficial lymph node metastases in melanoma. Eur J Radiol. 1997;24: 216–21.
83. Vassallo P, Wernecke K, Roos N, Peters PE. Differentiation of benign from malignant superficial lymphadenopathy: the role of high-resolution US. Radiology. 1992;183:215–20.
84. Vassallo P, Edel G, Roos N, Naguib A, Peters PE. In-vitro high-resolution ultrasonography of benign and malignant lymph nodes. A sonographic-pathologic correlation. Invest Radiol. 1993;28: 698–705.
85. Rettenbacher T. Sonography of peripheral lymph nodes part 1: normal findings and B-image criteria. Ultraschall Med. 2010;31: 344–62.
86. Rossi CR, Scagnet B, Vecchiato A, Mocellin S, Pilati P, Foletto M, Zavagno G, Casara D, Montesco MC, Tregnaghi A, Rubaltelli L, Lise M. Sentinel node biopsy and ultrasound scanning in cutaneous melanoma: clinical and technical considerations. Eur J Cancer. 2000;36:895–900.
87. Hocevar M, Bracko M, Pogacnik A, Vidergar-Kralj B, Besic N, Zgajnar J, Music MM. The role of preoperative ultrasonography in reducing the number of sentinel lymph node procedures in melanoma. Melanoma Res. 2004;14:533–6.
88. Sibon C, Chagnon S, Tchakérian A, Bafounta ML, Longvert C, Clerici T, Zimmermann U, Saiag P. The contribution of high-resolution ultrasonography in preoperatively detecting sentinel-node metastases in melanoma patients. Melanoma Res. 2007;17:233–7.

Cutaneous Lymphomas

12

Hong-Jen Chiou and Yi-Hong Chou

Contents

12.1 Introduction

Superficial soft-tissue tumors commonly manifest themselves as painless and benign masses that are hard to differentiate from malignant masses on physical examination alone. However, benign soft-tissue tumors are more common than malignant ones. Malignant soft-tissue tumors, especially those in the musculoskeletal and dermatological system, are rare and account for less than 1 % of all neoplasms. Most of these tumors are mesodermal in origin, such as malignant fibrous histiocytomas, leiomyosarcomas, liposarcomas, synovial sarcomas, and malignant peripheral nerve-sheath tumors, etc. [1, 2]. Superficial soft-tissue lymphomas are extremely rare, with approximately only 1.4 % of all malignant lymphomas [3].

The usual appearance of lymphoma, including both Hodgkin disease and non-Hodgkin lymphoma, is as localized or generalized lymphadenopathy. Extranodal lymphoma is relatively rare, occurring in bone, gut, and tonsils, for example, but rarely in peripheral soft tissue [4–16]. According the revised European-American lymphoma classification [17], the classification of superficial soft-tissue lymphomas is similar to that of whole-body lymphomas and is divided into B-cell lymphoma (precursor B-cell and mature [peripheral] B-cell tumor), T-cell lymphoma (precursor T-cell and mature [peripheral] T-cell tumor), and Hodgkin lymphoma. Superficial soft-tissue lymphomas might be the result of hematogenous or lymphatic pathways, continuous extension from surrounding primary bony lymphoma, or (in rare cases) from the soft tissue or muscle itself [18–24]. The management of superficial soft-tissue lymphomas differs from that of other soft-tissue sarcomas, and the proper treatment for these malignant tumors depends on accurate histopathologic diagnosis; in malignant lymphoma, nonsurgical therapy can be curative [25]. There have been few imaging studies of primary soft-tissue lymphoma. Most have been plain radiographic, computed tomographic (CT), magnetic resonance, and positron emission tomographic studies [12]. High-resolution ultrasonography (HRUS) applied to soft-tissue lymphoma was only recently developed [26, 27].

H.-J. Chiou (✉)
Division of Musculoskeletal Radiology, Taipei Veterans General Hospital and School of Medicine, National Yang-Ming University, No. 201, Section 2, Shih-Pa Road, Taipei 112, Taiwan
e-mail: hjchiou@gmail.com

Y.-H. Chou
Division of Ultrasound and Breast Imaging, Taipei Veterans General Hospital and School of Medicine, National Yang-Ming University, No. 201, Section 2, Shih-Pa Road, Taipei, Taiwan
e-mail: yhchou@vghtpe.gov.tw

X. Wortsman, G.B.E. Jemec (eds.), *Dermatologic Ultrasound with Clinical and Histologic Correlations*,
DOI 10.1007/978-1-4614-7184-4_12, © Springer Science+Business Media New York 2013

12.2 Technical Considerations

The gray scale ultrasonographic scanning should include both short and long axis views and evaluate the echogenicity, margin, and biggest diameter of the tumor. The echogenicity can be classified as high or low and as heterogeneous or homogeneous. Color Doppler ultrasonography was performed at various settings: the scale level and pulse repetition frequency were decreased; color gain was increased until color noise became apparent; and the probe pressure on the lesion was lowered to avoid compressing the small vessels and thereby causing disappearance of low–blood velocity signals [28]. A superficial soft-tissue mass is actually very sensitive to pressure. Therefore, we recommend that color Doppler ultrasound (CDU) and spectral analysis should be performed without pressure to obtain the most consistent results and will be the most sensitive to small vessel function. To achieve "pressureless" status, we recommended the use of a good supply of gel between the probe and skin. The Doppler spectral analysis technique was the same as the CDUS technique. CDUS findings were graded as 0 (no color signal), 1 (<5 spots or lines), 2 (5–15 color spots or lines), or 3 (>15 spots or lines).

The imaging systems will focus on the transducer, and we recommended using a high-frequency linear transducer with a lot of gel to put the lesion within the focus zone.

12.3 Pathology

Clinical presentations of superficial soft-tissue lymphomas could be classified as primary soft-tissue lymphoma, primary soft-tissue lymphoma with body involvement, and secondary soft-tissue lymphoma. Most of the superficial soft-tissue lymphomas occurred in the torso and lower limb [29].

The sonographic echogenicity and morphologic features of soft-tissue lymphoma usually presented as relatively homogeneous hypoechogenicity except for a panniculitis type lymphoma, possibly because most of the area of lymphocyte proliferation had less interface density to reflect the sound beam. Furthermore, most soft-tissue lymphomas had infiltrative margins, [28] which is related to the fact that lymphoma cells easily invade surrounding tissue except for the thick epimysium, and none had echo-free spaces within the tumor, suggesting that tumor necrosis is extremely rare in peripheral soft-tissue lymphoma. The homogeneously hypoechoic pattern of the lymphomas usually corresponded to the large-field, uniform cluster of lymphoma cells with correlation to histology (Fig. 12.1). In that pattern, acoustic impedances of the tumor were similar and differences in acoustic impedance were rare; therefore, the reflected echoes were less than those usually surrounding the soft tissue, resulting in homogeneous hypoechogenicity (Fig. 12.1). In lymphoma–cell infiltration and mixture of soft tissue (such as muscle fascicles), the acoustic impedance between uniform lymphoma cells and nonuniform soft tissue (perimysium or endomysium) varied and resulted in heterogeneous hypoechogenicity (Fig. 12.2). The appearance of soft-tissue lymphoma was variable and could be classified into five types: (1) big mass (>5 cm) (Fig. 12.1) (2) nodal (1–5 cm) (Fig. 12.3) or confluent nodal; (3) small nodular (<1 cm, most <5 mm) and disseminated (Fig. 12.4); (4) myositis (Fig. 12.2); and (5) panniculitis (Fig. 12.5). Most of the lymphomas were masses or nodal or confluent nodal.

Nodal or confluent nodal type means that lymphoma cells have infiltrated the lymph node, enlarging the node. In nodal-type lymphomas, the morphology of the lymph node (ovoid to round with a thin or absent echogenic central hilum) is usually preserved (Fig. 12.6). Therefore, the lymphoma may involve the superficial soft tissue, possibly by means of the lymphatic system, with proliferation in the lymph node. CDUS showed hypervascularity with proliferative vessels from the hilum and rarely from the peripheral capsule (Fig. 12.6).

Small nodular and disseminated lymphomas usually involve the salivary gland and have a diffuse, small and nodular pattern, which can be a result of cluster lymphocytic (hypoechoic) infiltration in the echogenic salivary gland (Fig. 12.4).

In the myositis type, the lymphoma usually grows via an infiltrative-like myositis if occurring within the muscle, rather than a focal process that usually presented on peripheral soft-tissue sarcoma. The sonographic pattern usually presents as heterogeneous hypoechogenicity with infiltration in the margin (Fig. 12.2). However, in some space-limited locations such as in the upper limb, rapid growth and infiltration within the muscle will result in compartment syndrome [12].

On modern HRUS equipment, the separation between adjacent normal adipose cells in subcutaneous fat lobules is difficult, the normal subcutaneous fat lobules therefore present as homogeneous hypoechogenicity except for some thick connective tissue bands. In the panniculitis form, the histologic examination showed that much lymphocytes proliferation and infiltration in the subcutaneous layer separated the small adipose cells from big fat lobules, increasing the number of the fat–soft tissue (lymphoma cells) interfaces and the amount of the sound beam reflected (Fig. 12.5c). Therefore, the infiltrated parts of the subcutaneous fat layer appear as variable homogeneous hyperechoic nodules (Fig. 12.7) distributed in the subcutaneous fat layer or occupied the whole layer of the subcutaneous layer (Fig. 12.5). Such homogeneous hyperechoic subcutaneous fat pattern could occur on other etiology, for example, when fluid or inflammatory cells (lymphocytes) infiltrate the subcutaneous fat layer. Therefore, the differential diagnosis should include entities such as subcutaneous edema (Fig. 12.8), hemorrhage, inflammatory myofibroblast cell tumor infiltration (Fig. 12.9), cellulites (Fig. 12.10), and panniculitis (Fig. 12.11). However, the panniculitic type is very rare in other malignant tumors such as malignantfibrous histiocytoma or other sarcomatous lesions. Subcutaneous panniculitis such as T-cell lymphoma is a rare disorder. Clinically, it is often confused with inflammatory panniculitis associated with connective tissue disease. Histologically, subcutaneous panniculitis-like T-cell

lymphoma is characterized by a lymphohistiocytic infiltrate confined primarily to the fat lobules in subcutaneous tissue.

Prominent hypervascularity in color Doppler sonography usually appears in peripheral soft-tissue lymphoma (Figs. 12.1b, 12.2b, and 12.7b). Although most other tumors (especially malignant tumors in peripheral soft tissue) are hypervascular, the degree of vascularity is more prominent in lymphomas than in other tumors [28–30]. The extreme hypervascularity in the lymphoma can be different from that in other types of soft-tissue sarcoma and result in no central necrosis in peripheral soft-tissue lymphoma. The spectral analysis showed that the resistive index of tumor vessels within the peripheral soft-tissue lymphoma was relatively low compared with that of normal vessels within the surrounding muscular tissue (Fig. 12.5b). The low resistive index was similar to that of vessels in other malignant soft-tissue tumors. Therefore, only the resistive index could not be differentiated from that of other soft-tissue sarcoma types. However, there were usually no arteriovenous shunts, which could be found in hemangiopericytoma, detected in peripheral soft-tissue lymphoma.

Patient survival is relatively independent to patient age, sex, tumor location or size, CDUS grade, or histology [30]. The prognosis of peripheral soft-tissue lymphoma possibly correlated to the cell type of lymphoma, tumor appearance, and clinical presentation; that is, poor prognosis in diffuse large B-cell lymphoma, myositis type, and secondary soft-tissue lymphoma [28, 30]

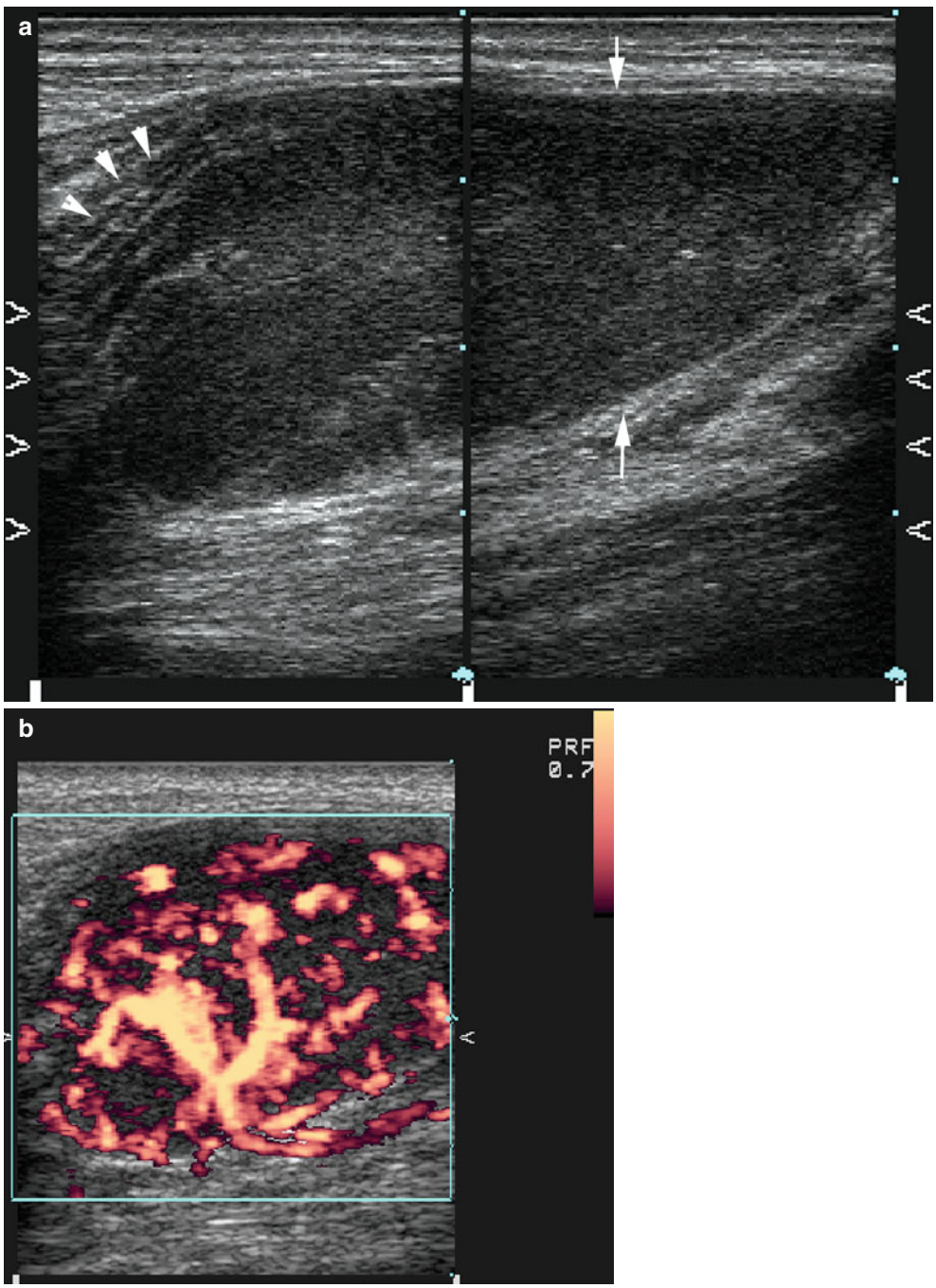

Fig. 12.1 A 60-year-old male patient complaining of a palpable mass over right calf. (**a**) Longitudinal section of the mass showing a homogeneous hypoechogenicity that infiltrated to the upper (*arrowheads*) and lower parts of the gastrocnemius muscle but well-defined margin in the anterior and posterior (*arrows*) aspect. (**b**) Power Doppler image showing hypervascularity in the tumor. This tumor turned out to be diffuse large T-cell lymphoma

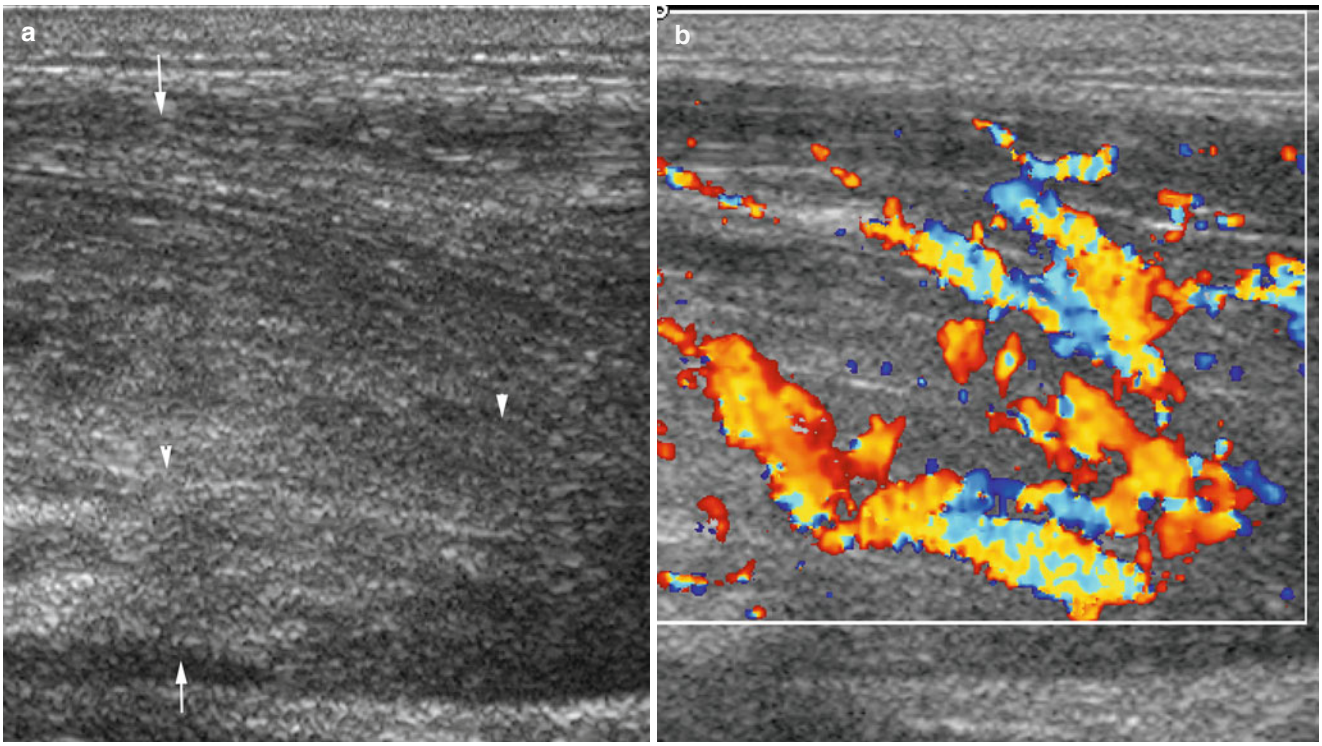

Fig. 12.2 A 79-year-old female patient complaining of severe swelling of the left arm. (**a**) Longitudinal section of left arm showing a heterogeneous echogenic lesion (*arrows*) infiltrating between the perimysium (*arrowheads*) in the muscle of the arm, as would be seen in a case of myositis. (**b**) Color Doppler ultrasound image showing hypervascularity in the tumor, that turned out to be diffuse large B-cell lymphoma

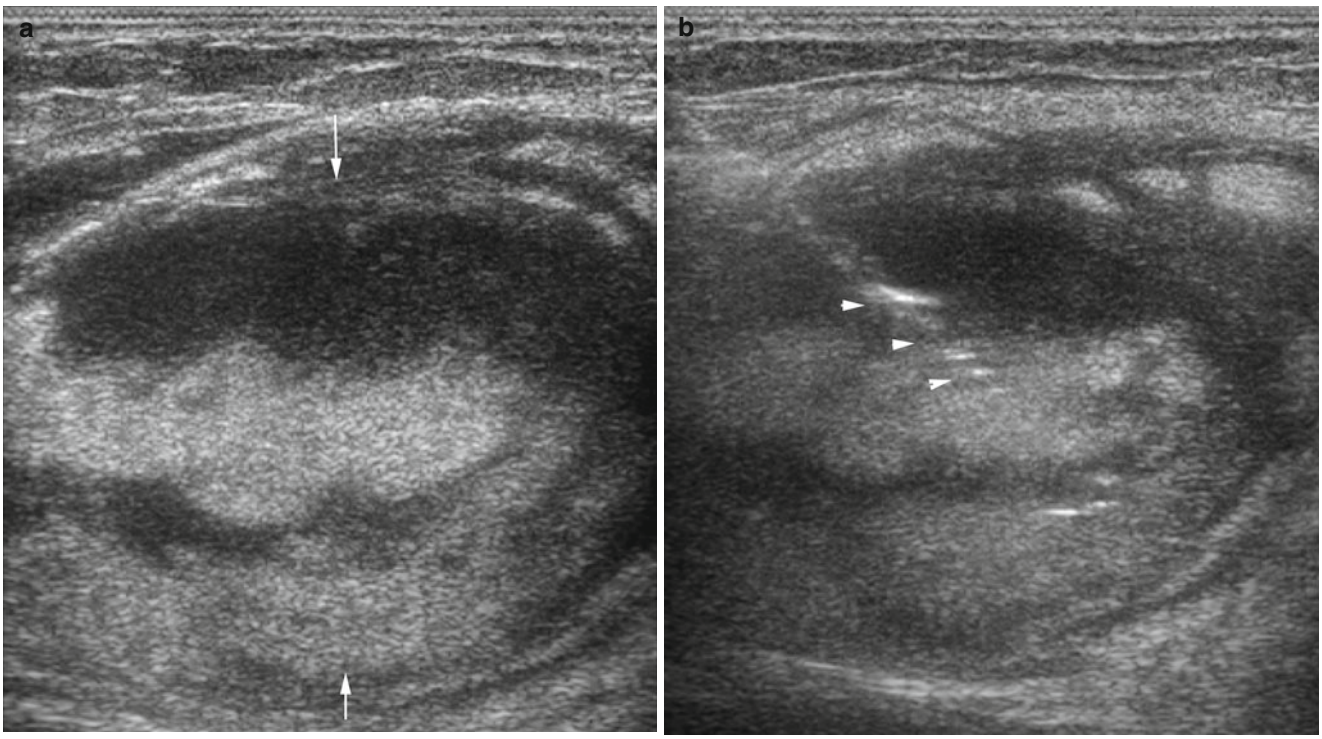

Fig. 12.3 A 77-year-old male, complaining of painless nodule in right inguinal region. (**a**) Grey-scale ultrasound image shows heterogeneous echoic nodule (*arrows*), mixed with hypoechoic and hyperechogenicity. (**b**) Ultrasound-guided core biopsy (*arrowheads*) through the hypoechoic and hyperechoic area. (**c**) Histologic photograph of specimen shows diffuse lymphoma cell infiltration and separated the adipose cell (*arrows*). This tumor turned out to be peripheral T-cell lymphoma

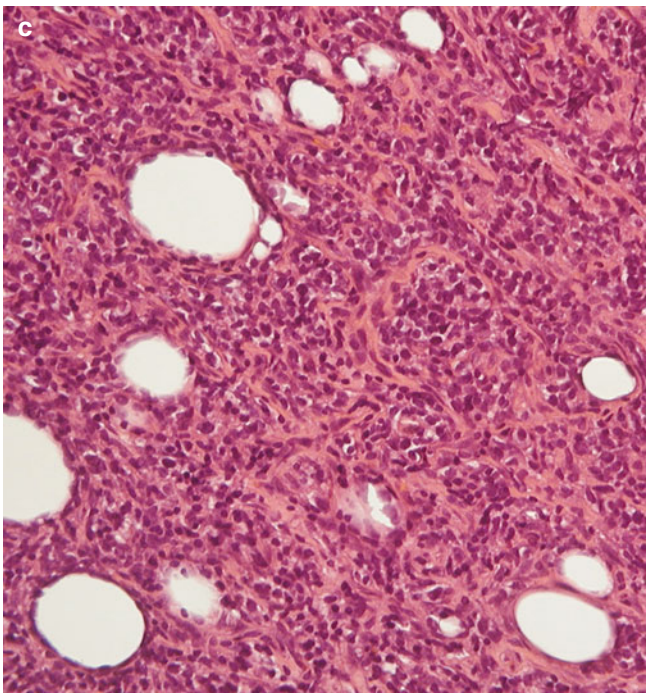

Fig. 12.3 (continued)

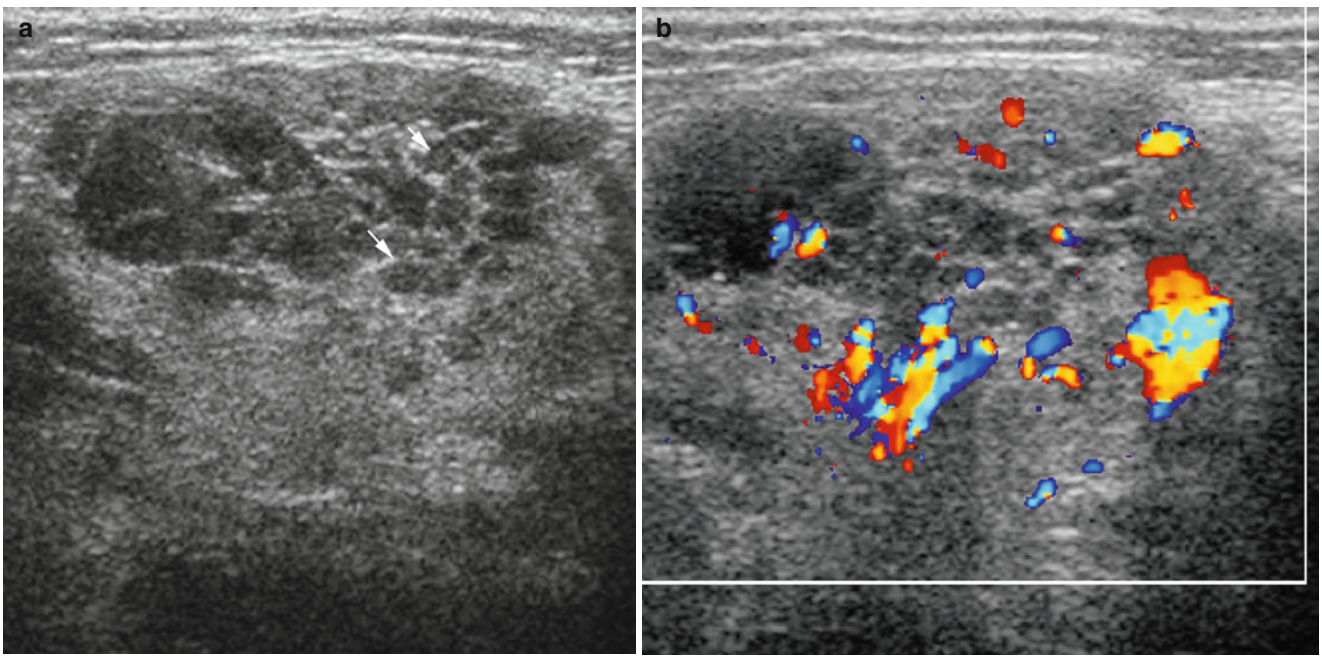

Fig. 12.4 A 53-year-old female patient complaining of swelling over billateral submandibular region. (**a**) Transverse section of left submandibular gland showing multiple small hypoechoic nodular lesions (*arrows*) within the echogenic submandibular gland. (**b**) Color Doppler ultrasound image showing prominent vascularity in left submandibular gland. Biopsy proved small B-cell lymphoma

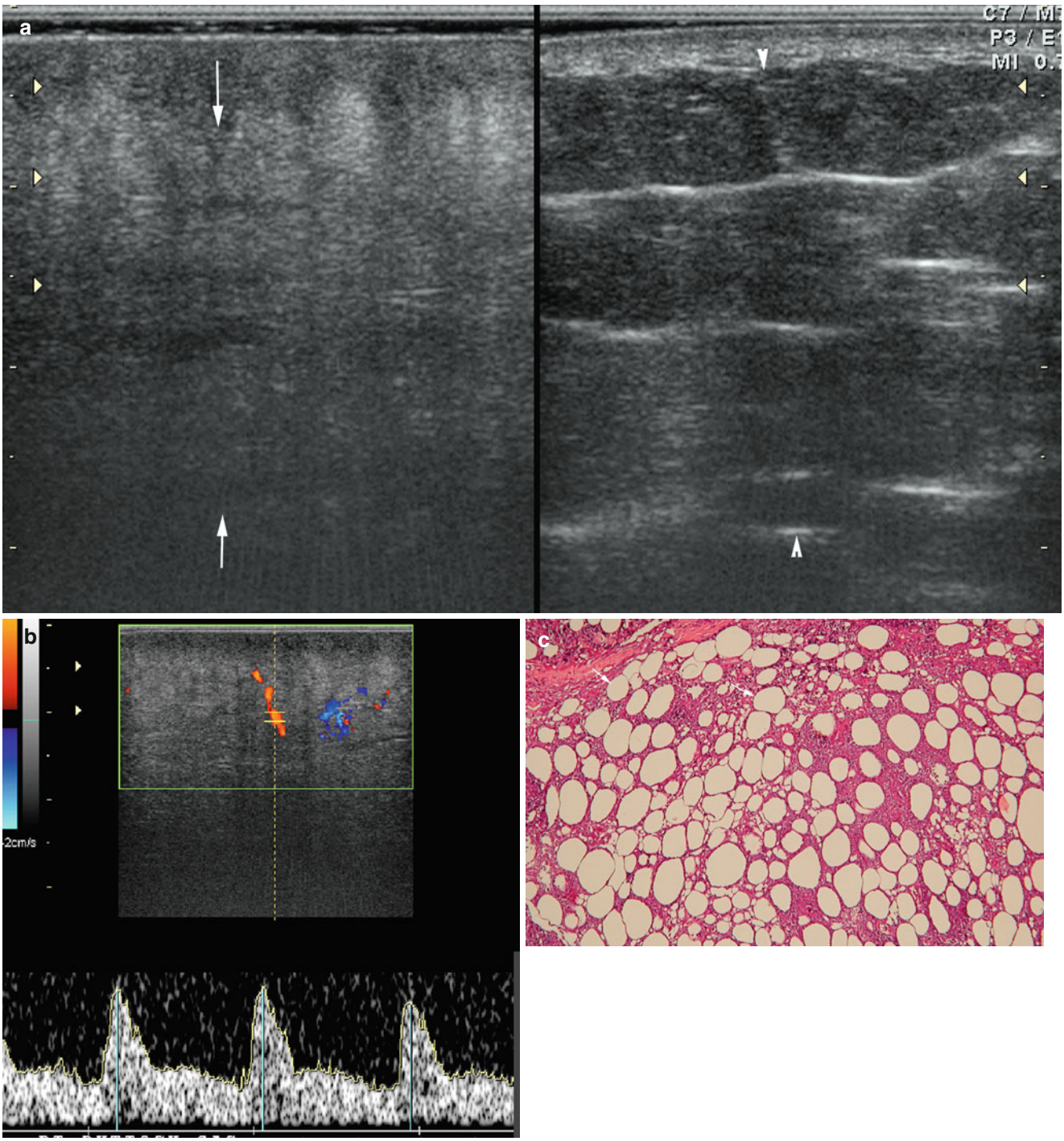

Fig. 12.5 A 25-year-old female patient complaining about painless nodule in right buttock region. (**a**) Grey scale ultrasound image shows homogeneous hyperechoic area (*arrows*) with infiltration in the subcutaneous layer compared with normal hypoechoic subcutaneous fat layer (*arrowheads*, left side). (**b**) Color Doppler ultrasound image shows grade 2 hypervascularity with low resistive index. (**c**) Histology image shows diffuse small lymphocyte infiltration and separated the adipose cells (*arrows*) in the subcutaneous layer. This lesion turned out to be T-cell lymphoma

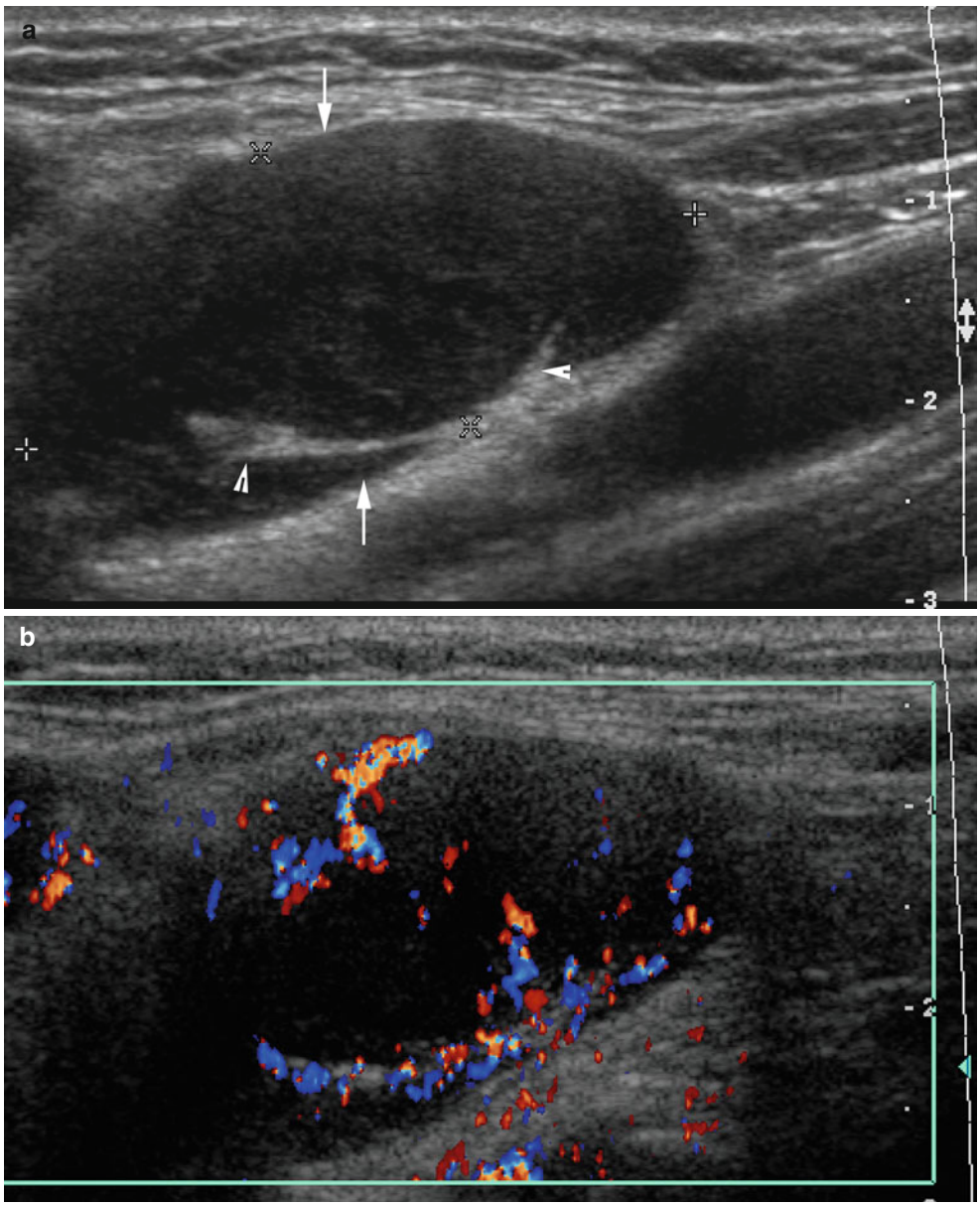

Fig. 12.6 A 57-year-old male patient complaining of firm mass in left neck that is movable for half a year. (**a**) Longitudinal section of left lateral neck showing an ovoid-shaped homogeneous hypoechoic nodule (*arrows*), size approximately 35 × 17 mm with compressed echogenic hilum (*arrowheads*). (**b**) Color Doppler ultrasound image showing vascularity from the hilum and capsule region. This turned out to be diffuse large B-cell lymphoma

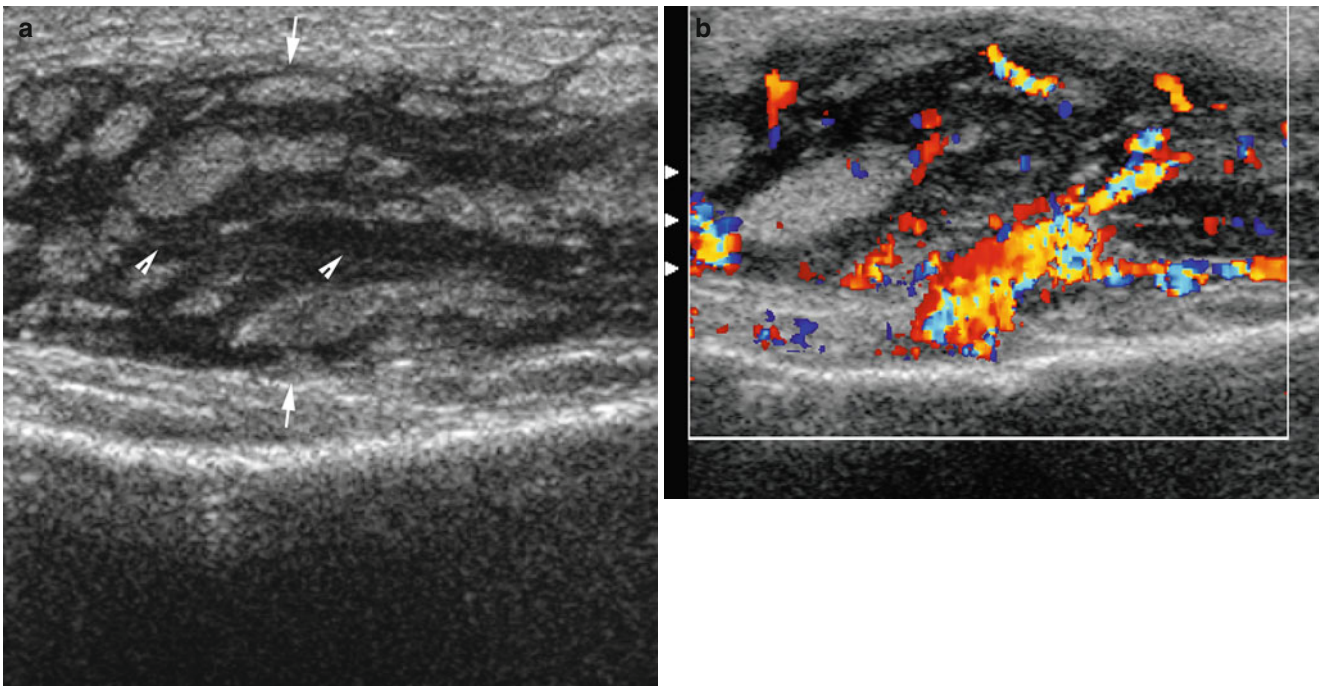

Fig. 12.7 A 72-year-old male patient complaining of painful mass over right anterior superior lower leg for 3 months. (**a**) Grey scale ultrasound image shows variable size homogeneous hyperechoic area (*arrows*) with thickening and hypoechogenicity of the septa (*arrowheads*) in subcutaneous fat layer. (**b**) Color Doppler ultrasound image showed grade 3 hypervascularity in the lesion. Sono-guide biopsy proved B-cell lymphoma

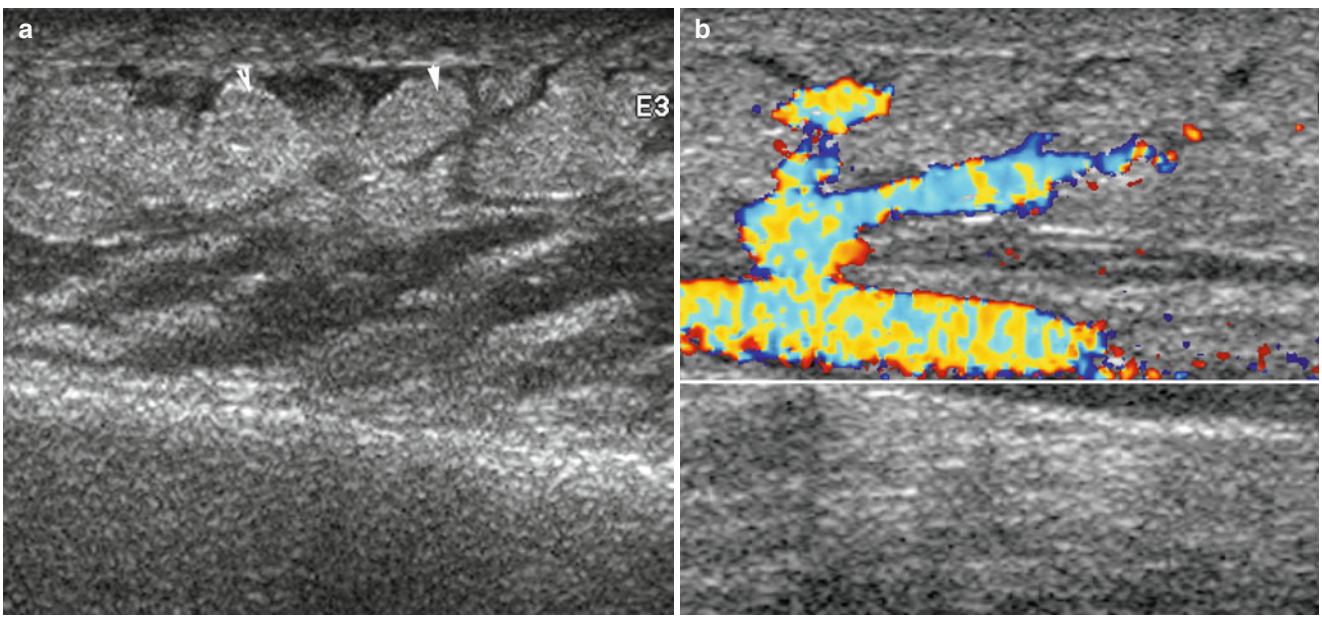

Fig. 12.8 A 58-year-old female patient complaining of bilateral lower leg edema. (**a**) Grey scale ultrasound image showing variable size homogeneous hyperechoic area (*arrowheads*) distributed in the subcutaneous fat layer. (**b**) Color Doppler ultrasound image showing grade 2 hypervascularity. This turned out to be lymphedema

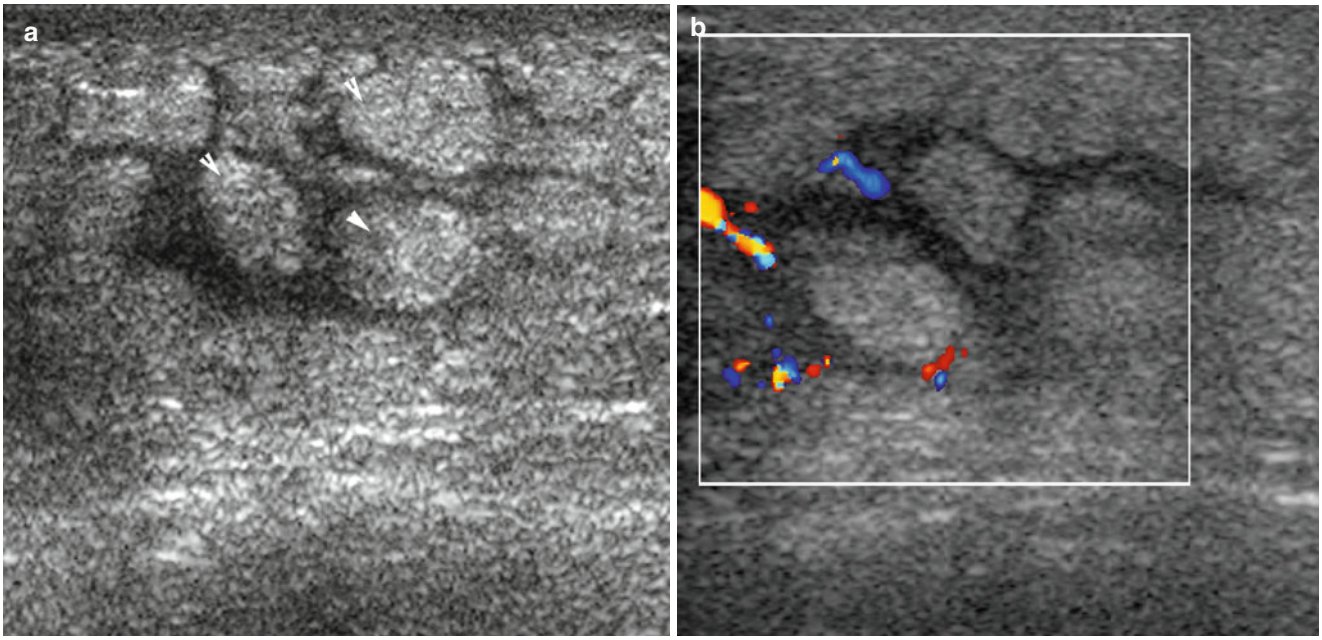

Fig. 12.9 A 57-year-old female patient complaining of palpable mass on left upper quadrant abdominal wall. a Grey scale ultrasound image showing variable size homogeneous hyperechoic nodules (*arrowheads*) distributed in subcutaneous fat layer. (**b**) Color Doppler ultrasound image showing grade 2 hypervascularity. Sono-guided biopsy proved to be inflammatory myofibroblastic tumor

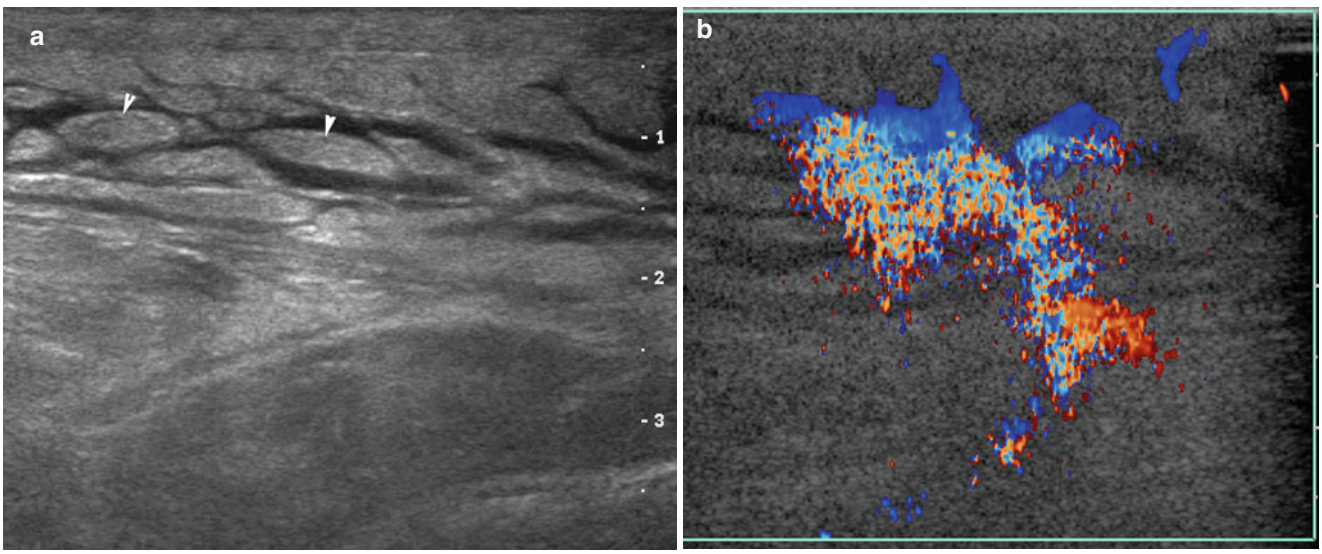

Fig. 12.10 A 40 y/o male patient complaint of painful swelling over left calf. (**a**) Grey scale ultrasonography showing variable size homogeneous hyperechoic nodules (*arrowheads*) distributed in subcutaneous layer. (**b**) Color Doppler ultrasonography showing grade 3 hypervascularity. This turned out to be cellulitis

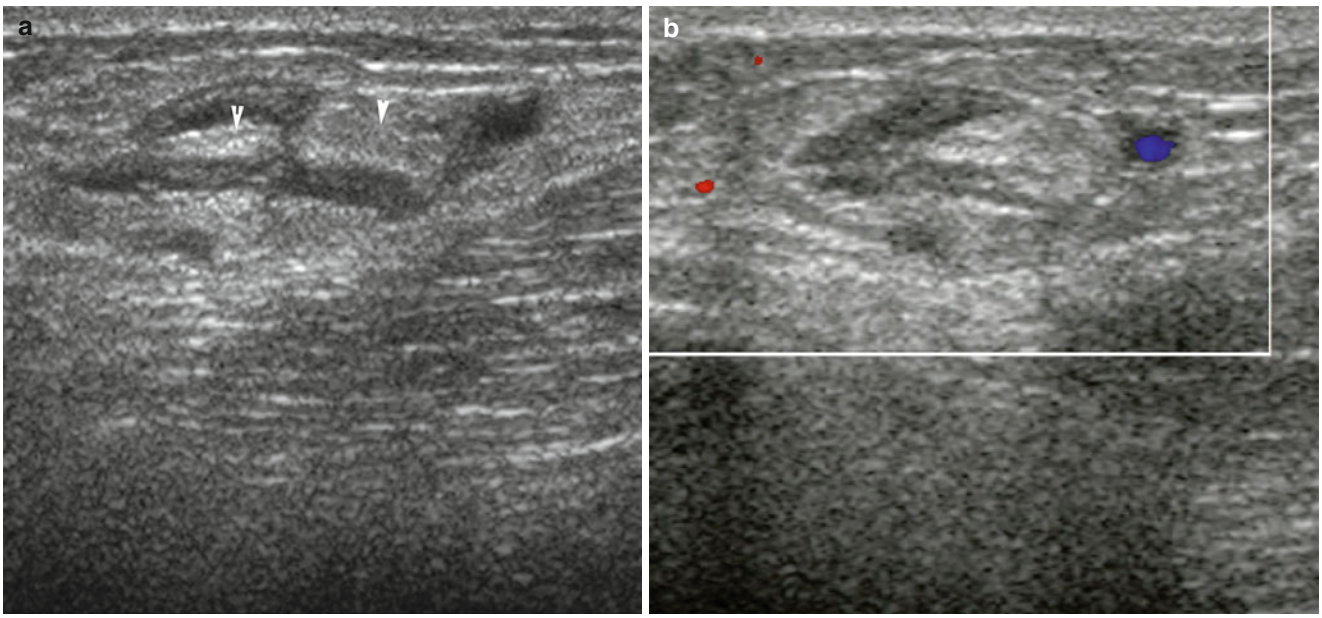

Fig. 12.11 A 27-year-old female patient complaining of painful nodule over RT upper lower leg that gradually enlarged within 2 weeks. (**a**) Grey scale ultrasound image showing heterogeneous echoic nodule (*arrowheads*) with ill-defined margin in RT upper leg subcutaneous layer. (**b**) Color Doppler ultrasound image showing grade 1 vascularity in the lesion. This turned out to be panniculitis

Conclusion

In conclusion, most of the superficial soft-tissue lymphomas were of the nodal or mass type. If the peripheral soft-tissue tumor appears as a nodal-type mass infiltrating the surrounding soft tissue, small nodular disseminated (<1 cm, most <5 mm), or a panniculitis-type lesion without signs of trauma or inflammation, lymphoma should be included in the differential diagnosis. The diagnostic protocol should begin with plain radiography, HRUS, CDUS, and then ultasound-guided biopsy. If malignancy is found, CT or magnetic resonance imaging should be performed for staging before treatment. The prognosis of patients with peripheral soft-tissue lymphoma is usually correlated with the clinical presentation and with tumor morphology, especially in patients with the myositis-type lymphoma and with secondary peripheral soft-tissue lymphoma.

References

1. Coindre JM, Terrier P, Guillou L, et al. Predictive value of grade for metastasis development in the main histologic types of adult soft tissue sarcomas: a study of 1240 patients from the French Federation of Cancer Centers Sarcoma Group. Cancer. 2001;91:1914–26.
2. Cormier JN, Pollock RE. Soft tissue sarcomas. Cancer J Clin. 2004;54:94–109.
3. Komatsuda M, Nagao T, Arimori S. An autopsy case of malignant lymphoma associated with remarkable infiltration in skeletal muscles. Rinsho Ketsueki. 1981;22:891–5 [in Japanese].
4. Ariad S, Hatskelzon L, Benharroch D, Geffen DB. Gluteal manifestation of advanced Hodgkin's disease. Skeletal Radiol. 1997;26:622–5.
5. Beggs I. Primary muscle lymphoma. Clin Radiol. 1997;52:203–12.
6. Cotran RS, Kumar V, Robbins SL. Diseases of white cells, lymph nodes, and spleen: malignant lymphomas. In: Cotran RS, Kumar V, Collins T, Robbins SL, editors. Robbins pathologic basis of disease. 6th ed. New York: WB Saunders Co; 1999. p. 708.
7. Ellstein J, Xeller C, Fromowitz F, Elias JM, Saletan S, Hurst LC. Soft tissue T cell lymphoma of the forearm: a case report. J Hand Surg [Am]. 1984;9:346–50.
8. Hung LK, Cheng JCY, McGuire LJ, Tsao SY. Primary malignant lymphoma of the deep tissues of the hand. J Hand Surg [Am]. 1988;13:683–6.
9. Koh HK, Foss FM, editors. Cutaneous T-Cell lymphoma: hematology/oncology clinics of North America. Philadelphia: WB Saunders Co; 1995.
10. Kumar S, Kingma DW, Weiss WB, Raffeld M, Jaffe ES. Primary cutaneous Hodgkin's disease with evolution to systemic disease: association with the Epstein-barr virus. Am J Surg Pathol. 1996;20:754–9.
11. Lanham GR. Malignant lymphoma: a study of 75 cases presenting in soft tissue. Am J Surg Pathol. 1989;13:1–10.
12. Lee VS, Martinez S, Coleman RE. Primary muscle lymphoma: clinical and imaging findings. Radiology. 1997;203:237–44.
13. Ostrowski ML, Unni KK, Banks PM, et al. Malignant lymphoma of bone. Cancer. 1986;58:2646–55.
14. Salamao DR, Nascimento AG, Lloyd RV, et al. Lymphoma in soft tissue: a clinicopathologic study of 19 cases. Hum Pathol. 1996;27:253–7.
15. Santucci M, Pimpinelli N, Arganini L. Primary cutaneous B-cell lymphoma: a unique type of low-grade lymphoma. Cancer. 1991;67:2311–26.
16. Wang CC, Fleischli DJ. Primary reticulum sarcoma of bone, with emphasis on radiation therapy. Cancer. 1968;22:994–9.
17. Harris NL, Jaffe ES, Stein H, et al. A revised European-American classification of lymphoid neoplasms: a proposal from the International Lymphoma Study Group. Blood. 1994;84:1361–92.
18. Eustace S, Winalski CS, McGowen A, Lan H, Dorfman D. Skeletal muscle lymphoma: observations at MR imaging. Skeletal Radiol. 1996;36:426–7.

19. Freeman C, Berg JW, Cutler SJ. Occurrence and prognosis of extranodal lymphomas. Cancer. 1972;29:252–60.
20. Grem JL, Neville AJ, Smith SC, Gould HR, Love RR, Trump DL. Massive skeletal muscle invasion by lymphoma. Arch Intern Med. 1985;145:1818–20.
21. Jeffery GM, Golding PF, Mead GM. Non-Hodgkin's lymphoma arising in skeletal muscle. Ann Oncol. 1991;2:501–4.
22. Kandel RA, Bedard YC, Pritzker KPH, Luk SC. Lymphoma presenting as an intramuscular small cell malignant tumor. Cancer. 1984;53:1586–9.
23. Scally J, Garrett A. Primary extranodal lymphoma in muscle. Br J Radiol. 1989;62:81.
24. Schwalke MA, Rodil JV, Vezeridis MP. Primary lymphoma arising in skeletal muscle. Eur J Surg Oncol. 1990;16:70–1673.
25. Vose JM, Bierman PJ, Weisenburger DD, Armitage JO. The therapy of non-Hodgkin's lymphomas: introduction and overview. Hematol Oncol Clin North Am. 1991;5:845–52.
26. Giovagnorio F, Galluzzo M, Andreoli C, De CM, David V. Color Doppler sonography in the evaluation of superficial lymphomatous lymph nodes. J Ultrasound Med. 2002;21:403–8.
27. Lee HJ, Im JG, Goo JM, et al. Peripheral T-cell lymphoma: spectrum of imaging findings with clinical and pathologic features. Radiographics. 2003;23:7–28.
28. Chiou HJ, Chou YH, Chiou SY, et al. High-resolution ultrasonography of primary peripheral soft tissue lymphoma. J Ultrasound Med. 2005;24:77–86.
29. Chiou HJ, Chou YH, Chiou SY, et al. HRUS of soft tissue neoplasms: the typical and atypical presentation. J Ultrasound Med. 2005;24:S99.
30. Chiou HJ, Chou YH, Chiou SY, Chen WM, Chen W, Wan HK, et al. Superficial soft tissue lymphoma: sonographic appearance and early survival. Ultrasound Med Biol. 2006;32:1287–97.

Anatomy of the Face for Cosmetic Purposes

13

Robert L. Bard

Contents

13.1 Introduction

Boney landmarks permit identification of overlying superficial structures. For example, the zygomatic arch is the upper limit of the parotid gland, the orbital rims mark the path of the infra- and supraorbital nerves, and the mastoid process reveals the emergence of the facial nerve. Similarly, the foramen imaged as boney notches affords a window to the orbital and mental nerves and arteries that run in the subcutaneous tissues.

The superficial musculoaponeurotic system (SMAS) interconnects the facial and neck musculature and is divided into two parts: the superficial SMAS, with the arterial supply and the deep SMAS, wherein lie most of the nerves. While the veins generally parallel the arteries, great variation occurs.

3D imaging is optimal to focus on the facial danger zones to avoid nerve damage. 2D cross-sectional imaging of the small facial nerves is difficult and C-plane reconstruction will confirm the linear and uninterrupted nature of the original picture.

13.2 Relevant Anatomic Structures and Regions

The following are important anatomical structures and regions for performing cosmetic procedures:

1. *Temporal branch of the facial nerve* located below a line drawn from approximately 0.5 cm below the tragus to 2 cm above the lateral eyebrow and above the zygoma (Fig. 13.1)
2. *Greater auricular nerve* located approximately 6.5 cm below the external auditory canal (Fig. 13.2)
3. *Marginal mandibular branch of the facial nerve* located mid mandible approximately 2 cm posterior to the oral commissure (Fig. 13.3)
4. *Zygomatic and buccal branches of the facial nerve* located in the triangle formed by connecting the dots of the malar

R.L. Bard, MD
Department of Radiology,
New York Medical College,
121 East 60th Street, Suite 6A, New York, NY 10022, USA
e-mail: rbard@cancerscan.com

X. Wortsman, G.B.E. Jemec (eds.), *Dermatologic Ultrasound with Clinical and Histologic Correlations*,
DOI 10.1007/978-1-4614-7184-4_13,

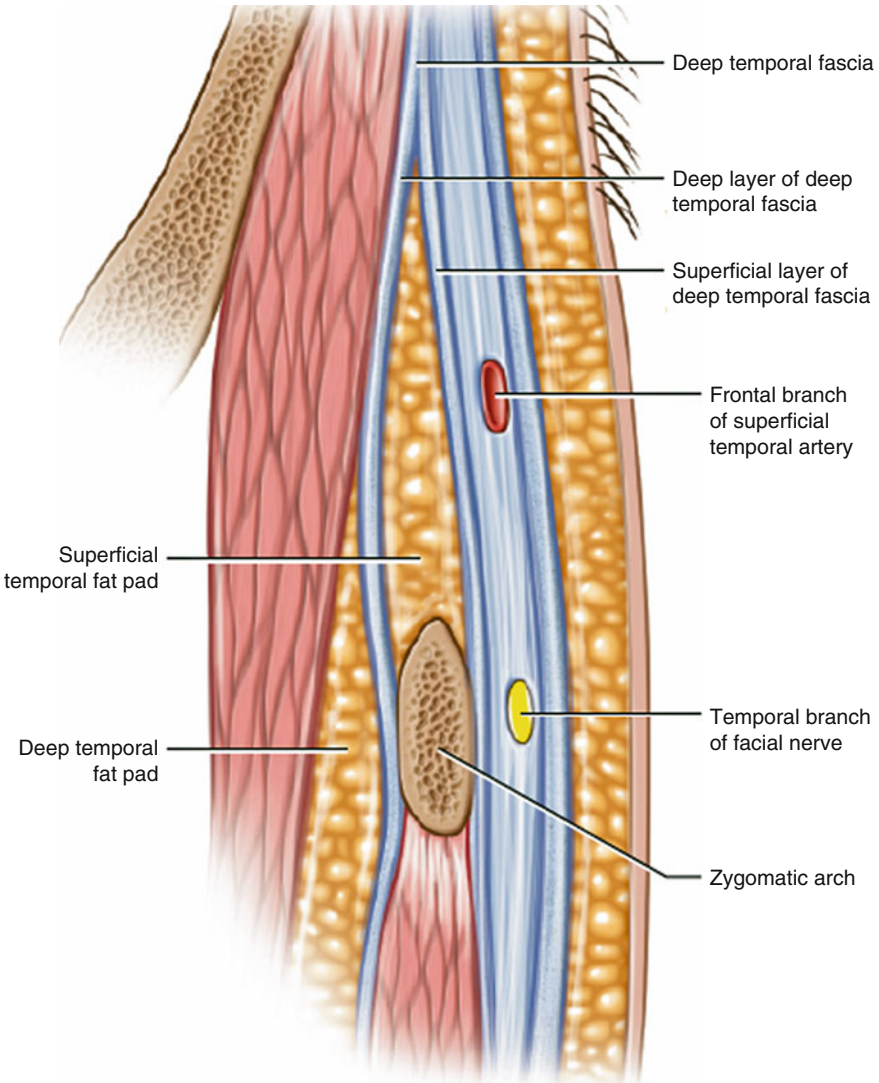

Fig. 13.1 Drawing (sagital axis of the temple and lateral cheek region) shows the location of the temporal branch of the facial nerve, besides other relevant structures

Fig. 13.1 (continued)

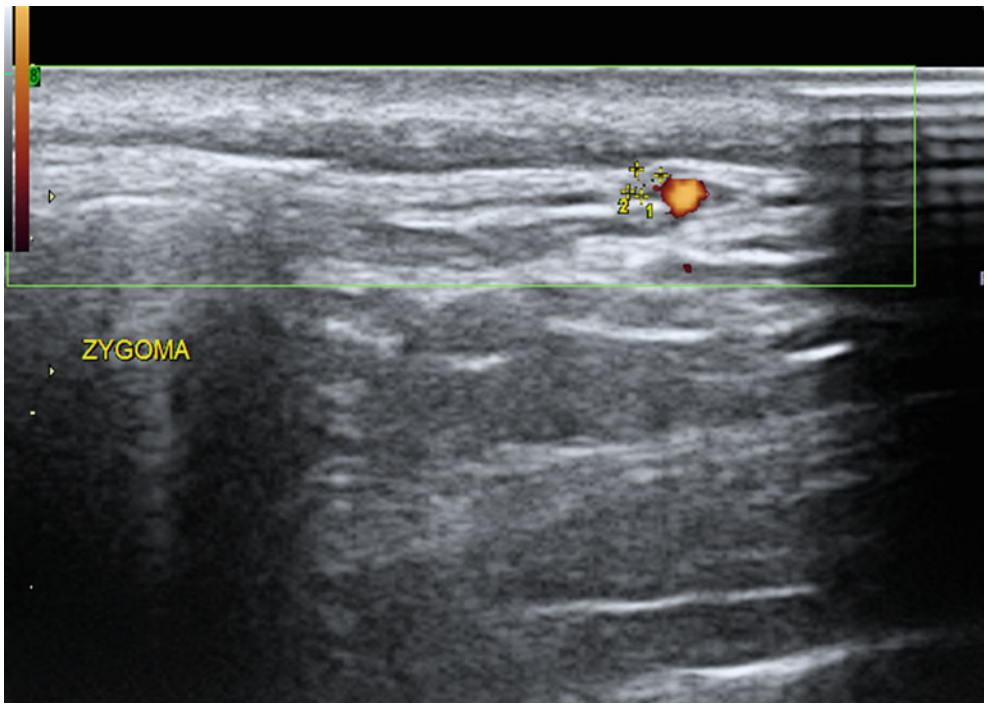

eminence, posterior border of the mandibular angle, and oral commissure (Fig. 13.4)

5. *Supraorbital and supratrochlear nerves* located at the superior orbital rim above the mid pupil (Fig. 13.5)
6. *Infraorbital nerve* located at the inferior orbital rim below the mid pupil (Fig. 13.6)
7. *Mental nerve* located midmandible below the second premolar (Fig. 13.7) [1–3]

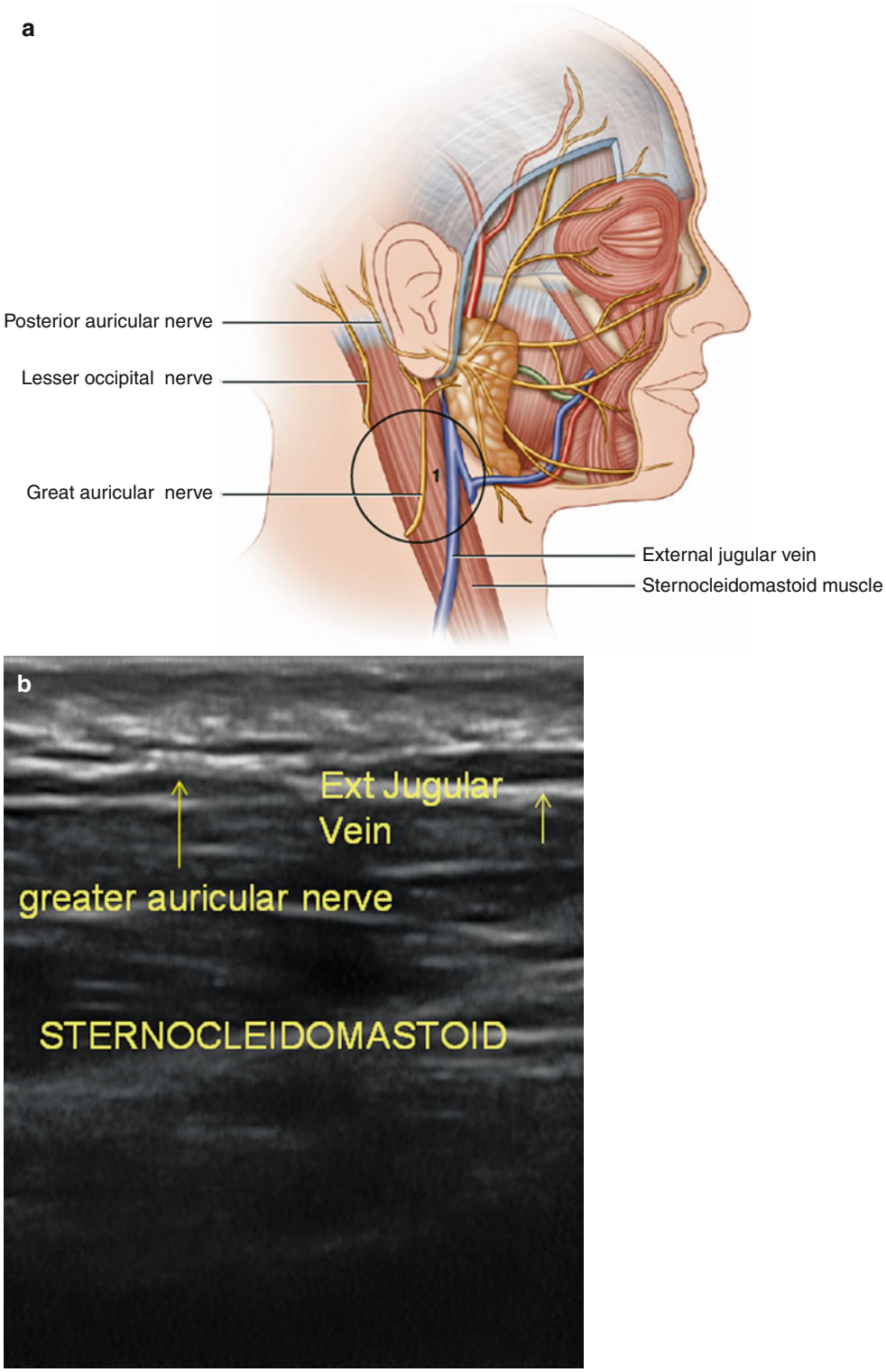

Fig. 13.2 (**a**) drawing, (**b**) ultrasound (longitudinal view) of the greater auricular nerve, located approximately 6.5 cm below the external auditory canal

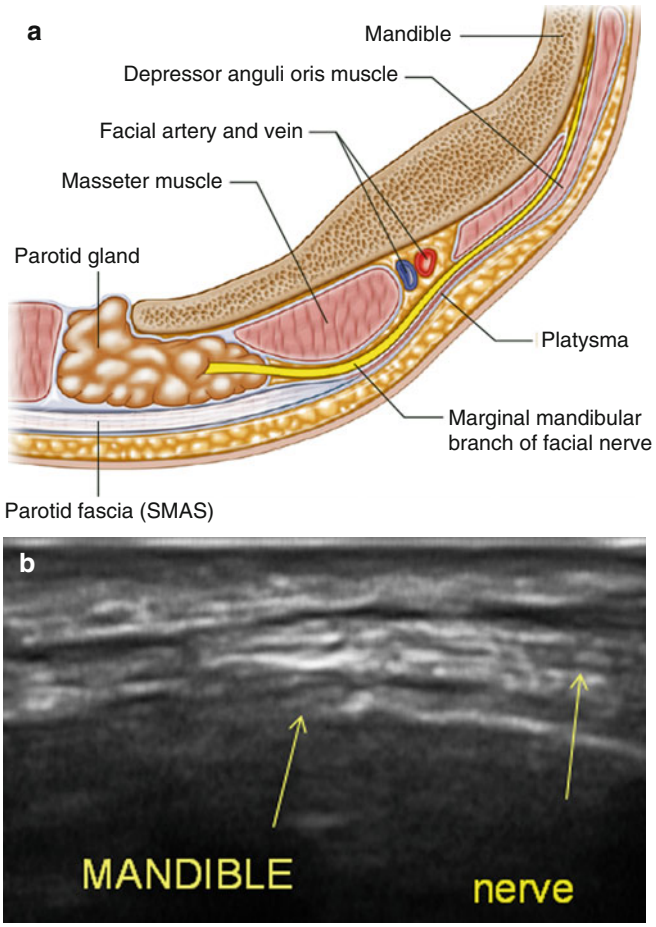

Fig. 13.3 (**a**) Drawing, (**b**) Ultrasound (longitudinal view) of the marginal mandibular branch of the facial nerve located in the mid mandible approximately 2 cm posterior to oral commissure

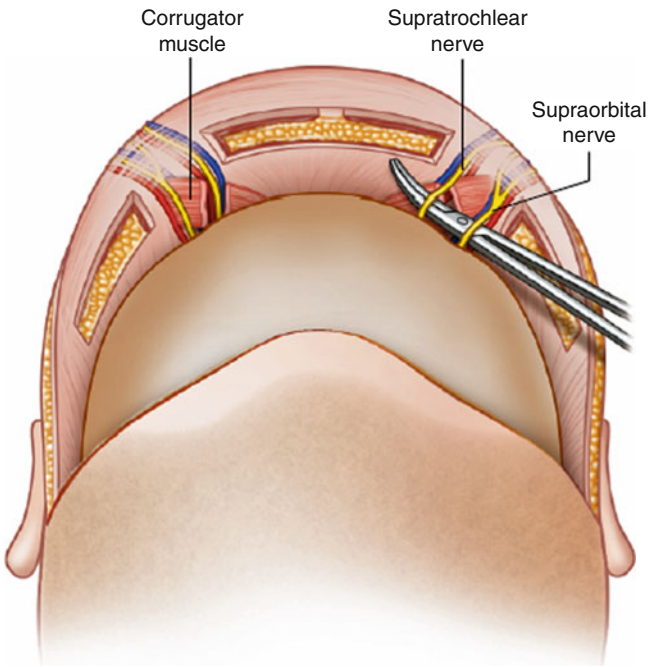

Fig. 13.4 Drawing of the supraorbital and supratrochlear nerves located at the superior orbital rim above mid pupil

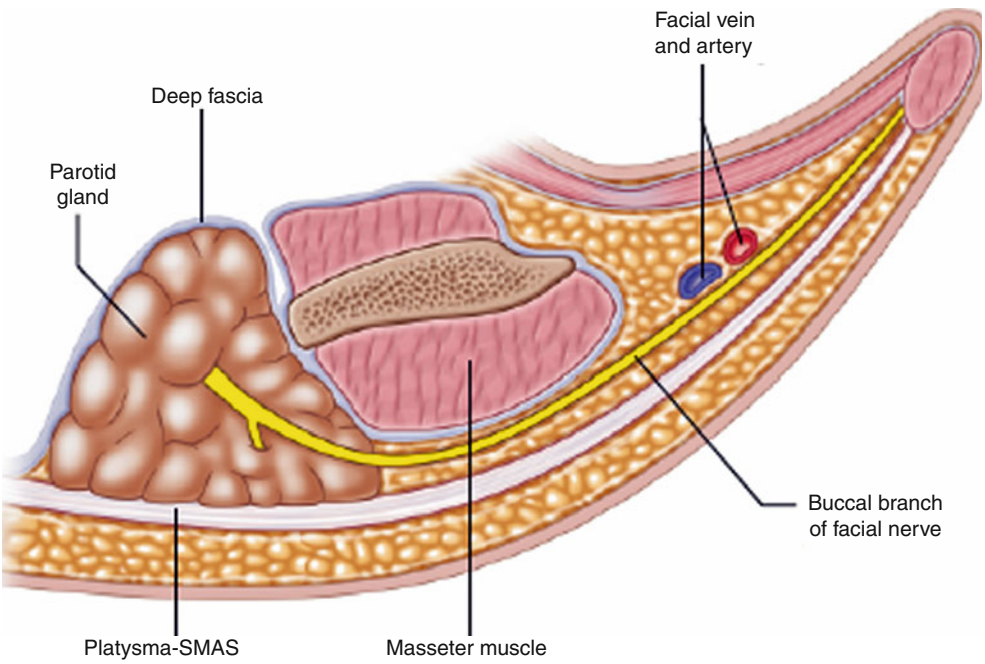

Fig. 13.5 Drawing of the zygomatic and buccal branches of facial nerve located in the triangle formed by connecting the dots of the malar eminence, posterior border of mandibular angle and oral commissure

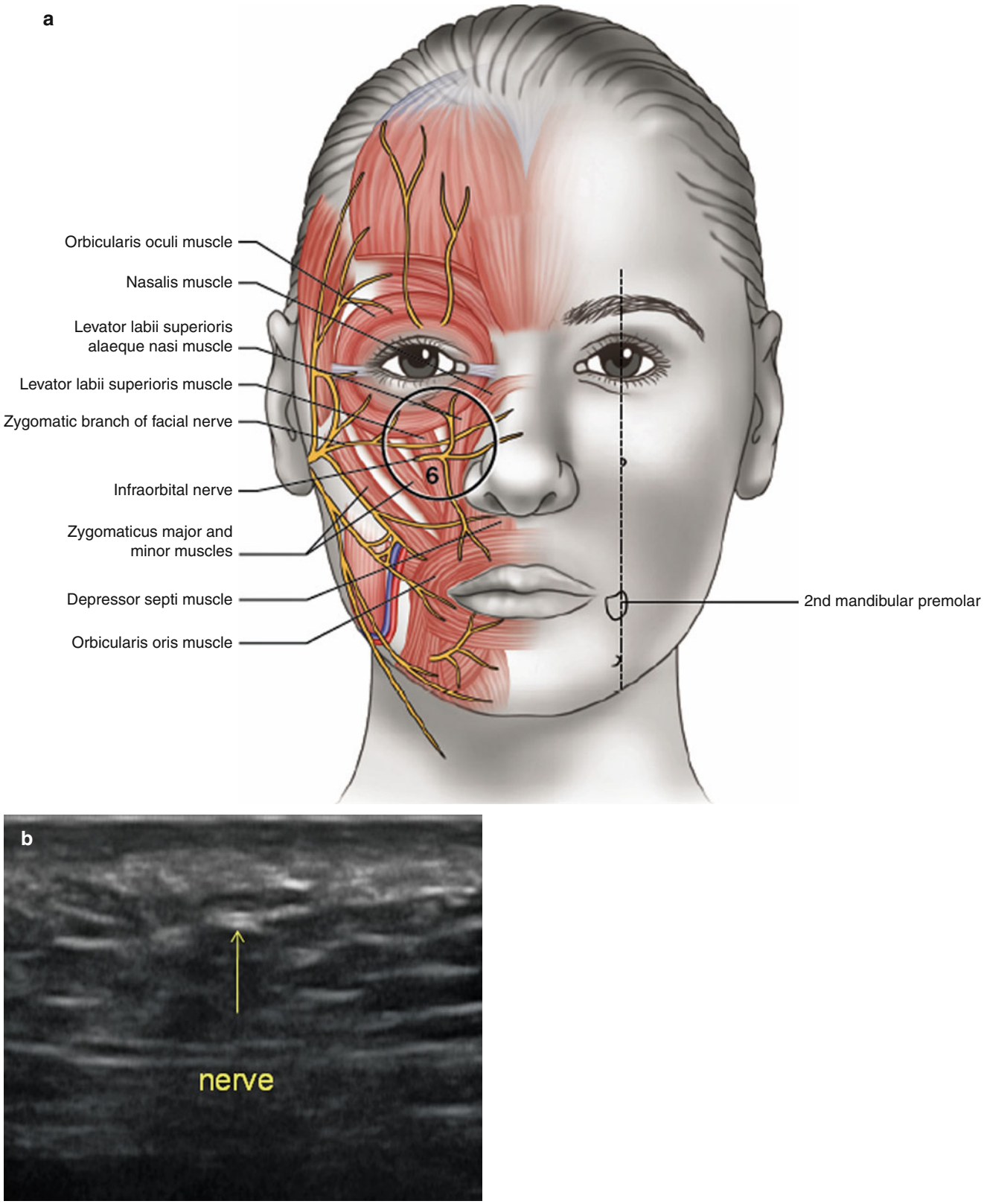

Fig. 13.6 (**a**) drawing (**b**) ultrasound (transverse view) of the infraorbital nerve (*arrow*) located at the inferior orbital rim below the mid pupil

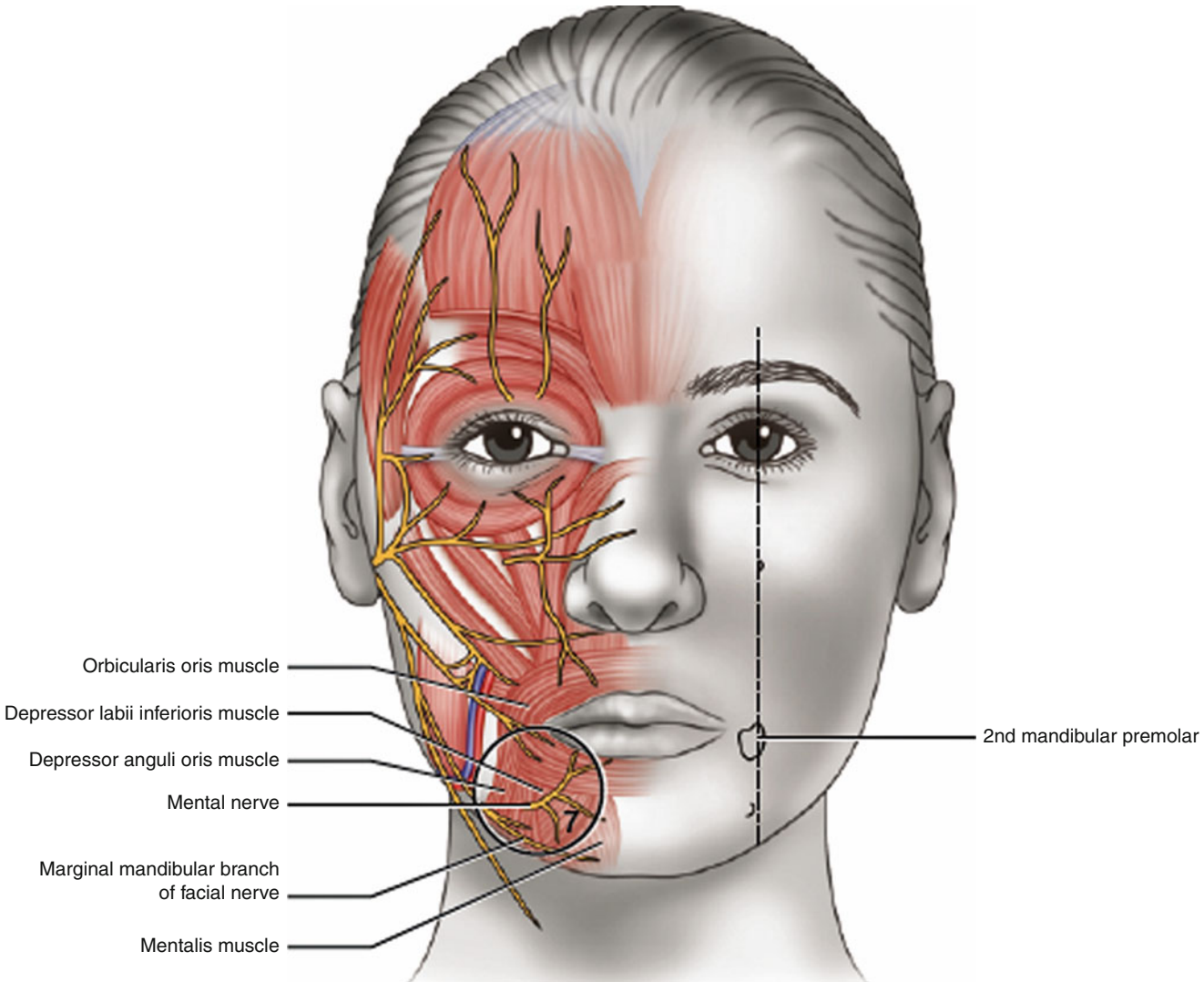

Fig. 13.7 Drawing of the mental nerve located midmandible below the second premolar

References

1. Owsley JQ. SMAS-platysma face lift. Plast Reconstr Surg. 1983;71:573–9.
2. Hamra ST. The tri-plane face lift dissection. Ann Plast Surg. 1984;12:268–81.
3. Rudolph R. Depth of the facial nerve in face lift dissections. Plast Reconstr Surg. 1990;85:537–42.

Concepts in Cosmetic Procedures

14

Robert L. Bard

Contents

14.1 Introduction

Cosmetic procedures, both surgical and nonsurgical, have entered the mainstream in the fast increasing quest of a youthful and healthy appearance. Nearly ten million procedures were performed in 2009 according to the American Society for Aesthetic Plastic Surgery, an increase of 147 % since the tracking first began in 1997. At that time there were approximately 1.5 million surgical procedures and 8.5 million non-surgical procedures [1]. Until recently, surgical procedures were generally a messy affair with swelling, bruising, drains, and other discomforts. To make matters worse, the affects of operations took weeks to heal, forcing many patients into temporary hiding. Despite dramatic advances, the concern regarding healing without lingering scars remains paramount in the minds of patients and their physicians. Even in non-surgical procedures, inflammation and scarring are a common cause of anxiety and discomfort. Recent scientific advances culminated in a new strategy for faster

R.L. Bard, MD
Department of Radiology,
New York Medical College,
121 East 60th Street, Suite 6A, New York, NY 10022, USA
e-mail: rbard@cancerscan.com

X. Wortsman, G.B.E. Jemec (eds.), *Dermatologic Ultrasound with Clinical and Histologic Correlations*,
DOI 10.1007/978-1-4614-7184-4_14, © Springer Science+Business Media New York 2013

healing and minimal scarring [2]. This approach combines internal and external interventions and ideally it is initiated prior to the procedure and continues during the healing period and beyond [3]. We will examine this holistic, science-based, and safe strategy.

14.2 Background Information

14.2.1 Risks of Cosmetic Surgery

Although no surgery is risk free, in the hands of an experienced surgeon, complications are rare and mostly correctable. These complications include bleeding and hematoma, infection, seroma (fluid collection), suture reactions, skin reactions, wound separation, necrosis (ischemia and tissue death), nerve damage, and scarring. Although all these risks are important and some (such as infections, necrosis, and nerve damage) are more serious than others, the most common by far, even in the hands of the most experienced surgeon, is scarring. All other complications contribute to increased scarring [4].

14.2.2 Wound Healing and Scarring

Surgery and other cosmetic procedures create trauma or injury to the skin. The proper healing of the resulting wound is critical to the final appearance and the degree of scarring. Wound healing proceeds through three phases:

- The inflammatory phase begins immediately after the operation. During this phase, bleeding stops, white blood cells fight bacterial infection, and collagen formation begins.
- The proliferative phase lasts several weeks. Collagen continues to be produced and new capillaries are formed to aid in healing.
- The remodeling or maturation phase, which continues for a period from several weeks to several years. There is more collagen produced to strengthen the wounds, and then excess collagen is removed to form a thin, flat, white scar.

14.2.3 Inflammation, Nutritional Status, and Immune System: Critical Factors in Wound Healing and Scarring

It is well known that smoking, poor nutritional status, and a weak immune system contribute directly or indirectly to poor wound healing. The emerging science, however, points to the direct and critical role of inflammation. Control of inflammation, which is closely interrelated to the nutritional status and the immune system, is the cornerstone of the strategy for accelerated wound healing and minimized scarring [5].

14.3 The Mechanisms at the Molecular and Cellular Levels

14.3.1 Free Radicals

Free radicals are the major causes of inflammation. Surgery, laser treatment, and many cosmetic treatments increase the production of free radicals–extremely reactive and harmful molecules. The half-life of one of the most damaging is one billionth of a second. This means that it will attack the first molecule in its path–fat, protein, DNA, sugar. Free radicals damage collagen, proteins, and lipids, which are key components in wound healing. Excess production of free radicals causes oxidative stress, a condition that weakens the immune system, accelerates aging, and increases the risk of chronic diseases.

14.3.2 The Critical Role of Nitric Oxide in Healing and Inflammation

Since its discovery 20 years ago, which resulted in the award of the Nobel Prize, nitric oxide has been shown to play an important role in wound healing. Nitric oxide affects diverse mechanisms involving inflammation, angiogenesis, and cell proliferation. Defined cytokine cascades control these processes; in many cases, nitric oxide appears to modulate these cytokines, especially those associated with inflammation. In addition, nitric oxide is an important component of the immune system in fighting infection.

While extremely useful at normal and modestly elevated amounts, excess production of nitric oxide can have devastating effects. For example, uncontrollable production of nitric oxide during infection causes sepsis, a potentially fatal condition. In less severe conditions, excess amounts of nitric oxide lead to increased production of nitrogen radicals, which accentuate inflammation and further production of nitric oxide and free radicals. Thus, control of inflammation and oxidative stress (from excess production of free radicals and especially nitrogen radicals) is key to accelerated wound healing and minimized scarring [6].

14.3.3 Controlling Production of Free Radicals and Inflammation

Reducing production of free radicals is essential for controlling inflammation. To achieve this objective, it is important to choose science-based compounds that combine antioxidant and anti-inflammatory properties. In addition, use of strong, natural anti-inflammatory compounds that act synergistically or complement the function of antioxidants enable effective management of inflammation.

14.3.4 The Special Role of Gamma Tocopherol and Tocotrienols

Gamma tocopherol and tocotrienols are key novel components in this strategy. These compounds are members of the vitamin E family.

14.4 Vitamin E

Most vitamins consist of a single compound, whether natural or synthetic makes little difference. Not so for vitamin E. Eight compounds, four tocopherols, and four tocotrienols make up the vitamin E family. Our food contains all eight and is particularly rich in gamma tocopherol.

- Gamma tocopherol, along with its metabolite produced in the body, is an effective quencher of nitrogen radicals and is anti-inflammatory.
- Research by the Armed Forces Radiobiology Research Institute has shown that tocotrienols, and particularly gamma and delta, provide powerful protection against radiation damage. Alpha tocotrienol is currently being evaluated in a clinical study for its wound healing properties. Tocotrienols accumulate preferentially in the skin.

Most vitamin E supplements contain only alpha tocopherol because it was thought that only that one was important [7]. Even worse, most vitamin E skin products contain a small amount of synthetic dl-alpha-tocopheryl acetate, which means that they contain only one of the eight members of the vitamin E family in the less-effective synthetic form. They do not contain gamma tocopherol and tocotrienols. In addition, its active group is blocked and cannot fight the free radicals on the surface of the skin. Even after penetration of the skin, only a very small amount becomes active [8]. It is for that reason that the role of vitamin E in wound healing and scarring has been controversial. Only products that supply the complete vitamin E family and are particularly rich in gamma tocopherol and tocotrienols in their natural unesterified form contribute to accelerated wound healing and minimized scarring [9–13].

14.5 Other Natural Compounds with Special Wound Healing and Anti-Scarring Properties

14.5.1 Antioxidants

The powerful antioxidant potential of tocopherols and tocotrienols described above can be strengthened by the synergistic antioxidant activity of other components such as carotenoids, vitamin A, and natural antioxidants in aloe vera [14–18].

14.5.2 Chondroitin Sulfate

Chondroitin sulfate stimulates collagen formation, cell proliferation, cell migration, and cell adhesion that accelerate wound healing [19, 20].

14.5.3 Beta-Glucans

Beta-glucans, an immunomodulator, stimulates fibroblast collagen biosynthesis.

14.5.4 Aloe Vera

Aloe vera supports wound healing through its moisturizing, anti-inflammatory, antimicrobial ,and other properties.

14.5.5 Zinc Oxide

Zinc oxide stimulates re-epithelialization and reduces inflammation and bacterial growth [21].

14.5.6 Vitamins A and D_3

Vitamin A and its natural metabolites affect epithelial cell proliferation and differentiation, immune modulation, and angiogenesis, and are used to treat acne, photoaging, and biologic skin aging.

Vitamin D_3 modulates the peptides kallikrein and cathelicidin that have antibiotic and immunomodulator properties including rosacea and psoriasis.

14.5.7 Wasabi

Wasabi is a derivative from the horseradish plant (wasabia japonica) and is useful as an adjuvant to the other antioxidants because it improves liver detoxification processes and promotes positive immunologic responses. A secondary function is to balance estrogen, progesterone, and testosterone metabolism.

14.6 The Major Applications

Research and clinical evidence on the function of its major components support the potential benefits of a topical product combining the above ingredients and formulation properties. Specifically, it can be used to help accelerate wound

healing therapies while minimizing scarring. Examples include:

- Wounds caused by minor burns including burns from exposure to ultraviolet radiation (sunlight).
- Skin ulcers often associated with chronic disease such as diabetes.
- Sores including those caused by viruses, microbes, fungi, and disease conditions such as dermatitis. It includes pressure sores (also known as bedsores, pressure ulcers, and decubitus ulcers) that are caused by poor blood supply to the skin and the tissues as a result of lying or sitting in one position for long periods of time.
- Skin damage caused by physiological conditions such as pregnancy (stretch marks) and exposure of the skin to pollutants, chemicals, and radiation.

Because of its anti-inflammatory properties, a topical product combining the above ingredients and formulation properties can be used as:

1. Adjunct treatment to reduce inflammation in major skin conditions that include eczema, acne, psoriasis, rosacea, and contact dermatitis.
2. Protection of the skin from the damaging effects of radiation thus reducing photoaging which is a major cause of the aging of the skin.

14.7 The Holistic Strategy

Localized wound healing and scarring is directly impacted by the overall antioxidant, immune, inflammatory, emotional, and wellness status. Many skin conditions reflect nutritional and metabolic imbalances and systemic disease conditions. The skin, like all tissues and organs in our body, gets nourishment from our diet through the bloodstream. The holistic approach integrates inner treatment and health with external skin treatment to achieve effective management of inflammation and antioxidant status resulting in accelerated wound healing and minimized scarring.

1. Lifestyle, which includes avoidance of smoking, excessive alcohol consumption, and long exposure to the sun (or use of appropriate protection), exercise, weight control, relaxation, stress management, and emotional health).
2. Diet, which includes plenty of water and is rich in fruits and vegetables, fiber, and antioxidants.
3. Supplements that include:
   - Vitamin E as natural tocopherols plus tocotrienols, unesterified.
   - Omega-3 fatty acids
   - Resveratrol (grape seed extract)

14.8 Medical Management of Scars

Advances in treatment are made possible by the application of immune response modifiers, immune modulators, antimetabolites, calcium channel blockade, and anti-oxidants such as vitamin E and onion extracts.

The immune response modifiers are: interferon, imiquimod, and hu-TGFbeta3. There is a low keloid recurrence rate after a keloid excision site is treated with imiquimod 5 % cream. Apoptosis (cell death) is enhanced with this modality. In double blind studies on dysplastic nevi (Berman B. AAD 2/04), imiquimod 5 % cream used to avoid post-surgical scarring produced no wound dehiscence or infection, it did however, produce an erythematous response one third greater than the vehicle cream treated control sites.

Immune modulators to treat scars include tumor necrosis factor (TNF)-alpha inhibitors (etanercept and tacrolimus) that decrease the local pro-inflammatory and profibrotic activity of TNF-alpha within keloids with intra-lesional injection have been mildly therapeutic.

Antimetabolites such as 5-FU (5-fluorouracil) showed a 47 % recurrence at 1 year in patients who responded to initial treatment.

Calcium channel blockers such as verapamil have shown promise in keeping keloids and hypertrophic scars from enlarging in width or growing in height.

Naturopathic products, such as vitamin E and onion extract, have been studied on burn patients and on new surgical scars with limited improvement in scar cosmesis and symptomatology compared with petrolatum based ointments. It must be noted that the vitamin E used in these studies was not separated into tocotrienol and tocopherol categories. In fact, the failure of partitioning the vitamin E has resulted in false claims in a large study that it made prostate cancers worse. This is in contrast to the effective subdivided use of vitamin E in Europe, which has proved clinically useful in many cancer treatments.

14.9 Adjuvant Supplement Protocols

Before analyzing treatment protocols, it must be understood that many dermal applications have their origins from other areas. For example, the popular treatment for skin tightening using collagen stimulation was initially used to treat prostate cancer. With this in mind, the dots need to be connected from the proven uses to the probable applications on the skin and the subcutaneous tissues. Another caveat is the type of technology utilized.

Specifically, vitamin E has been used widely and successfully in Europe to control inflammation and suppress cancer growth. The massive multicenter study on prostate cancer deduced the opposite effect–that vitamin E made prostate cancer worse. How to explain this contradiction? It appears that the effective substances must be taken at different times to be helpful, because when combined, the ingredients cancel the beneficial properties.

Resveratrol, from grape seed extract (GSE), has been shown to be an effective dietary supplement with chemoprevention properties in the breast, colon, prostate, and skin cancers (specifically squamous cell carcinoma). A study presented in the June 2011 issue of the *Journal of the*

American Academy of Dermatology noted a significant reduction in this type of dermatologic tumor in patients using the GSE formulation. The article cautioned its use because of potential side effects such as headache, hives, nausea, and dizziness.

Anecdotal reports of rose petal-based antioxidants as a successful chemopreventive agent have led to the formal study of this safe extract (absent allergy to the rose flower) that has the property to rehydrate the skin and increase collagen while taken orally in a tincture preparation.

14.10 Doppler Ultrasound Application for Improving Cosmetic Therapy

Doppler sonar, created in 1972, gives a picture of flow movement in the human body in the same way it shows motion in the weather patterns (Doppler radar) that can be seen on television weather reports. Doppler technology has been around for years.

Radiologists in Japan, England, the Netherlands, Belgium, and France, seeing the success of sonography in diagnosing malignant tumors in the breast, turned their attention to the study of the prostate, thyroid, and skin. They concluded that the vascular pattern shown using the Doppler technique held the key to the degree of malignancy. In 2002, German surgeons at the University of Ulm, the largest bone tumor center in Europe, proved that bone cancers that were highly malignant had high blood flows. The current clinical use of Doppler equipment in Europe is keeping patients from unnecessarily losing their arms and legs to surgery. Historically, the standard treatment for bone cancer has been amputation of the entire limb, but current surgical intervention has become more conservative, often removing a limited portion of the bone so that the tumor can be removed with a rim of normal bone without the need for an amputation. However, by distinguishing cancer aggressiveness, Doppler techniques have refined this even more because bone tumors that demonstrate no vascularity or low blood flows are now monitored or treated more conservatively [22–25].

14.11 Factors That Can Influence Repair

14.11.1 Inflammation

While only a relatively small percent of chronic inflammation is caused by bacterial infection, increasing evidence indicates a link to an imbalance in sex steroid hormones in all chronic diseases. Elevated levels of inflammatory cytokine interleukin (IL)-8 is a second and critical inflammation factor. IL-8 promotes stromal and epithelial cell proliferation and has been shown to have a pervasive role in promoting tumor cell survival and proliferation for all cancers [26].

14.11.2 Cell Membrane Elasticity

There is substantial evidence that disruption in the cell membrane's elasticity for increasing rigidity is a precursor for the development of cancer cells. It is also a factor in insulin resistance. On one hand, there is evidence that suggests that rigidity leads to focal adhesions and aberrant growth (cancer) by increasing tension in the cell that is normally generated by elevated Rho (Guanosine triphosphate (GTP)-binding protein family). On the other hand, ultrasound units that can read the elasticity of cell membranes are now being shown to accurately be able to detect cancer and fibrosis. The primary dietary reason for alteration to a cell's elasticity and fluidity is an imbalance between beta-sitosterol (β-Sit) and cholesterol in the cell membrane [27].

14.11.3 Membrane Permeability and Intra-Cellular Environment

There are many cell functions dependent on normal cell membrane permeability. Of interest here is an alteration in the isoprenoid pathway, the alteration of the balance of calcium and magnesium with excessive entry of Ca2+ and the release of calcium stores, which is a critical factor in cancer metastasis, that can be triggered when this imbalance is accompanied by critically low co-enzyme Q10 levels in the immediate intracellular fluids.

The same nutritional protocol described here that addresses the above issues also increases cell apoptosis, reduces proliferation, reduces excess estrogen production, supports and restores normal cell reproduction and differentiation, and reestablishes several mechanisms of homeostasis, especially for copper homeostasis. In other words, the β-Sit/AOX matrix provides the nutritional substructure missing from the current food supply for the body's normal, dynamic, anticancer functions and when balanced properly, accomplishes this at physiological levels [28].

It can be concluded from this literature, especially when it is looked at in a broader context, is that it is not just the diet, but the nutritional composition of the food consumed in that diet, that makes a critical difference, and that β-Sit is essential for health in general, and our body's anti-cancer mechanisms in particular.

Another way to look at it is to look at the effects of high levels of dietary and circulating β-Sit. A partial list of the effects produced with high levels of β-Sit includes: normalizing cholesterol, a reduction in insulin resistance, support for normal weight control and fat metabolism, a reduction in asthma incidents, acting as an anti-inflammatory and an immune modulator, a reduction in cardiovascular disease and arteriolosclerosis, and reduced rates of lung, prostate, and other cancers and chronic inflammatory disorders [29].

14.11.4 Natural Synergism and Potentiation

A possible explanation for the wide ranging effects of adequate dietary β-Sit, which can be measured by blood levels, is that it acts in synergy with other substances and also acts as a catalyst that potentiates antioxidant activity, as well as other antioxidant responses, especially for herb-based antioxidants that in turn potentiate the efficacy of vitamin D_3 [30]. It also is involved in a variety of processes throughout the body, from cell membrane structure to regulation of estrogen and Dihydrotestosterone (DHT) production, elimination of excess estrogens, apoptosis, and immune regulation among others.

14.11.5 The Ideal Phytosterol Composition

Based on the available literature and clinical observations, the ideal balance of phytosterols is comprised of β-Sit greater than 62 %; campesterol less than 25 %; stigmasterol less than 10 %; and brassticasterol less than 3 %. The following is a brief summary of the evidence for this composition.

(Note: most phytosterol supplements contain a maximum of 43 % β-Sit because it is derived from currently available soy. The problem with using it as a supplement is that merely provides the same balance found in the food supplies that are associated with higher rates of cancer, cardiovascular disease, obesity, and type II diabetes. Both population studies and clinical observation show that the balance of the sterols, from supplement and diet, is more important than the absolute amount. Therefore, higher supplemental amounts of properly balanced phytosterols are needed to offset the low β-Sit content and ratio from the food supply.)

14.11.5.1 Phytosterols Require Complementary Antioxidants

Two of the overlooked aspects of increasing dietary β-Sit are that it both stimulates the sphingomyelin cycle through increased Reactive Oxygen Specified (ROS) activity, increasing proliferation as demonstrated in prostate cancer cells; and high levels of both cholesterol and β-Sit can cause lipid peroxidation. For these reasons, β-Sit needs to always be administered in a composition that includes complementary antioxidants, countering the ROS activity and supporting its action in the cell membrane and intracellular environment. Regarding the effects on cancer, the practical effects of inadequate or incompatible antioxidants with β-Sit would be a leveling off at a balance between increased apoptosis and increased proliferation [31].

14.11.6 The β-Sit/AOX Matrix

The β-Sit/AOX Matrix interaction is complex, requiring multi-supplement support. In some ways the relationship is as symbiotic as it is synergistic. For example: β-Sit potentiates antioxidant activity and activates other antioxidant responses. β-Sit and plant-based antioxidants work together to protect cell membranes from lipid peroxidation. In addition, targeted antioxidants support activities of β-Sit (i.e., astragalus root and β-Sit work together to increase the activities of antioxidant enzymes, including Superoxide dismutase (SOD) and Glutathione peroxidase (GSH-Px).

A natural pairing of β-Sit and select antioxidants, forming a supportive nutritional matrix, is fundamental to a wide range of biological processes, therefore the components of the matrix need to be selected to fit the desired outcome. In this case, the matrix is comprised of β-Sit and antioxidants that work with it to improve membrane integrity and function, reestablish a healthy intracellular fluid environment, as well as support healthy cell reproduction and the body's mechanisms for controlling improperly reproduced cells–cancer cells.

A select group of antioxidants that form the β-Sit/AOX matrix for natural anti-cancer support are: astragalus, ellagic acid, gynostemma pentaphylum, ligustrum fruit, lutein, lycopene, quercetin, resveratrol, rhiodola, rosemary officinalis, schansandra fruit, trans-e-viniferin, wasabia japonica, and zinc.

14.11.7 Synergy Within the Matrix

Just like the components that make up foods, the matrix needs to be comprised of nutrients that work together to be efficient, for example:

- Quercetin+Resveratrol work together to naturally reduce Nitric oxide synthase (iNOS) gene expression and nitric oxide production, providing cardiovascular support and other benefits.
- Resveratrol+Ellagic Acid aid the structural ability of the cell to repair efficiently.
- Ellagic Acid+Quercetin synergistically support normal reproduction rates and proper apoptosis when balanced at dietary level concentrations.
- β-Sit+Resveratrol combine to provide a balanced ROS 1 level, and synergistically inhibit inappropriate cell growth. In addition, the systemic presence of β-Sit enhances resveratrol activity.

14.11.8 Coenzyme Q10 and the β-Sit/AOX Matrix

There are a number of key reasons why Coenzyme Q10 (CoQ10) should always be included in the matrix. First, it is essential for proper cell reproduction. Second, it has been shown that when the circumstances for metastases are set up, the process is not triggered if there is adequate CoQ10 present. CoQ10 has been demonstrated to reduce IL-8 to normal levels. As noted above, IL-8 is the primary inflationary

mechanism that drives the formation and survival of tumor cells for all cancers. Reducing IL-8 also works with the other components of the matrix to reduce angiogenesis. The efficiency of CoQ10 function in the cell membrane and overall cell function are restored in cancer cells through the reestablishment of membrane elasticity and permeability with β-Sit.

An ideal CoQ10 is highly absorbable and 100 % of what is supplemented needs to be available for absorption. The circulating Q10 needs to be readily able to cycle from the ubiquinone to ubiquinol forms, and be orthomolecular in nature, allowing it to be cellularly bioavailable. Preferably, the Q10 used should have a long clinical track record and have research-demonstrated efficacy. Recommended dose range is from 300 to 800 mg/day.

The above information forms the basis for the nutritional support we use. As appropriate for each individual, a more complete program is developed including: vitamin D3 to bring the D3 levels to a range of 65–90 ng/ml; mixed tocopherols with high gamma-tocopherol (taken in the morning) and 125–500 mg of a high-delta-tocotrienol supplement taken in the evening; a balanced calcium and magnesium supplement; vitamin K2; vitamin B bomplex; and 5 g of vitamin C.

The results shown here illustrate both the efficacy of restoring fundamental nutritional support that has been systematically removed from our diets by alterations in the food supply, and the need for a means to monitor each individual's response to treatment on a regular basis. Given the number of factors involved in nutritional support, this is the only way to know that an individual's body is capable of restoring its anti-cancer functions and anti-aging capabilities.

14.12 Thermal Ultrasound-Guided Treatments

14.12.1 Lasers

CO_2 and erbium skin resurfacing has been the gold standard for cosmetic surgeons. However, the pain and downtime has caused a demand for less invasive procedures. Fractional ablative skin resurfacing treats a small area of skin and leaves undamaged dermal tissues intact to act as a reservoir for rapid healing. The fractionally delivered energy into the skin creates clean channels of ablated tissue in the dermis that causes the injured collagen to plump the skin from the inside out because of the wound healing effect of fibroblast activity that stimulates new collagen production and rejuvenates the collagen matrix. Clinically, this improves skin tone and texture, wrinkles, acne scars and pigmentation. Epidermal pigmented lesions such as freckles and age spots can be treated with varying energies and wavelengths as clinically indicated. Pain control is improved by patient cooling with a skin cold air delivery system.

14.12.2 Photodynamic Therapy

Photodynamic therapy (PDT) involves the application of a chemical that is absorbed by cells with high metabolic activity. On exposure to light of appropriate wavelengths, a chemical reaction takes place releasing an oxygen free radical that is cytotoxic to the absorbed cells. Recent updates in photosynthesizer technology that accumulates preferentially in abnormal tissues have made this a viable modality in cancer treatments because the patient can resume normal exposure to light after 6 h. It is approved for the skin for treatment of actinic keratosis and uses the topical photosensitizers 5-aminolevulinic acid or methylaminolevulinate. Light sources include a variety of lasers, intense pulsed light sources, or 410 nm blue light. Side effects include erythema, pain, swelling, and peeling. Other uses of PDT include treatment of acne, non-melanoma skin cancer, and photorejuvenation. Photodamaged treated skin may show reduced fine lines, lentigines, and redness with improved texture resulting from collagen remodeling after 1 month.

14.13 Microfocused Ultrasound

The success of high intensity focused ultrasound cancer treatments has led to its targeted use in the cosmetic arena. This is technically a non-invasive procedure.

The beams of sound converge subcutaneously to damage the tissues, first on a deep level, and on a second pass, the superficial level. This spacing is important because ablated tissues degrade sound transmission. Collagen remodeling occurs as with other thermal treatments.

14.14 Radiofrequency

Electromagnetic energy applied to the face generates heat as a result of tissue resistance. Energy is delivered in various frequencies from 300 MHz to 3 kHz.

Different electrode configurations (mono-polar, bi-polar, or uni-polar) are used to treat the neck and facial areas. Radiofrequency is sometimes combined with other cosmetic modalities to improve collagen growth.

14.15 Cryolipolisis

Fat cells injured by freezing diminish in number. Cryolipolisis freezes an area of skin and subcutaneous fatty tissue over the period of 1 h. The effect of volume reduction occurs over a 4 month period. Because cold is, by itself, an anesthetic, the procedure is minimally uncomfortable. Ultrasonically, the ultrasound transmission decreases as the freezing occurs. Fifteen minutes after therapy stops, the through transmission in the tissues approaches normal. Analysis of the dermis will

show thickening that resolves as the edema subsides over several hours. There is a possibility of customizing this technology, which now takes 1 h per treated area, using the through-transmission pattern.

Studies are being performed to correlate the cooling necessary to be effective with the decreased penetration of the sound waves. This may make some treatments shorter, as in minimally vascularized tissues, and other treatments longer, as in richly vascularized tissues.

References

1. American Society for Aesthetic Plastic Surgery (ASAPS). 2009. ASAPS Statistics http://www.surgery.org/sites/default/files/2009stats.pdf
2. Shukla A, Rasik AM, Patnaik GK. Depletion of reduced glutathione, ascorbic acid, vitamin E and antioxidant defense enzymes in a healing cutaneous wound. Free Radic Res. 1997;26:93–101.
3. Thomas DR. Specific nutritional factors in wound healing. Adv Wound Care. 1997;10:40–3.
4. Wilgus TA, Bergdall VK, et al. The impact of cyclooxygenase-2 mediated inflammation on scarless fetal wound healing. Am J Pathol. 2004;165:753–61.
5. Rizk M, Witte MB, Barbul A. Nitric oxide and wound healing. World J Surg. 2004;28:301–6.
6. Schwentker A, Vodovotz Y, et al. Nitric oxide and wound repair: role of cytokines? Nitric Oxide. 2002;7:1–10.
7. Papas AM. The vitamin E factor. New York: HarperCollins Publishers Inc.; 1999.
8. Cooney R, Franke A, Harwood P, et al. Gamma-tocopherol detoxification of nitrogen dioxide: superiority to alpha-tocopherol. Proc Natl Acad Sci U S A. 1993;90:1771–5.
9. Ikeda S, Niwa T, Yamashita K. Selective uptake of dietary tocotrienols into rat skin. J Nutr Sci Vitaminol (Tokyo). 2000;46:141–3.
10. Scholl D, Langkamp-Henken B. Nutrient recommendations for wound healing. J Intraven Nurs. 2001;24:124–32.
11. Jiang et al. Gamma-tocopherol and its major metabolite, in contrast to alpha-tocopherol, inhibit cyclooxygenase activity in macrophages and epithelial cells. Proc Natl Acad Sci U S A. 2000;97:11494–9.
12. Wiser J et al. In vivo gamma-tocopherol supplementation decreases systemic oxidative stress and cytokine responses of human monocytes in normal and asthmatic subjects. Free Radic Biol Med. 2008;45:40–9.
13. Kumar KS et al. Preferential radiation sensitization of prostate cancer in nude mice by nutraceutical antioxidant gamma-tocotrienol. Life Sci. 2006;78:2099–104.
14. ClinicalTrials.gov Identifier NCT00700791. Efficacy of natural vitamin E tocotrienol on the treatment of surgical scars. http://clinicaltrials.gov/ct2/show/NCT00700791?term=tocotrienol+scar&rank=1
15. Kulkarni S et al. Gamma-tocotrienol protects hematopoietic stem and progenitor cells in mice after total-body irradiation. Radiat Res. 2010;173:738–47.
16. Murphy EA et al. Immune modulating effects of β-glucan. Curr Opin Clin Nutr Metab Care. 2010;13:656–61.
17. Delatte SJ et al. Effectiveness of beta-glucan collagen for treatment of partial-thickness burns in children. J Pediatr Surg. 2001; 36:113–8.
18. Eshghi F et al. Effects of Aloe vera cream on posthemorrhoidectomy pain and wound healing: results of a randomized, blind, placebo-control study. J Altern Complement Med. 2010;16:647–50.
19. Morizane S. Kallikrein expression and cathelicidin processing are independently controlled in keratinocytes by calcium, vitamin D(3), and retinoic acid. J Invest Dermatol. 2010;130:1297–306.
20. Yamada S, Sugahara K. Potential therapeutic application of chondroitin sulfate/dermatan sulfate. Curr Drug Discov Technol. 2008;5: 289–301.
21. Lansdown AB et al. Zinc in wound healing: theoretical, experimental, and clinical aspects. Wound Repair Regen. 2007;15:2–16.
22. Lassau N, Koscielny S, Avril M, Margulis A, Duvillard P, Baere T, et al. Prognostic value of angiogenesis evaluated with high frequency and color Doppler sonography for preoperative assessment of melanomas. AJR Am J Roentgenol. 2002;178:1547–51.
23. Cornud F, Hamida K, Flam T, Helenon O, Chretien Y, Thiounn N, et al. Endorectal color Doppler sonography and endorectal MR imaging features of non palpable prostate cancer. AJR Am J Roentgenol. 2000;175:1161–8.
24. Bard R. Dynamic contrast enhanced MRI of prostate cancer. New York: Springer; 2009.
25. Kenfield SA, Stampfer MJ, Giovannucci E, Chan JM. Physical activity and survival after prostate cancer diagnosis in the health professionals follow-up study. J Clin Oncol. 2011;29: 726–32.
26. Laffitte BA, Chao LC, Li J, Walczak R, Hummasti S, Joseph SB, et al. Activation of liver X receptor improves glucose tolerance through coordinate regulation of glucose metabolism in liver and adipose tissue. Proc Natl Acad Sci U S A. 2003;100(9):5419–24. Epub 2003 Apr 15.
27. Moraa-Ranjeva MP, Charveron M, Fabre B, Milon A, Muller I. Incorporation of phytosterols in human keratinocytes Consequences on UVA-induced lipid peroxidation and calcium ionophore-induced prostaglandin release. Chemistry 2003;44:93.
28. Toda S, Shirataki Y. Inhibitory effects of Astragali Radix, a crude drug in Oriental medicines, on lipid peroxidation and protein oxidative modification by copper. J Ethnopharmacol. 1999;68(1–3): 331–3.
29. Wang D, Shen W, Tian Y, Sun Z, Jiang C, Yuan S. Protective effect of active components extracted from radix Astragali on human erythrocyte membrane damages caused by reactive oxygen species [Article in Chinese]. Zhongguo Zhong Yao Za Zhi. 1996;21(12): 746–8, 763.
30. Chan MM, Mattiacci JA, Hwang HS, Shah A, Fong D. Synergy between ethanol and grape polyphenols, quercetin, and resveratrol, in the inhibition of the inducible nitric oxide synthase pathway. Biochem Pharmacol. 2000;60(10):1539–48.
31. Mertens-Talcott SU, Bomser JA, Romero C, Talcott ST, Percival SS. Ellagic acid potentiates the effect of quercetin on p21waf1/cip1, p53, and MAPKinases without affecting intracellular generation of reactive oxygen species in vitro. J Nutr. 2005;135: 609–14.

Sonography of Cosmetic Procedures

15

Ximena Wortsman

The usefulness of ultrasound for detecting fillers, implants, and cosmetic/plastic surgery complications

Contents

15.1 Introduction

In recent years, a significant growth in the numbers and variety of cosmetic procedures has taken place. Even though there are multiple reports of successful experiences, at the same time there are growing numbers of complications derived from these aesthetic procedures. Thus, this cosmetic field includes the non-surgical and surgical procedures that are executed with beauty purposes and are directed to decrease the anatomical signs of aging. Hence, this area includes a wide range of techniques that can go from botulinum toxin to cosmetic fillers and also a broad area of common plastic surgeries such as abdominoplasty, liposuction, and rhinoplasty, among others.

Frequently, adverse reactions or complications of cosmetic procedures elicit complex clinical manifestations that sometimes can mimic other common dermatologic entities. Moreover, patients may not provide a clear history of the cosmetic procedures, sometimes performed many years ago or by non-medical personnel.

Because biopsies present the inherent risk of scars, patients who are subject to aesthetic procedures try to avoid these invasive techniques. Therefore, the imaging support provided using sonography can be a powerful diagnostic and monitoring tool in the potential complications in these cases.

In this chapter we will discuss the sonographic signs and potential complications of common cosmetic procedures as well as the sonographic assessment of the anatomical effects of aging.

X. Wortsman, MD
Department of Radiology and Dermatology,
Institute for Diagnostic Imaging
and Research of the Skin and Soft Tissues,
Clinica Servet, Faculty of Medicine, University of Chile,
Almirante Pastene 150, Providencia, Santiago, Chile
e-mail: xwo@tie.cl, xworts@yahoo.com, www.sonoskin.com

X. Wortsman, G.B.E. Jemec (eds.), *Dermatologic Ultrasound with Clinical and Histologic Correlations*,
DOI 10.1007/978-1-4614-7184-4_15,

15.2 Photoaging

Photoaging is the process of damage of the skin derived from the continuous and chronic exposure to ultraviolet (UV, types A-UVA, and B-UVB) radiation that takes place on areas that are exposed to the sun such as the face, ears, neck, and hands. Histologically, it implies the deposit of glycosaminoglycans in the dermis, an entity also called elastosis. On sonography, the detection of a subepidermal low echogenicity band (SLEB) has been reported. The SLEB may provide an index of the magnitude of the photodamage to the patient. Thus, the thickness of the SLEB can be measured and can provide a tool for monitoring photoaging treatments [1, 2] (Fig. 15.1).

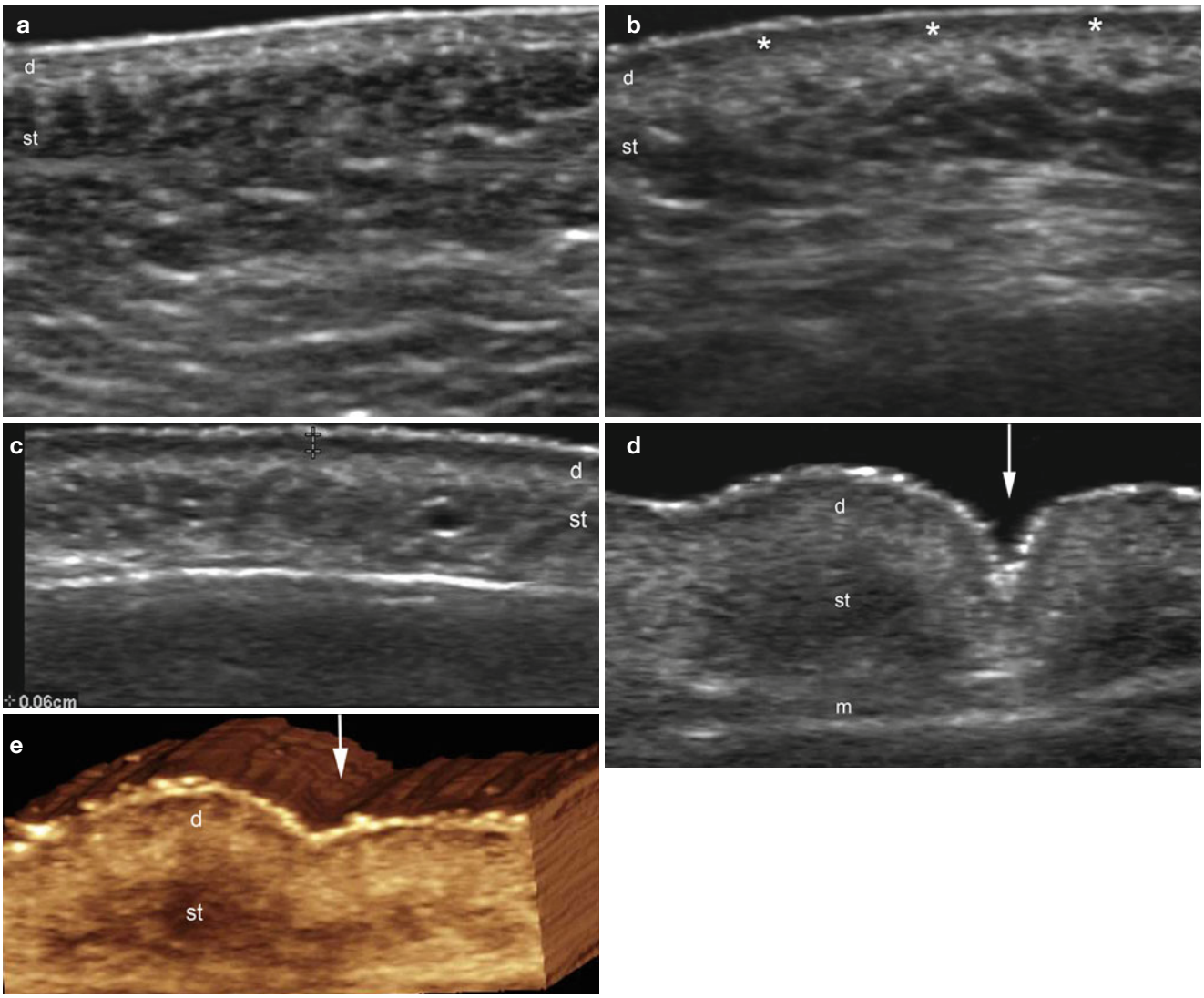

Fig. 15.1 (**a**–**e**) Photoaging. (**a**) The skin of a 1-year-old child (grey scale ultrasound image image, transverse view, right cheek). (**b**) The skin of a 50-year-old, sun-exposed woman (grey scale ultrasound image image, transverse view, right cheek). Notice the decreased echogenicity band in the upper dermis (in comparison with Fig. **a**) that corresponds to elastosis (*, subepidermal low echogenicity band-SLEB). (**c**) Grey scale ultrasound image image (transverse view, frontal region) shows a 0.6 mm depth SLEB (between markers). (**d**, **e**) Wrinkle and photoaging. Grey scale ultrasound image images (dynamic studies during frowning; transverse views; (**d**) 2D and (**e**) 3D reconstruction; at the glabellar region) show the hollow and retraction of the cutaneous layers in the site of the wrinkle (*arrow*). *Abbreviations*: *d* dermis, *st* subcutaneous tissue, *m* muscle

15.3 Botulinum Toxin

The botulinum toxin type A (BoNTA) is a flaccid paralysis-inducing agent, and the most common non-surgical aesthetic procedure in the United States. BoNTA is used for the removal of wrinkles in the glabella, superolateral orbicularis oculi, and depressor angulis oris. The effects usually last from 3 to 5 months, depending on dosage and injection site [3]. On sonography, BoNTA injections produce an increased echogenicity of the subcutaneous tissue and epicranius muscle with blurriness of the margin between the layers [4] (Fig. 15.2).

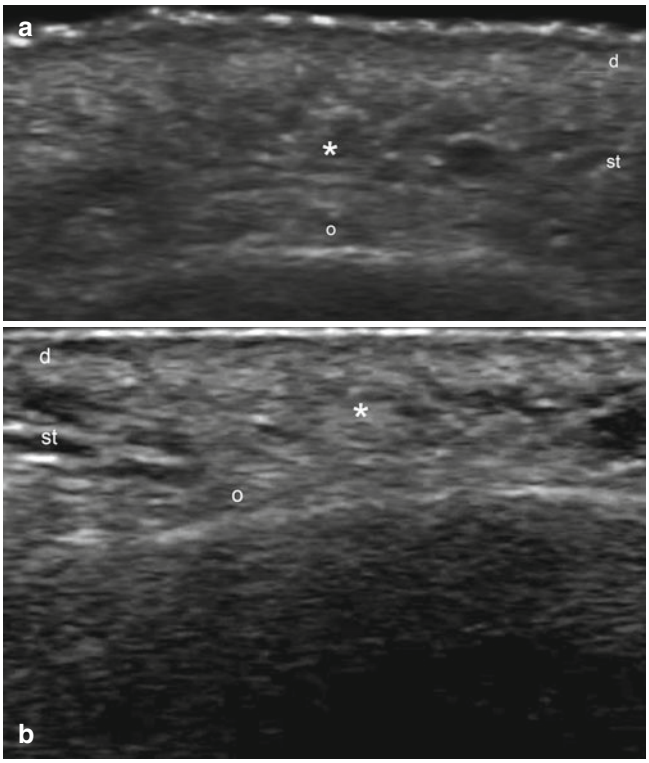

Fig. 15.2 (**a**, **b**) Botulinum Toxin. Grey scale ultrasound images (transverse views; **a** glabellar region and **b** right superciliary ridge, moments after injection). There is an increased echogenicity of the subcutaneous tissue (*) and epicranius muscle (o) with blurriness of the margin of the layers at the sites of injection. *Abbreviations*: *d* dermis, *st* subcutaneous tissue

15.4 Cosmetic Fillers

Cosmetic fillers are nanoparticles used for decreasing the effects of aging and sagging skin. Thus, these compounds are commonly injected into highly exposed areas such as the face [4, 5]. Cosmetic fillers were first used medically in HIV patients who presented significant lipoatrophy [6].

According to their origin these agents can be separated into two types, exogenous or endogenous. According to their nature and reabsorption capabilities they can be also separated in biologic (degradable) and synthetic (non-degradable). Currently, patients may present with deposits of one or more types of fillers in the skin and of different types that can sometimes complicate the clinical diagnosis and/or cosmetic procedures. Hence, in some cases there is contraindication to injecting cosmetic fillers (i.e., in patients receiving interferon or cases that present a history of previous injections of some synthetic fillers). Thus, ultrasound provides a mapping that allows the detection and identification of common cosmetic fillers [7] (Fig. 15.3).

15.4.1 Exogenous Fillers

15.4.1.1 Degradable

15.4.1.1.1 Hyaluronic Acid

Hyaluronic acid (HA) is the main biodegradable filler used, and commonly, HA presents complete reabsorption within 3 to 6 months [8]. There are pure and mixed formulations of HA (for e.g. with lidocaine).

Histologically, pure HA shows post-inflammatory cells, sparse histiocytes with cytoplasmic inclusions (macro and microvacuoles), but commonly with no foreign body reactions.

On sonography, the pure formulations appear as anechoic round subcutaneous pseudocysts that become smaller over time (months). The formulation mixed with lidocaine usually shows subcutaneous pseudocysts with inner echoes (debris) but also decreases in size over a short period of time, similar to the pure form. Occasionally, in patients that show complications, most commonly reported with the mixed formulations, the pseudocysts may present confluence and form fistulous tracts that drain into the subepidermal region [7] (Figs. 15.3 and 15.4).

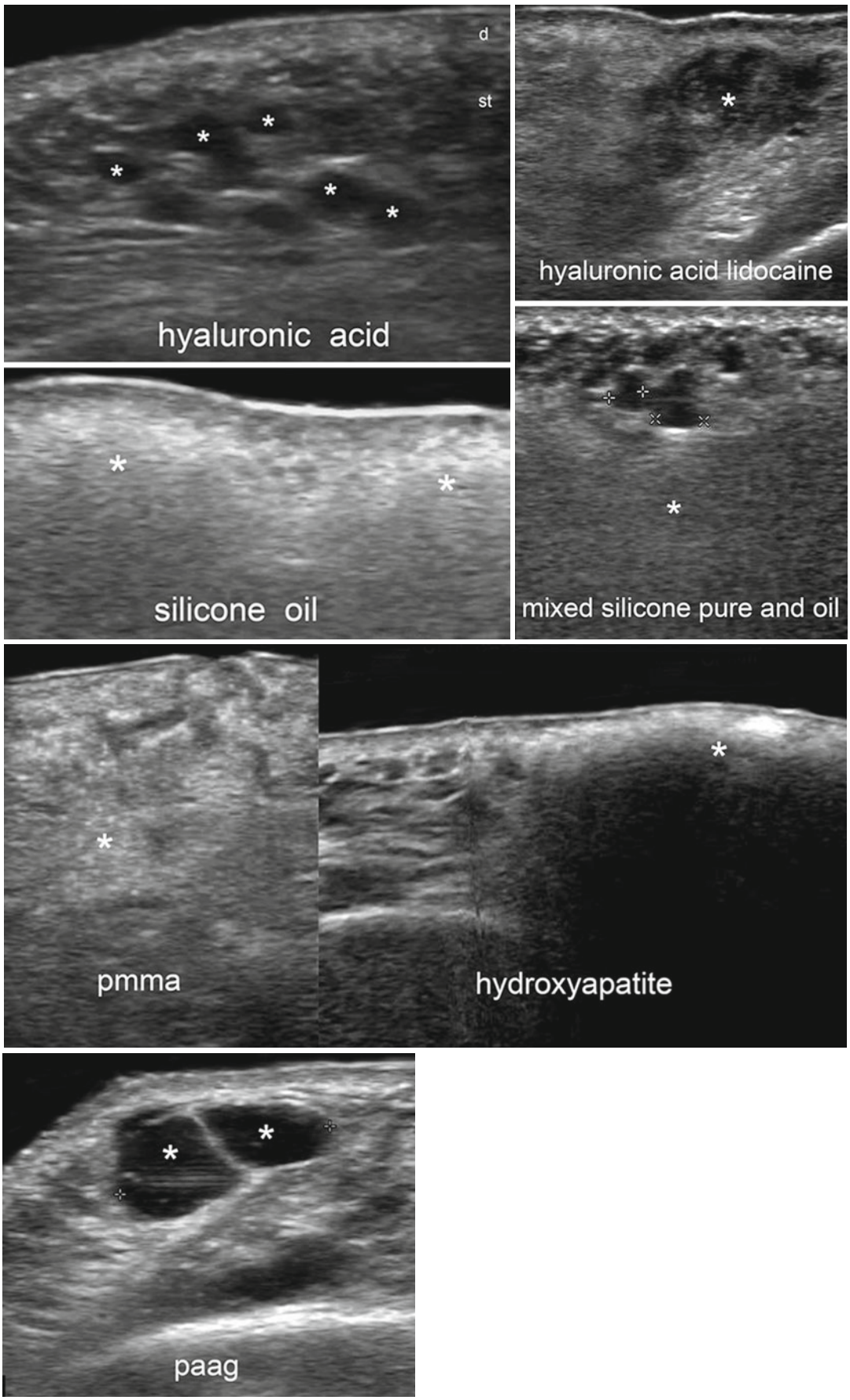

Fig. 15.3 The variable sonographic appearance of different types of fillers (*)

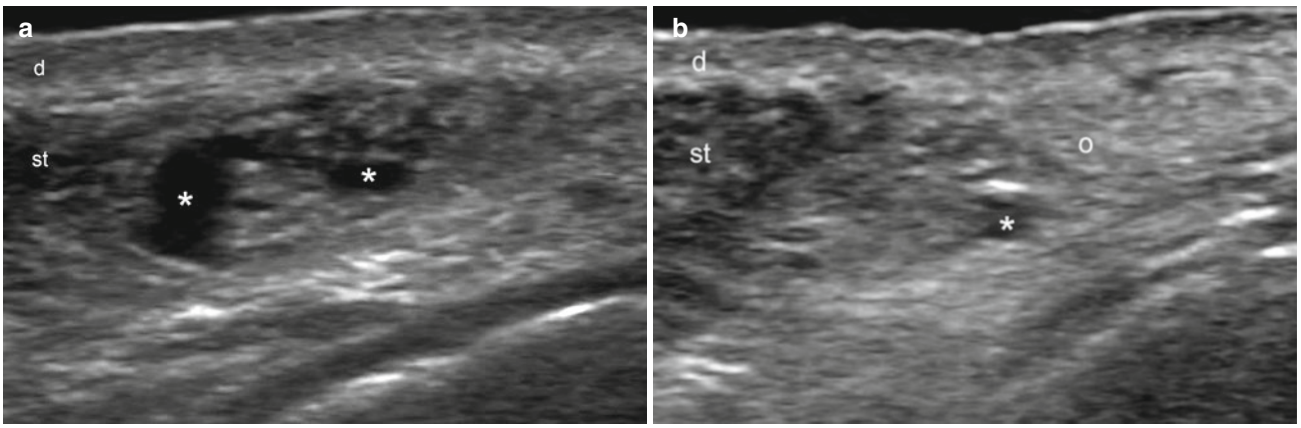

Fig. 15.4 (**a**, **b**) Hyaluronic acid (*, grey scale ultrasound images, transverse views, right nasofold line). (**a**) Immediately after injection, oval-shaped anechoic pseudocystic structures (*) are detected in the subcutaneous tissue. (**b**) 3 months after injection. Notice the scarce presence of anechoic pseudocysts (*) and the increased echogenicity (o) of the subcutaneous tissue. *Abbreviations*: *d* dermis, *st* subcutaneous tissue

15.4.1.2 Non-degradable

15.4.1.2.1 Silicone

There are two forms of silicone usually found in cosmetic procedures. The first is the pure form, and the second is the oily form, also called dimethylsilosane. Neither of these two silicone formulations have received Food and Drug Administration (FDA) approval for use in cosmetic procedures. Nevertheless, silicone oil has been approved for treating retinal detachment and a purified form of silicone called polydimethylsiloxane (PDMS-1000) is used for off-label purposes in the United States [9] and it is openly used in other countries [10]. Silicone is also present in many industrial components; therefore, its usage can be subject of malpractice in the non-medical field. Adverse reactions are commonly delayed and may take place 2–10 years post-injection. Additionally, silicone reactions can mimic frequent dermatologic diseases such as morphea, atopic dermatitis, angioedema, and actinic cheilitis, among others. Moreover, this agent can easily infiltrate into deeper layers such as muscles or lymph nodes.

Histologically, silicone shows a predominantly lymphocytic inflammatory infiltrate with extracellular vacuoles of different sizes and a exuberant foreign body granulomatous types of reaction.

On sonography, pure silicone appears as anechoic round or oval-shaped pseudocystic structures in the subcutaneous tissue, with similar echogenicity to the intact breast implants. These pseudocysts usually do not modify their morphology over time. Silicone oil, however, is hyperechoic, with a posterior reverberation artifact, similar to ruptured breast implants where the silicone becomes mixed with the fatty tissue. Mixed formulations that are composed of pure silicone and silicone oil can occasionally be detected. In the latter cases, the round or oval-shaped anechoic pure silicone pseudocysts can appear mingled within the reverberant hyperechoic areas that correspond to the silicone oil. The broad posterior reverberation artifact that is seen in silicone oil is also called the "snow storm" pattern and has also been reported in ruptured breast implants. The whitish appearance presents because of the strong mixing of pure silicone with the fatty tissue of the subcutaneous layer. Thus, the infiltration of deeper structures follows the same sonographic patterns as for the silicone forms. Additionally, subcutaneous venous thrombosis (Mondor's disease) has been reported in concomitance with the injected areas and appears on sonography as a dilated superficial subcutaneous vein with hypoechoic thrombotic material and without blood flow on color Doppler ultrasound [4, 7, 11] (Figs. 15.3, 15.5, 15.6, 15.7, 15.8, and 15.9).

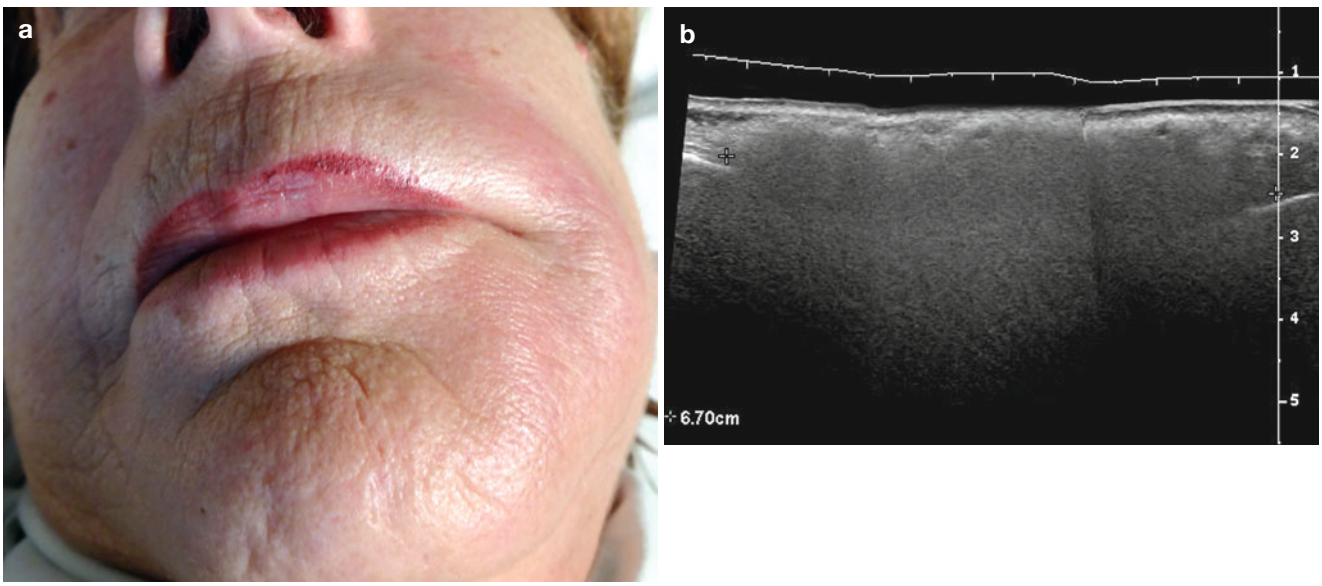

Fig. 15.5 (**a**, **b**) Silicone oil complication. (**a**) Clinical image shows erythema and edema in the left nasofold line, lips, and mandibular region. (**b**) Grey scale ultrasound image (extended field of view, longitudinal view) demonstrates a 6.7 cm long hyperechoic dermal and subcutaneous deposit (between markers) in the left nasolfold line and mandibular region. Notice the "snow storm" appearance of the silicone oil deposits

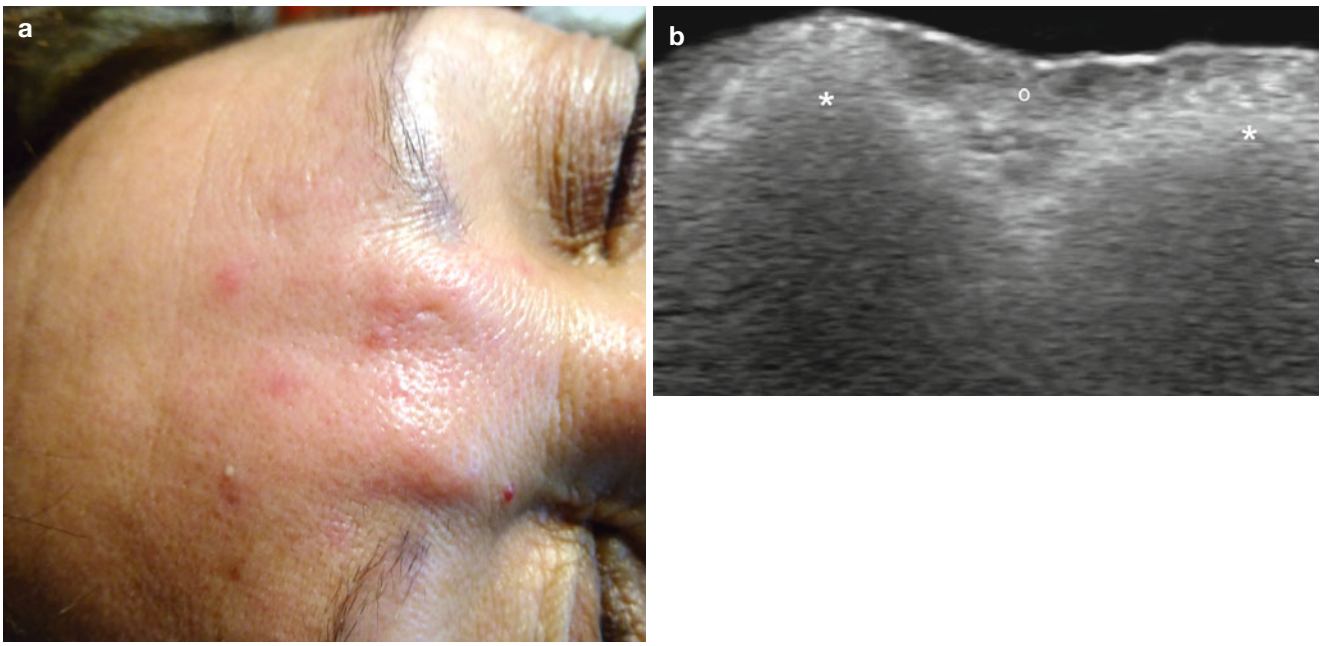

Fig. 15.6 (**a**, **b**) Silicone oil complication. (**a**) Clinical photograph demonstrates erythema and swelling in the glabellar region. (**b**) Grey scale ultrasound image (transverse view) shows hyperechoic deposits (*) in the dermis and subcutaneous tissue with a "snow storm" pattern. Hypoechogenicity of the dermis (o) between the deposits is also detected

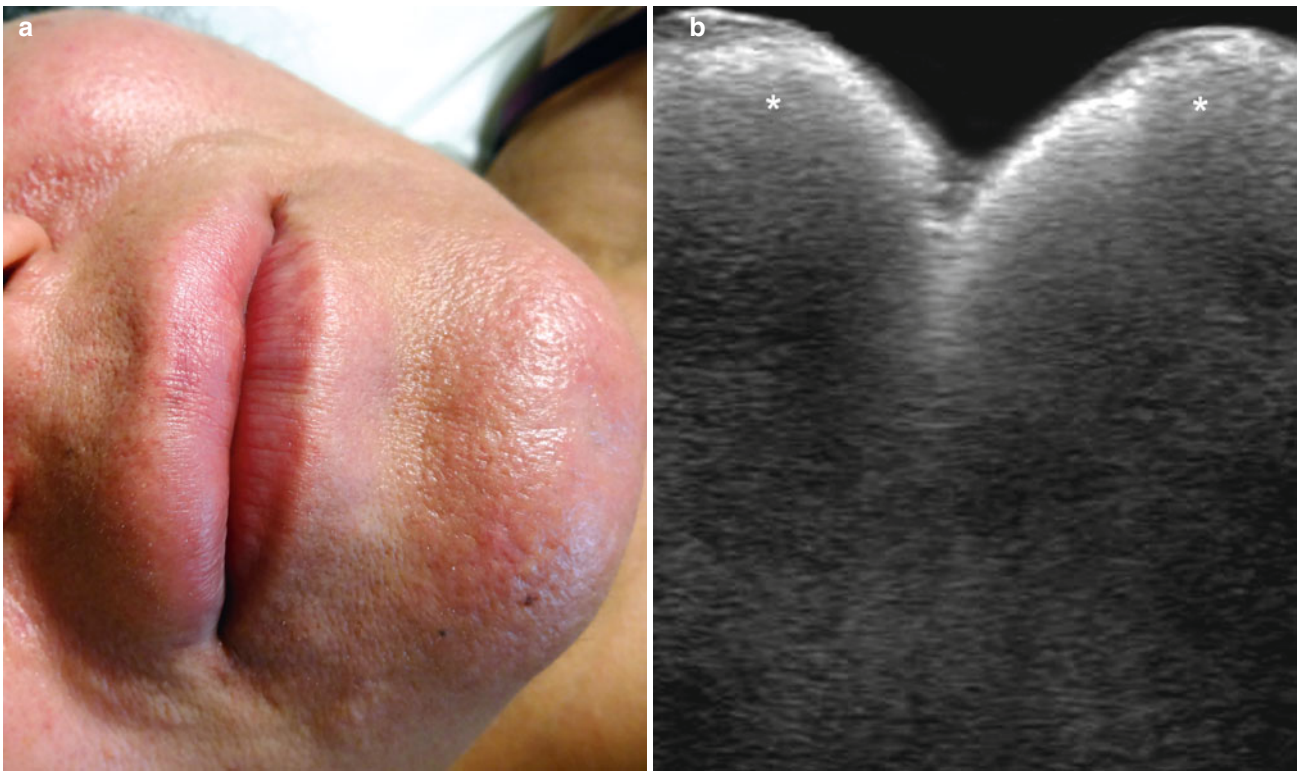

Fig. 15.7 (**a**, **b**) Silicone oil complication. (**a**) Clinical image shows erythema and edema of the lips and chin region. (**b**) Grey scale ultrasound image (longitudinal view) demonstrates hyperechoic deposits (*) with a "snow storm" pattern affecting the upper and lower lip

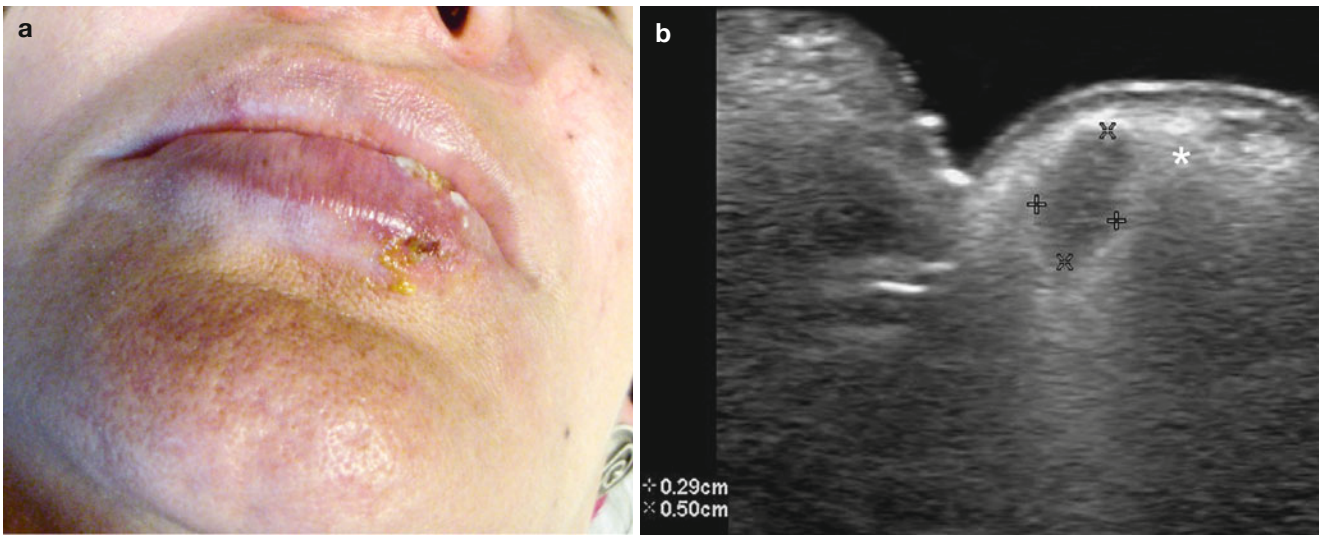

Fig. 15.8 (**a**, **b**) Silicone oil and hyaluronic acid complication. (**a**) Clinical image shows edema and ulceration in the lower lip 1 week after injection of a mixed formulation of hyaluronic acid and lidocaine. The patient had a history of injection of silicone oil in the lips 8 years ago (revealed after the hyaluronic acid injection). (**b**) Grey scale ultrasound image (longitudinal view, lips) demonstrates a 2.9 mm long × 5.0 mm depth oval-shaped hypoechoic deposit (between markers) in the lower lip that corresponds to the hyaluronic acid formulation which is surrounded by the hyperechoic deposits of the silicone oil (*, with posterior reverberance artifact). Notice that these deposits involve the cutaneous layers and the orbicularis muscle of the lips

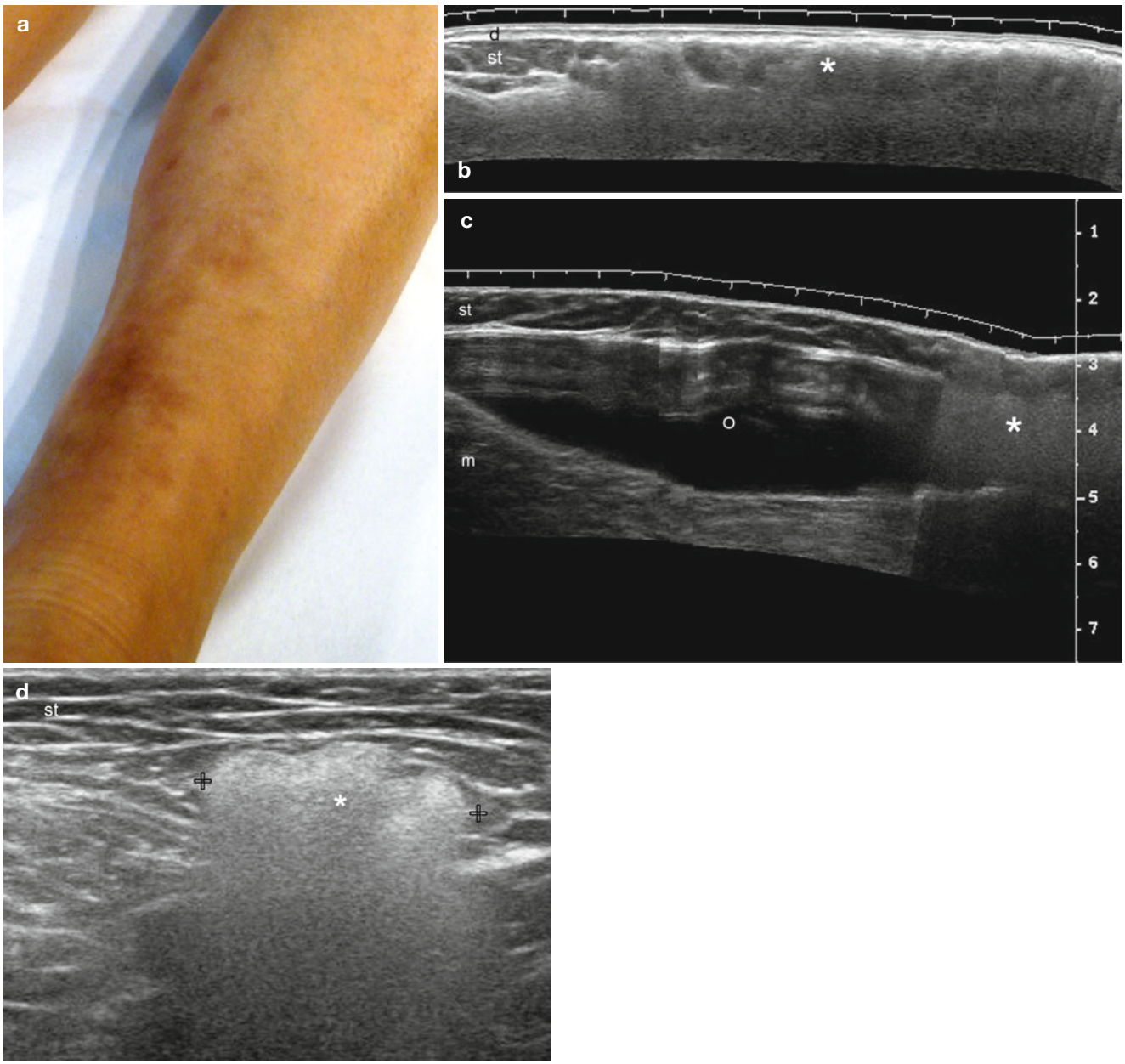

Fig. 15.9 (**a**–**d**) Pseudo-morphea generated by silicone oil and additional lymph node involvement. (**a**) Clinical photograph demonstrates pigmented bumps in the medial aspect of the left leg. (**b**, **c**) Grey scale ultrasound images (longitudinal views; **b** medial aspect; **c** medial gastrocnemius level) show extensive hyperechoic deposits in the subcutaneous tissue (*) that correspond to silicone oil. The patient also presented with a pure silicone implant (o) in the calf. (**d**) Grey scale ultrasound image (transverse view, left groin region) demonstrates a hyperechoic deposit with posterior reverberance artifact (*) that affects a lymph node (between markers). *Abbreviations*: *d* dermis, *st* subcutaneous tissue, *m* medial gastrocnemius muscle

15.4.1.2.2 Polymethylmethacrylate

Polymethylmethacrylate (PMMA) is an agent used in dermatology, plastic surgery, orthopaedics, and dentistry [12, 13] and is composed of microscopic beads (microspheres of a synthetic polymer of methylmethacrylate) that are suspended in collagen, hyaluronic acid, or other colloidal vehicle [14]. PMMA deposits usually appear as multiple bright hyperechoic dots producing a mini-comet-tail artifact (small posterior reverberance); later (more than 6 months after injection), some of the larger filler deposits may acquire posterior acoustic shadowing artifacts [4, 7, 11] (Figs. 15.3, 15.10, and 15.11).

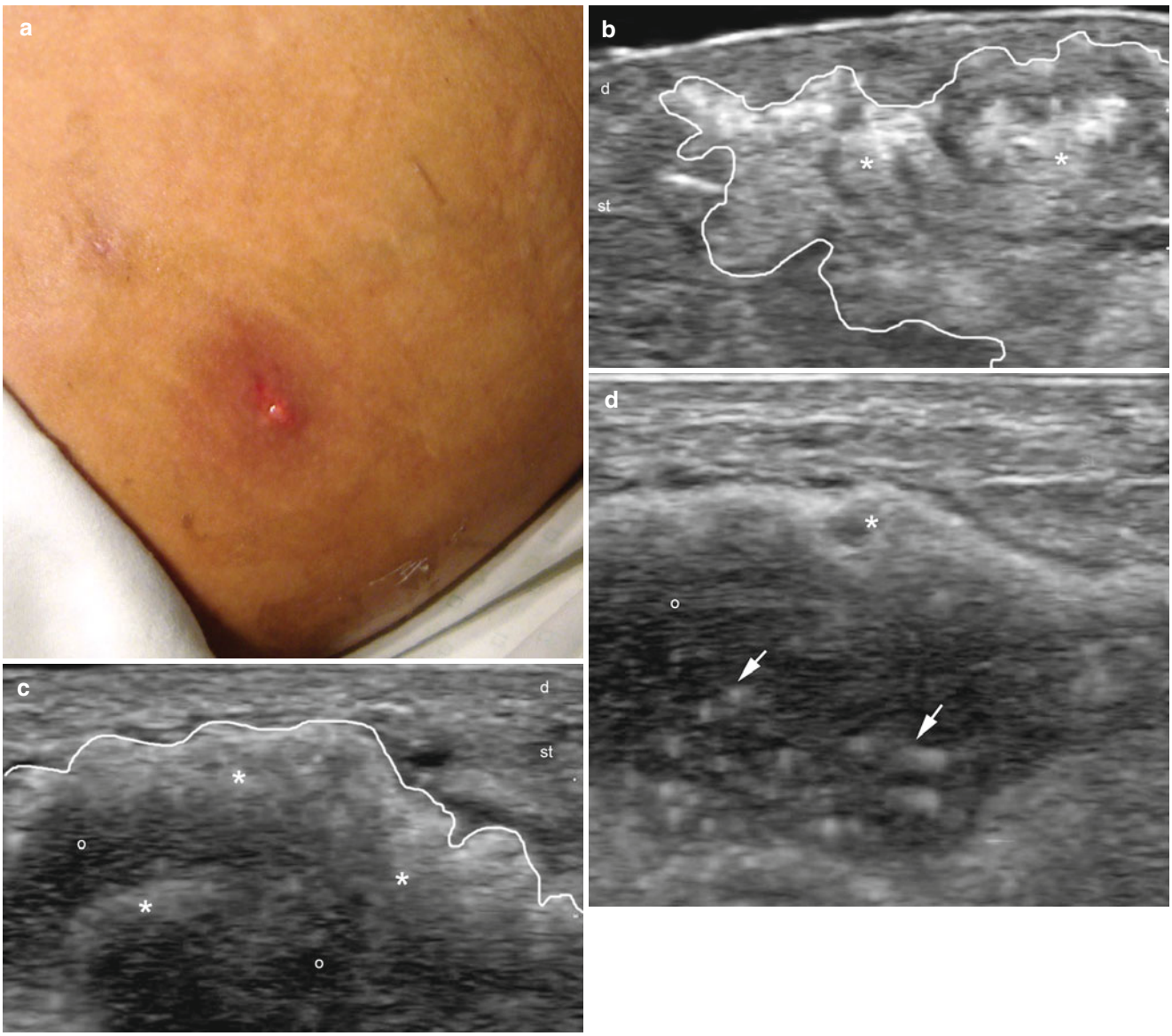

Fig. 15.10 (**a**–**d**) Complication of polymethylmethacrylate (PMMA). (**a**) Clinical photograph shows erythema, pigmentation, swelling, and drainage of oily material in the right gluteal region. (**b**–**d**) Grey scale ultrasound images (transverse views; right gluteal region; **b** upper third; **c** middle third; **d** lower third) demonstrate mainly subcutaneous deposits of hyperechoic dots (*) that present a mini-comet-tail artifact. Notice the subcutaneous anechoic fluid collection (o) that also contains the hyperechoic deposits (*, *arrows*) detected in Figs. (c) and (d). *Abbreviations*: *d* dermis, *st* subcutaneous tissue

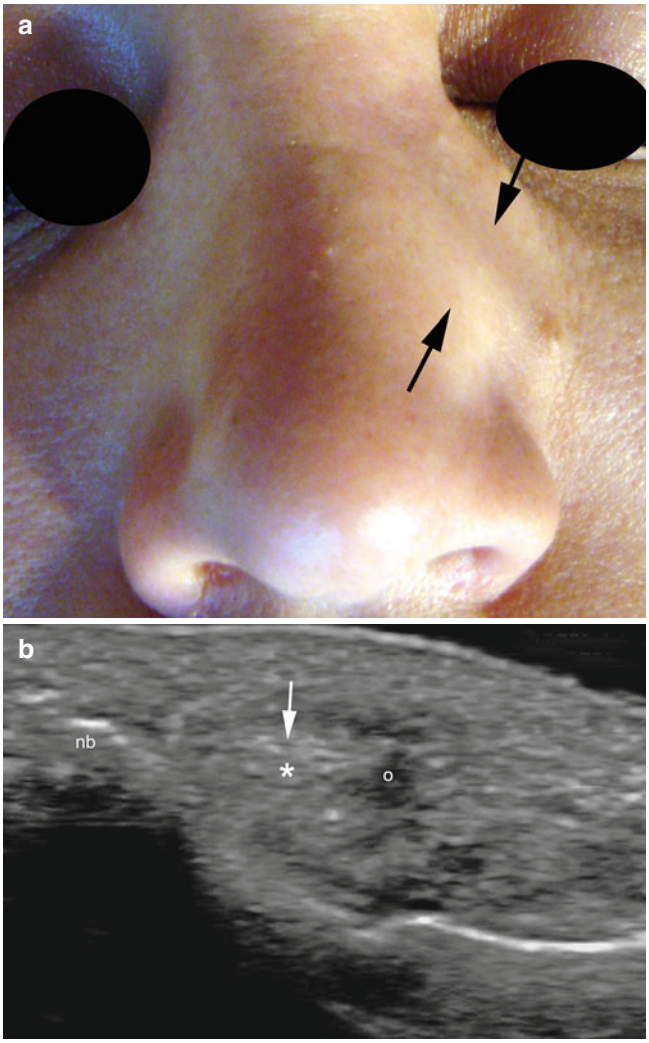

Fig. 15.11 (**a**, **b**) Complication of polymethylmethacrylate (PMMA) after Botox injection. (**a**) Clinical image demonstrates a left paranasal lump (*arrows*) that developed immediately after a Botox injection in the glabellar region. The patient presented with a history of PMMA injection in the left paranasal region for repairing a nasal fracture 5 years previously (revealed after the Botox injection). (**b**) Grey scale ultrasound image (transverse view, left paranasal region) shows subcutaneous hyperechoic dots (*, *arrow*)) with mini-comet-tail artifact surrounded by hypoechoic inflammatory/granulomatous tissue (o). *Abbreviation*: *nb* nasal bone

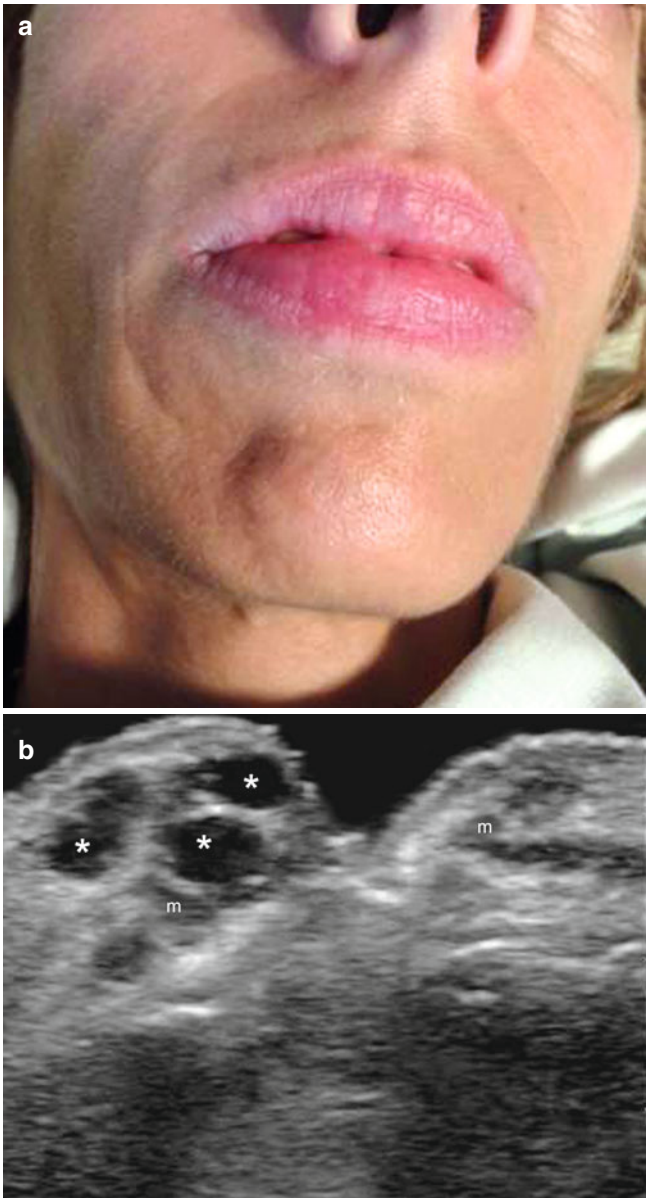

Fig. 15.12 (**a**, **b**) Polyacrylamide (PAAG). (**a**) Clinical image of a patient who was injected with PAAG in the lips and mandible region. (**b**) Grey scale ultrasound image (longitudinal view) shows round and oval-shaped anechoic deposits (*) in the dermis and muscularis oris muscle of the upper lip. The lower lip is unremarkable. *Abbreviation*: *m* muscularis oris muscle of the lip

15.4.1.2.3 Calcium Hydroxyapatite

Calcium hydroxyapatite is filler composed of microspheres suspended in a polysaccharide carrier [15]. On ultrasound, hydroxyapatite appears as hyperechoic deposits with variable degrees of posterior acoustic shadowing. The latter is produced by the calcium component of the filler [4, 7, 11] (Fig. 15.3).

15.4.1.2.4 Polyacrylamide

Polyacrylamide (PAAG) is a synthetic hydrogel that has been primarily used in the facial reconstruction of patients with HIV and later for cosmetic purposes [16, 17]. On ultrasound, PAAG deposits present as anechoic round or oval-shaped pseudocystic structures. A lack in modification of the size and shape of the deposits for at least 18 months has been reported. The latter characteristic can be useful in differentiating PAAG from hyaluronic acid. Thus, hyaluronic acid lasts for approximately 6 months and quickly modifies its size and shape. Additionally, PAAG can present increased echogenicity of the subcutaneous tissue in the vicinity of the deposits [18] (Figs. 15.3 and 15.12).

15.4.2 Endogenous Fillers

15.4.2.1 Autologous Fat

Autologous fat is a biologic agent that has been used to fill wrinkles or for gluteal or breast augmentation, through direct injection into the subcutaneous tissue or the muscle itself. Also, harvested fat can be transferred, usually from the abdominal wall, into the face for restoring the contour.

On sonography, liquefied autologous fat deposits appear as anechoic round or oval pseudocystic structures, sometimes with increased echogenicity of the subcutaneous and/or adjacent muscles [4]. Injection of non-liquefied harvested fat appears as lobulated hypoechoic deposits with some hyperechoic linear septa. Long-term follow-up may show mixed echogenicities and egg-like calcifications [19] (Figs. 15.13, 15.14, and 15.15).

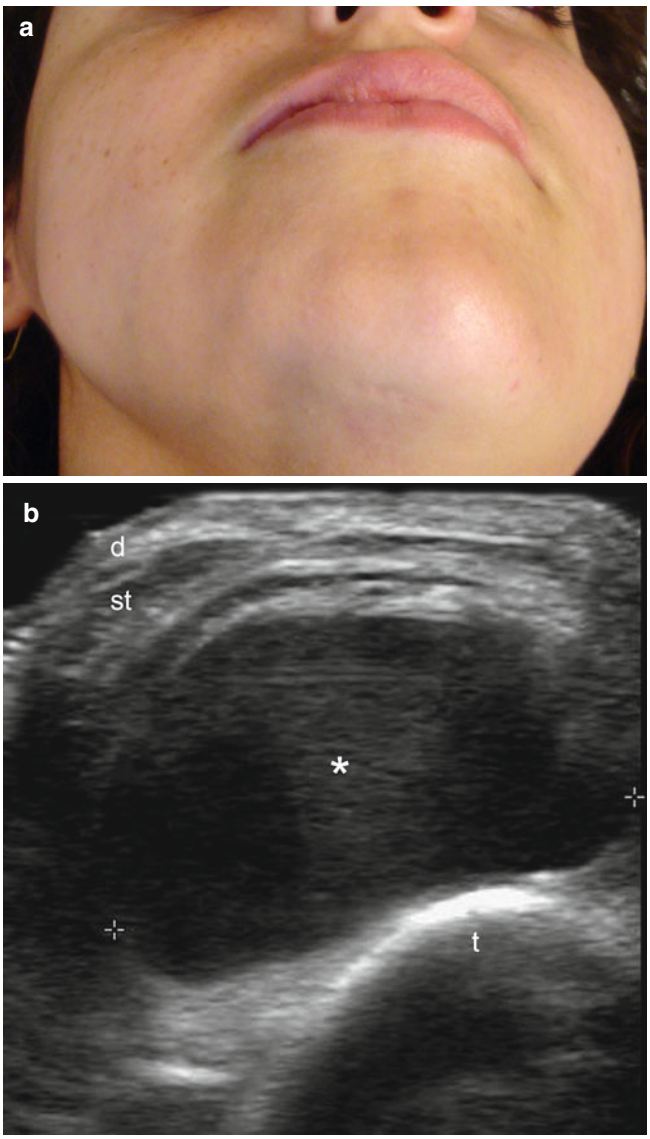

Fig. 15.13 (**a**, **b**) Autologous liquefied fat. (**a**) Clinical photograph shows hemifacial atrophy in a patient with Parry Romberg syndrome (progressive hemifacial atrophy) who also received an injection of liquefied autologous fat. (**b**) Grey scale ultrasound image (longitudinal view, right mandibular region) demonstrates well-defined subcutaneous round-shaped anechoic deposits (*) that correspond to the injected fat. *Abbreviations*: *st* subcutaneous tissue, *b* bone margin of the mandible

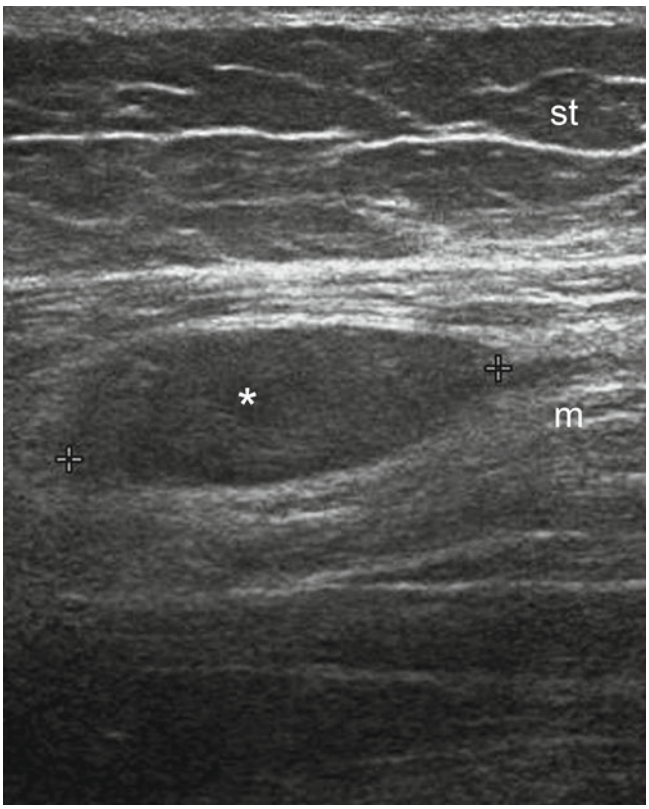

Fig. 15.14 Intramuscular liquefied autologous fat. Grey scale ultrasound image (longitudinal view, left gluteal region) demonstrates a well-defined oval-shaped anechoic deposit (*, between markers) within the left gluteus maximus muscle. *Abbreviations*: *st* subcutaneous tissue, *m* gluteus maximus muscle

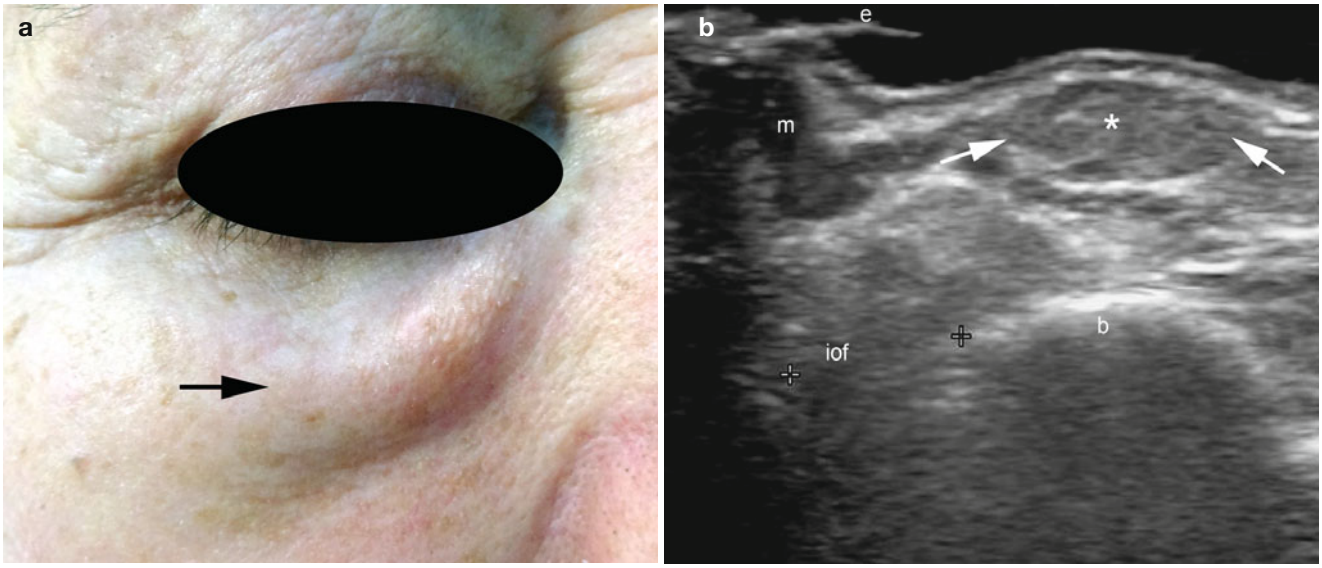

Fig. 15.15 (**a**, **b**) Autologous harvested fat. (**a**) Clinical image shows swelling (*arrow*) that appeared in the right lower eyelid after transfer of autologous harvested fat. (**b**) Grey scale ultrasound image demonstrates an oval-shaped hypoechoic deposit (*, *arrows*) in the subcutaneous tissue. *Abbreviations*: *e* eyelash, *m* orbicularis muscle of the eyelid, *iof* intraorbitary fat pad, *b* margin of the medial aspect of the zygomatic bone

15.4.2.2 Platelet Rich Plasma

Platelet-rich plasma (PRP), also called platelets concentrates, have been used for treating plantar fasciitis and currently, for stimulating healing and rejuvenation. PRP is commonly used for treating nasofold lines [20].

On sonography, heterogeneous or focal subcutaneous hyperechogenicity suggestive of local edema and/or anechoic interlobular fluid collections has been described [4]. Lipoatrophy (i.e., decreased or lack of the fatty component of the subcutaneous tissue) can occasionally be seen as a complication of this procedure (Figs. 15.16 and 15.17).

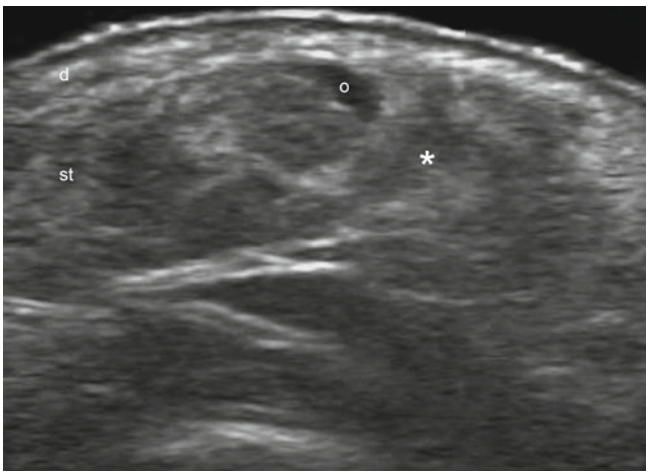

Fig. 15.16 Platelet-rich plasma (PRP). Grey scale ultrasound image demonstrates heterogeneous echogenicity (*) of the subcutaneous tissue immediately after injection of platelets in the dorsal forearm (testing). A small anechoic sero-hematic fluid collection (o) is also detected. *Abbreviations*: *d* dermis, *st* subcutaneous tissue

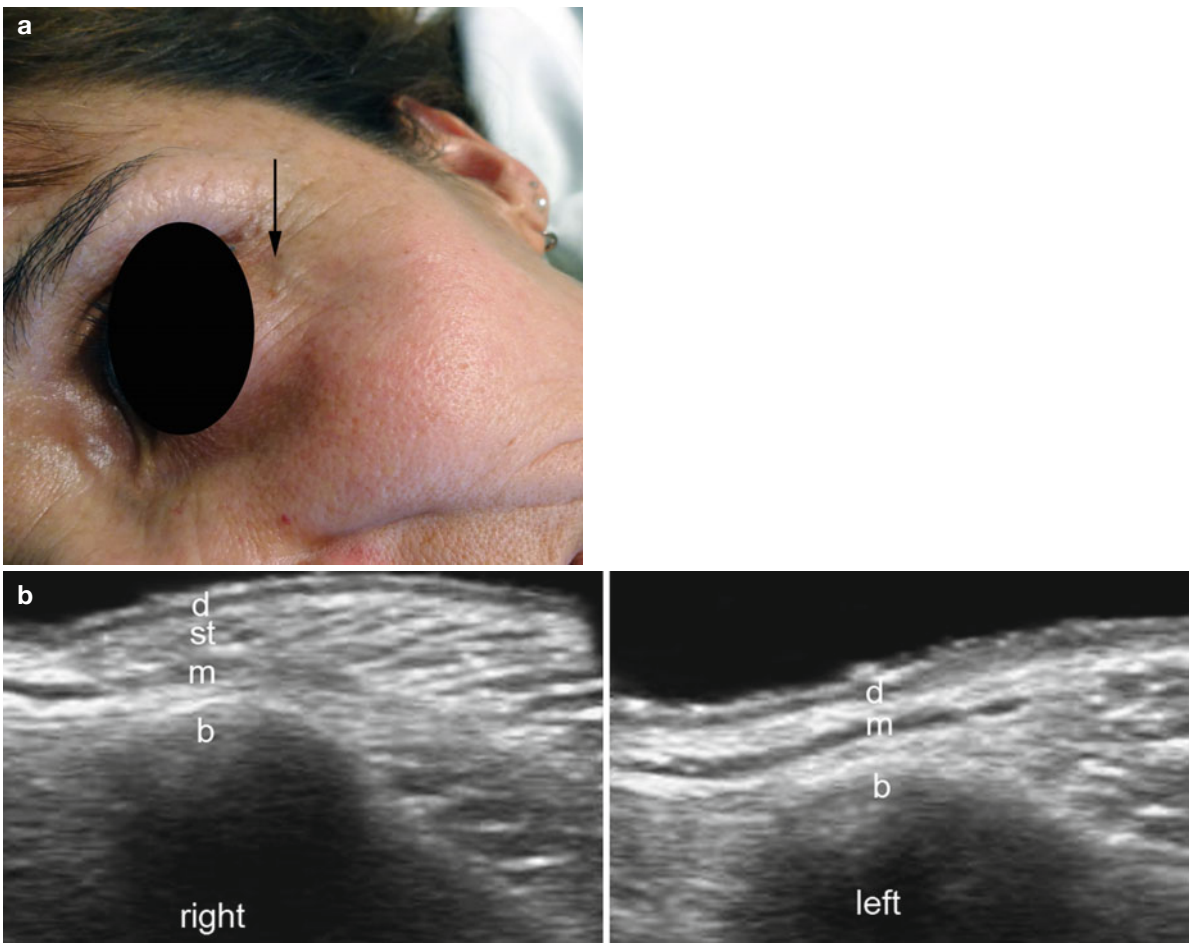

Fig. 15.17 Lipoatrophy post platelet-rich plasma (PRP) injection. (**a**) Clinical image shows atrophy (*arrow*) in the external aspect the left eyelid after platelet injection. (**b**) Grey scale ultrasound image (longitudinal views; side by side comparison, eyelid regions) demonstrates lack of subcutaneous tissue in the left lower eyelid. *Abbreviations*: *d* dermis, *st* subcutaneous tissue, *m* muscle, *b* margin of the zygomatic bone

15.5 Mesotherapy

Mesotherapy is a procedure used for treating cellulite, aging skin, body contouring, and hair loss and incorporates the use of agents that are natural or synthetic lipolytic factors that presumably present anti-aging properties [21]. These agents could be injected or directly applied over the skin surface, however, their mechanisms of action and efficacy are not clearly described in the literature, and currently, they are not approved by the FDA for use for cosmetic purposes [22].

On sonography, injected deposits from mesotherapy can appear as dermal echoic pseudonodules that may imply a foreign body granulomatous reaction, with an anechoic center that seems to be related to liquefaction and/or necrosis [4]. Cryotherapy and cryolipolysis can elicit heterogeneous echogenicity or increased echogenicity of the subcutaneous tissue and some anechoic pseudocystic structures suggestive of concomitant areas of liquefaction and/or necrosis of the fatty tissue (Figs.15.18 and 15.19).

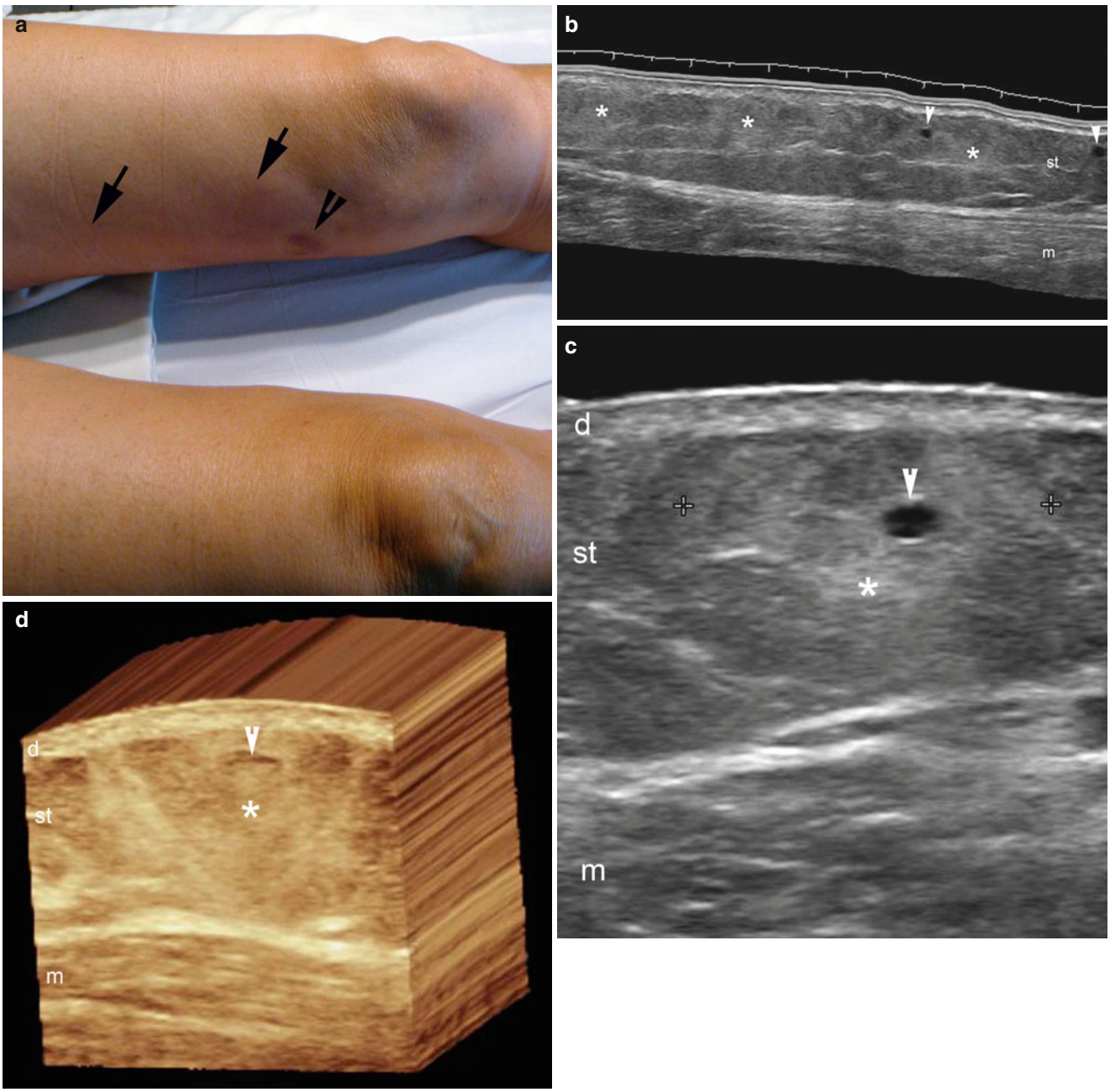

Fig. 15.18 (**a**–**d**) Mesotherapy-cryotherapy-cryolipolysis. (**a**) Clinical photograph of a patient with a history of recent cryotherapy and cryolipolysis (cool sculpting) in the medial aspect of the left thigh (*arrows*). There is a small hematoma (*arrowhead*) in the lower third of the thigh. (**b**–**d**) Grey scale ultrasound images (**b** longitudinal view; **c** transverse view; **d** 3D reconstruction transverse view) demonstrate increased echogenicity of the subcutaneous tissue (*, between markers) and some round-shaped, anechoic, pseudocystic structures (*arrowheads*) suggestive of liquefied fat (fat necrosis). *Abbreviations*: *d* dermis, *st* subcutaneous tissue, *m* muscle

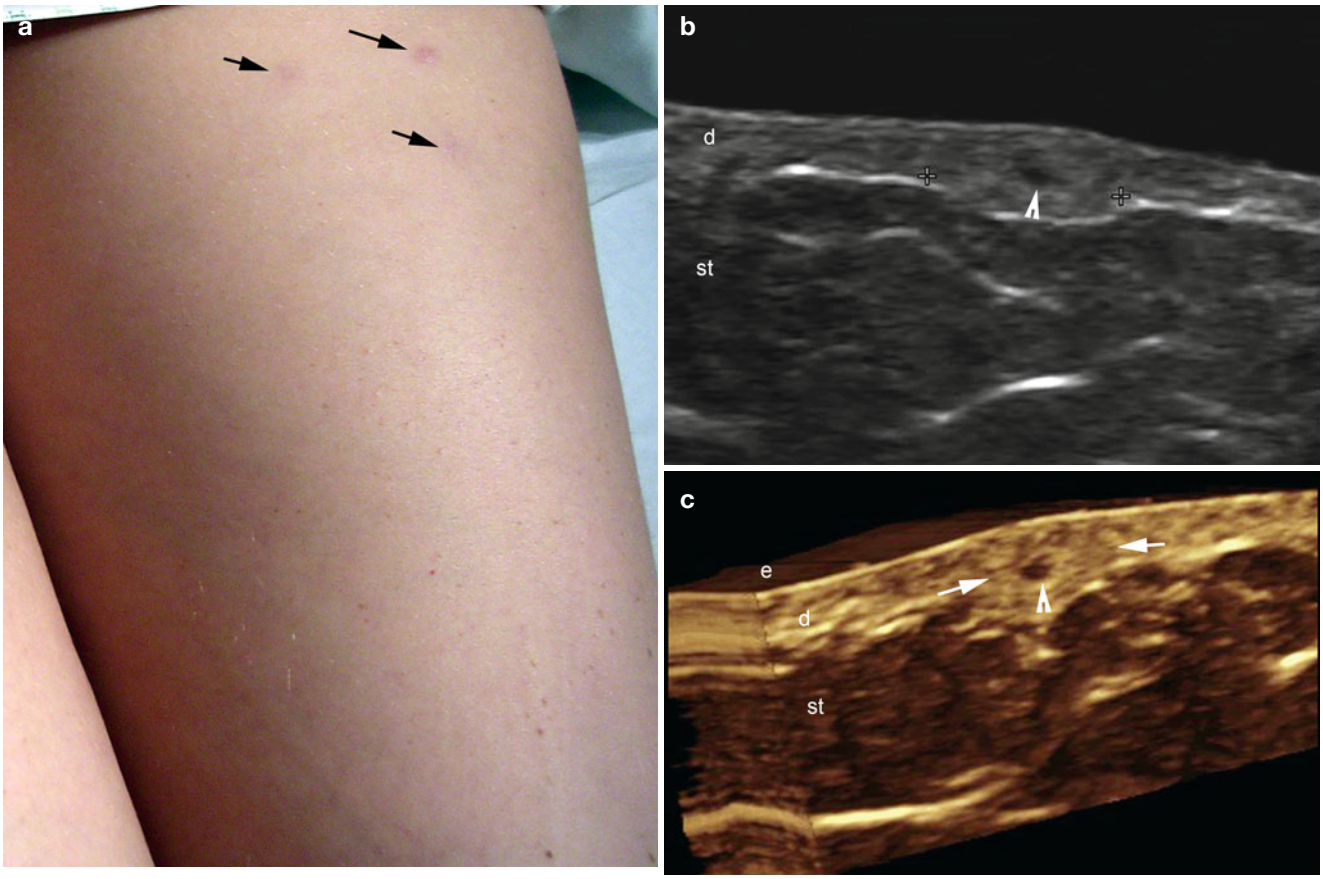

Fig. 15.19 (**a**–**c**) Mesotherapy. (**a**) Clinical image of a patient that developed erythematous papules (arrows) in the anterior aspect of the left thigh after mesotherapy. (**b**, **c**) Grey scale ultrasound images (**b** transverse view; **c** 3D reconstruction transverse view, right upper lesion) show a dermal oval shaped echoic pseudonodule (*markers* and *arrows*) with a small round shaped anechoic center (*arrowhead*). *Abbreviations*: *e* epidermis, *d* dermis, *st* subcutaneous tissue

15.6 Testosterone Injections

Testosterone injections are used by body builders to increase muscular volume, usually on both arms and thighs [23]. Self administration of this hormone, or administration of this agent by non-medical personnel, can produce muscle tears within the hypertrophied muscles. On sonography, hypoechoic focal linear lesions suggestive of partial thickness tears and/or hyperechoic areas within the muscles suggestive of edema are detected. Increased vascularity in the region can also be observed [4] (Fig. 15.20).

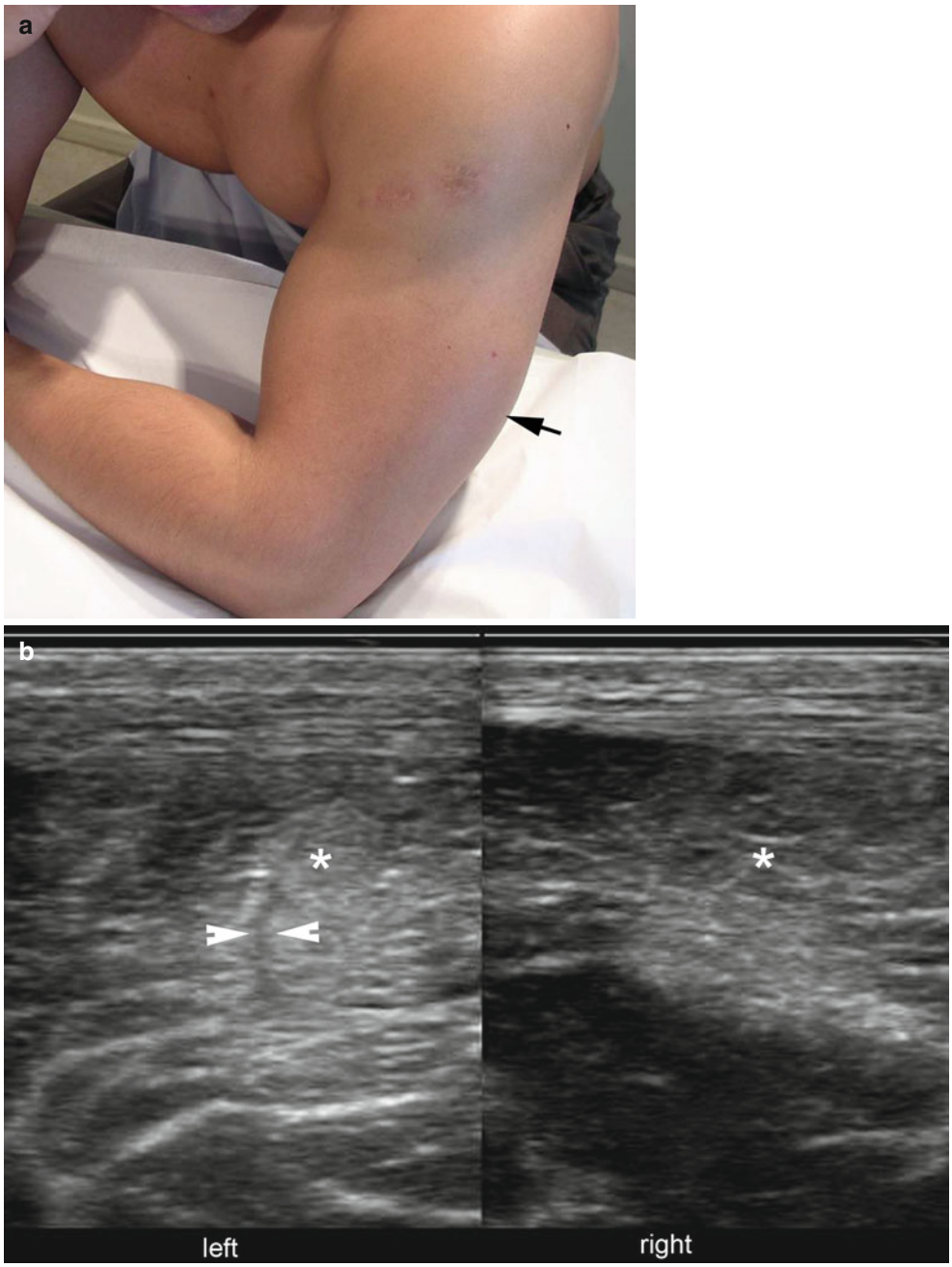

Fig. 15.20 (**a**, **b**) Testosterone injection. (**a**) Clinical image of a patient who presented with pain after self injection of testosterone in the posterior aspect of the left arm. The patient is a chronic user of self injections of testosterone in both arms. (**b**) Grey scale ultrasound image (transverse view, side by side comparison) shows increased echogenicity (*) and a hypoechoic band (*arrowheads*) consistent with a partial tear of the triceps muscle in the left side. There is also a focal increase of the echogenicity (*) of the right triceps muscle

15.7 Tensor Threads

Tensor threads are structures that are also called APTOS or "Russian Threads", that correspond to presumably non-reabsorbable polypropylene devices shaped like angled barbed threads that are commonly used for lifting facial area sagging [24]. These small barbs on each thread open in an umbrella-like fashion to form an anchoring structure that can lift the sagging skin. It is assumed that a fibroblastic reaction is produced that can generate new collagen bundles that would encapsulate each thread maintaining the lifting effect [24, 25]. Adverse effects have been reported in up to 69 % of patients, with 45 % of early recurrences, as well as instances of thread migration and partial expulsion of the device [26, 27].

On sonography, tensor threads appear as hyperechoic bilaminar structures with dots that are hyperechoic that correspond to the anchoring points or thorns [4] (Fig. 15.21).

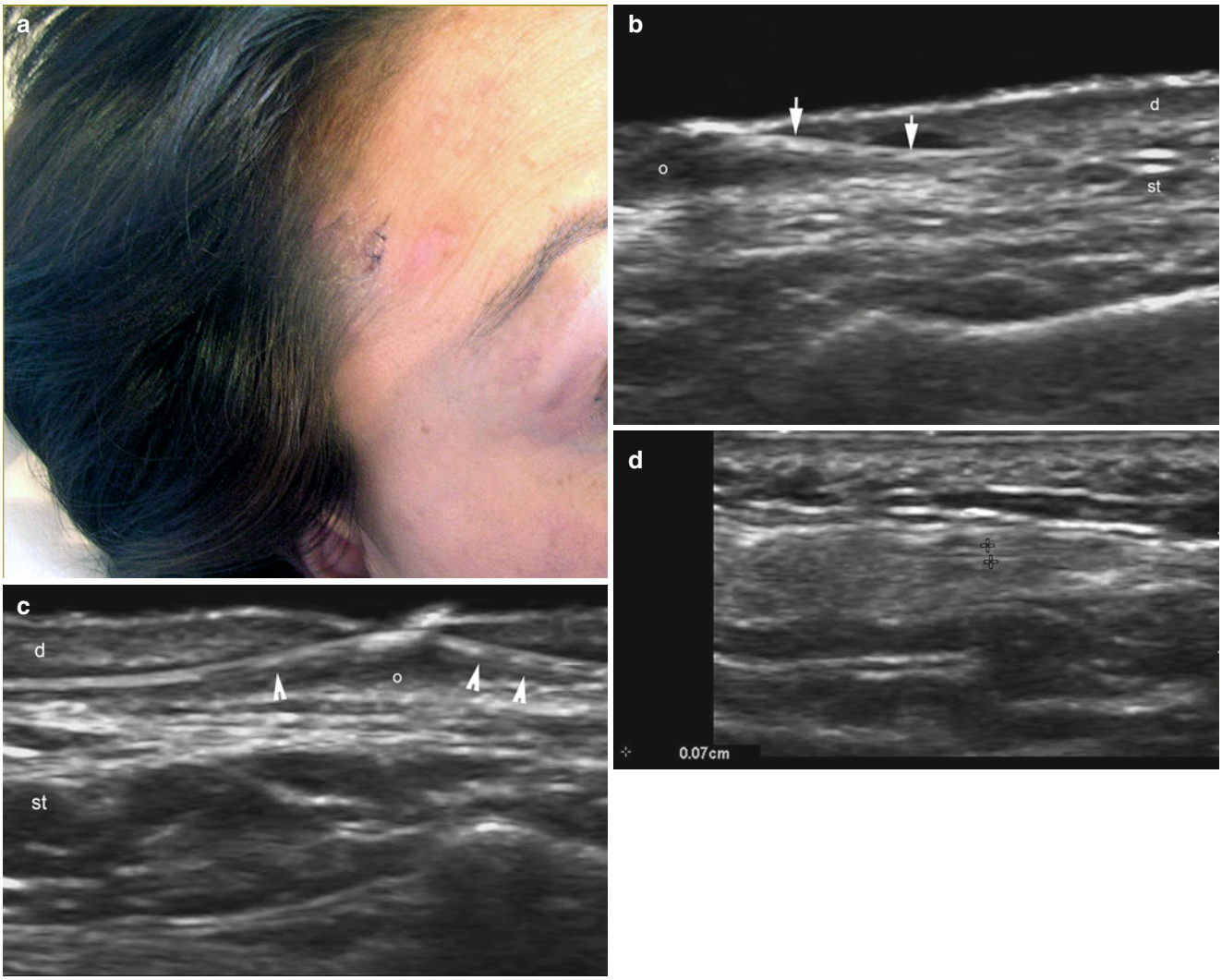

Fig. 15.21 (**a**–**d**) Tensor thread. (**a**) Clinical photograph of a patient with a history of an insertion of tensor threads in the temple and cheek regions. (**b**, **c**) Grey scale ultrasound images in the right temple region demonstrate a bilaminar hyperechoic structure (*arrows*) with hyperechoic dots (*arrowheads*). There is dermal hypoechoic tissue (o) surrounding the thread. (**d**) Grey scale ultrasound image (transverse view, left cheek) shows a 0.7 mm (thickness) bilaminar hyperechoic fragment of a thread (between markers) running through an accessory salivary gland on top of the masseter muscle. *Abbreviations*: *d* dermis, *st* subcutaneous tissue

15.8 Implants

Implants are commonly used for reshaping and augmentation, frequently in the breast, calf, and buttocks. Several types of implants are used that include the nose, chin, cheek, and jaws. Among the most common materials used in implants is silicone and less often, high-density porous polyethylene structures (HDPE). Implants may present multiple shapes such as convex, I-, or L-shaped structures [28, 29].

On sonography, pure silicone implants (including breast) present as an anechoic structure surrounded by a bilaminar hyperechoic layer. HDPE implants appear as hyperechoic bands and are commonly used in rhinoplasty. A hypoechoic inflammatory granulomatous reaction and/or cutaneous atrophy with shortening of the distance between the dermis and the implant can occasionally be detected under rupture or displacement of the implant [4] (Fig. 15.22).

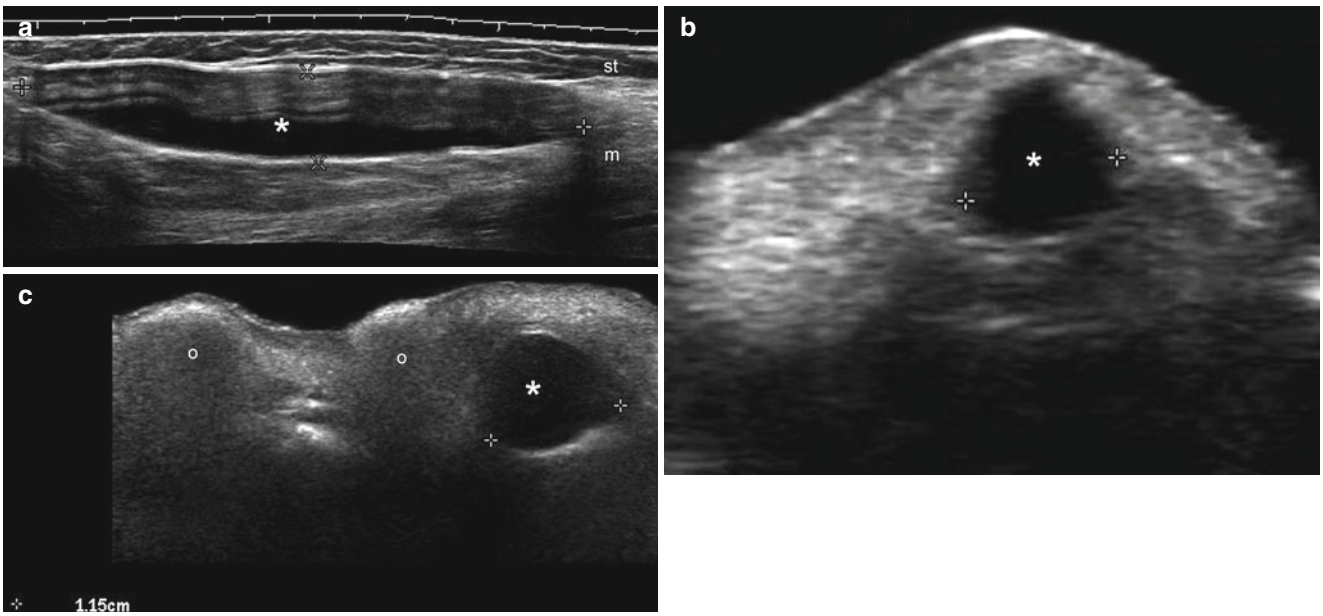

Fig. 15.22 (**a**–**c**) Silicone implants. (**a**) Calf implant. Grey scale ultrasound image (longitudinal view, right calf) shows a well-defined, oval-shaped, anechoic structure (*, between markers) located between the subcutaneous tissue (st) and the muscle (m) layer. (**b**) Nasal implant in the tip of the nose (longitudinal view) demonstrates a well-defined round-shaped, anechoic structure (*, between markers) located between the dermis and the nasal cartilages. (**c**) Chin implant. Grey scale ultrasound image (longitudinal view) shows a 1.15 cm well-defined round-shaped anechoic structure (*, between markers) in the subcutaneous tissue of the chin. Notice that there are also dermal and subcutaneous hyperechoic deposits (o) with a "snow storm" pattern that correspond to silicone oil in the same case

15.8.1 Acrylic Nails

Acrylic nails are common aesthetic implants used on the surface of the nails that consist of a synthetic non-degradable coating attached with glue to the ungual surface that covers the nail plates. Allergic reactions or interference with pulse oximetry measurements have been described [30–32]. Sound waves usually pass through the acrylic and therefore, do not alter the sonographic appearance of the nail unit. The acrylic agent presents as a hyperechoic linear structure attached to the normal bilaminar nail plates providing a trilaminar hyperechoic appearance [33]. Hyperechoic dots, corresponding to the adhesive agent (glue), can occasionally be detected between the acrylic deposits and nail plates [4] (Fig. 15.23).

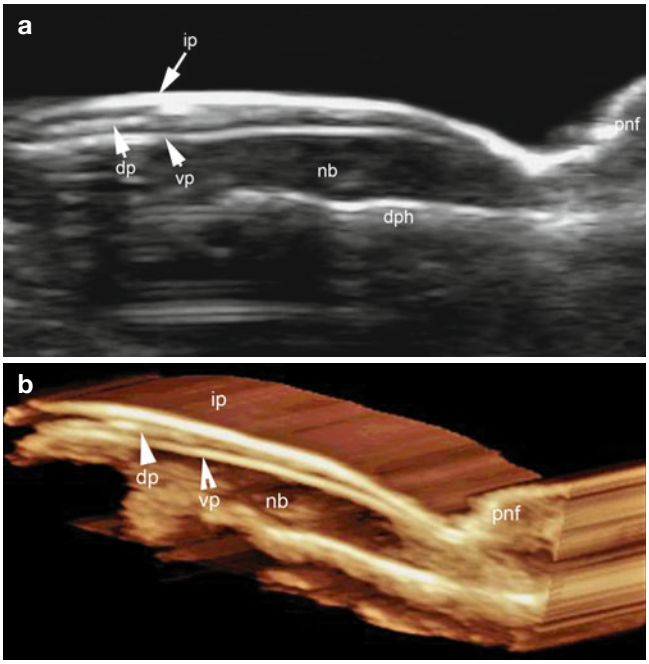

Fig. 15.23 (**a**, **b**) Acrylic nail implant. (**a** Grey scale ultrasound images (longitudinal view); and **b** 3D reconstruction) demonstrate a trilaminar hyperechoic pattern of the plates. The most superficial layer corresponds to the acrylic implant (ip, *arrow*). *Abbreviations*: *vp* ventral plate, *dp* dorsal plate, *nb* nail bed, *pnf* proximal nail fold, *dph* distal phalanx, *ip* acrylic implant

15.9 Plastic Surgery Procedures

15.9.1 Liposuction-Abdominoplasty

Liposuction implies a surgical aspiration of fatty lobules from the waist, arms, or hips and abdominoplasty is the surgical removal of subcutaneous abdominal fatty tissue with replacement of the rectus abdominis muscles and reconstruction of the umbilical zone [34]. The combination of these procedures is frequently performed, but higher risks of seroma of serohematomas are present with abdominoplasty, especially when performed in combination with liposuction of the flanks or on patients who are severely overweight [35, 36]. The fluid collections are usually close to the incision sites, such as the hypogastric region and the iliac fossa. In the early stages, these collections appear as predominantly exudates that turn into lymph-like deposits during later stages [37, 38].

On sonography, the areas of liposuction show a lack of hypoechoic fatty lobules, and instead show hyperechoic areas with interspersed deposition of anechoic bands of fluid or larger size collections [39]. Anechoic fluid collections of variable size and shape can be seen in the adjacent subcutaneous tissue. Changes in the morphology of the sheath of the rectus abdominis muscles, such as thickening and decreased echogenicity of the sheath, are also commonly detected. Anechoic round-shaped pseudocysts that represent fat liquefaction and/or necrosis may also be seen [4]. Rarely, a fragment from a broken catheter (bilaminar hyperechoic duct with an anechoic center) as a complication of abdominoplasty can be detected using sonography. Thus, ultrasound may guide the retrieval of the foreign body (Figs. 15.24, 15.25, 15.26, 15.27, and 15.28).

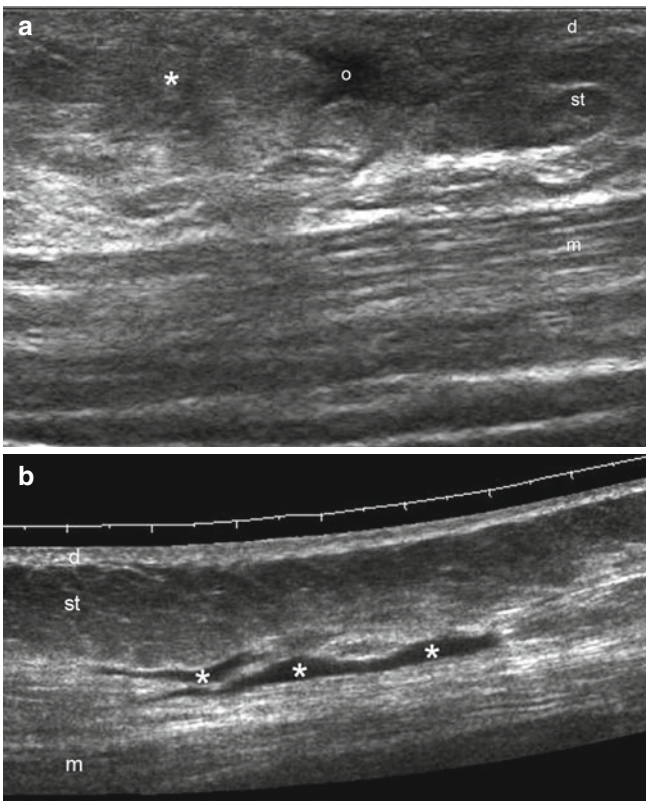

Fig. 15.24 (**a**, **b**) Liposuction. (**a**) Grey scale ultrasound image (longitudinal view) of the left flank of a patient with a history of recent liposuction. Notice the hyperechogenicity (*) of the subcutaneous tissue that lacks fatty lobules and presents a anechoic fluid sero-hematic collection (o). (**b**) A different case (longitudinal view, right flank) demonstrates anechoic bands of sero-hematic fluid collections (*) in the subcutaneous tissue. *Abbreviations*: *d* dermis, *st* subcutaneous tissue, *m* muscle

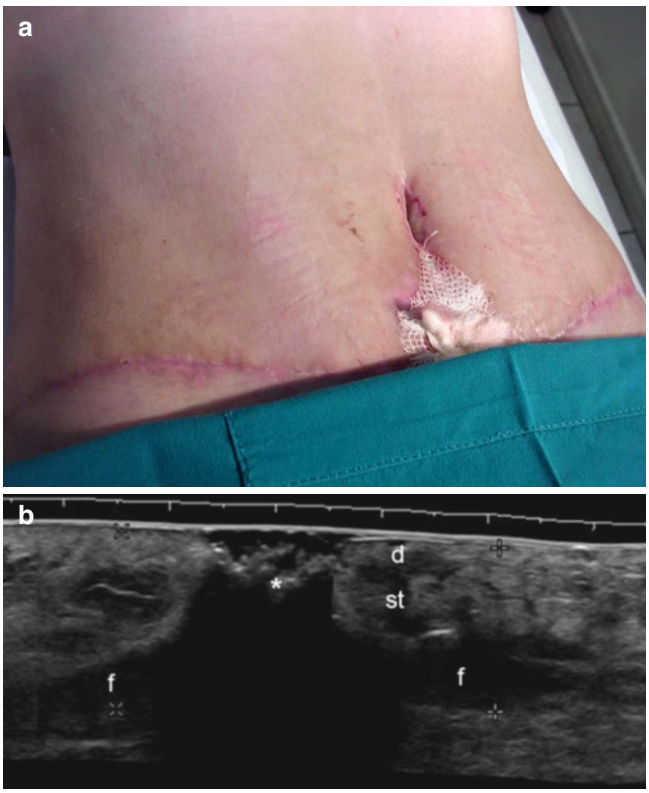

Fig. 15.25 (**a**, **b**) Abdominoplasty. (**a**) Clinical image of a patient with a history of recent abdominoplasty. (**b**) Grey scale ultrasound image (transverse view) shows a anechoic fluid collection (*f*) located between the subcutaneous tissue and the rectus abdominis muscles. The hyperechoic structure (*) in the surface that generates posterior acoustic shadowing artifact corresponds to the visible gauze. *Abbreviations*: *d* dermis, *st* subcutaneous tissue

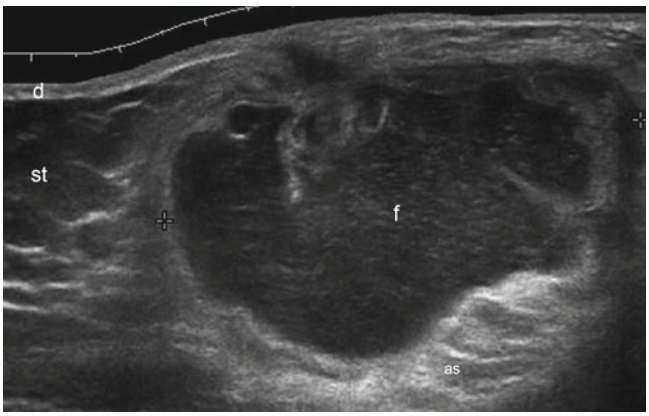

Fig. 15.26 Fluid collection after abdominoplasty. Grey scale ultrasound image (transverse view, anterior wall) demonstrates an oval-shaped anechoic fluid collection that presents echoes (debris) and posterior acoustic reinforcement (ar). *Abbreviations*: *d* dermis, *st* subcutaneous tissue

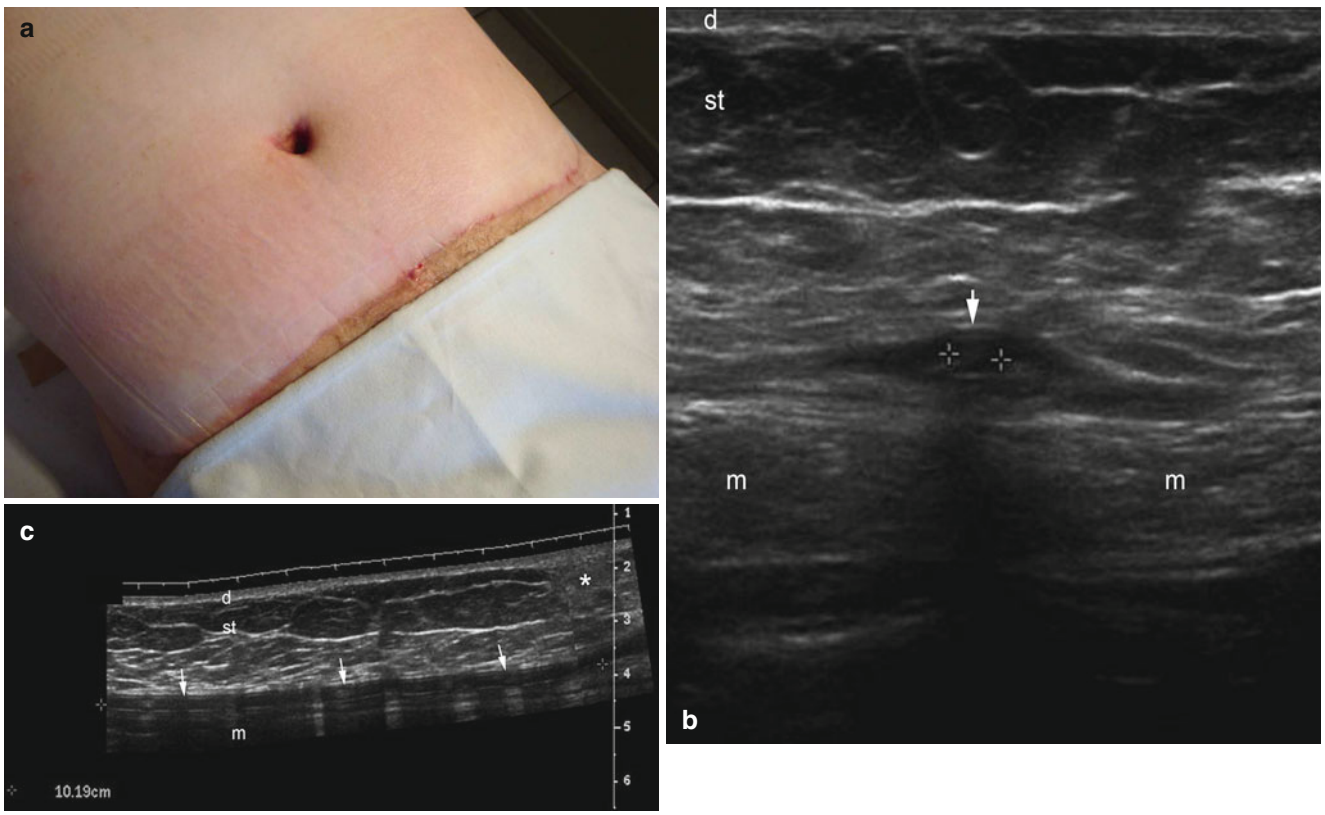

Fig. 15.27 (**a**–**c**) Catheter fragment after abdominoplasty. (**a**) Clinical photograph of a patient who presented with a history of a recent abdominoplasty and tenderness in the left flank. (**b**, **c**) Grey scale ultrasound images (**b** transverse view and **c** longitudinal view) demonstrate a 10.19 cm long duct (catheter) with bilaminar hyperechoic walls and anechoic center (*arrows*, between markers) located between the subcutaneous tissue and the left rectus abdominis muscle (m). Notice a focal area of increased echogenicity (inflammation) in the subcutaneous tissue (*, Fig. **c**). *Abbreviations*: *d* dermis, *st* subcutaneous tissue

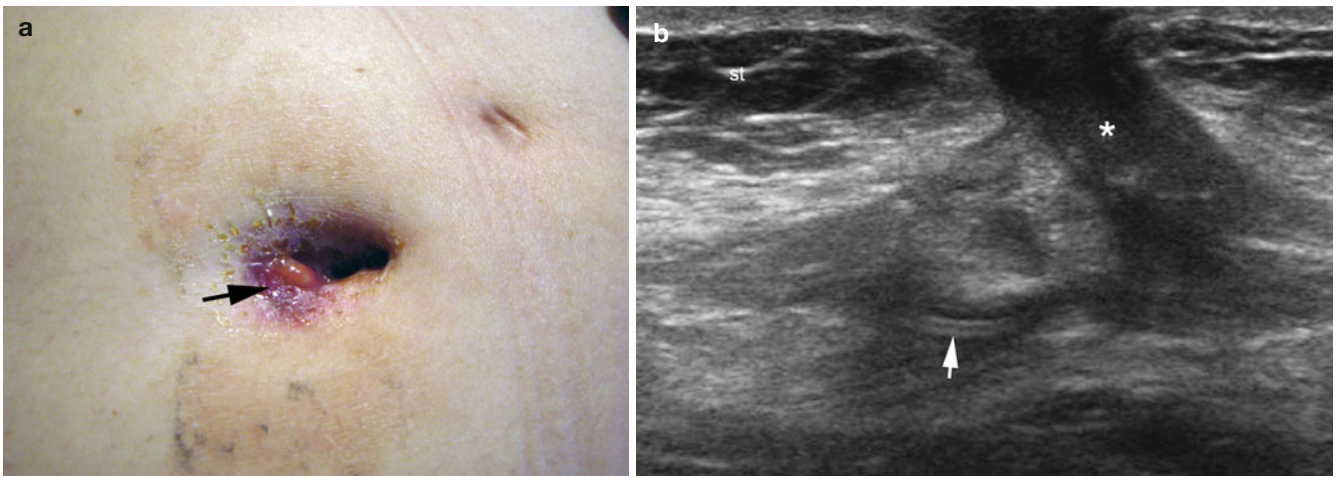

Fig. 15.28 (**a**, **b**) Fluid collection, fistulous tract, and fragment of a catheter after abdominoplasty. (**a**) Clinical image of the umbilical region in a patient with a history of abdominoplasty demonstrates erythematous swelling (*arrow*). (**b**) Grey scale ultrasound image (transverse view, umbilical region) shows hypoechoic fluid collection that connects through a fistulous tract (*) to the subepidermal region. Notice a bilaminar hyperechoic structure at the bottom of the collection that corresponds to a fragment of catheter (*arrow*). *Abbreviation*: *st* subcutaneous tissue

15.9.2 Blepharoplasty

Blepharoplasty is a procedure performed for the aesthetic remodeling of the eyelids. It implies the removal of excess (sagging) skin from the upper and/or lower lids usually caused by aging or severe exophthalmus. There are several different surgical techniques for approaching the upper and lower eyelids. Occasionally, there are complications derived from extensive skin removal, damage to tarsal structures, or orbicular muscles, but rarely orbital abscesses. It is possible that granulomas may develop after blepharoplasty as a foreign body reaction. Additionally, transfer of harvested fat can be used for filling hollow–looking eyelids.

Sonography allows characterization of the extent of skin removal, demonstrates fluid collections, and may confirm suture loosening [4, 40–42]. On ultrasound, granulomas appear as well-defined round or oval-shaped hypoechoic structures. Sonography can also show the extent of harvested fat that is transferred into the eyelids (Figs. 15.29 and 15.30).

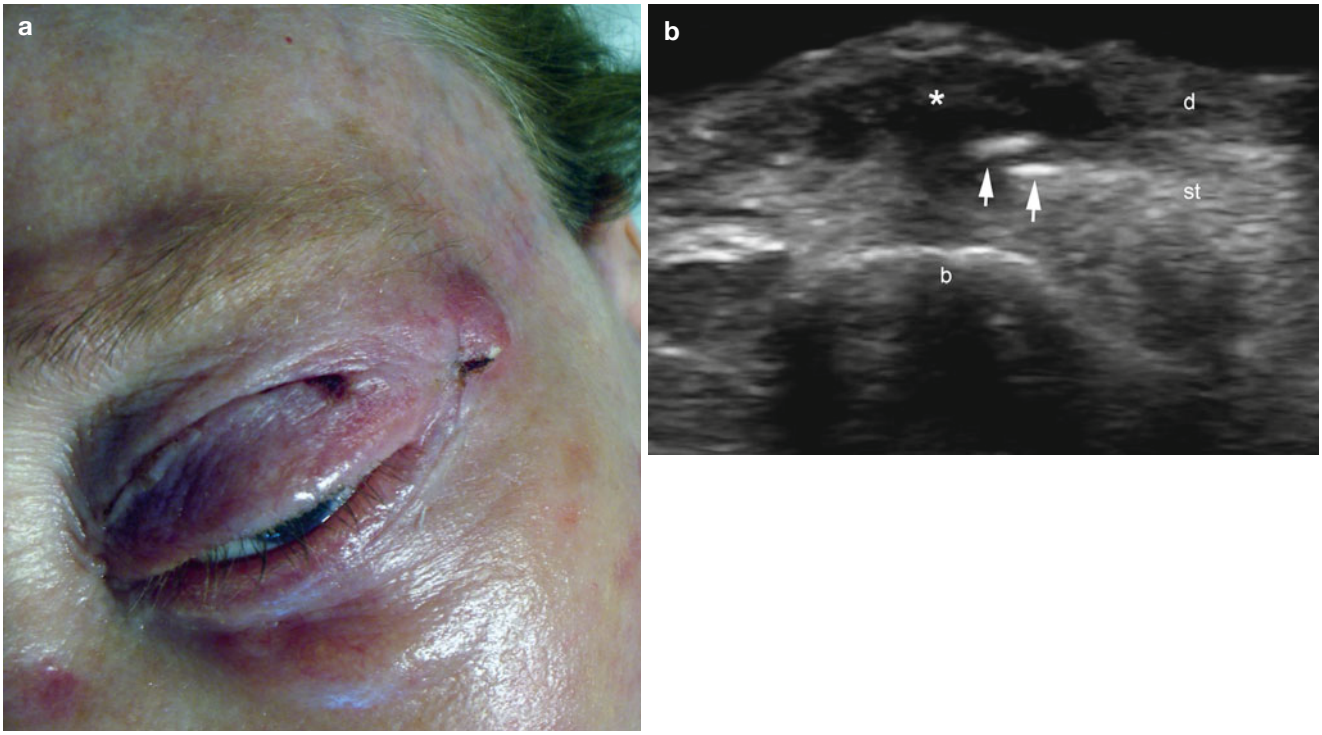

Fig. 15.29 (**a**, **b**) Loose sutures after blepharoplasty. (**a**) Clinical photograph shows erythema and edema of the eyelids and the external periocular region after blepharoplasty. (**b**) Grey scale ultrasound image (longitudinal view) demonstrates two hyperechoic linear fragments (*arrows*) that correspond to loose sutures in the subcutaneous tissue. An anechoic sero-hematic fluid collection (*) is surrounding the sutures. *Abbreviations*: *d* dermis, *st* subcutaneous tissue, *b* bony margin

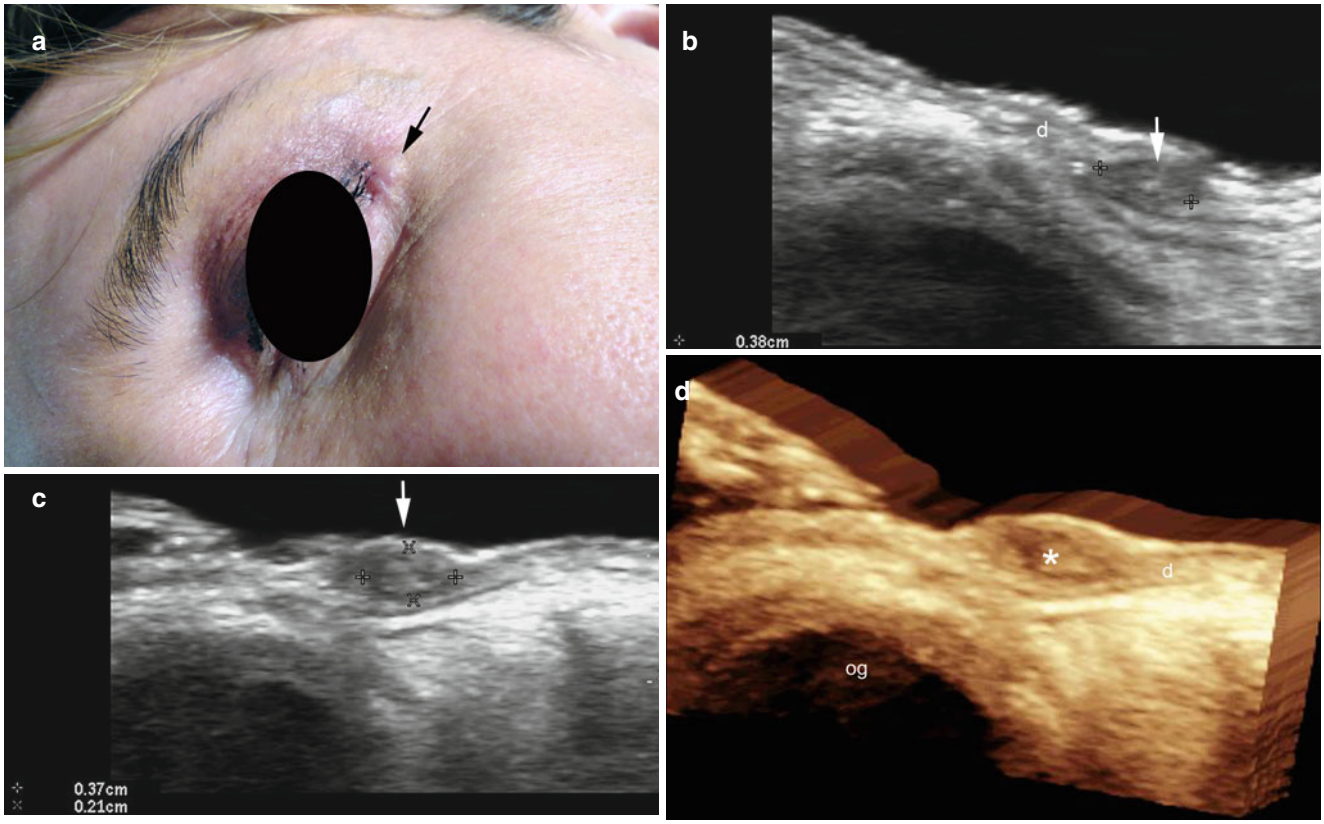

Fig. 15.30 (**a**–**d**) Granuloma after blepharoplasty. (**a**) Clinical image demonstrates a erythematous lump (*arrow*) in the external canthus of the left eye. (**b**–**d**) Grey scale ultrasound images (**b** longitudinal view; **c** transverse view and **d** 3D reconstruction longitudinal view) show a 3.8 mm (long) × 3.7 mm (transverse) × 2.1 mm (depth) well-defined, oval-shaped dermal hypoechoic solid structure (*, between markers, arrow). *Abbreviations*: *d* dermis, *og* ocular globe

15.9.3 Rhinoplasty

Rhinoplasty, also called "nose reshaping," is a type of plastic surgery usually performed for aesthetic or reconstructive purposes and includes partial or complete remodeling of the nose. Rhinoplasty can be combined with other plastic surgery procedures such as chin augmentation. Augmentation rhinoplasty most commonly uses synthetic agents such as alloplastic implants that include: silicone, supramid mesh, Proplast, Mersiline, Medpor, Porex, polytetrafluoroethylene (Gore-Tex), and hydroxyapatite [43–45]. Additionally, this procedure involves a remodeling of the nasal bones and cartilages, therefore, complications can include anechoic serohematic fluid collections, loosening of sutures commonly used for anchoring the nasal cartilage, and irregularities in the nasal cartilage or bones. Late complications of rhinoplasty include the deposition of granulomatous tissue under the dorsum of the nose that can increase the local vascularity and mimic rosacea.

Irregularities or lack of the normal smooth contour of nasal cartilages can be detected using sonography. Granulomas are mostly seen at the tip of the nose and appear as hypoechoic tissue with blurriness of the margins between the granuloma and the nasal cartilages, as well as variable degrees of vascularity. Bony grafts within the nose are hyperechoic and generate a posterior acoustic shadowing artifact typically seen in calcified structures. Secondary vascular malformations, commonly related to the surgical trauma, can occur and ultrasound can support the diagnosis and characterization of the lesion (high flow or low flow) and determine the predominant type of vessel (e.g., arterial, venous, or mixed) as well as the velocity of the blood flow. Pre- or post-surgical anatomical details about the extension of the changes and the nasal cartilage condition can also be derived from the ultrasound report [4, 46, 47] (Fig. 15.31).

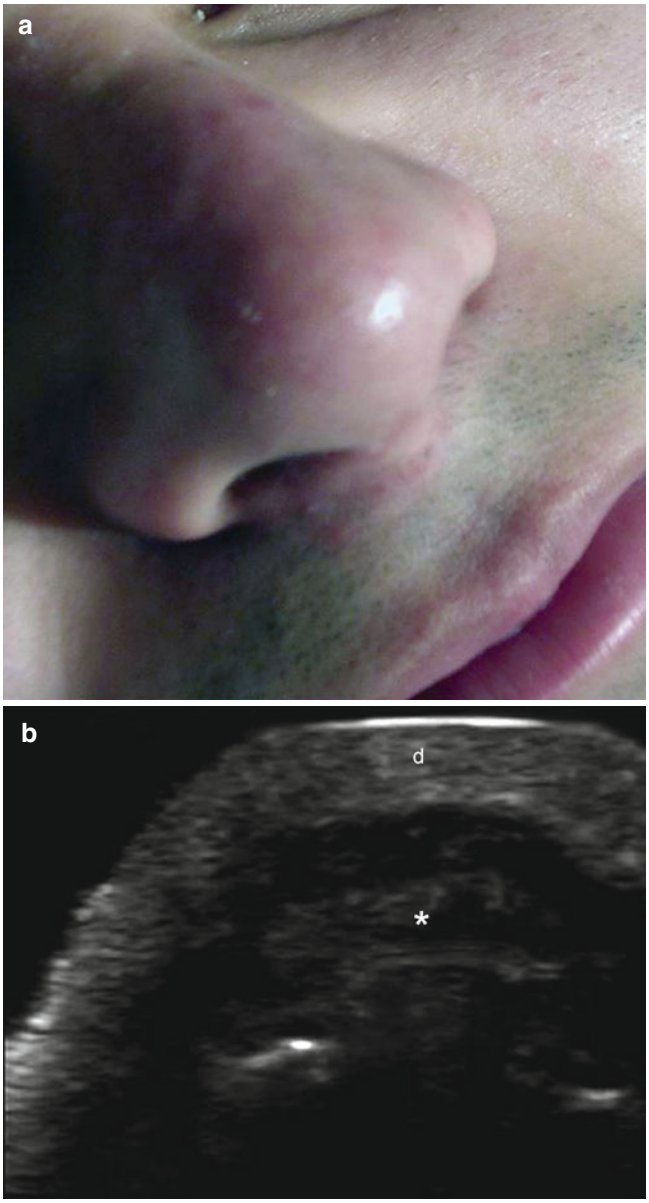

Fig. 15.31 (**a**, **b**) Granuloma after rhinoplasty. (**a**) Clinical photograph shows erythema and edema in the dorsum and tip of the nose. (**b**) Grey scale ultrasound image (transverse view) demonstrates hypoechoic granulomatous tissue (*) attached to the nasal cartilages without a clear definition of the borders of the granuloma and the nasal cartilages. *Abbreviation*: *d* dermis

References

1. Gniadecka M, Gniadecki R, Serup J, Søndergaard J. Ultrasound structure and digital image analysis of the subepidermal low echogenic band in aged human skin: diurnal changes and interindividual variability. J Invest Dermatol. 1994;102:362–5.
2. Sanders V, Herane MI, Orlandi C, Zegpi E, Valdes P, Ancic X. Clinical efficacy of adapalene (Differin®) 0.3 % gel in Chilean women with cutaneous photoaging. J Dermatolog Treat. 2012;23:57–64.
3. Flynn TC. Botulinum toxin: examining duration of effect in facial aesthetic applications. Am J Clin Dermatol. 2010;11:183–99.
4. Wortsman X, Wortsman J. Sonographic outcomes of cosmetic procedures. AJR Am J Roentgenol. 2011;197:W910–8.
5. Werschler WP, Weinkle S. Longevity of effects of injectable products for soft-tissue augmentation. J Drugs Dermatol. 2005;4:20–7.
6. Burgess CM, Quiroga RM. Assessment of the safety and efficacy of poly-L-lactic acid for the treatment of HIV-associated facial lipoatrophy. J Am Acad Dermatol. 2005;52:233–9.
7. Wortsman X, Wortsman J, Orlandi C, Cardenas G, Sazunic I, Jemec GBE. Ultrasound detection and identification of cosmetic fillers in the skin. J Eur Acad Dermatol Venereol. 2012;26:292–301.
8. Bailey SH, Cohen JL, Kenkel JM. Etiology, prevention, and treatment of dermal filler complications. Aesthet Surg J. 2011;31:110–21.
9. Hevia O. Six-year experience using centistokes silicone oil in 916 patients for soft tissue augmentation in a private practice setting. Dermatol Surg. 2009;35:1646–52.
10. Jacinto SS. Ten-year experience using injectable silicone oil for soft tissue augmentation in the Philippines. Dermatol Surg. 2005;31:1550–4.
11. Wortsman X. Common applications of dermatologic sonography. J Ultrasound Med. 2012;31:97–111.
12. Carvalho Costa IM, Salaro CP, Costa MC. Polymethylmethacrylate facial implant: a successful personal experience in Brazil for more than 9 years. Dermatol Surg. 2009;35:1221–7.
13. Bagal A, Dahiya R, Tsai V, Adamson PA. Clinical experience with polymethylmethacrylate microspheres (Artecoll) for soft-tissue augmentation: a retrospective review. Arch Facial Plast Surg. 2007;9:275–80.
14. Haneke E. Polymethyl methacrylate microspheres in collagen. Semin Cutan Med Surg. 2004;23:227–32.
15. Ridenour B, Kontis TC. Injectable calcium hydroxylapatite microspheres (Radiesse). Facial Plast Surg. 2009;25:100–5.
16. Rauso R, Freda N, Parlato V, Gherardini G, Amore R, Tartaro G. Polyacrylamide gel injection for treatment of human immunodeficiency virus-associated facial lipoatrophy: 18 months follow-up. Dermatol Surg. 2011;37:1584–9.
17. Mansor S, Breiting VB, Dahlstrøm K, Andersen AB, Andersen O, Christensen LH. Polyacrylamide gel treatment of antiretroviral therapy-induced facial lipoatrophy in HIV patients. Aesthetic Plast Surg. 2011;35:709–16.
18. Wortsman X, Wortsman J. Polyacrylamide fillers on skin ultrasound. J Eur Acad Dermatol Venereol. 2012;26:660–1.
19. Wang H, Jiang Y, Meng H, Zhu Q, Dai Q, Qi K. Sonographic identification of complications of cosmetic augmentation with autologous fat obtained by liposuction. Ann Plast Surg. 2010;64:385–9.
20. Sclafani AP. Applications of platelet-rich fibrin matrix in facial plastic surgery. Facial Plast Surg. 2009;25:270–6.
21. Brown SA. The science of mesotherapy: chemical anarchy. Aesthet Surg J. 2006;26:95–8.
22. Atiyeh BS, Ibrahim AE, Dibo SA. Cosmetic mesotherapy: between scientific evidence, science fiction, and lucrative business. Aesthetic Plast Surg. 2008;32:842–9.
23. Sinha-Hikim I, Artaza J, Woodhouse L, Gonzalez-Cadavid N, Singh AB, Lee MI, et al. Testosterone-induced increase in muscle size in healthy young men is associated with muscle fiber hypertrophy. Am J Physiol Endocrinol Metab. 2002;283:154–64.
24. Sulamanidze M, Sulamanidze G. APTOS suture lifting methods: 10 years of experience. Clin Plast Surg. 2009;36:281–306.
25. Sulamanidze MA, Fournier PF, Paikidze TG, Sulamanidze GM. Removal of facial soft tissue ptosis with special threads. Dermatol Surg. 2002;28:367–71.
26. Rachel JD, Lack EB, Larson B. Incidence of complications and early recurrence in 29 patients after facial rejuvenation with barbed suture lifting. Dermatol Surg. 2010;36:348–54.
27. Silva-Siwady JG, Díaz-Garza C, Ocampo-Candiani J. A case of Aptos thread migration and partial expulsion. Dermatol Surg. 2005;31:356–8.
28. Binder WJ. Facial rejuvenation and volumization using implants. Facial Plast Surg. 2011;27:86–97.
29. Deshpande S, Munoli A. Long-term results of high-density porous polyethylene implants in facial skeletal augmentation: an Indian perspective. Indian J Plast Surg. 2010;43:34–9.
30. Haughton AM, Belsito DV. Acrylate allergy induced by acrylic nails resulting in prosthesis failure. J Am Acad Dermatol. 2008;59:123–4.
31. Lazarov A. Sensitization to acrylates is a common adverse reaction to artificial fingernails. J Eur Acad Dermatol Venereol. 2007;21:169–74.
32. Hinkelbein J, Koehler H, Genzwuerker HV, Fiedler F. Artificial acrylic finger nails may alter pulse oximetry measurement. Resuscitation. 2007;74:75–82.
33. Wortsman X, Jemec GB. Ultrasound imaging of nails. Dermatol Clin. 2006;24:323–8.
34. Berry MG, Davies D. Liposuction: a review of principles and techniques. J Plast Reconstr Aesthet Surg. 2011;64:985–92.
35. Kim J, Stevenson TR. Abdominoplasty, liposuction of the flanks, and obesity: analyzing risk factors for seroma formation. Plast Reconstr Surg. 2006;117:773–9.
36. Najera RM, Asheld W, Sayeed SM, Glickman LT. Comparison of seroma formation following abdominoplasty with or without liposuction. Plast Reconstr Surg. 2011;127:417–22.
37. Di Martino M, Nahas FX, Barbosa MV, Montecinos Ayaviri NA, Kimura AK, Barella SM, et al. Seroma in lipoabdominoplasty and abdominoplasty: a comparative study using ultrasound. Plast Reconstr Surg. 2010;126:1742–51.
38. Andrades P, Prado A. Composition of postabdominoplasty seroma. Aesthetic Plast Surg. 2007;31:514–8.
39. Mohammad JA, Warnke PH, Stavraky W. Ultrasound in the diagnosis and management of fluid collection complications following abdominoplasty. Ann Plast Surg. 1998;41:498–502.
40. Perkins SW, Prischmann J. The art of blepharoplasty. Facial Plast Surg. 2011;27:58–66.
41. Rousso DE, Brys AK. Extended lower eyelid skin muscle blepharoplasty. Facial Plast Surg. 2011;27:67–76.
42. Rees TD, Craig SM, Fisher Y. Orbital abscess following blepharoplasty. Plast Reconstr Surg. 1984;73:126–7.
43. Sajjadian A, Guyuron B. Primary rhinoplasty. Aesthet Surg J. 2010;30:527–39.
44. Menick FJ. Nasal reconstruction. Plast Reconstr Surg. 2010;125:138–50.
45. Arneja JS, Chim H, Drolet BA, Gosain AK. The Cyrano nose: refinements in surgical technique and treatment approach to hemangiomas of the nasal tip. Plast Reconstr Surg. 2010;126:1291–9.
46. Hong JP, Yoon JY, Choi JW. Are polytetrafluoroethylene (Gore-Tex) implants an alternative material for nasal dorsal augmentation in Asians? J Craniofac Surg. 2010;21:1750–4.
47. Rettinger G, Steininger H. Lipogranulomas as complications of septorhinoplasty. Arch Otolaryngol Head Neck Surg. 1997;123:809–14.

Inflammatory Diseases of the Nail: Clinical Overview

16

Robert Baran

Contents

R. Baran, MD
Nail Diseases Center,
42, rue des Serbes, Cannes 06400, France

Department of Dermatology,
Gustave Roussy Cancer Institute, Villejuif, France
e-mail: baran.r@wanadoo.fr, baran.r@club-internet.fr

16.1 Introduction

Diseases of the nail and its adjacent tissues rank among the most interesting and fascinating diseases that "flesh is heir to." Diagnosis for these diseases may require examinations such as histology, hematology, radiography, magnetic resonance imaging, and scintigraphy. Advancing technology has recently taken a leap forward with the development of 2D and 3D ultrasound. This development in investigative techniques combines ease of use with economy of cost.

16.2 Psoriasis

Five per cent of patients with nail psoriasis do not show any skin involvement [1].

The histology of psoriasis is an inflammatory parakeratotic papule. This same inflammatory papule occurs in the nails of psoriatic patients and the location of the papule determines the clinical presentation [2].

Erythematous scaly papules and plaques can be seen on the cutaneous surface of the proximal nail fold (PNF) and hyponychium. Their appearance is similar to psoriasis in other areas of the skin. A psoriatic lesion of the undersurface of the PNF produces a separation of the PNF from the nail plate with a secondary paronychia.

Psoriatic lesions can occur in the proximal portion of the matrix or in the distal matrix. A cluster of abnormal parakeratotic cells is incorporated into the dorsal surface of the nail if the lesion is present in the proximal matrix. These loosely arranged cells might travel with the nail plate for a short distance but are lost quickly, and pits (Fig. 16.1) mark the prior location of these cells. If the parakeratotic cells are in the central or distal portion of the matrix, they are "trapped" within the nail plate and reflected light gives the nail plate an opaque white appearance.

Psoriatic lesions can occur in the nail bed. The subungual area can frequently present with hyperkeratosis (Fig. 16.2) or

X. Wortsman, G.B.E. Jemec (eds.), *Dermatologic Ultrasound with Clinical and Histologic Correlations*,
DOI 10.1007/978-1-4614-7184-4_16,

Fig. 16.1 Nail pitting

Fig. 16.2 Onycholysis with proximal erythematous border

onycholysis, whereas typical cases are proximally surrounded by an erythematous line (Fig. 16.3). A deeply erythematous macule can be seen through the translucent nail plate. Psoriatic lesions produce glycoproteins that accumulate under the nail and present clinically with the "oil dropping"' sign.

Fig. 16.3 Subungual hyperkeratosis

Fig. 16.4 Transverse leuconychia of the thumb

A constellation of the findings described here is usually seen, depending on the location of the psoriatic lesions. A completely dystrophic nail characterized by mounds of keratinaceous debris can be seen if the psoriatic lesion is particularly large, especially in pustular psoriasis or acrodermatitis continua of Hallopeau. The severity of nail disease can be correlated with skin disease that is severe and psoriatic arthritis that is advanced [3–8].

Intermittent inflammation of the nail matrix can produce Beau's lines. Other less common nail changes described in psoriasis are nail fold telangiectasias, red lunulae, punctuate red spots in the lunula, transverse leukonychia (Fig. 16.4), and leukonychia punctata.

Ten to twenty percent of patients with psoriasis present with psoriatic arthritis (PsA), and patients with PsA commonly have nail involvement (53–86 %).

Psoriatic onychopathy may present varying degrees of alterations on ultrasound in both the nail bed and the nail

plate. These abnormalities (from early to late phases) are the thickening of the nail bed (increased distance between the ventral plate and the bony margin of the distal phalanx); increased blood flow within the nail bed; loss of definition of the ventral plate; hyperechoic focal involvement of the ventral plate (that can be subclinical) usually correlating with the subungual keratosis and can present without involvement of the dorsal plate. Thickening, loss of definition, and undulation of both nail plates can be detected in the late phases.

The assessment of activity in psoriatic onychopathy is possible using sonography. On color Doppler ultrasound, registration of the basal activity (blood flow and sonographic anatomical changes) can be compared with the modifications detected on a follow-up examination.

Fig. 16.5 Discoid type of lupus erythematosus (Courtesy B. Richert, Belgium)

16.3 Lupus Erythematous

Lupus erythematous is a multisystemic connective tissue disease, characterized by the presence of numerous auto-antibodies, circulating immune complexes, and widespread immunologically determined tissue damage [9, 10] (Figs. 16.5 and 16.6).

16.3.1 Arthritis, Arthralgia, and Fever

Arthritis can be transient, migratory, or a more persistant seronegative polyarthritis.

16.3.2 Skin Lesions

Skin lesions are seen in more than two thirds of patients. In addition to the classic, photosensitive, erythematous butterfly rash across the face, a vasculitic rash can present as purpura or periungual erythema with "chilblain-like" lesions or digital infarcts.

Cardiopulmonary features, renal, and central nervous system involvement can be associated with the joint and cutaneous signs.

Interestingly, blood flow abnormalities that involve the digital arteries and nail bed can be detected using color Doppler ultrasound. These changes include thrombotic phenomena within the distal end of the digital arteries that can cause secondary hypovascular changes in the nail bed leading to dystrophic changes. Thus, variable areas of thickness can be seen in the nail bed, together with thickening and thinning areas associated with this secondary dystrophy that can be accompanied by a discontinuity of the nail plates.

Fig. 16.6 Ulceration of the proximal nail fold in lupus erythematosus (Courtesy B. Richert, Belgium)

16.4 Scleroderma

Initially, there is often well-demarcated non-pitting oedema and induration associated with 'sausage' swelling and restriction of movement of the fingers seen in scleroderma [11]. Later, the skin becomes shiny, with atrophy and ulceration of the fingertips, with or without associated calcinosis. The skin of the face, limbs, and torso is variably affected and there can be striking pigmentation and telangiectasia. As the disease progresses, the face can become taut and mask-like, with 'beaking' of the nose and difficulty in opening the mouth. The tightening of the skin over bony prominences results in flexion contractures and liability to trauma. Often there is erythema and dilated capillaries of the PNFs.

Systemic sclerosis can affect both microvascular structures and functions of the nail unit. These changes have been previously registered by using other imaging modalities such as laser, Doppler, thermal imaging, and nailfold capillaroscopy. Giant capillaries, hemorrhages, and/or avascular areas have been described in scleroderma using such imaging modalities. Thus, vascular abnormalities are one of the primary pathologic components of scleroderma (Figs. 16.7 and 16.8).

Thickening and decreased echogenicity of the nail bed with an upward displacement of the nail plates can be seen using ultrasound, and is probably related to edema and/or chronic inflammatory changes. Hypovascularity of the nail bed is sometimes detected and can be related to changes at the microvascularity level.

Fig. 16.7 Systemic sclerodermia with vascular impairment of the distal digits

Fig. 16.8 Same patient as in Fig. 16.7, late stage (Courtesy N. Rowell)

16.5 Dermatomyositis

16.5.1 Adult Dermatomyositis [11]

Adult dermatomyositis is more common in women than in men. Acute or subacute muscle weakness is accompanied by periorbital edema and a characteristic violet "heliotrope" rash on the upper eyelids. Additionally, a photosensitive, erythematous, scaling rash on the face, shoulders, upper arms, and chest with red patches over the knuckles, elbows, and knees can be seen. Muscle pain, tenderness, and weight loss are common, as are arthralgia and mild inflammatory polyarthritis.

Inflammatory myositis can be associated with malignancy.

16.5.2 Childhood Dermatomyositis [11]

Childhood dermatomyositis most commonly affects children between the ages of 4 and 10 years old. Muscle weakness is usually accompanied by the typical rash of dermatomyositis and muscle atrophy, contractures, and subcutaneous calcification can be widespread and severe.

Many periungual capillary changes have been described in active juvenile dermatomyositis, among them dilated and tortuous blood vessels, areas of atrophy, telangiectases, central areas of hemorrhages, splinter hemorrhages, and bushy capillary loop formation in the PNF.

Color Doppler ultrasound may register vascularity changes in the nail bed and also detect periungual calcinosis deposits that are frequently located in the fingertips. Calcinosis appears on ultrasound as hyperechoic focal deposits frequently presenting posterior acoustic shadowing typical of the calcium component.

16.6 Rheumatoid Arthritis

Rheumatoid arthritis (RA) is the most common form of chronic inflammatory joint disease. In its typical form, RA is a symmetrical, destructive, and deforming polyarthritis affecting small and large synovial joints, with associated systemic disturbance, a variety of extra-articular features, and the presence of circulating antiglobulin antibodies (rheumatoid factors).

RA is a chronic progressive disorder characterized by symmetric inflammatory arthritis in association with systemic symptoms. Although considered a "joint disease," RA is associated with involvement in diverse organ systems, including the skin and nails. Clinical nail abnormalities that are commonly described that are associated with RA are longitudinal ridging and clubbing [11].

Identification of anatomic changes in the joint, bony margins, tendons, and soft tissues can be visualized using color Doppler ultrasound. The alterations include narrowing of the joint space, tendinosis (degeneration of the fibrillar pattern of the tendon), tear or atrophy of extensor and flexor tendons, erosions of the bony margin, periarticular and peritendinous edema, thickening decreased echogenicity, and increased blood flow in the nail bed.

16.7 Lichen Planus

The etiology of lichen planus is unknown, there is however, some evidence for a genetic susceptibility. Primary immunological disturbance is another likely hypothesis. Nail involvement of one or all the nail components occurs in 10 % of patients with lichen planus, and clinical features depend on the site affected by the pathological process [2].

16.7.1 Nail Fold Involvement

The dorsum of the PNF can be blue or red with or without swelling, and indicates that the proximal matrix is the origin of the lesion and that nail plate changes are likely to occur soon afterward.

16.7.2 Matrix Disease

A small focus of lichen planus in the matrix can present as a bulge under the PNF. The nail gradually reflects the disease process with a longitudinal red line indicating a thinned nail plate evolving into a distal split. The lunula can also be red, either in a focal or generalized pattern, and the next stage is a complete split. The matrix disease is relatively advanced and there can be pterygium formation between the underlying matrix disease and the overlying PNF. The most drastic form of matrix disease is seen in ulcerative lichen planus (Fig. 16.9) where complete, and sometimes irreversible, nail

Fig. 16.9 Ulcerative lichen planus

loss combines with large areas of bullae formation and erosion, usually on the soles of the feet and sometimes on the palms of the hands.

Focal disease that does not proceed to significant scarring may leave pigmentary changes similar to lesions seen on the skin. Longitudinal ridging can be a manifestation of lichen planus where disease matrix involvement results in selective atrophy of the nail plate.

16.7.3 Nail Bed Disease

Lichen planus seldom exclusively involves the nail as subungual hyperkeratosis or onycholysis.

16.7.4 Prognosis

The prognosis of the disease depends on the degree of matrix involvement and scarring with pterygium formation.

16.8 Lichen Striatus

Lichen striatus is a linear dermatosis of unknown etiology. It is characterized by the sudden appearance of erythematous, squamous, or lichenoid papules arranged on a continuous or interrupted streak involving the entire length of an extremity. It can extend along a finger or a toe as far as the PNF and affect the nail plate [12]. Several types of nail dystrophy include fraying, longitudinal splitting, punctuate or transverse leuconychia, shredding, onycholysis, and total nail loss. The nail dystrophy may precede the onset of the rash and an isolated assymetrical nail dystrophy in a young person should raise suspicion about the diagnosis.

16.8.1 Prognosis

All these lesions are transient, usually resolving in 1 year. However, the presence of nail involvement indicates a protracted course and the deformity of the nail plate may persist for several years.

16.9 Retronychia

Retronychia is a new pattern of ingrown nail that is characterized by a proximal embedding of the nail plate. De Berker et al. [13, 14] presented a series of 10 cases with a mild-to-moderate paronychia (Fig. 16.10) as a result of 2–4 nail plates being superimposed on each other. Pain, inflammation, and varying degrees of granulation tissue reaction are observed. These symptoms subside rapidly after avulsion. A transitory growth arrest produces a Beau's line, and if the arrest ranges from 3 to 8 weeks, the nail plate separates from the subungual tissues leading to latent onychomadesis with secondary nail shedding [15].

Fig. 16.10 Finger retronychia (Courtesy X. Wortsman)

Important sonographic criteria for diagnosing retronychia are the reduced distance between the origin of the nail plate and the base of the distal phalanx (level of the distal interphalangeal joint compared with the contralateral digit), thickening; decreased echogenicity and increased blood flow in the dermis of the posterior nail fold and proximal nail bed (color Doppler ultrasound).

References

1. Baran R. The burden of nail psoriasis: an introduction. Dermatology. 2010;221 Suppl 1:1–5.
2. Holzberg M. Common nail disorders. Dermatol Clin. 2006;24:349–54.
3. Scarpa, Manguso F, Oriente A, Peluso R, Atteno M, Oriente P. Is the involvement of the DIP joint in psoriatic patient related to nail psoriasis? Clin Rheumatol. 2004;23:27–30.
4. McGonagle D, Ash Z, Dickie L, McDermott M, Aydin SZ. Ann Rheum Dis. 2011;Suppl 1:i71–6.

5. McGonagle D. Enthesis an autoinflammatory lesion linking nail and joint involvement in psoriatic disease. J Eur Acad Dermatol Venereol. 2009;1:9–13.
6. McGonagle D, Benjamin M, Tan AL. The pathogenesis of psoriatic arthritis and associated nail disease: not autoimmune after all? Curr Opin Rheumatol. 2009;21:340–7.
7. McGonagle D, Tan AL, Benjamin M. The nail as a musculoskeletal appendage-implications for an improved understanding of the link between psoriasis and arthritis. Dermatology. 2009;218:97–102.
8. McGonagle D, Tan AL, Benjamin M. The biomechanical link between skin and joint disease in psoriasis and psoriatic arthritis: what every dermatologist needs to know. Ann Rheum Dis. 2008;67:1–4.
9. Kanvar J, Sandipan D, Srabani G. Involvement of nails in discroid. LE JAP I. 1993;41:543.
10. Richert B, André J, Bourguignon R, de la Brassine M. Hyperkeratotic nail discoid lupus erythematosus evolving forwards systemic lupus erythematosus: therapeutic difficulties. J Eur Acad Dermatol Venereol. 2004;18:728–30.
11. Braverman I. Connective tissue (rheumatic) diseases, chapter 7. In: Skin signs of systemic disease. 3rd ed. Philadelphia/London: W. Sanders; 1998. p. 198–277.
12. Baran R, Dupré A, Lauret P, Puissant A. Lichen striatus with nail involvement. Report of 4 cases and review of the 4 cases in the literature. Ann Dermatol Venereol. 1979;106:885–91.
13. De Berker DA, Rendall JR. Retronychia-proximal ingrowing nail. J Eur Acad Dermatol Venereol. 1999;12 Suppl 2:S126.
14. De Berker DA, Richert B, Duhard E, et al. Retronychia: proximal ingrowing of the nail plate. J Am Acad Dermatol. 2008;58: 978–83.
15. Wortsman X, Calderon P, Baran R. Finger retronychias detected early by 3D ultrasound examination. J Eur Acad Dermatol Venereol. 2012;26(2):254–6.

Nail Tumors: Clinical Overview

17

Robert Baran

Contents

17.1 Introduction

The diagnostics of disease of the nail and adjacent tissues is frequently aided with the use of radiography, magnetic resonance imaging, and scintigraphy. However, the recent technological advances in sonography, particularly in 3D, have changed the appearance of the diagnosis and consequently the management of nail diseases. Ultrasound is an easy-to-use and more cost-effective tool that has rendered visible what was previously invisible, and clarified what was once difficult to see. It has become an essential tool in dermatological and surgical diagnosis.

17.2 Warts

Common warts are caused by human papilloma viruses of different DNA types. They are benign, weakly contagious, fibroepithelial tumors with a rough keratotic surface. They are most frequently located on the lateral aspect of the proximal nail fold (PNF) and they spread onto the dorsum of the entire fold (Fig. 17.1). Tender nodules beneath the PNF are infrequent [1, 2] and rarely result in longitudinal grooving. Subungual warts affect the hyponychium initially, growing as pseudotumors slowly toward the nail bed and finally elevating the nail plate, that is not often affected although surface ridging may occur. Subungual warts are painful and can mimic a glomus tumor.

Bone erosion from verruca vulgaris has been observed. However, some of those cases may have been keratoacanthomas because the latter, as well as epidermoid carcinoma and verruca vulgaris, are sometimes indistinguishable from clinical signs alone. Therefore, in longstanding warts in the nail area, histologic examination may be necessary to differentiate extensive periungual warts from verrucous Bowen's disease.

On sonography, subungual warts appear as hypoechoic structures mostly of a fusiform shape, associated with thickening of the nail plates and interplate spaces. Warts

R. Baran, MD
Nail Diseases Center, 42, rue des Serbes, Cannes 06400, France

Department of Gustave Roussy Cancer Institute, Villejuif, France
e-mail: baran.r@wanadoo.fr, baran.r@club-internet.fr

X. Wortsman, G.B.E. Jemec (eds.), *Dermatologic Ultrasound with Clinical and Histologic Correlations*,
DOI 10.1007/978-1-4614-7184-4_17,

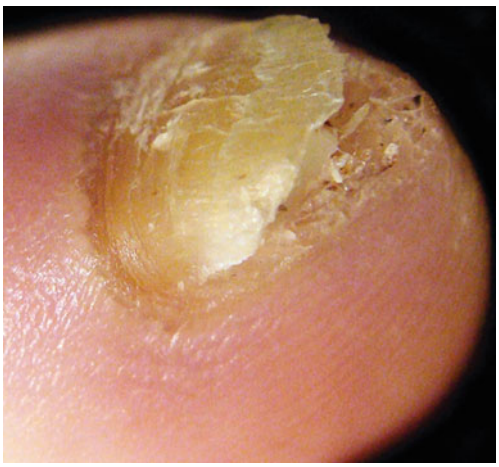

Fig. 17.1 Subungual wart

Fig. 17.2 Subungual keratoacanthoma

tend to have a nodular shape and can produce secondary thickening of the nail plates along the same axis when localized in the proximal nail bed. Warts are usually hypovascular, nevertheless, when they involve the hyponychium, they can produce dermal hypervascularity in the affected areas.

17.3 Distal Digital Keratoacanthoma

Subungual and periungual finger keratoacanthoma (KA) can occur as solitary or multiple tumors [3, 4]. KA is a rare, benign, but rapidly growing, seemingly aggressive tumor usually situated below the edge of the nail plate or in the most distal portion of the nail bed. Multiple subungual KAs without KAs on other sites are exceptional [5]. In three cases the distal phalanx of the toe was affected. Spontaneous resolution of KA is rare in the nail area [6].

The lesion can start as a small and painful keratotic nodule, visible beneath the free edge and growing rapidly to a 1–2 cm lesion within 4–8 weeks. Its typical gross appearance as a dome-shaped nodule with a central plug of horny material filling the crater is not often seen subungually, although histology of an adequate biopsy specimen will clearly show the characteristic pattern. Less frequently, the tumor grows out from under the PNF, which becomes inflamed and can cover or surround it with a cushion of swollen tissue (Fig. 17.2). The tumor then erodes the bone which can be seen radiologically as a fairly well-defined crescent-shaped lytic defect of tuft adjacent to the overlying nail bed. Reconstitution of the bony defect can be expected.

Diagnosis of distal digital keratoacanthoma is dependent on the rapid growth, bone erosion, and characteristic histology. Its clinical differentiation from squamous cell carcinoma is nevertheless difficult and the tumor is frequently diagnosed histologically as a squamous cell carcinoma (keratoacanthoma type). On sonography, well-circumscribed masses with mixed echogenicity (anechoic-hypoechoic), cortical remodeling or erosion of the bony margins, as well as associated posterior acoustic enhancement have been described.

17.4 Onychomatricoma

The are four main clinical signs that are striking enough to either make the diagnosis of onychomatricoma or at least to arouse suspicion of the condition that we described 25 years ago [7–19].

The first is a yellow longitudinal band of variable width that leaves a single or double portion of normal pink nail on either side (Fig. 17.3a). Splinter hemorrhages can be seen in the yellow area involving the proximal nail region in a characteristic manner and longitudinal ridging is prominent in the affected nail. The second sign is a tendency toward transverse overcurvature of the affected nail portion that becomes more pronounced as the yellow color becomes extended.

The third sign is shown after nail avulsion, exposing a villous tumor (Fig. 17.3b) emerging from the matrix while the nail appears as a thickened funnel, storing filamentous digitations of matrix fitting into the holes of the proximal nail, the fourth sign (Fig 17.3c). The villous projections in the nail plate can be so pronounced that nail trimming may produce bleeding [14]. However, in some cases the clinical presentation can be confusing: longitudinal melanonychia can hide the yellow hue and the PNF can become swollen at its junction with the lateral nail fold. The swelling gives the affected nail the texture of a cutaneous horn, and in some cases, the horn is completely separated from the nail plate. Histological examination establishes the diagnosis [15]. In some cases,

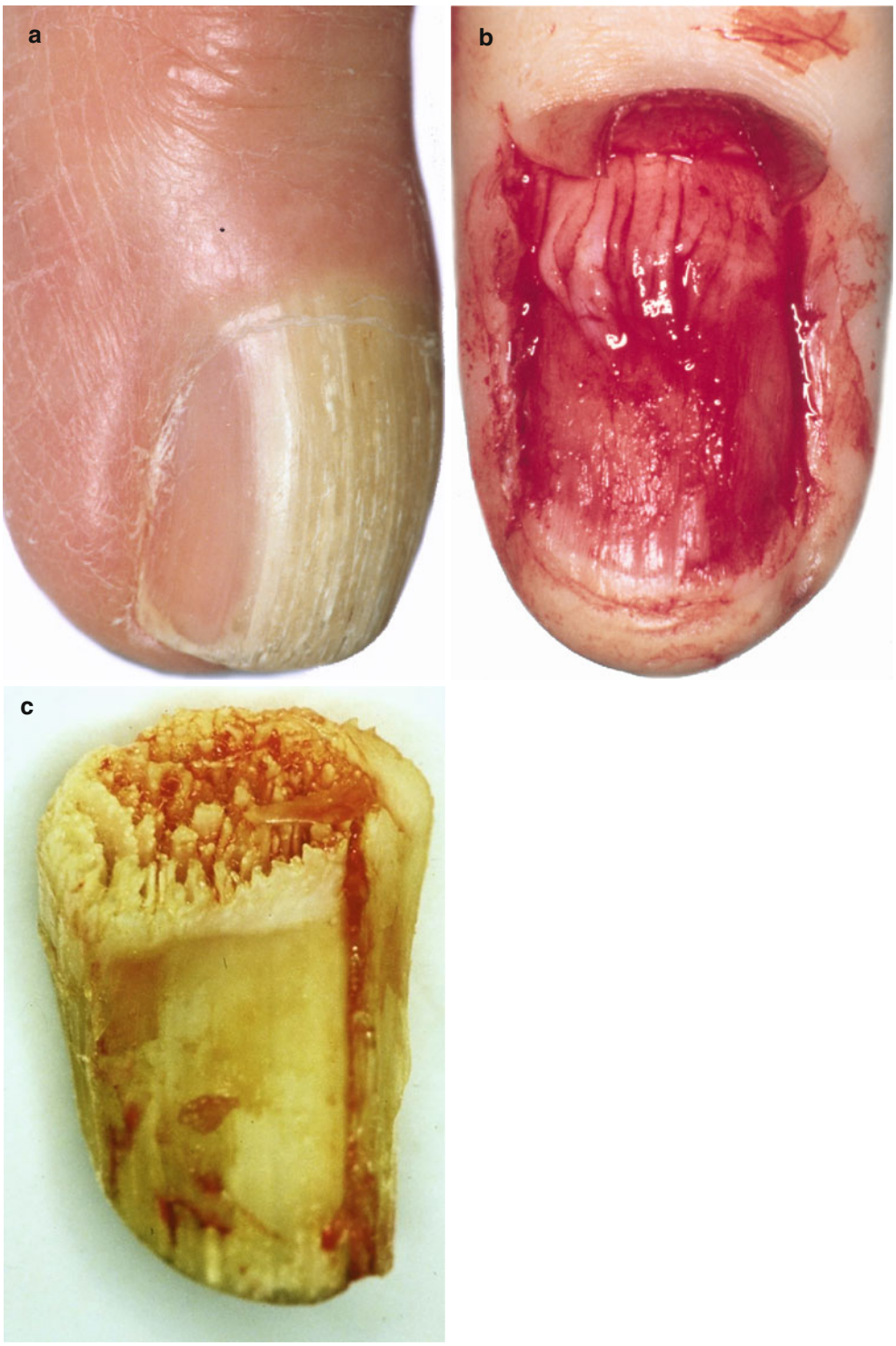

Fig. 17.3 (**a**) Onychomatricoma. (**b**) Digitations derived from the matrix. (**c**) Holes of the proximal nail extremity are clearly visible

the tumor is associated with onychomycosis and longitudinal melanonychia [18].

This fibroepithelial tumor consists of two anatomical zones and three histologic criteria are used for each [10]. The proximal zone is located beneath the PNF with a proximal border starting at the root of the nail and a distal border corresponding to the cuticle. It is characterized by (1) deep epithelial invaginations filled with a thick V-shaped keratogenous zone; (2) a thickened nail plate without cavitation but with an undulating inferior border ending in ungual spurs; and (3) a fibrillar stroma clearly demarcated from the undersurface.

There are two histologic differential diagnoses that can be discussed [15]. In the first, longitudinal sections in the

Fig. 17.4 (**a**) Fibrokeratoma (*arrow*) (**b**–**d**) Koenen's tumors (**e**) Koenen's tumor with longitudinal groove demonstrating presence of a very tiny tumor in front of the cuticle

structure are reminiscent of a fibrokeratoma. However, a diagnosis of fibrokeratoma of the nail matrix can be excluded on the basis of the multiplicity of fibroepithelial digitations, absence of a horny corn at the distal border of the thickened nail plate, and the presence of cavitation filled with serous fluid. In the second, the stroma of the lunular segment of the onychomatricoma can suggest a fibroma. However, the latter can be ruled out on the basis of the hyperplastic and onychogenic nature of the epithelium. Histologically, an ungual fibroma compresses the matrix epithelium and results clinically in thinning of the nail plate in the form of a longitudinal groove [18]. This type of tumor can bleed after extensive trimming of the distal nail margin.

On sonography, onychomatricoma presents with an eccentric location in the nail bed and affects one of the matrix wings. Hyperechoic linear dots are described within the hyperechoic tumor that also sends projections into the intraplate space and matrix region. Remodeling or erosive changes in the bony margin, hypervascularity, or expansion in the PNF have been reported.

17.5 Fibrous Tumors

17.5.1 Acquired Ungual Fibrokeratoma

Acquired ungual fibrokeratoma (Fig. 17.4) is probably a variant of acquired digital fibrokeratoma [20] and garlic clove fibroma [21]. Classically, they are acquired, benign, spontaneously developing, asymptomatic nodules with a hyperkeratotic tip and a narrow base that occur mostly in the periungual area or elsewhere on the fingers. They can be double and even triple and reach a considerable size. Most ungual fibrokeratomas emerge from beneath the PNF, growing on the dorsum of the nail where it causes a sharp longitudinal depression. Some of the lesions originate from within the matrix and grow in the nail plate to eventually emerge in the middle of the nail; these intraungual fibrokeratomas are also called "dissecting ungual fibrokeratomas" because they divide the nail plate [22]. Subungual fibrokeratomas that arise from the nail bed are rare.

17.5.2 Acquired Ungual Fibrokeratoma and Koenen's Tumors

Koenen's periungual fibromas develop in about 50 % of cases of tuberous sclerosis (epiloia or Bourneville-Pringle disease) (Fig. 17.4a, b, c), which is a dominantly inherited multisystem disease affecting the central nervous system, eyes, skin, cutaneous appendages, kidneys, heart, blood vessels, and bones. Two major gene loci have been identified where mutations can cause the tuberous sclerosis complex with apparently indistinguishable phenotypes: *TSC1* at 9q34 and *TSC2* at 16p13.3 [23].

In the Koenen's tumors that we have examined, we were able to distinguish two portions: (1) a small distal segment with loose collagen and many blood vessels, and (2) a larger proximal part built up of dense collagen bundles and fewer capillaries [24]. It thus appears that Koenen's tumor can be considered as a particular type of fibrokeratoma that can be

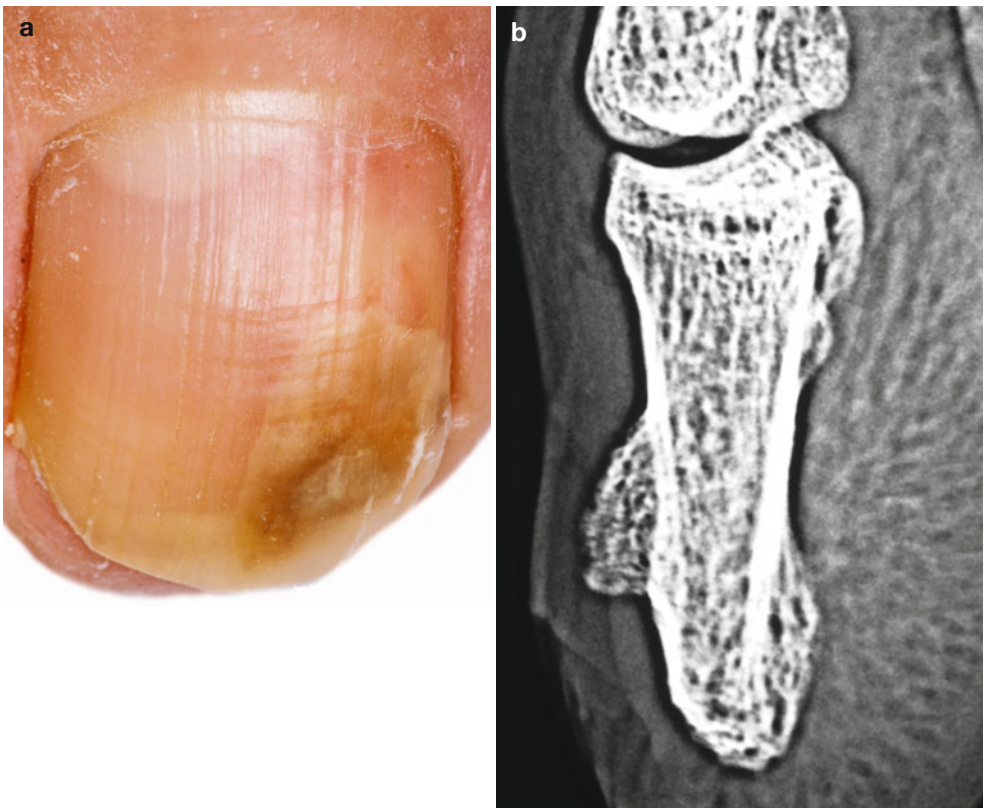

Fig. 17.5 (**a**) Distal subungual exostosis. (**b**) Exostosis radiograph

subdivided according to its clinical appearance, its location, and its origin into the following groups:

1. Fibrokeratomas originating from the dermal connective tissue. These fibrokeratomas are post-traumatic or appear spontaneously and are usually located on the fingers (acquired digital fibrokeratoma).
2. Fibrokeratomas originating from the PNF or the surrounding connective tissue. These fibrokeratomas are located in the nail fold [25] and can be hereditary [26] (tuberous sclerosis) or acquired (for example, garlic-clove fibroma).

Trauma is thought to be a major factor initiating acquired periungual fibrokeratoma. Biopsy is mandatory for the diagnosis of nail tumors because pseudo-fibrokeratoma should be considered as a clue for Bowen's disease [27].

On sonography, fibromas present uniform hypoechoic nodular or oval structures. Their location is commonly eccentric within the nail bed and they can affect the matrix region including its wings. They can present in a variety of sizes and usually, in large sized tumors, a remodeling of the bony margin can be detected.

Moreover, fibrous tumors can secondarily involve the lateral nail fold going from the dorsal aspect to the ventral aspect and attaching into the corresponding flexor sheath. On color Doppler ultrasound, fibrous tumors are usually hypovascular, with the exception of angiofibroma that can present with small sized vascular bundles with low velocity arterial and venous blood flow within the tumoral lesion.

17.6 Exostosis and Osteochondroma

Subungual exostoses are not true tumors, but rather outgrowths of normal bone or calcified cartilaginous remains. It is still unclear whether subungual osteochondroma [28] is a different entity [29] Subungual exostoses are rarely reported: there were only 60 subungual exostoses in a series of 6,034 benign osseous lesions [30]; however, they can be considerably under-diagnosed and underreported. They are bony growths that are painful with pressure and can elevate the nail. They are particularly frequent in young people and located mostly in the dorso-medial aspect of the tip of the great toe, although subungual exostoses can also occur in the lesser toes or less commonly in the thumb or index fingers [31].

Subungual exostoses start as small elevations of the dorsal aspect of the distal phalanx and can eventually emerge from under the nail edge or destroy the nail plate. If the nail is lost, the surface becomes eroded and secondarily infected, sometimes mimicking an ingrown toenail or even a melanoma, which can cause walking to be painful; however, solitary subungual exostoses have never been observed as undergoing malignant degeneration. Some authors believe that a history of trauma is only occasionally found in subungual exostosis [32].

The triad of pain (the leading symptom), nail deformation (Fig. 17.5a), and radiographic features (Fig. 17.5b) are usually diagnostic. The exostosis is an ill-defined trabeculated osseous growth with an expanded distal portion covered with radiolucent fibrocartilage.

Osteochondroma, commonly evoking the same symptoms as subungual exostosis, is believed to have a male predominance. Its onset is usually between the ages of 10–25 years, and there is also often a history of trauma [28]. Its growth rate is slow and radiographs shows a well-defined circumscribed pedunculated or sessile bone growth projecting from the dorsum of the distal phalanx near to the epiphyseal line, therefore, nail dystrophy can be pronounced [33]. A bony tumor with a hyaline cartilage cap can be seen histologically, however, on the basis of the histopathological pattern, de Palma et al. [29] have stated that most subungual bone masses exhibit the features of conventional osteochondromas and not of subungual exostoses independent of their location at the distal phalanx. It must be differentiated from primary subungual calcification (particularly seen in elderly women), secondary subungual calcification due to trauma or psoriasis [34], and primary osteoma cutis [35].

Subungual exostoses appear on ultrasound as linear echoic structures with posterior shadowing artifact, frequently seen and dependent on the reflective properties of the calcium component. These exostoses usually connect with their origin in the hyperechoic line of the bony margin of the distal phalanx. When they are associated with cartilaginous tissue, they are called osteochondroma, and a hypoechoic cap can be detected surrounding the calcified hyperechoic component. Hypoechoic ill-defined tissue can also be seen in the periphery of the exostoses as a part of secondary inflammatory and scarring reaction.

17.7 Myxoid Cysts

Myxoid cysts are cystic lesions that are usually connected to the distal interphalangeal (DIP) joint and extend into the periungual or subungual regions. They most commonly affect the PNF but also may extend into the nail bed secondarily compressing the ungual matrix [36] (Fig. 17.6).

They appear on ultrasound as round or oval-shaped anechoic structures that produce posterior acoustic reinforcement and lack of inner blood flow. Extension of the mucoid cyst into the nail bed and the usually tortuous anechoic connecting tract with the DIP joint can be assessed. They are commonly associated with osteoarthritis and synovitis of the DIP joint, and thickening and irregularities of the nail plate can be detected in the same axis of the ungual compression.

17.8 Pyogenic Granuloma

Pyogenic granuloma is a benign eruptive hemangioma which typically occurs following a minor penetrating skin injury. It begins around the nail with a minute red papule that rapidly grows to the size of a pea or even a cherry. Its surface can become eroded with necrosis of the overlying epidermis. Crusting can mimic a malignant melanoma, although the typical collarette can usually be seen. Pyogenic granuloma is most commonly located at the PNF but can develop distally in the hyponychium region (Fig. 17.7) or in the nail bed associated with onycholysis [37] of the toe, often resulting from prolonged frictional trauma. The matrix can also be the site of this tumor after a penetrating wound of the nail plate, with tenderness and a ready tendency to bleed being characteristic features. Extensive granulation tissue resulting from an ingrown toenail can mimic a periungual pyogenic granuloma, and has also been observed in patients treated with aromatic retinoids [38], indinavir [39], cyclosporine [40], as well as with the new anti-cancer agents that act by inhibiting the epidermal growth factor receptor or

Fig. 17.6 Myxoid pseudocysts

Fig. 17.7 Pyogenic granuloma

Fig. 17.8 Glomus tumor with longitudinal erythronychia

its transduction: Iressa (ZD1839) [41], Cetuximab (C225) [42], and Gefitinib [43].

They appear on ultrasound as poorly defined hypoechoic structures that displace the nail plate and enlarge the nail bed. One or both nail layers of the nail plate can be thickened and/or wavy in shape, and variable degrees of blood flow can be detected within granulomas going from hypovascularity to hypervascularity (telangieltatic variant).

17.9 Glomus Tumor

Seventy-five percent of glomus tumors occur in the hand, most commonly in the fingertips and particularly in the subungual area. One to two percent of all hand tumors are glomus tumors [44], with seven cases of glomus tumors being reported in von Recklinghausen's neurofibromatosis [45].

Glomus tumors are characterized by intense, often pulsating, pain that can occur spontaneously or be provoked by the slightest trauma and exacerbation (such as placing an ice cube on the nail), and even changes in temperature, particularly from warm to cold, can trigger pain radiating up to the shoulder. The pain can sometimes be worse at night, however, a tourniquet placed at the base of the digit stops the pain, with a blood pressure cuff inflated to 300 mmHg before or immediately after minor trauma abolishing the pain response [46].

Glomus tumors are seen through the nail plate as small, bluish to reddish-blue spots several millimeters in diameter, rarely exceeding 1 cm in diameter. An erythematous focus that does not totally blanch with pressure, and is associated with sharp pain, probably represents a glomus tumor. Longitudinal erythronychia that can be associated with a distal fissure is a classic presentation of a glomus tumor (Fig. 17.8). A glomus tumor can sometimes cause a slight rise in surface temperature which can be detected by thermography; dynamic telethermography shows the lesion at

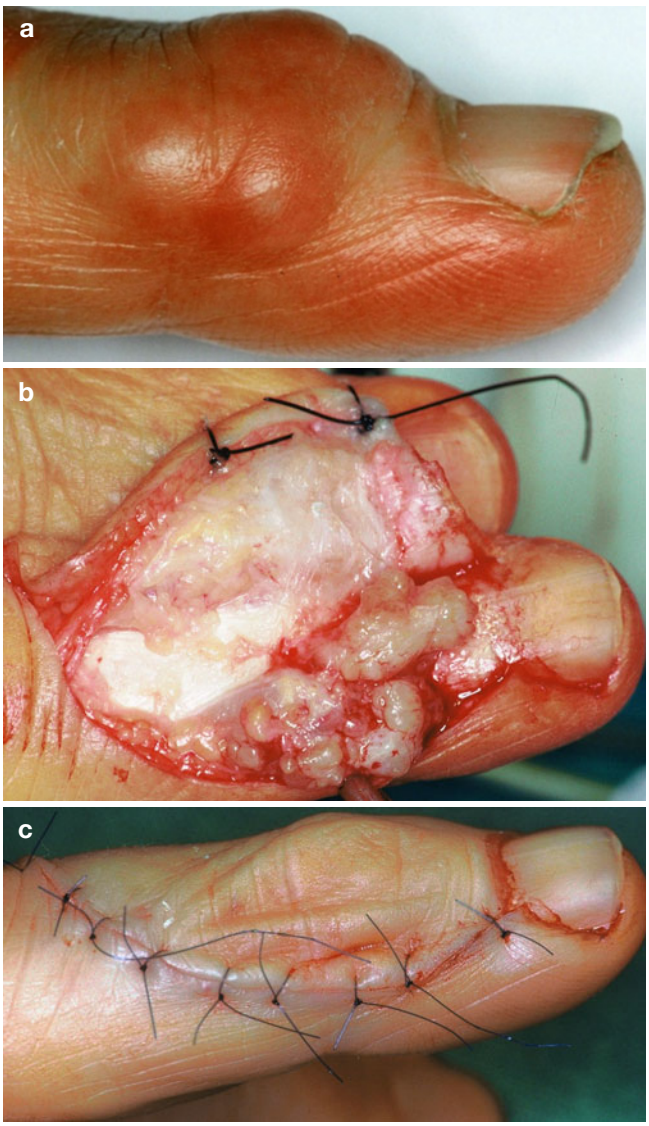

Fig. 17.9 (**a**) Giant cell tumor. (**b**) Exposed lesions. (**c**) After removal of the tumor

about three times its actual size [47]. One half of glomus tumors cause minor nail deformities with ridging and fissuring being the most common. Subungual hyperkeratosis with onycholysis is rare. About 50 % cause a depression on the dorsal aspect of the distal phalangeal bone or even a cyst visible on radiographic study [48], and an intraosseous location is unusual. Probing and transillumination may help to localize the tumor if it is not clearly visible through the nail as arteriography is no longer performed; this would reveal a star-shaped telangiectatic zone useful for diagnosis and localization of the tumor if it cannot be localized clinically or on radiography, although magnetic resonance imaging may be preferable because it offers the highest sensitivity and a better assessment of the extent of the lesion [49].

Glomus tumors appear as hypoechoic nodules on ultrasound, centrally located and frequently with increased vascularity. Variable peak arterial systolic velocities can be detected

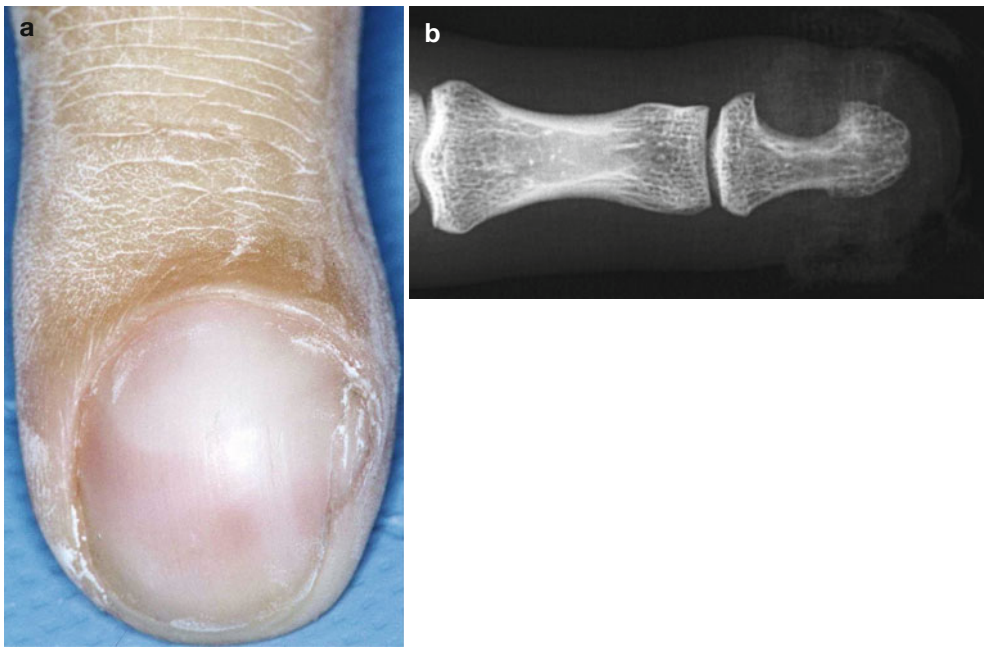

Fig. 17.10 (**a**) Perineurioma. (**b**) Perineurioma radiograph

within the intratumoral blood flow, and have been reported to be as low as 3.7 cm/s and as high as 21.1 cm/s, the latter exceeding the peak systolic velocity that had been described for the normal tibial artery (16 ± 10 cm/s). It is common to see remodeling of the bony margin of the distal phalanx beneath the tumor, probably reflecting the slow growth pattern of the tumor. On ultrasound, proximal locations of glomus tumors are described as more frequent than distal locations; therefore, pre-surgical knowledge of the location of the tumor can benefit the choice of the incision site.

17.10 Giant Cell Tumor

Giant cell tumors are neoplasms derived from the tendon sheath or the joint synovia. They are the second most common subcutaneous tumors of the hand and occur more frequently in women than they do in men. On the digits, giant cell tumors usually occur on the dorsum of the DIP joint and appear as solitary, often lobulated slow-growing, skin-colored and smooth-surfaced nodules that tend to feel firm and rubbery (Fig. 17.9a–c). The tumors may enlarge to the size of a cherry and may cause pain on flexion by virtue of their dimensions. Only rarely do the tumors interfere with the nail unit in the region of the lateral nail fold. Periodic inflammation and drainage may occur, but in contrast to malignant synovioma, no calcification is demonstrable on radiographs [50], and giant cell tumors in a subungual location are unusual [51]. A cystic-appearing lesion adjacent to the nail can cause a wide longitudinal groove in the nail plate [52], and a giant cell tumor involving the lateral nail fold and nail bed can interfere with nail growth [53].

17.11 Perineurioma of the Nail

Perineuriomas can be distinguished by their positive immunoreactivity for epithelial membrane antigen and lack of reactivity to the S-100 protein and α-smooth muscle actin. They appear clinically as swelling, clubbing (Fig. 17.10a, b), or dystrophy of the nail and can mimic other tumoral entities such as fibrous tumors or subungual exostoses.

Poorly defined hypoechoic eccentric masses have been reported when using ultrasound. Perineuriomas can involve the matrix region (particularly one of the wings) and the ipsilateral nail fold, presenting on color Doppler ultrasound as a hypovascular tumors. Remodeling of the bony margin has not been described, although this finding could be hypothetically present in larger size tumors. To our knowledge, neither involvement of the inter-plate space nor hyperechoic dots within the perineuriomas have been reported to date. Some authors were fortunate enough to see three cases of perineurioma in the nail apparatus [54–56]; however, these benign tumors, derived from neural tissue, are extremely rare in this location. Additionally, they differ from other common neurogenic tumors such as schwanomas or neurofibromas.

References

1. Holland TT, Weber CB, James WD. Tender periungual nodules. Arch Dermatol. 1992;128:105–10.
2. Laüchli S, Eichmann A, Baran R. Swelling of the proximal nail fold caused by underlying warts. Dermatology. 2001;202:328–9.
3. Baran R, Goettmann S. Distal digital keratoacanthoma: a report of 12 cases and review of the literature. Br J Dermatol. 1998;139:512–5.
4. Baran R, Mikhail G, Costini B, Tosti A, Goettmann S. Distal digital keratoacanthoma. Two cases with a review of the literature. Dermatol Surg. 2001;27:575–9.

5. Haneke E. Multiple subungual keratoacanthomas. XII Int cong dermatol surg Munich. Zbl Haut-Geschl Kr. 1991;159:337–8.
6. Sinha A, Marsh R, Langtry J. Spontaneous regression of subungual keratoacanthoma with reossification of underlying distal lytic phalanx. Clin Exp Dermatol. 2005;30:20–2.
7. Baran R, Kint A. Surgical treatment of a filamentous tufted tumour in the matrix of a funnel-shaped nail – a new entity. Zbl Haut-Geschl Kr. 1991;159:337.
8. Baran R, Kint A. Onychomatricoma. Filamentous tufted tumour in the matrix of a funnel-shaped nail: a new entity. Br J Dermatol. 1992;126:510–5.
9. Van Holder C, Dumontier C, Abimelec P. Onychomatricoma. J Hand Surg. 1999;24B:120–1.
10. Fraga GR, Patterson JW, McHargue CA. Onychomatricoma. Report of a case and its comparison with fibrokeratoma of the nail bed. Am J Dermatopathol. 2001;23:36–40.
11. Nagamatsu S, Tozawa A, Nakuoka H, Ohtsuka H, Hashimoto K. A case of onychomatricoma. JPN J Plast Reconstr Surg. 2002;45:875–80.
12. Laxmisha C, Thappa DM, Karthikeyan K, Jayanthi S. Onychomatricoma. Indian J Dermatol. 2003;48:94–5.
13. Ko CJ, Shi L, Barr RJ, Mölne L, Termesten-Bradel A, Headington JT. Ungioblastoma und unguioblastic fibroma – an expanded spectrum of onychomatricoma. J Cutan Pathol. 2004; 31:207–311.
14. Raison-Peyron N, Alirezai M, Meunier L, Barnéon G, Meynadier J. Onychomatricoma: an unusual cause of nail bleeding. Clin Exp Dermatol. 1998;23:138.
15. Perrin C, Goettmann S, Baran R. Onychomatricoma: clinical and histopathologic findings in 12 cases. J Am Acad Dermatol. 1998;39:560–4.
16. Fayol J, Baran R, Perrin C, Labrousse F. Onychomatricoma with misleading features. Acta Dermato Venereol. 2000;80:370–2.
17. Goettmann S, Drapé JL, Baran R, Perrin C, Haneke E, Bélaïch S. Onychomatricome: 3 nouveaux cas, intérêt de la résonance magnétique nucléaire. Ann Dermatol Venereol. 1994;121:S145.
18. Haneke E, Fränken J. Onychomatricoma. Dermatol Surg. 1995;21:984–7.
19. Kint A, Baran R, Geerts ML. The onychomatricoma: an electron microscopic study. J Cutan Pathol. 1997;24:183–8.
20. Bart RS, Andrade R, Kopf AW, Leider M. Acquired digital fibrokeratomas. Arch Dermatol. 1968;97:120–9.
21. Steel HH. Garlic-clove fibroma. J Am Med Assoc. 1965;191:1082–3.
22. Haneke E. Intraoperative differential diagnosis of onychomatricoma, Koenen's tumours, and hyperplastic Bowen's disease. J Eur Acad Dermatol Venereol. 1998;11:S 199.
23. Sampson JR, Harris PC. The molecular genetics of tuberous sclerosis. Hum Mol Genet. 1994;3:1477–80.
24. Kint A, Baran R. Histopathologic study of Koenen tumours. Are they different from acquired digital fibrokeratoma? J Am Acad Dermatol. 1988;18:369–72.
25. Colomb D, Racouchot J, Jeune R. Les lésions des ongles dans la sclérose tubéreuse de Bourneville isolées ou associées aux tumeurs de koenen. Ann Dermatol Syph. 1976;103:431–7.
26. Webb DW, Clarke A, Fryer A, Osborne JP. The cutaneous features of tuberous sclerosis: a population study. Br J Dermatol. 1996;135:1–5.
27. Baran R, Perrin C. Pseudo-fibrokeratoma of the nail apparatus: a new clue for Bowen disease. Acta Derm Venereol. 1994;74:449–50.
28. Apfelberg DB, Druker D, Maser M, Lash H. Subungual osteochondroma. Differential diagnosis and treatment. Arch Dermatol. 1979;115:472–3.
29. De Palma L, Gigante A, Specchia N. Subungual exostosis of the foot. Foot Ankle Int. 1996;17:758–63.
30. Dahlin DC, Unni KK. Bone tumors. In: Dahlin DC, Unni KK eds, Dahlin's Bone tumors, 4th ed. Springfield: Charles C Thomas; 1986. p. 18–30.
31. Baran R, Sayag J. Exostose sous-unguéale de l'index. Ann Dermatol Venereol. 1978;105:1075–6.
32. Norton LA. Nail disorders. J Am Acad Dermatol. 1980;2:451–67.
33. Kim SW, Moon SE, Kim JA. A case of subungual osteochondroma. J Dermatol. 1998;25:60–2.
34. Fischer E. Subunguale verkalkungen. Fortschr Röntgenst. 1982;137:580–4.
35. Burgdorf W, Nasemann T. Cutaneous osteomas: a clinical and histopathologic review. Arch Dermatol Res. 1977;260:121–35.
36. Wortsman X, Jemec GB. Ultrasound imaging of nails. Dermatol Clin. 2006;24:323–8.
37. Richert B. Frictional pyogenic granuloma of the nail bed. Dermatology. 2001;202:80–1.
38. Baran R. Retinoids and the nails. J Dermatol Treat. 1990;1:151–4.
39. Bouscarat F, Bouchard C, Bachour D. Paronychia and pyogenic granuloma of the great toes in patients treated with indinavir. VEJ Med. 1998;338:1776–7.
40. Higgins EM, Hughes JR, Snowden S, Pembroke AC. Cyclosporin-induced periungual granulation tissue. Br J Dermatol. 1995;132:829–30.
41. Lee MW, Seo CW, Kim SW, et al. Cutaneous side effects in non-small cell lung cancer patients treated with iressa (ZD1839), an inhibitor of epidermal growth factor. Acta Derm Venereol. 2004;84:23–6.
42. Busam KJ, Capodieci P, Motzer R, Kiehn T, Phelan D, Halpern AC. Cutaneous side-effects in cancer patients treated with the antiepidermal growth factor receptor antibody C225. Br J Dermatol. 2001;144:1169–76.
43. Nakano J, Nakamura M. Paronychia induced by gefitinib, an epidermal growth factor receptor tyrosine kinase inhibitor. J Dermatol. 2003;30:261–2.
44. Rettig AC, Strickland JW. Glomus tumor of the digits. J Hand Surg. 1977;2:261–5.
45. Sawada S, Honda M, Kamide R, Niimura M. Three cases of subungual glomus tumors with von Recklinghausen neurofibromatosis. J Am Acad Dermatol. 1995;32:277–8.
46. Hildreth DH. The ischemia test for glomus tumor: a new diagnostic test. Rev Surg. 1970;27:147–8.
47. Corrado EM, Passareti U, Messore L, Lanza F. Thermographic diagnosis of glomus tumour. Hand. 1982;14:21–4.
48. Van Geertruyden J, Lorea P, Goldschmidt D, de Fontaine S, Schuind F, Kinnen L, et al. Glomus tumours of the hand. A retrospective study of 51 cases. J Hand Surg. 1996;21:257–60.
49. Van Ruyssevelt CE, Vranckx P. Subungual glomus tumor: emphasis of MR angiography. AJR Am J Roentgenol. 2004;182:263–4.
50. Wright CJE. Benign giant-cell synovioma. An investigation of 85 cases. Br J Surg. 1951;38:257–71.
51. Abimelec P, Cambiaghi S, Thioly D, Moulonguet I, Dumontier C. Subungual giant cell tumor of the tendon sheath. Cutis. 1996;58:273–5.
52. Batta K, Tan CY, Colloby P. Giant cell tumour of the tendon sheath producing a groove deformity of the nail plate and mimicking a myxoid cyst. Br J Dermatol. 1999;140:720–81.
53. Richert B, André J. Latero-subungual giant cell tumor of the tendon sheath: an unusual location. J Am Acad Dermatol. 1999; 41:347–8.
54. Baran R, Perrin C. Subungual perineurioma: a peculiar location. Br J Dermatol. 2002;164:125–8.
55. Baran R, Perrin C. Perineurioma: a tendon sheath fibroma-like variant in a distal subungual location. Acta Derm Venereol. 2003;83:60–1.
56. Wortsman X, Merino D, Catalan V, Morales C, Baran R. Perineurioma of the nail on sonography. J Ultrasound Med. 2010;29:1379–82.

Sonography of the Nail

18

Ximena Wortsman

What for, how to study and what to look in nail and periungual lesions

Contents

18.1 Introduction

The nail unit is a complex enthesis that is composed of several structures such as the nail bed, nail plate, periungueal region, distal interphalangeal (DIP) joint, and the distal insertion of the extensor tendon. This appendage grows from the 15th week of gestation until death and can be primarily or secondarily affected by multiple causes [1, 2].

Clinical diagnosis in the ungual region can present difficulties. The ungual matrix is very sensitive to trauma of any kind, therefore biopsies of the nail can be hard to perform and leave a permanent scar in a highly exposed area of the body. Additionally, the natural covering of the nail plates may complicate the identification of the underlying pathology [3]. Therefore, the use of imaging modalities such as ultrasound may facilitate early diagnosis and management. Furthermore, the anatomical information provided by ultrasound can affect important decisions such as the site and size of a surgical incision or the modification of a medical treatment plan.

In the past, sonography of the nail began with fixed frequency ultrasound machines that used 20 MHz probes [4]. Currently, the ultrasound examination of the ungual unit is commonly performed with variable frequency machines that vary in frequency from 7 to 22 MHz and present the capability to detect the blood flow of the nail bed in real time. 3D ultrasound reconstructions may also provide valuable information for the clinician who can usually better understand the dimension of the lesion.

18.2 Technical Considerations

It is suggested to perform the ungual examination with the finger or toe fully extended using a variable frequency compact linear (hockey stick-shaped) probe that can adapt better to the ungual shape. If necessary, a pad can be used to support the thumbs. A copious amount of gel should be applied over the ungual and periungual regions. A sweep

X. Wortsman, MD
Department of Radiology and Dermatology,
Institute for Diagnostic Imaging
and Research of the Skin and Soft Tissues,
Clinica Servet, Faculty of Medicine, University of Chile,
Almirante Pastene 150, Providencia, Santiago, Chile
e-mail: xwo@tie.cl, xworts@yahoo.com, www.sonoskin.com

X. Wortsman, G.B.E. Jemec (eds.), *Dermatologic Ultrasound with Clinical and Histologic Correlations*,
DOI 10.1007/978-1-4614-7184-4_18,

that includes at least two perpendicular axes should then be performed. Grey scale, color, and power Doppler imaging modalities with spectral curve analysis are used. 3D reconstructions are obtained by making 5–8 s sweeps of the nail and periungual region for improving the presentation and the understanding of the images [5].

18.3 Normal Sonographic Anatomy of the Nail

The nail unit is composed of three parts: the nail bed, the nail plate, and the periungual tissue. Thus, the nail plate is subdivided in two aspects or plates. The dorsal and ventral plates appear on ultrasound as a bilaminar parallel hyperechoic structures separated by a hypoechoic, almost virtual space that tends to present as more hyperechoic on higher frequencies (>20 MHz). The origin of the nail plates is normally far from the level of the DIP joint. The nail bed appears as hypoechoic and turns to slightly hyperechoic in the proximal region underlying the ungual matrix. Small and low flow arteries and veins are usually detectable within the normal nail bed. The periungual region is divided into the proximal and lateral nail folds. The lateral nail folds are termed radial or ulnar, and medial or lateral according to the respective location in the fingers or toes. The cutaneous layers in the periungual regions present the same echogenicities of the normal skin as in any other part of the body. Thus, a bilaminar hyperechoic epidermis is seen in the palmar and plantar regions (glabrous skin) and becomes a hyperechoic epidermal monolayer in the dorsum of the fingers and toes (non-glabrous skin). Additionally, the lateral and proximal nail folds lack hypoechoic fatty subcutaneous tissue. In contrast, the fatty component of the subcutaneous tissue is prominent in the pulp of the fingers or toes [6] (Figs. 18.1 and 18.2).

Fig. 18.1 (**a**–**c**) Nail surface anatomy and examination technique. (**a**, **b**) The photographs (**a** anteroposterior view; **b** lateral view) show the different parts of the nail. (**c**) The sonographic examination technique for studying the nail. *Abbreviations*: *np* nail plate, *lnf* lateral nail fold, *pnf* proximal nail fold, *h* hyponychium, *l* lunula

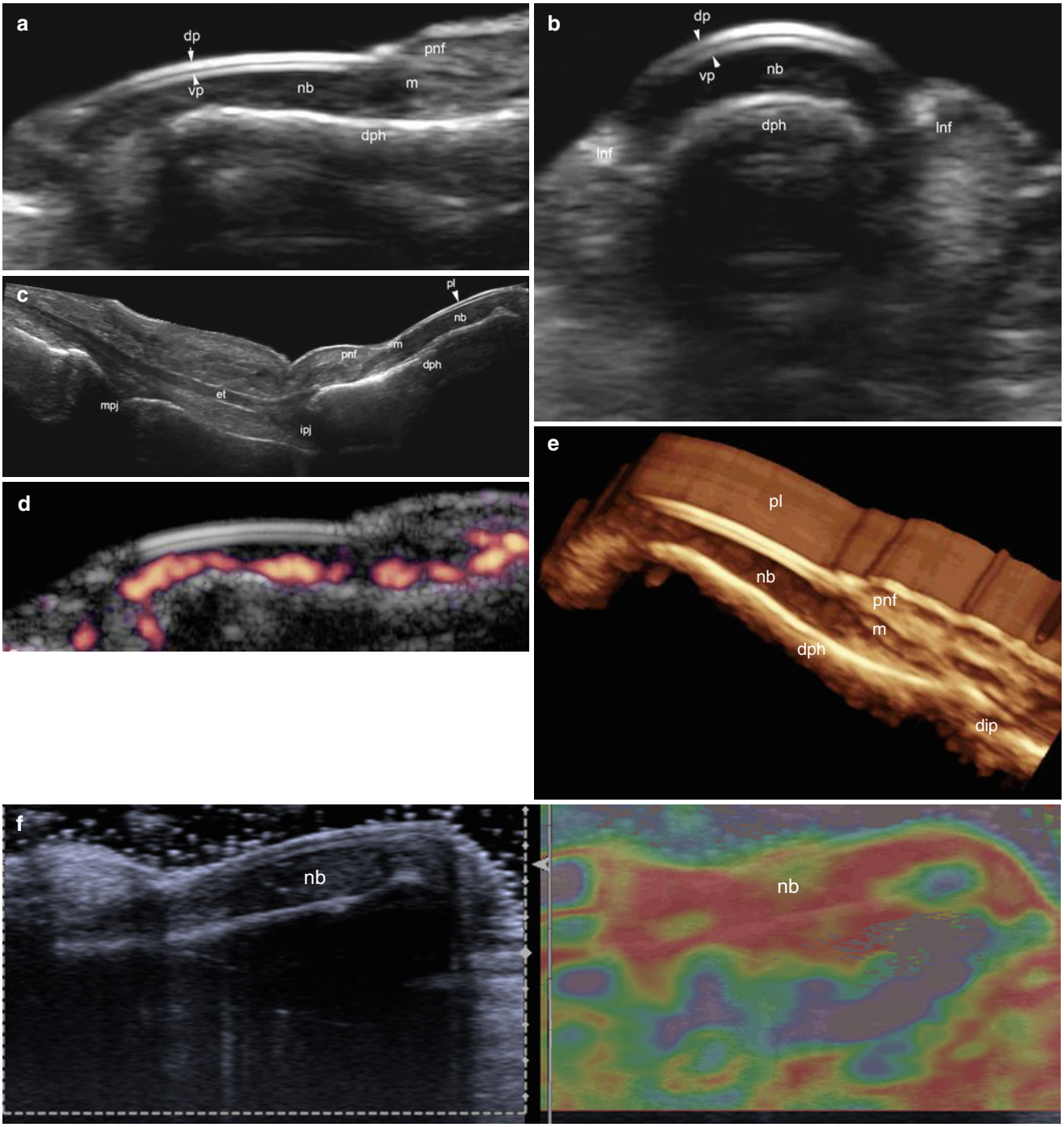

Fig. 18.2 (**a**–**f**) Sonographic anatomy of the nail. (**a**–**c**) Grey scale ultrasound images (**a** longitudinal view; **b** transverse view; **c** extended field of longitudinal view) show the different parts of the nail unit. (**d**) Power Doppler ultrasound image (longitudinal view) shows the normal blood flow within the nail bed. (**e**) 3D reconstruction of the nail (5–8 s sweep) highlights the different components of the nail unit. (**f**) Sonoelastography of the nail (side by side comparison: grey scale–elastography, longitudinal view). Notice the soft appearance (*red*) of the nail bed. *Abbreviations*: *nb* nail bed, *dp* dorsal plate, *vp* ventral plate, *pl* ungual plate, *m* ungual matrix, *pnf* proximal nail fold, *lnf* lateral nail fold, *dip* distal interphalangeal joint, *ipj* interphalangeal joint, *mph* metacarpophalangeal joint, *et* extensor tendon, *dph* distal phalanx

18.4 Pathology of the Nail Unit

18.4.1 Benign Growth and Congenital, Inflammatory, and Cosmetic Pathology

18.4.1.1 Growth and Location Alterations

18.4.1.1.1 Ingrowing Toenail

Ingrowing toenail, also called onychocryptosis, is an abnormal growth or embedding of the nail plates into the lateral fold. There are several causes among which are overcurvature of the nail plates (pincer nails), congenital malalignment, anomalous growth axis or hypertrophy of the lateral nail fold, improper trimming, repetitive or inadvertent trauma, genetic predisposition, hyperhidrosis, and poor foot hygiene [7]. The treatment is most commonly surgical and the recurrence rates are high (up to 70 %) [8].

On sonography, the fragment of the nail plates that is embedded in the lateral nail fold is detected as a bilaminar hyperechoic structure usually surrounded by hypoechoic inflammatory and granulomatous tissue. Hypervascularity can be detected on color Doppler ultrasound in the periphery to the fragment (Figs. 18.3 and 18.4).

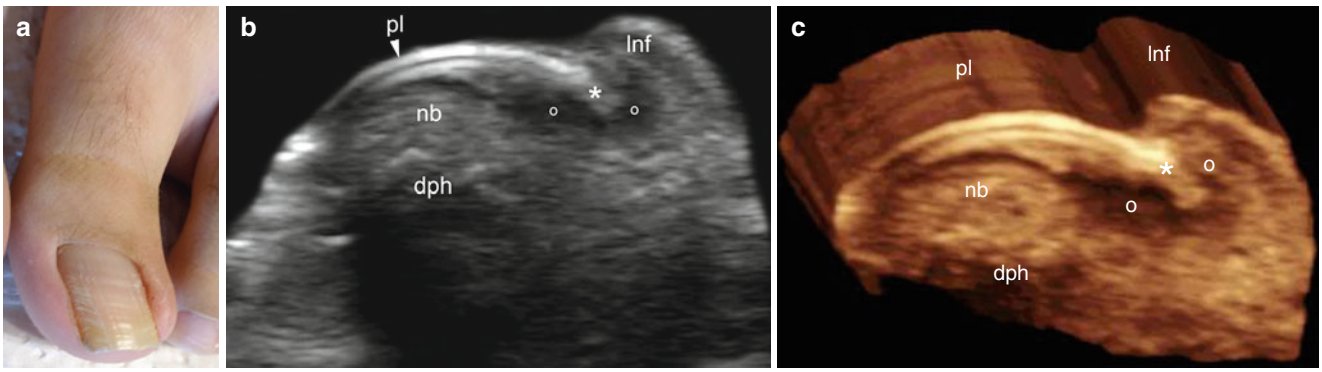

Fig. 18.3 (**a**–**c**) Ingrowing toenail (onychocryptosis). (**a**) Clinical photograph shows erythema and swelling in the lateral nail fold of the left toenail. The patient also presents a congenital malalignment of the nail (lateral deviation of the nail unit). (**b**) Grey scale ultrasound image (transverse view) shows a hyperechoic linear fragment (*) of the nail plate embedded in the lateral nail fold. There is hypoechoic granulomatous and inflammatory tissue (o) surrounding the fragment. (**c**) 3D reconstruction (transverse view, 5–8 s sweep) of the ingrown toenail. *Abbreviations*: *nb* nail bed, *pl* nail plate, *lnf* lateral nail fold, *dph* distal phalanx, * embedded nail plate fragment, *o* granulomatous and inflammatory tissue

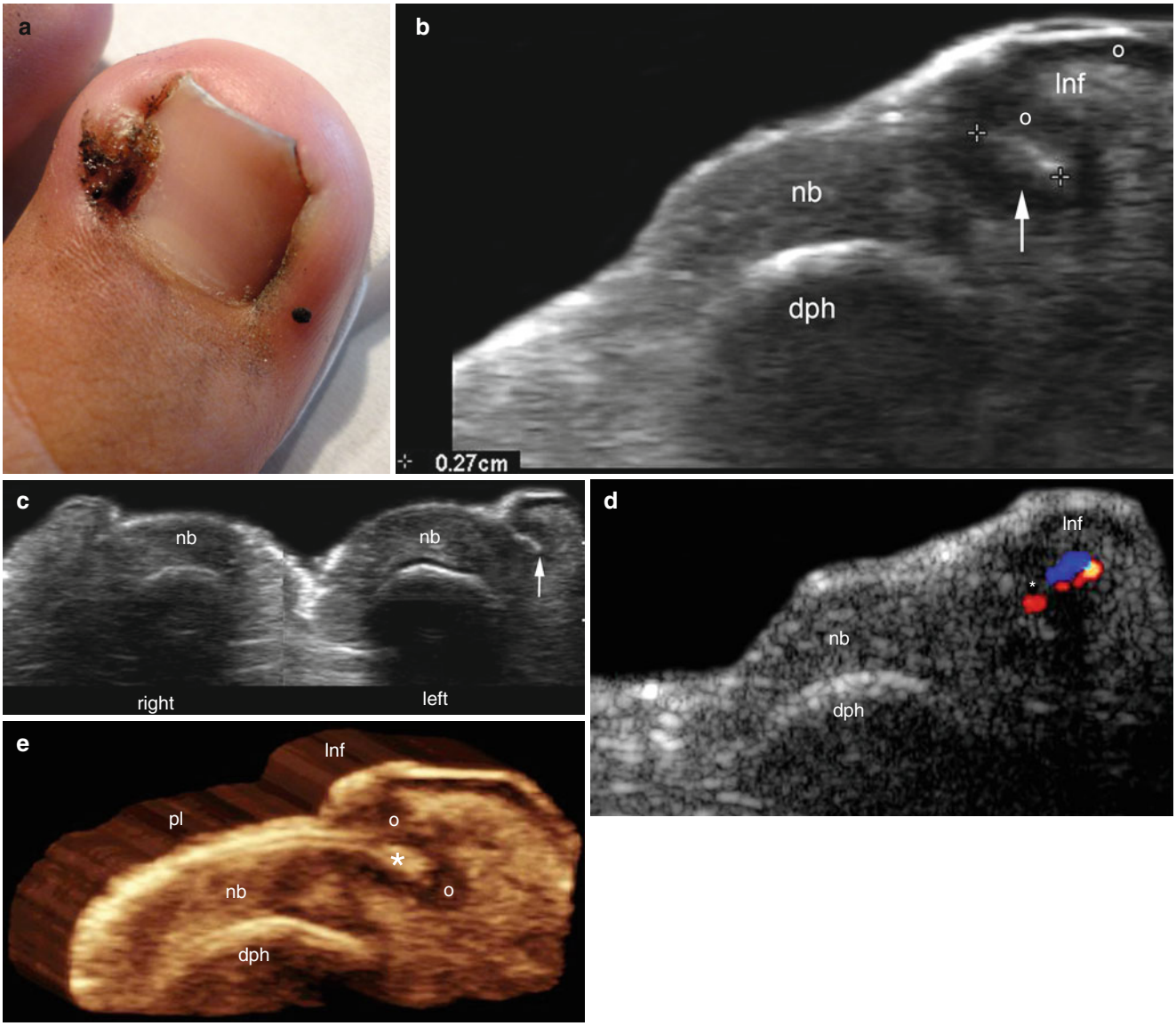

Fig. 18.4 (**a**–**e**) Ingrowing toenail (onychocriptosis). (**a**) Photograph of the left toenail shows an erythematous lesion that easily bleeds in the lateral nail fold. (**b**, **c**) Grey scale ultrasound images (**b** transverse view; **c** comparative side by side transverse view) show a 2.7 mm hyperechoic linear nail plate fragment (*, between markers, and *arrow*) embedded in the lateral nail fold. There is hypoechoic inflammatory and granulomatous tissue (o) in the periphery of the nail fragment. (**d**) Color Doppler ultrasound image (transverse view) shows increased vascularity in the periphery of the nail plate fragment. (**e**) 3D reconstruction (transverse view; 5–8 s sweep) of the ingrown toenail (*). *Abbreviations*: *nb* nail bed, *pl* nail plate, *lnf* lateral nail fold, *dph* distal phalanx, * embedded nail plate fragment, *o* granulomatous and inflammatory tissue

18.4.1.1.2 Onychomadesis

Onychomadesis is the spontaneous separation of the nail plate from the matrix, and a common phenomenon resulting from arrest of nail formation for a certain period. Short-term slowing of nail formation leads to Beau's lines (i.e., transverse lines or depressions across the nail plate), while long-term stop of nail growth will cause onychomadesis and even nail shedding [9]. Onychomadesis is typically seen 4–8 weeks after a severe systemic illness or traumatic event.

On sonography, two or more separated fragments of the nail plates can be identified, sometimes with an additional anechoic pseudobullous disruption in the ventral plate. Thickening and decreased echogenicity of the nail bed can also be detected [6, 10] (Fig. 18.5).

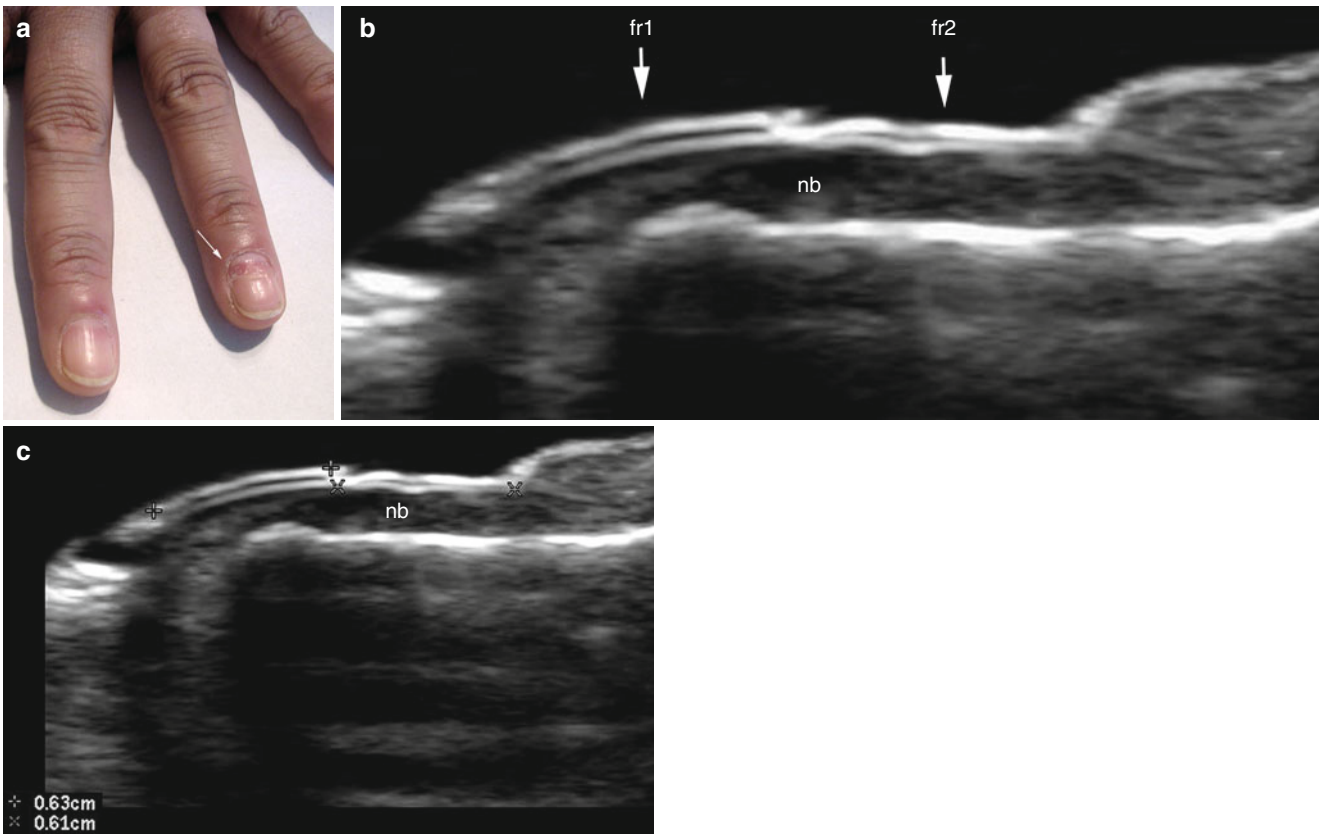

Fig. 18.5 (**a**–**c**) Onychomadesis. (**a**) Clinical image shows nail shedding (*arrow*) in the nail of the left index finger. (**b**, **c**) Grey scale ultrasound images (longitudinal views; **b** with *arrows*; **c** with *markers*) show two bilaminar hyperechoic nail plate fragments (fr1: 6.3 mm long and fr2: 6.1 mm long). *Abbreviations*: *nb* nail bed, *fr* nail plate fragment

18.4.1.1.3 Retronychia

Retronychia represents a proximal ingrowth of the nail that occurs when the nail unit embeds backward into the proximal nail fold [10]. Clinically, retronychia presents 3–6 months after a severe inflammatory or systemic disease and shows as persistent or chronic proximal paronychia with a disrupted nail appearance. Retronychia can occasionally be associated with onychomadesis and can clinically mimic a nail tumor.

On sonography, an abnormal shorter distance between the origin of the nail plates and the base of the distal phalanx (DIP joint level) can be seen in retronychia. Thickening and decreased echogenicity of the proximal nail fold and the proximal nail bed as, well as variable degrees of thickening of the ungual matrix, can be detected. This abnormality can also appear as a total or partial posterior embedding of the nail unit. 3D ultrasound has been reported as being useful in the early detection and better clinical understanding of retronychia [10, 11] (Figs. 18.6 and 18.7).

Fig. 18.6 (**a**–**c**) Retronychia. (**a**) Clinical photograph shows edema and posterior embedding of the nails of the right index, middle and ring fingers. (**b**, **c**) Sonographic comparison of side by side images (longitudinal views) of the index fingers (**b** grey scale ultrasound image and **c** 3D reconstruction) show a decrease of the distance (*white line*) between the origin of the nail plates and the base of the distal phalanx in the right side (abnormal) versus the left side (normal). Notice that the origin of the nail plates in the affected side is closer to the distal interphalangeal joint level. *Abbreviations: pl* ungual plate, *nb* nail bed, *dph* distal phalanx, *pnf* proximal nail fold, *dip* distal interphalangeal joint

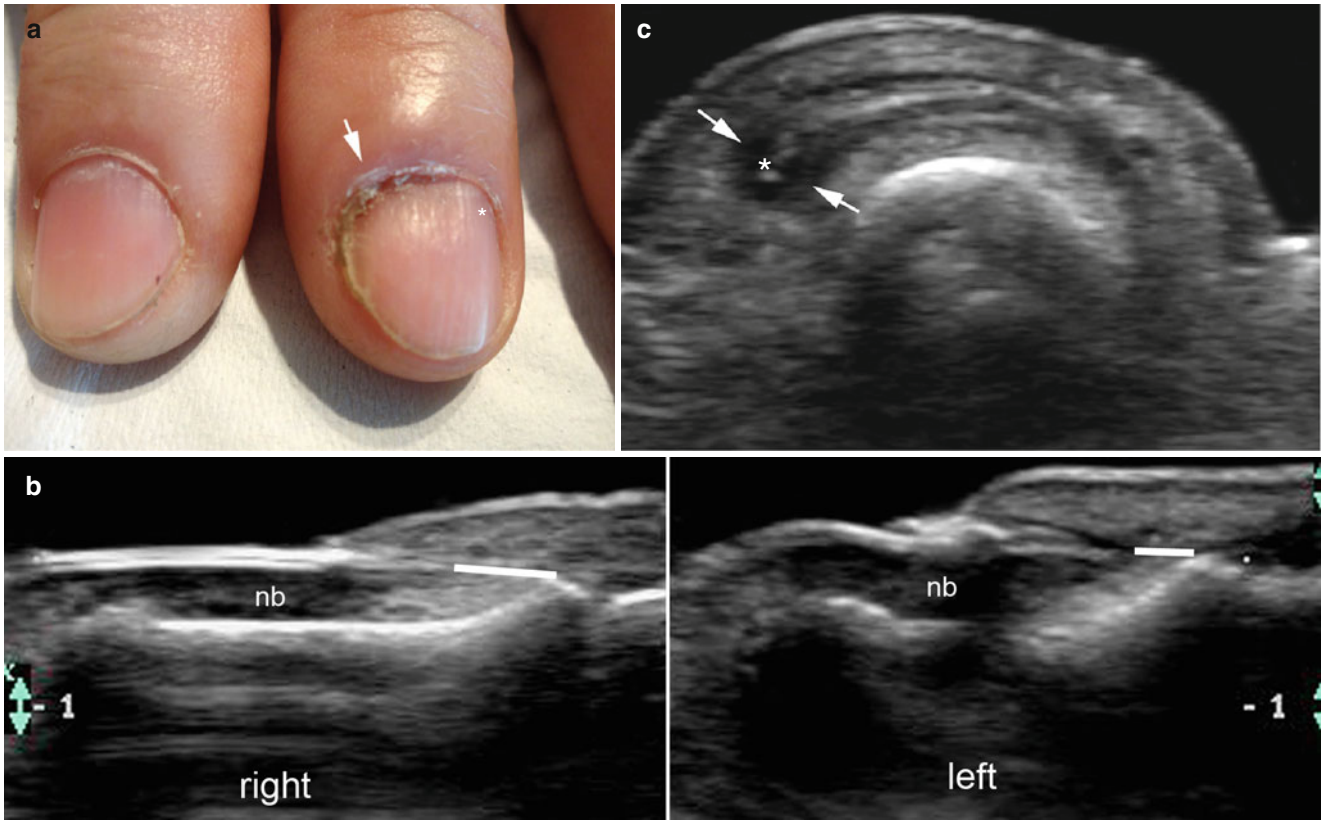

Fig. 18.7 (**a**–**c**) Partial Retronychia. (**a**) Clinical photograph shows edema in the radial aspect of the proximal nail fold of the nail (*arrow*) in the left index finger. (**b**) Grey scale ultrasound image (longitudinal view, side by side (right/left) comparison of the radial aspect of the index finger) shows a posterior embedding of the nail plate in the left index that is located closer to the base of the distal phalanx and interphalangeal joint. Notice the bilaminar and thick pattern of the nail plate fragment in the abnormal side. Thickening and hypoechogenicity of the nail bed is also detected in the affected side. The *white horizontal lines* mark the distance from the origin of the nail plate to the base of the distal phalanx. The radial aspect of the left finger shows a shorter distance. (**c**) Grey scale ultrasound image (transverse view, left index finger) shows the nail plate fragment (*, *arrows*) embedded in the radial aspect of the proximal nail fold. The ulnar aspect of the proximal nail fold in the left index is unremarkable. *Abbreviations*: *nb* nail bed

18.4.1.2 Congenital Diseases, Anatomical Variants, and Secondary Involvement

18.4.1.2.1 Congenital Malalignment

The three main types of nail malalignment are: congenital malalignment of the big toe nail, traumatic nail malalignment, and iatrogenic malalignment of the nail plate. Congenital malalignment (CM) of the big toe nail is based on a lateral deviation of the nail plate. This longitudinal axis shift is the result of a deviation of the nail matrix, possibly caused by increased traction of a hypertrophic extensor tendon of the hallux. CM of the big toe nail is typically present at birth. It is commonly bilateral but can also appear unilateral. Ingrown toenails and onychogryphosis (i.e., prominent thickening and curving of the nails) are among the most common complications [12, 13].

On ultrasound, CM appears as thickening of the nail plates and nail bed with hypoechogenicity of the ungual bed. Hyperechoic and bilaminar fragments of nail plates can be detected in the lateral folds when CM is complicated by onychocriptosis. The nail bed typically appears hypovascular on color Doppler ultrasound (Figs. 18.8 and 18.9).

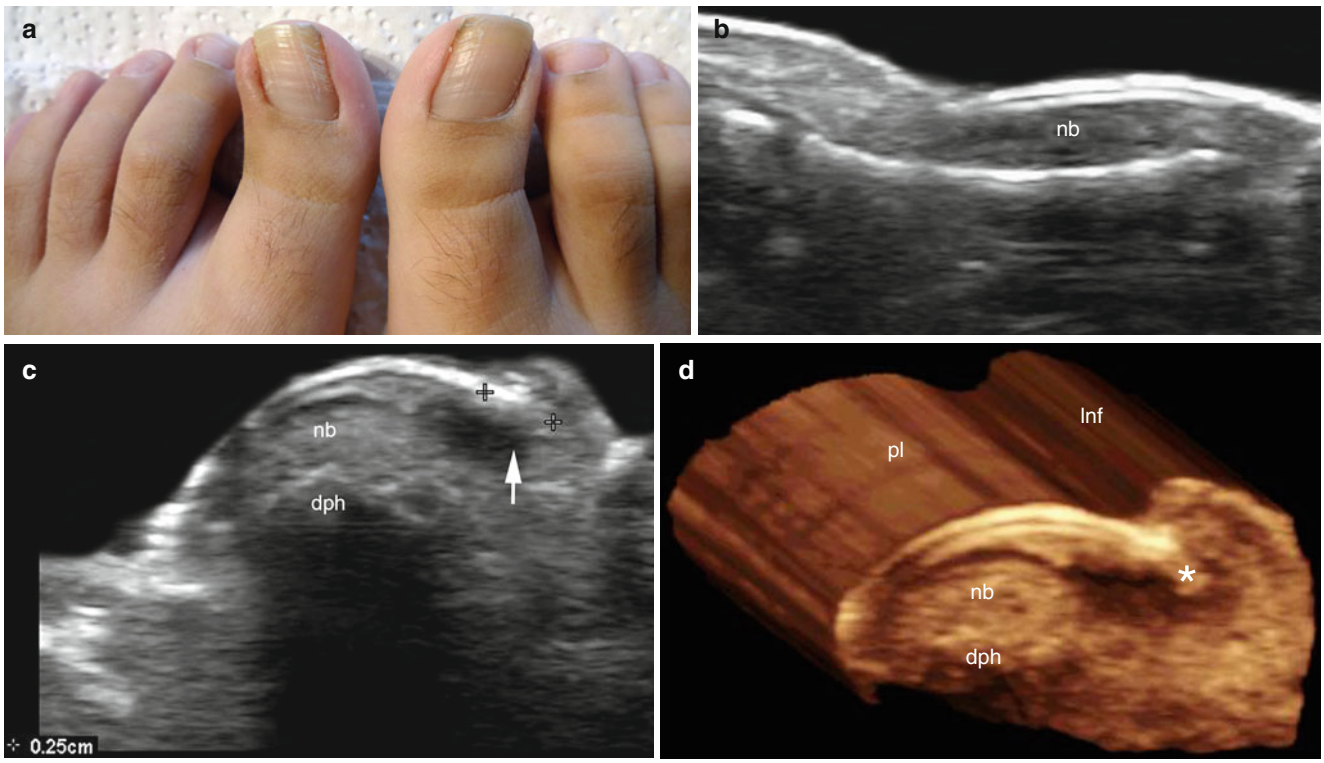

Fig. 18.8 (**a**–**d**) Bilateral congenital nail malalignment of the big toenail. (**a**) Clinical photograph shows a lateral deviation of the nails as well as erythema and swelling in the lateral nail folds in both big toenails. (**b**) Grey scale ultrasound image (longitudinal view, left big toenail) shows a mild thickening of the nail bed. (**c**, **d**) Sonographic studies (transverse views; **c** grey scale and **d** 3D reconstruction; left big toenail) show embedding of a 2.5 mm wide nail plate fragment (*) into the lateral nail fold. Hypoechoic inflammatory and granulomatous tissue (*arrow*) surrounds the nail fragment. *Abbreviations*: *nb* nail bed, *pl* ungual plate, *lnf* lateral nail fold, *dph* distal phalanx

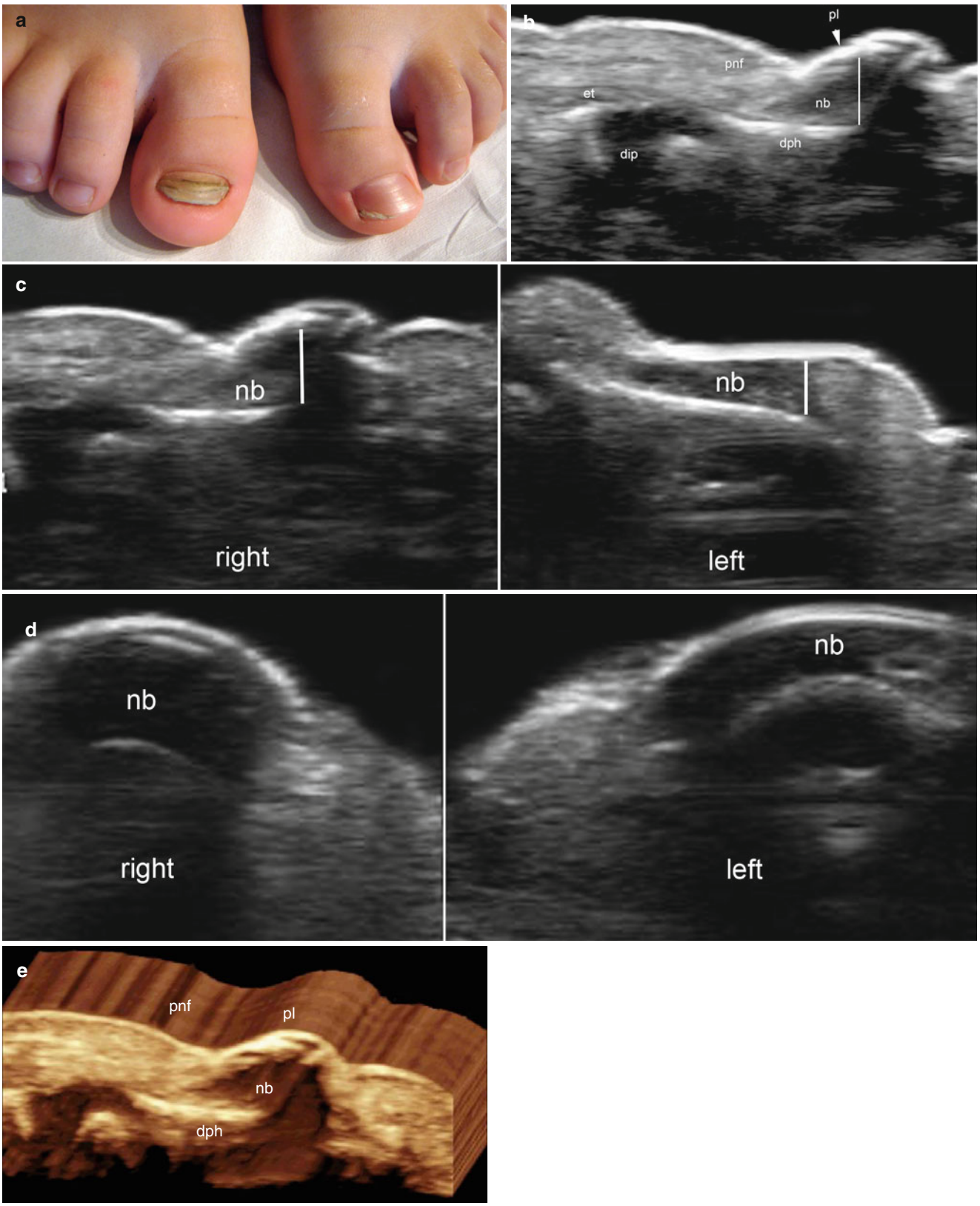

Fig. 18.9 (**a**–**e**) Unilateral congenital nail malalignment of the big toenail. (**a**) Clinical photograph shows mild lateral deviation, dystrophic changes, brownish and greenish color, transverse ridging and thickening of the nail plate of the right big toenail. (**b**–**e**) Ultrasound images (**b**–**d** Grey scale ultrasound images (**b** longitudinal view right big toenail; **c** longitudinal view comparison side by side; **d** transverse view, comparison side by side); **e** 3D longitudinal reconstruction of the right big toenail) show thickening and decreased echogenicity of the nail bed (*white line*) that involves the ungual matrix region. Thickening of the nail plate and disruption with loss of the interplate space in parts of the nail plate are also detected. *Abbreviations*: *nb* nail bed, *pnf* proximal nail fold, *pl* ungual plates, *dph* distal phalanx, *dip* distal interphalangeal joint, *et* extensor tendon

18.4.1.2.2 Congenital Hypertrophic Lip of the Hallux

Congenital hypertrophic lip of the hallux also called as pseudodigital fibrous tumor of the hallux, corresponds to a commonly bilateral and symmetric hypertrophy of the medial nail fold that is present at birth and mostly affects the hallux. Clinically, it is composed of red and firm swellings that may resemble recurrent digital fibrous tumors of childhood [14–16].

On sonography, these benign conditions or pseudotumors present as hypertrophic skin layers with decreased echogenicity of the upper dermis, probably related to inflammation. The condition affects the medial nail fold and does not compromise the ungual beds. Fragments of nail plates can occasionally be found embedded in the lateral nail fold [6] (Fig. 18.10).

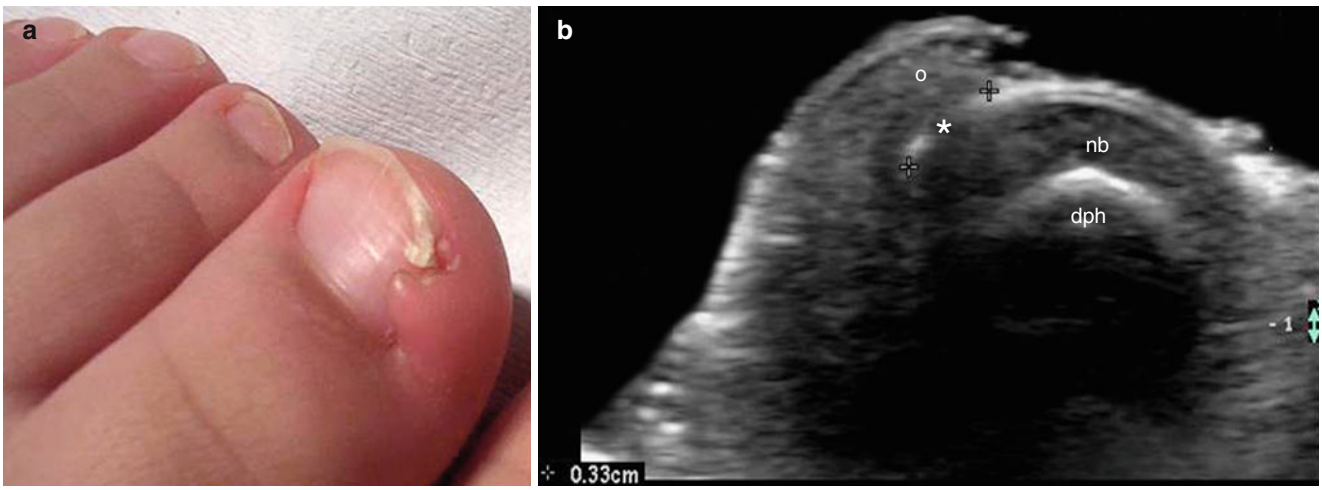

Fig. 18.10 (**a**, **b**) Congenital hypertrophic lip of the hallux. (**a**) Clinical image shows erythematous and hypertrophic swelling in the medial nail fold of the left hallux. (**b**) Grey scale ultrasound image (transverse view) shows hypertrophy of the dermal layer (o) in the medial nail fold. Notice that there is a 3.3 mm nail plate fragment (*) embedded in the medial nail fold (onychocryptosis). Hypoechoic inflammatory and/or granulomatous tissue surrounds the nail plate fragment. *Abbreviations*: *nb* nail bed, *dph* distal phalanx

18.4.1.2.3 Alopecia Areata

Alopecia areata (AA) is an autoimmune non-scarring hair loss disorder with a 2 % lifetime risk. This condition usually affects young adults and children. Nail affection in AA seems occur more frequently in the pediatric population. In addition to the scalp and body hair, the eyebrows, eyelashes, and nails can be affected [17–20]. Clinically, pitting and variable degrees of nail dystrophy are seen that may precede the presentation of the abnormalities in the scalp, and these clinical changes can resemble psoriatic onychopathy [6].

On ultrasound, thickening of the proximal nail bed that involves the matrix region can be detected. Hyperechogenicity, thickening, and a wavy shape of the nail plates have been described. Upward displacement of the nail plates also can be seen. Hypovascularity is commonly detected in the nail bed that may differ from the usual hypervascularity detected in active psoriatic onychopathy [6] (Figs. 18.11 and 18.12).

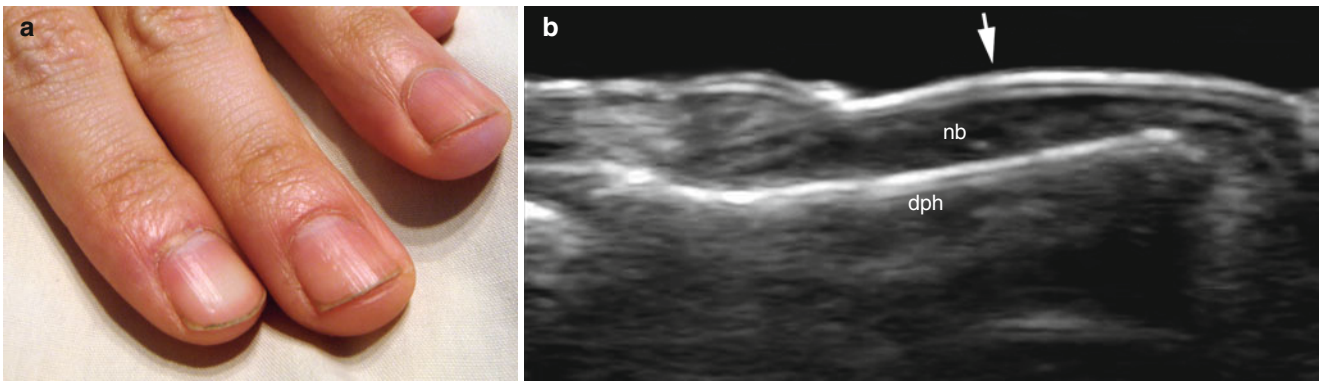

Fig. 18.11 (**a**, **b**) Alopecia areata. (**a**) Clinical photograph shows irregular pitting in the right index, middle, and ring fingers. (**b**) Grey scale ultrasound image (longitudinal view, middle finger) shows mild increase of the thickness of the nail bed and an upward displacement of the nail plates (convexity, *arrow*). *Abbreviations*: *nb* nail bed, *dph* distal phalanx

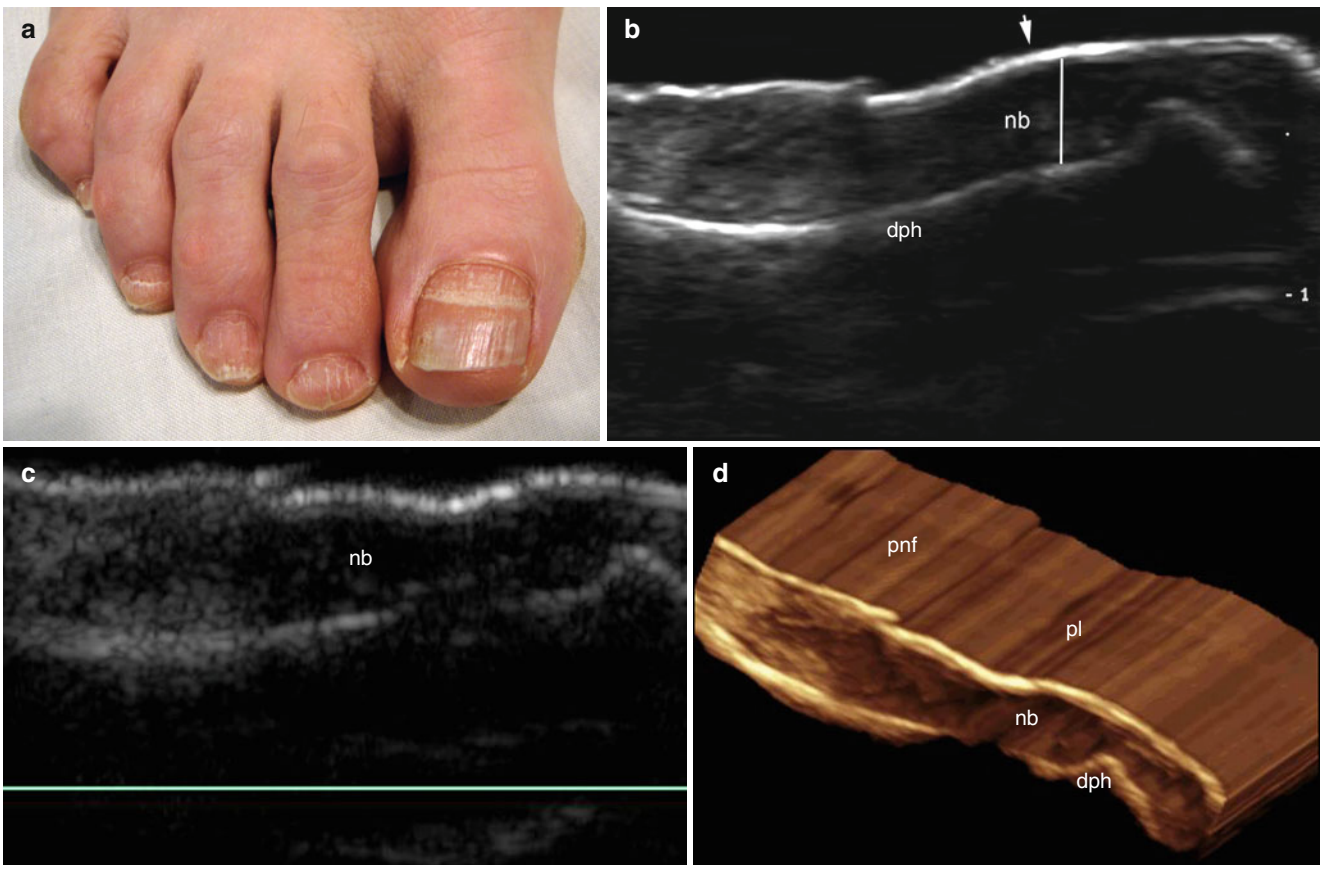

Fig. 18.12 (**a**–**d**) Alopecia areata. (**a**) Clinical image shows dystrophic changes in the toenails of the right foot. (**b**) Grey scale image (longitudinal view, right big toenail) shows thickening (*white line*) and decreased echogenicity of the nail bed that additionally affects the ungual matrix region. A wavy nail plate with loss of definition of the ventral plate is also detected (*arrow*). (**c**) 3D reconstruction (longitudinal view, 5–8 s sweep) of the right big toenail highlights the changes. (**d**) Color Doppler ultrasound image (longitudinal view) shows diffuse hypovascularity of the nail bed. *Abbreviations*: *nb* nail bed, *dph* distal phalanx, *pl* nail plate, *pnf* proximal nail fold

18.4.1.2.4 Ichthyosis

Ichthyosis is a group of genetic disorders with defective cornification, clinically characterized by scaling of the skin. There are inherited and acquired forms of ichthyosis. The congenital autosomal recessive ichthyosis is usually present at birth, most often in collodion babies. Ichthyosis vulgaris is the most common form of ichthyosis and is inherited in an autosomal dominant pattern [6, 21, 22].

On sonography, thickening of the nail plates with loss of the interplate space and thickening of the epidermal layer in the periungual region can be detected [6, 23] (Fig.18.13).

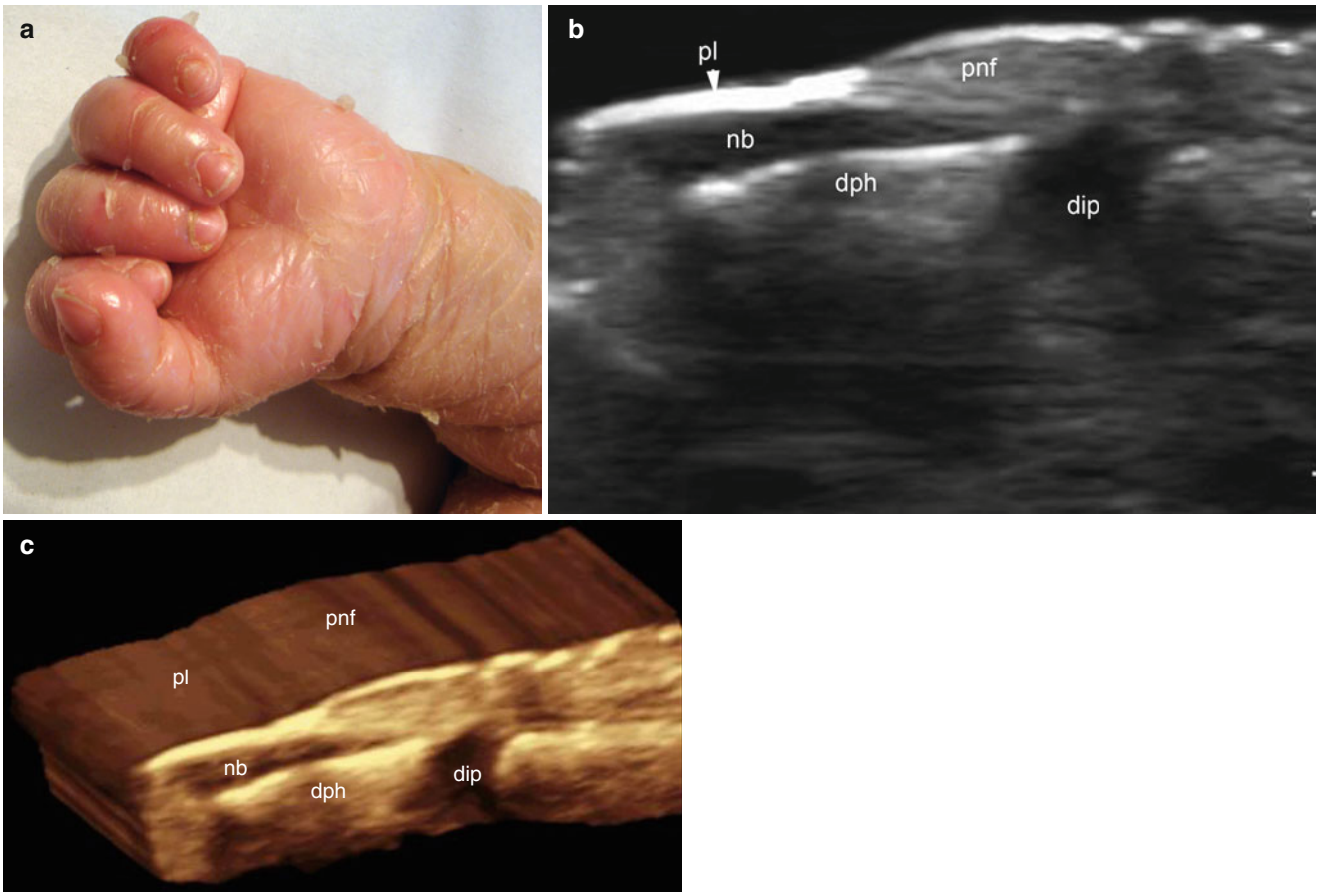

Fig. 18.13 (**a**–**c**) Ichthyosis. (**a**) Clinical photograph shows prominent scaling of the skin in a child with congenital autosomal recessive ichthyosis (CARI). (**b**, **c**) Images (**b** Grey scale ultrasound image and **c** 3D reconstruction longitudinal views) of the right middle fingernail show thickening of the nail plate with loss of the interplate space between the dorsal and ventral plates. Thickening of the epidermis in the proximal nail fold is also detected. *Abbreviations*: *nb* nail bed, *pl* nail plate, *dph* distal phalanx, *dip* distal interphalangeal joint

18.4.2 Inflammatory Diseases

18.4.2.1 Psoriasis

A significant association exists between the severity of nail and skin involvement in psoriasis [24]. Psoriatic onychopathy can be the single manifestation, or precede the appearance, of psoriatic plaques in the skin. It is estimated that 5 % of the psoriatic patients with an affected nail do not show any cutaneous involvement and nail disease has a greater magnitude of underlying systemic subclinical enthesopathy than those with normal nails. Additionally, 10–20 % of psoriatic patients present with psoriatic arthritis, although patients that present with psoriatic arthritis will most commonly show nail involvement (53–86 %).

On ultrasound, psoriasis can be seen usually affecting both the nail bed and the nail plates. The most common sonographic manifestations (from early to late phases) are: thickening of the nail bed (increased distance between the ventral plate and the bony margin of the distal phalanx); increased blood flow within the nail bed; loss of definition of the ventral plate; hyperechoic focal involvement of the ventral plate (that can be subclinical), thickening, loss of definition, irregularities, and undulation of one or both nail plates in late phases [25, 26]. The assessment of activity in psoriatic onychopathy using color or power Doppler ultrasound can also be traced through the patterns of blood flow that allow monitoring of the disease [27]. Hypervascularity is often detected during the active phases that usually begin in the proximal nail bed (partial involvement) and can diffusely extend to the whole nail bed (total involvement) (Figs.18.14, 18.15, and 18.16).

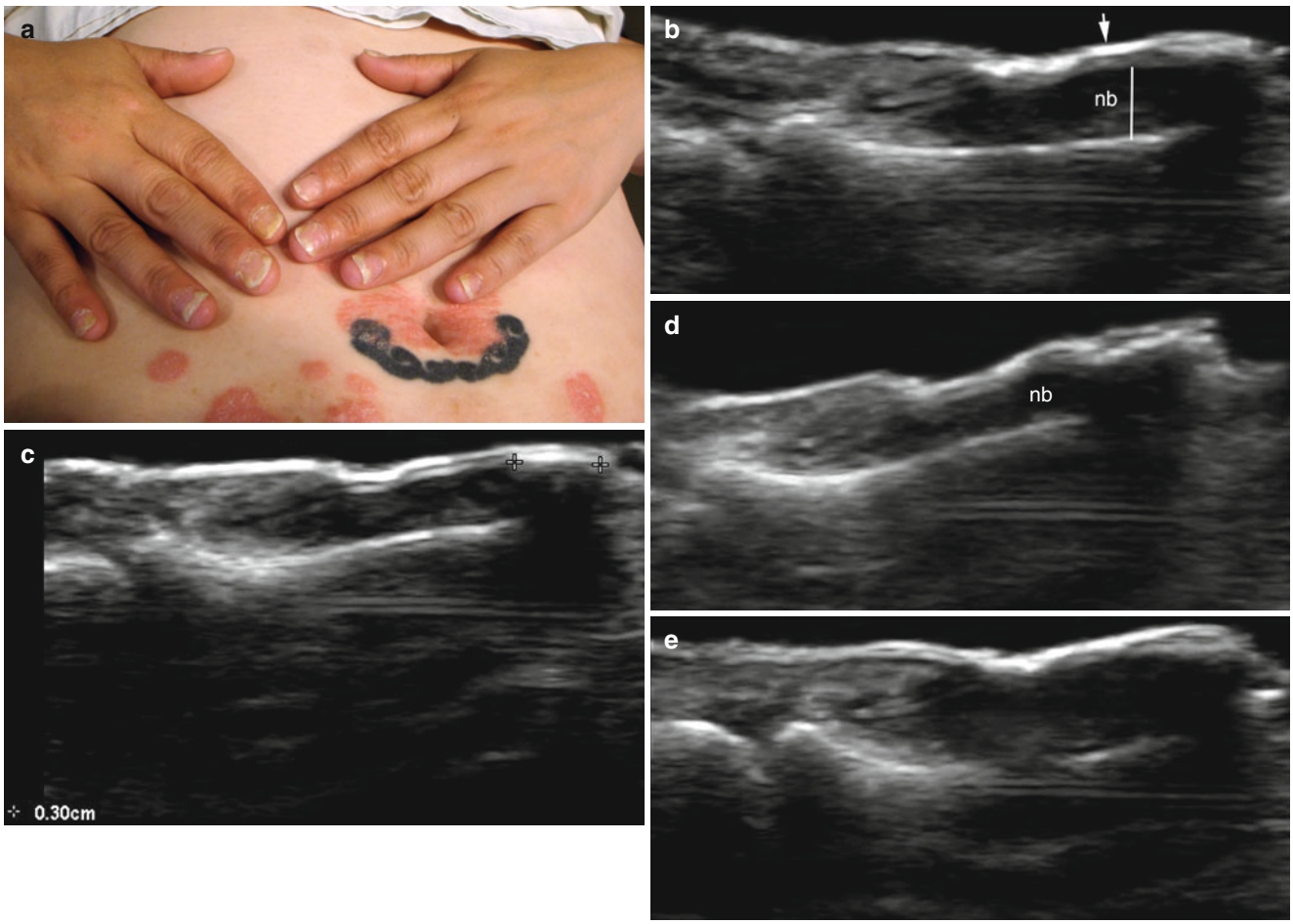

Fig. 18.14 (**a**–**e**) Psoriasis. (**a**) Clinical image shows extensive dystrophic changes in the fingernails of a patient with psoriatic plaques. (**b**) Grey scale ultrasound image (longitudinal view, right middle finger): thickening and decreased echogenicity of the nail bed (*white line*) that includes the ungual matrix region. Thickening of the dorsal plate (*arrow*) and loss of definition of the ventral plate are also detected. (**c**) Grey scale ultrasound image (longitudinal view, right ring finger): 3.0 mm hyperechoic focal deposit in the distal ventral plate that produces posterior acoustic shadowing artifact. Diffuse hypoechogenicity of the nail bed and wavy nail plates are also detected. (**d**) Grey scale ultrasound image (longitudinal view, right little finger): loss of definition, irregularities, and thickening of the nail plates. Increased thickness of the proximal nail bed is seen with diffuse hypoechogenicity of the nail bed. (**e**) Grey scale ultrasound image (longitudinal view right index finger): prominent thickening and hypoechogenicity of the nail bed. Loss of definition of the ventral nail plate and thickening of the dorsal plate are detected. The inter-plate space is also partially lost. *Abbreviation*: *nb* nail bed

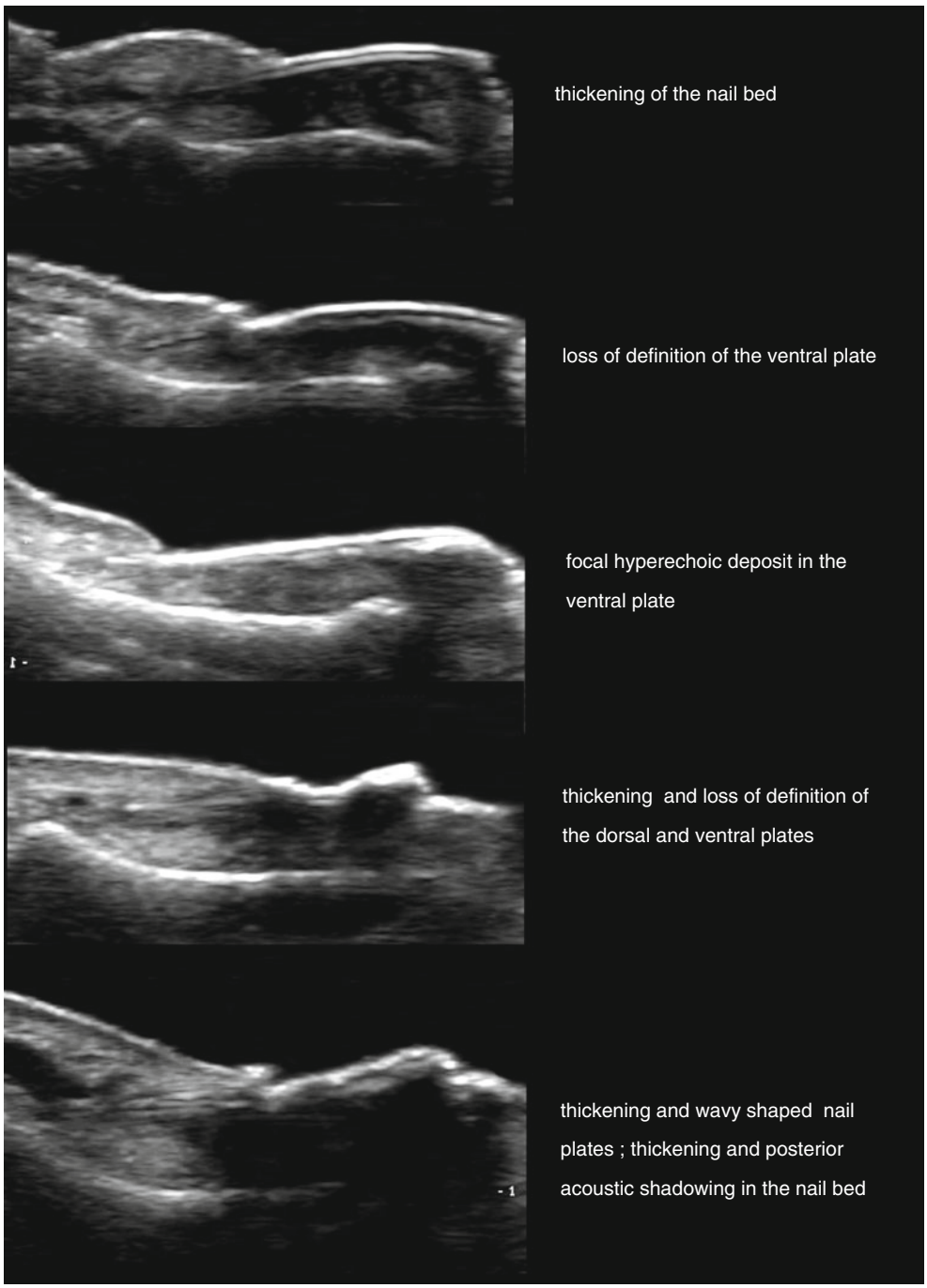

Fig. 18.15 Psoriatic onychopathy echogenicity patterns. Grey scale ultrasound image (longitudinal views) shows the wide variety of morphological changes in psoriasis from early to late phases

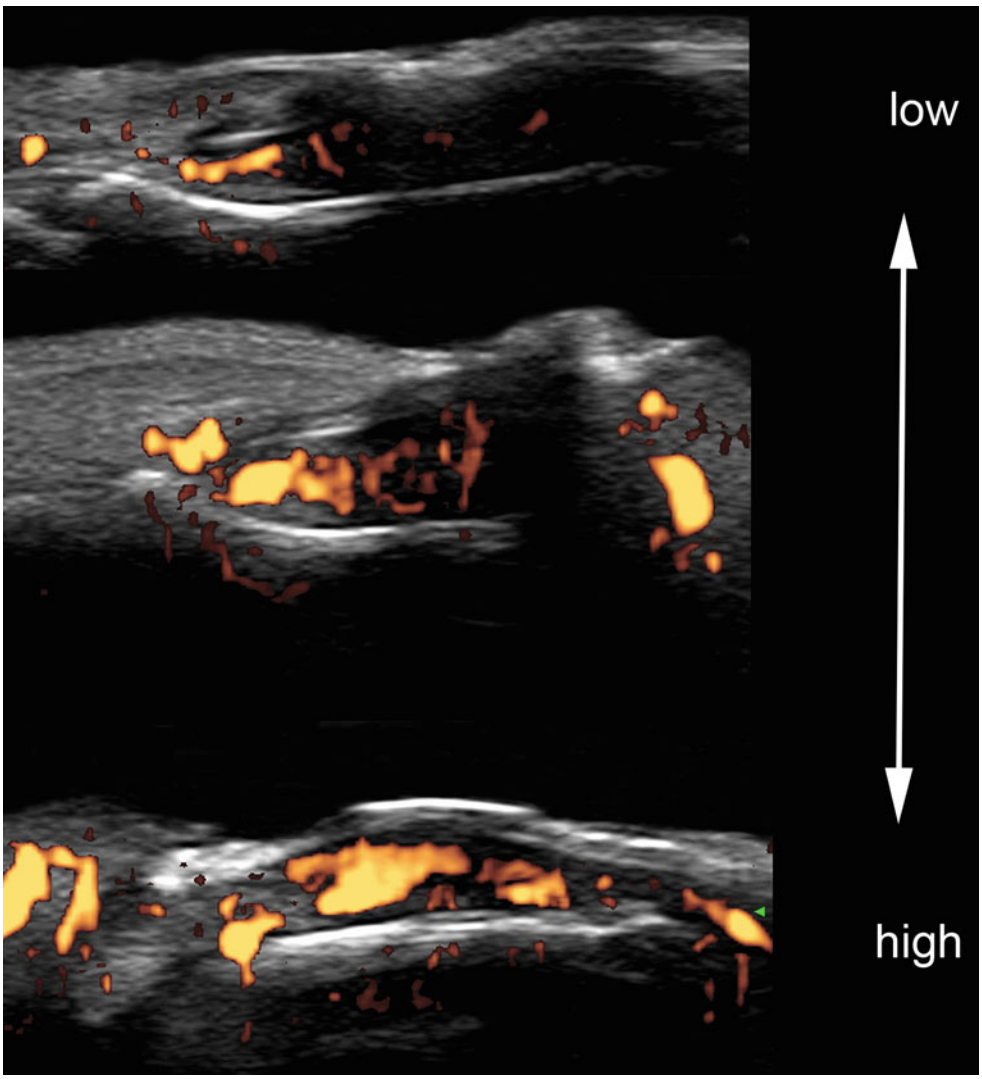

Fig. 18.16 Psoriatic onychopathy blood flow patterns. Power Doppler ultrasound image (longitudinal views) shows the variable degrees of blood flow in the psoriatic nail bed going from a low (partial and proximally located) to high level (total and diffuse) of vascularity within the nail bed

18.4.2.2 Scleroderma

Systemic sclerosis (SSC) is a connective tissue disease characterized by vascular damage and interstitial fibrosis of many organs. SSC can affect the microvascular structure and functionality of the nail unit; therefore, vascular abnormalities are common findings in scleroderma. Other imaging modalities have been used to track the vascular changes in the nail such as laser Doppler, thermal imaging, and nail fold capillaroscopy [28–30].

On sonography, upward displacement of the nail plates with thickening and decreased echogenicity of the nail bed are commonly detected that are probably related to edema and/or chronic inflammatory changes. Variable degrees of vascularity that end to mostly show low flow (hypovascularity) within the nail bed are detected that can be related to the slow capillary flow (velocity ≤2 cm/s) which is difficult to catch with the current machines [6, 31] (Fig.18.17).

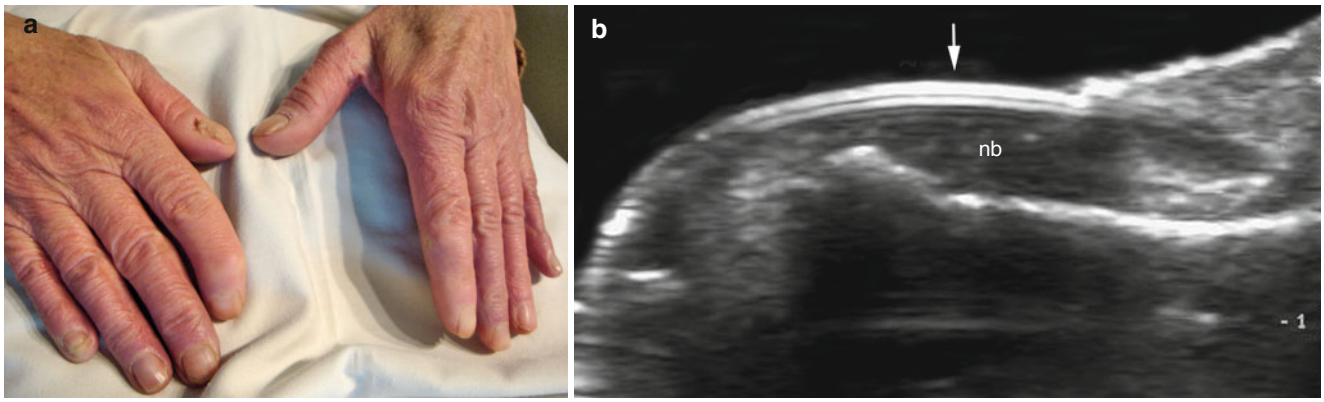

Fig. 18.17 Scleroderma. (**a**) Clinical photograph shows brownish zones and areas of discoloration in the fingernails. (**b**) Grey scale ultrasound image (longitudinal view of the left thumb) shows an upward displacement of the nail plates (*arrows*). Thickening and decreased echogenicity of the nail bed (*nb*), that includes the ungual matrix region, is detected in the fingernail.

18.4.2.3 Dermatomyositis-Calcinosis

Changes in nail-fold capillaries have been reported to reflect disease activity in dermatomyositis [32]. Thus, periungual capillary changes such as dilated and tortuous blood vessels, areas of atrophy, telangiectasias, central areas of hemorrhages, splinter hemorrhages, and bushy capillary loop formation in the proximal nail fold have been reported [30, 33]. Calcinosis is a recognized manifestation of many connective tissue diseases, particularly juvenile dermatomyositis, and it is common in patients with sustained disease activity and longer disease duration [34].

On ultrasound, the periungual calcinosis deposits are usually located in the tip of the fingers and can be seen on ultrasound as hyperechoic focal spots that present posterior acoustic shadowing, a typical artifact generated by the properties of the calcium [6, 31]. Variable degrees of hypoechogenicity in the upper dermis that is close to the calcium deposits (suggestive of edema) can also be found. Additionally, mild degrees of hypervascularity in the nail bed can additionally be detected using color Doppler ultrasound (Fig. 18.18).

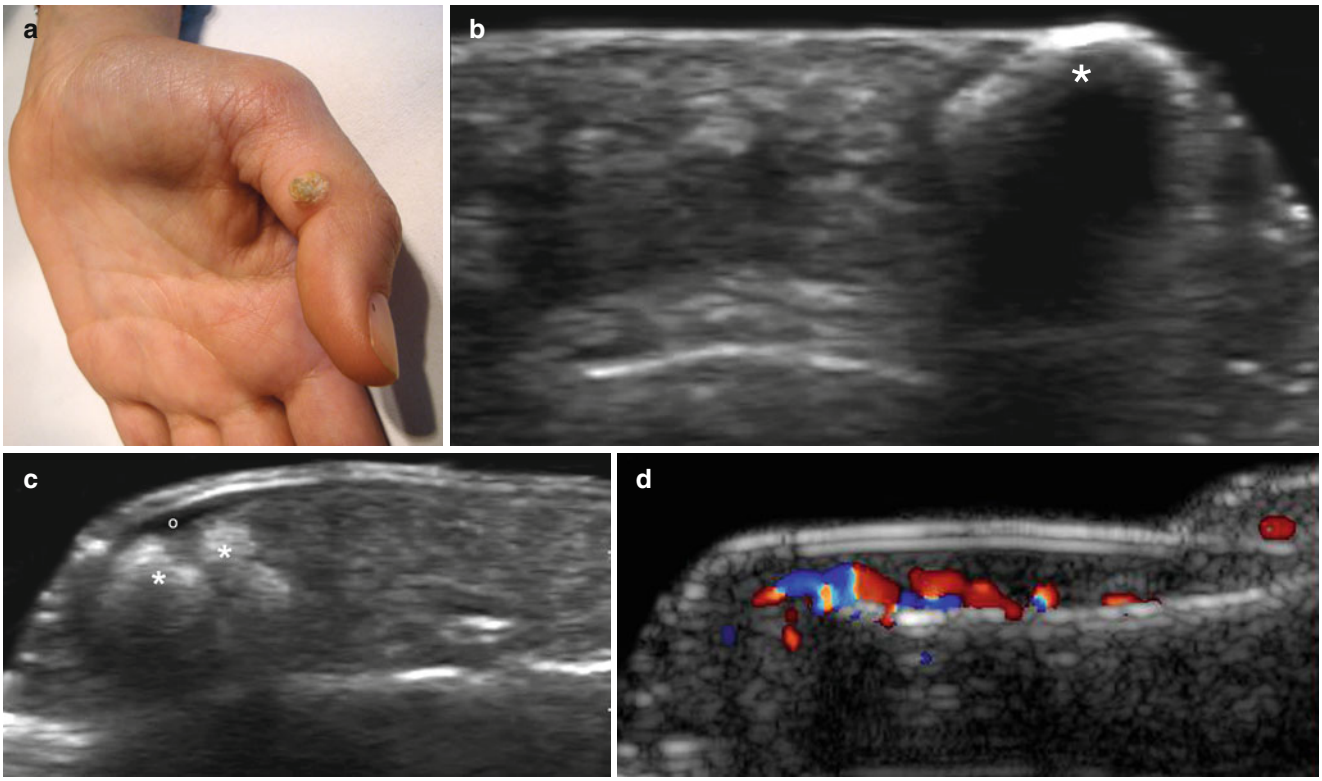

Fig. 18.18 (**a**–**d**) Dermatomyositis–calcinosis. (**a**) Clinical image shows a whitish swelling in the radial aspect of the left thumb. (**b**) Grey scale ultrasound image (longitudinal view, radial aspect of the left thumb) shows a hyperechoic spot (*) in the dermis that produces a posterior acoustic shadowing artifact and corresponds to a calcium deposit. (**c**) Grey scale ultrasound image (longitudinal view, pulp of the right index finger) shows hyperechoic dermal and subcutaneous spots (*) suggestive of calcium deposits. Hypoechogenicity of the upper dermis (o) is also detected. (**d**) Color Doppler ultrasound image (longitudinal view, left thumb) shows a mild increase in the vascularity of the nail bed

18.4.2.4 Lupus Erythematosus

Angiogenesis and microvascular endothelial injuries play a role in the pathogenesis of systemic lupus erythematosus [35]. The vascular changes also involve the digital arteries and nail bed. Thrombotic phenomena within the distal end of the digital arteries can produce secondary hypovascular changes and secondary dystrophic changes in the nail bed [36].

On sonography, variable thickness and hypoechogenicity of the nail bed can be seen, including thickening and thinning areas in the nail bed and/or the nail plates. Ungual dystrophy that reflects the affected ungual matrix can be characterized by a discontinuity and irregularities in the nail plates. Hypovascularity is usually detected in the nail bed using color Doppler ultrasound [6, 31] (Figs. 18.19 and 18.20).

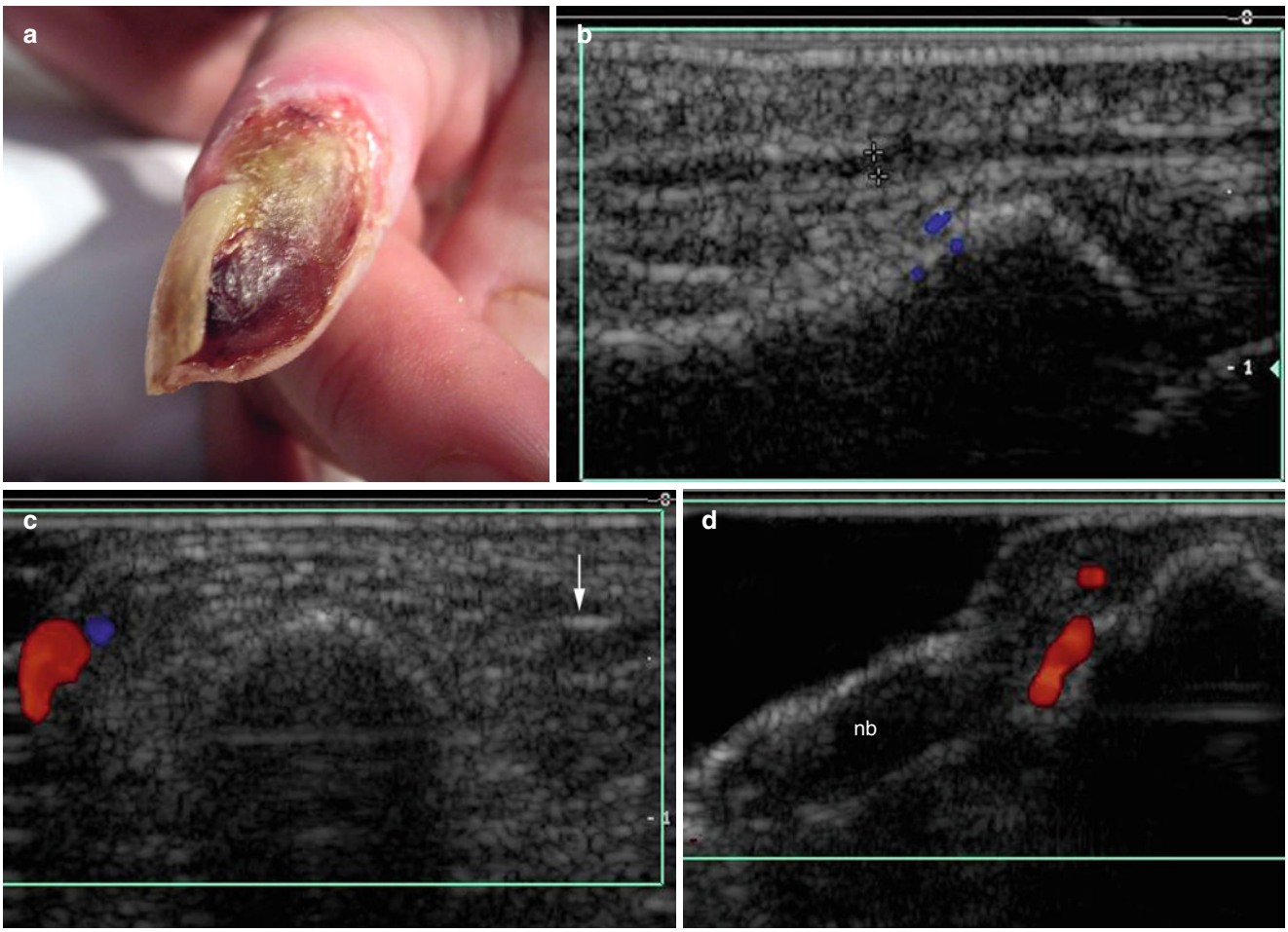

Fig. 18.19 (**a**–**d**) Lupus erythematous. (**a**) Clinical image shows ulceration of the tip of the right index finger and dystrophic changes in the nail. (**b**, **c**) Color Doppler ultrasound image (**b** longitudinal view; **c** transverse view; right index finger) shows hypoechoic thrombotic material filling the dorsal digital artery (between *markers* and *arrow*) of the radial aspect of the finger. (**d**) Color Doppler ultrasound image (longitudinal view; right index fingernail) shows diffuse hypovascularity within the nail bed. *Abbreviation*: *nb* nail bed

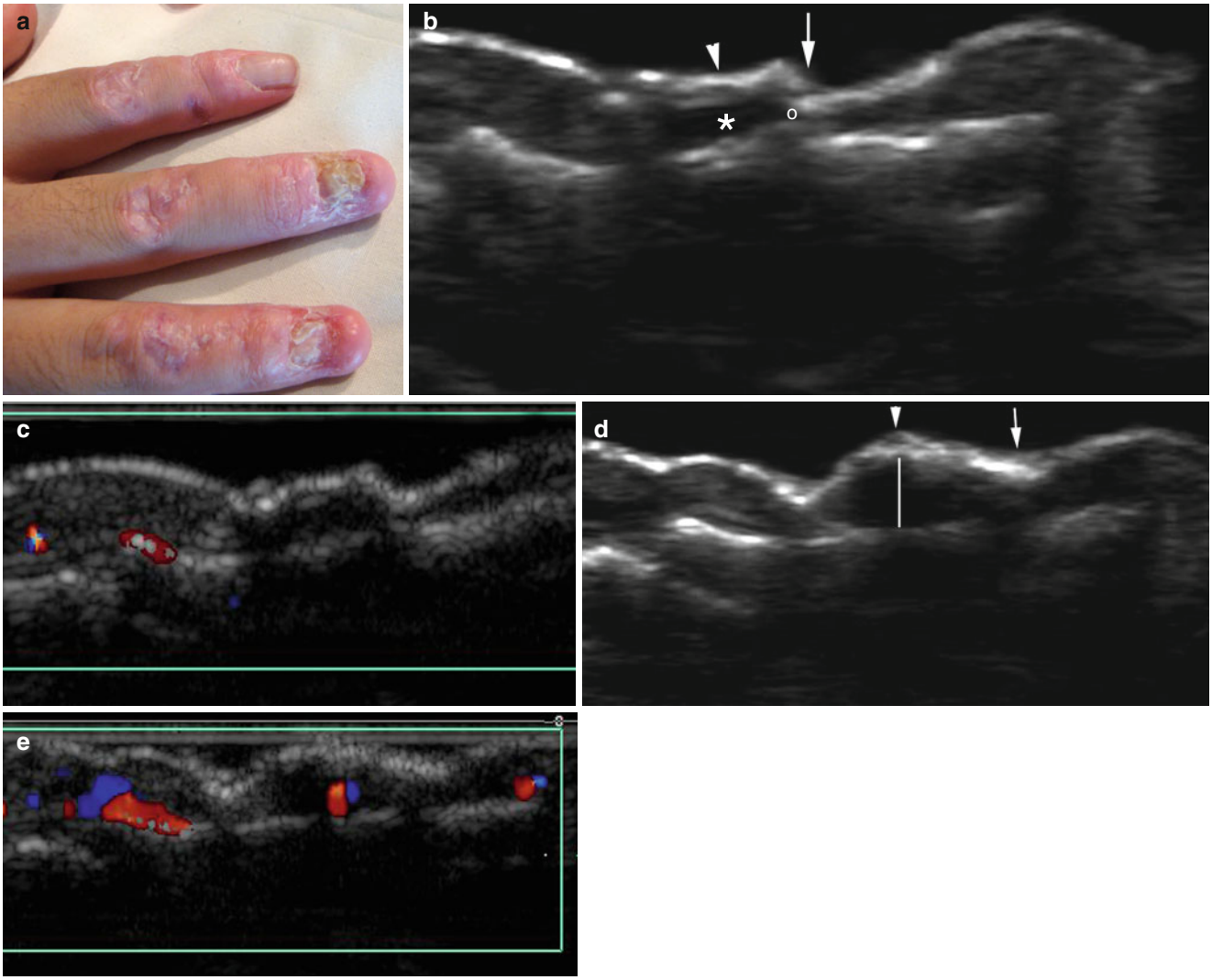

Fig. 18.20 (**a**–**e**) Lupus erythematous. (**a**) Clinical photograph shows extensive dystrophic changes in the fingernails and erythematous and scaly plaques in the dorsum of the fingers. (**b**) Grey scale ultrasound image (longitudinal view, right ring finger) shows thinning (* and o) of the nail bed with disruption (*arrow*) and irregularities (*arrowhead*) in the nail plates (dorsal and ventral). (**c**) Color Doppler ultrasound image (longitudinal view, right ring finger) shows hypovascularity within the nail bed. (**d**) Grey scale ultrasound image (longitudinal view, right middle finger) shows a variable thickness within the nail bed with thickening of the proximal nail bed (*vertical white line*) and thinning of the distal nail bed (*arrow*). Thickening, convexity (*arrowhead*), and irregularities in the nail plates are also detected. (**e**) Color Doppler ultrasound image (longitudinal view, right middle finger) shows partial hypovascularity within the nail bed

18.4.2.5 Rheumatoid Arthritis

Patients with autoimmune disorders can have a broad spectrum of nail changes. The proximal nail fold is the most important site of alterations in all collagen-related diseases. Erythema and telangiectasia, associated with visualization of the capillary loops, are frequent findings; nail fold capillary hemorrhages and focal necrosis are also observed [37].

Rheumatoid arthritis (RA) is a long-term disease characterized by symmetric inflammatory arthritis in association with systemic symptoms. RA involves diverse organ systems that include the skin and nail. Clinically, longitudinal ridging and clubbing are common findings in RA [38].

On ultrasound, an identification of the anatomic details of the joint space, extensor and flexor tendons, bone margin, periarticular and peritendinous soft tissues, nail, and blood vessels is possible [39]

Alterations in the anatomical parts include: narrowing of the joint space; tendinosis (i.e., tendinopathy or degeneration of the fibrillar pattern of the tendon); tear or atrophy of extensor and flexor tendons; erosions of the bony margin; periarticular and peritendinous edema; thickening, decreased echogenicity, and increased blood flow within the nail bed [6, 31] (Fig. 18.21).

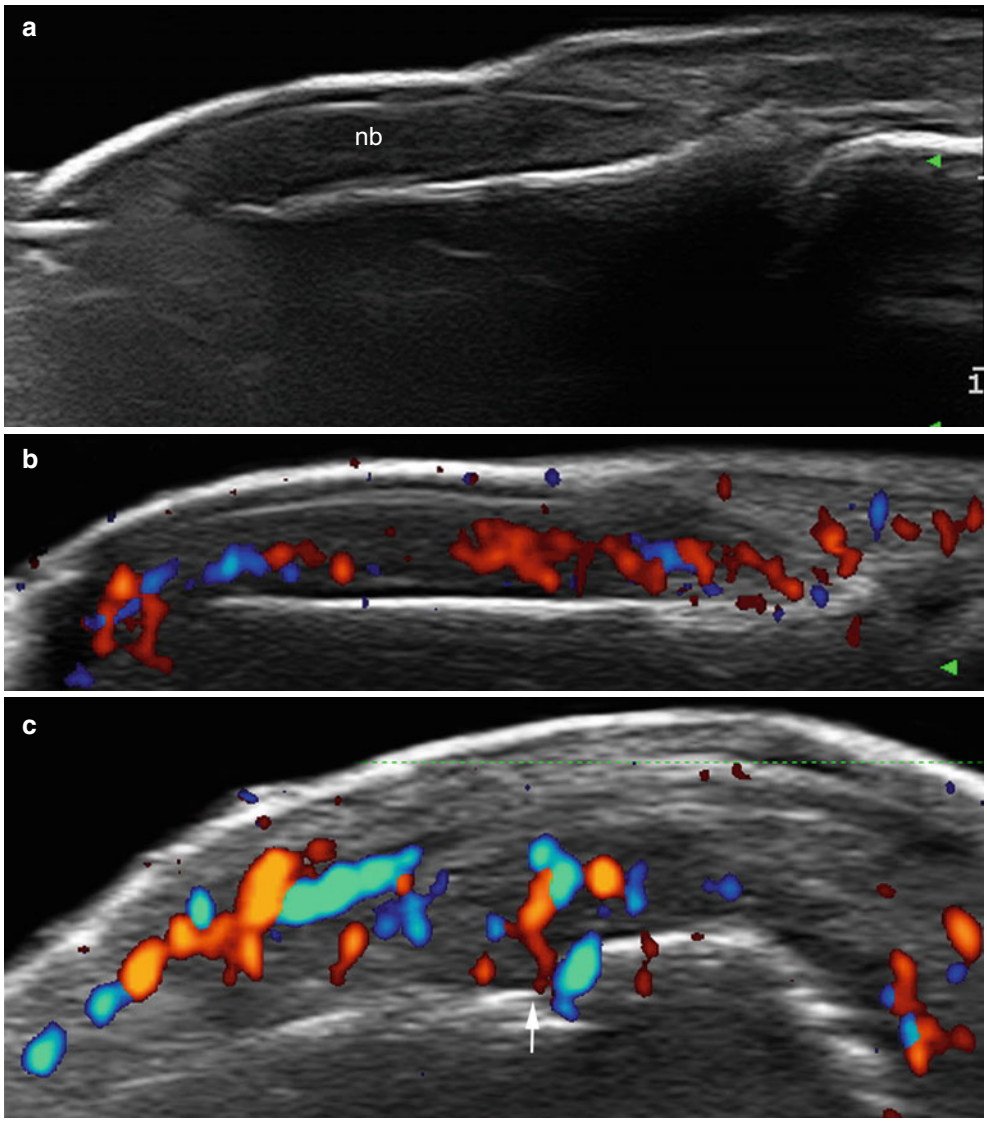

Fig. 18.21 (**a**–**c**) Rheumatoid arthritis. (**a**) Grey scale ultrasound image (longitudinal view, right index finger) shows diffuse thickening and hypoechogenicity of the nail bed. Loss of definition of the ventral plate, thickening of the dorsal plate, and a slight upward displacement of the nail plates (dorsal and ventral) are also detected. (**b**) Color Doppler ultrasound image (longitudinal view, right index finger) shows a mild increase of vascularity, mainly in the proximal region of the nail bed. (**c**) Color Doppler ultrasound image (longitudinal view, radial aspect of the base of the middle phalanx in the right index finger) shows a bony erosion (*arrow*) and hypervascularity of the surrounding soft tissues

18.4.2.6 Subungual Abscess: Periungual Fistula

Immmunosuppression secondary to drugs and/or systemic diseases can be associated with severe infections of the nail bed that often require surgical drainage [40–43].

On ultrasound, fluid collections or abscesses appear as anechoic areas within the nail bed usually accompanied by thickening of the subungual space. When the infections generate air bubbles, a hyperechoic band with reverberance and posterior acoustic shadowing can be seen. Furthermore, the free air can be displaced within the nail bed according to the changes in the position of the fingernail or toenail of the patient. Periungual hypoechoic and tortuous fistulous tracts can connect with the bony margin of the distal phalanx, the distal interphalangeal joint, and/or the nail bed and can be followed using sonography [6] (Figs. 18.22, 18.23, 18.24, and 18.25).

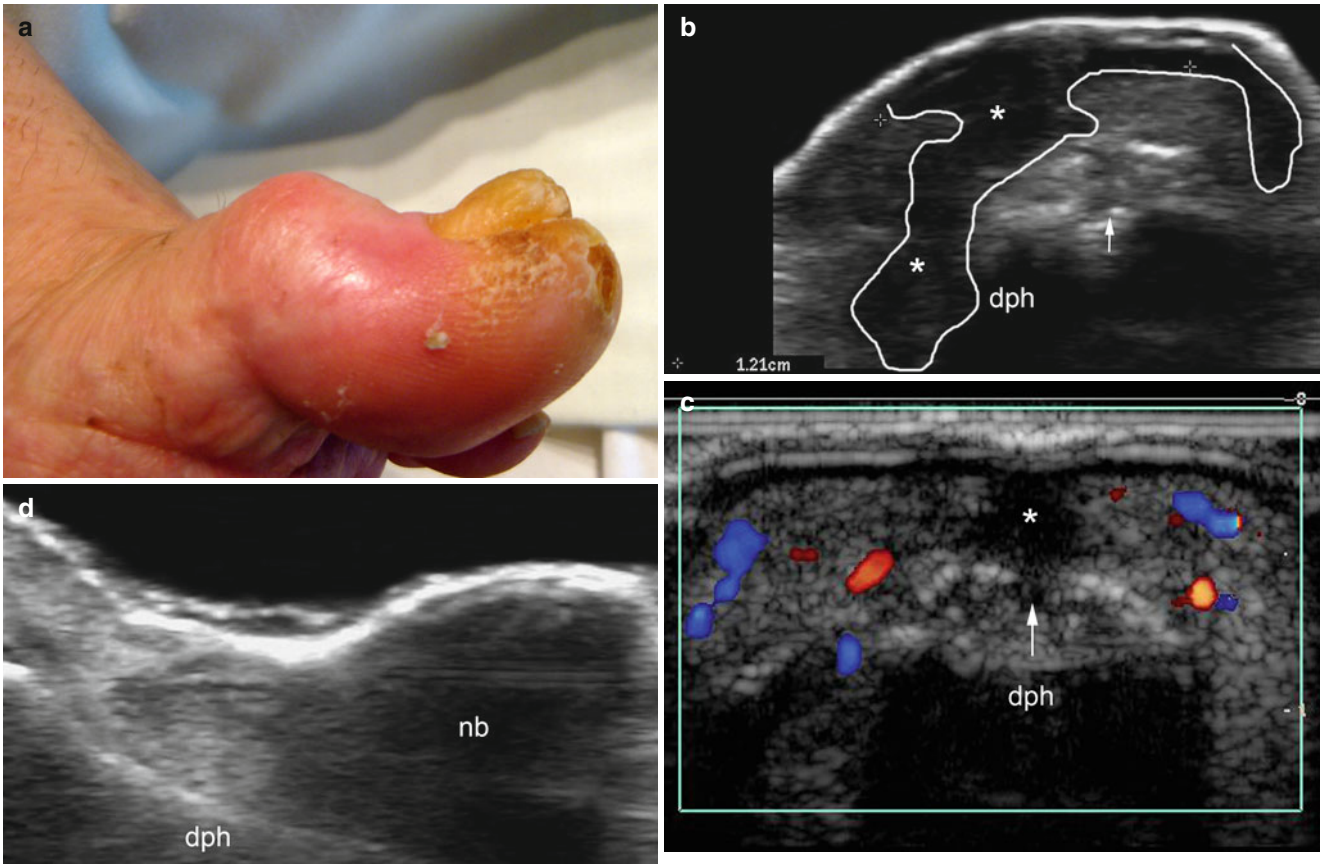

Fig. 18.22 (**a**–**d**) Periungual fistula. (**a**) Clinical photograph shows erythema and swelling in the medial aspect of the left big toe. A yellowish color and dystrophic changes are seen in the nail plate. Hyperkeratotic plaques are detected in the medial fold and the hyponichium. (**b**) Grey scale image (longitudinal view, medial aspect of the left hallux) shows a 1.21 cm fistulous tract (*, outlined) that connects the subepidermal region with the bony margin of the distal phalanx. Erosion of the hyperechoic bony margin of the distal phalanx is also detected (*arrow*). (**c**) Color Doppler ultrasound image (transverse view) shows a mild increase of vascularity in the periphery of the fistulous tract (*). Erosion (*arrow*) in the bony margin is well depicted. (**d**) Grey scale ultrasound image (longitudinal view, ungual region) shows thickening and decreased echogenicity of the nail bed. Thickening and irregularities in the nail plates are also detected. *Abbreviations*: *dph* distal phalanx, *nb* nail bed

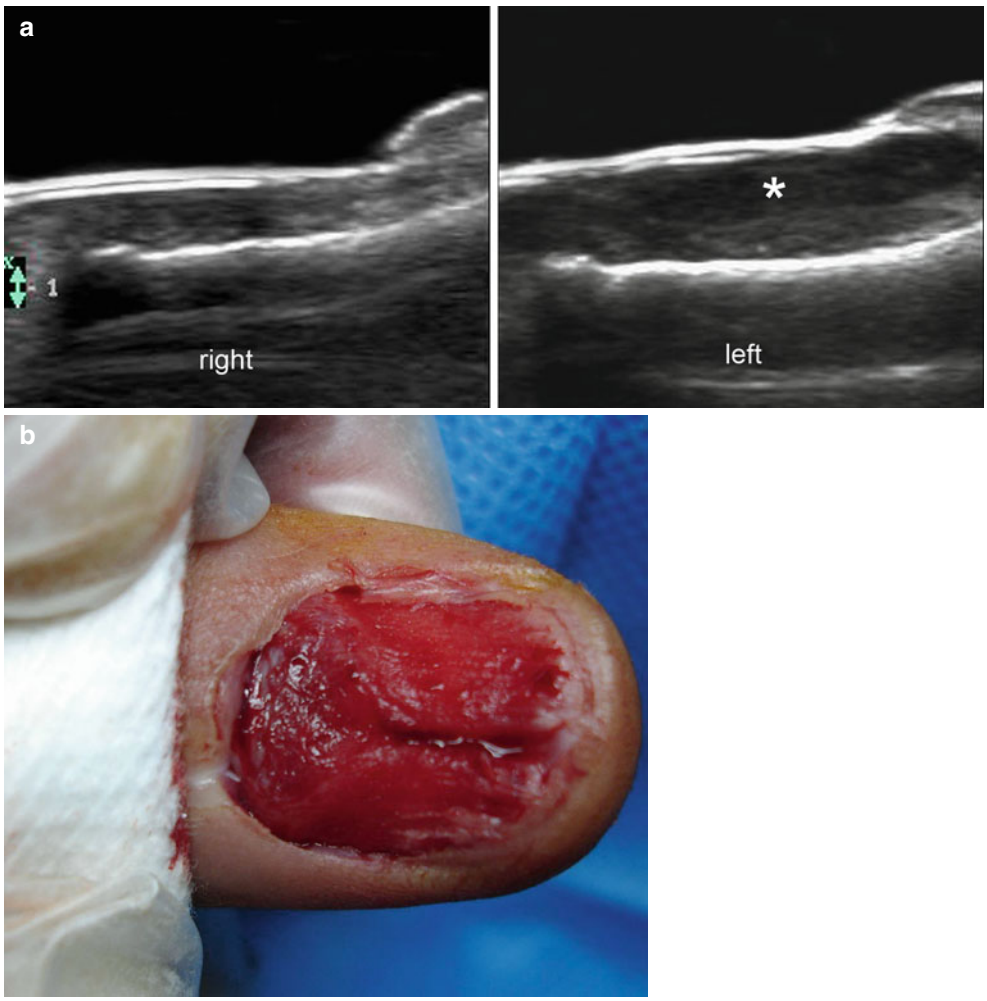

Fig. 18.23 (**a**, **b**) Subungual abscess. (**a**) Grey scale ultrasound image (comparative side by side longitudinal view) shows anechoic subungual fluid collection (*) in the nail bed of the left thumb. The nail bed of the right thumb is unremarkable. (**b**) The nail bed after drainage of the fluid collection (Courtesy of Dr. Rosamary Soto)

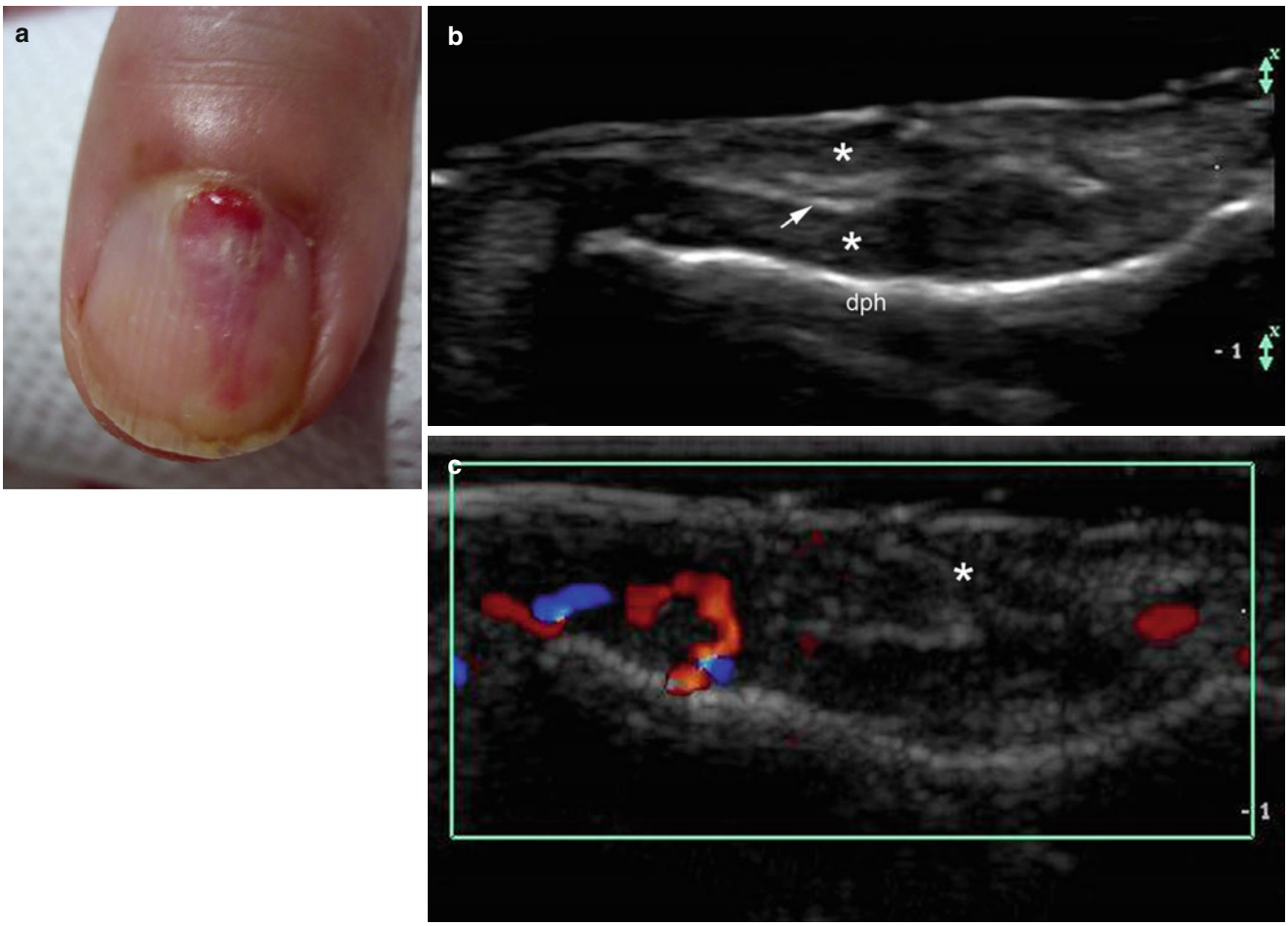

Fig. 18.24 (**a**–**c**) Subungual abscess. (**a**) Clinical image shows discharge of sero-hematic material and erythema in the nail of the left thumb. (**b**) Grey scale ultrasound image (longitudinal view, left thumb) shows hypoechoic subungual collection (*) that surrounds a nail plate fragment (*arrow*) embedded in the nail bed. A diffuse thickening of the nail bed is also detected. (**c**) Color Doppler ultrasound image (longitudinal view, left thumb) shows hypervascularity in the periphery of the fluid collection

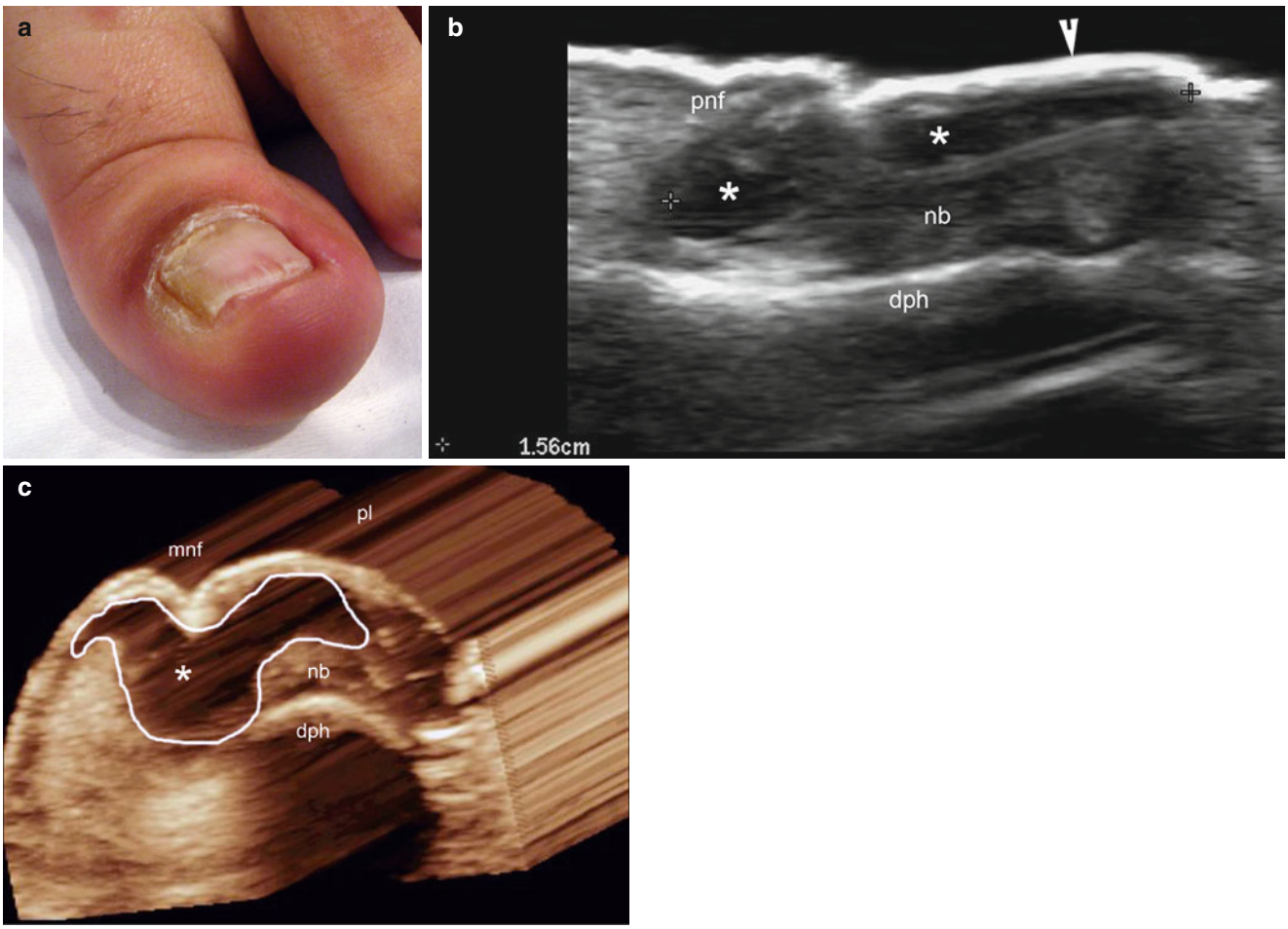

Fig. 18.25 (**a**–**c**) Subungual and periungual abscess. (**a**) Clinical image shows dystrophic changes in the nail plate, erythema, and edema in the medial and lateral nail fold of the left hallux. (**b**) Grey scale ultrasound image (longitudinal view, left hallux) shows 1.56 cm long anechoic fluid collection (*) in the nail bed. Thickening of the nail bed (*) and the nail plates (*arrowhead*) is well depicted. (**c**) 3D reconstruction (transverse view, left hallux) shows the extension of the collection (*) into the medial nail fold. *Abbreviations*: *nb* nail bed, *pl* nail plates, *mnf* medial nail fold, *pnf* proximal nal fold, *dph* distal phalanx

18.4.2.7 Trauma, Foreign Bodies, and Median Canaliform Nail Dystrophy

Nail trauma is common and is one of the most frequent causes of hand injury in the pediatric population. Among the most common traumatic lesions are subungual hematoma, wounds, simple or stellate lacerations of the nail bed and/or matrix, avulsion of the nail bed, ungual matrix defect, nail bed injuries associated with fractures of the distal phalanx, and associated fingertip injuries. The fingernail plays an important role in hand function, facilitating pinch and increasing the sensitivity of the fingertip. Therefore, immediate and proper strategy in treating fingernail injuries is essential to avoid aesthetic and functional impairment. Moreover, the ungual matrix is sensitive to trauma, and therefore a prompt diagnosis can decrease the possibility of long-term cosmetic complications such as a nail dystrophy [44–46].

Foreign bodies can also be found within the nail bed and can accidentally be embedded in the ungual bed; additionally, they can also be inserted during surgical corrections in the finger or toe that use prosthetic devices [6].

Median canaliform dystrophy is a condition most commonly related to prior local trauma and less commonly to drugs and a familial link. Clinically, there is longitudinal splitting of the nail or a central nail groove, beginning at or distal to the proximal nail fold, where small lateral fissures can be found [47–49].

On ultrasound, subungual fluid collections such as hematomas appear as anechoic deposits that can be associated with thickened and decreased echogenicity within the nail bed. In presence of incised or penetrating wounds the path of the injury can usually be recognized on ultrasound as a hypoechoic linear band that can reach the matrix region. The appearance of foreign bodies can vary in appearance on sonography according to the type of material. There are organic types of foreign bodies such as splinters of wood or rose thorns as well as synthetic materials such as pieces of glass or metal. The foreign bodies that are of an organic nature appear on ultrasound typically as laminar or bilaminar hyperechoic structures within the nail bed; synthetic materials such as glass and metal can be associated with reverberation artifact; and surgical implants can be seen as echoic bands attached to the bony margin. Typically, all types of foreign bodies are surrounded by hypoechoic inflammatory and/or granulomatous tissue with variable degrees of hypervascularity. Ultrasound can be useful in confirming the existence, nature, and exact location of the foreign body as well, facilitating the decision for the site and size of the excision and for guiding their extraction [5, 6] (Fig. 18.26).

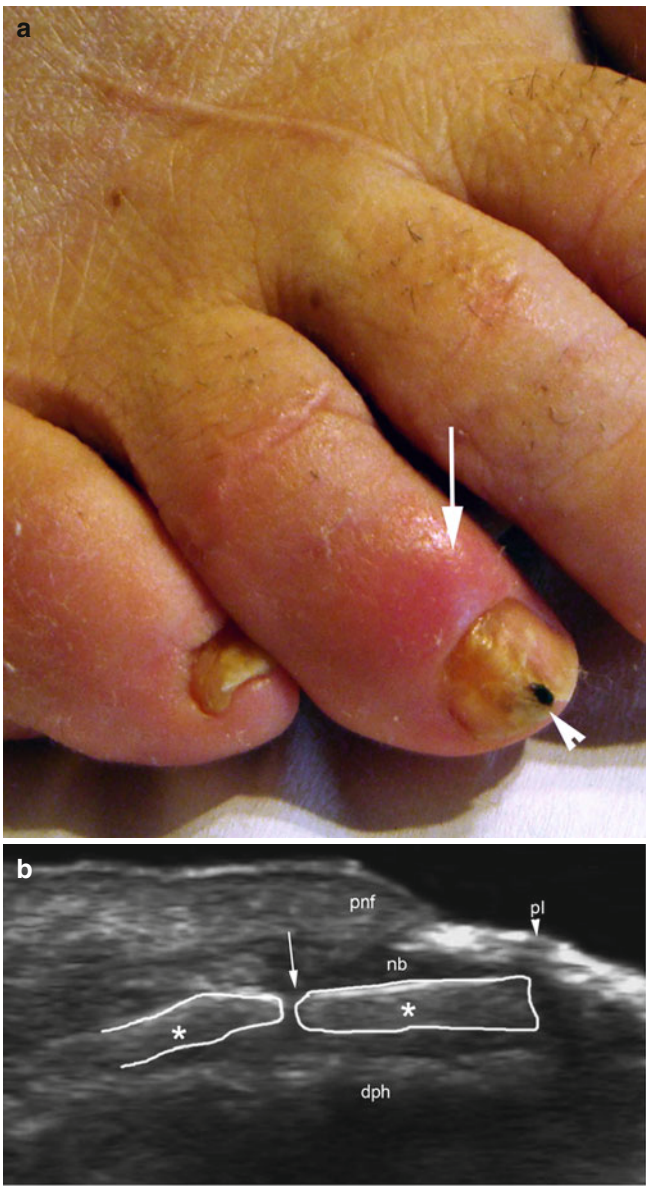

Fig. 18.26 (**a**, **b**) Subungual foreign body. (**a**) Clinical photograph shows a dark pigmented spot in the nail plate (*arrowhead*) as well as erythema and swelling of the proximal nail fold (*arrow*). The patient presented with a history of corrective surgery in the right foot. (**b**) Grey scale ultrasound image (longitudinal view, right fourth toe) shows two hyperechoic cylinder-shaped structures on top of the distal phalanx that correspond to fragments of a synthetic material (*, fiber tape, *outlined*). The fiber tape was fractured (*arrow*) and the distal fragment was embedded into the nail bed. Thickening and decreased echogenicity of the nail bed and thickening of the nail plates are also detected. *Abbreviations*: *nb* nail bed, *dph* distal phalanx, *pnf* proximal nail fold, *pl* nail plates

The sonographic findings in the median canalicular nail dystrophy (MCD) are the changes in the thickness (thickening or thinning), as well as the hypoechogenicity, of the proximal nail bed and nail fold (usually centrally located) that involves the ungual matrix region. The changes may suggest scarring and a chronic inflammatory reaction. The nail plates can secondarily present thickening, loss of definition, discontinuity, and irregularities following the same axis of the proximal nail bed alteration. Hypovascularity is a common finding in nails affected by MCD [6] (Fig. 18.27).

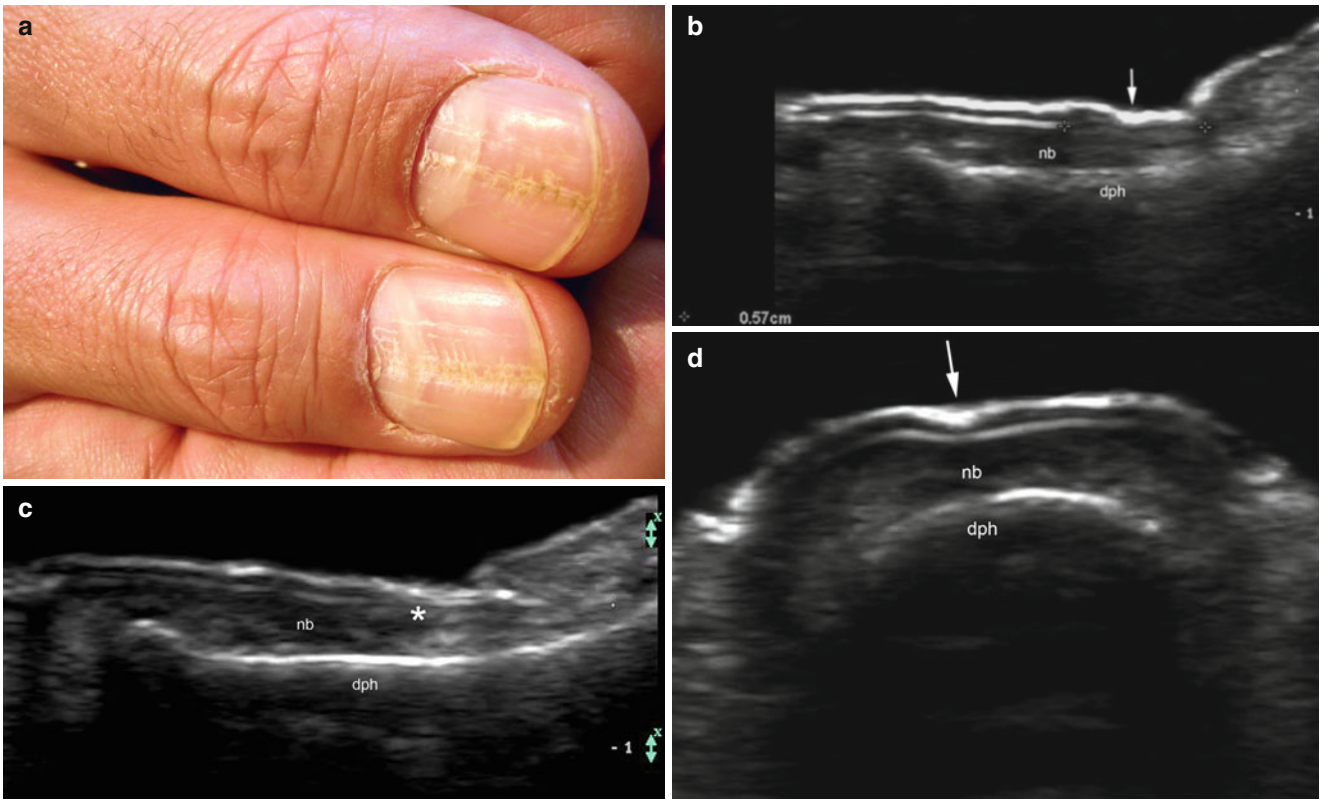

Fig. 18.27 (**a**–**d**) Median canaliform nail dystrophy. (**a**) Clinical photograph shows wide median grooves (longitudinal) with steep edges and transverse defects in both thumbs. (**b**) Grey scale ultrasound image (longitudinal view, right thumb) shows a 5.7 mm long hypoechogenicity and thickening area in the proximal nail fold that also affects the matrix region. Loss of definition of the proximal ventral plate (between markers) and thickening of the dorsal plate (*arrow*) in the same region are also detected. (**c**) Grey scale ultrasound image (longitudinal view, left thumb) shows diffuse thickening and hypoechogenicity of the nail bed that includes the matrix region (*). Loss of definition of the ventral plate is also detected. (**d**) Grey scale ultrasound image (transverse view, right thumb) shows a mild concavity in the median region of the nail plates in concordance with the visible nail defect. Thickening of the dorsal plate is observed. *Abbreviations*: *nb* nail bed, *dph* distal phalanx

18.4.3 Cosmetic Alterations

18.4.3.1 Implants: Acrylic Nails

Acrylic resin monomers, particularly acrylates and methacrylates, are well-known sensitizers responsible for allergic contact dermatitis [50]. Currently, sculptured nails with acrylic components are commonly used for cosmetic purposes. Problems in detecting pulse oximetry, onychodystrophy, and contact dermatitis are among the secondary effects of artificial nails that have been reported in the literature [51–53].

On ultrasound, the acrylic deposits appear as an extra hyperechoic linear deposit over the dorsal plate providing a trilaminar appearance. Hyperechoic spots are typically seen between the extra hyperechoic acrylic line and the dorsal plate, and correspond to the glue that is used to attach the cosmetic implant to the surface of the nail [6] (Fig. 18.28).

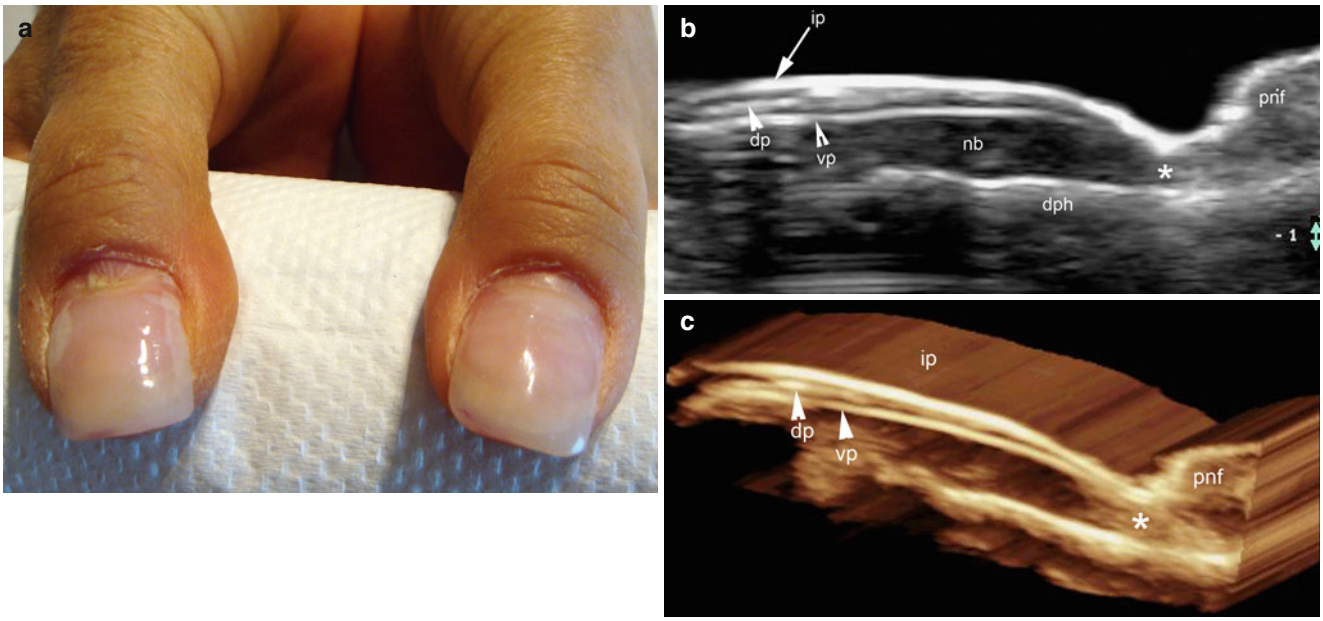

Fig. 18.28 (**a**–**c**) Acrylic implant. (**a**) Clinical image of acrylic implants in the thumbs. (**b**, **c**) Sonographic images (longitudinal views; **b** grey scale and **c** 3D reconstruction of the right thumb) show a trilaminar hyperechoic structure in the surface of the nail. The upper hyperechoic line corresponds to the acrylic implant (*arrow, ip*) and the middle and lower layer to the dorsal and ventral plate, respectively. Notice the thinning of the proximal nail bed (*) that involves the matrix region. *Abbreviations*: *dp* dorsal plate, *vp* ventral plate, *dph* distal phalanx, *pnf* proximal nail fold

18.4.4 Tumors and Pseudotumors of the Ungual and Periungual Region

There are several tumors that affect the ungual and periungual regions that can constitute a clinical challenge because of the regional complex anatomy and the usual masking generated by the nail plates and lateral nail folds [54, 55].

Sonography provides pre-surgical information on:

(a) Origin of the lesion (ungual or periungual)
(b) Exact location (proximal or distal nail bed; ulnar, radial, medial, or lateral aspects of the nail unit; central or eccentric position)
(c) Involvement of nail unit components and surrounding structures
(d) Size (in every axis)
(e) Composition (solid, cystic), and
(f) Blood flow (hypo- or hypervascular)

Tumors of the nail can be classified according to their ungual or periungual origin as well as to their nature in solid or cystic conditions [55].

18.4.4.1 Benign Tumors and Pseudotumors

18.4.4.1.1 Ungual origin

Solid Tumors

Glomus Tumors These are rare neoplasms that arise from the neuromyoarterial apparatus and account for 1–5 % of soft-tissue tumors of the upper extremity, in most cases occurring in the nail bed. The typical clinical presentation includes paroxysmal pain and hypersensitivity to cold that limit the use of the affected hand causing practical, professional, and often emotional discomfort for the patient [56]. Glomus tumors are benign subungual tumors that can be difficult to excise because of their small size and relatively high rates of recurrence in up to 20 % of cases [57]. A high correlation between ultrasound and intraoperative location and size, including tumors that measure less than 1 mm, has been reported. Thus, reported recurrence rates of glomus tumors after pre-surgical ultrasound are very low in comparison with tumors without pre-surgical imaging [58].

Histologically, glomus tumors present as well-circumscribed nodules composed of vessels with a normal endothelium surrounded by round glomus cells with pale eosinophilic cytoplasm. They are usually positive α-smooth-muscle actin (SMA), a muscle specific actin, and CD 34 can also be positive on immunohistochemistry. Glomangiomas are the most common histological form of presentation (variant) of glomus tumors (60 %). Glomangiomas usually present a prominent vascular component with dilated lumina, hyalinization of the vessel walls, and often thrombosis. There are other less common variants, such as symplastic glomus tumor (high nuclear grade), glomangiomyoma (15 %, a rare subtype, with larger and more numerous smooth cells), glomangiomatosis (a tumor with features of angiomatosis and excess glomus cells), infiltrating glomus tumor (a very rare variant with infiltrative growth and high recurrence rate), and malignant transformation of glomus tumor (extremely rare variant with deep location, with tumors that measure more than 2 cm, presenting moderate to high nuclear grade diagnosis and five or more mitotic figures per 50 high power fields) [59].

On ultrasound, glomus tumors usually present as single hypoechoic nodules, centrally located, and with increased vascularity. Nevertheless, eccentric involvement of the nail bed can also be seen. Peak arterial systolic velocities within the glomus tumor have been reported to vary between 3.7 cm/s and 26.1 cm/s. The glomangiomyoma variant can be hypovascular in comparison with the most common form of glomus tumor (glomangioma). Secondary scalloping of the bony margin beneath the tumor (that probably reflects the slow growth pattern of the tumor) is a frequent finding and can be a key sonographic sign for finding small-sized glomus tumors. Additionally, proximal locations of glomus tumors in the nail bed are seen more frequently than distal locations [55–61] (Figs. 18.29, 18.30, 18.31, and 18.32).

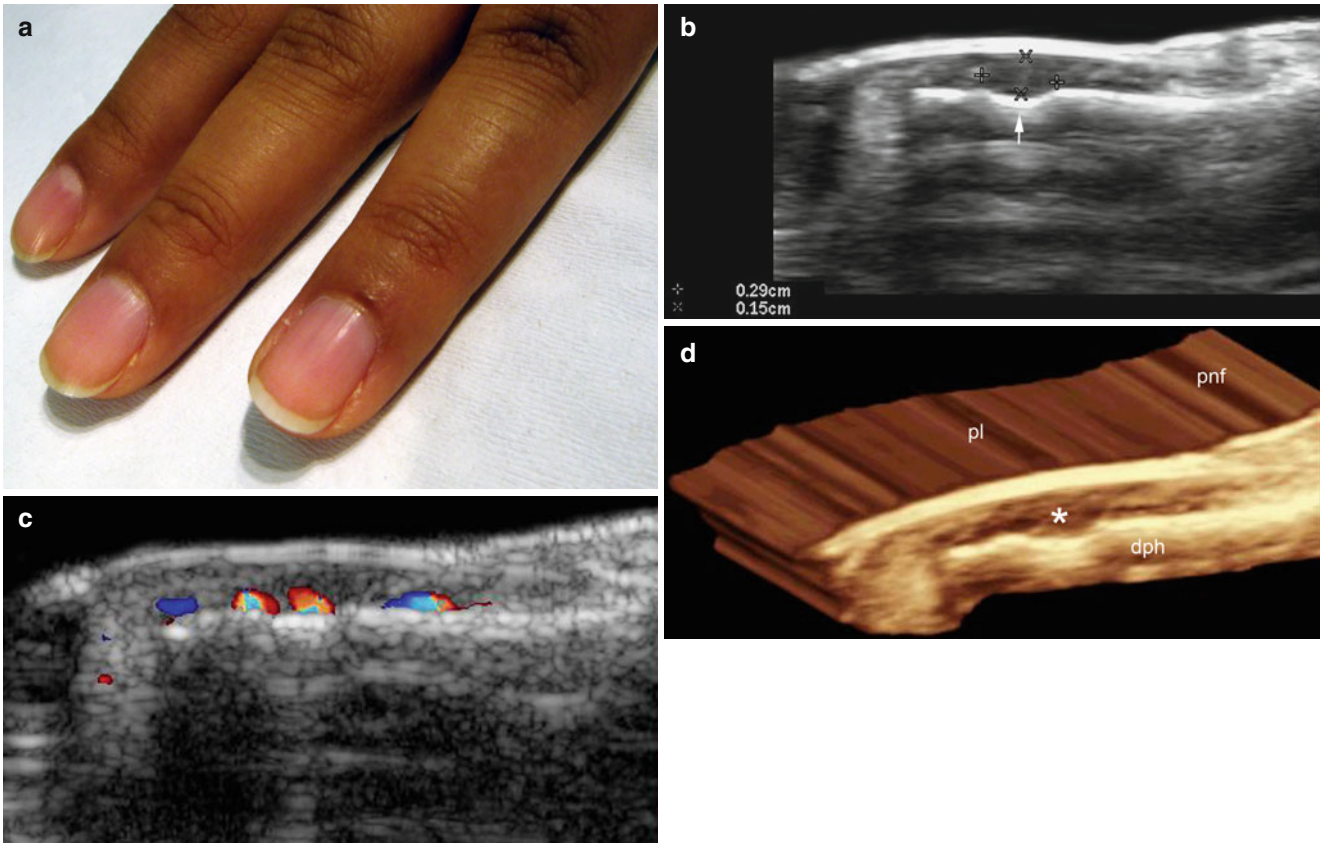

Fig. 18.29 (**a**–**d**) Glomus tumor. (**a**) Clinical photograph shows no abnormalities in the fingers. The patient presented with excruciating pain in the nail of the left ring finger. (**b**) Grey scale ultrasound image (longitudinal view, left ring finger) shows a 2.9 mm (long) × 1.5 mm (depth) well-defined, hypoechoic nodule (*) in the nail bed. Notice the scalloping of the bony margin (*arrow*) underlying the nodule. (**c**) Color Doppler ultrasound image (longitudinal view) shows hypervascularity within the nodule. (**d**) 3D reconstruction (longitudinal view) of the tumor (*). *Abbreviations*: *pl* nail plates, *dph* distal phalanx, *pnf* proximal nail fold

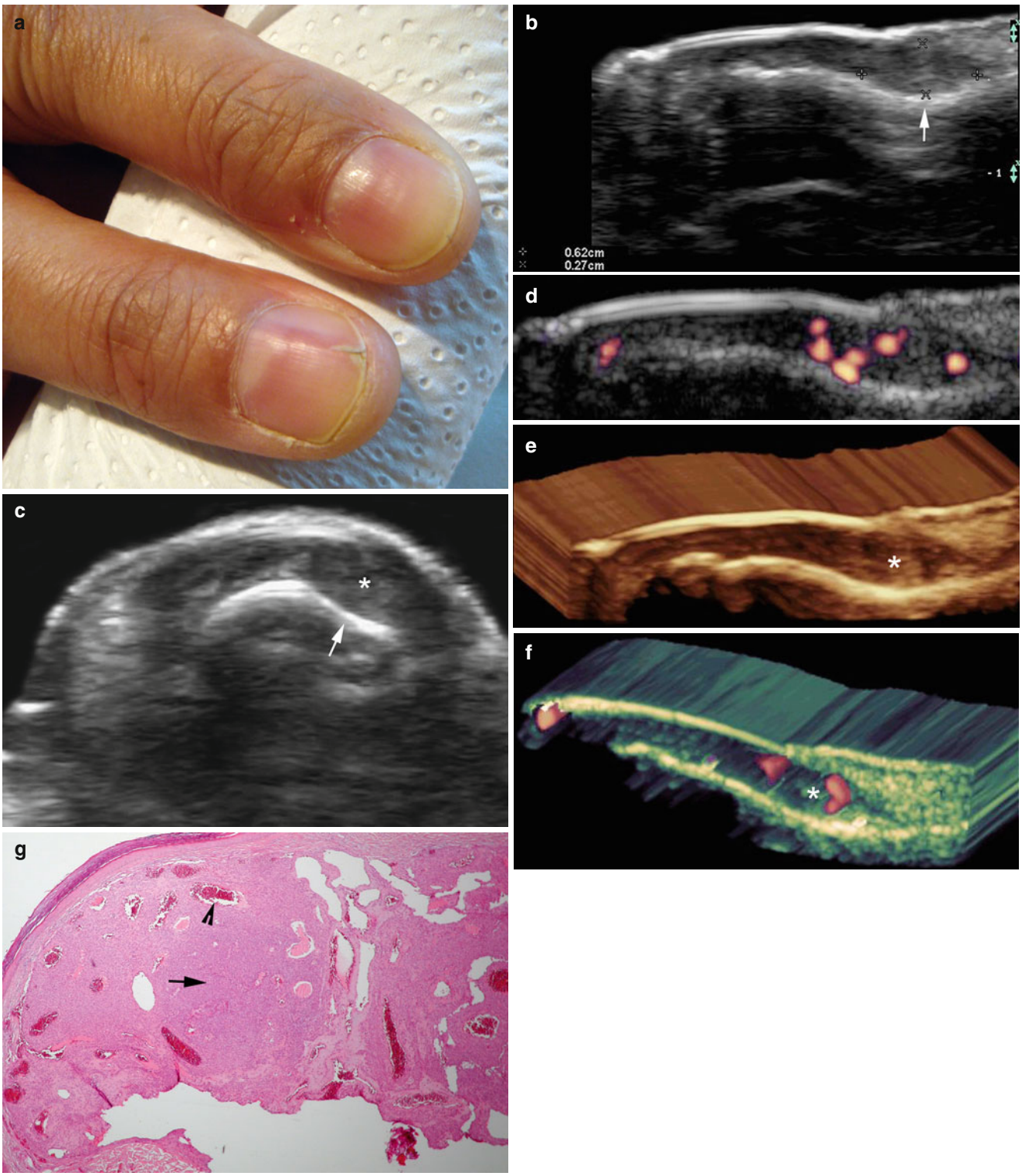

Fig. 18.30 (**a**–**g**) Glomus tumor. (**a**) Clinical image shows a longitudinal defect in the distal nail plate of the right thumb. (**b**, **c**) Grey scale ultrasound images (**b** longitudinal view; **c** transverse view, right thumb) show a 6.2 mm (long) × 2.7 mm (depth), well defined, hypoechoic nodule (*, between markers) in the radial aspect of the proximal nail bed (same axis of the visible lesion). Scalloping of the bony margin (*arrow*) is also detected. (**d**) Power Doppler ultrasound image (longitudinal view) shows increased vascularity within the nodule. (**e**, **f**) 3D reconstructions of the tumor (**e** grey scale; **b** power angio) highlighting the tumor (*) and its vascularity (f). (**g**) Histology (HE × 40 zoom): proliferation of blood vessels in the dermis surrounded by a stromal proliferation of round cells (*arrow*). Some of the vessels are dilated and show prominent red blood cells (*arrowhead*) (Histology image is courtesy of Dr. Laura Carreño)

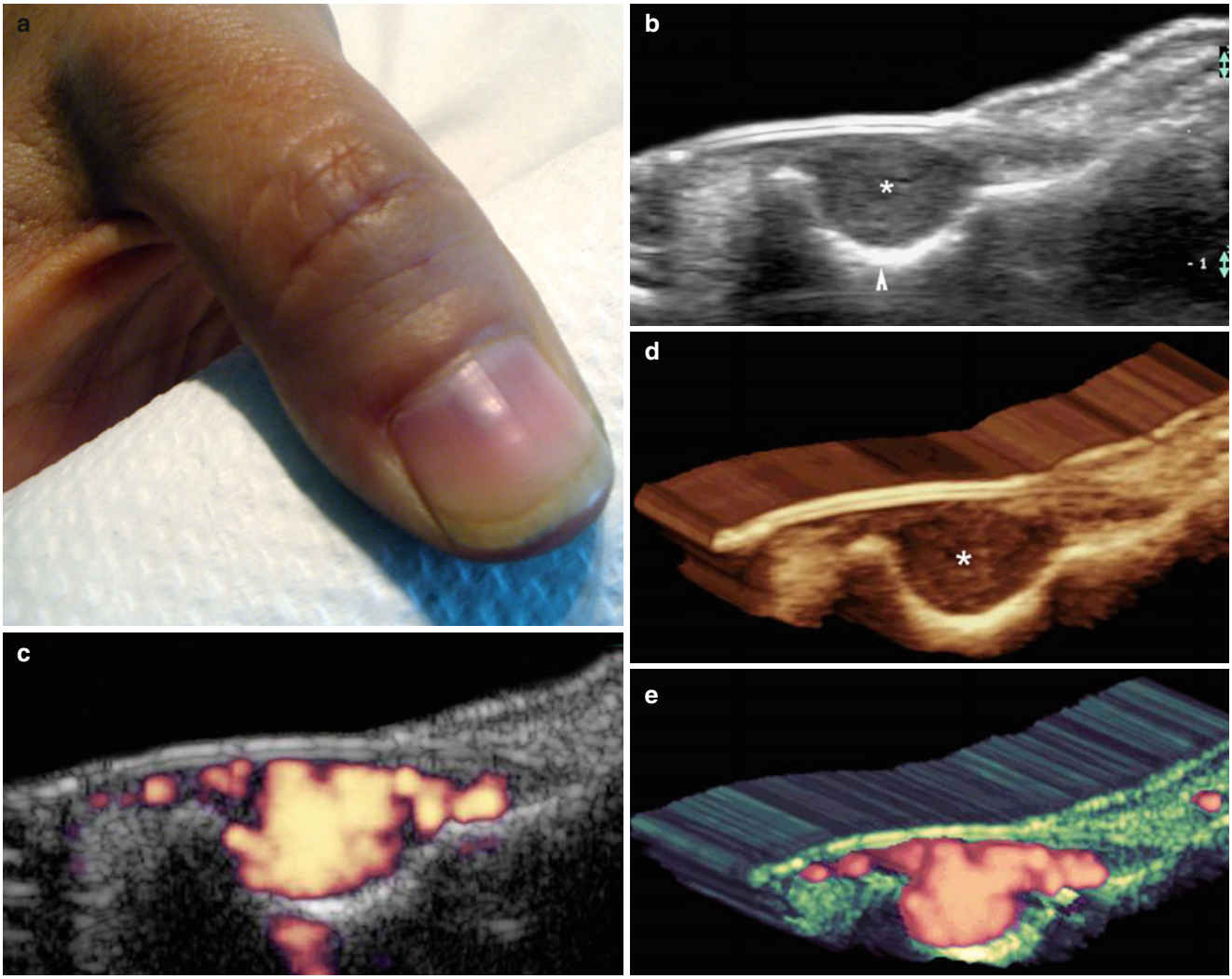

Fig. 18.31 (**a**–**e**) Glomus tumor. (**a**) Clinical photograph shows mild erythema in the proximal nail plate of the right thumb. (**b**) Grey scale ultrasound image (longitudinal view) shows a well-defined, hypoechoic nodule (*) in the middle third of the nail bed. Marked scalloping of the bony margin of the distal phalanx is detected (*arrowhead*). (**c**) Power angio Doppler ultrasound image (longitudinal view) shows strong vascularity within the nodule. (**d**, **e**) 3D reconstructions of the tumor (*) (**b** grey scale; **e** power angio) highlight the lesion

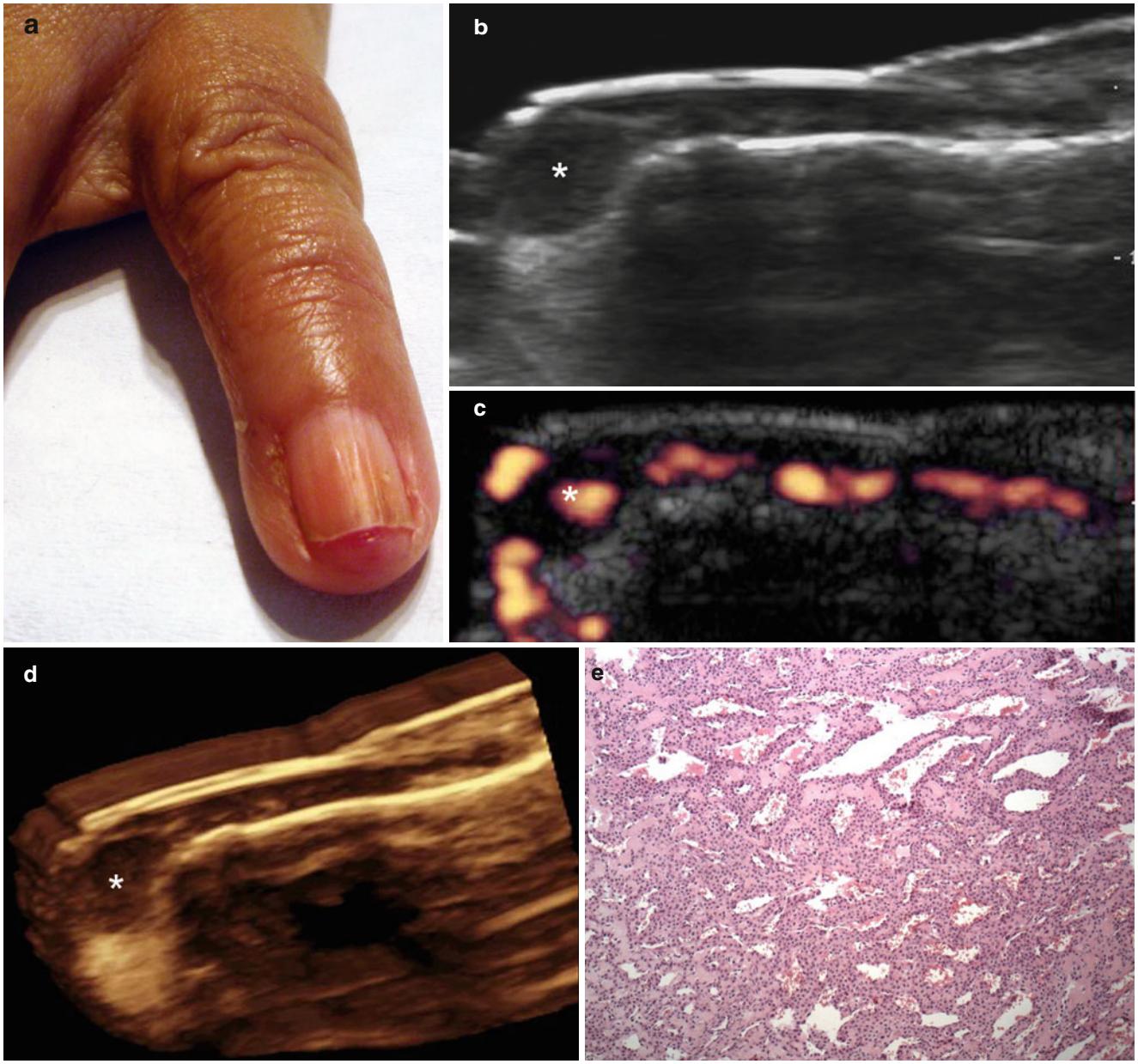

Fig. 18.32 (**a**–**e**) Distal glomus tumor. (**a**) Clinical photograph shows mild longitudinal ridging of the nail plate of the left little finger. (**b**) Grey scale ultrasound image (longitudinal view) shows a well-defined, hypoechoic solid nodule (*) in the hyponychium. (**c**) Color Doppler ultrasound image (longitudinal view) shows hypervascularity within the nodule (*). (**d**) 3D reconstruction (longitudinal view) highlighting the lesion (*). (**e**) Histology (HE × 100 zoom): proliferation of vessels of variable shape and size surrounded by nests of monomorphic cuboidal cells without mitosis (Histology image is courtesy of Dr. Laura Carreño)

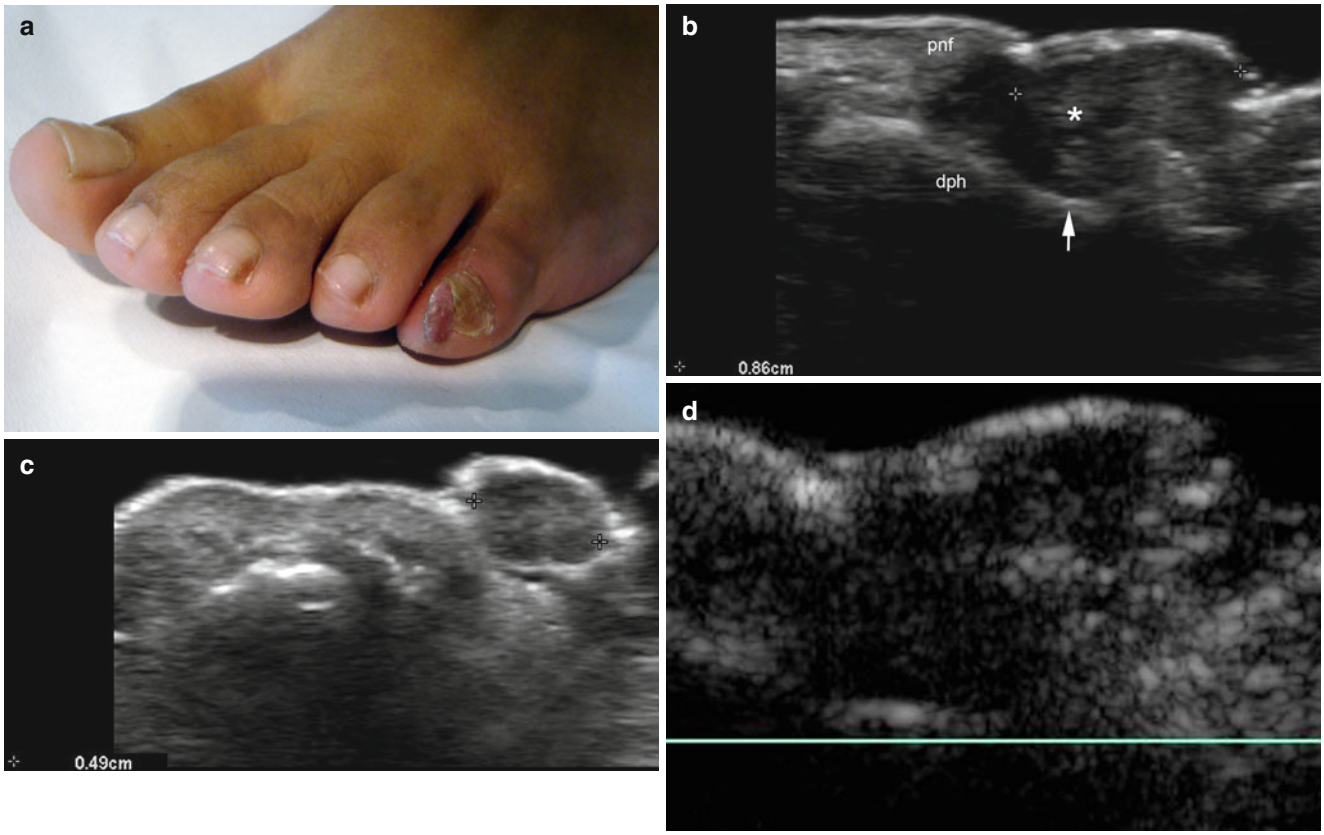

Fig. 18.33 (**a**–**d**) Subungual and periungual fibroma. (**a**) Clinical image shows a periungual reddish bump in the medial aspect of the left fifth toenail. (**b**) Grey scale ultrasound image (longitudinal view) shows a 8.6 mm long subungual hypoechoic solid structure (*, between markers) that remodels the bony margin (*arrow*) of the distal phalanx. (**c**) Grey scale ultrasound image (transverse view) shows a 4.9 mm extension of this structure that bulges into the surface of the periungual region at the medial nail fold. (**d**) Color Doppler ultrasound image (longitudinal view) shows hypovascularity within the lesional area. *Abbreviations*: *dph* distal phalanx, *pnf* proximal nail fold

Fibrous Tumors This in an heterogeneous group with several histological subtypes and forms of presentation that include congenital entities such Koenen's fibromas (associated with tuberous sclerosis) and acquired fibrous tumors, such as garlic clove-shaped fibromas [62, 63].

On ultrasound, the heterogeneous group of fibrous tumors can appear as oval-, round-, fusiform-, or polypoid-shaped hypoechoic structures; these are commonly eccentric (i.e., away from the central part of the nail bed) within the nail bed; and can affect the matrix region, including matrix wings and periungual region. Fibromas can involve both the subungual and periungual regions at the same time. Remodeling of the bony margin can be detected in large-sized tumors, and on color Doppler ultrasound they often present with hypovascularity, with the exception of angiofibromas, that can present small-sized vessels with low velocity arterial and venous blood flow within the tumor [6] (Figs. 18.33, 18.34, 18.35, and 18.36).

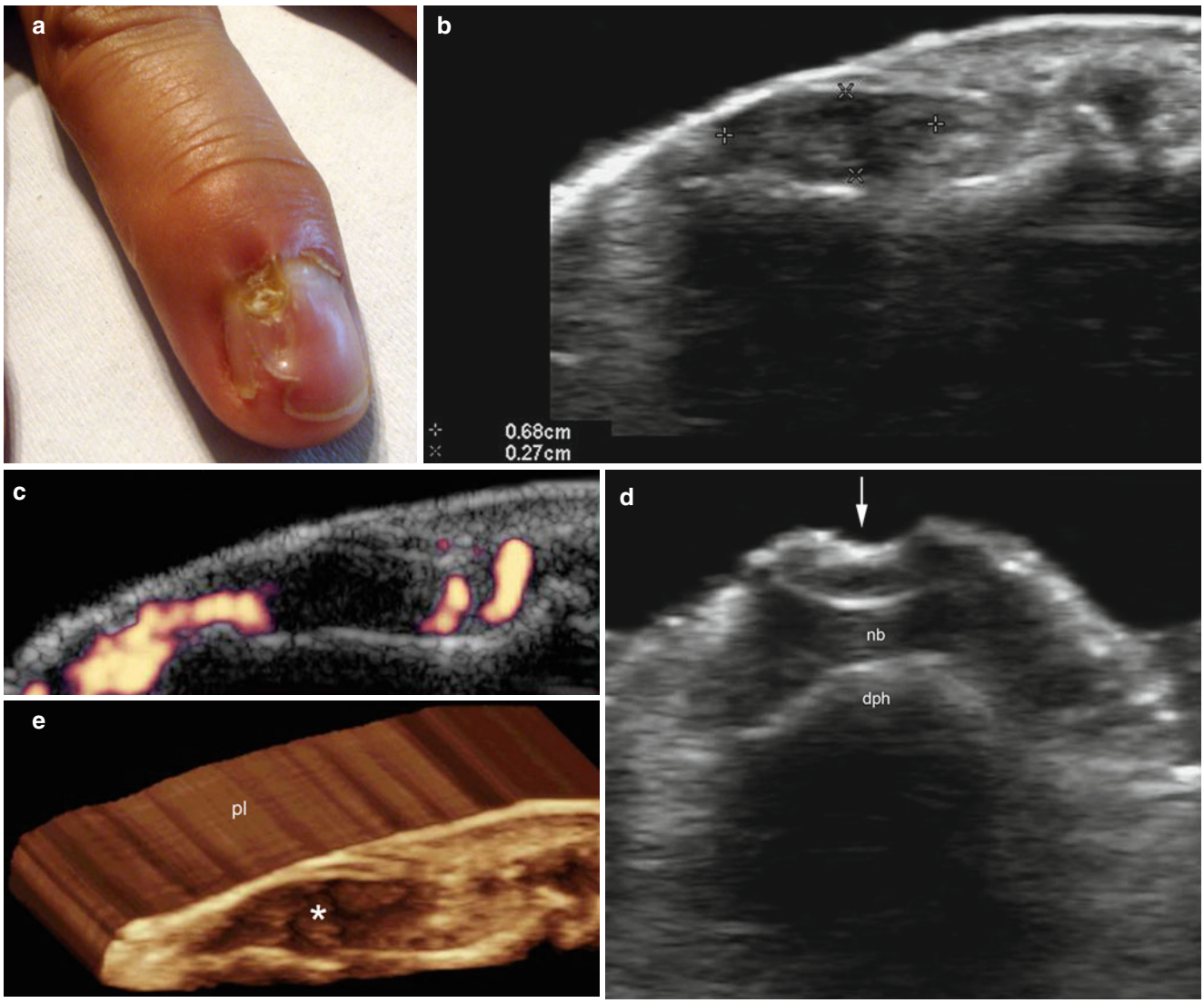

Fig. 18.34 (**a**–**e**) Subungual fibroma. (**a**) Clinical photograph shows dystrophic changes and concavity in the radial aspect of the nail plate of the left middle finger. (**b**) Grey scale ultrasound image (longitudinal view, radial aspect left middle finger) shows a 6.8 mm (long) × 2.7 mm (depth) hypoechoic structure in the nail bed that affects the ungual matrix region and displaces the nail plates upward. (**c**) Grey scale ultrasound image (transverse view, distal nail, left middle finger) shows concavity of the nail plates (*arrow*) and thickening of the interplate space. (**d**) Power Doppler ultrasound image shows hypovascularity within the lesional area. (**e**) 3D reconstruction of the tumor (*). *Abbreviations*: *nb* nail bed, *dph* distal phalanx

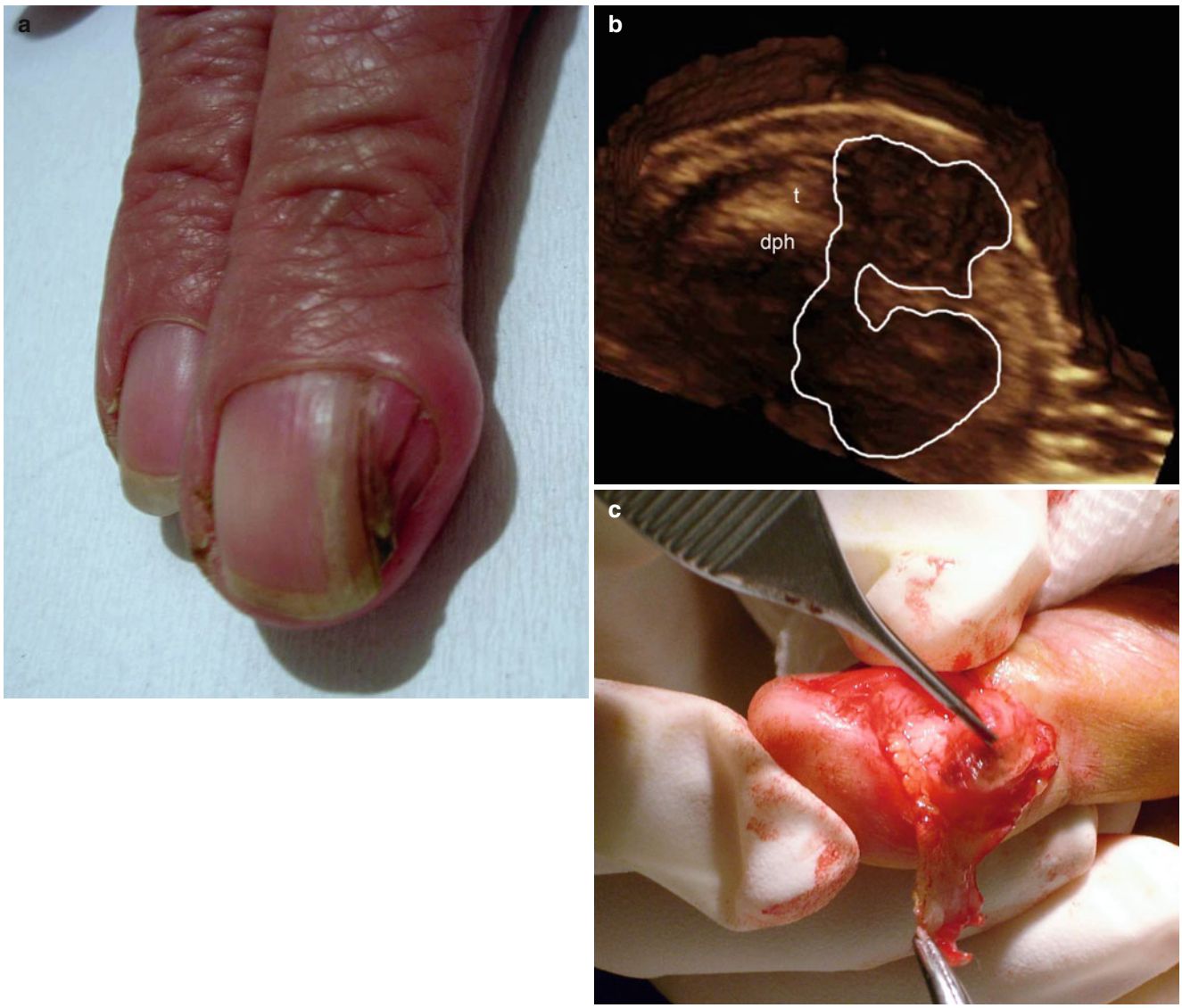

Fig. 18.35 (**a**–**c**) Subungual and periungual fibroma. (**a**) Clinical image shows swelling in the ulnar aspect of the nail plate and lateral nail fold of the left middle finger. (**b**) 3D reconstruction of the tumor shows the mass (outlined) that affects the ulnar aspect of the fingernail from the dorsal to the flexor region of the finger. (**c**) The tumor at surgery (courtesy of Dr. Rosamary Soto). *Abbreviations*: *t* extensor tendon, *dph* distal phalanx

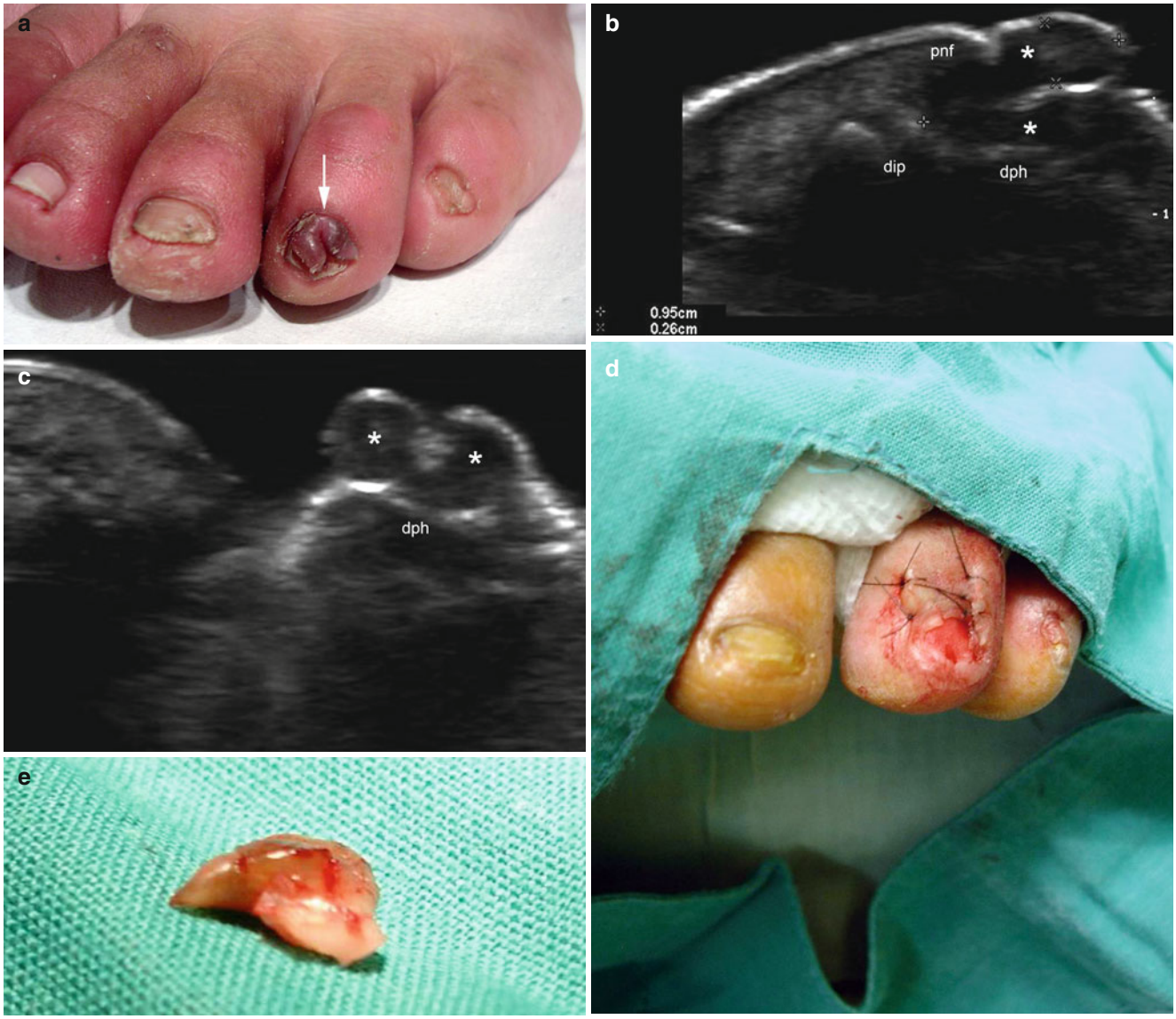

Fig. 18.36 (**a**–**e**) Angiofibroma. (**a**) Clinical photograph shows a reddish lump in the nail of the left fourth toe. (**b**) Grey scale ultrasound image (longitudinal view) shows a 9.5 mm long hypoechoic structure that bulges into both the surface of the nail plate and the nail bed (*). (**c**) Grey scale image (transverse view) shows the lobulated hypoechoic mass over the surface of the nail plates in the distal nail. Notice the mild concavity of the nail plates secondary to the extrinsic compression from the tumor. (**d**, **e**) The surgery of the mass (**d** post-operative image of the nail unit; **e** gross image of the tumor; both surgical images are courtesy of Dr. Rosamary Soto). *Abbreviations*: *dph* distal phalanx, *dip* distal interphalangeal joint, *pnf* proximal nail fold

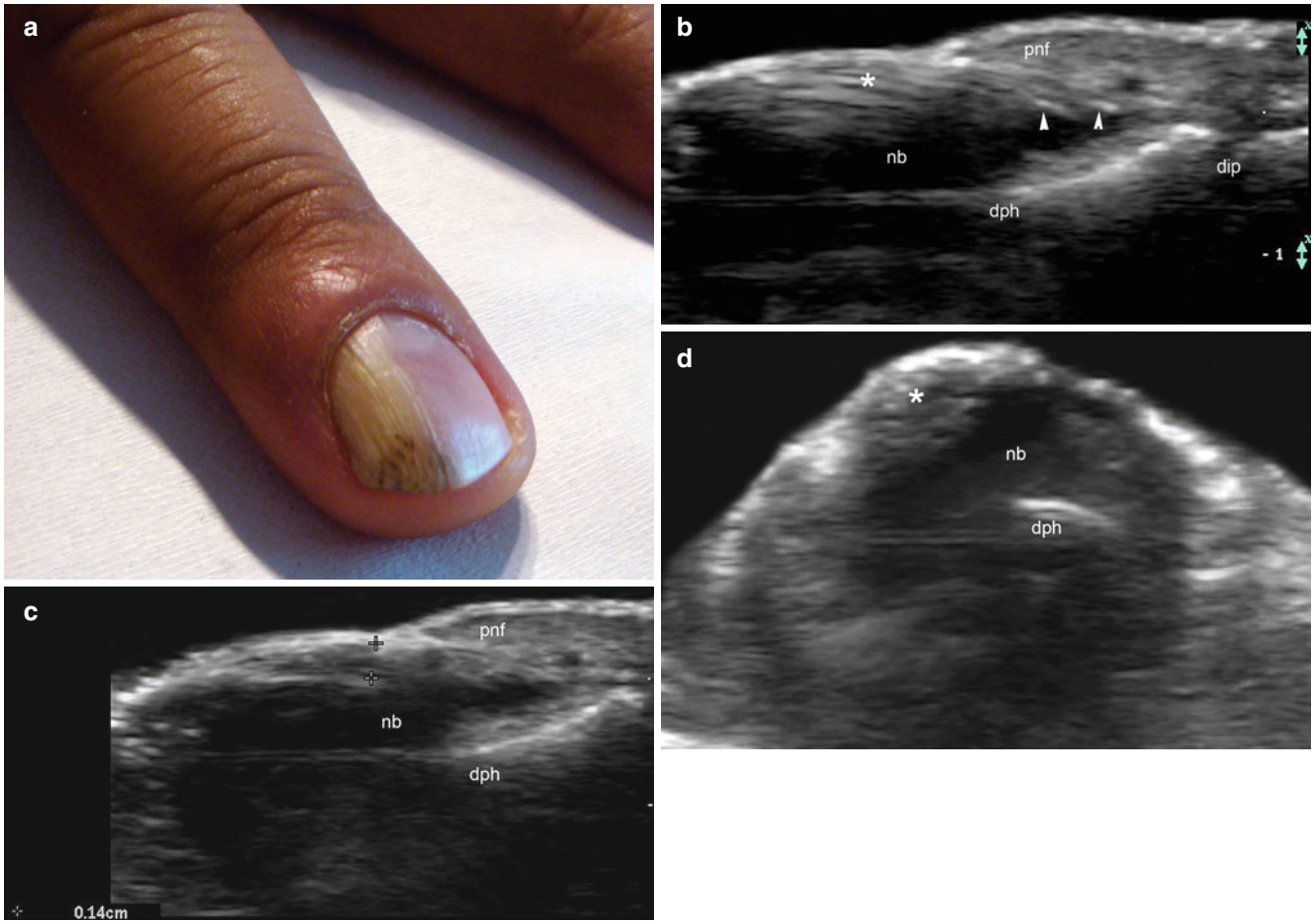

Fig. 18.37 (**a**–**d**) Onychomatricoma. (**a**) Clinical photograph shows a yellow longitudinal thick band with ridging, overcurvature, and splinter hemorrhages in the radial aspect of the nail of the left middle finger. (**b**) Grey scale ultrasound image (longitudinal view) shows a hyperechoic longitudinal band-like structure composed of hyperechoic lines (*) that affects the ungual matrix region (*arrowheads*) and bulges into both the nail plates and the nail bed. (**c**) Grey scale ultrasound image (longitudinal view) shows thickening of the interplate space (1.4 mm, between markers). (**d**) Grey scale ultrasound image (transverse view) highlights the hyperechoic dots within the tumor. *Abbreviations*: *nb* nail bed, *dph* distal phalanx, *pnf* proximal nail fold, *dip* distal interphalangeal joint

Onychomatricomas (OMs) These are fibroepithelial tumors of the nail matrix that occur in the digits of both the hands and feet. Clinically, they present as asymmetric longitudinal thick yellows bands in the nail with increased transverse convexity of the nail and splinter hemorrhages that provide a thickened funnel-shaped nail [64, 65].

Two main patterns are described histologically: a lobulated or foliated pattern, observed principally on the transverse section, and a gloved-finger mono- or multidigitate pattern, observed mainly on the longitudinal section [66].

OMs typically present as ill-defined mixed echogenicity structures on sonography that involve the interplate space and the ungual matrix region. Thus, the tumors are commonly hypoechoic and present prominent hyperechoic spots. Also they can present a hyperechoic band-like appearance with hyperechoic lines. The hyperechoic spots or lines usually send projections into the interplate space and matrix region. OMs are most commonly seen in an eccentric location within the nail bed and affect a matrix wing. Remodeling or erosive changes in the bony margin, hypervascularity, or involvement of the proximal nail fold have not been reported [6, 67] (Fig. 18.37).

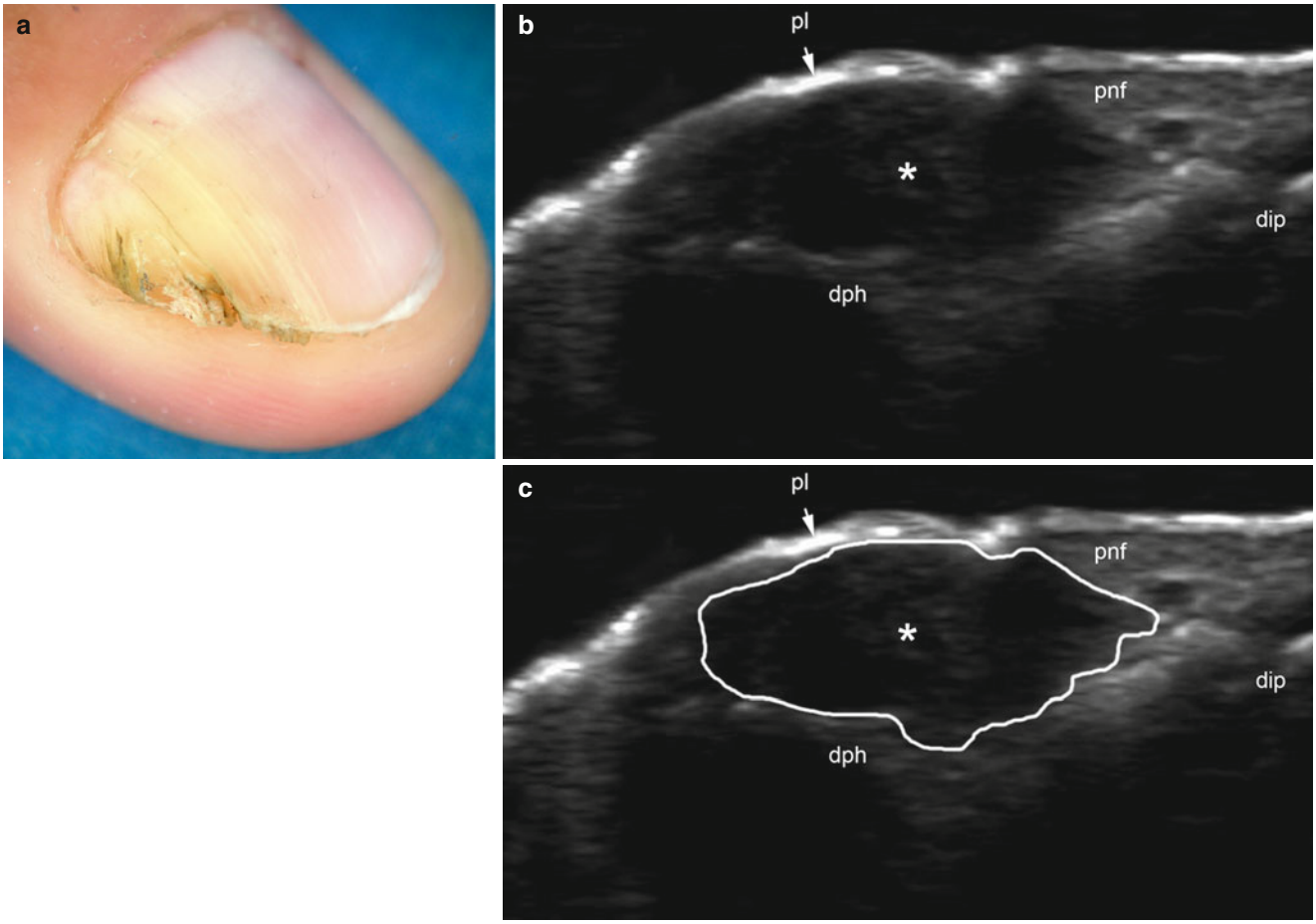

Fig. 18.38 (**a**–**c**) Perineurioma. (**a**) Dermoscopy image shows a yellowish swelling and dystrophic changes in the radial aspect of the left middle finger (Courtesy of Dr. Veronica Catalan). (**b**, **c**) Grey scale ultrasound images (**b** longitudinal view, and **c** same view with the tumor outlined) show a hypoechoic ill-defined mass that affects the radial aspect of the nail bed and displaces the nail plate upward. Notice the diffuse loss of the bilaminar structure of the nail plate. *Abbreviations*: *nb* nail bed; *dph* distal phalanx, *pl* nail plates, *pnf* proximal nail fold, *dip* distal phalanx

Perineuriomas These are neurogenic tumors that differ from schwannomas or neurofibromas in their positive immunoreactivity for the epithelial membrane antigen (EMA) and lack of reactivity for the S-100 protein and α-smooth muscle actin (SMA). Clinically they show as swelling, clubbing or dystrophy of the nail and may mimic other tumoral entities such as fibrous tumors or subungual exostoses [6, 68].

Ill-defined hypoechoic eccentric masses have been reported seen on ultrasound. Perineuriomas can involve the matrix region, particularly the wings, and the ipsilateral nail fold. Hypovascularity has been demonstrated using color Doppler ultrasound. Remodeling of the bony margin, involvement of the inter-plate space, and hyperechoic dots within the perineuriomas have not been described [6, 69] (Fig. 18.38).

Keratoacanthomas These are rare, squamoproliferative neoplasms that occur at the nail bed and can cause erosion and/or scalloping of the underlying bone and present with a characteristic central keratin-filled crater. In contrast to other types of keratoacanthomas (out of the ungual region), this type of tumor may not show spontaneous regression, sometimes grows progressively, and can clinically mimic a digital squamous cell carcinoma (SCC).

On sonography, a well circumscribed solid-cystic mass that shows a mixed echogenicity pattern (anechoic center and hypoechoic rim), with remodeling or erosion of the bony margins, as well as a posterior acoustic enhancement artifact has been described [6, 70–72] (Fig. 18.39).

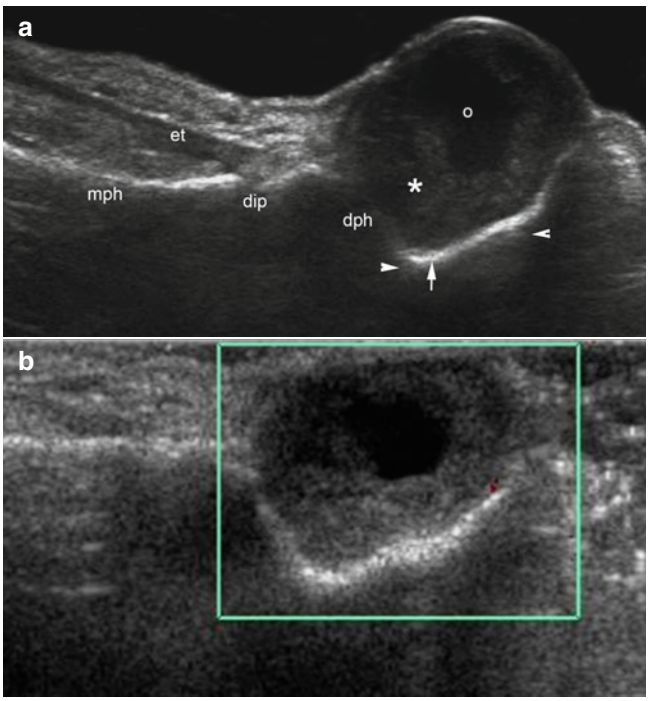

Fig. 18.39 (**a**, **b**) Keratoacanthoma. (**a**) Grey scale ultrasound image (longitudinal view, left hallux) shows a mixed echogenicity mass that presents a hypoechoic rim (*) and anechoic center (o). This mass displaces the nail plates upward and produces scalloping of the bony margin of the distal phalanx (*arrowheads*). (**b**) Color Doppler ultrasound image (longitudinal view) shows hypovascularity within the mass. *Abbreviations*: *nb* nail bed, *dph* distal phalanx, *dip* distal interphalangeal joint, *mph* middle phalanx, *et* extensor tendon

Solid Pseudotumors

Granulomas These are composed of a proliferative scarring and fibrous reaction with extensive and chronic inflammatory changes in the nail bed that elicit a mass-like effect. The chronic inflammatory process can involve the ungual matrix and generate secondary dystrophic changes in the nail plates. A telangiectatic (vascular) variant of granulomas is present in up to 9 % of cases and is characterized by local tenderness and easy bleeding.

On sonography, granulomas present as ill-defined hypoechoic structures that increase the thickness of the nail bed and displace the nail plates upward. Thickening and wavy-shaped nail plates (one or both, dorsal or ventral) can also be seen. Variable degrees of vascularity within granulomas are usually seen on color Doppler ultrasound that can go from hypo- to hypervascular (telangiectatic variant) [6, 55, 63] (Figs. 18.40 and 18.41).

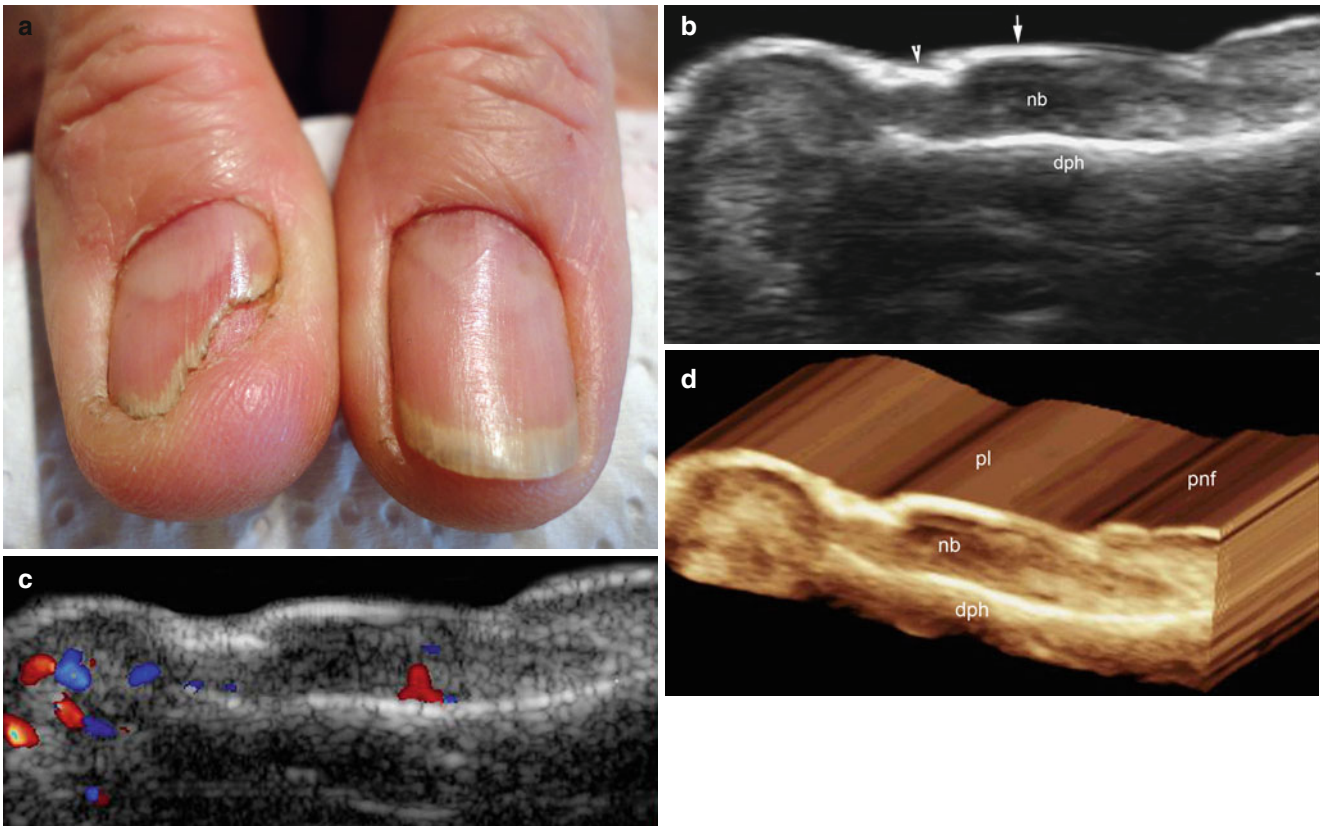

Fig. 18.40 (**a**–**d**) Granuloma. (**a**) Clinical photograph shows swelling, disruption, and dystrophic changes in the radial aspect of the nail of the right thumb. (**b**) Grey scale ultrasound image (longitudinal view, right thumb) shows thickening and hypoechogenicity of the proximal nail bed. There is thickening and convexity of the dorsal plate and loss of definition of the ventral plate. Disruption of the contour of the nail plate is detected in the distal third of the fingernail. (**c**) Color Doppler ultrasound image (longitudinal view, right thumb) shows no sign of hypervascularity within the nail bed. (**d**) 3D reconstruction of the fingernail (right thumb, longitudinal view) highlighting the changes. *Abbreviations*: *nb* nail bed, *dph* distal phalanx, *pl* nail plates, *pnf* proximal nail fold

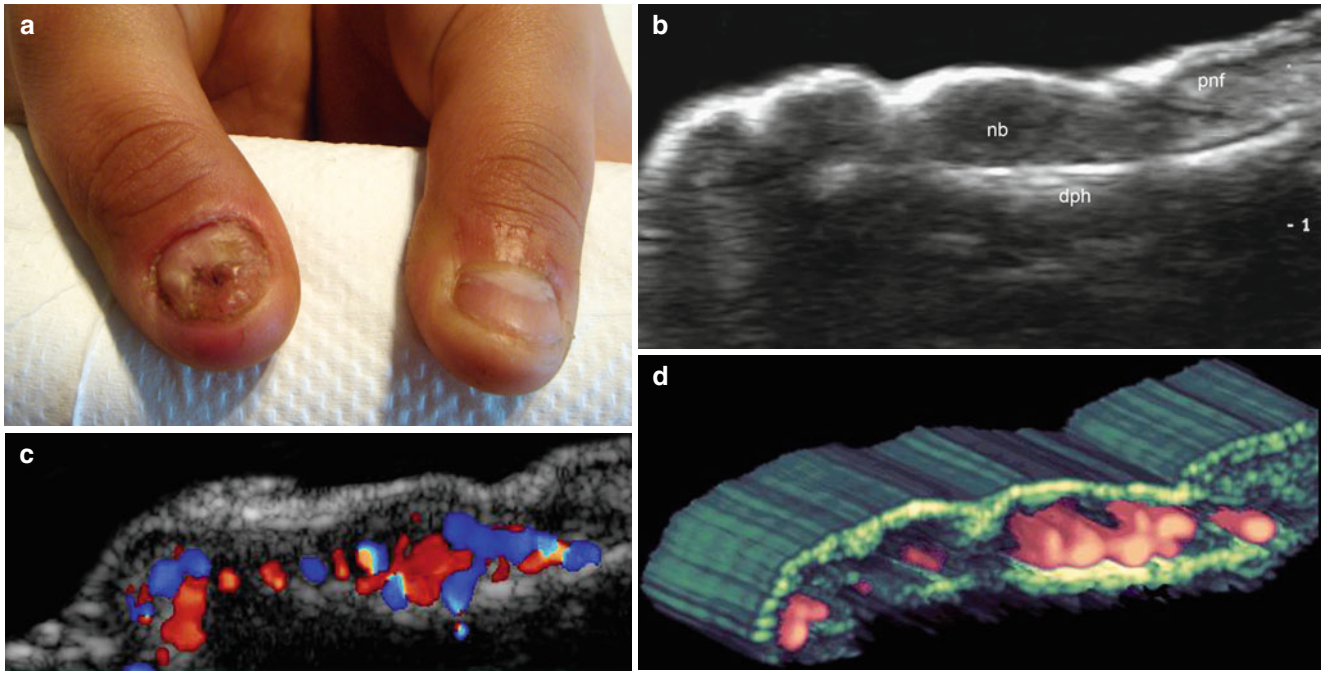

Fig. 18.41 (**a**–**d**) Granuloma. (**a**) Clinical image shows swelling and dystrophic changes in the nail of the right thumb. (**b**) Grey scale ultrasound image (longitudinal view) shows thickening and hypoechogenicity of the nail bed that also affects the matrix region. Notice the wavy shaped nail plate with loss of the bilaminar pattern. (**c**) Color Doppler ultrasound image (longitudinal view) shows the increased vascularity within the nail bed. (**d**) 3D power angio reconstruction (longitudinal view) highlights the prominent the blood flow within the lesional area. *Abbreviations*: *nb* nail bed, *pnf* proximal nail fold, *dph* distal phalanx

Subungual Warts These are caused by the infection of the human papilloma virus that induces a proliferative fibroepithelial response. Subungual warts are lesions that usually grow slowly from the hyponychium toward the nail bed, affecting the nail matrix and causing a secondary upward displacement and dystrophy of the nail plates. Subungual warts can have involvement of both the nail bed and lateral nail folds [55, 63].

On ultrasound, subungual warts frequently present as eccentric hypoechoic fusiform structures associated with thickening of the nail plates and interplate spaces, which is similar to the classic sonographic appearance already described for plantar warts [55, 63, 73]. Subungual warts can present a nodular shape and secondary thickening of the nail plates in the same axis when they are located in the proximal nail bed. Subungual warts are seen as hypovascular on color Doppler ultrasound, but may occasionally present hypervascularity in the underlying or surrounding dermis [6, 55] (Figs. 18.42 and 18.43).

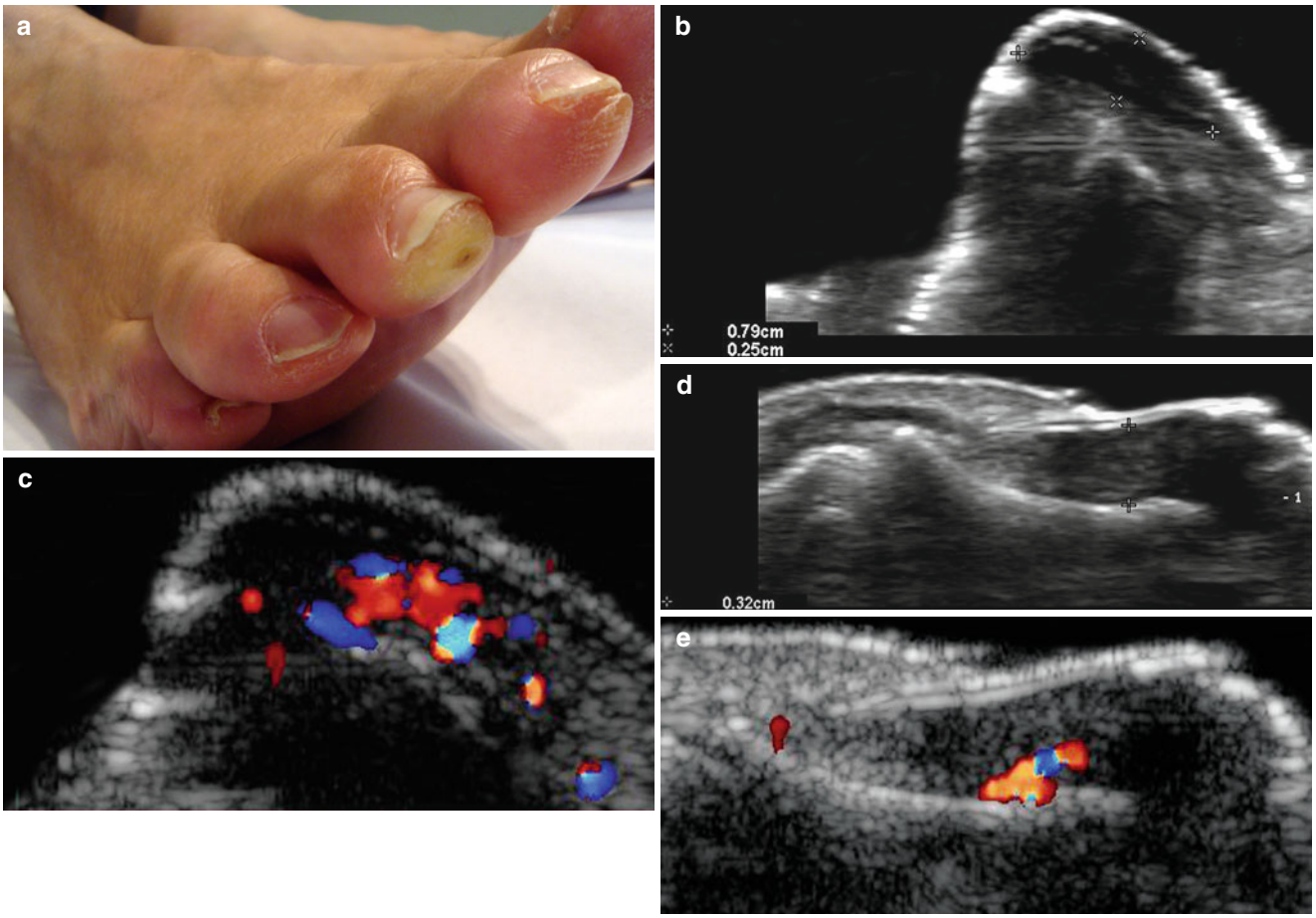

Fig. 18.42 (**a**–**e**) Wart. (**a**) Clinical photograph shows prominent hyperkeratosis in the plantar aspect and hyponychium of the right second toe. (**b**) Grey scale ultrasound image (transverse view, plantar region, right second toe) shows a 7.9 mm (transverse) × 2.5 mm (depth) fusiform-shaped hypoechoic epidermal and dermal lesion (between markers). (**c**) Color Doppler ultrasound image (transverse view, plantar region) shows increased vascularity in the sublesional area. (**d**) Grey scale ultrasound image (longitudinal view, right second toenail) presents a mild increase of the thickness of the nail bed and undulation of the ventral plate. **e** Color Doppler ultrasound image (longitudinal view, right second toenail) shows no signs of hypervascularity within the nail bed

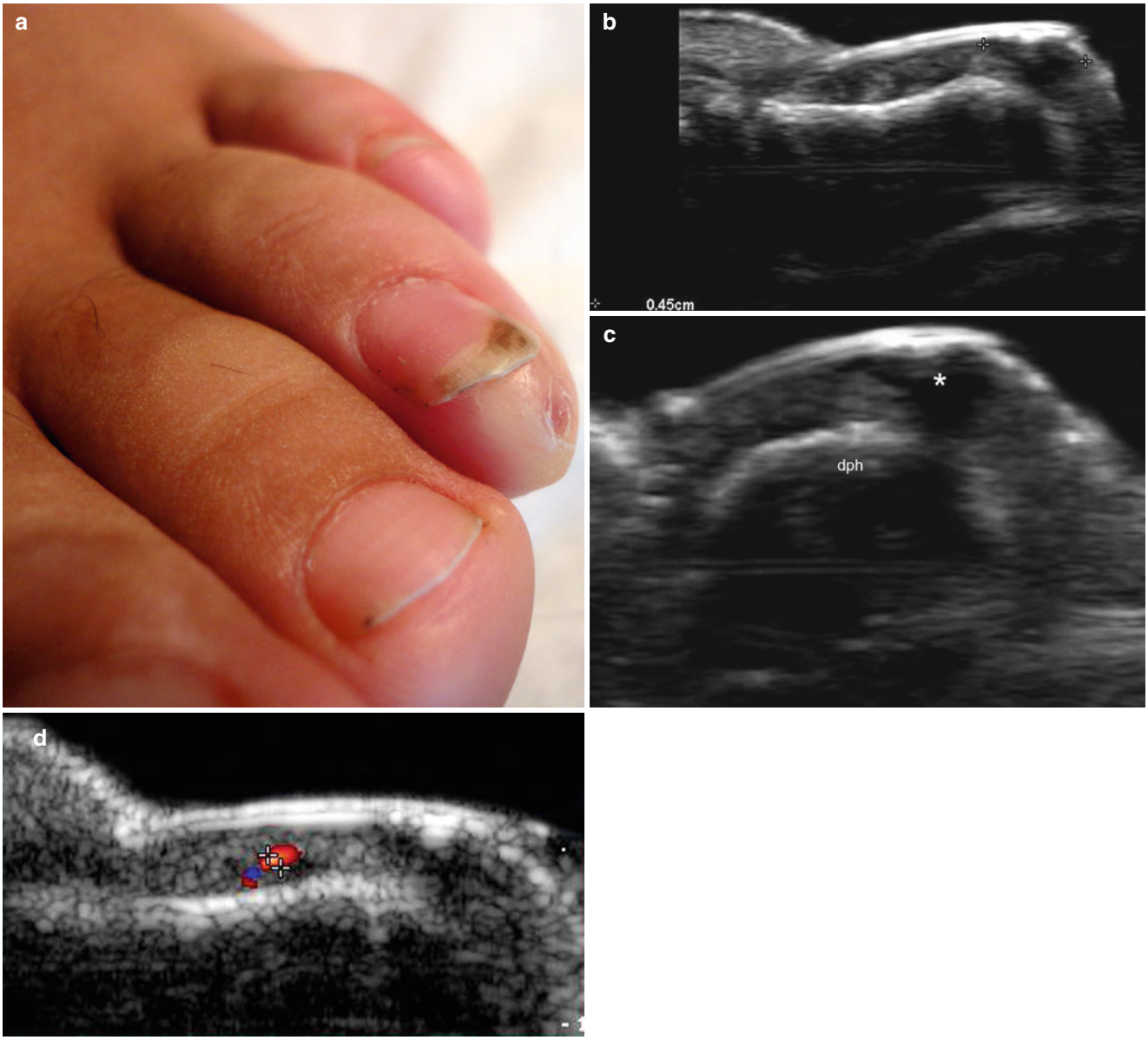

Fig. 18.43 (**a**–**d**) Wart. (**a**) Clinical image shows pigmentation and dystrophic changes in the nail plate of the left fourth toe. Hyperkeratosis and small erosion in the skin are also detected in the hyponychium. (**b**, **c**) Grey scale ultrasound images of the left fourth toe (**b** longitudinal view; **c** transverse view) show a 4.5 mm long well-defined fusiform-shaped hypoechoic structure (between markers) in the lateral aspect of the distal nail bed. Notice the thickening of the ventral plate in contact with the lesion. (**d**) Color Doppler ultrasound image (longitudinal view) shows no signs of hypervascularity in the lesional area. Only thin vessels (colors and between markers) are detected. *Abbreviation*: *dph* distal phalanx

Cysts

Mucous Cysts These also called mucinous cysts, are entities that contain degenerated collagen and mucoid viscous fluid. The difference between mucous and synovial cysts is usually determined histologically. Clinically, mucous cysts can present as painless lumps, swelling, nodules, or deformities of the nail and periungual tissues. Mucous cysts can cause dystrophic changes in the nail plates when compressing the nail matrix, and frequently do not connect with the distal interphalangeal joint.

Mucous cysts appear as round- or oval-shaped, sometimes lobulated, anechoic structures when seen on ultrasound that can present inner echoes suggestive of viscous debris. If the cyst compresses the ungual matrix region, irregularities or thickening of the nail plates can be detected. Additionally, the nail plates can be displaced upward by the mass effect of the cyst. A posterior acoustic enhancement artifact, typical of fluid-filled cystic lesions, is commonly detected. When viewed on color Doppler ultrasound, mucous cysts lack blood flow [6, 55, 63, 74] (Fig. 18.44).

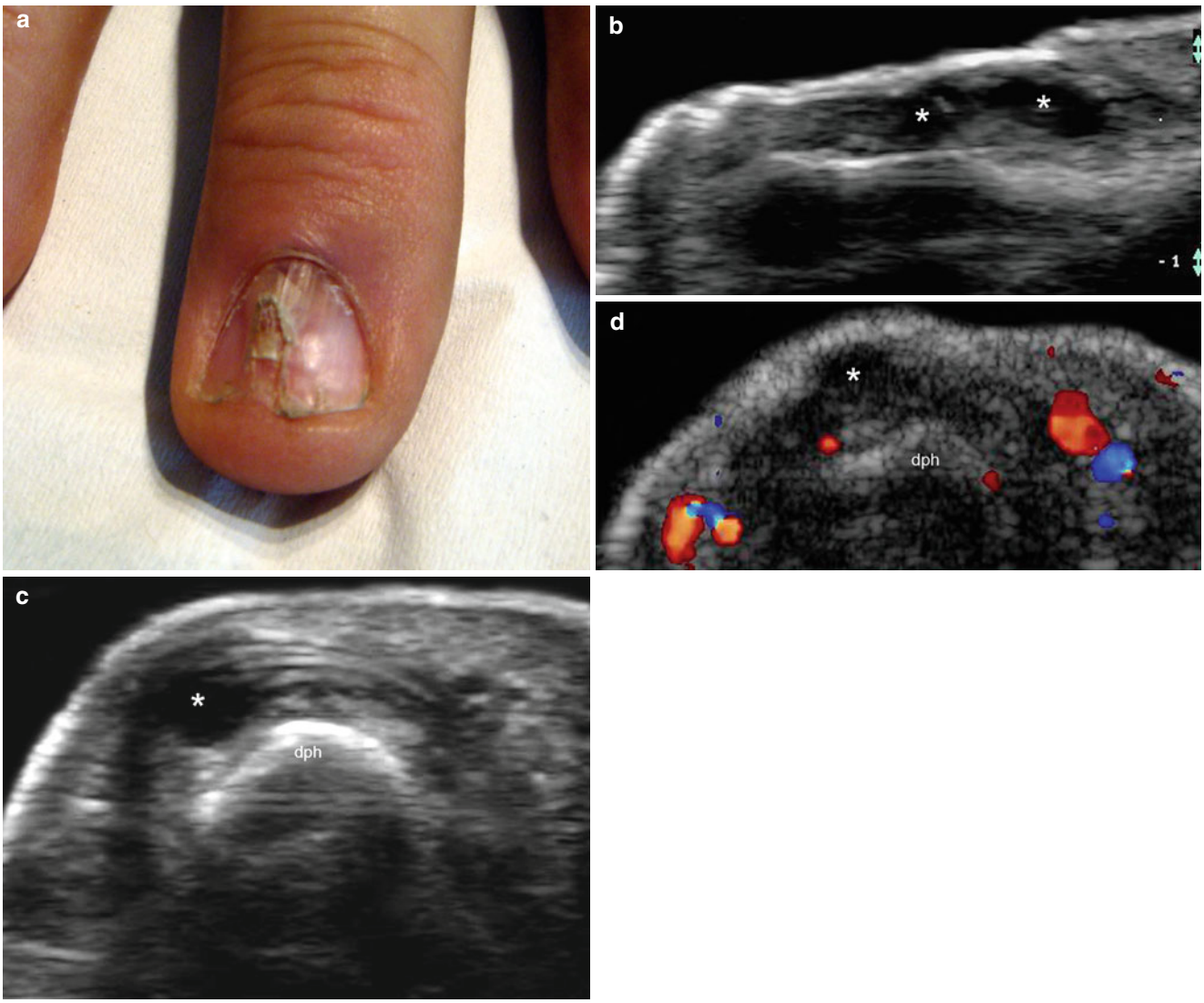

Fig. 18.44 (**a**–**d**) Mucous cyst. (**a**) Clinical photograph shows a lump and dystrophic changes in the nail of the right middle finger. (**b**) Grey scale ultrasound image (longitudinal view) shows a bilobulated anechoic cystic structure (*) in the nail bed. An upward displacement of the nail plate with thickening of the dorsal plate and loss of definition of the ventral plate is detected. (**c**) Grey scale ultrasound image (transverse view) shows involvement of the ulnar wing of the ungual matrix by the cyst (*). (**d**) Color Doppler ultrasound image (transverse view) shows lack of vascularity within the cyst. *Abbreviation*: *dph* distal phalanx

18.4.4.1.2 Periungual Origin

Solid

Subungual Exostosis This is a slow-growing, benign outgrowth of normal bone and/or calcified cartilaginous tissue beneath or beside the nail unit. The most common location for subungual exostosis in the foot is the dorsal surface of the distal phalanx of the great toe. Clinically, subungual exostosis can produce elevation and deformity of the nail plates and be associated with inflammatory changes that can easily mimic ungual tumors or onychomycosis.

On ultrasound, subungual exostoses appear as linear or band-like hyperechoic structures with posterior acoustic shadowing, an artifact that is typically seen in calcified structures. The hyperechoic structures are usually continuous with the hyperechoic bony margin of the distal phalanx. A hypoechoic cap surrounding the calcified hyperechoic component can be detected when subungual exostoses are associated with cartilaginous tissue (osteochondroma). Hypoechoic ill-defined tissue can be seen surrounding the exostosis that corresponds with secondary inflammation and scarring [6, 55, 74, 75] (Figs. 18.45, 18.46, 18.47, and 18.48).

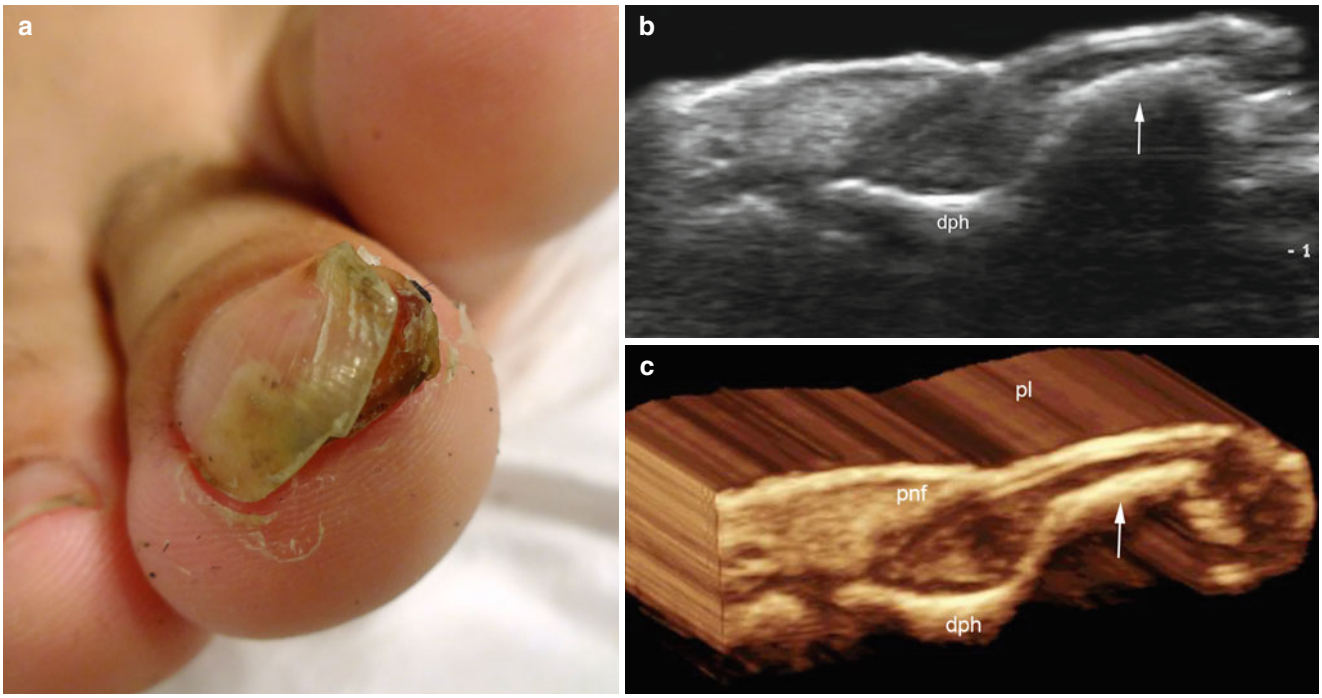

Fig. 18.45 Subungual exostosis. (**a**) Clinical photograph shows an erythematous subungual lump with deformation and dystrophic changes in the nail of the right second toe. (**b**) Grey scale ultrasound image (longitudinal view) shows a hyperechoic linear bony outgrowth (*arrow*) that emerges from the bony margin of the distal phalanx. There is posterior acoustic shadowing underlying the bone. (**c**) 3D reconstruction (grey scale, longitudinal view) of the exostosis (*arrow*). *Abbreviations*: *dph* distal phalanx, *pnf* proximal nail fold, *pl* nail plates

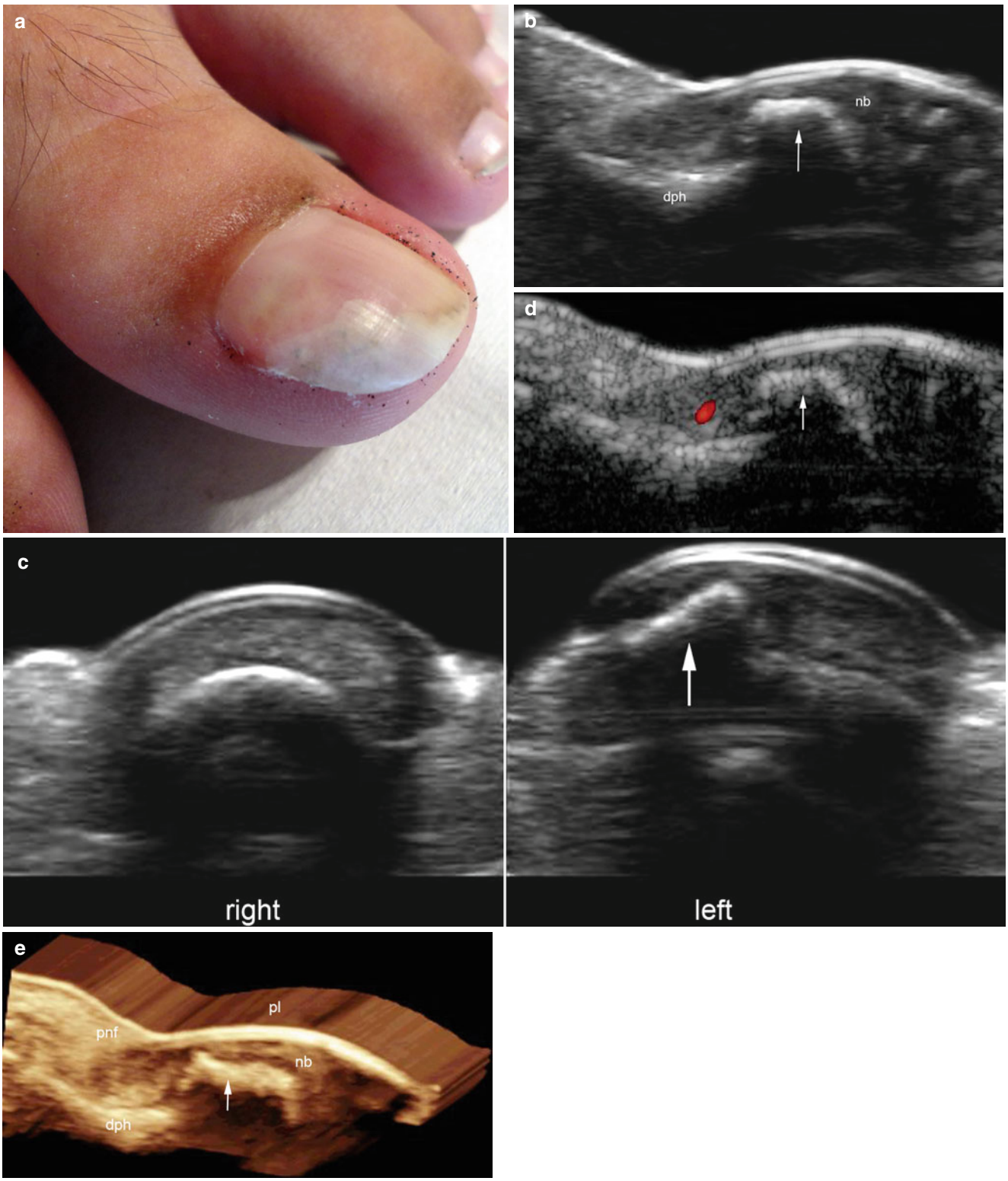

Fig. 18.46 (**a**–**e**) Subungual exostosis. (**a**) Clinical image shows dystrophic changes in the nail plate of the left hallux. Tests for onychomycosis were negative for over 6 months. (**b**) Grey scale ultrasound image (longitudinal view) shows a hyperechoic band (*arrow*) that bulges into the nail bed and connects with the bony margin of the distal phalanx. (**c**) Grey scale image (transverse view, side by side comparison): well-depicted hyperechoic bony outgrowth (*arrow*, exostosis) is detected in the medial aspect of the nail bed of the left hallux. In contrast, no sign of exostosis is detected in the nail bed of the right hallux. (**d**) Color Doppler ultrasound image (longitudinal view) shows lack of hypervascularity within the lesional area (*arrow*). (**e**) 3D reconstruction (longitudinal view) of the exostosis (*arrow*). *Abbreviations*: *nb* nail bed, *dph* distal phalanx, *pnf* proximal nail fold, *pl* nail plates

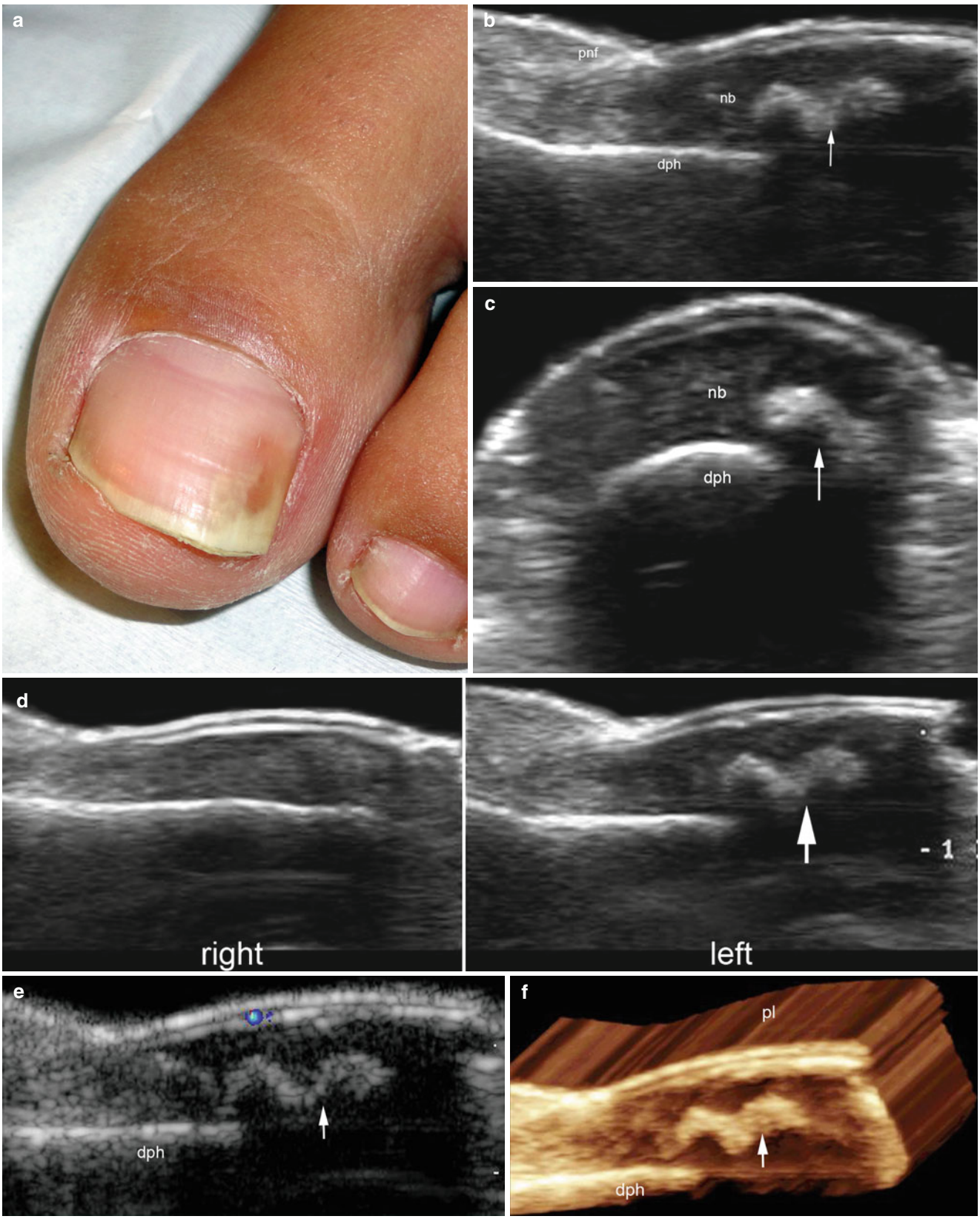

Fig. 18.47 (**a**–**f**) Subungual exostosis. (**a**) Clinical image shows brownish and dystrophic changes in the nail plate of the left hallux. Tests for onychomycosis were negative for the previous 4 months. (**b**, **c**) Grey scale ultrasound images (**b** longitudinal view; **c** transverse view) show a wavy hyperechoic band (*arrow*) in the lateral aspect of the nail bed that produces posterior acoustic shadowing. (**d**) Grey scale ultrasound image (longitudinal view, side by side comparison) shows an hyperechoic band that corresponds to the exostosis (*arrow*) in the nail bed of the left hallux. No sign of exostosis is detected in the nail bed of the right hallux. (**e**) Color Doppler ultrasound image (longitudinal view) shows lack of hypervascularity within the nail bed. (**f**) 3D reconstruction (longitudinal view) highlights the exostosis (*arrow*). *Abbreviations*: *nb* nail bed, *dph* distal phalanx, *pnf* proximal nail fold, *pl* nail plates

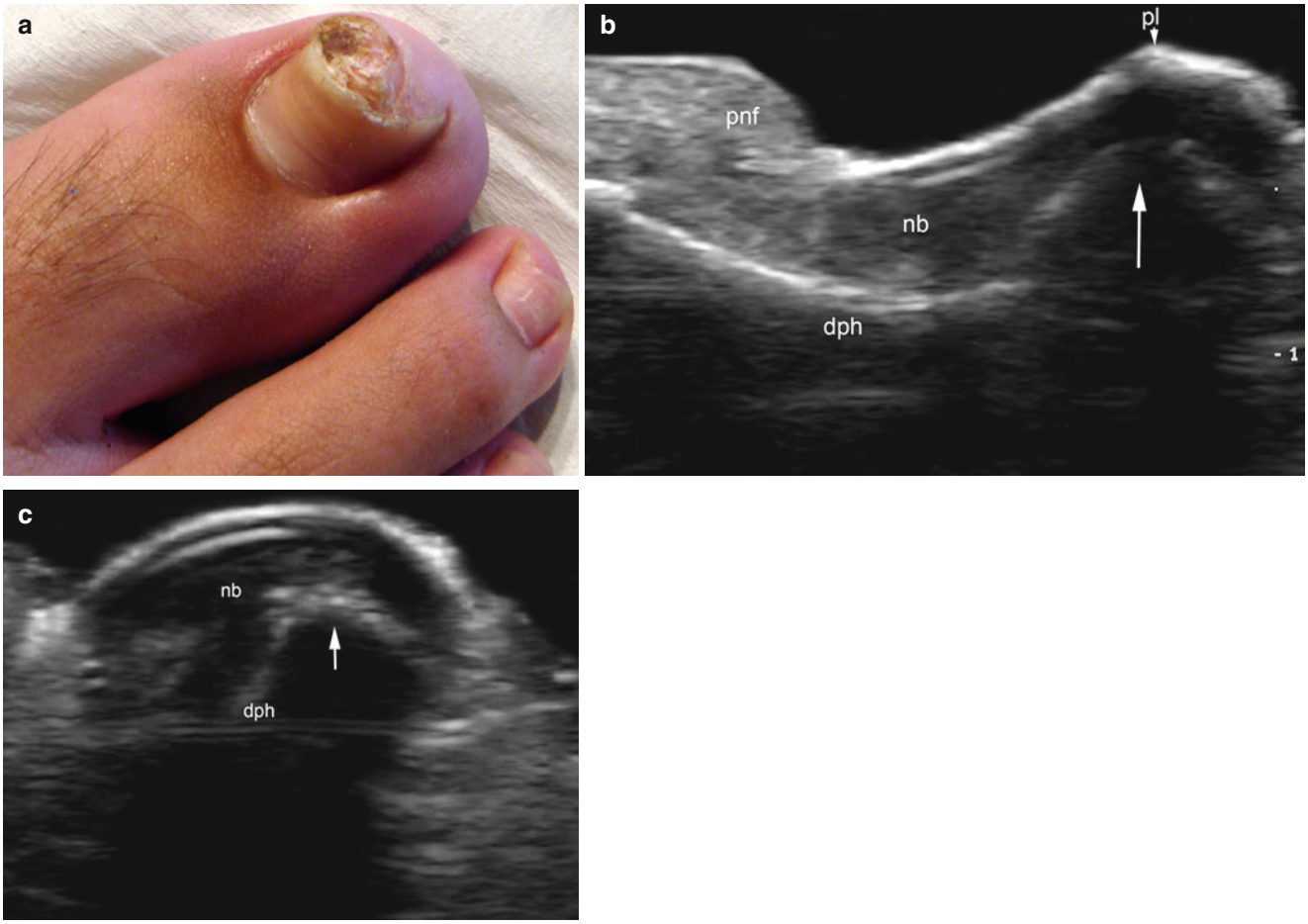

Fig. 18.48 (**a**–**c**) Subungual exostosis. (**a**) Clinical image shows a brownish subungual lump in the nail of the right hallux. (**b**, **c**) Grey scale ultrasound images (**b** longitudinal view; **c** transverse view) show a hyperechoic convex band (*arrow*) in the medial aspect of the right hallux that produces posterior acoustic shadowing artifact. *Abbreviations*: *nb* nail bed, *dph* distal phalanx, *pnf* proximal nail fold, *pl* nail plates

Periungual Pyogenic Granuloma This is a proliferative and reactive condition also called periungual telangiectatic granuloma, and presents histological similarities to the subungual variant. Periungual pyogenic granulomas can present complications in the periungual region elicited by their direct exposure to trauma, and have been described as being bleeding nodules [76]. There are also reports that show association of periungual pyogenic granulomas with certain medications [77, 78].

On ultrasound, periungual pyogenic granulomas present as round- or oval-shaped hypoechoic lesions located in the dermis of the proximal or lateral nail folds. The degree of vascularity is variable and can vary from hypervascular to hypovascular. A low presence of vascularity is usually related to the high content of slow flow capillary vessels within the lesion that can make detection of the flow by the current machines difficult [6] (Fig. 18.49).

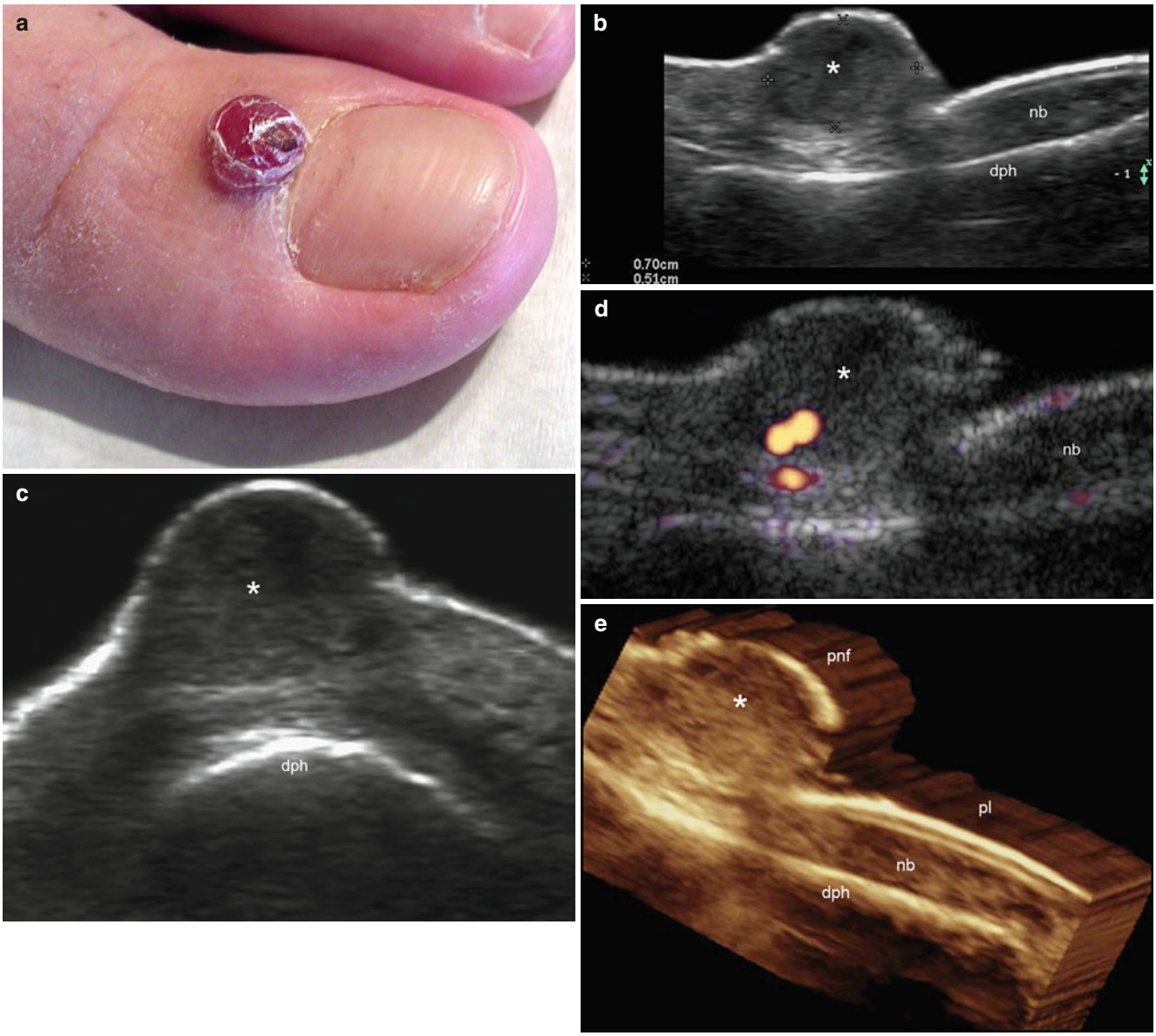

Fig. 18.49 (**a**–**e**) Periungual pyogenic granuloma. (**a**) Clinical photograph shows a reddish lump in the proximal nail fold of the left hallux. (**b**, **c**) Grey scale ultrasound images (**b** longitudinal view; **c** transverse view) show a 7.0 mm long×5.1 mm depth well-defined, round-shaped hypoechoic solid nodule (*, between markers) in the dermis of the proximal nail fold. (**d**) Power Doppler ultrasound image (longitudinal view) shows a mild increase of the blood flow within the nodule. (**e**) 3D reconstruction of the lesion (*). *Abbreviations*: *nb* nail bed, *dph* distal phalanx, *pnf* proximal nail fold, *pl* nail plates

Periungual Fibrokeratomas These are elongated and polypoid fibrous tumors that lie over the nail plates and frequently connect with the proximal or lateral nail folds, as well as the nail bed. Thus, periungual fibrokeratomas are tumors that can involve the ungual matrix in the same axis [6].

Histologically, capillaries are typically found in the distal part of the periungual fibrokeratomas surrounded by thin collagen bundles, whereas the proximal part present dense, closely packed collagen fibers. The epidermis that covers the tumor appears to be connected with the nail fold, and the dense collagen of the lesion also fades into the normal structure of the dermis of the proximal nail fold [79].

On sonography, periungual fibrokeratomas appear as eccentrically located hypoechoic polypoid structures that are usually hypovascular and frequently cover an aspect of the nail plates. Rarely these tumors can elicit scalloping of the bony margin of the distal phalanx. Sonographic examination of the involvement of the proximal or lateral nail fold, ungual matrix, or nail bed can provide useful pre-surgical information and prevent recurrences [6, 55] (Fig. 18.50).

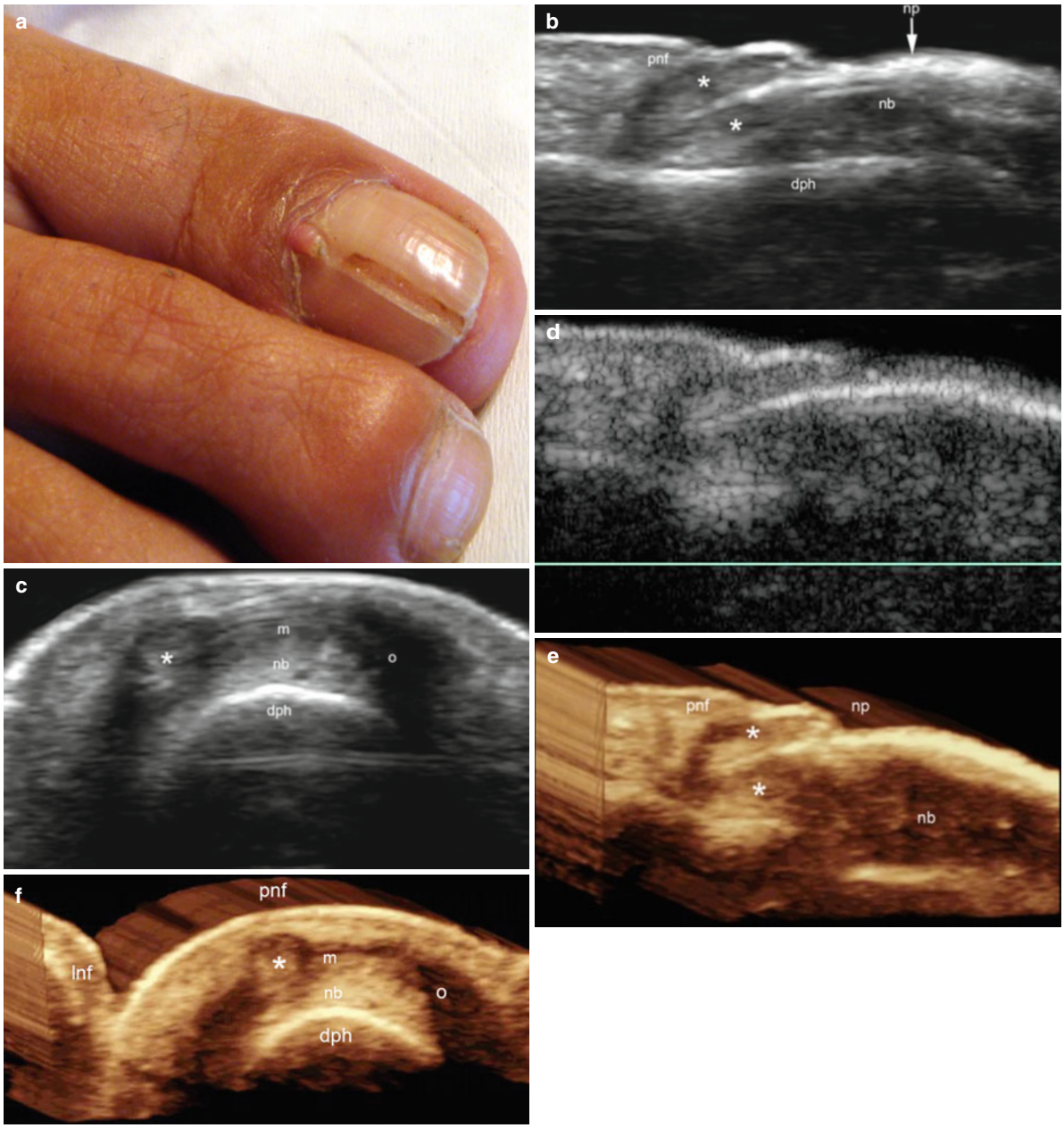

Fig. 18.50 (**a**–**f**) Periungual fibrokeratoma. (**a**) Clinical image shows an erythematous, elongated and polypoid lesion attached to the proximal nail fold. A longitudinal groove is also seen in the nail plate following the same axis of the lesion. (**b**, **c**) Grey scale ultrasound images (**b** longitudinal view; **c** transverse view) show a polypoid hypoechoic solid structure (*) over the proximal part of the nail plates that also bulges into the nail bed affecting the lateral wing of the ungual matrix (Fig. C). Notice that the medial wing of the ungual matrix (o) is unremarkable. (**d**) Color Doppler ultrasound image (longitudinal view) shows no signs of hypervascularity within the nail bed. (**e**, **f**) 3D reconstructions (**e** longitudinal view; **f** transverse view) of the lesion (*). *Abbreviations*: *nb* nail bed, *dph* distal phalanx, *pnf* proximal nail fold, *np* nail plates

Cysts

Synovial Cysts These also called myxoid cysts are entities usually caused by a leakage of fluid and/or synovial proliferation in the adjacent joint that extends into the periungual region. Therefore, synovial cysts are usually connected to the distal interphalangeal (DIP) joint through thin and tortuous ducts that run through lateral aspects of the finger or toe. This connection between the cyst and the joint has been identified by means of a methylene blue injection in 89 % of cases in some studies [80]. Additionally, synovial cysts frequently affect the proximal nail fold and can also extend into the nail bed and secondarily compress the ungual matrix.

On ultrasound, synovial cysts appear as round or oval-shaped, tortuous or lobulated, anechoic structures with posterior acoustic reinforcement that lack inner blood flow. Assessment of the extension of the synovial cyst into the nail bed and the anechoic connecting tract with the DIP joint can be useful for diagnosis. Osteoarthrosis and synovitis of the DIP joint are commonly seen. Thickening and irregularities of the nail plates in the same axis of the secondary compression of the ungual matrix are also frequently found [55, 74] (Figs. 18.51, 18.52, and 18.53).

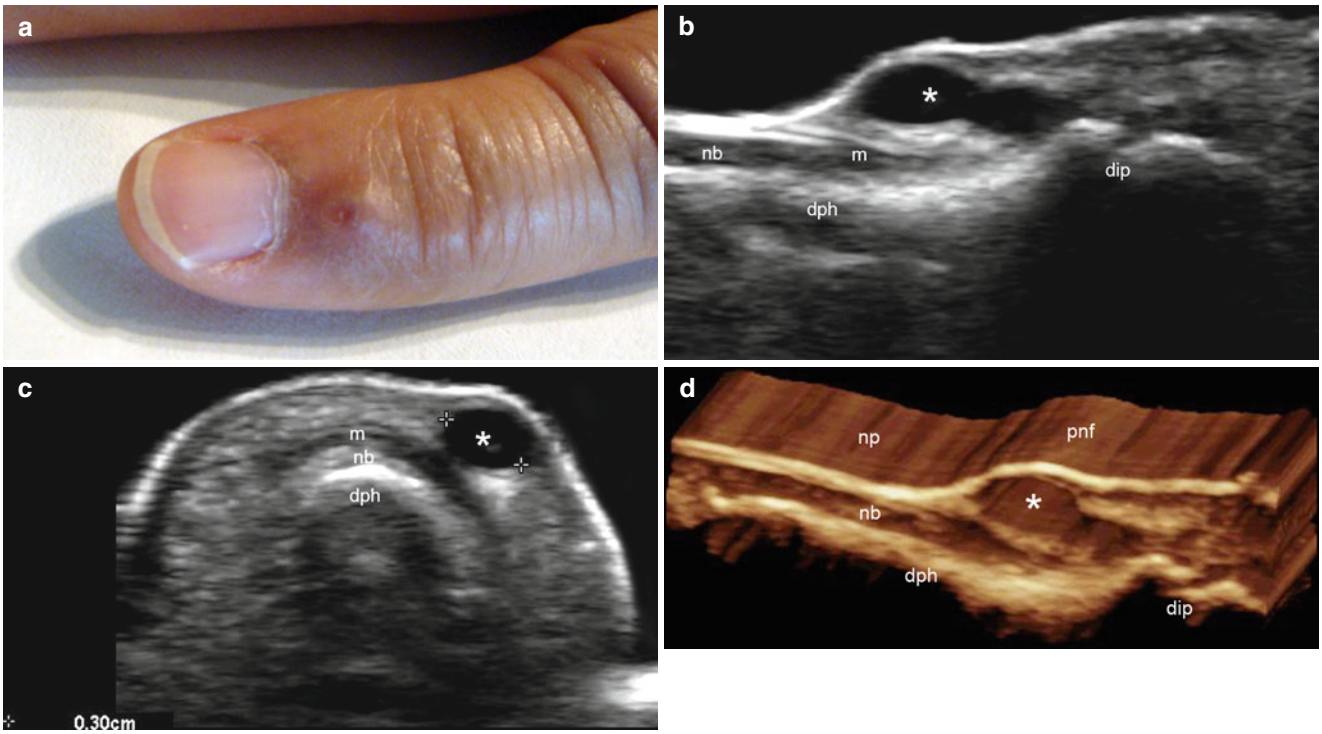

Fig. 18.51 (**a**–**d**) Synovial (myxoid) cyst. (**a**) Clinical photograph shows erythematous swelling in the ulnar aspect of the proximal nail fold of the little finger. (**b**, **c**) Grey scale ultrasound images (**b** longitudinal view; **c** transverse view) show a well-defined, lobulated anechoic cystic structure that connects with the ulnar aspect of the distal interphalangeal joint. (**d**) 3D reconstruction (longitudinal view, 5–8 s sweep) highlights the cyst (*). *Abbreviations*: *nb* nail bed, *m* ungual matrix, *dph* distal phalanx, *pnf* proximal nail fold, *np* nail plates, *dip* distal interphalangeal joint

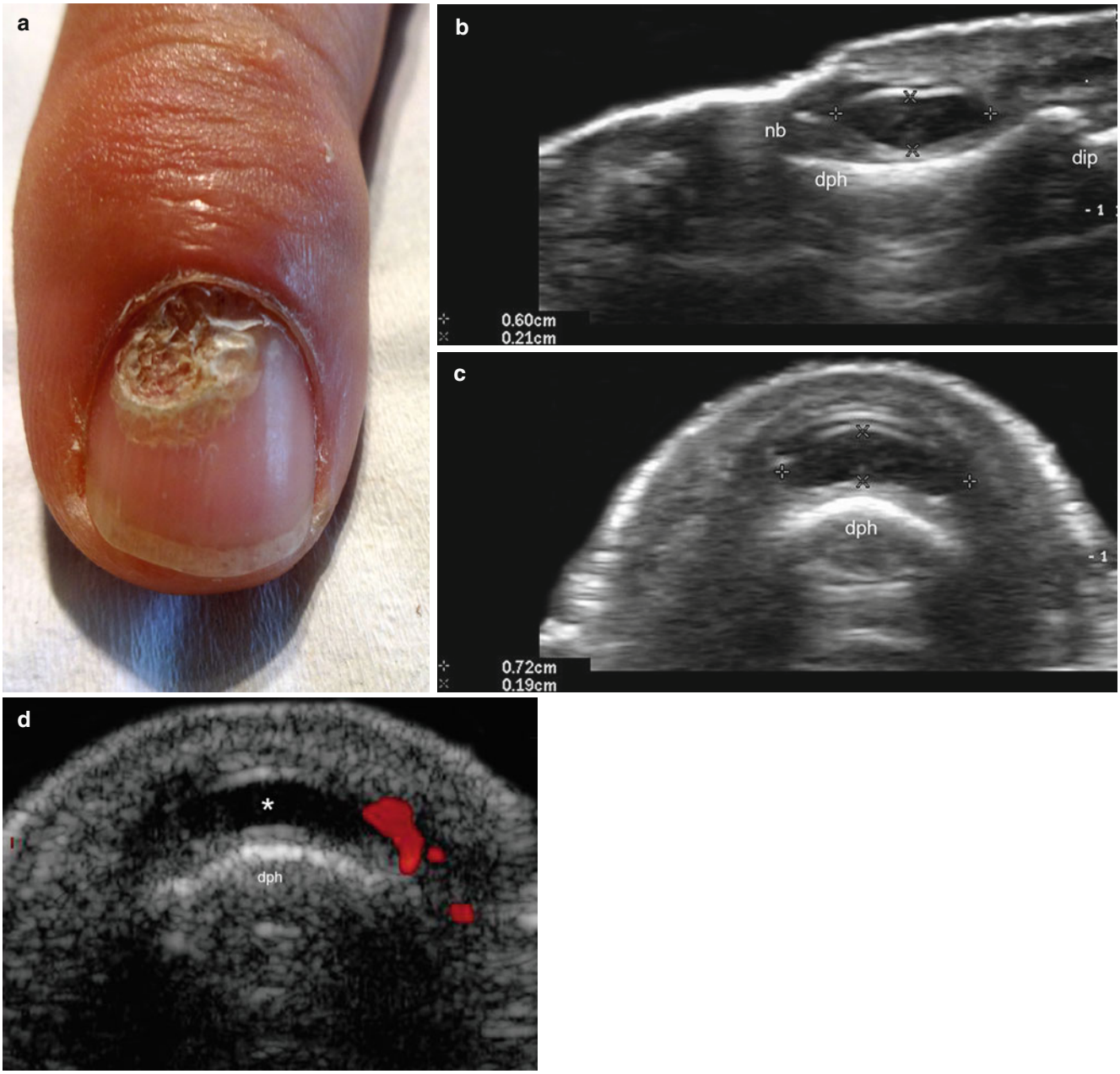

Fig. 18.52 (**a**–**d**) Synovial (myxoid) cyst. (**a**) Clinical image shows deformation and dystrophic changes in the proximal region of the nail plate of the left index finger. (**b**, **c**) Grey scale ultrasound images (**b** longitudinal view; **c** transverse view) show a 6.0 mm (long) × 2.1 mm (depth) × 7.2 mm (transverse) well-defined, oval-shaped anechoic structure in the proximal nail fold that bulges into the nail bed and mildly compress the ungual matrix. Notice the thickening of the nail plate with loss of the bilaminar pattern. (**d**) Color Doppler ultrasound image (transverse view) shows lack of vascularity within the cyst (*). *Abbreviations*: *nb* nail bed, *dph* distal phalanx, *pnf* proximal nail fold, *dip* distal interphalangeal joint

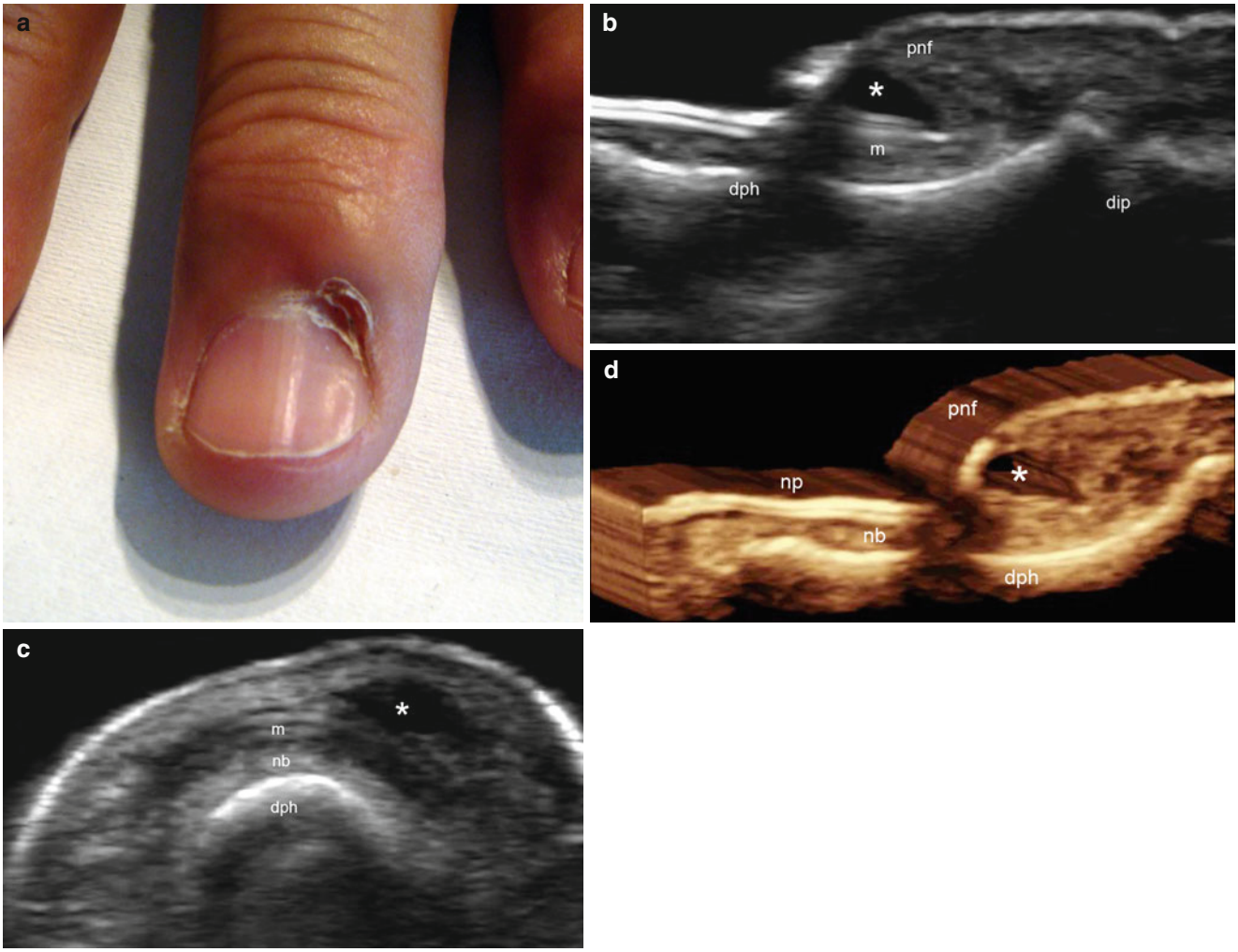

Fig. 18.53 (**a**–**d**) Synovial (myxoid) cyst. (**a**) Clinical photograph shows swelling in the proximal nail fold and a concavity of the radial aspect of the nail plate in the right middle finger. (**b**, **c**) Grey scale ultrasound images (**b** longitudinal view; **c** transverse view) show a well-defined, oval-shaped anechoic cystic structure (*) in the proximal nail fold that slightly compresses the radial wing of the ungual matrix. (**d**) 3D reconstruction (longitudinal view) highlights the cyst (*). *Abbreviations*: *nb* nail bed, *m* ungual matrix, *dph* distal phalanx, *pnf* proximal nail fold, *np* nail plates, *dip* distal interphalangeal joint

18.4.4.2 Malignant Tumors

18.4.4.2.1 Melanoma

Acral lentiginous melanoma (i.e., located in the extremities) is rare, and represents approximately 1 % of malignant melanomas. This type of melanoma shows a 5-year survival rate that is disproportionately poor (25–51 %) compared with other histological subtypes, and can be the result of delay in the diagnosis that can generate a more advanced or aggressive form at presentation [81]. Ungual melanoma (UM) is uncommon, and composes 1–13 % of all acral lentiginous melanomas, accounting for 0.7–3.5 % of all cutaneous melanomas. Clinically, UM presents as a brownish-black or darkly pigmented linear patch or band that has widened and darkened over time and typically involves the lunula, hyponychium and/or lateral nail folds. Discoloration of the nail followed by a recalcitrant wound, a visible tumor, nail splitting, and bleeding can also be detected. Histology shows atypical melanocytes and inflammatory cells along the basal layer of the epidermis or deeper layers. UM, a type of acral lentiginous melanoma, arises from the nail matrix, most commonly in the big toe or thumb. Hutchinson's nail sign is an important clinical clue to UM and is characterized by extension of brown or black pigment from the nail bed, matrix, and nail plate to the adjacent cuticle and proximal or lateral nail folds [82]. Misdiagnosis of UM as a subungual hematoma, chronic trauma, or onychomycosis is currently still a frequent occurrence, significantly reducing the chances for early treatment. An appropriate diagnostic approach is crucial to allow diagnosis in the early state. The proper management of UM hinges on early diagnosis and selection of the most appropriate surgical technique. Curative treatment of UM currently entails surgical excision when the extent of invasion is limited [83].

Fortunatly, the in situ type of UM is the most common form of presentation which on the other hand can limit the diagnostic support of sonography. The early form of presentation of UM is difficult to catch on sonography because of the current limitations of the ultrasound equipment that include the lack of pigment detection or difficulties to detect flat lesions measuring less than 0.1 mm [84]. Nevertheless, in some early cases of UMs, sonographic abnormalities such as focal hypervascularity and/or ill-defined hypoechoic areas can be detected. A hypoechoic well-defined solid mass can be detected in the late phases [61]. Ultrasound may also be an adjunct tool in cases with congenital or acquired melanonychia (i.e., benign pigmentation of the nail plate) that can potentially undergo sonographic examination to rule out the development of a solid mass and to avoid the cosmetic disfigurements that may be elicited through serial biopsies [6] (Fig. 18.54).

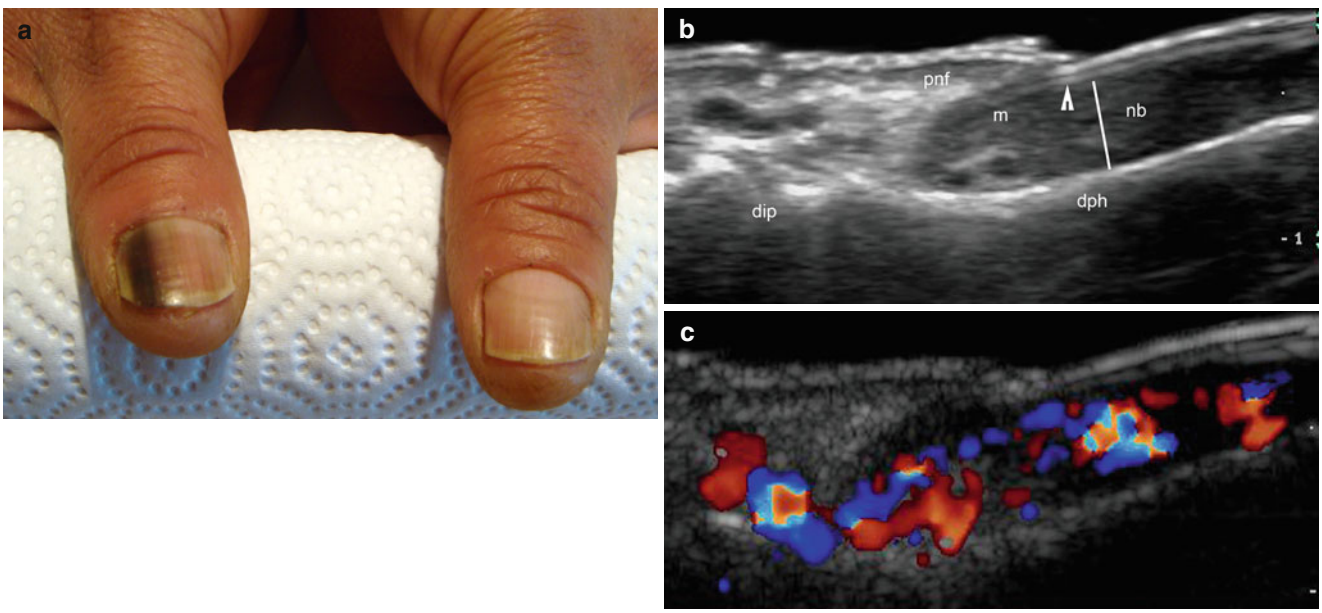

Fig. 18.54 (**a**–**c**) Melanoma in situ. (**a**) Clinical image shows a longitudinal pigmented band in the ulnar aspect of the nail of the right thumb. (**b**) Grey scale ultrasound image (longitudinal view) shows increased thickness of the nail bed and a mild loss of definition of the ventral plate (*arrowhead*). No solid mass is detectable. (**c**) Color Doppler ultrasound image (longitudinal view, ulnar aspect of the nail) shows diffuse hypervascularity within the nail bed in the same axis of the lesion. *Abbreviations*: *nb* nail bed, *m* ungual matrix, *dph* distal phalanx, *pnf* proximal nail fold, *np* nail plates, *dip* distal interphalangeal joint

Squamous Cell Carcinoma

Subungual involvement because of SCC occurs most frequently on the fingernails, and has rarely been reported on the toes [85]. Detection of in situ SCC (Bowen's disease) in ungual locations is limited by the resolution of sonography that can currently be obtained. Nevertheless, a hypoechoic ill-defined solid mass that erodes the nail plates can be detected in the late stages. Destruction of the bony margin and hypervascularity within the tumor can also be seen [6, 86] (Fig. 18.55).

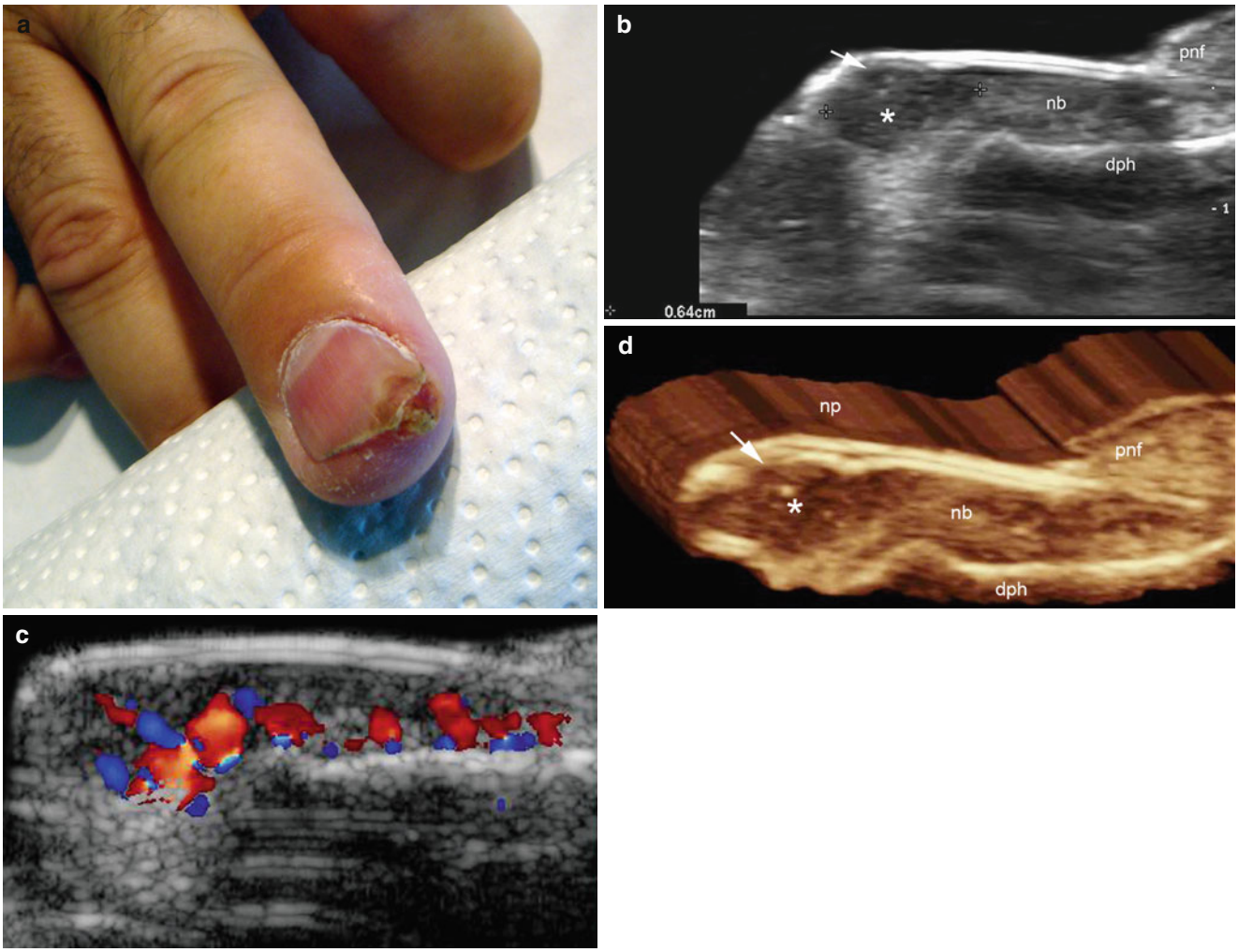

Fig. 18.55 (**a**–**d**) Squamous cell carcinoma. (**a**) Clinical photograph shows an erosive reddish swelling in the distal part of nail of the middle finger. (**b**) Grey scale ultrasound image (longitudinal view) shows a 6.4 mm long oval-shaped hypoechoic nodule (*, between markers). Notice the disruption (*arrow*) of the ventral plate in contact with the nodule. (**c**) Color Doppler ultrasound image (longitudinal view) shows increased vascularity in the distal part of the nail bed in the same axis of the lesion. (**d**) 3D reconstruction (longitudinal view) highlights the lesion (*) and the disruption of the ventral plate (*arrow*). *Abbreviations*: *nb* nail bed, *m* ungual matrix, *dph* distal phalanx, *pnf* proximal nail fold, *np* nail plates, *dip* distal interphalangeal joint

References

1. Gonagle M, Tan AL, Benjamin M. The nail as musculoskeletal appendage – implications for an improved understanding of the link between psoriasis and arthritis. Dermatology. 2009;218:97–102.
2. Hanecke E. Surgical anatomy of the nail apparatus. Dermatol Clin. 2006;24:291–6.
3. Wortsman X, Jemec GBE. Ultrasound imaging of nails. Dermatol Clin. 2006;24:323–8.
4. Jemec GB, Serup J. Ultrasound structure of the human nail plate. Arch Dermatol. 1989;125:643–6.
5. Wortsman X. Common applications of dermatologic sonography. J Ultrasound Med. 2012;31:97–111.
6. Thomas L, Vaudaine M, Wortsman X, Jemec GBE, Drapé JL. Imaging the nail unit. In: Baran R, de Berker D, Holzberg M, Thomas L, editors. Baran & Dawber's diseases of the nails and their management. 4th ed. Chichester: Wiley; 2012. p. 132–53.
7. Heidelbaugh JJ, Lee H. Management of the ingrown toenail. Am Fam Physician. 2009;15(79):303–8.
8. Chapeskie H, Kovac JR. Case series: soft-tissue nail-fold excision: a definitive treatment for ingrown toenails. Can J Surg. 2010;53:282–6.
9. Haneke E. Onychomadesis and hand, foot and mouth disease-is there a connection? Euro Surveill. 2010;6(15 pii):19664.
10. Wortsman X, Wortsman J, Guerrero R, Soto R, Baran R. Anatomical changes in retronychia and onychomadesis detected using ultrasound. Dermatol Surg. 2010;36:1615–20.
11. Wortsman X, Calderon P, Baran R. Finger retronychias detected early by 3D ultrasound examination. J Eur Acad Dermatol Venereol. 2012;26:254–6.
12. Baran R, Haneke E. Etiology and treatment of nail malalignment. Dermatol Surg. 1998;24:719–21.
13. Wagner G, Sachse MM. Congenital malalignment of the big toe nail. J Dtsch Dermatol Ges. 2012;10:326–33.
14. Hammerton MD, Shrank AB. Congenital hypertrophy of the lateral nail folds of the hallux. Pediatr Dermatol. 1988;5:243–5.
15. Rufli T, von Schulthess A, Itin P. Congenital hypertrophy of the lateral nail folds of the hallux. Dermatology. 1992;184:296–7.
16. Piraccini BM, Parente GL, Varotti E, Tosti A. Congenital hypertrophy of the lateral nail folds of the hallux: clinical features and follow-up of seven cases. Pediatr Dermatol. 2000;17:348–51.
17. Finner AM. Alopecia areata: clinical presentation, diagnosis, and unusual cases. Dermatol Ther. 2011;24:348–54.
18. Alkhalifah A, Alsantali A, Wang E, McElwee KJ, Shapiro J. Alopecia areata update: part I. Clinical picture, histopathology, and pathogenesis. J Am Acad Dermatol. 2010;62:177–88.
19. Baran R, Dawber RP, Haneke E. Hair and nail relationship. Skinmed. 2005;4:18–23.
20. Noronha PA, Zubkov B. Nails and nail disorders in children and adults. Am Fam Physician. 1997;1(55):2129–40.
21. DiGiovanna JJ, Robinson-Bostom L. Ichthyosis: etiology, diagnosis, and management. Am J Clin Dermatol. 2003;4:81–95.
22. Van Gysel D, Lijnen RL, Moekti SS, de Laat PC, Oranje AP. Collodion baby: a follow-up study of 17 cases. J Eur Acad Dermatol Venereol. 2002;16:472–5.
23. Wortsman X, Aranibar L, Morales C. Postnatal 2- and 3-dimensional sonography of the skin and nail in congenital autosomal recessive ichthyosis correlated with cutaneous Histologic findings. J Ultrasound Med. 2011;30:1437–9.
24. Hallaji Z, Babaeijandaghi F, Akbarzadeh M, Seyedi SZ, Barzegari M, Noormohammadpour P, et al. A significant association exists between the severity of nail and skin involvement in psoriasis. J Am Acad Dermatol. 2012;66:e12–3.
25. Wortsman X, Holm EA, Jemec GBE, Gniadecka M, Wulf H. 15 MHz high resolution ultrasound examination of psoriatic nails. Rev Chil Rad. 2004;10:6–9. Spanish.
26. Gutierrez M, Wortsman X, Filippucci E, De Angelis R, Filosa G, Grassi W. High-frequency sonography in the evaluation of psoriasis: nail and skin involvement. J Ultrasound Med. 2009;28:1569–74.
27. Gutierrez M, Filippucci E, De Angelis R, Bertolazzi C, Becciolini A, Ariani A, et al. The ultrasound assessment of the psoriatic arthritis: from joint to skin. Reumatismo. 2009;61:309–15.
28. Di Franco M, Paradiso M, Riccieri V, Basili S, Mammarella A, Valesini G. Autonomic dysfunction and microvascular damage in systemic sclerosis. Clin Rheumatol. 2007;26:1278–83.
29. Murray AK, Moore TL, Manning JB, Taylor C, Griffiths CE, Herrick AL. Noninvasive imaging techniques in the assessment of scleroderma spectrum disorders. Arthritis Rheum. 2009;15(61):1103–11.
30. Tunc SE, Ertam I, Pirildar T, Turk T, Ozturk M, Doganavsargil E. Nail changes in connective tissue diseases: do nail changes provide clues for the diagnosis. J Eur Acad Dermatol Venereol. 2007;21:497–503.
31. Wortsman X, Gutierrez M, Saavedra T, Honeyman J. The role of ultrasound in rheumatic skin and nail lesions: a multi-specialist approach. Clin Rheumatol. 2011;30:739–48.
32. Mugii N, Hasegawa M, Matsushita T, Hamaguchi Y, Horie S, Yahata T, et al. Association between nail-fold capillary findings and disease activity in dermatomyositis. Rheumatology (Oxford). 2011; |50:1091–8.
33. Rider LG, Atkinson JC. Images in clinical medicine. Gingival and periungual vasculopathy of juvenile dermatomyositis. N Engl J Med. 2009;9(360):e21.
34. Chander S, Gordon P. Soft tissue and subcutaneous calcification in connective tissue diseases. Curr Opin Rheumatol. 2012;24: 158–64.
35. Moneib HA, Salem SA, Aly DG, Khedr HT, Wafaey HA, Hassan HE. Assessment of serum vascular endothelial growth factor and nail fold capillaroscopy changes in systemic lupus erythematosus with and without cutaneous manifestations. J Dermatol. 2012;39:52–7.
36. Trüeb RM. Involvement of scalp and nails in lupus erythematosus. Lupus. 2010;19:1078–86.
37. Tosti A. The nail apparatus in collagen disorders. Semin Dermatol. 1991;10:71–6.
38. Michel C, Cribier B, Sibilia J, Kuntz JL, Grosshans E. Nail abnormalities in rheumatoid arthritis. Br J Dermatol. 1997;137:958–62.
39. Grassi W, Filippucci E, Farina A, Cervini C. Sonographic imaging of the distal phalanx. Semin Arthritis Rheum. 2000;29:379–84.
40. Fleming TE, Brodell RT. Subungual abscess: a bacterial infection of the nail bed. J Am Acad Dermatol. 1997;37:486–7.
41. Vanhooteghem O, Richert B, Vindevoghel A, Vandenbossche L, Vandeveire A, de la Brassinne M. Subungual abscess: a new ungual side-effect related to docetaxel therapy. Br J Dermatol. 2000; 143:462–4.
42. Vidal S, Barcala L, Barberán J, Heras JA, Tovar JA, Baran R. A suppurating fistula from a cement foreign body presenting as a tumour of the nail. Acta Derm Venereol. 2000;80:313–4.
43. Freiman A, Bouganim N, O'Brien EA. Case reports: mitozantrone-induced onycholysis associated with subungual abscesses, paronychia, and pyogenic granuloma. J Drugs Dermatol. 2005;4:490–2.
44. Newmeyer WL, Kilgore Jr ES. Common injuries of the fingernail and nail bed. Am Fam Physician. 1977;16:93–5.
45. Salazard B, Launay F, Desouches C, Samson P, Jouve JL, Magalon G. Fingertip injuries in children: 81 cases with at least one year follow-up. Rev Chir Orthop Reparatrice Appar Mot. 2004;90: 621–7. French.
46. Hart RG, Kleinert HE. Fingertip and nail bed injuries. Emerg Med Clin North Am. 1993;11:755–65.
47. Wu CY, Chen GS, Lin HL. Median canaliform dystrophy of Heller with associated swan neck deformity. J Eur Acad Dermatol Venereol. 2009;23:1102–3.
48. Sweeney SA, Cohen PR, Schulze KE, Nelson BR. Familial median canaliform nail dystrophy. Cutis. 2005;75:161–5.

49. Dharmagunawardena B, Charles-Holmes R. Median canaliform dystrophy following isotretinoin therapy. Br J Dermatol. 1997;137: 658–9.
50. Cruz MJ, Baudrier T, Cunha AP, Ferreira O, Azevedo F. Severe onychodystrophy caused by allergic contact dermatitis to acrylates in artificial nails. Cutan Ocul Toxicol. 2011;30:323–4.
51. Hinkelbein J, Koehler H, Genzwuerker HV, Fiedler F. Artificial acrylic finger nails may alter pulse oximetry measurement. Resuscitation. 2007;74:75–82.
52. Peters SM. The effect of acrylic nails on the measurement of oxygen saturation as determined by pulse oximetry. AANA J. 1997;65: 361–3.
53. Torres MC, Linares T, Hernandez MD. Acrylates induced rhinitis and contact dermatitis. Contact Dermatitis. 2005;53:114.
54. Richert B, Lateur N, Theunis A, Andre J. New tools in nail disorders. Semin Cutan Med Surg. 2009;28:44–8.
55. Wortsman X, Wortsman J, Soto R, Saavedra T, Honeyman J, Sazunic I, et al. Benign tumors and pseudotumors of the nail: a novel application of sonography. J Ultrasound Med. 2010;29:803–16.
56. Paliogiannis P, Trignano E, Trignano M. Surgical management of the glomus tumors of the fingers: a single center experience. Ann Ital Chir. 2011;82:465–8.
57. Wortsman X, Jemec GB. Role of high-variable frequency ultrasound in preoperative diagnosis of glomus tumors: a pilot study. Am J Clin Dermatol. 2009;10:23–7.
58. Chen SH, Chen YL, Cheng MH, Yeow KM, Chen HC, Wei FC. The use of ultrasonography in preoperative localization of digital glomus tumors. Plast Reconstr Surg. 2003;112:115–9.
59. Matsunaga A, Ochiai T, Abe I, et al. Subungual glomus tumour: evaluation of ultrasound imaging in preoperative assessment. Eur J Dermatol. 2007;17:67–9.
60. MacKee P, Calonje E, Granter S. Tumors of perivascular cells. In: MacKee P, Calonje E, Granter S, editors. Pathology of the skin with clinical correlation. 3rd ed. Philadelphia: Elsevier/Mosby; 2005. p. 1848–51.
61. Baek HJ, Lee SJ, Cho KH, Choo HJ, Lee SM, Lee YH, et al. Subungual tumors: clinicopathologic correlation with US and MR imaging findings. Radiographics. 2010;30:1621–36.
62. Baran R, Haneke E, Drape JL, Zook EG. Tumors of the nail and adjacent tissues. In: Baran, Dawber RPR, de Berker D, Haneke E, Tosti A, editors. Diseases of the nails and their management. 3rd ed. Oxford: Blackwell and Science; 2001. p. 515–601.
63. Baran R, Richert B. Common nail tumors. Dermatol Clin. 2006;24:297–311.
64. Baran R, Klint A. Onychomatrixoma. Filamentous tufted tumor in the matrix of a funnel-shaped entity (report of three cases). Br J Dermatol. 1992;126:510–5.
65. Haneke E, Fränken J. Onychomatricoma. Dermatol Surg. 1995; 21:984–7.
66. Perrin C, Goettmann S, Baran R. Onychomatricoma: clinical and histopathologic findings in 12 cases. J Am Acad Dermatol. 1998;39: 560–4.
67. Soto R, Wortsman X, Corredoira Y. Onychomatricoma: clinical and sonographic findings. Arch Dermatol. 2009;145:1461–2.
68. Baran R, Perrin C. Subungual perineurioma: a peculiar location. Br J Dermatol. 2002;146:125–8.
69. Wortsman X, Merino D, Catalan V, Morales C, Baran R. Perineurioma of the nail on sonography. J Ultrasound Med. 2010;29: 1379–82.
70. Macaulay WL. Subungual keratoacanthoma. Arch Dermatol. 1976;112:1004–5.
71. Connolly M, Narayan S, Oxley J, de Berker DA. Immunohistochemical staining for the differentiation of subungual keratoacanthoma from subungual squamous cell carcinoma. Clin Exp Dermatol. 2008;33: 625–8.
72. Choi JH, Shin DH, Shin DS, Cho KH. Subungual keratoacanthoma: ultrasound and magnetic resonance imaging findings. Skeletal Radiol. 2007;36:769–72.
73. Wortsman X, Sazunic I, Jemec GB. Sonography of plantar warts: role in diagnosis and treatment. J Ultrasound Med. 2009;28: 787–93.
74. Wortsman X, Wortsman J. Skin ultrasound, chapter 9. In: Dogra V, Gaitini D, editors. Musculoskeletal ultrasound with CT and MRI correlation. 1st ed. New York: Thieme; 2010. p. 147–70.
75. García Carmona FJ, Pascual Huerta J, Fernández Morato D. A proposed subungual exostosis clinical classification and treatment plan. J Am Podiatr Med Assoc. 2009;99:519–24.
76. Piraccini BM, Bellavista S, Misciali C, Tosti A, de Berker D, Richert B. Periungual and subungual pyogenic granuloma. Br J Dermatol. 2010;163:941–53.
77. Armstrong K, Weinstein M. Pyogenic granulomas during isotretinoin therapy. J Dermatol Case Rep. 2011;26(5):5–7.
78. Paul LJ, Cohen PR. Paclitaxel-associated subungual pyogenic granuloma: report in a patient with breast cancer receiving paclitaxel and review of drug-induced pyogenic granulomas adjacent to and beneath the nail. J Drugs Dermatol. 2012;11:262–8.
79. Kint A, Baran R. Histopathologic study of koenen tumors. Are they different from acquired digital fibrokeratoma. J Am Acad Dermatol. 1988;18(2 Pt 1):369–72.
80. de Berker D, Lawrence C. Ganglion of the distal interphalangeal joint (myxoid cyst): therapy by identification and repair of the leak of joint fluid. Arch Dermatol. 2001;137:607–10.
81. Miranda BH, Haughton DN, Fahmy FS. Subungual melanoma: an important tip. J Plast Reconstr Aesthet Surg. 2012;65:1422.
82. Yun SJ, Kim SJ. Images in clinical medicine. Hutchinson's nail sign. N Engl J Med. 2011;5(364):e38.
83. De Giorgi V, Saggini A, Grazzini M, Gori A, Rossari S, Scarfì F, et al. Specific challenges in the management of subungual melanoma. Expert Rev Anticancer Ther. 2011;11:749–61.
84. Wortsman X, Wortsman J. Clinical usefulness of variable-frequency ultrasound in localized lesions of the skin. J Am Acad Dermatol. 2010;62:247–56.
85. Nasca MR, Innicenzi D, Micalli G. Subungual squamous cell carcinoma of the toe: report on three cases. Dermatol Surg. 2004;30: 345–8.
86. Choughri H, Villani F, Sawaya E, Pelissier P. Atypical squamous cell carcinoma of the nail bed with Phalangeal involvement. J Plast Surg Hand Surg. 2011;45:173–6.

Sonography of the Scalp and Hair

19

Ximena Wortsman and Jacobo Wortsman

Contents

19.1 Introduction

Scalp hair is traditionally considered a conveyor of self image, identity, ethnicity, and health [1, 2]. Understandably, pathologies affecting the scalp, and hence scalp hair, frequently result in serious impacts on the quality of life. Improvement in scalp appearance and hair density are the main goals of cosmetic products and plastic surgery hair restoration procedures. Physiological studies have shown that adult body hair is not homogeneous, but rather it is subject to remarkable interregional differences. For example, eyelashes are structurally similar to scalp hair, but differ notably in the distribution of the mitotically active K-19 positive stem cells reservoirs that are distributed along the outer root sheath (ORS) of eyelash follicles, but are separated into two ORS reservoirs in the upper and lower third of scalp hair. Also, the human gene dopachrome tautomerase, involved in melanin synthesis, is expressed only in eyelash melanocytes, being strikingly absent in scalp hair melanocytes. Finally, the hair cycle is shorter in eyelashes than scalp hair [3].

In this chapter we will discuss the potential of ultrasound in the evaluation of diseases of the scalp and the corresponding structural changes in scalp hair.

19.2 Technical Considerations

The sonographer should face the lesion site(s) directly; a copious amount of gel is applied over the scalp and the hair tracts are displaced to the borders of the lesion site; testing (grey scale and color Doppler ultrasound with spectral curve analysis) routinely includes panoramic scalp readings obtained along at least the two main perpendicular axes (transverse and longitudinal), while hair follicles are followed along their main axis and also on two perpendicular views. Hair tracts can better be observed after trimming and being embedded in saline in a small plastic receptacle. The use of stand-off pads or contrast medium is usually not necessary in baseline studies [4].

X. Wortsman, MD (✉)
Department of Radiology and Dermatology,
Institute for Diagnostic Imaging
and Research of the Skin and Soft Tissues, Clinica Servet,
Faculty of Medicine, University of Chile, Almirante Pastene 150,
Providencia, Santiago, Chile
e-mail: xwo@tie.cl, xworts@yahoo.com, www.sonoskin.com

J. Wortsman, MD
Department of Medicine,
Southern Illinois University School of Medicine,
3128 Temple Drive, Springfield, IL 62704, USA

X. Wortsman, G.B.E. Jemec (eds.), *Dermatologic Ultrasound with Clinical and Histologic Correlations*,
DOI 10.1007/978-1-4614-7184-4_19,

19.3 Sonographic Anatomy of Scalp Skin

The skin of the scalp maintains the echostructure already described for other corporal segments [5], the frontal skin being thinner than the occipital skin [6]; therefore, the epidermis appears as a hyperechoic line; the dermis, as a hyperechoic band; and the subcutaneous tissue, as a hypoechoic band. A thin hypoechoic band seen under the subcutaneous tissue corresponds to the epicranius muscle or galeal layer (i.e. the epicranius muscle and its aponeurosis), and a deeper hyperechoic line marks the bony margin of the skull. The blood supply to the scalp comes from a centripetal network, with larger trunks running subcutaneously in the periphery and reaching the midline through branches of the external and internal carotid arteries [6].

The longitudinal structure of the hair follicle includes the dermal follicle bulb most proximally and the hair tract (shaft) more proximally, and their position within the scalp depends on rhythmic growth cycles (the "hair cycle clock") [7], for example, the telogen or resting phase when the hair bulb is in a superficial subdermal location; the anagen or active growth phase with a deeply located hair bulb almost in the subcutaneous tissue; and the catagen or transition phase, between the telogen and anagen. The growth cycle independently affects each individual follicle and therefore, human hairs are not shed simultaneously as in the case of many animals. Normally, 90 % of scalp hairs are in the anagen phase, and the remaining 10 % are in the telogen and catagen phases [4, 8] (Figs. 19.1, 19.2, 19.3, 19.4, 19.5, 19.6, 19.7, and 19.8).

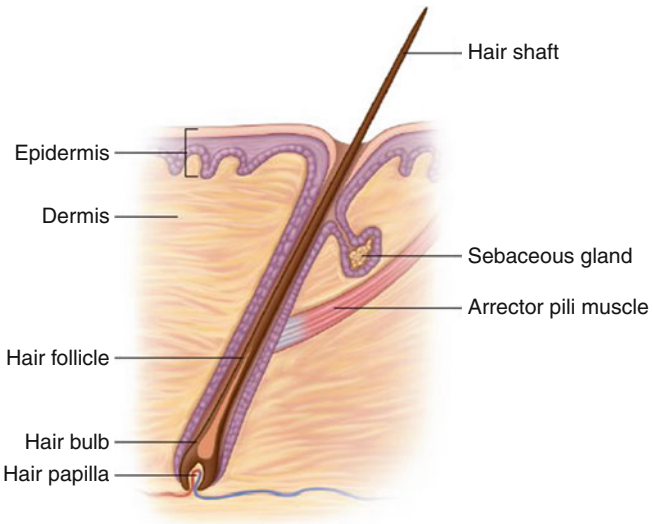

Fig. 19.1 Drawing of the anatomy of the hair follicle and tract

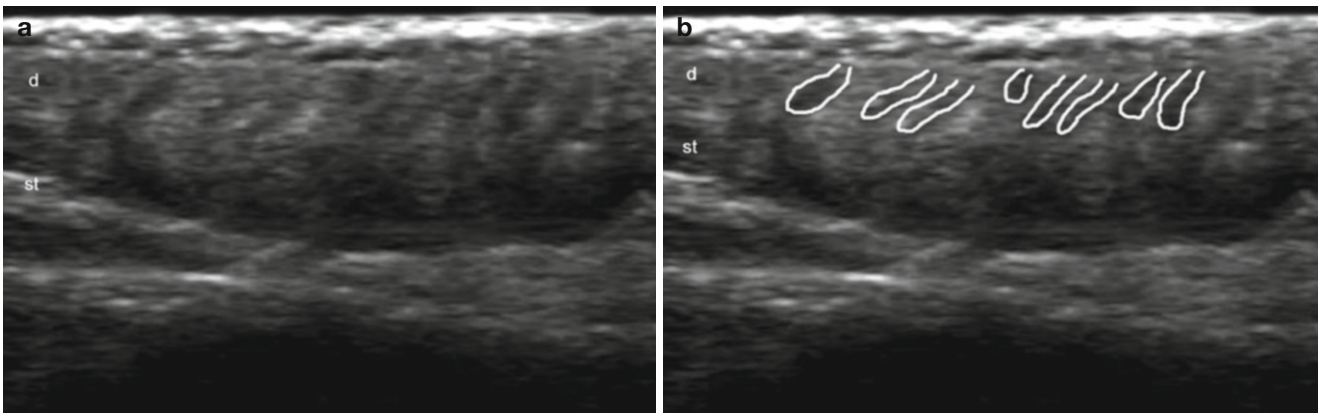

Fig. 19.2 (**a**–**d**) Sonoanatomy of the scalp and hair follicles (occipital region). (**a**, **b**) Grey scale ultrasound images (scalp); (**b**) with the hair follicles outlined. (**c**, **d**) 3D reconstructions of the hair follicles (axilla); (**d**) with the hair follicles outlined. *Abbreviations*: *d* dermis, *st* subcutaneous tissue

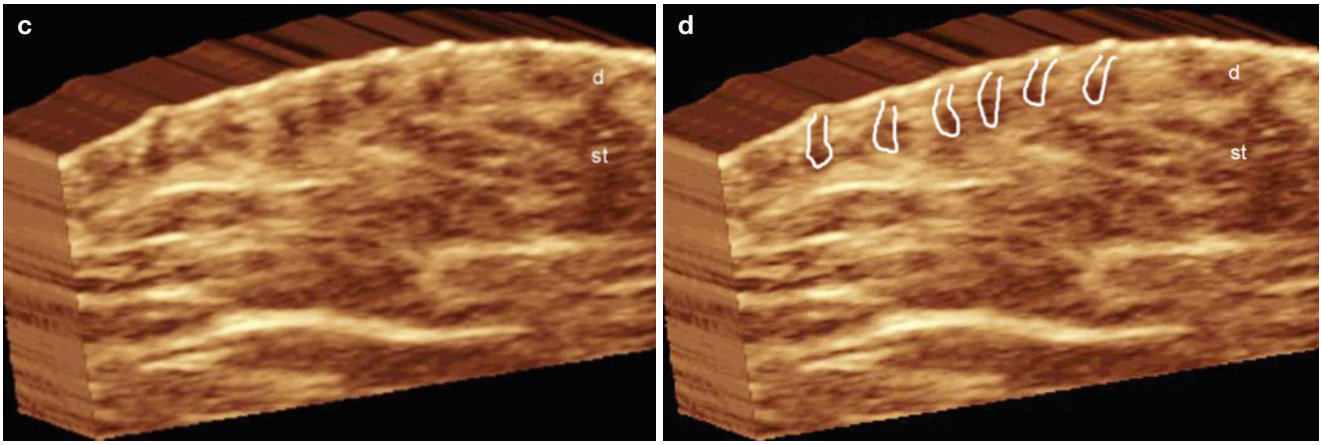

Fig. 19.2 (continued)

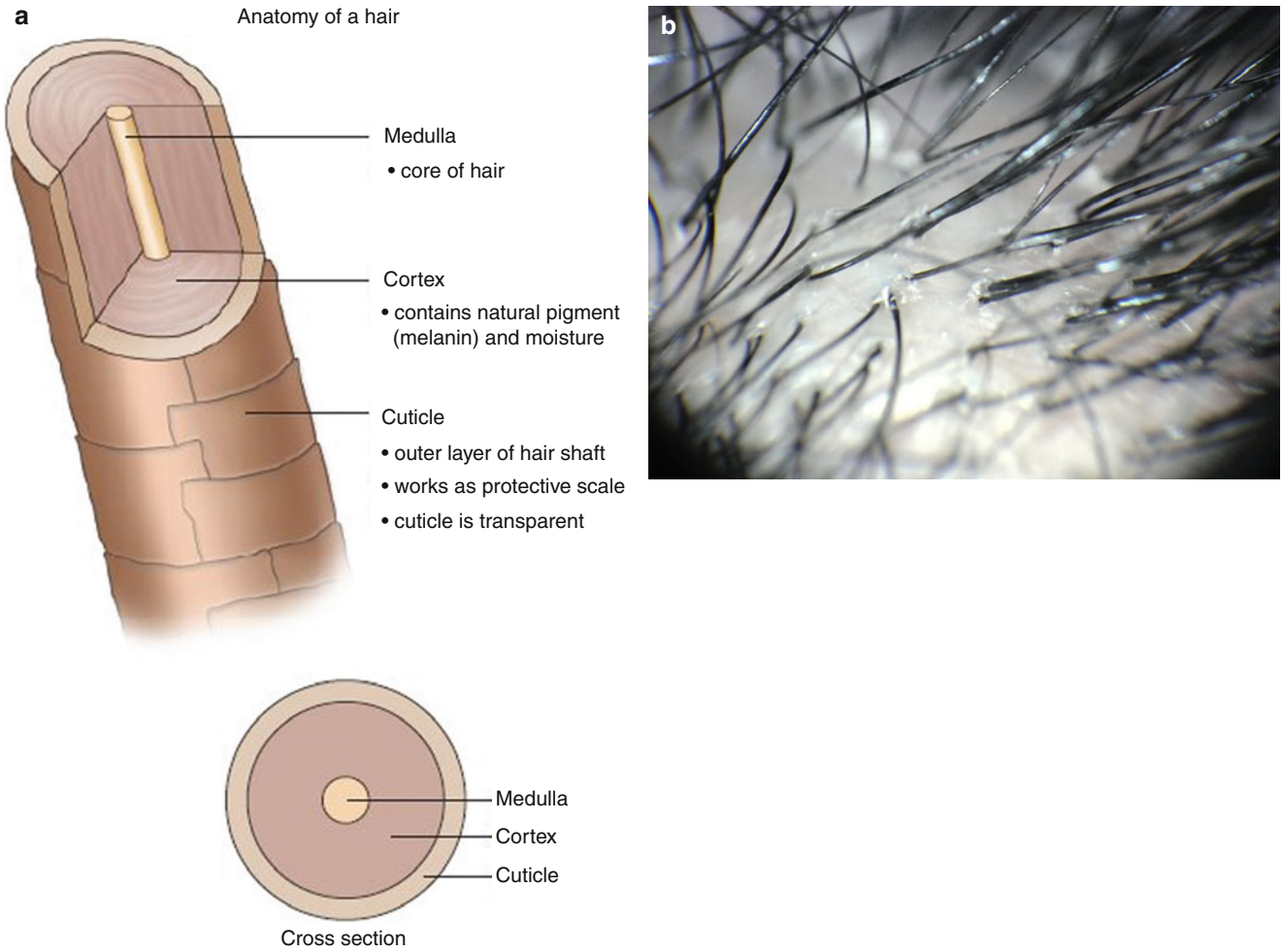

Fig. 19.3 (**a**–**e**) Hair tract. (**a**) Anatomical drawing of the parts of a hair tract. (**b**) Dermoscopy image of the hair tracts in the scalp. (**c**) Sonoanatomy of the hair tract (grey scale). (**d**) Sweep electron microscope image of a hair tract shows the cuticle layer. (**e**) Histology (HE ×25 zoom, courtesy of Dr. Laura Carreño): skin of the scalp shows mature hair follicles (*arrows*). The bulbs (base) of the hair follicles (*arrows*) anchor in the upper subcutaneous tissue

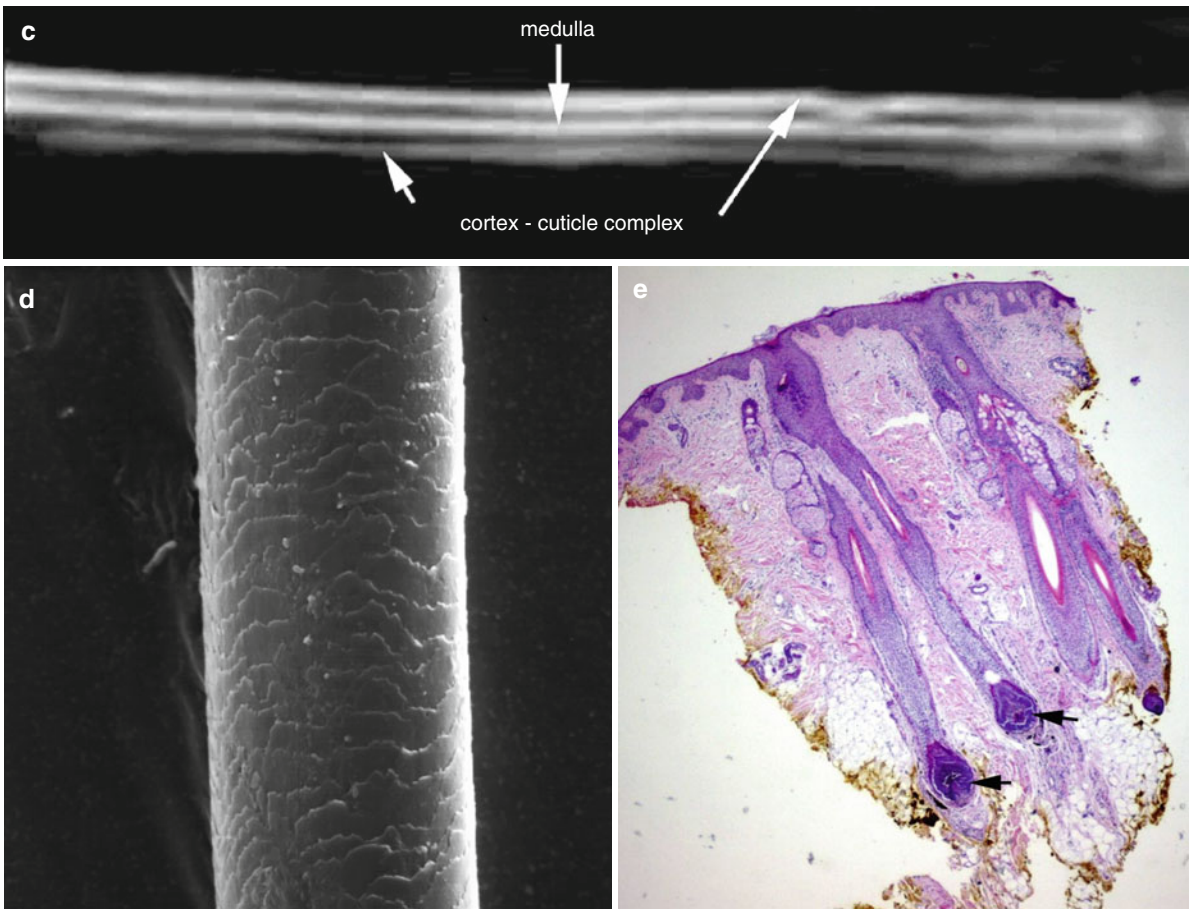

Fig. 19.3 (continued)

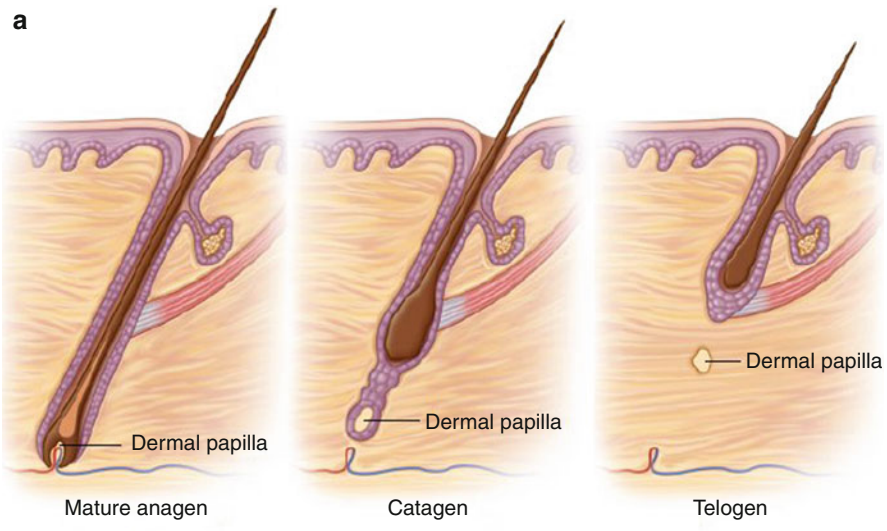

Fig. 19.4 (**a**, **b**) Hair follicle cycle. (**a**) Drawing. (**b**) Histology (HE ×25 zoom, courtesy of Dr. Laura Carreño): shows immature (*arrowheads*) and mature (*arrows*) hair follicles

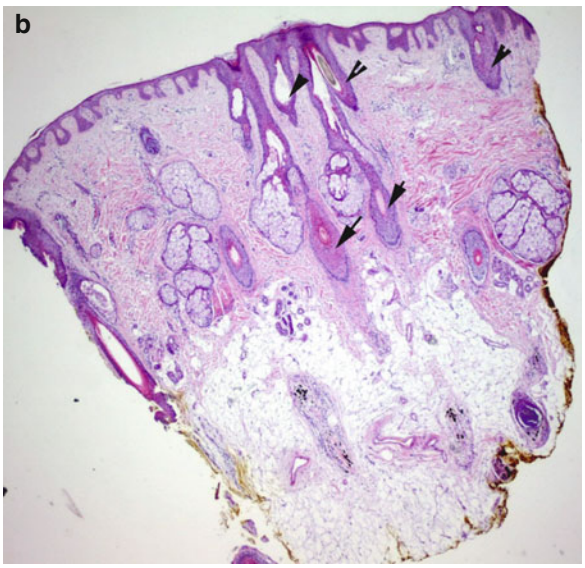

Fig. 19.4 (continued)

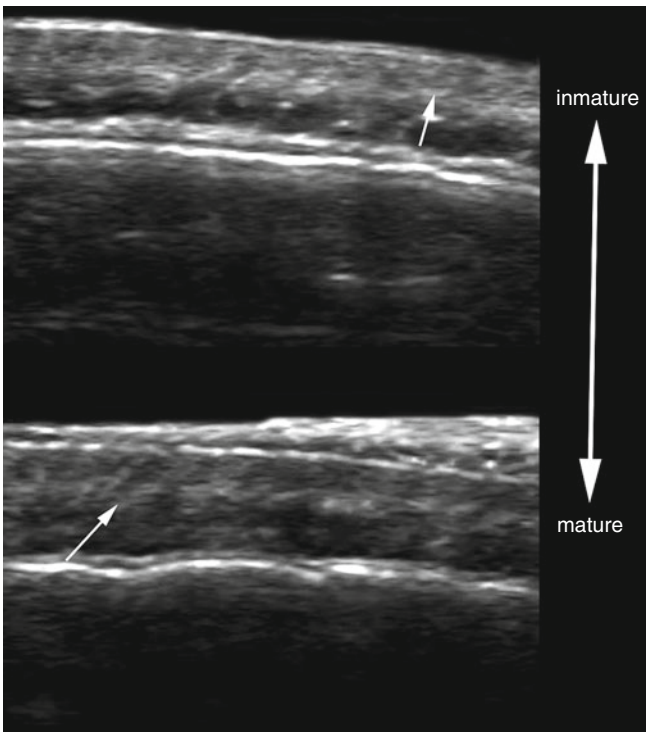

Fig. 19.5 Grey scale image showing sonographic appearance of the hair follicle cycle. The arrows show the location of the hair follicles in the dermis

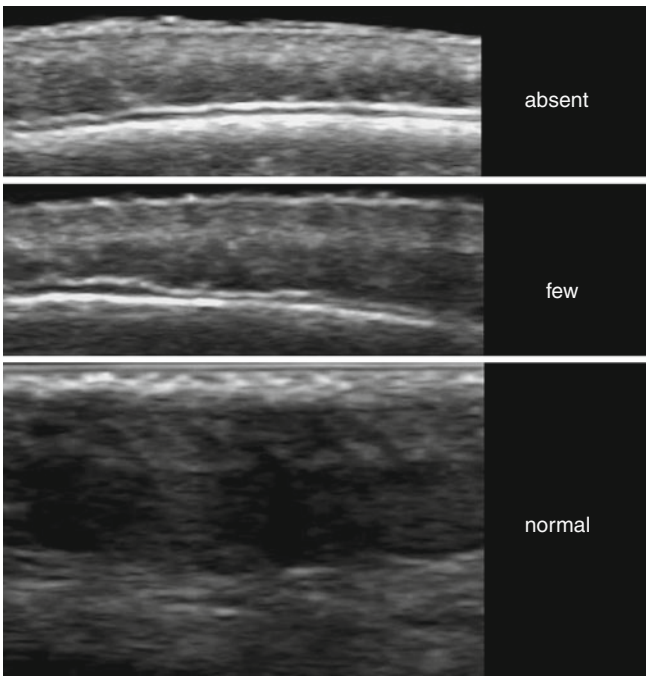

Fig. 19.6 Grey scale image showing sonographic grading of the density of the hair follicles in the scalp

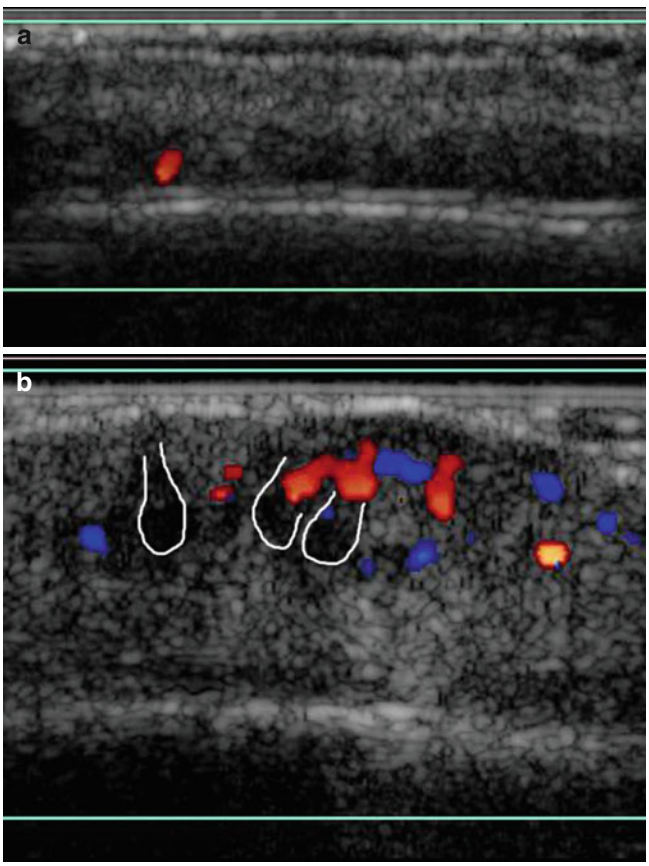

Fig. 19.7 (**a**, **b**) Color Doppler sonographic image showing grading of vascularity of the scalp. (**a**) Normal. (**b**) Increased (hair follicles outlined)

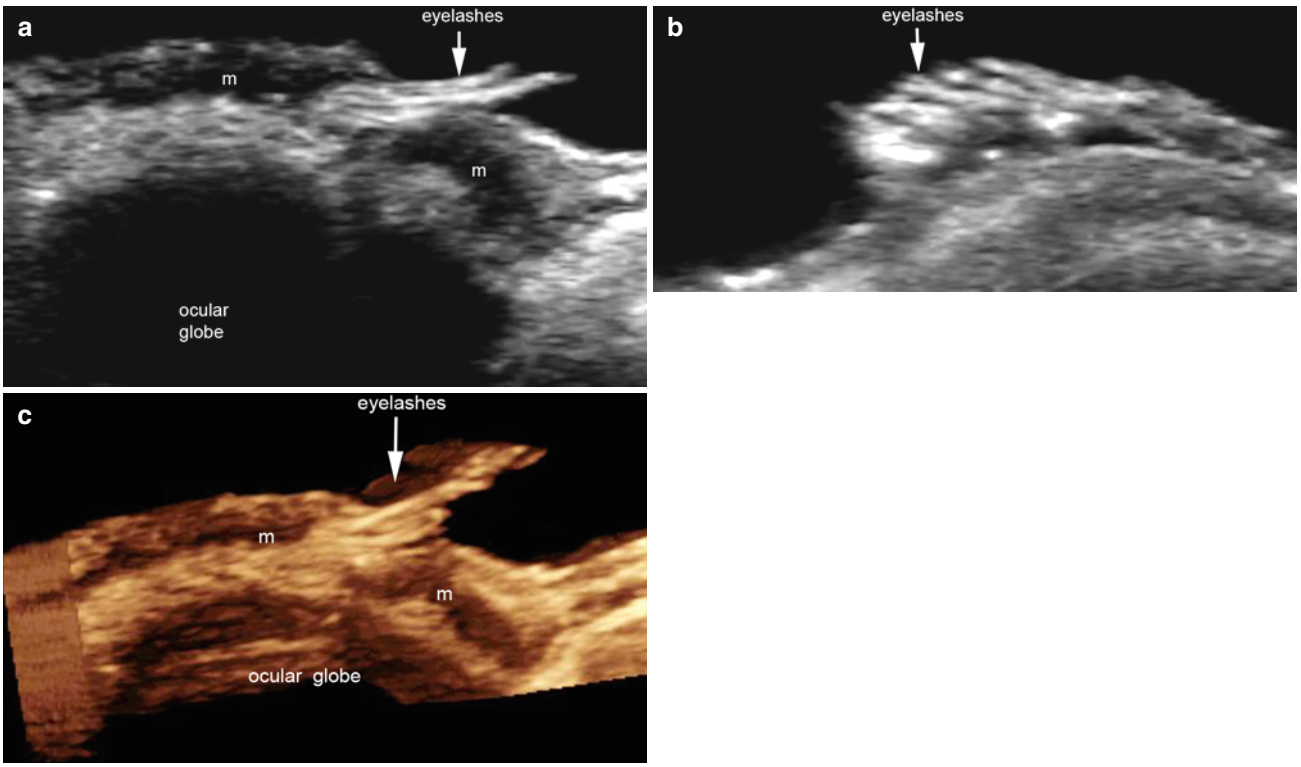

Fig. 19.8 (**a**–**c**) Eyelashes (*arrows*). (**a**, **b**) Grey scale ultrasound images (**b** longitudinal view; **c** transverse view). (**c**) 3D reconstruction (longitudinal view; 5–8 s sweep). *Abbreviations*: *m* orbicularis muscle of the eyelid

19.4 Sonographic Anatomy of the Hair Tract

Histologically, the hair tract (shaft) consists of an outer sheath, comprising the complex cuticle-cortex and an inner central medulla. In recent imaging studies using experimental magnetic resonance imaging machines, the same morphology has been observed with clear separation of the cortex and medulla [9]. Ultrasound provides additional structural details because scalp hair shafts from the scalp mainly present a trilaminar hyperechoic structure presumably reflecting the longitudinal arrangement of the keratin chains. This structure resembles the sonographic bilaminar appearance of another keratinized organ, the ungual plaque of the nail [10]. The trilaminar organization of scalp hair tracts is nevertheless unique because the eyelashes are uniformly monolaminar. It is not clear if the eyelashes present this appearance because of the current limitations in the resolution of ultrasound machines or whether this represents a true morphology of the keratinous component [4] (Figs. 19.3 and 19.8).

19.5 Hair Follicle Quantification

Ultrasound provides a qualitative estimation of the density of scalp hair follicles from their total absence, in alopecia or post-chemotherapy status, to a reduction in follicle number; thus, ultrasound detects not only abnormalities in the actual appearance of the hair follicles, but also alterations of the local hair growth cycle, properties clinically helpful in comprehensive monitoring of treatments directed at correcting baldness [4] (Fig. 19.6).

19.6 Hair Follicle Inflammation

Hair follicle inflammation, also called folliculitis, implies an active inflammatory process within the hair follicle itself or in the surrounding tissues that produces changes in hair follicle diameter and/or echogenicity. Thus, the follicle is both swollen and markedly hypoechoic in the presence of inflammation. Adding determination of the vascularity pattern by color Doppler ultrasound can further show increased blood flow, another sign of inflammation [4] (Fig. 19.7)

19.7 Disorders of Scalp Skin and Scalp Hair

19.7.1 Benign Conditions

19.7.1.1 Trichilemmal Cyst

Trichilemmal cysts (TCs) are cystic structures originating from the trichilemma or exposed outer root of the hair sheath. TCs are thought to be derived from the isthmus of the hair follicle (the zone between hair bulb and hair shaft), and comprise approximately 20 % of epithelial cysts (the remaining 80 % is represented by epidermis-derived, epidermal cysts), with the most common locations being the scalp (78 %) and torso (13 %) [11]. TCs present clinically as smooth, firm nodules often accompanied by hair loss. Histologically, TC is typically seen as a sharply circumscribed cystic wall with abrupt transition between the epidermal stratum spinosum and hair keratin, without the intervening granular layer. The cysts often contain keratinous debris and cholesterol crystals from keratin liquefaction, and occasional focal calcifications and trapped hair tracts [12, 13]. Sonography of TCs usually presents as anechoic or hypoechoic round or oval-shaped structures in the dermis and subcutaneous tissue, usually without connecting tracts to the epidermal layer. Detectable echoes within the cyst generally correspond to keratinous and dense cholesterol elements [4]. TCs can occasionally present as target nodules with a hypoechoic rim and heterogeneous center that contains hyperechoic lines that correspond to hair tracts fragments. In contrast to the calcium deposits that are seen in the "target nodule" sonographic appearance of pilomatrixomas, the hyperechoic hair fragments tend to not present posterior acoustic shadowing artifact (Figs. 19.9, 19.10, 19.11, and 19.12).

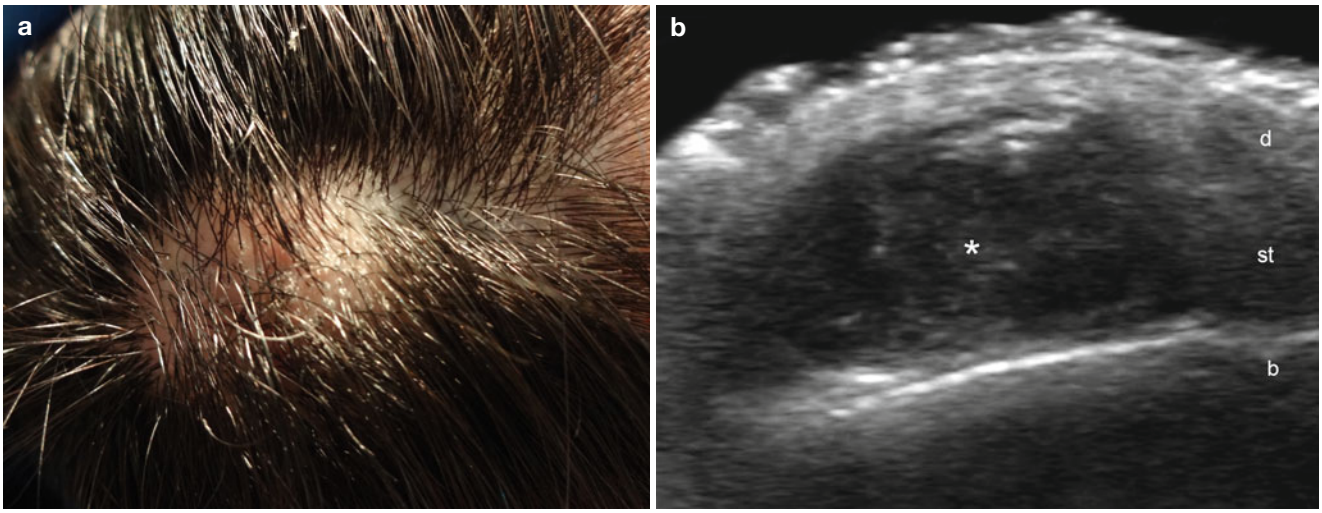

Fig. 19.9 (**a**–**e**) Trichilemmal cyst. (**a**) Clinical photograph shows focal alopecia and swelling. (**b**) Grey scale ultrasound image (longitudinal view; frontal scalp) demonstrates a well-defined, oval-shaped, anechoic structure (*) that presents echoes (debris) and is located in the dermis and subcutaneous tissue. (**c**) Color Doppler ultrasound image (longitudinal view; frontal scalp) demonstrates a lack of vascularity within the cyst. (**d**) 3D reconstruction of the cyst (*). (**e**) Histology (HE ×100 zoom, courtesy of Dr. Claudia Morales) shows compact keratin in the lumen of the cyst. The cyst is lined by epithelium without a granular layer. *Abbreviations*: *d* dermis, *st* subcutaneous tissue, *b* bony margin of the skull, *k* keratin, *e* epithelium

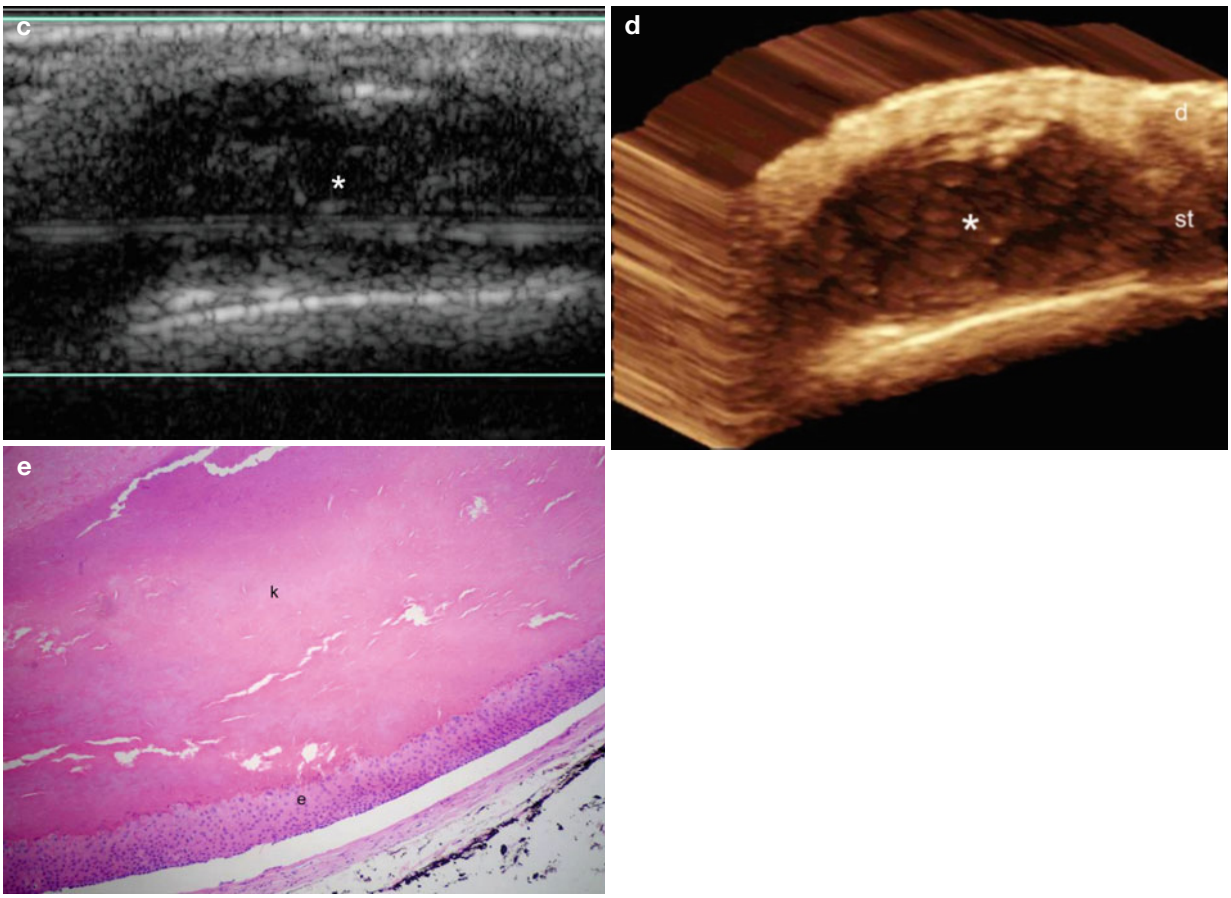

Fig. 19.9 (continued)

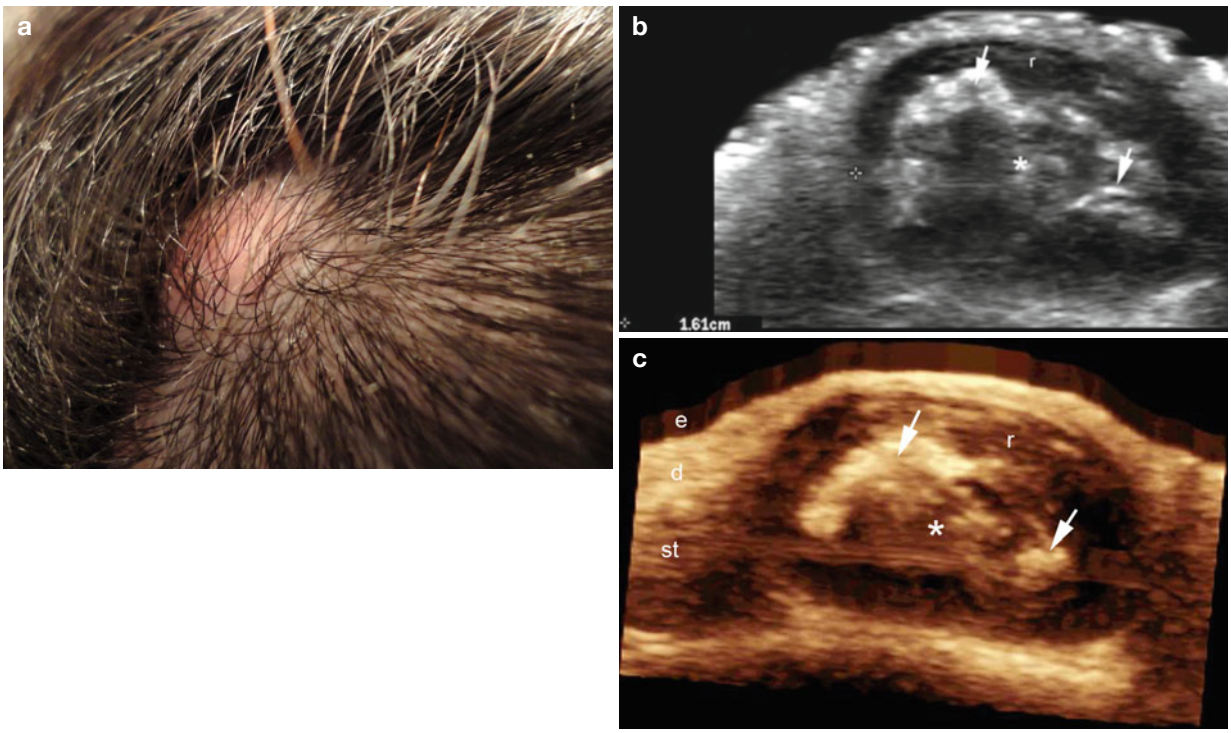

Fig. 19.10 (**a**–**c**) Trichilemmal cyst. (**a**) Clinical image shows swelling and focal alopecia. (**b**, **c**) Grey scale ultrasound images (**b** 2D and **c** 3D; transverse view, left parietal region) demonstrate a 1.61 cm well-defined, oval-shaped nodule that presents a hypoechoic rim (*r*) and heterogeneous center (*). Notice the hyperechoic lines in the center that correspond to trapped hair tracts fragments (*arrows*). *Abbreviations*: *e* epidermis, *d* dermis, *st* subcutaneous tissue

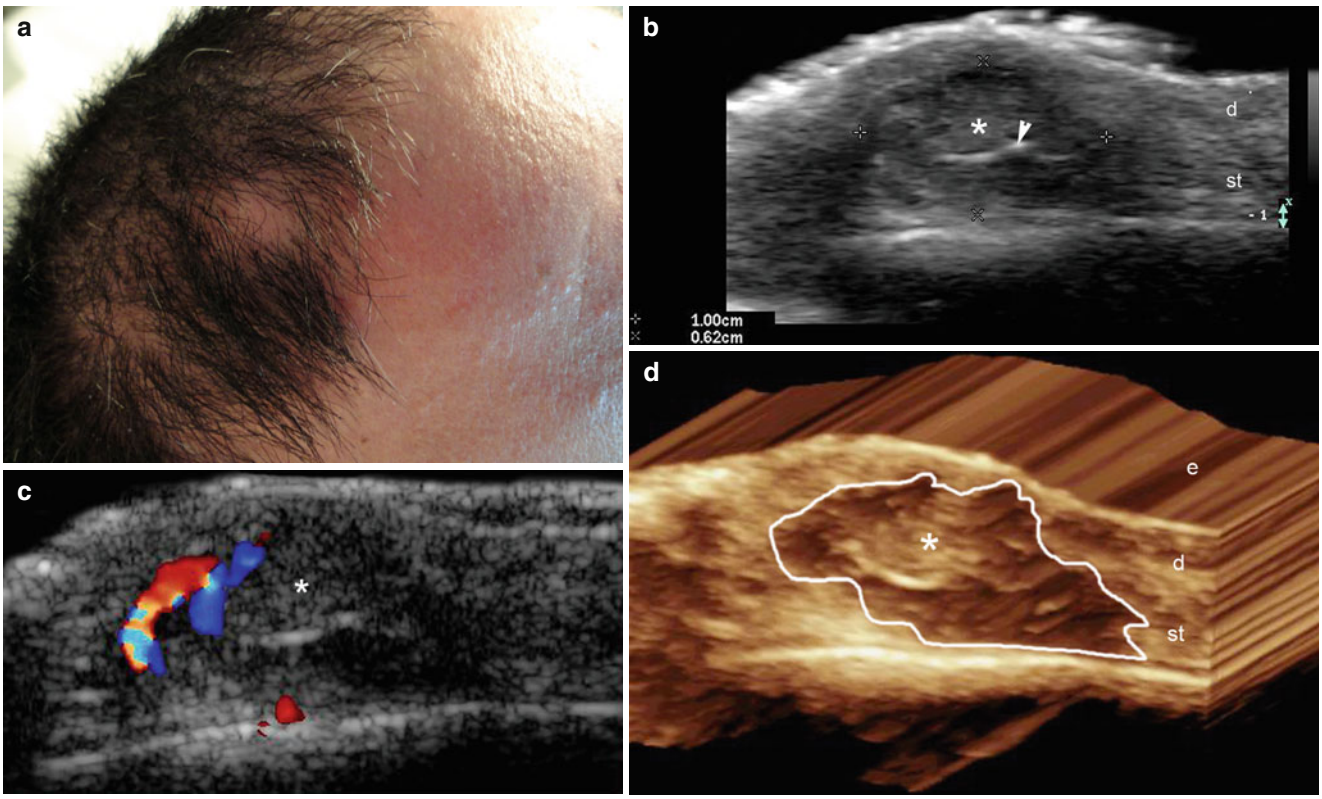

Fig. 19.11 (**a**–**d**) Trichilemmal cyst. (**a**) Clinical photograph demonstrates focal alopecia. (**b**) Grey scale ultrasound image (longitudinal view; right frontal region) shows a 1.0 cm (long)×0.62 cm (depth) well-defined oval-shaped hypoechoic structure (*, between markers) located in the dermis and subcutaneous tissue. Notice the fragment of hair tract (*arrowhead*) within the cyst. (**c**) Color Doppler ultrasound image (longitudinal view) demonstrates a mildly increased vascularity in the periphery of the cyst . (**d**) 3D reconstruction (longitudinal view, 5–8 s sweep) of the cyst (*, outlined). *Abbreviations*: *e* epidermis, *d* dermis; *st* subcutaneous tissue

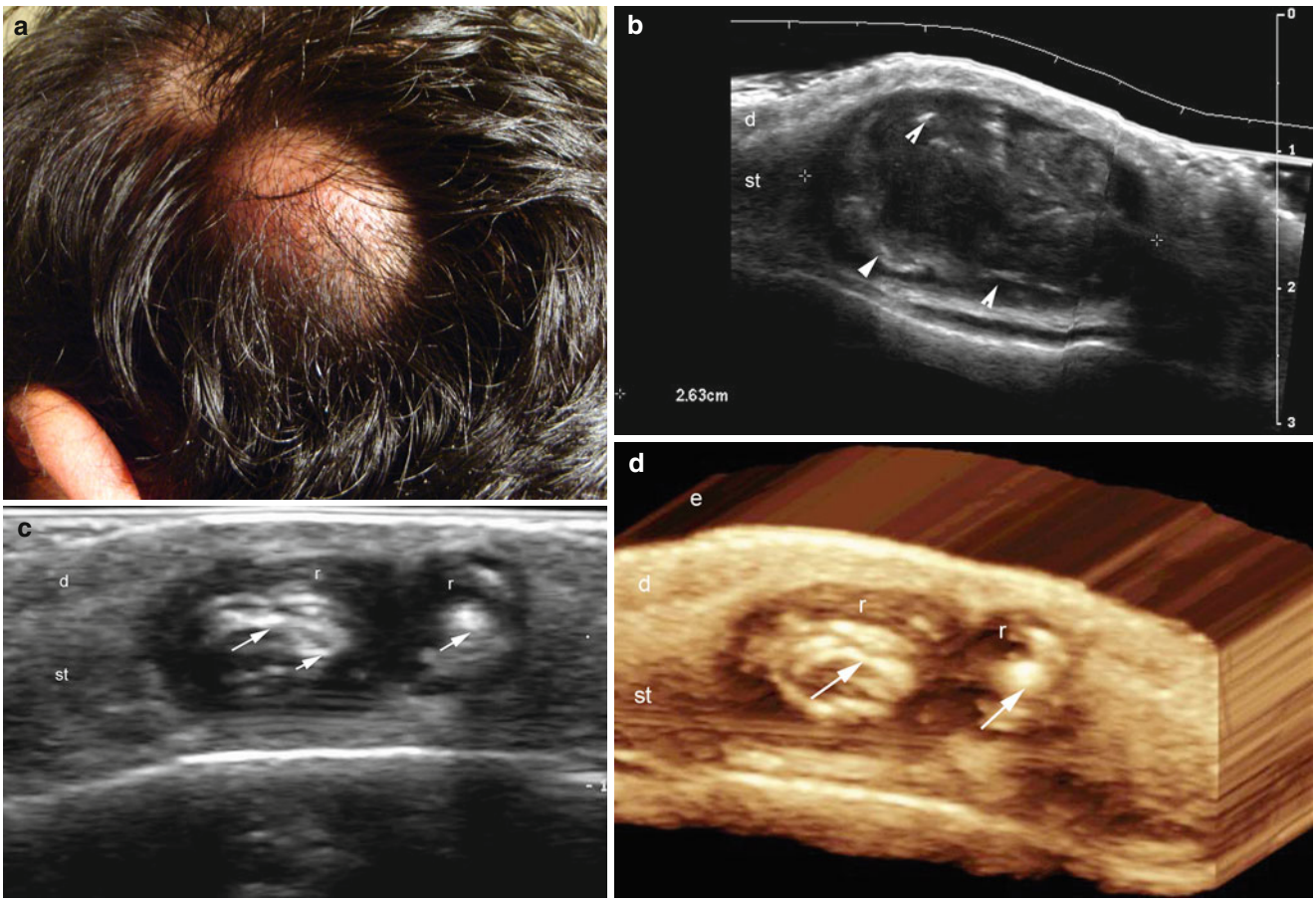

Fig. 19.12 (**a**–**d**) Multiple trichilemmal cysts. (**a**) Clinical photograph demonstrates a lump with focal alopecia. (**b**) Grey scale ultrasound image (longitudinal view) shows a 2.63 cm (long) well-defined oval-shaped hypoechoic and heterogeneous structure (between markers) in the subcutaneous tissue. Notice the hyperechoic lines that correspond to hair tracts fragments (*arrowheads*). (**c**, **d**) Grey scale ultrasound images (**b** 2D longitudinal view and **c** 3D reconstruction in same patient) show two additional well-defined oval-shaped structures that present hypoechoic rim (*r*) and heterogeneous center with hyperechoic lines that represent trapped hair tracts (*arrows*). *Abbreviations*: *e* epidermis, *d* dermis, *st* subcutaneous tissue

19.7.1.2 Pilomatrixoma

Pilomatrixoma, also known as pilomatricoma or calcifying epithelioma of Malherbe, is a benign tumor arising from the hair follicle matrix. Pilomatrixomas are most frequently found in children and young adults, especially in the head and neck, with 9 % of them located in the scalp [14]. The tumor often goes unrecognized until the time of surgery because of the non-specific clinical history of a painless, irregular, slowly enlarging hard nodule [15, 16]. Clinically, pilomatrixomas may also cause focal baldness in the scalp. Sonography of typical pilomatrixomas commonly shows a target-like lesion with a hyperechoic center and hypoechoic rim; hyperechoic dots are commonly seen within the nodule and correspond to calcium deposits. According to the size of the calcium deposits, a posterior acoustic shadowing can be detected [4, 17, 18] (Fig.19.13).

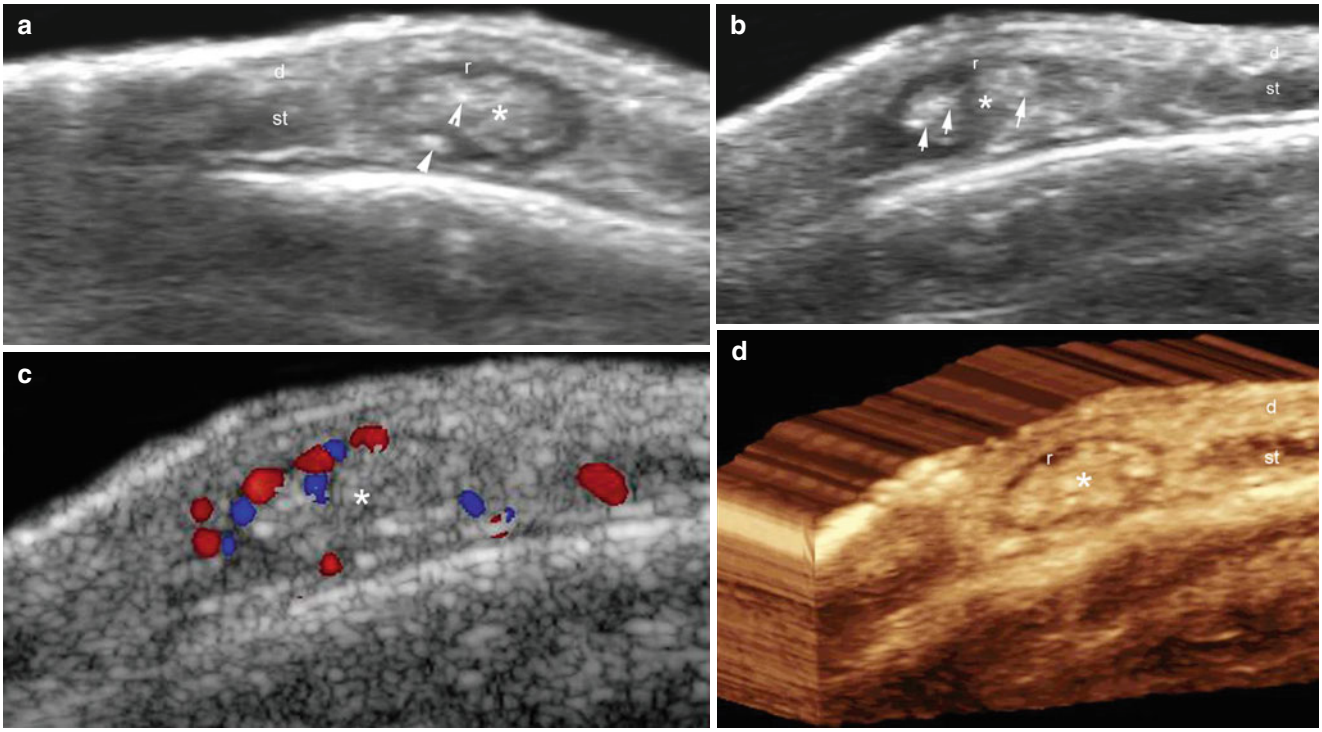

Fig. 19.13 (**a**–**d**) Pilomatrixoma. (**a**, **b**) Grey scale ultrasound images (**a** transverse view and **b** longitudinal view) demonstrate a target-like nodule that presents a hypoechoic rim (r) and a hyperechoic center (*) with hyperechoic spots (*arrows*) that correspond to calcium deposits. (**c**) Color Doppler ultrasound image (longitudinal view) shows increased vascularity in the periphery of the nodule. (**d**). 3D reconstruction (longitudinal view) highlights the lesion (*). *Abbreviations*: *d* dermis, *st* subcutaneous tissue, *r* rim

19.7.1.3 Hemangioma

Hemangiomas of infancy are the most common benign tumors of infancy, appearing shortly after birth in 5–10 % of infants. Clinically, many hemangiomas are discrete and well-circumscribed soft, reddish tumors of the head or neck; others are segmental and diffuse and often involve larger areas [19]. On sonography, hemangiomas present as ill-defined structures that can vary in their echogenicity according to the phase of activity. Thus, they show hypoechogenicity during the proliferative phase, and hyperechogenicity in the total regression phase. During the partial regression phase, hemangiomas can appear as heterogeneous structures (i.e., mixed hyper- and hypoechoic areas). Hemangiomas present prominent arterial and venous vessels or arteriovenous shunts [4, 20, 21] in the proliferative phase and turn hypovascular in the total regression phase. Deep vascular tumoral involvement extending to the epicranius muscle or bony margins of the skull can occasionally be detected [22, 23] (Figs. 19.14, 19.15, and 19.16).

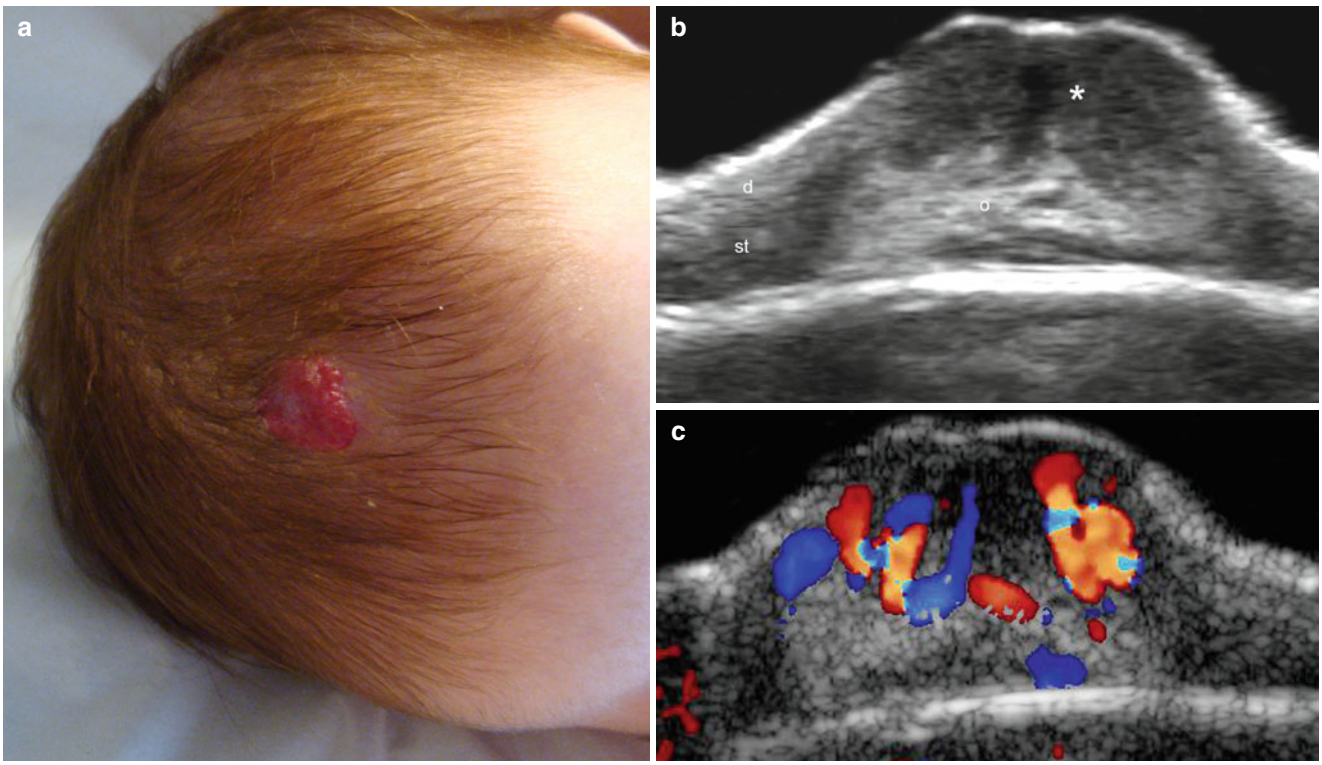

Fig. 19.14 (**a**–**c**) Hemangioma. (**a**) Clinical image shows a reddish swelling in the scalp. (**b**) Grey scale ultrasound image (transverse view) demonstrates an ill-defined heterogeneous structure that presents an upper hyperechoic area (*, mostly proliferative zone) and a lower hyperechoic area (o, mostly regression zone). (**c**) Color Doppler ultrasound image (transverse view) shows increased vascularity mostly in the upper region of the lesion. *Abbreviations*: *d* dermis, *st* subcutaneous tissue

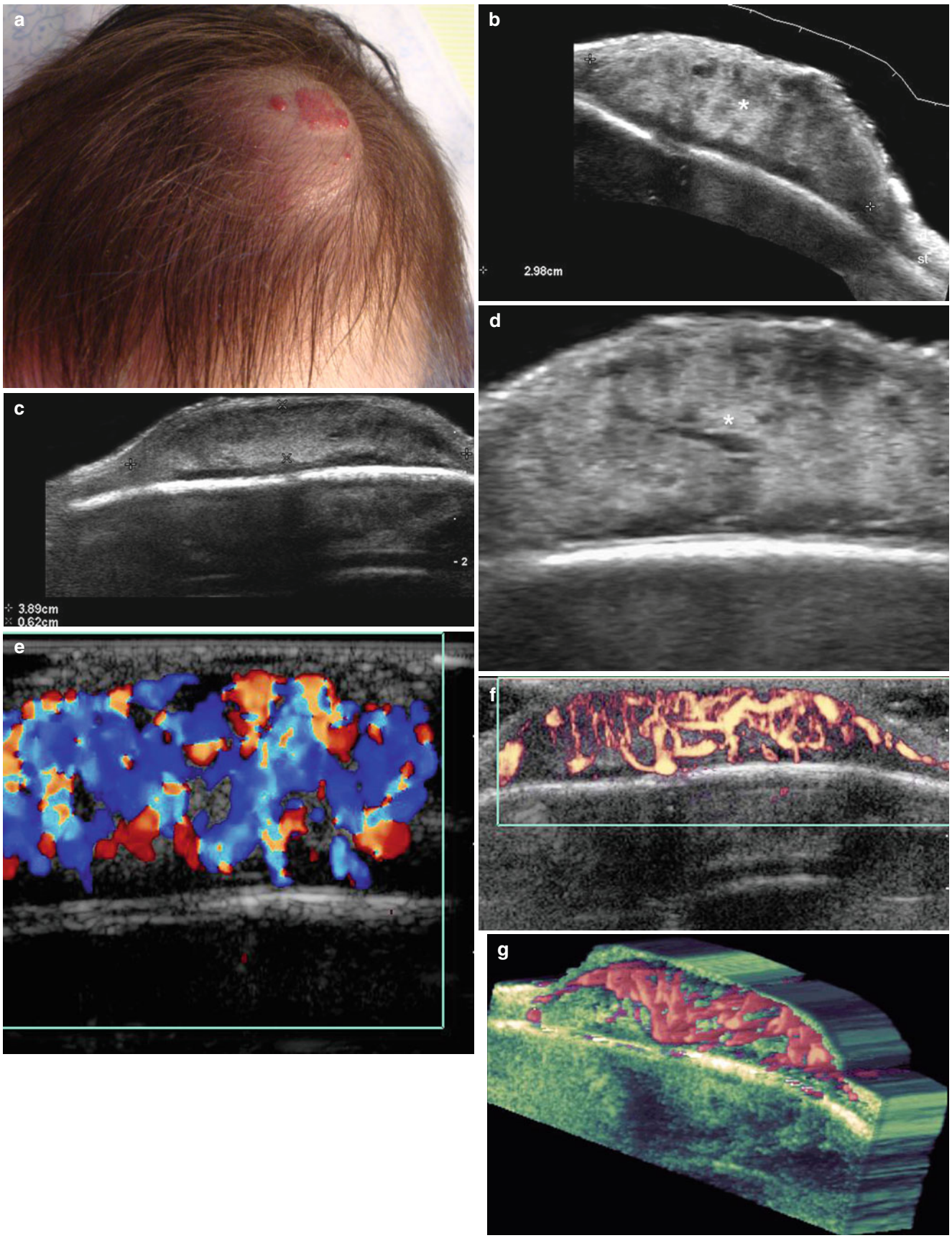

Fig. 19.15 (**a**–**g**) Hemangioma. (**a**) Clinical photograph shows a reddish lump. (**b**), (**c**, **d**) Grey scale ultrasound images (**b** longitudinal; **c** transverse and **d** zoomed transverse view) demonstrate a 3.98 cm (long) × 3.9 cm (transverse) × 0.62 (depth) ill-defined heterogeneous structure (*) mostly hyperechoic, located in the dermis and subcutaneous tissue. (**e**–**g**) Color and power Doppler ultrasound images (**e** color; **f** power; **g** 3D power angio reconstruction) show increased vascularity within the lesion

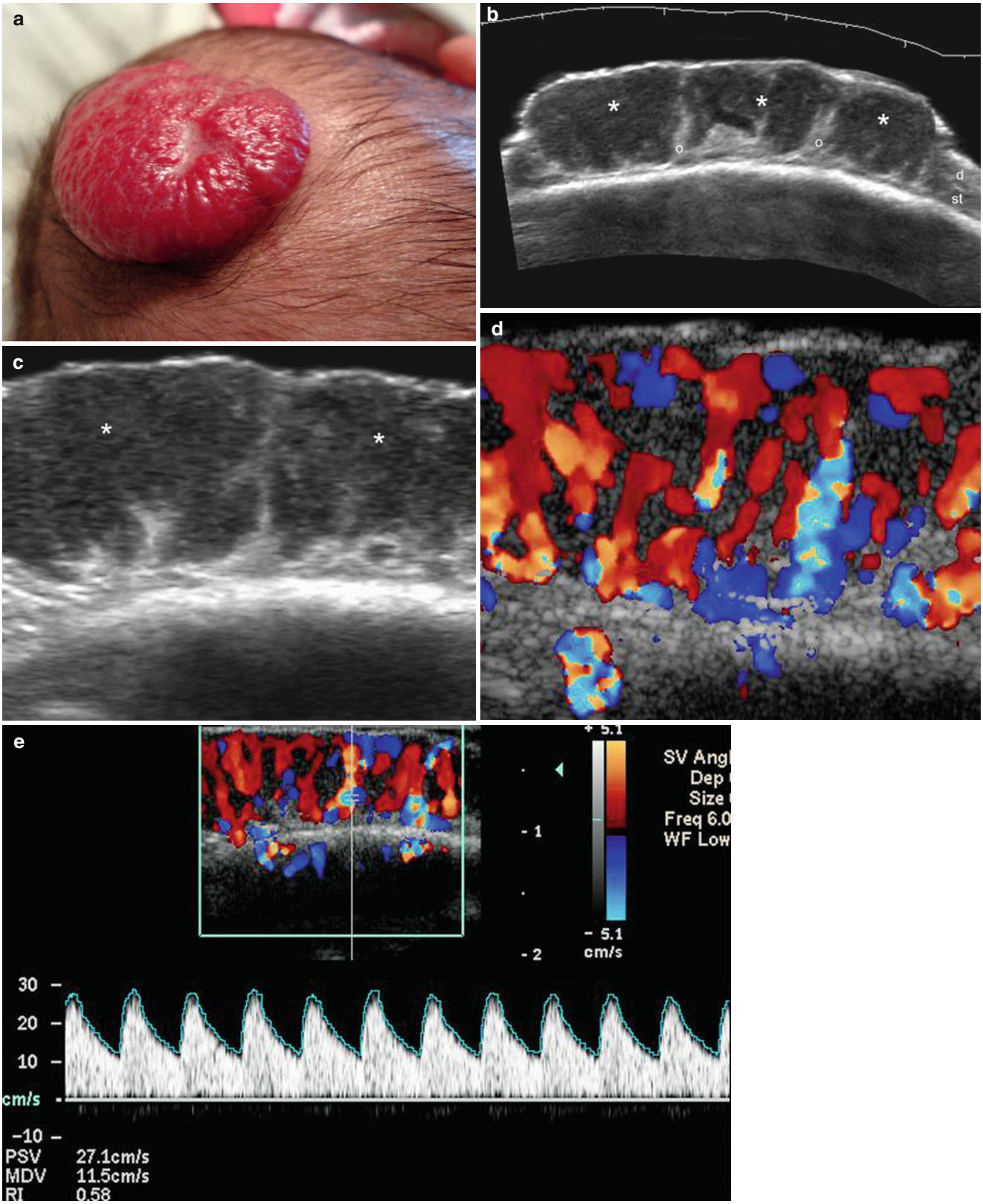

Fig. 19.16 (**a**–**g**) Hemangioma. (a) Clinical image shows a reddish lump in the left parietal region of the scalp. (**b**, **c**) Grey scale ultrasound images (**b**: extended field of transverse view; **c**: zoomed transverse view) demonstrate an ill-defined heterogeneous structure predominantly hypoechoic (*, mostly proliferative zone) and also presenting some hyperechoic deep areas (o, mostly regression zone). (**d**–**g**) Color Doppler ultrasound images (**d** zoomed image; **e** and **f** spectral curves; **g** 3D power angio reconstruction) show increased blood flow within the lesion. Notice that arterial (**e**) and venous (**f**) vessels are detected within the hemangioma. *Abbreviations*: *d* dermis, *st* subcutaneous tissue

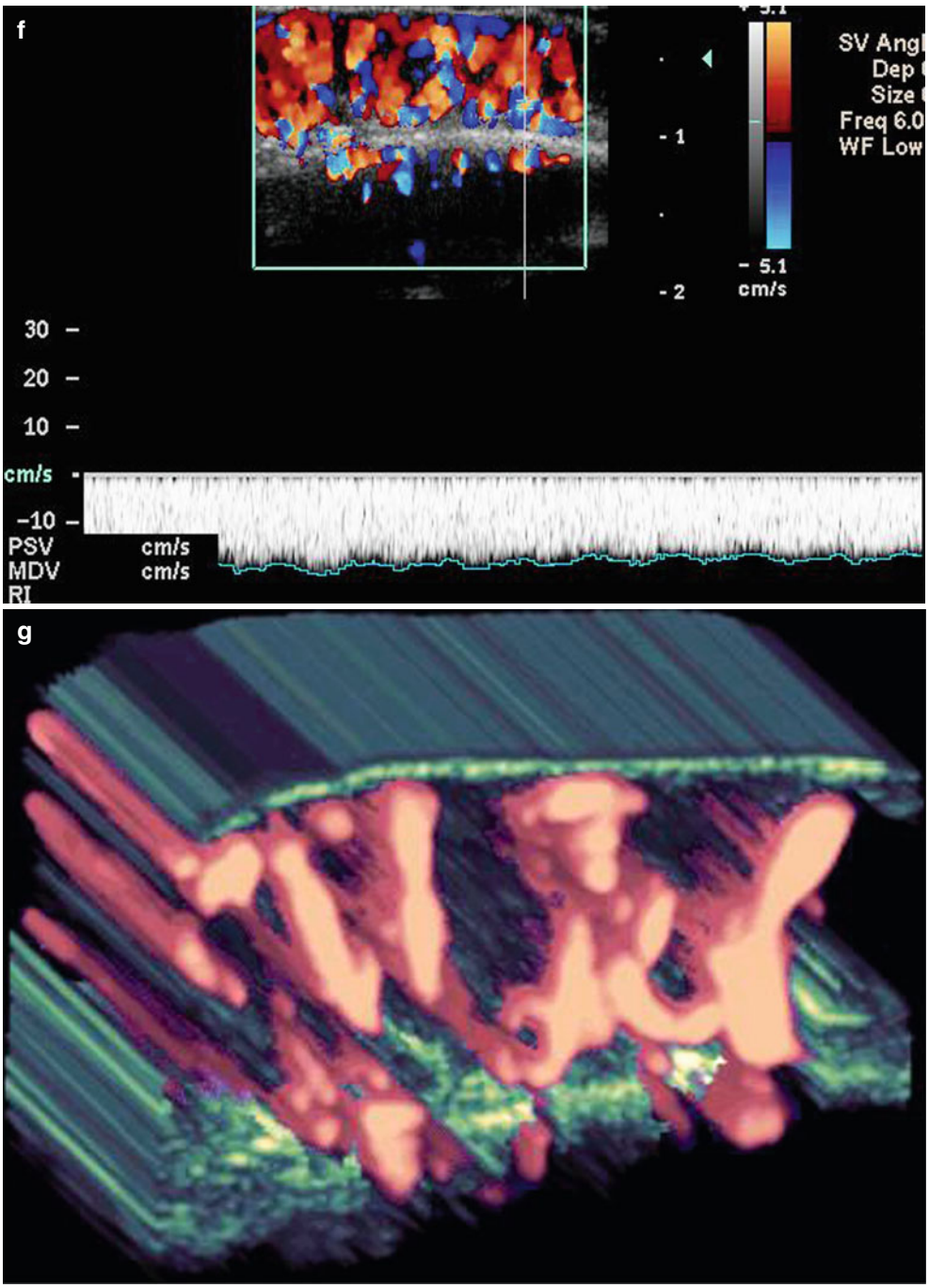

Fig. 19.16 (continued)

19.7.1.4 Scarring Alopecias

Scarring alopecias comprise a complex group of disorders with poorly defined origins that present with inflammation and scarring as common components [24, 25]. Sonography allows the characterizing of these entities on an anatomical basis and shows the different degrees of inflammation of the dermis and subcutaneous tissue. The latter findings appear on ultrasound as hypoechogenicity for the dermis, and hyperechogenicity for the subcutaneous tissue. Hypervascularity can be increased within the lesioned areas.

19.7.1.4.1 Acne Keloidalis Nuchae

Acne keloidalis nuchae (AKN) is a chronic scarring folliculitis seen mostly in young adult men who present with follicular papules and pustules coalescing occasionally into firm, shiny, smooth plaques and nodules on the nape of the neck. Acanthosis nigricans, a skin marker for the metabolic syndrome, obesity, curly hair, or wearing of a helmet has been associated with AKN. Additionally, AKN can present with some clinical similarities to acne inversa (hidradenitis suppurativa) [26]. Although AKN is infrequent, it has an important impact on the quality of life and may require aggressive treatment [26–29]. Sonography can show inflammation through all the cutaneous layers, hypoechoic connecting fistulous tracts, and enlargement of hair follicles [4] (Fig. 19.17).

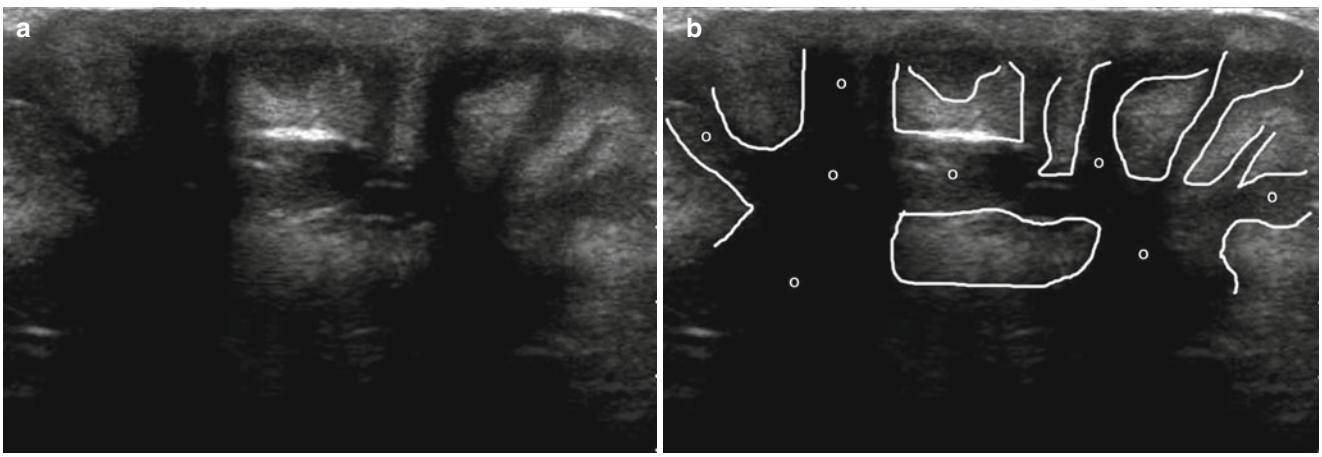

Fig. 19.17 (**a**, **b**) Acne keloidalis nuchae. (**a**, **b**) Grey scale ultrasound images (transverse view; **c** outlined) demonstrate multiple and connecting fistulous tracts (o) in the occipital region of the scalp

19.7.1.4.2 Perifolliculitis Capitis Abscedens et Suffodiens

Perifolliculitis capitis abscedens et suffodiens (PCAS) is a dissecting cellulitis or folliculitis of the scalp. PCAS is rare and presents as severe progressive inflammation with painful nodules and purulent drainage, with burrowing tracts connecting cutaneous fluid collections or abscesses and scarring as well as cicatricial alopecia [30, 31]. The etiology of PCAS is unknown but thought to follow episodes of follicular occlusion with reactive hyperkeratosis, secondary infection, and deep inflammation. PCAS may share its pathogenesis with acne conglobata and hidradenitis suppurativa, occurring as a triad [32]. Histologically, PCAS is a cicatricial neutrophilic alopecia with deep pustular inflammation at the reticular dermal or hypodermal levels. It starts with an episode of perifolliculitis that leaves deep abscesses and destroys the sebaceous glands that are then replaced by lymphoplasmocytic and giant cells granulomas [33]. Sonography of PCAS shows debris-filled fluid collections and/or abscesses with multiple connecting hypoechoic fistulous tracts that reach the hair bulb in the dermis and can cause follicular swelling. PCAS can affect large areas or the entire scalp, producing multiple areas of baldness [4] (Figs. 19.18 and 19.19).

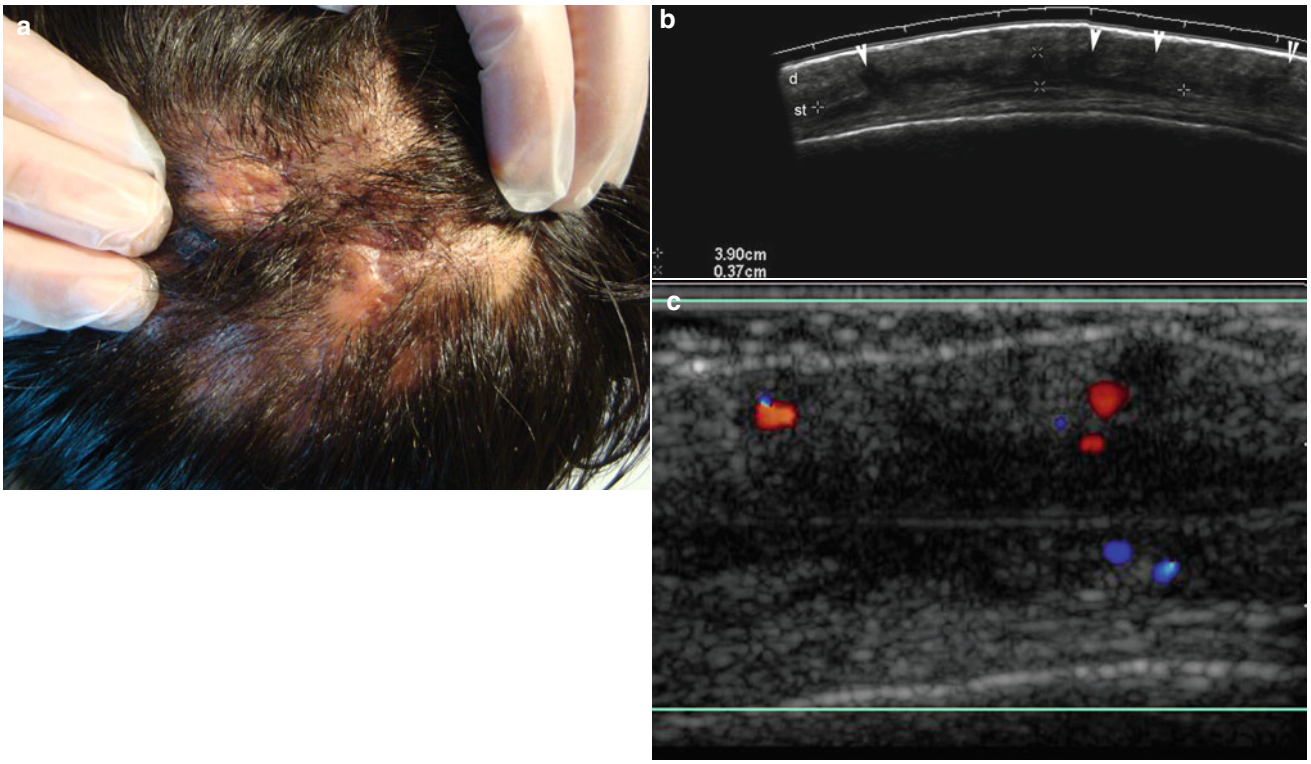

Fig. 19.18 (**a**–**c**) Perifolliculitis capitis abscedens et suffodiens. (**a**) Clinical image shows patchy alopecia. (**b**) Grey scale ultrasound image (transverse view) demonstrates a 3.9 cm (transverse) × 0.37 cm (depth) anechoic fluid collection (between markers) in the subcutaneous tissue with several connecting tracts (*arrowheads*) to the dermal region. (**c**) Color Doppler ultrasound image (transverse view) shows midly increased blood flow in the periphery of the fluid collection. *Abbreviations*: *d* dermis, *st* subcutaneous tissue

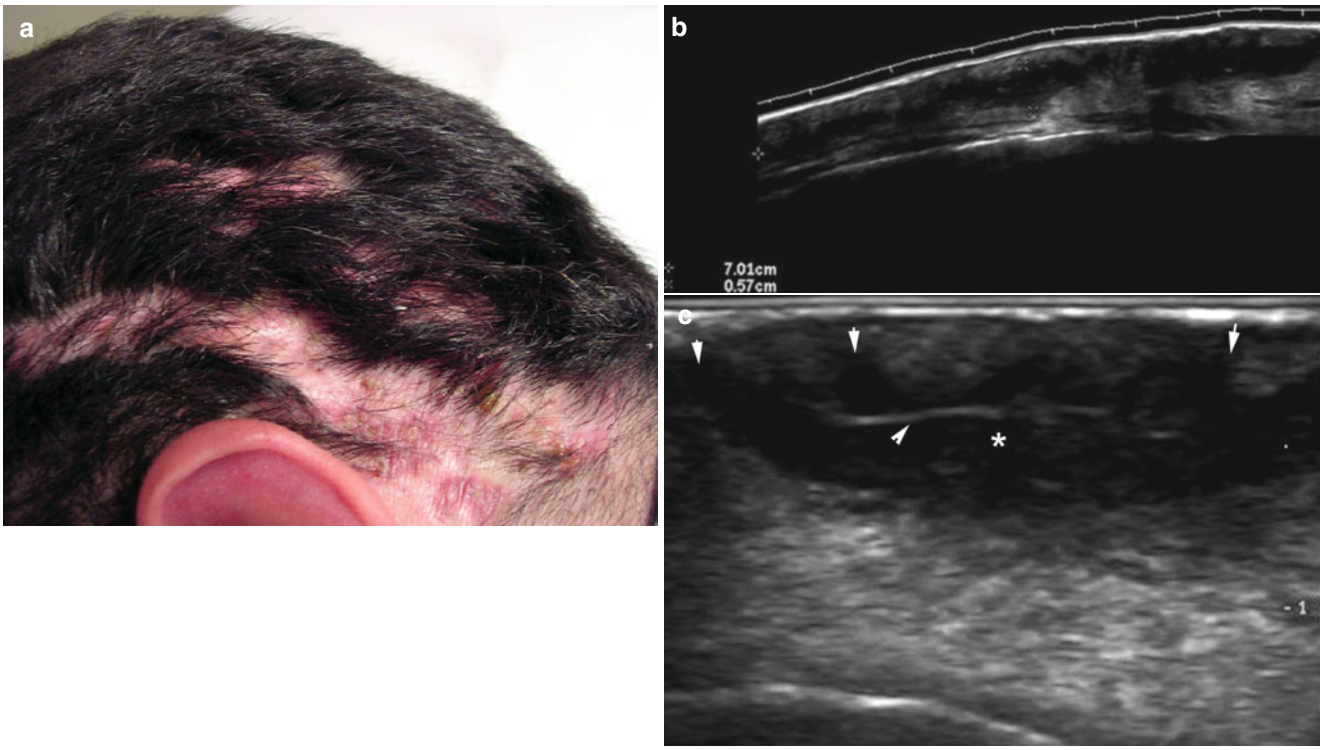

Fig. 19.19 (**a**–**c**) Perifolliculitis capitis abscedens et suffodiens. (**a**) Clinical photograph demonstrates patchy alopecia. (**b**) Grey scale ultrasound image (longitudinal view) shows a 7.0 cm (long) × 0.57 cm (depth) anechoic fluid collection (between markers) in the subcutaneous tissue. (**c**) Grey scale ultrasound image (zoomed transverse view) presents hyperechoic lines that correspond to hair tracts fragments (*arrowhead*) within the collection (*). Notice the connecting tracts (*arrows*) of the collection to dermis

19.7.1.4.3 Folliculitis Decalvans

Folliculitis decalvans (FD) is a chronic form of deep folliculitis that occurs on the scalp as patches of scarring alopecia at the expanding margins of which are the follicular pustules [34]. FD is a rare and recurrent purulent inflammation of the hair follicle in middle-aged adults that leads to scarring alopecia [35]. Both infection with *Staphylococcus aureus* and a deficient immune response by the host seem to be important for the development of this disfiguring disease [36]. The lesions typically occur in the vertex and occipital areas and consist of follicular pustules without external openings (ostia); there is also follicular tufting, surrounding diffuse or perifollicular erythema, and often hemorrhagic crusts and erosions can be seen. Early histology shows an inflammatory infiltrate of mainly neutrophils, followed by the additional recruitment of lymphocytes and plasma cells in more advanced stages [37]. Sonography shows inflammation of cutaneous layers, usually without fistulae, and thickening of hair follicles in the affected area. Hypoechoic scarring tissue and atrophy of the subcutaneous tissue can also be detected [4] (Fig. 19.20).

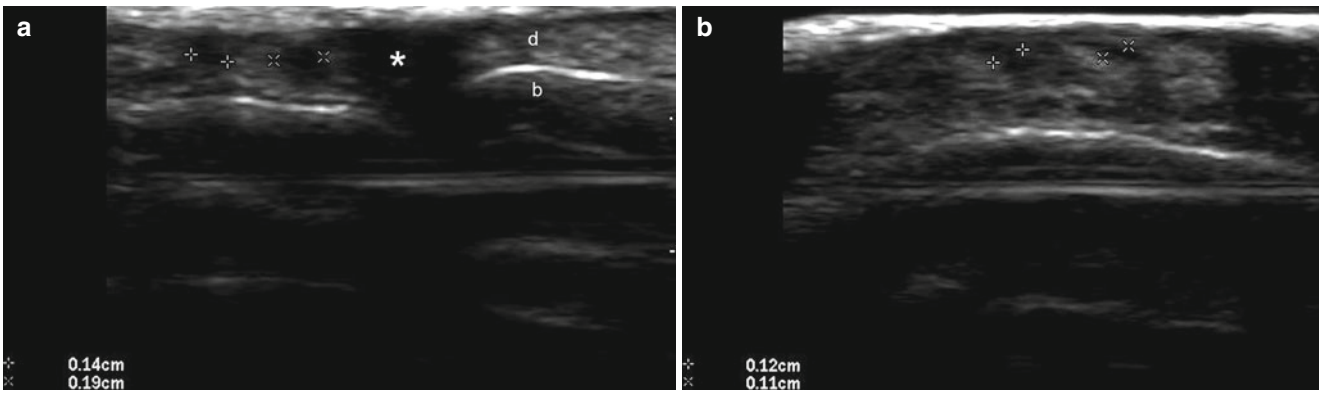

Fig. 19.20 (**a**, **b**) Folliculitis decalvans. (**a**, **b**) Grey scale ultrasound images (transverse views; parietal region) demonstrate thickening of the hair follicles (between markers) in the dermis and atrophy (post surgery and radiotherapy) of the subcutaneous tissue. There is a hypoechoic scar (*) in the site of a previous surgery. *Abbreviations*: *d* dermis, *b* bony margin of the skull

19.7.1.5 Pseudolymphoma

Pseudolymphoma, also called lymphocytoma cutis and cutaneous lymphoid hyperplasia implies a proliferation of lymphocytes in response to a foreign antigen or unknown stimuli [38]. Cutaneous pseudolymphomas comprise a heterogeneous group of lymphoproliferative disorders with dermal infiltrates of benign reactive T-cells or B-cells that tend to regress spontaneously over time [39]. Pseudolymphomas can simulate cutaneous lymphomas at both clinical and histological levels, developing as reactions to antigenic stimuli as varied as arthropod bites, vaccinations, tattoos, infections, or drugs; pseudolymphoma can also be idiopathic [40–44]. Sonography shows a focal and sometimes fusiform- or oval-shaped thickening of the dermis; this focal region presents hypoechogenicity but can become heterogeneous. Additionally, there is usually increased blood flow within the lesion and the periphery [4] (Fig. 19.21).

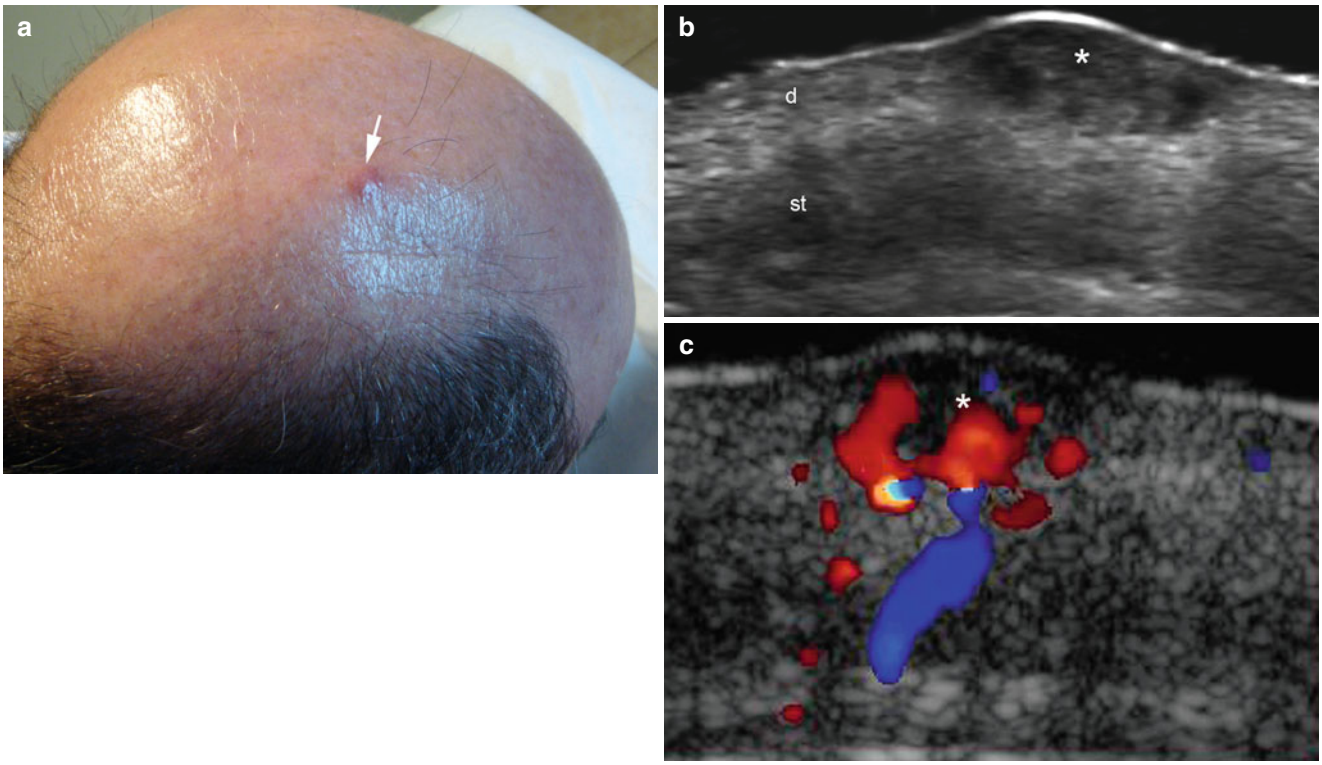

Fig. 19.21 (**a**–**c**) Pseudolymphoma. (**a**) Clinical image demonstrates a reddish lump (*arrow*) in the scalp (right parietal region). (**b**) Grey scale ultrasound image (transverse view) demonstrates an oval-shaped hypoechoic and heterogeneous structure (*) that affects the dermis. (**c**) Color Doppler ultrasound image (transverse view) shows increased blood flow within the lesion (*) and the surrounding tissues *Abbreviations*: *d* dermis, *st* subcutaneous tissue

19.7.2 Malignant Conditions

19.7.2.1 Skin Cancer

Malignant tumors occurring in the scalp are not common and when asymptomatic or small in size, may be covered by hair and neglected by the patient, leading to a potential risk of delay in detection and resulting in poorer outcomes [45]. Thus, cutaneous cancers of the scalp represent approximately 2 % of all skin cancers, with basal cell carcinoma being the most frequent in women and squamous cell carcinoma in men [46, 47]. Risk factors for developing skin cancer of the scalp include actinic damage, prior treatment with ionizing radiation, immunosuppresion, chronic scarring, and coexisting genodermatosis [48]. Alopecia favors the development of skin cancer from the direct exposure of the skin to solar radiation in men [48]. Features associated with recurrences include prior anticancer treatment, immunosuppression, and tumors of a large size; in fact, scalp cancer may already extend microscopically for a significant distance away from the primary site at the time of diagnosis, because the subgaleal plane offers little resistance to tumor spread. Furthermore, if the tumor penetrates the periosteum, it can spread laterally for even greater distances [46, 49]. Sonography of scalp cancer shows hypoechoic solid lesions of generally increased vascularity [50], and in basal cell carcinoma, hyperechoic spots can be detected within the tumor [51] (Figs. 19.22, 19.23, 19.24, 19.25, and 19.26).

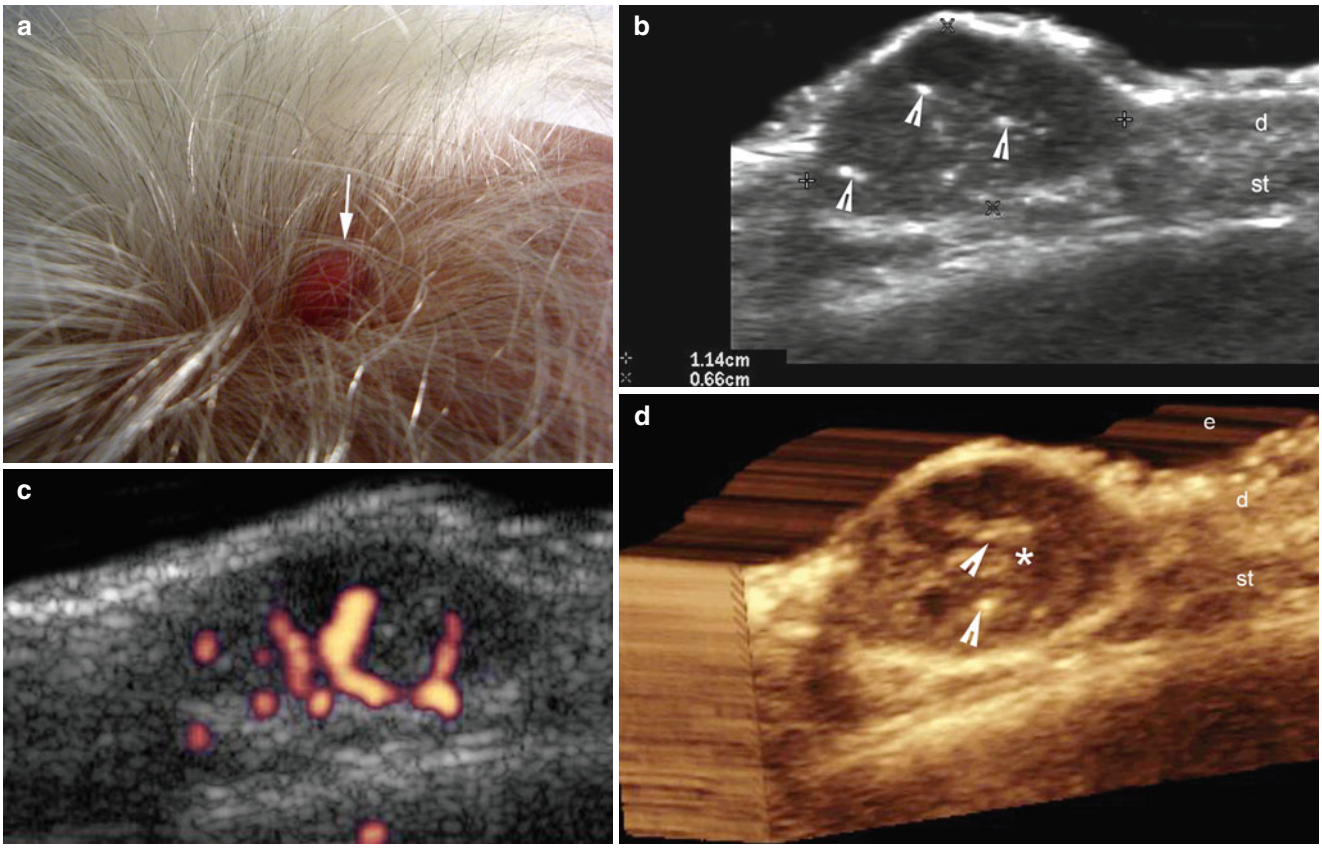

Fig. 19.22 (**a**–**d**) Basal cell carcinoma. (**a**) Clinical photograph demonstrates a reddish lump (*arrow*) in the scalp. (**b**) Grey scale ultrasound image (transverse view; right frontal region of the scalp) shows 1.14 cm (transverse) × 0.66 cm (depth) well-defined hypoechoic and heterogeneous structure (between markers) that involves the dermis and subcutaneous tissue. Notice the hyperechoic spots (*arrowheads*) within the lesion. (**c**) Power Doppler ultrasound image (longitudinal view) demonstrates increased vascularity within the lesional area. (**d**) 3D reconstruction (transverse view) highlights the tumor (*) and its hyperechoic spots (*arrowheads*). *Abbreviations*: *e* epidermis, *d* dermis, *st* subcutaneous tissue

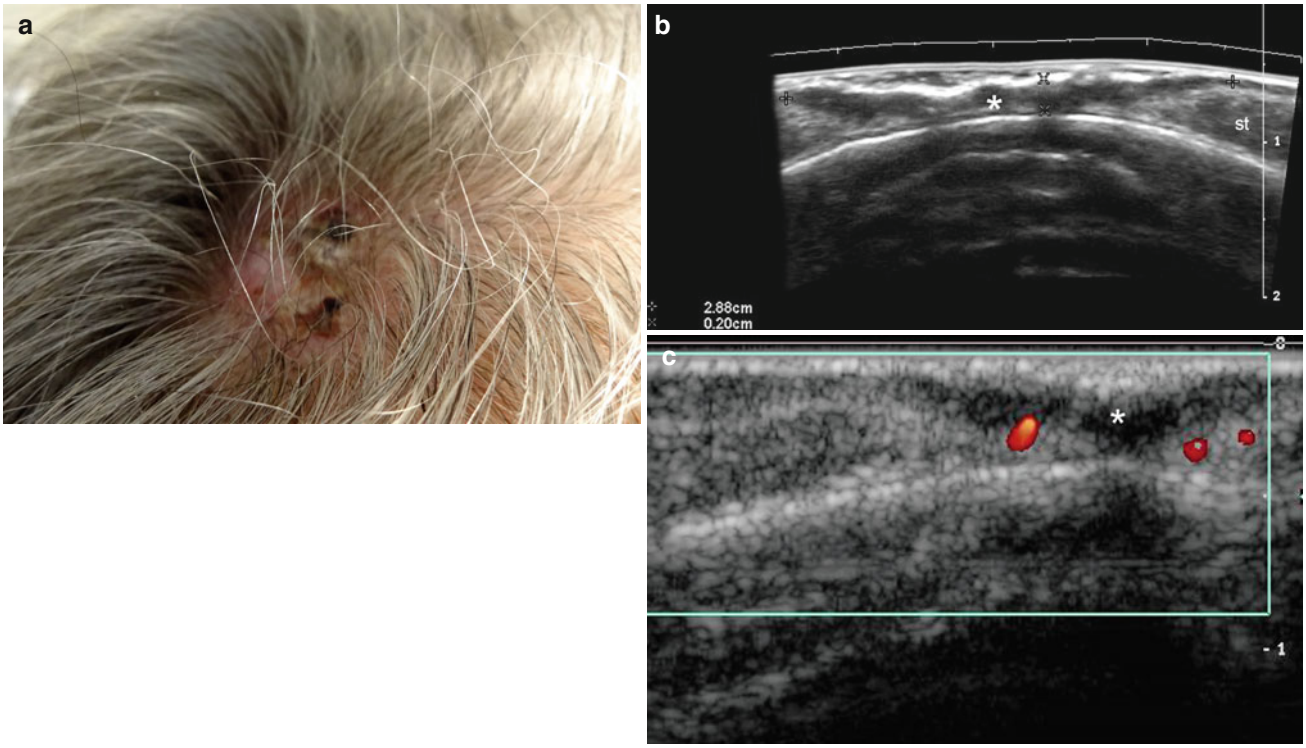

Fig. 19.23 (**a**–**c**) Basal cell carcinoma. (**a**) Clinical image shows erythematous, pigmented, crusty, and scaly lesion in the right frontal region of the scalp. (**b**) Grey scale ultrasound image (transverse view) demonstrates a 2.88 cm (transverse) × 0.37 cm (depth) hypoechoic structure (*, between markers) that affects the epidermis, dermis, and subcutaneous tissue. Notice the hyperechoic epidermal thickening in the lesional region. (**c**) Color Doppler ultrasound image (longitudinal view) shows mildly increased vascularity in the periphery of the lesion

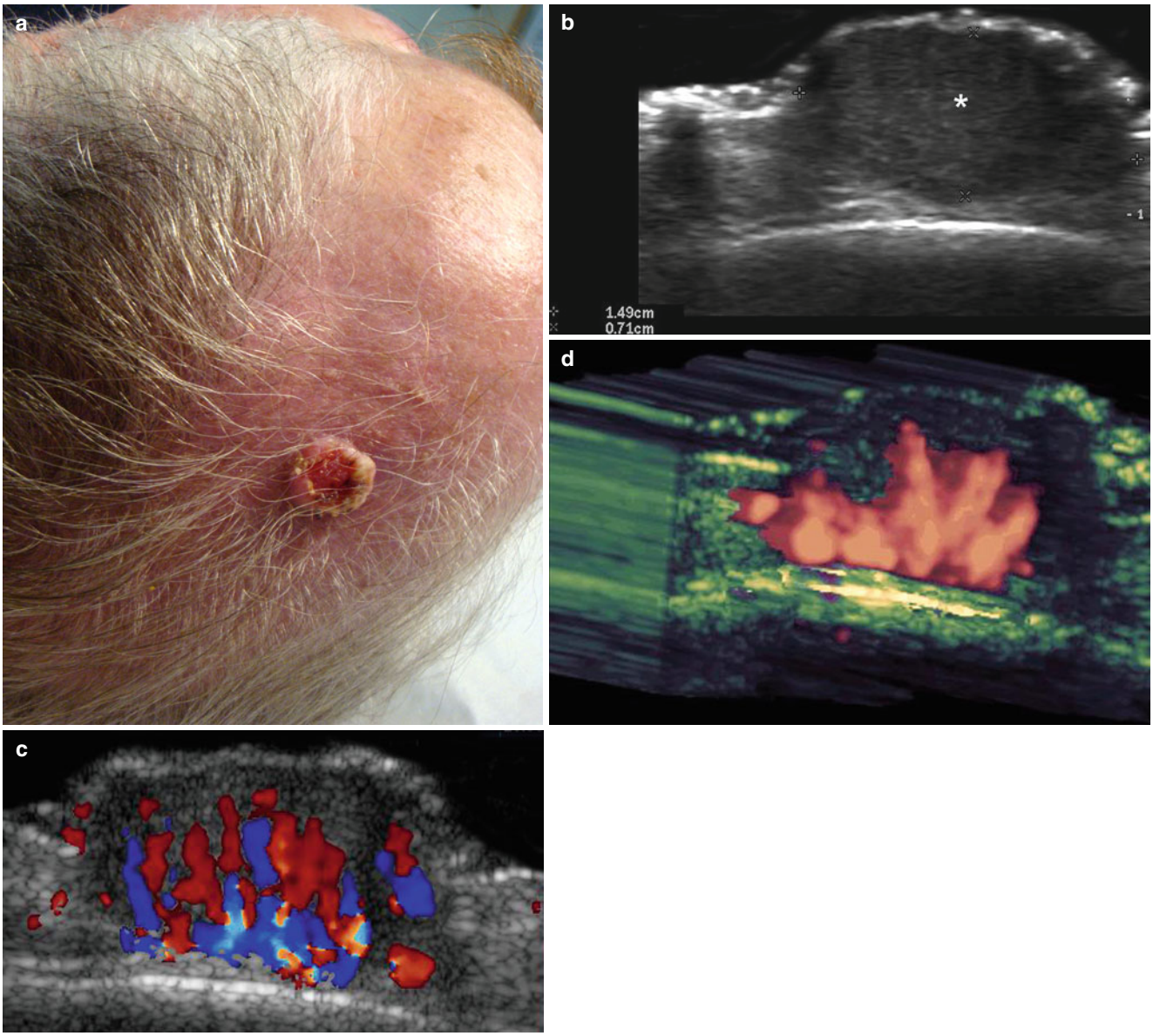

Fig. 19.24 (**a**–**d**) Squamous cell carcinoma. (**a**) Clinical image demonstrates erythematous and ulcerated lump in the left parietal region of the scalp. (**b**) Grey scale ultrasound image (transverse view) shows a 1.49 cm (transverse) × 0.71 (depth) well-defined hypoechoic solid mass (*) that affects the dermis and subcutaneous tissue. (**c**) Color Doppler ultrasound image (longitudinal view) shows strong vascularity within the mass. (**d**) 3D power angio reconstruction highlights the blood flow of the mass

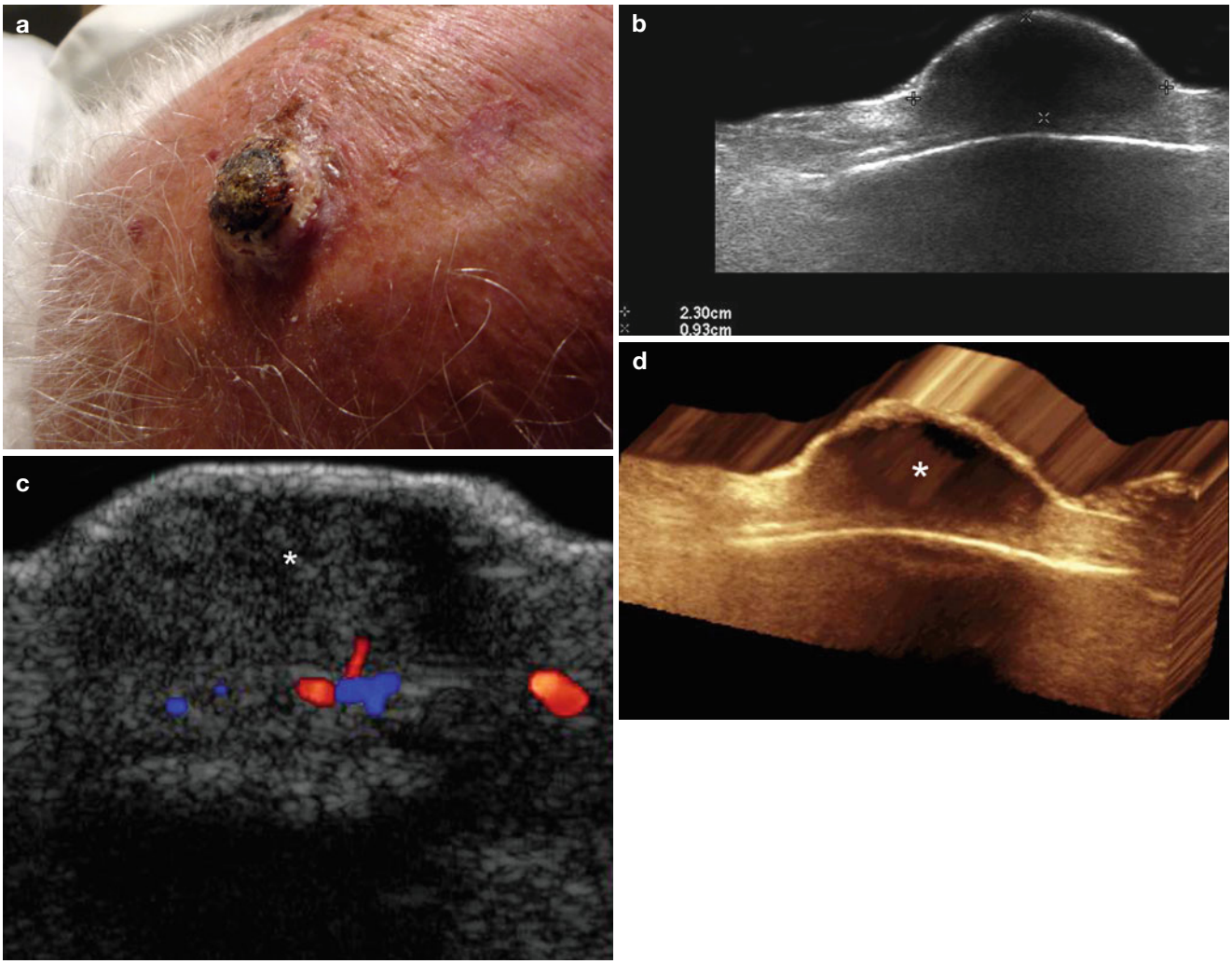

Fig. 19.25 (**a**–**d**) Squamous cell carcinoma. (**a**) Clinical photograph demonstrates a pigmented outgrowth in the left parietal region of the scalp. (**b**) Grey scale ultrasound image (transverse view) shows a 2.3 cm (transverse) × 0.93 cm (depth) hypoechoic mass (*, between markers) that involves the dermis and subcutaneous tissue. (**c**) Color Doppler ultrasound image (longitudinal view) demonstrates slightly increased blood flow in the periphery of the mass. (**d**) 3D reconstruction of the mass (*)

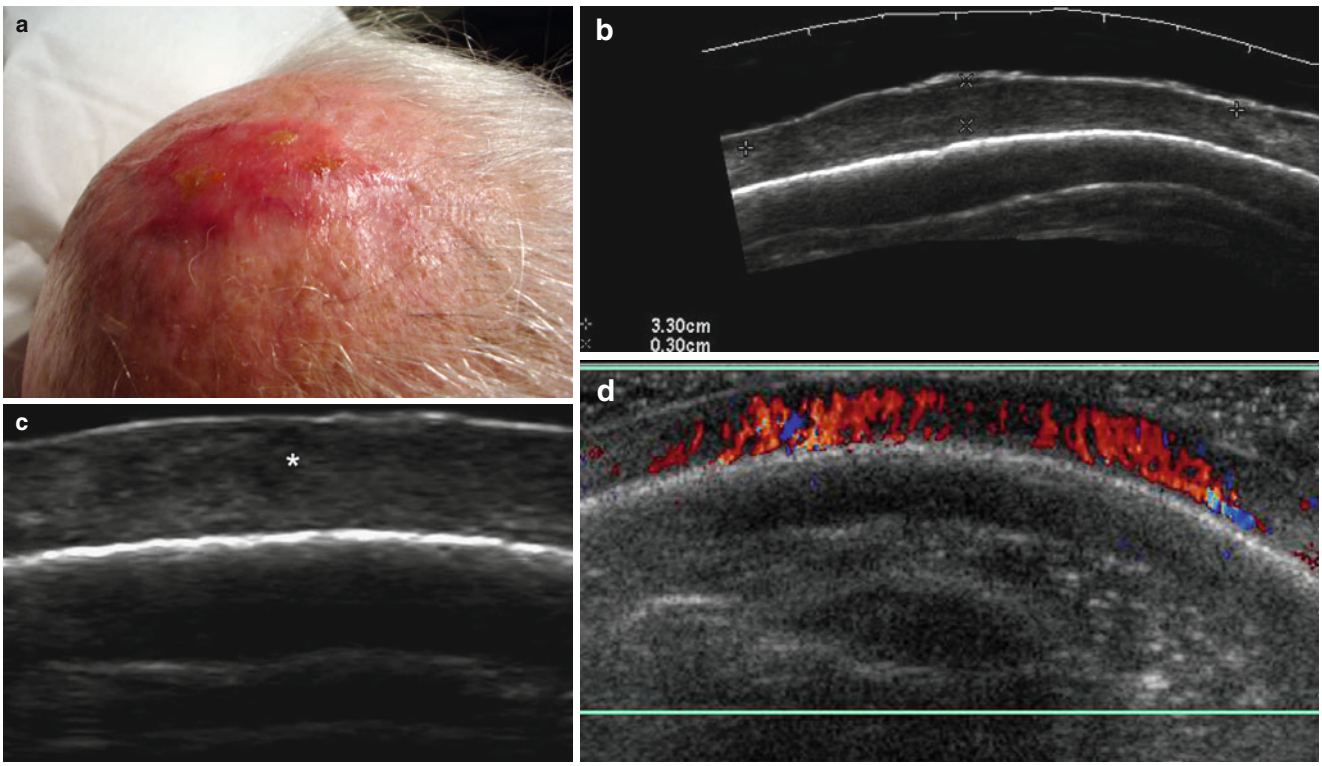

Fig. 19.26 (**a**–**d**) Squamous cell carcinoma. (**a**) Clinical photograph shows erythematous plaque-like swelling in the left parietal region of the scalp. (**b**, **c**) Grey scale ultrasound images (**b** extended transverse field of view; **c** zoomed longitudinal view) demonstrate a 3.3 cm (transverse) × 0.3 cm (depth) hypoechoic and heterogeneous thickening (*, between markers) of the dermis and subcutaneous tissue. (**d**) Color Doppler ultrasound image (longitudinal view) shows strong vascularity in the lesion area

Folliculotropic mycosis fungoides (FMF), a low-grade lymphoproliferative disorder, is a rare variant of cutaneous T-cell lymphoma where the neoplastic T lymphocytes display tropism for the follicular epithelium [52]. It presents clinically with patches, plaques, acneiform lesions (comedo-like and/or epidermal cysts), palpable tumors, and/or erythroderma. The most common site of involvement of the folliculotropic form of mycosis fungoides is the head and neck (80 %), with alopecia as a frequent sequel to head involvement. Histologically, FMF shows selective infiltration of the follicular epithelium by atypical lymphocytes and mucinous degeneration of the follicular epithelium in 60 % of cases [53, 54]. Sonography will show general thickening of the skin, decreased echogenicity of the upper dermis, thickening of the hair follicles, and hyperechoic deposits surrounding large hypoechoic hair follicles in the scalp or any FMF-affected area of the body [4] (Fig. 19.27).

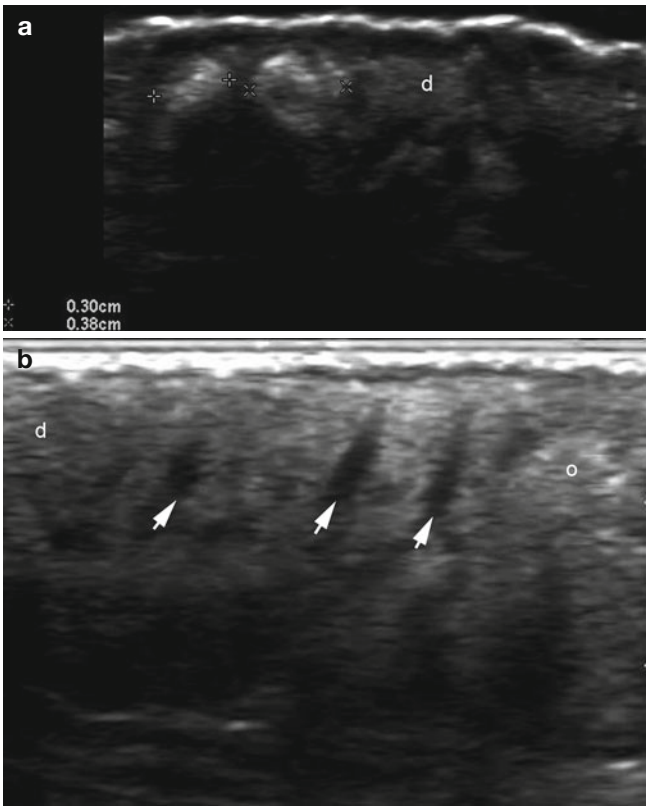

Fig. 19.27 (**a**, **b**) Folliculotropic mycosis fungoides. (**a**, **b**) Grey scale ultrasound images (occipital region of the scalp (**a** transverse; **b** longitudinal view). (**a**) Ultrasound image demonstrates hyperechoic deposits (between markers) surrounding the dermal hair follicles. (**b**) Ultrasound image shows thickening of the dermal hair follicles (*arrows*) and some hyperechoic deposits (o). *Abbreviation*: *d* dermis

References

1. Miyakoshi K, Tanaka M, Matsumoto T, Hattori Y, Minegishi K, Ishimoto H, et al. Occipital scalp hemangioma: prenatal sonographic and magnetic resonance images. J Obstet Gynaecol Res. 2008;34:666–9.
2. Wolfram LJ. Human hair: a unique physicochemical composite. J Am Acad Dermatol. 2003;48:S106–14.
3. Thibaut S, De Becker E, Caisey L, Baras D, Karatas S, Jammayrac O, et al. Human eyelash characterization. Br J Dermatol. 2010;162:304–10.
4. Wortsman X, Wortsman J, Matsuoka L, Saavedra T, Mardones F, Saavedra D, et al. Sonography in pathologies of scalp and hair. Br J Radiol. 2012;85(1013):647–55.
5. Wortsman X, Wortsman J. Clinical usefulness of variable-frequency ultrasound in localized lesions of the skin. J Am Acad Dermatol. 2010;62(2):247–56.
6. Seery GE. Surgical anatomy of the scalp. Dermatol Surg. 2002;28:581–7.
7. Al-Nuaimi Y, Baier G, Watson RE, Chuong CM, Paus R. The cycling hair follicle as an ideal systems biology research model. Exp Dermatol. 2010;19:707–13.
8. Yagyu K, Hayashi K, Chang SC. Orientation of multi-hair follicles in nonbald men: perpendicular versus parallel. Dermatol Surg. 2006;32:651–60.
9. Mattle E, Weiger M, Schmidig D, Boesiger P, Fey M. MRI of human hair. MAGMA. 2009;22:181–6.
10. Wortsman X, Wortsman J, Soto R, et al. Benign tumors and pseudotumors of the nail: a novel application of sonography. J Ultrasound Med. 2010;29:803–16.
11. Sau P, Graham JH, Helwig EB, Sau P, Graham JH, Helwig EB. Proliferating epithelial cysts. Clinicopathological analysis of 96 cases. J Cutan Pathol. 1995;22:394–406.
12. Satyaprakash AK, Sheehan DJ, Sangüeza OP. Proliferating trichilemmal tumors: a review of the literature. Dermatol Surg. 2007;33:1102–8.
13. Anolik R, Firoz B, Walters RF, Meehan SA, Tsou HC, Whitlow M, et al. Proliferating trichilemmal cyst with focal calcification. Dermatol Online J. 2008;14:25.
14. Agarwal RP, Handler SD, Matthews MR, Carpentieri D. Pilomatrixoma of the head and neck in children. Otolaryngol Head Neck Surg. 2001;125:510–5.
15. Roche NA, Monstrey SJ, Matton GE. Pilomatricoma in children: common but often misdiagnosed. Acta Chir Belg. 2010;110:250–4.
16. Cecen E, Ozguven AA, Uysal KM, Gunes D, Ozer E, Olgun N, et al. Pilomatricoma in children: a frequently misdiagnosed superficial tumor. Pediatr Hematol Oncol. 2008;25:522–7.
17. Choo HJ, Lee SJ, Lee YH, Lee JH, Oh M, Kim MH, et al. Pilomatricomas: the diagnostic value of ultrasound. Skeletal Radiol. 2010;39:243–50.
18. Hwang JY, Lee SW, Lee SM. The common ultrasonographic features of pilomatricoma. J Ultrasound Med. 2005;24:1397–402.
19. Peer S. The place of sonography in the diagnostic work-up of haemangiomas and vascular malformations. Handchir Mikrochir Plast Chir. 2009;41:70–7.
20. Giovagnorio F, Andreoli C, De Cicco ML. Color Doppler sonography of focal lesions of the skin and subcutaneous tissue. J Ultrasound Med. 1999;18:89–93.
21. Wortsman X. Common applications of dermatologic sonography. J Ultrasound Med. 2012;31(1):97–111.
22. Verity DH, Rose GE, Restori M. The effect of intralesional steroid injections on the volume and blood flow in periocular capillary haemangiomas. Orbit. 2008;27:41–7.

23. Sans V, de la Roque ED, Berge J, et al. Propranolol for severe infantile hemangiomas: follow-up report. Pediatrics. 2009;124:423–31.
24. Al-Zaid T, Vanderweil S, Zembowicz A, Lyle S. Sebaceous gland loss and inflammation in scarring alopecia: a potential role in pathogenesis. J Am Acad Dermatol. 2011;65(3):597–603.
25. Stefanato CM. Histopathology of alopecia: a clinicopathological approach to diagnosis. Histopathology. 2010;56:24–38.
26. Verma SB, Wollina U. Acne keloidalis nuchae: another cutaneous symptom of metabolic syndrome, truncal obesity, and impending/overt diabetes mellitus? Am J Clin Dermatol. 2010;11(6):433–6.
27. Sterling JB, Sina B, Gaspari A, Deng A. Acne keloidalis: a novel presentation for tinea capitis. J Am Acad Dermatol. 2007;56:699–701.
28. Bajaj V, Langtry JA. Surgical excision of acne keloidalis nuchae with secondary intention healing. Clin Exp Dermatol. 2008;33:53–5.
29. Gloster Jr HM. The surgical management of extensive cases of acne keloidalis nuchae. Arch Dermatol. 2000;136:1376–9.
30. Brănişteanu DE, Molodoi A, Ciobanu D, et al. The importance of histopathologic aspects in the diagnosis of dissecting cellulitis of the scalp. Rom J Morphol Embryol. 2009;50:719–24.
31. Mihić LL, Tomas D, Situm M, Krolo I, Sebetić K, Sjerobabski-Masnec I, et al. Perifolliculitis capitis abscedens et suffodiens in a Caucasian: diagnostic and therapeutic challenge. Acta Dermatovenerol Croat. 2011;19(2):98–102.
32. Ljubojevic S, Pasic A, Lipozencic J, Skerlev M. Perifolliculitis capitis abscedens et suffodiens. J Eur Acad Dermatol Venereol. 2005;19:719–21.
33. Williams CN, Cohen M, Ronan SG, Lewandowski CA. Dissecting cellulitis of the scalp. Plast Reconstr Surg. 1986;77:378–82.
34. Castaño-Suárez E, Romero-Maté A, Arias-Palomo D, Borbujo J. Photodynamic therapy for the treatment of folliculitis decalvans. Photodermatol Photoimmunol Photomed. 2012;28(2):102–4.
35. Otberg N, Kang H, Alzolibani AA, Shapiro J. Folliculitis decalvans. Dermatol Ther. 2008;21:238–44.
36. Gemmeke A, Wollina U. Folliculitis decalvans of the scalp: response to triple therapy with isotretinoin, clindamycin, and prednisolone. Acta Dermatovenerol Alp Panonica Adriat. 2006;15:184–6.
37. Chiarini C, Torchia D, Bianchi B, Volpi W, Caproni M, Fabbri P. Immunopathogenesis of folliculitis decalvans: clues in early lesions. Am J Clin Pathol. 2008;130:526–34.
38. Nnebe NV, Woon C, Haines S, Dayton V, Weigel BJ. Cutaneous pseudolymphoma: an unusual presentation of a scalp mass. Pediatr Blood Cancer. 2009;52(2):283–5.
39. Bergman R. Pseudolymphoma and cutaneous lymphoma: facts and controversies. Clin Dermatol. 2010;28:568–74.
40. Bachelez H. The uncertain status of cutaneous pseudolymphoma. Actas Dermosifiliogr. 2009;100:33–7.
41. Cerroni L, Borroni RG, Massone C, Chott A, Kerl H. Cutaneous B-cell pseudolymphoma at the site of vaccination. Am J Dermatopathol. 2007;29:538–42.
42. Gutermuth J, Hein R, Fend F, Ring J, Jakob T. Cutaneous pseudolymphoma arising after tattoo placement. J Eur Acad Dermatol Venereol. 2007;21:566–7.
43. Colli C, Leinweber B, Müllegger R, Chott A, Kerl H, Cerroni L. Borrelia burgdorferi-associated lymphocytoma cutis: clinicopathologic, immunophenotypic, and molecular study of 106 cases. J Cutan Pathol. 2004;31:232–40.
44. Ploysangam T, Breneman DL, Mutasim DF. Cutaneous pseudolymphomas. J Am Acad Dermatol. 1998;38:877–95.
45. Greco M, Vitagliano T, Fiorillo MA, Atzeni M, Corona A, Ribuffo D. Rare malignant tumors of the scalp: a report of four cases, their treatment and a review of the literature. Eur Rev Med Pharmacol Sci. 2010;14(11):993–7.
46. Lang Jr PG, Braun MA, Kwatra R. Aggressive squamous carcinomas of the scalp. Dermatol Surg. 2006;32:1163–70.
47. Katz TM, Silapunt S, Goldberg LH, Jih MH, Kimyai-Asadi A. Analysis of 197 female scalp tumors treated with mohs micrographic surgery. J Am Acad Dermatol. 2005;52:291–4.
48. Neubauer KE, Goldstein GD, Plumb SJ. Squamous cell carcinoma of the scalp in organ transplant recipients: exploring mechanisms for recurrence and treatment guidelines. Dermatol Surg. 2010;36:185–93.
49. Leibovitch I, Huilgol SC, Richards S, Paver R, Selva D. Scalp tumors treated with mohs micrographic surgery: clinical features and surgical outcome. Dermatol Surg. 2006;32:1369–74.
50. Bobadilla F, Wortsman X, Muñoz C, Segovia L, Espinoza M, Jemec GBE. Pre-surgical high resolution ultrasound of facial basal cell carcinoma: correlation with histology. Cancer Imaging. 2008;22:163–72.
51. Uhara H, Hayashi K, Koga H, Saida T. Multiple hypersonographic spots in basal cell carcinoma. Dermatol Surg. 2007;33:1215–9.
52. Muniesa C, Estrach T, Pujol RM, Gallardo F, Garcia-Muret P, Climent J, Servitje O. Folliculotropic mycosis fungoides: clinicopathological features and outcome in a series of 20 cases. J Am Acad Dermatol. 2010;62:418–26.
53. Nashan D, Faulhaber D, Ständer S, Luger TA, Stadler R. Mycosis fungoides: a dermatological masquerader. Br J Dermatol. 2007;156:1–10.
54. Iorizzo M, El Shabrawi Caelen L, Vincenzi C, Misciali C, Tosti A. Folliculotropic mycosis fungoides masquerading as alopecia areata. J Am Acad Dermatol. 2010;63:50–2.

Conditions That Can Mimic Dermatologic Diseases: "Simulators"

20

Ximena Wortsman, Patricio Azocar,
and Jose Antonio Bouffard

Entities that can present challenging clinical or sonographic diagnosis that belong to the surrounding tissues (foreign bodies, accessory structures, abnormalities of the lymph nodes, tendons, muscles, fascia, vessels, nerves, and glands in the vicinity of the skin)

Contents

20.1 Introduction

Simulators of dermatologic pathology are common findings among soft-tissue lesions. These pseudodermatologic entities originate in the surrounding structures and can bulge into the skin, therefore, they can generate challenging clinical presentations. Simulators include pathology derived from a wide spectrum of structures such as lymph nodes, vessels, glands, muscles, tendons, cartilage, and bone, among others. These conditions can also be composed of exogenous material that could have been inserted accidentally (e.g., foreign bodies), for surgical purposes (e.g., prosthetic devices), or for cosmetic purposes (e.g., implants).

Clinically, many patients present with bumps or lumps that are associated with some cutaneous alterations such as redness or edema, and/or can appear in concomitance with cutaneous diseases. Hence, these entities can easily mimic

X. Wortsman, MD (✉)
Department of Radiology and Dermatology,
Institute for Diagnostic Imaging
and Research of the Skin and Soft Tissues, Clinica Servet,
Faculty of Medicine, University of Chile,
Almirante Pastene 150, Providencia, Santiago, Chile
e-mail: xwo@tie.cl, xworts@yahoo.com, www.sonoskin.com

P. Azocar, MD
Department of Radiology, Hospital del Trabajador,
Francisco Solano Astaburuaga 405, Ñuñoa, Santiago, Chile
e-mail: patricioazocar@gmail.com

J.A. Bouffard, MD
Department of Orthopaedic Surgery and Sports Medicine,
Sports Medicine Ultrasound, Detroit Medical Center,
Sports Medicine Institute, 30671 Stephenson Hwy,
Madison Heights, Detroit, MI 48071, USA
e-mail: jabouffar@dmc.org

X. Wortsman, G.B.E. Jemec (eds.), *Dermatologic Ultrasound with Clinical and Histologic Correlations*,
DOI 10.1007/978-1-4614-7184-4_20,

common dermatologic lesions such as epidermal cysts, pilomatrixomas, morphea plaques, or plantar warts, among others.

These simulators are key factors that must be taken into consideration during the ultrasound examination of skin lesions, especially when no abnormality is detected within the cutaneous layers. In such cases, the sonographer should explore deeper into the layers and it is highly probable that a lower frequency probe and/or an adjustment of the depth and focal zones of the ultrasound machine will be needed.

In this chapter we will review some challenging clinical entities that could mimic dermatologic pathology. For academic purposes, we have divided the simulators according to the structure that abnormality originates from.

20.2 Simulators

20.2.1 Lymph Nodes

Lymph nodes are common causes of swelling or lumps and usually follow the distribution of the lymphatic drainage.

Normal lymph nodes appear on ultrasound as oval-shaped solid structures with a hypoechoic rim that corresponds to the cortex and a hyperechoic center that represents the medulla, the latter usually being a little bet eccentric within the nodule. A low flow vascular pedicle is generally found in one of the aspects of the lymph node that commonly contains a feeding artery and a draining vein (hilum). Therefore, the normal pattern of vascularization predominantly shows a central location in the medullae. Lymph nodes normally present a transverse axis ≤1 cm [1], with the exception of the jugulodigastric and groin regions where lymph nodes that reach 1.5–2 cm can be found in unaffected individuals.

20.2.1.1 Benign

20.2.1.1.1 Inflammatory Lymph Nodes

Under inflammation, lymph nodes tend to increase in size but maintain their oval shape and echostructure. The cortex usually becomes thickened and the vascularity becomes more prominent within the nodule. The medulla may present as a hyperechoic band-like and eccentric area. On color Doppler ultrasound, the vascularity conserves the regular shape of the vessels and shows a prominent and centrally located hilum (Figs. 20.1 and 20.2).

Cat Scratch Disease

Catch scratch disease, also called cat scratch fever or subacute regional lymphadenitis, is an infectious disease that affects the lymph nodes and is caused by a bacterium called *Bartonella henselae* (gram negative rod). This bacterial infection is transmitted through the draining lymph nodes of the site of the bite or scratch that is usually gotten from a cat [2]. Cat scratch disease has recently been reported in organ transplanted patients [3]. Clinically, this disease can produce erythematous lumps close to the sites of the scratch, sometimes overlooked by the patient. On sonography, enlarged lymph nodes that present inflammatory characteristics (increased size, hypoechogenicity, thick cortex, and prominent vascularity) can be found on the neck, parotid, or upper limbs. The affected nodes have been reported to retain their oval shape and present a short axis to long axis ratio of 0.5 or more in 61 % of patients [2]. Posterior sound enhancement has been significantly associated with larger and abscessed lymph nodes. Increased echogenicity of the surrounding subcutaneous tissue can also be noticed [2, 3] (Fig. 20.3).

20.2.1.1.2 Lymphoid Hyperplasia

Lymphoid hyperplasia is an entity that implies the reactive proliferation of lymphoid tissue usually concomitant with other conditions such as sarcoidosis; acquired toxoplasmosis; infectious mononucleosis (Epstein-Barr virus); vaccinal reactions; Destombes-Rosai-Dorfman syndrome or massive lymphadenopathy by sinusal histiocytosis with hemophagocytosis; angiofollicular lymphoid hyperplasia or pseudotumor of Castleman; angio-follicular and plasmocytic polyadenopathy; adenopathies of collagenosis; rheumatoid arthritis; systemic erythematous lupus; and those caused by protein deposits [4–6]. Clinically, the neck, axillae, and groin regions are most commonly affected with palpable nodules. Histologically, the majority of reactive lymph node lesions exhibit reactive follicular hyperplasia with interfollicular polyclonal plasmacytosis. There is usually increased size and number of the lymph nodes seen on ultrasound that exhibit a prominent hypoechoic cortex and blood flow that is similar to the reactive inflammatory presentation. Nevertheless, hyperplastic lymph nodes can be larger in size and sometimes measure more than 2 cm, although they usually maintain the normal echostructure of the lymphoid tissue (oval shape, hypoechoic cortex, hyperechoic center, and prominent central vascularity) (Fig. 20.4).

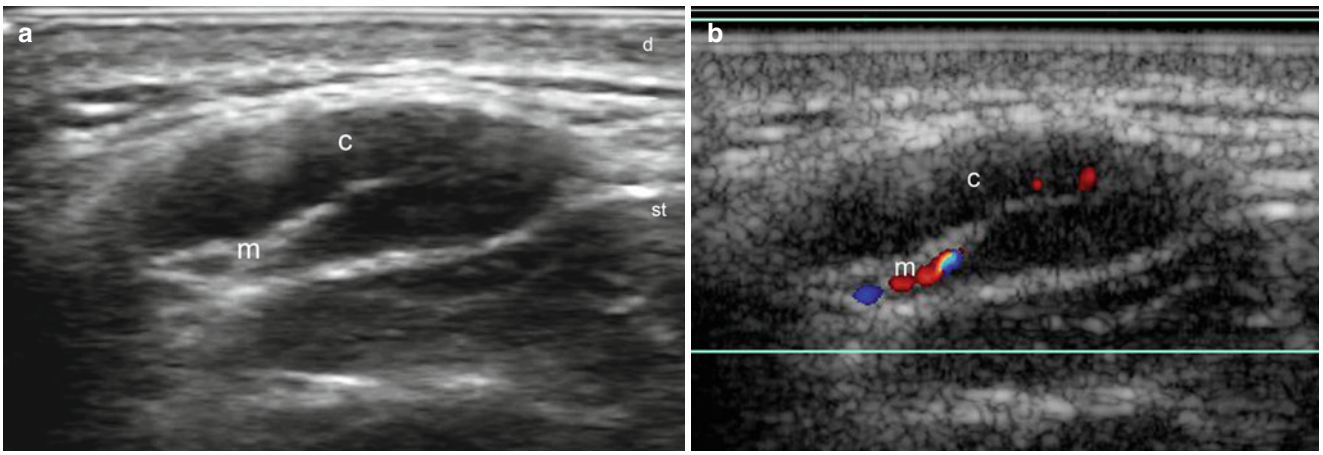

Fig. 20.1 (**a**, **b**) Inflammatory lymph node. (**a**) Grey scale ultrasound image (transverse view) shows a well-defined, oval-shaped subcutaneous structure that presents a thick hypoechoic rim (cortex) and band-like hyperechoic center (medulla). (**b**) Color Doppler ultrasound image (transverse view) demonstrates blood flow in the hilum of the medulla and a mild increase of the vascularity within the cortex of the lymph node. *Abbreviations*: *c* cortex, *m* medulla, *d* dermis, *st* subcutaneous tissue

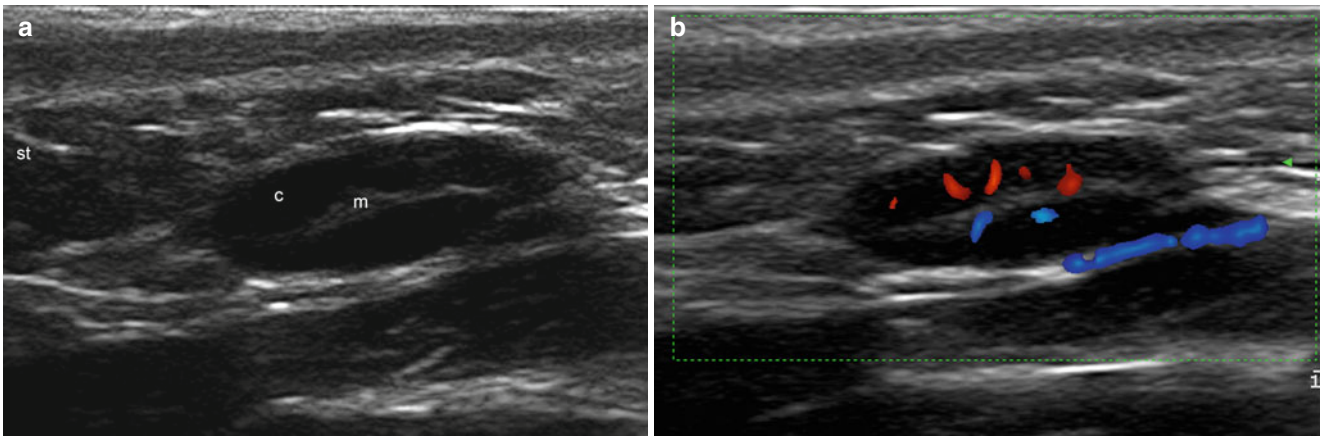

Fig. 20.2 (**a**, **b**) Inflammatory lymph node. (**a**) Grey scale ultrasound image (transverse view) shows a well-defined oval-shaped subcutaneous nodule with a thick hypoechoic cortex and a band-like hyperechoic medulla. (**b**) Color Doppler ultrasound image (transverse view) demonstrates increased vascularity in the cortex of the lymph node. *Abbreviations*: *c* cortex, *m* medulla, *st* subcutaneous tissue

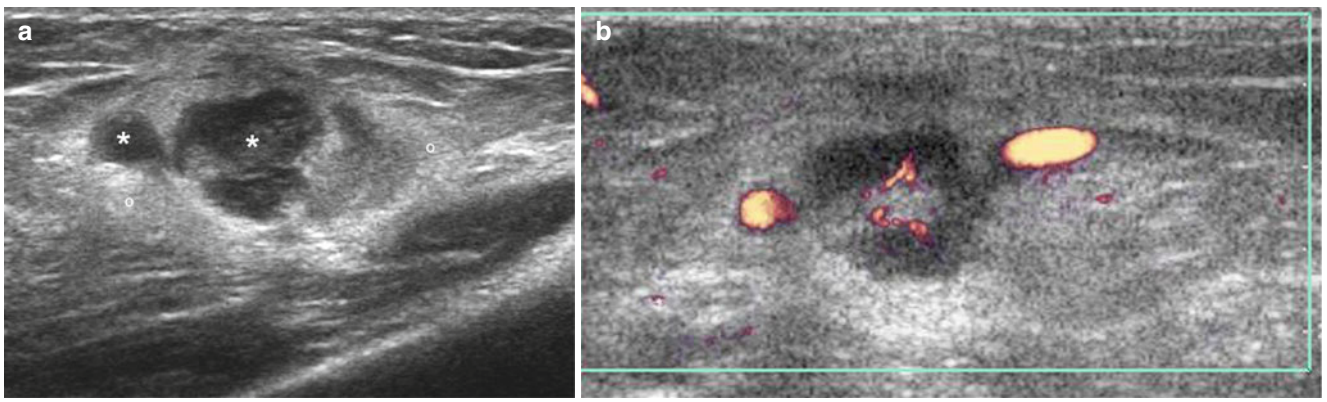

Fig. 20.3 (**a**, **b**) Cat scratch disease lymph node. (**a**) Grey scale ultrasound image (transverse view, ulnar aspect, distal part of the left arm) shows two well-defined oval-shaped subcutaneous nodules (*) that correspond to inflammatory lymph nodes. There is a thick cortex and an eccentric hyperechoic medulla. Notice the hyperechogenicity (edema) of the surrounding subcutaneous tissue (*o*). (**b**) Color Doppler ultrasound image (transverse view) demonstrates blood flow in the medulla and cortex of the lymph node

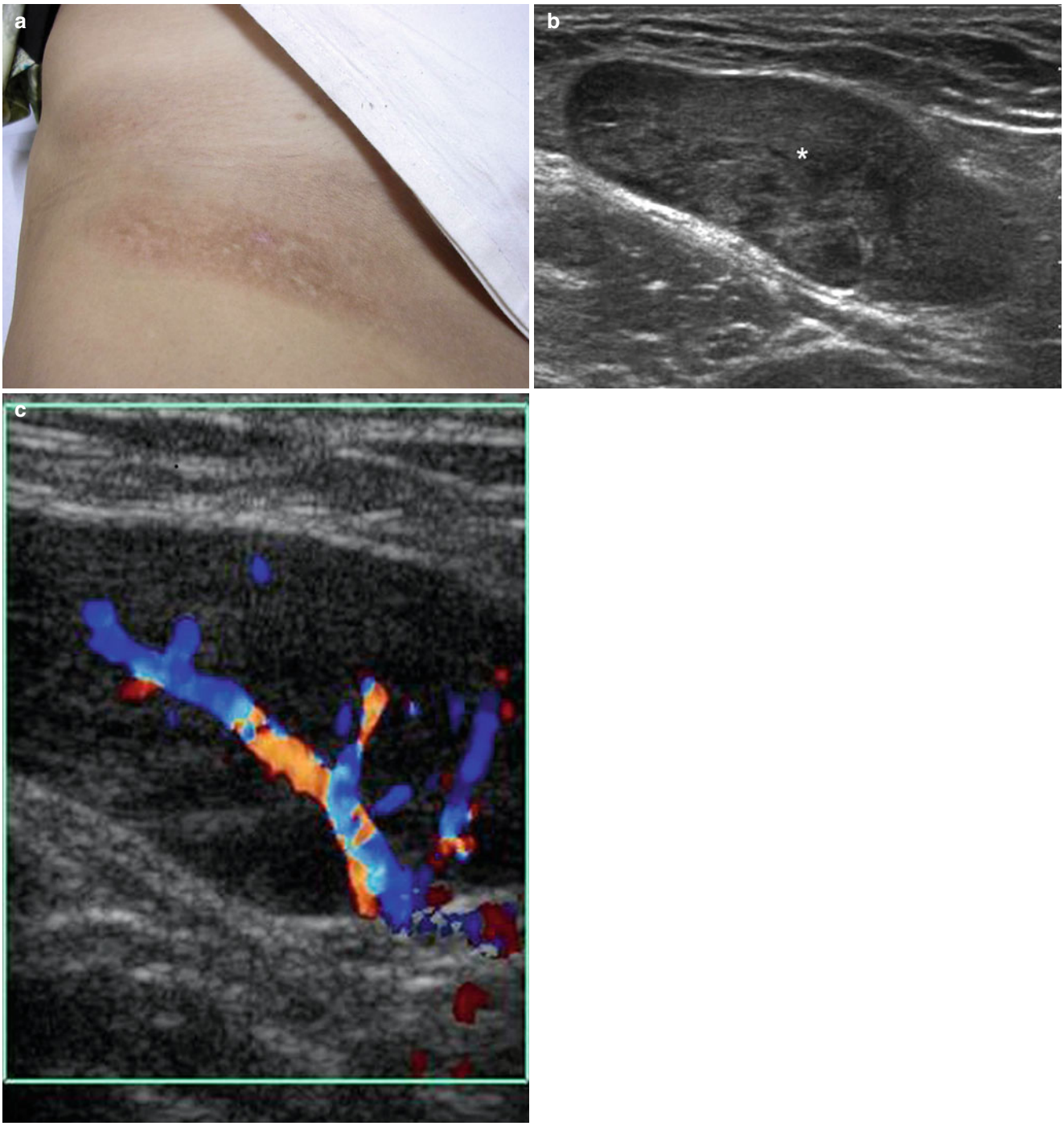

Fig. 20.4 (**a**–**c**) Lymphoid hyperplasia lymph node. (**a**) Clinical image shows pigmentation in the right groin. A mass was also palpable in the same region. (**b**) Grey scale ultrasound image (transverse view) demonstrates a well-defined, oval-shaped, hypoechoic and slightly heterogeneous subcutaneous structure (*). (**c**) Color Doppler ultrasound image (transverse view) shows prominent blood flow in the hilum and medulla

20.2.1.2 Malignant

20.2.1.2.1 Metastatic Lymph Nodes

Malignant infiltration in the echostructure of the lymph nodes typically produces morphological changes such as loss of the hyperechoic center and oval shape, adopting a rounder shape and hypoechoic echostructure, both in the medulla (center) and cortex. Moreover, a round shape with a longitudinal/transverse ratio of less than two within these hypoechoic nodes, the absence of an echogenic hilum, and the presence of cystic portions and calcifications have been reported as being significantly greater in malignant lesions than in benign lesions in thyroid cancer [7]. Thus, size is increased and in addition to the loss of the hyperechoic pattern of the medulla, hypoechoic nodules can be found in the cortex (Table 20.1). The malignant lymph nodes can sometimes show an anechoic structure that resembles abscesses or fluid collections. The latter appearance has been reported in metastasis of cutaneous melanoma and is probably a result of the hypercellularity and not the presence of necrosis [8]. Increase of the gain parameters to check the echostructure and the detection of vascularity within the lymph nodes can support the diagnosis because fluid collections are prone to show compressibility, peripheral vascularity and anechogenicity with some floating echoes (debris). On color Doppler ultrasound, malignant vessels tend to show a peripheral distribution that includes prominent vessels in the cortex with irregularities and stumps. Resistive indexes ≥0.7 have been indicated as criteria for malignant infiltration [9]. In spite of some promising results, the role of sonolelastography still seems controversial for the assessment of malignancy in lymph nodes and will probably require further investigation [10] (Fig. 20.5).

Table 20.1 Sonographic signs suggestive of benign/malignant lymph nodes

	Benign	Malignant
Characteristic		
Shape	Oval	Round
Center	Hyperechoic	Hypoechoic/anechoic
Thickening cortex	Diffuse	Nodular
Ratio longitudinal/transverse	>2	<2
Vascularity	Regular	Irregular
Cortex vessels	Absent/few	Present/prominent

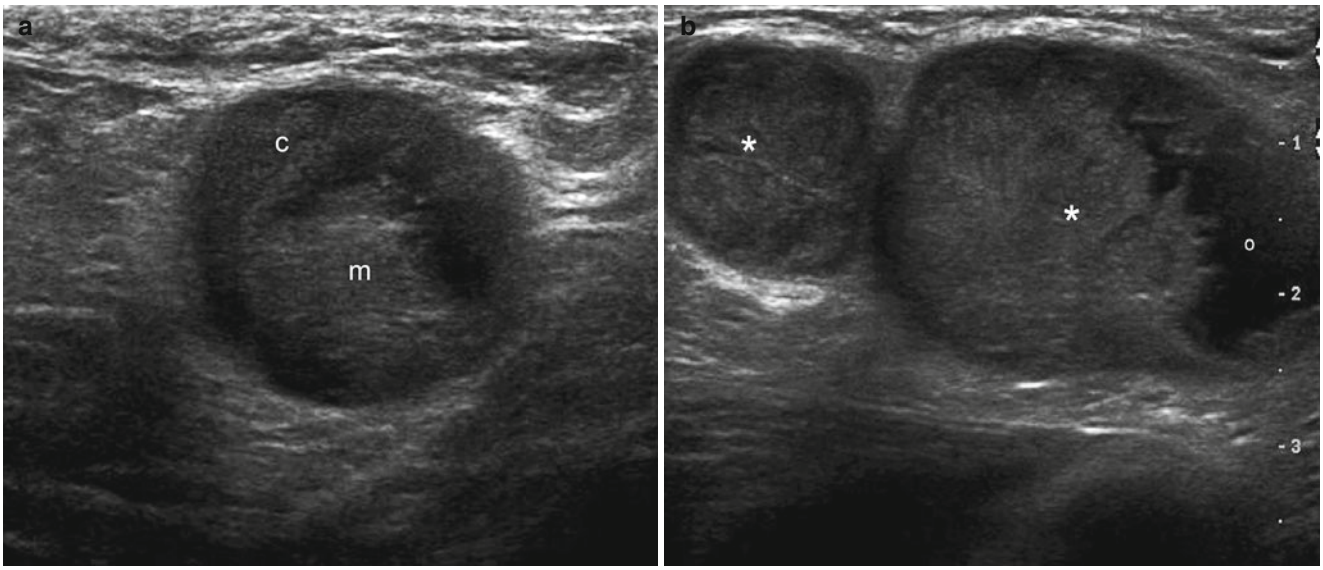

Fig. 20.5 (**a**, **b**) Metastatic lymph nodes (melanoma). (**a**) Grey scale ultrasound image (transverse view, right axilla) demonstrates a well-defined round-shaped subcutaneous nodule that presents a thick hypoechoic cortex (*c*) and a slightly hyperechoic medulla (*m*). (**b**) Grey scale ultrasound image (transverse view, right axilla) demonstrates two well-defined round and oval-shaped hypoechoic subcutaneous nodules (*). Notice the lack of the central hyperechoic medulla and the anechoic areas within the nodules (*o*)

20.2.2 Fistulae/Sinus Tracts

A fistula is an abnormal pathological pathway between two anatomic spaces/layers or a pathway that leads from an internal cavity or organ to the surface of the body. A sinus tract is an abnormal channel that originates or ends in one opening [11]. The fistulous and sinus tracts can originate from the infectious involvement of deeper layers that can rise to the surface. Clinically, they appear as erythematous and sometimes ulcerated points or nodules that drain purulent, serosanguineous, and/or oily material. On sonography, hypoechoic tracts with prominent echoes (debris) that connect the deeper layers with the skin layers are found. These tracts are usually associated with increased vascularity in the periphery (Figs. 20.6 and 20.7).

20.2.2.1 Odontogenic Cutaneous Fistulae

Odontogenic cutaneous fistulae is an abnormal communication between the cutaneous layers of the face and the oral cavity. This fistula arises as a continuation of bacterial invasion of

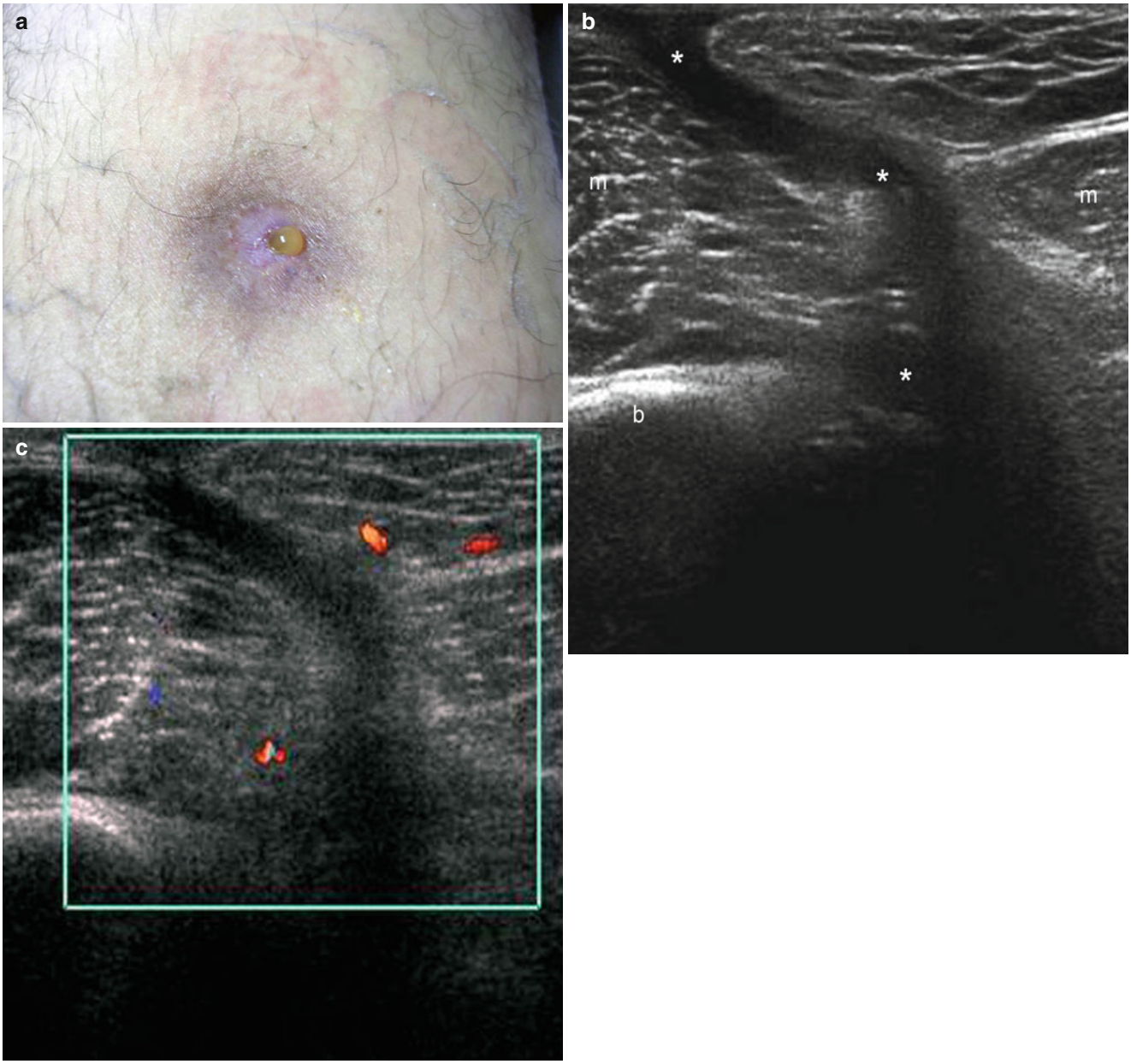

Fig. 20.6 Fistula (osteomyelitis). (**a**) Clinical image shows an erythematous and pigmented macule that drains purulent material in the antero-medial aspect of the right thigh. (**b**) Grey scale ultrasound image (transverse view) demonstrates a hypoechoic fistulous tract (*) that connects the skin layers with the bony margin of the femur. (**c**) Color Doppler ultrasound image (transverse view) shows increased vascularity in the periphery of the fistulous tract. *Abbreviations*: *m* muscle (quadriceps and adductor muscles), *b* bony margin of the femur

the dental pulp through a breach in the enamel and the dentine from a carious lesion, trauma, or other causes. If treatment is not initiated at this stage, the pulp becomes necrotic and infection spreads beyond the confines of the tooth into the peri-radicular area resulting in apical periodontitis that subsequently dissects along the path of least resistance and erupts through the skin. Clinically, odontogenic fistulae show as erythematous and smooth nodules, with or without drainage. The chronic lesion often leads to retraction of skin secondary to scarring. A cord-like tract can be felt attached to the underlying bony structure and patients can experience intermittent remission of symptoms. Intra-oral examination may reveal dental caries or restorations and periodontal disease, but the examiner should keep in mind that the tooth involved can appear normal [11–13]. On sonography, they appear as hypoechoic tracts with rich–debris echoes that connect the skin layers with the bony margins of the upper maxillae or mandible. There is generally an erosion of the cortical bone at the connecting site. Increased blood flow is detected in the periphery of the fistula [14, 15] (Figs. 20.8 and 20.9).

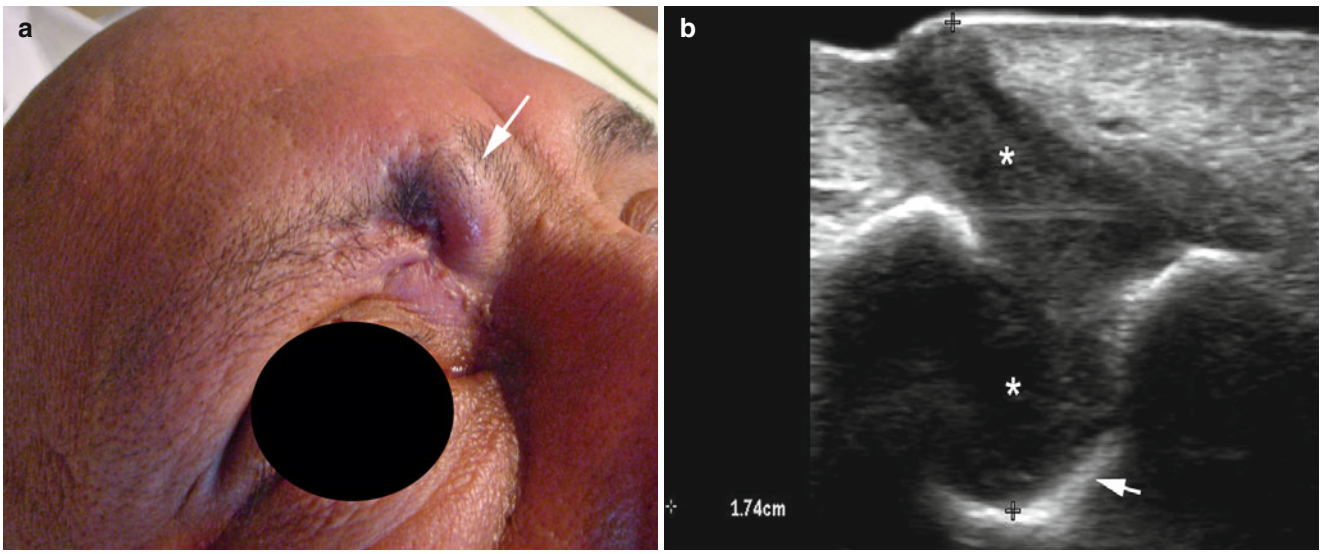

Fig. 20.7 (**a**, **b**) Frontal sinocutaneous fistula. (**a**) Clinical photograph demonstrates an erythematous lump (*arrow*) in the right fronto-nasal region. (**b**) Grey scale ultrasound image (transverse view) shows a 1.74 cm deep hypoechoic fistulous tract (*) that connects the subepidermal region to the bony margin of the skull. Notice the scalloping of the bony margin (*arrow*)

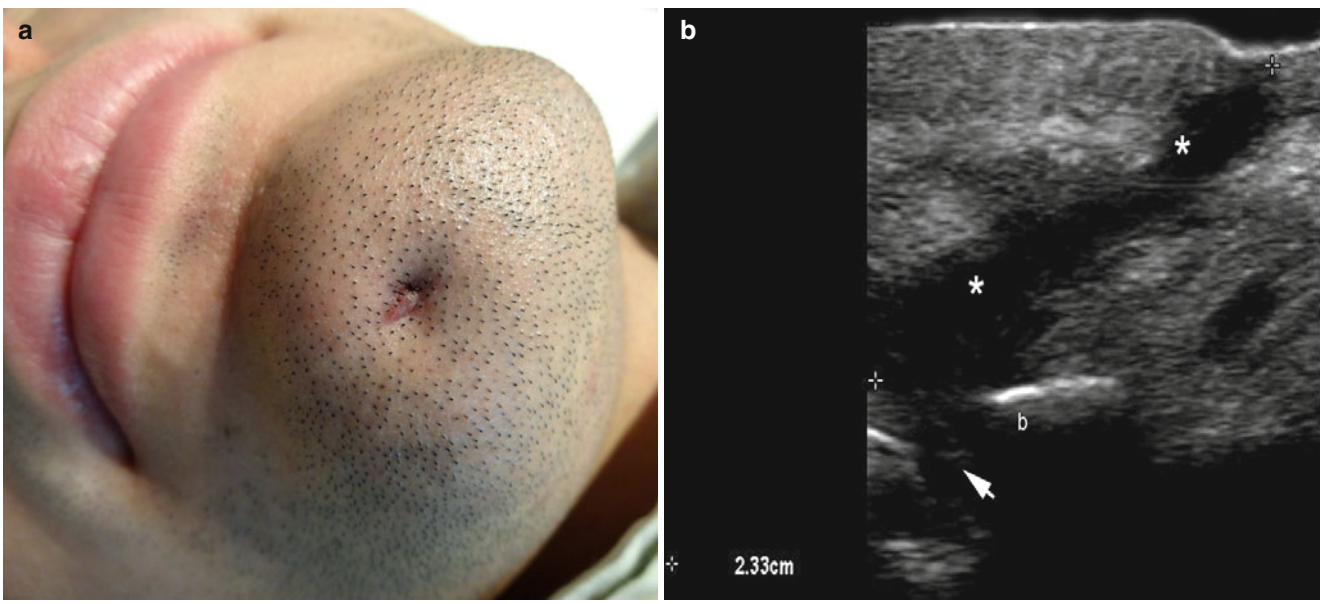

Fig. 20.8 (**a**, **b**) Odontogenic fistula. (**a**) Clinical image shows a depressed erythematous scar-like lesion in the right aspect of the chin. (**b**) Grey scale ultrasound image (longitudinal view) demonstrates a 2.3 cm deep hypoechoic fistulous tract (*) that connects the subepidermal region to the bony margin of the mandible. Notice the erosion of the bony margin (*arrow*)

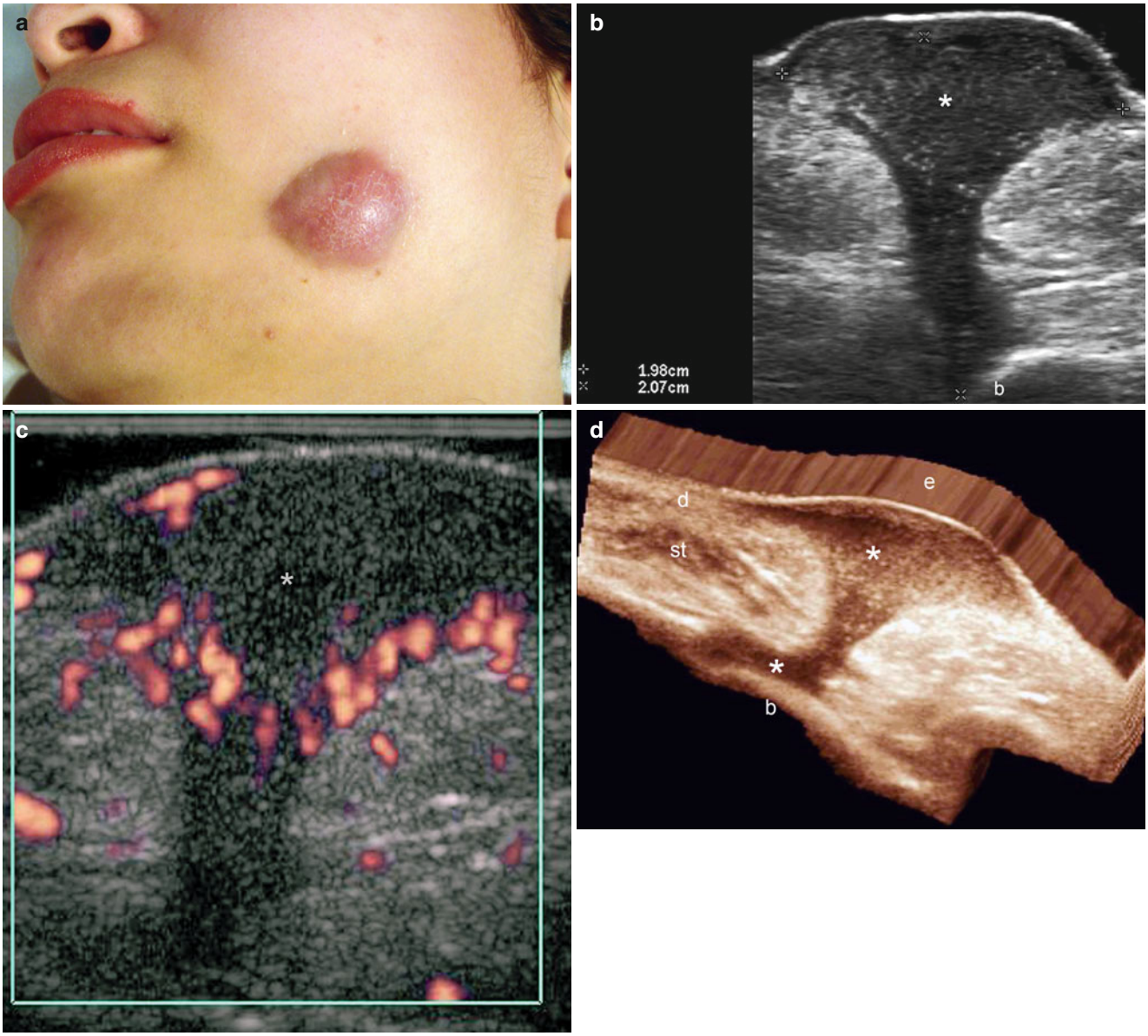

Fig. 20.9 (**a**–**d**) Odontogenic fistula. (**a**) Clinical photograph shows a reddish swelling in the left cheek. (**b**) Grey scale ultrasound image (longitudinal view) demonstrates a 1.98 cm (wide)×2.07 cm (deep) hypoechoic fistulous tract (*) that connects the subepidermal area with the bony margin of the mandible (*b*). Notice the widening of the fistula in the dermis and the rich debris echoes within the tract. (**c**) Color Doppler ultrasound image (transverse view) shows increased blood flow in the periphery of tract. (**d**) 3D reconstruction (grey scale, longitudinal view) highlights the fistulous tract (*) and the connection to the bony margin of the mandible (*b*). *Abbreviations*: *e* epidermis, *d* dermis, *st* subcutaneous tissue

20.2.3 Congenital Cysts

20.2.3.1 Thyroglossal Cyst

Thyrodglossal cysts are one of the most common congenital neck masses occurring in children, representing approximately 70 % of the congenital lesions that occur in the neck [16, 17]. Thyroglossal cysts are composed of a remnant thyroglossal duct that extends from the foramen caecum at the base of the tongue to the pyramidal lobe of the thyroid gland and involutes by the eighth week of gestation. Remnants of a portion of the duct can lead to cyst formation or ectopic thyroid tissue. Thyroglossal cysts typically affect children and young adults. Clinically, they present as painless palpable masses at the anterior neck that can be found at any level from the base of the tongue to the isthmus of the thyroid gland. Most of the cysts are located in the midline at the hyoid level or infrahyoid. The cysts become enlarged secondary to infection and can present as tender or erythematous nodules or masses in the neck that can be clinically confused with skin lesions. On sonography, intact tyroglossal cysts appear as well-defined, thin-walled, single anechoic masses with posterior acoustic enhancement. A thyroglossal cyst that presents with mixed echogenicity (anechogenicity-hypoechogenicity or thick walls), septae, or a multilocular appearance suggests inflammation and/or infection. Thus, in the latter cases, increased blood flow can be found in the periphery of the cyst on color Doppler ultrasound [18–21] (Fig. 20.10).

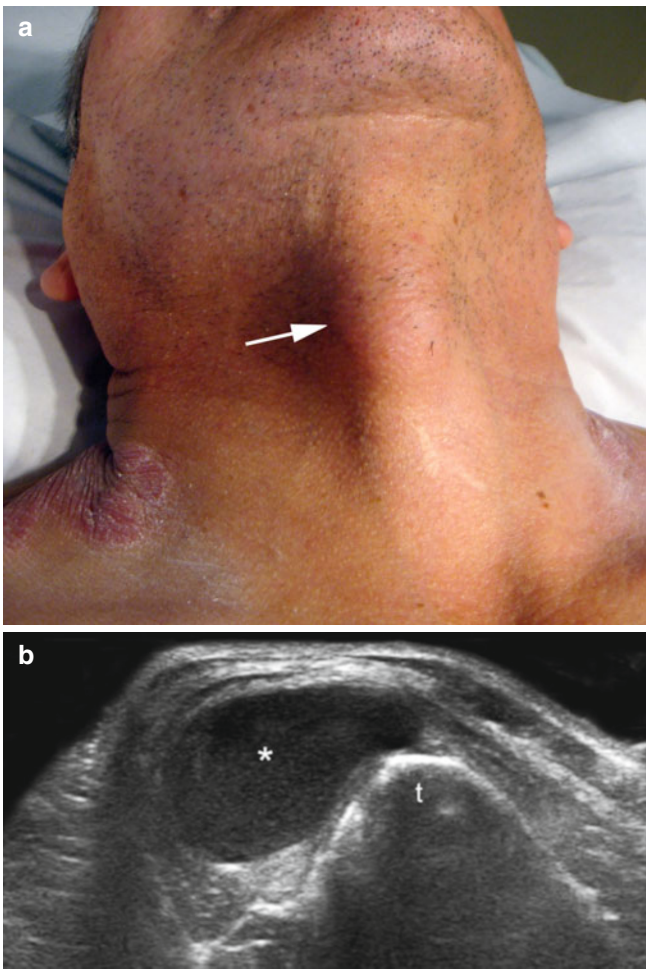

Fig. 20.10 (**a**, **b**) Thyroglossal cyst. (**a**) Clinical photograph demonstrates a palpable lump in the right aspect of the neck (paratracheal region) in a patient with psoriasis. (**b**) Grey scale ultrasound image (transverse view) shows a well-defined oval-shaped anechoic cystic structure (*) attached to the right aspect of the hyoid bone (*t*)

20.2.3.2 Branchial Cysts

Branchial cysts are congenital anomalies and are important lesions to consider in the differential diagnosis of head and neck masses in children. They are composed of a heterogeneous group of congenital malformations that occur from incomplete obliteration of pharyngeal clefts and pouches during embryogenesis. Although present at birth, many abnormalities do not become evident until later in infancy or childhood. Moreover, it is common for branchial anomalies to become infected, causing significant morbidity [22]. The branchial system is composed of six branchial arches separated by five branchial clefts and appears by the 15th day of gestation. Incomplete obliteration of the branchial apparatus, predominately the cleft, is postulated to lead to branchial cleft anomalies such as cysts, sinuses, or fistulae. Most of the cysts (75 %) develop along the course of the second branchial cleft, however, they can affect any branchial cleft. Clinically, they most commonly present in children and young adults as palpable masses in the lateral neck, located anterior to the sternocleidomasteideous muscle, and close to the angle of the mandible. On sonography, intact branchial cysts appear as well-defined, thin-walled and anechoic fluid-filled cysts. Under inflammation or infection, branchial cysts can present hypoechogenicity with internal debris, heteroechogenicity, thick walls, septae, and increased vascularity in the periphery. Posterior acoustic enhancement can be seen in most branchial cysts (70 %) [20–23] (Fig. 20.11).

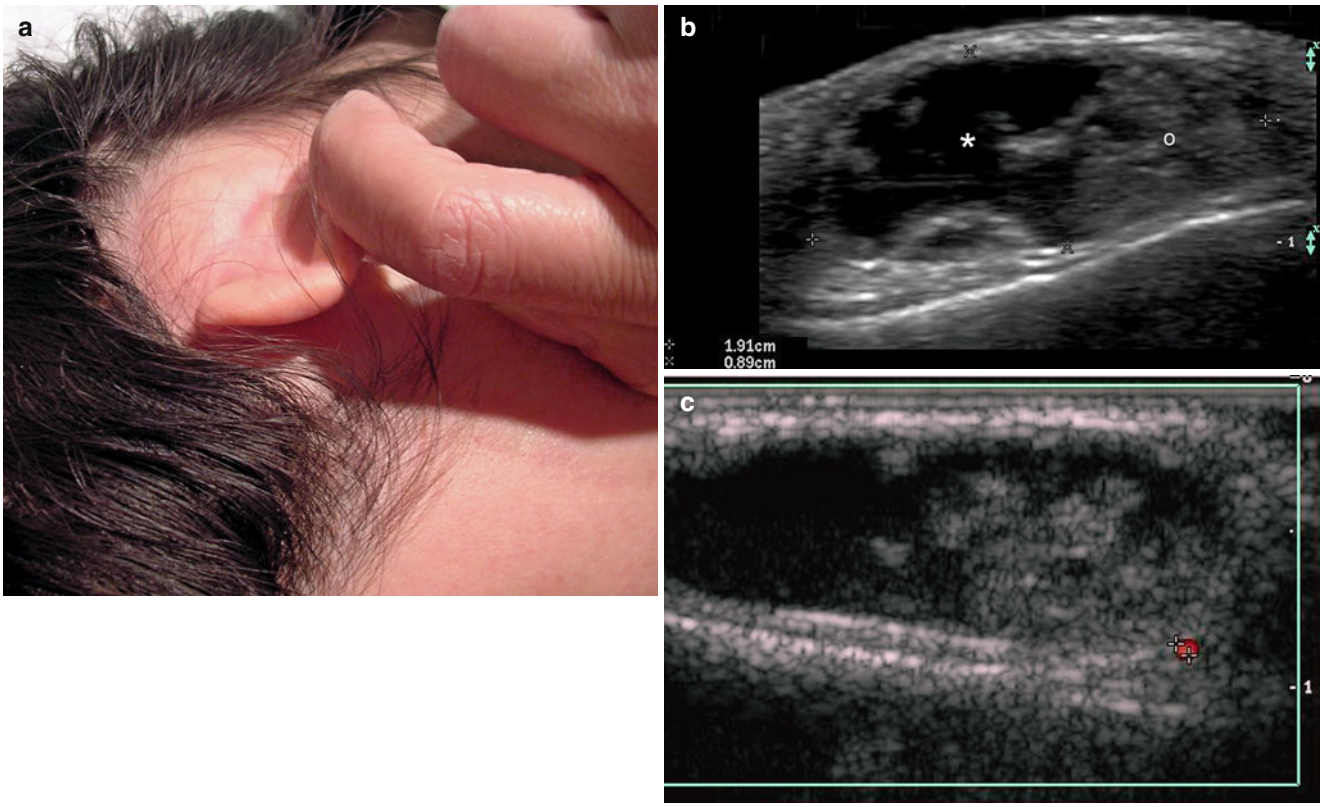

Fig. 20.11 (**a**–**c**) Branchial cyst. (**a**) Clinical photograph shows swelling in the right retroauricular region. (**b**) Grey scale ultrasound image (transverse view) demonstrates a 1.91 cm (transverse axis)×0.89 cm (depth), well-defined, oval-shaped, anechoic subcutaneous and dermal structure (*) with thick walls that contains prominent echoes (*o*, debris). (**c**) Color Doppler ultrasound image (transverse view) shows lack of vascularity within the cyst and a small vessel (between markers) in the vicinity

20.2.4 Vessels

20.2.4.1 Arteries

20.2.4.1.1 Variants

Caliber Persistent Artery of the Lip

This is a vascular anomaly in which a primary artery penetrates the submucosal tissue without division or caliber loss. Clinically, this anatomical variant can generate painless erythematous, blue or skin-colored papules sometimes ulcerated that can occasionally simulate malignant pathology, and bleed easily. Caliber persistent arteries are most commonly reported in the lower lip and can vary in size and pulsatility. Differential diagnoses include other vascular lesions such as vascular malformations or hemangiomas as well as mucoceles, irritative fibromas, sclerosing sialoadenitis, and cutaneous basal and squamous cell carcinoma, among others. On sonography, the thick anechoic tubular, and sometimes serpiginous, arterial tract can be detected in the submucosal tissue crossing the orbicularis oris and usually presenting low velocity flow on color Doppler spectral curve analysis [14, 24, 25] (Fig. 20.12).

20.2.4.1.2 Inflammation

Giant Cell Temporal Arteritis

This is a benign inflammatory vasculopathy that affects large- and medium-sized arteries of the head and involves the temporal artery and its branches (parietal and frontal). Giant cell arteritis is a disease affecting middle-aged and older persons, with a reported incidence of 30 cases per 100,000 patients per year among individuals older than 70 years. The diagnosis of the disease is often suspected from clinical

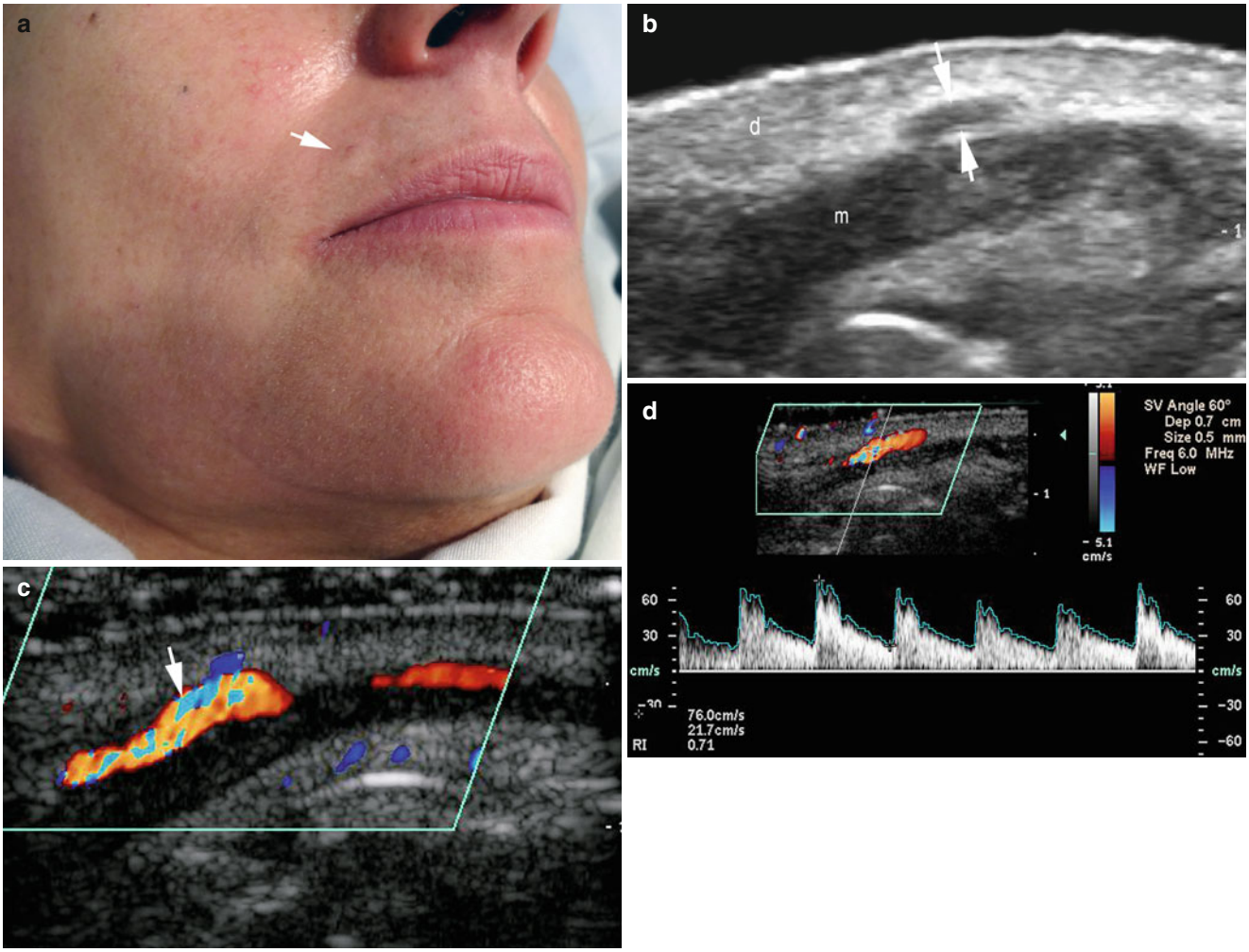

Fig. 20.12 (**a**–**d**) Caliber persistent artery of the lip. (**a**) Clinical image shows a tiny erythematous lump in the right border of the upper lip. (**b**) Grey scale ultrasound image (transverse view) shows a prominent hypoechoic duct (*arrows*) in the dermis of the upper lip. (**c**) Color Doppler ultrasound image (transverse view) presents the vascular nature of the duct (*arrow*). (**d**) Color Doppler spectral curve analysis shows high peak systolic arterial velocity (76 cm/s) within the vessel. *Abbreviations*: *d* dermis, *m* orbicularis oris muscle of the upper lip

symptoms such as localized headache and temporal artery tenderness in older individuals. The condition can occasionally present as swelling in the temple region. Biopsy can confirm diagnosis and shows the segmental involvement of the arterial walls and its periphery with mononuclear cells (histiocytes and lymphocytes), granulomatous inflammatory infiltration, and giant cells. In the final stages, necrosis and destruction of the internal elastic lamina and fibrosis can be seen. Nevertheless, biopsy can be risky and difficult to perform, and sonography has been reported to have a high accuracy for diagnosing giant cell arteritis. On sonography, the pathognomonic sign is the presence of a segmental, and occasionally bilateral, hypoechoic halo surrounding the anechoic arterial tract. This halo is expected to be related to the presence of edema and inflammatory infiltration in the arterial wall and its periphery. Additionally, focal areas of stenosis and/or occlusion have been described that seem to present an atherosclerosis origin most commonly seen in older individuals, and are not specific signs for diagnosing giant cell arteritis [26, 27] (Fig. 20.13).

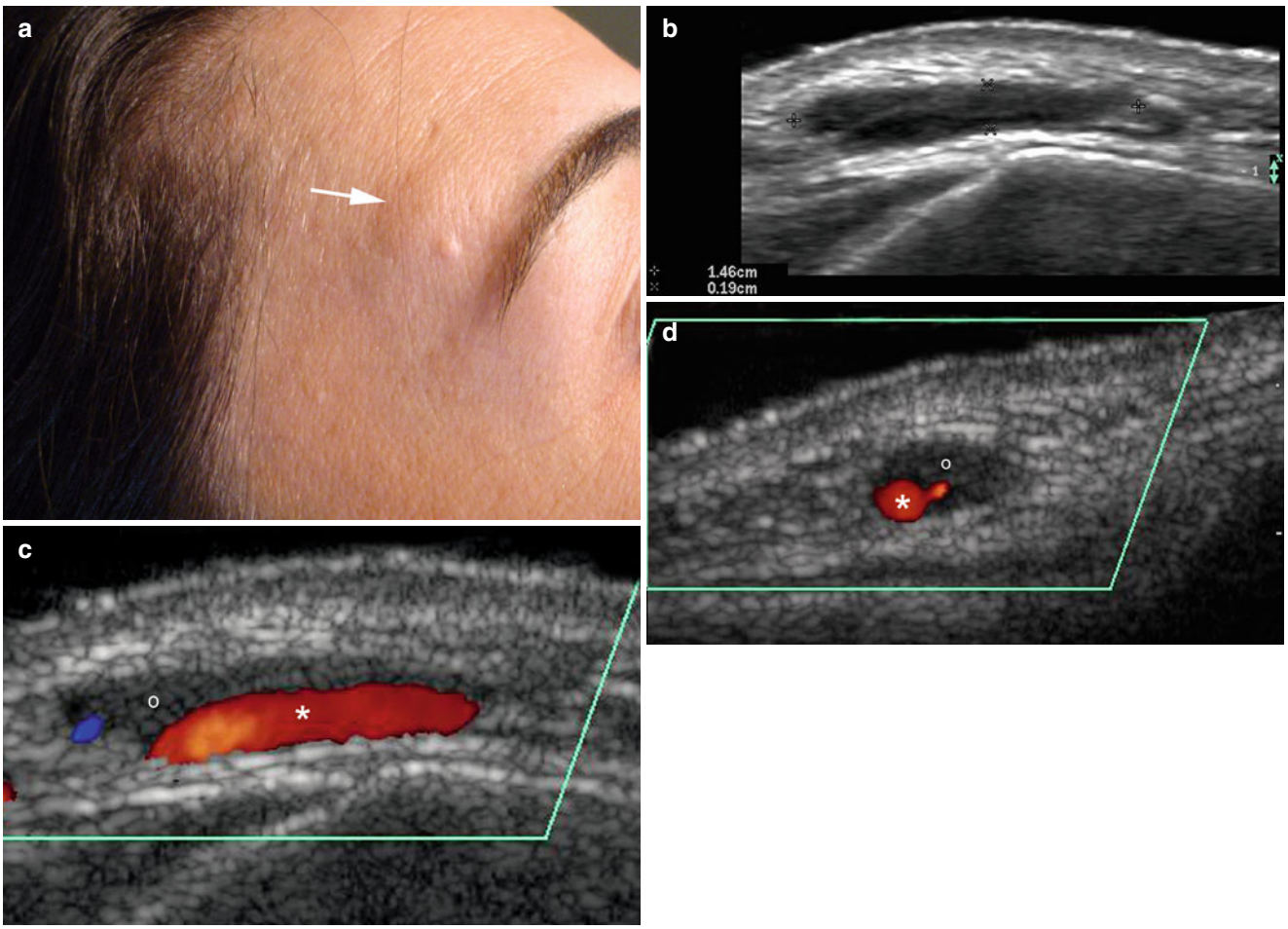

Fig. 20.13 (**a**–**d**) Giant cell temporal arteritis. (**a**) Clinical photograph demonstrates swelling (*arrow*) in the right temple region. (**b**) Grey scale ultrasound image (longitudinal view) shows a 1.46 cm (long) × 0.19 cm (deep) well-defined hypoechoic dilated tubular structure (between markers) in the subcutaneous tissue. (**c**) Color Doppler ultrasound image (longitudinal view) demonstrates blood flow within the structure (*) that corresponds to the frontal branch of the superficial temporal artery. Notice the hypoechoic tissue (*o*) attached to the vessel. (**d**) Color Doppler ultrasound image (transverse view) shows the hypoechoic halo (*o*) that surrounds the artery (*)

20.2.4.1.3 Abnormal Dilation

Pseudoaneurysm

Also called false aneurysm, is a leakage of arterial blood into the surrounding tissue through a persistent connection between the originating artery and the resultant adjacent sac-like hematic cavity. These contained ruptures of the arterial vessels are usually secondary to trauma or invasive procedures such as surgeries, punctures, or catheterizations. Clinically, they present as a firm, occasionally pulsatile swelling. Thus, the palpation of the pulse in the surface of the pseudoaneurysm is not a permanent clinical finding because of the presence of partial thrombosis filling the lumen of the neo-cavity. On sonography, there is a anechoic or hypoechoic oval-shaped sac-like structure connected to a feeding vessel. Turbulent "to-and-fro" type of blood flow at the neck, and arterial flow within the cavity of the pseudoaneurysm, can be detected on color Doppler, and can be mixed with avascular partially or totally thrombosed areas. Ultrasound-guided compression therapy of the pseudoaneurysm is a treatment option that seems effective in the early phases [28, 29] (Fig. 20.14).

20.2.4.2 Veins

20.2.4.2.1 Superficial Thrombophebitis

Superficial thrombophlebitis most commonly affects varicose veins and rarely non-varicose veins [30]. This condition

is characterized by a thrombus that fills the lumen of a subcutaneous vein(s) associated with an inflammatory process in the walls of the vessel and/or surrounding tissues. The superficial thrombosis affects the veins located in the lower extremities, including the plantar region [31]. Clinically, it can appear as a painful or tender erythematous, blue or skin-colored swelling or cord-like structure that can mimic vascular lesions or fibromatous entities. Associations with local trauma, excessive exercise, and paraneoplastic conditions have been reported. On sonography, there are single or multiple dilated and non-compressible subcutaneous venous tracts that show hypoechoic thrombotic material filling their lumen. On color Doppler ultrasound, the affected vessel(s) does not show blood flow (Fig. 20.15).

Mondor's Disease

Also called acute or sclerosing thrombophlebitis of superficial veins, it has been reported in the breast, anterior thoracic/abdominal wall, and penis. It appears clinically as a palpable, painful cord associated with erythema or discoloration of the overlying skin that can mimic a cutaneous scleroderma (morphea). This condition is usually most commonly found in women and presents a self- limited course that tends to

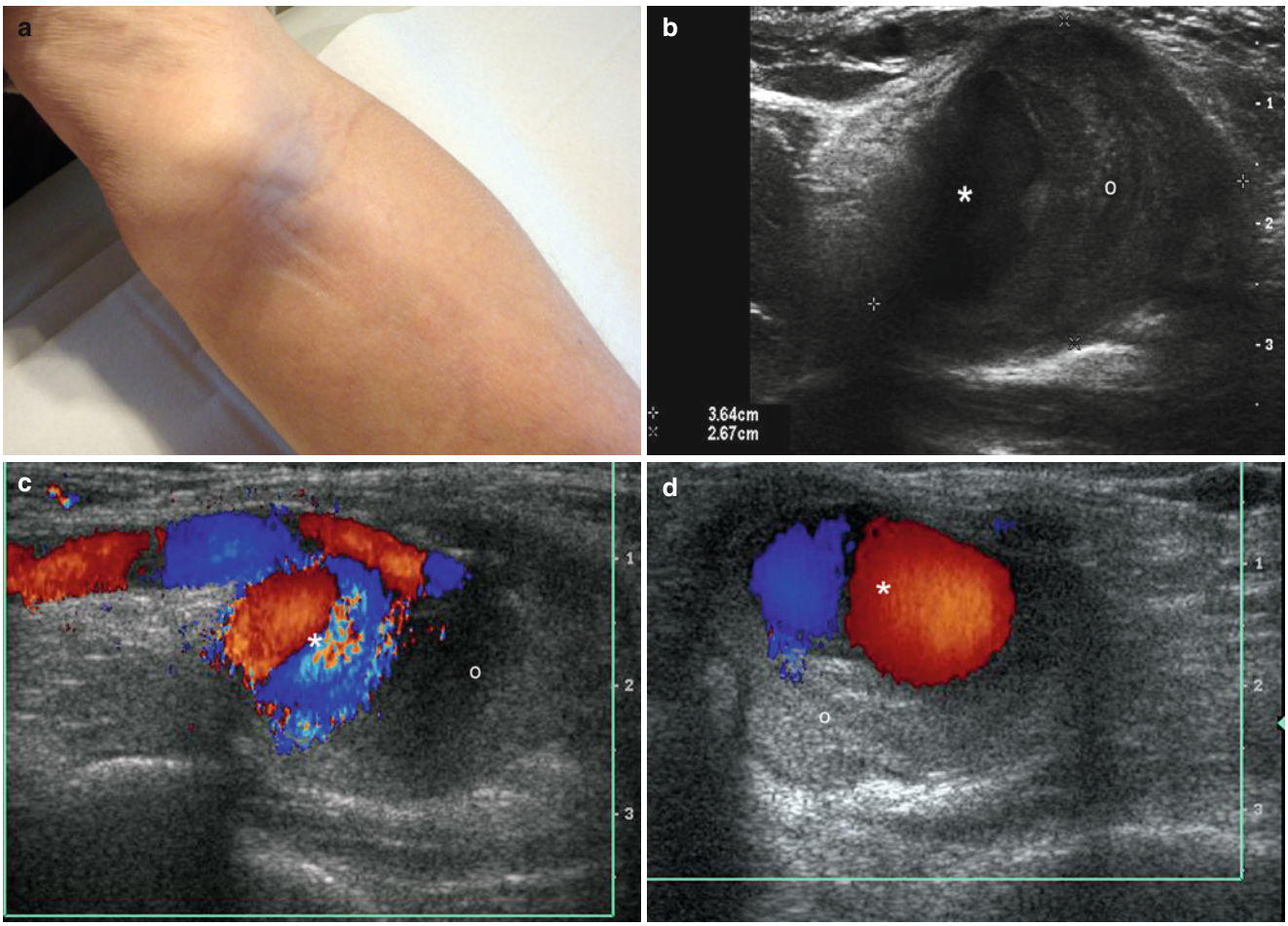

Fig. 20.14 (**a**–**d**) Pseudoaneurysm. (**a**) Clinical photograph shows swelling in the anterior aspect of the left elbow. (**b**) Grey scale ultrasound image (longitudinal view) demonstrates a 3.64 cm (long)×2.67 cm (deep) oval-shaped structure in the subcutaneous tissue. Notice the mixed echogenicity with anechoic (*) and hypoechoic (*o*) areas. (**c**) Color Doppler ultrasound image (longitudinal view) shows prominent and turbulent blood flow (*) within the structure that connects with an arterial vessel. The hypoechoic area (*o*) corresponds to thrombotic material within the pseudoaneurysm. (**d**) Color Doppler ultrasound image (transverse view) highlighting the central blood flow (*) and the thrombotic material (*o*) in the periphery

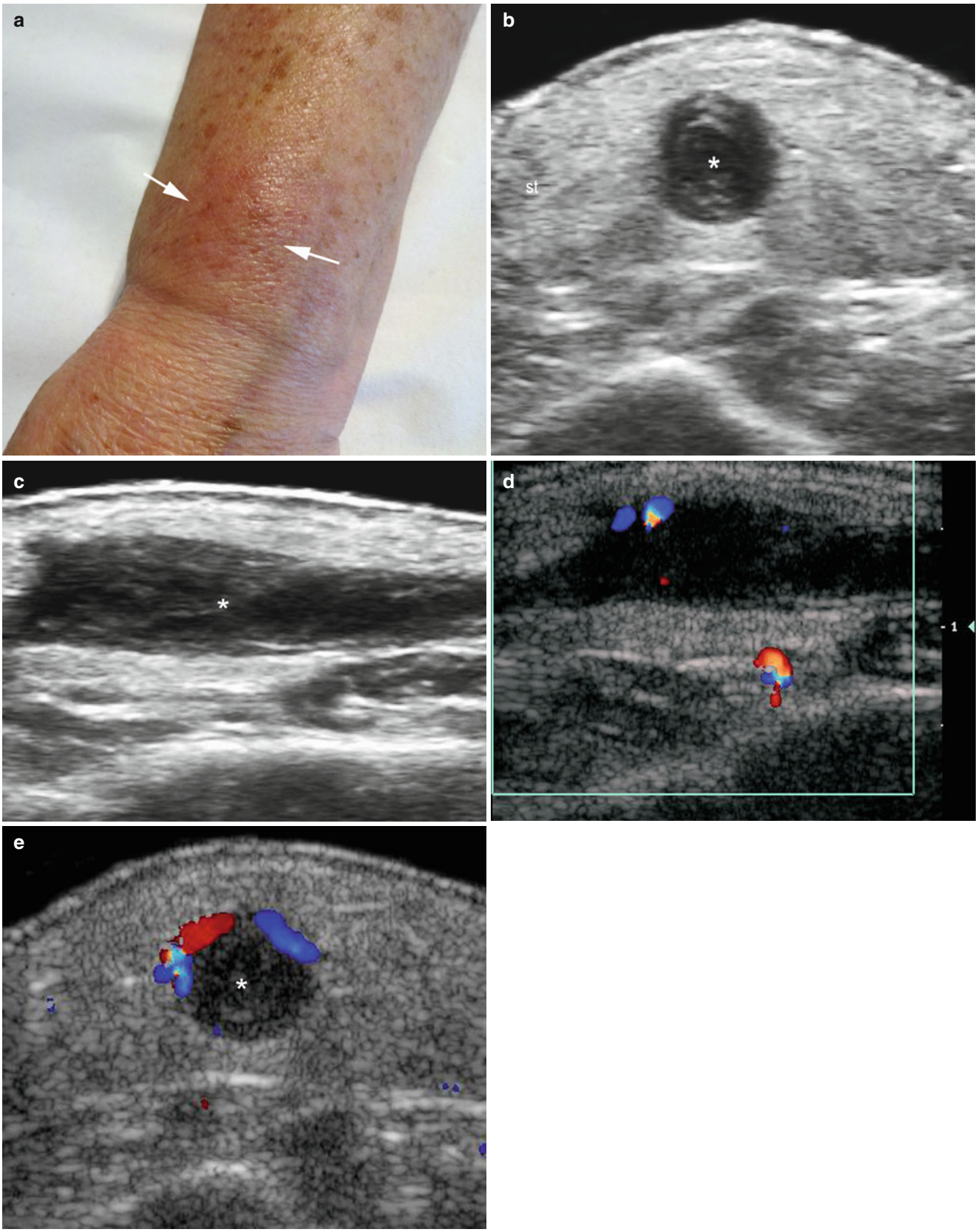

Fig. 20.15 (**a**–**e**) Superficial thrombophebitis. (**a**) Clinical photograph depicts erythema and swelling (*arrows*) in the distal part of the dorsal right forearm. (**b**, **c**) Grey scale ultrasound images (**b** transverse view; **c** longitudinal view) demonstrate a dilated venous vessel (*) with hypoechoic thrombotic endoluminal material. There is increased echogenicity of the surrounding subcutaneous tissue (edema). (**d**, **e**) Color Doppler ultrasound images (**d** longitudinal view; **e** transverse view) demonstrate lack of vascularity within the vessel (*) and increased blood flow in the wall of the vessel

resolve during the following days or weeks and/or with the use of anti-inflammatory topical medication. On sonography, a non-compressible, hypoechoic, tubular venous structure in the subcutaneous tissue is detected. The lumen is filled with hypoechoic thrombotic material and no flow is detectable on color Doppler imaging [14, 32, 33] (Figs. 20.16 and 20.17).

20.2.4.2.2 Insufficiency of Perforant Veins

The incompetence of perforant (i.e., veins that connect the deep venous system and cutaneous layers crossing the fascial planes) can generate swelling, ulcers, and hyperpigmentation changes in the skin. On sonography, the incompetent perforant veins appear as dilated and tortuous venous vessels usually associated with reflux flow during the Valsalva maneuver. This insufficiency can be confused with Pyoderma Gangrenosum, a rare ulcerative inflammatory cutaneous condition that clinically presents as chronic and painful ulcerations associated with inflammatory bowel diseases, arthritis, monoclonal gammopathies, or cancer. In the latter condition, superficial veins are frequently normal or can show thickening of the walls of the veins in the presence of phlebitis. Additionally, inflammatory changes in the subcutaneous tissue (hyperechogenicity) can be seen [14, 34] (Fig. 20.18).

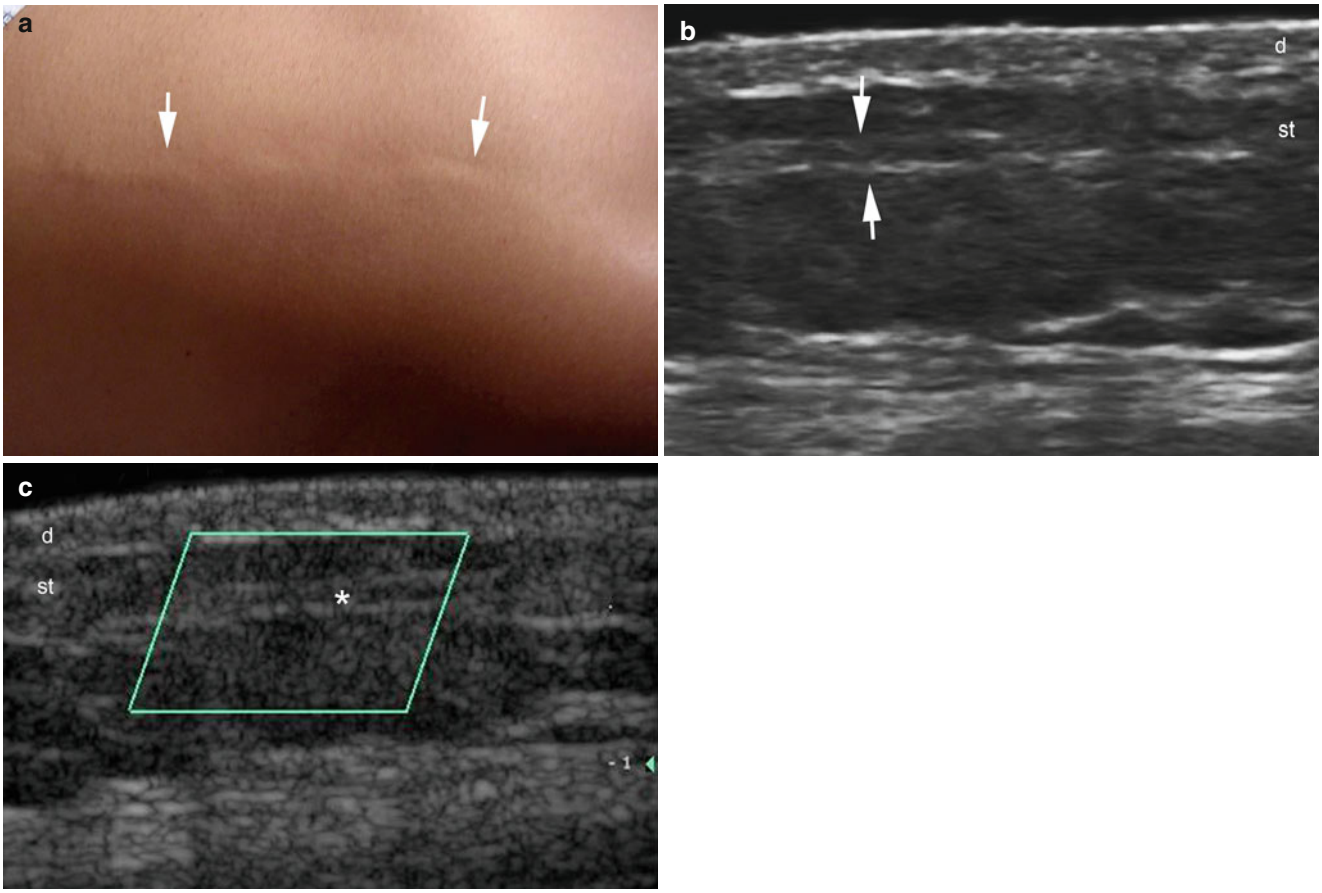

Fig. 20.16 (**a**–**c**) Mondor's disease. (**a**) Clinical image demonstrates a cord-like band (*arrows*) in the right aspect of the abdominal wall. (**b**) Grey scale ultrasound image (longitudinal view) shows a dilated subcutaneous vessel (*arrows*) with hypoechoic thrombotic material filling the lumen. (**c**) Color Doppler ultrasound image (longitudinal view) depicts lack of vascularity within the vessel (*). *Abbreviations*: *d* dermis, *st* subcutaneous tissue

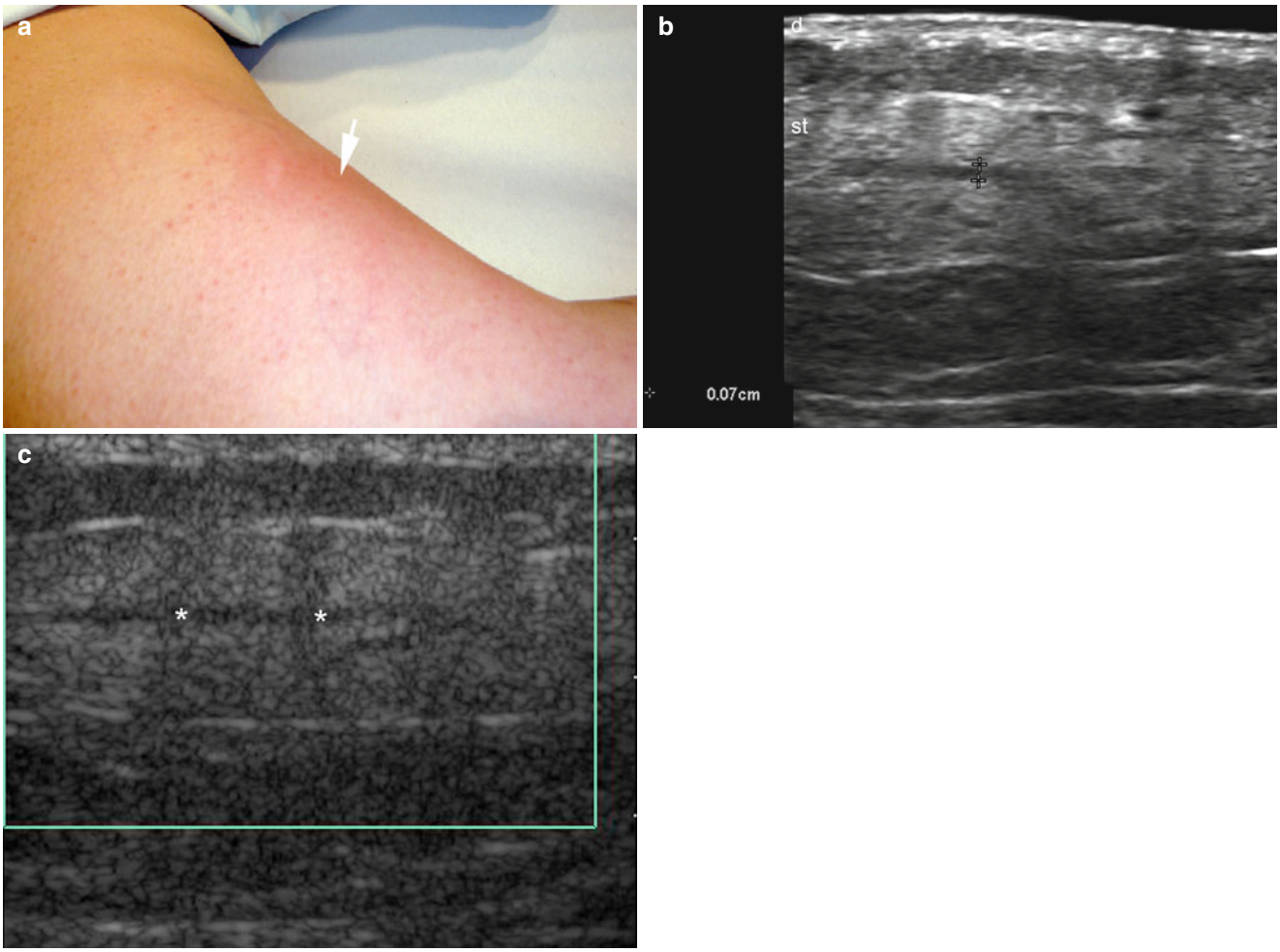

Fig. 20.17 (**a**–**c**) Mondor's disease. (**a**) Clinical image shows erythema (*arrow*) in the lateral aspect of the left flank. (**b**) Grey scale ultrasound image (longitudinal view) demonstrates a 0.7 mm (thickness) dilated, non-compressible and hypoechoic subcutaneous vessel (*, between markers). Increased echogenicity of the subcutaneous tissue in the periphery of the vessel also was detected. (**c**) Color Doppler ultrasound image (longitudinal view) shows the lack of vascularity within the vessel (*). *Abbreviations*: *d* dermis, *st* subcutaneous tissue

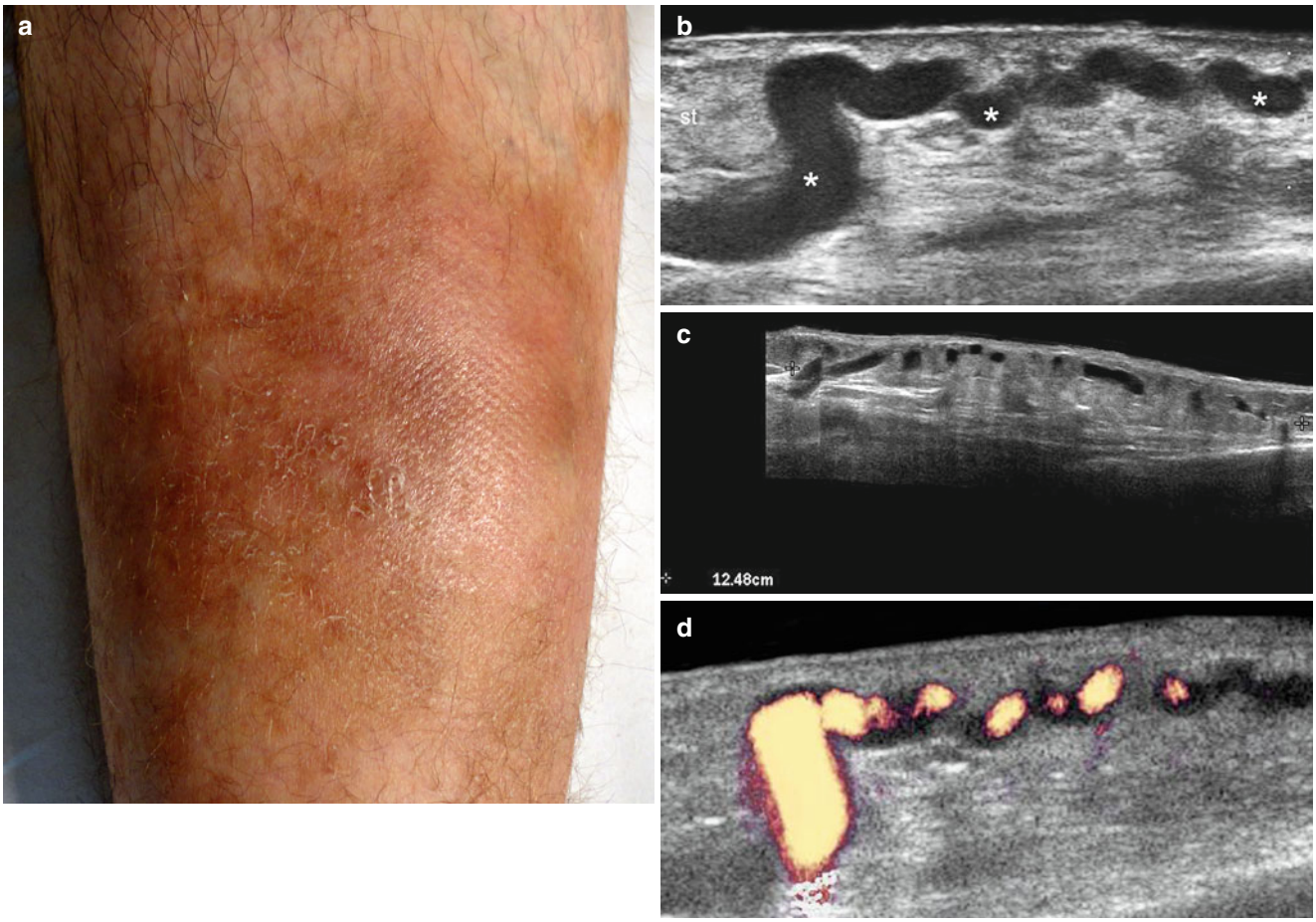

Fig. 20.18 (**a**–**d**) Insufficiency of perforant veins. (**a**) Clinical image showing pigmentation and swelling in the anterior aspect of the left leg. (**b**, **c**) Grey scale ultrasound images (**b** zoomed longitudinal view; **c** extended field of longitudinal view) show dilated and tortuous, anechoic, venous vessels (*) in the subcutaneous tissue. (**d**) Power Doppler ultrasound image depicts venous reflux under Valsalva maneuver. *Abbreviation*: *st* subcutaneous tissue

20.2.5 Nerves

20.2.5.1 Carpal Tunnel Syndrome

Carpal tunnel syndrome (CTS) is the most frequent type of peripheral entrapment neuropathy and is most commonly seen in individuals who perform repetitive motion at the wrist, pregnant women, and patients with diabetes or arthritis. Clinically, CTS presents as pain, numbness, a tingling sensation of the fingers excluding the little finger, and loss of sensation in the hands and fingers.

The following are some criteria for diagnosis CTS using sonography:

1. Abnormalities in the median nerve:
   - Swelling in the proximal tunnel
   - Nerve flattening in the distal tunnel
   - Nerve thickening (cross-sectional area in the transverse axis greater than 10 mm^2). The normal area of the nerve is usually less than 10 mm^2 (indirect method-ellipsoid area) or greater than 9 mm^2 (direct method-continuous boundary trace)
   - Decreased echogenicity of the nerve with loss of the fascicular pattern
   - Vascularity within the neural fascicles
2. Abnormalities in the flexor retinaculum:
   - Bulging of the volar flexor retinaculum (distance from the retinaculum to a line that joins the tip of the hook of the hamate and the tubercle of the trapezium greater than 4 mm is abnormal)
   - Thickening of the flexor retinaculum in comparison with the contralateral side
3. Abnormalities in the carpal tunnel content
   - Enlargement of the flexor tendons most commonly related to tenosynovitis
   - Tunnel-occupying lesions such as volar ganglia or synovial cysts

A high correlation has been reported between the electrophysiological and sonographic changes as well as between the blood flow on color Doppler and severity grading of this condition [14, 35–38] (Fig. 20.19).

20.2.5.2 Benign Peripheral Neurogenic Tumors

20.2.5.2.1 Neurofibromas and Schwannomas

Neurogenic tumors can be divided into two main types: *neurofibromas* and *schwannomas* (neurilemomas). Clinically they often show as a painless or tender swelling or lump in the upper or lower limbs. Sonographic differentiation among the

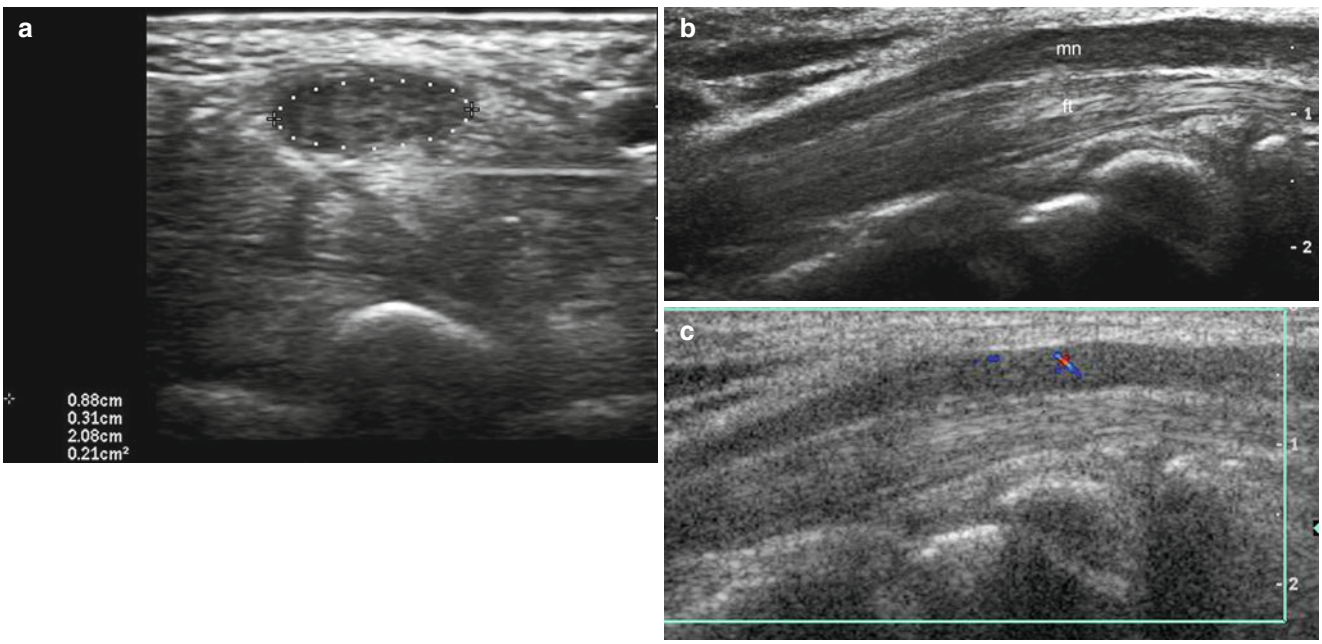

Fig. 20.19 (**a**–**c**) Carpal tunnel syndrome. (**a**, **b**) Grey scale ultrasound images (**a** transverse view; **b** longitudinal view) demonstrate a median nerve (*mn*) with increased thickness and area (21 mm^2). (**c**) Color Doppler ultrasound image (longitudinal view) shows increased vascularity within the nerve

types is difficult and both can appear as oval-shaped hypoechoic and sometimes lobulated structures with posterior acoustic transmission. Hyperechoic focal spots resulting from calcium deposits and anechoic areas secondary to myxoid cystic degeneration are usually more common in schwannomas. Identification of a nerve (hypoechoic tract with a fascicular pattern) entering and exiting a mass is virtually pathognomonic for a peripheral nerve sheath tumor, although is seen in rare instances. An eccentric relationship with the parent nerve is suggestive of a schwannoma, whereas a centric relationship commonly would not be distinguishable between the two tumors. On color Doppler ultrasound, blood flow is variable (from hypo to hypervascular) and hypervascularity has been reported in both schwannomas and neurofibromas [39–41] (Figs. 20.20 and 20.21).

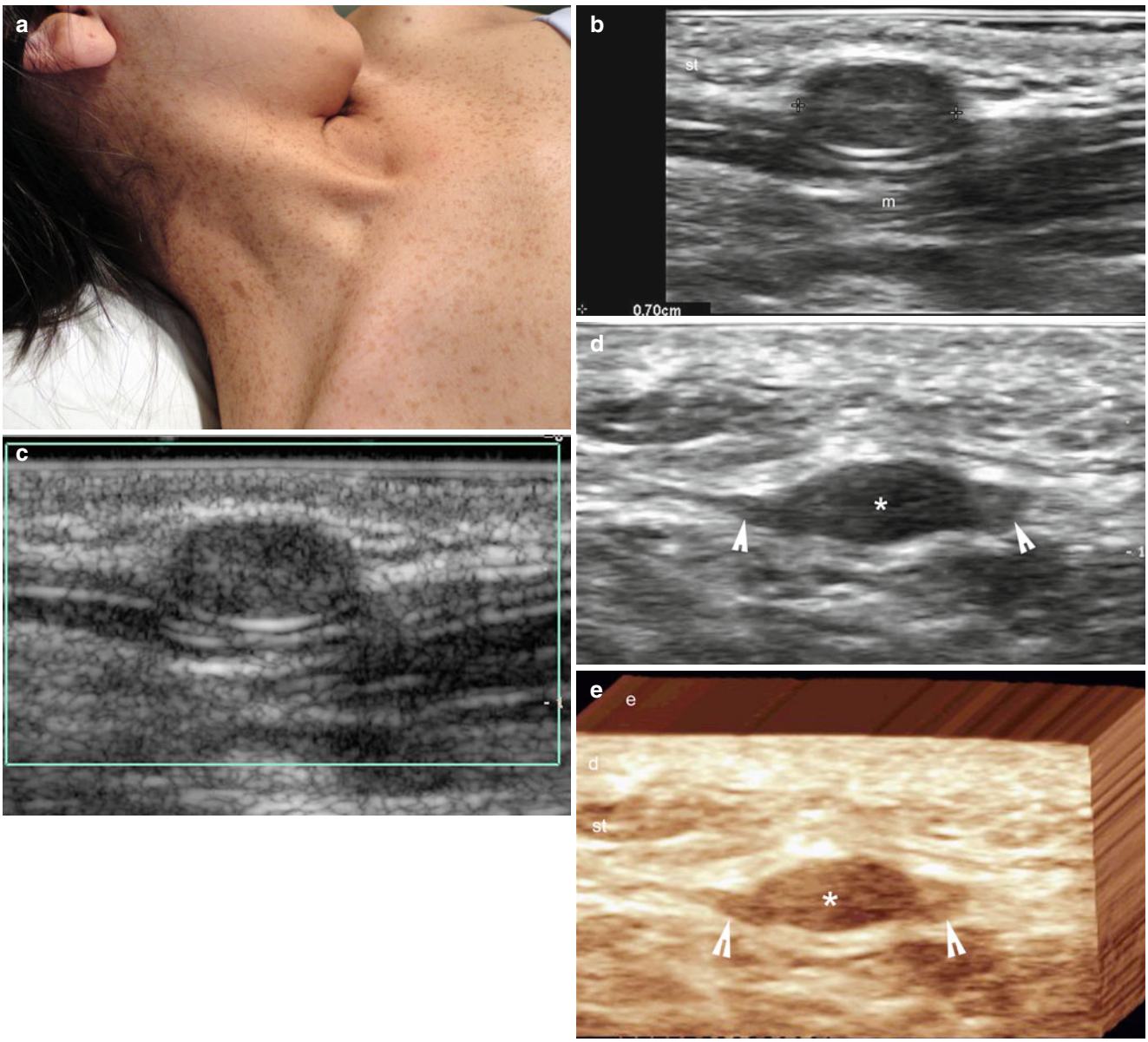

Fig. 20.20 (**a**–**e**) Neurofibromatosis. (**a**) Clinical photograph of patient who presented with neurofibromatosis type I. Several "café-au-lait" spots and palpable lumps in the right aspect of the neck and gluteal regions are seen. (**b**) Grey scale ultrasound image (longitudinal view, right aspect of the neck) demonstrates a 7.0 mm well-defined, oval-shaped, hypoechoic solid subcutaneous nodule (between markers). The nodule elicits a mild extrinsic compression of the sternocleidomastoid muscle (*m*). (**c**) Color Doppler ultrasound image (longitudinal view, same location of figure **b**) shows lack of vascularity of the nodule. (**d**) Grey scale ultrasound image (longitudinal view, medial aspect of the right gluteal region) demonstrates a well-defined, oval-shaped, hypoechoic solid subcutaneous nodule (*). Notice the afferent and efferent tracts (*arrowheads*) to the nodule. (**e**) 3D ultrasound reconstruction highlights the nodule (*) and the afferent and efferent tracts (*arrowheads*). *Abbreviations*: *d* dermis, *st* subcutaneous tissue

20.2.5.2.2 Morton's Neuroma

Morton's neuroma is a reactive and mechanically induced degenerative neuropathy of a plantar digital nerve. It does not correspond to a true tumor because it has a perineural fibrotic reaction with vascular proliferation and axonal degeneration. Morton's neuromas are most commonly seen in middle-aged women in the third interdigital nerve, although they can affect any web space. Clinically, Morton's neuroma presents as a painful condition on the feet (i.e., metatarsalgia) that can limit the quality of life. On sonography, it appears as a hypoechoic ill- or well-defined ovoid, hypoechoic mass oriented parallel to the long axis of the metatarsals structures, most commonly hypovascular on color Doppler. Concomitant intermetatarsal bursitis has been reported and can be detected as anechoic and compressible fluid sacs attached to the neuromas. Dynamic maneuvers during the sonography examination can be necessary to detect and displace the Morton's neuroma that is anchored in the web space and includes dorsal or plantar compression using the digit of the examiner and the probe, respectively. A dorsal approach with the probe is preferred because the skin is thin in this region in comparison with the plantar zone that presents a thick epidermis mainly because of the prominent stratum corneum. Ultrasound can also be helpful for guiding the percutaneous treatments used for this condition [42–44] (Fig. 20.22).

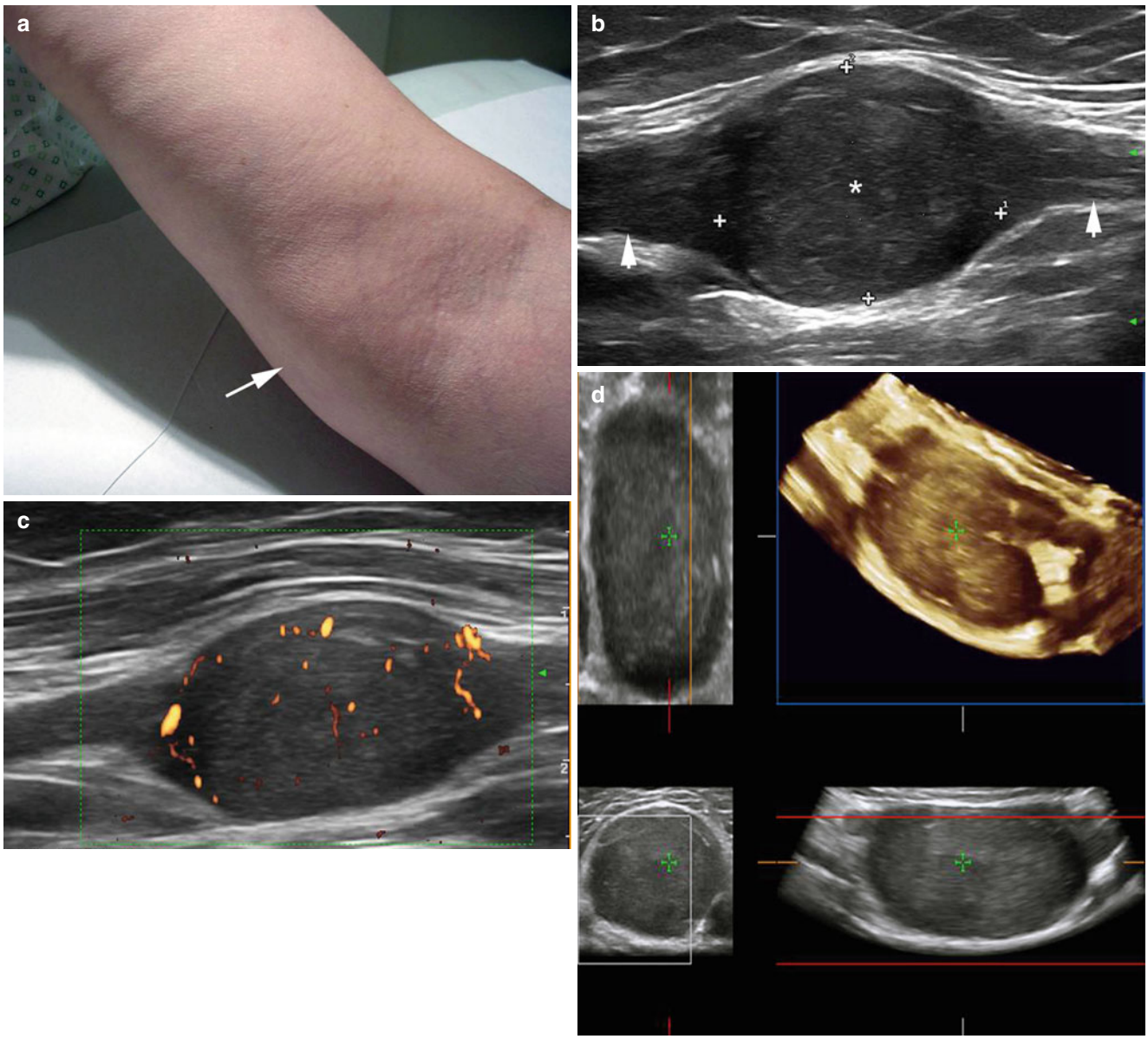

Fig. 20.21 (**a**–**e**) Schwannoma. (**a**) Clinical photograph demonstrates a lump (*arrow*) in the medial aspect of the left elbow. (**b**) Grey scale ultrasound image (longitudinal view) shows a well-defined, oval-shaped hypoechoic subcutaneous nodule (*, between markers) that presents afferent and efferent tracts (*arrowheads*). (**c**) Power Doppler ultrasound image depicts increased blood flow within the nodule. (**d**) Sagittal, coronal, transverse, and 3D reconstructions of the nodule. (**e**) Sonoelastography of the nodule shows a soft pattern suggestive of benignancy

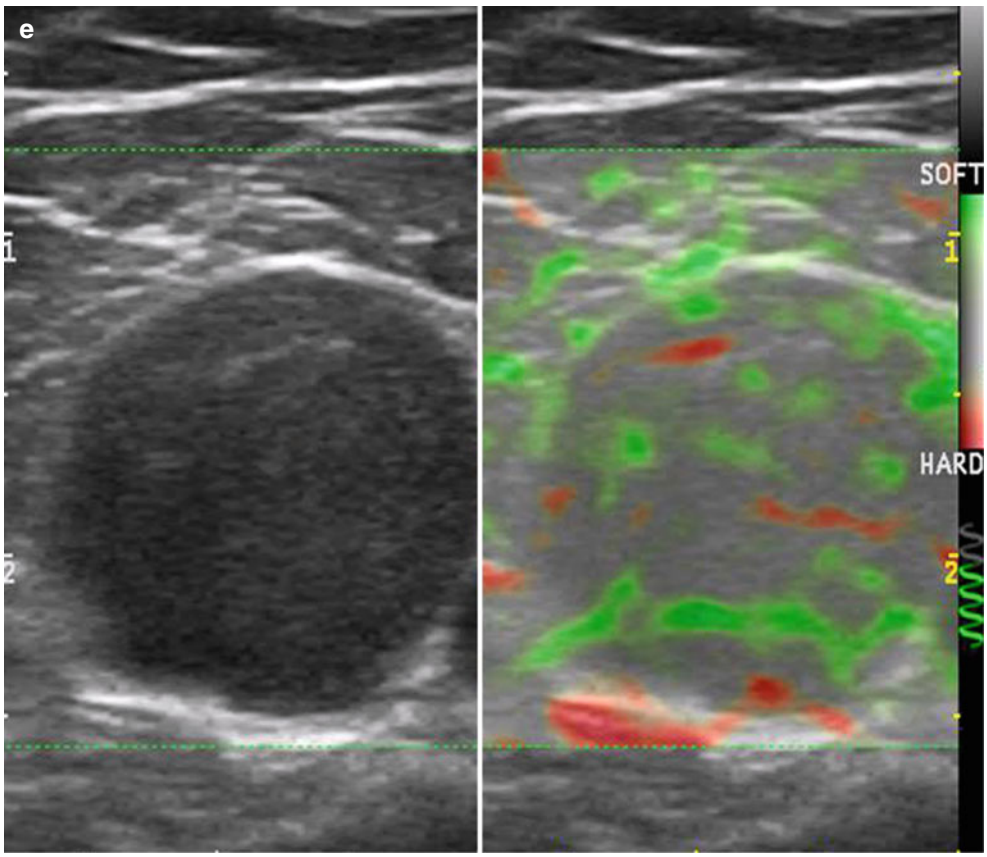

Fig. 20.21 (continued)

20.2.6 Salivary Glands

20.2.6.1 Inflammation

Clinically, the inflammation of the salivary glands (i.e., sialadenitis) can elicit a painful or painless, uni- or bilateral swelling in the facial or submandibular regions. Acute sialadenitis can be viral (e.g., mumps infection) or bacterial in origin, related to a parotid or submandibular calculi or systemic disease causing immunosuppression. On sonography of acute inflammation, the salivary gland enlarges and appears hypoechoic or heterogenous, sometimes with blurry margins (Fig. 20.23). Increased vascularity within the gland can be seen using color Doppler ultrasound. Sonographic detection of a concomitant calculus in the gland or duct, sometimes with dilated intraglandular ducts, can explain the acute and/or recurrent episodes of inflammation. The stones appear as hyperechoic spots within the glands or ducts because of their calcium component. Salivary stones are most commonly formed in the submandibular rather than in the parotid gland. Thus, the submandibular duct, also called Wharton's duct or submaxillary duct, is much thinner than the parotid duct and extends from the submandibular gland to the posterior edge of the mylohyoid muscle, curves around the muscle, then enters the sublingual space on the surface of the mylohyoid muscle, and finally drains into the sublingual papilla. The parotid duct is also called Stensen's duct and passes through the buccal fat, buccopharyngeal fascia, and buccinator muscle and opens into the vestibule of the mouth next to the maxillary second molar tooth. Recurrent infections can cause gland atrophy and fibrous tissue replacement of the normal gland. The parotid gland can also be involved with chronic infectious and non-infectious granulomatous diseases such as sarcoidosis and Sjögren's syndrome. Infective causes of granulomatous parotitis include mycobacterial infection, actinomycosis, and histoplasmosis. Tuberculous parotitis typically presents as painless enlargement of an involved intraparotid lymph node, although diffuse enlargement of the whole gland can occur. Sjögren's syndrome is

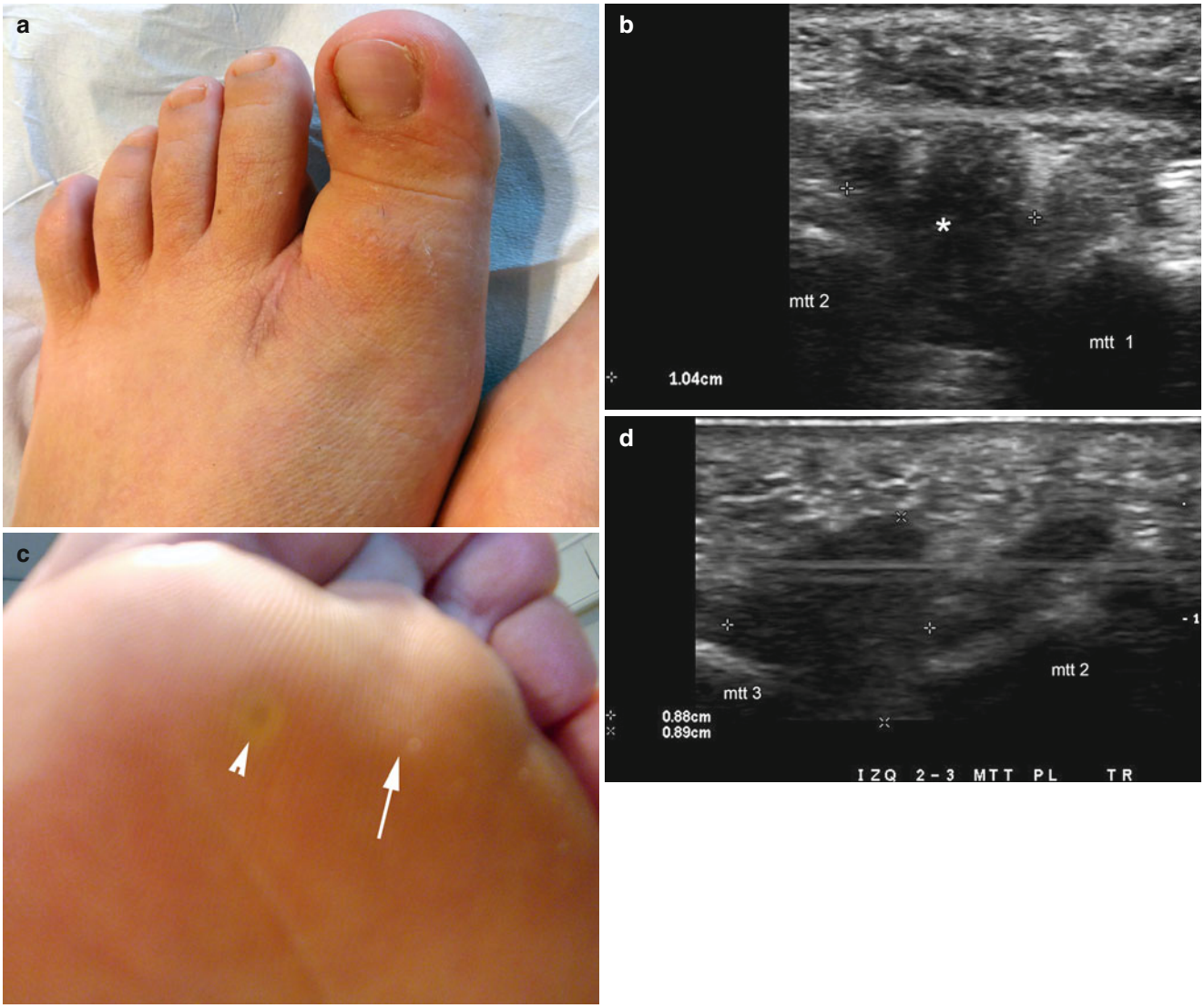

Fig. 20.22 (**a**–**d**) Morton's neuroma. (**a**) Clinical image of a patient that presented with a history of corrective surgery and excruciating pain in the first intermetatarsal space of the right foot. (**b**) Grey scale ultrasound image (transverse view, same patient of figure **a**) demonstrates a 1.04 cm (wide), ill-defined lobulated hypoechoic solid structure (*) in the space between the first and second metatarsal bones. (**c**) Clinical image of a patient that presented with a plantar wart (*arrowhead*) and excruciating pain in the second metatarsal space (*arrow*) of the left foot. (**d**) Grey scale ultrasound image (transverse view, same patient of figure **c**) shows a 8.8 mm (wide)×8.9 mm (long) ill-defined lobulated hypoechoic solid structure in the space between the second and third metatarsal bones. *Abbreviation*: *mtt* metatarsal bone

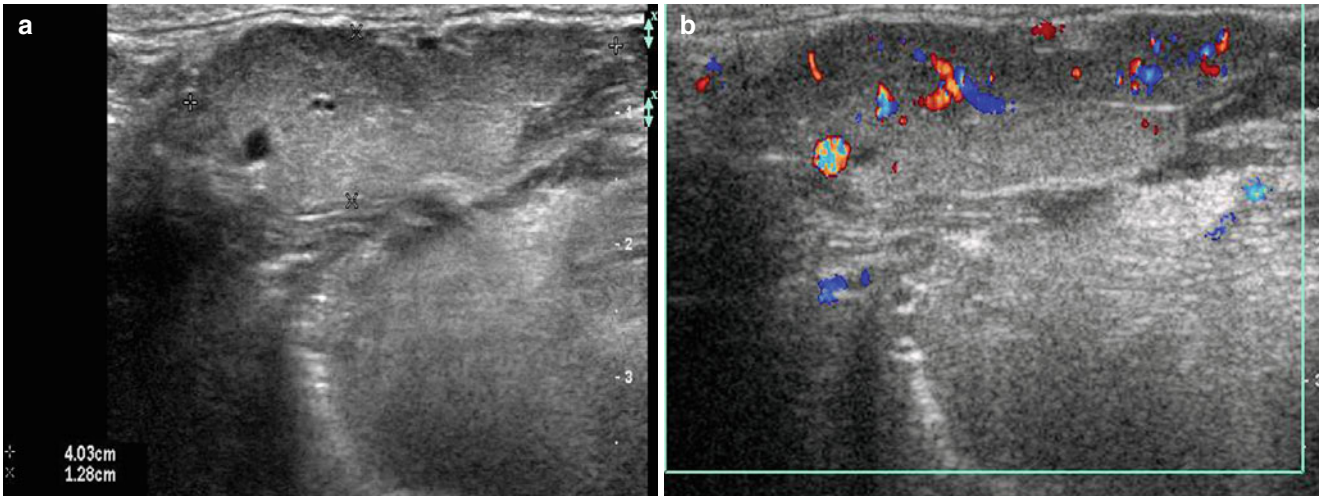

Fig. 20.23 (**a**, **b**) Sialadenitis. (**a**) Grey scale ultrasound image (transverse view) shows diffuse enlargement of the right submandibular gland. (**b**) Color Doppler ultrasound image (transverse view) demonstrates increased vascularity within the submandibular gland

an auto-immune disease presenting with a typical triad of keratoconjunctivitis sicca, xerostomia, and auto-immune disorder. In the early stages, the gland can appear normal on ultrasound but later the gland enlarges, appearing of heterogeneous echotexture, and multiple 2–3 mm hypoechoic foci are observed. The hypoechoic areas, also seen in other chronic inflammatory conditions of the salivary glands, represent areas of non-obstructive sialectasis and large, septated cysts can also develop before the end-stage atrophic phase. In acute inflammatory diseases, sonography can help to differentiate between obstructive or non-obstructive sialoadenitis. Abscess formations can be detected, the maturation of the colliquation can be controlled, and can be punctured using ultrasound guidance [45–47] (Fig. 20.24).

20.2.6.2 Tumors

20.2.6.2.1 Pleomorphic Adenomas

Most of parotid tumors are benign and 85–90 % of the lesions correspond to *pleomorphic adenomas*, which are thought to occur from myoepithelial cells. Clinically, they present as slow-growing, painless masses in middle-aged patients and the majority occur in the superficial lobe of the gland. On sonography, pleomorphic adenoma typically appears as a round-shaped, well-circumscribed, sometimes lobulated and hypoechoic structure with posterior acoustic enhancement. On color Doppler ultrasound, pleomorphic adenomas can demonstrate a, internal and peripheral "basket-like" pattern of flow. As pleomorphic adenomas enlarge, they can develop more atypical characteristics with internal heterogeneity, cystic changes, poor defined margins, and internal hyperechoic spots resulting from calcifications (Figs. 20.25 and 20.26).

20.2.6.2.2 Warthin's Tumor (Cystadenolymphoma)

Warthin's tumor is the second most common benign tumor of the parotid gland and arises from heterotopic parotid tissue within parotid lymph nodes. This tumor is most common in elderly males and tends to occur in the superficial lobe near the angle of the mandible. The tumors present a bilateral or multiple appearance in 10–15 % of cases. On sonography,

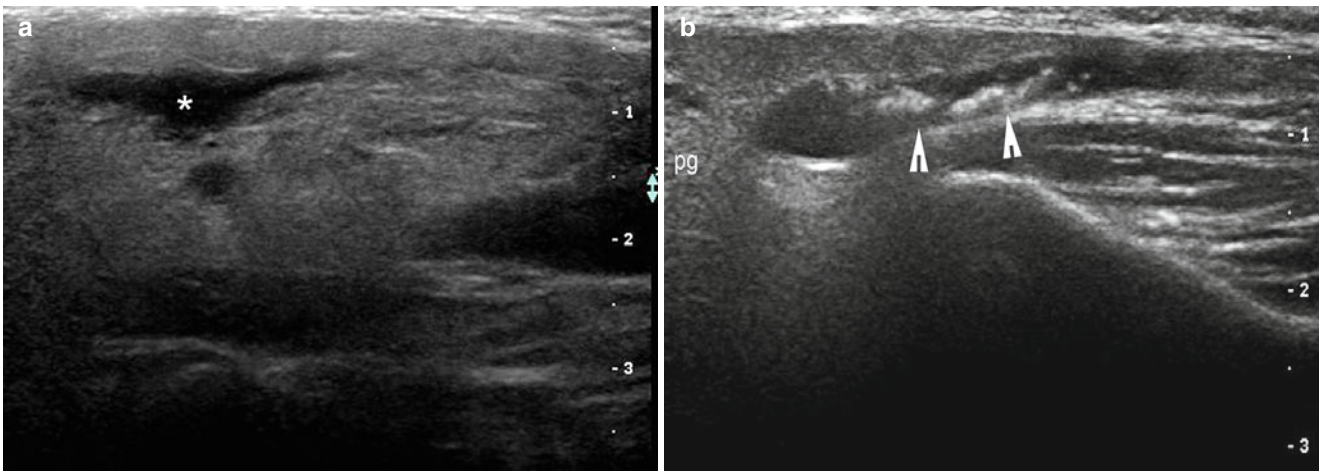

Fig. 20.24 (**a**, **b**) Sialadenitis, ductal ectasia and stones of the parotid gland. (**a**) Grey scale ultrasound image (longitudinal view) demonstrates enlargement and ductal ectasia (*) of the right parotid gland. (**b**) Grey scale ultrasound image (transverse view) shows dilation of the main parotid duct that contains multiple hyperechoic stones (*arrowheads*). *Abbreviation*: *pg* parotid gland

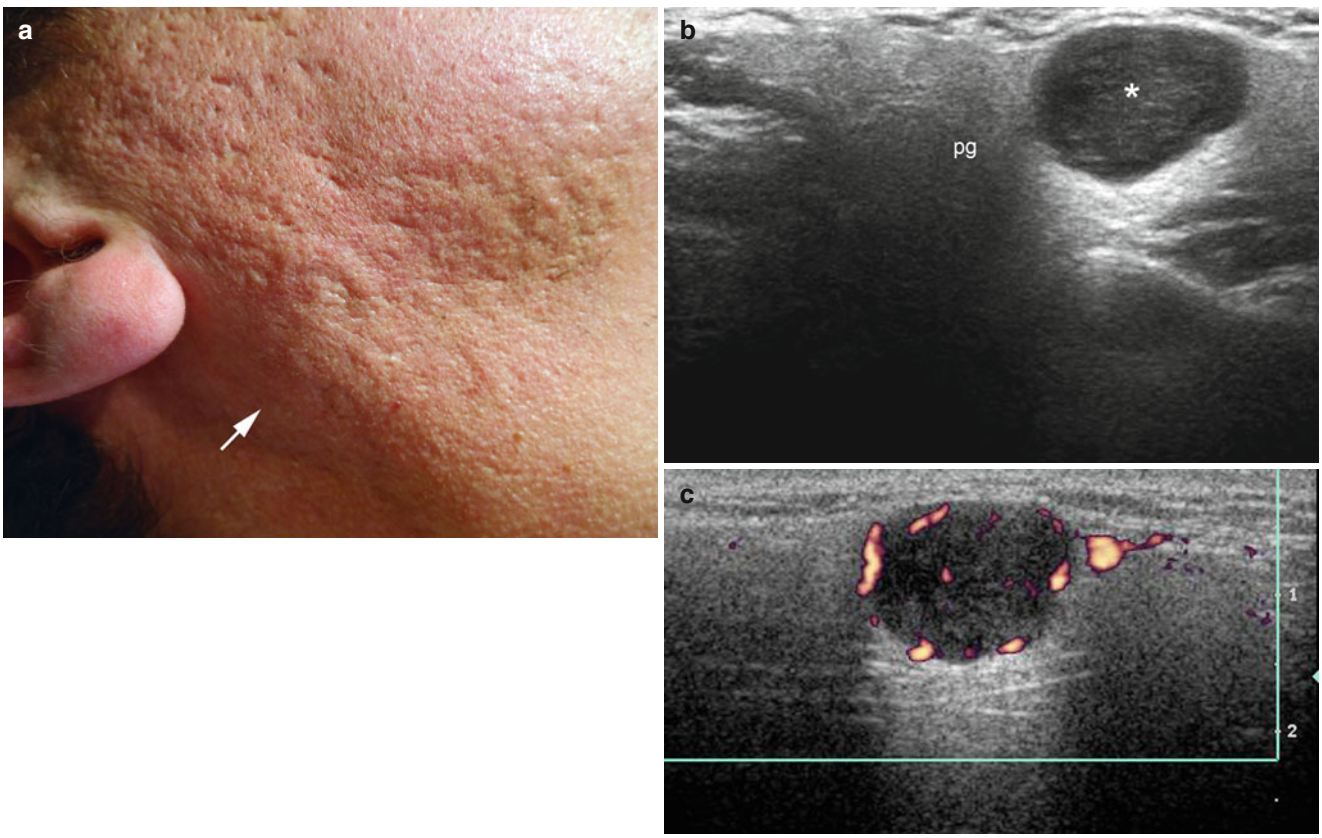

Fig. 20.25 (**a**–**c**) Pleomorphic adenoma. (**a**) Clinical image of a patient that presented with a palpable lump (*arrow*) in the right infra-auricular region. The patient also had several atrophic acne scars. (**b**) Grey scale ultrasound image (transverse view) shows a well-defined oval-shaped hypoechoic nodule (*) in the right parotid gland that bulges into the subcutaneous tissue. (**c**) Power Doppler ultrasound image (transverse view) demonstrates increased blood flow within the nodule. *Abbreviation*: *pg* parotid gland

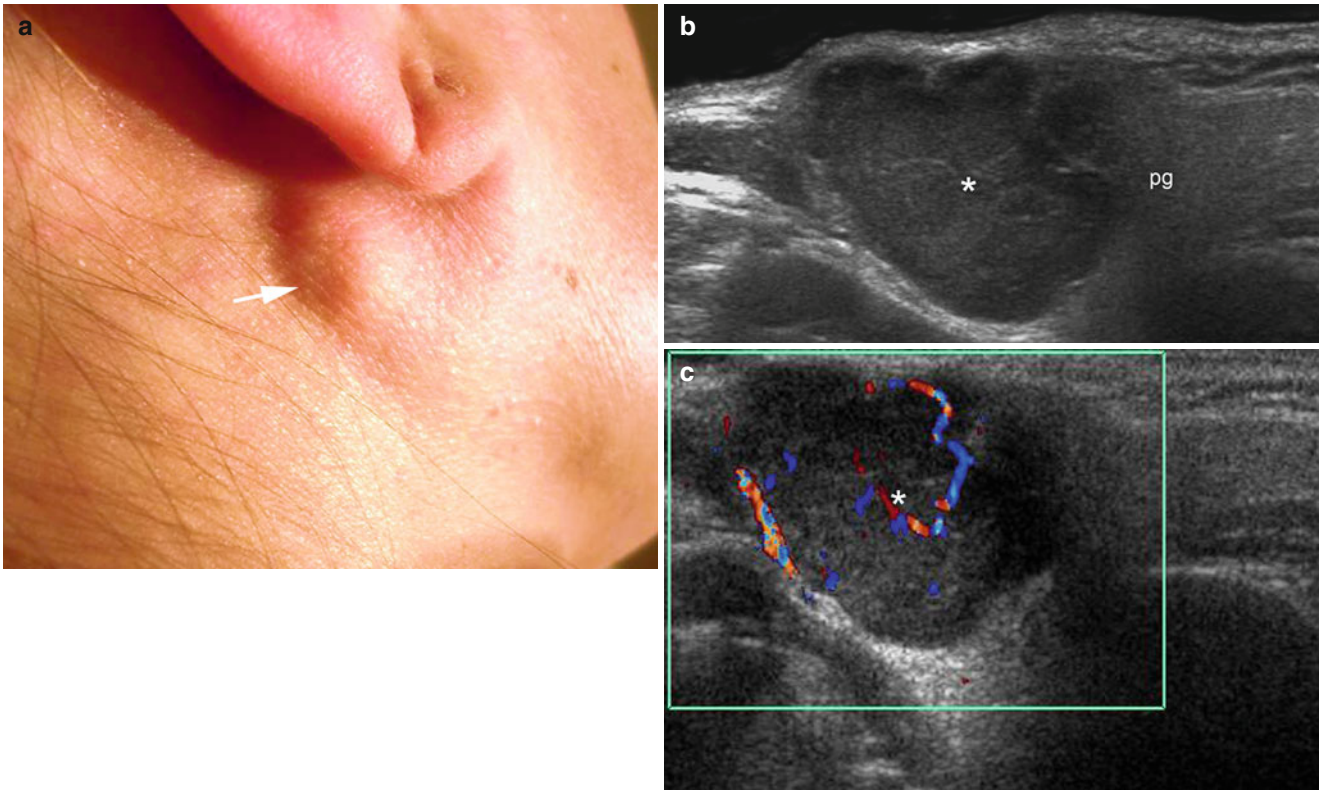

Fig. 20.26 (**a**–**c**) Pleomorphic adenoma. (**a**) Clinical photograph shows a lump (*arrow*) in the right infra- and retro-auricular region. (**b**) Grey scale ultrasound image (transverse view) demonstrates a well-defined lobulated hypoechoic solid structure (*) in the posterior part of the right parotid gland. The mass bulges into the subcutaneous tissue. (**c**) Color Doppler ultrasound image (transverse view) shows increased vascularity within the tumor (*). *Abbreviation*: *pg* parotid gland

Warthin's tumors appear as rounded or lobulated, well-circumscribed masses with internal anechoic cystic changes and septae (Fig. 20.27).

20.2.6.2.3 Intraparotid Lipomas

Intraparotid lipomas are benign fibro-fatty tumors that appear on ultrasound as oval-shaped, well-defined hypoechoic and avascular masses with appearance similar to the lipomatous tumors detected in the rest of the body (Fig. 20.28).

Sonographic pre-surgical anatomical support can provide relevant information about these tumors that could help in avoiding complications such as injuries of the facial nerve and its branches [45].

It was recently reported that shear wave elastography has higher elasticity indices for pleomorphic adenomas (i.e., stiffer) than Warthin's tumors. Nevertheless, further studies are needed for assessing the role of sonoelastography in salivary gland tumors [48].

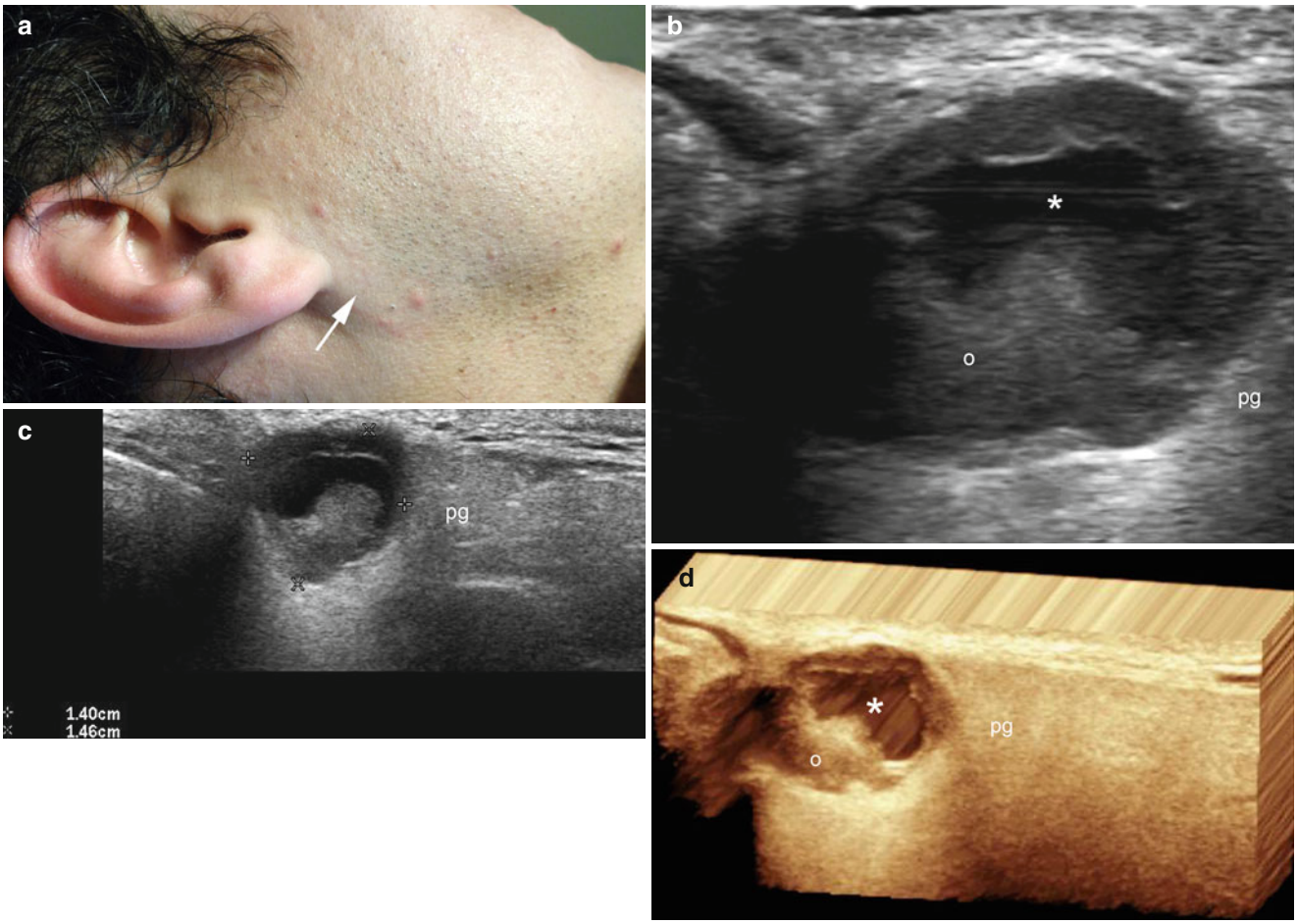

Fig. 20.27 (**a**–**d**) Warthin's tumor (cystadenolymphoma). (**a**) Clinical photograph demonstrates a lump (*arrow*) in the right infra-auricular region. (**b**, **c**) Grey scale ultrasound images (**b**: zoomed transverse view; **c** extended transverse view) show a 1.40 cm (wide)×1.46 cm (deep) mixed echogenicity mass with a thick hypoechoic rim (*o*) and anechoic center (*) that is located in the posterior part of the right parotid gland. (**d**) 3D ultrasound reconstruction highlights the solid (*o*) and cystic (*) parts of the mass. *Abbreviation*: *pg* parotid gland

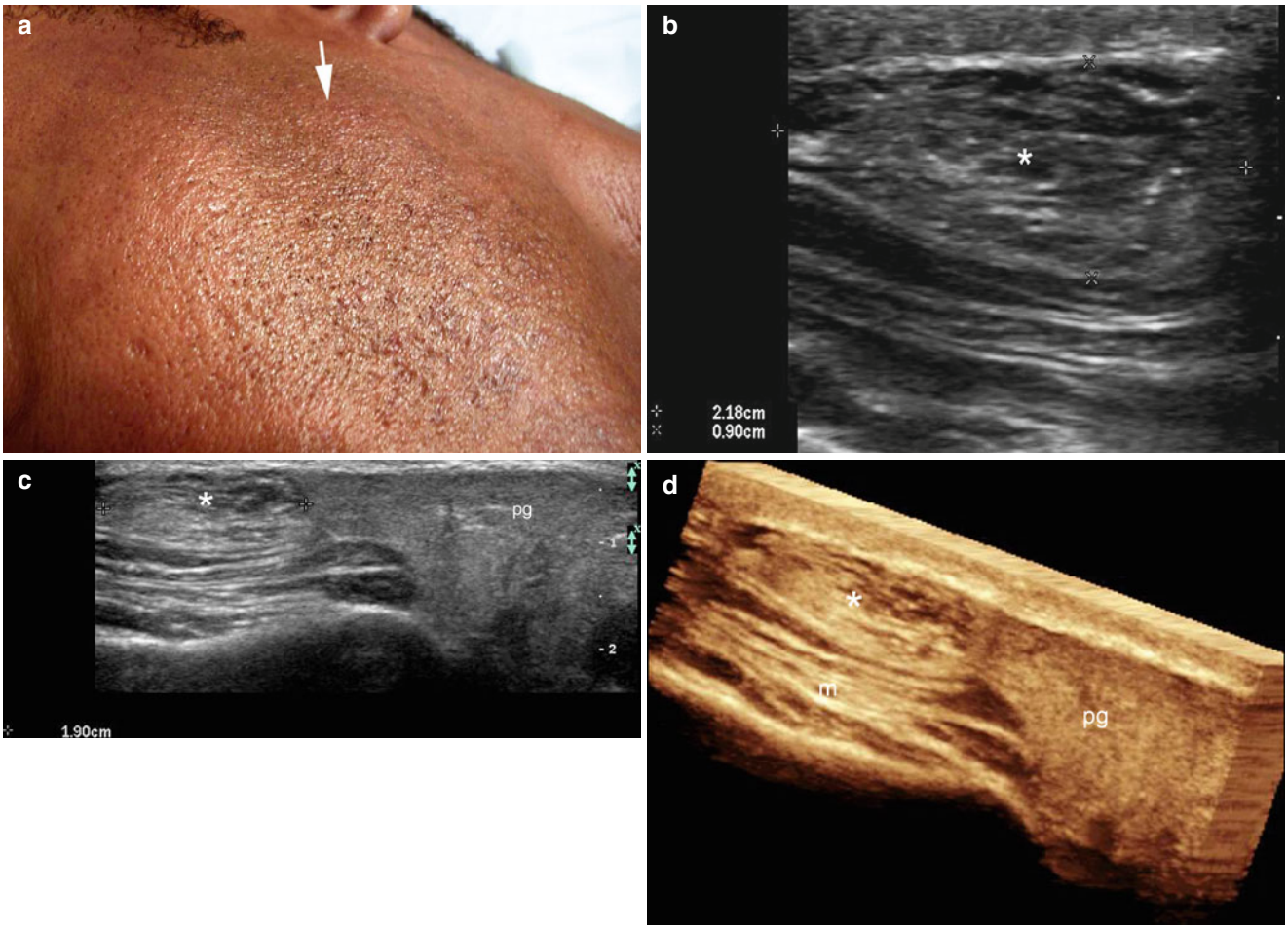

Fig. 20.28 (**a**–**d**) Intraparotid lipoma. (**a**) Clinical photograph shows a patient with a palpable lump (*arrow*) in the left cheek. (**b**, **c**) Grey scale ultrasound images (**b** zoomed transverse view; **c** extended transverse view) demonstrate a 2.18 cm (wide) × 0.90 cm (deep) well-defined oval-shaped hypoechoic solid structure that presents hyperechoic septa and is located in the anterior aspect of the left parotid gland and also on top of the masseter muscle. (**d**) 3D ultrasound depicts the solid mass (*). *Abbreviations*: *pg* parotid gland, *m* masseter muscle

20.2.6.3 Variants

20.2.6.3.1 Accessory Parotid Gland

The accessory parotid gland is an anatomical variant that is a common clinical occurrence and usually drains into the main Stenson's duct by small ductules and thereby, into the buccal cavity. Accessory parotid glands can be uni- or bilateral and are usually located anteromedially or laterally to the masseter muscle and are isolated from the main parotid gland. These accessory glands can show inflammation episodes and can produce facial asymmetry that can confuse the clinician. The inflammatory changes can also be secondary to sialolithiasis. The consultation is most often motivated by a painful nodule in the facial region. The presence of these anatomical variants can also potentially complicate facial cosmetic procedures such as tensor threads that can unexpectedly pass through the accessory glands or a prominent anterior lobe of the main parotid gland. Tumors of the accessory salivary glands have been reported to represent 71.4 % of tumors of the salivary glands. Similar to the usual salivary glands, the majority of benign tumors are pleomorphic adenomas, and adenoid cystic carcinoma is the principal malignant tumor [49–51] (Fig. 20.29).

20.2.7 Muscles

20.2.7.1 Inflammation

Muscular inflammation can be secondary to local trauma or a systemic condition such as *dermatomyositis* or *polymyositis*. Clinically, patients present with pain, tenderness, and/or swelling in the affected region(s). In inmunosuppressed patients, such as those with HIV or diabetes, *pyomyositis*, a suppurative bacterial infection of the muscle, can be seen. A contiguous source of infection is usually detected in these patients, with skin infection being the most frequent cause (40 %). The most common pathogen is *Staphylococcus aureus* followed by

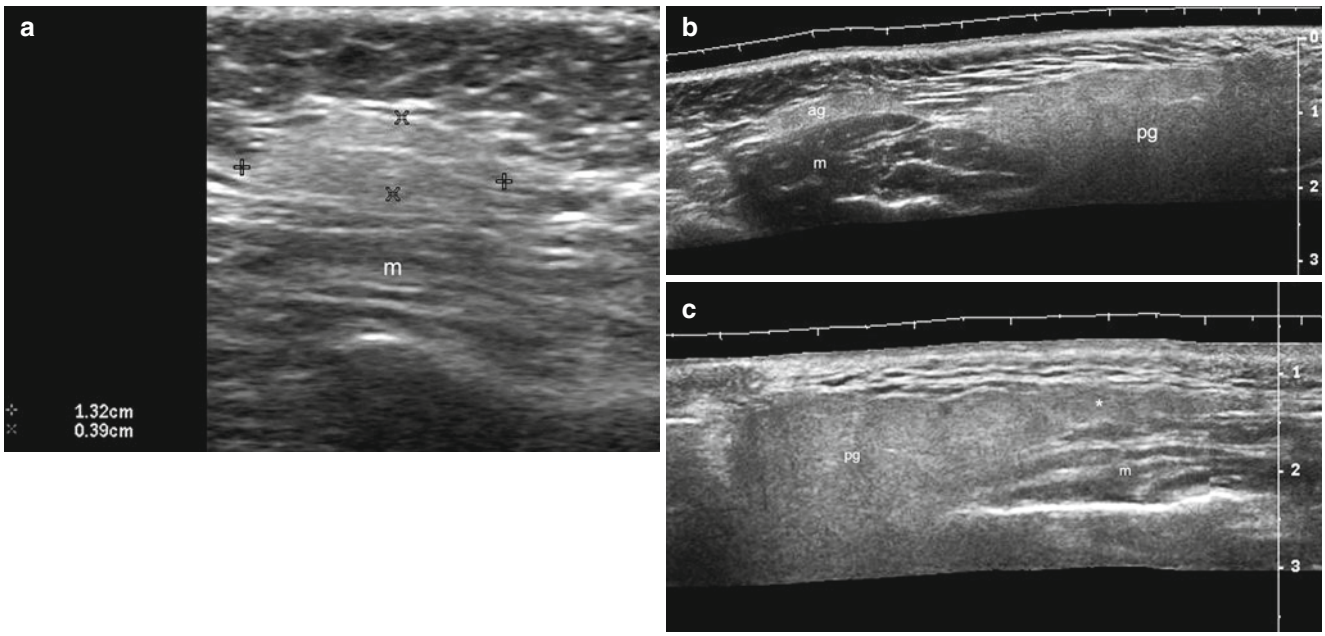

Fig. 20.29 (**a**–**c**) Accessory parotid gland and prominent anterior lobe of the parotid gland. (**a**) Grey scale ultrasound image (transverse view) demonstrates a 1.39 cm (wide) × 0.39 cm (deep) well-defined, oval-shaped, hyperechoic structure (between markers) that corresponds to an accessory parotid gland. This variant is located on top of the masseter muscle. (**b**) Grey scale ultrasound image (extended transverse view) shows a well-defined oval-shaped hyperechoic structure (accessory parotid gland) that is separated from the main parotid gland and located on top of the masseter muscle in the left cheek. (**c**) Grey scale ultrasound image (extended transverse view) depicts a prominent anterior lobe of the parotid gland in the right cheek of the same case. *Abbreviations*: *m* masseter muscle, *ag* accessory parotid gland, *pg* parotid gland

coagulase-negative staphylococci. On sonography, variable degrees of increased echogenicity and enlargement of the affected muscle(s) reflecting the edema and inflammation, and sometimes miofascial or intramuscular anechoic fluid collections, can be found. Anechoic or mixed echogenicity fluid collections with septae and posterior enhancement can be seen in cases presenting with purulent abscesses. Hyperechoic deposits of calcium are possible to detect within the muscle, miofascial, or surrounding subcutaneous tissue in chronic inflammatory conditions. Increased blood flow can occasionally be detected on color Doppler ultrasound within the affected muscle(s) during the acute or active phases. Sonoelastography has recently been reported as useful in the follow-up of patients with myositis [52–54] (Fig. 20.30).

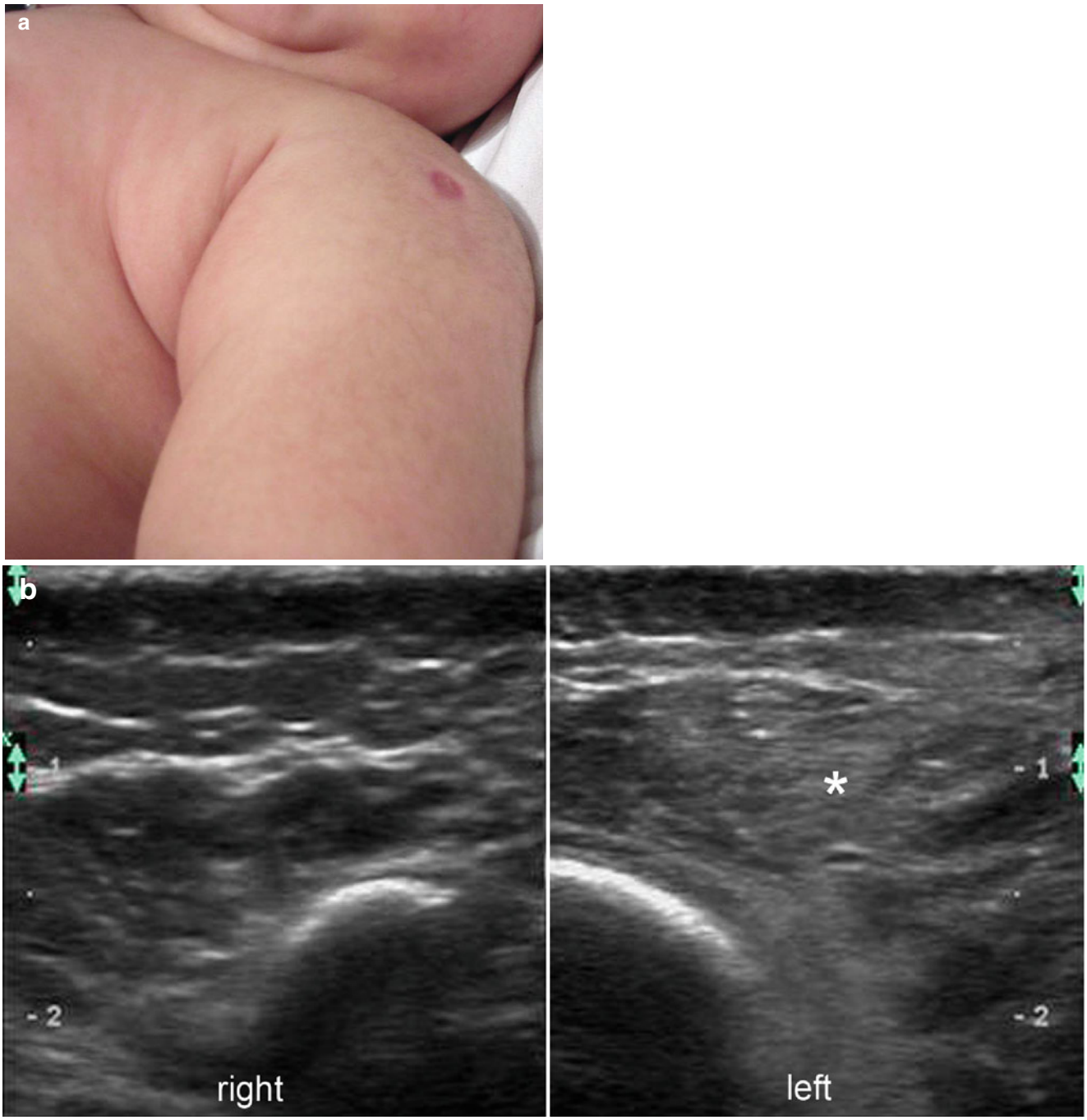

Fig. 20.30 (**a**, **b**) Myositis. (**a**) Clinical photograph of a child that presented with tenderness of the left arm after a vaccination. (**b**) Grey scale ultrasound image (comparative side by side transverse views) demonstrates increased thickness and echogenicity of the left deltoid muscle (*). The right deltoid muscle is unremarkable

20.2.7.2 Hernia

Muscle herniation is defined as a protrusion of a portion of a muscle through a defect of the muscle fascia. Although muscle herniation can be only a cosmetic problem, the condition can lead to spontaneous pain, cramps, or local tenderness [55]. Most muscle hernias occur in the lower leg and affect the tibialis anterior muscle; nevertheless, other sites can be involved. Occupational and sporting activities, trauma, chronic compartment syndrome, and weakness in the overlying fascia as a result of perforating vessels have been implicated as causes. Muscular hernias are common in adolescents or young adults, and patients present with swelling that typically appears or enlarges when the affected muscle is contracted or the patient is standing erect. The swelling shrinks when the muscle is relaxed or the patient is supine but the hernia can be reproduced with muscle contraction. Thus, the muscle protrudes through a defect in the fascia into the subcutaneous fat and presents clinically as a soft-tissue mass. On sonography the herniated hypoechoic muscular component is detected bulging into the subcutaneous tissue through the fascial defect. A "mushroom-like" appearance results when the herniated muscle overlaps the fascial defect and has a convex superficial contour. A dynamic sonography examination during contraction-relaxation or stand up-rest maneuvers, to catch the fascial defect, are usually required. On color Doppler ultrasound, arterial vessels adjacent to the hernia site can be identified in some cases which supports the theory that muscle hernia occurs at sites of weakness where vessels penetrate the fascia [56] (Figs. 20.31, 20.32, and 20.33).

20.2.7.3 Musculotendinous Tear

Acute or chronic full-thickness tears in tendinous insertions are associated with retraction of the muscular belly that can elicit lumps. Recent trauma history and bruising can support the clinical diagnosis during the acute phase. Nevertheless, the patient may not provide a clear history after time passes and the bruises have disappeared; the

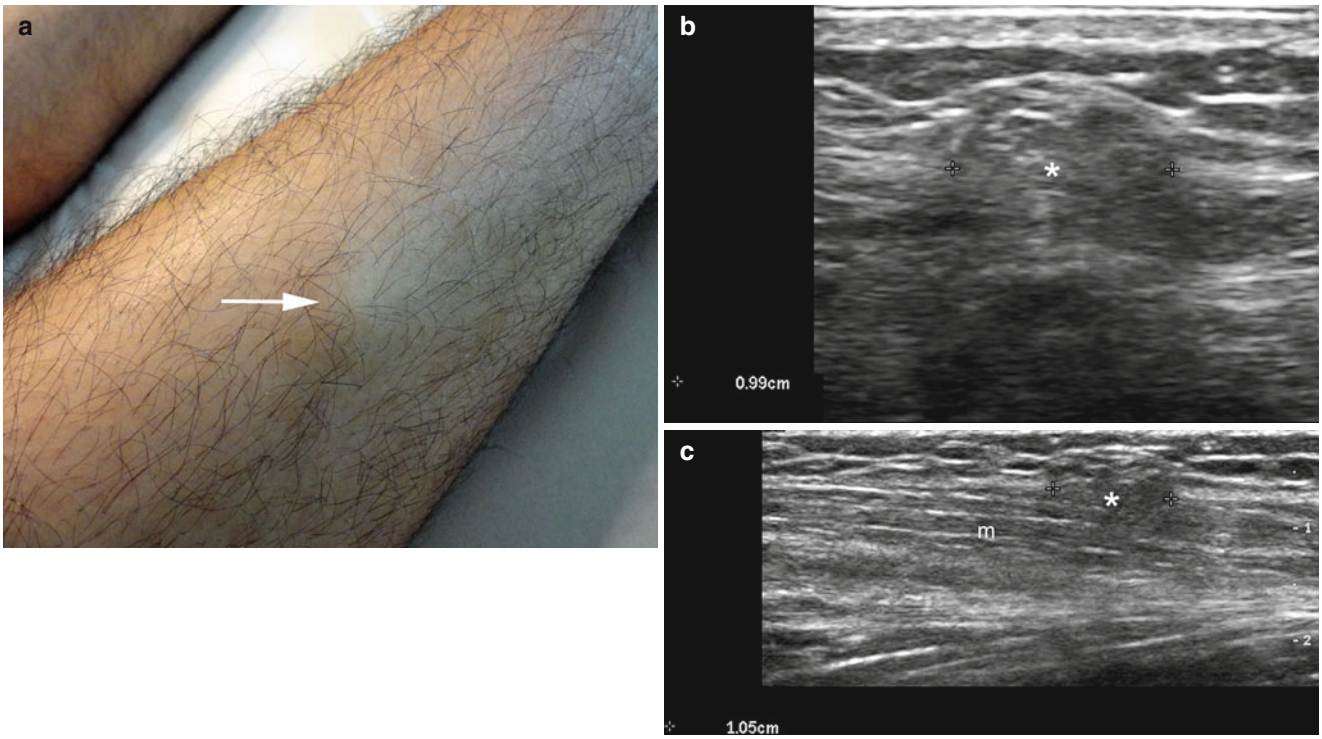

Fig. 20.31 (**a**–**c**) Muscle herniation. (**a**) Clinical photograph demonstrates a bump (*arrow*) in the anterior aspect of the right leg. (**b**, **c**) Grey scale ultrasound images (**b** zoomed longitudinal view; **c** extended longitudinal view) show a 1.05 cm long focal bulge (*, between markers) in the surface of the right tibialis anterior muscle. This bulge is more prominent under contraction. *Abbreviation*: *m* tibialis anterior muscle

soft-tissue lump can become a challenging diagnosis for a clinician. Examples of these conditions are the full-thickness tears of the long head of the biceps and the pectoralis major muscles. Partial thickness tears with prominent edema of the muscle belly can also occasionally cause swelling. On sonography the hypoechoic interruption of the muscle belly, musculotendineous junction, or tendineous insertion can be seen (sometimes with anechoic serohematic fluid and distal retraction of the muscular belly). Hyperechogenicity of the surrounding muscle tissue can be detected in cases that present with prominent edema [57–59] (Figs. 20.34, 20.35, 20.36, and 20.37).

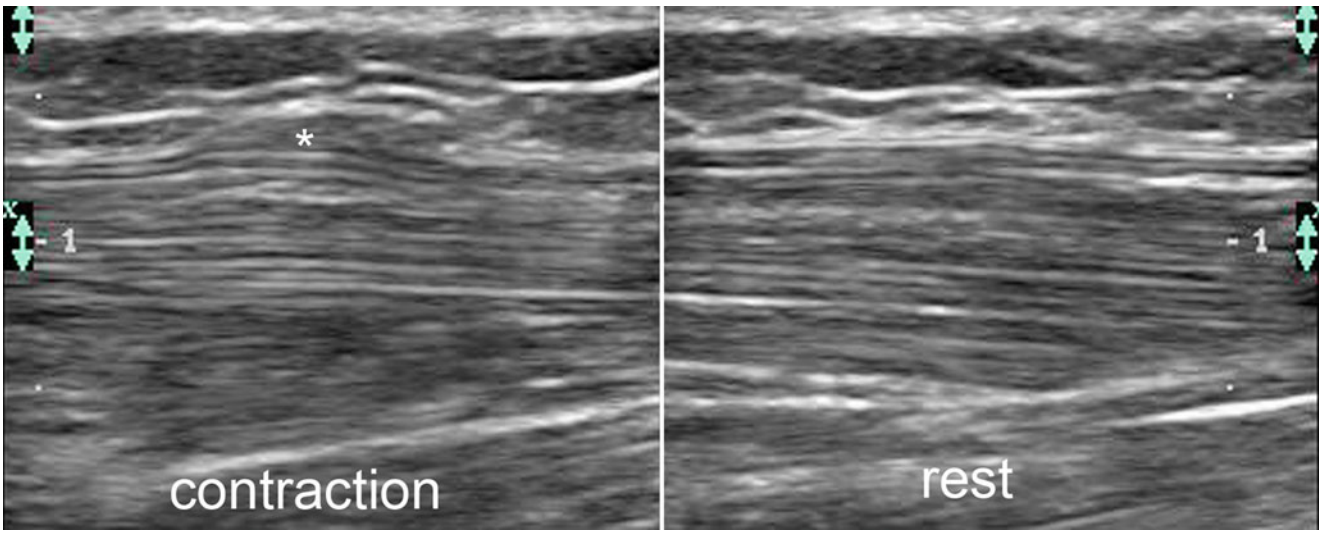

Fig. 20.32 Herniation of the musculotendinous junction. Dynamic grey scale ultrasound image (dynamic study under contraction and rest) shows a focal bulge (*) of the surface of the tibialis anterior musculotendinous junction under contraction

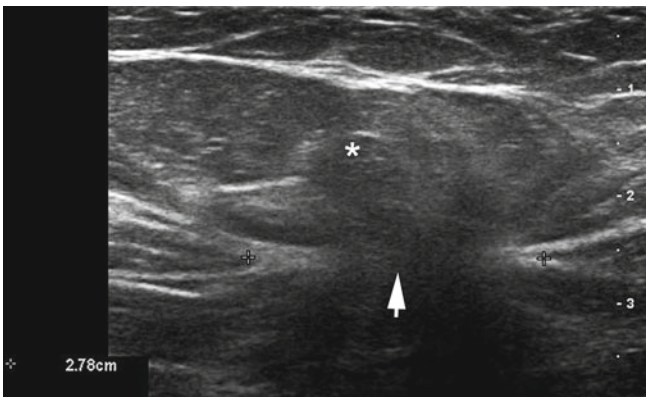

Fig. 20.33 Abdominal wall hernia. Grey scale ultrasound image (transverse view) demonstrates a herniation of fatty tissue (*) through a defect (*arrow*) in the aponeurosis. There is a 2.78 cm (wide) diastasis (between markers) of the bellies of the rectus abdominis muscles

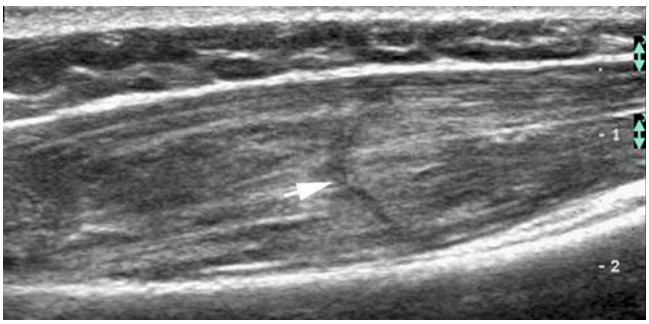

Fig. 20.34 Partial-thickness tear. Grey scale ultrasound image (longitudinal view, lateral aspect of the left arm) shows hypoechoic band (*arrow*) that corresponds to a partial-thickness tear in the deltoid muscle. Notice the increased echogenicity and thickness of the surrounding muscle tissue secondary to edema

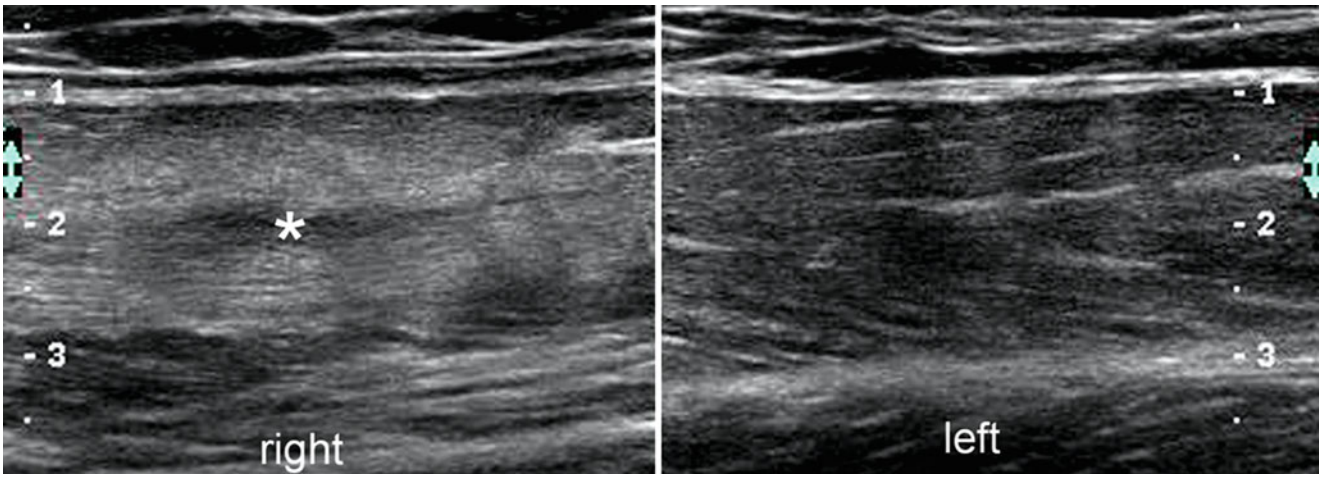

Fig. 20.35 Partial-thickness tear. Grey scale ultrasound image (longitudinal view, side by side view, anterior thigh) shows a hypoechoic band (*) that corresponds to a partial tear in the right rectus femoris muscle. There is increased echogenicity and thickness of the muscle belly. The left rectus femoris muscle is unremarkable

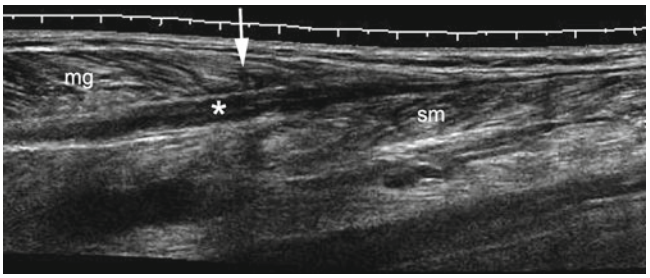

Fig. 20.36 Partial-thickness tear. Grey scale ultrasound image (longitudinal view, right calf) shows a partial disruption (*arrow*) of the distal part of the medial gastrocnemius muscle with an anechoic myofascial band (*) of serohematic fluid between the medial gastrocnemius and soleus muscles. *Abbreviations*: *mg* medial gastrocnemius, *sm* soleus muscle

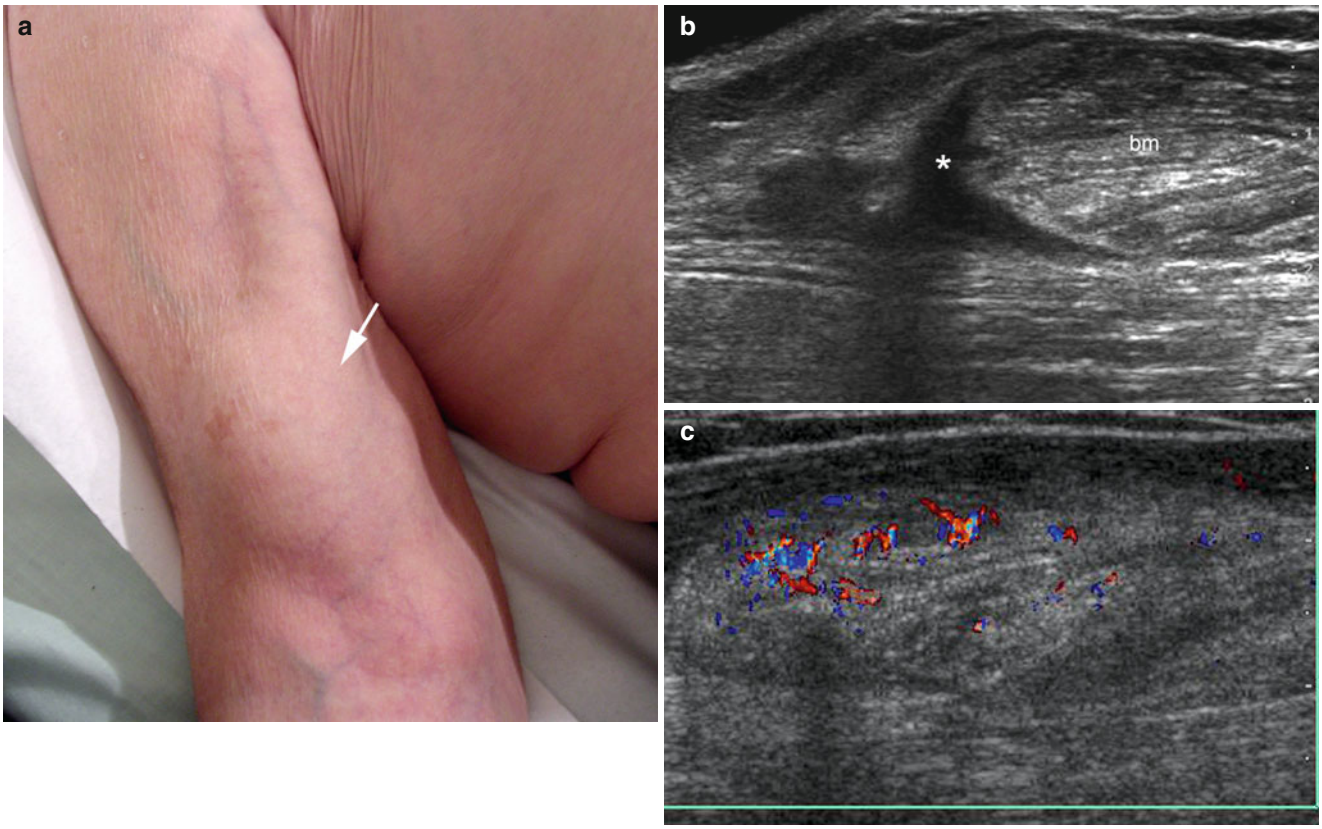

Fig. 20.37 (**a**–**c**) Full-thickness tear. (**a**) Clinical photograph demonstrates a lump in the anterior aspect of the right arm. (**b**) Grey scale ultrasound image (longitudinal view) shows a curved anechoic band of fluid (*) in the site of the full thickness tear of the musculotendinous junction of the long head of the biceps brachii. Notice the retraction of the muscle belly (*bm*). (**c**) Color Doppler ultrasound image (longitudinal view) shows increased vascularity within the muscle belly

20.2.7.4 Variants

Accessory, *hypertrophic or reversed* (i.e., distal location of the muscle belly) *muscles* are common and can produce swelling and asymmetry. The most common examples of this condition are the accessory extensor digitorum brevis manus, the abductor digiti minimi, the extensor medii propitous, accessory extensor carpi radialis, and the variations of the palmaris longus muscles in the wrist and hands; the accessory brachialis, anconeus epitrochlearis, the accessory head of the flexor pollicis longus, and the bifurcated distal biceps brachii muscles on the elbow; the accessory slips of the medial and lateral gastrocnemius, tensor fasciae suralis, and accessory popliteus muscles on the knee; the accessory peroneal muscles, flexor digitorum accessorius longus, peroneouscalcaneous internus, accessory soleus, and tibiocalcaneus internus on the ankle [60].

On sonography these muscles present the same hypoechoic pattern that the rest of the muscular tissue show and present anteroposterior enlargement during contraction. Moreover, they show specific anatomical locations in the different corporal regions that the sonographer should recognize (Figs. 20.38, 20.39, 20.40, and 20.41).

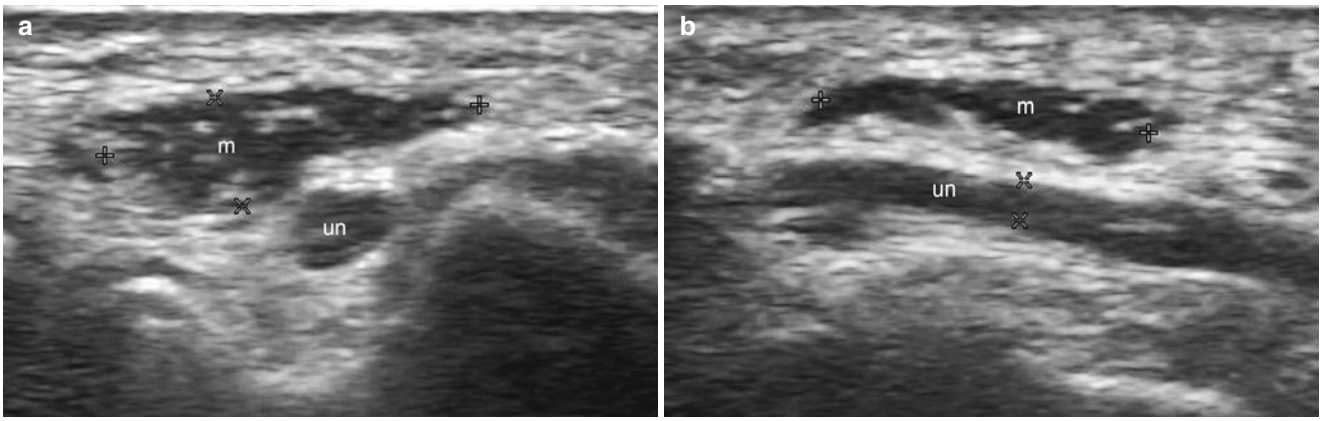

Fig. 20.38 (**a**, **b**) Accessory muscle anconeus epitrochlearis. (**a**, **b**) Grey scale ultrasound images (**a** transverse view; **b** longitudinal view) demonstrate a hypoechoic solid muscular structure (m, between markers) located on top of the ulnar nerve (*un*, between markers) in the posterior aspect of the elbow

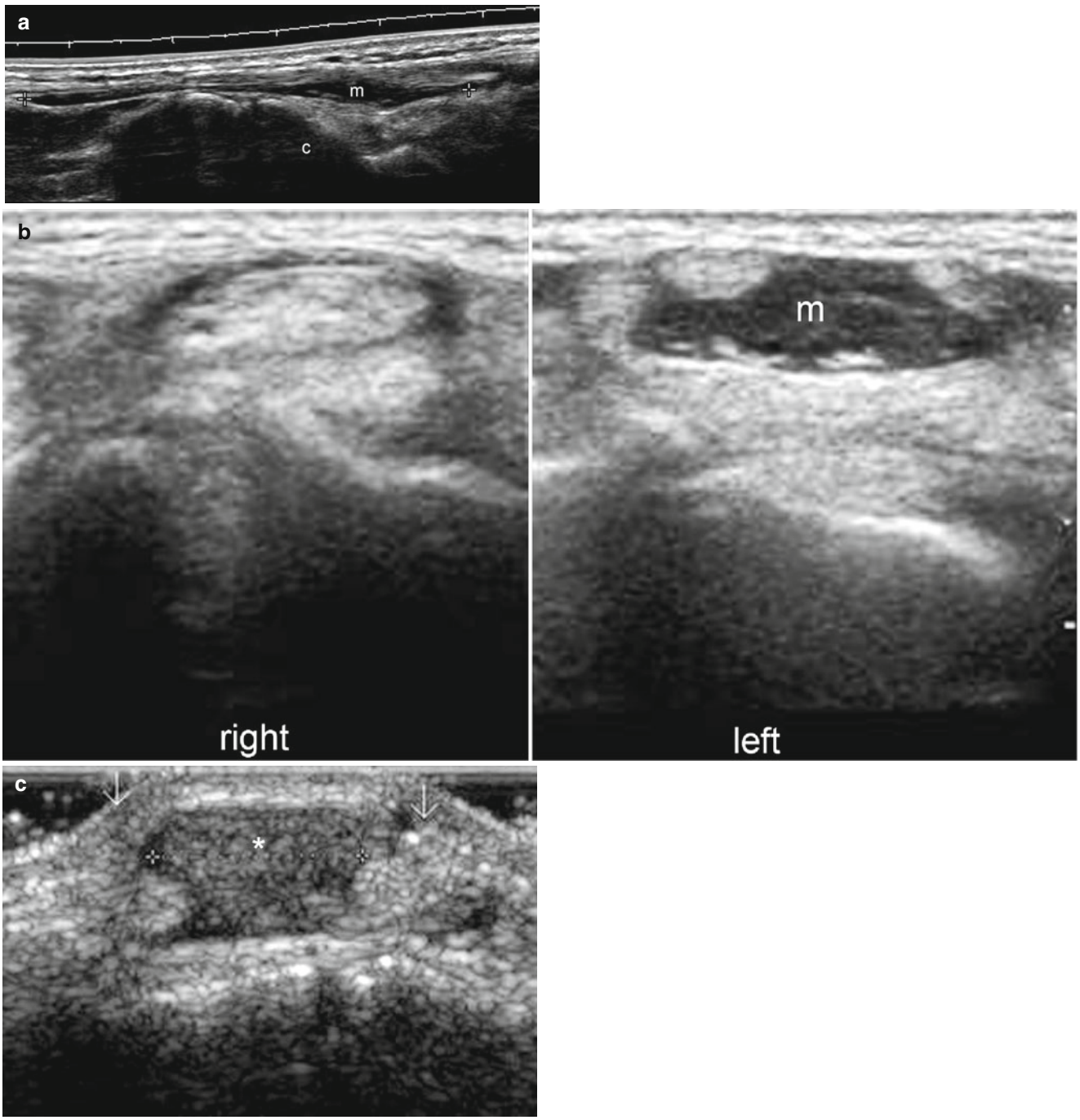

Fig. 20.39 (**a**–**c**) Accessory muscle extensor digitorum brevis manus. (**a**–**c**) Grey scale ultrasound images in different patients (**a** longitudinal view of the dorsal aspect of the right wrist and hand; **b** comparative side by side transverse view of the dorsal wrist; **c** transverse view dorsal aspect of the left wrist under contraction) show hypoechoic structure (*m*, *) attached to the fourth extensor tendon compartment (tendons of extensor digitorum muscle and extensor indicis tendon). Notice the bulge of the accessory muscle under contraction in figure (c). *Abbreviations*: *m* accessory muscle, *c* capitate bone

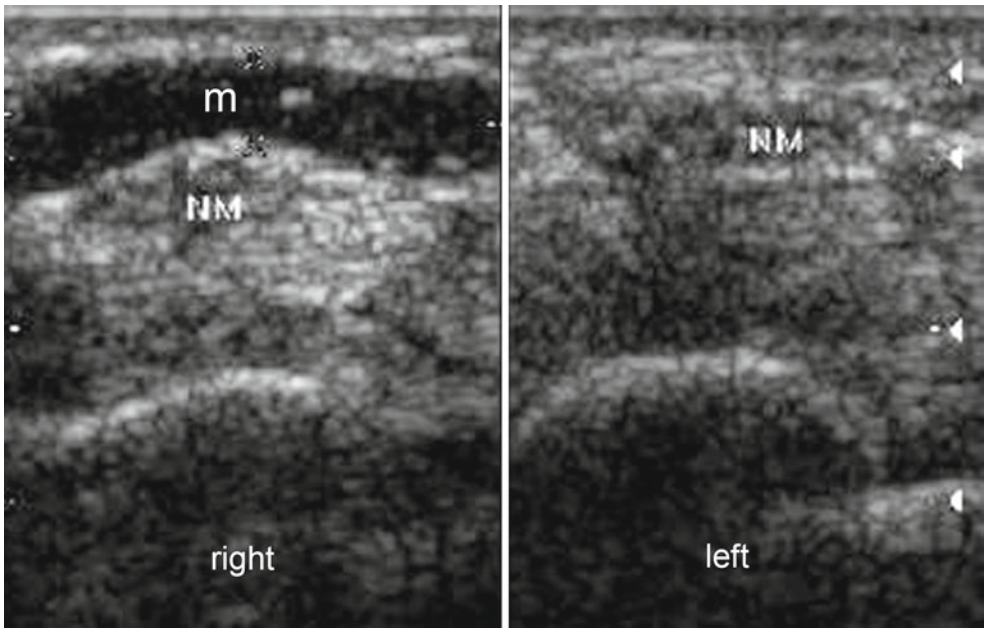

Fig. 20.40 Reversed palmaris longus muscle. Comparative side-by-side transverse view shows hypoechoic solid structure (*m*) on top of the median nerve and flexor tendons in the palmar aspect of the right wrist. The left side is unremarkable. *Abbreviations*: *m* accessory muscle, *nm* median nerve

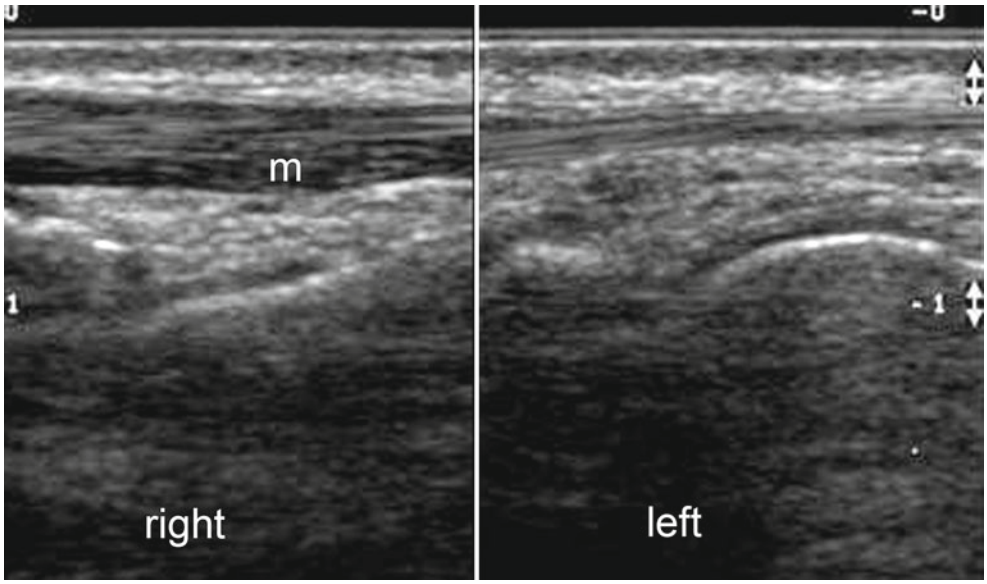

Fig. 20.41 Accessory extensor indicis muscle. Grey scale ultrasound image (comparative side-by-side longitudinal view in the dorsum of the hand) shows a hypoechoic structure (*m*) attached to the extensor indicis tendon in the right side. The left side is unremarkable

20.2.8 Pulley System and Fascia

20.2.8.1 Trigger Finger

The pulley system is composed of focal thickened areas of the flexor tendon sheaths and is of paramount biomechanical importance in flexion, not only for accurate tracking of the tendon but also to maintain the apposition of tendon and bone across the joint and provide a fulcrum to elicit flexion and extension [61]. When these pulleys become thickened and/or are associated with tenosynovitis, the patient can clinically present with finger stiffness (particularly in the morning); a popping or clicking sensation when moving the finger; tenderness or a bump (nodule) at the base of the affected finger; finger catching or locking in a bent position that occurs more frequently on the dominant, thumb, middle, or ring fingers. The most commonly affected pulley is the A1, an annular and thin structure situated at the level of the metacarpophalangeal (MCP) joint that surrounds the flexor tendon sheath. In most cases, the cause of trigger fingers is idiopathic, although a number of congenital forms have been noted. Its incidence is increased in patients with rheumatoid arthritis, diabetes mellitus, De Quervain tenosynovitis, osteoarthritis, carpal tunnel syndrome, mucopolysaccharidoses, and hypothyroidism. The diagnosis is usually made clinically; however, the development of ultrasound-guided injections allows the appearance of trigger fingers to be depicted on sonography. On sonography, A1 pulleys appear as hypoechoic bands superficial to the flexor tendon sheath. In the axial plane, lateral expansions are oblique and appear hypoechoic because of anisotropy. The thickness of the A1 pulley in the trigger fingers has been reported to vary from 1.1 mm to 2.9 mm with an average of 1.8 mm. Hypervascularization of the A1 pulley on power or color Doppler imaging has been reported in up to 91 % of cases and tendinosis or tenosynovitis of the flexor tendon has been found in 63 % of the trigger fingers. For the thumb, tendinosis has been reported located proximal to the A1 pulley because the normal position of rest for the thumb is in semi-flexion. The pulley thickening is sometimes associated with a cystic lesion of the pulley (ganglion cyst) that may increase the probability of a nodular palpation on clinical examination [62]. Intrasheath ultrasound-guided first annular (A1) pulley release has been reported to be safe and effective according to literature [63] (Fig. 20.42).

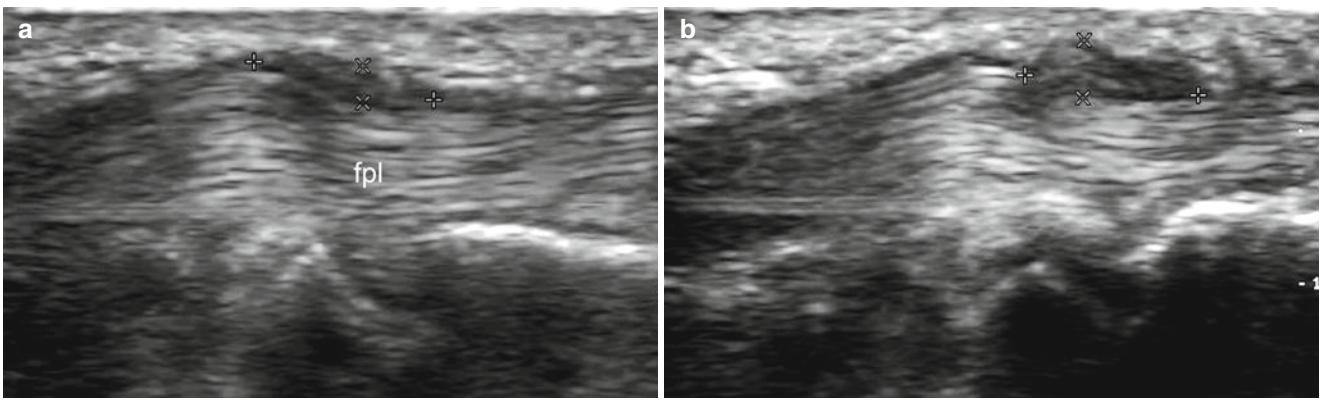

Fig. 20.42 (**a**, **b**) Trigger finger. Grey scale ultrasound images (longitudinal views, left thumb; **a**: rest; **b**: under flexion). There is thickening of the A1 pulley (between markers) that is located on top of the flexor pollicis longus tendon (*fpl*) at the level of the metatarsophalangeal joint. The tendon becomes trapped under the A1 pulley during the flexion phase (b)

20.2.8.2 Tumors and Pseudotumors

20.2.8.2.1 Plantar and Palmar Fibromatoses

Fibromatoses are divided into two main groups: superficial (fascial) and deep (musculoaponeurotic). Superficial fibromatoses are usually small, slow-growing lesions that arise from the fascia and aponeuroses. The most common superficial entities are the palmar and plantar (Ledderhose's disease) fibromatoses

Palmar Fibromatosis

Also called Dupuytren's disease, is the most common of the superficial fibromatoses, affecting 1–2 % of the general population and is most commonly seen in male patients over 65 years of age. Bilateral involvement has been reported in up to 40–60 % of patients. Trauma, microvascular injury, immunologic processes, and genetic factors have been described among the possible causes. Other associations include diabetes mellitus (20 % of patients), epilepsy (50 % of male patients and 25 % of female patients), alcoholism (particularly liver disease related to alcoholism), and keloids. Clinically, patients present with slow-growing, painless, palpable nodules, cords, or bands that attach to and cause traction on the underlying flexor tendons, resulting in flexion contractures of the digits (Dupuytren contractures). The ulnar-sided rays, particularly the fourth and fifth digits, are most commonly involved. Palmar fibromatosis can be concomitant with other types of fibromatoses such as plantar fibromatosis (5–20 % of cases), Peyronie disease, and knuckle pads (i.e., dorsal focal fibrous thickening at the proximal interphalangeal or metacarpophalangeal joint) that may precede the development of palmar fibromatosis. On gross specimen examinations, these fibromatous lesions appear gray-white or gray-yellow, depending on their collagen content.

Histologically, palmar fibromatosis shows a fibroblastic-myofibroblastic proliferation of spindle-shaped cells with variably vascularity. Younger lesions are usually more hypercellular (proliferative phase) and the older lesions have greater collagen content. Moderate mitotic activity can be present but is not indicative of malignancy.

On sonography, hypoechoic or heterogeneous, ill-defined focal thickening or well-defined oval-shaped nodules or cord-like structures are seen in the palmar fascia superficial to the flexor tendons. Thus, these structures bulge into the palmar subcutaneous tissue. On color Doppler ultrasound they present variable degrees of vascularity [64, 65]. Management of Dupuytren contracture with ultrasound-guided lidocaine injection and needle aponeurotomy coupled with osteopathic manipulative treatment have also been reported in literature [66] (Fig. 20.43).

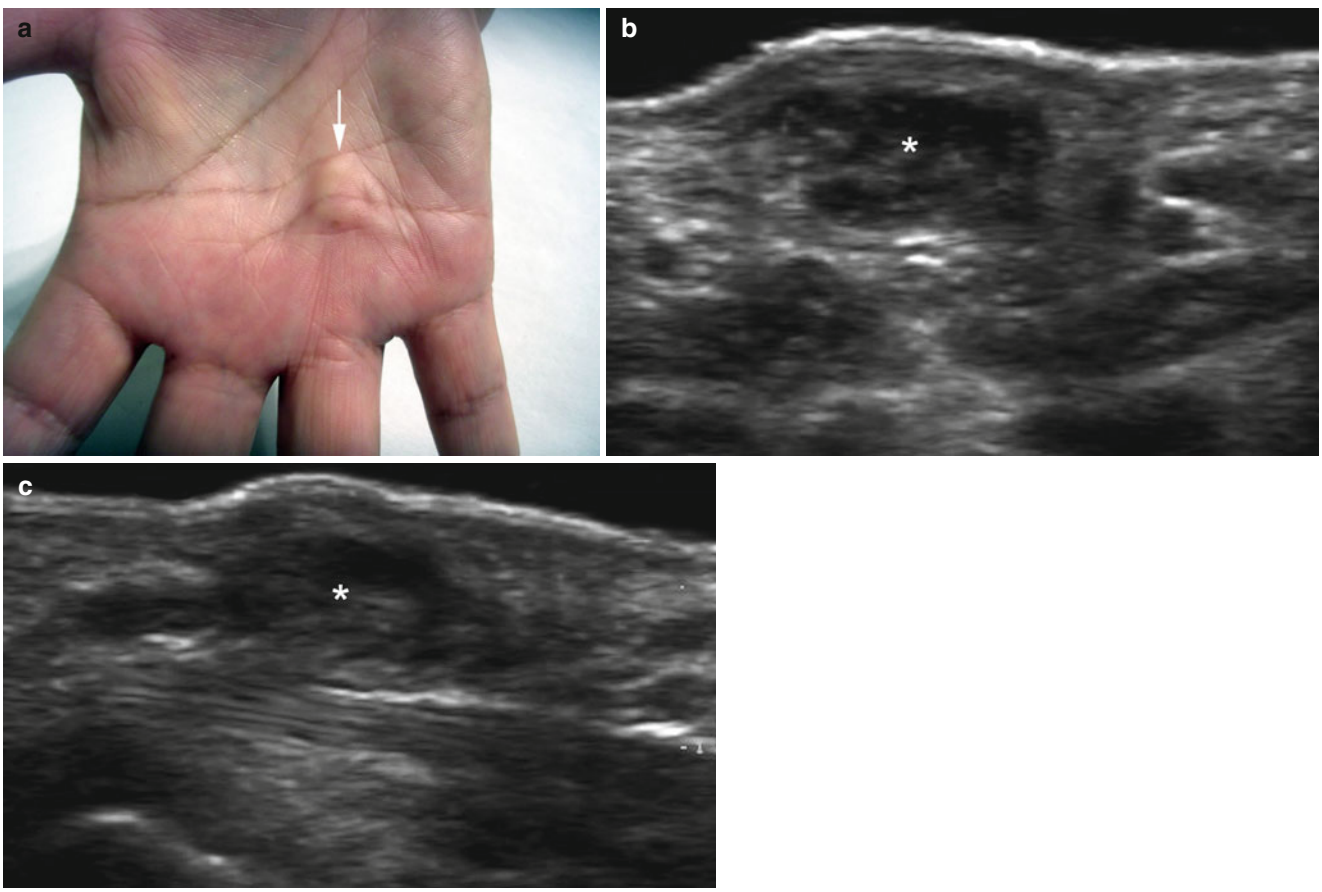

Fig. 20.43 (**a**–**c**) Palmar fibromatosis-Dupuytren's disease. (**a**) Clinical image demonstrates a lump (*arrow*) in the palmar aspect of the right hand. (**b**, **c**) Grey scale ultrasound images (**b** transverse view; **c** longitudinal view) show a hypoechoic and heterogeneous solid structure (*) that follows the palmar fascia

Plantar Fibromatosis

Also called Ledderhose's disease, shows less prevalence than palmar fibromatosis. Plantar fibromatosis is most commonly seen in male patients ages 30–50 years, although there is a marked female predilection among the pediatric age group. Bilateral involvement has been reported in up to 20–50 % of patients. Concomitant palmar disease occurs in 10–65 % and knuckle pads are seen in 42 % of patients. Etiology includes genetic and traumatic causes and associations with diabetes mellitus, epilepsy, keloids, and alcoholism with liver disease.

Clinically, one or more slow-growing, painless or tender, firm nodules are palpated on the medial aspect of the sole of the foot. The nodules are not usually associated with contracture although they can in rare cases affect an adjacent structure such as the muscles or neurovascular bundles.

Histologically, prominent spindle-shaped cells similar to those described in palmar fibromatosis are detected [64, 65].

On sonography, single or multiple hypoechoic or heterogeneous oval-shaped, sagittally elongated nodules are detected in the plantar fascia. Sixty percent of the lesions are located medially and the remaining 40 % are located centrally in the fascia [67, 68]. Anechoic cystic areas within the nodules and involvement of the subcutaneous tissue have been also reported. On color Doppler ultrasound they tend to present hypovascularity, although blood flow can be detected in large-sized lesions [69] (Fig. 20.44).

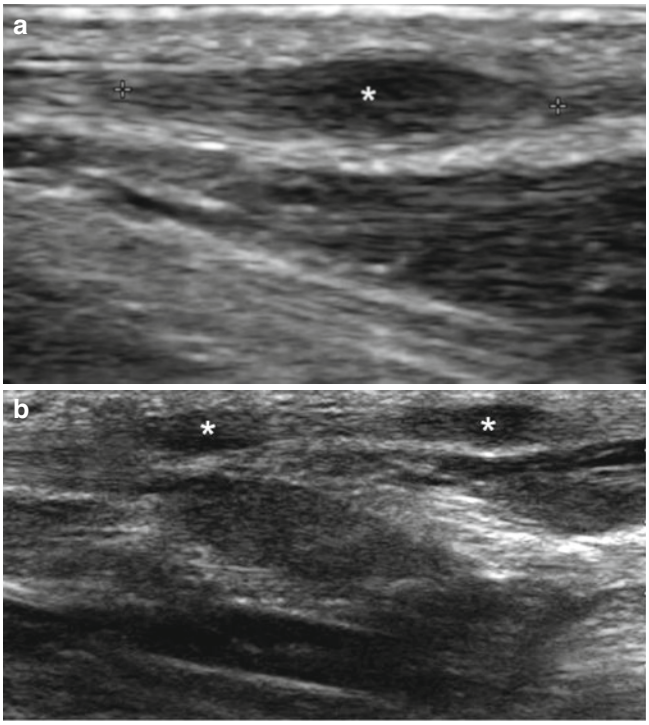

Fig. 20.44 (**a**, **b**) Plantar fibromatosis-Ledderhose's disease. (**a**, **b**) Grey scale ultrasound images (**b** zoomed longitudinal view; **c** extended longitudinal view) show fusiform shaped hypoechoic nodules (*, between markers) within the medial aspect of the plantar fascia in the right foot

20.2.8.2.2 Fibroma of the Tendon Sheath

Fibroma of the tendon sheath (FTS) is an uncommon and benign soft-tissue tumor, predominantly seen in the fingers, hands, and wrists of young, adult men. FTS appears clinically as painless, slow-growing, solid nodules. The nodules are usually single but multiple presentations have also been reported. Histologically, the tumors are composed of a dense fibrocollagenous stroma with scattered spindle-shaped fibroblasts and narrow slit-like vascular spaces. Recurrence has been reported in up to 24 % of lesions. On sonography, FTS appears as a well-defined, oval-shaped hypoechoic nodule near the tendons. The degree of vascularity is variable but it often shows increased blood flow with thin vessels [70, 71] (Fig. 20.45).

20.2.8.2.3 Nodular Fasciitis

Nodular fasciitis is a reactive fibrous disorder that affects young adults usually in the upper extremities and the torso, including the breast. When see in children, the head and neck regions have also described as sites of involvement, and the eyelid and anterior orbit have been also reported to be affected. Clinically, a rapidly growing swelling that frequently involves the volar aspect of the forearm is the most common form of presentation. The lesion develops over several weeks and in up to 10–15 % of patients, a history of trauma can be elicited; however, the cause of these reactive lesions is still unknown. The rapid growth of the lesions can simulate malignant conditions such as sarcoma. On histology, spindle cells, prominent collagen, and/or myxoid ground substance are founded. On sonography, nodular fasciitis appears as a hypoechoic or mildly heterogeneous, round or oval-shaped, well-defined miofascial and subcutaneous structure sometimes with lobulated or slightly irregular margins, with posterior acoustic enhancement (probably a result of the mix of myxoid component and perhaps closely packed cells) and increased echogenicity of the surrounding subcutaneous tissue. Multiple punctate echogenic foci within the mass have also been reported. On color Doppler ultrasound, vascularity can appear as a variable pattern but this may demonstrate increased blood flow in the periphery and within the mass, usually with thin and slow flow vessels [72–75] (Fig. 20.46).

Fig. 20.45 (**a**–**d**) Fibroma of the tendon sheath. (**a**) Clinical image shows a lump in the palmar aspect of the right thumb. (**b**) Grey scale ultrasound image (transverse view) shows two well-defined, oval-shaped hypoechoic solid subcutaneous nodules (between markers) that measure 5.9 and 9.5 mm (wide), respectively. (**c**) Color Doppler ultrasound image (transverse view) demonstrates increased blood flow within the larger-sized nodule (*). (**d**) The tumors at surgery (Courtesy of Dr Andres Figueroa). *Abbreviations*: *ph* phalanx, *bu* ulnar aspect, *br* radial aspect

20.2.9 Bursae

20.2.9.1 Bursitis

Bursitis is the inflammation of the virtual sac-like structures located between the tendons and the subcutaneous tissue or the tendons and the bones. This inflammatory process elicits synovial fluid-filled cystic structures, sometimes with prominent synovial proliferation in its walls. Clinically, they present as painless or painful and sometimes erythematous lumps or swelling that can be associated with overuse, repetitive or acute trauma, inflammatory arthropathy, obesity, chronic degenerative arthritis, rheumatoid arthritis, and gout. There are anatomical regions where the bursae are located superficially and can become easily inflamed and palpated, among them are the posterior elbow (olecranon bursa), the popliteal fossae (Baker's cyst, semimembranous-medial gastrocnemius bursa), the shoulder (the lateral recess of the subacromiosubdeltoid bursa), and the anterior aspect of the knee (pre- and infra-patellar bursae). Histologically, the synovial lined structure shows non-specific inflammatory granule-like tissue, sometimes similar to the synovial pannus. On sonography these sac-like subcutaneous structures present classic anatomical sites and are filled with anechoic fluid, occasionally floating echoes (debris), and may also show septation, lobulation, thick walls (from synovial proliferation), adjacent joint effusion, and posterior acoustic enhancement. The bursae can sometimes rupture into the subcutaneous tissue and generate anechoic band-like fluid collections and increased echogenicity of the adjacent subcutaneous tissue [76]. Complications such as rupture or secondary infection can mimic other clinical entities such as phlebitis, deep venous thrombosis, or soft-tissue tumors [77] (Figs. 20.47 and 20.48).

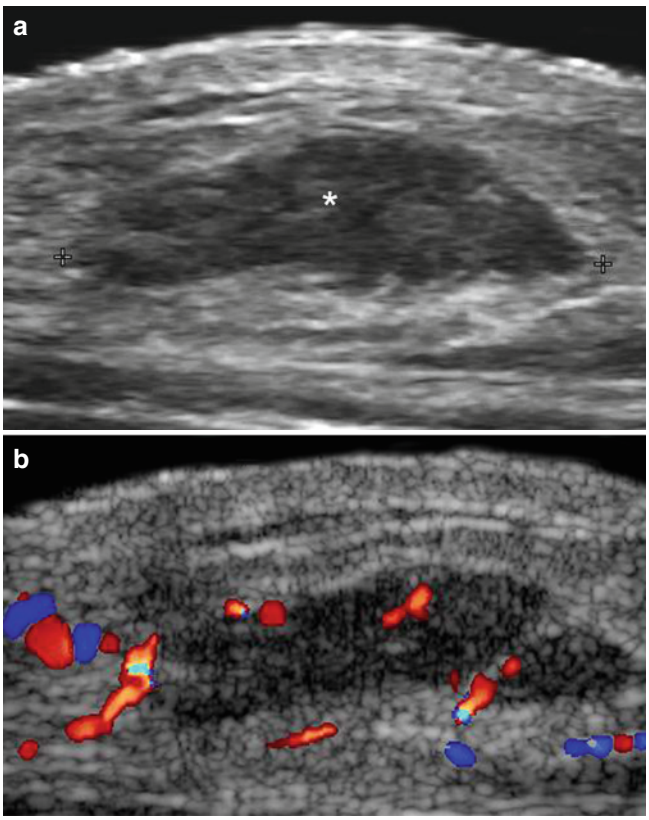

Fig. 20.46 (**a**, **b**) Nodular fasciitis. (**a**) Grey scale ultrasound image (transverse view dorsal aspect of the right forearm) shows a well-defined oval-shaped mildly lobulated hypoechoic subcutaneous structure (*, between markers). (**b**) Color Doppler ultrasound image (transverse view) demonstrates increased vascularity within the muscle and the surrounding tissues

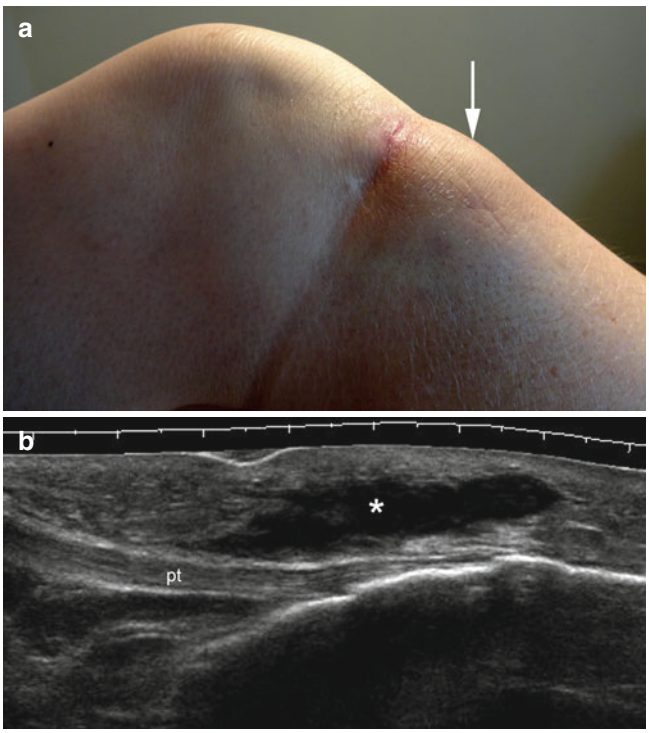

Fig. 20.47 (**a**, **b**) Infrapatellar bursitis. (**a**) Clinical photograph shows a lump (*arrow*) in the right infrapatellar region. (**b**) Grey scale ultrasound image (longitudinal view) demonstrates distention and fluid (*) in the infrapatellar bursa. *Abbreviation*: *pt* patellar tendon

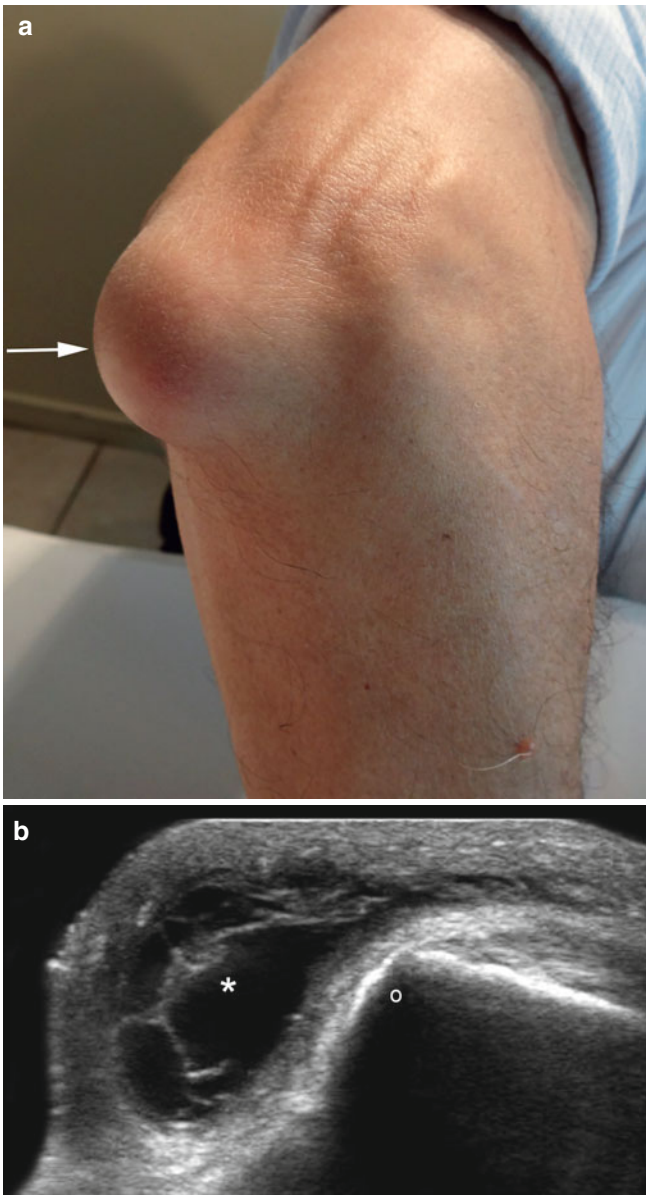

Fig. 20.48 (**a**, **b**) Olecranon bursitis. (**a**) Clinical photograph shows a lump (*arrow*) in the posterior aspect of the right elbow. (**b**) Grey scale ultrasound image (transverse view) demonstrates distention and fluid of the olecranon bursa. Notice the septa and echoes (debris) within the bursa (*). *Abbreviation*: *o* olecranon

20.2.10 Tendinous and/or Peritendinous

20.2.10.1 Inflammation: Tendinitis-Tenosynovitis

The inflammatory involvement of tendinous and peritendinous structures can generate a painful swelling. An example is the inflammation of the first extensor compartment in the wrist, also called *Quervain's tenosynovitis*. De Quervain disease is a tenosynovitis that affects the synovial sheath of the tendons of the abductor pollicis longus and extensor pollicis brevis muscles (first extensor compartment in the wrist); it is associated with pain and functional impairment and progresses to cause local fibrosis with blockage or triggering of the thumb. On sonography, thickening of the tendons and sheath can be detected. Anechoic fluid and hypervascularity in the tendon sheath, as well as thickening of the retinaculum, may be evident [78, 79] (Figs. 20.49 and 20.50).

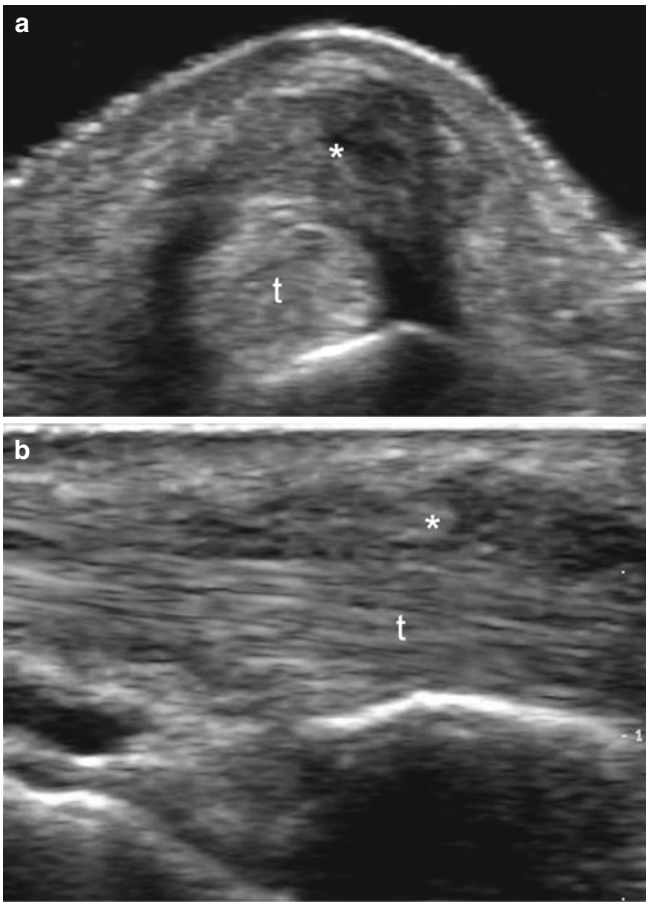

Fig. 20.49 (**a**–**c**) Quervain's tenosynovitis. (**a**, **b**) Grey scale ultrasound images (**a** transverse view; **b** longitudinal view; left wrist) show prominent thickening of the synovial sheath (*) of the abductor pollicis longus tendon (first compartment of the wrist). The tendon (*t*) is also enlarged. (**c**) 3D reconstruction highlights the thickening of the tendon and sheath. *Abbreviation*: *t* tendon

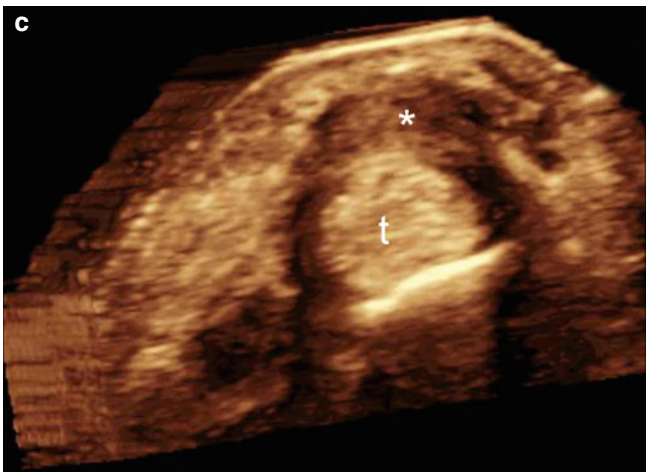

Fig. 20.49 (continued)

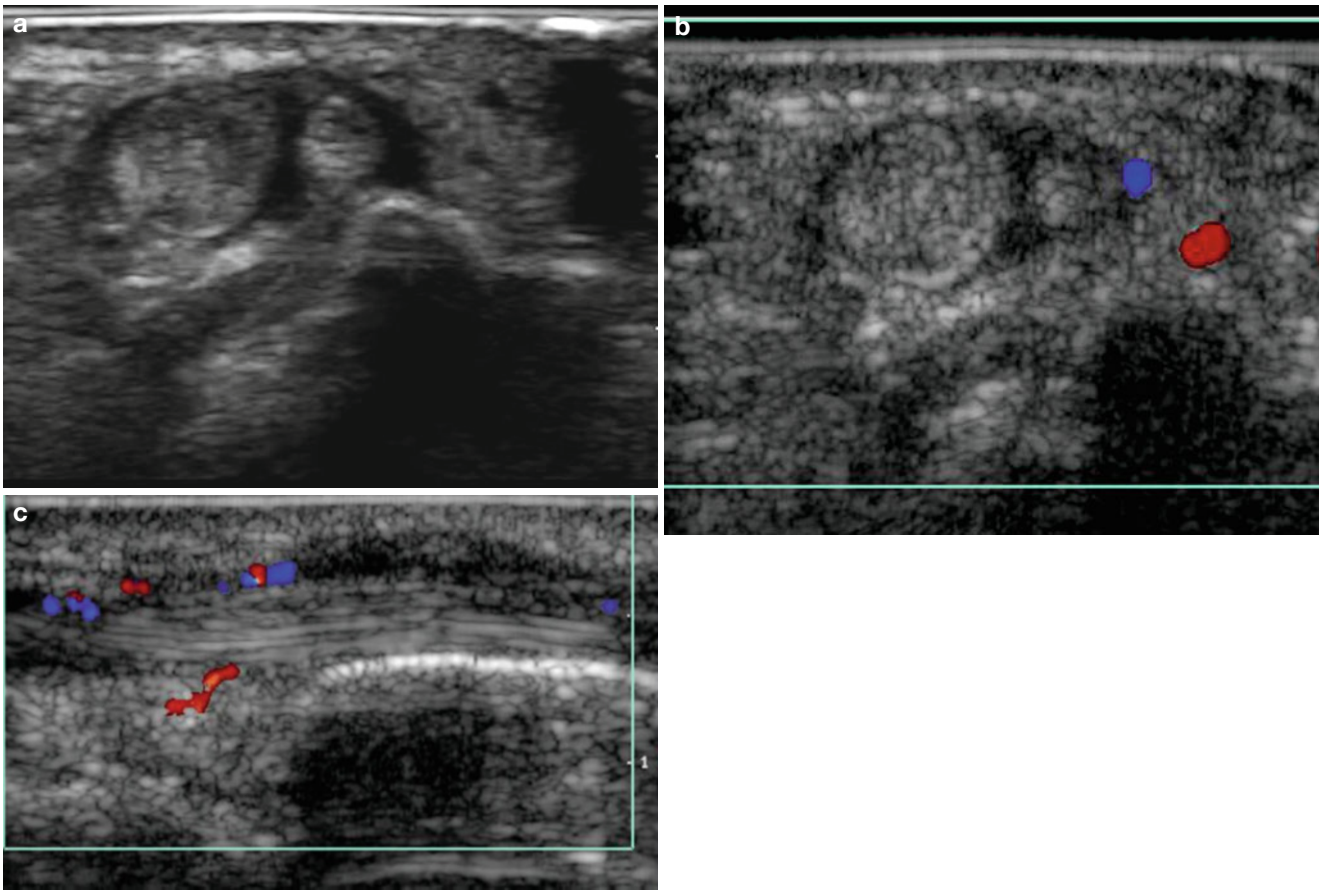

Fig. 20.50 (**a**–**c**) Quervain's tenosynovitis. (**a**) Grey scale ultrasound image (transverse view, right wrist) shows thickening of the abductor pollicis longus and extensor pollicis brevis tendons and their synovial sheath (first extensor compartment of the wrist). (**b**, **c**) Color Doppler ultrasound images (**b** transverse view; **c** longitudinal view) demonstrate increased vascularity in the synovial sheath and surrounding tissues

20.2.10.2 Variants

Accessory tendons can generate lumps or asymmetry and elicit painless swelling that also can become inflamed or ruptured. A common location is the accessory abductor pollicis longus in the first extensor compartment of the wrist, the accessory flexor pollicis longus in the ventral aspect of the wrist and hand, and the accessory extensor hallucis longus and peroneal tendons in the ankle. These variants should not be confused with tears or split of the tendinous structures. On sonography, they present the same fibrillar hyperechoic pattern that do the normal tendons and are surrounded by a virtual synovial sheath, usually running along the same axis than the corresponding accessory muscular structure [60, 80, 81].

20.2.10.3 Pseudotumors and Tumors

20.2.10.3.1 Synovial Cysts-Ganglion Cysts

Synovial and ganglion cysts are usually attached to musculotendinous structures. The distinction between synovial cysts (i.e., with synovial lining) and ganglion cysts (i.e., without a synovial lining) is made by histology. These cysts are most commonly caused by the leakage of fluid from the joint into the surrounding tissue and are frequently associated with osteoarthrosis. Ganglion cysts predominantly contains mucous or myxoid material. Synovial and ganglion cysts are the most common cause of lumps in the hands and are usually connected to the joint through thin tracts and can become larger in size when the joints become inflamed. These cysts are filled with a myxoid viscous material that can sometimes drain into the skin layers, particularly when located in the proximal nail fold of the fingers where the skin is thin. On sonography, synovial and ganglion cysts present as anechoic round or oval-shaped structures that communicate with the joint through an anechoic tract that usually runs in the lateral aspect of the joints in the fingers. These cysts may dissect between the extensor or flexor tendons and pop up into the surface when they are located in the wrist and hands. The cysts usually present a valve-like mechanism that produces transient distension of the cystic cavity during episodes of inflammation of the connected joint. Synovial and ganglion cysts are common in the hands and periungual regions and may cause secondary tenosynovitis and ungual dystrophies by compressing the adjacent tendons or ungual matrix, respectively [14] (Figs. 20.51 and 20.52).

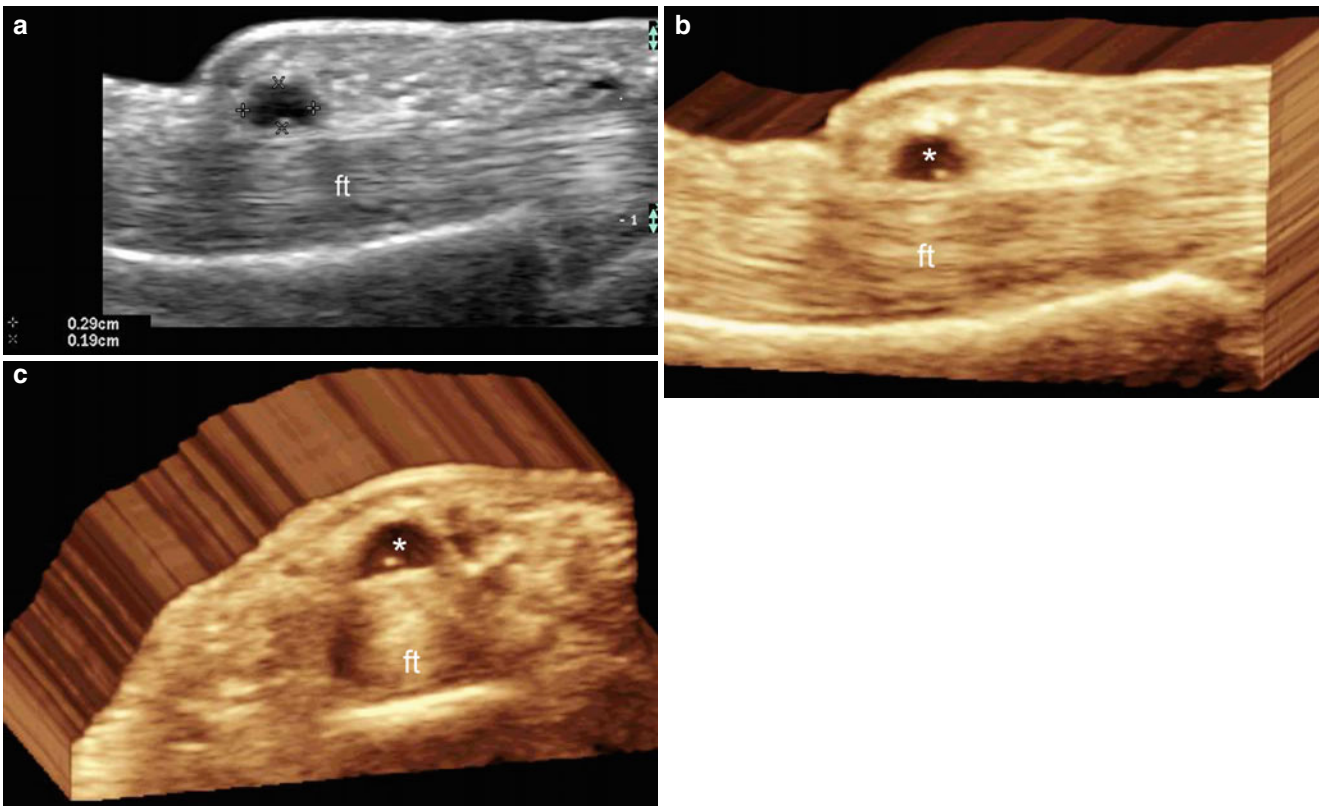

Fig. 20.51 (**a**–**c**) Synovial cyst. (**a**) Grey scale ultrasound image (longitudinal view; left middle finger) shows a 2.9 mm (long) × 1.9 mm (deep) well-defined round-shaped anechoic cystic structure attached to the flexor digitorum superficialis tendon. (**b**, **c**) 3D grey scale ultrasound reconstructions (**b**: longitudinal view; **c**: transverse view) highlight the cystic lesion (*). *Abbreviation*: flexor digitorum

20.2.10.3.2 Giant Cell Tumors

Giant cell tumors are a common soft-tissue mass in the hands, also known as localized nodular tenosynovitis. They may occur at any age but typically presents in the third to fifth decades. A traumatic etiology has been suggested, and a history of trauma has been noted in up to 15 % of cases in some reports. It presents clinically as a skin-colored, painless or tender palpable nodule, most often in the volar aspect of the digits that can cause distal numbness. Thus, they are most common in the hand, exceeded only by synovial and ganglion cysts in that location. The second most frequent site of occurrence is the ankle-foot region and in rare cases they affect the large joints. Nevertheless, in children, these tumors may reveal an equal predilection for the upper and lower extremities. Histologically, giant cell tumors contain histiocyte-like foamy or multinucleated cells and fibroblast-like cells and may have hemosiderin deposits. Pathologically, giant cell tumors are identical to pigmented villonodular synovitis, the intrarticular form of the same entity. On sonography, they appear as a hypoechoic or heterogeneous, slightly lobulated well-defined mass adjacent to the flexor or extensor tendon sheath commonly embracing the tendon. Hence, they can encase the tendon and extend from the dorsal aspect to the ventral aspect of the digit. Additionally, giant cell tumors can appear as well-defined hypoechoic, subcutaneous solid nodules. Close contact of the tumor to the interphalangeal joint has also been reported. Bone erosions or scalloping resulting from pressure effects of swelling have been variably reported in 9–25 % of cases. On color Doppler ultrasound, they present variable degrees of vascularity that go from hypovascular to hypervascular with thin and slow flow vessels [82, 83] (Figs. 20.53 and 20.54).

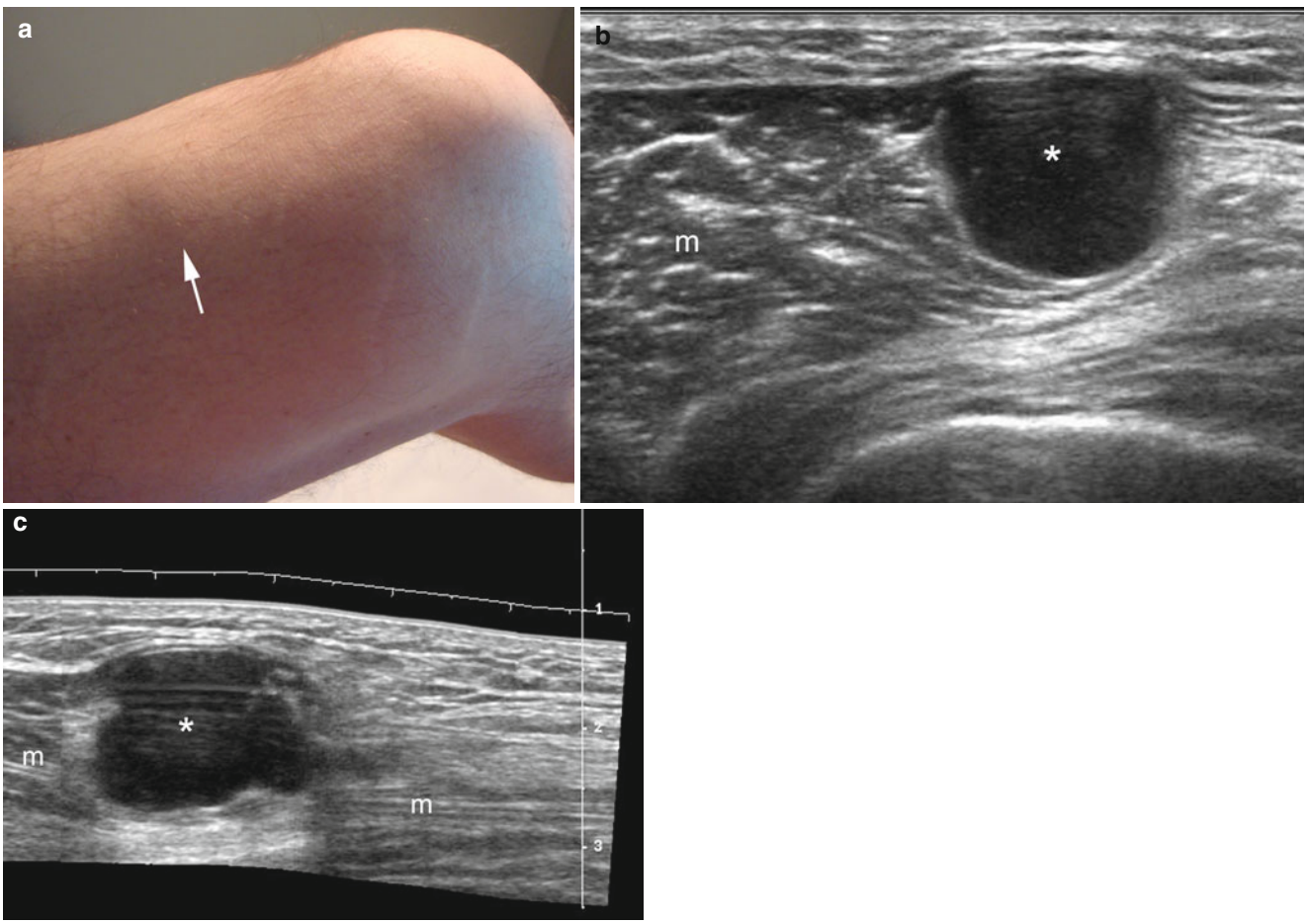

Fig. 20.52 (**a**–**c**) Ganglion cyst. (**a**) Clinical photograph of patient that presented with a lump in the anteromedial aspect of the left thigh. (**b**, **c**) Grey scale ultrasound images (**b** transverse view; **c** longitudinal view) demonstrate a well-defined round-shaped lobulated anechoic cyst (*, between markers) attached to the anterior aspect of the vastus medialis muscle

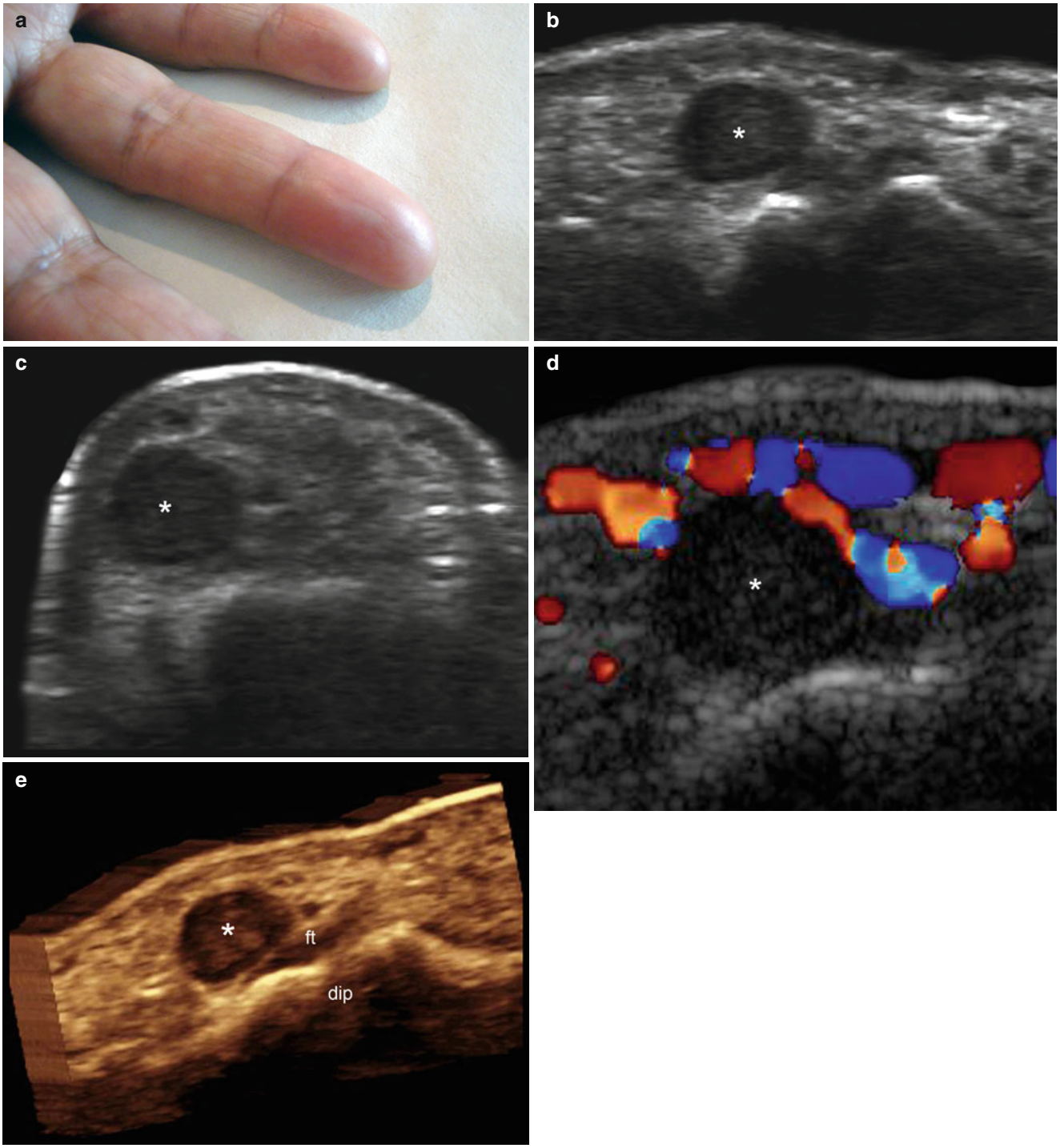

Fig. 20.53 (**a**–**e**) Giant cell tumor. (**a**) Clinical image of a patient who presented with a palpable lump (*arrow*) in the pulp of the right ring finger. (**b**, **c**) Grey scale ultrasound images (**b** longitudinal view; **c** transverse view) demonstrate a well-defined round-shaped hypoechoic subcutaneous nodule (*) in the radial aspect of the pulp of the ring finger. (**d**) Color Doppler ultrasound image (longitudinal view) depicts hypovascularity within the nodule (*). (**e**) 3D reconstruction (longitudinal view) highlights the closeness of the tumor (*) with the insertion of the flexor digitorum profundus tendon (ft). *Abbreviation*: *dip* distal interphalangeal joint

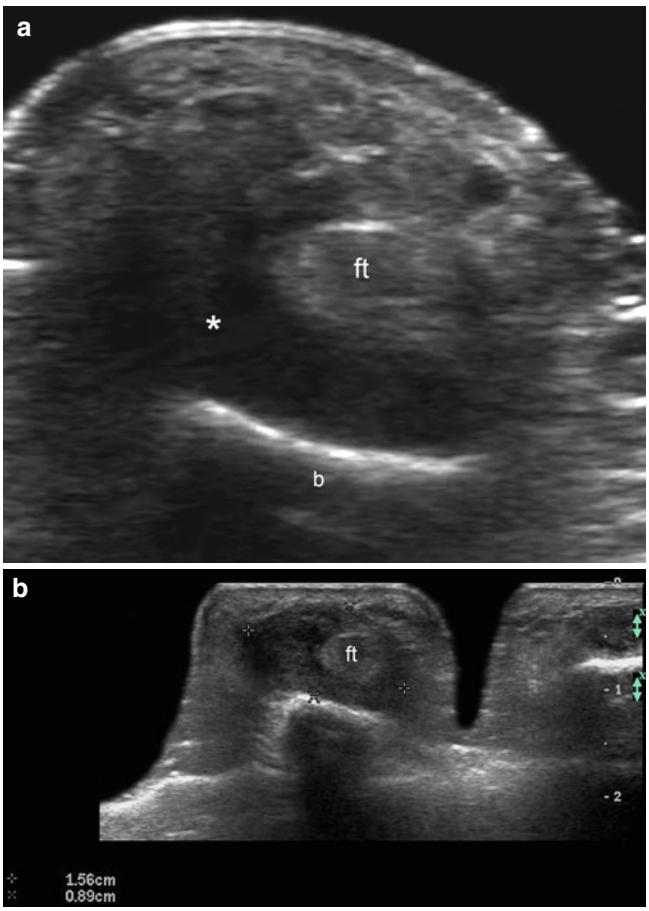

Fig. 20.54 (**a**, **b**) Giant cell tumor of the tendon sheath. (**a**, **b**) Grey scale ultrasound images (transverse views; **b**: zoomed image; **c**: extended image) show a 1.56 cm (wide)×0.89 cm (deep) hypoechoic solid structure (*, between markers) that embraces the flexor digitorum tendons of the right index finger. *Abbreviation*: *b* bony margin of the proximal phalanx

20.2.11 Joints and/or Periarticular Tissues

20.2.11.1 Inflammation: Synovitis

Joint synovitis is defined as the presence of intra-articular effusion. There are multiples causes for joint synovitis, among them trauma, osteoarthrosis, and inflammatory diseases such as rheumatoid arthritis. Synovitis presents clinically as skin-colored or erythematous, tender or painless, swelling over the articular or peri-articular sites. Thus, the fingers are commonly affected by synovitis. Histologically, there is hyperplasia and enlargement of the synovial lining cell layer with inflammatory cell infiltration. A reactive proliferative synovium with prominent neovascularization can be observed in severe stages of inflammation. An example of the latter case is the pannus, usually present in rheumatoid arthritis. On sonography, synovitis shows in the early phases as intra-articular anechoic fluid that occasionally is associated with floating echoes. In cases presenting prominent synovial hyperplasia there is a poorly compressible anechoic fluid, with hypoechoic tissue resulting from synovial proliferation and variable degrees of increased vascularity in the synovium (on color Doppler) can be detected in late and/or severe phases [84–86] (Fig. 20.55).

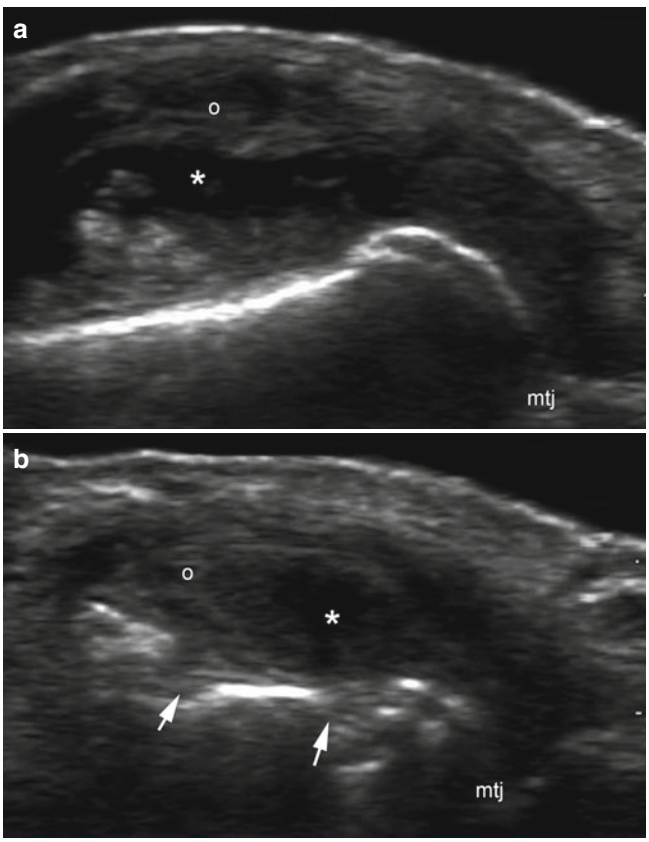

Fig. 20.55 (**a**, **b**) Synovitis (Rheumatoid Arthritis). (**a**, **b**) Grey scale ultrasound images (longitudinal views; metacarpophalangeal joints; **a**: ring finger; **b**: little finger) demonstrate anechoic fluid (*, effusion) and synovial proliferation (*o*) in the joint. Notice the erosions (*arrows*) of the bony margin of the proximal phalanx in figure (b). *Abbreviation*: *mtj* metacarpophalangeal joint

20.2.11.2 Pseudotumors

20.2.11.2.1 Rheumatoid Nodule

Rheumatoid nodules are local and firm swelling usually near pressure points or bony prominences that is commonly seen in patients presenting with rheumatoid arthritis. Rheumatoid nodules are detected most frequently on the olecranon or the knuckles of the fingers. Histologically, central fibrinoid necrosis associated with proliferations of the fibroblastic cells and mononuclear cells is seen. Extensive mucin deposition can produce mucinous exudates from the nodule. On sonography, they appear as hypoechoic or heterogeneous subcutaneous nodules with anechoic areas in correlation to necrosis [87–89].

20.2.11.2.2 Gouty Tophi

Gout is a metabolic disorder characterized by hyperuricemia that causes the deposition of monosodium urate crystals, triggering gouty arthritis if the deposits are in the joints and gouty tophi if the crystals are located in the soft tissues. Tophi can develop as a first sign of gout or present later during the course of the disease. Histologically, these urate crystal deposits can be surrounded by histiocytes. Clinically, patients present with painless or tender swelling or lumps that may release white or yellowish-white, cheesy or chalky material. On sonography, gouty tophi can be seen as subcutaneous and/or periarticular-intrarticular, hyperechoic deposits that may additionally present slightly increased vascularity in the periphery on color Doppler ultrasound. The gouty material can resemble "wet sugar clumps" on sonography and can be associated with hyperechoic deposits of the same crystals in the surface of the hyaline cartilage and/or erosions of the bony margin [90–93] (Figs. 20.56 and 20.57).

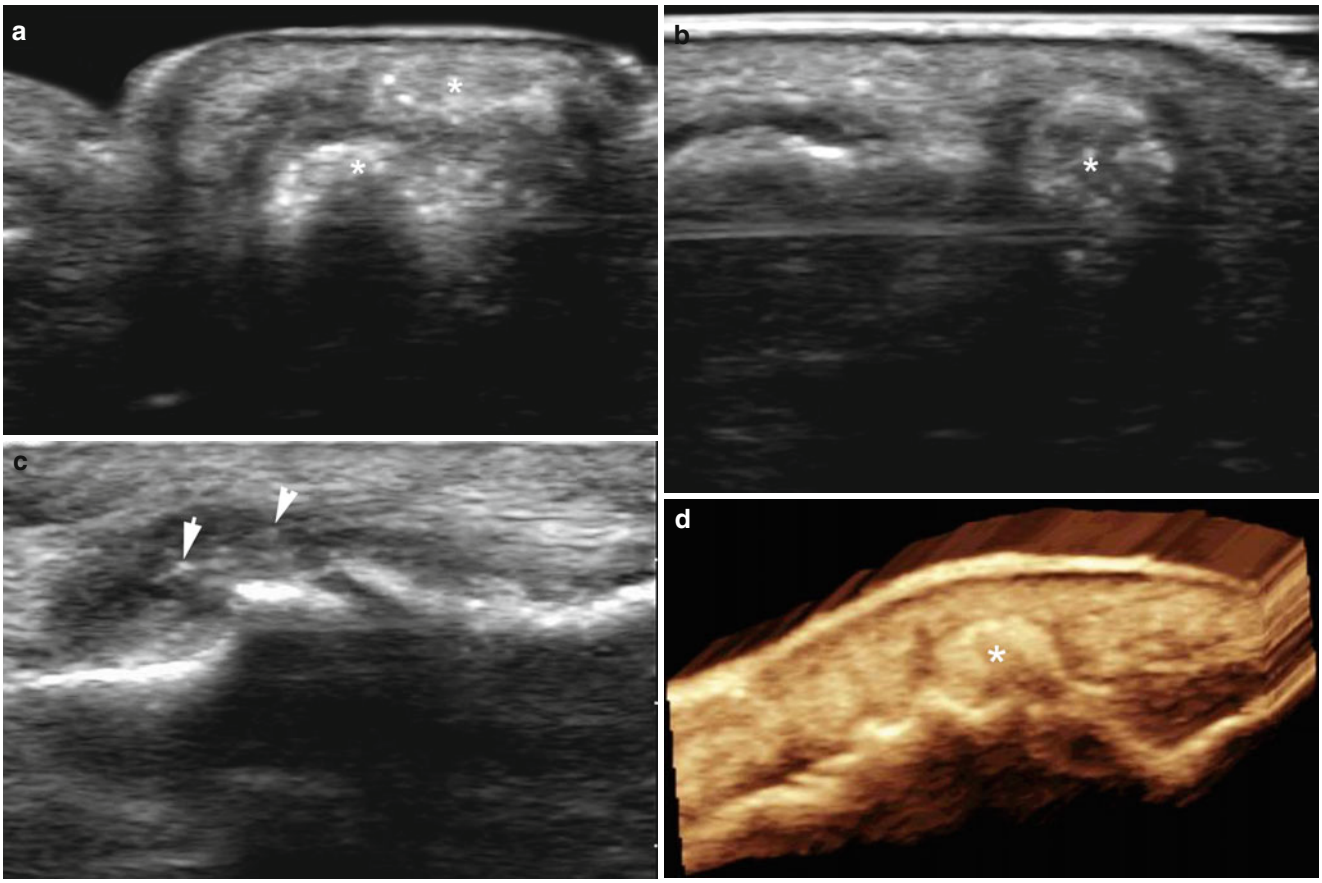

Fig. 20.56 (**a**–**d**) Gouty tophi. (**a**, **b**) Grey scale ultrasound images (lateral aspect of the left big toe; **a** transverse view; **b** longitudinal view) show hyperechoic subcutaneous periarticular deposits (*, gouty tophi). (**c**) Grey scale ultrasound image (longitudinal view, interphalangeal joint, left big toe) demonstrates synovitis with hyperechoic dots that correspond to crystal deposits (*arrow-arrowhead*) in the same case. (**d**) 3D ultrasound reconstruction highlights the periarticular gouty tophi (*)

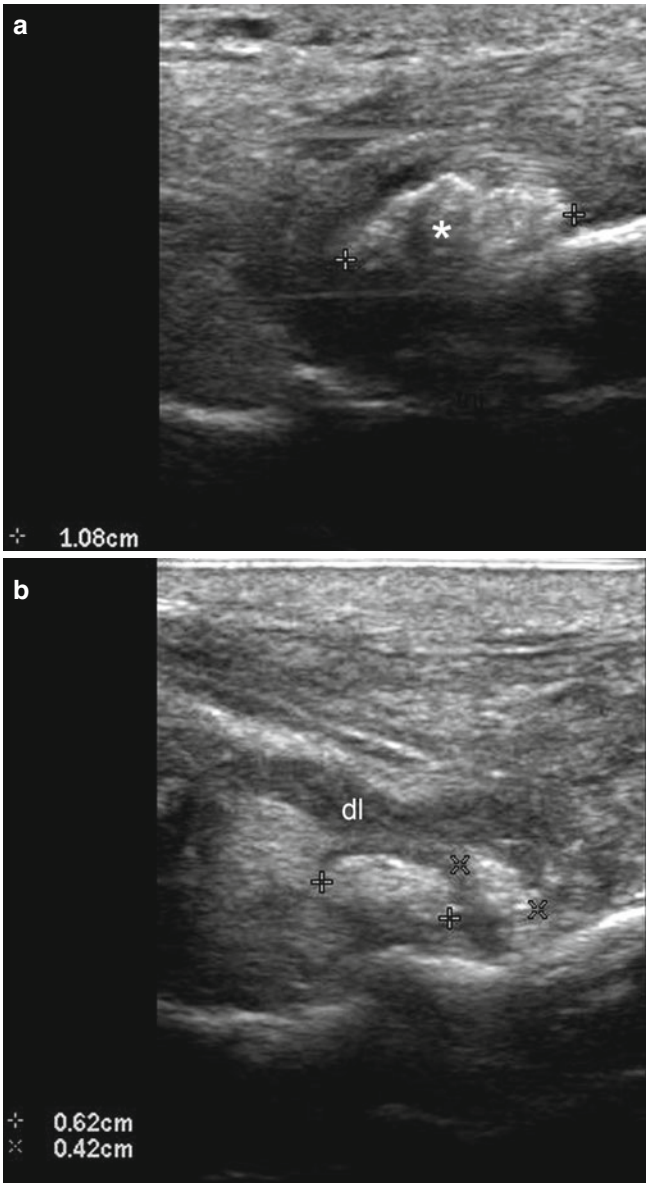

Fig. 20.57 (**a**, **b**) Gouty tophi. (**a**, **b**) Grey scale ultrasound images (longitudinal views; left foot; **a** talonavicular joint region; **b** deltoid ligament area) demonstrate hyperechoic deposits that resemble "wet sugar clumps". (**a**) 1.08 cm (long) deposit of crystals (*, between markers) is detected in the dorsum of the talonavicular joint. (**b**) Two deposits (between markers) that measure 0.62 cm and 0.42 cm (long), respectively, are well depicted in the medial aspect of the ankle close to deltoid ligament. *Abbreviations*: *tnj* talonavicular joint, *dl* deltoid ligament

20.2.12 Cartilage

20.2.12.1 Inflammation: Chondritis

Chondritis is inflammation of the cartilage and can affect superficial locations such as the ear pinna or the nasal tip. It can be associated with trauma or a history of piercing. Nevertheless, when several corporal regions are affected, it can be part of a rare autoimmune systemic disease called relapsing polychondritis. In the latter case, there are nasal, ear, and laryngotracheobronchial types of chondritis. Clinically, patients present with erythematous and sometimes painful swelling most commonly on the ear pinna or the nasal tip. When the ear pinna is affected, the ear lobe is not involved because anatomically it does not have cartilage. The red ears may resemble infectious cellulitis in advanced stages of auricular chondritis [94–96]. On sonography, thickening and increased echogenicity of the cartilage can be detected. In chronic or late phases, the cartilage can also present a beaded appearance and the perichondral tissues can become hypoechoic secondary to the inflammatory process. Variable degrees of vascularity can often be detected within the cartilage and surrounding tissues [97] (Figs. 20.58, 20.59, and 20.60).

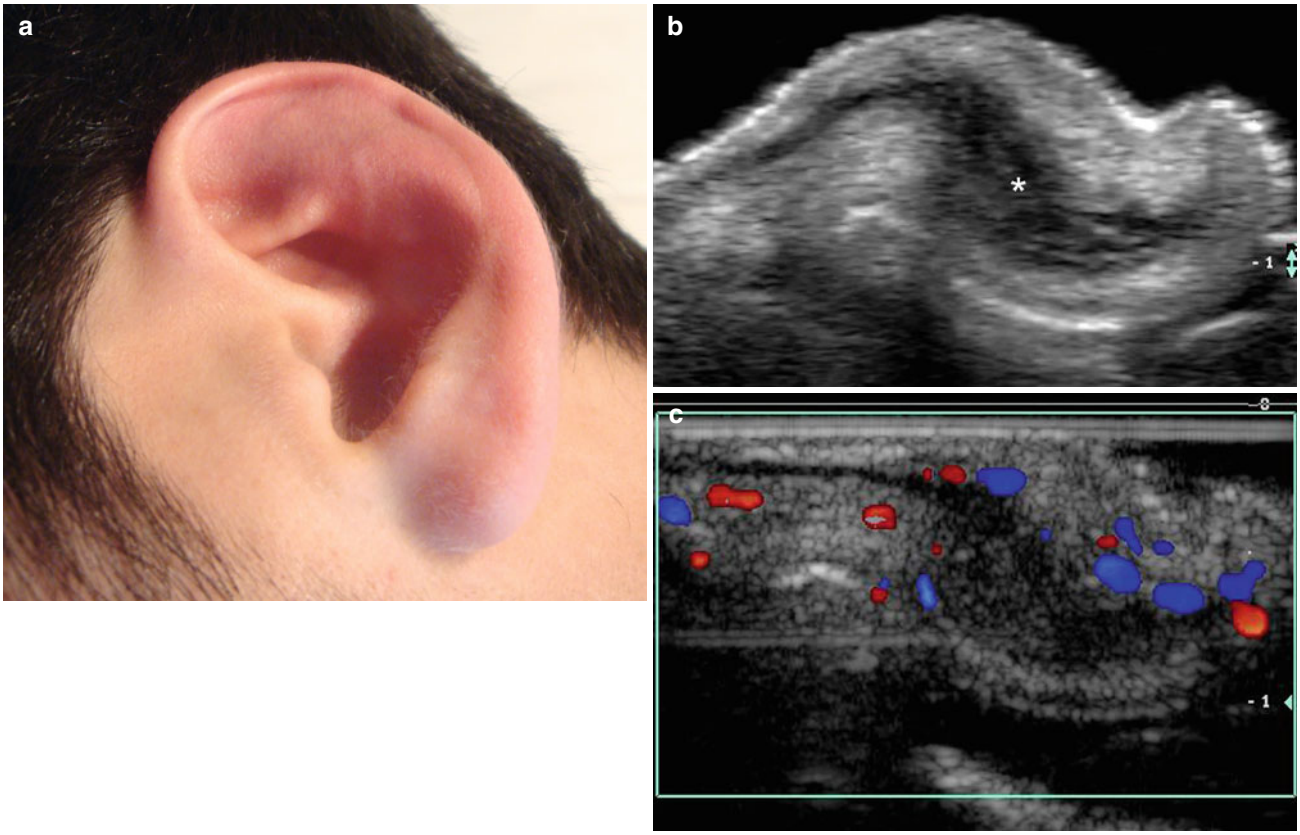

Fig. 20.58 (**a**–**c**) Chondritis and perichondritis. (**a**) Clinical photograph shows erythema and swelling of the left ear pinna. (**b**) Grey scale ultrasound image (transverse view) demonstrates a focal hypoechoic thickening (*) of the auricular cartilage. (**c**) Color Doppler ultrasound image (transverse view) shows increased blood flow in the periphery of the cartilage

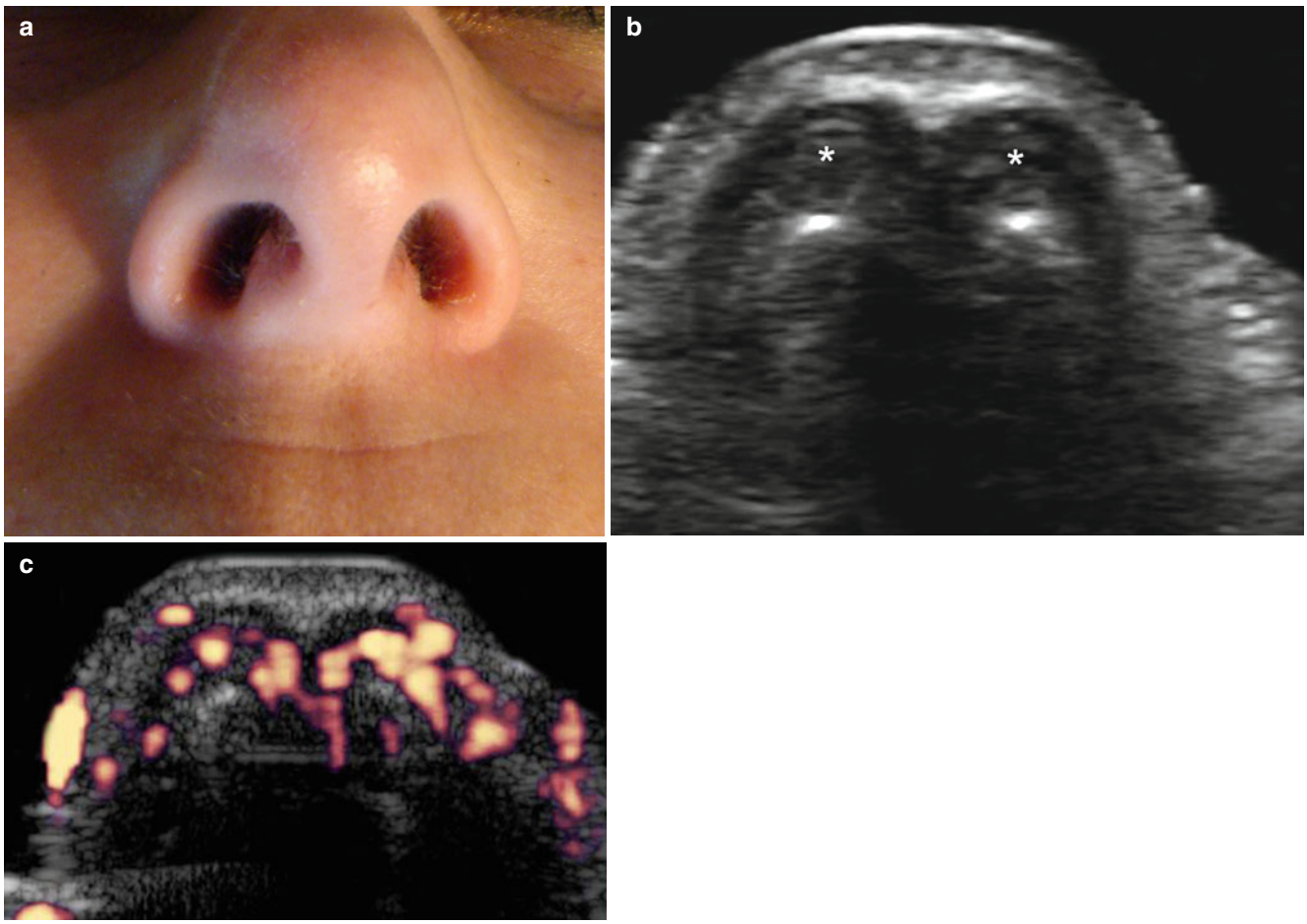

Fig. 20.59 Chondritis. (**a**) Clinical image shows mild erythema and swelling of the tip of the nose. (**b**) Grey scale ultrasound image (transverse view) demonstrates a mild diffuse thickening of the nasal cartilages (*). (**c**) Power Doppler ultrasound image (transverse view) shows increased blood flow within the nasal cartilages

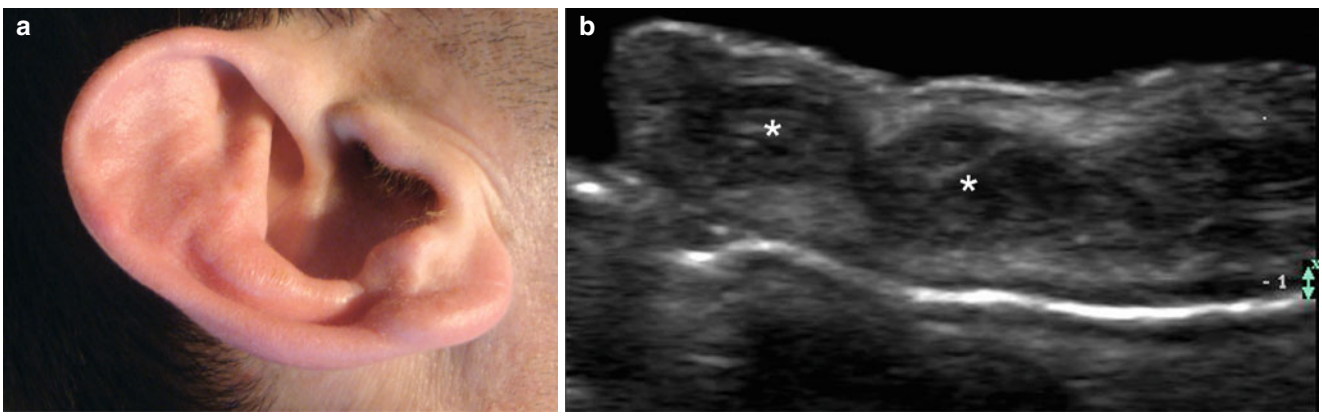

Fig. 20.60 (**a**, **b**) Chronic chondritis. (**a**) Clinical photograph shows erythema and swelling of the right ear pinna. (**b**) Grey scale ultrasound image (transverse view) demonstrates thickening of the auricular cartilage (*) that presents a beaded appearance

20.2.13 Bone

20.2.13.1 Heterotopic Ossification

Heterotopic ossification is the formation of bone outside the skeleton, usually related to trauma that includes injuries or surgeries. Nevertheless, heterotopic ossification can also affect the soft tissues, particularly in some neurologic or genetic diseases that do not present any history of trauma. Histologically, it is composed of well-differentiated compact bone [98–100]. Heterotopic ossification differs from *calcinosis cutis* because the latter implies deposit of calcium without lamellar mature bone. When the heterotopic bone deposits are located within the muscle the condition is called *myositis ossificans* [101, 102], and when the bone deposits are located in the subcutaneous tissue it is called *panniculitis ossificans* [103, 104]. In rare instances, a genetic autosomal dominant condition called *fibrodysplasia ossificans progressiva* (FOP), or Münchmeyer disease, produces progressive ossification of the fascial planes, muscles, tendons, and ligaments. Nearly all cases of FOP are caused by the identical mutation in the *ACVR1* gene that causes a single amino acid substitution (R206H) in the bone morphogenetic protein type I receptor ACVR1 (formerly known as ALK2) [105].

On sonography, the heterotopic bone deposits appear as hyperechoic spots, bands, or nodules that frequently produce posterior acoustic shadowing. Some deposits can show a low echogenicity in the center, associated with an outer sheet-like hyperechoic peripheral rim. The differentiation between heterotopic ossification (mature lamellar bone) and calcinosis (calcium deposits) is usually made histologically, although small or punctate hyperechoic deposits on the ultrasound examination will suggest calcinosis cutis, and large hyperechoic areas with strong acoustic shadowing will probably correspond to heterotopic ossification. Usually, no evidence of hypervascularity is detected on color Doppler ultrasound, although some slow flow and thin vessels may be detected in the periphery of the deposits (Fig. 20.61)

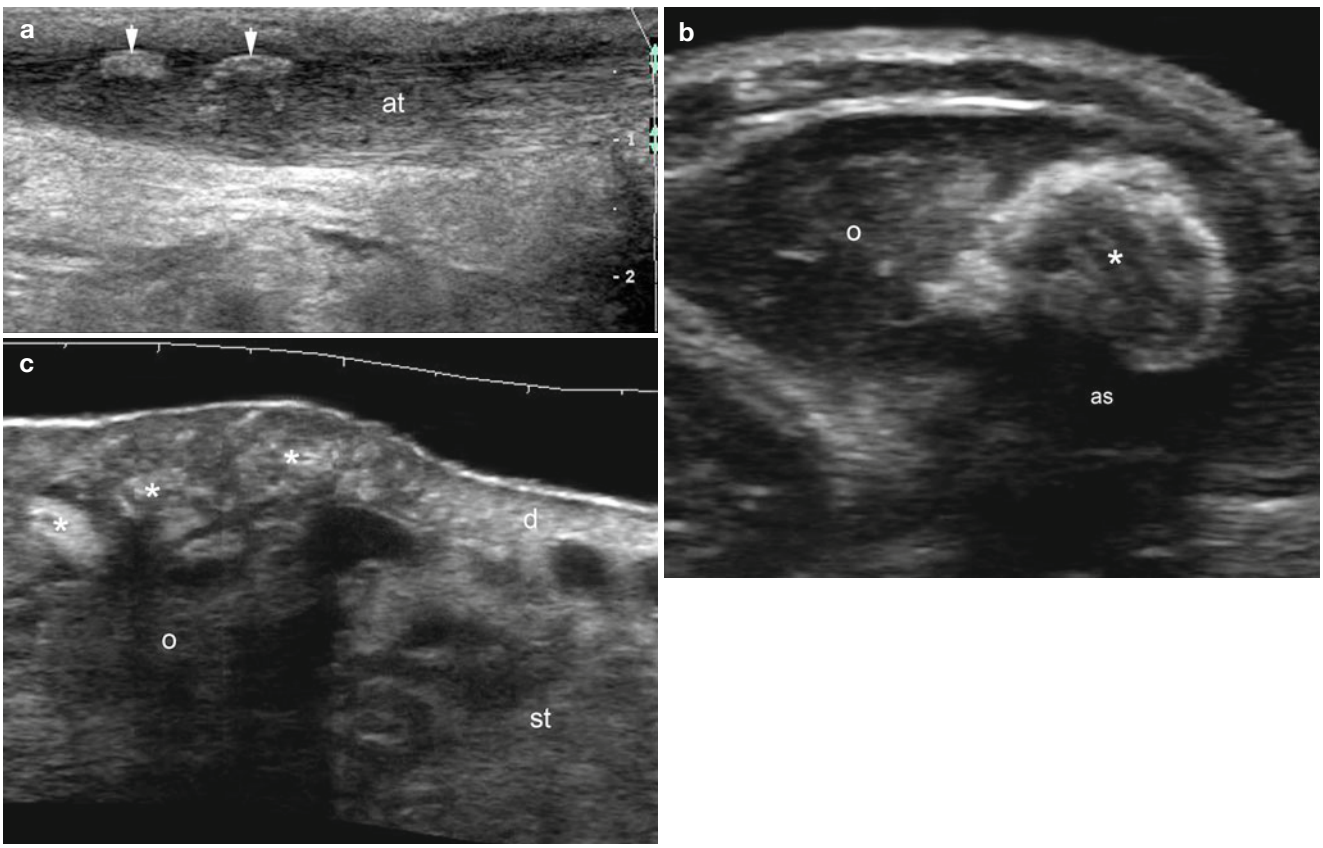

Fig. 20.61 (**a**–**c**) Heterotopic ossification. (**a**) Grey scale ultrasound image (longitudinal view, posterior aspect of the left ankle) demonstrates hyperechoic calcium deposits (*arrows*) within the Achilles tendon (*at*). Thickening and hypoechogenicity of the tendon are also detected (i.e., tendinosis and/or enthesopathy). (**b**) Grey scale ultrasound image (transverse view; lateral aspect of the left knee) shows a large hyperechoic calcium deposit within a fluid collection. The hyperechoic calcified structure generates a posterior acoustic shadowing artifact (*as*). Echoes (*o*, debris) are also seen within the collection. (**c**) Grey scale ultrasound image (longitudinal view, anterior aspect of the left leg) shows dermal and subcutaneous hyperechoic calcium deposits (*). The patient also presented with dilation and insufficiency of the perforant veins in the subcutaneous tissue (st). Hypoechogenicity (*o*) secondary to chronic inflammation is detected in the subcutaneous tissue

20.2.13.2 Tumors and Pseudotumors

20.2.13.2.1 Osteoma Cutis

Osteoma cutis is a focal deposit of well-differentiated bone in the dermis, subcutaneous tissue, and/or epicranius muscle and can be seen in the frontal region, scalp, and face. Clinically, osteoma cutis generates painless papules or lumps. Histologically, it is composed of lamellar bone with osteocytes in the center and osteoclasts in the external area. Osteoma cutis can be either primary, arising de novo in healthy skin, or secondary, developing in association with pre-existing neoplastic or inflammatory skin lesion (e.g., acne or trauma history) [106, 107]. On sonography, osteoma cutis appears as an hyperechoic oval-shaped or fusiform nodule or hyperechoic structure that produces posterior acoustic shadowing artifact (Fig. 20.62).

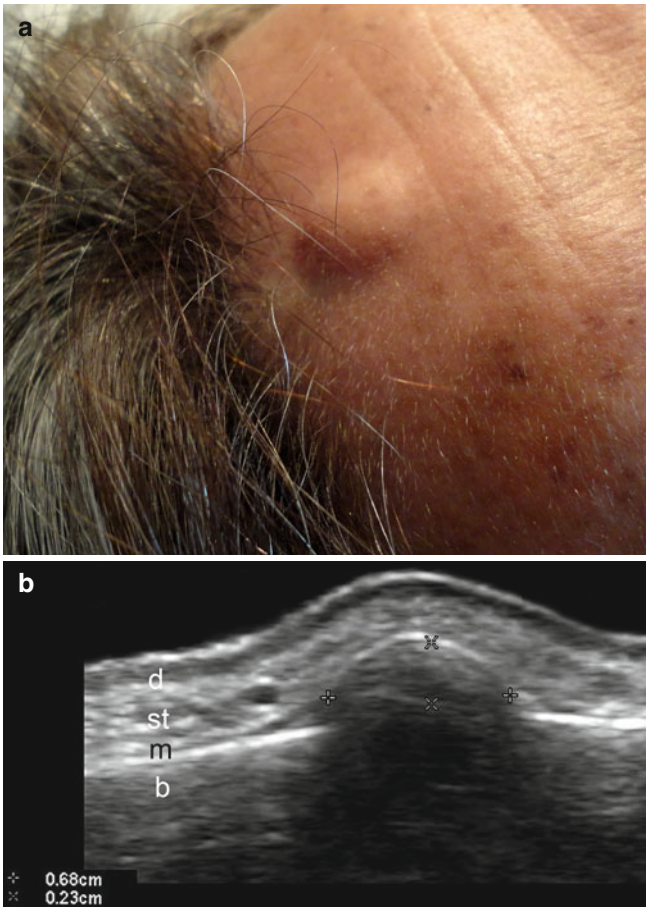

Fig. 20.62 (**a**, **b**) Osteoma cutis. (**a**) Clinical image shows a lump in the frontal region. (**b**) Grey scale ultrasound image (transverse view) demonstrates a 6.8 mm (wide) × 2.3 mm (deep) fusiform oval-shaped hyperechoic structure located between the epicranius muscle and the bony margin of the skull. The structure produces acoustic shadowing artifact. *Abbreviations*: *d* dermis, *st* subcutaneous tissue, *m* epicranius muscle, *b* bony margin of the skull

20.2.13.2.2 Exostoses

Exostoses are benign outgrowths of bone and/or calcified cartilaginous tissue (osteochondromas). They may bulge into the cutaneous layers or ungual plates and generate lumps, bumps, or challenging clinical appearances in areas where the skin is thin. They are histologically composed of mature lamellar bone that can be associated with an actively growing cartilaginous cap. On sonography, exostoses appear as hyperechoic bands connected to the bony margin. A common location for exostoses is the ungual bed where they can be associated with hypoechogenicity resulting from chronic inflammatory signs. On color Doppler imaging, hypovascularity in the periphery of the exostosis can be seen because of the long-term inflammation and granulomatous response [108] (Fig. 20.63).

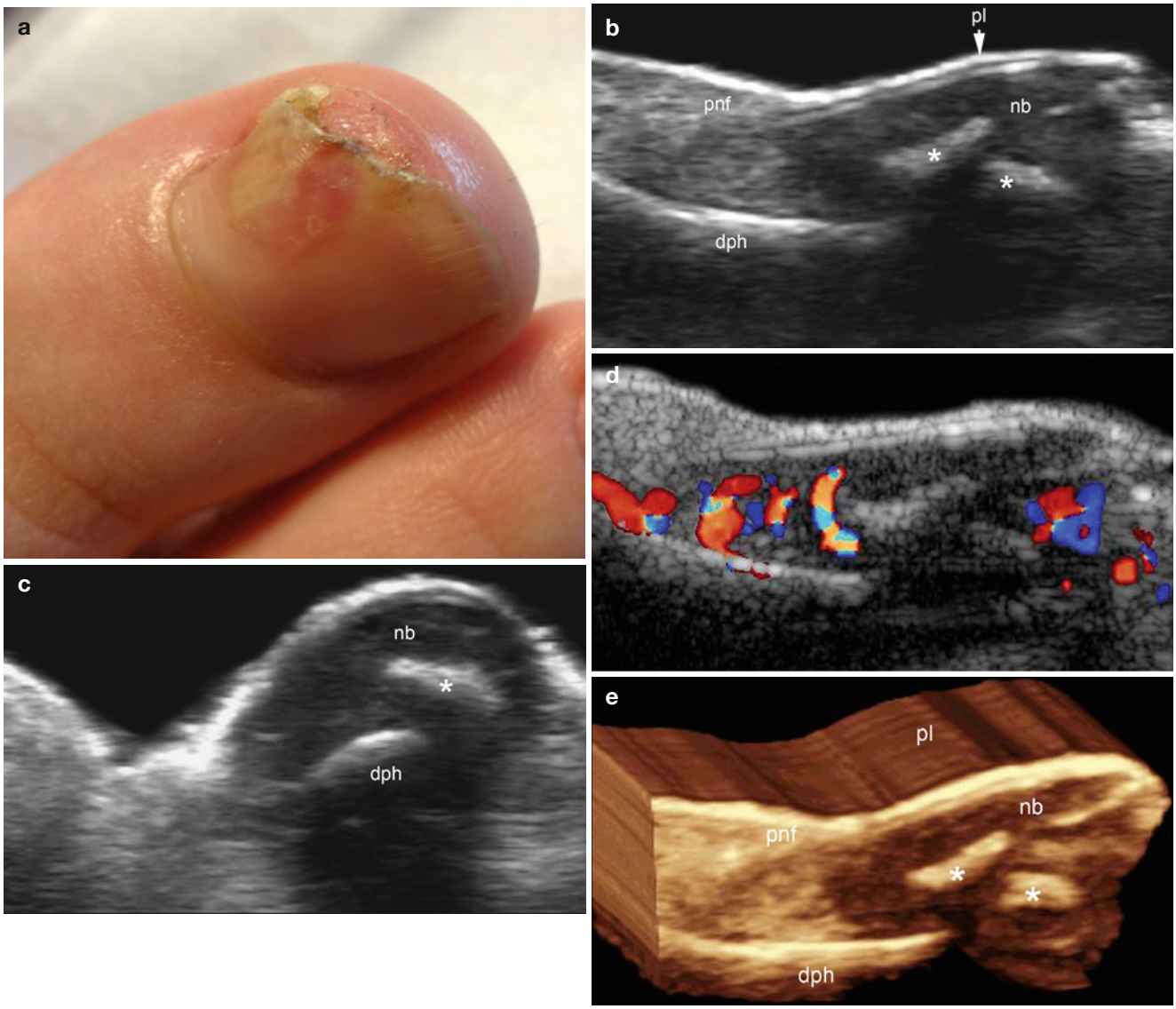

Fig. 20.63 (**a**–**e**) Subungual exostosis. (**a**) Clinical photograph shows erythema and swelling in the medial aspect of the nail of the right big toe. Dystrophic changes in the nail plate are also detected. (**b**, **c**) Grey scale ultrasound images (**b**: longitudinal view; **c**: transverse view) demonstrate a hyperechoic structure composed of two fragments (*) that bulge into the nail bed. (**d**) Color Doppler ultrasound image (longitudinal view) shows a mild increase in the vascularity of the nail bed. (**e**) 3D reconstruction (longitudinal view) highlights exostosis (*). *Abbreviations*: *nb* nail bed, *pl* nail plates, *dph* distal phalanx, *pnf* proximal nail fold

20.2.14 Fluid Collections

20.2.14.1 Hematomas-Serohematomas

Trauma is a common cause of hematic or sero-hematic fluid collections in the subcutaneous tissue and adjacent structures. On sonography, hematomas can appear as anechoic laminar band-like or large-sized sac-like, fluid-filled collections with thick walls and floating echoes (debris). In some types of plastic surgery (i.e., abdominoplasty), there is a high frequency of seromas or hematomas in the anterior abdominal wall that appear as exudates and become easily compressible anechoic lymph-like collections. The surrounding subcutaneous tissue often presents increased echogenicity because of edema [50] (Fig. 20.64).

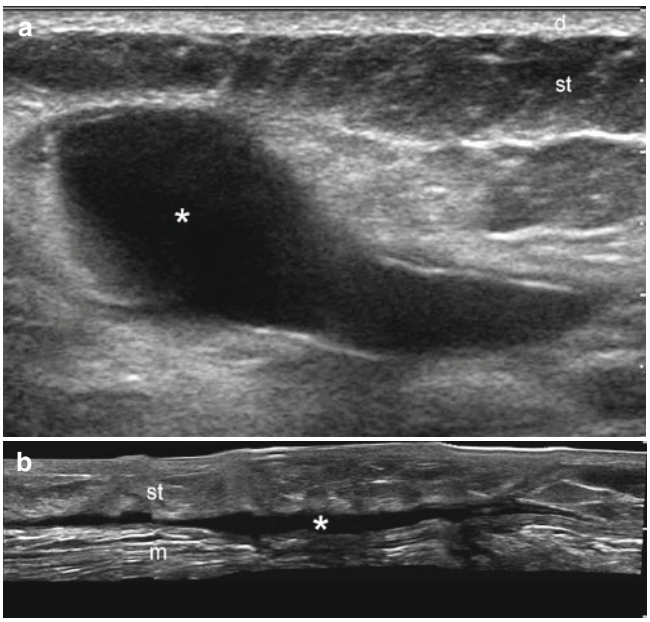

Fig. 20.64 (**a**, **b**). Serohematoma. (**a**) Grey scale ultrasound image (transverse view; lateral aspect of the left thigh) shows a well-defined anechoic fluid collection (*) in the subcutaneous tissue (post-trauma). Increased echogenicity of the surrounding subcutaneous tissue is also detected. (**b**) Grey scale ultrasound image (transverse view; abdominal wall; hypogastrium region) demonstrates anechoic band of fluid (*) in the deep subcutaneous tissue (post-abdominoplasty). Increased echogenicity of the subcutaneous tissue (*st*) is also seen in the vicinity of the collection. *Abbreviations*: *d* dermis, *st* subcutaneous tissue, *m* rectus abdominis muscle

20.2.15 Exogenous Components

20.2.15.1 Foreign Bodies

According to their nature, foreign bodies can be classified into two groups: organic (e.g., splinters of wood or thorns, fish hooks) or inert (e.g., pieces of glass and metal). Clinically, there is induration, erythema, and edema in the affected region. On sonography they present as hyperechoic laminar or billaminar bands frequently associated with hypoechoic granulomatous tissue in the periphery. Glass fragments and metallic foreign bodies usually show posterior reverberation artifact. On color Doppler ultrasound they can present variable degrees of vascularity in the periphery. Sonography supports early diagnosis by confirming the existence, nature of the exogenous material, and exact location and helps in guiding their removal [109] (Figs. 20.65, 20.66, 20.67, 20.68, 20.69, and 20.70).

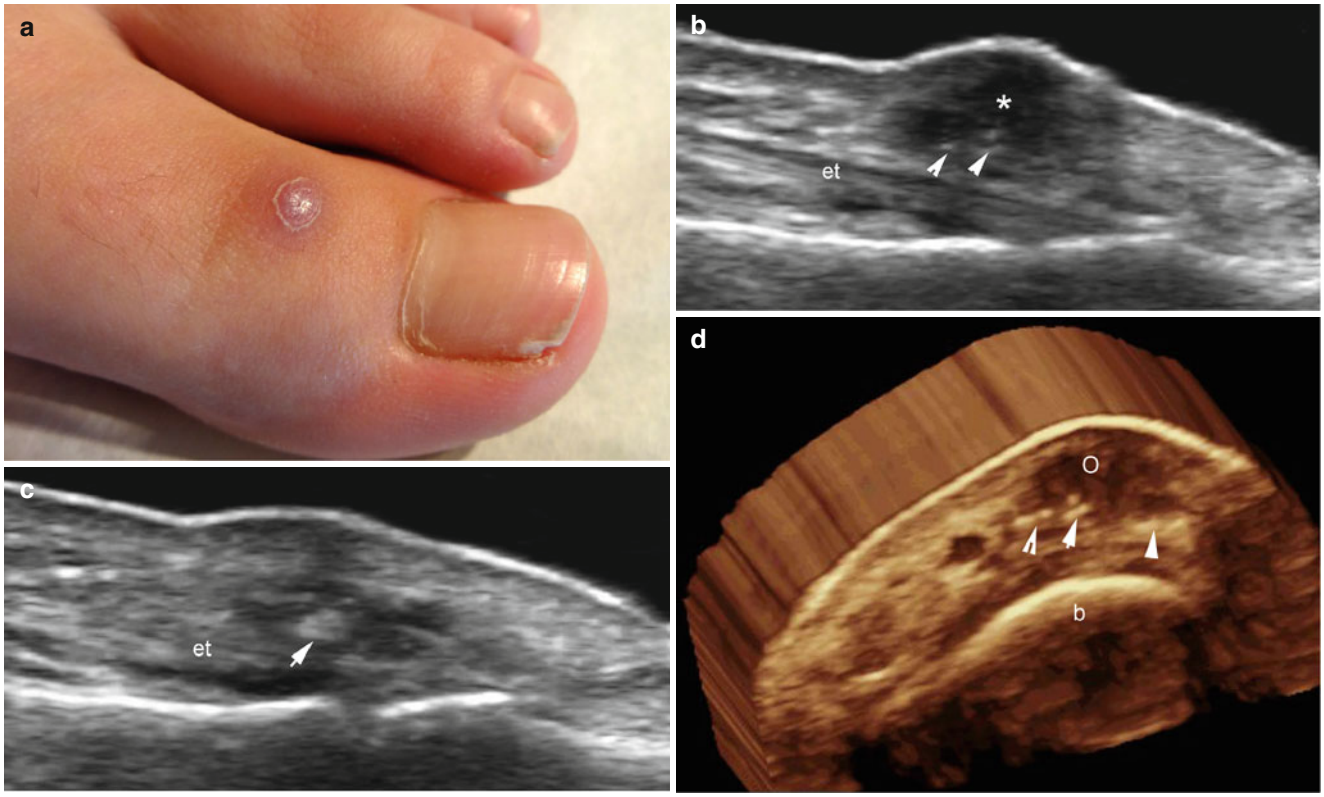

Fig. 20.65 (**a**–**d**) Foreign body-coral fragments. (**a**) Clinical image shows an erythematous swelling in the dorsum of the left big toe. (**b**, **c**) Grey scale ultrasound images (longitudinal views; **b** lateral to the interphalangeal (ip) joint; **c** at the ip joint level) demonstrate subcutaneous hyperechoic linear spots (*arrowheads*) and fragments (*arrow*) near the distal insertion of the extensor tendon (*et*). There is hypoechoic dermal and subcutaneous granulomatous tissue (*o*) surrounding the deposits. (**d**) 3D ultrasound reconstruction highlights the foreign body fragments (*arrowheads* and *arrow*) and the granulomatous tissue (*o*). *Abbreviations*: *b* bony margin of the proximal phalanx

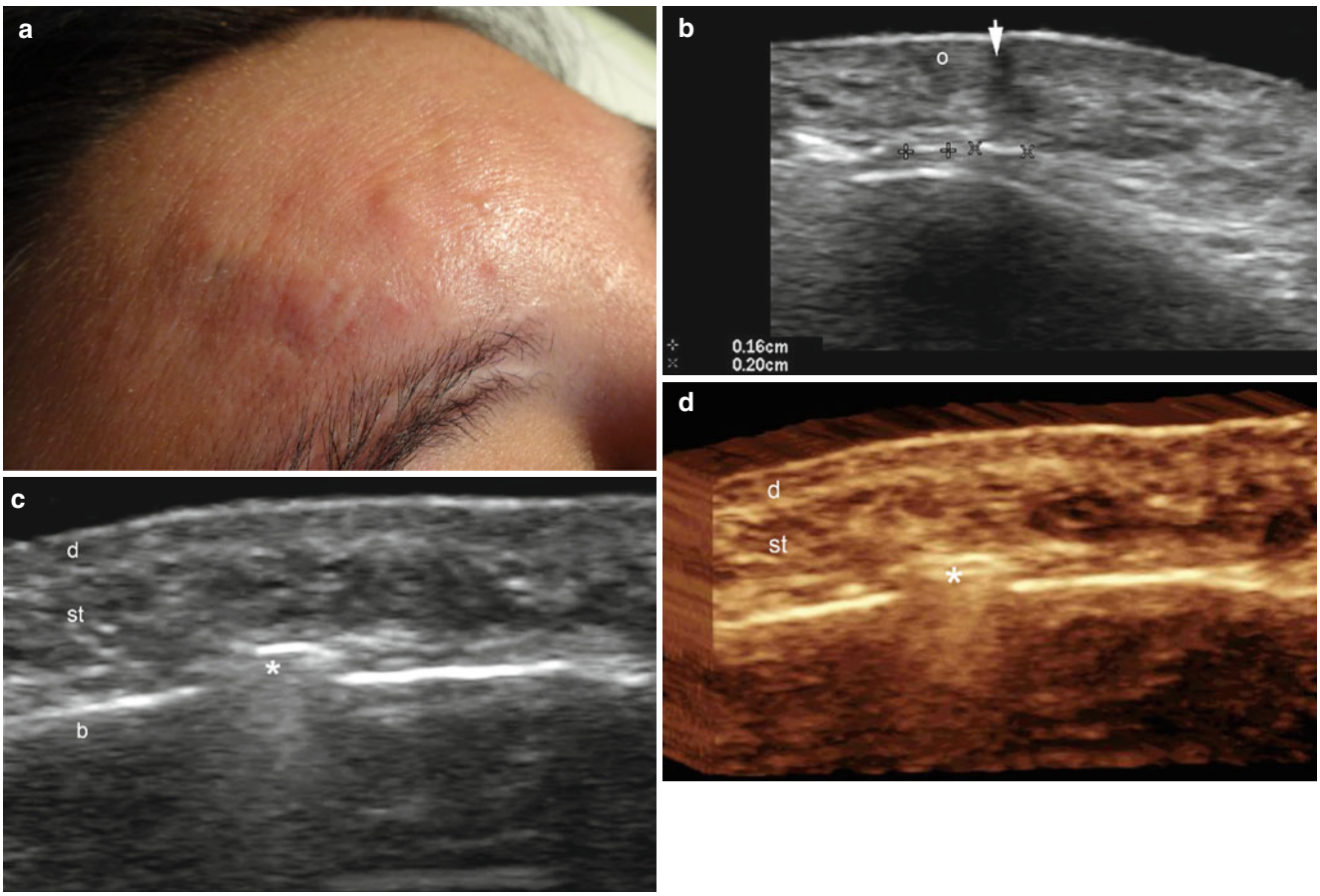

Fig. 20.66 (**a**–**d**) Foreign body-glass fragments. (**a**) Clinical image shows several erythematous papules in the frontal region. (**b**, **c**) Grey scale ultrasound images (transverse views at different levels of the same region) demonstrate multiple hyperechoic deep subcutaneous fragments (*, between markers, 1.6 to 2.6 mm wide) that generate a posterior reverberation artifact. Hypoechoic dermal granulomatous (*o*) and scarring areas (*arrow*) are also detected (b). *Abbreviations*: *d* dermis, *st* subcutaneous tissue

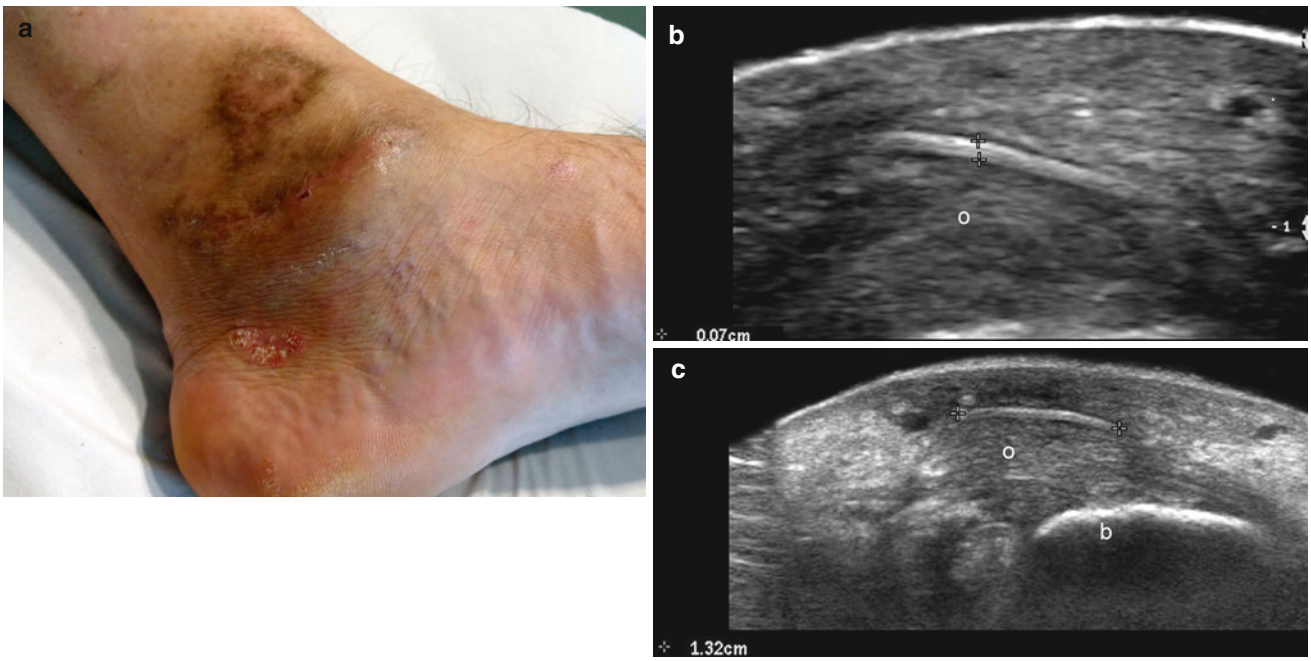

Fig. 20.67 (**a**–**c**) Foreign body-metallic wire. (**a**) Clinical photograph shows pigmentation, erythema, and swelling of the medial aspect of the left ankle and foot after corrective surgery. (**b**, **c**) Grey scale ultrasound images (transverse views; **b** zoomed image; **c** extended image) demonstrate a 13.2 mm (long) × 0.7 mm (thick) linear hyperechoic structure (fragment of metallic wire between markers) in the subcutaneous tissue. Hypoechoic granulomatous and scarring tissue (*o*) surrounds the wire. *Abbreviations*: *b* bony margin of the medial malleolus of the tibia

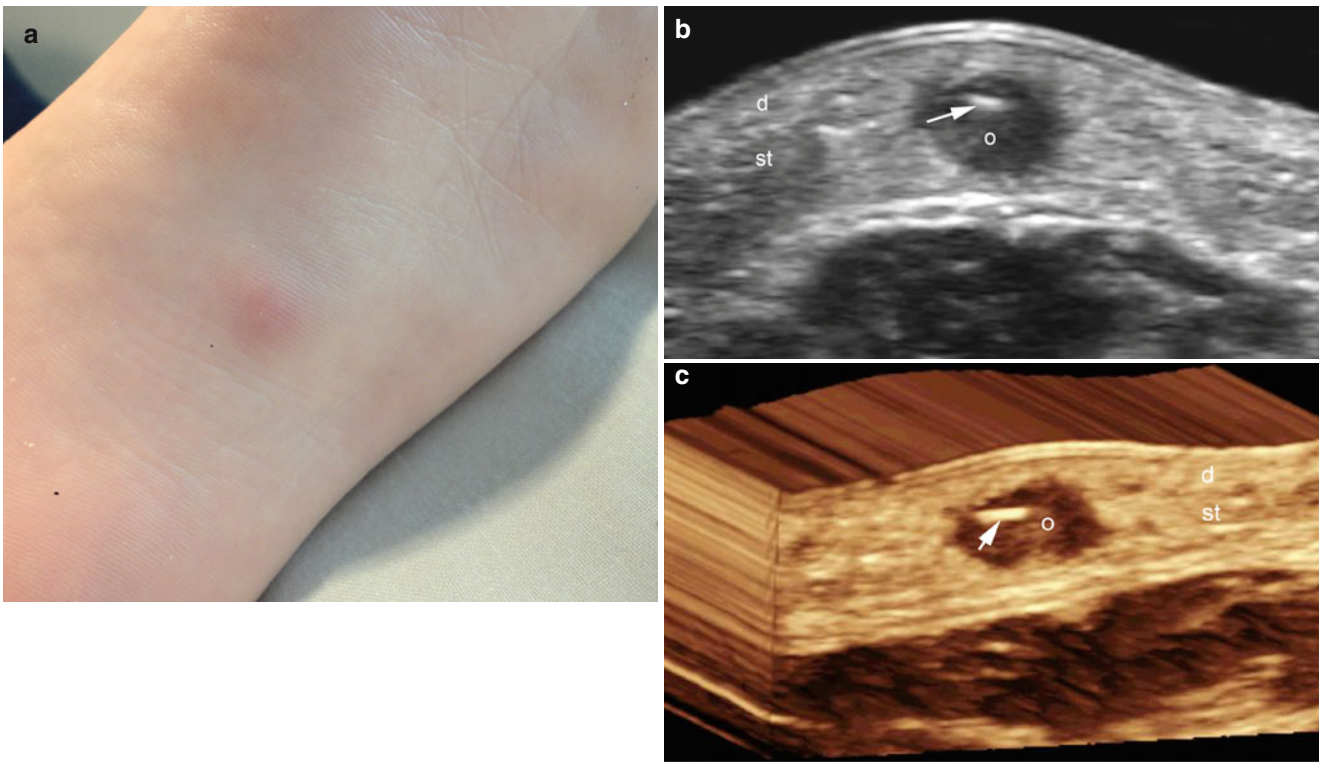

Fig. 20.68 (**a**–**c**) Foreign body-splinter of wood. (**a**) Clinical photograph demonstrates an erythematous swelling in the sole of the left foot. (**b**) Grey scale ultrasound image (transverse view) shows a hyperechoic linear structure (*arrow*, splinter of wood) surrounded by hypoechoic granulomatous tissue (*o*). Increased echogenicity of the surrounding subcutaneous tissue is also detected. (**c**) 3D ultrasound reconstruction (transverse view) highlights the foreign body (*arrow*) and the granulomatous reaction (*o*) in the vicinity. *Abbreviations*: *d* dermis, *st* subcutaneous tissue

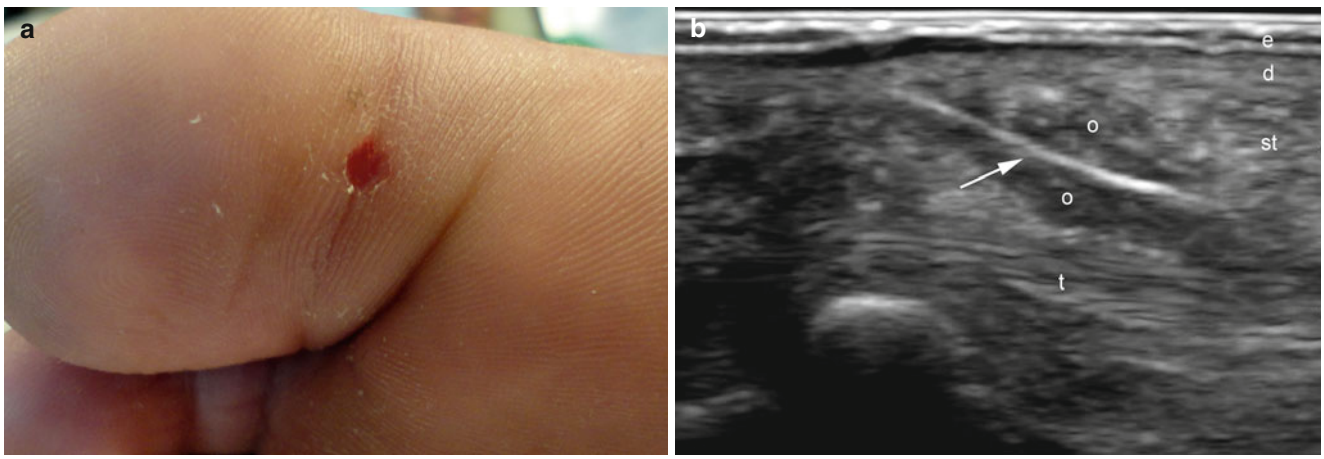

Fig. 20.69 (**a**–**c**) Foreign body-fragment of coral. (**a**) Clinical photograph shows a reddish disruption of the plantar skin in the right big toe. (**b**) Grey scale ultrasound image (longitudinal view) shows a hyperechoic linear fragment (*arrow*, coral fragment) surrounded by hypoechoic granulomatous tissue (*o*). (**c**) Color Doppler ultrasound image (longitudinal view) shows a mild increase of the regional vascularity. *Abbreviations*: *e* epidermis, *d* dermis, *st* subcutaneous tissue, *t* flexor hallucis longus tendon

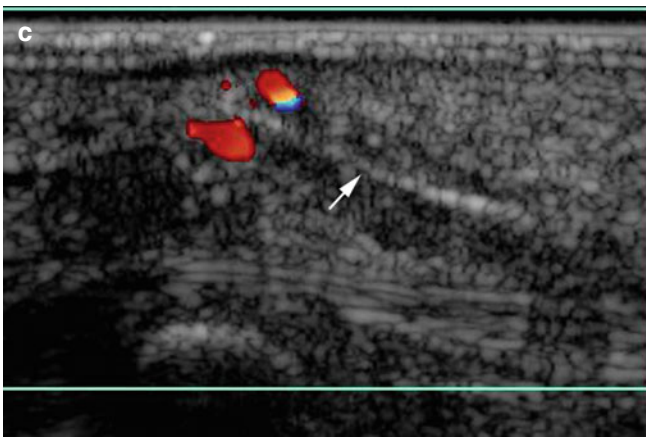

Fig. 20.69 (continued)

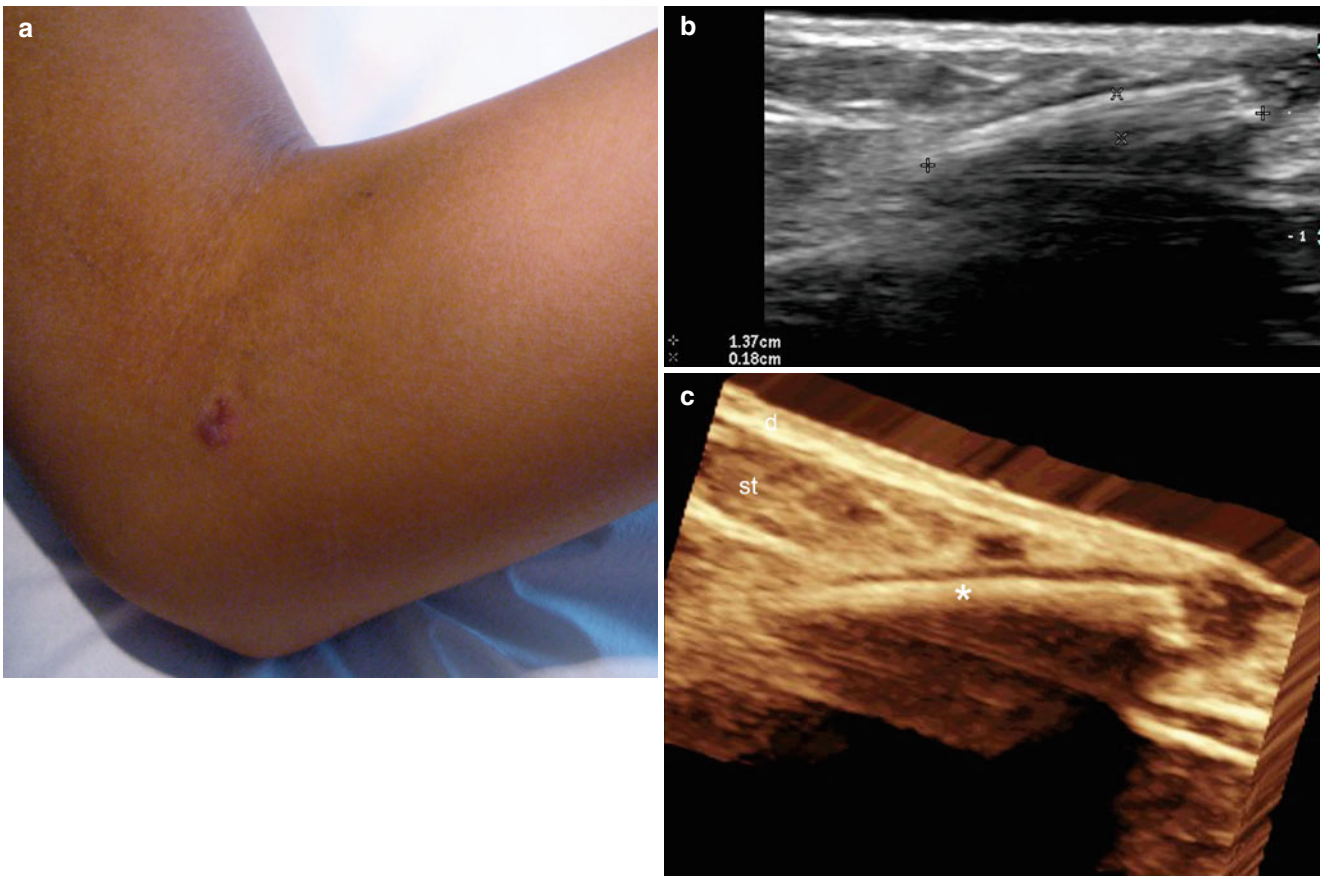

Fig. 20.70 (**a**–**c**) Foreign body-splinter of wood. (**a**) Clinical photograph shows a reddish papule in the ulnar aspect of the left elbow. (**b**) Grey scale ultrasound image (longitudinal view) demonstrates a 1.37 cm (long) × 0.18 cm (thick) hyperechoic band (*, splinter of wood) in the dermis and subcutaneous tissue. (**c**) 3D ultrasound reconstruction (longitudinal view) highlights the splinter of wood (*). *Abbreviations*: *d* dermis, *st* subcutaneous tissue

20.2.15.2 Prosthetic Devices-Implants-Exogenous Synthetic Materials

Several prosthetic devices are used in corrective surgeries. These materials are usually composed of pure silicone, high-density porous polyethylene structures, or metallic materials that may rupture, fracture, and/or migrate to the skin or subungual regions. On sonography, pure silicone devices appear as oval or round-shaped, well-defined anechoic structures that when ruptured in the subcutaneous tissue, turn to hyperechoic material with posterior reverence artifact. The modification of the echogenicity is probably a result of the mix of fat and pure silicone that provides a dense oily material. On sonography, silicone oil has a hyperechoic appearance with posterior reverberation artifact also termed the "snow storm" pattern. The high-density porous polyethylene components appear as hyperechoic bands of variable sizes that can be associated with hypoechoic inflammatory tissue in the periphery. Metallic devices are usually hyperechoic bands or spots that most commonly present as posterior reverberation artifact [50, 109] (Fig. 20.71, 20.72, 20.73, and 20.74).

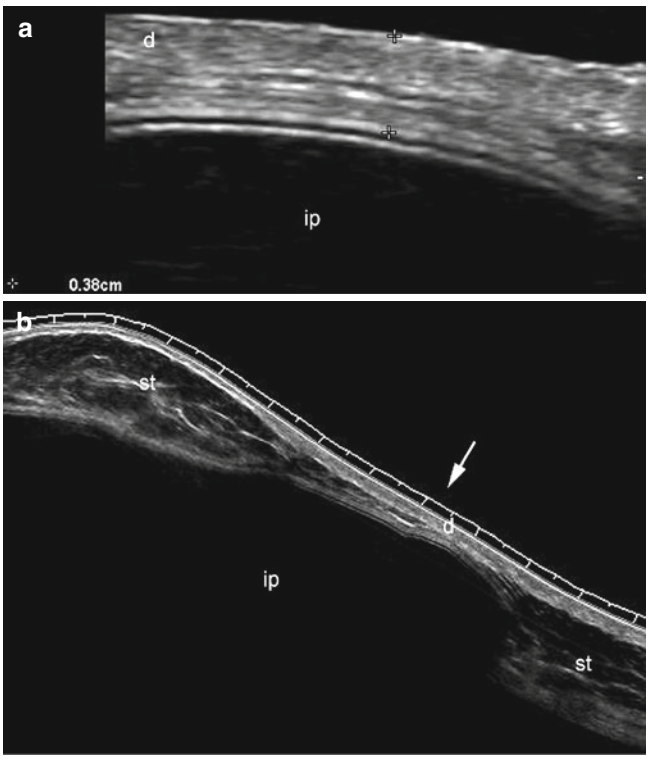

Fig. 20.71 (**a**, **b**) Breast implant. (**a**, **b**) Grey scale ultrasound images (longitudinal views; **a** zoomed image; **b** extended field of view) show a region with atrophy of the subcutaneous tissue (*arrow*) and almost direct contact between the anechoic well-defined silicone implant (*ip*) and the dermis. The distance between the epidermal layer and the implant is 3.8 mm in this location. The patient presented with erythema in the same region. *Abbreviations*: *d* dermis, *st* subcutaneous tissue

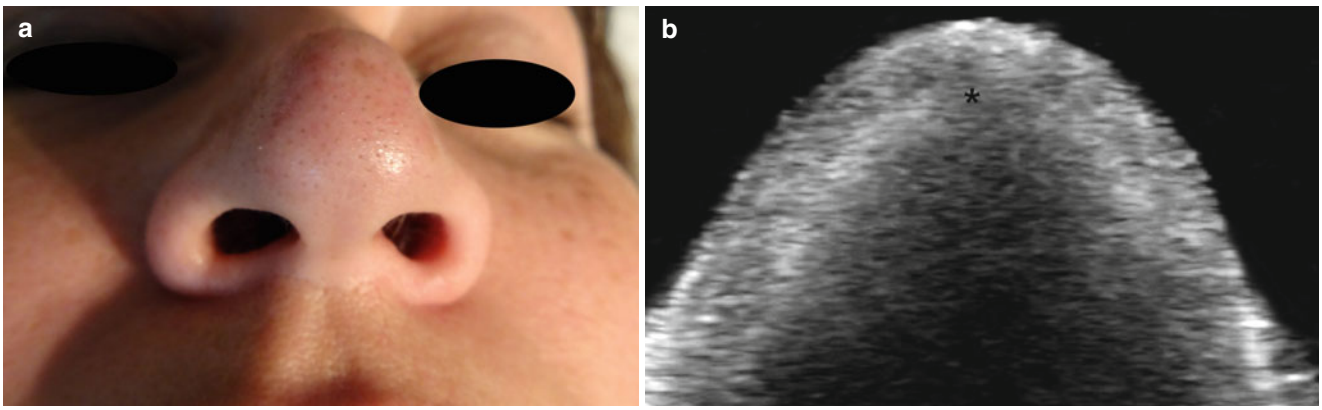

Fig. 20.72 (**a**–**c**) Silicone oil. (**a**) Clinical photograph shows erythema and swelling of the tip of the nose. (**b**, **c**) Grey scale ultrasound images (**b** transverse view; **c** longitudinal view; tip of the nose) demonstrate extensive deposit of hyperechoic material (*) that presents a posterior reverberation artifact and a "snow storm" pattern in the dermis and subcutaneous tissue. Notice that the exogenous material passes through the nasal cartilages. Therefore, the nasal cartilages are covered by the silicone oil

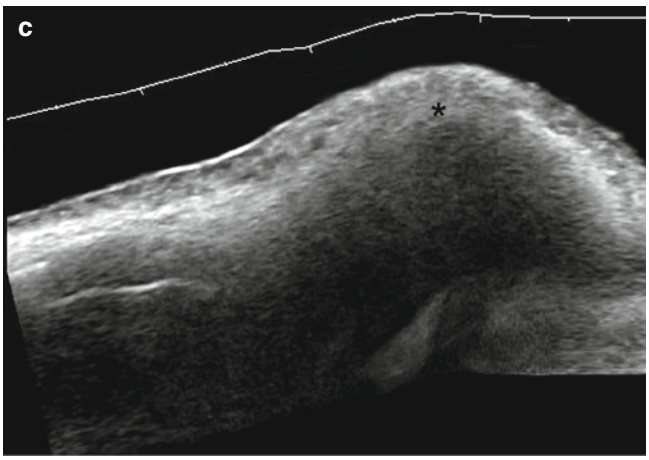

Fig. 20.72 (continued)

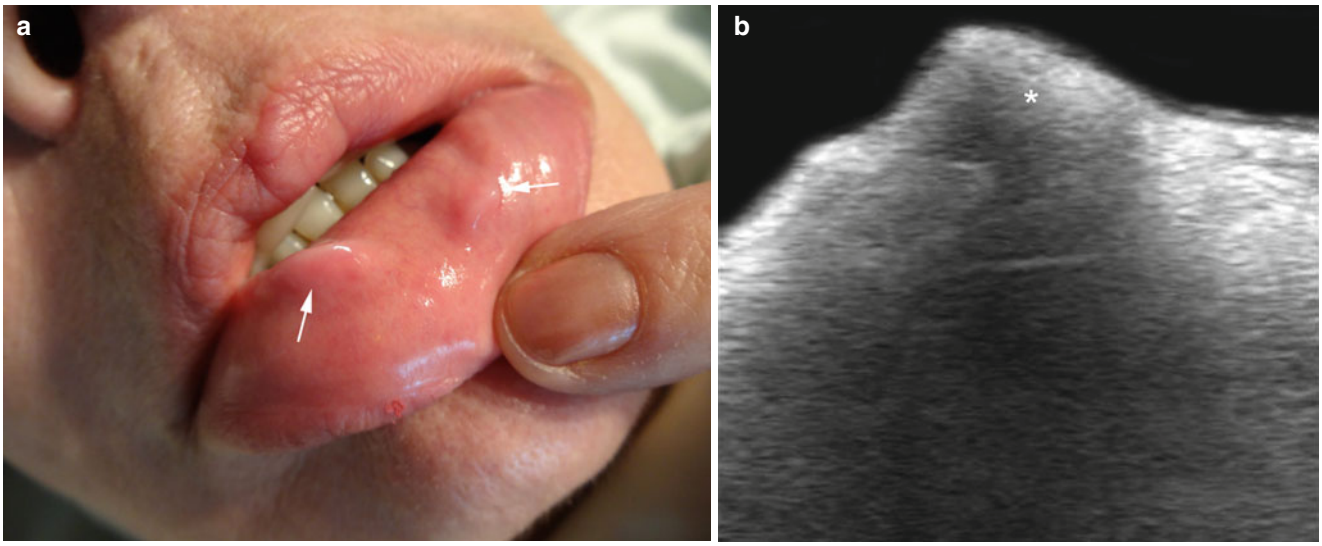

Fig. 20.73 (**a**, **b**) Silicone oil. (**a**) Clinical image shows lumps (*arrows*) in the vestibule of the oral cavity. (**b**) Grey scale ultrasound image (transverse view) demonstrates hyperechoic material (*) that produces posterior reverberation artifact and a "snow storm" pattern affecting the lower lip layers (submucosal and orbicularis muscle)

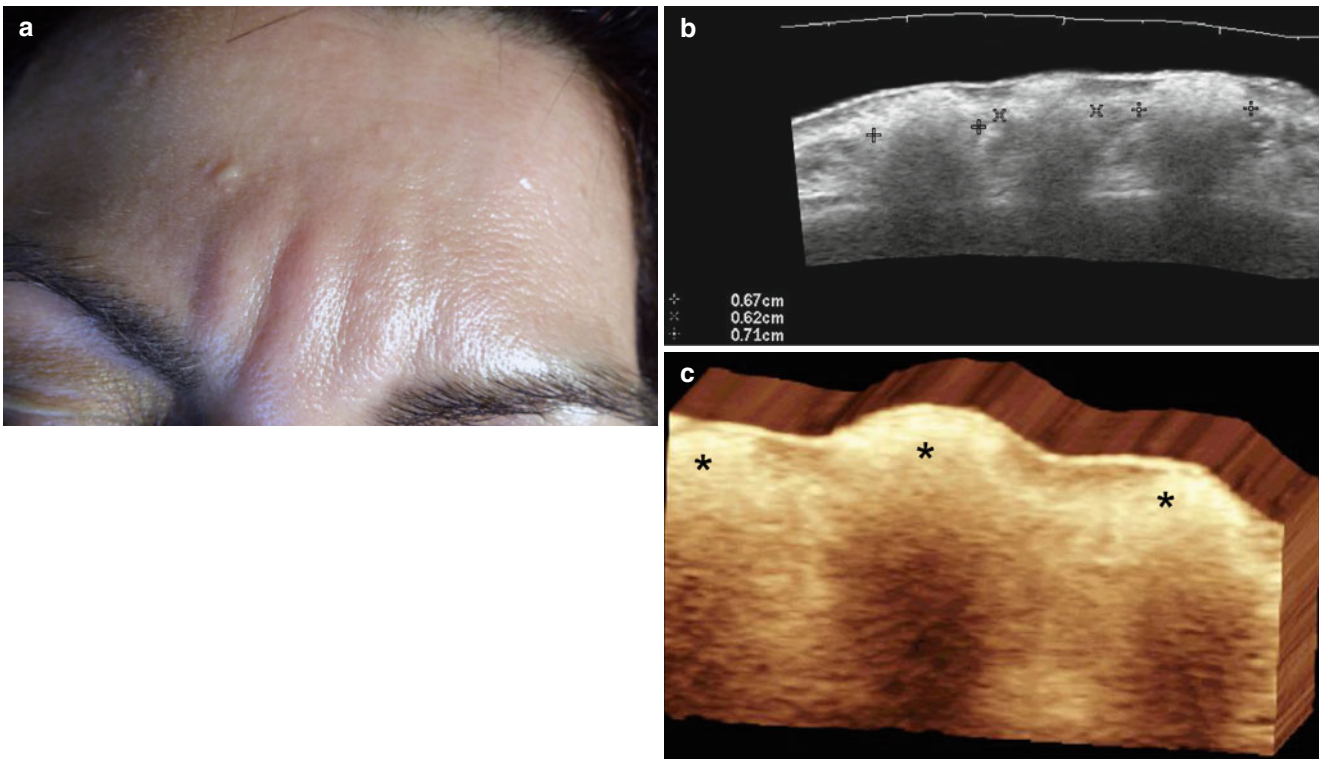

Fig. 20.74 (**a**–**c**) Silicone oil. (**a**) Clinical photograph shows three bumps in the glabellar region. (**b**) Grey scale ultrasound image (transverse view) demonstrates three hyperechoic dermal and subcutaneous deposits that measure 6.7, 6.2 and 7.1 mm (wide), respectively. The deposits generate posterior reverberation and present a "snow storm" pattern. (**c**) 3D ultrasound reconstruction (transverse view) highlights the exogenous deposits

Tips

- Anatomical location is a key factor for assessing the differential diagnosis in this wide spectrum of simulators.
- The addition of a lower frequency probe can provide a better image of the deeper layers, therefore, a more complete image of the lesion site and adjacent structures will be obtained.

References

1. Restrepo R, Oneto J, Lopez K, Kukreja K. Head and neck lymph nodes in children: the spectrum from normal to abnormal. Pediatr Radiol. 2009;39:836–46.
2. Ridder GJ, Richter B, Disko U, Sander A. Gray-scale sonographic evaluation of cervical lymphadenopathy in cat-scratch disease. J Clin Ultrasound. 2001;29:140–5.
3. Psarros G, Riddell J, Gandhi T, Kauffman CA, Cinti SK. Bartonella henselae infections in solid organ transplant recipients: report of 5 cases and review of the literature. Medicine (Baltimore). 2012;91:111–21.
4. Diebold J. Reactive hyperplasia and pseudo-lymphomas with hypergammaglobulinemia. I. Benign lymphadenopathies. Ann Pathol. 1983;3:269–83 (French).
5. Kojima M, Motoori T, Asano S, Nakamura S. Histological diversity of reactive and atypical proliferative lymph node lesions in systemic lupus erythematosus patients. Pathol Res Pract. 2007;203:423–31.
6. Kojima M, Motoori T, Nakamura S. Benign, atypical and malignant lymphoproliferative disorders in rheumatoid arthritis patients. Biomed Pharmacother. 2006;60:663–72.
7. Kuna SK, Bracic I, Tesic V, Kuna K, Herceg GH, Dodig D. Ultrasonographic differentiation of benign from malignant neck lymphadenopathy in thyroid cancer. J Ultrasound Med. 2006;25:1531–7.
8. Catalano O, Voit C, Sandomenico F, Mandato Y, Petrillo M, Franco R, et al. Previously reported sonographic appearances of regional melanoma metastases are not likely due to necrosis. J Ultrasound Med. 2011;30:1041–9.
9. Gupta A, Rahman K, Shahid M, Kumar A, Qaseem SM, Hassan SA, et al. Sonographic assessment of cervical lymphadenopathy: role of high-resolution and color Doppler imaging. Head Neck. 2011;33:297–302.
10. Ying L, Hou Y, Zheng HM, Lin X, Xie ZL, Hu YP. Real-time elastography for the differentiation of benign and malignant superficial lymph nodes: a meta-analysis. Eur J Radiol. 2012;81:2576–84.
11. Samir N, Al-Mahrezi A, Al-Sudairy S. Odontogenic cutaneous fistula: report of two cases. Sultan Qaboos Univ Med J. 2011;11:115–8.
12. Cioffi GA, Terezhalmy GT, Parlette HL. Cutaneous sinus tract: an odontogenic etiology. J Am Acad Dermatol. 1986;14:94–100.
13. Stoll HL, Solomon HA. Cutaneous sinuses of dental origin. JAMA. 1963;184:120–4.
14. Wortsman X, Wortsman J. Skin ultrasound, chapter 9. In: Dogra V, Gaitini D, editors. Musculoskeletal ultrasound with CT and MRI correlation. 1st ed. New York/Stuttgart: Thieme; 2010. p. 147–70.

15. Wortsman X, Gutierrez M, Saavedra T, Honeyman J. The role of ultrasound in rheumatic skin and nail lesions: a multi-specialist approach. Clin Rheumatol. 2011;30:739–48.
16. Santiago W, Rybak LP, Bass RM. Thyroglossal duct cyst of the tongue. J Otolaryngol. 1985;14:261–4.
17. Allard RH. The thyroglossal cyst. Head Neck Surg. 1982;5: 134–46.
18. Kutuya N, Kurosaki Y. Sonographic assessment of thyroglossal duct cysts in children. J Ultrasound Med. 2008;27:1211–9.
19. Ahuja AT, King AD, Metreweli C. Sonographic evaluation of thyroglossal duct cysts in children. Clin Radiol. 2000;55:770–4.
20. Turkington JR, Paterson A, Sweeney LE, Thornbury GD. Neck masses in children. Br J Radiol. 2005;78:75–85.
21. Ahuja AT, King AD, King W, Metreweli C. Thyroglossal duct cysts: sonographic appearances in adults. AJNR Am J Neuroradiol. 1999;20:579–82.
22. Waldhausen JH. Branchial cleft and arch anomalies in children. Semin Pediatr Surg. 2006;15:64–9.
23. Warren MJ, Spencer K, Nayagam M. Sorographic appearance of branchial cysts. Clin Radiol. 1994;49:359–60.
24. Wortsman X, Calderón P, Arellano J, Orellana Y. High-resolution color Doppler ultrasound of a caliber-persistent artery of the lip, a simulator variant of dermatologic disease: case report and sonographic findings. Int J Dermatol. 2009;48:830–3.
25. Arellano J, Antoniazzi C, Wortsman X. Early diagnosis of a calibre persistent labial artery in a child: usefulness of ultrasonography. Australas J Dermatol. 2012;53:e18–9.
26. Romera-Villegas A, Vila-Coll R, Poca-Dias V, Cairols-Castellote MA. The role of color duplex sonography in the diagnosis of giant cell arteritis. J Ultrasound Med. 2004;23:1493–8.
27. Ball EL, Walsh SR, Tang TY, Gohil R, Clarke JM. Role of ultrasonography in the diagnosis of temporal arteritis. Br J Surg. 2010;97:1765–71.
28. Celik H, Yücel C, Oktar S, Karadag Z, Ozdemir H. Iatrogenic pseudoaneurysm of the superior thyroid artery: color Doppler ultrasonographic diagnosis and treatment approach. J Ultrasound Med. 2004;23:1675–8.
29. Lee KH, Ko EY, Han BK, Shin JH, Kang SS, Hahn SY. Thrombosed pseudoaneurysm of the breast after blunt trauma. J Ultrasound Med. 2009;28:233–8.
30. Blättler W, Schwarzenbach B, Largiadèr J. Superficial vein thrombophlebitis – serious concern or much ado about little? Vasa. 2008;37:31–8.
31. Bernathova M, Bein E, Bendix N, Bodner G. Sonographic diagnosis of plantar vein thrombosis: report of 3 cases. J Ultrasound Med. 2005;24:101–3.
32. Yanik B, Conkbayir I, Oner O, Hekimo lu B. Imaging findings in Mondor's disease. J Clin Ultrasound. 2003;31:103–7.
33. Machan K, Rojo-Carmona LE, Marquez-Moreno AJ, Herrera-Imbroda B, Ruiz-Escalante JF, Herrera-Gutierrez D, et al. Ultrasound diagnosis of three cases of Mondor's disease. Arch Esp Urol. 2012;65:262–6.
34. Stiegler H, Rotter G, Standl R, Mosavi S, von Kooten HJ, Weichenhain B, et al. Value of color duplex ultrasound in diagnosis of insufficiency of perforant veins. A prospective study of 94 patients. Vasa. 1994;23:109–13.
35. Klauser AS, Faschingbauer R, Bauer T, Wick MC, Gabl M, Arora R, et al. Entrapment neuropathies II: carpal tunnel syndrome. Semin Musculoskelet Radiol. 2010;14:487–500.
36. Guan J, Ji F, Chen W, Chu H, Lu Z. Sonographic and electrophysiological detection in patients with carpal tunnel syndrome. Neurol Res. 2011;33:970–5.
37. Ghasemi-Esfe AR, Khalilzadeh O, Vaziri-Bozorg SM, Jajroudi M, Shakiba M, Mazloumi M, et al. Color and power Doppler US for diagnosing carpal tunnel syndrome and determining its severity: a quantitative image processing method. Radiology. 2011;261: 499–506.
38. Mohammadi A, Ghasemi-Rad M, Mladkova-Suchy N, Ansari S. Correlation between the severity of carpal tunnel syndrome and color Doppler sonography findings. AJR Am J Roentgenol. 2012;198:W181–4.
39. Tsai WC, Chiou HJ, Chou YH, Wang HK, Chiou SY, Chang CY. Differentiation between schwannomas and neurofibromas in the extremities and superficial body: the role of high-resolution and color Doppler ultrasonography. J Ultrasound Med. 2008;27:161–6.
40. Martinoli C, Bianchi S, Derchi LE. Ultrasonography of peripheral nerves. Semin Ultrasound CT MR. 2000;21:205–13.
41. Lee JY, Kim SM, Fessell DP, Jacobson JA. Sonography of benign palpable masses of the elbow. J Ultrasound Med. 2011;30:1113–9.
42. Wu KK. Morton neuroma and metatarsalgia. Curr Opin Rheumatol. 2000;12:131–42.
43. Redd RA, Peters VJ, Emery SF, Branch HM, Rifkin MD. Morton neuroma: sonographic evaluation. Radiology. 1989;171:415–7.
44. Bianchi S, Martinoli C. Foot. In: Bianchi S, Martinoli C, editors. Ultrasound of the musculoskeletal system. Berlin/New York: Springer; 2007. p. 835–88.
45. Howlett DC. High resolution ultrasound assessment of the parotid gland. Br J Radiol. 2003;76:271–7.
46. Jäger L, Menauer F, Holzknecht N, Scholz V, Grevers G, Reiser M. Sialolithiasis: MR sialography of the submandibular duct – an alternative to conventional sialography and US? Radiology. 2000;216: 665–71.
47. Gritzmann N, Rettenbacher T, Hollerweger A, Macheiner P, Hübner E. Sonography of the salivary glands. Eur Radiol. 2003;13:964–75.
48. Bhatia KS, Cho CC, Tong CS, Lee YY, Yuen EH, Ahuja AT. Shear wave elastography of focal salivary gland lesions: preliminary experience in a routine head and neck US clinic. Eur Radiol. 2012;22:957–65.
49. Bahadir O, Caylan R, Bektas D, Korkmaz O. Sialolithiasis of an accessory parotid gland. Ann Otol Rhinol Laryngol. 2004;113:52–4.
50. Wortsman X, Wortsman J. Sonographic outcomes of cosmetic procedures. AJR Am J Roentgenol. 2011;197:W910–8.
51. Boko E, Napo-Koura G, Kpemissi E, Boko-Bessi L. Tumours of the accessory salivary glands. Epidemiological and anatomopathological aspects. Rev Laryngol Otol Rhinol (Bord). 2004;125:233–7.
52. Martín-Millán M, García-Ibarbia C, Gutiérrez-Cuadra M, Gutiérrez-Santiago M, Fernández-Sampedro M, González-Macías J, et al. Pyomyositis: retrospective review in a third-level hospital in the north of Spain. Enferm Infecc Microbiol Clin. 2006;24:173–7.
53. Chiu NC, Hsieh MC, Chi H, Huang FY. Clinical characteristics of pyomyositis in children: 20-year experience in a medical center in Taiwan. J Microbiol Immunol Infect. 2009;42:494–9.
54. Botar-Jid C, Damian L, Dudea SM, Vasilescu D, Rednic S, Badea R. The contribution of ultrasonography and sonoelastography in assessment of myositis. Med Ultrasound. 2010;12:120–6.
55. Bianchi S, Abdelwahab IF, Mazzola CG, Ricci G, Damiani S. Sonographic examination of muscle herniation. J Ultrasound Med. 1995;14:357–60.
56. Beggs I. Sonography of muscle hernias. AJR Am J Roentgenol. 2003;180:395–9.
57. Meyer DC, Gerber C, Von Rechenberg B, Wirth SH, Farshad M. Amplitude and strength of muscle contraction are reduced in experimental tears of the rotator cuff. Am J Sports Med. 2011;39:1456–61.
58. Skendzel JG, Jacobson JA, Carpenter JE, Miller BS. Long head of biceps brachii tendon evaluation: accuracy of preoperative ultrasound. AJR Am J Roentgenol. 2011;197:942–8.
59. Weaver JS, Jacobson JA, Jamadar DA, Theisen SE, Ebrahim F, Kalume-Brigido M. Sonographic findings of pectoralis major tears with surgical, clinical, and magnetic resonance imaging correlation in 6 patients. J Ultrasound Med. 2005;24:25–31.

60. Sookur PA, Naraghi AM, Bleakney RR, Jalan R, Chan O, White LM. Accessory muscles: anatomy, symptoms, and radiologic evaluation. Radiographics. 2008;28:481–99.
61. Hauger O, Chung CB, Lektrakul N, Botte MJ, Trudell D, Boutin RD, et al. Pulley system in the fingers: normal anatomy and simulated lesions in cadavers at MR imaging, CT, and US with and without contrast material distention of the tendon sheath. Radiology. 2000;217:201–12.
62. Guerini H, Pessis E, Theumann N, Le Quintrec JS, Campagna R, Chevrot A, et al. Sonographic appearance of trigger fingers. J Ultrasound Med. 2008;27:1407–13.
63. Rojo-Manaute JM, Rodríguez-Maruri G, Capa-Grasa A, Chana-Rodríguez F, Soto Mdel V, Martín JV. Sonographically guided intrasheath percutaneous release of the first annular pulley for trigger digits, part 1: clinical efficacy and safety. J Ultrasound Med. 2012;31:417–24.
64. Robbin MR, Murphey MD, Temple HT, Kransdorf MJ, Choi JJ. Imaging of musculoskeletal fibromatosis. Radiographics. 2001;21: 585–600.
65. Murphey MD, Ruble CM, Tyszko SM, Zbojniewicz AM, Potter BK, Miettinen M. From the archives of the AFIP: musculoskeletal fibromatoses: radiologic-pathologic correlation. Radiographics. 2009;29:2143–73.
66. Sampson S, Meng M, Schulte A, Trainor D, Montenegro R, Aufiero D. Management of Dupuytren contracture with ultrasound-guided lidocaine injection and needle aponeurotomy coupled with osteopathic manipulative treatment. J Am Osteopath Assoc. 2011; 111:113–6.
67. Griffith JF, Wong TY, Wong SM, Wong MW, Metreweli C. Sonography of plantar fibromatosis. AJR Am J Roentgenol. 2002; 179:1167–72.
68. Bedi DG, Davidson DM. Plantar fibromatosis: most common sonographic appearance and variations. J Clin Ultrasound. 2001;29: 499–505.
69. Haun DW, Cho JC, Kettner NW. Symptomatic plantar fibroma with a unique sonographic appearance. J Clin Ultrasound. 2012;40:112–4.
70. Moretti VM, de la Cruz M, Lackman RD, Fox EJ. Fibroma of tendon sheath in the knee: a report of three cases and literature review. Knee. 2010;17:306–9.
71. Lee MH, Kim NR, Ryu JA. Cyst-like solid tumors of the musculoskeletal system: an analysis of ultrasound findings. Skeletal Radiol. 2010;39:981–6.
72. Nikolaidis P, Gabriel HA, Lamba AR, Chan NG. Sonographic appearance of nodular fasciitis. J Ultrasound Med. 2006;25:281–5.
73. Hayashi H, Nishikawa M, Watanabe R, Sawaki M, Kobayashi H, Shibata A, et al. Nodular fasciitis of the breast. Breast Cancer. 2007;14:337–9.
74. Ozben V, Aydogan F, Karaca FC, Ilvan S, Uras C. Nodular fasciitis of the breast previously misdiagnosed as breast carcinoma. Breast Care (Basel). 2009;4:401–2.
75. Damasceno RW, Heindl LM, Szentmáry N, Schlötzer-Schrehardt U, Kruse FE, Holbach LM. Nodular fasciitis of the eyelid and anterior orbit in children: case report and review of the literature. Ophthalmologe. 2009;106:829–31.
76. Jin W, Lee JH, Yang DM, Kim HC, Ryu CW, Shin HP, et al. Olecranon bursitis communicating with an olecranon cyst in rheumatoid arthritis. J Ultrasound Med. 2007;26:857–61.
77. Handy JR. Popliteal cysts in adults: a review. Semin Arthritis Rheum. 2001;31:108–18.
78. De Maeseneer M, Marcelis S, Jager T, Girard C, Gest T, Jamadar D. Spectrum of normal and pathologic findings in the region of the first extensor compartment of the wrist: sonographic findings and correlations with dissections. J Ultrasound Med. 2009;28:779–86.
79. Giovagnorio F, Andreoli C, De Cicco ML. Ultrasonographic evaluation of de Quervain disease. J Ultrasound Med. 1997;16:685–9.
80. Wang XT, Rosenberg ZS, Mechlin MB, Schweitzer ME. Normal variants and diseases of the peroneal tendons and superior peroneal retinaculum: MR imaging features. Radiographics. 2005;25:587–602.
81. Timins ME, O'Connell SE, Erickson SJ, Oneson SR. MR imaging of the wrist: normal findings that may simulate disease. Radiographics. 1996;16:987–95.
82. Wang Y, Tang J, Luo Y. The value of sonography in diagnosing giant cell tumors of the tendon sheath. J Ultrasound Med. 2007;26:1333–40.
83. Middleton WD, Patel V, Teefey SA, Boyer MI. Giant cell tumors of the tendon sheath: analysis of sonographic findings. AJR Am J Roentgenol. 2004;183:337–9.
84. Porta F, Radunovic G, Vlad V, Micu MC, Nestorova R, Petranova T, et al. The role of Doppler ultrasound in rheumatic diseases. Rheumatology (Oxford). 2012;51:976–82.
85. Mandl P, Balint PV, Brault Y, Backhaus M, D'Agostino MA, Grassi W, et al. Metrologic properties of ultrasound versus clinical evaluation of synovitis in rheumatoid arthritis: results of a multicenter, randomized study. Arthritis Rheum. 2012;64:1272–82.
86. Chen HH, Lan JL, Hung GD, Chen YM, Lan HH, Chen DY. Association of ultrasonographic findings of synovitis with anticyclic citrullinated Peptide antibodies and rheumatoid factor in patients with palindromic rheumatism during active episodes. J Ultrasound Med. 2009;28:1193–9.
87. Nalbant S, Corominas H, Hsu B, Chen LX, Schumacher HR, Kitumnuaypong T. Ultrasonography for assessment of subcutaneous nodules. J Rheumatol. 2003;30:1191–5.
88. Highton J, Hessian PA, Stamp L. The Rheumatoid nodule: peripheral or central to rheumatoid arthritis? Rheumatology (Oxford). 2007;46:1385–7.
89. Honda A, Fujimoto E, Kuroda K, Tajima S. Cutaneous mucinous nodule in a patient with rheumatoid arthritis. J Dermatol. 2008;35: 98–101.
90. Gentili A. The advanced imaging of gouty tophi. Curr Rheumatol Rep. 2006;8:231–5.
91. Koley S, Salodkar A, Choudhary S, Bhake A, Singhania K, Choudhury M. Tophi as first manifestation of gout. Indian J Dermatol Venereol Leprol. 2010;76:393–6.
92. Fernandes EA, Lopes MG, Mitraud SA, Ferrari AJ, Fernandes AR. Ultrasound characteristics of gouty tophi in the olecranon bursa and evaluation of their reproducibility. Eur J Radiol. 2012;81:317–23.
93. Wiesner T, Fried I. Images in clinical medicine. Gouty tophi. N Engl J Med. 2009;361:e49.
94. Rapini RP, Warner NB. Relapsing polychondritis. Clin Dermatol. 2006;24:482–5.
95. Fisher CG, Kacica MA, Bennett NM. Risk factors for cartilage infections of the ear. Am J Prev Med. 2005;29:204–9.
96. Fonseca AR, de Oliveira SK, Rodrigues MC, Aymoré IL, Domingues RC, Sztajnbok FR. Relapsing polychondritis in childhood: three case reports, comparison with adulthood disease and literature review. Rheumatol Int. 2012.
97. Wortsman X, Jemec GB. Sonography of the ear pinna. J Ultrasound Med. 2008;27:761–70.
98. Mavrogenis AF, Soucacos PN, Papagelopoulos PJ. Heterotopic ossification revisited. Orthopedics. 2011;34:177.
99. Stołtny T, Koczy B, Wawrzynek W, Miszczyk L. Heterotopic ossification in patients after total hip replacement. Ortop Traumatol Rehabil. 2007;9:264–72.
100. Falsetti P, Acciai C, Lenzi L. Sonographic diagnosis of neurogenic heterotopic ossification in patients with severe acquired brain injury in a neurorehabilitation unit. J Clin Ultrasound. 2011;39:12–7.
101. Abate M, Salini V, Rimondi E, Errani C, Alberghini M, Mercuri M, et al. Post traumatic myositis ossificans: sonographic findings. J Clin Ultrasound. 2011;39:135–40.

102. Okayama A, Futani H, Kyo F, Maruo S, Koezuka A, Kinoshita G. Usefulness of ultrasonography for early recurrent myositis ossificans. J Orthop Sci. 2003;8:239–42.
103. Wollina U, Koch A, Schönlebe J, Witzigmann H, Kittner T. Panniculitis ossificans of the lower leg. Int J Low Extrem Wounds. 2009;8:165–8.
104. Müller CS, Rass K, Tilgen W. Panniculitis ossificans non-traumatica of the scalp. J Cutan Pathol. 2010;37:703–4.
105. Shore EM. Fibrodysplasia ossificans progressiva (FOP): a human genetic disorder of extra-skeletal bone formation, or – How does one tissue become another? Wiley Interdiscip Rev Dev Biol. 2012;1:153–65.
106. Aneiros-Fernandez J, Husein-ElAhmed H, Orgaz-Molina J, O'Valle Ravassa F, Arias-Santiago S. A man with infiltrated and indurated plaque on the forehead. Dermatol Online J. 2010;16:12.
107. Ntuen EC, Guzmán-Sánchez DA, McMichael AJ. Osteoma cutis as a sequela to facial acne: a case report. Cutis. 2010;86:100–2.
108. Wortsman X, Wortsman J, Soto R, Saavedra T, Honeyman J, Sazunic I, et al. Benign tumors and pseudotumors of the nail: a novel application of sonography. J Ultrasound Med. 2010;29:803–16.
109. Wortsman X. Common applications of dermatologic sonography. J Ultrasound Med. 2012;31:97–111.

Part III

Terms, Classifications, and Protocols

Glossary of Dermatological Terms

21

Maria Francisca Daza and Gregor B.E. Jemec

Contents

21.1 Introduction

There are dermatological terms that should be known by the sonographers, and these concepts are commonly used in daily practice. This chapter contains a glossary composed of terms that the reader may hear frequently when exposed to dermatologic conditions. Drawings were added to represent the most common primary and secondary lesions in dermatology (Figs. 21.1 and 21.2) [1, 2].

M.F. Daza, MD (✉)
Department of Dermatology, Clinica Alemana de Santiago,
Avenida Bicentenario, 3951, Dept 91D, Vitacura,
Santiago 7630659, Chile
e-mail: frandazap@gmail.com

G.B.E. Jemec, MD, DMSci
Department of Dermatology, Health Sciences Faculty,
Roskilde Hospital, University of Copenhagen,
Køgevej 7-13, Roskilde 4000, Denmark
e-mail: gbj@regionsjaelland.dk

X. Wortsman, G.B.E. Jemec (eds.), *Dermatologic Ultrasound with Clinical and Histologic Correlations*,
DOI 10.1007/978-1-4614-7184-4_21,

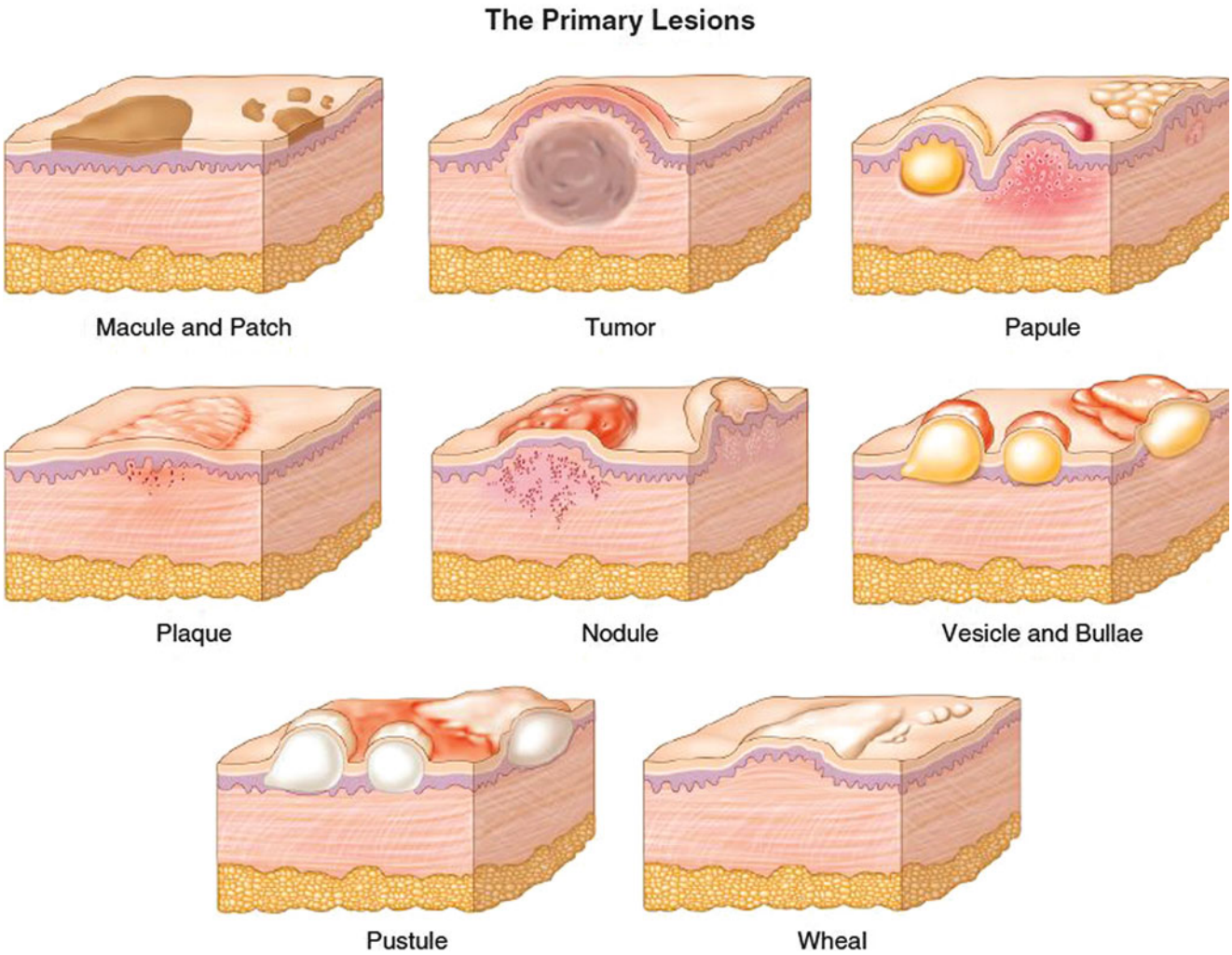

Fig. 21.1 The primary dermatological lesions

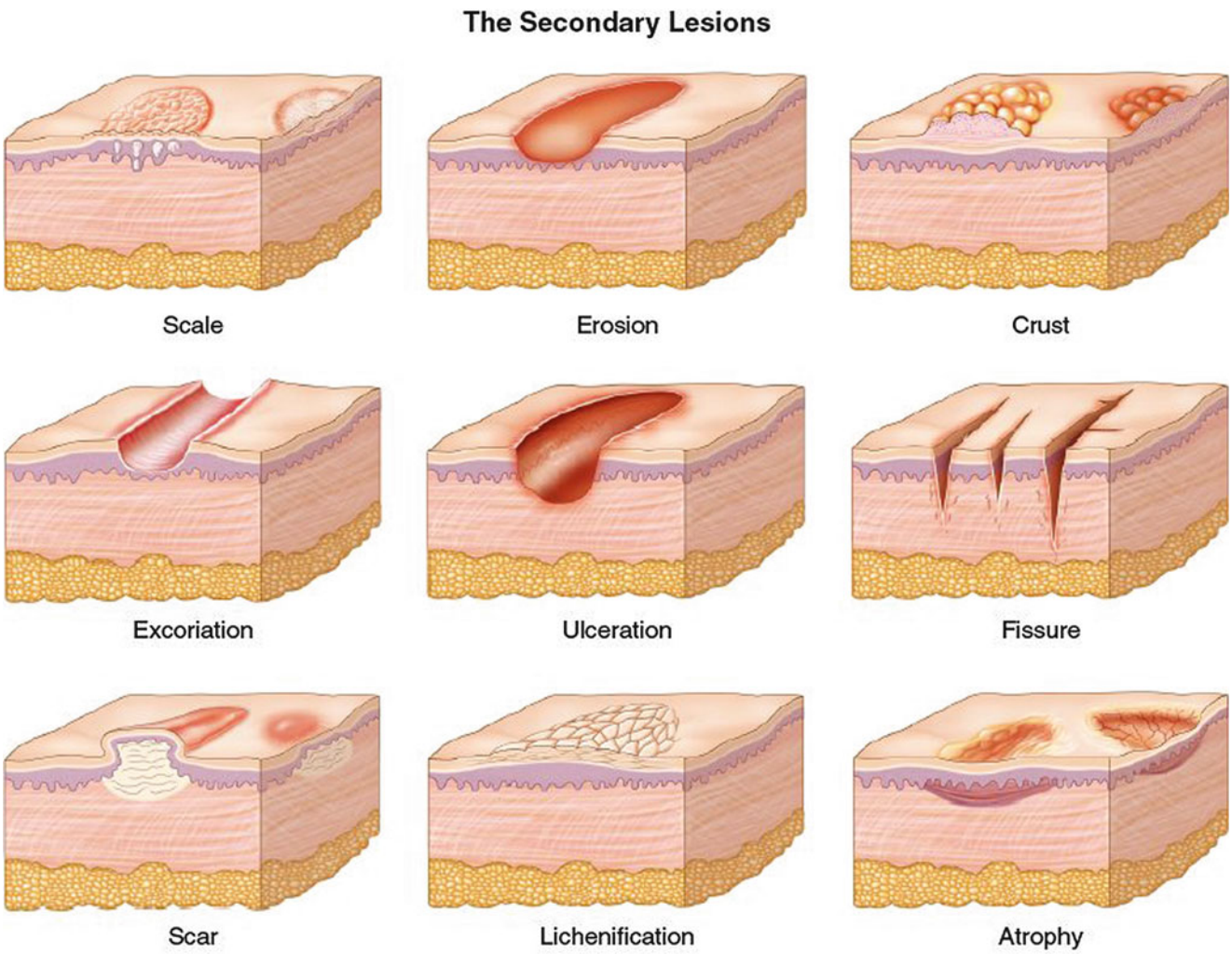

Fig. 21.2 The secondary dermatological lesions

21.2 A

Abscess: a localized collection of pus in the tissue in a non-preformed cavity, formed by accumulation of polymorphonuclear leukocytes with tissue necrosis.

Acanthosis Nigricans: an asymptomatic area of darkening and thickening of the skin. It is characterized by symmetrical, hyperpigmented, velvety plaques that can occur in almost any location but appear most commonly on the intertriginous areas of the axilla, groin, and posterior neck. It is often idiopathic, but can be associated with other diseases such as obesity, insulin resistance, or internal malignancy.

Acne keloidalis nuchae: a form of chronic folliculitis that manifests as follicular-based papules and pustules that evolve in keloid-like lesions. The final result is scarring alopecia. The lesions are most pronounced on the occipital scalp and the posterior part of the neck. Note that the lesions, however, do not occur as a result of acne vulgar and are not keloidal histologically.

Acne vulgaris: characterized by comedones, papules, pustules, and in severe cases, nodules in a sebaceous gland distribution. Comedones are non-inflamatory lesions and can be closed (whiteheads) or open (blackheads). The primary inflammatory lesions are papules and pustules. No inflammatory lesions are present in comedonal acne. Comedonal lesions are the earliest lesions of acne, and closed comedones are the precursor lesion of inflammatory lesions. The pathogenesis of acne vulgaris is multifactorial. The key factor is genetics. The propensity for follicular epidermal hyperproliferation with subsequent plugging of the follicle is inherited. Additional aggravating factors include excess sebum, the presence and activity of Propionibacterium acnes, and inflammation.

Acquired digital fibrokeratoma: manifests as a solitary, skin-colored papule or a tall finger-like protrusion with a hyperkeratotic surface. Most acquired digital fibrokeratoma lesions are small and do not exceed 1.5 cm in height or diameter. The etiology of acquired digital fibrokeratomas is unknown.

Acrochordon: a benign pedunculated neoplasm. It is soft, skin-colored or hyper-pigmented, and it can appear as surface nodules or papillomas on healthy skin. Most acrochordons are small and the most frequent locations of presentation are the neck and the axillae.

Acrokeratosis verruciformis: an autosomal dominant trait usually manifesting in early childhood. It a disorder of keratinization characterized by multiple flat-topped, skin-colored keratotic lesions resembling plane warts typically observed on the dorsum of the hands and feet.

Actinic keratoses: an ultraviolet light–induced lesion of the skin that can progress into invasive squamous cell carcinoma. It appears as pink, scaly patches and plaques on sun-exposed skin.

Actinic prurigo: a chronic, pruritic skin disease caused by an abnormal reaction to sunlight. Lesions appear hours or days following sun exposure as itchy plaques, mainly on photo-exposed areas, cheilitis, and conjunctivitis. Actinic prurigo frequently affects individuals of mixed descent from Latin America and American Indians with skin photo-types IV or V.

Actinic purpura: a benign clinical entity resulting from sun-induced damage to the connective tissue of the dermis. It is characterized by ecchymoses on the extensor surfaces of the forearms and the dorsa of the hands that usually lasts 1–3 weeks. It is common in elderly individuals and usually occurs after unrecognized minor trauma to the respective areas.

Actinomycosis: a chronic, suppurating, granulomatous condition caused by bacteria producing branching hyphae, such as *Actinomyces israelii*. Typically, there a group of dull red nodules, with sinuses draining colonies of organisms called "sulfur" granules. The most common clinical forms of actinomycos are cervicofacial, thoracic, and abdominal.

Adiposis dolorosa (**Dercum disease**): a disorder that is comprised of chronic progressive, painful, sometimes ecchymotic, plaques of fat. It is often associated with obesity and sometimes associated with systemic symptoms, including emotional upset. The criteria for diagnosis consist of four cardinal symptoms: multiple painful fatty masses; generalized obesity; asthenia, weakness, and fatigability; and mental disturbances.

Alopecia: hair loss. **Androgenetic alopecia** is the progressive miniaturization, and finally hair loss, secondary to the presence of androgens. **Alopecia areata** a recurrent non-scarring type of hair loss that can affect any hair-bearing area. Clinically, is most commonly seen as well-defined round patches of hair loss on the scalp. It can occasionally become generalized.

Another type of alopecia is **Telogen Effluvium,** which occurs when the hair cycle is disturbed causing an increase in the number of hairs to be produced that are in the falling out phase. This usually occurs after childbirth, infections, surgery, or other stressful events and usually resolves spontaneously. **Scarring alopecias** are a collection of conditions typically seen on the scalp that cause destruction of the hair follicle resulting in permanent hair loss. Examples are Lichen plano pilaris or Discoid lupus.

Anetoderma: a benign condition with focal loss of dermal elastic tissue, resulting in localized areas of flaccid or herniated sac-like skin. It is classified as either primary anetoderma, which an idiopathic occurrence of atrophic lesions in areas of skin that appear normal prior to the onset of

atrophy, or secondary anetoderma, which is preceded by an inflammatory dermatosis in the same location. Both can be associated with systemic diseases.

Angioedema: the swelling of deep dermis, or subcutaneous or submucosal tissue resulting from vascular leakage. Angioedema can be hereditary or acquired. Clinically, there is swelling of the face (eyelids, lips), tongue, hands, and feet. It can be acute or chronic, and each episode of angioedema can last from a few hours to a few days. A local burning sensation and pain can be observed without pronounced itchiness or local erythema. Angioedema can also be categorized as allergic, pseudoallergic, nonallergic, or idiopathic.

Angiokeratoma: a group of vascular ectasias that involve the papillary derm and that may produce papillomatosis, acanthosis, and hyperkeratosis of the epidermis. These lesions are most commonly found on the lower extremities as an asymptomatic solitary papule or plaque, but they can also be found in the upper extremities and the torso. The lesions are of clinical importance because they can clinically mimic a malignant melanoma.

Angiokeratoma corporis diffusum (**Fabry's disease**): an x-linked recessive disease characterized by the deposition of ceramides within blood vessel walls. It a lysosomal storage disease that is caused by deficient activity of lysosomal enzyme α-galactosidase A. Clinically, it manifests with angiokeratomas on the thighs, scrotum, or buttocks, although lesions can be anywhere. Other systemic manifestations are corneal dystrophy, acroparesthesias, and vasomotor disturbances. Cardiac and renal disease is common, with death typically occurring by age 40 years.

Angiolymphoid hyperplasia with eosinophilia (**ALHE**): an uncommon idiopathic condition that manifests in adults as isolated or grouped papules, plaques, or nodules in the skin of the head and neck. Most patients present with lesions in the periauricular region, forehead, or scalp. Rare sites of involvement include the hands, shoulders, breasts, penis, oral mucosa, and orbit. This condition is marked by a proliferation of blood vessels with distinctive large endothelial cells. The blood vessels are accompanied by a characteristic inflammatory infiltrate that includes eosinophils.

Angiomas: are benign vascular tumors of the skin. Clinically, they appear as red to purple small circumscribed domed lesions scattered over the body surface. The first lesions typically appear by age 40 years, increasing in number subsequent to that. They are asymptomatic.

Aplasia cutis congenital: is part of a heterogenous group of disorders characterized by the absence of a portion of skin in a localized or widespread area at birth. It most commonly manifests as a solitary defect on the scalp. The lesions are non-inflammatory and well demarcated, and they range in size from 0.5 to10 cm. It may be circular, oval, linear, or stellate in configuration. At birth, the lesions may have already healed with scarring or may remain superficially eroded to deeply ulcerated, occasionally involving the dura or the meninges.

Aplasia cutis congenita is most often a benign isolated defect, but it can be associated with other physical anomalies or malformation syndromes.

Apocrine hidrocystoma: benign cystic proliferations of the apocrine secretory glands that most commonly appear as solitary, soft, dome-shaped, translucent papules or nodules and most frequently are located on the eyelids, particularly the inner canthus. Apocrine hidrocystomas grow slowly and usually persist indefinitely.

Ashy dermatosis: an idiopathic condition with a primary lesion that is characterized by a central, gray macule, often surrounded by an erythematous, slightly indurated edge. Lesions expand and tend to coalesce. The erythematous edge eventually disappears leaving only the gray macules. Extensive areas of the skin surface can eventually be involved. It is usually asymptomatic. It is also called Erythema dyschromicum perstans.

Atopic dermatitis: a pruritic disease that usually begins in early infancy and is characterized by pruritus, eczematous lesions, xerosis (dry skin), and lichenification (thickening of the skin and an increase in skin markings). It can be associated with other atopic diseases such as asthma or allergic rhinit and urticaria.

Atrophia maculosa varioliformis cutis: a rare disease that presents as spontaneously formed facial scars in young adults. The scars vary in shape and size, resembling those from smallpox, most commonly located on the cheeks. Its etiology remains unknown, but elastic tissue pathology has been reported on histologic findings.

Atrophoderma of Pasini and Pierini: a form of dermal atrophy that manifests as single or multiple sharply demarcated, hyperpigmented, non-indurated patches. The disorder usually begins during adolescence or early adulthood with a slightly erythematous lesion appearing on the torso, most commonly on the back or lumbosacral region, followed in frequency by the chest, arms, and abdomen. Its cause is not known.

Atypical fibroxanthoma: a benign tumor usually found on the sun-damaged skin of elderly faces. It appears as a red, dome-shaped nodule approximately 2 cm in diameter. Clinically, lesions are suggestive of malignancy because they arise rapidly in skin where other skin cancers have been found and treated. Histologically, lesions show a highly atypical and pleomorphic cellular appearance, but they typically respond to simple excision.

21.3 B

Bacillary angiomatosis: a systemic disease caused by two Bartonella species, *Bartonella henselae* and *Bartonella quintana*. Most cases occur in people with concomitant AIDS. It appears as multiple subcutaneous nodules characterized histologically by a vascular proliferation. Skin lesions can resemble those seen in Kaposi's sarcoma.

Balanoposthitis: is the inflammation of the foreskin and glans in uncircumcised males. It can have any of a multiple of bacterial or fungal origins or be caused by contact dermatitis.

Basal cell carcinoma: a nonmelanocytic skin cancer that develops from basal cells of the follicular epidermis. It presents as a well-demarcated, translucent papular or nodule with evident telangiectasia. There can be central ulceration, the so-called "rodent ulcer". They most commonly occur in areas of significant actinic damage, but can appear in sun-protected areas as well. Tumor size can vary from a few millimeters to several centimeters in diameter. Basal cell carcinoma is predominantly locally invasive but only seldom metastatizes.

Basaloid follicular hamartoma: a superficial malformation of hair follicles. It is a rare benign adnexal tumor that appears most often on the face and scalp. The lesions can range in size from 1- to 2-mm papules to 3-cm plaques. Lesions can appear hypopigmented, hyperpigmented, or flesh colored. Additionally, hypotrichosis or alopecia can develop at sites of solitary basaloid follicular hamartoma.

Becker's nevus: a cutaneous hamartoma that generally appears in late childhood or adolescence in boys. It is manifested by a well-demarcated hyperpigmented patch with darkly pigmented terminal hairs and acneform lesions. It is most commonly located on the shoulder, upper chest, or back.

Behçet's syndrome: consists of recurrent painful aphthous stomatitis in association with genital ulcers and inflammatory eye disease. Pustulosis, arthritis, fever, and general malaise also occur, and the disease can be associated with central nervous system complications. It has a strong association with HLA-B5.

Benign lymphangioendothelioma: an uncommon vascular tumor that consists of a proliferation of lymphatic endothelial cells. It is a single, asymptomatic, slowly expanding patch, plaque, or nodule that usually manifests during adolescence or young adulthood. It can be confused histologically with Kaposi's sarcoma or angiosarcoma.

Black heel: a subcutaneous hemorrhage on the heel caused by trauma. Clinically it looks like a darkening of the posterior or posterolateral aspect of the heel that occurs primarily in young adult athletes.

Blue nevi: solitary small tumours with a bluish color. Blue nevi are believed to represent dermal arrest in embryonal migration of neural crest melanocytes that fail to reach the epidermis. The clinically noted blue color is a result of the depth of melanin in the epidermis and the Tyndall effect. The Tyndall effect is the preferential absorption of long wavelengths of light by melanin, and the scattering of shorter wavelengths representing the blue end of the spectrum, by collagen bundles.

Blue rubber bleb nevus syndrome: a syndrome characterized by multiple cutaneous venous malformations in association with visceral lesions, most commonly affecting the gastointestinal tract.

Bowen disease: a form of intra-epidermal carcinoma, a malignant tumor of keratinocytes with the potential for significant lateral spread. Larger lesions can reach several centimeters in diameter and can ultimately progress into an invasive squamous cell carcinoma. Patients often present with an asymptomatic, slowly enlarging, erythematous, well-demarcated scaly patch or plaque. It may occur anywhere on the mucocutaneous surface.

Bowenoid papulosis: a focal epidermal hyperplasia and dysplasia induced by infection from the human papillomavirus. Bowenoid papulosis typically occurs in young sexually active people and presents as solitary or multiple, small, pigmented papules with a flat-to-verrucous surface. Bowenoid papulosis lesions can coalesce into larger plaques. Lesions most commonly occur on the shaft of the penis or the external genitalia of women.

Branchial cleft cysts: congenital epithelial cysts that appear on the lateral part of the neck from a failure of obliteration of the second branchial cleft in embryonic development. Branchial cleft cysts commonly present as solitary, painless masses in the necks of children or a young adults.

Bullous pemphigoid: an autoimmune, subepidermal, blistering skin disease. It is characterized by the presence of immunoglobulin G autoantibodies specific for the hemidesmosomal bullous pemphigoid antigens BP230 (BPAg1) and BP180 (BPAg2). Clinically, it is characterized by tense, thin-roofed bullae that arise on any part of the skin surface, with a predilection on the flexural areas. It rarely involves mucous membranes.

21.4 C

Café-au-lait macule: well-demarcated light to dark brown patch that is present from early childhood. Multiple café-au-lait macules are uncommon and more than six big macules or patches are strongly suggestive of neurofibromatosis. Café-au-lait macules can also occur in association with Albright's syndrome, tuberous sclerosis, and other genodermatoses.

Calcinosis cutis: a term used to describe a group of disorders in which calcium deposits form in the skin. It is classified into four major types according to etiology: dystrophic,

metastatic, iatrogenic, and idiopathic. In all cases, insoluble compounds of calcium are deposited within the skin resulting from local and/or systemic factors. The calcium salts consist primarily of hydroxyapatite crystals or amorphous calcium phosphate.

Cellulitis: a diffuse inflammation of connective tissue with severe inflammation of dermal and subcutaneous layers of the skin resulting from bacterial infection.

Chancroid: a sexually transmitted disease caused by *Hemophilus ducreyi* characterized by painful necrotizing genital ulcers that can be accompanied by inguinal lymphadenopathy.

Cheilitis Granulomatous: a chronic swelling of the lip as a result of granulomatous inflammation. The earliest manifestation is sudden diffuse or nodular swellings of the lips. Once chronicity is established, the enlarged lip appears cracked and fissured with reddish brown discoloration and scaling. The lip becomes painful and eventually acquires the consistency of firm rubber.

Chondrodermatitis Nodularis Helices: a common, benign, painful papule of the helix or antihelix of the ear. Pain is experienced when sleeping. The exact cause is unknown, although it is believed that it is caused by prolonged and excessive pressure or ultraviolet exposure.

Clavus: a thickening of the skin as a result of intermittent pressure and frictional forces. These forces result in hyperkeratosis, clinically and histologically. The extensive thickening of the skin in a clavus can result in chronic pain, particularly in the forefoot.

Clear cell acanthoma: a benign tumor of the epidermis. It clinically appears as a well-demarcated pink nodule or plaque, often with a scale. The characteristic sharply demarcated edge shows a raised rim of keratin at the base.

Congenital nevi: present at birth and result from a proliferation of benign melanocytes in the dermis, epidermis, or both. Congenital nevi have been stratified into three groups according to size. Small nevi are less than 1.5 cm in greatest diameter, medium nevi are 1.5–19.9 cm in greatest diameter, and large or giant nevi are greater than 20 cm in greatest diameter.

Connective tissue nevi: hamartomatous malformations of the skin containing elements of dermal connective tissue. These elements include collagen, elastin, and glycosaminoglycans. They may occur as isolated skin lesions, or they can be associated with a number of syndromes.

Cutis laxa: a rare, inherited or acquired connective tissue disorder where the skin becomes inelastic and hangs loosely in folds. Patients report progressive laxity and sagging of the skin as they notice the development of loose, wrinkled skin.

Cutis marmorata telangiectatica congenital: an uncommon, sporadic, congenital cutaneous vascular anomaly. It is generally present at birth or shortly thereafter with a reticulated mottling that frequently becomes more prominent in a cold environment but tends not to disappear with rewarming.

Cutis verticis gyrate: a descriptive term for a condition of the scalp manifesting as convoluted folds and furrows formed from thickened skin of the scalp resembling cerebriform pattern. It mainly occurs in males after puberty in the vertex and occipital region.

Cylindroma: a benign skin appendage tumor. It begins during middle age or later as a slow-growing, rubbery asymptomatic nodule located on the head and neck.

21.5 D

Dermatitis herpetiformis: an autoimmune blistering disorder often associated with a gluten-sensitive enteropathy. Patients typically present with erythematous excoriated papules or plaques with herpetiform (small, clustered) vesicles that are symmetrically distributed over extensor surfaces, including the elbows, knees, buttocks, and shoulders. The eruption is intensely pruritic.

Dermatofibroma: a common cutaneous nodule that consists of a benign proliferation of fibroblasts in association with an increased number of mast cells and, often, blood vessels. Clinically, the lesion a tethered, firm, intracutaneous nodule of 0.5–2 cm in diameter, often with associated hyperpigmentation in the overlying skin. Because of the tethering, squeezing the lesion results in a central umbilication, the dimple sign.

Dermatofibrosarcoma protuberans: a cutaneous malignancy that arises from the derma and invades deeper subcutaneous tissue. It a very slowly growing tumor that usually presents as a large, indurated plaque that most commonly occurs on the torso, followed by the proximal extremities.

Dermatopathia pigmentosa reticularis: a very rare disorder with the diagnostic triad of generalized reticulate hyperpigmentation, noncicatricial alopecia, and onychodystrophy. Other dermatologic findings are hypohidrosis or hyperhidrosis, palmoplantar hyperkeratosis, and acral dorsal nonscarring blisters.

Dermatosis papulosa nigra: a benign cutaneous condition characterized by multiple, small, hyperpigmented, asymptomatic papules on the face of adults with Fitzpatrick skin type V or VI.

Desmoid tumors: cytologically bland fibrous neoplasms originating from the musculoaponeurotic structures throughout the body. Peripheral desmoid tumors are firm, smooth, and mobile. They often adhere to surrounding structures. The overlying skin is usually unaffected.

Digital mucous cysts: benign ganglion cysts of the digits, typically located at the distal interphalangeal joints or in the proximal nail fold. They usually occur on the hands as solitary, round-to-oval, dome-shaped, firm-to-fluctuant papulonodules

from 1 to 10 mm in diameter that have overlying skin that ranges from very thin to moderately thick. The cysts contain a viscous, gelatinous fluid.

Discoid lupus erythematosus: a chronic, scarring, atrophy producing, photosensitive dermatosis. The primary lesion has an erythematous papule or plaque with slight-to-moderate scaling. As the lesion progresses, the scale may thicken and become adherent, and pigmentary changes may develop, with hypopigmentation in the central or inactive area and hyperpigmentation at the active border.

Dyshidrotic eczema: a recurrent or chronic relapsing form of vesicular palmoplantar dermatitis of unknown etiology. It is considered a reaction pattern caused by various endogenous conditions and exogenous factors.

Dyskeratosis congenita: a rare, progressive bone marrow failure syndrome characterized by the triad of reticulated skin hyperpigmentation, nail dystrophy, and oral leukoplakia. The mucocutaneous features typically develop between the ages of 5 and 15 years.

21.6 E

Ecthyma: an ulcerative pyoderma of the skin caused by group A beta-hemolytic streptococci. Because ecthyma extends into the dermis, it is often referred to as a deeper form of impetigo. It usually arises on the lower extremities of children, people with diabetes, and neglected elderly patients as a vesicle or pustule overlying an inflamed area of skin that deepens into a dermal ulceration with overlying crust.

Ehlers-Danlos syndrome: a group of inherited disorders of collagen metabolism. There are at least 10 subtypes with a variable expression of skin fragility, hyperelasticity of the skin, and hypermobility of the joints.

Elastofibroma: a rare, benign, slow-growing connective-tissue tumor that occurs most often in the subscapular area in elderly women. It is characterized by accumulated abnormal elastic fibers and is generally regarded as a reactive process, an unusual fibroblastic pseudotumor.

Elastosis perforans serpiginosum: a rare skin disease in which abnormal elastic tissue fibers, other connective tissue elements, and cellular debris are expelled from the papillary dermis through the epidermis. Primary lesions are eruptive, dome-shaped papules. They are small in size, flesh colored to red, and they are grouped into linear, arciform, circular, or serpiginous patterns.

Epidermal nevi: congenital hamartomas of embryonal ectodermal origin classified on the basis of their main component; the component can be sebaceous, apocrine, eccrine, follicular, or keratinocytic. They are patches, plaques, or nodules that can be bilateral or distributed on most of the body. Usually, no symptoms of the nevi are present, with the exception of inflammatory linear verrucous epidermal nevus.

Epidermoid cysts: a closed cavity with an epithelial lining that contain keratin. The cyst begins as a nidus of epidermis below the epidermis. Keratin is produced, and with nowhere to be expelled, the cyst slowly enlarges. As the epidermis grows over the cyst, it stretches allowing the white to yellow color of the cyst to be evident. Cysts may become inflamed and resemble furuncles. Epidermoid cysts represent the most common cutaneous cysts.

Epidermolysis bullosa: a group of inherited bullous disorders characterized by blister formation in response to mechanical trauma.

Eruptive vellus hair cysts: follicular papules that are thought to arise as a developmental abnormality of vellus hair follicles. A predisposition exists for follicular occlusion at the level of the infundibulum that results in cystic dilatation of the proximal hair follicle and secondary atrophy of the hair bulb. They typically develop as an acneiform eruption on the chest and extremities.

Erysipelas: a superficial bacterial skin infection that characteristically extends into the cutaneous lymphatics. It is often caused by Streptococcus spp. and Staphlococci may also be found. Clinically, it begins as a small erythematous patch which progresses to a fiery-red, indurated, tense, and shiny plaque with associated fever and general malaise.

Erythema ab igne: characterized as localized areas of reticulated erythema and hyperpigmentation resulting from chronic and repeated exposure to heat at a lower level than that which causes a thermal burn. Initially, the skin is mildly erythematous; however, after repeated heat exposure, a classic blue, purple, or brown reticulated hyperpigmentation develops.

Erythema annulare centrifugum: characterized by a scaling or nonscaling, nonpruritic, annular or arcuate, erythematous eruption. It tends to spread peripherally while clearing centrally. Histologically, an intense lymphohistiocytic infiltrate occurs about the superficial and deep dermal vessels without epidermal involvement. Its etiology is uncertain, but it can result from a hypersensitivity to malignancy, infection, drugs, or chemicals, or it can be idiopathic.

Erythema elevatum diutinum: a rare type of leukocytoclastic vasculitis characterized by red, purple, brown, or yellow papules, plaques, or nodules. These lesions are usually distributed symmetrically on the extensor surfaces of the body. Its etiology is unknown.

Erythema induratum (**nodular vasculitis**): considered a multifactorial syndrome of lobular panniculitis where tuberculosis may or may not be one of a multitude of etiologic components. Clinically, it consists of persistent or recurrent ill-defined nodules that usually occur on the posterior calves of women. Nodules can develop irregular, shallow ulcers, often with a violaceous edge.

Erythema nodosum: an acute, nodular, erythematous eruption that usually is limited to the extensor aspects of the

lower legs. It is presumed to be a hypersensitivity reaction and may occur in association with several systemic diseases or drug therapies, or it can be idiopathic. The inflammatory reaction occurs in the panniculus.

Erythrasma: a chronic superficial infection of the intertriginous areas of the skin by *Corynebacteria*. These organisms invade the upper third of the stratum corneum; under favorable conditions such as heat and humidity, they proliferate. The coral-red fluorescence of scales seen under Wood light is secondary to the production of porphyrin by these diphtheroids. The typical appearance of erythrasma is well-demarcated, brown-red macular patches.

21.7 F

Favre-Racouchot syndrome: a disorder consisting of multiple open and closed comedones in the presence of actinically damaged skin. It is related to elastosis resulting from severe prolonged ultraviolet damage.

Fibrous papule of the nose: a solitary, firm, skin-colored or pink papule occurring on the nose, less commonly elsewhere on the face. There a distinct histological picture of fibrosis, ecstatic vessels, and multinucleate cells of undetermined origin.

Follicular infundibulum tumor: a rare benign adnexal tumor arising from the follicular infundibulum. The histopathology of the tumor is distinctive, which occurs as a plate-like dermal nodule with multiple thin connections to the overlying epidermis. The tumor usually manifests as a scaly nodule up to 1.5 cm in diameter and is located on the head or neck.

Folliculitis: a primary inflammation of the hair follicle that occurs as a result of various infections or can be secondary to follicular trauma or occlusion. It is defined histologically as the presence of inflammatory cells within the wall and ostia of the hair follicle, creating a follicular-based pustule.

21.8 G

Granuloma annulare: a benign inflammatory dermatosis. It is characterized clinically by dermal papules and annular plaques. The precise cause is unknown. Histological examination reveals foci of degenerative collagen associated with palisaded granulomatous inflammation.

Glomus tumor: benign lesions that typical present in young adults as small, blue-red papules or nodules of the distal extremities, with a predilection for subungual sites. Glomus tumors are typically painful, often causing paroxysmal pain in response to temperature changes or pressure. Glomus tumors are thought to arise from the glomus body, a thermoregulatory shunt concentrated in the fingers and toes. Two variants are noted: solitary glomus tumors and multiple glomus tumors that are also known as glomangiomas or glomu-venous malformations.

21.9 H

Hailey-Hailey disease: a chronic autosomal dominant disorder with incomplete penetrance that is characterized by vesicles and erythematous plaques with overlying crusts. The lesions typically occur in the genital area as well as the chest, neck, and axillary areas. Multiple asymptomatic longitudinal white bands on the fingernails have also been described.

Halo nevi: common benign skin lesions that represent melanocytic nevi in which a reactive inflammatory infiltrate develops, resulting in a zone of depigmentation surrounding the nevus.

Hemangiomas: benign vascular neoplasms that have a characteristic clinical course marked by early proliferation and are followed by spontaneous involution. During the proliferative phase in the neonatal period or early infancy, a rapidly dividing endothelial cell proliferation is responsible for the enlargement of infantile hemangiomas. Finally, an involutional phase occurs, whereby most infantile hemangiomas are clinically resolved by age 9 years.

Hematoma: a localized, tumor-like collection of blood in a non-preformed cavity.

Herpes Zoster: a common dermal and neurologic disorder caused by the varicella-zoster virus. Classic physical findings include painful grouped herpetiform vesicles on an erythematous base confined to the cutaneous surface innervated by a single unilateral sensory nerve.

Hidradenitis suppurativa: a chronic condition characterized by swollen, painful, inflamed lesions in the axillae, groin, and other parts of the body rich in apocrine glands. The disease is a chronic acneiform infection of the cutaneous apocrine gland bearing skin that also can involve adjacent subcutaneous tissue and fascia. The hallmarks of the disease are cutaneous nodules and sinus tracts that can become draining fistulas.

Hypomelanosis of Ito: a syndrome with hypopigmented whorls of skin along the Blaschko lines. Congenital abnormalities, mental retardation, and seizures are the most commonly associated conditions.

21.10 I

Impetigo: an acute, contagious, superficial pyogenic skin infection that occurs most commonly in children. The two causative organisms are *Streptococcus pyogenes* and *Staphylococcus aureus*. Lesions first begin as vesicles or

pustules on an erythematous base. Then they promptly rupture, releasing their serum, which dries and forms a light brown, honey-colored crust.

Incontinentia pigmenti: an X-linked dominant neurocutaneous syndrome with cutaneous, neurologic, ophthalmologic, and dental manifestations. The cutaneous manifestations usually appear in a characteristic, chronologic sequence: vesicular, then verrucous, hyperpigmented, and finally atrophic or hypopigmented.

21.11 J

Juvenile xanthogranuloma: an idiopathic benign tumor of histiocytes. Usually asymptomatic; self-healing; red, yellow, or brown papules and nodules composed of histiocytic cells that predominantly occur during infancy and childhood. Papules or nodules occur in the skin, eyes, and viscera.

21.12 K

Kaposi's sarcoma: a neoplasm of proliferating blood vessels that often manifests with multiple vascular nodules in the skin and other organs.

Keloid: the result of an overgrowth of dense fibrous tissue that usually develops after healing of a skin injury. The tissue extends beyond the borders of the original wound, does not usually regress spontaneously, and always recurs after excision.

Keratoacanthoma: a low-grade malignancy that originates in the pilosebaceous glands and closely and pathologically resembles squamous cell carcinoma. It is characterized by a rapidly evolving nodule with a "volcano-like" appearance, rising sharply from the surrounding skin as a smooth edge tumor. Centrally, within the cone of the "volcano", is rough, keratotic tissue. Keratoacanthomas usually spontaneously resolve within 8 weeks.

Keratosis follicularis (**Darier disease**): an autosomal dominantly inherited genodermatosis characterized by greasy hyperkeratotic papules in seborrheic regions, nail abnormalities, and mucous membrane changes.

Keratosis pilaris: a genetic disorder of keratinization of hair follicles of the skin. It is an extremely common benign condition that manifests as small, rough folliculocentric keratotic papules, often described as chicken skin, in characteristic areas of the body, particularly the outer-upper arms and thighs. It associated with other dry skin conditions.

Koebner's phenomenon: the induction by, and at the site of, trauma to the skin, of disease manifestations typical of the disease elsewhere. It is typically seen in psorias and lichen planus.

21.13 L

Leiomyoma: a benign tumor of smooth muscle usually derived from the erector pili muscle. A variant, angioleiomyoma arises from the muscle of blood vessels. A leiomyoma is typically a round nodule less than 1 cm in diameter. Lesions can be painful. Secondary to contraction of the muscle elements, some lesions show evident clinical contraction associated with pain development.

Lentigo: a small, sharply circumscribed, pigmented macule surrounded by normal-appearing skin. Histologic findings include hyperplasia of the epidermis and increased pigmentation of the basal layer. A variable number of melanocytes are present; the melanocytes can increase in number, but they do not form nests.

Leukocytoclastic vasculitis: a histopathologic term commonly used to denote a small-vessel vasculitis. Palpable purpura is the most common presentation.

Lichen planus: a pruritic, papular eruption characterized by its violaceous color, polygonal shape, and sometimes fine scale. Lichen planus is most commonly found on the flexor surfaces of the upper extremities, on the genitalia, and on the mucous membranes. It a cell-mediated immune response of unknown origin.

Lichen sclerosus et atrophicus: a chronic inflammatory dermatosis that results in white plaques with epidermal atrophy. It is typically found on the genitals with porcelain white macules and papules, often with a fine wrinkled, "cigarette-paper" surface. In later stages the lesions may actually become depressed. Atrophic genital lesions develop into painful erosions and are associated with secondary development of malignancy if left untreated.

Lichen simplex chronicus: thickening of the skin with variable scaling that arises secondary to repetitive scratching or rubbing.

Lichen striatus: a self-limited linear dermatosis of unknown origin that predominantly affects children. It appears as a continuous or interrupted, linear band consisting of small pink, brown, or skin-colored lichenoid papules. It has a characteristic developmental pattern following the lines of Blaschko.

Lipodystrophy syndromes: represent a group of heterogeneous disorders characterized by progressive loss of fat tissue, mainly from the subcutaneous compartment and occasionally from visceral fat.

Lipomas: benign tumors arising from adipocytes. They are clinically seen as soft and occasionally tender masses in the subcutaneous tissue.

Liposarcoma: a malignancy of fat cells. In adults, it is the most common soft-tissue sarcoma. It normally appears as a slowly enlarging, painless, nonulcerated submucosal mass in middle-aged people, but some lesions grow rapidly and become ulcerated early. The development of a liposarcoma

from a preexisting benign lipoma is rare. Most cases arise de novo.

Lobular Capillary Hemangioma (**Pyogenic granuloma**): an exophytic vascular proliferation, usually in response to obvious trauma. The deep red to red-black nodule or polyp is typically 3–5 mm in diameter, although larger lesions can occur. Pyogenic granulomas are misnamed; they are neither infectious nor granulomatous.

Lymphangioma: hamartomatous congenital malformations of the lymphatic system that involve the skin and subcutaneous tissues. The classification most frequently used divides these lesions into two major groups based on the depth and the size of these abnormal lymph vessels. The superficial vesicles are called lymphangioma circumscriptum. The more deep-seated group includes cavernous lymphangioma and cystic hygroma.

Lymphangioma circumscriptum: consist of clusters of transparent to red vesicles and papules, resembling "frog spawn". There may be a lymphangioma (clear) and hemangioma (purple-red) component in a single lesion. Lesions commonly present in early childhood.

Lymphocytoma cutis: a response to a variety of known and unknown stimuli that results in the accumulation of lymphocytes and other inflammatory cells in a localized region. It is not a specific disease, instead, a reactive process and generally has a benign course. Patients present with a red to purpule nodule or group of discrete nodules, usually with minimal associated symptoms.

Lymphomatoid papulosis: a chronic papulonecrotic skin disease with histologic features suggestive of a malignant lymphoma. The disease is characterized by recurrent crops of pruritic papules at different stages of development that predominantly arise on the torso and limbs. The papules heal spontaneously over 1–2 months, usually leaving slightly depressed oval scars.

21.14 M

Majocchi granuloma: a deep folliculitis as a result of a cutaneous dermatophyte infection. Clinically it appears as a nonpruritic solitary or multiple persistent papulopustules or plaques. The legs are common sites for Majocchi granuloma in young women who shave frequently.

Malignant melanoma: a malignant neoplasm of melanocytes. It accounts for only 4 % of all skin cancers; however, it causes the greatest number of skin cancer-related deaths worldwide. The development of melanoma is multifactorial and appears to be related to multiple risk factors, including fair complexion, excessive childhood sun exposure with blistering sunburns, an increased number of dysplastic nevus, a family history of melanoma, the presence of a changing mole or evolving lesion on the skin, and older age. The most common warning sign for melanoma is a new or changing mole. Variation in color and/or an increase in diameter, height, or asymmetry of borders of a pigmented lesion are noted by more than 80 % of patients with melanoma at the time of diagnosis.

Mastocytomas: localized collections of mast cells. Clinically, they appear as yellow-red-brown macules. Stroking the lesion elicits an urticarial response called Darrier's sign. Extensive mast cell involvement of the skin is called urticaria pigmentosa.

Melanocytic nevi: benign neoplasms or hamartomas composed of melanocytes, the pigment-producing cells that constitutively colonize the epidermis. Junctional melanocytic nevi are macular or thinly popular and typically range from brown to brownish-black. Compound and intradermal melanocytic nevi display elevation relative to surrounding uninvolved skin. Compound melanocytic nevi are often lighter in color than junctional nevi and range from tan to light brown. Many wholly intradermal melanocytic nevi display no significant pigmentation.

Melanonychia: brown or black pigmentation of the nail unit. Melanonychia commonly presents as pigmented band arranged lengthwise along the nail unit, and this presentation is known as melanonychia striata. The most important cause of melanonychia is subungual melanoma, although a variety of other causes includes physiologic longitudinal melanonychia, systemic disorders, trauma, inflammatory disorders, fungal infections, drugs, and benign melanocytic hyperplasias.

Microcystic adnexal carcinoma: a malignant appendage tumor commonly classified as a low-grade sweat gland carcinoma that typically occurs on the head and neck, particularly the central face. It shows aggressive local invasion. Clinically it appears as plaques or nodules flesh colored, yellow, or erythematous in color.

Milia: benign, keratin-filled cysts. Primary milia are typically seen in infants but also may occur in children and adults. Secondary milia are observed in a number of blistering disorders and following dermabrasion.

Molluscum contagiosum: an infectious cutaneous eruption consisting of one or more, 1–3 mm diameter, flesh-colored papules with a central umbilication. It is caused by a member of the pox virus family.

Mondor disease: a condition characterized by a sclerosing thrombophlebitis of the subcutaneous veins of the anterior chest wall. The sudden appearance of a subcutaneous cord, which is initially red and tender, and subsequently becomes a painless fibrous band that accompanied by tension and skin retraction, is characteristic.

Morphea (**Localized scleroderma**): a disorder characterized by excessive collagen deposition leading to thickening of the dermis, subcutaneous tissues, or both. Morphea is classified into plaque, generalized, linear, and deep subtypes according to the clinical presentation and depth of tissue involvement.

21.15 N

Necrobiosis lipoidica: a disorder of collagen degeneration with a granulomatous response, thickening of blood vessel walls, and fat deposition. The exact cause of necrobiosis lipoidica is unknown, but the leading theory of necrobiosis lipoidica has focused on diabetic microangiopathy. Skin lesions begin as small well-circumscribed papules or nodules that expand with an active border to become waxy, atrophic, round plaques centrally. Initially, these plaques are red-brown in color but progressively become more yellow and atrophic in appearance.

Neurofibroma: a neural tumor that can evolve from a papule to a nodule. These lesions can be single or multiple. When multiple, they can be indicative of the presence of neurofibromatosis. With direct pressure, the lesion seems to "button hole" into the skin. Malignant transformation, while possible, is uncommon.

Nevus sebaceus: a circumscribed hamartomatous lesion predominantly composed of sebaceous glands. Most frequently, a solitary, hairless patch is noted on the scalp at birth or in early childhood. In adolescence, the lesion becomes verrucous and nodular, round, oval, or linear in shape, varying in length from about 1 cm to more than 10 cm. Later in life, some lesions may develop various types of appendageal tumors including basal cell carcinoma.

21.16 O

Onycholysis: a spontaneous separation of the nail plate starting at the distal free margin and progressing proximally.

Onychomatricoma: a subungual tumor of the fingers and toes. The clinical presentation includes discoloration, longitudinal ridging, splinter hemorrhage, and notable overcurvature of the nail plate.

Onychomycosis: a fungal infection that affects the toenails or the fingernails. Typically, the nail shows a yellow-white color, subungual hyperkeratos and onycholysis.

21.17 P

Pemphigus: a group of autoimmune blistering diseases of the skin and mucous membranes characterized histologically by intraepidermal blister and immunopathologically by the finding of in vivo bound and circulating immunoglobulin G antibody directed against the cell surface of keratinocytes. The primary lesion is a flaccid blister that usually arises on healthy-appearing skin but can also be found on erythematous skin. Affected skin is very painful.

Pilomatrixoma: a benign appendageal tumor with differentiation toward hair cells. It usually manifests as a solitary, asymptomatic, firm nodule on the head. It is characterized by a lobular appearance and can be hard when palpated if there is extensive calcification within. It is more common in children, but occurrence in adults is increasingly being recognized. There may be an associated inflammation. Malignant transformation can occur, but is uncommon.

Pityriasis rubra pilaris: a chronic papulosquamous disorder of unknown etiology characterized by reddish orange scaly plaques, palmoplantar keratoderma, and keratotic follicular papules.

Poroma: a benign adnexal neoplasm composed of epithelial cells that show tubular differentiation. Poromas typically manifest as skin-colored papules or nodules smaller than 2 cm in diameter. They are asymptomatic and slow-growing lesions. The malignant counterpart of a poroma is referred to as porocarcinoma.

Pseudocyst of the auricle: a noninflammatory, asymptomatic swelling on the lateral or anterior surface of the pinna, usually in the scaphoid or triangular fossa. It ranges from 1 to 5 cm in diameter and contains clear or yellowish viscous fluid, with a consistency similar to that of olive oil. It manifests as a painless swelling on the lateral or anterior surface of the pinna, developing over a period of months. A history of minor trauma may accompany the clinical history.

Pseudoxanthoma elasticum: an inherited neuro-cutaneous disorder of connective tissue, characterized by abnormal elastotic fibers in the skin, blood vessels, and eye. Both autosomal dominant and recessive variants show skin laxity, 1–3 mm yellowish papules involving the lateral aspect of the neck, upper torso and elsewhere, and angioid streaks of the retina. Biopsy of the papules shows the characteristic elastotic change with calcium deposition.

Psoriasis: a chronic inflammatory skin disorder with a strong genetic basis. It is most typically characterized by circular-to-oval red plaques distributed over extensor body surfaces and the scalp. The plaques usually exhibit scaling as a result of epidermal hyperproliferation and dermal inflammation.

Pyoderma gangrenosum: an uncommon ulcerative cutaneous condition of uncertain etiology. The initial lesion is usually a small, red papule or pustule that then changes into a larger ulcerative lesion. In addition to ulceration, pain is the predominant complaint.

21.18 R

Rosacea: a condition characterized by symptoms of facial flushing and a spectrum of clinical signs, including erythema, telangiectasia, coarseness of skin, and an inflammatory papulopustular eruption resembling acne.

21.19 S

Schwannoma: a tumor of the nerve sheath composed of Schwann cells. Typically firm 1-2 cm nodules on the head and neck of middle-aged individuals, these tumors are usually sporadic and solitary. When multiple, they are associated with an increased incidence of neurofibromatosis.

Sebaceous adenomas: benign skin tumors that show histological differentiation toward sebaceous gland structures. Lesions of yellowish color that are usually 2–4 mm, but can reach 1 cm in size.

Sebaceous carcinoma: a firm, yellowish, translucent nodule, most commonly on the face. Histologically, it a malignant tumor with sebaceous differentiation. Metastases can occur.

Seborrheic keratoses: a universally occurring, very common benign tumor that develops from the proliferation of epidermal cells. They arise on normal skin as one or more sharply defined, light brown, flat lesions that develop with a velvety to finely verrucous surface.

Squamous carcinoma: a malignant tumor of epidermal keratinocytes. It frequently arises on the sun-exposed skin of middle-aged and elderly individuals. It is usually seen as an erythematous to skin-colored scaling plaque or nodule. Squamous carcinoma can also occur at the site of chronic irritation such as a chronic ulcer from any cause.

Syringoma: a benign adnexal neoplasm formed by well-differentiated ductal elements. They are skin-colored or yellowish, small, dermal papules. They are usually multiple in number, arranged in clusters, and symmetrically distributed. Syringomas are most commonly limited to the upper parts of the cheeks and lower eyelids.

21.20 T

Tinea corporis: a superficial dermatophyte infection characterized by a pruritic, annular plaque on the glabrous skin.

Trichilemmal cyst: a scalp cyst containing keratin, with a cell wall histologically similar to the external hair root sheath. While often intracutaneous, lesions may become polypoidal. Asymptomatic lesions can become tender from trauma or secondary infection. The tendency for multiple lesions can be inherited as an autosomal dominant trait.

Trichoepitheliomas: are hamartomas with pilosebaceous differentiation. Clinically, these small, skin-colored papules can resemble milia, syringomas, or other benign skin tumors, in addition to nodular basal cell carcinomas.

Trichofolliculoma: a hamartoma of the hair follicle. Clinically, it appears as a small, solitary, skin-colored nodule on the face or scalp in adults. Often, a tuft of wool-like hair protrudes from a central pore.

Tuberous xanthomas: yellow-orange nodules up to 2 cm in diameter, often located over the knees and elbows in patients with hypercholesterolemia and other lipid abnormalities.

21.21 U

Ulerythema ophryogenes: inflammatory hyperkeratotic facial papules giving the skin an abrasive feel to the touch. Scarring and alopecia may occur. Appears clinically as a fulminant form of keratosis pilaris, but may be associated with various syndromes.

21.22 V

Vitiligo: an acquired pigmentary disorder of the skin and mucous membranes. It is characterized by circumscribed depigmented macules and patches. It a progressive disorder in which some or all of the melanocytes in the affected skin are selectively destroyed.

21.23 W

21.24 X

Xanthelasma: a soft, superficial, yellow-orange papule, most common on the medial upper eyelid. They are usually multiple and symmetrical in distribution. Although they are of considerable value in identifying hyperlipemic patients at risk for occlusive vascular disease, lesions can occur in normolipemic individuals.

Xanthomas: lesions characterized by accumulations of lipid-laden macrophages, forming yellow-pink lesions visible to the eye. Xanthomas can develop in the setting of altered systemic lipid metabolism or as a result of local cell dysfunction.

References

1. Urbina F. Atlas de diagnostic diferencial en dermatología. 1st ed. Chile: Editorial Mediterraneo Ltda; 2008.
2. Bolognia JL, Jorizzo JL, Rapini RP, Horn TD, Mascaró JM, et al. Dermatología. 1st ed. Madrid: Elsevier; 2004.
3. Freedberg MI, Eisen ZA, Wolff K, Austen FK, Goldsmith AL, Katz IS, et al. Fitzpatrick's dermatology in general medicine, vol. 1 and 2. 7th ed. New York: McGraw-Hill; 2008.

Useful Dermatologic Classifications

22

Perla E. Calderon, Fernando A. Valenzuela,
and Gregor B.E. Jemec

The most common dermatologic classifications: a must read for anyone embedded in dermatologic ultrasound

Contents

P.E. Calderon, MD (✉) • F.A. Valenzuela, MD
Department of Dermatology,
Hospital Clínico Universidad de Chile, Faculty of Medicine,
University of Chile, Santos Dumont 999, Santiago 8380456, Chile
e-mail: perlacald@yahoo.com; dr.fvalenzuela@gmail.com

G.B.E. Jemec, MD, DMSci
Department of Dermatology, Health Sciences Faculty,
Roskilde Hospital, University of Copenhagen,
Køgevej 7-13, Roskilde 4000, Denmark
e-mail: gbj@regionsjaelland.dk

22.1 Introduction

In clinical dermatology, there are a great number of different diagnoses, and many of them have more than one name, that can overwhelm non-dermatologists when studying this complex discipline. Furthermore, many different classifications are involved in common dermatologic conditions and are frequently used in daily practice.

The purpose of this chapter is to provide a brief review of relevant dermatologic classifications or indexes that may impact the management of the lesions in order to coordinate the vocabulary and background between physicians involved in the clinical and the imaging fields. Topographic classifications for many dermatological diseases are also provided as additional support and to remind the reader of some of the differential diagnoses.

Dermatologic lesions must be considered as evolving entities, clinically and histopathologically, and must be considered when approaching a specific lesion. A particular disease may present different and multiple morphologies that can be a challenge to the clinician.

22.2 Main Differential Diagnosis According to Lesion Morphology

1 Blisters
1.1 Thick roof of blister
1.1.1 Bullous pemphigoid
1.1.2 Linear IgA disease
1.1.3 Friction blisters
1.1.4 Cicatricial pemphigoid
1.1.5 Pemphigoid gestationis
1.1.6 Epidermolyisis bullosa acquisita
1.1.7 Chronic bullous dermatosis of childhood
1.1.8 Bullous lichen planus pemphigoides
1.2 Thin roof of blister
1.2.1 Pemphigus vulgaris
1.2.1.1 Pemphigus vegetans

X. Wortsman, G.B.E. Jemec (eds.), *Dermatologic Ultrasound with Clinical and Histologic Correlations*,
DOI 10.1007/978-1-4614-7184-4_22,

1.2.2 Pemphigus erythematosus (Senear-Usher syndrome)
1.2.3 Porphyria or pseudoporphyiria
1.2.4 Pemphigus foliaceus
1.2.5 Perniosis
1.2.6 Bullous dermatosis of diabetes mellitus and uremia
1.3 Small blisters with a thin roof
1.3.1 Dermatitis herpetiformis
1.3.2 Keratosis follicularis (Darier's disease)
1.3.3 Neonatal sucking blisters
1.3.4 Transient acantholytic dermatosis (Grover's disease)
1.3.5 Benign familial pemphigus (Hailey-Hailey disease)
1.3.6 Subcorneal pustular dermatosis
1.3.7 Neonatal sucking blisters
1.4 Blisters with varying roof thickness
1.4.1 Burns
1.4.2 Epidermolysis bullosa
1.4.3 Graft vs. host disease

2 Vesicle

2.1 Dermatitis
2.2 Eczematous dermatitis – acute and subacute
2.3 Pompholyx
2.4 Phytophotodermatitis
2.5 Impetigo
2.6 Herpesvirus infections: herpes simplex, herpes varicella-zoster
2.7 Insect bites
2.8 Miliaria cristalina
2.9 Miliaria rubra
2.10 Chilblains
2.11 Cutaneous candidiasis
2.12 Erythema ab igne
2.13 Erythema toxicum neonatorum
2.14 Picornavirus infection: hand-foot-mouth disease
2.15 Pityriasis lichenoides et varioliformis acuta (PLEVA)
2.16 Hidrocystoma
2.17 Transient neonatal pustular melanosis
2.18 Acropustulosis of infancy
2.19 Incontinencia pigmenti, first stage
2.20 Mastocytosis

3 Pustule

3.1 Folliculitis
3.2 Rosacea
3.3 Acne
3.4 Demodicosis
3.5 Pustular psoriasis
3.6 Staphylococcal scalded skin syndrome
3.7 Benign cephalic pustulosis (neonatal acne)
3.8 Subcorneal pustular dermatosis (Sneddon-Wilkinson)
3.9 Langerhans cell histiocytosis
3.10 Miliaria pustulosa

4 Papule

4.1 Verruca plana
4.2 Seborrheic keratoses
4.3 Condyloma acuminatum
4.4 Sebaceous hyperplasia
4.5 Xanthoma (isolated, eruptive, planar)
4.6 Lichen planus
4.7 Basal cell carcinoma
4.8 Accessory nipple
4.9 Angiokeratoma
4.10 Trichoepitelioma isolated or multiple
4.11 Lichen nitidus
4.12 Syphilis, secondary
4.13 Darier's disease
4.14 Dermatosis papulosa nigra
4.15 Granuloma faciale
4.16 Sebaceous carcinoma
4.17 Trichofolliculoma
4.18 Syringoma
4.19 Ecrine poroma
4.20 Syringocystadenoma papilliferum
4.21 Accessory tragi

5 Plaques

5.1 Hyperkeratotic plaques
5.1.1 Callus
5.1.2 Actinic keratosis
5.1.3 Knuckle pads
5.1.4 Psoriasis
5.1.5 Pityriasis rosea
5.1.6 Pityriasis rubra pilaris
5.2 Non hyperkeratotic plaques
5.2.1 Scars
5.2.2 Keloid
5.2.3 Granuloma annulare
5.2.4 Nevus sebaceous
5.2.5 Morphea
5.2.6 Erythema elevatum diutinium
5.2.7 Dermatofibrosarcoma protuberans
5.2.8 Scleredema
5.2.9 Angiosarcoma
5.2.10 Infantile digital fibromatosis

6 Nodule

6.1 Lipoma and variants
6.2 Dermatofibroma
6.3 Foreign body granuloma
6.4 Scabies
6.5 Gout
6.6 Panniculitis
6.7 Neuroma
6.8 Neurofibroma
6.9 Injection granulomas

6.10 Piezogenic nodules
6.11 Chondrodermatitis nodularis helicis
6.12 Rheumatoid nodule
6.13 Tuberous xanthoma
6.14 Giant cell tumor of tendon sheath
6.15 Branchial sinus and/or cyst
6.16 Cephalohematoma of the newborn
6.17 Amyloidosis
6.18 Tuberous sclerosis–shagreen patch
6.19 Mycetoma
6.20 Lymphogranuloma venereum–sign of the Groove
6.21 Halogenoderma
7 Tumor
7.1 Exophytic/Pedunculated/papilliform
7.1.1 Warts
7.1.2 Acrochordon
7.1.3 Seborrheic keratosis
7.1.4 Nevus sebaceous
7.1.5 Keratoacanthoma
7.1.6 Supernumerary digit
7.1.7 Hypertrophic lichen planus
7.1.8 Hypertrophic lupus erythematosus
7.1.9 Sebaceous adenoma
7.1.10 Syringocystoadenoma papilliferum
7.1.11 Cylindroma
7.1.12 Tuberculosis verrucosa cutis
7.1.13 Verrucous carcinoma
7.1.14 Warty dyskeratoma
7.1.15 Acrokeratosis verruciformis
7.2 Solid tumor
7.2.1 Superficial
7.2.1.1 Non-melanocytic
7.2.1.1.1 Epidermal nevus
7.2.1.2 Melanocytic
7.2.1.2.1 Melanocytic nevi
7.2.1.2.1.1 Congenital or acquired
7.2.1.2.1.2 Blue nevus
7.2.1.2.2 Nevus of Ota
7.2.1.2.3 Nevus spilus
7.2.1.2.4 Halo nevus (Sutton's nevus)
7.2.1.2.5 Mayerson's nevus
7.2.1.2.6 Spitz Nevus
7.2.1.2.7 Malignant melanoma (variants)
7.2.1.2.7.1 Lentigo maligna melanoma
7.2.1.2.7.2 Intraepidermal malignant melanoma
7.2.1.2.7.3 Superficial spreading malignant melanoma
7.2.1.2.7.4 Papular and nodular malignant melanoma
7.2.1.2.7.5 Acral lentiginous malignant melanoma
7.2.1.2.7.6 Mucosal melanoma
7.2.1.2.7.7 Subungual melanoma
7.2.1.2.7.8 Amelanotic melanoma
7.2.1.2.7.9 Desmoplastic melanoma
7.2.1.3 Lymphocytic
7.2.1.3.1 Pseudolymphoma
7.2.1.3.2 Mycosis fungoides
7.2.1.3.3 B cell lymphoma
7.2.1.3.4 Jessner's lymphocytic infiltrate
7.2.1.3.5 Lymphocytoma cutis
7.2.2 Dermal (not mentioned above)
7.2.2.1 Metastatic neoplasm
7.2.2.2 Merkel cell carcinoma
7.2.2.3 Vasculitis
7.2.2.3.1 Large vessel vasculitis
7.2.2.3.1.1 Giant cell arteritis
7.2.2.3.1.2 Takayasu's arteritis
7.2.2.3.2 Medium vessel vasculitis
7.2.2.3.2.1 Polyarteritis nodosa
7.2.2.3.2.2 Kawasaki disease
7.2.2.3.3 Small vessel vasculitis
7.2.2.3.3.1 Cutaneous leukocytoclastic vasculitis
7.2.3 Hyperplasias and neoplasms affecting the subcutis
7.2.3.1 Benign
7.2.3.1.1 Lipoma
7.2.3.1.2 Angiolipoma
7.2.3.1.3 Angioleiomioma
7.2.3.1.4 Connective tissue nevus
7.2.3.2 Malignant
7.2.3.2.1 Liposarcoma
7.2.3.2.2 Dermatofibrosarcoma protuberans
7.2.3.2.3 Metastatic tumor
7.2.4 Miscellaneous
7.2.4.1 Calcinosis cutis
7.2.4.2 Osteoma cutis
7.2.4.3 Gouty tophi
7.2.4.4 Pilomatrixoma
7.3 Cyst
7.3.1 Cysts with stratified squamous epithelium
7.3.1.1 Epidermoid cyst
7.3.1.2 Trichilemmal cyst
7.3.1.3 Pilonidal cyst
7.3.1.4 Dermoid cyst
7.3.1.5 Steatocytoma
7.3.1.6 Ear pit cyst
7.3.1.7 Pigmented follicular cyst
7.3.1.8 Villous hair cyst
7.3.1.9 Cystic hygroma
7.3.2 Cysts with non-stratified squamous epithelium
7.3.2.1 Hydrocystoma: eccrine and apoccrine
7.3.2.2 Ciliated cyst of the vulva
7.3.2.3 Bronchogenic cyst

7.3.2.4 Thyroglossal duct cyst
7.3.2.5 Brachial cleft cyst
7.3.2.6 Median raphe cyst
7.3.2.7 Omphalomesenteric duct cyst
7.3.3 Cysts with absence of epithelium:
7.3.3.1 Mucocele
7.3.3.2 Digital mucous cyst
7.3.3.3 Ganglion
7.3.3.4 Pseudocyst of the auricle
7.3.3.5 Cutaneous metaplastic synovial cyst
7.4 Vascular tumour
7.4.1 Pyogenic granuloma
7.4.2 Infantile hemangiomas
7.4.3 Congenital hemangioma
7.4.3.1.1 Rapidly involuting congenital hemangioma (RICH)
7.4.3.1.2 Non-involuting congenital hemangioma (NICH)
7.4.4 Kaposiform hemangioendothelioma
7.4.5 Tufted angioma
7.4.6 Congenital hemangiopericytoma
7.4.7 Spindle cell hemangioma
7.5 Vascular malformations
7.5.1 Simple
7.5.1.1 Slow flow
7.5.1.1.1 Capillary malformation
7.5.1.1.2 Venous lake
7.5.1.1.3 Venous malformation
7.5.1.1.4 Lymphatic malformation
7.5.1.1.5 Glomuvenous malformation
7.5.1.2 Fast-flow
7.5.1.2.1 Arterial malformation
7.5.2 Combined:
7.5.2.1 Slow-flow
7.5.2.1.1 Lymphatic/Venous Malformation
7.5.2.1.2 Capillary/Lymphatic/Venous Malformation
7.5.2.1.3 Capillary/Venous Malformation
7.5.2.2 Fast-flow
7.5.2.2.1 Arteriovenous malformation
7.5.2.2.2 Capillary malformation plus arteriovenous malformation
7.5.2.2.3 Arteriovenous fistula
8 Ulcer
8.1 Venous ulcer
8.2 Stasis ulcer
8.3 Pressure ulcer
8.4 Snake or spider bites
8.5 Neuropathic
8.5.1 Ulcer (trophic ulcer)
8.5.2 Decubitus
8.5.3 Diabetes
8.5.4 Neuropathy
8.5.5 Paraplegias
8.5.6 Tabes dorsalis
8.5.7 Trigeminal trophic syndrome
8.6 Leprosy
8.7 Arterial ulcer
8.8 Traumatic ulcer
8.9 Pyoderma gangrenosum
8.10 Septic emboli
9 Hives
9.1 Dermographism
9.2 Urticaria
9.3 Angioedema
9.4 Urticarial vasculitis
9.5 Histamine releasing agents
9.6 Toxocariasis (urticarial migratory lesions)
10 Macules
10.1 Macular erythematous rashes
10.2 Depigmented macules:
10.2.1 Vitiligo
10.2.2 Idiopathic guttate hypomelanosis
10.2.3 Nevus achromicus
10.3 Hyper pigmented macules
10.3.1 Café-au-lait patch
10.3.2 Macular amyloidosis

22.3 Guide to Dermatologic Diagnosis by Affected Region

1. Hair and Scalp
- Inflammatory
  - Seborrheic dermatitis
  - Contact dermatitis
  - Benign neoplasm
  - Psoriasis
  - Acne keloidalis nuchae
  - Nevus sebaceous
  - Pityriasis amiantacea
  - Pilar cyst
  - Dissecting folliculitis
  - Juvenile xanthogranuloma
- Cutaneous malignancies
  - Actinic keratosis
  - Basal cell carcinoma
  - Squamous cell carcinoma
  - Follicular mucinosis
  - Angiosarcoma
- Infections
  - Folliculitis
  - Tinea capitis
  - Kerion
- Infestations
  - Pediculosis capitis
- Immunologic
  - Contact dermatitis
  - Alopecia areata
  - Lupus erythematosus
  - Benign mucous membrane pemphigoid

2. Face
- Inflammatory
  - Acne
  - Rosacea
  - Eczema/Contact dermatitis
  - Lichen simplex
- Benign neoplasms
  - Intradermal nevus
  - Syringoma
  - Calcifying epithelioma of Malherbe
  - Nevus of Ota
  - Blue nevus
  - Nevus despigmentosus
- Cutaneous malignancy
  - Actinic keratosis
  - Basal cell carcinoma
  - Keratoacanthoma
  - Squamous cell carcinoma
  - Bowen's disease
  - Lentigo maligna
- Infections
  - Impetigo
  - Erysipelas
  - Tinea
  - Molluscum contagiosum
  - Warts
  - Herpes simplex
  - Herpes zoster
  - Kaposi's sarcoma
- Immunologic causes
  - Lupus erythematosus
  - Dermatomyositis
  - Scleroderma
- Pigmentary
  - Melasma
  - Pityriasis alba
  - Solar lentigo
  - Vitiligo
- Systemic disorders
  - Xanthelasma
  - Sweet's syndrome
  - Sarcoidosis
  - Myxedema
  - Porphyria

3. Oral Disorders
- Inflammatory
  - Contact dermatitis
  - Lichen planus
- Infections
  - Impetigo
  - Herpes simplex
  - Warts
  - Candidiasis
  - Varicella zoster
  - Coxsackievirus
  - Measles
  - Oral hairy leukoplakia
  - Kaposi's sarcoma
  - Dental sinus
- Benign neoplasms
  - Venous lakes
  - Mucous cysts
  - Lentigines
  - Pyogenic granuloma
- Mucosal malignancies
  - Actinic cheilitis
  - Squamous cell carcinoma
- Drugs
  - Fixed drug eruption
  - Erythema multiforme
- Developmental disorders
  - Geographic tongue
  - Hemangioma
  - Fordyce spots
  - Black hairy tongue
- Immunologic causes
  - Lupus erythematosus
  - Pemphigus vulgaris
  - Cicatricial pemphigoid
- Systemic disorders
  - Trauma
  - Granulomatous cheilitis
  - Crohn's disease
  - Behçet disease
  - Addison's disease
  - Lipoid proteinosis

4. Torso
- Inflammatory
  - Acne
  - Contact dermatitis
  - Eczema
  - Folliculitis
  - Pityriasis rosea
  - Psoriasis
  - Pityriasis lichenoides
  - Pityriasis rubra pilaris
  - Erythroderma
- Skin tumors
  - Dysplastic nevi
  - Lipomas
  - Epidermal cyst
- Skin malignancies
  - Superficial basal cell carcinoma
  - Melanoma
- Infections
  - Viral exanthems
  - Pityriasis versicolor
  - Herpes zoster
  - Tinea corporis
  - Secondary syphilis

- Drugs/reactive
  - Urticaria
  - Phototoxicity
  - Drug eruptions
  - Toxic erythema
- Immunologic causes
  - Lupus erythematosus
  - Pemphigus
  - Pemphigoid
  - Pityriasis lichenoides morphea
- Developmental disorders
  - Darier's syndrome
  - Neurofibromatosis
  - Ichtyosis
- Systemic disorders
  - Mycosis fungoides
  - Sarcoidosis
  - Urticaria pigmentosum
  - Eruptive xanthoma

5. Groin and Pubic Area

- Inflammatory
  - Seborrheic or contact eczema
  - Lichen simplex
  - Napkin eruption
  - Inverse psoriasis
  - Lichen planus
  - Hidradenitis suppurativa
- Nevi and tumors
  - Angiokeratomas
  - Lymphangioma
  - Idiopathic calcinosis of the scrotum/vulva/penis skin
- Infections
  - Warts
  - Herpes simplex
  - Molluscum contagiosum
  - Candidiasis
  - Tinea cruris
  - Syphilis
  - Lymphogranuloma venereum
- Infestations
  - Pediculosis
  - Scabies
- Drugs (reactive)
  - Fixed drug eruption
  - Steroid-induced striae
  - Erythema multiforme
- Developmental disorders
  - Hailey-Hailey disease
  - Pseudoacanthosis nigricans
- Immunologic causes
  - Vitiligo
  - Lichen sclerosus et atrophicus
  - Benign mucous membrane pemphigoid
  - Pemphigus
- Systemic disorders
  - Behçet's syndrome
  - Pyoderma gangrenosum
  - Reiter's syndrome
- Benign tumors
  - Pearly penile papules
- Cutaneous neoplasms
  - Bowenoid papulosis
  - Squamous cell carcinoma
  - Bowen's disease
- Pigmentary
  - Melanotic macules
- Psychological causes
  - Dermatitis artefacta

6. Hands

- Inflammatory
  - Contact dermatitis
  - Pompholyx
  - Psoriasis
  - Lichen planus
  - Pityriasis rubra pilaris
- Common benign neoplasms
  - Pyogenic granuloma
  - Blue nevus
- Cutaneous malignancies
  - Actinic keratosis
  - Bowen's disease
  - Squamous cell carcinoma
  - Mycosis fungoides
- Infections
  - Warts
  - Impetigo
  - Herpes simplex
  - Tinea
  - Candidal paronychia
  - Secondary syphilis
  - Gonococcaemia
  - Orf
- Infestations
  - Scabies
  - Larva migrans
- Drugs (reactive)
  - Erythema multiforme
  - Photosensitivity
  - Fixed drug eruption
- Developmental disorders
  - Accessory digits
  - Acquired digital fibrokeratoma
- Immunologic causes
  - Dermatomyositis
  - Chilblain lupus erythematosus
  - Scleroderma
  - Graft-versus-host disease

Pigmentary
- Vitiligo
- Solar lentigines

Systemic disorders
- Granuloma annulare
- Sarcoidosis
- Porphyria cutanea tarda

7. Feet

Inflammatory
- Contact eczema
- Pompholyx
- Juvenile plantar dermatosis
- Psoriasis
- Lichen planus
- Infantile acropustulosis

Benign neoplasms
- Eccrine poroma

Infections
- Warts
- Tinea
- Secondary syphilis

Infestations
- Insect bites
- Scabies

Drugs (reactive)
- Erythema multiforme

Developmental disorders
- Punctate keratoderma
- Congenital Keratoderma
- Epidermolysis bullosa

Vascular
- Arteriosclerosis
- Gangrene

Systemic disorders
- Hyperhidrosis
- Trauma
- Corns
- Granuloma annulare
- Necrobiosis lipoidica diabeticorum
- Reiter's syndrome
- Kaposi's sarcoma

8. Midline Cutaneous Lesions

Scalp Midline Lesions (may extend intracranial)
- Vascular lesions
- Port stain wine
- Dermoid cysts
- Cephaloceles
- Heterotopic brain or meningeal tissue
- Aplasia cutis congenital

Nasal Midline Lesions
- Dermoid cysts (located at the external side of the eyebrows)
- Nasal gliomas
- Encephaloceles

Neck Midline Lesions
- Midline cervical clefts
- Thyroglossal duct cysts
- Sternal clefts
- Bronchogenic cysts (also located over the clavicles)

Spine Midline Lesions (may have an underlying dysraphism, most of them located in the lumbosacral region)
- Hemangiomas and vascular malformations
- Dimples
- Hypertricosis
- Curved gluteal cleft (may be hiding a intraspinal lipoma or a lypomyelomeningocele)
- Dermal sinuses
- Achrocordons
- Aplasia cutis congenital
- Hypo or hyperpigmentation
- Congenital melanocytic nevi
- Subcutaneous tumours

9. Nail Diseases

Onichomychosis

Traumatic
- Onychotillomania
- Medial canalicular dystrophy
- Subungueal hematoma

Nail Plate or Matrix Tumors and Pseudotumors

Benign:
- Warts
- Pyogenic granuloma
- Melanocytic nevi of the nail matrix
- Fibromas
- Subungueal exostosis
- Myxoid cysts
- Glomus tumors
- Onychomatricoma

Malignant:
- Bowen's disease
- Keratoacanthoma
- Squamous cell carcinoma
- Verrucous carcinoma
- Melanoma

22.4 Indexes, Scoring, and Classifications

22.4.1 Psoriasis

22.4.1.1 Psoriasis Area and Severity Index (PASI) (Range, 0–72)

PASI is a clinical scoring system commonly used for the assessment of disease severity (higher score indicates a more severe disease). It is used mostly for clinical trials, but also to document clinical improvement in patients treated with highly expensive medications (e.g., tumor necrosis factor-alpha inhibitors).

Table 22.1 Psoriasis Area and Severity Index (PASI)

	Head	Trunk	Upper limbs	Lower limbs
Severity of psoriasis lesions: 0, none; 1, slight; 2, moderate; 3, severe; 4, very severe				
Erythema	0–4	0–4	0–4	0–4
Induration	0–4	0–4	0–4	0–4
Scaling	0–4	0–4	0–4	0–4
Total score = 1	Sum of above	Sum of above	Sum of above	Sum of above
Area of psoriatic involvement: 0, none; 1, <10 %; 2, 10–<30 %; 3, 30–<50 %; 4, 50–<70 %; 5, 70–<90 %; 6, 90–100 %				
Degree of involvement = 2	0–6	0–6	0–6	0–6
Multiply 1 × 2	1 × 2	1 × 2	1 × 2	1 × 2
Correction factor = 3	0,1	0,3	0,2	0,4
1 × 2 × 3	A	B	C	D
A + B + C + D = total PASI				

Procedure: After a complete examination, the physician must summarize the psoriatic lesions in terms of erythema, induration, and scaling of each corporal segment as follows: head, torso, upper limbs, and lower limbs from 0 to 4 according to severity and add the three values (parameter 1 = total score). The physician must then calculate the percentage of psoriatic involvement in each corporal segment (parameter 2 = degree of involvement) that can range from 0 (no compromise) to 6 (≥ 90 % of the segment compromised).

Thus, the physician must calculate 1 × 2 and then multiply for the correction factor [1] according to the relative importance of each segment in the total body surface in order to get the A, B, C, and D scores. Finally, all the scores must be added to complete the PASI score (Table 22.1).

22.4.1.2 Nail Psoriasis Severity Index (NAPSI) (Range, 0–80 or 160 [If Toenails Are Included])

NAPSI is a commonly used clinical score for the assessment of disease severity (higher score indicates a more severe disease). NAPSI is used mostly in connection with trials, but can also be used to document the effect in high-cost treatments (e.g., tumor necrosis factor-alpha inhibitors).

Procedure: The nail is divided into quadrants with imaginary horizontal and longitudinal lines. Each nail is given a score for nail bed psoriasis (0–4) and nail matrix psoriasis (0–4) depending on the presence of any of the features of nail psoriasis in that quadrant.

A. Evaluation 1: Nail matrix. In each quadrant of the nail, nail matrix psoriasis is evaluated by presence of any of the nail matrix features (pitting, leukonychia red spots in the lunula, crumbling):
   0 for none, 1 if present in one quadrant of the nail, 2 if present in two quadrants of the nail, 3 if present in three quadrants of the nail, and 4 if present in four quadrants of the nail.
B. Evaluation 2: Nail bed. Nail bed psoriasis is evaluated by the presence of any of the nail bed features (onycholysis, splinter hemorrhages, subungual hyperkeratosis, "oil drop", salmon patch dyschroma):
   0 for none, 1 if present in one quadrant of the nail, 2 if present in two quadrants of the nail, 3 if present in three quadrants of the nail, and 4 if present in four quadrants of the nail.
C. Each nail is assigned a matrix score and a nail bed score, the total of which is the score for that nail (0–8).
D. Each nail is evaluated, and the sum of all the nails is the total NAPSI score.

Table 22.2 The Physician Global Assessment (PGA) Scale

Erythema (E)	Induration (I)	Scaling (S)
Severity 0–4	Severity 0–4	Severity 0–4
(E + I + S)/3		
0 = clear, 1 = almost clear, 2 = mild, 3 = moderate, 4 = severe		

22.4.1.3 Physician Global Assessment (PGA) Scale (Range, 0–4)

The PGA scale is a commonly used clinical score for the assessment of disease severity (higher score indicates more severe disease). It is used mainly for clinical trials, but also to document clinical improvement in cases that use costly medications (e.g., tumor necrosis factor-alpha inhibitors).

Procedure: The PGA scale is the summary of all individual lesions of a patient with psoriasis. After complete physical examination the physician must score the lesions in terms of plaques erythema, induration, and scaling; the mean value finally interprets psoriasis activity (Table 22.2).

Table 22.3 Breslow Classification (thickness)

Breslow thickness (mm)	Prognosis (5-year survival) (%)
<1	95–100
1–2	80–96
2.1–4	60–75
>4	37–50

Table 22.4 Clark Classification (level of invasion)

Level I	Confined to the epidermis; called "in situ" melanoma
Level II	Invasion of the papillary (upper) dermis
Level III	Filling of the papillary dermis, but no extension into the reticular (lower) dermis
Level IV	Invasion of the reticular dermis
Level V	Invasion of the deep, subcutaneous tissue

22.4.2 Melanoma

22.4.2.1 Breslow Thickness

Breslow thickness is defined as the total vertical height of a melanoma, from the very top (called the "granular layer") to the area of deepest penetration into the skin. In general, the higher the Breslow thickness, the worse the prognosis (Table 22.3).

22.4.2.2 Clark Level of Invasion

The Clark level refers to how deep the tumor has penetrated into the layers of the skin (Table 22.4).

Conclusion

Knowledge of the differential diagnoses, indexes, scoring, and classification may help in facilitating performance and interpretation of dermatologic ultrasound examinations [1–16].

References

1. Habif TP. Clinical dermatology: a color guide to diagnosis and therapy. 4th ed. St Louis: Mosby; 2003.
2. Bolognia J, Jorizzo J, Rapini R, editors. Dermatology, vol. 2. 2nd ed. Spain: Mosby; 2008.
3. du Vivier A. Atlas of clinical dermatology. 3rd ed. Edinburgh: Churchill Livingstone; 2002.
4. Wolff K, Johnson RA, Suurmond R. Fitzpatrick's color atlas and synopsis of clinical dermatology. 5th ed. New York: McGraw-Hill; 2005.
5. James WD, Berger TG, Elston DM. Andrew's diseases of the skin: clinical dermatology. 10th ed. Philadelphia: Saunders; 2006.
6. Wolff K, Goldsmith LA, Katz SI, et al., editors. Fitzpatrick's dermatology in general medicine. 7th ed. New York: McGraw-Hill; 2007.
7. James WD, Elston D, editors. eMedicine dermatology. St Petersburg: eMedicine Corporation; 2011. Online at emedicine.com.
8. Schachner LA, Hansen RC. Pediatric dermatology. 3rd ed. New York: Churchill Livingstone; 2003.
9. Schneiderman PI, Grossman ME. A clinician's guide to dermatologic differential diagnosis, vol. I: The text and vol. II: The atlas. New York: Informa Healthcare; 2006.
10. Ackerman AB, Kerl H, Sanchez J, et al. A clinical atlas of 101 common skin diseases with histopathologic correlation. New York: Ardor Scribendi; 2000.
11. Weedon D. Skin pathology. 2nd ed. Edinburgh: Churchill Livingstone; 2002.
12. Rich P, Scher R. Nail psoriasis severity index: a useful tool for evaluation of nail psoriasis. J Am Acad Dermatol. 2003;49:206–12.
13. Mulliken JB, Glowacki J. Hemangiomas and vascular malformations in infants and children: a classification based on endothelial characteristics. Plast Reconstr Surg. 1982;69:412–22.
14. Huang JT. Vascular malformations. Pediatr Clin North Am. 2010;57:1091–110.
15. Willemze R, Jaffe ES, Burg G, et al. WHO-EORTC classification for cutaneous lymphomas. Blood. 2005;105:3768–85.
16. Hood A, Kwan T, Mihm M, Horn T, Smoller B. Primer of dermatopathology. 3rd ed. Philadelphia: Lippincott Williams & Wilkins; 2002.

How to Start on Skin, Nail, and Hair Ultrasound: Guidance and Protocols

23

Ximena Wortsman

Suggested guidance and protocols for performing the examinations within a practical approach

Contents

X. Wortsman, MD
Department of Radiology and Dermatology,
Institute for Diagnostic Imaging
and Research of the Skin and Soft Tissues,
Clinica Servet, Faculty of Medicine, University of Chile,
Almirante Pastene 150, Providencia, Santiago, Chile
e-mail: xwo@tie.cl, xworts@yahoo.com, www.sonoskin.com

23.1 Introduction

The implementation of any medical technique can present difficulties. Thus, many questions can emerge from the sonographer, the referring physician, and of course the patient. In this chapter, recommendations and guidance to facilitate the process are suggested. The suggestions are the result of our experience, but are of course susceptible to modification or improvement according to the reality of your own place of work. Hence, the application of the technique relies mainly on three points: the sonographic anatomy, the technical requirements, and the team of work necessary to optimize the results.

We assume at this point that the reader is been well-informed regarding the sonographic anatomy, and has reviewed the technical requirements and common dermatologic entities that he or she will most often deal with. Moreover, ideally, a team of work between the following departments has been initiated: Imaging (Radiology), Clinical (e.g., Dermatology, Rheumatology, Plastic Surgery, etc.), and Pathology. Therefore, we will focus on practical issues, such as suggested protocols for dealing with common conditions and providing examples of dermatologic reports. We hope that this guide will help to facilitate the implementation of this technique at your work place.

23.2 Protocol for Studying Skin Lesions

The sonographer is an active part of the examination and it is suggested that before beginning the test, a visual inspection of the lesion and a conversation with the patient be performed. This interactive pre-test is of paramount importance and can provide clinical data that can assist in the final interpretation of the results or help with proper probe placement. Therefore, the sonographer can potentially guess the questions or doubts of the referring physician and the differential diagnoses. An algorithm for studying skin lesions is proposed, which shows ultrasound as the first-line imaging modality for assessing dermatologic entities (Algorithm 23.1).

X. Wortsman, G.B.E. Jemec (eds.), *Dermatologic Ultrasound with Clinical and Histologic Correlations*,
DOI 10.1007/978-1-4614-7184-4_23, © Springer Science+Business Media New York 2013

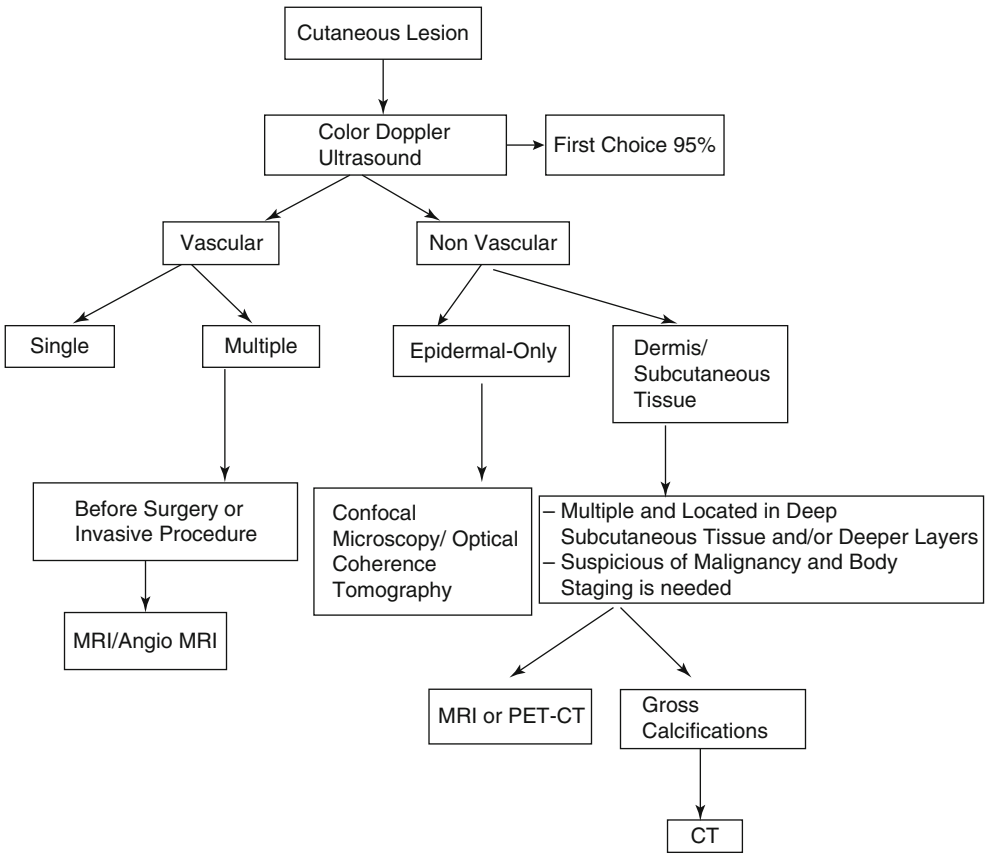

Algorithm 23.1 Proposal for approaching a dermatological lesion on imaging. *Abbreviations: MRI* magnetic resonance imaging, *CT* computed tomography, *PET* positron emission tomography

23.2.1 Visual Inspection of the Lesion

Performing a visual inspection in a well-illuminated room is recommended (Figs. 23.1 and 23.2). A dimmer can be used to regulate the intensity of the light in the room during the different parts of the sonographic examination. The visual inspection should determine such clinical characteristics of the lesion:

- Location (body region[s])
- Skin color (erythema, blue or purple colored, pigmented, etc.)
- Ulceration (yes or no)
- Palpation (soft, firm, hard)
- Pain (painful, painless)
- History (recent, old, slow-growing, fast-growing, without changes, surgeries, biopsies, etc.)

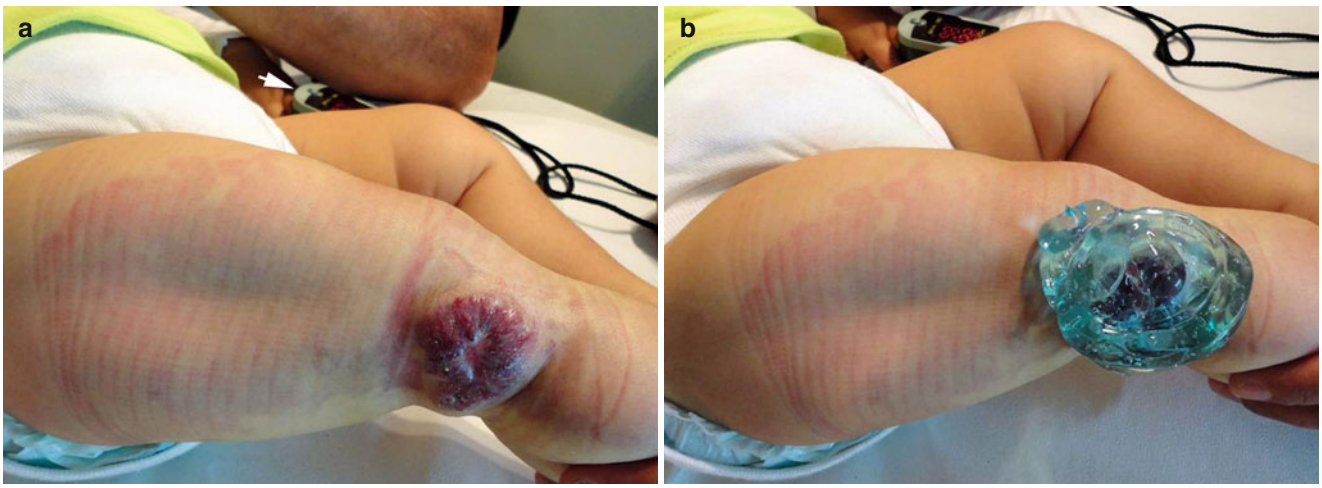

Fig. 23.1 (**a**) Inspection of the lesion in a well-illuminated room. Notice the pulse oximeter (*arrow*) that is used for monitoring the child under sedation. (**b**) Use a copious amount of gel to cover the lesion

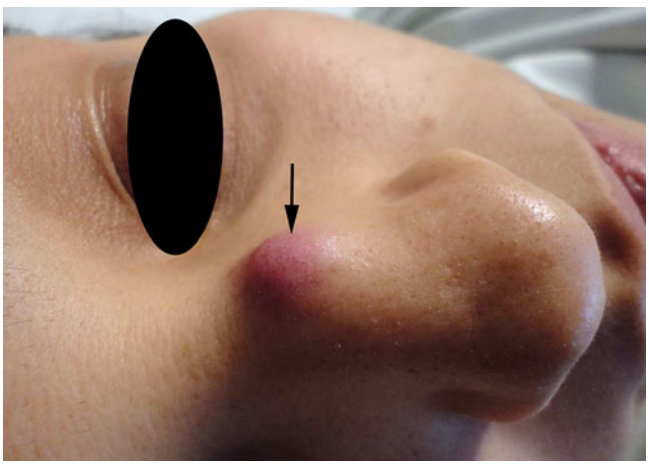

Fig. 23.2 Palpation of the lesion (*arrow*) is recommended

23.2.2 Tips for the Sonographic Examination of the Skin

- Use a copious amount of gel (Fig. 23.3).
- Sedation is used in children (<4 year-old, for e.g. Chloral Hydrate, 50 mg/kg, orally, 30 min before the examination after informed consent has been signed by the parent or guardian). The modified Aldrete scoring system can be used for monitoring the child during the sedation process.
- When studying lesions in the ear pinna, a small piece of cotton can be used to cover the meatus (Fig. 23.4).
- Grey scale ultrasound: a sweep in at least two perpendicular axes is recommended.
- Color Doppler ultrasound: look for the lesional and perilesional blood flow
- Spectral curve analysis: registration of at least three curves in non-vascular and six curves in vascular lesions (three curves per each/axis) is recommended.

Fig. 23.3 A copious amount of gel is also applied in the non-lesional areas or contralateral regions for comparison

Fig. 23.4 For studying the ear pinna region, a small piece of cotton is used to cover the external meatus (*arrow*)

23.3 Protocol for Studying Lesions of the Nail

1. Visual inspection
2. Sonographic examination

Tips for the sonographic study of the nail:

- Compare with the contralateral side (Fig. 23.5)
- Use a towel or pad beneath the thumbs (Fig. 23.6)

Use the following sequence:

1. Grey scale ultrasound
   - A sweep in at least two different axes (e.g., from medial to lateral and from proximal to distal) including the periungual tissue and the distal interphalangeal joint is recommended.

     Set your focus and depth for observing both the complete nail bed and the bony margin of the distal phalanx.
2. Color Doppler ultrasound: register the ungual and periungual blood flow
3. Spectral Curve Analysis

   At least three spectral curves in non-vascular and six in vascular lesions are suggested.

Fig. 23.5 A comparison with the contralateral nail is recommended

Fig. 23.6 A towel or pad beneath the thumbs can help to better support the fingers

23.4 Protocol for Studying the Scalp

- Visual Inspection
- Sonographic Examination:
- Displace the hair tracts to apply the gel (Fig. 23.7).
- Try to avoid software that softens the images (i.e., median filtering that comes with some machines) because you may lose definition of the hair follicles in the dermis.
- The rest is similar to the protocol for studying localized skin lesions.

Fig. 23.7 When studying a lesion in the scalp, try to displace the hair tracts

23.5 Suggested Settings for the Ultrasound Machine

- Power Doppler to detect slow flow
- Lowest repetition pulse frequencies and wall filters
- Color gain below the noise threshold that does not cause artifacts
- Extended field of view
- Compound software
- 3D reconstruction (optional)
- Try to use compact linear probes (hockey stick) that adapt well to the different concavities and convexities of the skin surface and small structures such as the fingers or the nail.

23.6 Tips for Studying Multiple Skin Lesions

1. Visual Inspection
   If necessary, consider scheduling the patient for two or more sessions (Fig. 23.8)
2. Manage the light in the examination room
   It will probably be necessary to turn the lights on and off in order to properly position the probe
3. If you are dealing with an inflammatory disease such as morphea or psoriasis, try to position the probe in the transition zone between the lesional and non-lesional tissue and/or perform a comparison with the contralateral region (Fig. 23.9). These observations may provide a clearer view of the abnormalities.
4. Sonographic Examination
   Similar for studying localized lesions

Remember that a high-frequency probe does not necessarily mean high definition. In addition to high frequency you will need:

- A multi-channeled ultrasound machine with a potent processor
- Focus that goes from superficial to deep, ideally from the skin to the bony margin. If necessary, change the probe (to a lower frequency) for observing deeper structures.

Fig. 23.8 In patients with multiple lesions, more than one ultrasound session may be needed

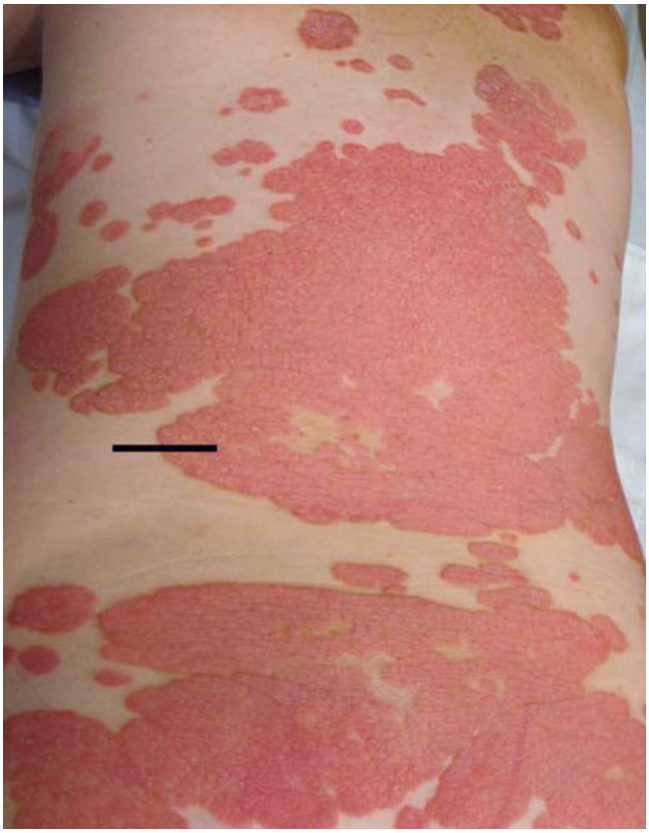

Fig. 23.9 For inflammatory diseases, a study of the transitional zone (*black line*) between the lesional and non-lesional tissue is suggested

23.7 Tips for the Examination

- Use a copious amount of gel including on the lesion and surrounding tissue.
- If necessary, apply gel on the contralateral side
- Try to not use stand-off pads and first view the lesion without any artificial compression.
- During the examination you can try compression maneuvers as a dynamic test
- Try the nearest position of the lesion to the examiner's hand and probe

23.8 Tips on How to Perform Sonographic Locoregional Staging in Melanoma

- Start from the primary lesion or scar.
- Follow 10–20 cm around the primary region and study the entire extremity
- Follow the superficial vein tracts and the distribution of the probable lymphatic drainage
- Go to the ipsilateral and contralateral nodal stations (axillae-groin)
- If the primary tumor is located in the head and neck region, also study the supra- and infraclavicular stations.

23.9 Sonography Report of Cutaneous Lesions

23.9.1 Key Questions

As in any other imaging technique, the report is of paramount importance and should include relevant data unavailable from the naked eye clinical examination. Thus, the sonography report should ideally provide the following answers of the clinician:

1. Is the lesion originated in the skin?
2. Where is the exact anatomical location?
3. Is there any relevant surrounding anatomical structure that can affect the planning of surgery or the medical treatment?
4. Is it cystic or solid?
5. What are the diameters of the lesion in every axis?
6. Is it a vascular lesion? Does it present high or low flow ? Is it arterial or venous flow? What is the diameter of the vessels? Is there any arterio-venous shunt? Is it a vascular lesion (e.g., a hemangioma) in a proliferative or regression phase?
7. Is it suggestive of a benign or malignant cutaneous lesion?
8. If the lesion is an inflammatory condition, is it in the active, inactive, or atrophic phase?
9. Differential diagnoses?

Once the questions and answers are clear in the mind of the sonographer, the practical outputting of the report can take place.

23.9.2 Examples of Sonography Reports of Common Dermatologic Lesions

Some practical examples of reports of common dermatologic lesions are provided below. These fictitious examples are based on the most common forms of presentation of cutaneous lesions but it should be kept in mind that there are variants of these presentations that can be reviewed in the other chapters of this book.

23.9.2.1 Reporting an Epidermal Cyst

23.9.2.1.1 Clinical History

A 28-year-old male patient presenting with a 6-month history of a painless and occasionally erythematous bump on the left cheek.

23.9.2.1.2 Technique

Grey scale and color Doppler multiplanar sonographic sweep is performed of the left cheek.

23.9.2.1.3 Sonography Report

A round-shaped well-defined anechoic cystic structure with internal echoes and posterior acoustic transmission is detected in the dermis and subcutaneous tissue of the left cheek.

The measurements of the cyst are 2.5 mm (longitudinal axis) × 2.3 mm (transverse axis) and 0.8 mm (depth axis).

There is a 0.4 mm (transverse axis) × 1.1 mm (depth axis) anechoic tract that connects the surface of the cyst with the subepidermal region.

No signs of hypervascularity are detected within the lesion area or in the surrounding tissues.

The left parotid gland and masseter muscle appear normal.

The rest of the examination is unremarkable.

23.9.2.1.4 Impression on Sonography

These findings are suggestive of an intact epidermal cyst.

23.9.2.2 Reporting a Pilomatrixoma

23.9.2.2.1 Clinical History

A 8-year-old female patient presenting with an 8-month history of slow-growing, erythematous, firm and painless swelling located in the right arm.

23.9.2.2.2 Technique

Grey scale and color Doppler multiplanar sonographic sweep is performed of the right arm.

23.9.2.2.3 Sonographic Report

A round-shaped well-defined solid nodule with a hypoechoic rim and hyperechoic center is detected in the dermis and subcutaneous tissue of the right arm.

The nodule measures 3.4 mm (longitudinal axis) × 3.7 mm (transverse axis) and 3.2 mm (depth axis). There are several 0.5–0.8 mm focal hyperechoic spots suggestive of calcium deposits within the center of the lesion.

Increased echogenicity of the subcutaneous tissue that surrounds the lesion consistent with edema is noted.

On color Doppler ultrasound, thin arterial and venous vessels that measure between 0.4 mm and 0.8 mm (thickness) are detected in the periphery and the center of the tumor.

Spectral curve analysis shows low velocity flow within the vessels. The maximum peak systolic velocity of the arterial vessels is 6.2 cm/s.

The deeper layers are unremarkable.

23.9.2.2.4 Impression on Sonography

The findings are consistent with Pilomatrixoma.

23.9.2.3 Reporting a Hemangioma

23.9.2.3.1 Clinical History

A 4-month-old male infant presenting with a 3-month history of a fast-growing reddish and soft lesion of the right cheek.

23.9.2.3.2 Technique

Grey scale and color Doppler multiplanar sonographic sweep is performed of the right cheek.

23.9.2.3.3 Sonography Report

The study shows a heterogeneous ill-defined mass in the dermis and subcutaneous tissue of the left cheek, predominantly hypoechoic in the dermal layer.

The mass also involves the ipisilateral parotid gland and masseter muscle.

The measurements of the lesional tissue are 6.2 cm (longitudinal axis) × 5.1 cm (transverse axis) × 3.2 cm (depth axis).

On color Doppler ultrasound, prominent vascularity is detected within the mass, particularly in the dermal region. The lesion shows high flow arterial vessels, low flow venous vessels, and a few arterio-venous shunts. The thickness of the vessels within the mass ranges between 0.6 and 1.6 mm.

The maximum peak systolic velocity of the arterial vessels is 42.3 cm/s.

The bony margin of the maxillae is unremarkable.

23.9.2.3.4 Impression on Sonography

The findings are consistent with infantile hemangioma in the proliferative phase with involvement of the ipsilateral parotid gland.

23.9.2.4 Reporting a Vascular Malformation

23.9.2.4.1 History

A 5-year-old female patient presenting with a slow-growing, blue-colored painless bump of the lower lip

23.9.2.4.2 Technique

Grey scale and color Doppler multiplanar sonographic sweep is performed of the lower lip

23.9.2.4.3 Sonography Report

Multiple, serpiginous, easily compressible, anechoic thin ducts are detected in the submucosal layer of the lower lip that extends into the orbicularis oris muscle. The thickness of the ducts varies between 0.6 and 1.8 mm. The lesion area measures 1.7 cm (longitudinal axis), 3.8 cm (transverse axis), and 0.7 cm (depth axis).

On color Doppler ultrasound, low-velocity venous flow is detected within the vessels.

No signs of thrombosis are seen in the venous tracts on sonography.

There are a few low flow arterial vessels in the periphery of the lesional tissue that seem to correspond to normal stromal vessels of the lower lip.

There are no signs of involvement of the deeper layers or at the oral cavity.

23.9.2.4.4 Impression on Sonography

The findings are consistent with a low flow venous vascular malformation with involvement of the orbicularis muscle of the lower lip.

23.9.2.5 Reporting a Basal Cell Carcinoma

23.9.2.5.1 History

A 75-year-old male patient presenting with a 1-year history of an erythematous and ulcerated lesion located in the right wing of the nasal tip suspicious of basal cell carcinoma (BCC).

23.9.2.5.2 Technique

Grey scale and color Doppler multiplanar sonographic sweep is performed at the nasal tip.

23.9.2.5.3 Sonography Report

Ovoid-shaped, well-defined, hypoechoic solid lesion that involves the dermis and the anterior aspect of the right nasal cartilage.

The lesion has multiple hyperechoic spots and measures 3.8 mm (longitudinal axis), 3.5 mm (transverse axis), and 2.5 mm (depth axis). The lesion involves the anterior aspect of the right nasal cartilage through a 2.1 mm (transverse axis) × 1.8 mm (longitudinal axis) and 0.5 mm (depth axis) area.

On color Doppler ultrasound, increased vascularity with low flow arterial vessels is detected at the bottom of the lesion. The thickness of the lesion vessels varies between 0.4 mm and 1.6 mm. The maximum peak systolic velocity of the arterial vessels is 9.8 cm/s.

No satellite extensions are detected in the periphery of the primary lesion.

23.9.2.5.4 Impression on Sonography

The findings are consistent with a neoplastic lesion, probably BCC that involves the skin and the anterior aspect of the right nasal cartilage.

23.9.2.6 Reporting a Melanoma

23.9.2.6.1 History

A 54-year-old female patient presenting with a 4-month history of painless, fast-growing, hyper-pigmented lesion located in the anterior aspect of the distal third of the left lower leg that is suspicious of melanoma.

23.9.2.6.2 Technique

Grey scale and color Doppler multiplanar sonographic sweep is performed in the left lower extremity and groin regions

23.9.2.6.3 Sonography Report

In correlation with the cutaneous hyper-pigmented lesion, an ovoid-shaped, well-defined, hypoechoic solid structure is detected. The lesion involves the dermis and measures 2.8 mm (longitudinal axis) × 1.4 mm (transverse axis) and 1.6 mm (depth axis).

The underlying subcutaneous tissue and muscles are unremarkable.

On color Doppler ultrasound, prominent vascularity is detected within the lesion tissue with low flow arterial vessels that present a thickness that varies between 0.5 and 1.1 mm. The maximum peak systolic velocity of the arterial vessels is 9.8 cm/s.

At the ipisilateral popliteal fossa, the subcutaneous tissue shows a hypoechoic well-defined structure with slightly lobulated and irregular margins that measures 1.7 mm (longitudinal axis) × 2.5 mm (transverse axis) × 0.8 mm (depth axis). On color Doppler ultrasound, slow flow arterial and venous vessels are detected within the structure. The maximum peak systolic velocity of the arterial vessels is 8.6 cm/s.

Bilateral enlarged round-shaped inguinal lymph nodes are seen in the subcutaneous tissue. The lymph nodes present thickening and hypoechogenicity of their cortex, lack of the nodal well-defined hyperechoic center, and presence of low flow vessels in the cortex region. Additionally, some lymph nodes have a nodular appearance in the cortex. The lymph nodes located on the left inguinal region vary in their measurements (transverse axis) between 1.5 and 2.8 cm, and the lymph nodes located in the right inguinal region vary between 1.7 and 2.3 cm.

23.9.2.6.4 Impression on Sonography

The findings are consistent with a melanoma, that shows a sonographic Breslow index type II and a satellite lesion in the ipsilateral popliteal fossa as well as bilateral inguinal nodal involvement as described.

23.9.2.7 Reporting a Plantar Wart

23.9.2.7.1 Clinical History

A 38-year old-male patient presenting with a 9-month history of a painful hyperkeratotic lesion located in the sole of the right foot. A foreign body or a plantar wart is suspected clinically.

23.9.2.7.2 Technique

Grey scale and color Doppler multiplanar sonographic sweep is performed in the sole of the right foot.

23.9.2.7.3 Sonography Report

The study shows a fusiform-shaped, well-defined, hypoechoic solid structure in the epidermis and dermis in correlation with the visible cutaneous lesion.

The structure measures 2.9 cm (anteroposterior axis) × 2.8 cm (transverse axis) and 1.8 cm (depth axis).

On color Doppler ultrasound, increased vascularity is detected in the dermis underlying the lesion with slow flow arterial vessels that present a thickness that varies between 0.4 and 0.9 mm and a maximum peak systolic velocity of 8 cm/s.

There is a distension of the plantar bursa underlying the lesion located in the subcutaneous tissue and superficial to the flexor tendon at the level of the third metatarsophalangeal joint. No signs of hypervascularity are detected within the bursa.

The plantar fascia, flexor tendons of the foot, and the flexor digitorum brevis muscle are unremarkable.

There are no signs of a foreign body on ultrasound.

The metartasophalangeal joints demonstrate no signs of distension.

The bony margins are well defined with no signs of erosions.

23.9.2.7.4 Impression on Sonography

- The findings are consistent with a plantar wart.
- A mild plantar bursitis underlying the lesion is noted, probably secondary to the inflammation induced by the wart.

23.9.2.8 Reporting Morphea

23.9.2.8.1 Clinical History

A 18-year-old female patient presenting with a 6-month history of two painless, indurated, and hyperpigmented plaques located in the abdominal wall and right arm, respectively.

23.9.2.8.2 Technique

Grey scale and color Doppler multiplanar sonographic sweep is performed in the abdominal wall and right arm in correlation with the lesional tissue. Side-by-side sonography views and comparisons with the non-lesional tissue are also performed.

23.9.2.8.3 Sonography Report

Focal hypoechoic thickening and decreased echogenicity of the dermis at the lesion areas are detected. The lesion located at the abdominal wall also presents increased echogenicity of the subcutaneous tissue and measures 5.6 cm (longitudinal axis) × 3.8 cm (transverse axis) and 3.5 cm (depth axis). On color Doppler ultrasound there is increased vascularity in the dermis and subcutaneous tissue in the abdominal wall lesion with low flow arterial vessels that measure between 0.6 and 0.9 mm (thickness) with a maximum peak systolic arterial velocity of 6 cm/s.

The lesion located in the right arm measures 3.5 cm (longitudinal axis) × 2.8 cm (transverse axis) and 1.6 cm (depth axis). No signs of involvement of the subcutaneous tissue or hypervascularity at the cutaneous layers are noted in the right arm.

The muscular layer is unremarkable at both lesion sites.

23.9.2.8.4 Impression on Sonography

The findings are consistent with morphea that shows sonographic signs of activity in the plaque located in the abdominal wall and inactivity in the plaque at the right arm.

23.9.2.9 Reporting a Glomus Tumor of the Nail

23.9.2.9.1 Clinical History

A 53-year-old female presenting with a 1-year history of a painful fingernail with ungual dystrophy that affects the right middle finger.

23.9.2.9.2 Technique

Grey scale and color Doppler multiplanar sonographic sweep of the ungual and periungual region is performed.

23.9.2.9.3 Sonography Report

The study shows an oval-shaped, well-defined hypoechoic solid nodule in the proximal nail bed that affects the matrix region. The nodule is centrally located and measures 1.2 mm (longitudinal axis) × 1.6 mm (transverse axis) and 0.8 mm (depth axis).

On color Doppler ultrasound, there is increased vascularity within the nodule with low flow arterial vessels that measure between 0.4 and 0.6 mm (thickness) and show a maximum arterial peak systolic velocity of 8 cm/s.

The ungual plate is displaced upward in correlation with the nodule and become thickened and slightly irregular at the distal fingernail in the same axis of the nodule.

Scalloping of the underlying bony margin of the distal phalanx underlying the nodule is detected.

The distal interphalangeal joint and the insertion of the lateral bands of the extensor tendon are unremarkable.

23.9.2.9.4 Impression on Sonography

- Hypervascular solid nodule located in the proximal nail bed that shows a benign appearance and is compatible with a glomus tumor.
- Secondary dystrophic changes of the nail plates.

23.10 Final Suggestions

The learning curve of the operator can be accelerated if a strong clinical, sonographic, and pathological correlation of the lesions is performed. Thus, ultrasound can be suggested as the first imaging modality in the study of common dermatological lesions, and will probably answer approximately 95 % of the questions of the referring physician that are generated from the clinical examination of these entities. Depending on the primary characteristics of the cutaneous lesion(s), it may be necessary to perform additional imaging studies (See Algorithm 23.1). The imaging studies can include well-known imaging modalities such as magnetic resonance imaging (MRI), computed tomography (CT), confocal microscopy (CFM), or optical coherence tomography (OCT). The use of additional imaging techniques can complement the information delivered using ultrasound. The imaging techniques that can be performed for the presence of multiple or deeper involvement are MRI and CT, or when dealing with epidermal or subepidermal lesions, CFM and OCT can be performed. As in any field of medicine, the use of these imaging modalities will depend on the availability of the machines and the presence of a well-trained operator.

A major advantage of the ultrasound examination is that it non-invasively provides both anatomical and functional information of the lesions, a concept that we call "Two-for-One". The latter broad sonography conceptual analysis may support the understanding of the physiopathology of dermatologic entities and improve the final cosmetic prognosis of patients [1–5].

Finally, we encourage the reader to learn, enjoy, and develop this technique, taking advantage of the tools provided in this book and also from the on-line information that can be found on the skin ultrasound educational website www.sonoskin.com, a virtual on-line community dedicated to this type of sonography examination.

References

1. Wortsman X, Wortsman J. Clinical usefulness of variable-frequency ultrasound in localized lesions of the skin. J Am Acad Dermatol. 2010;62(2):247–56.
2. Wortsman X. Common applications of dermatologic sonography. J Ultrasound Med. 2012;31(1):97–111.
3. Wortsman X, Wortsman J, Soto R, Saavedra T, Honeyman J, Sazunic I, et al. Benign tumors and pseudotumors of the nail: a novel application of sonography. J Ultrasound Med. 2010; 29(5):803–16.
4. Wortsman X, Wortsman J, Matsuoka L, Saavedra T, Mardones F, Saavedra D, et al. Sonography in pathologies of scalp and hair. Br J Radiol. 2012;85(1013):647–55.
5. Wortsman X. Sonography of cutaneous and ungual lumps and bumps. Ultrasound Clin. 2012;7(4):505–23. doi:10.1016/j.cult.2012.08.006.

Pre-surgical Sonographic Assessment of the Margins in Skin Lesions

24

Fernando Alfageme

Contents

24.1 Introduction

Correct margin assessment in skin lesions is mandatory to avoid recurrence in malignant lesions, which is very unpleasant above all.

24.2 Assessment of Lateral Margins

Two methods can be suggested to determine lateral margins:

(a) After establishing clinical margins and marking with a pen, tracking of the lesional margins on ultrasound is performed using probes with frequencies that usually go from 13 to18 MHz. This method is used if lesions present superficial involvement. An increase in gain may help if the dermal contrast of the lesion is not apparently evident.

(b) Perform a parallel scanning for checking the free borders of the tumor and draw a line (Fig. 24.1). Take special care with the elastotic areas that commonly show a subepidermic low echogenicity band. Importantly, the minimum number of lines required to delineate a lesion is three. The more lines drawn, the more tissue that is unaffected can be spared.

F. Alfageme, MD, PhD
Department of Dermatology, Hospital Puerta de Hierro Majadahonda,
Universidad Autonoma de Madrid,
Manuel de Falla 1, Majadahonda, Madrid 28222, Spain
e-mail: dermalfageme@gmail.com

X. Wortsman, G.B.E. Jemec (eds.), *Dermatologic Ultrasound with Clinical and Histologic Correlations*,
DOI 10.1007/978-1-4614-7184-4_24,

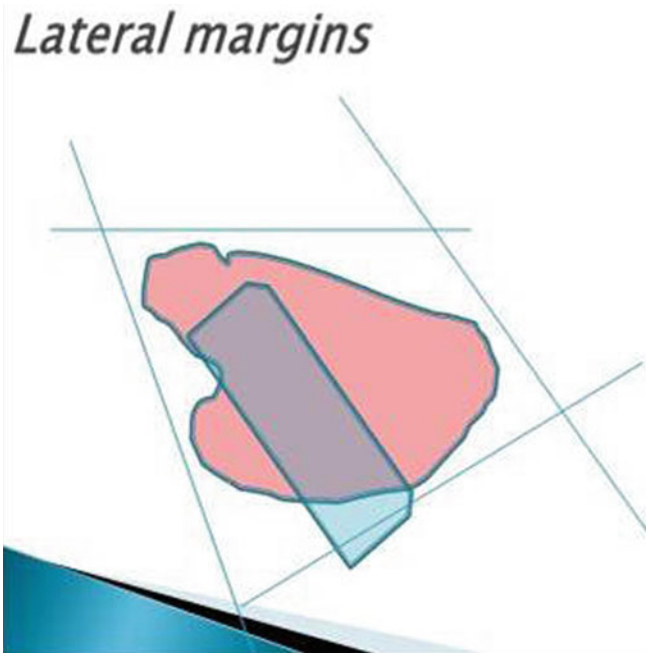

Fig. 24.1 Marking of the lateral margins on ultrasound (drawing)

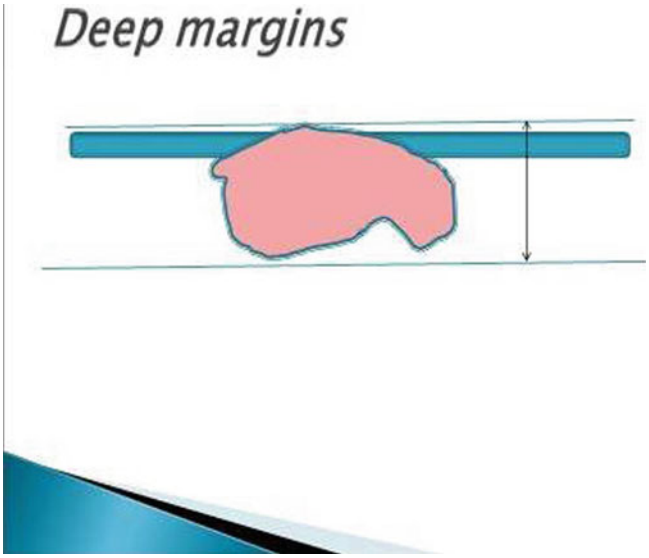

Fig. 24.2 Marking of deep margins on ultrasound (drawing)

24.3 Assessment of Deep Margins

Two methods can be recommended for the assessment of deep margins depending on tumor echogenicity and size

(a) Determine the deepest point after scanning the entire lesion. Measure and use these measures as tumor-free deep margin (Fig. 24.2). At surgery, maintain this measurement constantly.
(b) Determine the deepest point and use an anatomic reference instead of a measurement (superficial fascia deep fascia, muscle, dermis).

Some authors use another method that begins from the middle of the lesion and determining measurements in a radial fashion, whereas other authors use metallic pointers, staplers, and harpoons.

It is important to remember that if the lesion is marked outside the operating room, the position of the patient should be the same one that he or she will experience under surgery (decubitus, lateral, flexion, extension, etc.) (Figs. 24.3, 24.4, and 24.5).

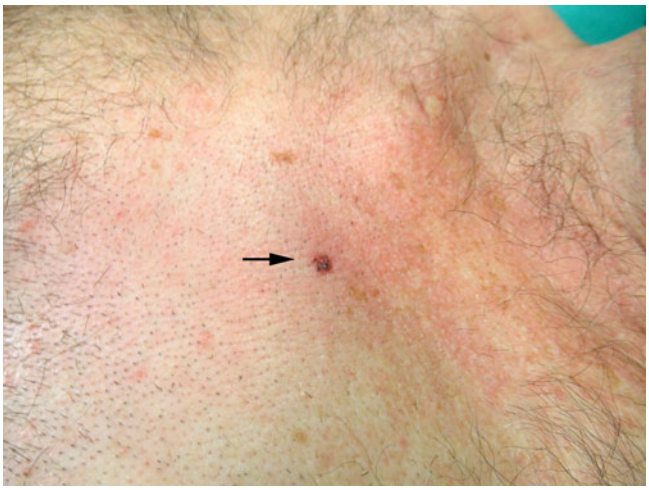

Fig. 24.3 Chest basal cell carcinoma (BCC, *arrow*) before margin assessment

Fig. 24.4 Cutaneous marking of the tumor at the beginning

Fig. 24.5 Cutaneous marking of the tumor at the end using a polygonal design

24.4 Comments

Large studies on margins assessed in different types of tumors are lacking. Bobadilla et al. published an interesting article on deep margin assessment of basocelular carcinoma and includes some useful tips [1]. Jambusaria-Pahlajani et al. [2] from Pennsylvania compare it with Mohs surgery, favoring Mohs (in that article, the technician and not the surgeon marks the limits). The latest work on epithelial tumor assessment by the group from Mount Sinai shows a favorable experience in the use of high-frequency ultrasound in the preoperative assessment of patients prior to Mohs surgery [3].

Margin assessment using ultrasound is an interesting tool that may not substitute histological assessment but may reduce the number of Mohs steps, therefore, saving surgical time. It can be a useful technique when Mohs surgery is not available [1–3].

References

1. Bobadilla F, Wortsman X, Muñoz C, Segovia L, Espinoza M, Jemec GB. Pre-surgical high resolution ultrasound of facial basal cell carcinoma: correlation with histology. Cancer Imaging. 2008;8:163–72.
2. Jambusaria-Pahlajani A, Schmults CD, Miller CJ, Shin D, Williams J, Kurd SK, et al. Test characteristics of high-resolution ultrasound in the preoperative assessment of margins of basal cell and squamous cell carcinoma in patients undergoing Mohs micrographic surgery. Dermatol Surg. 2009;35:9–15.
3. Marmur ES, Berkowitz EZ, Fuchs BS, Singer GK, Yoo JY. Use of high-frequency, high-resolution ultrasound before Mohs surgery. Dermatol Surg. 2010;36:841–7.

Index

X. Wortsman, G.B.E. Jemec (eds.), *Dermatologic Ultrasound with Clinical and Histologic Correlations*,
DOI 10.1007/978-1-4614-7184-4, © Springer Science+Business Media New York 2013